AD-A258 028

Volume 58, Nos. 1–4
15 September 1992

ISSN 0167-2789

DTIC
ELECTE
NOV 3 0 1992
S D
C

PHYSICA D
NONLINEAR PHENOMENA

Interpretation of Time Series from Nonlinear Systems

Proceedings of the IUTAM Symposium and NATO Advanced Research Workshop on the Interpretation of Time Series from Nonlinear Mechanical Systems
University of Warwick, England
26–30 August 1991

92-30299

Editors:

P.G. Drazin
G.P. King

PDNPDT 58 (1–4) 1–506 (1992)

NORTH-HOLLAND

DISTRIBUTION STATEMENT A
Approved for public release
Distribution Unlimited

92 11 27 006

Physica A, Physica B, Physica C and Physica D are published by Elsevier Science Publishers B.V., Amsterdam

PHYSICA D

Coordinating editors:
H. FLASCHKA, Mathematics Department, Building 89, University of Arizona, Tucson, AZ 85721, USA, Telefax: (602) 621 8322, Email: FLASCHKA@MATH.ARIZONA.EDU
F.H. BUSSE, Physikalisches Institut, Universität Bayreuth, Postfach 101251, W-8580 Bayreuth, Germany, Telex: 921824 = ubt/

Fields of interest:
Integrable systems, Geometry, Differential equations
Nonlinear fluid dynamics (in particular thermal convection and rotating fluids, dynamo theory, geophysical fluid dynamics)

Editors:

Fields of interest:
G. AHLERS, Department of Physics, University of California at Santa Barbara, Santa Barbara, CA 93106, USA — Experimental nonlinear phenomena
V.I. ARNOL'D, Department of Mathematics, University of Moscow, 117234 Moscow B-234, Russia — Dynamical systems, Singularities
J.M. BALL, Department of Mathematics, Heriot-Watt University, Edinburgh EH14 4AS, Scotland — Solid mechanics, Infinite-dimensional dynamical systems
B.V. CHIRIKOV, Institute of Nuclear Physics, 630090 Novosibirsk 90, Russia — Classical and quantum chaos
U. FRISCH, Observatoire de Nice, B.P. 229, 06304 Nice Cedex 4, France — Turbulence, Lattice gases, Asymptotic methods
A.V. HOLDEN, Department of Physiology, University of Leeds, Leeds LS2 9NQ, UK — Dynamical systems and chaos in physiology
E. JEN, Theoretical Division, Los Alamos National Laboratory, Los Alamos, NM 87545, USA — Cellular automata, Interacting particle systems, Adaptive dynamics
C.K.R.T. JONES, Division of Applied Mathematics, Box F, Brown University, Providence, RI 02912, USA — Dynamical systems, Dissipative waves
M. MIMURA, Department of Mathematics, Faculty of Science, Hiroshima University, Hiroshima 730, Japan — Mathematical biology
A.C. NEWELL, Mathematics Department, Building 89, University of Arizona, Tucson, AZ 85721, USA — Convection patterns, Nonlinear optics, Turbulence
P.E. RAPP, Department of Physiology and Biochemistry, The Medical College of Pennsylvania, 3300 Henry Avenue, Philadelphia, PA 19129, USA — Dynamical systems, Biophysics
R. TEMAM, Université de Paris-Sud, Laboratoire d'Analyse Numérique, Bâtiment 425, 91405 Orsay Cedex, France — Fluid mechanics, Navier-Stokes equations, Dissipative dynamical systems (finite infinite dimensional)
V.E. ZAKHAROV, USSR Academy of Sciences, L.D. Landau Institute for Theoretical Physics, Kosygina 2, 117940, GSP-1, Moscow V-334, Russia — Integrable systems, Turbulence, Wave motion

Administrative assistant: Mrs. B. Flaschka

Desk editor: **B. WAGE,** Elsevier Science Publishers B.V. (North-Holland), P.O. Box 103, 1000 AC Amsterdam, The Netherlands, - Tel: (020) 5862 631, Telefax: (020) 5862 319, Email: (X400) C = NL; A = 400NET; P = SURF; O = ELSEVIER; S = NHPDESKED or (RFC822) NHPDESKED@ELSEVIER.NL, Telex: 10704 espom nl

1992 Subscription data. All prices are **inclusive** of postage and handling. The Dutch Guilder price is definitive, the currency equivalent is for guidance only.
Physica A: The subscription price per volume is Dfl. 371.00 ($203.00). 10 volumes have been announced at a total price of Dfl. 3710.00 ($2027.00). Physica A is published semimonthly.
Physica B: The subscription price per volume is Dfl. 371.00 ($203.00). 8 volumes have been announced at a total price of Dfl. 2968.00 ($1622.00). Physica B is published monthly.
Physica C: The subscription price per volume is Dfl. 371.00 ($203.00). 17 volumes have been announced at a total price of Dfl. 6307.00 ($3446.00). Physica C is published semimonthly.
Physica D: The subscription price per volume is Dfl. 371.00 ($203.00). 8 volumes have been announced at a total price of Dfl. 2968.00 ($1622.00). Physica D is published monthly.
Physica A, Physica B, Physica C and **Physica D:** The total price of a combined subscription (43 volumes in all) is Dfl. 12943.00 ($7073.00).
Please contact the Publisher for special rates for other combinations of Physica sections.

Subscriptions should be sent to the Publisher, Elsevier Science Publishers B.V., Journals Department, P.O. Box 211, 1000 AE Amsterdam, The Netherlands, or to any subscription agent.
Journals are sent by surface delivery to all countries, except the following countries where SAL air delivery (Surface Airlifted Mail) is ensured: USA, Canada, Japan, Australia, New Zealand, The People's Republic of China, Israel, India, Brazil, Malaysia, Singapore, South Korea, Taiwan, Pakistan, Hong Kong, South Africa. Air mail rates for other countries are available upon request.
Claims for missing issues should be made within three months of their publication. The Publisher expects to supply missing issues free only if losses have been sustained in transit and when stocks permit.

Elsevier Science Publishers B.V. All rights reserved. No part of this publication may be reproduced, stored in a retrieval system or transmitted in any form or by any means, electronic, mechanical, photocopying, recording or otherwise, without the written permission of the Publisher, Elsevier Science Publishers B.V., Copyright & Permissions Department, P.O. Box 521, 1000 AM Amsterdam, The Netherlands.
Special regulations for authors. Upon acceptance of an article by the journal, the author(s) will be asked to transfer copyright of the article to the Publisher. This transfer will ensure the widest possible dissemination of information.
Special regulations for readers in the USA. This journal has been registered with the Copyright Clearance Center, Inc. Consent is given for copying of articles for personal or internal use, or for the personal use of specific clients. This consent is given on the condition that the copier pays through the Center the per-copy fee stated in the code on the first page of each article for copying beyond that permitted by Sections 107 or 108 of the U.S. Copyright Law. The appropriate fee should be forwarded with a copy of the first page of the article to the Copyright Clearance Center, Inc., 27 Congress Street, Salem, MA 01970, USA. If no code appears in an article, the author has not given broad consent to copy and permission to copy must be obtained directly from the author. All articles published prior to 1981 may be copied for a per-copy fee of US $2.25, also payable through the Center. (N.B. For review journals this fee is $0.25 per copy per page.) This consent does not extend to other kinds of copying, such as for general distribution, resale, advertising and promotion purposes, or for creating new collective works. Special written permission must be obtained from the Publisher for such copying.
US mailing notice - Physica D (ISSN 0167-2789) is published monthly in 1992 (except in October and November, when it will appear twice) by Elsevier Science Publishers (Molenwerf 1, 1000 AE Amsterdam, The Netherlands). Annual subscription price in the USA US $1622.00 (subject to change), including air speed delivery. Application to mail at second class postage is pending at Jamaica, NY 11431.
USA Postmasters: Send address changes to: Physica D Publications Expediting, Inc., 200 Meacham Avenue, Elmont, NY 11003. Airfreight and mailing in the USA by Publication Expediting.
No responsibility is assumed by the Publisher for any injury and/or damage to persons or property as a matter of products liability, negligence or otherwise, or from any use or operation of any methods, products, instructions or ideas contained in the material herein.

Printed in The Netherlands

PHYSICA D

© 1992 Elsevier Science Publishers B.V. All rights reserved.

No part of this publication may be reproduced, stored in a retrieval system or transmitted in any form or by any means, electronic, mechanical, photocopying, recording or otherwise without the written permission of the Publisher, Elsevier Science Publishers B.V., Copyright & Permissions Department, P.O. Box 521, 1000 AM Amsterdam, The Netherlands.

Special regulations for authors. Upon acceptance of an article by the journal, the author(s) will be asked to transfer copyright of the article to the Publisher. This transfer will ensure the widest possible dissemination of information.

Submission to this journal of a paper entails the author's irrevocable and exclusive authorization of the Publisher to collect any sums or consideration for copying or reproduction payable by third parties (as mentioned in article 17 paragraph 2 of the Dutch Copyright Act of 1912 and in the Royal Decree of June 20, 1974 (S. 351) pursuant to article 16b of the Dutch Copyright Act of 1912) and/or to act in or out of Court in connection therewith.

Special regulations for readers in the USA. This journal has been registered with the Copyright Clearance Center, Inc. Consent is given for copying of articles for personal or internal use, or for the personal use of specific clients. This consent is given on the condition that the copier pays through the Center the per-copy fee stated in the code on the first page of each article for copying beyond that permitted by Sections 107 or 108 of the U.S. Copyright Law. The appropriate fee should be forwarded with a copy of the first page of the article to the Copyright Clearance Center, Inc., 27 Congress Street, Salem, MA 01970, USA. If no code appears in an article, the author has not given broad consent to copy and permission to copy must be obtained directly from the author. All articles published prior to 1981 may be copied for a per-copy fee of US $2.25, also payable through the Center. (N.B. For review journals this fee is $0.25 per copy per page.) This consent does not extend to other kinds of copying, such as for general distribution, resale, advertising and promotion purposes, or for creating new collective works. Special written permission must be obtained from the Publisher for such copying.

No responsibility is assumed by the Publisher for any injury and/or damage to persons or property as a matter of products liability, negligence or otherwise, or from any use or operation of any methods, products, instructions or ideas contained in the material herein.

This journal is printed on acid-free paper.

Published monthly

Printed in The Netherlands

Volume 58, 1992

PHYSICA D

NONLINEAR PHENOMENA

Coordinating Editors:

H. FLASCHKA
F.H. BUSSE

Editors:

G. AHLERS
V.I. ARNOL'D
J.M. BALL
B.V. CHIRIKOV
U. FRISCH
A.V. HOLDEN
E. JEN
C.K.R.T. JONES
M. MIMURA
A.C. NEWELL
P.E. RAPP
R. TEMAM
V.E. ZAKHAROV

DTIC QUALITY INSPECTED 4

Accession For
NTIS GRA&I ☑
DTIC TAB ☐
Unannounced ☐
Justification
By Per Form 50
Distribution/
Availability Codes
Dist | Avail and/or Special
A-1

NORTH-HOLLAND

Members of the International Scientific Committee

Dr. M.-P. Chauve	I.M.S.T., Marseille, France
Prof. P.G. Drazin	University of Bristol, UK, Co-chairman
Prof. J.-P. Eckmann	Université de Genève, Switzerland
Prof. P. Grassberger	University of Wuppertal, Germany
Dr. G.P. King	University of Warwick, UK, Co-chairman
Prof. V.Ya. Levchenko	USSR Academy of Sciences, Novosibirsk, USSR
Prof. J.L. Lumley	Cornell University, USA
Prof. F.C. Moon	Cornell University, USA
Prof. S.A. Orszag	Princeton University, USA
Prof. H. Sato	Institute of Flow Research, Japan
Prof. W.O. Schielen	University of Stuttgart, Germany

Members of the Local Organizing Committee

Dr. G.P. King (chairman)
Dr. M.R. Muldoon
Dr. G. Rowlands
Dr. L.A. Smith

Interpretation of Time Series from Nonlinear Systems

Proceedings of the IUTAM Symposium and NATO Advanced Research Workshop
on the Interpretation of Time Series from Nonlinear Mechanical Systems
University of Warwick, England
26–30 August 1991

Editors:

P.G. Drazin

Department of Mathematics
University of Bristol
Bristol BS8 1TW, England

G.P. King

Department of Mathematics
University of Warwick
Coventry CV4 7AL, England

1992

NORTH-HOLLAND

Physica D 58 (1992) vii–xi
North-Holland

PHYSICA D

Introduction*

P.G. Drazin[a] and G.P. King[b]

[a]*Department of Mathematics, University of Bristol, Bristol, UK*
[b]*Department of Mathematics, University of Warwick, Coventry, UK*

This is a report of the proceedings of the IUTAM Symposium and NATO Advanced Research Workshop on "The Interpretation of Time Series from Nonlinear Mechanical Systems", held at the University of Warwick, England, from 26–30 August 1991. It contains a brief and partial review of the state of the art of the subject, and an account of a few highlights of the Symposium. This paper also introduces the papers which follow in this volume, papers which report some of the contributions to the Symposium.

1. Introduction

Whether a time series is produced by a linear, chaotic or stochastic process, the aims of its interpretation are the same:

(1) to detect useful and interesting patterns by exploring the data;

(2) to construct a model by using the data and as much other knowledge of the process as possible; and

(3) to verify that the model can both reproduce and predict the patterns, and, if necessary, to improve the model further.

Statisticians and communications engineers have analysed time series for several decades, using primarily linear methods of analysis, such as Fourier transforms and filters. The explosive growth of research in nonlinear systems in the 1970s and 1980s led to new goals of, and new approaches to, the interpretation of time series. The need to use observations of the output of a nonlinear system, whether the system is in nature, a laboratory or a computer, in order to ascertain the character of the system, and the need to predict the future behaviour of the system, drove both theoreticians and experimentalists to devise new methods to interpret time series (and sometimes to re-discover old methods). It drove them to seek to reconstruct the phase space rather than use the tools of stochastic and linear analysis.

The discovery of deterministic chaos, with the appearance of randomness, directed research along lines somewhat similar to those followed by statisticians earlier, although different kinds of information from the data were sought. If the system has homed in on an attractor, it is valuable to reconstruct, from the time series alone, the fractal dimension and other topological invariants of the attractor, the attractor in its phase space, or even the governing differential equations themselves. Early claims of successful analysis evoked the dream of putting a thermometer outside one's window, measuring the temperature at regular intervals, and finding the dynamics of the whole atmosphere, so that the future climate would be predictable. This violates physical intuition, and violates it for good reasons.

Chaos is fascinating, beautiful and intriguing, but also dangerous. Its temptations are so great

* This work relates to Department of the Navy Grant N00014-91-J-9049 issued by the Office of Naval Research European Office. The United States has a royalty-free license throughout the world in all copyrightable material contained herein.

0167-2789/92/$05.00 © 1992 – Elsevier Science Publishers B.V. All rights reserved

that many scientists think of it and see it wherever they look. The danger was anticipated by Eddington, who wrote (in an astrophysical context)

> "We have found that where science has progressed the farthest, the mind has but regained from nature that which the mind put into nature. We have found a strange foot-print in the shores of the unknown. We have devised profound theories, one after the other, to account for its origin. At last, we have succeeded in reconstructing the creature that made the foot-print. And lo! It is our own".

This is uncomfortably close to a description of some modern work, in particular the calculation of fractal dimension. Many difficulties of interpreting time series from a chaotic system became apparent in the 1980s. The difficulty of keeping even a carefully controlled laboratory system stationary, the difficulty of measuring data over long enough times, the difficulty of making measurements frequently enough, the difficulty of making measurements accurately enough, and the difficulty of distinguishing chaos from noise, were recognized as imposing severe practical limitations on methods of interpreting time series.

These developments, some fast moving, made it timely to hold an international meeting on the topic.

2. The Symposium

The Symposium set out to examine critically modern methods and to ensure that reconstruction of chaotic states will reveal nature's footprints, not our own. We sought how to learn about any physical system of interest from measurements of the system which are contaminated by extraneous physical effects. We concluded that we are nearing the stage when several algorithms will be widely available for use by those with no specialist knowledge of the theory of dynamical systems, and that these algorithms will not confuse chaos with correlated noise. In discussion some said that some makers of algorithms had been unjustly blamed for poor results by those who had misused the algorithms because they misunderstood the theory. This emphasizes that the algorithms will not be magic solutions of all nonlinear problems, but will require careful application and merely be added to the repertoire of scientific methods, which require thoughtful modelling and verifying. In short, common sense is essential.

The method of delays is fundamental to much of the work reported at the Symposium. This method was proposed independently by Packard, Crutchfield, Farmer and Shaw [1], Takens [2], and Ruelle in a private communication (cf. ref. [3]), whereby time series of a few state variables are used to generate a large-dimensional vector. For example, with a single time series $y(t)$ sampled $N+1$ times at intervals τ, i.e. at $t=0, \tau, 2\tau, \ldots, N\tau$, the l-vector $y_n = [y(n\tau), y((l+1)\tau), \ldots, y((n+l-1)\tau)]^{\mathrm{T}}$ can easily be constructed. Takens went on to use the Whitney embedding theorem to show that the method of delays can be used to reconstruct finite-dimensional chaotic attractors. Tong told, or reminded, the Symposium that these ideas are rooted in the scatter diagram used by Yule [4] in 1927 and its subsequent developments by statisticians. The essential novelty in these methods lies in reconstructing the dynamics, or at least topological invariants of the dynamics, of the system which has produced the data.

So, although the idea of constructing a delay vector was not new, Takens' [2, p. 371] embedding theorem was. It is so fundamental to many of the papers in this volume that we state it here, albeit informally. It is assumed that a smooth dynamical system has an attractor in a compact manifold M of dimension m, and that the observable y: $M \to \mathbb{R}$ is determined smoothly from any given state $\boldsymbol{x}$ of the system and measured at time $t = n\tau$. Thus $y = y(\boldsymbol{x}(n\tau))$ as $\boldsymbol{x}$: $\mathbb{R} \to M$ evolves, i.e. as the system changes with time. Then

Takens' theorem states that it is a *generic* property that $\Phi_y: M \to \mathbb{R}^{2m+1}$ defined by

$$\Phi_y(x) = [y(x(t)), y(x(t+\tau)), \ldots, y(x(t+2m\tau))]^T$$

is an embedding. (Mañé [5, p. 232] proved a similar embedding theorem in which M is a compact subset of a Banach space and the embedding dimension $2m+1$ is the least integer greater than or equal to one plus twice the Hausdorff dimension of M.) Of course, measurements of the series $y(x(nt))$ do not tell us directly what the unknown dynamical system, attractor, manifold M and dimension m are, but Takens' theorem indicates that the dimension of the delay vector may have to be as large as $2m+1$ before we can be assured that it is sufficient for the reconstruction of the topological behaviour of the attractor. For more recent work on embedding see, e.g., Sauer, Yorke and Casdagli [6].

This reconstruction is an ideal unrealizable in practice, because measurements are of finite duration and noisy. One method to reduce noise is to choose an appropriate basis of vectors to represent the time series, the vectors being determined by the data themselves. In fact the basis is chosen to be the set of eigenvectors of the two-point correlation matrix computed from the series. The method was given different names by different lecturers. It was originated by statisticians, who call it principal component analysis. Others call it the method of singular-value decomposition, singular system analysis, singular spectrum analysis, bi-orthogonal decomposition, or proper orthogonal decomposition; or call the vectors Karhunen–Loève vectors or empirical orthogonal functions. The method emerged as a tool in many lectures. We suggest that the name singular-value decomposition is better reserved as the title of the method of factorizing a matrix, a method which dates back to Beltrami's work in the nineteenth century (cf. ref. [7]), because it is only one part of the method of noise reduction.

Another tool of increasing use is the wavelet transform. It is a generalization of the Fourier transform which represents the translation as well as the scaling of components of a signal. Arnéodo's lecture was a masterly review of wavelets, and Grossman's an example of their modern use.

A prevalent theme of the Symposium was the hard task of distinguishing between the signal and noise, between chaos and extraneous effects or errors. We could not agree on a definition of noise, but we did agree that it is important. The problem of determining what portion of a time series is due to deterministic chaos and what to noise was the subject of several lectures and many animated discussions. New approaches to this problem are described in the papers in the section *Chaos or noise?* of this volume.

Concepts of phase space and time delay reconstruction have led to new approaches to modelling time series from nonlinear systems. Applications to prediction, control, noise reduction, filtering and signal extraction were described in several lectures.

Another recurring theme in the Symposium was the parallel developments of the interpretation of time series by theoreticians of statistics, signal processing and dynamical systems. Theoreticians have belatedly seen how to apply the tools of statistics and signal processing to the interpretation of time series from real dynamical systems. Conversely, the concepts of deterministic chaos, phase space, fractal dimension etc. are beginning to lead to new developments of statistics and signal processing.

The Symposium was dominated by specialists in dynamical systems, but the statisticians were represented eloquently and cogently by Tong. He reminded us of the priority of statisticians in making many discoveries, and illuminated several lectures with a statistical point of view. The interest of the statistical community in chaos in general, and in the subject of the Symposium in particular is aptly marked by Chaos Day, a meeting which was organized by the Royal

Statistical Society on 16 October 1991, so close to the Symposium. The reader may wish to see the proceedings [8] of that meeting.

Until recently, low-dimensional systems have been emphasized in nonlinear dynamics. Now interpretation of time series from spatially extended systems is being developed rapidly. Excellent examples are found in spatiotemporal chaos, and in fluid mechanics, where we see a low-dimensional system, then spatiotemporal chaos and finally turbulence as a fluid system is driven more strongly. Several papers in this volume illuminate this; also there were some valuable lectures on identification of coherent structures in turbulence (by Otaguro and Sato, by van de Water, and by Vassilicos). But, of course, applications of the interpretation of time series to many other fields, e.g. the instrumentation of analysis of signals in real time (by Namajūnas and Tamaševičius), are equally valuable.

It was encouraging also to hear lectures and to see posters on interpreting time series of natural phenomena in the earth and life sciences. They offer new insights into some very important and useful, but formidable, problems.

Our original intention was to build a data bank of time series to make it available world wide for analysis, and to hold a competition for participants to apply their algorithms on the same sets of data. However, our plans were overtaken by events. For the Santa Fe Institute has set up similar arrangements and fortunately has the resources to sustain the programme at a higher level and for a longer time than we could. It will run a workshop in May 1992, and retain a repository of interesting data and analysis programs thereafter. For further information, the interested reader may write to Andreas Weigend or Neil Gershenfeld at the Santa Fe Institute, 1660 Old Pecos Trail, Santa Fe, NM 87501, USA.

Nonetheless, the participants at the Symposium not only took an evening to watch videos of computer and laboratory experiments, but also worked on computers to demonstrate algorithms and exchange software.

There were 66 participants at the Symposium, joined by a few observers and several young scientists. The names of the participants, the observers, the young scientists, and their lectures and posters are listed at the end of this volume.

This is our description of interpretation of time series from nonlinear systems and of the proceedings of the symposium, but the best description of the state of the art of interpretation of time series is the lectures, posters and discussion at the symposium itself and the papers which follow in this volume. The papers are grouped in sections by subject. The subjects merge with one another, so our intention in the grouping is to help the reader rather than belittle the papers.

Acknowledgements

We are grateful to the International Union of Theoretical and Applied Mechanics, NATO, the US Air Force European Office of Aerospace Research and Development, the European Research Office of the US Army, the Office of Naval Research European Office, the London Mathematical Society, the Royal Society of London and British Petroleum Plc for their generous financial support of the Symposium. We thank the Symposium Secretary, Terri Moss, whose work beyond the call of duty contributed so much to the success of the Symposium; the Local Organizing Committee, Dr. M.R. Muldoon, Dr. G. Rowlands and Dr. L.A. Smith, for their many and varied contributions to the Symposium, its organization, this volume and this paper; and the local helpers, Sophia Castro, Hermann Haaf, John Marshall, John Phelps and Ian Redfern. We are indebted to the International Committee, especially Peter Grassberger and John Lumley, for their helpful advice and encouragement.

References

[1] N.H. Packard, J.P. Crutchfield, J.D. Farmer and R.S. Shaw, Phys. Rev. Lett. 45 (1980) 712.

[2] F. Takens, in: Dynamical Systems and Turbulence, eds. D. Rand and L.-S. Young (Springer, Berlin, 1981) p. 366.
[3] J.C. Roux, A. Rossi, S. Bachelart and C. Vidal, Phys. Lett. A 77 (1980) 391.
[4] G.U. Yule, Phil. Trans. R. Soc. London A 226 (1927) 267.
[5] R. Mañé, in: Dynamical Systems and Turbulence, eds. D. Rand and L.-S. Young (Springer, Berlin, 1981) p. 230.
[6] T. Sauer, J.A. Yorke and M. Casdagli, J. Stat. Phys. 65 (1991) 579.
[7] E. Beltrami, Giornale Mat. 11 (1873) 98; C. Eckart and G. Young, Psychometrika 1 (1936) 211; C. Eckart and G. Young, Bull. Am. Math. Soc. 45 (1939) 118; G.H. Golub and C.F. Van Loan, Matrix Computations (Johns Hopkins Univ. Press, Baltimore, 1983).
[8] D.S. Broomhead and others, J. R. Stat. Soc. B 54 (1992).

Contents

Introduction
P.G. Drazin and G.P. King vii

Chapter 1. Chaos or noise?

Using neural nets to look for chaos
A.M. Albano, A. Passamante, T. Hediger and M.E. Farrell 1

Power spectra of noise-driven nonlinear systems and stochastic resonance
M.I. Dykman and P.V.E. McClintock 10

Distinguishing between low-dimensional dynamics and randomness in measured time series
A. Provenzale, L.A. Smith, R. Vio and G. Murante 31

Identification and prediction of low dimensional dynamics
L.A. Smith 50

Testing for nonlinearity in time series: the method of surrogate data
J. Theiler, S. Eubank, A. Longtin, B. Galdrikian and J.D. Farmer 77

Singular-spectrum analysis: A toolkit for short, noisy chaotic signals
R. Vautard, P. Yiou and M. Ghil 95

Chapter 2. Prediction, control and noise reduction

Comparison of algorithms calculating optimal embedding parameters for delay time coordinates
Th. Buzug and G. Pfister 127

Problems in estimating dynamics from data
E.J. Kostelich 138

Controlling chaotic dynamical systems using time delay coordinates
G. Nitsche and U. Dressler 153

Controlling chaotic dynamical systems
F.J. Romeiras, C. Grebogi, E. Ott and W.P. Dayawansa 165

A noise reduction method for signals from nonlinear systems
T. Sauer 193

Chapter 3. Modelling

Construction of phenomenological models from numerical scalar time series
G. Gouesbet and J. Maquet 202

Phase space reconstruction for symmetric dynamical systems
G.P. King and I. Stewart 216

Topological analysis and synthesis of chaotic time series
G.B. Mindlin and R. Gilmore 229

Dynamical signatures
L. Noakes and A. Mees 243

Extraction of dynamical equations from chaotic data
G. Rowlands and J.C. Sprott 251

Global unpredictability in nonlinear dynamics: capture, dispersal and the indeterminate bifurcations
J.M.T. Thompson 260

Chapter 4. Statistics and dynamical systems

Nonlinear analysis of data sampled nonuniformly in time
J.L. Breedon and N.H. Packard 273

Analysis of noisy signals
A. Rabinovitch and R. Thieberger 284

Using cluster analysis to classify time series
C.T. Shaw and and G.P. King 288

Some comments on a bridge between nonlinear dynamicists and statisticians
H. Tong 299

Chapter 5. Topological analysis

Hierarchical resolution of power spectra
R. Badii, M. Finardi, G. Broggi and M.A Sepúlveda 304

Evaluation of probabilistic and dynamical invariants from finite symbolic substrings –comparison between two approaches
R. Stoop and J. Parisi 325

Chapter 6. Spatiotemporal chaos

Dynamical description of spatial disorder
V.S. Afraimovich, A.B. Ezersky, M.I. Rabinovich, M.A. Shereshevsky and A.L. Zheleznyak 331

Spatiotemporal pattern formation and chaos in passive optical systems
M. Brambilla, G. Broggi and F. Prati 339

Thermodynamic aspects of the transition to spatiotemporal chaos
M. Caponeri and S. Ciliberto 365

Invariant measure in coupled maps
A. Politi and G.P. Puccioni 384

Chapter 7. Applications to fluids

Phase-space analysis of bursting behavior in Kolmogorov flow
D. Armbruster, R. Heiland, E.J. Kostelich and B. Nicolaenko 392

Low dimensional models of the wall region in a turbulent boundary layer: New results
G. Berkooz, P. Holmes and J.L. Lumley 402

Complex bi-orthogonal decomposition of a chain of coupled wakes
M.P. Chauve and P. Le Gal 407

Turbulent convection in helium gas
E.S.C. Ching, L.P. Kadanoff, A. Libchaber and X.-Z. Wu 414

Combined approaches and characterizations of experimental chaotic attractors in thermal lensing
S. Meunier-Guttin-Cluzel, B. Maheu and G. Gouesbet 423

Characterization of experimental time series from Taylor–Couette flow
G. Pfister, Th. Buzug and N. Enge 441

Applications of singular systems analysis to 'Baroclinic chaos'
P.L. Read 455

Chapter 8. Other applications

Correlation of local stretchings as a way of characterising chaotic dynamics amid noise
C.D. Bertram and X. Tian 469

A technique for measuring fractal dimensions from time series on a real-time scale
A. Namajūnas and A. Tamaševičius 482

Estimation of the persistence of strain from experimental recordings from cardiac tissue
H. Zhang, A.V. Holden, M. Lab and M. Moutoussis 489

List of participants 497
List of observers 499
List of young scientists 500
List of lectures 501
List of posters 503
List of contributors 505

Physica D 58 (1992) 1–9
North-Holland

PHYSICA D

Using neural nets to look for chaos

A.M. Albano
Department of Physics, Bryn Mawr College, Bryn Mawr, PA 19010, USA

A. Passamante, T. Hediger and Mary Eileen Farrell
Naval Air Warfare Center, Warminster, PA 18974, USA

Received 27 August 1991
Revised manuscript received 31 January 1992
Accepted 7 February 1992

Backpropagating neural networks are used to reconstruct the attractors of two low-dimensional chaotic systems using small input sets of noise-corrupted data. The nets are able to reconstruct attractors that are visually similar to, and have the same correlation dimensions as, attractors constructed from noise-free data.

1. Introduction

In recent years, a vocabulary for the quantitative characterization of chaos has been developed, and has been used to describe and analyze an incredible variety of phenomena in practically all fields of science and engineering (see e.g. ref. [1]). Procedures for the calculation of the quantities that make up this vocabulary – dimensions, entropies, Lyapunov exponents, topological indices, etc. – typically presume the availability of copious amounts of data measured with high precision, and with minimal noise contamination. Unfortunately, this is rarely the case with data from real experiments which usually provide only noise-corrupted data sets of limited size and limited precision. Thus, when confronted with a data set that is known to be noise-contaminated, one often cannot just ask, "is it chaos or is it noise?". Rather, one is forced to ask, "is it just noise, or is there some potentially meaningful dynamical information being masked by the noise?". Before any of the powerful nonlinear dynamical techniques of analysis can be applied, the effects of noise need to be eliminated or at least minimized.

The most obvious procedure for minimizing the effects of noise is by filtering. There is increasing evidence, however, that filtering changes the values of some nonlinear dynamical indices, notably the correlation dimension. Some types of filters increase the system's calculated dimension [2]), others decrease it [3]). There are some chaotic systems – the Hénon map is an example – which have remarkably flat spectra so that any filtering is sure to have serious effects on the dynamical information contained by a time series generated by the system. Conventional filters should be used with the greatest of care, if at all.

There are other noise-reduction techniques that do not rely on conventional digital filtering [4]. Some of these make use of singular value decomposition or principal component analysis and have been shown to be effective for relatively low noise levels.

Neural networks present another possibility. Recently, there has been considerable progress

0167-2789/92/$05.00 © 1992 – Elsevier Science Publishers B.V. All rights reserved

in the use of neural networks to recognize spatial as well as temporal patterns [5–7]. The use of neural networks in this context has capitalized on their ability to generalize as well as on their remarkable fault tolerance. The first of these properties means that they can successfully classify patterns that have not been previously presented; the second means that they can recognize corrupted patterns [5]). The first characteristic makes them candidates for the analysis of nonlinear signals as has, in fact, been done by Lepedes and Farber [6]. The second suggests that they may remain effective even in cases when the signal is corrupted by noise.

In this contribution we present evidence that neural networks may, indeed, be able to extract geometric information about the attractors of some chaotic systems from noise-corrupted data. In the following, we specify the relative amount of noise by the signal-to-noise ratio (SNR) in decibels, defined by SNR = 10 log(signal variance/noise variance). We will be considering situations for which SNR = 10 dB – i.e. when the variance of the noise is as large as that of the signal.

In section 2 we present some details of the backpropagation algorithm and describe the simple networks we use. In section 3 we present results on the use of these networks to analyze chaotic time series calculated from the logistic equation and from the Hénon equations. The analysis involves both "clean" data (i.e. values calculated from the equations of motion) and "noisy" data obtained by adding Gaussian random noise to the clean data to get a signal-to-noise ratio (SNR) of 10 dB. The performance of the nets is judged by their ability to reconstruct attractors that are visually similar, and have essentially the same correlation dimensions, as the systems being studied. The results show that the networks are capable of satisfying these criteria even when using remarkably small, noise-corrupted data sets as inputs.

Section 4 summarizes the results and discusses some problems. One set of problems arises from the very same fault-tolerance which is one of the greatest strengths of neural networks. An aspect of this property is that once trained, a network can still function satisfactorily even if some nodes are damaged [5]. This means that there is no unique relationship between the architecture of the network, or its internal state, and the task which it has learned to perform, or the time series it has learned to predict. This points to the need to develop techniques that would make neural networks perform more robustly (see, in this regard, the paper by de Groot and Würtz elsewhere in this volume [12]), and to define criteria that could be used for optimizing their performance.

2. Backpropagating neural networks

Backpropagating neural networks have been used to predict chaotic time series using presumably noise-free data as input [6]. Figure 1 shows a neural net of the type we use in this work: M input units, H units in a single hidden layer, and one output unit. Inputs and outputs of all units are real numbers. A time series, $\{x(k),\ k = 1, \ldots, N\}$ is used as a training set. Using the architecture shown in fig. 1, M successive values of the time series, $x(k-M), \ldots, x(k-2)$, $x(k-1)$, are used to predict the next value, $x(k)$. These inputs are weighted with weights,

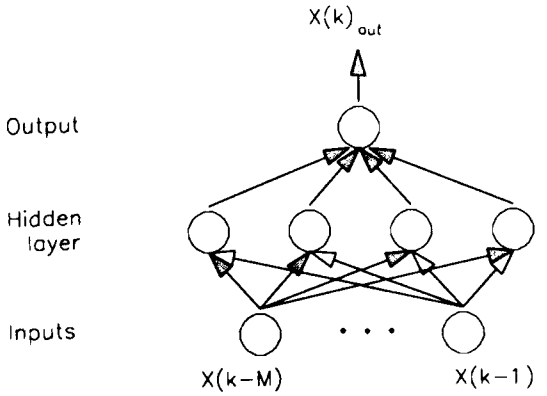

Fig. 1. Backpropagating neural network with M inputs, one hidden layer, and one output.

$w_{j,i}^{(h)}$; a bias, $b_j^{(h)}$, is added and the result is fed to a hidden unit. The input to the jth hidden unit for this set of inputs is thus

$$I(k)_j = b_j^{(h)} + \sum_{i=1}^{M} w_{j,i}^{(h)} x(k-i) . \tag{2.1}$$

The superscript (h) means that the quantities pertain to the hidden units. The activation function of the hidden units is a sigmoid – that is, with eq. (2.1) as input, the output of the jth hidden unit is

$$O(k)_j = 0.5(1.0 + \tanh I(k)_j) . \tag{2.2}$$

This is sometimes referred to as a "threshold" function or an "activation" function. One may use other functions. One form that is widely used is $O(x) = 1/(1 + \exp(-kx))$, which is also called sigmoid by some [5], or the "logistic function" by others [7]. It may also be symmetrized so that its range is $(-1, 1)$ rather than $(0, 1)$ as in the above. Some of the details of the threshold function may not be crucial, but it is essential for the function to be monotonic, bounded from above as well as from below, and be everywhere differentiable [5, 7].

The output of the net is a biased and weighted sum of the hidden unit outputs:

$$x(k)_{out} = b^{(o)} + \sum_{j=1}^{H} w_j^{(o)} O(k)_j , \tag{2.3}$$

the superscript (o) on the weights and biases signifying that these refer to the output unit.

The net is trained as follows: (1) start with a random set of weights and biases, (2) calculate the outputs for all possible input sets, (3) evaluate the "error"

$$Q = \sum_{k=1}^{N'} [x(k) - x(k)_{out}]^2 , \tag{2.4}$$

where N' is the total number of input sets, $N' = N - M - 1$. The crucial step is: (4) adjust the weights and biases to minimize the error. The name "backpropagating rule" was given to this procedure by Rumelhart et al. [4, 6], because the behavior of the error function is propagated backward to adjust the weights and biases that produced it.

The minimization of the error is performed by means of the usual method of steepest descent, or a variant of it called the "generalized delta rule" in the neural net literature [5–7]. The error Q is taken as a function of the weights and biases which, for convenience, we collectively denote by $\{\alpha_i\}$, the index i taking on as many values as there are weights and biases. When the parameter α_k, say, changes by $\delta\alpha_k$, then Q changes by

$$\delta Q = (\partial Q/\partial \alpha_k)\, \delta\alpha_k , \tag{2.5}$$

where $\partial Q/\partial\alpha_k$ is evaluated using the current values of the parameters. To insure that changes in α_k result in a decrease in Q, one chooses

$$\delta\alpha_k = -\gamma(\partial Q/\partial\alpha_k) , \tag{2.6}$$

where γ is a positive constant called the "learning rate". γ is to be large enough so that the training can be accomplished in a reasonable amount of time, but small enough so that one does not "overshoot" the sought-after minimum. As an attempt to avoid overshooting when using relatively large values of γ, a term $\mu\, \delta\alpha_k^p$ is sometimes added to eq. (2.6), where $\delta\alpha_k^p$ is the *previous* change in α_k and μ is another positive constant called the "momentum". As the name suggests, inclusion of this term tends to keep changes in the parameter going in the same direction, regardless of the direction determined by the gradient.

3. Results

When used for time series prediction and modeling as in ref. [6], the performance of the net is judged by its ability to predict future values of the time series given an appropriate number of

its values in the past. Although we use this criterion in training the net, we do not use it in the evaluation of its performance. In the training phase, we expect that a minimum of the error function reflects values of the weights and biases that average out the effects of noise, and that when a trained net is used for prediction, what is predicted are not future values of the noisy data set, but of the signal that was obscured by the noise in the original data.

The examples we study here are data from chaotic systems. This introduces an additional complication. Since chaos is characterized by sensitive dependence on initial conditions, we do not expect to achieve reliable long-term predictions, in part because of this sensitivity, and in part because we are dealing with noisy data which means that successive points in the time series are not necessarily successive points in the same trajectory. We therefore cannot expect to get a reliable prediction of the system's dynamics – that is, of the precise temporal evolution of its dynamical variables. Rather, as we show below, we get some geometrical information on the system's attractor – namely, the form of the attractor and its correlation dimension.

Data sets calculated from the logistic equation,

$$x_{n+1} = 4x_n(1 - x_n)\,, \tag{3.1}$$

and values of the x variable calculated from the Hénon equations,

$$(x_{n+1}, y_{n+1}) = (y_n + 1 - 1.4x_n^2, 0.3x_n)\,, \tag{3.2}$$

are used as inputs. Values calculated from the above equations as well as those to which random Gaussian has been added are used in the subsequent analysis. The parameters in both of the above systems are those known to yield chaotic behavior. Logistic data were analyzed using a net with one input, four hidden units, and one output while Hénon data were analyzed with a net of two inputs, four hidden units, and one output. Learning rates and momenta were between 0.0 and 1.0. The network architecture (i.e. the number of input and hidden units) as well as values of the learning rate and momentum were chosen from among a few combinations to give the fastest convergence of Q to a minimum.

Once a minimum of Q is reached, the net is used to calculate a predicted time series. In the examples presented here, we calculated 1024 points by iteration starting from the last M points of the input time series, $M = 1$ for the logistic data, $M = 2$ for Hénon. Each newly calculated value of the variable is appended to the input time series, and the last M values of the augmented time series are used to calculate the next entry. Comparison of the time series generated by the net with those calculated from the equations of motion with the same initial conditions showed that the net's predictions diverged from the values given by the equations very quickly. As mentioned earlier, this is not a surprise. Instead of comparing trajectories, the predicted time series are used to reconstruct the attractors.

3.1. Reconstructed attractors

We use the method of time delays [8] to reconstruct the systems' attractors in two-dimensional phase spaces and visually compare attractors constructed from the input data with those constructed using the nets' predictions. This comparison is necessarily qualitative and subjective, but is very much in the spirit of the use of neural networks for pattern recognition. There is, however, one important and novel difference in that the pattern that is presented to the network here is not merely a spatial configuration, but dynamical information encoded in a scalar time series that is used to reconstruct what may be a complex geometrical object in a multidimensional phase space. Indeed, for a chaotic time series, one may be trying to reconstruct a fractal. The next section gives a quantitative comparison of the results discussed here in qualitative terms.

Figures 2 and 3 are plots of x_{n+1} vs. x_n for both systems. Figures 2a and 3a show the familiar attractors of the logistic and the Hénon maps while figs. 2b and 3b show how well these attractors are obscured with the addition of enough noise to get a signal-to-noise ratio (SNR) of 10 dB. What the networks are asked to accomplish is, first of all, to determine that there are patterns embedded in figs. 2b and 3b and secondly, that the pattern hidden in fig. 2b is that shown in fig. 2a, and that hidden in fig. 3b is that shown in fig. 3a.

Figures 4a and 4b are reconstructions of the logistic attractor using input data sets of only eight points (marked by crosses) from the "clean" and "noisy" data sets, respectively. Here "clean" means data points calculated from the equation of motion while "noisy" means a set with SNR = 10 dB. Although distorted, the

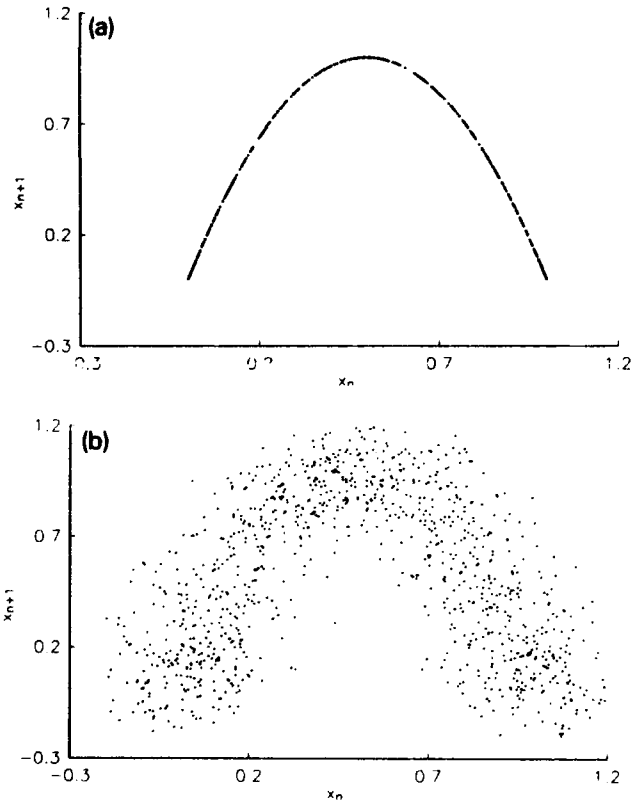

Fig. 2. Logistic attractor: (a) Delay plot, x_{n+1} versus x_n, of "clean" input data calculated from the logistic equation. (b) Delay plot of "noisy" logistic input data (SNR = 10).

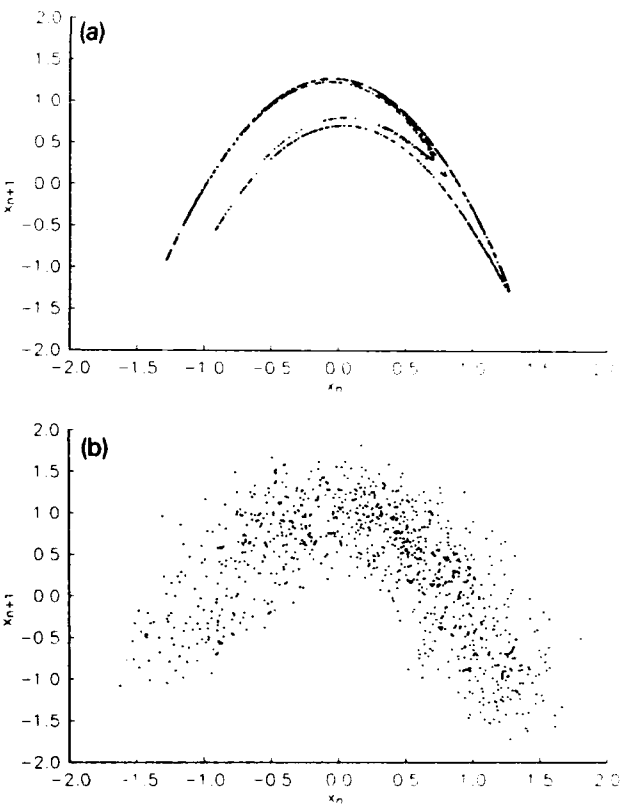

Fig. 3. Hénon attractor: (a) Delay plot of "clean" input data calculated from the Hénon equations. (b) Delay plot of "noisy" Hénon data.

similarity of the reconstructions with fig. 2a is obvious. We note that in fig. 4b, the net does not faithfully reproduce the behavior of the noisy input set. Rather, it produces a smooth shape that may represent an "averaging out" of the noise.

The attractor of the logistic map (fig. 2a) is just a parabola, and one might argue that it could more simply be obtained by a polynomial fit involving no more than three parameters. The Hénon attractor (fig. 3a), however, is quite a different matter. Its form is not describable by an expression in closed form that gives x_{k+1} in terms of x_k. The network needs to extract from the input time series, information equivalent to that embodied in the two coupled difference equations of the Hénon map.

Figure 5a is a reconstruction of the Hénon attractor using eight values of clean data. Even

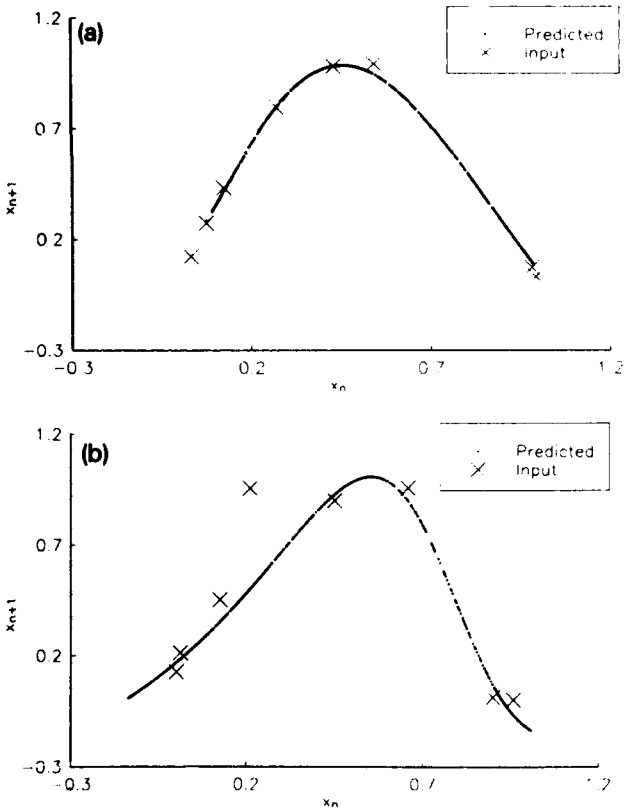

Fig. 4. Reconstructed logistic attractor: (a) using 8 points of clean input; (b) using 8 points of noisy input.

with such a small input set, the net has obviously captured visually recognizable details of the attractor with remarkable fidelity. This, however, it cannot do using eight points of the noisy data set. The first recognizable reconstruction occurs with a training set of 16 points (fig. 5b). Here, one has a distorted, but still recognizable version of the attractor. Increasing the size of the training set improves the net's performance, as indicated in fig. 5c which uses 64 points. However, it does not seem to do as well with a training set of 128 points (fig. 5d).

3.2. Correlation dimension

To provide a more quantitative comparison of the clean, noisy, and reconstructed attractors, we calculated their correlation dimensions using the Grassberger–Procaccia algorithm [9]. 1004 values of x_n were used to create 1000 points in a

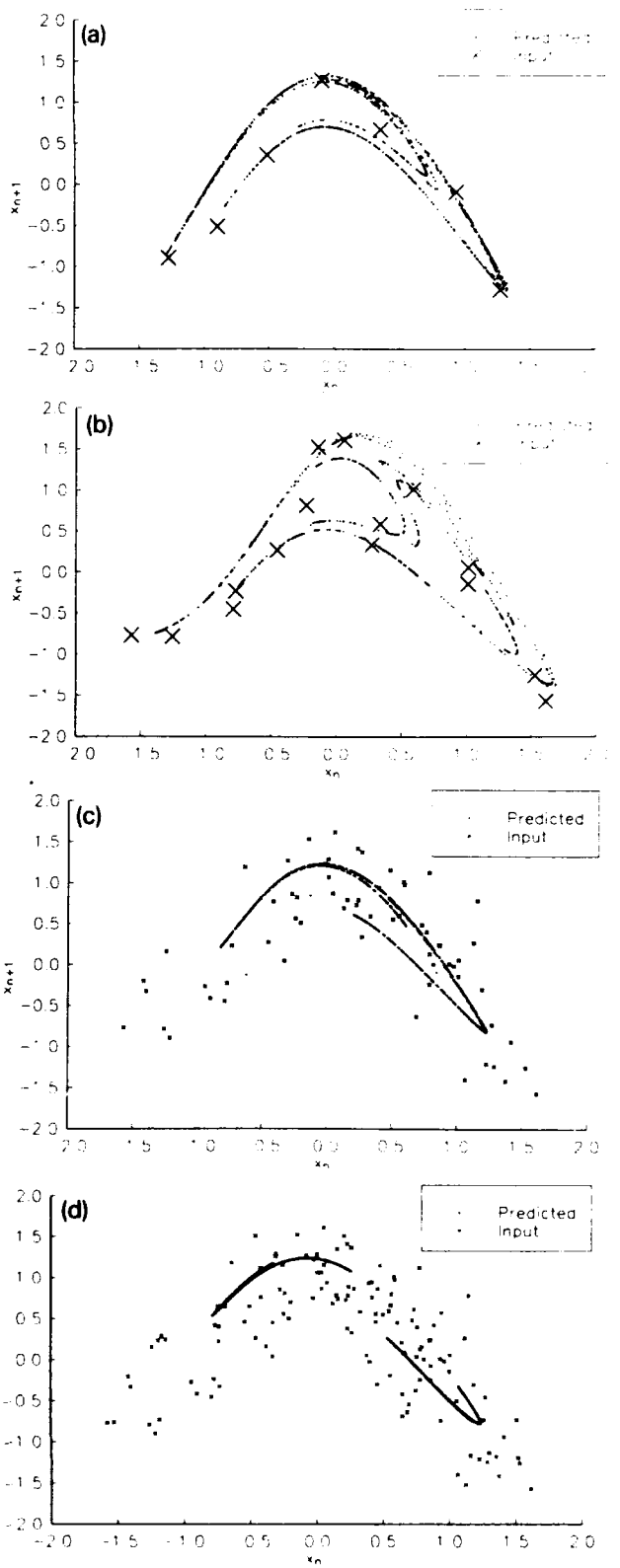

Fig. 5. Reconstructed Hénon attractor: (a) using 8 points of clean input, (b)–(d); using 16, 64, and 128 points, respectively, of noisy input.

five-dimensional embedding space:

$$Y_1 = (x_1, x_2, \ldots, x_5),$$
$$Y_2 = (x_2, x_3, \ldots, x_6),$$
$$\ldots$$
$$Y_k = (x_k, x_{k+1}, \ldots, x_{k+4}),$$
$$\ldots .$$

Since the correlation dimensions of the attractors are both less than 2.0, the choice of a 5-dimensional embedding space guarantees satisfaction of Takens' criterion [10] which requires a space of dimension $\geq 2d+1$ to embed an object of dimension d. Using 1000 embedding vectors makes it possible to do the necessary calculations relatively quickly while still satisfying the usual estimate that one needs some 10^d points to resolve a d-dimensional attractor. The embedding vectors Y_k are used to calculate the correlation integral

$$C(r) = \frac{1}{N_p} \sum_{i<j}^{1000} \Theta(r - |Y_i - Y_j|), \tag{3.3}$$

where Θ is the Heaviside function, $|\times|$ is the Euclidean distance operator, and N_p is the number of distinct pairs of points in the embedding space. Grassberger and Procaccia have shown that under appropriate conditions, the function $\ln C(r)$ versus $\ln r$ has a linear region, called the "scaling region". The slope of the function in that scaling region is the correlation dimension D_2.

Figure 6 shows a superposition of plots of the slope, $d \ln C(r)/d \ln r$, of the function $\ln C(r)$ versus $\ln r$ for the logistic map using clean data, noisy data, and reconstructions from noisy data using 8- and 128-point training sets. Figure 7 shows similar plots for the Hénon map with the difference that the reconstructions use 64- and 256-point training sets taken from the noisy data.

We note first of all that, as expected, the plot for the noisy data for both attractors do not have scaling regions which means that if either noisy data set is at all characterizable by a dimension, its dimension cannot be resolved by this implementation of the Grassberger–Procaccia algorithm. On the other hand, plots for the clean data and for the reconstructed attractors in fig. 6 are practically coincident in an easily identifiable scaling region between $\ln r \approx -3$ and $\ln r \approx -6$.

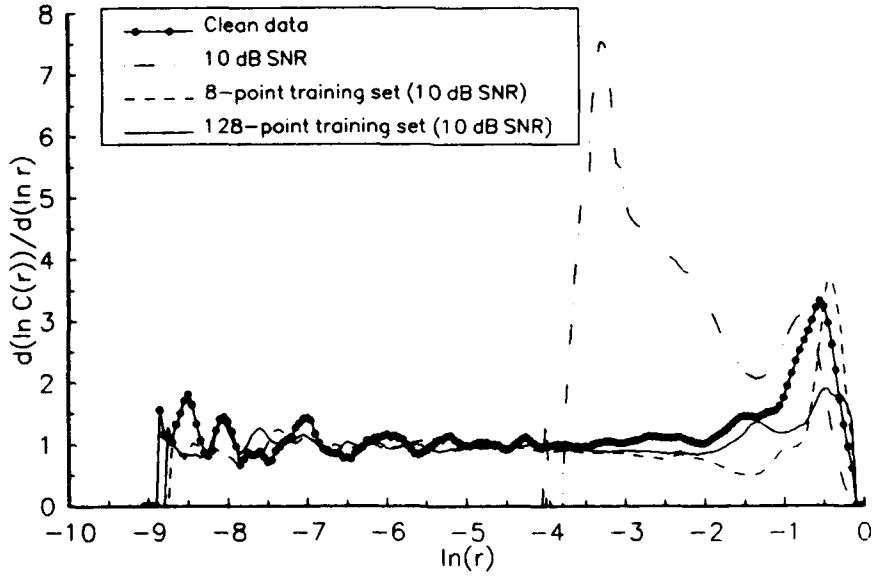

Fig. 6. Correlation dimension of the logistic attractor: Slope of $\ln C(r)$ versus $\ln r$ plotted as a function of $\ln r$. Noisy data: dot-dot-dash; clean data: solid with open circles; data reconstructed from a 8-point noisy input set: dashes; data reconstructed from a 128-point noisy input set: solid.

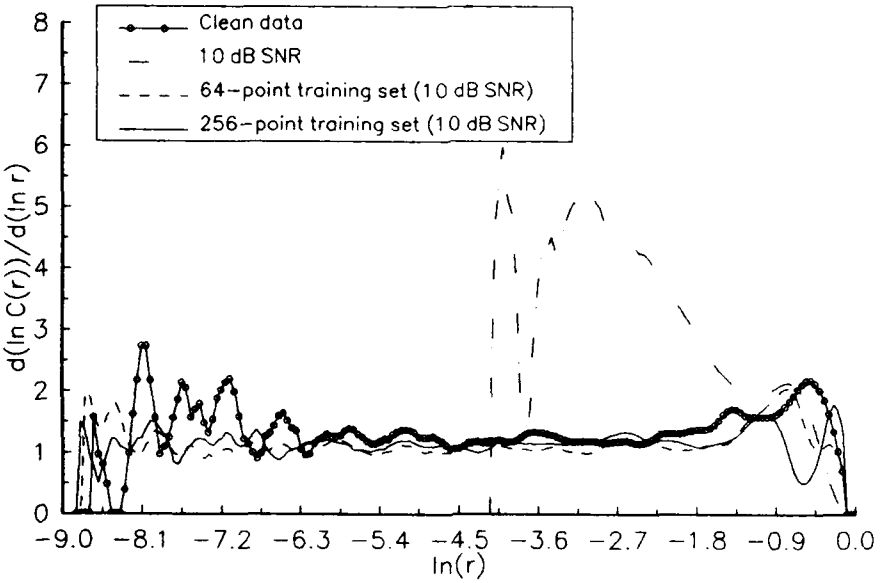

Fig. 7. Correlation dimension of the Hénon attractor: Slope of $\ln C(r)$ versus $\ln r$ plotted as a function of $\ln r$. Noisy data: dot-dot-dash; clean data; solid with open circles; data reconstructed from a 64-point noisy input set: dashes; data reconstructed from a 256-point noisy input set: solid.

All three calculations yield a correlation dimension of approximately 1.0, which is the expected value for the parameter we used. Similar observations hold for the Hénon map (fig. 7). Calculations using the clean data and reconstructions using 64- and 256-point training sets taken from the noisy data have a common scaling region between $\ln r \approx -2$ and $\ln r \approx -6$, and all three yield a correlation dimension of approximately 1.2, which is well within 10% of the value obtained by using much larger data sets (a rigorous upper bound for the correlation dimension of the Hénon attractor obtained by using its equations of motion, is its Lyapunov dimension, 1.25826 ± 0.00006 [11].

4. Summary

The examples presented above suggest that in trying to answer the question posed in the Introduction, "is it just noise or is there some potentially meaningful information being masked by the noise?", backpropagating neural nets may prove to be useful tools. These examples show that neural nets have the capability of extracting some geometric properties of the attractors of chaotic signals immersed in large amounts of noise, and that they can do this extraction using relatively small input data sets.

However, there are problems. Most notable among these is that the performance of the neural nets is quite inconsistent. The training of the net is started by assigning random values to the weights and biases. Different initial random weights can evolve to different minima of the error function, resulting in different levels of performance even when using the same input data. One set of initial weights and biases might lead to a time series that reconstructs almost the entire attractor, another might reconstruct only short segments, or get trapped in a periodic motion on a small set of points. This behavior can sometimes be alleviated by calculating several sets of output, each output starting from randomly chosen starting points in the input data set.

In addition, there do not exist consistent criteria for determining the optimum architecture of the net, or of the optimum size of the training set. In fig. 5, the performance of the net seems to improve in that it gives a less-distorted

attractor (although with less folding) as the size of the training set is increased from 16 to 64. Then it seems to deteriorate when the size is further increased to 128. Calculations with training sets consisting of 256, 512 and 1024 points show that the quality of the reconstruction again increases as one goes from 128 to 256, but then deteriorates with the larger training sets.

These problems are by no means unique to the application which we have presented here, and extensive efforts are underway to alleviate them [5, 7]. Inspite of these problems, examples such as those we have discussed indicate that neural nets can become very powerful tools for extracting signals from noise-corrupted data sets, but there is a need for the development of techniques that would make them perform this task more consistently, and for the definition of easily implementable criteria for optimizing their performance.

Acknowledgements

Part of this work was done while A.M.A. was on a Navy-ASEE Summer Faculty appointment at the Naval Air Warfare Center, and part was supported by a contract from the NAWC. He is grateful for the kind hospitality extended to him at the Center.

References

[1] G. Mayer-Kress, ed., Dimensions and Entropies in Chaotic Systems (Springer, Berlin, 1986);
N.B. Abraham, A.M. Albano, A. Passamante and P.E. Rapp, eds., Measures of Complexity and Chaos, (Plenum, New York, 1989);
S. Krasner, ed., The Ubiquity of Chaos (AAAS, Washington, 1990).

[2] R. Badii, G. Broggi, B. Derighetti, M. Ravani, S. Ciliberto, A. Politi and M.A. Rubio, Phys. Rev. Lett. 60 (1988) 979;
F. Mitschke, M. Moller and W. Lange, Phys. Rev. A 37 (1988) 4518.

[3] P.-C. Lo and J. Principe, Proc. Ann. Conf. IEEE Eng. Biol. Soc. 89 (1989) 638;
L.O. Chua and T. Lin, IEEE Trans. Circuits Systems 35 (1988) 648;
P.E. Rapp, A.M. Albano, T.I. Schmah and L. Farwell, preprint Medical College of Pennsylvania (1991).

[4] D.S. Broomhead and G.P. King, Physica D 20 (1986) 217;
A.M. Albano, J. Muench, C. Schwartz, A.I. Mees and P.E. Rapp, Phys. Rev. A 38 (1988) 3017;
E. Kostelich and J.A. Yorke, Phys. Rev. A 38 (1988) 1649.

[5] R. Beale and T. Jackson, Neural Computing: An Introduction (Adam Hilger, Bristol, 1990)
B. Müller and J. Reinhardt, Neural Networks: An Introduction (Springer, Berlin, 1991).

[6] A. Lapedes and R. Farber, Los Alamos preprint LAUR-87-2662.

[7] D. Rummelhart and J. McClelland, *Parallel Distributed* Processing (MIT Press, Cambridge, MA 1986).

[8] N.H. Packard, J.P. Crutchfield, J.D. Farmer and R.S. Shaw, Phys. Rev. Lett. 45 (1980) 712.

[9] P. Grassberger and I. Procaccia, Physica D 9 (1983) 189; Phys. Rev. Lett. 50 (1983) 346; Phys. Rev. A 28 (1983) 2591.

[10] F. Takens, in: Proc. Dynamical Systems and Turbulence, Warwick, 1980, Lecture Notes in Mathematics 898 (Springer, Berlin, 1981);
J.-P. Eckmann and D. Ruelle, Rev. Mod. Phys. 57 (1985) 617.

[11] W.E. Caswell and J.A. Yorke, in: Dimensions and Entropies in Chaotic Systems, ed. G. Mayer-Kress (Springer, Berlin, 1986).

[12] C. de Groot and D. Würtz, Presented at this Workshop.

Physica D 58 (1992) 10–30
North-Holland

PHYSICA D

Power spectra of noise-driven nonlinear systems and stochastic resonance

M.I. Dykman[1] and P.V.E. McClintock
School of Physics and Materials, Lancaster University, Lancaster, LA1 4YB, UK

Received 4 October 1991
Revised manuscript received 17 January 1992
Accepted 17 January 1992

The results of recent experimental and theoretical investigations of the spectral densities of fluctuations (SDFs) of noise-driven nonlinear dynamical systems are reviewed. Emphasis is placed on the analysis of the shapes and intensities of peaks in the SDFs. Three different types of phenomena are considered. First, the SDFs of a class of monostable underdamped nonlinear systems, in which the variation of eigenfrequency with energy is nonmonotonic, are investigated. It is shown that they exhibit zero-dispersion peaks and noise-induced spectral narrowing, as well as zero-frequency peaks. Secondly, it is demonstrated that systems bistable in an external periodic field can exhibit supernarrow spectral peaks within the range of a kinetic phase transition. Finally, recent results in stochastic resonance (SR) are reviewed, including phase shifts, giant nonlinearities for weak noise, SR for periodically modulated noise intensity, and high-frequency SR for periodic attractors.

1. Introduction

Spectral densities of fluctuations (SDFs) provide an important means of characterising physical systems, because they can be measured directly in a variety of experiments: in particular, the optical and neutron spectra of systems in thermal equilibrium (or quasiequilibrium) – one of the main sources of information about the microscopic characteristics of many such systems – are immediately related to SDFs. The investigation of SDFs also makes possible to observe and analyse the interplay between the fluctuations, relaxation and nonlinearity that are inherent to real macroscopic physical systems. This interplay provides one of the most challenging problems of modern nonlinear physics.

In many cases of interest, the physical system to be investigated can be modelled by a more or less complicated damped dynamical system that is subject to noise. If the noise and the relaxation are both due to coupling to a thermal bath, then they will satisfy the fluctuation-dissipation relations [1] and the characteristic intensity of the noise will be equal to the temperature T of the bath. In the general case, a nonthermal noise is also present. Certain properties of the systems, and of their SDFs in particular, are highly sensitive to the characteristics of the noise, while others are universal and depend only weakly on these characteristics. Both types of property are clearly of importance in different contexts. In what follows, our main aim will be to consider *phenomena* exhibited by noise-driven archetypal models. Similar phenomena may of course then be predicted for real systems, over a very wide range of contexts in science and technology, whenever they are described by equations of the same general form as those we will discuss.

[1] Now at: Department of Chemistry, Stanford University, Stanford, CA 94305, USA.

0167-2789/92/$05.00 © 1992 – Elsevier Science Publishers B.V. All rights reserved

In the present paper we outline recent results on the SDFs of relatively simple, although nontrivial, nonlinear systems. Emphasis is placed on the shapes and intensities of the peaks of the SDF. Three sorts of effects are considered. In section 2 we analyse the shapes of the peaks for monostable underdamped nonlinear systems and investigate effects related to nonmonotony of the dependence of the frequency of eigenvibrations $\omega(E)$ on the energy E of a system. Such nonmonotony is inherent in a number of vibrational systems. Examples include the localised vibrations in solids, where nonmonotony will arise provided that the "stiffness" of the system increases with energy for small E (see [2] for a review) and where it can be controlled by external electric field and/or pressure. For systems of this kind, the widths of the SDF peaks at first increase in the usual way with increasing noise intensity, relative to their low noise values (which are determined by damping). Surprisingly, however, they can sometimes *decrease* again, by a large factor, as the noise intensity continues to rise. Moreover, for very small damping, a specific zero-dispersion peak can arise at the frequency of the extremum [3].

In section 3 the SDF is investigated for bistable systems, with the emphasis on bistability arising in an external periodic field where the coexisting stable states correspond to forced periodic vibrations with different amplitudes and phases. Bistable systems driven by a sufficiently weak noise have a very large characteristic relaxation time that is given by the reciprocal probabilities of fluctuational transitions between the stable states. Associated with this time is an extremely small spectral width of the peaks of the SDF (supernarrow peaks) that arise at the frequency of the driving field and its overtones, and also at zero frequency. The peaks exhibit a critical-type behaviour for the parameters of the system lying in the vicinity of a kinetic "phase transition" where the stationary populations of the coexisting stable states are of the same order of magnitude.

In section 4 a phenomenon directly related to the aforementioned super-narrow peaks is investigated, namely, the onset of a strong response of a bistable noise-driven system to a comparatively weak (trial) periodic field [4] and the dome-like (bell-shaped) dependence of the response on the noise intensity called *stochastic resonance* by Benzi et al. [5] (see also [6]). This phenomenon has attracted considerable interest recently and has been observed in both active [7] and passive [8] optically bistable systems and also in analogue electronic experiments [9–12].

2. Noise-induced narrowing of the spectral peaks of monostable underdamped systems

In view of its importance and a wide variety of applications, the problem of the power spectra of nonlinear vibrational systems has been considered by many authors, both numerically and analytically (see refs. [13–24] and the reviews [4b, 25]). Underdamped systems, in particular, are of the utmost interest, because of their association with resonant phenomena, including, e.g. resonant light absorption and neutron scattering in condensed matter that is directly described just by the SDFs. It is generally accepted that the peaks of the SDF usually become substantially broader as the external noise intensity increases. This is due to the growth of fluctuations in the system. However, as is shown below, in some systems the broadening is followed, remarkably, by a narrowing of the peaks with further increase of the noise intensity.

We shall investigate evolution of the peaks for the simplest model of a fluctuating nonlinear system, a nonlinear oscillator performing Brownian motion. It is described by the equation

$$\ddot{q} + 2\Gamma\dot{q} + U'(q) = f(t)\,,$$
$$\langle f(t)\, f(t')\rangle = 4\Gamma T\delta(t-t') \qquad (1)$$

If its fluctuations correspond to thermal equilibrium, then T in (1) is the temperature, whereas

in the more general case it simply characterises the intensity of the driving noise which, in the present ection, is supposed to be white and Gaussian. The damping Γ is assumed small,

$$\Gamma \ll \omega_0 , \quad \omega_0 \equiv \omega(0) = [U''(q_{eq})]^{1/2} , \tag{2}$$

where $\omega(E)$ is the eigenfrequency of conservative vibrations with a given energy E,

$$E = \tfrac{1}{2}\dot{q}^2 + U(q) \tag{3}$$

(the energy is measured from the value of the potential $U(q)$ in the equilibrium position q_{eq}: $U(q_{eq}) = U'(q_{eq}) = 0$).

In what follows (see, however, section 4) we shall consider the SDF of the coordinate defined as

$$Q(\omega) = \lim_{t_0 \to \infty} (4\pi t_0)^{-1} \times \left| \int_{-t_0}^{t_0} dt\, [q(t) - \langle q(t) \rangle] \exp(i\omega t) \right|^2 . \tag{4}$$

Here, $\langle \ldots \rangle$ implies the ensemble average (which is well known [1, 4b] to differ from the time average for the periodically driven systems considered below; for such systems the time axis is evidently "inhomogeneous").

2.1. Peak of the SDF for "small" noise intensities

For very weak noise (small T) the oscillator (1) can be assumed effectively harmonic, with an eigenfrequency ω_0 and damping parameter Γ. The SDF $Q(\omega)$ for such an oscillator is well known (cf. [1]) to have a Lorentzian peak at the frequency ω_0, with a halfwidth at halfmaximum just equal to Γ. With increasing noise intensity the shape of the peak changes, and this change can be strong even for relatively small noise intensities (which was probably noticed for the first time in ref. [26] where the quantum theory of the spectra of localised vibrations was considered).

The origin of the strong noise-induced broadening of the spectral peak can easily be understood from fig. 1. Because of fluctuations, a distribution of the oscillator is formed over the energy E. Its characteristic width is given by the driving-noise intensity T. In its turn, because of nonlinearity, this distribution gives rise to a distribution of the oscillator over the corresponding range of vibrational eigenfrequencies $\omega(E)$ i.e., there arises a noise-induced frequency straggling $\delta\omega_{fl}$ which for small noise intensities is equal to

$$\delta\omega_{fl} = T|\omega_0'| , \quad \omega_0' \equiv [d\omega(E)/dE]_{E=0} , \quad \delta\omega_{fl} \ll \omega_0 . \tag{5}$$

The frequency straggling (5) "competes" with the frequency "uncertainty" Γ arising from damping. The shape of the peak in the SDF depends just on the ratio of these two quantities:

$$\alpha = \tfrac{1}{2}(\delta\omega_{fl}/\Gamma) \operatorname{sgn} \omega_0' .$$

For arbitrary α, but for both weak damping, $\Gamma \ll \omega_0$, and "weak" noise, $\delta\omega_{fl} \ll \omega_0$, the peak is

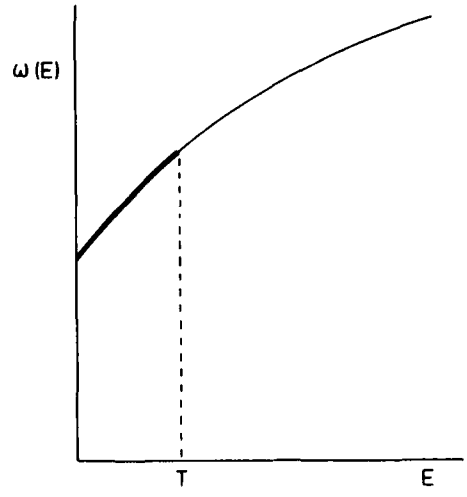

Fig. 1. Variation of eigenfrequency $\omega(E)$ with the energy E for a general nonlinear oscillator. If the oscillator is driven by noise of intensity T, its energy will be described by a distribution whose width is approximately equal to T, so that the frequencies of the thermally excited vibrations are mostly those on the thickened portion of the curve.

described by a comparatively simple expression [15]

$$Q(\omega) = \frac{T}{2\pi\omega_0^2}\,\mathrm{Re}\int_0^\infty \mathrm{d}t\,\exp[\mathrm{i}(\omega-\omega_0)t]\,\tilde{Q}^*(t)\,,$$

$$|\omega-\omega_0| \ll \omega_0\,,$$

$$\tilde{Q}(t) = \exp(\Gamma t) \times \left(\cosh(at) + \frac{\Gamma}{a}(1-2\mathrm{i}\alpha)\sinh(at)\right)^{-2}\,,$$

$$a = \Gamma(1-4\mathrm{i}\alpha)^{1/2}\,. \qquad (6)$$

It follows from (6) that for $|\alpha| \gg 1$, i.e. for $\delta\omega_{\mathrm{fl}} \gg \Gamma$ it is fluctuational broadening that determines the shape of the peak in the SDF near its maximum. It also follows that, in contrast to the case $|\alpha| \ll 1$ where $Q(\omega) \propto \Gamma T/[\Gamma^2 + (\omega-\omega_0)^2]$ is symmetrical near the maximum, for $|\alpha| \gg 1$ the peak is strongly asymmetric. The shape of the peak in the latter case can readily be understood by noting that the amplitude of the eigenvibrations increases with increasing energy (as $E^{1/2}$ for small E), while the probability of the system having an energy E decreases exponentially, according to the Gibbs law. The product of the squared amplitude times $\exp(-E/T)$ is "mapped" onto the spectral distribution $Q(\omega)$ via the relation $\omega = \omega(E) = \omega_0 + \omega_0' E$, so that $Q(\omega)$ near the maximum is proportional to $[(\omega-\omega_0)/\omega_0'] \exp[-(\omega-\omega_0)/\omega_0' T]$. The position of the maximum itself is given by $\omega_0 + T\omega_0' = \omega(T)$ and the peak increases rapidly in width with the noise intensity, being much steeper on the side of the sharp low-energy threshold (cf. fig. 1).

The above picture has been completely confirmed by analogue electronic experiments [24, 27]. The evolution of the SDF with increasing noise intensity for an oscillator (1) with the potential

$$U(q) = \tfrac{1}{2}q^2 + \tfrac{1}{4}q^4 + \lambda q \qquad (7)$$

at $\lambda = 0$, when the eigenfrequency $\omega(E)$ increases monotonically with E, as observed in [27], is shown in fig. 2. The stronger the noise the broader the peak, and its width for the values of T in fig. 2 substantially exceeds the relaxational broadening Γ.

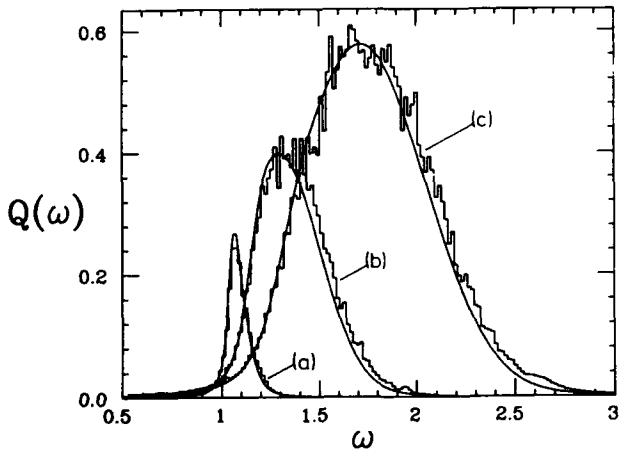

Fig. 2. Spectral density $Q(\omega)$ of the fluctuations of the oscillator described by (1) and (7) for damping $\Gamma = 0.0143$ and the asymmetry parameter $\lambda = 0$, as measured (histograms) in an analogue experiment [27] for comparison with theoretical predictions (curves), for noise intensities: (a) $T = 0.078$; (b) 0.687; (c) 3.04.

Strikingly similar behaviour has been observed [28] in the optical absorption spectra of localised and resonant vibrations in solids as shown, for example, by the results of fig. 3. Just as in the

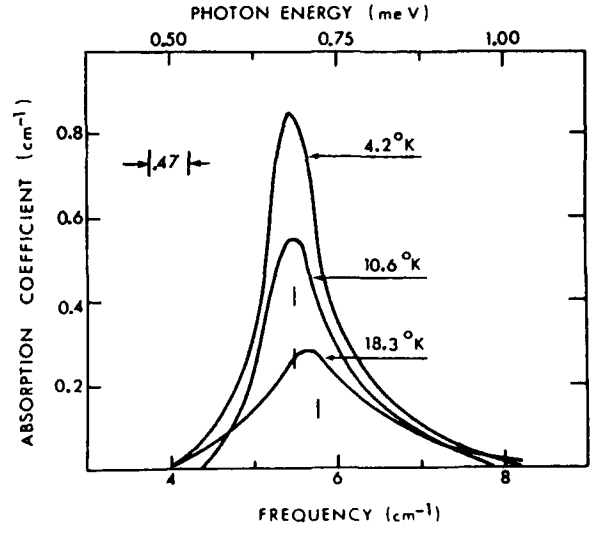

Fig. 3. Temperature dependence of the far-infrared absorption in an NaI crystal doped with 0.4% NaCl [28].

case of the Duffing oscillator SDFs of fig. 2, the absorption spectrum of the resonant mode in fig. 3 broadens rapidly and becomes noticeably asymmetric with increasing temperature. (The dependences of the intensity on temperature in the two graphs differ because the optical absorption cross-section in the experiment of fig. 3 varies approximately as the SDF divided by temperature.) We note that, in many physical systems, effects arising from quantum statistics (i.e. related to the discreteness of the energy levels) of the localised modes are important: such effects are beyond the scope of the present review.

2.2. *Noise-induced narrowing and onset of the zero-dispersion peak*

A peculiar situation of particular interest arises when the dependence of the eigenfrequency $\omega(E)$ on the vibration energy E is nonmonotonic and for some energy E the derivative $\omega'(E)$ passes through zero,

$$[\mathrm{d}\omega(E)/\mathrm{d}E]_{E=E_e} = 0\,, \quad \omega(E_e) \equiv \omega_e \tag{8}$$

(cf. fig. 4; for convenience in understanding the experimental data in figs. 2, 5 we have chosen in fig. 4 an initial slope $\omega_0' = [\mathrm{d}\omega(E)/\mathrm{d}E]_{E=0}$ that is opposite in sign to that in fig. 1, but which corresponds to the particular system considered below). If (8) is fulfilled there are two "cutoff" frequencies, ω_0 and ω_e. For small noise intensities, $T \ll E_e$, when the vibrations with the eigenfrequencies close to ω_e do not come into play, the behaviour of $Q(\omega)$ with increasing T is described by the results of the preceding subsection.

However, for T approaching E_e and the position of the maximum of $Q(\omega)$ approaching ω_e, respectively, the "flattening" of $\omega(E)$ becomes more and more marked. In essence, as is obvious from the above arguments, the peak of $Q(\omega)$ is "pressed" against the frequency ω_e: vibrations with higher and higher amplitudes are being excited, and their eigenfrequencies approach ω_e.

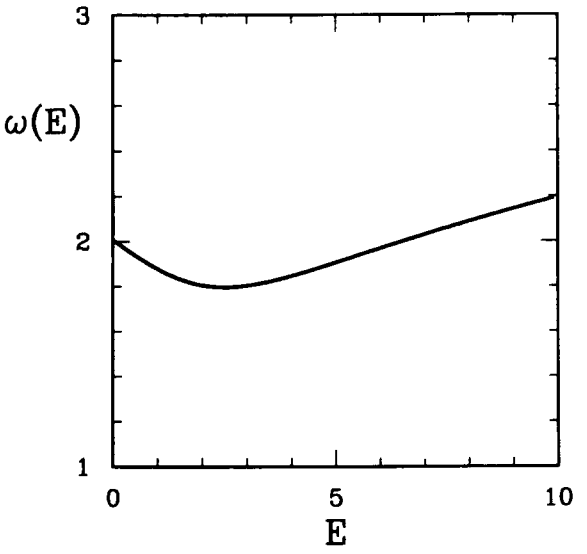

Fig. 4. Variation of eigenfrequency $\omega(E)$ with energy E for the particular oscillator described by (1), (7), with $\lambda = 2$. It is the existence of an extremum in $\omega(E)$ that is responsible for the noise-induced spectral narrowing and zero-dispersion spectral peaks discussed in the text.

But there are no eigenfrequencies beyond this cutoff. As a result the peak becomes narrower with increasing T and also becomes steeper on the ω_e-side, i.e. the exact opposite of the situation for small T.

Spectral narrowing was first observed in an analogue experiment and then described in detail theoretically [27]. The theory reduced the problem of calculating the peak of the SDF to a boundary-value problem for an ordinary differential equation related to the Fokker–Planck equation for a noise-driven oscillator: the former equation was a Fourier-transformed (over time) equation for diffusion in energy, but, in contrast to Kramer's paper [29], it was the equation not for the phase-independent, but for the phase-dependent (as $\exp(in\phi)$, with $|n| = 1$ in the present case) part of the distribution function.

The experimental and theoretical results for the model (1), (7), demonstrating the noise-induced narrowing of the spectral peak, are shown in fig. 5. We would note that the model (7) is extremely simple in that it contains only one control parameter λ which might be associ-

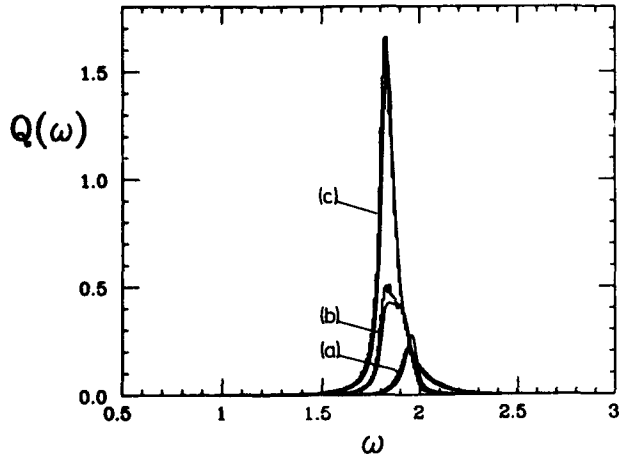

Fig. 5. Spectral densities $Q(\omega)$ of the fluctuations of the oscillator described by (1), (7) for $\Gamma = 0.0143$ and the asymmetry parameter $\lambda = 2$, as measured (histograms) in an analogue electronic experiment [27] for comparison with theoretical predictions (curves) for noise intensities: (a) $T = 0.078$; (b) 0.687; (c) 3.04. Note the narrowing of the width at the half-height as the noise intensity is increased between (b) and (c).

ated, e.g., with an electric field for an oscillating charged particle, or a static pressure. For $\lambda = 0$ the eigenfrequency $\omega(E)$ increases monotonically with E and there is no spectral narrowing (cf. fig. 2). The nonmonotony of $\omega(E)$ arises for $|\lambda| > 8/7^{3/2} \cong 0.43$, and starting with slightly higher $|\lambda|$ (because of finite damping; the data refers to $\Gamma \cong 0.015$) the nonmonotony of the peak width vs T was observed. The theory is evidently in excellent agreement with the experiment, and we would stress that it does not contain any adjustable parameter.

A very interesting phenomenon arises in systems with nonmonotonic $\omega(E)$ for still smaller damping Γ/ω_e [3]: the onset of an additional narrow peak in the SDF at the extreme frequency ω_e for sufficiently high noise intensities. Qualitatively, such a zero-dispersion peak arises because the system spends a relatively long time oscillating at frequencies close to ω_e: for $E \cong E_e$ fluctuations over energy have little effect on the frequency or phase of the eigenvibrations. The characteristic width $\delta\omega_{zd}$ of the peak can be readily obtained by noting that $\delta\omega_{zd}$ is due to the frequency diffusion over the time $\delta t \sim (\delta\omega_{zd})^{-1}$; in its turn, the frequency diffusion is due to energy diffusion over the time δt; $\delta E \sim (4\Gamma T I_e \omega_e \delta t)^{1/2}$ (cf. [29]), where I_e is the action for the vibrations with the energy E_e. Therefore,

$$\delta\omega_{zd} = (2\Gamma|\omega_e''|TI_e\omega_e)^{1/2},$$

$$\omega_e'' \equiv [d^2\omega(E)/dE^2]_{E_e},$$

$$I_e = \int_0^{E_e} \omega^{-1}(E)\,dE. \qquad (9)$$

We note that the change in frequency $\omega(E)$ over a time $(\delta\omega_{zd})^{-1}$ due to the drift in energy is of

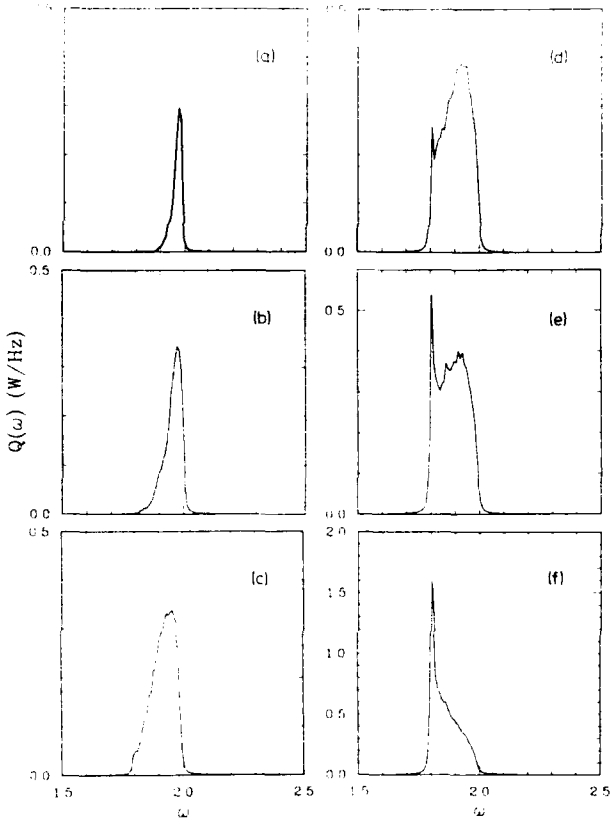

Fig. 6. Spectral densities $Q(\omega)$ of the fluctuations of an electronic model [30] of the oscillator described by (1), (7) for very small damping $2\Gamma = 1.70 \times 10^{-3}$ and the asymmetry parameter $\lambda = 2$, for several noise intensities: (a) $T = 0.100$; (b) 0.203; (c) 0.320; (d) 0.409; (e) 0.485; (f) 0.742. The zero-dispersion peak is the sharp "spike" that first appears in (d); it rapidly grows, overwhelming the usual spectral peak as T increases, in (f).

order $\omega_e''(\Gamma\omega_e I_e/\delta\omega_{zd})^2 \ll \delta\omega_{zd}$, and can thus be neglected, i.e. the broadening of the peak is purely diffusional. The shape of the zero-dispersion peak is described by the expression [3]

$$\delta Q_{zd}(\omega) = \text{const.} \times \exp(-E_e/T) \times |S[(\omega - \omega_e)\,\mathrm{sgn}(\omega_e'')/\delta\omega_{zd}]|\,,$$

$$S(x) = \mathrm{Re}\int_0^\infty \mathrm{d}t \exp(-\mathrm{i}xt) \times [(1-\mathrm{i})\sinh((1-\mathrm{i})t)]^{-1/2}\,. \qquad (10)$$

Analogue simulations of the model (1), (7) have made it possible to reveal the zero-dispersion peak [30]. The evolution of the SDF with increasing temperature for very small damping, $\Gamma = 8.5\times10^{-4}$, is shown in fig. 6. It is obvious from this figure that the zero-dispersion peak emerges very suddenly with increasing temperature, and then grows rapidly to dominate the spectrum. The sharp "outburst" of the peak (due to the competition of the exponentially small occupation of the energies $E \sim E_e$ for small T and the sharpness of the peak itself) has recently been described analytically [31], and the theory has been demonstrated [30] to be in good agreement with the experiment.

2.3. Zero-frequency peaks in SDFs of monostable system

A well-known feature of nonlinear vibrations is that they are not strictly sinusoidal: in addition to the fundamental frequency $\omega(E)$ there also exist overtones $n\omega(E)$ $(n = 2, 3, \ldots)$ in their Fourier spectrum. It is to be expected, therefore, that in addition to the peak in the SDF corresponding to the main tone (see above) there will also be peaks corresponding to the overtones. Peaks of this sort have indeed been observed, e.g., in the absorption spectra of localized vibrations in solids [32] (see [2] for a review). Their width increases with the number n of the overtone (cf. [33]) and exceeds that for the main tone.

For an underdamped oscillator fluctuating in an asymmetric potential well there arises, in addition, a well-resolved comparatively narrow peak in the SDF at zero frequency [24, 34] (we note that for overdamped oscillators the peak at zero frequency is the only one in the spectrum). The quantum theory of a corresponding peak in the absorption spectra of weakly nonlinear localized vibrations was given in ref. [35].

The zero-frequency peak in the SDF of the coordinate q is related to the fact that, in asymmetric potential wells, the fluctuations of the oscillator energy E give rise to fluctuations of the *centre* of the vibrations with a given energy, $q_0(E)$. These fluctuations are "slow", with a characteristic time scale equal to the relaxation time Γ^{-1}. They are purely relaxational and are not associated with any finite frequency, and thus the corresponding SDF peak should be positioned at zero frequency and have a half-width of order Γ. A simple theory shows that, for small noise intensities, the shape of the zero-frequency peak is given by the expression [34]

$$Q_0(\omega) = \frac{1}{\pi}\, q_0'^2 T^2\, \frac{2\Gamma}{4\Gamma^2+\omega^2} \times \left[1 + 4T\left(\frac{q_0''}{q_0'} - \frac{4(\omega_0'/\omega_0)\Gamma^2}{4\Gamma^2+\omega^2}\right)\right],$$

$$q_0' \equiv [\mathrm{d}q_0(E)/\mathrm{d}E]_{E=0}\,,$$

$$q_0'' \equiv [\mathrm{d}^2 q_0(E)/\mathrm{d}E^2]_{E=0} \qquad (11)$$

An important feature of the zero-frequency peak is that it is not affected by the straggling of the frequencies of eigenvibrations induced by the combined effects of noise and nonlinearity (see above). Therefore it does not broaden rapidly with increasing noise intensity. It is because of this that the zero-frequency peak in the SDF is resolved much better than the peaks at the overtones: peaks of both types are due to nonlinearity of the vibrations, and therefore their intensities increase with noise strength, but the width of the zero-frequency peak becomes much smaller for noise strengths beyond $T \sim \Gamma/|\omega_0'|$ and,

correspondingly, it is much higher. In addition, for relatively small noise, the intensity of the peak at the second overtone (the "main" overtone for weak noise) contains an extra numerical factor $\frac{1}{9}$ [33] compared to that of the zero-frequency peak. An overall view of the SDF for the oscillator (1), (7) as obtained for the relevant electronic model and described theoretically, with a clearly visible zero-frequency peak, is shown in fig. 7. The insert demonstrates that the broadening of this peak with increasing noise is indeed small and that sometimes, rather than broadening, noise-induced narrowing may occur; this follows from eq. (11).

In concluding this section, we note that the shape of the fundamental peak for not very weak noise, when the main broadening mechanism is the fluctuational one, reflects the stationary distribution of the system over its energy (the peak gives the "projection" of this distribution on the distribution over the frequencies $\omega(E)$). Therefore it is quite sensitive to the characteristics of the driving noise, whereas the shape of the zero-frequency peak is much less sensitive to these characteristics.

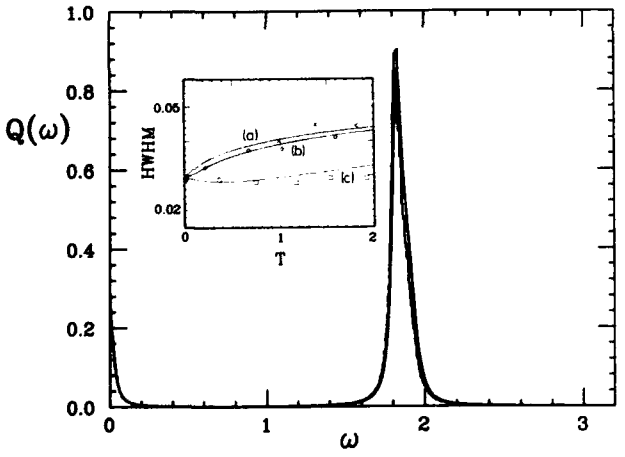

Fig. 7. Spectral density $Q(\omega)$ of the fluctuations of the oscillator described by (1), (7) for damping $\Gamma = 0.0143$ and with the asymmetry parameter $\lambda = 2.0$, for a noise intensity $T = 0.814$. The full spectrum (except for the overtones) is plotted, with the zero-frequency peak on the left-hand side and the peak corresponding to eigenvibrations at the fundamental frequency on the right-hand side. The histogram represents data from an electronic model, and the full curve represents the theory [34]. Inset: the variation of the width (defined as the half-width at half-maximum) of the zero-frequency peak, as a function of noise intensity T for three values of the asymmetry parameter: (a) $\lambda = 0.2$; (b) 0.43; (c) 2.0. The data points represent measurements on the electronic model, and the full curves represent the theory.

3. Super-narrow spectral peaks in the SDFs of bistable systems

Many physical systems of particular interest have not one, but two or more coexisting attractors. These may be potential minima for a diffusing particle (e.g., for an impurity in a solid, or a reorientating molecule) or coexisting regimes of laser generation, passive optical transmission, or forced oscillations of an electron in a Penning trap [36], etc. A quite general feature of fluctuations in bistable (or multistable) systems is that, in addition to the relaxation time (times) $\tau_{\rm rel}$ characterising the dynamics in close vicinity to one of the attractors, the fluctuations are also characterised by much larger times associated with the noise-induced transitions between the attractors. These are equal to the reciprocal transition probabilities W_{ij}^{-1} (i, j enumerate the attractors, i, $j = 1$, 2). For a broad class of systems driven by Gaussian noise the dependence of W_{ij} on the characteristic noise intensity D is of the activation type (see [4, 37–41] and references therein),

$$W_{ij} = \text{const.} \times \exp(-R_i/D)\,. \tag{12}$$

Here, R_i can be associated with the activation energy of the transition from the state i (in Kramers' model [29] of the activation of a Brownian particle over a potential barrier, R_i is the height of the barrier and D is the temperature). It is obvious from (12) that for sufficiently weak noise

$$W_{ij} \ll \tau_{\rm rel}^{-1} \quad (R_i \gg D)\,. \tag{13}$$

It is the inequality (13) that makes the concept of transition probabilities sensible.

Fluctuational transitions give rise to fluctuations of the instantaneous populations $\tilde{w}_1(t)$, $\tilde{w}_2(t)$ of coexisting attractors. The kinetics of the populations is described by the balance equation.

$$\dot{\tilde{w}}_1(t) = -W_{12}\tilde{w}_1(t) + W_{21}\tilde{w}_2(t)\,,$$
$$\tilde{w}_2(t) = 1 - \tilde{w}_1(t) \qquad (14)$$

The interwell fluctuations become pronounced in the range of parameters where the stationary values of the populations, w_1 and w_2, are of the same order of magnitude (obviously, because otherwise a system spends practically all its time near one of the attractors). This parameter range is quite narrow for weak noise, since according to (14) the ratio of the stationary populations,

$$w_1/w_2 = W_{21}/W_{12} = \text{const.} \times \exp[(R_1 - R_2)/D]\,, \qquad (15)$$

is either exponentially large or small: for most parameter values, $|R_1 - R_2| \gg D$ at small D (cf. (13)). The region where $R_1 \approx R_2$ can reasonably be called the range of a kinetic phase transition, by analogy with first-order phase transitions in thermal equilibrium systems where the populations of the phases (e.g. molar volumes, for a liquid–vapour transition) are of the same order of magnitude.

The fluctuations of the populations cause large (of the order of the distance between the attractors) fluctuations of the coordinate, momentum, amplitude of forced vibrations, etc. It would be expected therefore that, in the region of a kinetic phase transition, there will arise very intense and very narrow (with a width of the order of the transition probability) peaks in the SDFs of bistable systems [42] (similar peaks in susceptibilities were considered in [4]; cf. also [43]). In the case of bistability displayed in a periodic field with frequency ω_F, such supernarrow fluctuational-transition-induced peaks are positioned at ω_F and its overtones $n\omega_F$, including $n = 0$; those in the SDF of the coordinate of the bistable system are described by the expression [42]

$$Q_{tr}^{(n)}(\omega) = \frac{1}{\pi}\,\frac{w_1 w_2 |q_1(n) - q_2(n)|^2 W}{W^2 + (\omega - n\omega_F)^2}\,,$$
$$|\omega - n\omega_F| \ll \tau_{rel}^{-1}\,,$$
$$W = W_{12} + W_{21}\,. \qquad (16)$$

Here, $q_j(n)$ is the value of the nth Fourier component of the coordinate for the attractor j: because of the periodicity of the forced vibrations, the coordinate $q(t)$ for the jth attractor can be expanded as

$$[q(t)]_j = \sum_{n=-\infty}^{\infty} q_j(n)\exp(in\omega_F t)\,. \qquad (16a)$$

(in practice, for finite noise intensities, $q_j(n)$ differ slightly from their zero-noise values; this difference is neglected in what follows). We note that, for the particular case of an overdamped system performing Brownian motion in a static bistable potential, an expression of the type (16) (with $n = 0$) was given in [44]; the supernarrow zero-frequency peak was considered also in [24, 25, 45].

A supernarrow peak at the frequency of a driving periodic field was observed and the variation of its intensity with the parameters of the system was investigated in [46]. The system analysed was an analogue electronic model of an underdamped single-well Duffing oscillator described by (1), (7) with $\lambda = 0$, and the driving field $F\cos(\omega_F t)$ was nearly resonant, $|\omega_F - \omega_0| \ll \omega_F$. This system is closely related in particular to the case of a relativistic electron in a Penning trap: the motion of such an electron displays bistability in a sufficiently strong field with a frequency close to the cyclotron frequency [36]. The sharp onset of the supernarrow peak with variation of the dimensionless field intensity β,

$$\beta = 3F^2/32\omega_F^3|\omega_F - \omega_0|^3 \qquad (17)$$

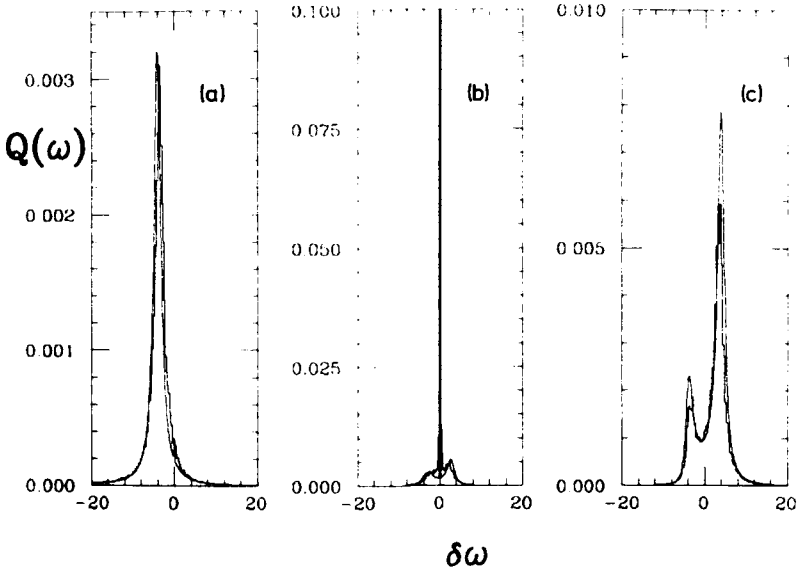

Fig. 8. Spectral densities $Q(\omega)$ of the fluctuations of the oscillator (1), (7) with $\lambda = 0$ driven by a strong, nearly resonant, periodic force $F\cos(\omega_F t)$, plotted as a function of $\delta\omega = (\omega_F - \omega_0)/\Gamma$ for three values of the dimensionless field intensity: (a) $\beta = 0.048$; (b) 0.078; (c) 0.150. The histograms are measurements from the electronic model, and the full curves are theoretical predictions [46]. The supernarrow spectral peak appears at $\delta\omega = 0$ in (b).

is shown in fig. 8. The width of the peak could not be resolved. The critical dependence of the intensity of the peak on the distance (in parameter space) to the phase-transition point is clearly evident in fig. 9. The full curves correspond to the expression

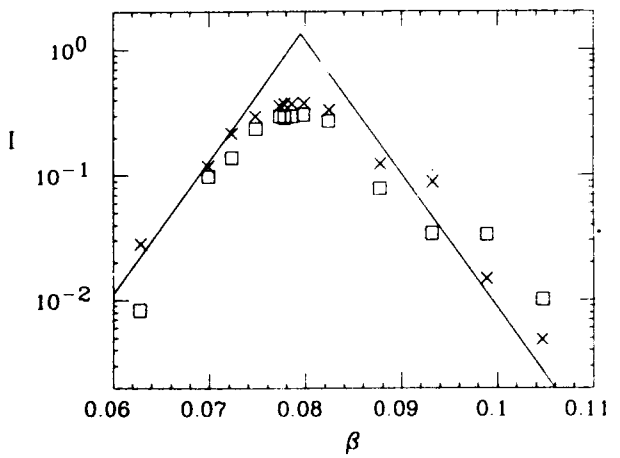

Fig. 9. Variation of the intensity I of the supernarrow peak with distance from the kinetic phase transition [46]. The square data points represent direct measurements. The crosses are theoretical values calculated from *measured* transition rates, and the full lines represent (18).

$$\ln(w_1 w_2) \simeq -|R_1' - R_2'|\,|\beta - \beta_c|/D\,, \qquad (18)$$

which gives the logarithm of the intensity of the peak (16) with account taken of (15). The quantities R_1', R_2' in (18) are the derivatives of the transition activation energies (cf. (12)) with respect to the controlling parameter β, evaluated at the phase-transition point β_c; they were determined quite independently from measurements of the transition probabilities. The data clearly demonstrate that the experimental results are self-consistent and also provide some insight into the origin of the supernarrow peak.

A related problem of considerable interest is that of the influence of the characteristics of the noise on the supernarrow peaks. The only such characteristics entering the expression for the peak shape (16) are the transition probabilities that, from (12), seem to depend on the noise only in terms of its intensity (for Gaussian noise). However, the values of the activation energies are highly sensitive to the shape of the power spectrum of the noise [37–41] and, by varying this shape, one can not only produce

marked changes in R_1, R_2, but also shift the position of the phase-transition point.

We note in conclusion of this section that the supernarrow peaks in the SDF's and the susceptibilities of bistable systems, in particular systems displaying bistability in a strong periodic field, are not only of interest as a means of studying kinetic critical phenomena e.g. in revealing the phase transition itself; they also provide a basis for the tunable filtering and detection of weak periodic signals.

4. Stochastic resonance in bistable systems: linear and nonlinear effects

An important phenomenon inherent to fluctuating bistable systems, one that occurs in the range of the kinetic phase transition, is stochastic resonance (SR). In fact, there are two distinct groups of phenomena both called SR. Originally [5], the term was used of periodically driven bistable systems to describe the dome-like (bell-shaped), seemingly resonant, dependence on noise intensity of the depth of the periodic modulation [4] of the instantaneous populations $\tilde{w}_1(t)$, $\tilde{w}_2(t)$ of the stable states. The other, more general, perception of SR [7] (which includes the first type of SR as a subset) is simply as the increase and subsequent decrease with increasing noise intensity of the response to a periodic field, i.e. of the susceptibility of the system. Viewed in the latter way, SR is no longer restricted to bistable systems, but can arise in monostable ones as well, as has been demonstrated very recently [47].

In what follows, however, we concentrate on SR in bistable systems and we consider the phenomena associated with the modulation of the instantaneous populations of the stable states. It is clear that this modulation will give rise, in turn, to a strong modulation of the coordinates, momenta, and other dynamic characteristics, i.e. it represents a strong overall response of the system to the field. Of course, the effect will only come into play when the noise intensity is large enough for transitions to occur between the stable states: thus, the effect can be promoted by noise and, consequently, in a certain interval of noise intensity, the coherent periodic response of the system *increases* with increasing noise. It is also evident that, being associated with the redistribution over the wells, SR is closely related to the onset of the supernarrow peaks considered in the preceding section.

There are several physical observables displaying an SR-type dependence on noise (cf. refs. [4–7, 11, 12, 48]). We shall analyse first a (slightly modified compared to (4)) SDF of a bistable system driven by trial field. It follows from the general concepts of statistical physics [1] that the average value of the coordinate of a system driven by a periodic force $A\cos(\Omega t)$ oscillates with the period $2\pi/\Omega$:

$$\langle q(t)\rangle = \sum_{n=0}^{\infty} a(n)\cos(n\Omega t + \phi(n)) \tag{19}$$

(if the system is driven by two fields there are terms in (19) with both frequencies, and also with their combinations: see below). It is clear from (19) that if we define the SDF of the coordinate as

$$S(\omega) = \lim_{t_0\to\infty} (4\pi t_0)^{-1}\left|\int_{-t_0}^{t_0} \mathrm{d}t\, q(t)\exp(\mathrm{i}\omega t)\right|^2 \tag{4a}$$

it will contain δ-shaped peaks at the frequency Ω and its overtones. The intensity S_n (total area) of the peak at the frequency $n\Omega$ is

$$S_n = \tfrac{1}{4}a^2(n)\,. \tag{20}$$

It was suggested in [7] that SR could conveniently be characterized by the ratio ρ of the trial-field-induced spike in $S(\omega)$ at the frequency Ω to the value $Q(\Omega) = S(\Omega)$ of the SDF in the absence of trial field,

$$\rho = S_1/Q(\Omega) \tag{21}$$

(the so-called signal-to-noise-ratio). It is quite straightforward to determine this ratio experimentally and it provides an important measure of the system's response to a trial field.

4.1. Linear response approximation

The easiest way to gain insight into SR and to find ρ is based on the fact that, for sufficiently weak trial fields (see below), the amplitudes of the harmonics $a(n)$ in (19) decrease very rapidly with increasing n so that, to a good approximation, it suffices to allow for the forced oscillations at the frequency Ω only, i.e., to retain in (19) only the terms with $n = 0, 1$. The term with $n = 0$ describes the time-independent part of $\langle q(t) \rangle$, and it remains unchanged to first order in the field amplitude; the main effect of the weak field is the onset of the term with $n = 1$. Taking account only of these two terms constitutes the linear response approximation [1]. The linear response is fully characterised by a susceptibility $\chi(\omega)$ [1, 49]:

$$a(1) = A|\chi(\Omega)|\,, \quad \rho = \tfrac{1}{4}A^2|\chi(\Omega)|^2/Q(\Omega)\,, \tag{22}$$

$$\phi(1) \equiv \phi = -\arctan[\mathrm{Im}\,\chi(\Omega)/\mathrm{Re}\,\chi(\Omega)]\,.$$

The susceptibility $\chi(\omega)$ can be calculated analytically for some simple model systems [4, 8, 10, 50]. It should be noted, however, that there is a broad class of systems of interest where $\chi(\omega)$ can be obtained from experimental measurements of the SDF in the *absence* of periodic driving, while a simple-minded analytical theory works only for a narrow range of parameters. This is the class of systems which are in thermal equilibrium (or quasiequilibrium). If a perturbing field is potential, i.e., its effect on a system can be determined by an extra term $-Aq\cos(\Omega t)$ in the Hamiltonian of the system, $\chi(\omega)$ can be expressed in terms of $Q(\omega)$ via the fluctuation-dissipation relations:

$$\mathrm{Re}\,\chi(\omega) = \frac{2}{T}\int_0^{\infty} \mathrm{d}\omega_1\, Q(\omega_1)\,\omega_1^2(\omega_1^2 - \omega^2)^{-1}\,,$$

$$\mathrm{Im}\,\chi(\omega) = \frac{\pi\omega}{T}\,Q(\omega)\,, \tag{23}$$

where the bar on the integral implies that we should take the Cauchy principal part. Some experimental data demonstrating, on one hand, the onset of SR in the signal-to-noise ratio ρ, and, on the other hand, the applicability of the relations (23) are shown in fig. 10. They refer to a Brownian "particle" (1) fluctuating in a symmetric double-well potential

$$U(q) = -\tfrac{1}{2}q^2 + \tfrac{1}{4}q^4\,. \tag{24}$$

The two sets of data were obtained from an analogue electronic circuit [51] simulating (1), (24) in two different ways: first (squares) by measuring ρ directly for the periodically driven system; and secondly (pluses) by making use of the measured $Q(\omega)$ obtained in the absence of periodic driving and of eqs. (22), (23). It is

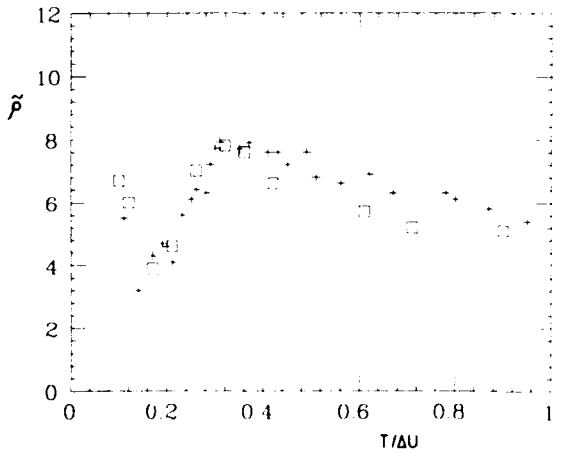

Fig. 10. Stochastic resonance [10]: the signal/noise ratio $\tilde{\rho} = 1.54 \times 10^1\rho$, defined by (21), measured for an electronic model of the oscillator (1), (24) driven by a weak periodic field, is plotted as a function of reduced noise intensity $T/\Delta U$. The square data points are direct measurements; the crosses are derived from (22), (23), based on measurements of the SDF in the *absence* of the periodic force. There are no adjustable parameters.

immediately evident from fig. 10 that ρ has a distinct maximum as a function of the noise intensity T thus demonstrating stochastic resonance, and also that the two ways of obtaining ρ give identical results.

Explicit expressions for $Q(\omega)$ and $\chi(\omega)$ for a Brownian particle (1) fluctuating in a bistable potential $U(q)$ can be obtained in the range of relatively small noise intensities,

$$T \ll \Delta U_1, \Delta U_2 ,$$
$$\Delta U_i = U(q_s) - U(q_i) \quad (i = 1, 2) , \tag{25}$$

where $q_{1,2}$ are the positions of the minima of the potential $U(q)$ and q_s is that of the local maximum, so that $U'(q_{1,2}) = U'(q_s) = 0$, $q_1 < q_s < q_2$. In this range, $Q(\omega)$ and $\chi(\omega)$ are given [42] by the sums of the "partial" contributions from fluctuations about the equilibrium positions $q_{1,2}$ and those from interwell transitions:

$$Q(\omega) = \sum_{i=1,2} w_i Q_i(\omega) + Q_{tr}^{(0)}(\omega) ,$$
$$\chi(\omega) = \sum_{i=1,2} w_i \chi_i(\omega) + \chi_{tr}^{(0)}(\omega) . \tag{26}$$

In eq. (26) w_i are the stationary populations of the stable states 1, 2 (cf. eqs. (14), (15)). The partial spectra $Q_i(\omega)$ in the low-noise range (25) for underdamped systems at ω close to $(U''(q_i))^{1/2}$ are given by eq. (6), while in the range of interest for SR, $\omega \leqslant (U''(q_i))^{1/2}$,

$$Q_i(\omega) = 2\Gamma T/\pi U_i''^2 + Q_{i0}(\omega), \quad U_i'' \equiv U''(q_i) ,$$
$$\Gamma, \omega \ll (U_i'')^{1/2} . \tag{27}$$

Here, $Q_{i0}(\omega)$ is the zero-frequency peak due to the local asymmetry of the potential about the bottom of the ith well; it is described by the expression (11) for $Q_0(\omega)$, with q_0', q_0'' calculated for the corresponding well. Alternatively, for overdamped systems,

$$Q_i(\omega) = 2\Gamma T/\pi(U_i''^2 + 4\Gamma^2\omega^2) , \quad \Gamma \gg (U_i'')^{1/2} \tag{27a}$$

(a more detailed expression that allows for the corrections $\sim T/\Delta U_i$ is given in [50]). The expression for the interwell-transition-induced contribution $Q_{tr}^{(0)}(\omega)$ in (26) is given by eq. (16); only the term with $n = 0$ in (16) contributes to (26) in the particular case under consideration. The values of the "partial" susceptibilities $\chi_i(\omega)$ and of the interwell-transition-induced term $\chi_{tr}^{(0)}(\omega)$ in the susceptibility are expressed in terms of $Q_i(\omega)$, $Q_{tr}^{(0)}(\omega)$ by the relations (23).

The expressions (16), (26), (27), (27a) explain (cf. also [52]) the dependence of ρ on T plotted in fig. 10: for very small noise intensities the inequality $W \ll \Omega$ holds, and the interwell transitions contribute neither to the SDF nor to the susceptibility so that, according to (23), (27), (27a) ρ decreases roughly as T^{-1} with increasing T. This is because the partial spectra $Q_i(\omega)$ are proportional to T, whereas the susceptibilities $\chi_i(\omega)$ are seen from (23) to be T-independent. The increase of ρ starts for those T where W becomes of order of Ω. In the range where the interwell-transition-induced terms are dominant both in the SDF and susceptibility, one arrives at the simple expression

$$\rho = \tfrac{1}{4}\pi A^2 w_1 w_2 W (q_1 - q_2)^2/T^2 ,$$
$$W = W_{12} + W_{21} ,$$
$$Q_{tr}^{(0)}(\omega) \gg Q_{1,2}(\omega) , \quad |\chi_{tr}^{(0)}(\omega)| \gg |\chi_{1,2}(\omega)| . \tag{28}$$

It is seen from (12), (18), (28) that the dependence of the signal-to-noise ratio on the noise intensity is of the activation type, $\rho \propto \exp(-\Delta U_{max}/T)$ where ΔU_{max} is the depth of the deeper well.

Because the onset of SR is related to the supernarrow interwell-transition-induced peak, a strong amplification of the response to a weak trial periodic field would be expected to occur (for the present case of motion in a static potential) at comparatively small frequencies where the supernarrow peak at zero frequency can dominate the SDF:

$$\Omega \ll \Gamma, (U''_{1,2})^{1/2} . \tag{29}$$

The dependence of ρ on T for the range of the parameters outside the restrictions in (28) is still greatly simplified (compared to that given by (23), (27a)) for the particular situation of overdamped motion in a symmetric double-well potential,

$$U(q) = U(-q) , \quad 2\Gamma \gg (U'')^{1/2}$$
$$(U'' \equiv U''(q_{1,2})) . \tag{30}$$

In this case, for sufficiently small frequencies,

$$\rho = (\pi A^2/4T)(f^2U''^2 + \Omega^2)/(fU''^2 + 2\Gamma\Omega^2) ,$$
$$f = (q_2 - q_1)^2 W/4T ,$$
$$\Omega, W, [T/2\Gamma(q_2 - q_1)^2] \ll U''/2\Gamma , \tag{31}$$

For the same model, and in the same range of parameters, the phase shift between the signal $\langle q(t) \rangle$ and the driving force

$$\phi = -\arctan[(\Omega/U'')$$
$$\times (fU''^2 + 2\Gamma\Omega^2)/(fWU'' + \Omega^2)] . \tag{32}$$

According to (31) the signal-to-noise ratio is minimal for the value of T given by the expression $fU'' \cong \Omega$, and it increases rapidly for higher T(cf. (28)). The maximum of ρ vs. T is reached in the region $T \sim \Delta U$, which is not described by the above analytic expressions for $Q(\omega)$, $\chi(\omega)$, but is still described by the fluctuation–dissipation relations.

It is evident from (32) that the phase shift also displays an SR-type behaviour [50]. From physical intuition, we may expect ϕ to provide a measure of the extent to which the external field is absorbed by the system. For very small noise, where the interwell transitions do not come into play, it follows from (32) that $|\phi| = 2\Gamma\Omega/U''$ is also very small: intrawell absorption of a low-frequency field is weak (the absorption band is broad, with the width $U''/2\Gamma \gg \Omega$). The increase of $|\phi|$ with T starts, however, for quite small T where ρ is still decreasing; $|\phi|$ reaches its maximum value when $T = T_{max}$ is still small compared with ΔU:

$$(-\phi)_{max} = \arctan(\tfrac{1}{2}[(q_2 - q_1)^2 U''/4T_{max}]^{1/2}) ,$$
$$W(T_{max}) = \Omega[4T_{max}/(q_2 - q_1)^2 U'']^{1/2} . \tag{33}$$

It can be seen from (33) that $|\phi|_{max}$ is quite large, i.e., there then is a strong absorption of the periodic field. This absorption is due primarily to the interwell transitions. We note that the absorption coefficient itself, which is proportional to Im $\chi(\Omega)$, also displays an SR-type behaviour. Both $|\phi|$ and Im $\chi(\Omega)$ are much steeper on the small-T side of their maxima, because it is the activation dependence of the transition probabilities on T that determines the behaviour of $\chi(\Omega)$ in this range.

The stochastic-resonance-like dependence of the phase shift upon noise intensity has been clearly demonstrated in analogue electronic experiments [50]. Some data for an overdamped

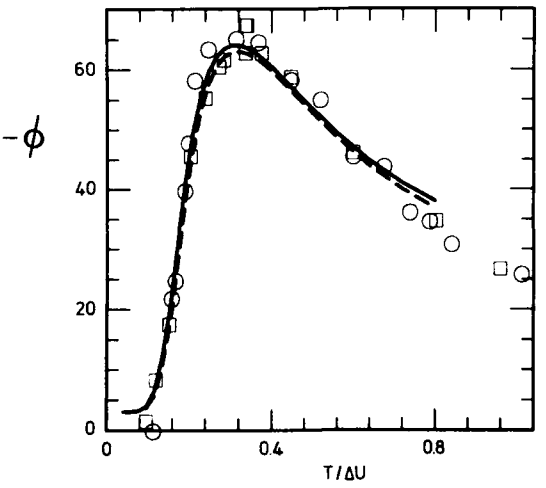

Fig. 11. The phase shift $-\phi$ (degrees) between the weak periodic force $A \cos \Omega t$ and the averaged coordinate $\langle q(t) \rangle$, measured for an electronic model of the overdamped oscillator described by (1), (24), (3) with $\Omega = 0.1$ for $A/2\Gamma = 0.04$ (circle data points) and $A/2\Gamma = 0.2$ (squares). The dashed curve represents the simple linear response prediction (31); the full curve takes account of nonlinear corrections for $A/2\Gamma = 0.04$ [50].

oscillator with the potential (24) are shown in fig. 11. The simple expression (31) is evidently in excellent agreement with the experimental data (the prefactor in the expression (12) for the transition probability of an overdamped system was taken to be of the standard form [29]); the comparison of theory with experiment does not involve any adjustable parameters.

4.2. Nonlinear effects

One of the more intriguing features of the response of a bistable system to a low-frequency field (the effects for high-frequency fields will be considered below) is the possibility of observing strongly nonlinear effects, even for small field amplitudes A. Such a possibility arises because the field-induced modulation of the populations of the attractors comes about primarily through a modulation of the activation energies of fluctuational transitions; and the effect of the latter modulation is enhanced exponentially, because it is with the small noise intensity that this modulation should be compared (cf. (12)). It is seen from the expressions (15) that the parameter g describing the redistribution over the attractors is of the form

$$g = \frac{A}{D}\left|\frac{\partial}{\partial A}[R_1(A) - R_2(A)]\right|_{A=0}. \tag{34}$$

Here, $R_i(A)$ is the activation energy of the transition from the state i for the initial system driven additionally by a weak force A, and the derivatives are calculated for $A = 0$ (see [10a]; the importance of a parameter of this kind was also recognised recently in [11]). The variation of R_1, R_2 under the weak force A is assumed small: accordingly, only terms of the first order in A will be taken into account in $R_i(A)$.

In considering nonlinear effects we shall assume the field $A\cos(\Omega t)$ to be slowly varying, $\Omega \ll U''/2\Gamma, \Gamma$ (cf. (31)), so that the transition probabilities can be considered in the adiabatic approximation. In this case their values depend on the instantaneous value of the field as they would if it were a fixed parameter. Then according to (12) the instantaneous transition probability $\tilde{W}_{ij}(t)$ is given by the expression

$$\tilde{W}_{ij}(t) = W_{ij}\sum_{k=-\infty}^{\infty} I_k(g_i)\exp(ik\Omega t),$$

$$g_i = -\frac{A}{D}\left(\frac{\partial R_i}{\partial A}\right)_{A=0}, \tag{35}$$

where W_{ij} are the values of the transition probabilities in the absence of the field, i.e., for $A = 0$; I_k are modified Bessel functions [53]. The periodic dependence of the transition probabilities on time, which is strongly nonsinusoidal for $|g_i| > 1$, gives rise to the nonsinusoidal time dependence of the instantaneous state populations $\tilde{w}_{1,2}(t)$. Eqs. (14), (35) result in the following set of linear algebraic equations for the Fourier components $\tilde{w}_{1k}$:

$$\tilde{w}_1(t) = \sum_{k=-\infty}^{\infty}\tilde{w}_{1k}\exp(ik\Omega t),$$

$$[ik\Omega + W_{12}I_0(g_1) + W_{21}I_0(g_2)]\tilde{w}_{1k} + \sum_{s\neq 0}[W_{12}I_s(g_1) + W_{21}I_s(g_2)]\tilde{w}_{1k-s} = W_{21}I_k(g_2). \tag{36}$$

It is straightforward to express the amplitudes $a(k)$ and phases $\phi(k)$ of the forced vibrations of the system (cf. eq. (19)) in terms of $\tilde{w}_{1k}$. For $k > 1$,

$$a(k) = 2|(q_1 - q_2)\tilde{w}_{1k}|,$$

$$\phi(k) = \arg[(q_1 - q_2)\tilde{w}_{1k}] \quad (k > 1), \tag{37}$$

while the expressions for $a(1)$, $\phi(1)$ are of the form (22) with the susceptibility $\chi(\Omega)$ having been replaced by $\tilde{\chi}(\Omega)$:

$$\tilde{\chi}(\Omega) = \tilde{w}_{10}\chi_1(\Omega) + (1 - \tilde{w}_{10})\chi_2(\omega) + 2A^{-1}w_{11}^*(q_1 - q_2). \tag{38}$$

Eqs. (35)–(38) make it straightforward to com-

pute the response to a slowly varying field for arbitrary nonlinearity. They obviously go over into the results of linear-response theory in the limit of weak field where $|g_{1,2}| \ll 1$.

The extreme nonlinear case $|g_{1,2}| \gg 1$ can be also analysed analytically, by application of a quite different approach [10a]. In this case inter-well transitions from the state i, for example, happen, with an overwhelming probability during that part of the period of the driving field $2\pi/\Omega$ where the activation energy $R_i(A)$ is minimal, i.e., the field works as a shutter (we stress that the field itself is weak; this is not a deterministic, but a probabilistic shutter). As a result, the average signal at the output will be rectangular. In particular, in the case of Brownian motion in a symmetric double-well potential (30) in the neglect of intrawell contributions,

$$\langle q(t)\rangle = 2\bar{q}\sum_{n=-\infty}^{\infty}\left[\Theta\left(t-\frac{2\pi n}{\Omega}\right) - \Theta\left(t-\frac{\pi(2n+1)}{\Omega}\right)\right] - \bar{q}\,,$$

$$\bar{q} = -q_1 \tanh \bar{g}\,,$$

$$\bar{g} = \left(\frac{2\pi T}{|Aq_1|}\right)^{1/2}\frac{W_{12}}{2\Omega}\exp(|Aq_1|/T)\,, \qquad (39)$$

where $\Theta(t)$ is the unit step-function. We note that the "amplitude" $\bar{q}$ of the rectangular wave (39) saturates quite quickly as a function of $\bar{g}$ (starting with $\bar{g} \gtrsim 1.5$), and therefore the intensities of the spectral peaks in the SDF $S(\omega)$ as defined by (4a) depend only weakly on the field amplitude A.

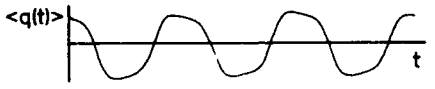

Fig. 12. The averaged coordinate $\langle q(t)\rangle$ measured for an electronic model [50] of the overdamped oscillator (1), (24), (30), driven by a periodic force $A\cos\Omega t$ with $A/2\Gamma = 0.1$, $T/2\Gamma = 0.0644$, for a very low frequency $\Omega = 1.9\times10^{-5}$. As predicted theoretically (39), the result approximates a square wave. Its tops and bottoms are curved due to intra-well vibrations, and tilted due to the phase shift between the latter and the inter-well transitions.

The nearly rectangular signal under sinusoidal driving by a slowly varying field has been observed in an analogue electronic experiment [50]. The result is shown in fig. 12. The distortion of the signal is related to the contribution of the forced intrawell vibrations. We stress that the periodic driving force was itself comparatively weak, so that the nonlinearity of this effect is indeed quite remarkably strong.

4.3. *"Nonconventional" stochastic resonance*

Until recently, stochastic resonance was considered purely as an effect that arises for Brownian motion in a static bistable potential with a superimposed slowly varying field (cf. [5–12, 50, 52]). It follows from the above formulation, however, that it is actually a quite general phenomenon for fluctuating bistable systems in the range of a kinetic phase transition. Consequently, it may also be expected to occur for systems displaying bistability under strong periodic driving [46] (the onset of a large susceptibility with respect to an additional weak trial field was predicted for systems of just this kind in [4]). In this latter case SR will be inherent to the response, not only to a low-frequency, but also to a high-frequency field [54]. Also, since bistable systems are strongly nonlinear, periodic driving of various parameters (not only of their coordinates or momenta) can also give rise to a periodic signal (i.e. to periodic variation of the coordinate), and in some cases this signal can display a dome-like dependence on the noise intensity. One such parameter could be the noise intensity itself [55]. The results for these two new types of SR are described briefly below.

First, we consider high frequency stochastic resonance for periodic attractors. As pointed out above, the onset of SR is related to a comparatively strong noise-enhanced modulation of the populations of the attractors $\tilde{w}_1(t)$, $\tilde{w}_2(t)$ by a trial field. Since the characteristic time-scale for the variation of the populations is given by the reciprocal transition probabilities, the modula-

tion can be effective provided it is slow. A feature of nonlinear systems is that they perform mixing of the frequencies of external fields. Therefore, if a system is driven by a (strong) field $F\cos(\omega_F t + \phi_F)$ and a (weak) trial field $A\cos(\Omega t)$ then the variables of the system will oscillate at combination frequencies $|\pm n\omega_F + \Omega$ $(n = 0, 1, 2, \ldots)$ and thus if one of these is small the corresponding oscillations can give rise to effective redistribution over the attractors.

The simplest case is just $|\omega_F - \Omega| \ll \tau_{rel}^{-1}$. The dynamics of the system in this case can be considered as that in the strong field $\mathrm{Re}[F(t)\exp(i\omega_F t + i\phi_F)]$, but with the complex amplitude $F(t)$ slowly varying in time,

$$F(t) = F + A\exp[i(\Omega - \omega_F)t - i\phi_F]\,. \tag{40}$$

The activation energies $R_{1,2}$ of the transitions between the attractors depend on F (strictly, on F^2, since they are determined by the intensity rather than by the fast oscillating phase of the field). For small $|\Omega - \omega_F|$, they get modulated at frequency $|\Omega - \omega_F|$ and, for a sufficiently weak trial field, R_i in the expression (12) should be replaced by $\tilde{R}_i(t)$,

$$\tilde{R}_i(t) = R_i + \frac{\partial R_i}{\partial F^2}\,2AF\cos[(\Omega - \omega_F)t - \phi_F]\,. \tag{41}$$

The further analysis of the redistribution over the attractors is closely similar to that in the preceding subsection. It should be stressed, however, that the modulation of the populations of the attractors at frequency $|\Omega - \omega_F|$ gives rise to periodic oscillations, not only at the trial-field frequency Ω, but also at the mirror-reflected frequency $|2\omega_F - \Omega|$. For small A, where the linear-response approximation holds, the trial-field-induced addition to the average value of the coordinate is of the form

$$\delta\langle q(t)\rangle = A\,\mathrm{Re}\{\chi(\Omega)\exp(-i\Omega t) + \bar{\chi}(\Omega) \times \exp[-i(2\omega_F - \Omega)t]\}\,. \tag{42}$$

In the case of weak noise, the susceptibilities $\chi(\Omega)$, $\bar{\chi}(\Omega)$ can be written in the form (26), and the transition-induced contributions are of the form

$$\chi_{tr}(\Omega) = \frac{2F}{D}\,w_1 w_2[q_1^*(1) - q_2^*(1)] \times \frac{\partial(R_1 - R_2)}{\partial F^2}\,\frac{W}{W - i(\Omega - \omega_F)}\,,$$

$$\bar{\chi}_{tr}(\Omega) = \chi_{tr}(2\omega_F - \Omega)\exp(-2i\phi_F)\,. \tag{43}$$

Both of them display SR.

High-frequency stochastic resonance (HFSR) of this type has been observed for periodic attractors in analogue electronic experiments [54]. The system simulated was the one already discussed above in section 3: an underdamped nonlinear oscillator with a single-well potential given by eq. (7) with $\lambda = 0$, which has two types of coexisting vibrational states under a sufficiently strong nearly resonant field. When the oscillator was driven, in addition, by a trial field of frequency $\Omega \cong \omega_F$ there occurred two clearly resolved extra δ-shaped spikes in the SDF of the coordinate $S(\omega)$. The dependence of the intensity of these spikes on the noise intensity can be seen from fig. 13 to be just of the SR-type. The theoretical curves are based on measured values of the activation energies of the transitions (cf. fig. 9); the experimental uncertainty arising from the latter data is shown by the bars. Given the large systematic errors inherent in these measurements – arising e.g. from β (17) which contains the small difference between two large quantities $|\omega_F - \omega_0|$ raised to its third power – the agreement can be regarded as very satisfactory; in particular, the theoretical and experimental curves are of a similar shape, and their maxima lie at nearly the same T. Fig. 14 demonstrates that high-frequency SR is a purely critical phenomenon: the intensities of the spikes decrease exponentially as the control parameter β (17) moves away from its critical value. We note that these experiments are quite delicate, since an extremely high resolution is necessary to

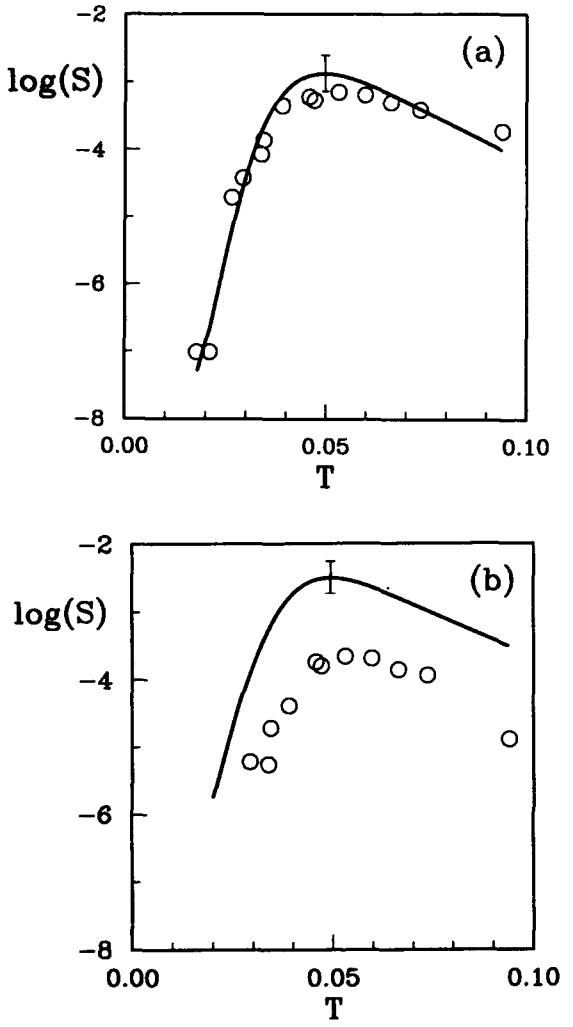

Fig. 13. High frequency stochastic resonance for periodic attractors, measured for an electronic model of the oscillator described by (1), (7) with $\lambda = 0$, driven by a strong periodic field $F\cos(\omega_F t + \phi_F)$ and a weak trial force $A\cos\Omega t$ [54]. The logarithms of the intensities S of the δ-shaped spikes in the spectral density of the fluctuations (a) at frequency Ω and (b) at $2\omega_F - \Omega$ are plotted (data points) as a function of the noise intensity T. The curves are theoretical predictions based on *measured* values of the activation energies; they are subject to the systematic uncertainties indicated by the bars. There are no adjustable parameters.

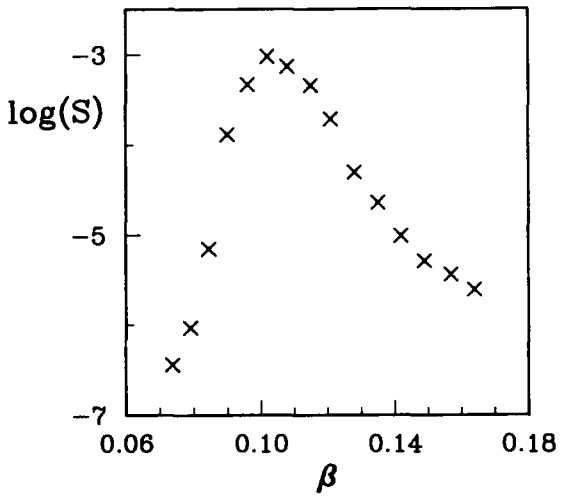

Fig. 14. The logarithm of the intensity S of the δ-shaped spike at frequency Ω in the spectral density of the fluctuations for high-frequency stochastic resonance [54], plotted as a function of the dimensionless field intensity β (17) which gives a measure of the distance from the kinetic phase transition line.

observe and investigate the peaks, given that they must be separated by a frequency difference much smaller than the reciprocal relaxation time which, in its turn, is much smaller than the frequencies ω_F, Ω themselves.

The second nonconventional form of SR refers to physical situations where the noise and signal acting upon a system are not additive, but multiplicative: it is noise (or noise intensity) that is modulated directly by the signal, and it may be such a periodically modulated noise that drives the system itself. If the initial noise is of zero mean, the driving field will also be of zero mean. Nonetheless, a nonlinear system can still detect the modulating signal via nonlinear transformations. It is demonstrated below that, for bistable systems, the quality of detection may increase with increasing noise intensity and display an SR-type behaviour.

We shall consider SR in the response to modulated noise for the simplest bistable system: an overdamped particle oscillating in a bistable potential and described by the equation

$$2\Gamma\dot{q} + U'(q) = \xi(t)\,,$$
$$\xi(t) = [\tfrac{1}{2}A\cos(\Omega t) + 1]f(t)\,,$$
$$U(q) = -\tfrac{1}{2}q^2 + \tfrac{1}{4}q^4 + \lambda q\,,$$
$$\langle f(t)\, f(t')\rangle = 4\Gamma T\delta(t - t')\,. \qquad (44)$$

In contrast to the former analysis it is the amplitude of the noise that is assumed to be

periodically modulated here; the potential is assumed to be asymmetric, with the asymmetry parameter λ (the asymmetry turns out to be crucial for obtaining a well-pronounced SR).

If the amplitude A is sufficiently weak, we can characterise the response of the system to the corresponding modulation in terms of a generalised susceptibility $\aleph(\omega)$ and write the signal-induced term in the average value of the coordinate as

$$\delta\langle q(t)\rangle = A\,\mathrm{Re}[\aleph(\Omega)\exp(-\mathrm{i}\Omega t)]\,. \tag{45}$$

For weak noise intensities and for a slowly varying field, $\Omega \ll U''/2\Gamma$, the function $\aleph(\Omega)$ (just as for the "normal" susceptibility $\chi(\Omega)$) is a sum of contributions from the vibrations in the vicinities of the stable states q_1, q_2 and from the interwell transitions (cf. (26)):

$$\aleph(\Omega) = \sum_{i=1,2} w_i \aleph_i(\Omega) + \aleph_{\mathrm{tr}}(\Omega)\,. \tag{46}$$

The contribution from the interwell transitions, which is the one of primary interest, originates from the fact that the transition probabilities depend on the instantaneous value of the noise intensity (it varies slowly because of the modulation) and, provided that the potential is asymmetric so that $W_{12} \neq W_{21}$, the periodic variation of W_{ij} gives rise to a periodic change of the state populations; for a symmetric potential, the variation of the noise intensity does not break the symmetry, and so the populations remain equal. The resulting expression for $\aleph_{\mathrm{tr}}(\Omega)$ is of the form [55]

$$\aleph_{\mathrm{tr}}(\Omega) = -\frac{1}{T}\,\frac{(q_1 - q_2)(\Delta U_1 - \Delta U_2)w_1 w_2 W}{(W - \mathrm{i}\Omega)}\,. \tag{47}$$

Thus, a periodic signal will indeed occur under driving by a zero-mean periodically modulated noise for an *asymmetric* potential ($\Delta U_1 \neq \Delta U_2$); furthermore, the amplitude of the signal $|\aleph_{\mathrm{tr}}(\Omega)|$ is seen from (47) to increase sharply with the increasing noise intensity T.

The dependence of the signal-to-noise ratio, defined by analogy to (21) as the ratio of the δ-shaped spike in the SDF $S(\omega)$ at frequency Ω to the value of $S(\Omega) = Q(\Omega)$ in the absence of modulation, is shown in fig. 15: the theoretical prediction is compared with the results from an analogue electronic experiment (the lower full curve and square data points, respectively). The phenomenon of stochastic resonance is clearly evident in this situation, although slightly less pronounced than for "conventional" periodic driving (upper curve and circle data), i.e. driving the system rather than the noise. It is evident from the lower curve and data of fig. 16 that this type of SR is intimately connected with the asymmetry of the potential (44), i.e. with the finiteness of the parameter λ; for $\lambda = 0$ the signal could not be detected. At the opposite extreme for very strong asymmetry, there will again be no SR because in practice only one well will be populated for weak noise and the interwell tran-

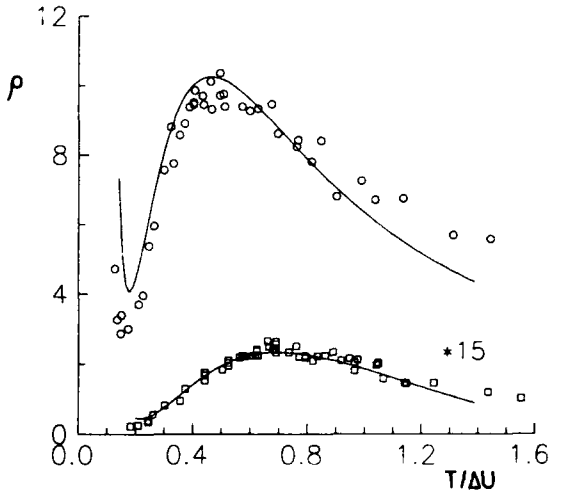

Fig. 15. Stochastic resonance for periodically modulated noise [55]. Measurements (×15) of the signal/noise ratio ρ defined by (21) for an electronic circuit model of (44) with $A = 0.14$, $\lambda = 0.2$, $\Omega = 0.029$ are plotted (data points) as a function of the reduced noise intensity $\Delta U = 1/4$; the full curve represents the theoretical prediction. The upper curve and circle data show the theory and measurements using the same circuit with *additive* periodic forcing (conventional stochastic resonance) under similar conditions (theoretical results are valid for $T \ll \Delta U_{1,2}$, strictly speaking).

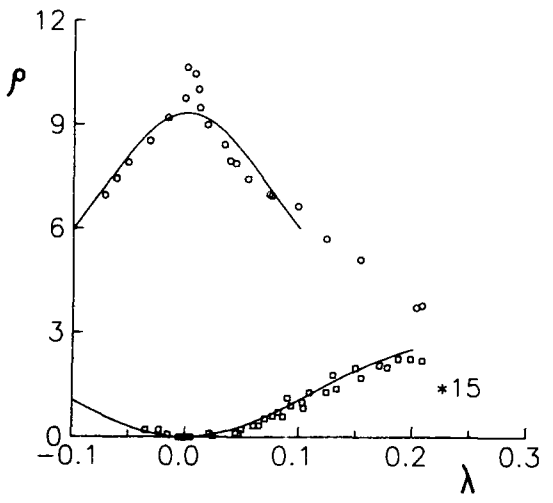

Fig. 16. Effect of the asymmetry parameter λ on stochastic resonance [55]. Measurements (×15) of the signal/noise ratio ρ defined by (21) for an electronic circuit model of (44) with $A = 0.15$, $(T/\Delta U)_{\lambda=0} = 0.303$, $\Omega = 0.029$ are plotted (square data points) as a function of λ; the full curve represents the theoretical prediction. The upper curve and circle data show the theory and measurements using the same circuit with *additive* periodic forcing (conventional stochastic resonance) under similar conditions.

sitions will be "frozen out". Therefore, in order to investigate SR under these conditions, it is necessary to optimise the asymmetry of the system.

5. Conclusions

It follows from the above results that the traditional field of noise-driven dynamics and, in particular, investigations of the spectral densities of fluctuations of noise-driven systems, is far from being exhausted. There still arise new and unexpected phenomena like the noise-induced narrowing of spectral peaks, the onset of extra peaks such as the zero-dispersion and supernarrow ones, and also stochastic resonance. All of these phenomena are very general. They are not "pinned" to particular models, and thus they are of fundamental interest. At the same time, they are also rich in potential applications, ranging from solid state physics, through electrons localised in Penning traps, to neurons and neural networks, as mentioned above. There still remain a number of significant problems that have not been solved, or even addressed. Many of these are related to the interplay of dynamical chaos and noise. We hope, therefore, that these investigations will continue, and that our understanding of noise-driven nonlinear dynamics will thereby be substantially enriched.

Acknowledgements

It is our great pleasure to acknowledge our indebtedness to those people in immediate collaboration with whom the above ideas have been worked out and the results obtained. These are the late M.A. Krivoglaz, D.G. Luchinsky, R. Mannella, S.M. Soskin, N.D. Stein and N.G. Stocks. The work has been supported by the Science and Engineering Research Council (UK).

References

[1] L.D. Landau and E.M. Lifshitz, Statistical Physics, 3rd ed. (Pergamon, New York, 1980), Part 1, revised by E.M. Lifshitz and L.P. Pitaevskii.
[2] A.S. Barker Jr. and A.J. Sievers, Rev. Mod. Phys. 47 Suppl. No. 2 (1975) S1.
[3] S.M. Soskin, Physica A 155 (1989) 401.
[4] (a) M.I. Dykman and M.A. Krivoglaz, Zh. Eksp. Teor. Phys. 77 (1979) 60 [Sov. Phys. JETP 50 (1979) 30]; (b) in: Soviet Physics Reviews, ed. I.M. Khalatnikov (Harwood, New York, 1984) Vol. 5, p. 265.
[5] R. Benzi, A. Sutera and A. Vulpiani, J. Phys. A 14 (1981) L453; R. Benzi, G. Parisi, A. Sutera and A. Vulpiani, Tellus 34 (1982) 10.
[6] C. Nicolis, Tellus 34 (1982) 1.
[7] B. McNamara, K. Wiesenfeld and R. Roy, Phys. Rev. Lett. 60 (1988) 2626.
[8] M.I. Dykman, A.L. Velikovich, G.P. Golubev, D.G. Luchinsky and S.V. Tsuprikov, JETP Lett. 53 (1991) 193.
[9] S. Fauve and F. Heslot, Phys. Lett. A 97 (1983) 5; L. Gammaitoni, F. Marchesoni, E. Menichella-Saetta and S. Santucci, Phys. Rev. Lett. 62 (1989) 349; G. Debnath, T. Zhou and F. Moss, Phys. Rev. A 39 (1989) 4323.

[10] (a) M.I. Dykman, P.V.E. McClintock, R. Mannella and N.G. Stocks, JETP Lett. 52 (1990) 141; (b) M.I. Dykman, R. Manella, P.V.E. McClintock and N.G. Stocks, Phys. Rev. Lett. 65 (1990) 2606.
[11] T. Zhou, F. Moss and P. Jung, Phys. Rev. A 42 (1990) 3161.
[12] A. Longtin, A. Bulsara and F. Moss, Phys. Rev. Lett. 67 (1991) 656.
[13] J.B. Morton and S. Corssin, J. Stat. Phys. 2 (1970) 153.
[14] M.A. Krivoglaz and I.P. Pinkevich, Ukr. Fiz. Zh. 15 (1970) 2039; Y. Onodera, Prog. Theor. Phys. 44 (1970) 1477.
[15] M.I. Dykman and M.A. Krivoglaz, Phys. Stat. Sol. (b) 48 (1971) 497.
[16] K. Sture, J. Nordholm and R. Zwanzig, J. Stat. Phys. 11 (1974) 143.
[17] R.F. Rodriguez and N.G. van Kampen, Physica A 85 (1976) 347.
[18] S.H. Crandall, in: Random Vibrations, ed. S.H. Crandall (MIT Press, Cambridge, MA, 1963), Vol. 2, p. 85.
[19] A.B. Budgor, K. Lindenberg and K.E. Shuler, J. Stat. Phys. 15 (1976) 375; A.R. Bulsara, K. Lindenberg and K.E. Shuler, J. Stat. Phys. 27 (1982) 787.
[20] M.I. Dykman and M.A. Krivoglaz, Physica A 104 (1980) 495.
[21] B. Carmeli and A. Nitzan, Phys. Rev. A 32 (1985) 2439.
[22] W. Renz, Z. Phys. B 59 (1985) 91; L. Fronzoni, P. Grigolini, R. Mannella and B. Zambon, J. Stat. Phys. 41 (1985) 553; Phys. Rev. A 34 (1986) 3293; W. Renz and F. Marchesoni, Phys. Lett. A 112 (1985) 124.
[23] J.J. Brey, J.M. Casado and M. Morillo, Physica A 123 (1989) 481.
[24] M.I. Dykman, R. Mannella, P.V.E. McClintock, F. Moss and S.M. Soskin, Phys. Rev. A 37 (1988) 1303.
[25] H. Risken, The Fokker–Planck Equation, 2nd ed. (Springer, Berlin, 1989).
[26] M.A. Ivanov, L.B. Kvashnina and M.A. Krivoglaz, Fiz. Tverd. Tela 7 (1965) 2047 [Soviet Phys. – Solid State 7 (1965) 1652].
[27] M.I. Dykman, R. Mannella, P.V.E. McClintock, S.M. Soskin and N.G. Stocks, Phys. Rev. A 42 (1990) 7041.
[28] B.P. Clayman, Phys. Rev. B 3 (1971) 2813.
[29] H.A. Kramers, Physica 7 (1940) 284.
[30] N.G. Stocks, P.V.E. McClintock and S.M. Soskin, Phys. Rev. A (1992).
[31] S.M. Soskin, Physica A 180 (1992) 386.
[32] R.J. Elliott, W. Hayes. G.D. Jones, H.F. McDonald and C.T. Sennett, Proc. R. Soc. A 289 (1965) 1.
[33] M.I. Dykman and M.A. Krivoglaz, Ukr. Fiz. Zh. 17 (1972) 1971.
[34] M.I. Dykman, R. Mannella, P.V.E. McClintock, S.M. Soskin and N.G. Stocks, Phys. Rev. A 43 (1991) 1701.
[35] M.A. Krivoglaz and I.P. Pinkevich, Zh. Eksp. Teor. Fiz. 51 (1966) 1151 [Sov. Phys. – JETP 24 (1966) 772].
[36] G. Gabrielse, H. Dehmelt and W. Kells, Phys. Rev. Lett. 54 (1985) 537.
[37] J.F. Luciani and A.D. Verga, Europhys. Lett. 4 (1987) 255; J. Stat. Phys. 50 (1988) 567.
[38] A.J. Bray and A.J. McKane, Phys. Rev. Lett. 62 (1989) 493; A.J. McKane, Phys. Rev. A 40 (1989) 4050; A.J. McKane, H.C. Luckock and A.J. Bray, Phys. Rev. A 41 (1990) 644.
[39] M.M. Klosek-Dygas, B.J. Matkowsky and Z. Schuss, SIAM J. Appl. Math. 48 (1988) 425; J. Stat. Phys. 54 (1989) 1309.
[40] H.S. Wio, P. Colet, M. San Miguel, L. Pesquera and M.A. Rodriguez, Phys. Rev. A 40 (1989) 7312.
[41] M.I. Dykman, Phys. Rev. A 42 (1990) 2020; M.I. Dykman, P.V.E. McClintock, N.D. Stein and N.G. Stocks, Phvs. Rev. Lett. 67 (1991) 933.
[42] M.I. Dykman, M.A. Krivoglaz and S.M. Soskin, in: Noise in Nonlinear Dynamical Systems, eds. F. Moss and P.V.E. McClintock (Cambridge Univ. Press, Cambridge, 1989) Vol. 2, p. 347.
[43] M.R. Beasley, D. D'Humieres and B.A. Huberman, Phys. Rev. Lett. 50 (1983) 1328.
[44] P. Hanggi and H. Thomas, Phys. Rep. 88 (1982) 207.
[45] F.T. Arecchi and F. Lisi, Phys. Rev. Lett. 49 (1982) 94; 50 (1983) 1330; R.F. Voss, Phys. Rev. Lett. 50 (1983) 1329; F.T. Arecchi, R. Badii and A. Politi, Phys. Rev. A 32 (1985) 402; F.T. Arecchi and A. Califano, Europhys. Lett. 3 (1987) 5.
[46] M.I. Dykman, R. Mannella, P.V.E. McClintock and N.G. Stocks, Phys. Rev. Lett. 65 (1990) 48.
[47] N.G. Stocks, N.D. Stein and P.V.E. McClintock, Stochastic resonance in monostable systems, submitted to Phys. Rev. Lett.
[48] Hu Gang, G. Nicolis and C. Nicolis, Phys. Rev. A 42 (1990) 2030.
[49] R. Kubo, J. Phys. Soc. Jpn. 12 (1957) 570.
[50] M.I. Dykman, R. Mannella, P.V.E. McClintock and N.G. Stocks, Phys. Rev. Lett. 68 (1992) 2985; and to be published.
[51] P.V.E. McClintock and F. Moss, in: Noise in Nonlinear Dynamical Systems, eds. F. Moss and P.V.E. McClintock, (Cambridge, Univ. Press, Cambridge, 1989), vol. 3, p. 243.
[52] B. McNamara and K. Wiesenfeld, Phys. Rev. A 39 (1989) 4854.
[53] M. Abramovitz and I. Stegun, eds., Handbook of Mathematical Functions (Dover, New York, 1970).
[54] M.I. Dykman, R. Mannella, P.V.E. McClintock, N.D. Stein and N.G. Stocks, High-frequency stochastic resonance for periodic attractors, to be published.
[55] M.I. Dykman, D.G. Luchinsky, P.V.E. McClintock, N.D. Stein and N.G. Stocks, Stochastic resonance for periodically modulated noise intensity, submitted to Phys. Rev. A.

Physica D 58 (1992) 31–49
North-Holland

PHYSICA D

Distinguishing between low-dimensional dynamics and randomness in measured time series

A. Provenzale[a], L.A. Smith[b], R. Vio[c] and G. Murante[a]

[a]*Istituto di Cosmogeofisica del CNR, Corso Fiume 4, I-10133 Turin, Italy*
[b]*Department of Engineering, Warwick University, Coventry CV4 7AL, UK*
[c]*Dipartimento di Astronomia, Università di Padova, V.lo Dell'Osservatorio 5, I-35122 Padua, Italy*

Received 5 November 1991
Revised manuscript received 2 March 1992
Accepted 2 March 1992

The success of current attempts to distinguish between low-dimensional chaos and random behavior in a time series of observations is considered. First we discuss stationary stochastic processes which produce finite numerical estimates of the correlation dimension and K_2 entropy under naive application of correlation integral methods. We then consider several straightforward tests to evaluate whether correlation integral methods reflect the global geometry or the local fractal structure of the trajectory. This determines whether the methods are applicable to a given series; if they are we evaluate the significance of a particular result, for example, by considering the results of the analysis of stochastic signals with statistical properties similar to those of observed series. From the examples considered, it is clear that the correlation integral should not be used in isolation, but as one of a collection of tools to distinguish chaos from stochasticity.

1. Introduction

In the past ten years, a variety of methods to extract phase space dynamical information from experimentally observed or computer generated time series have been developed, see e.g. refs. [1–28]. These methods are generally based on a phase space reconstruction (typically a "time embedding" procedure, see refs. [22, 29]) and are devoted to the calculation of the properties of a (supposed) underlying attractor (such as the correlation dimension [12, 14, 20, 23, 25], the K_2 entropy [13] and the Lyapunov exponents [1, 9, 18, 28]), to the determination of the approximate number of the (empirical) modes excited in the system through singular value decomposition (SVD) [3], to the issue of predicting the future evolution of the system from the knowledge of its past, in a spirit which is the extension of classical autoregressive (AR) approaches [5, 10, 11, 21, 30], or even toward reconstructing the equations of motion of the system [7, 10].

The "static" methods based on the correlation integral [12–14, 24, 25] differ from prediction methods in that the former do not explicitly take into account information from the ordering of the points in the time series. The methods mentioned above provide information on systems which are known to be dominated by low-dimensional deterministic dynamics and there exists a noticeable difference in the results from low-dimensional chaotic systems and uncorrelated (white) noise. Applications to well-controlled laboratory experiments have led to determining the presence of low-dimensional chaos in several experimental contexts, see e.g. refs. [31–33]; note that these systems were characterized by a limited degree of space complexity and by the ability to adjust control parameters.

The situation turns out to be much more com-

0167-2789/92/$05.00 © 1992 – Elsevier Science Publishers B.V. All rights reserved

plicated for natural (uncontrolled) systems, see e.g. refs. [34–46], where claims and counterclaims for low-dimensional attractors coexist for the same data, as well as for systems dominated by the presence of "colored" noises with power-law power spectra [43, 47–49] or for non-linear stochastic processes [27]. In this paper we briefly review some of the problems encountered in the study of systems characterized by the presence of correlated stochastic processes and we discuss a few simple tests which can be of use in the attempt of distinguishing between low-dimensional (dissipative) determinism and stochastic noise.

2. Behavior of correlated noises

The majority of quantitative attempts to detect low-dimensional attractors from time series data have focused on the estimation of the correlation dimension and of the correlation entropy K_2. Given a scalar time series $x(t_i)$, the first step in the analysis is to employ an embedding procedure to reconstruct the system phase space. Here we consider the method of delays [22, 29], where a vector time series is defined as

$$\boldsymbol{x}(t_i) = \{x(t_i), x(t_i + \tau), \ldots, x(t_i + (M-1)\tau)\} . \tag{2.1}$$

Here $\tau = m\,\Delta t$ is an appropriate time delay, Δt is the effective sampling time and M is the dimension of the vector $\boldsymbol{x}(t_i)$. Recent discussions of embedology are given in refs. [6, 19]. The crucial idea underlying the embedding procedure (2.1) is that the observed variable $x(t)$ contains information on all the other phase space variables of the system. In the case of weakly coupled phase space variables, however, the above method may lead to misleading results [40]. Note that the choice of the time delay τ is somewhat arbitrary [17, 50]; there may not even be a unique good selection criterion for this parameter [15].

The correlation integral $C_M(r)$ of the reconstruction is defined as [12]

$$C_M(r) = \frac{1}{N'^2} \sum_{i,j}^{N'} \theta\{r - \|\boldsymbol{x}(t_i) - \boldsymbol{x}(t_j)\|\} , \tag{2.2}$$

where θ is the Heaviside step function, N is the number of points in the time series, $N' = N - m(M-1)$ and the vertical bars indicate the norm of the vector. Efficient implementations of (2.2) are available [14, 24] and a clear overview of the analysis is presented in ref. [25]. One is then interested in the scaling properties of the correlation integral, in particular whether $C_M(r)$ is a power-law at small scales, that is

$$C_M(r) \underset{N\to\infty,\, r\to 0}{\sim} r^{\nu_M} , \tag{2.3}$$

where we have ignored any effects due to lacunarity [2, 51]. If (2.3) holds, the next step is to examine the behavior of the estimated correlation exponent ν_M with increasing M. For point distributions with a low-dimensional geometry, one may show that at sufficiently large M [6, 8, 12]

$$\nu_M \to \nu , \tag{2.4}$$

where ν is the correlation dimension; for *deterministic* dynamical systems, this quantity provides an estimate of the number of degrees of freedom excited in the system. We stress that eqs. (2.3) and (2.4) assume a very large data set and that the results should be independent of τ over an appropriate range of values.

The K_2 entropy [13] may be estimated from the correlation integrals $C_M(r)$. This is computed (in the limit as $M \to \infty$) as the distance between two successive correlation integrals in log–log coordinates. Specifically

$$\frac{1}{\Delta t} \log \frac{C_M(r)}{C_{M+1}(r)} \underset{r\to 0}{\sim} K_2(M) \tag{2.5}$$

and then

$$K_2(M) \underset{M\to\infty}{\sim} K_2 . \tag{2.6}$$

The K_2 entropy is zero for periodic or quasi-periodic systems, it is positive for chaotic systems and diverges for a white noise. Since low-dimensional strange attractors *do* produce a small and usually non-integer value of the correlation dimension and a converging K_2 entropy, the above statements have on occasion been reversed and a finite, small value of the correlation dimension and a converging K_2 entropy have been taken as "proof" of the presence of a strange attractor. As a counterexample to this belief, Osborne and Provenzale [47], and Provenzale et al. [48] have shown that simple stochastic processes, characterized by a power-law power spectrum with random, independent, uniformly distributed Fourier phases, generate time series with finite correlation dimension and converging K_2 entropy estimates, both of which are determined by the logarithmic spectral slope.

The stochastic signals considered in refs. [47, 48] are defined through their Fourier representation, i.e., by

$$x(t_i) = \sum_{k=1}^{N/2} A(\omega_k)\cos(\omega_k t_i + \phi_k)\,, \quad i = 1, N\,,$$
$$A^2(\omega_k) \propto \omega_k^{-\alpha}\,, \tag{2.7}$$

where $\omega_k = 2\pi k/N\,\Delta t$ and the ϕ_k are random uncorrelated phases. The "saturation" value of the correlation dimension ν is determined by the logarithmic spectral slope α through $\nu = 2/(\alpha - 1)$ for $1 < \alpha < 3$ [47]. In addition, the numerical estimates of the K_2 entropy were found to be convergent when $\alpha > 1$ [48]. The extension of these results to systems whose power spectrum has a power-law behavior only on a limited frequency range has been considered by Theiler [49]. A similar problem was also considered by Harding et al. [37], who studied a stochastic signal generated by a random walk in Fourier space which leads to a finite value of the correlation dimension. Clearly, the noises (2.7) are not associated with any low-dimensional system. The above results simply show that the standard time-embedding techniques and dimension and entropy calculations should not be used without a careful evaluation of the conditions for their applicability and an examination of the consistency of the results obtained. A naive application of these methods may lead to erroneous conclusions.

The colored noise example discussed above is certainly not the only class of random noises which give a finite estimate of ν and a convergent K_2 when finite-time series are considered [27, 49]. Following Vio et al. [27], we consider the two time series generated by a *linear* and by a *non-linear* stochastic process, given respectively by

$$\frac{dx}{dt} = \theta x(t) + w(t)\,, \tag{2.8}$$

$$\frac{dy(t)}{dt} = (\alpha - 0.5)\beta - y(t) + [2\beta y(t)]^{1/2} w(t)\,, \tag{2.9}$$

where $w(t)$ is a standard gaussian white noise process. Two such time series are shown in figs. 1a (linear case) and 1b (non-linear case) for the parameter values $\theta = -0.9$ and $\alpha = \beta = 1$. The discrete version of the process in formula (2.8) is a classical AR(1) linear model; the numerical integration of eq. (2.9) is pursued by the local linearization method of Ozaki [52] with $\Delta t = 0.02$ for both series. Unless noted otherwise, we consider time series composed of $N = 4000$ data points. This corresponds to a length of about 15 correlation times, similar to signals commonly encountered in the study of natural systems.

Both the linear and the non-linear processes (2.8) and (2.9) generate *stationary* time series for parameters values in an appropriate range [27]. It is important to note that both the linear and the non-linear time series possess very similar power spectra (a power-law power spectrum $P(\omega) \approx \omega^{-2}$ over a large frequency range) and very similar structure functions (defined below). As shown in ref. [27], the two series differ in that the linear signal $x(t)$ is statistically self-similar

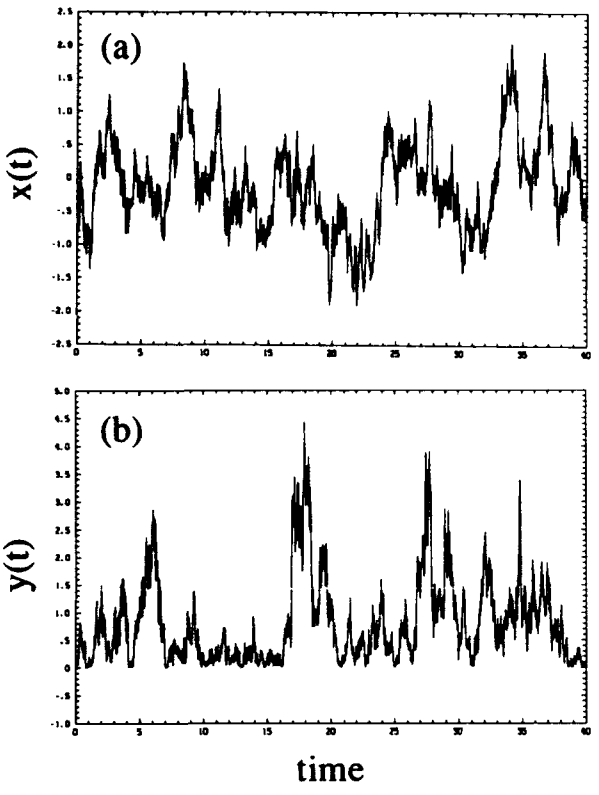

Fig. 1. (a) Time series obtained from the linear stochastic process (2.8) with $\theta = -0.9$ and $\Delta t = 0.02$. (b) Time series generated by the non-linear stochastic process (2.9) with $\alpha = \beta = 1$ and $\Delta t = 0.02$.

(an homogeneous fractal signal), while the non-linear signal $y(t)$ is multifractal and intermittent. This is reflected by the fact that the Fourier phases of the linear system (2.8) are random uniformly distributed with no correlation with each other, while some of the Fourier phases of the non-linear signal (2.9) have a non-zero correlation, as revealed for example by the bispectrum analysis. This implies that the stochastic signal given by formula (2.8) has close analogies with those studied in refs. [47, 48], while the signal (2.9) is a truly new entity.

Figs. 2a and 2b report the correlation integrals for the linear and non-linear time series respectively; figs. 2c and 2d show the correlation exponent ν_M and $K_2(M)$ versus the embedding dimension for the two time series, as computed by linear least-squares fit of log $C_M(r)$ versus log r on the scaling range $0.002 \leq C_M(r) \leq 0.02$. Note the "knee" in the correlation integrals for large M, at a value $C_M(r) \approx 0.02$, consistent with the results by Theiler [49] on stationary random processes with a power-law spectrum on a finite frequency range. The procedure of phase space reconstruction and the subsequent dimension and entropy calculations give the similar value $\nu \approx 2.5$ (at embedding dimension $M = 8$) and an equally converging K_2 entropy for both time series, independent on the linear or non-linear nature of the signals. For both signals, the time delay τ used in the time embedding procedure, $\tau = 250\,\Delta t$, is near the first zero of the autocorrelation function. In any event, the convergence of the correlation dimension and of the entropy does not significantly depend on the choice of the time delay over a large range of values of τ.

The computed value of the correlation dimension for both signals is slightly larger than the value indicated by the expression $\nu = 2/(\alpha - 1) = 2$ when $\alpha = 2$. This is due to the fact that the power spectrum of the signals (2.8) and (2.9) tend to become flat at low frequencies, consistent with the stationary nature of the processes [27]. When the length of the time series increases, the noises (2.8) and (2.9) tend to become space-filling, as required for stationary stochastic processes. However, this convergence is slow, and for a finite number of points an apparently finite estimate of the correlation dimension is typically obtained. Increasing the length of the signal produces somewhat larger estimates of the dimension. Clearly, an increase of the dimension estimates with the length of the time series should warn about misleading conclusions; unfortunately, such a test is often not available in the study of natural systems.

In the case of noises with a power-law spectrum and a low-frequency cutoff ω_0 (below which the spectrum becomes flat), Theiler [49] has recently derived an analytic expression for the correlation integral; the existence of different scaling regimes at different scales has been detected, the fractal behavior being associated with

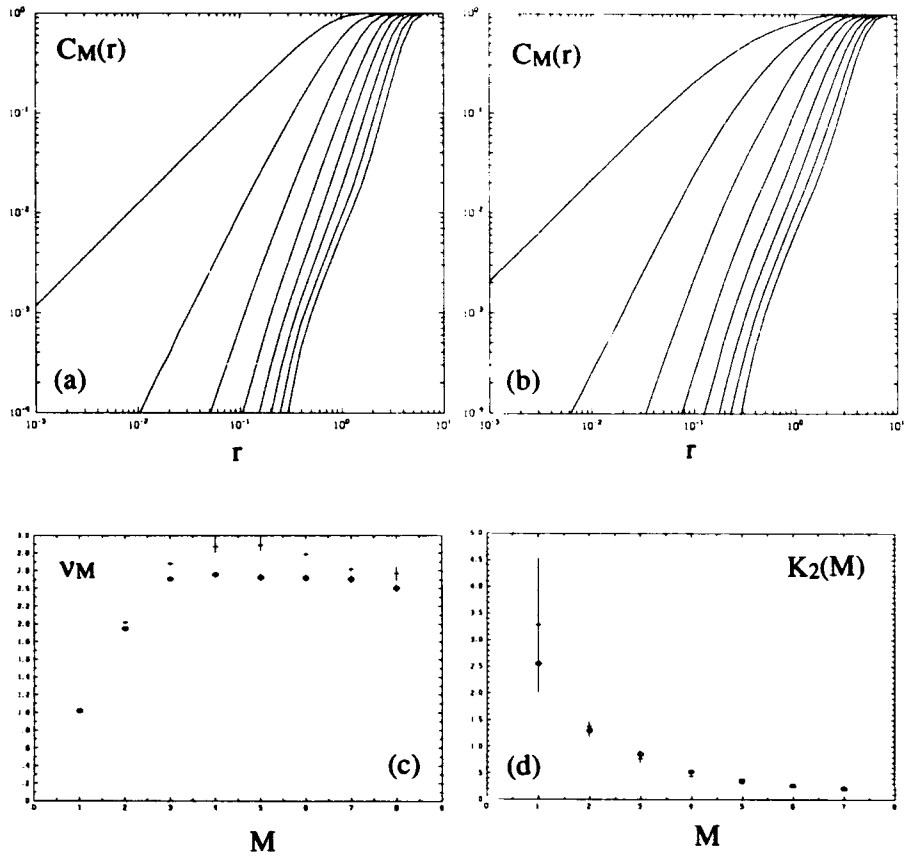

Fig. 2. (a) and (b) report the correlation integrals $C_M(r)$ for the linear (2.8) and non-linear (2.9) stochastic processes shown in fig. 1. The time delay τ in the embedding procedure has been chosen to be $\tau = 250\,\Delta t$, approximately corresponding to the first zero of the autocorrelation of the signals. The embedding dimension varies from $M = 1$ to $M = 8$. (c) and (d) report the correlation exponent ν_M and the correlation entropy $K_2(M)$ versus the embedding dimension M for both the linear and non-linear signals. Crosses refer to the linear signal and circles to the non-linear process. The error bars on ν_M are the 95% confidence limits of the least-squares-fit slope of $\log C_M(r)$ versus $\log r$; the error bars on $K_2(M)$ are the standard deviation on the mean value of $[\log C_M(r) - \log C_{M+1}(r)]/\Delta t$ in the scaling range.

the scale range where the spectrum is power-law. Theiler also estimated a lower bound N_0 to the number of points required in order to observe the space-filling scaling regime; N_0 "may have to be extremely large for this regime to be achieved". The power spectral properties of the noises considered in the present paper are similar to those discussed in ref. [49]; note, however, that the signal generated by (2.9) has been defined through a non-linear stochastic differential equation (not by its spectrum) and that its Fourier phases are not independent. Tests for the presence of non-linearity (such as the BDM test [53]) should give a positive result. Nevertheless, the present results show that finding that a time series is *non-linear* is certainly not sufficient to infer the presence of low-dimensional deterministic dynamics.

Another class of random processes which provide a finite correlation dimension estimate is obtained by considering a white noise with randomly superposed jumps of random amplitude (a random saw-tooth). One realization of such a process is shown in fig. 3a. In this example, the

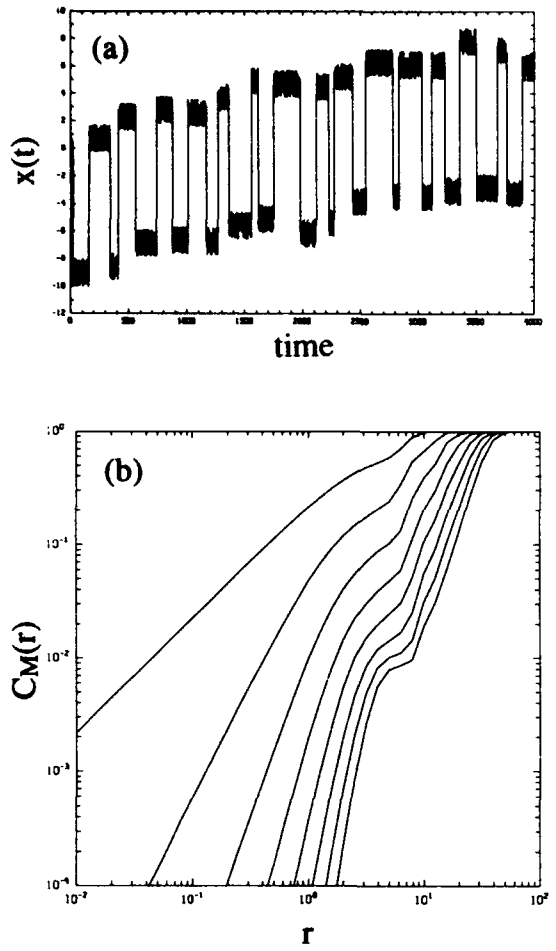

Fig. 3. (a) The "random saw-tooth" signal obtained by superposing random jumps of large amplitude onto a white noise background. (b) Correlation integrals $C_M(r)$ for the signal in fig. 3a; $\tau = 100\,\Delta t$ and $M = 1, \ldots, 8$.

"fast" dynamics is a white noise uniformly distributed between -1 and 1; we superposed onto it a random number of consecutively positive and negative jumps with amplitude $A_j = A_0 + \eta_j$, where $A_0 = 10$ and η_j is uniformly random distributed in $(-1, 1)$. The average time separation between jumps is about $100\,\Delta t$. The correlation integrals obtained from this time series are shown in fig. 3b; again, a value of the time delay corresponding to the first zero of the autocorrelation function has been chosen ($\tau = 100\,\Delta t$, here $\Delta t = 1$). A scaling regime in $C_M(r)$, with saturating correlation exponent, is clearly visible at large values of r for the higher embedding dimensions, leading to a correlation dimension $\nu \approx 2.7$. A similar structure was observed by Voges et al. [46] in the analysis of the X-ray variability of Hercules X-1 (their fig. 5); this behavior was ascribed to a two-amplitude-range process, where the low-amplitude fluctuations are due to high-dimensional dynamics and the large-amplitude fluctuations determined by a low-dimensional chaotic dynamics. However, such a behavior can be simulated by a purely stochastic process, as in the example above.

3. Some tests toward the goal of distinguishing between some chaos and some noise

The examples given in the previous section suggest that the distinction between low-dimensional dissipative chaos and (correlated) random noise should not be based solely on correlation dimension estimates. In addition to those considered here, other types of stochastic processes certainly exist which mimic the properties of low-dimensional chaos in finite data sets. Methods other than dimension calculations should be applied to measured time series in order to extract as much dynamical information as possible. In this regard, however, we recall that also predictability algorithms may have difficulty in distinguishing between chaos and correlated noise when a finite number of points is considered [21].

In a sense, simply examining the time series and its recurrence plots often indicates whether a meaningful correlation integral analysis can be performed (more precisely, such an examination often indicates the analysis should not be performed). For a system believed to contain a very-low-dimensional attractor (say, dimension less than three), one can directly inspect phase space trajectories and Poincaré sections; if these yield either "messy" distributions with no discernible structure or isolated, non-recurrent

patches of points, the correlation integral estimates should be interpreted with extreme caution. Analogously, time series which show rare bursts in otherwise unexplored regions of phase space, as well as an obvious non-stationarity and/or the absence of close returns in phase space are not promising candidates for the search of low-dimensional dissipative chaos.

Clearly, real time series are a mixture of deterministic components and random noise; it is nevertheless of some interest to attempt to disentangle the two components (when possible). In this section we discuss simple tests which may be applied to an experimental time series in order to interpret correlation dimension estimates and distinguish low-dimensional dynamics from stochastic processes. These tests are based on the idea of modifying some of the properties of a time series (i.e., on generating appropriate "surrogate" data, in a language similar to that used in refs. [26, 30]), in order to determine whether the convergence of the dimension and of the entropy (or some other measured quantity) does or not depend on the modified property.

It is important to stress the fact that each test *in se* is not an absolute proof; at best we are able to evaluate the probability that a series would produce the observed result by chance if it were chosen from an ensemble of signals with some given set of properties. These properties are chosen in an attempt to fool the algorithm tested and the usefulness of the test depends on the choice of good surrogate signals. The comparison between several of the above approaches increases the confidence in a distinction between chaos and noise. Finally, we recall that we tend to include in the term "randomness" the behavior of a dynamical system which cannot be represented in terms of a few active degrees of freedom, but which must instead be characterized by a large number of excited modes. The definitions of "few" and "large numbers" are vague and will depend on the level of technology and the theory available. This means that one will (mis)classify sufficiently "high" dimensional chaos as randomness.

3.1. Space–time-separation plots

The first test simply recasts the data in the correlation integral to make the bias due to dynamical correlations more obvious. We recall that Theiler [23] demonstrated that short-time correlations can produce "knees" in the correlation integral due to the one-dimensional nature of the trajectory. Analysis of fractal trajectories may result in similar knees with non-integer dimension.

The correlation integral represents the probability that a pair of randomly chosen points on the reconstruction will be less that a distance r apart. When making the standard calculations, one assumes the distance between pairs of points is due to the geometry of the reconstruction, *not* because the points are dynamically correlated and their separation in space reflects their being neighbors in time. These temporal correlations led Theiler to restrict the sums in eq. (2.2) to i, j pairs where $|i - j| > W$ for some constant W. The graphs presented below may be interpreted as providing a method for choosing W; in the case of non-stationary power-law noises they indicate that there is no value of W for which the correlation integral reflects global scaling due to recurrence.

For reconstructions from a single time series, each pair of points on the reconstruction is separated in phase space by some distance r and in time by some Δt. Our approach is to consider the time separation of points explicitly, first, through a scatter plot of the separation between two points in the space against their separation in time. This is illustrated for a three-dimensional reconstruction of the x series from the Lorenz equation [54] with $\sigma = 10$, $b = \frac{8}{3}$ and $r = 24.74$; in fig. 4 where the horizontal axis is separation in time and the vertical axis is the base 2 logarithm of the separation in space. For small Δt points

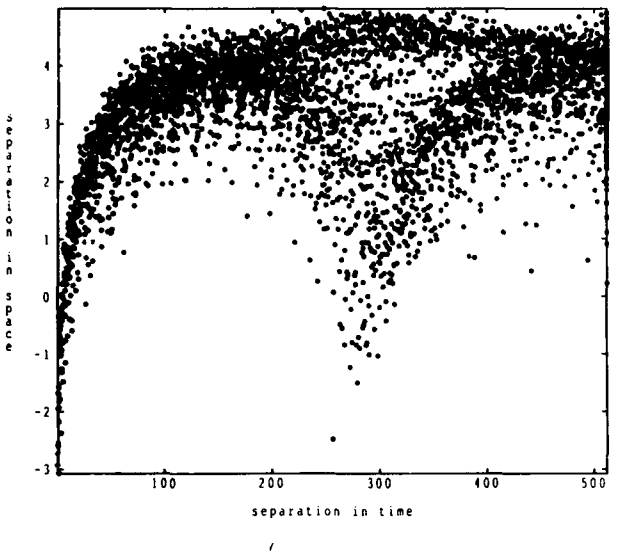

Fig. 4. Scatter plot of the spatial separation versus time separation between pairs of points on a trajectory on the Lorenz attractor. The horizontal axis is separation in time and the vertical axis is the (base 2 logarithm of) the separation in space.

are always near neighbors in space, as their time separation increases so, initially, does their separation in space.

For large data sets, scatter plots are difficult to interpret. An alternative is to plot contour maps of the fraction of points closer than a distance r at a given time separation Δt as a function of Δt, equivalently $P(|x(t+\Delta t)-x(t)|<r)$ for arbitrary t. For large N and Δt (in systems in which correlations decay with time), this distribution converges to the correlation integral for each Δt. The purpose of these contour maps is to observe the manner in which this convergence comes about.

Fig. 5 shows the space–time-separation contour map for the Lorenz case shown in fig. 4. The first zero of the autocorrelation function corresponds to 295 in the integer units of the graph. Fig. 5b shows the distribution over longer time scales. The length of time for which memory effects are significant is surprisingly long. The correlation integral is usually computed including these time separations with the implicit assumption that the visible oscillations average out.

Fig. 6 shows the corresponding results for a $1/f$ power-law noise. It is clear in this example that the only points with small spatial separation are dynamically near neighbors: The series is non-recurrent in phase space. The key point here is that there is no analogue of fig. 5b for the power-law noise signal: There exist no time scales on which the distribution is stable. As the correlation integral effectively projects this graph onto the vertical axis, biased estimates of the correlation integral will result when the contributions of this projection are disturbed by structure at small t. In the plots for the power-law noise this is always the case; whatever time threshold is chosen, the smallest length scales will always be dominated by the smallest time scales. For the Lorenz attractor, Theiler's approach removes the contribution of the region $|i-j|<W$; from fig. 5a it is clear that for, say, $W<32$ the distribution contains many near neighbors due to dynamical correlations. For a chaotic system, the decay of correlations with time results in the convergence of slices at constant Δt to the correlation integral at large Δt. The memory of initial conditions, reflected here in the persistence of long time structure of this plot is greater than might have been expected.

The connection with the correlation integral is straightforward: $C(r)$ is simply the sum over "large" Δt for a given r; the usefulness of this graph is that (a) it provides a quantitative estimate of what constitutes "large Δt" (namely those values where the contours have reached their asymptotic behavior), (b) it is sensitive to the specific reconstruction parameters used and the full non-linear structure in M dimensions as opposed to the (linear) autocorrelation function or the one-dimensional mutual information, and (c) computationally, it is a subset of the correlation integral. Note that these distributions may also be used to estimate the inside cutoff to scaling range in the spatial separation of points with minimal dynamic correlation.

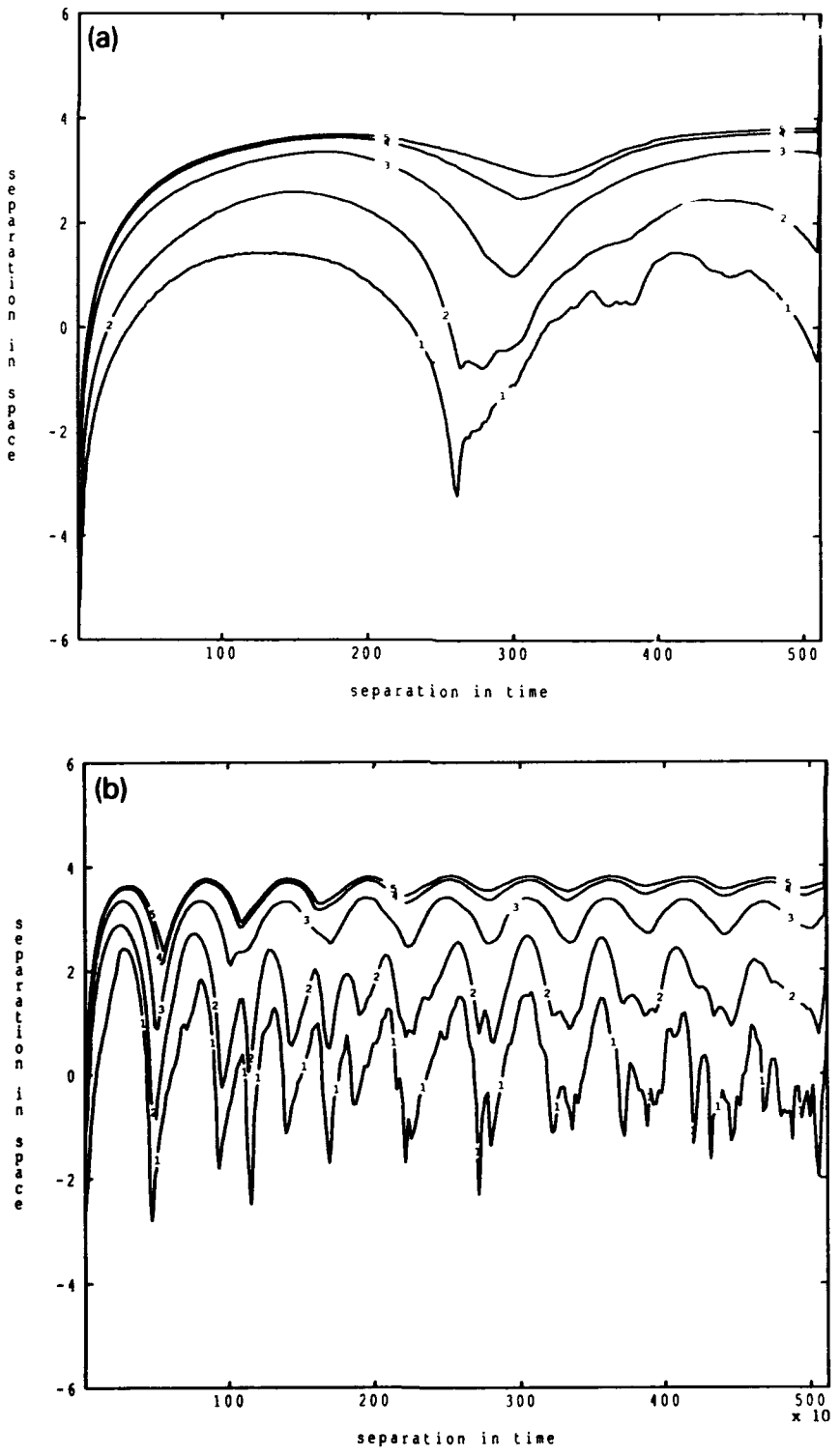

Fig. 5. Space–time-separation plots for the Lorenz attractor as in fig. 4. In this case the scatter diagram is replaced by a contour map at short time scales (a) and at longer time scales (b). The contours indicate the fraction of points closer than a distance r at a given time separation Δt. The different curves correspond to different fractions; curve 1 refer to a fraction of 1%, curve 2 to 10%, curve 3 to 50%, curve 4 to 90% and curve 5 to 99%.

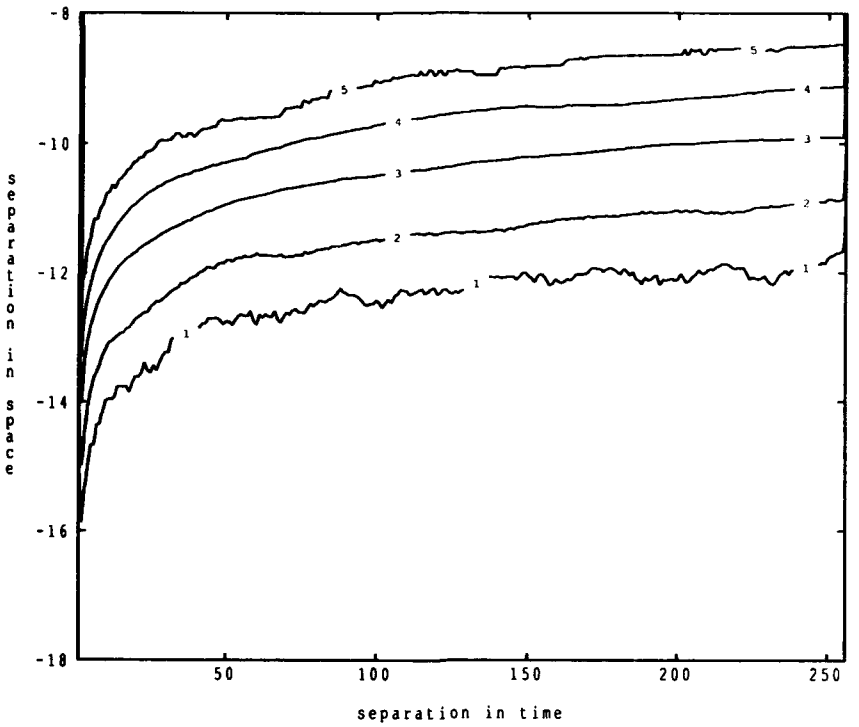

Fig. 6. Space–time-separation contour map for a $1/f$ power-law noise, as a function of Δt. Same details as in fig. 5.

For very long series with low sampling rates, the effects discussed here become small as one eventually finds near returns closer to a given point than its dynamical next neighbor. For reasonable sampling rates, however, the data set lengths required for this to occur can be extremely long.

The power-law noise is employed here as a clear example of a series which is non-recurrent in phase space. In this case, the non-stationarity of the signal should be obvious by inspection of the time series itself. The space–time-separation maps quantify the occurrence (or absence) of near returns in more subtle time series.

Finally, we note a secondary bias in the correlation integral when high sampling rates are used. Even when near neighbors of a given point are omitted from the calculation centered at that point, they can still bias the probability distribution centered on points far away in time. This appears as a change in the conditional probability $P(\Delta x_{ij} < r + \Delta r \,|\, \Delta x_{ij-1} < r)$ through the correlation of $x(t_{j-1})$ and $x(t_j)$ for arbitrarily large values of $i - j$.

3.2. Phase randomization

A very useful test is to consider the distribution of the Fourier phases of the signal under study. In fact, in the case of fractal noise processes the convergence of the correlation dimension is forced mainly by the shape of the power spectrum (consistent with the fact that both the power spectrum and the correlation integral are related to the second moment of the distribution), while for a low-dimensional dynamics phase correlations play an essential role. Thus, given an experimentally measured signal $x(t)$ thought to be chaotic, it is useful to consider the stochastic surrogate signals obtained by inverting a power spectrum exactly equal to that of the signal under study and random, independent and uniformly distributed Fourier phases. If the convergence is determined only by

the shape of the spectrum (equivalently, by the autocorrelation function), then the results are not affected by phase randomization; the invariance of the correlation dimension and entropy estimates under phase randomization strongly implies that these estimates are not indicative of low-dimensional dynamics. To our knowledge, this test was first applied in the study of the motion of freely drifting buoys in the Pacific Ocean [43].

As an example of this approach, in fig. 7a we show the time series obtained by randomizing the Fourier phases of the non-linear stochastic process shown in fig. 1b, and in fig. 7b we report the corresponding correlation integrals. The difference between the original and the phase-randomized time series is visually apparent, since the phase randomization has destroyed the delicate phase couplings associated with the intermittent and multifractal nature of the process (2.9). The average correlation dimension estimates, however, do not show any significant differences between the original (non-liner) and the phase-randomized (linearized) signal, as shown in fig. 7c, which reports ν_M versus M for the two time series. For both signals, the correlation dimension saturates at approximately the same value. By repeating this procedure over an ensemble of ten different surrogate signals, corresponding to different choices of the random phases, we have always obtained saturating correlation dimension estimates with mean value $\langle \nu \rangle = 2.65$ and standard deviation $\sigma_\nu = 0.17$ (at embedding dimension $M = 8$). In general, we have noted that the scatter in the saturation values of ν_M obtained for an analogous ensemble of ten surrogates of the linear signal (2.8) is smaller ($\langle \nu \rangle = 2.47$ and $\sigma_\nu = 0.08$ at $M = 8$); this difference, however, is in general not sufficient to infer the linear or non-linear nature of the original signal.

The above results can be understood by recalling that the correlation dimension is related to the second moment of the probability distribution associated with the time series (in a given

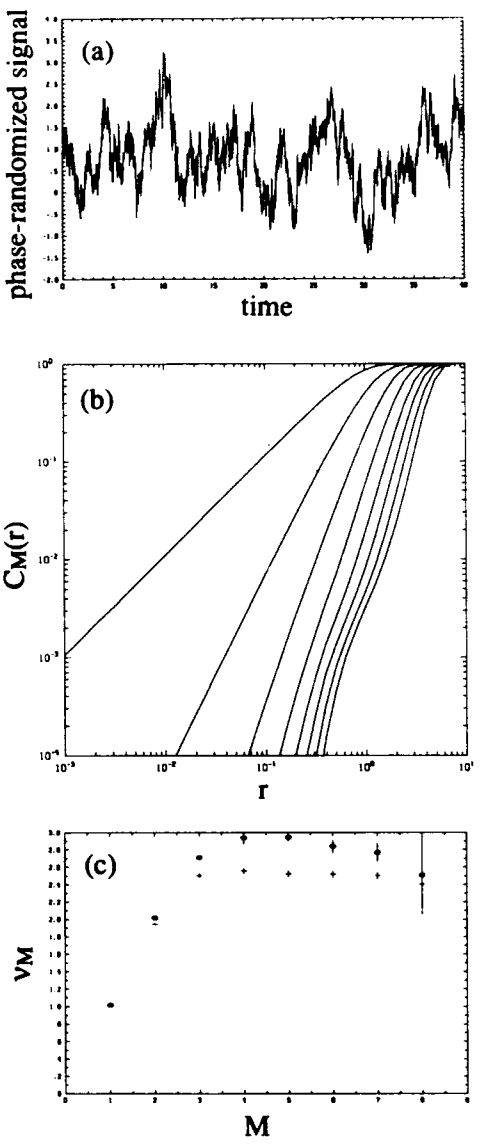

Fig. 7. (a) Signal obtained by randomizing the Fourier phases of the non-linear time series shown in fig. 1b. (b) Correlation integrals for the phase-randomized time series shown in fig. 7a; $\tau = 250\,\Delta t$ and $M = 1, \ldots, 8$. (c) Correlation exponent ν_M versus the embedding dimension M for the original (crosses) and phase randomized (circles) time series. Error bars are the 95% confidence limits on the least-squares fit.

embedding space), i.e., it is related to the autocorrelation or to the power spectrum. For a stochastic signal, the phase information determines the behavior of higher moments, i.e., it is related to the generalized fractal dimensions (as-

sociated with the intermittency properties) and to higher-order spectral quantities such as the bispectrum. All these higher-order measures are obviously modified by phase randomization in the case of the non-linear signal. Along these lines, a useful test to detect the presence of non-linearity and phase correlations in a given stochastic signal is to verify how the spectrum of multifractal dimensions is changed under phase randomization [27]. Clearly, for the purpose of distinguishing between chaos and noise one should attempt to choose stochastic surrogates which resemble the original series as much as possible (even in the higher moments). For example, the sunspot series has a number of non-linear characteristics; in this case, rather than simply use phase randomization one might consider non-linear stochastic model simulations, as discussed in refs. [30, 55].

On the other hand, if the convergence is due to an underlying deterministic dynamics, phase randomization destroys the convergence of the dimension and of the entropy estimates. As an example, figs. 8a and 8b report a 4000-point time series of the x component from the Lorenz attractor, with the same parameters as above, before and after the phase randomization. The time step used is $\Delta t = 0.05$. The appearance of the two time series is completely different and the correlation dimension results differ as well, see figs. 8c and 8d. In fact, there is no clear scaling range in $C_M(r)$ for the phase-randomized signal, as shown in figs. 8e and 8f which report the local logarithmic slope of $C_M(r)$ for each case. For the phase-randomized signal, ν_M may be defined as an average slope over a specified range of length scales. Fig. 8g shows ν_M versus M for both signals; as one can see, the average correlation exponent for the phase-randomized signal does not saturate. By repeating the analysis over an ensemble of ten surrogate signals we have always obtained non-convergent correlation dimension estimates for the phase-randomized signals.

We caution, however, that a change in the correlation integrals under phase randomization does not necessarily imply the existence of an underlying strange attractor. For example, phase randomization of signals with strong periodic or quasi-periodic components in their spectrum will be more difficult to interpret. In principle, quasi-periodic signals with the geometry of tori can be detected by their integer dimension. In reality, however, the uncertainty in dimension estimates makes identifying integers impractical. Other tests better designed to identify signals such as these exist (see e.g. ref. [56]). The combined use of several methods is often a crucial step in the correct analysis of the source of difficulties with correlation integral techniques. Alternatively, the use of some noise-filtering algorithms [11, 15, 16] may help in elucidating the true nature of the system, although non-linear cleaning should be kept distinct from "bleaching" the data [26].

3.3. *Signal differentiation*

Another test considers the correlation integral analysis of the first (numerical) derivative of the signal. For a system governed by a low-dimension strange attractor, the value of the correlation dimension is the same for the original signal as well as for the first (or for a higher) derivative (note that the time delay may have to be modified). In the case of a stochastic signal, The first derivative (or difference) of the signal has a correlation dimension which, when well defined, is often much larger than that of the original signal, consistent with the change in the logarithmic spectral slope under signal differentiation. Fig. 9a reports the first difference signal $\Delta x(t) = x(t + \Delta t) - x(t)$ of the x component of the Lorenz attractor; fig. 9b reports the correlation integrals for $\Delta x(t)$ and fig. 9c shows the values of the correlation exponent versus the embedding dimension for the original time series and for the first difference signal $\Delta x(t)$. The same value of τ has been used for both time series ($\tau = 5\,\Delta t$,

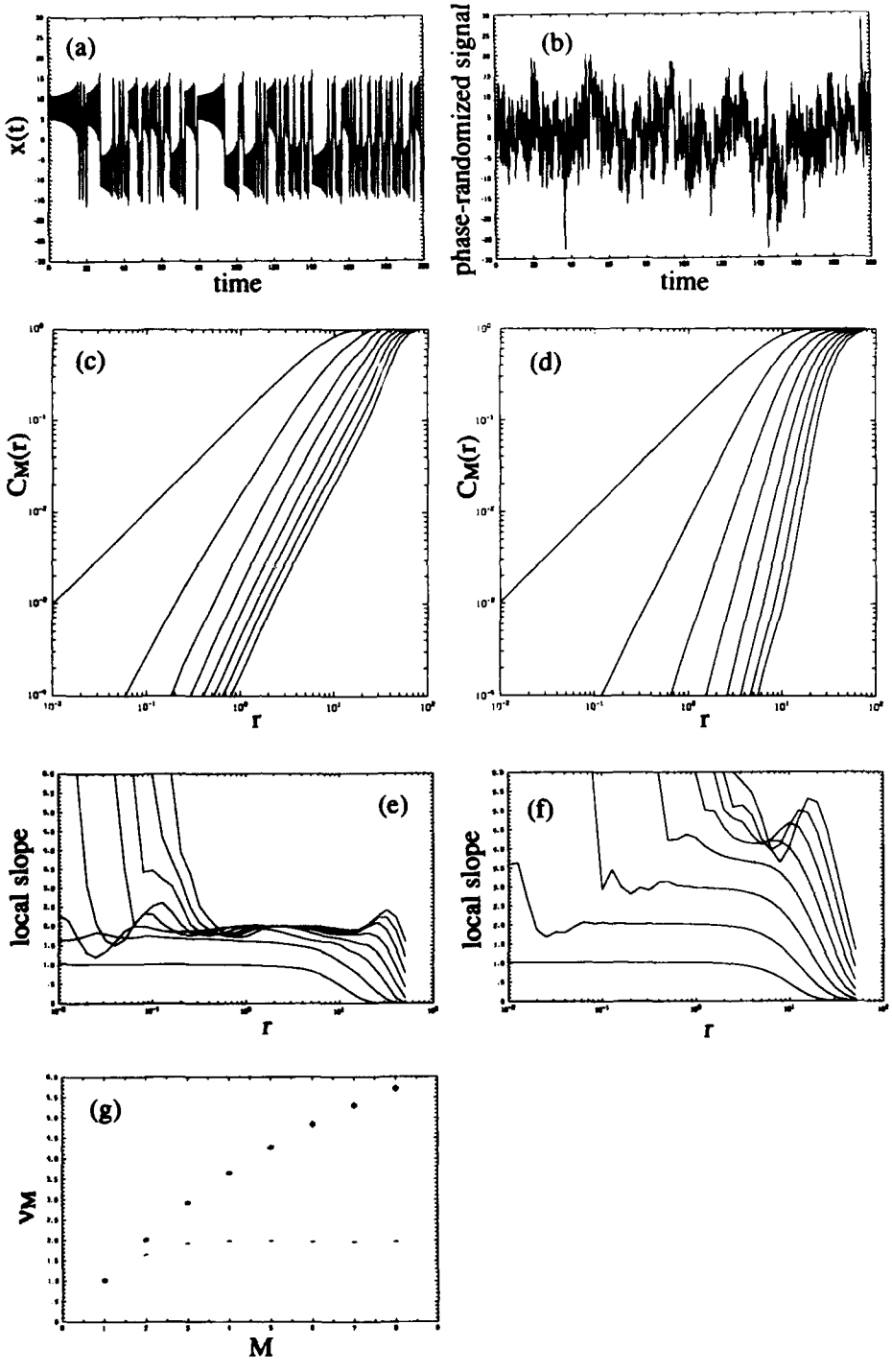

Fig. 8. (a) and (b) report respectively a time series obtained from the three-dimensional Lorenz model [28] and its phase-randomized counterpart; we use the standard values $\sigma = 10$, $b = 8/3$ and $r = 24.74$. A similar behavior is obtained for $r = 28$. The time step is $\Delta t = 0.05$. (c) and (d) report the corresponding correlation integrals with $\tau = 5\,\Delta t$ and $M = 1, \ldots, 8$; (c) and (f) report the local logarithmic slopes of the correlation integrals as obtained from a moving five-point linear regression of $\log C_M(r)$ versus $\log r$. (g) shows the (average) correlation exponent ν_M versus M for the original (crosses) and phase-randomized (circles) time series.

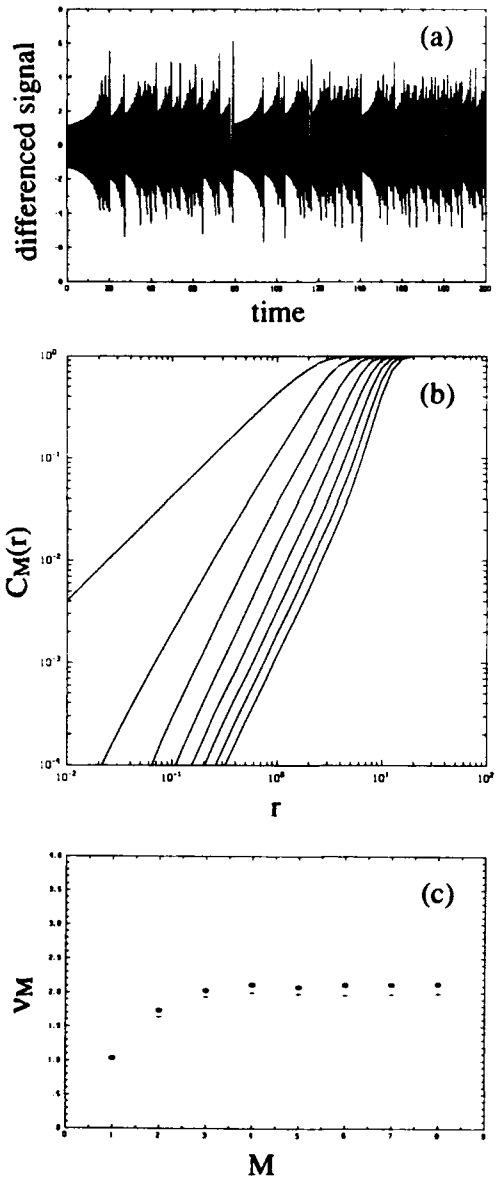

Fig. 9. (a) reports the first difference signal $\Delta x(t) = x(t + \Delta t) - x(t)$ obtained from the signal in fig. 8a, $\Delta t = 0.05$. (b) reports the correlation integrals for this signal, with $\tau = 5\,\Delta t$ and $M = 1, \ldots, 8$, and (c) reports the correlation exponents ν_M versus M for the original (crosses) and first difference (circles) signals.

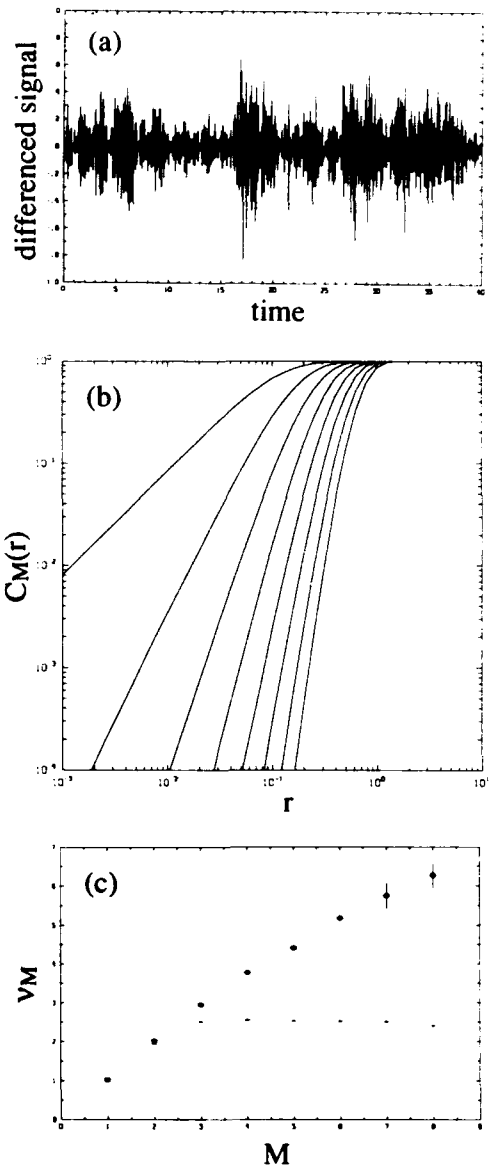

Fig. 10. (a) reports the first difference signal obtained from the non-linear stochastic process (2.9), $\alpha = \beta = 1$ and $\Delta t = 0.02$. (b) reports the corresponding correlation integrals for $\tau = 250\,\Delta t$ and $M = 1, \ldots, 8$. (c) shows the correlation exponent versus the embedding dimension for the original (crosses) and differenced (circles) signals. From panel (a) the intermittent nature of the process (2.9) is particularly evident.

where $\Delta t = 0.05$); as expected, results are very similar.

The first difference signal $\Delta y(t) = y(t + \Delta t) - y(t)$ obtained from the non-linear stochastic process (2.9) and the resulting analysis are shown in fig. 10; again, the same time delay $\tau = 250\,\Delta t$ has been used for both signals. As one can see, no saturation is observed in the correlation exponent of the difference signal. This is due to the fact that the increments $\Delta y(t)$ have essentially a white noise spectrum in this case, and have

consequently a much shorter correlation time. Thus, when a clear estimate of the derivative of a signal is available, the existence of a strong difference in the correlation dimension between the measured signal and its first derivative is a good indication that the dynamics has a significant stochastic component. Conversely, if the results of the correlation analysis do not change under signal differentiation, one has strong indication that the dynamics is not simply a fractal noise. Clearly, there may be severe difficulties in estimating the derivatives of measured signals.

Another possibility (similar in spirit to signal differentiation) is to consider a generic diffeomorphism $z = F\{x\}$ of the observed variable. For a sufficiently long series from a deterministic system, no difference should be observed between the correlation dimension of the signal $x(t)$ and that of $z(t)$, apart from the effects due to the amplification of measurement noise. In contrast, the dimension of a stochastic fractal signal should drastically change under this operation, since the characteristics of the process will be modified [34]. Changes in the correlation integrals may depend crucially upon $F\{x\}$; a careful examination of different classes of transformations must be pursued. We also note that transformation of the distribution (effectively, a change in the measurement function) has been applied by Theiler et al. [26].

3.4. *Independent realizations*

A useful test is based on considering several independent realizations of the dynamics, with different initial conditions. In the case of a low-dimensional dissipative dynamics, the correlation dimension of the set of points obtained by considering all realizations at once is equal to that of a single realization, provided that the different realizations start in the same basin of attraction. On the other hand, for a stochastic system the different realizations tend to fill the entire space, and one should observe an increase of the correlation dimension estimate with the number of realizations considered. In fact, the convergence of the dimension estimates for the noises considered here are due to the existence of long time correlations, the effect of which is diminished by considering *independent* realizations.

To illustrate this behavior, fig. 11a contrasts the correlation exponent versus the embedding dimension for a set obtained by combining five independent time series of the x component of the Lorenz attractor against the results for a single time series of the same total length. Fig. 11b reports the correlation exponent versus the embedding dimension for a set of points obtained by composing five independent realizations of the non-linear stochastic process (2.9), together with the correlation exponent obtained

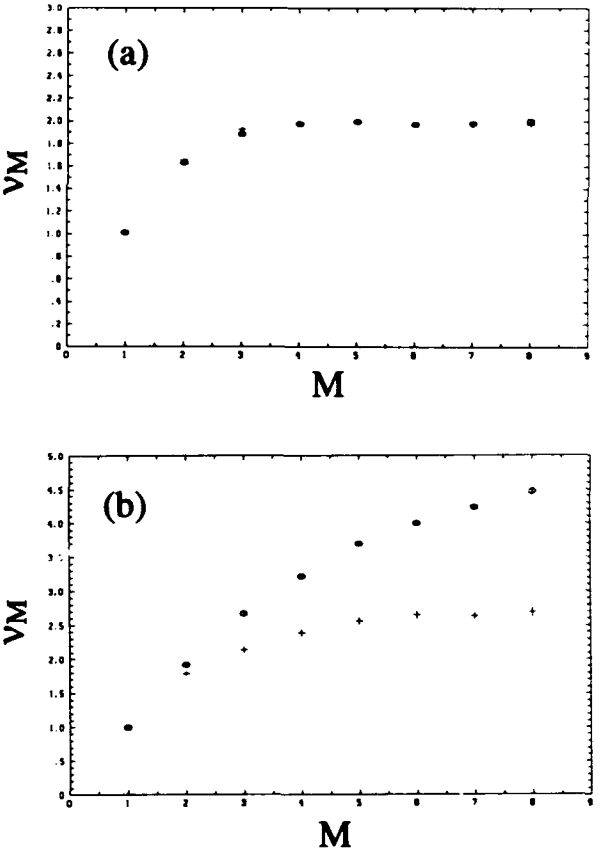

Fig. 11. Correlation exponent versus the embedding dimension for the Lorenz attractor (a) and for multiple realizations of the non-linear stochastic process (2.9) (b). Crosses are for a single realization, circles refer to the results obtained by superposing five independent realizations.

from the analysis of a single realization. The growth of the correlation dimension estimate with the number of realizations is clearly visible in this case. Another approach in this vein is to consider simultaneous measurement of several quantities. When the quantities measured reflect different aspects of the process, then the information content in two simultaneous signals of length T can be much greater than gaining "twice as many points" in either one of the signals by doubling the sampling rate (due in part to projection effects).

3.5. Structure function

A classic quantity in the study of measured time series is the structure function (SF), which is given by

$$S(n) = \sum_{i=1}^{N-n} [x(t + n\,\Delta t) - x(t)]^2 , \qquad (3.1)$$

where $x(t)$ is a scalar signal. For a fractal signal, the structure function has a scaling behavior

$$S(n) \propto n^{2H} \qquad (3.2)$$

at small values of n, where H is called the scaling exponent (see e.g. refs. [47, 57, 58]). A fractal signal whose SF is given by formula (3.2) has a power-law power spectrum $P(\omega) \approx \omega^{-\alpha}$, where $\alpha = 2H + 1$ [47]. By composing independent realizations $x_k(t)$ of a fractal signal on the different axes of an N-dimensional space, one obtains a fractal trajectory which is parametrically represented by the set of $x_k(t)$. The correlation dimension ν of the trajectory is related to the scaling exponent by the expression $\nu = 1/H$, if $\nu \leq M$ [47, 57, 58]. The different signals $x_k(t)$ may be independent realizations or time-delayed versions of the same signal.

The structure function of the stochastic processes (2.8) and (2.9) displays a scaling behavior

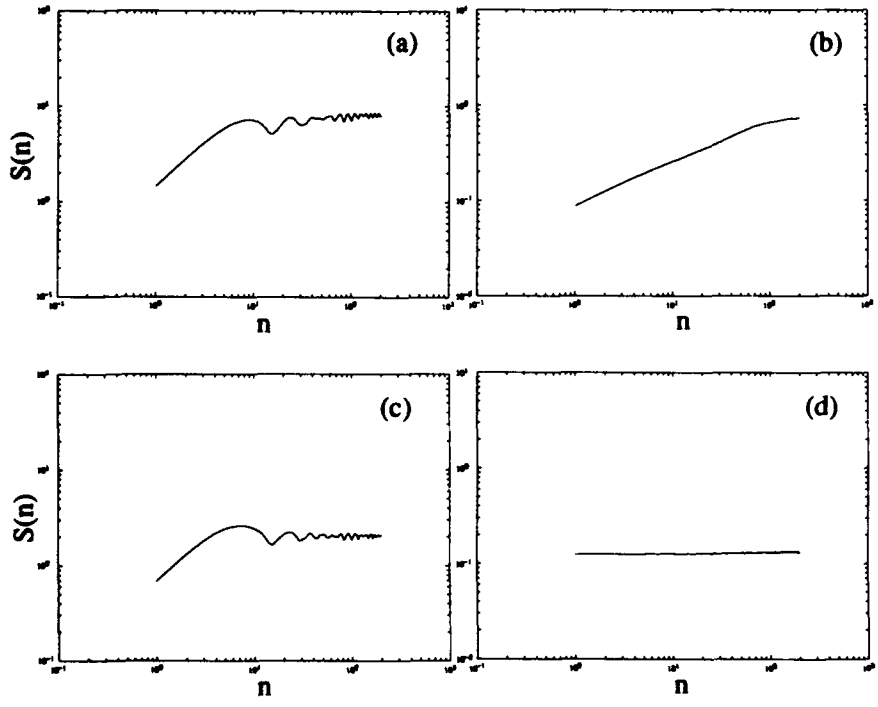

Fig. 12. (a) Structure function (SF) for the x component of the Lorenz attractor shown in fig. 8a. (b) SF for the non-linear stochastic process shown in fig. 1b. (c) SF for the first difference deterministic signal shown in fig. 9a. (d) SF for the first difference stochastic signal shown in fig. 10a.

of the kind (3.2) (at least on the time scales corresponding to the power-law regime in the spectrum). Alternatively, for motion on a strange attractor, which is differentiable in the direction of motion (and whose fractal structure is due to "close returns" in phase space), the SF has a scaling exponent $H = 1$ at small values of n. The SF tends to oscillate and then to become constant at increasing n, due to the limited region of the phase space visited by the system. As an example of the above statements, in fig. 12 we report the SF versus n for the x component of the Lorenz attractor (a) and for the non-linear noise (2.9) (b). The difference between the two structure functions is striking; the SF for the non-linear noise shows an extended scaling regime while the SF for the Lorenz attractor displays the typical behavior discussed above.

By combining the test of the signal differentiation and the SF calculation one obtains an even more clear difference between chaos and fractal noise. Fig. 12c shows the SF versus n for the first difference signal obtained from the x component of the Lorenz attractor and fig. 12d reports the SF for the first numerical derivative of the non-linear process (2.9). The SF of the differentiated signal from the Lorenz attractor is practically equal to that of the original time series, while the SF of the noise is now flat, indicating $H = 0$ and a non-convergent dimension estimate for the first differenced signal.

4. Discussion and conclusions

The (re)discovery of low-dimensional deterministic chaos and the development of data analysis methods which can be easily implemented have stimulated many works devoted to the study of experimental signals from the "chaotic" viewpoint. This work has often focused on deciding whether apparently unpredictable behavior should be ascribed to the presence of a low-dimensional strange attractor rather than "random" behavior. In many cases, however, the desire for finding a chaotic attractor has led to a naive application of the analysis methods; as a result, the number of claims on the presence of strange attractors in vastly different physical, chemical, biological and astronomical systems has grown (exponentially?). Difficulties in interpreting correlation integral results led for example Grassberger et al. [15] to state that ". . . most (if not all) of these claims have to be taken with very much caution". Analogously, in a more specific context, Lorenz [40], based on the analysis of a dynamical system with several *weakly coupled* degrees of freedom, has recently concluded that there is "no reason to believe that an extensive weather or climate system possesses a low-dimensional attractor".

The most convincing evidence for low-dimensional chaos most commonly arises when the spatial complexity of the system is limited. Examples include carefully controlled laboratory experiments, transitional regimes (for example from laminar to turbulent flows) and some natural systems where physical reasons clearly imply the presence of only a few active collective modes [39]. Extended systems (e.g. fluids) may require long (global) space correlations for a low-dimensional dynamics to exist. Systems with short space-correlations, as well as systems with weakly coupled phase space variables, need not be (globally) described by low-dimensional dynamics. For the latter systems, the standard correlation integral approach may (again in Lorenz's words) "attempt to measure the dimension of a subsystem" [40].

In this paper we have extended the results given in refs. [47, 48] and we have considered several different types of random noises which can result in convergent estimates of the dimension and of the entropy. In particular, we have considered two types of *stationary* stochastic processes, generated by linear and by non-linear stochastic processes. It has been shown that both noises provide a very similar output of the dimension and entropy (numerical!) estimates. These results are of some interest since they

remove the objection that only non-stationary noises are associated with convergent dimension and entropy estimates. In the case of stochastic signals, the convergence of dimension estimates are a result of the fractal nature of the trajectories. As it is crucial to distinguish which aspect of the signal the estimate is reflecting, we have examined this question directly through space–time-separation plots and structure functions.

Given the interest of distinguishing between low-dimensional chaos and random behavior in observed signals, we have considered a series of tests which can assist (or circumvent) the interpretation of the correlation integral. These tests employ appropriate surrogate data which must then be analysed by the same methods employed with the original time series to determine whether the estimates of the dimension, entropy or any other statistic depend on the characteristics of the time series which have been modified. In particular, we have considered the procedures based on randomizing the Fourier phases of the signal, numerically differentiating the original time series, and the analysis of several independent realizations of the same dynamics. We have also discussed how the structure function can be used for contrasting low-dimensional chaos and fractal noises. In general, we have shown that low-dimensional dynamics may be distinguished from fractal noises by using these tests. The case of randomly modulated periodic (or quasi-periodic) oscillations could be much more complicated, and a clear distinction between chaos and random modulations might best employ other techniques (see e.g. ref. [56]).

In conclusion, we stress that there is no simple test which automatically and unequivocally indicates the presence or the absence of chaotic dynamics; it is only through the comparison of several different methods that the dynamical processes underlying a given system may be assessed. As always, a minimal physical insight into the dynamics of the system under study is a great asset. In this regard, we think it would be extremely useful to produce a collection of signals (both deterministic and random) and provide a detailed description of the output of the various analysis techniques when applied to each of them. In this way, safer conclusions on the presence of chaos, low-dimensional dynamics and/or noise from the analysis of measured time series could be obtained.

Acknowledgements

The present work has benefitted by several discussion with Jean-Guy Caputo, Peter Grassberger, Mark Muldoon, James Theiler and Risheng Wang during the IUTAM Meeting on interpretation of time series from mechanical systems (Warwick University, UK, August 1991), as well as by fruitful visits of two of us (A.P. and L.S.) to Professor Klaus Fraedrich at the Free University of Berlin. L.S. would also like to acknowledge profitable discussions with Professor Mike Gaster which led to the space–time-separation graphs.

References

[1] H.D.I. Abarbanel, R. Brown and J.B. Kadtke, Phys. Rev. A 41 (1990) 1742.
[2] R. Badii and A. Politi, Phys. Rev. Lett. 52 (1984) 1661.
[3] D.S. Broomhead and G.P. King, Physica D 20 (1986) 217.
[4] D.S. Broomhead and R. Jones, Proc. R. Soc. London A 423 (1989) 103.
[5] M. Casdagli, Physica D 35 (1989) 335.
[6] M. Casdagli, S. Eubank, J.D. Farmer and J. Gibson, Physica D 51 (1991) 52.
[7] J.P. Crutchfield and B.S. McNamara, Compl. Syst. 1 (1987) 417.
[8] J.-P. Eckmann and D. Ruelle, Rev. Mod. Phys. 57 (1985) 617.
[9] J.-P. Eckmann, S. Oliffson Kamphorst, D. Ruelle and S. Ciliberto, Phys. Rev. A 34 (1986) 4971.
[10] J.D. Farmer and J.J. Sidorovich, Phys. Rev. Lett. 59 (1987) 845.
[11] J.D. Farmer and J.J. Sidorovich, Physica D 47 (1991) 373.
[12] P. Grassberger and I. Procaccia, Physica D 9 (1983) 189.

[13] P. Grassberger and I. Procaccia, Phys. Rev. A 28 (1983) 2591.
[14] P. Grassberger, Phys. Lett. A 148 (1990) 63.
[15] P. Grassberger, T. Schreiber and C. Schafrath, preprint (1991).
[16] E.J. Kostelich and J.A. Yorke, Phys. Rev. A 38 (1988) 1649.
[17] W. Liebert and H.G. Schuster, Phys. Lett. A 142 (1989) 107.
[18] M. Sano and Y. Sawada, Phys. Rev. Lett. 55 (1985) 1082.
[19] T. Sauer, J.A. Yorke and M. Casdagli, J. Stat. Phys. 65 (1991) 579.
[20] L.A. Smith, Phys. Lett. A 133 (1988) 283.
[21] G. Sugihara and R.M. May, Nature 344 (1990) 734.
[22] F. Takens, Detecting strange attractors in turbulence, in: Lecture Notes in Mathematics, Vol. 898, eds. D.A. Rand and L.S. Young (Springer, Berlin, 1981) p. 366.
[23] J. Theiler, Phys. Rev. A 34 (1986) 2427.
[24] J. Theiler, Phys. Rev. A 36 (1987) 4456.
[25] J. Theiler, J. Opt. Soc. Am. A 7 (1990) 1055.
[26] J. Theiler, B. Galdrikian, A. Longtin, S. Eubank and J.D. Farmer, Los Alamos Preprint LA-UR-91-2615 (1991).
[27] R. Vio, S. Cristiani, O. Lessi and A. Provenzale, Time series analysis in astronomy: an application to quasar variability studies, Astrophys. J., in press (1992).
[28] A. Wolf, J.B. Swift, H.L. Swinney and J.A. Vastano, Physica D 16 (1985) 285.
[29] N.H. Packard, J.P. Crutchfield, J.D. Farmer and R.S. Shaw, Phys. Rev. Lett. 45 (1980) 712.
[30] L.A. Smith, Physica D, submitted.
[31] P. Atten, J.G. Caputo, B. Malraison and Y. Gagne, J. Mech. Theor. Appl., Special Issue (1984) 133.
[32] A. Brandstater, J. Swift, H.L. Swinney, A. Wolf, J.D. Farmer, E. Jen and P.J. Crutchfield, Phys. Rev. Lett. 51 (1983) 1442.
[33] S. Cilberto and J.P. Gollub, J. Fluid Mech. 158 (1985) 381.
[34] J.K. Cannizzo, D.A. Goodings and J.A. Mattei, Astrophys. J. 357 (1990) 235.
[35] K. Fraedrich, J. Atmos. Sci. 43 (1986) 419.
[36] P. Grassberger, Nature 323 (1986) 609; 326 (1986) 524.
[37] A.K. Harding, T. Shinbrot and J.M. Cordes, Astrophys. J. 353 (1990) 588.
[38] C.L. Keppenne and C. Nicolis, J. Atmos. Sci. 46 (1989) 2356.
[39] Z. Kollath, Mon. Not. R. Astron. Soc. 247 (1990) 377.
[40] E.N. Lorenz, Nature 353 (1991) 241.
[41] C. Nicolis and G. Nicolis, Nature 311 (1984) 529.
[42] J.P. Norris and T.A. Matilsky, Astrophys. J. 346 (1989) 912.
[43] A.R. Osborne, A.D. Kirwan, A. Provenzale and L. Bergamasco, Physica D 23 (1986) 75.
[44] L.-H. Shan, P. Hansen, C.K. Goertz and R.A. Smith, Geophys. Res. Lett. 18 (1991) 147.
[45] A.A. Tsonis and J.B. Elsner, Nature 333 (1988) 545.
[46] W. Voges, H. Atmanspacher and H. Scheingraber, Astrophys. J. 320 (1987) 794.
[47] A.R. Osborne and A. Provenzale, Physica D 35 (1989) 357.
[48] A. Provenzale, A.R. Osborne and R. Soj, Physica D 47 (1991) 361.
[49] J. Theiler, Phys. Lett. A 155 (1991) 480.
[50] A.M. Fraser and H.L. Swinney, Phys. Rev. A 33 (1986) 1134.
[51] L.A. Smith, J.-D. Fournier and E.A. Spiegel, Phys. Lett. A 114 (1986) 465.
[52] T. Ozaki, in: Handbook of statistics, eds. E.J. Hannah and P.R. Krishnaiah (Elsevier, Amsterdam, 1985).
[53] W. Brock, W. Dechert and J. Scheinkman, A test for independence based on the correlation dimension, University of Wisconsin-Madison, SSRI paper 8702.
[54] E.N. Lorenz, J. Atmos. Sci. 20 (1963) 130.
[55] N. Weiss, Phil. Trans. R. Soc. London A 330 (1989).
[56] G.L. Bretthorst Bayesian spectral analysis and parameter estimation, Lecture Notes in Statistics (Springer, Berlin, 1988).
[57] B.B. Mandelbrot, The fractal geometry of nature (Freeman, San Francisco, 1982).
[58] A. Provenzale, A.R. Osborne, A.D. Kirwan and L. Bergamasco, The study of fluid parcel trajectories in large-scale ocean flows, in: Nonlinear topics in ocean physics, ed. A.R. Osborne (Elsevier, Amsterdam, 1991).

Physica D 58 (1992) 50–76
North-Holland

PHYSICA D

Identification and prediction of low dimensional dynamics

Leonard A. Smith [1,2]
Department of Engineering, University of Warwick, Coventry CV4 7AL, UK

Received 14 November 1991
Revised 15 March 1992
Accepted 15 March 1992

This contribution focuses upon extracting information from dynamic reconstructions of experimental time series data. In addition to the problem of distinguishing between deterministic dynamics and stochastic dynamics, applied questions, such as the detection of parametric drift, are addressed. Nonlinear prediction and dimension algorithms are applied to geophysical laboratory data, and the significance of these results is established by comparison with results from similar surrogate series, generated so as not to contain the property of interest. A global nonlinear predictor is introduced which attempts to correct systematic bias due to the inhomogeneous distribution of data common in strange attractors. Variations in the quality of predictions with location in phase space are examined in order to estimate the uncertainty in a forecast at the time it is made. Finally, the application of these methods to truly stochastic systems is discussed and the distinction between deterministic, stochastic, and low dimensional dynamics is considered.

1. Introduction

It is now generally recognized that complex dynamical behavior is not restricted to systems with many active degrees of freedom, and examples of low dimensional nonlinear systems with complex and apparently unpredictable behavior are commonly cited [1–5]. One imagines that Laplace would have no difficulty with chaos, for given the *exact* state of the universe, prediction of a modern chaotic future is no more difficult than Newton's laws. In Laplace's words, for an intellect "vast enough to submit this information to Analysis, ...nothing would remain uncertain, and the future, as well as the past, would lay before its eyes" [6]. Yet few would dispute that there exist many systems which are, in fact, not *deterministic* within any known physical framework. A recurring theme in time series analysis is the attempt to characterize these two types of systems in order to distinguish determinism and indeterminism, chaos and stochasticity. In many cases of interest, this cannot be resolved definitely and we shall focus on a simpler question: given a particular set of observations (and current technological constraints), can we detect low dimensional dynamics in a time series?

This question will be directed either at phenomena outside the lab or at experiments designed to investigate such phenomena. There is no question that numerical experiments have taught us much about the nature of chaos. A more interesting question now appears to be what chaos can teach us about Nature. The particular experiment discussed here investigates dynamical processes related to the motion of planetary atmospheres, and provides an instance of the reoccurring attempt to distinguish "red" noise from nonlinear determinism. This distinction is central in determining the direction of future research; the best model for an atmosphere which amplifies small scale stochas-

[1] Present address: Mathematics Institute, University of Oxford, Oxford, OX1 3LB, UK.
[2] E-mail address: lenny@uk.ac.warwick.eng.

0167-2789/92/$05.00 © 1992–Elsevier Science Publishers B.V. All rights reserved

tic disturbances differs from an optimal model of the complex deterministic interaction of a reasonable number of modes. Long term prediction of the first is possible only in a statistical sense, the present state does not define the future state after some (nonlinear) decorrelation time. Prediction in the second case is difficult, but possible in principle as the information needed is contained in the state of the system. In this paper, we discuss techniques for this test and report initial results indicating that there is low dimensional behavior in some systems (including the experiment) and not in others. The analysis of such systems is notoriously difficult; what we desire are tests for low dimensional behavior which are reliable, in the sense that they do not yield false positives.

There are now a large number of algorithms for detecting and quantifying low dimensional behavior and chaos. The known weaknesses of individual tests may be addressed through the analysis of *surrogate data*: non-deterministic time series constructed to be similar in appearance to the original data. Such an analysis aims to establish what aspect of the data set an algorithm is quantifying, by determining whether original data can be reliably distinguished from an ensemble of surrogates, when each data set is processed in precisely the same way. The construction of these surrogate data sets is discussed in section 2 (also see [7–9]). The usefulness of this test will depend on the quality of the generator of the surrogate sets, as a poor choice of surrogate generator will result in sets which are distinguished, not because of any underlying determinism, but by some other factor. Indeed we argue in section 6 that some stochastic series may be more predictable than surrogates generated with similar statistics.

Section 3 addresses the construction and evaluation of dynamic reconstructions from observational data, where the vector field is approximated in phase space. The desirability of this approach has been discussed previously (e.g. [10,11]). We note that by using additional information about the macroscopic state of the system, more useful dynamical reconstructions can be obtained from the same data set(s). Once a dynamic reconstruction is in hand, a variety of other questions may be asked. The existence of a good reconstruction provides an estimate of a minimal embedding dimension for the system; clearly if one has a six-dimensional flow by which the observed dynamics are well described, then a six-dimensional embedding is a practical one. In addition, many characteristics of the system can be estimated from the reconstructed flow much more easily than from the raw data directly, for example the spectrum of unstable periodic orbits, or Lyapunov exponents. As these quantities are well defined for a given reconstruction, one must address the question of how quickly the properties of the flow approach those of the underlying system. In the case of unstable periodic orbits, this can be very rapid [12].

Dynamic reconstructions can also clarify experimental uncertainties. In section 4, we analyze time series from a thermally stressed rotating fluid annulus [13]. Comparison with surrogate signals demonstrates that the organization in the reconstructed phase space dynamics is greater than that arising from either autocorrelation or simple advection alone. We also show how dynamic reconstructions offer a natural method for the detection of slow parametric drift. In addition, one may use the flow to make predictions providing a direct test of determinism. We stress the importance of what is predicted and, in general, of which aspect of the time series is reconstructed. The quality of predictions (the difference between the predicted and observed values) may vary with time due to differences in the volatility of different states of the system, variations in the quality of the predictor, or errors in observation. We demonstrate a method of estimating the expected uncertainty in a given prediction, and discuss how to distinguish between these various causes. Additional evidence that the time series are in fact

low dimensional is given in section 5, where we apply the Grassberger–Procaccia Algorithm (GPA) [14] to analyze the geometric structure of the experimental data sets and establish the significance of the results through comparison with those from surrogate data sets.

Finally, in section 6, the results of applying these prediction techniques to stochastic series is considered. Laplacian determinism requires that, in the limit of perfect initial data, the future of the system is uniquely defined, so the systems considered in this section are not deterministic in this sense. There is, however, either a low dimensional or a deterministic component in their evolution, due to which many stationary stochastic systems will appear deterministic relative to some surrogate series. We discuss some of the implications this holds for distinguishing between low dimensional determinism and stochasticity from time series.

2. The data sets: observed and manufactured

2.1. Experiments

The primary data sets considered in this paper come from the geophysically inspired experiments reported by Read et al. [13,15]. These experiments were performed within a fluid filled, rotating annulus with thermally conducting side walls and insulating boundaries top and bottom. A temperature difference was maintained between the inner (cooler) and outer side walls providing an infinite dimensional simulation of the mid-latitude circulation of the Earth's atmosphere. The temperature in the fluid was measured by an array of 32 thermocouples, uniformly distributed in azimuth at mid-height and mid-radius. By monitoring the flow rate (volume) and temperature of the coolant water, simultaneous measurements of the total heat transport through the inner boundary were obtained.

Of the many reported results, two realizations are considered here. They correspond to the temperature series b and d of table 1 of ref. [13] and are shown in figs. 1a and 1c. The heat flux differs from the temperature series as it is averaged around the entire annulus and thus does not display the roughly periodic structure seen in the local temperature probe; this structure is due to the advection of (an evolving) wave pattern around the annulus. Fourier spectra of these series are given by Read et al. [13]. Both Read et al. [13] and R. Smith [16] conclude that these time series are low dimensional; series b coming from a strange attractor with a correlation dimension, $d_2 \approx 3$, while series d with $d_2 \approx 2$, is considered to reflect a two-torus [13,15].

The isolation of an experiment from external forces is a major concern of experimentalists. To obtain the long time series for the rotating annulus, experimental runs of 20 hours were required. One may ask whether the environment has been sufficiently isolated, for example from diurnal temperature variations, so that no systematic parameter drift has occurred during the experiment. Might not an evolving three-torus present a geometric structure with properties similar to those observed? A method of detecting slow parametric drift with dynamic reconstructions is introduced in the next section. First we discuss the construction and use of surrogate data sets.

2.2. Surrogate data sets

A common objection to the dynamical systems analysis of data from poorly understood systems is that the significance of a given result is rarely established [17–21]. This objection can be addressed directly by considering a class of non-deterministic surrogate signals. The significance of a result is then established by comparing it with the outcome of the same test applied to these surrogate data sets.

The choice of surrogate signals will also depend on the known weaknesses of the algorithm

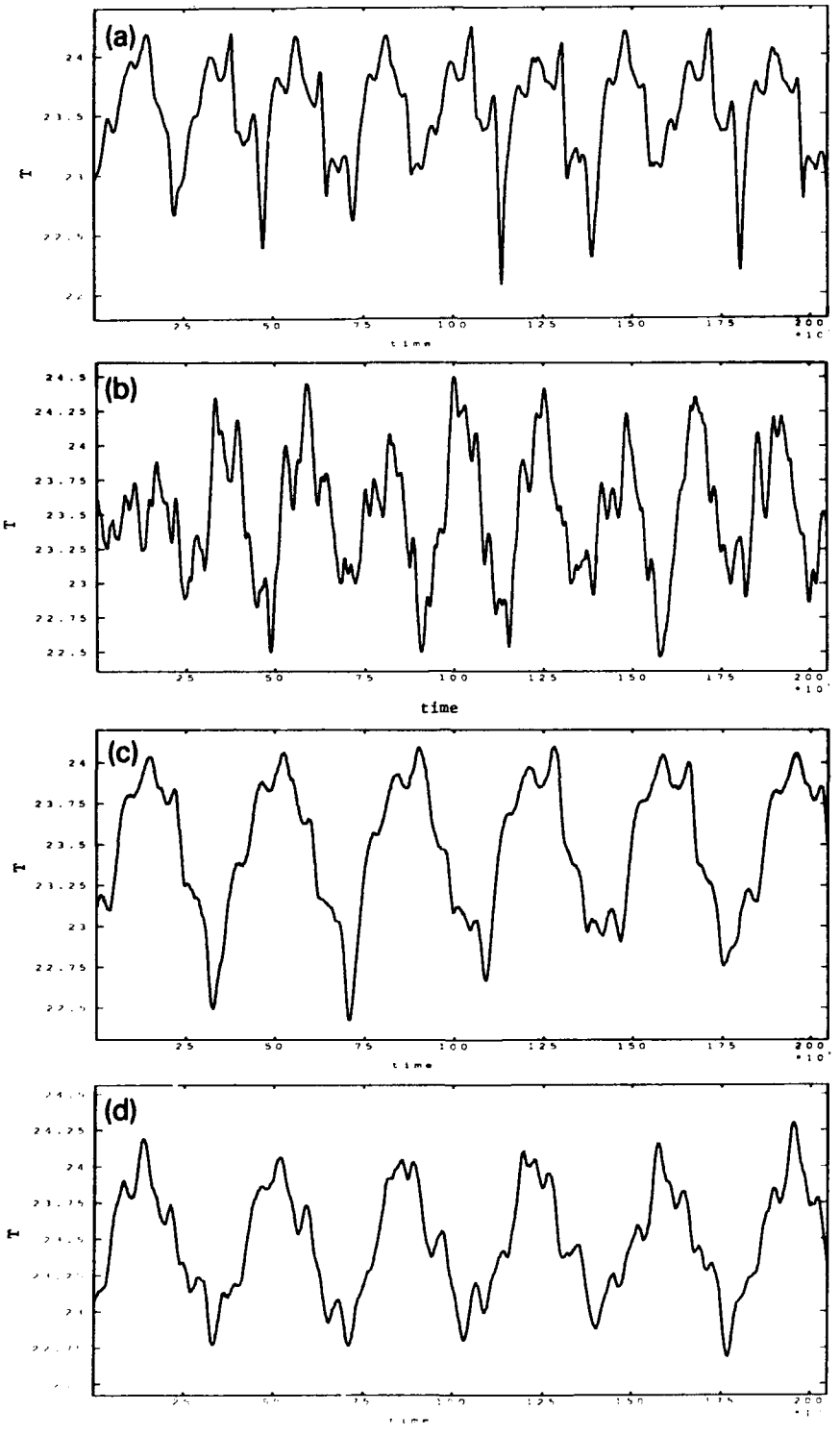

Fig. 1. A sample of the measurements of temperature, T, from the rotating annulus experiment and surrogate signals with the same autocorrelation function. (a) Time series b, (b) surrogate series for b, (c) time series k, (d) surrogate series for k.

employed to analyze the data. While any comparison with surrogate signals can quantify differences, only careful choice of the *surrogate generator* allows qualitatively new information. The goal is to generate signals with similar properties with respect to this weakness, but not containing "the physics" of the original signal. A result is significant with respect to the weakness tested if the algorithm can distinguish the true signal from the surrogates. In cases where a quantitative result (or distribution) is produced for both observed and surrogate signals, one may estimate the probability that observed value would occur by chance in an ensemble of surrogate realizations, and thereby evaluate the null hypothesis that the observed signal was a realization of the surrogate generator. Note that the second formulation is more difficult than the qualitative comparison of results, in that it requires the algorithm to converge for the surrogate signals. This poses a problem for dimension estimates via the GPA [#1].

Hypothesis testing and model evaluation with surrogate data has a long history in statistics [22,23]. There are often two conflicting motivations in choosing surrogates: ease of analysis and similarity to the observed data. One of the most common surrogate series is independent, uniformly distributed white noise which has the advantage that the expected distributions can often be calculated analytically. Most time series, however, are not uniformly distributed, neither are consecutive observations independent; at reasonable sampling rates the series should display some structure. A simple IID surrogate generator provides the correct distribution by simply shuffling the data, while series longer than the observed signal may be obtained by randomly sampling the observed distribution.

Temporal correlations are reflected in the Fourier spectrum of the series. "White" series have a flat spectrum, while those with less power at high frequencies are called "red". The methods of the previous paragraph destroy temporal correlations in the original data. Perhaps the simplest method to amend this is to produce the time series where the next observation is chosen from a distribution determined by the current state. For digital data, the amount of data required to estimate this conditional distribution will depend on the resolution of the analog to digital conversion. In this paper we will be concerned primarily with yet another surrogate generator which preserves the autocorrelation function of the original data.

The point here is to show that there are a variety of methods available for constructing surrogate series and note that signals may be indistinguishable from one set, and not another. The insight gained from testing surrogate signals depends on the particular surrogate generator(s) adopted.

When searching for low dimensional deterministic dynamics, an alternate approach for generating surrogates is to use a simple stochastic model of the system. While care must be taken not to overfit the model to the data (e.g. to construct epicycles), this approach may be particularly useful in evaluating dimension calculations from short, highly structured series. Used by Grassberger when considering climate data [18,20], this approach is discussed below for the sunspot data.

Both predictability and correlation dimension estimates may be biased through autocorrelated signals. To test if a given result is significant with respect to signals with the same autocorrelation function the following surrogate generator (suggested by Osborne et al. [24]) may be used : first compute the Fourier transform of the original signal, then compute a set of random phases, and finally invert the transform using the orig-

[#1] In their discussion of the method of surrogate data, Theiler et al. [7] point out that, strictly speaking, an algorithm need not converge for the null hypothesis to be rejected. While this is true, it is important to note the difference between distinguishing the observed series from the surrogates and estimating a statistic (e.g. a dimension) from the observed series which describes the dynamics.

inal amplitudes and a particular set of random phases to generate a particular surrogate series. Since both the original and surrogate series will have the same Fourier amplitude spectrum, their autocorrelation functions will be identical. An ensemble of surrogate signals may then be subjected to exactly the same analysis as the original data; surrogates for the annulus data generated in this way are shown in figs. 1b and 1d. Note that we are concerned with relatively long series here, where many linear decorrelation times are available, so that calculation of the Fourier transform is not a problem. Signals from this FT surrogate generator will be used to demonstrate the significance of the dynamic reconstructions in section 4 and correlation integral calculations in section 5.

Note that it is not necessary for a surrogate generator to completely destroy the phase coherence in a signal, and in some cases, it is not desirable. Consider a signal containing some understood frequencies, such as a diurnal cycle in a temperature record. Complete phase randomization will distort the daily cycles obvious in the data and the true signal may be distinguished from the surrogates for this reason alone. A stronger result is obtained (in the sense that a more relevant null hypothesis is rejected) if the observed signal can be distinguished from an ensemble of surrogates which also contain a diurnal cycle. Such surrogate series may be generated by retaining a subset of the Fourier phases unaltered and randomizing the remainder. (Note that the fine structure of a fractal attractor will be destroyed simply by randomizing only the phases corresponding either to high frequencies or to those frequencies with relatively low power thus retaining some macroscopic structure.)

For some data sets, reconstructions *cannot* be distinguished from those of the surrogate generators discussed above; but for many interesting systems the construction of good surrogates will require a more detailed examination of the system. The underlying desire is often not to identify either nonlinearity or chaos, but low dimensional, deterministic dynamics. This may be pursued by employing the best stochastic model available for a given process as a source of surrogate signals. One must balance overfitting the model to the data (allowing unduly complex models) against setting up "straw man" surrogates. An excellent example is provided by the annual mean sunspot numbers. The basic asymmetries of the sunspot number (it is strictly positive, increases more rapidly than it decays, etc.) and the presence of events like the Maunder minimum [25] make the simple FT surrogates inappropriate for this series. It is nonlinear by inspection. Analysis calls for either a modification of the data set (e.g. Spiegel and Wolf [26]) or an improved surrogate generator. By modifying the dynamics of a linear ARMA model, Barnes et al. [27] have constructed a nonlinear stochastic model of sunspot number, which, fortuitously, produces Maunder minima. Treating this model as a surrogate generator, the significance of correlation integral results for the sunspot series is examined by Weiss [28], along with a discussion of solar aperiodicity in the context of nonlinear dynamical systems.

In summary, different surrogates will test different effects. The better the surrogate generator, the more relevant the class of signals that the data set (and by implication the system) can be distinguished from. Even then, the comparison with the best surrogate signals provides only a necessary condition for the detection of low dimensional dynamics; it is not sufficient. As we are showing what the signal is not, this approach cannot establish what the system is; in this sense proving moderate dimensional chaotic dynamics by this method is similar to proving true randomness, one only knows when one cannot do it.

3. Reconstructions

3.1. Static reconstructions

The methods of nonlinear dynamical systems theory discussed here require time series to be *reconstructed* in a geometrical framework [29]. Consider a single signal measured as a function of time, $s(t)$. Once the signal is recorded digitally in discrete time we have

$$s_i = s(i\tau_s), \quad i = 1,2,\ldots,n_s, \tag{3.1}$$

where τ_s is the sampling time (and s_i is digitized to one of a finite number of values).

Consider a deterministic system with phase space dimension M_s. A trajectory, $\boldsymbol{x}(t)$, of this system is reconstructed in M dimensions from a time series of a single observable, s(t), by the method of delays [30,31] to yield

$$\boldsymbol{x}(t) = (s(t), s(t-\tau_d), \ldots, s(t-(M-1)\tau_d)), \tag{3.2}$$

where τ_d is called the delay time. The delay time need not equal τ_s (although it must, of course, be an integer multiple of τ_s). In fact the $M-1$ delays used in defining $\boldsymbol{x}(t)$ need not be equal, although they will be treated as such here. Methods for choosing τ_d vary (see e.g. [32–34]); it is usually related to the decay of information in the signal with time, either from linear autocorrelation time (τ_{auto}) or more general methods [35]. When constructing nonlinear predictors, the delay may be chosen to optimize the predictor as demonstrated in section 4. Breeden and Packard [36] discuss the case of time series sampled nonuniformly in time.

The arguments which follow do not depend on the use of this method of delays. We have achieved similar results with singular value decomposition (SVD) reconstructions (see [37,38,35]). Multi-variate series also work well, often with significantly shorter time series in terms of the total duration of the "experiment". This is easily understood as multivariate probes can distinguish states in phase space which appear similar to univariate probes due to projection effects. When working with finite data sets, the use of multi-probe data can add crucial information on the state of the system, either by directly characterizing macroscopic patterns or through direct (and much more efficient) evaluation of mode amplitudes. We return to this issue in section 7. Typically, each series is transformed to have zero mean and unit standard deviation, however the standard deviation can be varied to change the weighting between different variables in the interpolation scheme. When we are concerned with predicting a fixed period in the future, we consider a third time scale, τ_p, the prediction time. Each point $\boldsymbol{x}(t)$ on the trajectory has a scalar image $s(t+\tau_p)$ and we wish to construct a predictor to determine this image for any $\boldsymbol{x}$. In other applications the time of the prediction is determined through some geometric constraint. For example, when working on a surface of section the time of the next crossing must be predicted as well as its location. Alternatively, when predicting recurrence times, the main goal of the analysis is to determine τ_p.

3.2. Dynamic reconstructions

Recently there has been much interest in predicting nonlinear deterministic systems and a wide variety of approaches and algorithms have been proposed (see [39–43,33,44–48]). While these systems differ in detail they all attempt the same task, since in the context of deterministic analysis, prediction in time becomes a question of interpolation in phase space. To predict a deterministic system given a description of its current state, one is faced with the basic problem of interpolating the future behavior based on a sample of the "nearby" points. Like all interpolation problems, success depends on having a sufficient number of nearby points to satisfy the smoothness assumptions of the chosen algorithm. In the presence of noise, this require-

ment is increased so that the variations due to the noise may be, in some sense, averaged out. We shall use a global radial basis function predictor [43] and account for noise by fitting the predictor to the data in a least squares sense [41]. Further, we can account for the systematic bias introduced by extreme inhomogeneities in the distribution by adjusting the weighting scheme. This method provides a smooth flow over the entire region of the reconstruction (which may or may not be an "attractor"). As we are interested in finding global structures (e.g. periodic orbits), this smoothness, lost in most local methods, is important (see, however [48]).

When the underlying dynamics are not known in advance, we both construct and evaluate a dynamic reconstruction from the same data set. To do so, the data set is typically divided into two sections of unequal length: the *learning set* consisting of n_L points from which a reconstruction is derived and the *test set* on which various *reconstructions are evaluated.* It is crucial that this distinction should be maintained for out-of-sample evaluation of the predictor. That is not to say that statistics from the ability to fit the learning set are not of interest, but that these two types of statistics measure essentially different things. Statistics generated within the learning set reflect how well the data can be forced into a given mold and may be useful, for example, for internal consistency checks and locating outliers. Those generated from the test set reflect how well the predictor generalizes from the learning set to new data. Only the latter are of use for cross-validation. Predictor "error" in the two sets is a very different quantity. For example, with the exact radial basis function predictor described below, the in-sample predictor error can be made zero for almost any data set.

The predictor is based upon a set of n_c centers in an M-dimensional space:

$$\boldsymbol{x}_j^c,\ j = 1,2,\ldots,n_c; \quad \boldsymbol{x}_j^c \in \mathbb{R}^M.$$

The choice of centers will be discussed below, but, in the simplest case, each center might correspond to a data point in the learning set. Associated with each of the n_L points, $\boldsymbol{x}_i$, in the learning set is an observation, s_i; s_i may be a future value of the system, a simultaneous value of another state variable, or even a past observation thought to contain noise [49]. In general, the problem is to construct a predictor (or map), $F(\boldsymbol{x})$: $\mathbb{R}^M \to \mathbb{R}^1$ which estimates s for any $\boldsymbol{x}$. We will consider $F(\boldsymbol{x})$ of the form

$$F(\boldsymbol{x}) = \sum_{j=1}^{n_c} \lambda_j \phi(||\boldsymbol{x} - \boldsymbol{x}_j^c||), \tag{3.3}$$

where $\phi(r)$ are radial basis functions and the λ_j are constants which are determined by observations in the learning set:

$$F(\boldsymbol{x}_i) \approx s_i. \tag{3.4}$$

Determining the λ_j corresponds to the solution of the (linear) problem

$$\boldsymbol{b} = \mathbf{A}\boldsymbol{\lambda}, \tag{3.5}$$

where $\boldsymbol{\lambda}$ is a vector of length n_c whose jth component is λ_j and $\mathbf{A}$ and $\boldsymbol{b}$ are given by

$$A_{ij} = \omega_i \phi(||\boldsymbol{x}_i - \boldsymbol{x}_j^c||) \tag{3.6}$$

and

$$b_i = \omega_i s_i, \tag{3.7}$$

where $i = 1,\ldots,n_L$ and $j = 1,\ldots,n_c$. Traditionally, the weights ω_i reflect the varying confidence associated with the ith observation.

Casdagli [43] was the first to solve this problem in the context of predicting chaotic systems, considering the special case of exact interpolation where centers are chosen from the learning set and only their images are considered in eq. (3.4). In this case the interpolation on the centers is exact; the matrix $\boldsymbol{A}$ is square and the solution for $\boldsymbol{\lambda}$ depends on the $\boldsymbol{A}$ being nonsingular. This is guaranteed when the $\boldsymbol{x}_j^c$ are distinct and $\phi(r)$ is a radial basis function [50,51].

Typical radial basis functions are $\phi(r) = r$, r^3, $\sqrt{r^2 + c}$, $1/\sqrt{r^2 + c}$, and $e^{-r^2/c}$ where c denotes a constant often based on the average distance between neighboring centers.

Casdagli demonstrated the effectiveness of this approach and showed that interpolation in both time and parameter space was possible. There are, however, several drawbacks when applying it to noisy data; in this form, the interpolation fits the centers exactly, and no information from the points in the learning set not chosen as centers, is used. It is desirable to use this information, and important to avoid overfitting or fitting the noise in data exactly (especially since when making the choice of centers, one may tend to select outliers). Even with numerical systems, computational constraints limit the number of centers used.

In order to include the information available from the learning set, Broomhead and Lowe [41] solved this problem in a least squares sense and studied the behavior of the logistic map. For the least squares case, the entire learning set is included in eq. (3.5) ($\boldsymbol{b}$ is of length $n_L > n_c$), but a smaller number of centers are employed, and thus A is not square. Further there is no need to know the images of the centers, so they need not correspond to observations from the series. We seek a λ which minimizes $\chi^2 = ||\boldsymbol{b} - \mathbf{A}\lambda||^2$

Choosing the solution which also minimizes $||\lambda||^2$ corresponds to

$$\lambda = \mathbf{A}^+ \boldsymbol{b}, \tag{3.8}$$

where $\mathbf{A}^+$ is the Moore–Penrose pseudo-inverse of A. Efficient methods of calculating $\mathbf{A}^+$ via singular value decomposition are discussed in [23]. Noting that the guaranteed solubility of the original system is lost in this generalization, Broomhead and Lowe [41] quantified the effect of increasing the number of centers and considered this modeling approach as a special case of a neural network with a guaranteed learning rule.

We continue this approach, introducing the weights w_i, and investigate the sensitivity of the solution to the choice of centers and the effects of observational noise. Given the inhomogeneous (often singular) distribution of data on a chaotic attractor (see e.g. [52]), these weights can also be used to provide a more uniform prediction error across the attractor by reducing the importance of the dense regions of the reconstruction.

One common objection to the use of radial basis function interpolation arises from the large number of free parameters employed, one per center in the original formulation. The least squares formulation addresses this question of parsimony. When determining the coefficients of eq. (3.5), we perform a SVD of the matrix A. In doing so, a tolerance is set as to the smallest meaningful value an eigenvalue can take [23]. Values below this threshold are considered superfluous and suppressed (set equal to zero). This prevents "extra" degrees of freedom in the model from overfitting "noise fluctuations". As the threshold is raised, the estimated uncertainty in the modeling parameters (the λ_i) decreases dramatically, with little effect on the χ^2 or the in-sample predictor error. This might be taken to mean that higher tolerances were preferred to avoid fitting noise in the learning set. Out-of-sample prediction error statistics often conflict with this interpretation: there are examples for which, although the estimated uncertainty of the λ_i is greater, low threshold models consistently yield better out-of-sample prediction statistics. This implies that the model is *not* fitting noise in the learning set. It is here that a difference between radial basis functions is observed: for a fixed tolerance and an identical choice of centers, models with $\phi(r) = e^{-r^2/c}$ consistently use fewer degrees of freedom than those with $\phi(r) = r^3$ or $\phi(r) = r$.

Predictions more than one sampling time into the future can be made either by *direct forecasts*. constructing a predictor for this time scale, or through *iterative forecasts* repeatedly using a predictor which forecasts a smaller time step. Farmer and Sidorowich [49] conclude that iterative forecasts are generally better than direct

forecasts, but also present an experimental example where the reverse is observed. Stokbro [48] also compares the two as a function of the forecast time and comments on the choice for the basic time step. Direct forecasts are used in this paper.

As noted above, minimization of $||\boldsymbol{b} - \mathbf{A}\lambda||^2$ with all ω_i equal results in a bias in favor of the frequently visited regions of phase space. In order to achieve a good reproduction throughout phase space, such weighting is not desirable, as argued in the next section. One method to account for this is to partition the phase space and allow only a specified number of points in each partition. In the presence of noise it is preferable to retain all the observations and adjust the ω_i so that the partitions are more equally weighted.

3.2.1. The choice of reconstruction centers

We now consider the question of how to determine the centers. Four approaches to this question are to choose the centers either

(i) randomly (or uniformly) in the region of phase space explored by the data,

(ii) with respect to the probability density (measure) on the reconstruction,

(iii) spatially uniform on the reconstruction,

(iv) with respect to the local divergence on the reconstruction.

Methods (iii) and (iv) appear the most robust in terms of providing good reconstructions with a limited number of centers, but unfortunately, these results appear to be system dependent. There are several shortcomings in methods (i) and (ii) . Placing the centers uniformly in space works well when the system explores the entire region, as with the logistic map in one dimension. In higher dimensional spaces, there are often large lacunae into which the system does not venture; placing many centers in such gaps is counter-productive, at least when localized basis functions are employed [#2] . Numerical experiments indicate this is particularly relevant in cases where the underlying dynamics is not determined by a simple analytic formulation (contrast a true surface of section of a flow with that of an analytically defined map) perhaps due to the smoothness of the dynamics.

Centers may be placed uniformly with respect to the probability density on the reconstruction either by choosing them equally spaced in time or randomly sampling the series. This initially attractive idea often yields poor results. One reason for this can be understood in the case of flows where the speed in phase space varies from point to point. An ideal illustration of this effect is provided by the Duffing oscillator near homoclinic bifurcation (see [53,54]). In this case, a trajectory spends most of its time near the fixed point, while the centers "should" be distributed over the relatively rare excursions. With maps, inhomogeneities in the measure also result in a poor distribution of centers.

One method to distribute the centers uniformly on the reconstruction is simply to disallow centers closer than some nearest center distance d_{nc}. This succeeds in the Duffing case and will, in general, avoid the accumulation of centers in the slow moving regions of the reconstruction which are relatively easy to predict. But that is the real point. Once the basic skeleton of the reconstruction is covered, it is reasonable to place additional centers in regions where the fine structure of the flow is greatest and where prediction is most difficult. Note that this need not correspond to the fine structure of the probability density or geometry, the fine structure here is in the vector field of the phase space flow, not that of the attractor. Also note that, while the location of additional centers allows the predictor to develop fine structure, this will not occur unless the data are weighted toward the recovery of that fine structure. Returning to the Duffing oscillator, we would like to combine (iii) and (iv) , covering the excursions and also the region about the unstable manifold near the origin so that the beginning of an ex-

[#2] I would like to thank James Theiler for pointing out this qualification.

cursion is predicted. Locations where the flow is contracting need not be sampled so densely.

The importance of these effects in a given reconstruction may be determined by dividing the reconstruction space into partitions and examining the errors made in each region. When the centers are distributed uniformly on the reconstruction, a straightforward way to partition the reconstruction is to classify each point according to the center to which it is nearest. This is now demonstrated for rotating annulus data.

4. Applications to laboratory data

We now apply the ideas of the last section to the rotating annulus data. Consider first a dynamic reconstruction of data set series *b* built from a learning set consisting of 2K points ($1K = 2^{10}$) from the first 16K data points of this 50*K* point data set. The reduction from 16K to 2K was achieved by increasing the sampling time by a factor of 8, thus all time steps considered in reconstruction will be multiples of 8 τ_s. A total of $n_c = 128$ centers were chosen such that no two were closer than a nearest center distance, d_{nc}; this was implemented by choosing an initial value of d_{nc} large enough so that less than half the desired number of centers were found on the first pass through the learning set. The value of d_{nc} was then decreased by a factor of 0.7 and the process repeated iteratively in order to avoid over-sampling any one segment of the learning set. In this case, the delay time $\tau_d = 4$ $(8\tau_s)$ and an embedding dimension, $M = 5$, were also chosen taking into account the results of the correlation integral calculations of section 5. We shall refer to this model with $\phi(r) = e^{-r^2/c}$ as reconstruction A.

The initial results are presented in fig. 2. The three panels show (a) the observed (solid) and predicted (symbol) time series as a function of time, (b) the absolute value of the prediction error, and (c) the distance between the point being predicted and the nearest center to it, d_{nc}. The prediction time ($\tau_p = 18$ $(8\tau_s)$) was chosen as twice τ_{auto} (the first zero of the linear autocorrelation function). Each of the predictions was made at this fixed distance into the future, the series shown is taken from the beginning of the test set and represents completely out-of-sample testing. In panel 2a, the prediction time is just over $\frac{1}{3}$ of the separation of the tick marks. Comparing the first 2 panels, it is observed that large errors often correlate with extreme values of the measured signal. Occasionally, there are episodes of poor predictions (not shown) which do not correspond to extreme values of the signal but do correspond to large values of d_{nc}; this implies that the trajectory is located in a region of phase space not explored during the learning set. Predictions in such regions are extrapolations and generally not reliable.

The effect of varying reconstruction parameters and choice of basis function is illustrated in fig. 3, which shows the cumulated predictor error profile, $P(\epsilon)$, for three different reconstructions. These graphs display the fraction of the learning set predicted to within a given error. For example, the solid line denoting the reconstruction of fig. 2 shows that half the learning set was predicted with $\log_2(\text{error}) < -3$ corresponding to an accuracy of approximately 6 bits. The right most (short-dashed line) corresponds to a similar reconstruction with $\tau_d = 8\tau_s$ (a factor of 4 shorter than reconstruction A). The corresponding predictions are about 0.5 bits worse; more so for small errors. τ_d was chosen to optimize this distribution, although for τ_d slightly greater than the chosen value the variation was small.

The long-dashed line in fig. 3 shows the distribution for a reconstruction similar to reconstruction A, but using $\phi(r) = r^3$; as was often observed, the exponential provided a slightly better fit. Although we shall not discuss the effect of different basis functions further, it is interesting to note that the two predictors tend to yield similar predictions across phase space. Indeed, they are in closer agreement with each other than with the observations. This is shown in fig. 4b

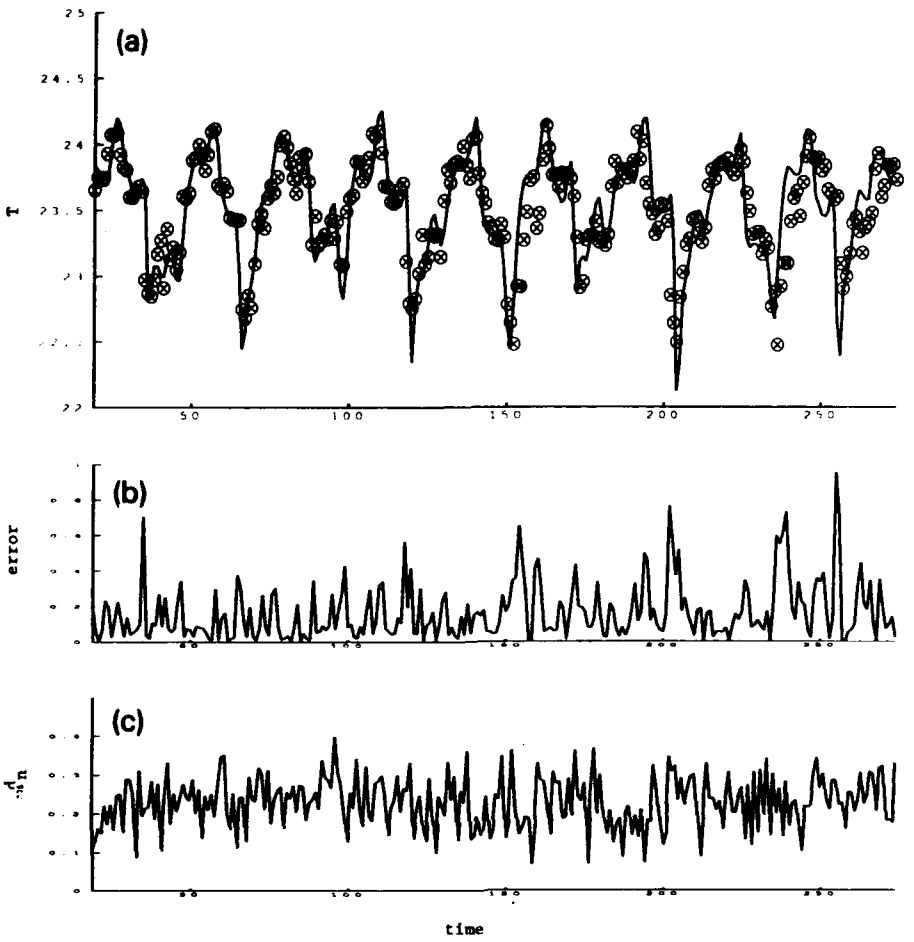

Fig. 2. An extract of the results of applying reconstruction A to time series *b*. (a) the observed (solid) and predicted (symbol) temperature values, (b) the error, and (c) nearest center distance for the point from which the prediction was made.

which is a scatter plot of the prediction of reconstruction A, where $\phi(r) = e^{-r^2/c}$, against that with $\phi(r) = r^3$. Panel 4a is a similar plot with reconstruction A against the observations. For small observed values, the two predictors remain in rough agreement although both are inaccurate; the inaccuracy results, in part, from the low weighting the least squares fit assigns to the less commonly observed values. By adjusting the the weights, w_i, we can force the distribution of errors to be more uniform over the reconstruction.

The cumulated predictor error profiles show a slow decay in predictability as τ_p increases comparable to Read's Lyapunov estimate of 1.79×10^{-3} bits per second (or one bit per advection period). As these values are small, it may be argued that they are numerically zero and the system is not, in fact, chaotic. One alternative is the parametric drift mentioned above. We give evidence below that this is not the case. Of course, the significance of the Lyapunov exponent can be addressed directly via comparison with the distribution of values obtained from surrogate sets; where the Lyapunov exponent estimates from the surrogate signals are used to define the expected range of values to be considered as computationally equivalent to zero. It should also be noted that a different predictor was constructed for each of these prediction times (i.e. a direct predictor for each value of τ_p). The decay of predictability with time in this instance may differ from the case of

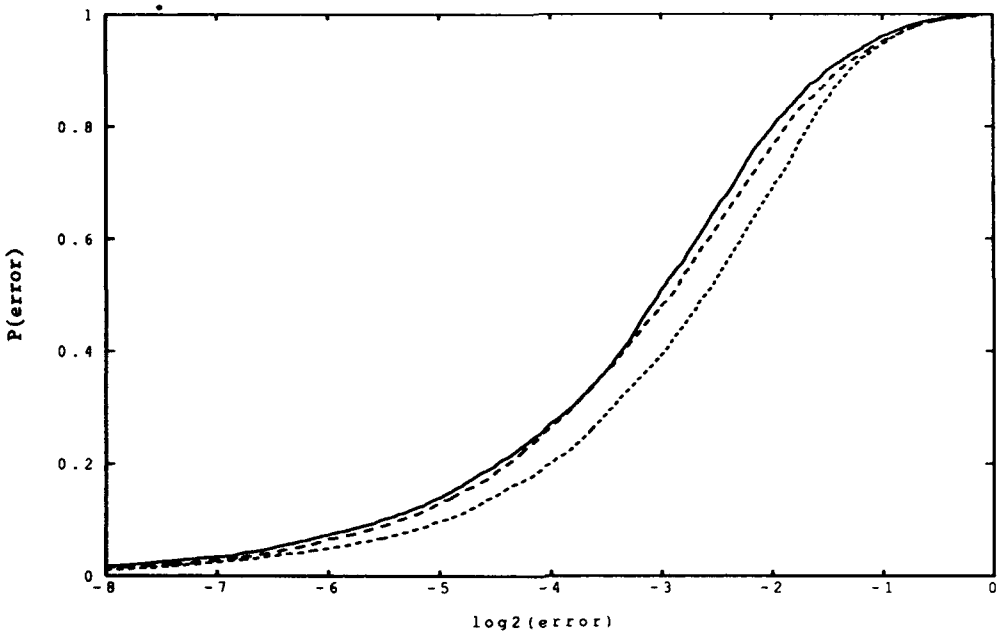

Fig. 3. Cumulated predictor error profile for a reconstruction with $n_c = 128$, $M = 5$, $\tau_p = 18$ $(8\tau_s)$ and $\phi(r) = e^{-r^2/c}$, $\tau_d = 4$ $(8\tau_s)$ (solid), $\phi(r) = r^3, \tau_d = 4$ $(8\tau_s)$ (long dashed), $\phi(r) = e^{-r^2/c}, \tau_d = 1$ $(8\tau_s)$ (short dashed). The horizontal axis is the base-2 logarithm of the error.

an iterated fixed-step predictor.

Rather than estimate the Lyapunov exponents of surrogate series, we investigate the significance of observing this level of predictability. In particular, whether predictions of similar accuracy would be found in other signals with the same autocorrelation function. To do so we construct surrogate series with a FT surrogate generator and consider the prediction of a reconstruction with parameters identical to those of reconstruction A above. The resulting cumulative error profiles are shown in fig. 5. Eight surrogate series, each with a different set of random phases was analyzed, the results shown have the lowest (best) average absolute predictor error. Considering the error to which 50% of the series is predicted, reconstruction A is almost one bit lower, implying that the prediction error is almost a factor of 2 less, easily distinguishing the observed data from the surrogate series.

Noting that the distributions do not appear to be Gaussian, we can reject the hypothesis that these two realizations either have the same mean (via the t-test) or were generated from the same distribution (via the Kolmogorov–Smirnov test) at well over the 0.99 confidence level. We wish to stress both the significance and limitations of this statement. The surrogate generator here preserved the autocorrelation function of the data set, and the radial basis function predictor easily distinguished five-dimensional reconstructions of these two signals. What we have really shown is that this 5D reconstruction is more coherent than that of these surrogate data sets. This is somewhat different from establishing that the data arise from a deterministic five-dimensional system. Further evidence that the data do in fact reflect low dimensional dynamics in provided by the correlation integral results.

As an additional test, we construct a "surrogate predictor" to determine whether the predictability of this signal is only due to the advection of a slowly evolving signal. Look again at the observational and the surrogate version of series *b* in fig. 1; the coherence between one "wave" and the next is stronger in the real signal than in the surrogate data. The surrogate predictor sim-

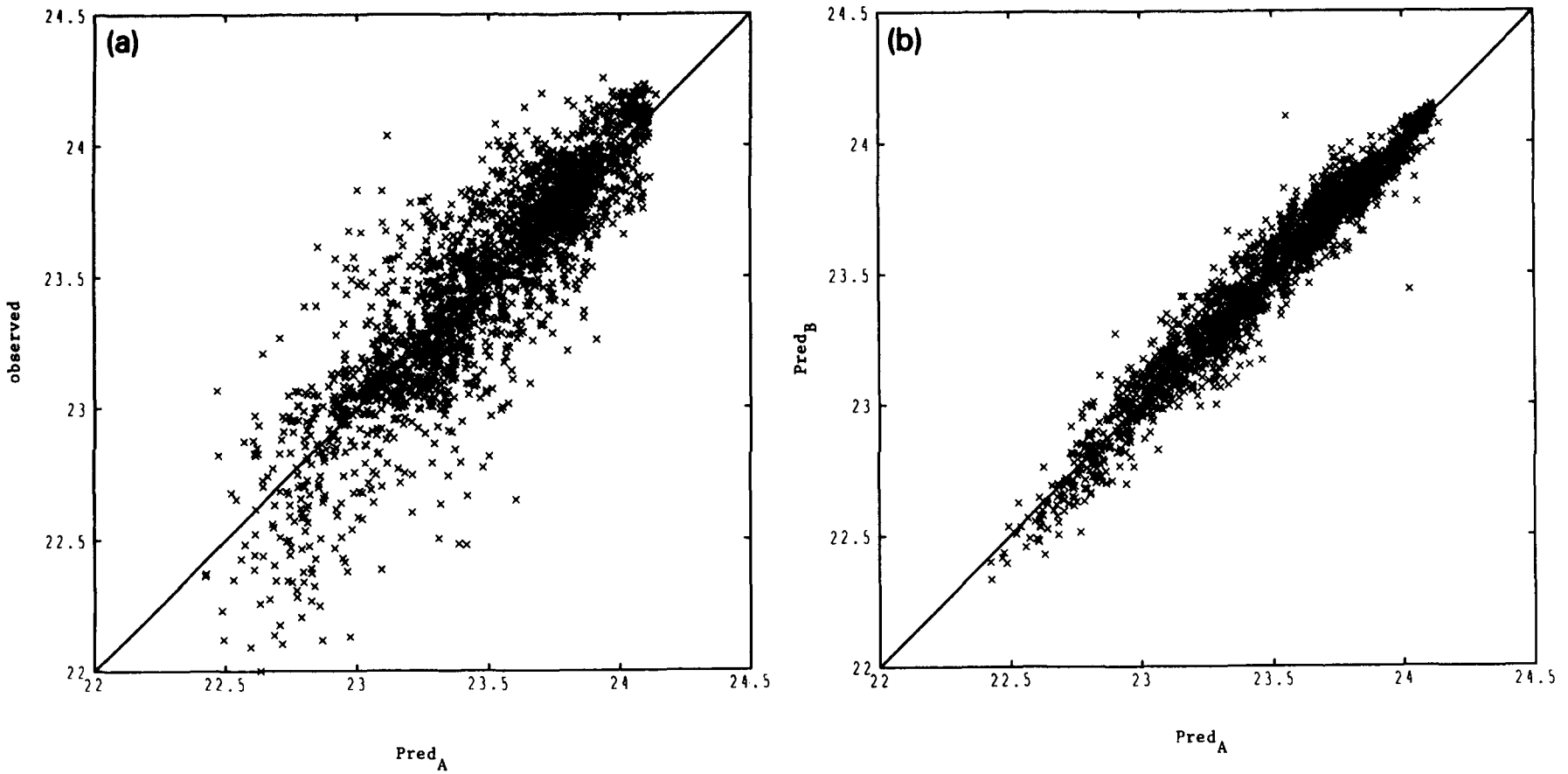

Fig. 4. Scatter plots of the predictions of reconstruction A (horizontal) against (a) the observed value and (b) the prediction of a similar reconstruction, Pred_B, using $\phi(r) = r^3$.

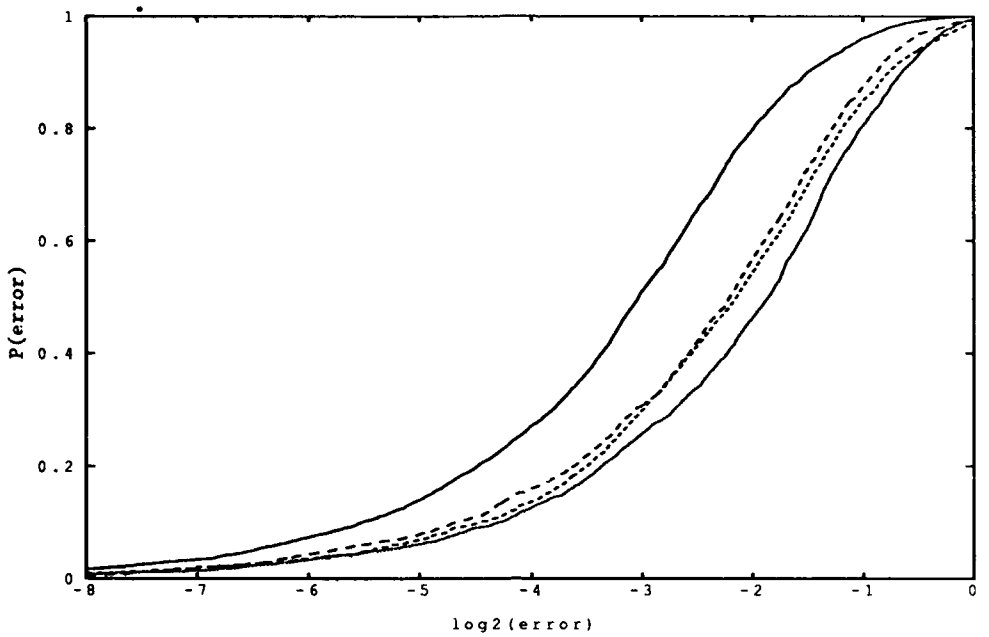

Fig. 5. Cumulated predictor error profile for reconstruction A on (a) observed (solid) and (b) surrogate (long dashed) series. And the period 1 surrogate predictor in (a) observed (short dashed) and (b) surrogate (dotted) series.

ply projects forward the last observed point an integer number of advection periods in the past. The cumulative error profile for this predictor is shown in fig. 5 for both the observed data set (short-dashed line) and the surrogate (the right most, fine dotted line). Although it is not as accurate as reconstruction A, this one dimensional predictor clearly differentiates between the true signal and these surrogates, demonstrating one limitation of the FT surrogate generator in this case. (This originates, in part, from the loss of phase coherence of the periodic advection signal in the FT surrogates, as noted above.) To establish that a system is chaotic through surrogate signals, we would have to reject all nonchaotic surrogates; this is clearly not feasible, and highlights the importance of the selection of surrogate signals.

The inhomogeneity of the spatial distribution of points in the series *b* reconstruction is reflected in fig. 6 which shows a histogram of the number of times each center is nearest to the point from which a prediction is made in the test set. It is convenient to use this partition of the phase space by nearest center to examine the variation of predictor error with location as well. This is shown in fig. 7 which will be used to predict the error associated with each prediction of the time series below. Examining the distribution of errors in the learning set about individual centers provides examples where the data density is high and the average error is below the global average. Simultaneously, the error distribution about some other center with fewer associated points may be very broad. On the assumption that this is due to additional structure in the flow near the latter center, additional resolution should be placed in this region instead of the denser region where the flow is already well described.

4.1. Predicting predictability

We have seen that the predictability of a reconstruction varies with location, due to both the underlying dynamics of the system and the weighting scheme used in the construction of the predictor itself. We now quantify this variability and, in so doing, estimate the uncertainty associated with each individual prediction. This will

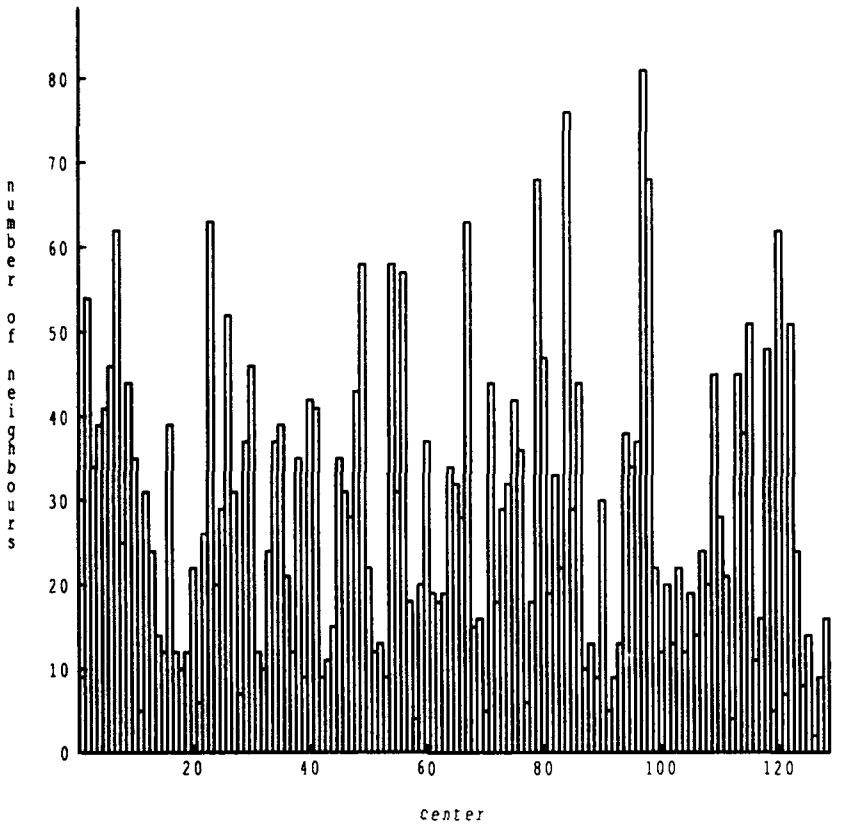

Fig. 6. Histogram of number of predictions made as classified by the nearest center to the point from which the prediction was made. The data is from the test set of reconstruction A.

allow us to estimate the error associated with a prediction at the time the prediction is made and thus forecast error bars as well as expected values.

When estimating the probable errors associated with each location in the reconstruction we again use the partition provided by the centers. Let $n_N(x)$ equal the index of the center nearest to the point x, that is

$$n_N(x) = j, \tag{4.1}$$

where $(||x - x_j^c||)$ is the minimum value of $(||x - x_k^c||)$ over all centers k.

At the beginning of the test set, initial estimates can be drawn from the histograms of the learning set. When very large quantities of data are available, one may estimate the mean and standard deviation error associated with each center (or even examine each distribution). We note that, in some examples, the distributions are far from Gaussian (e.g. bimodal) and the distribution of positive errors is very different from that of negative errors. In shorter sets where many centers may have only a few (< 3) tests, we have found it useful to define the average positive predictor error associated with the jth center as

$$E_j^+ = \frac{\sum_k e_k \delta_{j,n_N(x_k)}}{\sum_k \delta_{j,n_N(x_k)}}, \tag{4.2}$$

where δ is the Kronecker delta, e_k is the error associated with the kth prediction (i.e. the predicted value minus the observed) and the sum is over all k such that $e_k > 0$. E_j^- is similarly defined for $e_k < 0$. These average positive and negative errors are then used as predicted error bars for future x such that $n_N(x) = j$. Positive and negative errors are considered separately, so

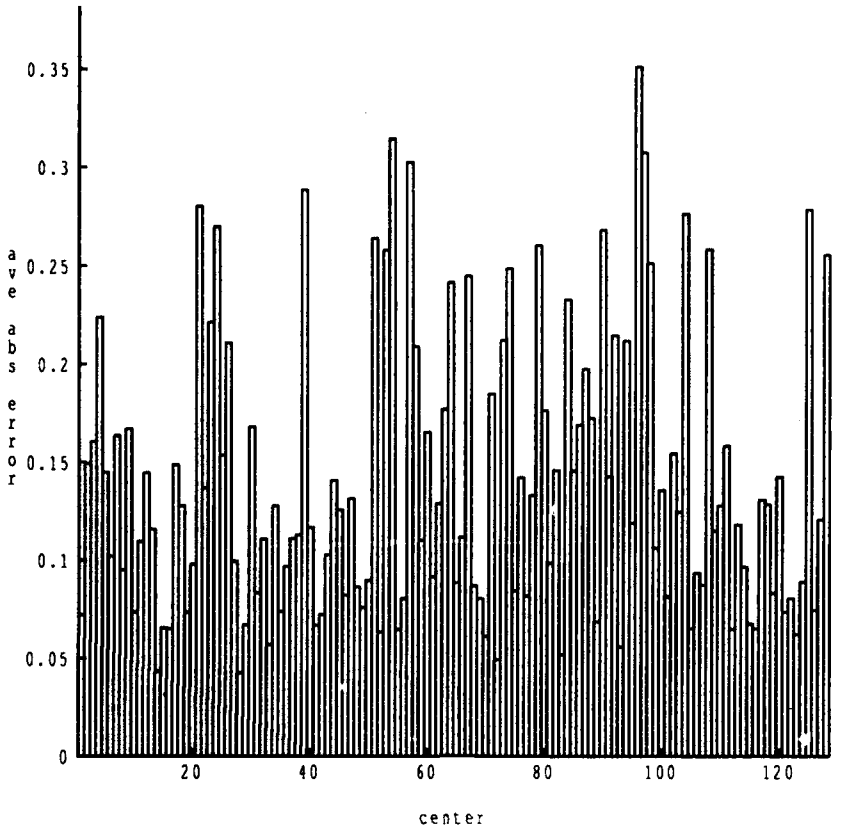

Fig. 7. Histogram of local error from the test set of reconstruction A classified according to the center nearest to the point predicted as in fig. 6.

asymmetries in the predictability are preserved.

Two short sequences taken from the annulus temperature series *b* are shown in fig. 8 where the time scale is increased from that of fig. 2 to make individual predictions more clear. In this case, the predictions were made 18 ($8\tau_s$) steps ahead corresponding to almost two horizontal tick marks. Panel A shows a typical result; note that the expected error is often asymmetrically distributed about zero. This implies that the absolute value of the average prediction error could be reduced by adding a constant to each prediction, the value of which was dependent upon the nearest center, $n_N(x)$. This would improve the predictions but at the cost of a smooth predictor (local nonlinear predictors should provide even lower predictor error, and can function at lower data densities than local linear methods). Modifying the weighting scheme used in constructing the predictor provides an alternative global approach which preserves smoothness.

The more striking result is the reliability of the estimated error; predictions which lie in portions of the time series with sharp vertical displacements have large estimated errors, the slowly changing portions expected to be more predictable tend to have smaller estimated errors which are reflected in the observed error.

In addition to their practical value, these estimates can be used to identify regions of the reconstruction with greater instability and to distinguish outliers from variation due to this instability. The only instances of persistently misleading results noted thus far occur when the trajectory explores a portion of the phase space not visited in the learning set; this condition can often be identified by an increase in the nearest neighbor distance as noted above. Persistently

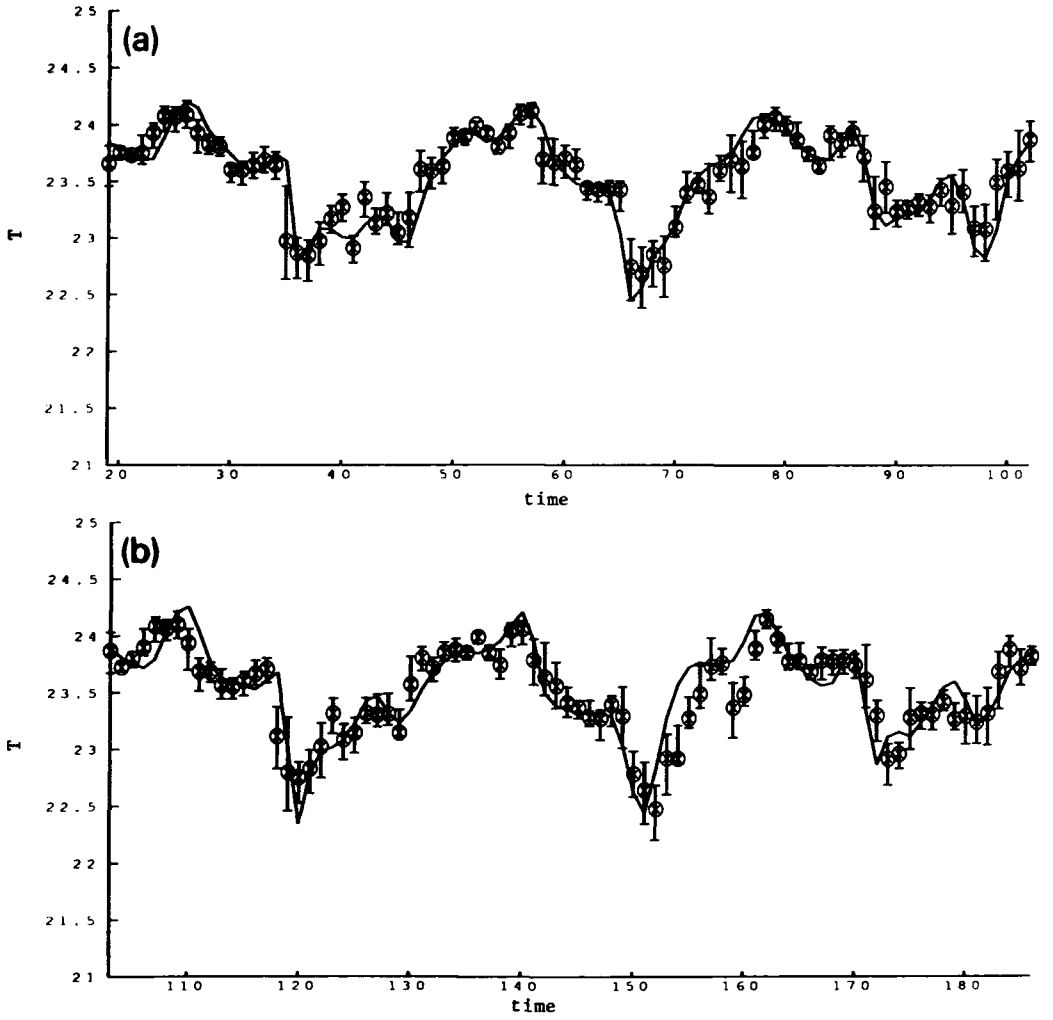

Fig. 8. A section from the learning set of reconstruction A where the temperature, its forecast value and the predicted uncertainty are plotted. Here $\tau_p = 18$ $(8\tau_s)$.

poor predictions and error estimates may also indicate sensor failure or a change in the dynamics of the physical system, an application developed in refs. [55,56].

4.2. Parametric drift

To conclude this section we address the question of slow parametric drift over the course of the experiment. If this were to occur, the dynamics at different points in time would be best determined from learning sets located nearby in time. To see if this is indeed the case, the learning set above (from the initial 4096 points) was tested on the remaining time series divided into thirds. Computing the Kolmogorov–Smirnov statistic, d, between the out-of-sample error distributions from a given predictor on different sections of the series [23], we find that the null hypothesis that the observed distributions arise from the same distribution function cannot be rejected at the 90% level of confidence. If this test is applied directly to the two halves of series b, we have $d_{obs} \approx 0.04$ and probability$(d > d_{obs}) \approx 0.86$. When applied to the data series, the Kolmogorov–Smirnov test indicates that the range and distribution of the data did not change; when applied to the error distributions,

it indicates that the quality of the predictor did not change and hence is evidence against slow parametric drift. It does not, of course, rule out recurrent parametric drift on time scales short relative to the length of the series. There exists no definitive method to do so as, in practice, the distinction between "parameters" and "system variables" becomes a philosophical question when both vary on small time scales.

5. Correlation dimension

The Grassberger–Procaccia Algorithm or GPA [14], which estimates the correlation dimension, d_2, provides a direct measure of the geometry of a distribution and has become perhaps the most widely used tool in the search for low dimensional dynamics. It is described in detail in [57,58]. Briefly stated, one wishes to estimate the correlation integral $C_2(\ell)$ of a distribution of points $\boldsymbol{x}$:

$$C_2(\ell) = \frac{\text{number of pairs of points separated by less than } \ell}{\text{total number of pairs of points}} = \text{probability}(\|\boldsymbol{x}_i - \boldsymbol{x}_j\| < \ell), \tag{5.1}$$

where $\boldsymbol{x}_i$ and $\boldsymbol{x}_j$ are two randomly chosen points in the set. It is implicitly assumed here that one is selecting from the set of all possible pairs of points on the attractor. This is not the case with reconstructions from time series when the spatial separation between a pair of points reflects that they are close in time. Theiler [59] demonstrated that for smooth dynamical systems, consideration of points close in time can lead to one-dimensional "knees" in correlation integral estimates. More recently, Osborne and Provenzale [60] have found finite correlation dimensions for power law noises, but these are another case of this same effect and need not foil dimension estimates in practice [61]. A simple test for detecting such effects is given in ref. [9]. Taking care that these effects are minimal, the correlation integral is approximated as

$$C_2(\ell) = \lim_{N\to\infty} \frac{1}{N^2} \sum_{i=1}^{N} \sum_{j=1}^{N} \Theta(\ell - |\boldsymbol{x}_i - x_j|), \tag{5.2}$$

where ℓ is the length scale and $\Theta(x)$ is the Heaviside function which is equal to zero for negative argument and one otherwise. When the limit is not taken, the sums over i and j should be restricted so that $|i - j| > W$ [59]. Numerically efficient methods for evaluating the correlation integral are available [62,63].

In the limit of small ℓ, we expect $C_2(\ell)$ to be scaling, that is

$$C_2(\ell) \sim \chi(\ell)\, \ell^{d_2}, \tag{5.3}$$

which defines d_2, the correlation exponent and $\chi(\ell)$ accounts for lacunarity effects [64,65]. At finite length scales, one can inspect the local slope of $\log_2 C_2(\ell)$ as a function of $\log_2(\ell)$ for a scaling range over which to estimate d_2. When estimating d_2, the $i = j$ terms in the sum should be neglected, although it is useful to compute $C_2(\ell)$ with both normalizations (this involves negligible computational cost) and compare their slopes as functions of $\log \ell$. Both curves provide useful information in judging the quality and evolution of reconstructions with changes in the embedding dimension.

There has been a great deal of discussion in the literature regarding the amount of data required to obtain a meaningful estimate of the characteristics of chaotic dynamical systems. For the correlation exponent, several authors [66–69] have provided estimates of the minimum "number of data points" required. Unfortunately, it is not easy to determine the number of data points in a time series in this sense. The difficulty lies in assumptions which require the data to be spread uniformly with respect to some underlying probability density (measure). Appeals to ergodicity are of no use when the sampling rate is such that consecutive measurements are dynamically correlated, for this biases the correlation integral by

increasing the probability of a pair of points at separation $\ell + \delta$, given that there is a pair with separation ℓ. The dynamical correlation time is also very difficult to estimate *a priori*, it is certainly not the linear correlation time (i.e. the first zero of the linear autocorrelation function, τ_{auto}) or the first minimum of the one dimensional mutual information [68]. A second drawback of these scaling arguments is that they provide necessary but not sufficient conditions, and the former are of much less use than a measure of success. It is easily shown that through smooth deformation of a reconstruction, one can always increase the number of data points required to obtain a good estimate of a dimension.

Like all analysis techniques, the GPA must be applied with some insight. There has been much discussion about the *a priori* knowledge of the system required to apply this algorithm. We would liken application of the GPA to that of the Fast Fourier Transform (FFT): one must understand the algorithm and its limitations when interpreting the results. To push the analogy, one rarely hears reports of strong power in a frequency beyond Nyquist limit, or public arguments over whether it is really necessary to have a stationary time series to apply the FFT. Such results would reveal a false application of the algorithm, not a flaw in it. Nor is it claimed that one must understand the physics of the system to gain useful information from a power spectrum. The analogy holds.

The analogy fails when the difficulty of coding the algorithm is considered, and the general knowledge of its limitations. Particular errors of application are well documented [59,66,58,57,70] although they are still common. Even so, these are again necessary, not sufficient conditions. Even when precautions are taken, one would like to estimate the probability that a given result, with specified reconstruction parameters (delay times or SVD window lengths, etc) is not due to such factors as the length of the data set. This is the strength of employing surrogate signals.

5.1. *Surrogate signals and the correlation integral*

The FT surrogate generator is now used to evaluate the results obtained for the rotating annulus data. Rather than attempt to automate the choice of a scaling region, fig. 9 presents the slope of the correlation integral from series *b* data along with that of a representative surrogate set. The solid (short-dashed) lines represent the slope of the $\log_2 C_2(\ell)$ against $\log_2 \ell$ including (excluding) the $i = j$ points in the sum. The regular long-dashed line is the expected slope for white noise with the same diameter (see [66]). The difference between observed and surrogate graphs is striking both in the value of the plateau (if one can be said to exist for the surrogate set) and the relative location of the nearest neighbor distances as reflected by the value of $\log_2(\ell)$ at which the curve including the $i = j$ points returns to zero. It is tempting to define a scaling range and determine the probability of observing the value $d_2 \approx 3$ for the surrogate sets. Such a calculation is questionable as the algorithm has not converged in the case of this surrogate series and there is no saturation as the embedding dimension is increased. This detracts little from the argument that the observed series has a significantly different correlation integral than expected due to its autocorrelation function.

We now examine the series *d* data set, considered to be quasi-periodic (two incommensurate frequencies) by Read et al. [13]. The slope of the correlation integral with length scale for this set is shown in fig. 10. Note that it does appear to be about two-dimensional. The feature at length scales $-2.5 < \log_2(\ell) < -1$, reflects the macroscopic structure of the reconstruction and not an artifact of the analysis. Assuming that the reconstruction is a two-torus, this would indicate that it has greater extent in "one direction", the true dimension of the distribution is not observed until length scales smaller than $\frac{1}{8}$ are reached. Even if a surrogate generator preserves the geometry of the two-torus, this particular macroscopic struc-

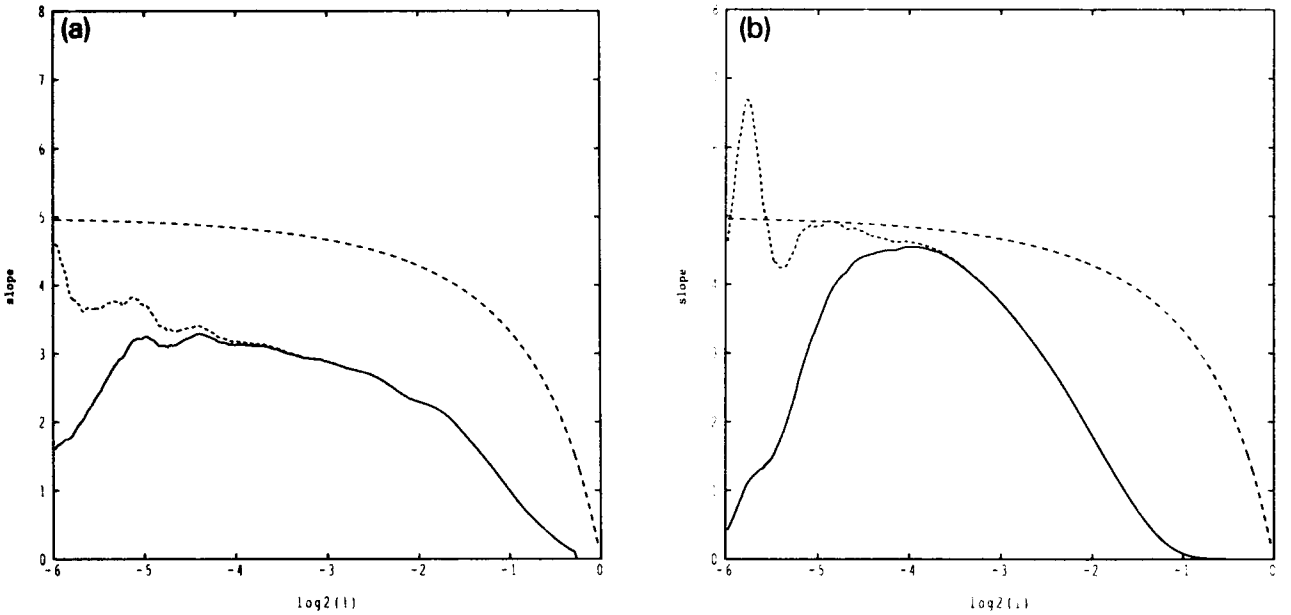

Fig. 9. Local slope of the correlation integral from series *b* This analysis utilized 2^{15} data points. (a) observed and (b) and surrogate.

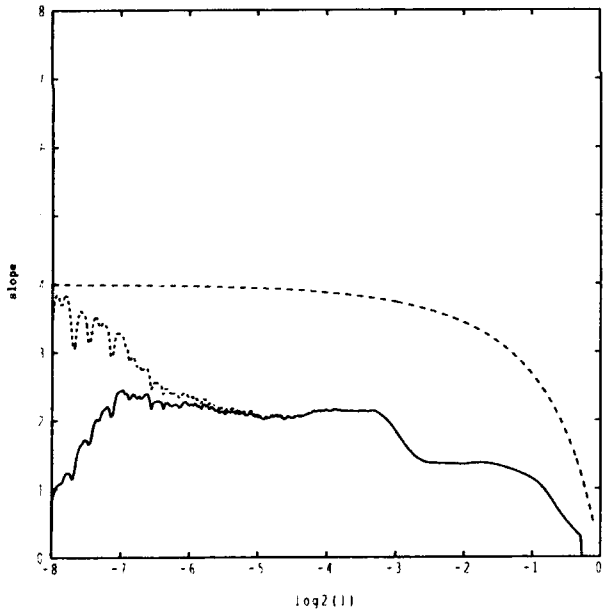

Fig. 10 Local slope of the correlation integral from series *k*.

ture need not be maintained; macroscopic distortions will shift the scaling range, confounding attempts to compare correlation dimension estimates between observed and surrogate signals even in a case where they both converge in the limit of small ℓ. The point here is that two topologically equivalent distributions with different macroscopic structure will have different correlation integrals at large scales. This is a fundamental limitation inherent in the geometric analysis of reconstructions, and provides an example where the lower bounds on data requirements for dimension calculations are vast *under*estimates of the true amount of data required for this type of analysis. (In this particular case, the Fourier spectrum indicated a quasi-periodic attractor.) It also provides an example of where surrogate series can provide misleading results if a fixed scaling range is used.

6. Nonlinear prediction of stochastic systems

The arguments above demonstrate that nonlinear predictors can distinguish dynamical systems with a structured phase space flow from those whose motion in phase space is incoherent. If we identify the former systems as deterministic and the latter as stochastic, we have a good test for determinism. Unfortunately such a classification will consider many classic "stochas-

tic" systems as deterministic as it fails to distinguish "determinism" from stochastic systems which are "low dimensional" in the sense that they are associated with a probabilistic flow in a low dimensional phase space.

In this section we shall consider two systems, the disturbed pendulum of Yule [71] and the Ornstein–Uhlenbeck process[72,73]. The disturbed pendulum provides an example of a deterministic system where noise feeds back into the dynamics (dynamic noise) rather than being superimposed on the measurements (observational noise). The Ornstein–Uhlenbeck process has become a paradigm of stationary stochastic systems. We demonstrate that nonlinear deterministic predictors provide a good approximation to optimal prediction of this system and indicate the difficulties this implies for tests of determinism using surrogate signals. We are not interested here in establishing whether one type of nonlinear deterministic predictor is better than another, but in their common properties.

Yule considered two simple models to account for the lack of simple periodicity in the 15 sunspot cycles then available. Both models are based on observations of a pendulum. In the first, the observations of perfect periodicity are subject to *superposed fluctuations* or observational noise. In this case, for sufficiently long series, Fourier analysis will detect the underlying periodicity. Any deterministic predictors which allow for observational noise should do so as well. In the second case, the observational noise is considered negligible, but *disturbances* to the pendulum's motion (caused by boys with pea shooters) change the energy of the pendulum and feed back into the systems dynamics. When the shocks are well separated in time, nonlinear deterministic predictors will give excellent predictions (between the shocks) due to the structure of the underlying two-dimensional phase space of the pendulum. Good predictions are possible as long as the expected time interval between impacts, Δt, is not small relative to the sum of the reconstruction window and prediction time or

$$\Delta t \gtrsim (m-1)\tau_d + \tau_p. \tag{6.1}$$

The Ornstein–Uhlenbeck process models the velocity of a Brownian particle. From a dynamical systems perspective, it is preferable to consider the velocity, $u(t)$, rather than the displacement, as the velocity time series is stationary. The change in the velocity, $\mathrm{d}u(t)$, is given by

$$\mathrm{d}u(t) = -\beta u(t)\,\mathrm{d}t + \sigma\gamma(t)\sqrt{\mathrm{d}t}, \tag{6.2}$$

where $\gamma(t)$ is a random Gaussian process with zero mean and unit variance, $\mathrm{d}t$ is the time step, and the parameters β and σ are related to frictional drag and the driving impacts respectively. The optimal (statistical) predictor for this process is known; given the initial condition u_0, the expected value of $u(t)$ is

$$P_{\text{theory}}(u(t)) = E(u(t) \mid u(0) = u_0) = u_0\, \mathrm{e}^{-\beta t}. \tag{6.3}$$

Estimates for the variance are also available [73]. To test whether the reconstructed dynamics finds this structure, a 2048 point learning set ($\beta = 0.5$, $\sigma = 1.0$, $\mathrm{d}t = 0.05$) with $m = 1$, $n_c = 64$ and $\phi(r) = r$ was constructed and tested out-of-sample on an additional 2048 points. The point here is not whether this radial basis function predictor is optimal, but is merely to demonstrate that *any* good dynamic reconstruction should identify this structure in an Ornstein–Uhlenbeck series (or a series from a stochastic model like that of Barnes et al. [27]).

We compare the predictor with P_{theory} by plotting the predicted future value against the current observed value in fig. 11. The solid line corresponds to P_{theory}. A scatter plot of the observed future value against the current observed value shows a wide distribution. Both the agreement and disagreement between the deterministic predictor and the expected value displayed in fig. 11 is understood. The largest values of u in the

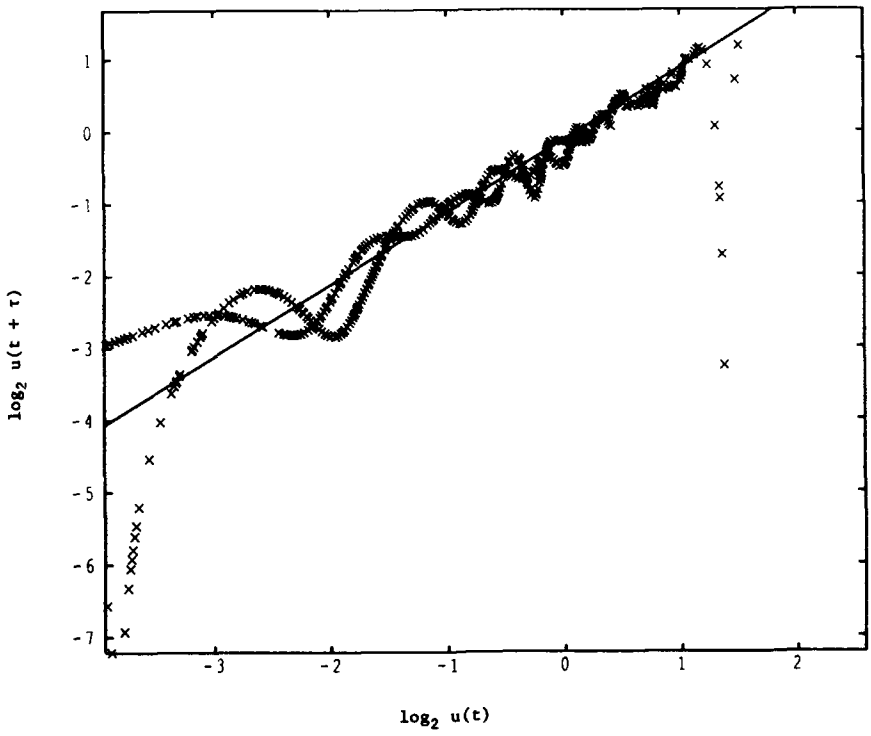

Fig. 11. Prediction of an Ornstein–Uhlenbeck process. The solid line denotes the optimal prediction. The predictor appears to be double valued because predictions for both positive and negative x are superimposed. The very inaccurate predictions at large x occur when the system explores a region of phase space not visited in the learning set. At small x, the variance in the expected value is large and the ability of the predictor to find the expected value is diminished.

test set correspond to very poor predictions (the markers on the right side of the plot well below the ideal line); these points have large nearest center distances and correspond to values of u not visited in the learning set. For slightly smaller u_0 there is good agreement between the two predictors; the two images of the deterministic predictor are the superimposed values for positive and negative u_0. For small u_0 there is poor agreement between the two predictors; due to both the magnification of small distortions by the logarithmic scales and the increase in uncertainty of future values of initial conditions near $u = 0$.

To the extent that these systems are deterministic, the dynamic reconstructions quantify their behavior. Yet they are stochastic in the sense that the current state of the system does not completely define its future. Once the deterministic structure is quantified, the quality of the predictions should not improve regardless of increases in the amount of data available. The lack of improved precision with increasing data, embedding dimension or changing delay time (for infinite data sets) provides an indication of the stochastic component of the process but is difficult to establish with finite data sets. In these particular cases, examining the predictor error series of the pendulum, and its spatial variation in the O-U process, could help identify the dynamics of the processes. The situation is more complicated in stochastic systems with more complex (higher-dimensional) phase space structure. Here nonlinear dynamics comes from nonlinear structure in the governing equations regardless of whether they are stochastically or deterministically driven. As the structure of the governing equations increases, the nature of the stochastic forcing may become less apparent. This holds implications for the use of surrogate data, in that surrogate generators which destroy this structure will be distinguished regard-

less of whether the underlying driving force is stochastic or deterministic.

One approach to recover this distinction is to look to longer time scales. Stone [54] has considered a Duffing oscillator driven either sinusoidally (chaos) or by random perturbations (stochasticity) and shown that the signals from these two systems are similar in terms of power spectra and symbolic dynamics. The short time predictability of these signals is similar as well; however if one considers long time phenomena the two cases can be distinguished. In particular, the series of time intervals between departures from the origin is distinguished by the predictor presented here. These return times are effectively independent and identically distributed in the stochastically forced system while the chaotic system is, initially, predictable and the distribution of predictor error for return times appears to relax to the same distribution as the stochastic case as predictions are made farther into the future. As the nonlinear structure of these two systems is identical, they provide a useful example of the similarities and differences of stochastic and deterministic behavior.

7. Discussion

It is customary to consider low dimensional determinism and stochasticity as two clearly distinct types of behavior. As we have seen, distinguishing between these alternatives is sometimes difficult. We have presented a general approach to evaluating algorithms, which attempts this distinction through contrasting the results a given algorithm produces on the observed data with those produced from surrogate data. The importance of choosing a good surrogate generator has been stressed and the general effectiveness of this approach has been demonstrated for correlation exponent calculations and prediction algorithms on laboratory data.

We have focused our attention primarily on the rotating annulus experiments and established that these data sets differ significantly from the surrogate series considered. This gives us confidence that dynamical systems techniques can provide a better understanding of this system, in particular in determining the nature of the underlying driving mechanisms. This goal is difficult to obtain with the data in the form presented here for, while it may display deterministic, "low dimensional" behavior, the physics in delay space is not at all simple. Dynamical systems texts often give the impression that a system which evolves on a low dimensional (say $d_2 < 5$) attractor has simple physics. This is somewhat misleading. For a set of five ordinary differential equations (ODE's) it is true, perhaps even for a set of 10 ODE's which collapse onto such an attractor.

For a large physical system with many degrees of freedom, the dynamics in 5D is certainly more simple than not under such restriction, but the physics is a mess in 5D. The equations of motion need not correspond to the macroscopic physical properties of the system and will almost certainly not correspond to a set of simple ODE's. While a great deal can be learnt from such systems, it is misleading to imply that the physics, in a traditional sense, will become clear. Indeed, we may need to develop a new way of interpreting physics and it is tempting to draw an analogy with the way statistical mechanics answers different questions than classical dynamics. An alternate approach which we are currently pursuing with the annulus data is to recast the data into a form in which the physics is more assessable. The spatial distribution of probes allows a spatial Fourier transform into wavenumber space. With the data in this form, a multivariable reconstruction can address the general question of predictability directly, as well as particular questions concerning which mode interactions drive the dynamics of the system. For example, suppose the data is recast into a multivariate series of the amplitudes of modes A, B, C, ... Using the predictor discussed above, we plan to examine the extent to which the energy in modes A

and B determine the future behavior of mode C, thereby directly testing cascade and mode–mode interaction hypotheses. Through this type of study we hope to clarify what physical processes dominate the dynamics of this system.

We have also shown how dynamic reconstructions can be used to address open questions concerning the experiment itself. By demonstrating that predictors formed from one segment of the time series yield statistically indistinguishable errors when applied to different segments of the time series, we have shown that the complexity observed is not due to slow parametric drift over the duration of the experiment. The statistically significant difference, between both the predictability and the correlation integrals of the observed signals and surrogates generated with identical autocorrelation functions, provides a strong case for low dimensional dynamics in this system. This case is further supported by the demonstration that a simple prediction by memory scheme, while capable of distinguishing between the FT surrogates and the observations, is much less accurate than the deterministic radial basis function predictor.

In this paper, we have applied a global, nonlinear predictor based on radial basis function interpolation which explicitly considers noise in the data set and the inhomogeneity of the reconstruction in phase space. This type of predictor may be improved in several ways. For example, the reconstruction may be altered to include known physics in the problem at hand: in a problem where diurnal cycles are known to be important, the time of day could be included by placing the reconstruction on a circle. In systems like the annulus, the predictability may be improved by recasting the data set into a form in which the physics is more assessable as discussed above. It is often the case that additional information regarding the macroscopic state of the system is available in addition to time series data. Examples under investigation include laboratory data where the phase of a forcing function is known [74], and meteorological series, where the general structure of the regional weather pattern is included to improve the prediction of local temperature series [75]. For finite, noisy data sets, considerations such as these may be crucial to obtaining a significant result.

In addition to better embeddings, improvements in the prediction scheme are also possible but are likely to involve system specific answers. For example, the choice between iterative forecasting and direct forecasting may vary with the particular dynamical system, the data density, the noise level and even the details of the predictor itself (local or global, linear or nonlinear, ...). The system specific nature of this problem is likely to reoccur in other details of reconstructions, such as the importance of the method employed for choosing centers. For the predictor presented here, one may improve the method used to account for noise; we have applied a straightforward least squares approach. Implicit in this approach is the assumption that the "noise" is located in the quantity being predicted (s), not the base point ($\boldsymbol{x}$). For delay reconstructions this is certainly not the case, the same noise level is present in the base point as in the prediction. One approach to this problem would be to consider total least squares. This is analogous to performing an SVD fit in two dimensions rather than a least squares fit when it is known that there is error in both coordinates.

In the attempt to distinguish between deterministic and stochastic dynamics through prediction, one complication has been noted: the ability of deterministic predictors to identify the expected values for some stochastic systems, and thereby differentiate them from (some) surrogates. This is particularly true in effectively low dimensional stochastic systems, systems which exhibit stochastic motion within a structured low dimensional phase space. (Although as stochastic systems they remain, of course, infinite dimensional.) While such systems clearly fail to follow strict Laplacian determinism, it is not clear how they are best classified. Their detection by nonlinear prediction will depend

on the particulars of what quantities and length scales are analyzed, and useful classification in the presence of these effects may require consideration of second order properties of the predictor. In the event, these distinctions may require a more precise definition of what constitutes determinism.

Acknowledgements

I thank M. Muldoon for many stimulating discussions and mutual information calculations. I am happy to acknowledge helpful discussions and disagreements with J. Theiler, D. Broomhead, K. Fraedrich, G. King and B. Mestel, and would like to thank P. Read, M. Gaster, T. Mullin for supplying data the analysis of which provided the insights reported here. M. Chappell, C. Lanone, P. Read and J. Theiler have provided very useful criticisms of a draft of this paper. Finally, I thank N. Weiss for discussions about chaos in the sun and the sunspot record. This research has been supported by the Science and Engineering Research Council and the US Office of Naval Research.

References

[1] E.N. Lorenz, J. Atmos Sci. 20 (1963) 130.
[2] D.W. Moore and E. A Spiegel, Astrophys. J. 143 (1966) 871–887.
[3] J. Crutchfield, J.D. Farmer, N.H. Packard and R.S. Shaw, Sci. Am. 254 (1986) 46–57.
[4] N. Gershenfeld, in: Directions in Chaos, ed. B.-l. Hao (World Scientific, 1988) pp. 310–383.
[5] S. Eubank and D. Farmer, An introduction to chaos and randomness, in: Proc. SFI Summer School, ed. E. Jen (Addison-Wesley, 1990).
[6] Marquis de Laplace and Pierre-Simon, Théorie Analytique des Probabilitiés (Paris, 1820), reproduced in the Oeuvres complètes de Laplace, Volume 11 (Paris, 1886).
[7] J. Theiler, B. Galdrikan, A. Longtin, S. Eubank and J. D. Farmer, in: Nonlinear Prediction and Modelling, eds. M. Casdagli and S. Eubank (Addison-Wesley, 1992) pp. 163–188.
[8] J. Theiler, S. Eubank, A. Longtin, B. Galdrikan and J. D. Farmer, Physica D 58 (1992) 77, these Proceedings.
[9] A. Provenzale, L.A. Smith, R. Vio and G. Murante, Physica D 58 (1992) 31, these Proceedings.
[10] E. Kostelich and J. Yorke, Physica D 41 (1990) 183–196.
[11] L.A. Smith, Quantifying chaos with predictive flows and maps: locating unstable periodic orbits, in: Measures of Complexity and Chaos, eds. N.B. Abraham et al. (Plenum, 1990).
[12] L.A. Smith, Applied chaos: computing unstable periodic orbits through predictive flows and maps, in: Information Dynamics, eds. H. Atmanspacher et al. (Plenum, 1991).
[13] P. Read, M.J. Bell, D.W. Johnson and R.M. Small, Chaotic regimes in rotating baroclinic flow, J. Fluid Mech. (1991), to appear.
[14] P. Grassberger and I. Procaccia, Phys. Rev. Lett. 50 (1983) 346.
[15] P. Read, Applications of singular value decomposition to the analysis of "baroclinic chaos", Physica D 58 (1992) 455, these Proceedings.
[16] R.L. Smith, in: Nonlinear Prediction and Modelling, eds. M Casdagli and S. Eubank (Addison-Wesley, 1992) pp. 115–136.
[17] C. Nicolis and G. Nicolis, Nature 311 (1984) 529.
[18] P. Grassberger, Nature 323 (1986) 609.
[19] C. Nicolis and G. Nicolis, Nature 326 (1987) 523.
[20] P. Grassberger, Nature 326 (1987) 524.
[21] I. Procaccia, Nature 333 (1988) 498–499.
[22] R. von Mises, Probability Statistics and Truth, (George Allen and Unwin, London, 1957).
[23] W.H. Press, B.P. Flannery, S.A. Teukolsky and W.T. Vetterling, Numerical Recipes, (Cambridge Univ. Press, Cambridge, 1987).
[24] A.R. Osborne, A.D. Kirwan, A. Provenzale and L. Bergamasco, Physica D 23 (1986) 75–83.
[25] J.A. Eddy, Science 192 (1976) 1182–1202.
[26] E.A. Spiegel and A. Wolf, Chaos and the solar cycle, in: Chaos in Astrophysics Ann. NY Acad. Sci. Vol. 497 (1987) pp. 55–60.
[27] J.A. Barnes, H.H. Sargent and P.V. Tryon, Sunspot cycle simulation using random noise, in: The ancient sun eds. R.O. Pepin, J.A. Eddy and R.B. Merrill (Pergamon, New York, 1980).
[28] N.O. Weiss, Phil. Trans. R. Soc. London A 330 (1990) 617–625.
[29] D.S. Broomhead and R. Jones, Time-series analysis, Proc. R. Soc. London 423 (1989) 103–121.
[30] N.H. Packard, J.P.Cruchfield, J.D. Farmer and R.S. Shaw, Phys. Rev. Lett. 45 (1980) 712.
[31] F. Takens, in: Dynamical Systems and Turbulence, eds. D. Rand and L.-S. Young (Springer, 1981) p. 366.
[32] Th. Buzug, T. Reimers and G. Pfister, Europhys. Lett. 13 (1990) 605–610.
[33] M. Casdagli, Chaos and deterministic versus stochastic non-linear modeling, J. R. Statist. Soc. B submitted (1991).
[34] T. Sauer, J.A. Yorke and M. Casdagli, J. Stat. Phys. 65 (1991) 579–616.

[35] A.M. Fraser, Physica D 34 (1989) 391–404.
[36] J.L. Breeden and N.H. Packard, Nonlinear analysis of data sampled nonuniformly in time, Technical Report CCSR-91-15, Center for Complex Systems Research, Urbana, Il 61801. (1991).
[37] D.S. Broomhead and G.P. King, Physica D 20 (1986) 217.
[38] G. King, R. Jones and D.S. Broomhead, Nucl. Phys. B (Proc. Suppl.) 2 (1987) 379.
[39] J.D. Farmer and J. Sidorowich, Phys. Rev. Lett. 59 (1987) 8.
[40] J. Crutchfield and B.S. McNamara, J. Compl. Syst. 1 (1987) 417–452.
[41] D.S. Broomhead and D. Lowe, J. Compl. Syst. 2 (1988) 321–355.
[42] A.I. Mees, Modelling complex systems, in: Proc. Conf. on Modelling Complex Systems, eds. L.S. Jennings, A.I. Mees and T.L. Vincent (Birkhaüser, 1989).
[43] M. Casdagli, Physica D 35 (1989) 335–356.
[44] N.H. Packard, J. Compl. Syst. 4 (1990) 543.
[45] A.S. Weigend, B.A. Huberman and D. E. Rumelhart, Predicting the future: A connectionist approach, Intern. J. Neural Syst. (1990), submitted.
[46] G. Sugihara and R.M. May, Nature 344 (1990) 734.
[47] H. Tong, Non-Linear Time Series Analysis, (Oxford Univ. Press, 1990).
[48] K. Stokbro, Predicting chaos with weighted maps, Nordita preprint (1991).
[49] J.D. Farmer and J. Sidorowich, in: Evolution, Learning, and Cognition, ed. Y.C. Lee (World Scientific, 1988) p. 277.
[50] M.J.D. Powell, Radial basis functions for multivariate interpolation: a review, in: Proc. IMA Conf. on Algorithms for the Approximation of Functions and Data (RMCS Shrivenham, 1985).
[51] C.A. Michelli, Constr. Approx. 2 (1986) 11–22.
[52] A. Arneodo, G. Grasseau and E.J. Kostelich, Phys. Lett. A 131 (1987) 426.
[53] J. Guckenheimer and P. Holmes, Nonlinear Oscillations, Dynamical Systems and Bifurcations of Vector Fields, Vol. 42 of Applied mathematical sciences (Springer, 1983).
[54] E. Stone, Phys. Lett. A 148 (1990) 434–442.
[55] L.A. Smith, K. Godfrey, P. Fox and K. Warwick, A new technique for fault detection in multi-sensor probes, in: Control 91 (1991) p. 1062.
[56] L.A. Smith and K. Godfrey, Nonlinear methods of fault detection in multi-sensor probes, in preparation (1992).
[57] P. Grassberger, T. Schreiber and C. Schaffrath, Nonlinear time sequence analysis, Preprint WUB 91-14 (1991).
[58] J. Theiler, J. Opt. Soc. Am. A7 (1990) 1055–1073.
[59] J. Theiler, Phys. Rev. A 34 (1986) 2427–2432.
[60] A.R. Osborne and A. Provenzale. Physica D 35 (1989) 357–381.
[61] J. Theiler, Phys. Lett. A 155 (1991) 480-493.
[62] J. Theiler, Phys. Rev. A 36 (1987) 4456–4462.
[63] P. Grassberger, Phys. Lett. A 148 (1990) 63.
[64] R. Badii and A. Politi, Phys. Lett. A 104 (1984) 303–305.
[65] L.A. Smith, J.-D. Fournier and E.A. Spiegel, Phys. Lett. A 114 (1986) 465.
[66] L.A. Smith, Phys. Let*. A 133 (1988) 283.
[67] D. Ruelle, Proc. R. Soc. London A 427 (1990) 241–248.
[68] J. Theiler, Phys. Rev. A 41 (1990) 3038–3051.
[69] C. Essex and M. and Nerenberg, Proc. R. Soc. London A 435 (1991) 287–292.
[70] K. Judd and A.I. Mees, Estimating dimensions with confidence, Aust. J. Bif. Chaos (June 1991).
[71] G.U. Yule, Phil. Trans. R. Soc. London A 226 (1927) 267–298.
[72] G.E. Uhlenbeck and L.S. Ornstein, Phys. Rev. 36 (1930) 823–841.
[73] D.R. Cox and H.D. Miller, The theory of stochastic procesesses, (Chapman and Hall, New York, 1965).
[74] M. Gaster, Proc. R. Soc. London A 430 (1990) 3–24.
[75] K. Fraedrich, C. Ziehmann-Schlumbohm and L.A. Smith, Estimating state dependent predictability: Some meteorological applications, Ann, Geophys. (1992), 1992 General Assembly Supplement Volume.

Physica D 58 (1992) 77–94
North-Holland

PHYSICA D

Testing for nonlinearity in time series: the method of surrogate data

James Theiler[a,b], Stephen Eubank[a,b,c,d], André Longtin[a,b], Bryan Galdrikian[a,b] and J. Doyne Farmer[a,c,d]

[a]*Theoretical Division, Los Alamos National Laboratory, Los Alamos, NM 87545, USA*
[b]*Center for Nonlinear Studies, Los Alamos National Laboratory, Los Alamos, NM 87545, USA*
[c]*Santa Fe Institute, 1660 Old Pecos Trail, Santa Fe, NM 87501, USA*
[d]*Prediction Company, 234 Griffin Street, Santa Fe, NM 87501, USA*

Received 4 October 1991
Revised manuscript received 11 February 1992
Accepted 3 March 1992

We describe a statistical approach for identifying nonlinearity in time series. The method first specifies some linear process as a null hypothesis, then generates surrogate data sets which are consistent with this null hypothesis, and finally computes a discriminating statistic for the original and for each of the surrogate data sets. If the value computed for the original data is significantly different than the ensemble of values computed for the surrogate data, then the null hypothesis is rejected and nonlinearity is detected. We discuss various null hypotheses and discriminating statistics. The method is demonstrated for numerical data generated by known chaotic systems, and applied to a number of experimental time series which arise in the measurement of superfluids, brain waves, and sunspots; we evaluate the statistical significance of the evidence for nonlinear structure in each case, and illustrate aspects of the data which this approach identifies.

1. Introduction

The inverse problem for a nonlinear system is to determine the underlying dynamical process in the practical situation where all that is available is a time series of data. Algorithms have been developed which can in principle make this distinction, but they are notoriously unreliable, and usually involve considerable human judgement. Particularly for experimental data sets, which are often short and noisy, simple autocorrelation can fool dimension and Lyapunov exponent estimators into signalling chaos where there is none. Most authors agree that the methods contain many pitfalls, but it is not always easy to avoid them. While some data sets very cleanly exhibit low-dimensional chaos, there are many cases where the evidence is sketchy and difficult to evaluate. Indeed, it is possible for one author to claim evidence for chaos, and for another to argue that the data is consistent with a simpler explanation [1–4].

The real complication arises because low-dimensional chaos and uncorrelated noise are not the only available alternatives. The erratic fluctuations that are observed in an experimental time series owe their dynamical variation to a mix of various influences: chaos, nonchaotic but still nonlinear determinism, linear correlations, and noise, both in the dynamics and in the measuring apparatus. While we are motivated by the prospect of ultimately disentangling these influences, we take as a more modest goal the detection of nonlinear structure in a stationary time series. (We will not attempt to characterize non-stationary time series – see refs. [5–9] for a

0167-2789/92/$05.00 © 1992 – Elsevier Science Publishers B.V. All rights reserved

discussion of some of the problems arising in the estimation of nonlinear statistics from nonstationary data.)

Positive identification of chaos is difficult; the usual way to detect low-dimensional behavior is to estimate the dimension and then see if this value is small. With a finite time series of noisy data, the dimension estimated by the algorithm will at best be approximate and often, outright wrong. One can guard against this by attempting to identify the various sources of error (both systematic and statistical), and then putting error bars on the estimate (see, for example, refs. [10–18]). But this can be problematic for nonlinear algorithms like dimension estimators: first, assignment of error bars requires some model of the underlying process, and that is exactly what is not known; further, even if the underlying process were known, the computation of an error bar may be analytically difficult if not intractable.

The goal of detecting nonlinearity is considerably easier than that of positively identifying chaotic dynamics. Our approach is to specify a well-defined underlying linear process or null hypothesis, and to determine the distribution of the quantity we are interested in (dimension, say) for an ensemble of surrogate data sets which are just different realizations of the hypothesized linear stochastic process. Then, rather than estimate error bars on the dimension of the original data, we put error bars on the value given by the surrogates. This can be done reliably because we have a model for the underlying dynamics (the null hypothesis itself), and because we have many realizations of the null hypothesis, we can estimate the error bar numerically (from the standard deviation of all estimated dimensions of the surrogate data sets) and avoid the issue of analytical tractibility altogether.

While this article elaborates on preliminary work described in an earlier publication [19], our aim is to make this exposition self-contained. In section 2, we express the problem of detecting nonlinearity in terms of statistical hypothesis testing. We introduce a measure of significance, develop various null hypotheses and discriminating statistics, and describe algorithms for generating surrogate data. Section 3 demonstrates the technique for several computer-generated examples under a variety of conditions: large and small data sets, high and low-dimensional attractors, and various levels of observational and dynamical noise. In section 4, we illustrate the application of the method to several real data sets, including fluid convection, electroencephalograms (EEG), and sunspots. With real data, there is always room for human judgment, and we argue that besides formally rejecting a null hypothesis, the method of surrogate data can also be useful in an informal way, providing a benchmark, or control experiment, against which the actual data can be compared.

2. Statistical hypothesis testing

The formal application of the method of surrogate data is expressed in the language of statistical hypothesis testing. This involves two ingredients: a null hypothesis against which observations are tested, and a discriminating statistic. The null hypothesis is a potential explanation that we seek to show is inadequate for explaining the data; and the discriminating statistic is a *number* which quantifies some aspect of the time series. If this number is different for the observed data than would be expected under the null hypothesis, then the null hypothesis can be rejected.

It is possible in some cases to derive analytically the distribution of a given statistic under a given null hypothesis, and this approach is the basis of many existing tests for nonlinearity (e.g., see refs. [20–26]). In the method of surrogate data, this distribution is estimated by direct Monte Carlo simulation. An ensemble of surrogate data sets are generated which share given properties of the observed time series (such as mean, variance, and Fourier spectrum) but are

otherwise random as specified by the null hypothesis. For each surrogate data set, the discriminating statistic is computed, and from this ensemble of statistics, the distribution is approximated.

While this approach can be computationally intensive, it avoids the analytical derivations which can be difficult if not impossible. This leads to increased flexibility in the choice of null hypotheses and discriminating statistics; in particular, the hypothesis and statistic can be chosen independently of each other. The method of surrogate data is basically an application of the "bootstrap" method of modern statistics. These methods have by now achieved widespread popularity for reasons that are well described in Efron's 1979 manifesto [27]. A more recent reference, which applies the bootstrap in a context very similar to ours is by Tsay [28].

2.1. Computing significance

Let Q_D denote the statistic computed for the original time series, and Q_{H_i} for the ith surrogate generated under the null hypothesis. Let μ_H and σ_H denote the (sample) mean and standard deviation of the distribution of Q_H.

If multiple realizations are available for the observational data, then it may be possible to compare the two distributions (observed data and surrogate) directly, using for instance the Kolmogorov–Smirnov or Mann–Whitney test, which compare the full distributions, or possibly a Student-t test which only compares their means. For the present purposes, however, we consider that only one experimental data set is available[#1], and we use a kind of t test.

[#1] Of course, it is always possible to create several realizations out of that single set by chopping up the data; we have not tried this approach, but just as the convergence of numerical algorithms like correlation dimension and Lyapunov exponent estimation are compromised by shortened data sets, so we suspect will be their power to reject a null hypothesis. This is only a suspicion, however; it would be worthwhile to compare the relative power of several short data sets versus that of one long data set.

We define our measure of "significance" by the difference between the original and the mean surrogate value of the statistic, divided by the standard deviation of the surrogate values:

$$\mathcal{S} \equiv \frac{|Q_D - \mu_H|}{\sigma_H} . \tag{1}$$

The significance is properly a dimensionless quantity, but it is natural to call the units of $\mathcal{S}$ "sigmas". If the distribution of the statistic is gaussian (and numerical experiments indicate that this is often a reasonable approximation), then the p-value is given by $p = \mathrm{erfc}(\mathcal{S}/\sqrt{2})$; this is the probability of observing a significance $\mathcal{S}$ or larger if the null hypothesis is true.

A more robust way to define significance would be directly in terms of p-values with rank statistics. For example, if the observed time series has a statistic which is in the lower one precentile of all the surrogate statistics (and at least a hundred surrogates would be needed to make this determination), then a (two-sided) p-value of $p = 0.02$ could be quoted. We have used eq. (1) for the investigations reported here because the computational effort in that case is not as severe.

2.1.1. Estimating error bars on significance

Our plots of significance include error bars; these are meant only as a rough guide and are computed assuming that the statistics are distributed as a gaussian.

We write the error bar on $\mathcal{S}$ as $\Delta\mathcal{S}$, and it is computed by standard propagation of errors methodology. Here

$$\left(\frac{\Delta\mathcal{S}}{\mathcal{S}}\right)^2 = \left(\frac{\Delta|\mu_H - \mu_D|}{|\mu_H - \mu_D|}\right)^2 + \left(\frac{\Delta\sigma_H}{\sigma_H}\right)^2$$

$$= \frac{(\Delta\mu_H)^2 + (\Delta\mu_D)^2}{(\mu_H - \mu_D)^2} + \left(\frac{\Delta\sigma_H}{\sigma_H}\right)^2 . \tag{2}$$

Now the error of the sample mean based on N observations is given by $(\Delta\mu)^2 = \sigma^2/N$, and the error of the sample standard deviation is

$(\Delta\sigma)^2 = \sigma^2/2N$, so we can write

$$\left(\frac{\Delta\mathcal{S}}{\mathcal{S}}\right)^2 = \frac{\sigma_H^2/N_H + \sigma_D^2/N_D}{(\mu_H - \mu_D)^2} + \frac{1}{2N_H}. \quad (3)$$

The absolute error bar is then given by

$$\Delta\mathcal{S} = \sqrt{(1 + \tfrac{1}{2}\mathcal{S}^2)/N_H + (\sigma_D/\sigma_H)^2/N_D}. \quad (4)$$

When only a single realization of the time series is available, we take $\sigma_D = 0$ and ignore the second term in the above equation. This reports the error bar on the significance of the specific realization.

In our numerical experiments, we use several realizations of the time series under question. However, the significance we report is not based on the collective evidence of the several, but is the average significance of each realization taken individually. The error bar in that case describes the expected error of our estimate of this average. Note that this differs from the error reported for a single realization.

2.2. Toward a hierarchy of null hypotheses

The null hypothesis defines the nature of the candidate process which may or may not adequately explain the data. Our null hypotheses usually specify that certain properties of the original data are preserved – such as mean and variance – but that there is no further structure in the time series. The surrogate data is then generated to mimic these preserved features but to otherwise be random. There is some latitude in choosing which features ought to be preserved: certainly mean and variance, and possibly also the Fourier power spectrum. If the raw data is discretized to integer values, then the surrogate data should be similarly discretized.

Ultimately we envision a hierarchy of null hypotheses against which time series might be compared. Beginning with the simplest hypotheses, and increasing in generality, the following sections outline some of the possibilities that we have considered.

2.2.1. Temporally independent data

The first (and easiest) question to answer about a time series is whether there is evidence for any dynamics at all. The null hypothesis in this case is that the observed data is fully described by independent and identically distributed (IID) random variables. If the distribution is further assumed to be gaussian, then surrogate data can be readily generated from a standard pseudorandom number generator, normalized to the mean and variance of the original data.

To test the hypothesis of IID noise *with arbitrary amplitude distribution* in an analysis of stock market returns, Schienkman and LeBaron [29] generated surrogate data by shuffling the time-order of the original time series. The surrogate data is obviously guaranteed to have the same amplitude distribution as the original data, but any temporal correlations that may have been in the data are destroyed. Breeden and Packard also used a shuffling process along with a sophisticated nonlinear predictor to prove that there was some dynamical structure to a time series of quasar data which were sampled nonuniformly in time [30].

2.2.2. Ornstein–Uhlenbeck process

A very simple case of non-IID noise is given by the Ornstein–Uhlenbeck process [31]. A discrete sampling of this process yields a model of the form

$$x_t = a_0 + a_1 x_{t-1} + \sigma e_t, \quad (5)$$

where e_t is uncorrelated gaussian noise of unit variance. The coefficients a_0, a_1, and σ collectively determine the mean, variance, and autocorrelation time of the time series. In fact, the autocorrelation function is exponential in this case,

$$A(\tau) \equiv \frac{\langle x_t x_{t-\tau}\rangle - \langle x_t\rangle^2}{\langle x_t^2\rangle - \langle x_t\rangle^2} = e^{-\lambda|\tau|},$$

where $\langle\ \rangle$ denotes an average over time t, and $\lambda = -\log a_1$.

To make surrogate data sets, the mean μ, variance v, and first autocorrelation $A(1)$ are estimated from the original time series; from these the coefficients are fit: $a_1 = A(1)$, $a_0 = \mu(1 - a_1)$, and $\sigma^2 = v(1 - a_1^2)$. Finally, one generates the surrogate data by iterating eq. (5), using a pseudorandom number generator for the unit variance gaussian e_t.

2.2.3. Linearly autocorrelated gaussian noise

We can generalize the above null hypothesis by extending eq. (5) to arbitrary order. This leads to the hypothesis that is generally associated with linearity. We emphasize that we are discussing linear *gaussian* processes here (see Tong [26, pp. 13, 14] for a brief description of some of the surprising properties of linear nongaussian processes); Section 2.2.4 describes one approach toward a nongaussian null hypothesis. The model is described by fitting coefficients a_k and σ to a process

$$x_t = a_0 + \sum_{k=1}^{q} a_k x_{t-k} + \sigma e_t \,, \tag{7}$$

which mimics the original time series in terms of mean, variance, and the autocorrelation function for delays of $\tau = 1, \ldots, q$. This is an autoregressive (AR) model; a more general model includes a moving average (MA) of time delayed noise terms as well, and the combination is called an ARMA model. For large enough q, the models are essentially equivalent. The null hypothesis in this case is that all the structure in the time series is given by the autocorrelation function, or equivalently, by the Fourier power spectrum.

One algorithm for generating surrogate data under this null hypothesis is again to iterate eq. (7), where the coefficients have been fit to the original data. We describe an alternative algorithm in section 2.4.1 which involves randomizing the phases of a Fourier transform. (To our knowledge, this algorithm was first suggested in this context by Osborne et al. [5], and independently in refs. [15, 32].) The alternative algorithm generates surrogate data which by construction has the same Fourier spectrum as the original data. While the two algorithms are essentially equivalent, we use the Fourier transform method because it is numerically stabler. If the values of the coefficients in eq. (7) are mis-estimated slightly, it is possible that iterating the equation will lead to a time series which diverges to infinity; this is particularly problematic if the raw time series is nearly periodic or highly sampled continuous data.

We remark that this is the null hypothesis that is associated with residual-based tests for nonlinearity. For instance, see refs. [22–24, 33, 34]. In these tests, a model of the form of eq. (7) is fit to the data, and the residuals

$$\epsilon_t = x_t - \left(a_0 + \sum_{k=1}^{q} a_k x_{t-k}\right) \tag{8}$$

are tested against a null of temporally independent noise. In ref. [19], we argue that it is usually preferable to use the method of surrogate data on the raw data directly, rather than working with residuals.

2.2.4. Static nonlinear transform of linear gaussian noise

One way to generalize the above null hypothesis to cases where the data is nongaussian is to suppose that although the dynamics is linear, the observation function may be nonlinear. In particular, we hypothesize that there exists an "underlying" time series $\{y_t\}$, consistent with the null hypothesis of linear gaussian noise, and an observed time series $\{x_t\}$ given by

$$x_t = h(y_t) \,. \tag{9}$$

Since x_t depends only on the current value of y_t and not on derivatives or past values, the filter $h(\,)$ is said to be "static" or "instantaneous". To permit the generation of surrogate data, we must further assume (as part of the null hypothesis)

that the observation function $h(\ )$ is effectively invertible.

In section 2.4.3, an algorithm for generating surrogate data corresponding to this null hypothesis is described. Its effect is to shuffle the time-order of the data but in such a way as to preserve the linear correlations of the underlying time series $y_t = h^{-1}(x_t)$. One advantage of shuffling over, for example, a smooth fit to the function $h(\ )$, is that any discretization that was present in the original data will be reflected in the surrogate data.

Note that time series in this class are strictly speaking nonlinear, but that the nonlinearity is not in the dynamics. Most conventional tests for nonlinearity would (correctly) conclude that the time series is nonlinear, but would not indicate whether the nonlinearity was in the dynamics or in the amplitude distribution. By using surrogate data tailored to this specific null hypothesis, it becomes possible to make such fine distinctions about the nature of the dynamics.

2.2.5. *More general null hypotheses*

Eventually, we would like to extend this list to consider more general cases. A natural next step is a null hypothesis that the dynamics is a noisy limit cycle. Such time series cannot be described by a linear process, even if viewed through a static nonlinear transform. Yet it is often of great interest, particularly in systems driven by seasonal cycles, to determine the nature of the inter-seasonal variation.

There is another large class of nonlinear stochastic processes which are not predictable even in the mean; among these are the conditional heteroscedastic models (for which the variance is conditioned on the past, but not the mean) in favor among economists. While there is definite nonlinear structure in these time series, it is not manifested in enhanced predictability by nonlinear models. (For instance, it may be possible to predict the magnitude $|x_t|$ from past values of x, but not the sign.)

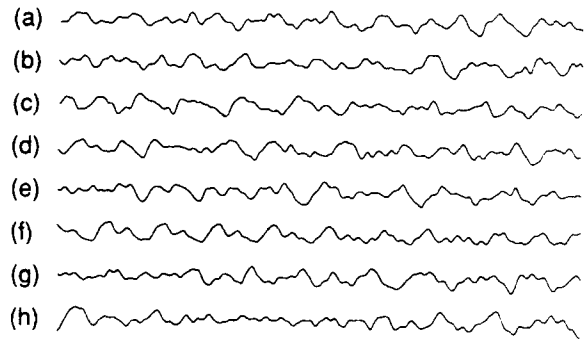

Fig. 1. Shown is a time series from the Mackey–Glass equation with $\tau = 30$, which is known to be low-dimensional and chaotic, and seven surrogate time series generated by the WFT algorithm. It is often not obvious by eye which is the actual data set and which are the surrogates. In this case it is series (f) which is the real one.

2.3. *Battery of discriminating statistics*

The method of surrogate data can in principle be used with virtually any discriminating statistic. Formally, all that is required to reject a null hypothesis is that the statistic have a different distribution for the data than for the surrogates. However, the method is more useful if the statistic actually provides a good estimate of a physically interesting quantity; in that case, one may not only formally reject a null hypothesis, but also informally characterize the nature of the nonlinearity.

Since we were motivated by the possibility that the underlying dynamics may be chaotic, our original choices for discriminating statistics were the correlation dimension, Lyapunov exponent, and forecasting error. Ideally, dimension counts degrees of freedom, Lyapunov exponent quantifies the sensitivity to initial conditions, and forecasting error tests for determinism. One of the ultimate aims in this project is to understand the conditions in which one or the other of these methods will be more effective.

We should remark that a danger in using a battery of statistics is that one of them, by chance, will show up as significant. This effect can be formally accounted for by keeping strict count of the number of tests used, and increasing

the threshold of significance accordingly. The formal approach tends to be more conservative than necessary, since the tests are not really independent of each other, but it is still a recommended practice to maintain a reasonably high threshold of significance.

2.3.1. Correlation dimension, ν

Dimension is an exponent which characterizes the scaling of some bulk measure with linear size. A number of algorithms are available [17, 35] for estimating the dimension of an underlying strange attractor from a time series; we chose a box-assisted variation [36] (see Grassberger [37] for an elegant alternative) of the Grassberger–Procaccia–Takens algorithm [38–40] to compute a correlation integral, and the best estimator of Takens [12] for the dimension itself. To compute a dimension, it is necessary to choose some range of sizes over which the scaling is to be estimated. The Takens estimator requires only an upper cutoff size; we used one-half of the rms variation in the time series for this value. (See Ellner [41] for an estimator that takes both an upper and a lower cutoff.)

We will concede that this choice is a bit arbitrary; one might prefer a more sophisticated algorithm for choosing a good scaling range. L. Smith (personal communication) has suggested choosing the range "by eye" for the raw data and then keeping this range for the surrogates. From the point of view of the formal test, it does not really matter, but if we are to ask for insight as well as a rejected null, then it is important to use a good dimension estimator. In the $N \to \infty$ limit, the estimator we describe will not converge to the actual precise dimension of the attractor, but we note that it will converge fairly rapidly to a number which is often reasonably close to actual dimension (of course, one can always contrive counterexamples); in particular, it will properly indicate low-dimensionality when it sees it. While we do not claim that this is the optimal dimension estimator, we believe that it is a useful one.

2.3.2. Forecasting error, ϵ

A system is deterministic if its future can be predicted. A natural statistic in this case is some average of the forecasting errors obtained from nonlinear modeling. The method we use entails first splitting the time series into a fitting set of length N_f, and a testing set of length N_t, with $N_f + N_t = N$, the length of the time series; then fitting a local linear model [42] to the fitting set, locality given by the number of neighbors k; and finally, using this model to forecast the values in the testing set, and comparing them with the actual values.

The prediction error $e_t = x_t - \hat{x}_t$ is the difference between the actual value of x and the predicted value, $\hat{x}$; we define our discriminating statistic as the log median absolute prediction error.

Several modeling parameters must be chosen, including the partitioning of the data set into fitting (N_f) and testing (N_t) segments, the number of steps ahead to predict (T), and number of neighbors (k) used in the local linear fit. We arbitrarily chose to divide the fitting and testing sets equally, with $N_f = N_t = \frac{1}{2}N$, and to predict one step ahead, so $T = 1$. For oversampled continuous data, a larger T would be more appropriate. The choice of k is also important. For the results in this article, we set $k = 2m$, which is twice the minimum number needed for a fit, but we note that this is often not optimal. Indeed, Casdagli [43, 44] has advocated sweeping the parameter k in a local linear forecaster as an exploratory method to look for nonlinearity in the first place.

2.3.3. Estimated Lyapunov exponent, λ

Following standard practices [45–47], we compute Lyapunov exponents by multiplying Jacobian matrices along a trajectory, with the matrices computed by local linear fits, and we use QR decomposition to maintain orthogonality.

We have found that numerical estimation of even the largest Lyapunov exponent can be problematic in the presence of noise. Indeed, for

our surrogate data sets, for which the linear dynamics is contracting, we often obtain positive Lyapunov exponents. This indicates that our Lyapunov exponent estimator (which, as we have described, is fairly standard) is seriously flawed, something we might not have noticed had we not tested with linear stochastic time series. We are aware of at least one group whose Lyapunov exponent estimator explicitly considers the effects of noise [48–50]. While our estimator is arguably still useful as a statistic which formally distinguishes original data from surrogate data, it would be better to use a discriminating statistic which correctly quantifies some feature of the dynamics. For that reason, we have avoided using the Lyapunov exponent estimator in this article.

2.3.4. *Other discriminating statistics*

We have found that using the correlation integral ($C(r)$ for some value of r) directly as a discriminating statistic generally provides a more powerful discrimination than the estimated dimension itself, but of course it is less useful as an informal tool. L. Smith (personal communication) has suggested using a statistic which characterizes the linearity of a $\log C(r)$ versus $\log r$ curve. We have also considered but not implemented two-sided forecasting – predicting x_t from the past *and* future values: $x_{t-1}, \ldots$; $x_{t+1}, \ldots$, instead of the usual forecasting which uses only the past (this was inspired by the simple noise reduction technique suggested by Schreiber and Grassberger [51]). In our forecasting, we are careful to distinguish the "training" set from the "testing" set, so that the forecasting statistic is an out-of-sample error; but the in-sample fitting error may also suffice as a discriminating statistic. We have found that the BDS test [33], which was designed to test for any temporal correlation at all – linear or nonlinear, can readily be extended to test other null hypotheses; we use the same statistic, but we do not pre-whiten the data, and instead of relying on an analytical derivation of the distribution function, we use surrogate data. Higher and cross moments provide another class of discriminating statistic; in fact, many of these are the basis of traditional tests for nonlinearity in a time series (e.g., see refs. [22–24]). We have found that a simple skewed difference statistic, defined by $Q = \langle (x_{t+m} - x_t)^3 \rangle / \langle (x_{t+m} - x_t)^2 \rangle$, is both rapidly computable and often quite powerful. Informally, this statistic indicates the asymmetry between rise and fall times in the time series. The most direct example we know is due to Brock, Lakonishok, and LeBaron [52], who used technical trading rules as discriminating statistics for financial data; here there is no difficulty interpreting the informal meaning of the statistic: it is how much money you should have made using that rule in that market.

2.4. *Algorithms for generating surrogate data*

In this section, we describe algorithms we use for generating surrogate data. The first two are consistent with the hypothesis of linearly correlated noise described in section 2.2.3, and the third adjusts for the possibility of a static nonlinear transform as discussed in section 2.2.4.

2.4.1. *Unwindowed Fourier transform (FT) algorithm*

This algorithm is based on the null hypothesis that the data come from a linear gaussian process. The surrogate data are constructed to have the same Fourier spectra as the raw data. The algorithm is described in more detail in ref. [19], but we briefly note the main features. First, the Fourier transform is computed for positive and negative frequencies $f = 0, 1/N, 2/N, \ldots, 1/2$, and without the benefit of windowing. Although windowing is generally recommended when it is the power spectrum which is of ultimate interest [53], we originally chose not to use windowing because what we wanted was for the real and surrogate data to have the same power spectrum; we were not concerned with the spectrum, *per se*. The Fourier transform has a complex am-

plitude at each frequency; to randomize the phases, we multiply each complex amplitude by $e^{i\phi}$, where ϕ is independently chosen for each frequency from the interval $[0, 2\pi]$. In order for the inverse Fourier transform to be real (no imaginary components), we must symmetrize the phases, so that $\phi(f) = -\phi(-f)$. Finally, the inverse Fourier transform is the surrogate data.

One limitation of this algorithm is that it does not reproduce "pure" frequencies very well. What happens is that nearby frequencies in Fourier space are "contaminated" and then because their phases are randomized, they end up "beating" against each other and producing spurious low-frequency effects. (We are grateful to S. Ellner for pointing this out to us.) This may not be too surprising since it is difficult to make a linear stochastic process with a long coherence time. Put another way, the time series should not only be much larger than the dominant periodicities but also much longer than the coherence time of any given frequency if one is to try and model it with a linear stochastic process.

A second problem, which is most evident for highly sampled continuous data, is that spurious high frequencies can be introduced. This can be understood as an artifact of the Fourier transform which assumes the time series is periodic with period N. This means that there is a jump-discontinuity from the last to the first point. We recommend tailoring the length N of the data set so that $x[0] \approx x[N-1]$. This should not be a problem if the time series is stationary and much longer than its dominant frequency. We have done this for the experimental results in this article.

2.4.2. *Windowed Fourier transform (WFT) algorithm*

The problem of spurious high frequencies can also be addressed by windowing the data before taking the Fourier transform. The time series is multiplied by a function $w(t) = \sin(\pi t/N)$ which vanishes at the endpoints $t = 0$ and $t = N$. This suppresses the jump discontinuity from the last to the first point, and seems to effectively get rid of the high frequency effect. However, it also introduces a spurious low-frequency from the power spectrum of $w(t)$ itself. We have done experiments where we simply set the magnitude of the offending frequency ($f = 1/N$) to zero; this seems to work well for stationary time series, but if there is significant power at that frequency in the original data, it too will be suppressed.

2.4.3. *Amplitude adjusted Fourier transform (AAFT) algorithm*

The algorithm in this section generates surrogate data sets associated with the null hypothesis in section 2.2.4, that the observed time series is a monotonic nonlinear transformation of a linear gaussian process. The idea is to first rescale the values in the original time series so they are gaussian. Then the FT or WFT algorithm can be used to make surrogate time series which have the same Fourier spectrum as the rescaled data. Finally, the gaussian surrogate is then rescaled back to have the amplitude distribution as the original time series.

Denote the original time series by $x[t]$, with $t = 0, \ldots, N-1$. The first step is to make a gaussian time series $y[t]$, where each element is generated independently from a gaussian pseudorandom number generator. Next, we re-order the time sequence of the gaussian time series so that the ranks of both time series agree; that is, if $x[t]$ is the nth smallest of all the x's, then $y[t]$ will be the nth smallest of all the y's. Therefore, the re-ordered $y[t]$ is a time series which "follows" the original time series $x[t]$ and which has a gaussian amplitude distribution. Using the FT or WFT algorithm, a surrogate, call it $y'[t]$, of the gaussian time series can be created. If the original time series $x[t]$ is time re-ordered so that it follows $y'[t]$ in the sense that the ranks agree, then the time-re-ordered time series provides a surrogate of the original time series which matches its amplitude distribution. Further, the

"underlying" time series ($y[t]$ and $y'[t]$) are gaussian and have the same Fourier power spectrum.

3. Experiments with numerical time series

To properly gauge the utility of the surrogate data approach will eventually require many tests with data from both numerical and laboratory experiments. In this section we illustrate several aspects of the method with data whose underlying dynamics is known. In the next section, we consider several examples with real data.

3.1. Linear gaussian data

First, we note that a time series which actually is generated by a linear process should by construction give a negative result (that is, the null hypothesis should *not* be rejected). We checked this by generating some time series with two simple linear processes, a moving average

$$x_t = e_t + ae_{t-1} \tag{10}$$

and an autoregressive

$$x_t = ax_{t-1} + e_t\,. \tag{11}$$

We used an embedding dimension $m = 3$ and computed correlation dimension from $N = 4096$ points. The "correct" dimension for both processes is $\nu = m = 3$, though as fig. 2 shows, the estimates were always biased low. The bias increases for data which are more highly autocorrelated ($|a|$ larger) but the point we wish to make is that the bias is the same for the original data and for the surrogates. The null hypothesis is not rejected.

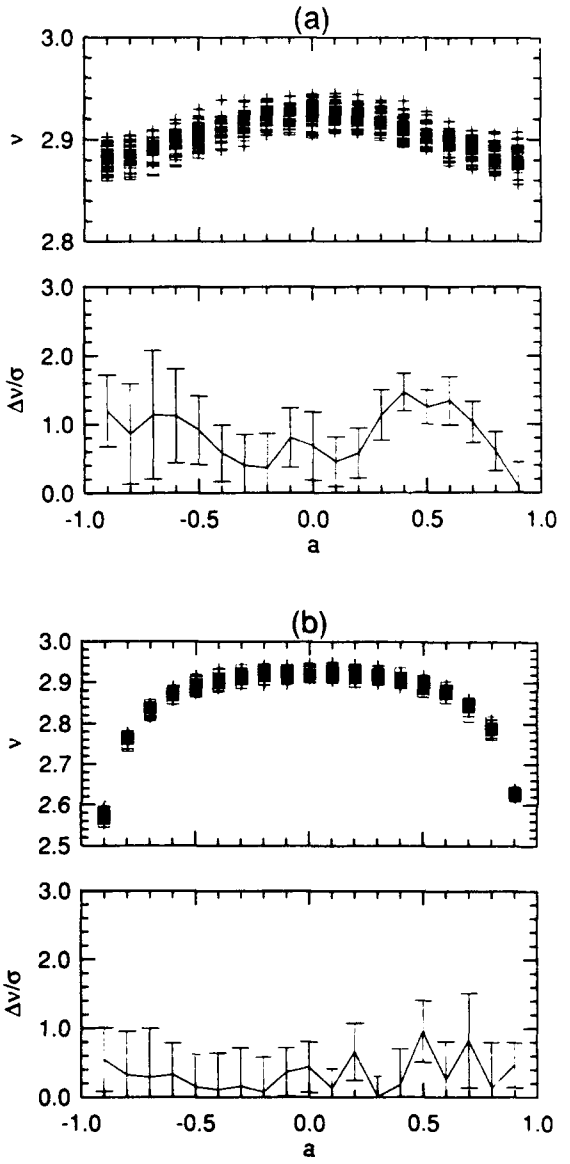

Fig. 2. Significance of evidence for nonlinearity for linear gaussian time series generated by (a) a moving average process, and (b) an autoregressive process. The coefficient in each case is a. The estimated dimension is shown for five realizations of the linear process (□) and thirty realizations of surrogate data (+). Note that the dimension does not distinguish the original from the surrogate data. The value we obtain for significance is shown in the lower panels and in neither case is significant.

3.2. Variation with number of data points and complexity of attractor

Using the FT algorithm, we showed in ref. [19] that increasing the number of points in a time series increases the significance with which nonlinearity can be detected in a time series that is known to be chaotic; and increasing the complexity of the chaotic time series decreases the ability to distinguish from linearity. This basic

point is illustrated again here using the AAFT algorithm (see fig. 3); while the significance is not as large using this more general null hypothesis, the qualitative behavior is the same. Time series are generated by summing n independent trajectories of the Hénon map [54]: such time series will have a dimension $n\nu$ where $\nu \approx 1.2$ is the dimension of a single Hénon trajectory. For the largest data sets, with $N = 8192$ points, our dimension estimator obtained correlation dimensions of 1.215 ± 0.008, 2.279 ± 0.014, 3.48 ± 0.02, and 4.81 ± 0.06 using embedding dimensions $m = 3$, 4, 5, and 6, for $n = 1$, 2, 3, and 4, respectively.

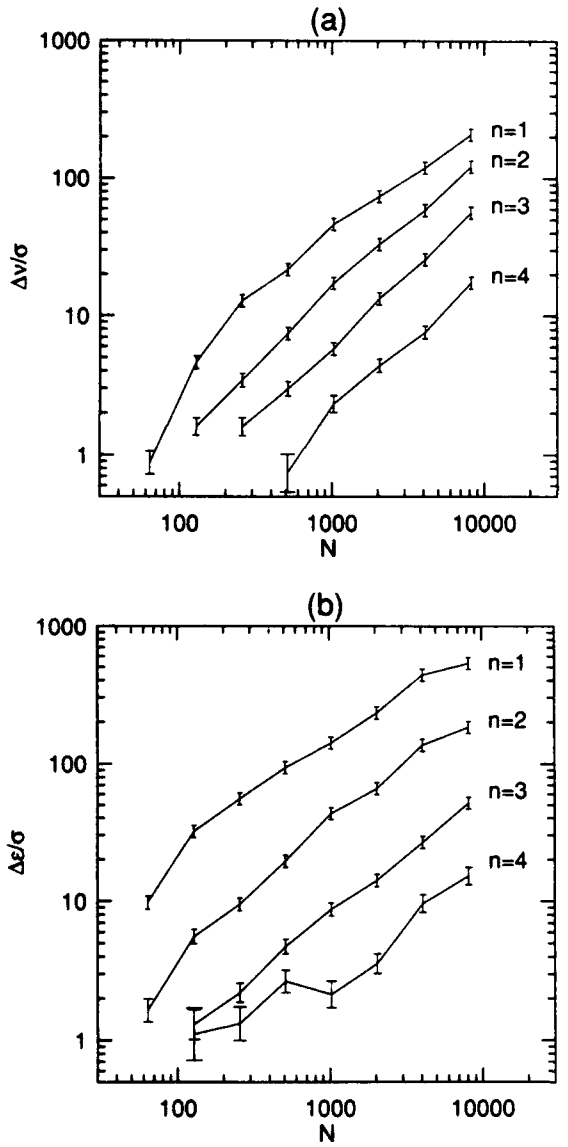

Fig. 3. Using the AAFT algorithm to generate surrogate data, the significance as a function of the number N of data points is computed for time series obtained by summing n independent trajectories of the Hénon map. For both (a) correlation dimension and (b) forecasting error, the significance increases with number of data points and decreases with the complexity of the system.

3.3. *Effect of observational and dynamical noise*

To test whether nonlinear determinism can be detected even when it is mixed with noise, we added both dynamical (η) and observational (ε) noise to the cosine map: $y_t = \lambda \cos(\pi y_{t-1}) + \eta_t$; $x_t = y_t + \varepsilon_t$. We chose a value $\lambda = 2.8$ which is in the chaotic regime when the external noise is zero. (The cosine map was used instead of the Hénon map because it does not "blow up" in the presence of too much dynamical noise.) In fig. 4,

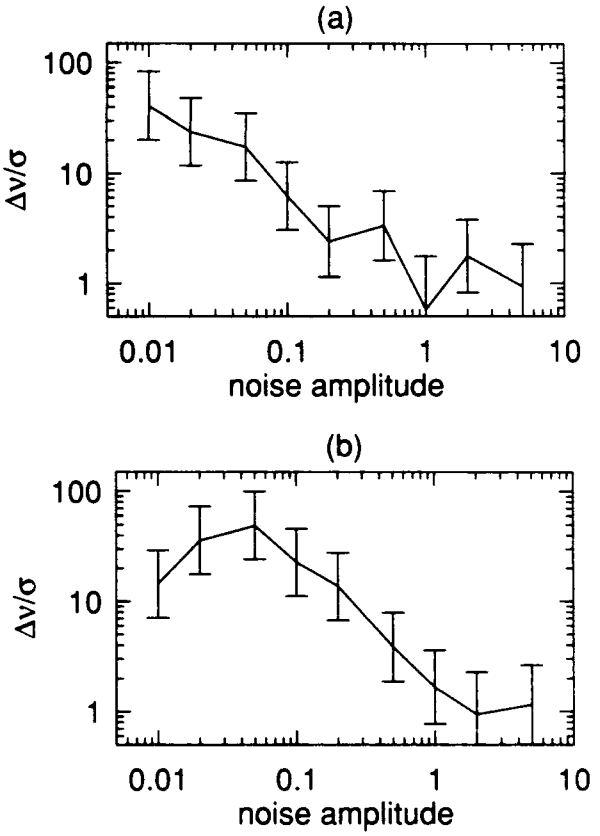

Fig. 4. Effect of noise on significance for a short time series of $N = 512$ points, derived from the cosine map with $\lambda = 2.8$: (a) observational noise; (b) dynamical noise.

we plot significance as a function of noise level for both dynamical and observational noise. As expected, significance decreases with increasing noise level, though we remark that the nonlinearity is still observable even with considerable noise. In the absence of noise, the rms amplitude of the signal is 0.36; thus we are able to detect significant nonlinearity even with a signal to noise ratio of one, using a time series of length $N = 512$. We also note that the decrease in significance with increased dynamical noise is not always monotonic; low levels of dynamical noise can make the nonlinearity more evident.

3.4. Continuous data

In most experiments, data is better described as a flow than a map. Although there is a formal equivalence, data which arise from processes that are continuous in time are often sampled at a much faster rate than is characteristic of the underlying dynamics. For these data sets, the effects of autocorelation can be quite large, and the importance of testing against a null hypothesis that includes autocorrelation becomes paramount.

We illustrate this point with numerical experiments on data obtained from the Mackey–Glass differential delay equation [55]

$$\frac{dx}{dt} = -bx(t) + \frac{ax(t-\tau)}{1+[x(t-\tau)]^{10}}, \qquad (12)$$

with $a = 0.2$, $b = 0.1$, and $\tau = 30$. Grassberger and Procaccia [39] compute a correlation dimension of $\nu \approx 3.0$ for these parameters.

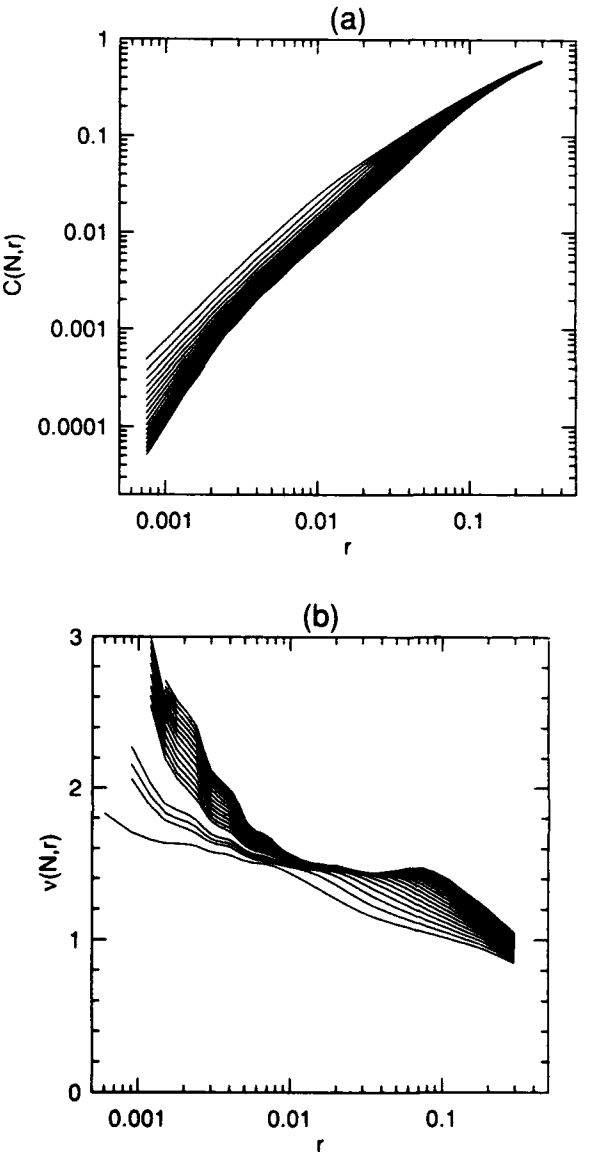

Fig. 5. (a) Correlation integral $C(N, r)$ for $N = 4096$ points and embedding dimensions $m = 3, \ldots, 19$ from oversampled Mackey–Glass data. (b) Estimated correlation dimension ν according to Takens estimator as a function of cutoff r.

3.4.1. A poor embedding

We oversample the data ($\Delta t = 0.1$) and use a deliberately poor embedding strategy – straight time-delay coordinates with a lag time of one sample period. We estimate correlation dimension with $N = 4096$ points and compute distances between all pairs of distinct vectors (despite the advice in refs. [2, 56]). Fig. 5 shows the correlation integral and estimated dimension as a function of the upper cutoff value R. There is about a decade of roughly constant slope, which might be taken to indicate convergence to a low correlation dimension.

For this example, the dimension statistic was computed as the Takens best estimator [12] at an upper cutoff of $R = 0.02$. (For comparison, the

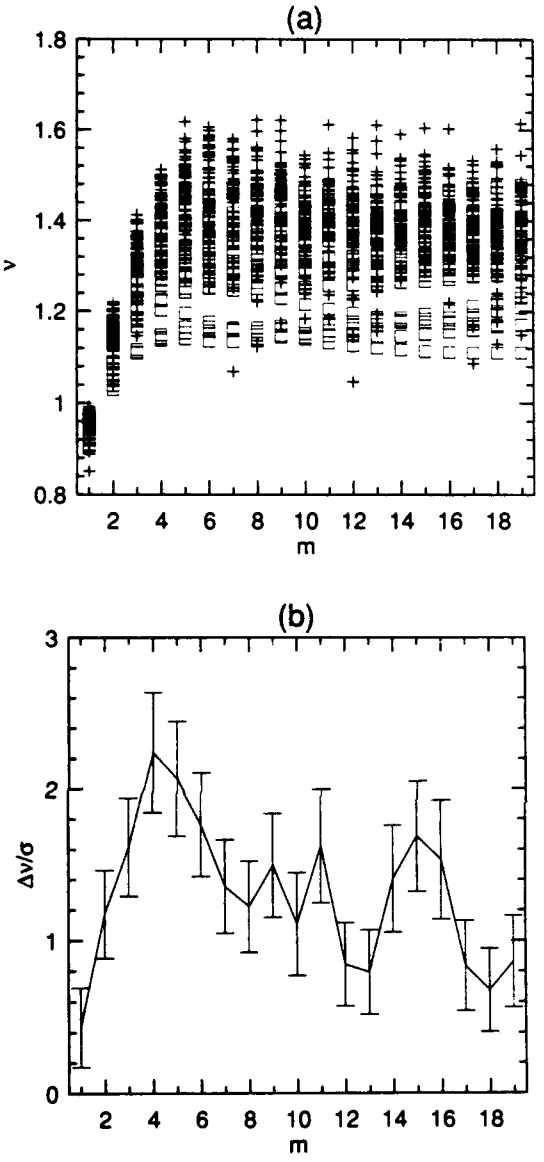

Fig. 6. (a) Estimated correlation dimension versus embedding dimension for oversampled ($\Delta t = 0.1$) Mackey–Glass data (□) and for surrogates generated using the WFT algorithm (+). (b) Significance of nonlinearity in no case exceeds three sigmas.

RMS value for this time series is $R_{\text{rms}} = 0.25$.) Fig. 6a shows an apparent convergence of the estimated dimension as a function of embedding dimension. A naive interpretation of this figure is that the time series arises from a low-dimensional strange attractor. However, as fig. 6a shows, the surrogate data also converge to a low dimension; the convergence is evidently an artifact of the autocorrelation. Indeed, fig. 6b shows that the dimension statistic in this case does not even provide evidence for nonlinearity.

3.4.2. *A better embedding*

From the same Mackey–Glass process, we recompute correlation dimension and the signifi-

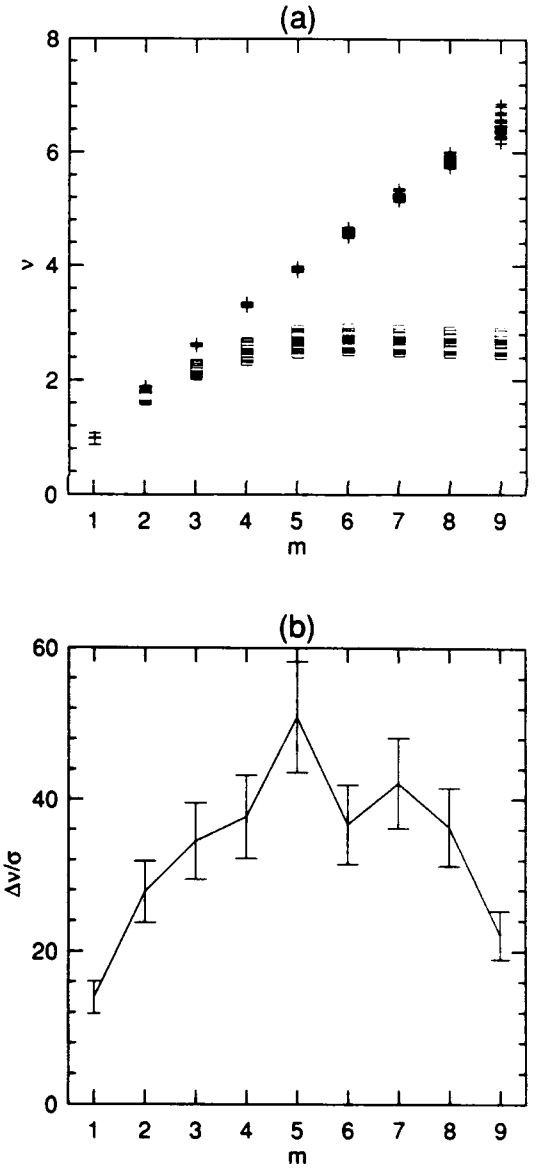

Fig. 7. Same as previous figure, except that a better embedding and a better algorithm were used for estimating the dimension. Not only is the evidence for nonlinearity extremely significant in this case, but it is also evident that the process is low-dimensional.

cance of evidence for nonlinearity using a better (though probably still not optimal) choice of embedding. We sample at a much lower rate, $\Delta t = 3.0$, and again use straight delay coordinates with lag time of one sample period. We estimate the correlation dimension as described in section 2.3.1 with $N = 4096$ points, and we avoid pairs of points which are closer together in time than one hundred sample periods. In fig. 7, we see that the evidence for nonlinearity is extremely significant. Indeed, we also see positive evidence of low-dimensional behavior (the estimated dimension ν converges with m) which we know is not an artifact of autocorrelation.

4. Examples with real data

We report some results on experimental time series from several sources. These results should be taken as illustrative, and not necessarily typical of the class which they represent. In particular, we have not yet attempted to "normalize" our findings with others that have previously appeared in the literature.

4.1. *Rayleigh–Benard convection*

Data from a mixture of ^{3}He and superfluid ^{4}He in a Rayleigh–Benard convection cell [57] provides an example where the evidence for nonlinear structure is extremely significant. The significance as obtained with the dimension and forecasting statistics from a time series of $N = 2048$ points are shown in fig. 8. Further, the dimension statistic indicates that the flow is in fact low-dimensional; while the measured dimension of 3.8 may be due to an artifact of some kind, we are at least assured that it is not an artifact of autocorrelation or of nongaussian amplitude distribution. Farmer and Sidorowich [42] used this data to demonstrate the enhanced predictability using nonlinear rather than linear predictors.

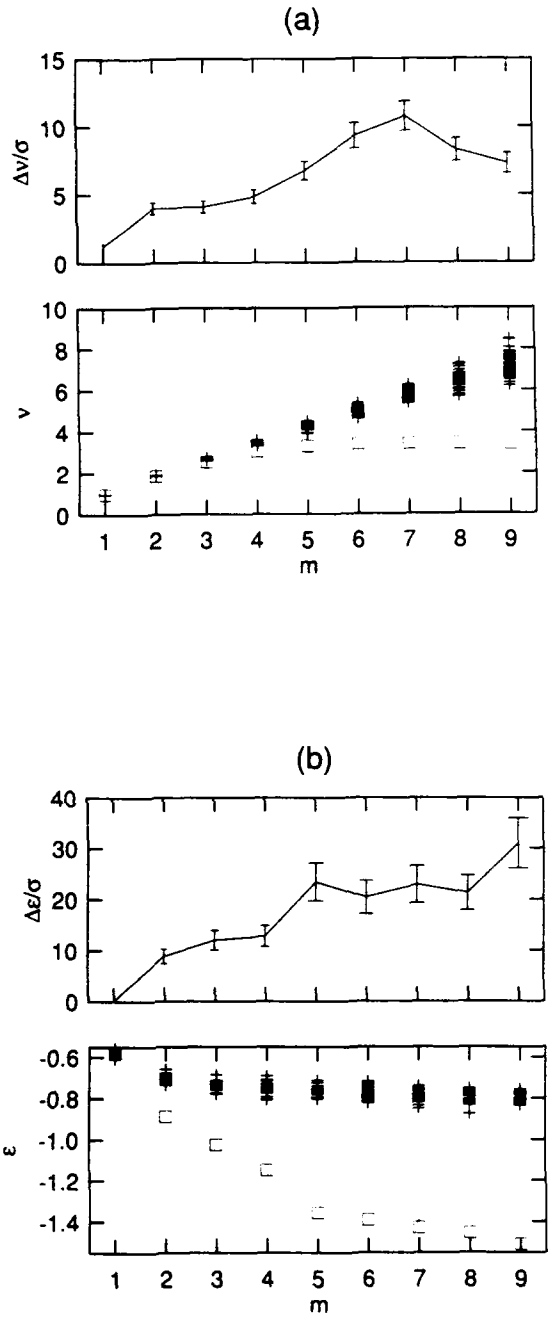

Fig. 8. Data from a fluid convection experiment exhibits very significant nonlinear structure, using (a) dimension, and (b) forecasting error. The top panel in these figures show the significance, measured in "sigmas", and the bottom panel shows the values of the statistics, with squares (□) for the original data and pluses (+) for the AAFT-generated surrogates. Both panels plot these statistics against the embedding dimension m. Not only is the evidence for nonlinear structure statistically significant, but the estimated dimension of about $\nu = 3.8$ suggests that the underlying dynamics is in fact low-dimensional chaos.

4.2. The human electroencaphalogram (EEG)

The electroencephalogram (EEG) is to the brain what the electrocardiogram (EKG) is to the heart. It has become a widely used tool for the monitoring of electrical brain activity, and its potential for diagnosis is still being explored. A number of researchers have applied the methods that were developed for the analysis of chaotic time series to EEG time series. While it was hoped that the characterization of deterministic structure in EEG would eventually lead to insights about the workings of the brain, the shorter term goal was to use the nonlinear properties of the time series as a diagnostic tool [58, 59].

Although we feel a more systematic survey is in order, we have not examined any EEG data which gives positive evidence of low-dimensional chaos. However, we have found examples where nonlinear structure was evident. We present here two cases, one positive and one negative. The two time series are from the same individual, eyes closed and resting; one is from a probe at the left occipital (O1), and the other from the left central (C3) part of the skull. The sampling rate is 150 Hz, and $N = 2048$ time samples are taken. The two time series are not necessarily contemporaneous. Using the dimension statistic, the first data set shows no significant evidence for nonlinearity, but the second data set exhibits about eight sigmas. Even in the significant case, we do not see any evidence that the time series is in fact low-dimensional (the correlation dimension ν does not converge with increasing embedding dimension m). We are formally able to reject the null hypothesis that the data arise from a linear stochastic process, but by comparing the surrogate data to the real data, we see no reason to expect that the "significant" data arises from a low-dimensional chaotic attractor.

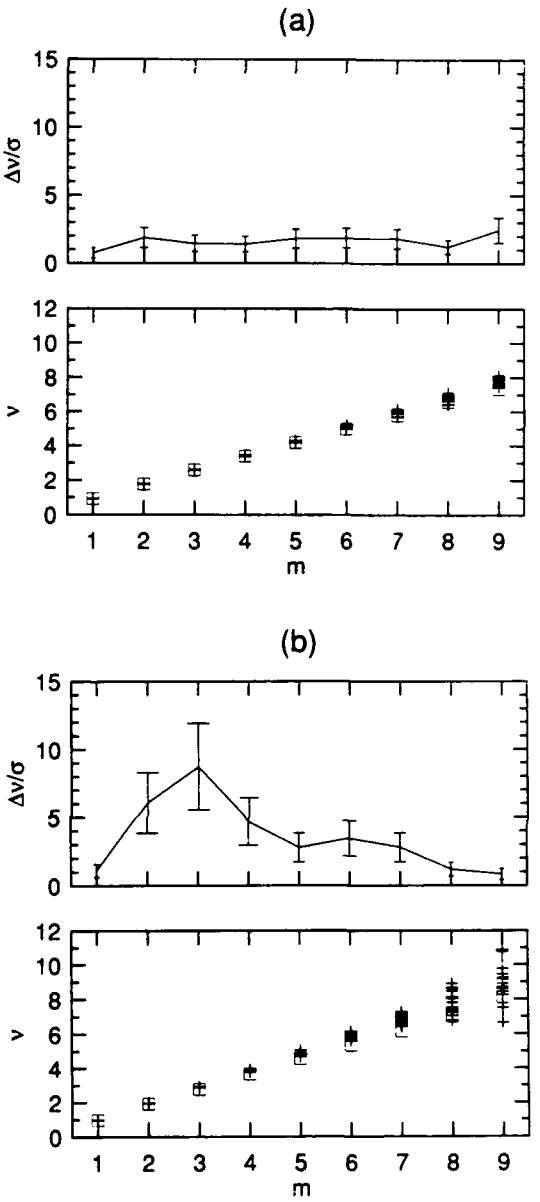

Fig. 9. Data from two electroencephalogram (EEG) time series. Using the dimension statistic, the first (a) shows no nonlinear structure, while the second (b) exhibits significant nonlinear structure at the eight sigma level. The evidence for low-dimensional chaos, however, is weak, since the estimated dimension increases almost as rapidly with embedding dimension for the original time series as it does for the surrogates.

4.3. The sunspot cycle

Our final example is the well known and much studied eleven year sunspot cycle [44, 60–66]. First, we used the FT algorithm for generating surrogate data, but we were careful to use a length of time series ($N = 287$) for which the first and last data point both corresponded to minima; this avoids introducing the spurious high

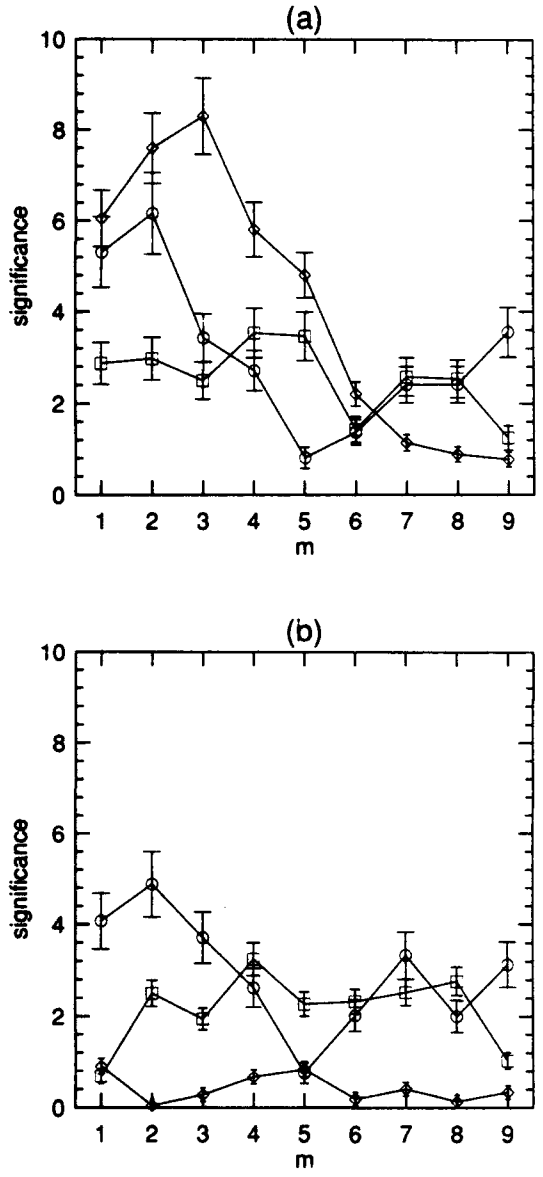

Fig. 10. Significance of nonlinearity in the annual sunspot series; (a) against the null hypothesis of linear gaussian noise (surrogates generated by FT algorithm), and (b) the null hypothesis of amplitude corrected linear gaussian noise (surrogates generated by AAFT algorithm). For both plots, the discriminating statistics are estimated dimension (◇), log median prediction error (□), and the skew statistic described in the text (○).

frequencies that we discussed in section 2.4.1. As fig. 10a shows, it is possible to quite confidently reject the null hypothesis of linear gaussian noise; this is in agreement with the numerous authors who obtained better agreement using nonlinear models instead of linear models. However, when we expand the null hypothesis to include a static nonlinear observation of an underlying linear gaussian process, the evidence for dynamical nonlinear structure is less dramatic. Using the dimension statistic, there is no significance; the prediction statistic gives that the evidence is just significant; the cubed difference statistic $Q = \langle (x_{t+m} - x_t)^3 \rangle / \langle (x_{t+m} - x_t)^2 \rangle$, which is a measure of the time irreversibility of the data, provides a more significant rejection of the hypothesis of static nonlinear filter of an underlying linear process.

5. Comparison to other work

Numerous authors have carefully compared their dimension estimates for real data against similar estimates for white noise. A few have extended this informal control to other forms of correlated noise. Grassberger [2] showed that a reported dimension for climate data could be reproduced with data from an Ornstein–Uhlenbeck process. Osborne et al. [5], criticized the Grassberger–Procaccia algorithm on the basis that the low dimension it gave to nonstationary data on ocean currents it also gave to data generated by randomizing the phases of the Fourier transform. Kaplan and Cohen [32] argued that fibrillation was not usefully described as chaotic, again since randomly phased data gave similar dimensions. Smith [67] has used the FT algorithm to generate surrogates which are used to assess the predictability of geophysical time series. Weiss [62], described a comparison of the sunspot time series against a particular stochastic model. Brock et al. [52] used technical trading rules to distinguish stock market data from surrogates generated by several stochastic models. And Ellner [68] showed that a variety of "plausible alternatives" might adequately explain measles and chickenpox data, despite earlier claims of chaos.

Brock and coworkers in particular [33, 52,

69–71], and the economics community in general [29, 34, 72, 73], have been extremely active in the development of statistical tools for time series analysis. While the choice of null hypotheses for financial time series tends to be different than for more physical time series (autocorrelation plays a lesser role, for example), the overall methodologies are quite similar. Classical statisticians [20–25, 28] have long considered tests for nonlinearity, and are becoming increasingly aware of low-dimensional chaos (just as physicists are becoming increasingly aware of the importance of the statistical approach); we cite Tong [26] as *the* review which most neatly and comprehensively ties these two fields together.

6. Conclusion

In this article, we have described an approach for evaluating the statistical significance of evidence for nonlinearity in a stationary time series. The test properly fails to find nonlinear structure in linear stochastic systems, and correctly identifies nonlinearity in several well-known examples of low-dimensional chaotic time series, even when contaminated with dynamical and observational noise. We illustrated the method with several experimental data sets, and confirmed the evidence for nonlinear structure in some systems, while failing to see such structure in other time series.

Acknowledgements

We are pleased to acknowledge Martin Casdagli, Xiangdong He, Willian Brock, Blake LeBaron, Steve Ellner, Peter Grassberger, Mark Berge, Tony Begg and Bette Korber for useful discussions. We are especially grateful to Lenny Smith for illuminating disagreements and a careful reading of the manuscript. We also thank Bob Ecke for providing convection data, and Paul Nuñez and Arden Nelson for providing EEG data. This work was partially supported by the National Institute for Mental Health under grant 1-R01-MH47184-01, and performed under the auspices of the Department of Energy.

References

[1] C. Nicolis and G. Nicolis, Nature 311 (1984) 529.
[2] P. Grassberger, Nature 323 (1986) 609.
[3] C. Nicolis and G. Nicolis, Nature 326 (1987) 523.
[4] P. Grassberger, Nature 326 (1987) 524.
[5] A.R. Osborne, A.D. Kirwin, A. Provenzale and L. Bergamasco, Physica D 23 (1986) 75.
[6] G. Mayer-Kress, in: Directions In Chaos, Vol .., ed. B.-L. Hao (World Scientific, Singapore, 1988), pp. 122–147.
[7] A.R. Osborne and A. Provenzale, Physica D 35 (1989) 357.
[8] A. Provenzale, A.R. Osborne R. Soj, Physica D 47 (1991) 361.
[9] J. Theiler, Phys. Lett. A 155 (1991) 480.
[10] J.B. Ramsey and J.-J. Yuan, Phys. Lett. A 134 (1989) 287.
[11] J. Theiler, Phys. Rev. A 41 (1990) 3038.
[12] F. Takens, in: Dynamical Systems and Bifurcations (Groningen, 1984), eds. B.L.J. Braaksma, H.W. Broer and F. Takens, Lecture Notes in Mathematics, Vol. 1125 (Springer, Berlin, 1985), pp. 99–106.
[13] W.E. Caswell and J.A. Yorke, in: Dimensions and Entropies in Chaotic Systems – Quantification of Complex Behavior, Springer Series in Synergetics, Vol. 32 (Springer, Berlin, 1986), pp. 123–136.
[14] J. Holzfuss and G. Mayer-Kress, in: Dimensions and Entropies in Chaotic Systems – Quantification of Complex Behavior, Springer Series in Synergetics, Vol. 32 (Springer, Berlin, 1986), pp. 114–122.
[15] J. Theiler, Quantifying Chaos: Practical Estimation of the Correlation Dimension, Ph.D. thesis (Caltech, 1988).
[16] M. Möller, W. Lange, F. Mitschke, N.B. Abraham and U. Hübner, Phys. Lett. A 138 (1989) 176.
[17] J. Theiler, J. Opt. Soc. Am. A 7 (1990) 1055.
[18] R.L. Smith, in: Nonlinear Modeling and Forecasting, eds. M. Casdagli and S. Eubank, of SFI Studies in the Sciences of Complexity, Vol. XII (Addison-Wesley, Reading, MA, 1992) pp. 115–136.
[19] J. Theiler, B. Galdrikian, A. Longtin, S. Eubank and J.D. Farmer, in: Nonlinear Modeling and Forecasting, eds. M. Casdagli and S. Eubank, SFI Studies in the Sciences of Complexity, Vol. XII (Addison-Wesley, Reading, MA, 1992) pp. 163–188.
[20] T. Subba Rao and M.M. Gabr, J. Time Series Anal. 1 (1980) 145.
[21] M.J. Hinich, J. Time Series Anal. 3 (1982) 169.
[22] A.I. McLeod and W.K. Li, J. Time Series Anal. 4 (1983) 269.

[23] D.M. Keenan, Biometrika 72 (1985) 39.
[24] R.S. Tsay, Biometrika 73 (1986) 461.
[25] R.S. Tsay, Stat. Sin. 1 (1991) 431.
[26] H. Tong, Non-linear Time Series: A Dynamical System Approach (Clarendon Press, Oxford, 1990).
[27] B. Efron, SIAM Rev. 21 (1979) 460.
[28] R.S. Tsay, Appl. Stat. 41 (1992) 1.
[29] J.A. Scheinkman and B. LeBaron, J. Business 62 (1989) 311.
[30] J.L. Breeden and N.H. Packard, Nonlinear analysis of data sampled nonuniformly in time, Physica D 58 (1992) 273, these Proceedings.
[31] G.E. Uhlenbeck and L.S. Ornstein, Phys. Rev. 36 (1930) 823; reprinted in: Noise and Stochastic Processes, ed. N. Wax (Dover, New York, 1954).
[32] D.T. Kaplan and R.J. Cohen, Circulation Res. 67 (1990) 886.
[33] W.A. Brock, W.D. Dechert and J. Scheinkman, A test for independence based on the correlation dimension, Social Systems Research Institute, University of Wisconsin at Madison, technical report 8702 (1986).
[34] T.-H. Lee, H. White and C.W.J. Granger, Testing for neglected nonlinearity in time series models: A comparison of neural network methods and alternative tests, J. Econometrics, to appear.
[35] E.J. Kostelich and H.L. Swinney, in: Chaos and Related Natural Phenomena, eds. I. Procaccia and M. Shapiro (Plenum, New York, 1987), p. 141.
[36] J. Theiler, Phys. Rev. A 36 (1987) 4456.
[37] P. Grassberger, Phys. Lett. A 148 (1990) 63.
[38] P. Grassberger and I. Procaccia, Phys. Rev. Lett. 50 (1983) 346.
[39] P. Grassberger and I. Procaccia, Physica D 9 (1983) 189.
[40] F. Takens, Invariants related to dimension and entropy, in: Atas do 13° Colóqkio Brasiliero de Matemática (1983).
[41] S. Ellner, Phys. Lett. A 133 (1988) 128.
[42] J.D. Farmer and J.J. Sidorowich, in: Evolution, Learning and Cognition, ed. Y.C. Lee (World Scientific, Singapore, 1988), pp. 277–330.
[43] M. Casdagli, in: Modeling Complex Phenomena, eds. L. Lam and V. Naroditsky (Springer, New York, 1992), p. 131.
[44] M. Casdagli, Chaos and deterministic versus stochastic nonlinear modeling, J. R. Stat. Soc. B 54 (1992) 303.
[45] M. Sano and Y. Sawada, Phys. Rev. Lett. 55 (1985) 1082.
[46] J.-P. Eckmann and D. Ruelle, Rev. Mod. Phys. 57 (1985) 617.
[47] J.-P. Eckmann, S.O. Kamphorst, D. Ruelle and S. Ciliberto, Phys. Rev. A 34 (1986) 4971.
[48] S. Ellner, A.R. Gallant, D. McCaffrey and D. Nychka, Phys. Lett. A 153 (1991) 357.
[49] D. McCaffrey, S. Ellner, A.R. Gallant and D. Nychka, Estimating the Lyapunov exponent of a chaotic system with nonparametric regression, J. Am. Stat. Assoc., to appear.
[50] D. Nychka, S. Ellner, D. McCaffrey and A.R. Gallant, J. R. Stat. Soc. B 54 (1992) 399.
[51] T. Schreiber and P. Grassberger, Phys. Lett. A 160 (1991) 411.
[52] W.A. Brock, J. Lakonishok and B. LeBaron, Simple technical trading rules and the stochastic properties of stock returns, J. Finance, to appear.
[53] R.B. Blackman and J.W. Tukey, The Measurement of Power Spectra (Dover, New York, 1959).
[54] M. Hénon, Commun. Math. Phys. 50 (1976) 69.
[55] M.C. Mackey and L. Glass, Science 197 (1977) 287.
[56] J. Theiler, Phys. Rev. A 34 (1986) 2427.
[57] H. Haucke and R. Ecke, Physica D 25 (1987) 307.
[58] P.E. Rapp, I.D. Zimmerman, A.M. Albano, G.C. deGuzman, N.N. Greenbaum and T.R. Bashore, in: Nonlinear Oscillations in Biology and Chemistry, ed. H.G. Othmer (Springer, Berlin, 1986), pp. 175–205.
[59] P.E. Rapp, T.R. Bashore, J.M. Martinerie, A.M. Albano, I.D. Zimmerman and A.I. Mees, Brain Topography 2 (1989) 99.
[60] G.U. Yule, Philos. Trans. R. Soc. London A 226 (1927) 267.
[61] H. Tong and K.S. Lim, J. R. Stat. Soc. B 42 (1980) 245.
[62] N.O. Weiss, Phil. Trans. R. Soc. London A 330 (1990) 617.
[63] J. Kurths and A.A. Ruzmaikin, Solar Phys. 126 (1990) 407.
[64] A. Weigend, B. Huberman and D. Rummelhart, Intern. J. Neural Systems 1 (1990) 193.
[65] M. Mundt, W.B. Maguire II and R.B. P. Chase, J. Geophys. Res. 96 (1991) 1705.
[66] A. Weigend, B.A. Huberman and D.E. Rummelhart, Predicting sunspots and exchange rates with connectionist networks, in: Nonlinear Modeling and Forecasting, eds. M. Casdagli and S. Eubank, SFI Studies in the Sciences of Complexity, Vol. XII (Addison-Wesley, Reading, MA, 1992), pp. 397–434.
[67] L. Smith, Identification and prediction of deterministic dynamical systems, this volume.
[68] S. Ellner, Detecting low-dimensional chaos in population dynamics data: a critical review, in: Chaos and Insect Ecology, eds. J.A. Logan and F.P. Hain (University of Virginia Press, Blacksburg, VA, 1991), pp. 65–92.
[69] W.A. Brock and C.L. Sayers, J. Monetary Econ. 22 (1988) 71.
[70] W.A. Brock and W.D. Dechert, Statistical inference theory for measures of complexity in chaos theory and nonlinear science, in: Measures of Complexity and Chaos, eds. N. Abraham et al. (Plenum, New York, 1989), pp. 79–98.
[71] W.A. Brock and S.M. Potter, in: Nonlinear Modeling and Forecasting, eds. M. Casdagli and S. Eubank, SFI Studies in the Sciences of Complexity, Vol. XII (Addison-Wesley, Reading, MA, 1992), pp. 137–162.
[72] D.A. Hsieh, J. Business 62 (1989) 339.
[73] D.A. Hsieh, J. Finance 46 (1991) 1839.

Physica D 58 (1992) 95–126
North-Holland

PHYSICA D

Singular-spectrum analysis: A toolkit for short, noisy chaotic signals

Robert Vautard, Pascal Yiou[1] and Michael Ghil[2]
Laboratoire de Météorologie Dynamique du CNRS, Ecole Normale Supérieure, F-75231 Paris Cedex 05, France

Received 18 October 1991
Revised manuscript received 18 February 1992
Accepted 2 March 1992

Singular-spectrum analysis (SSA) is developed further, based on experience with applications to geophysical time series. It is shown that SSA provides a crude but robust approximation of strange attractors by tori, in the presence of noise. The method works well for short, noisy time series.

The lagged-covariance matrix of the processes studied is the basis of SSA. We select subsets of eigenelements and associated principal components (PCs) in order to provide (i) a noise-reduction algorithm, (ii) a detrending algorithm, and (iii) an algorithm for the identification of oscillatory components. Reconstructed components (RCs) are developed to provide optimal reconstruction of a dynamic process at precise epochs, rather than averaged over the window length of the analysis.

SSA is combined with advanced spectral-analysis methods – the maximum entropy method (MEM) and the multi-taper method (MTM) – to refine the interpretation of oscillatory behavior. A combined SSA–MEM method is also used for the prediction of selected subsets of RCs.

The entire toolkit is validated against a set of four prescribed time series generated by known processes, quasi-periodic or chaotic. It is also applied to a time series of global surface air temperatures, 130 years long, which has attracted considerable attention in the context of the global warming issue and provides a severe test for noise reduction and prediction.

1. Introduction

1.1. Motivation

The analysis of observed time series is often a prerequisite for progress in modeling and forecasting the physical system which generates them. Three cases have to be distinguished. First, when the evolution equations governing the physical system are already known, and are relatively insensitive to initial data, forecasting is based on these equations and its accuracy depends largely on the quality of initial data. Such is the case of celestial mechanics [1], on the whole.

For other systems, the knowledge of exact evolution equations is useless for long-term forecasting purposes, even when good initial data are available. This typically happens when the dynamical system has instabilities and nonlinearities that give rise to deterministic chaos, as shown by Lorenz [2]. Chaos, however, does not mean that, for large time scales, the behavior is totally irregular or random. Some macroscopic regularities, such as near periodicities, may still contribute a large part of the variability of the system. This is the second possibility: we know the equations, detailed forecasting based on

[1]Now at Laboratoire de Modélisation du Climat et de l'Environnement/DSM, Commissariat à l'Energie Atomique, F-91191 Gif-sur-Yvette, France.

[2]On sabbatical leave from the Department of Atmospheric Sciences and the Institute of Geophysics and Planetary Physics, University of California, Los Angeles, USA.

0167-2789/92/$05.00 © 1992 – Elsevier Science Publishers B.V. All rights reserved

them for a long time is impossible because of the sensitivity to initial data, but there might be other ways to predict the regular part of the asymptotic behavior. Indeed, the phase-space trajectories of such a chaotic system converge generically to a *strange attractor*. Weakly unstable periodic orbits, contained in the latter, can attract trajectories intermittently, and therefore lead to spells of periodic activity. The underlying periodic orbits have to be identified by data analysis, and can help extended-range prediction.

The climatic system is such a dynamical system. The deterministic predictability limit of detailed weather is not longer than a couple of weeks [3, 4 pp. 182–190, 438–441]. On longer time scales, instabilities and nonlinearities make the atmosphere unpredictable. However, there are some near-periodicities such as the El Niño–Southern Oscillation (ENSO) cycle in the atmosphere and the oceans [5], with periods of two to five years, or the 40–50 day oscillation [6] in the tropical atmosphere. The regularity of these phenomena can make them easier to predict with empirical models [7], based on time-series analysis, than with elaborate general circulation models, based on the discretization and numerical solution of atmosphere–ocean-coupled systems of partial differential equations.

The third class includes systems with unknown evolution equations. An example is given by complex biomedical systems, such as the human brain [8]. Often, only noisy measurements of one variable from an intrinsically high-dimensional system are available, in either one of the two latter cases.

The purpose of this paper is to review the capabilities of a data-analysis method, called *singular-spectrum analysis* (SSA): SSA extracts as much reliable information as possible from short and noisy time series without using prior knowledge about the underlying physics or biology of the system; based on this information, it also provides prediction models. If only measurements of one variable are available, *single-channel* SSA applies. When several variables are measured, the cross-correlations between the time series can be taken into account by using *multi-channel* SSA.

SSA is essentially a linear analysis and prediction method. Its superiority over classical spectral methods, and the sense in which it can use concepts from and be useful in nonlinear dynamics, lies in the data-adaptive character of the eigenelements it is based on. Truly nonlinear information about and high predictive skill for intrinsically low-dimensional systems requires tens of thousands of data points [9], and many more for typical systems with intermediate and high phase-space dimensions. As we shall see, SSA can provide useful physical insight and modest, but unprecedented, medium-term predictive skill starting with the few hundred data points typically available for geophysical and other natural systems.

1.2. Background

SSA as a data-analysis method has been used for years in digital signal processing [10, 11]. It was introduced into oceanography by Colebrook [12], and into nonlinear dynamics by Broomhead and King [13] and by Fraedrich [14]. SSA is based on principal component analysis (PCA) in the vector space of delay coordinates for a time series. Classical PCA [15] is used with multichannel time series, and gives the principal axes of a sequence of M-dimensional vectors $(X_i, 1 \le i \le N)$, by expanding it with respect to an orthonormal basis $(E^k, 1 \le k \le M)$:

$$X_{ij} = \sum_{k=1}^{M} a_i^k E_j^k , \quad 1 \le j \le M . \tag{1.1}$$

The projection coefficients a_i^k are called the *principal components* (PCs), and the basis vectors E^k the *empirical orthogonal functions* (EOFs). The vectors E^k are the eigenvectors of the cross-covariance matrix of the sequence (X_i). For single-channel SSA, if the scalar series values are

denoted by $(x_i, 1 \le i \le N)$, the equivalent expansion is

$$x_{i+j} = \sum_{k=1}^{M} a_i^k E_j^k , \quad 1 \le j \le M . \tag{1.2}$$

The analogy is made by augmenting the single time series x_i into the multi-variate time series $X_i = (x_{i+1}, x_{i+2}, \ldots, x_{i+M})$. Aside from this definition, there is no formal difference between the two expansions (1.1) and (1.2). M in the latter is called the *window length*, or *embedding dimension* – and is chosen by the user – in contradistinction with classical PCA, where M is the fixed dimension of the data vectors.

The vectors E^k are the eigenvectors of the *Toeplitz matrix* of x, T_x, that contains in column j and row i the covariance of x at lag $i-j$. In both situations, the eigenvalue–eigenvector decomposition of the covariance matrix (with respect to space or lag) is related to singular-value decomposition (SVD [16]) of a rectangular matrix; in the case of SSA, the trajectory matrix has the $N - M$ augmented vectors X_i as its columns. SVD is a class of algorithms of great generality in numerical linear algebra; we prefer not to confuse matters and distinguish between it and SSA, which is a methodology for time-series analysis.

For multi-channel SSA [17–19], with original L-dimensional data vectors $X_{l,i}$, $1 \le l \le L$, $1 \le i \le N$, the expansion becomes

$$X_{l,i+j} = \sum_{k=1}^{L \times M} a_i^k E_{l,j}^k , \quad 1 \le l \le L, \; 1 \le j \le M . \tag{1.3}$$

Here, the state vector considered at time i is $(X_{1,i+1}, X_{1,i+2}, \ldots, X_{1,i+M}, X_{2,i+1}, \ldots, X_{2,i+M}, \ldots, X_{L,i+1}, \ldots, X_{L,i+M})$. M is still the window length, but now the problem is of embedding dimension $L \times M$. The kth basis vector is the eigenvector of the block-Toeplitz matrix T_x containing the cross-covariance coefficients of the different channels l at lags 0 to $M-1$.

The three formulae (1.1)–(1.3) are all applications of the general Karhunen–Loève bi-orthogonal expansion [20], and are most often used in signal processing for information compression and signal-to-noise (S/N) ratio enhancement. Usually, the eigenvalues λ_k of the symmetric, nonnegative covariance matrix of the problem are sorted in descending order. The orthogonality in both time (zero cross-covariance of two different PCs at lag 0) and "space" (orthogonality of the EOFs) imply in particular that λ_k is the variance of the kth PC. Therefore, truncating the sum in eq. (1.1) at an order $p < M$ reduces the information to the first p principal components, instead of the M initial components. This truncation is done, in PCA, in an optimal way: the first p principal directions describe the largest fraction of the total variance that one can obtain using a projection onto p orthogonal vectors.

Vautard and Ghil [21] (VG hereafter) showed that the SSA expansion (1.2) yields other powerful tools for time-series analysis than information compression and S/N enhancement, and applied these to a set of paleoclimatic time series. In particular, the near-equality of a pair of eigenelements is associated with periodic activity in the signal. In contradistinction from classical spectral analysis, where the basis functions are prescribed sines and cosines, SSA can easily and automatically localize in time intermittent oscillation spells. The shape of these oscillations is determined adaptively from the data, which makes SSA more flexible and better suited for the analysis of nonlinear, anharmonic oscillations.

SSA also provides a qualitative decomposition of the signal into its significant and noisy parts. Indeed, in the presence of white noise, the eigenvalue spectrum levels off after a certain order, and the PCs of higher order are dominated by noise. VG showed that the order S of this break in the eigenvalue spectrum and the capacity dimension D of the underlying dynamical system are not equal to each other, even approximately, but that SSA can help verify a

capacity estimate (see eqs. (4.2a)–(4.2d) of VG).

SSA has been applied by now to over a dozen geophysical data sets, on time scales from days to millenia, of various lengths and with spatial extents going from single channel to hundreds of grid points. Rasmusson et al. [22] showed that the irregular ENSO phenomenon in the coupled ocean–atmosphere system contains a rather regular quasi-biennial signal modulated by a lower-frequency, less regular 4–5 year oscillation. Ghil and Vautard [23] applied SSA to a 135 year long global-surface-temperature time series and found evidence of interannual and interdecadal oscillations, confirmed since then by Allen et al. [24]. Ghil and Mo [25] gave a comprehensive description of intraseasonal oscillations in the tropical and extratropical atmosphere. Multichannel SSA applied to geopotential height data in the Northern Hemisphere extratropics reveals cycles with periods of 40–50 days and 20–25 days [18, 19], and of 70 days [19]. Penland et al. [26] showed that SSA prefiltering allows the use of the maximum entropy method (MEM) with low-order autoregressive (AR) models in spectral estimation. Based on this combination of robust, low-order AR models with SSA, Keppenne and Ghil [7] predicted the Southern Oscillation index for ENSO with considerable skill at 30 month lead times.

Each one of these applications required a better understanding of SSA's properties, of its strengths and weaknesses. The present paper relies heavily on the experience thus accumulated, and goes considerably further in its methodological development of a coherent SSA toolkit.

1.3. Outline of the present study

In this paper we concentrate on single-channel SSA. The studies cited in the previous subsection raise four major, and several minor problems. First, the apparent arbitrariness in the choice of window length M gives pause. After analyzing further the eigenvalue problem central to SSA in section 2.1, we show in section 2.2 how the choice of M can influence the analysis and the results. The possibility to vary M makes in fact SSA much more adaptable to a large range of time scales than other statistical tools such as complex PCA [27], or principal oscillation patterns (POPs [28]).

Another major problem is that of robustness and statistical confidence. Analytical formulae for confidence levels on the eigenvalues [29] apply only to sets of independent realizations. We examine this problem in section 2.3, using the methodology described in section 1.4. Sections 2.4 and 2.5 are devoted to the interpretation of the time-dependent by-products of SSA. In particular, we derive in section 2.5 an algorithm capable of extracting the components of the signal corresponding to individual eigenelements, at a given epoch.

Third, the identification of noise plateaus in the eigenvalue spectrum was quite subjective in VG and most of the subsequent work in atmospheric and climatic applications. Indeed, observed time series do not, in general, provide the ideal break described above, nor is noise ever perfectly white. In section 3, objective algorithms for noise reduction are developed. The analyzed signal is decomposed explicitly as the sum of an intrinsic *dynamical component* and an external *noisy component.*

Noise reduction is a well-known signal-processing problem. Techniques like Kalman filtering, as well as more sophisticated nonlinear dynamical algorithms, like optimal shadowing [30] have shown very satisfactory results in noise reduction. This type of methods requires, however, a knowledge of the evolution equations. Approximations of the equations can be found empirically, as shown by Casdagli [31], but this in turn requires very long data sets in order to provide a useful reconstruction. Quite to the contrary, SSA is best at extracting – by essentially linear but data-adaptive methods – useful information about nonlinear systems from short,

noisy time series, in the absence of – or without using – the knowledge about governing equations.

Finally, the interpretation of the eigenelements has to be sharpened: When is SSA successful at removing trends and nonstationarities? How can SSA capture nearly periodic behavior – is the occurrence of a pair of degenerate eigenvalues always associated with a peak in the spectrum? We attempt to answer these two questions in sections 4.1 and 4.2, respectively. Maximum entropy spectral estimation [32–34] also uses the Toeplitz matrix T_x in order to determine the associated autoregression (AR) coefficients. We propose in section 4.3 an estimation of the power spectrum of a time series which is consistent with both MEM and SSA. In section 4.4, SSA is compared with multi-taper spectral estimation [35].

Linear forecasting algorithms, based on SSA expansion and AR models, are presented in section 5, following Keppenne and Ghil [7]. Concluding remarks appear in section 6.

1.4. Algorithm validation

In order to validate the algorithms we develop here, four single-channel processes with simple and known properties are analyzed by SSA. For each process, 100 Monte Carlo realizations of 150 points are generated. These sets are used to provide nonparametric estimates of the statistical confidence. For each realization of each process, SSA is applied using $M = 40$ and $M = 20$, in order to examine the influence of the window length. The processes x_n, $1 \le n \le 4$, are given below by defining y_n and w_n in

$$x_n = y_n + w_n \,. \tag{1.4}$$

For the processes 1, 2 and 3 (P1, P2 and P3)

$$y_{n,i} = 2\cos(\Omega_1 i + \phi_1) + \cos(\Omega_2 i + \phi_2) \,, \tag{1.5}$$

and $w_{n,i}$ is a Gaussian white-noise process with variance σ^2 and zero expectation. $\Omega_1 = \frac{2}{20}\pi$ and $\Omega_2 = \frac{2}{7}\pi$ are fixed frequencies, with a long common period (equal to 140), while ϕ_1 and ϕ_2 are constant, random phases depending on the realization; since the common period is of the same order of magnitude as the interval of 150 time units over which the processes P1–P3 are sampled, the behavior of P1–P3 approximates that of stochastically perturbed quasi-periodic signals, where *no* common period is present. For P1, we take $\sigma^2 = 2.5$, so that it has the same variance as the "signal" y_1. For P2, a larger noise variance is taken, $\sigma^2 = 4$. For P3, the noise variance is the same as the variance of the secondary oscillation, $\sigma^2 = 0.5$.

For the fourth process (P4) $y_{4,i}$ are the consecutive values of the Y-variable in an integration of the Lorenz [2] equations, with a predictor–corrector scheme using a time step of 0.02 and sampling rate of 0.1 (one value sampled every 5 time steps). The parameter values are those of Lorenz [2]. The variance of the white-noise process w_4 is taken equal to that of P2, $\sigma^2 = 4$. Fig. 1 shows the first realization of each process. The dashed curves represent the first 150 values of the noisy signal x_n to be analyzed, and the dotted ones the pure signal y_n. The light solid curves are the processed data using the noise-reduction algorithm described in section 4, where this figure is discussed further.

SSA is also applied to the IPCC global surface air temperature data [36]. The yearly averaged values are shown in fig. 2. The data studied by Ghil and Vautard [23] were slightly different [37], as was the method. The IPCC data are quite noisy, but show a marked trend as well as a significant year-to-year variability and interdecadal oscillations. This data set is studied as a worst-case example: the time series is short, noisy and nonstationary. Fortunately, the data are at least regularly sampled! As we do not dispose of independent realizations, the stability of the results is tested by repeating the analysis with data from 1861–1950, 1861–1951, and so on, up to 1861–1990.

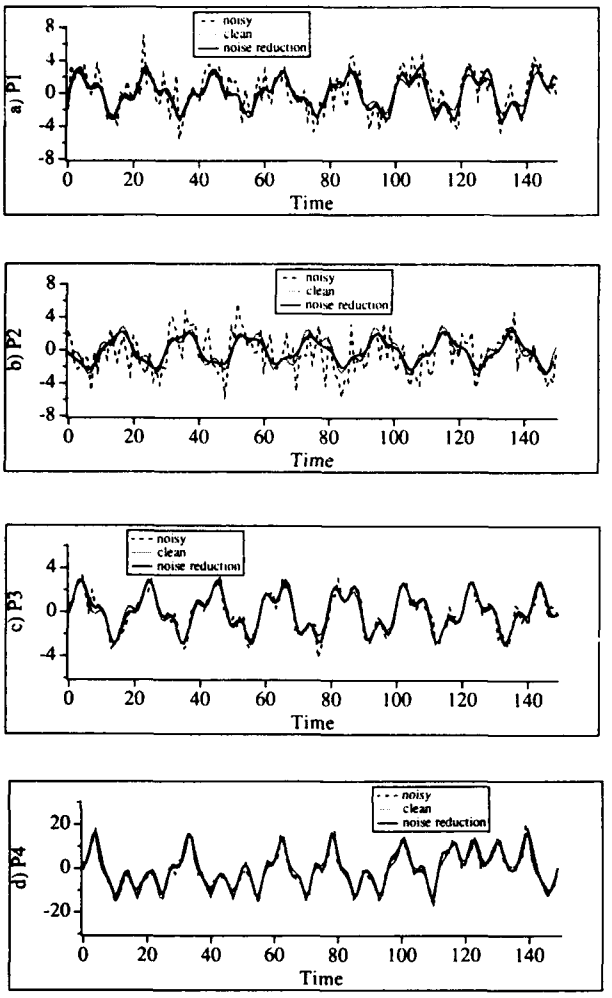

Fig. 1. One realization of the four synthetic processes under study, with the clean signal (dotted), the noisy time series (dashed), and the noisy series after application of the SSA noise-reduction filter (solid); $M = 40$. (a) P1, (b) P2, (c) P3 and (d) P4; note the scale difference on the ordinate between panels.

2. Theoretical and computational preliminaries

2.1. The Toeplitz matrix

The cornerstone of SSA is the Karhunen–Loève expansion theorem; this in turn is based on the lagged-covariance matrix of the process x, whose sample is the time series $(x_i, 1 \le i \le N)$, assumed – without loss of generality – to have zero expectation [38]. This matrix T_x has a Toeplitz structure, i.e., constant diagonals corresponding to equal lags:

$$T_x = \begin{pmatrix} c(0) & c(1) & \cdot & \cdot & \cdot & c(M-1) \\ c(1) & c(0) & c(1) & & & \cdot \\ \cdot & c(1) & \cdot & \cdot & & \cdot \\ \cdot & & \cdot & \cdot & \cdot & \cdot \\ \cdot & & & \cdot & \cdot & c(1) \\ c(M-1) & \cdot & \cdot & \cdot & c(1) & c(0) \end{pmatrix}. \tag{2.1}$$

where $c(j)$, $0 \le j \le M-1$, is the covariance of x at lag j.

There are different ways to estimate T_x [29, 39, 40]. Among the most frequently used are the Yule–Walker estimate

$$c(j) = \frac{1}{N} \sum_{i=1}^{N-j} x_i x_{i+j}, \tag{2.2}$$

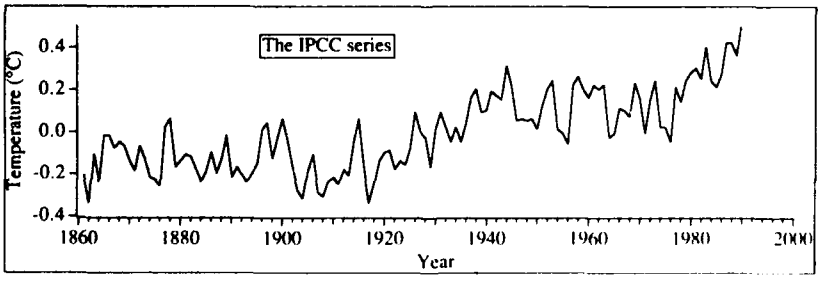

Fig. 2. The IPCC global temperature series [36] of yearly averages, as a function of time. The grand mean has been removed, i.e., the series is centered.

as well as the estimate

$$c(j) = \frac{1}{N-j} \sum_{i=1}^{N-j} x_i x_{i+j} . \qquad (2.3)$$

Burg's [32] algorithm, which gives the AR coefficients associated with MEM, also estimates implicitly $c(j)$; this estimate is again an average, like in (2.2, 2.3), but with larger weights toward the middle of the series than at the ends (see also refs. [26, 41]).

The first estimate, eq. (2.2), used by Box and Jenkins [39], is strongly biased when the number of data N is small; the estimate in (2.3) has larger variance but less bias [29]. When N is small, the Burg estimate can also be biased at large lags j, if there is power at periods larger than N, as shown by the following example: consider the process $x_i = \cos(\frac{2}{150}\pi i + \phi)$, where ϕ is a random constant phase, and $N = 100$. Fig. 3 shows the average of the various estimates. In this case, (2.3) is slightly biased, whereas both (2.2) and the Burg estimates are strongly biased. This problem occurs only when there are very low frequencies in the system, or trends. Once those frequencies are removed, both the Burg estimate and (2.3) are equivalent.

One could also estimate the covariance matrix of the process as in classical PCA, by averaging over lagged copies of the window [42]. This has a double disadvantage: (i) it does not conserve the Toeplitz properties of the sample covariance (see the next subsection), and (ii) it tends to give, like the Burg estimate, larger weights to the middle of the series and thus produce large biases as well. In the absence of prior information about the signal, we prefer therefore the estimate (2.3), and use it hereafter to compute the Toeplitz matrix.

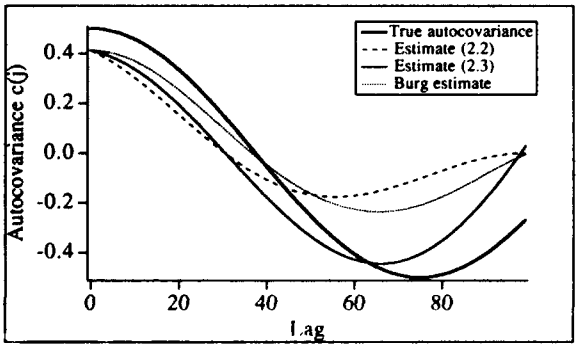

Fig. 3. Autocovariance function of the process $x_i = \cos(\frac{2}{150}\pi i)$: true (heavy solid curve) versus three different estimates from a 100 point long time series, as described in the text (see inset for legend).

2.2. Eigenelements and choice of window length

The Toeplitz matrix T_x is symmetric and nonnegative. Its eigenvalues λ_k are strictly positive, except when data are perfectly clean and come from a dynamical system with purely quasi-periodic behavior; in the latter case, all but a finite number – equal to twice the number of frequencies – are zero. They are sorted into decreasing order, and the eigenvectors E^k are normalized so that

$$\sum_{k=1}^{M} E_j^k E_l^k = \delta_{jl} , \quad 1 \le j \le M, \; 1 \le l \le M , \qquad (2.4)$$

and that the spectral decomposition formula should hold:

$$\sum_{k=1}^{M} \lambda_k E_j^k E_l^k = T_{x,jl} = c(j-l) ,$$
$$1 \le j \le M, \; 1 \le l \le M . \qquad (2.5)$$

An eigenvector here is a lag sequence of length M. Since T_x is a Toeplitz matrix, eigenvectors are either symmetric or antisymmetric with respect to $\frac{1}{2}M$. When the sampling rate of the signal is increased, for a given window length in time units, the shape of the first eigenvectors does not change much, as shown by VG; thus, the eigenvectors have a limit as the sampling interval goes to zero. On the other hand, if the embedding dimension is constant and the sampling interval goes to zero, i.e., the window length also goes to zero, the eigenvectors tend to

fixed linear combinations of the M successive time derivative operators [43].

For fixed, finite window length, Fortus [44] has shown that the largest eigenvalue corresponds to the maximum of the spectrum, under certain restrictive assumptions. In the asymptotic limit $M \to +\infty$, with fixed sampling interval, i.e., the window length goes to infinity, the eigenvectors tend to pairs of sines and cosines and the associated eigenvalues tend to the corresponding *spectral density* values [45, 21]. For finite M, all eigenvalues fall between the maximum and the minimum of the spectral density [46].

A key problem in SSA is the proper choice of M. As we shall see forthwith, SSA does not resolve periods longer than the window length. Hence, if one wishes to reconstruct a strange attractor, whose spectrum includes periods of arbitrary length, the larger M the better, as long as statistical errors do not dominate the last values of the autocovariance function. To prevent this, one should not exceed $M = \frac{1}{3}N$.

In many physical and engineering applications, however, one wishes to concentrate on oscillatory phenomena in a certain band, which may be associated with the least-unstable periodic orbits embedded in a strange attractor. Such periodic orbits typically generate oscillations of strongly varying amplitude [18, 19, 23, 25]: the system's trajectory approaches and follows them for a certain time – comparable to or longer than the period in question – only to wander off into other parts of phase space. When the ratio of M to the life time of such an intermittent oscillation – the typical time interval of sustained high amplitudes – is large, the corresponding eigenvector pair suffers from the same Gibbs effect as in classical spectral analysis (see section 2.4 below). Spells of the oscillation – weak or strong – will be smoothed out. The following arguments should help understand the difficulty and make the correct choice of M.

Let us denote, by analogy with the time-continuous case treated in section 2 of VG, by $\tilde{E}^k(f)$ the *reduced Fourier transform* of E^k, i.e.,

$$\tilde{E}^k(f) = \sum_{j=1}^{M} E_j^k \exp(2\pi i j f) . \tag{2.6}$$

$\tilde{E}^k(f)$ is also the response function of the filter transforming x into its kth PC. $\tilde{E}^k(f)$ is a sum of periodic functions of the frequency f with periods $1, \frac{1}{2}, \frac{1}{3}, \ldots, 1/M$. Therefore the spectral resolution is $1/M$.

If M is too small, the coarse resolution may cause several neighboring peaks in the spectrum of x to coalesce. When there is an intermittent oscillation, reflected by a broad spectral peak, on the contrary, large M values (high resolution) will split the peak into several components with neighboring frequencies. Eq. (2.6) also shows that the filters are unable to isolate peaks at frequencies lower than the resolution $1/M$, i.e., periods larger than M. Given a peak in the power spectrum $P_x(f)$ of x – with maximal spectral density at f_0 and width $2\,\delta f$, say – these considerations suggest that SSA will isolate correctly the intermittent oscillation if

$$\frac{1}{f_0} \leq M \leq \frac{1}{2\,\delta f} . \tag{2.7}$$

In other words, the window length has to be chosen between the period of the oscillation and the average life time of its spells. In practice, this latter quantity cannot be estimated a priori, but SSA is typically successful at analyzing periods in the range $(\frac{1}{5}M, M)$.

2.3. *Statistical stability of eigenvalues*

Statistical stability is crucial in spectral analysis. SSA is based on estimates of lagged autocovariances, i.e., on second-order moments. The eigenvalues should converge therefore at least as well as Blackman–Tukey spectral estimates, heuristically speaking. Estimating the statistical confidence to be placed in the eigenvectors, however, is rather difficult. Simple confidence-interval formulae were used by Fraedrich [14], VG, and Ghil and Mo [25], who all assume

the independence of successive points of the augmented time series, either one sampling time or one window length apart. Here we use a nonparametric Monte Carlo method to check for stability, as we dispose of several realizations of the synthetic processes P1–P4.

Fig. 4 shows the average of the eigenvalues λ_k, calculated with the 100 randomly generated data sets, for the four synthetic processes, with $M = 40$ (solid circles) and $M = 20$ (open circles). The 95% error bars are calculated as $\lambda_k \pm 1.96\sigma_k$, where σ_k is the variance – estimated with the 100 realizations – of λ_k. Also shown are the confidence intervals estimated with the heuristic variance formula of Ghil and Mo [25], $\sigma_k = \lambda_k\sqrt{M/2N}$, for P1 only; the latter is quite conservative, except for the smallest λ_k's.

For P1 (fig. 4a), the two spectra are quite similar, with two leading pairs standing out, and a regular weakly descending ramp after $k = 5$. These two pairs are associated with the periodic components of the signal, whereas the slowly decreasing part corresponds to the white-noise dominated components. Note that the tails of the spectra are not flat. This is essentially due to the finiteness of the data.

Processes P2 and P3 (figs. 4b, 4c) behave in the same way as P1, with different noise plateaus. The second pair of P2 stands out less from the rest of the spectrum, since it is reached by the noise. We anticipate that for P2 SSA would not, based on most realizations, identify the secondary oscillation of period 7 with great confidence. For P3, the level of noise is low, and the last average eigenvalue is even negative (not shown on this logarithmic plot). Indeed, the covariance estimate (2.3) may lead to a nonpositive Toeplitz matrix, but negative eigenvalues are quite rare, and small in absolute value. For the stochastically perturbed Lorenz process (P4: fig. 4d), no clear break is apparent, although an inflection point of the average spectrum lies at $k \cong \frac{1}{2}M$.

The near-disappearance of the second pair into the noise level for P2 and $M = 20$ raises another point to consider in choosing the win-

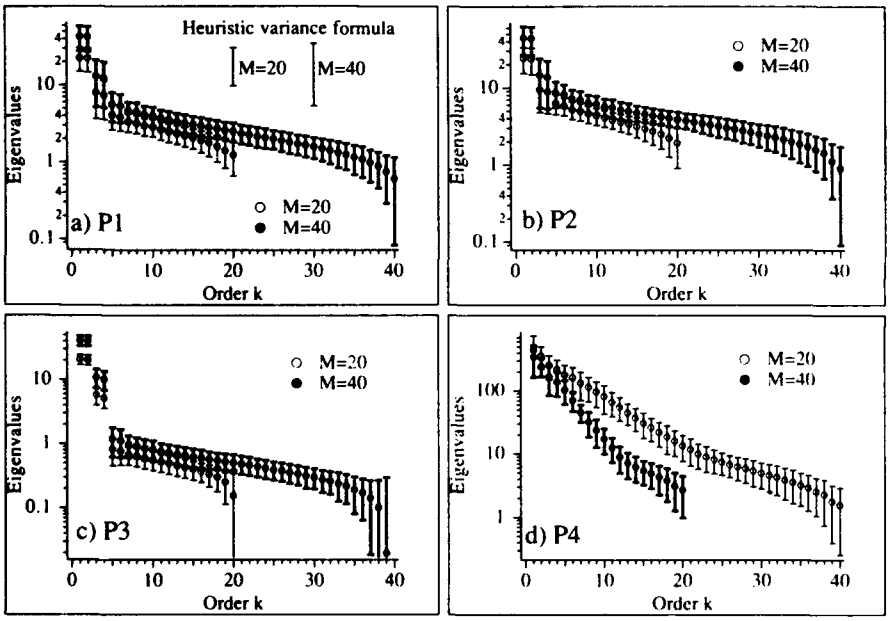

Fig. 4. SSA eigenvalue spectra, for $M = 40$ (averages shown as solid circles), and $M = 20$ (open circles), with the 95% confidence limits calculated using the actual variance of the 100 realizations (thick bars: $M = 40$; thin bars: $M = 20$). (a) P1, (b) P2, (c) P3 and (d) P4. At the top of panel (a) are represented also the error bars (thin long I's) estimated by the heuristic variance formula of Ghil and Mo [25]; note that the latter is quite conservative.

dow length: if the process is a pure sine function of variance v, the two nonvanishing eigenvalues are close to $v' = \frac{1}{2}Mv$ (compare eqs. (2.7a)–(2.7e) of VG). On the other hand, if the process is noisy, the noise floor always lies at the value of the noise variance, for all values of M (with different slopes). Therefore, some pairs can be extracted from the noise level by increasing M. The fact that the noisy part of the eigenvalue spectrum is flatter for larger M values enhances pair detection further as M is increased.

For the IPCC data, the eigenvalue spectra (not shown) present no evidence of a noise floor, and are rather similar to the spectrum [23] of the Jones et al. [37] data. Since the length of the record is small (130 numbers), however, white-noise floors may be steep and hardly recognizable from signal. The quantitative method developed in section 3 shows that, in fact, about 20 eigenvalues are above the noise floor. The first two eigenvalues, representing the nonstationarity of the data, are about one order of magnitude above the other ones.

When SSA is applied to the IPCC data, with the ending year varying continuously, the order of the eigenvalues is not stable, whereas the shape of the eigenvectors is, i.e., it is possible to follow the eigenvectors continuously, from ending year to ending year, but the associated eigenvalues may undergo exchanges in their respective order (see also refs. [24, 42]).

2.4. *Principal components (PCs)*

The kth PC is defined as the orthogonal projection coefficient of the original series onto the kth EOF:

$$a_i^k = \sum_{j=1}^{M} x_{i+j} E_j^k , \quad 0 \le i \le N - M . \tag{2.8}$$

PCs are therefore processes of length $N - M + 1$, which can be considered as weighted *moving averages* of the process x. If we denote by B the backward shift operator, and by Ψ_k the polynomial

$$\Psi_k(\zeta) = E_M^k + E_{M-1}^k \zeta + \cdots + E_1^k \zeta^{M-1} , \tag{2.9}$$

then the kth PC can be written as

$$a_i^k = \Psi_k(B) x_{i+M} . \tag{2.10}$$

Like in classical PCA, principal components are orthogonal to each other, i.e., $\mathcal{E}(a^k a^l) = \lambda_k \delta_{kl}$, where $\mathcal{E}$ is the expectation operator. It does not mean that the PCs are independent from each other, since this relation holds for SSA only at lag zero. PCs give the representation of the augmented time series in a new coordinate system, with most information represented along the first coordinates.

The PCs can be interpreted in another way. Let us consider the portion of signal x contained between instants $i+1$ and $i+M$, and, for a given k, the function

$$J(\alpha) = \sum_{j=1}^{M} (x_{i+j} - \alpha E_j^k)^2 . \tag{2.11}$$

It is easy to show that $J(\alpha)$ is minimum for $\alpha = a_i^k$, and hence that the PCs can be obtained from the local fit, in the least-squares sense, of the kth EOF to the original series x. This property is conserved if one fits several EOFs, i.e., the PCs are the coefficients of the linear combination of any subset of EOFs that minimizes the square distance to the series x over the window considered. The implication is, again, that if an intermittent oscillation has a typical life time shorter than the window length, Gibbs effects will reduce the amplitude of the fit within the spells and produce artificial periodicity off the spells.

From the spectral point of view, EOFs correspond to data-adaptive moving-average filters. The power spectrum $P_k(f)$ of a^k, at frequency f, is

$$P_k(f) = P_x(f) |\tilde{E}^k(f)|^2 , \tag{2.12}$$

with $\tilde{E}^k$ being given by (2.6), or

$$P_k(f) = P_x(f)|\Psi_k(\zeta)|^2 , \tag{2.13}$$

for $\zeta = \exp(2\pi i f)$. The orthogonality constraints of the problem give the identity

$$1 = \frac{1}{M} \sum_{k=1}^{M} |\tilde{E}^k(f)|^2 \tag{2.14}$$

for any frequency f, so that the sum of the spectra of the PCs is identical to the power spectrum of x, i.e.,

$$P_x(f) = \frac{1}{M} \sum_{k=1}^{M} P_k(f) . \tag{2.15}$$

It is thus interesting to build *stack spectra* by piling up the contributions of the various components (see section 4.3).

2.5. Reconstructed components (RCs)

PCs are filtered versions of the original series. However, they do not allow a unique expansion of the signal into a sum of the different components. Indeed, in the expansion (1.2), individual terms depend on the index j, varying from 1 to M. Therefore, there are M different ways of reconstructing the components of the signal, which do not give, in general, the same results. Another problem in using eq. (1.2) for filtering, and in particular for *real-time* filtering and prediction, is that the resulting series are of length $N - M + 1$, and not of length N as desired. We show here how to extract, in an optimal way, series of length N – corresponding to a given set of eigenelements – that we shall call *reconstructed components* (RCs).

Let us consider a subset $\mathcal{A}$ of eigenelements k over which the reconstruction is to be performed. By analogy with eq. (1.2), we seek a series of length N, $y = R_{\mathcal{A}}x$, such that the quantity

$$H_{\mathcal{A}}(y) = \sum_{i=0}^{N-M} \sum_{j=1}^{M} \left(y_{i+j} - \sum_{k \in \mathcal{A}} a_i^k E_j^k \right)^2 \tag{2.16}$$

is minimized. In other words, the optimal series y is the one whose augmented version Y is the closest, in the least-squares sense, to the projection of the augmented series X onto EOFs with indices belonging to $\mathcal{A}$. The solution $y = R_{\mathcal{A}}x$ to this least-squares problem is given by

$$(R_{\mathcal{A}}x)_i = \frac{1}{M} \sum_{j=1}^{M} \sum_{k \in \mathcal{A}} a_{i-j}^k E_j^k \quad \text{for } M \le i \le N - M + 1 , \tag{2.17a}$$

$$(R_{\mathcal{A}}x)_i = \frac{1}{i} \sum_{j=1}^{i} \sum_{k \in \mathcal{A}} a_{i-j}^k E_j^k \quad \text{for } 1 \le i \le M - 1 , \tag{2.17b}$$

$$(R_{\mathcal{A}}x)_i = \frac{1}{N-i+1} \sum_{j=i-N+M}^{M} \sum_{k \in \mathcal{A}} a_{i-j}^k E_j^k \quad \text{for } N - M + 2 \le i \le N . \tag{2.17c}$$

When $\mathcal{A}$ consists of a single index k, the series $R_{\mathcal{A}}x$ is called the kth RC, and will be denoted by x^k. RCs have additive properties, i.e.,

$$R_{\mathcal{A}}x = \sum_{k \in \mathcal{A}} x^k . \tag{2.18}$$

In particular, the series x can be expanded as the sum of its RCs:

$$x = \sum_{k=1}^{M} x^k . \tag{2.19}$$

Note that, despite its linear aspect, the transform changing the series x into x^k is, in fact, nonlinear, since the eigenvectors E^k depend nonlinearly on x. A drawback of RCs is that they are correlated even at lag 0.

The main advantage of using RCs instead of PCs is the recovery of the epochs: indeed, if there are short spells of oscillations in the signal, PCs do not allow to localize them precisely,

whereas RCs do. Moreover, there is no phase shift between x and x^k, except possibly near the ends of the series: In the middle of the data set – where (2.17a) is used – the transform from x to $R_{\mathscr{A}}x$ is a linear filter whose response function

$$\rho_{\mathscr{A}}(f) = \frac{1}{M} \sum_{k \in \mathscr{A}} |\tilde{E}^k(f)|^2 \qquad (2.20)$$

is real valued. Therefore, at no frequency is there a phase shift between x and x'. Within M points of the ends of the series, however, there might be some phase shift. This effect is small as long as $\mathscr{A}$ is large, or suitably chosen, and, of course, totally disappears when $\mathscr{A} = \{1, \ldots, M\}$. Based on a number of SSA experiments, we also found that there is no phase shift at the ends of the series when $\mathscr{A}$ is made up of an oscillatory pair $(k, k+1)$.

Our reconstruction algorithm may be compared to the Wiener filtering method [47], which also provides optimal filters in a least-squares sense. The main differences are (i) that the Wiener filter uses harmonic functions as a basis, and (ii) that it is not fully adaptive, in the sense that one has to prescribe the shape of the desired filtered spectral density. Smooth and very reliable estimates of the power spectrum are therefore required in the Wiener method, which are impossible to obtain with short data sets.

3. Noise reduction

The simplest kind of noise reduction is by applying a fixed, prescribed low-pass filter to the data. This procedure is successful when the power spectrum of the process is rapidly decreasing to zero. When the spectrum is not monotonic, and has lines or peaks distributed over a wide range, the problem is more complicated. The gaps between these significant elements in the spectrum are filled by spurious noise, and to filter out this noise requires more-complex filters. As stated at the end of the last section, it is still possible to use the Wiener method in this case, but only by assuming either accurate spectral estimates or prior hypotheses on the noise variance; the former is impossible with short data sets, the latter is arbitrary.

In this section we show that SSA is a powerful tool for signal reconstruction from noisy data. We assume that we have at our disposal a realization of a finite process x of length N, which is the sum of a dynamical process y and of some external noise process w due to measurement errors. In VG, we showed that the last PCs of such processes are dominated by noise, after the break in the eigenvalue spectra. We develop here a systematic method for determining the break, and derive a process $R_{\mathscr{A}}x$, with $\mathscr{A} = \{1, \ldots, S\}$, approximating y with the knowledge of only a few x-data.

Fig. 5 shows the average of the ratio $n(p)$ as a function of p, over the 100 realization sets of the four synthetic processes,

$$n(p) = \frac{\sum_{i=1}^{N} (y_i - \sum_{k=1}^{p} x_i^k)^2}{\sum_{i=1}^{N} \{y_i - x_i\}^2} \; ; \qquad (3.1)$$

$n(p)$ represents the noise-reduction ratio when p RCs are considered. For P1, P2 and P3 (figs. 5a–5c), the average optimum noise reduction is at $p = 3$ or $p = 4$, and the reduced noise is less than 10% of the original. With $M = 20$, the best reduction that can be achieved is not quite as good as with $M = 40$. Even with short data sets and dominant noise, like for P2, reconstruction with $p = 3$ or 4 is very close to the underlying signal. For the process P4 (fig. 5d), the optimal reduction – to about 0.6 – occurs around $p = \frac{1}{2}M$. This relatively bad score is due to the fact that the Lorenz system has a monotonically decreasing power spectrum, with no particular frequency standing out, and therefore any linear noise-reduction technique unavoidably filters out a part of the signal as well.

In the real world, we do not have several

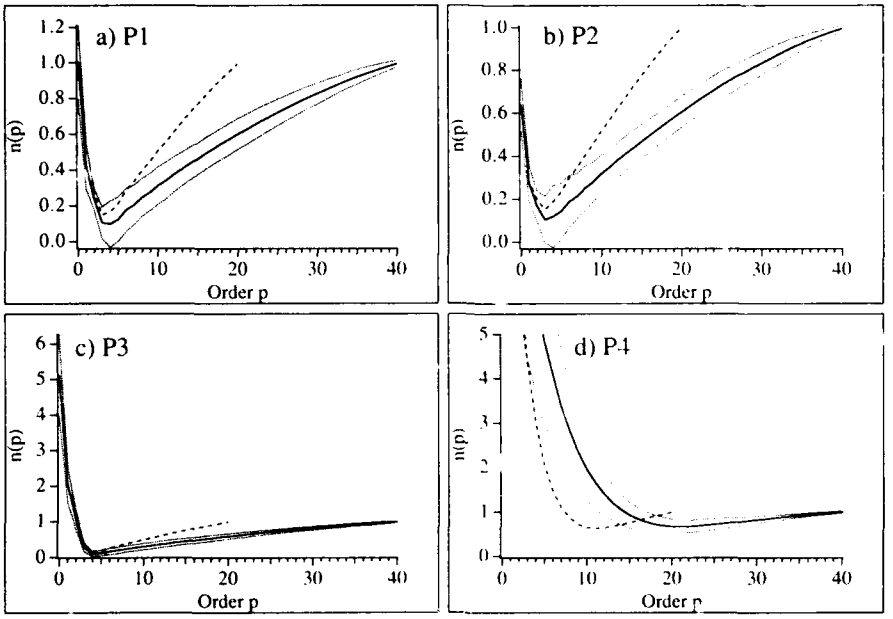

Fig. 5. Average error made when approximating the clean signal by the reconstruction filters $R_{\mathscr{A}}$, with $\mathscr{A} = \{1, \ldots, p\}$, divided by the noise variance, as a function of p, for $M = 20$ (dashed) and $M = 40$ (solid). Dotted curves show the 95% confidence interval for $M = 40$. (a) P1, (b) P2, (c) P3 and (d) P4.

realizations of the same process at our disposal, and the pure signal is not known. The optimal order, therefore, needs to be calculated in a different way. For a given order p, let us denote again by $\mathscr{A}$ the subset $\{1, \ldots, p\}$, and by $\mathscr{A}'$ the subset $\{p+1, \ldots, M\}$. The algorithm is based on the remark that if the reconstructed part of x involving the subset $\mathscr{A}'$ of indices is really dominated by white noise, it should not be significantly different from the reconstruction, using the same EOFs, of some pure gaussian white-noise process. Let v be a normal white-noise process. The problem is to find a positive number β, such that $R_{\mathscr{A}'}x$ behave like $R_{\mathscr{A}'}(\beta v)$. In this case, at least the autocovariance functions of $R_{\mathscr{A}'}x$ and $R_{\mathscr{A}'}(\beta v)$ should be nearly equal at lags 0 to $M-1$. That is, if SSA is reapplied to the two processes, it will provide statistically indistinguishable results.

To test this idea, we use again Monte Carlo simulation. This type of simulation, going back to the work of Ulam in the 1950s, has been used extensively of late in meteorological time-series analysis [48]; it has been applied recently in nonlinear dynamics under the name of the *surrogate-data* method [49]. We generate 100 normal realizations of length N of the white-noise process v. The operator $R_{\mathscr{A}'}$ is applied – for a given order p – to the 100 realizations of v and to the signal x. Let us denote by ω the realization, by $c_\omega(j)$, $0 \le j \le M-1$, the autocorrelation of the reconstructed ωth realization $R_{\mathscr{A}'}v$ at lag j, and by $c_p(j)$ the autocorrelation of $R_{\mathscr{A}'}x$. The average $c_v(j)$ over these realizations, the variances $s_v(j)$ of these estimates, and the 95% confidence intervals $(c_-(j), c_+(j))$, with $c_\pm(j) = c_v(j) \pm 1.96\sqrt{s_v(j)}$, are estimated. Then we look for β such that, for $0 \le j \le M-1$, $c_p(j)$ lies in the interval $(\beta^2 c_-(j), \beta^2 c_+(j))$; β must therefore lie in the intersection of M intervals and must be positive. If this intersection is empty, the null hypothesis of white-noise dominated behavior of the last $M-p$ components is rejected. Otherwise, this intersection is itself an interval (γ_p, δ_p), and the last $M-p$ RCs may be considered as a reconstruction of mere white noise. The smallest p satisfying the above condition is called the *statistical dimension* of the data set.

and is denoted here (as in VG) by S. The interval (γ_S, δ_S) gives bounds for the standard deviation β of the noise present in the data.

As shown by VG, S has nothing to do with the dimension of an underlying attractor: S simply gives the number of significant components in an SSA expansion; it depends almost linearly on the window M for synthetic and observed data, although VG only used a heuristic criterion for finding S. For almost all $p > S$, the conditions of nonrejection are fulfilled; sampling errors are responsible for the other cases. For $p = S$ and $\mathscr{A} = \mathscr{S} = \{1, \ldots, S\}$, we obtain

$$x = R_{\mathscr{S}} x + R_{\mathscr{S}^c} x \,. \tag{3.2}$$

$R_{\mathscr{S}} x$ is an approximation of y,

$$y = R_{\mathscr{S}} x + \varepsilon \,, \tag{3.3}$$

where

$$\varepsilon = R_{\mathscr{S}^c} y - R_{\mathscr{S}} w \,. \tag{3.4}$$

The error ε made when approximating y by the significant reconstructed part $R_{\mathscr{S}} x$ of x is due to the difference of two quantities. The first one describes the part of signal that has been removed by the reconstruction filter; the second one is the part of the noise that has not been removed by it. The skill of the noise-reduction algorithm depends on minimizing both of these spurious quantities. The quantity plotted in fig. 5 shows, in fact, the average variance ratio of ε to w as a function of p.

The first contribution to ε dominates for small values of p, and is a monotonically decreasing function, whereas the second contribution dominates for large values of p, and is monotonically increasing. Processes for which the noise reduction is successful are those for which the variance of the first contribution in ε decreases rapidly with p, i.e., processes for which a few components explain a large part of the variance. Quasi-periodic processes and processes dominated by low frequencies fall within this category. More generally, the algorithm will be successful when a significant part of the power lies within a small fraction of the frequency range of interest.

Fig. 6 shows the distribution of S obtained

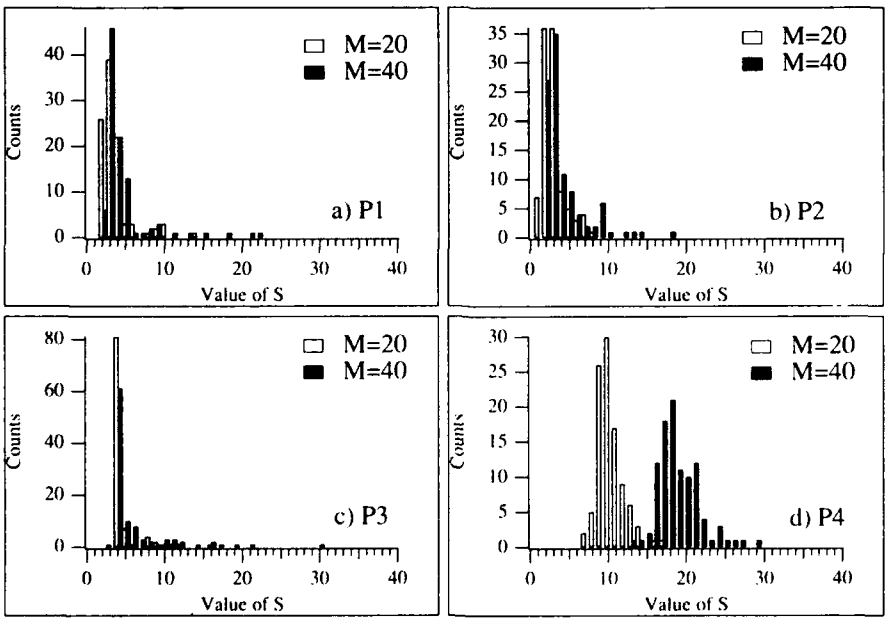

Fig. 6. Histograms of the statistical dimension estimate S, for $M = 40$ (solid) and $M = 20$ (open). Bars are placed to the left of the abscissa point for $M = 20$, and to the right for $M = 40$. (a) P1, (b) P2, (c) P3 and (d) P4.

with 100 realizations of the various test processes, using $M = 40$ and $M = 20$. For P1, P2, and P3 (figs. 6a–6c), there is but little difference between the distribution with $M = 20$ and $M = 40$, while the histogram peak is, as desired, at $S = 3$ or $S = 4$ (cf. fig. 5). Only for P2, the noisiest process, do many realizations actually give $S = 2$. For P3, most of the values are $S = 4$; therefore, both oscillations are recognized as significant, even though the noise has the same variance as the oscillation of period 7. For P4 (fig. 6d), the peak lies at $S = 10$ for $M = 20$ and at $S = 18$ for $M = 40$ (i.e., $S \cong \frac{1}{2}M$, like the p-value for optimal noise reduction).

For the IPCC data set, the estimates of S vary – with the ending year – from 14 to 22 (most of the values equaling 18) for $M = 40$, and from 7 to 12 for $M = 20$. S tends to increase towards the end of the time series, probably due to the increasing amount of data. The estimate of S is therefore almost proportional to M, as expected (cf. VG), and otherwise well behaved. The present values are larger than the estimate $S = 12$ of Ghil and Vautard [23], obtained for $M = 40$, but coming from a different data set [37] and using a different Monte Carlo method; the earlier method [23] compared the eigenvalue spectra (fig. 1 there) instead of the autocovariance function. For the Jones et al. [37] data set the present method also gives lower S-values.

The characteristics of the noise's estimated standard deviation β are summarized in table 1. The estimates γ_S and δ_S are stable, since their standard deviation at given M is about one tenth of their respective average values. These estimates are also fairly insensitive to the window length, since doubling M only changes the average by a few percent at most. For P1, P2, and P3, γ_S and δ_S are both nearly equal to the true noise standard deviation σ, all but 4 out of 12 values in the table being well within their own standard deviations. The error made in estimating the noise is not only small – about 10% for $\frac{1}{2}(\gamma_S + \delta_S)$ versus σ – it is also on the safe side.

The excess of variance for the estimated noise is due to the fact that the algorithm tries to fit $R_{\mathcal{J}} x = R_{\mathcal{J}} y + R_{\mathcal{J}} w$ to $R_{\mathcal{J}} v$, where v is a white-noise process. Since c_- and c_+ are, in fact, bounds on the variance of v, and y and w are uncorrelated, the excess arises from the fraction of the variance of y contained in the frequency bands involved by the filter $R_{\mathcal{J}}$. It follows that, while in principle $\gamma_S \leq \sigma \leq \delta_S$, the only completely reliable inequality in practice is $\sigma < \delta_S$. The closeness of individual reconstructions to the process y can be checked for the four processes in fig. 1a–1d. The values of γ_S and δ_S for the IPCC data set are also quite stable for the time intervals under study.

Fig. 7a shows the average and the standard deviation of the 41 reconstructions $R_{\mathcal{J}} x$ of the significant temperature signal, based on ending dates between 1950 and 1990. It is noteworthy that the standard deviation at all times is very

Table 1
Average and standard deviation of the bounds γ_S and δ_S on the standard deviation of the noise, as identified by the reduction algorithm. These values are calculated from the 100 synthetic realizations – for processes P1–P4 – and with the final year moving from 1950 to 1990 – for the IPCC data. Each column contains the average (left number) and the standard deviation (right number).

Process	$M = 40$		$M = 20$	
	γ_S	δ_S	γ_S	δ_S
P1	1.67 ± 0.17	1.78 ± 0.18	1.66 ± 0.21	1.83 ± 0.17
P2	2.09 ± 0.20	2.24 ± 0.18	2.07 ± 0.25	2.30 ± 0.20
P3	0.71 ± 0.08	0.77 ± 0.07	0.68 ± 0.09	0.79 ± 0.07
P4	2.43 ± 0.33	2.57 ± 0.31	2.29 ± 0.40	2.56 ± 0.34
IPCC	0.065 ± 0.007	0.070 ± 0.004	0.070 ± 0.007	0.074 ± 0.003

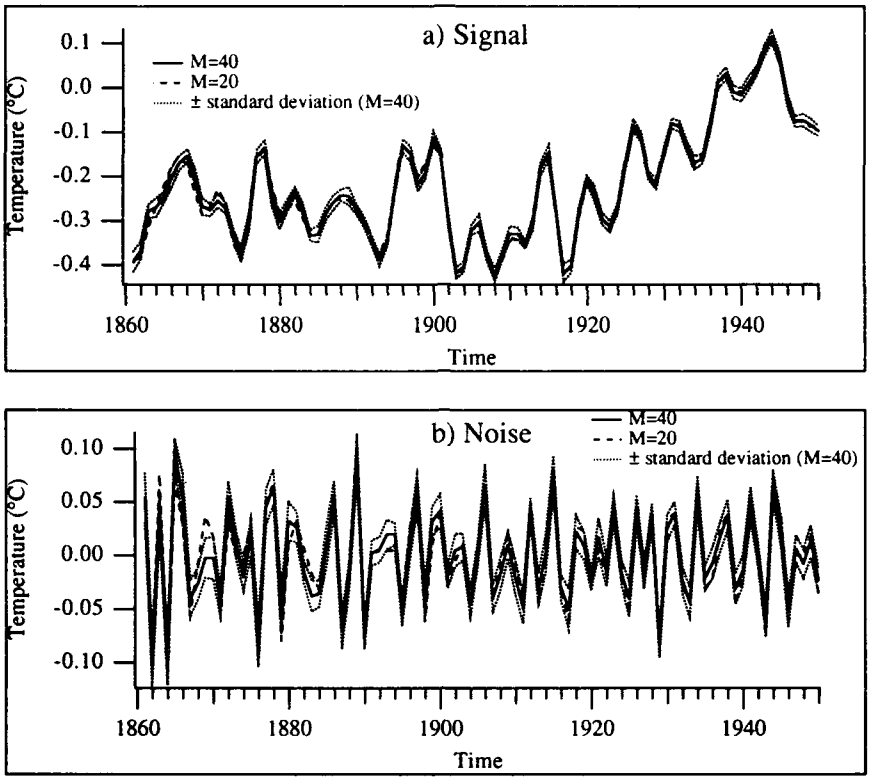

Fig. 7. (a) Noise-reduced IPCC series, calculated with the 41 ending dates running from 1950 to 1990, for $M = 40$ (solid) and $M = 20$ (dashed). The standard deviation of the noise-reduced data is represented by dotted lines (for $M = 40$ only). (b) Same as (a) for the noise part only. Curves for $M = 20$ and $M = 40$ are almost indistinguishable, for the noise as well as the signal.

small compared with the fluctuations over time of the average. The agreement between the filtered series for $M = 20$ and $M = 40$ is also quite remarkable, even at the ends, in spite of the dependence of S on M and on ending date.

In fig. 7b are plotted the same quantities for the reconstructed noise part $R_{\mathcal{S}'}x$ of the signal. Again, the variability from one estimate to another is considerably smaller than the noise variability itself. We conclude that, despite the fact that individual eigenelements in the tail of the expansion are not statistically stable, the global reconstruction process is stable – as the length of the data set as well as the window length M is varied.

The Monte Carlo method becomes rapidly untractable numerically as N increases, and the above algorithm can be shown to have a bias towards large values of S. Still, some experiments performed with $N = 10\,000$ on P4 showed that the noise-reduction factor (fig. 5) has a minimum value below 1 even when $N \to \infty$, and one can identify S as the order at which this minimum occurs. For large values of N, the eigenvalue spectrum itself becomes much more reliable and hence should provide a solution to this identification problem: as a noise plateau emerges more clearly with larger N, the break point should give an estimate of the best order $p = S$ to use for noise reduction. Other methods, like the Wiener filter, can also be used when N is large.

4. Interpretation of the eigenelements

4.1. Trends and nonstationarities

The interpretation of SSA results relies on the assumption that the process x under study is

stationary in the weak sense, i.e., that the second-order moments are invariant under translation, although the Karhunen–Loève expansion theorem does *not* require the stationarity of the process [38]. Individual realizations of a process of length N may indeed appear nonstationary. This happens typically when periods larger than N are present in the system, even if the process is stationary, like in the example of fig. 3 in section 2.1.

When several realizations are available, it is possible to check for stationarity. For instance, let us assume that the visual trend present in the IPCC temperature data (figs. 2 and 7a) results from a natural climatic oscillation with a period of, say, 500 years; then another realization of this process might show a decreasing trend. However, when only one realization is available, it is impossible to distinguish between actual trends or nonstationarities and the presence of ultra-low frequencies. In practice, SSA still works quite well, just as if the stationarity of the process, along with the ergodicity of the realizations, were satisfied.

The distinction between trend and stationary ultra-low frequency can be crucial in a given application. For instance, if the temperature data over the last century reflect a true trend, and this trend is caused by anthropogenic increases in greenhouse trace gases, such as carbon dioxyde (CO_2), then a number of technological and socio-economic consequences follow [36]. The statistical significance of the trend in the data was established by Kuo et al. [50], while the causal role played by CO_2 increases is plausible but not definitively confirmed.

From the point of view of studying the higher frequencies clearly manifest in a time series, the presence of either a trend or an ultra-low frequency is a major impediment. Various detrending methods, such as prewhitening [40], polynomial fits [51] and spline fits [52] exist. They all have some advantages and serious drawbacks. Ghil and Vautard [23] showed that SSA provides an effective and adaptive method of detrending, with little if any undesirable aliasing. We derive here a systematic data-adaptive algorithm for removing trends or ultra-low frequencies in a given data set.

The algorithm is based on the same principle as noise reduction. If the trend is sizable, it should appear in the first few PCs. Bearing this in mind, we use the nonparametric test of Kendall for global trend identification [29]: consider a sequence of values $(x_i, 1 \le i \le n)$ and count the number K_r of pairs of indices (i, j), with $i < j$, such that $x_i < x_j$. Roughly speaking, if K_r is large, there is a positive trend in the series, and if K_r is small, there is a negative trend in the series. More precisely, the distribution of the coefficient

$$\tau = \frac{4K_r}{n(n-1)} - 1 \tag{4.1}$$

tends rapidly to a normal distribution with zero expectation and standard deviation

$$s = \sqrt{\frac{2(2n+5)}{9n(n-1)}} \,. \tag{4.2}$$

The hypothesis of no trend is rejected, therefore, when the measured value of τ is outside the interval $(-1.96s, +1.96s)$, with a 5% chance of being wrong.

The test is applied to the successive PCs, using $n = N - M + 1$, and we denote by T_1 the first order such that the corresponding PC has no significant trend. Detrending is then performed by reconstruction over the set $\mathcal{T}' = \{T_1, T_1 + 1, \ldots, M\}$. Since the ends of the time series may lead to artificial trends, a second Kendall test is performed on the detrended series. If a trend is still detectable, reconstruction over the set $\mathcal{T}' = \{T_1 + 1, \ldots, M\}$ is performed and again tested, and so on. The first order T^* for which the reconstructed series has no significant trend determines the order of the detrending process, and – in obvious notation – $R_{T^*}.x$ is the detrended series.

For the processes P1–P4, T^* was always found to be 1. For the IPCC data T^* was found to lie between 2 and 4, the variations being mainly due to changes in the order of the eigenvalues and to our restricting attention – for simplicity – to the leading eigenelements, as far as the trend is concerned. Fig. 8 shows the average estimate of the IPCC temperature trend $R_{\mathcal{T}}x$, $\mathcal{T} = \{1, \ldots, T^* - 1\}$, calculated with different ending dates, for $M = 40$ and $M = 20$, in the same format as figs. 7a, 7b. Again, individual trend estimates are almost identical. For $M = 20$, a low-frequency component is mixed in with the trend, justifying the use of larger windows by Ghil and Vautard [23]. The detrending algorithm is quite stable, even at the ends of the series, for $M = 40$.

4.2. *Pairs of eigenelements*

In VG, we showed that when a vigorous – albeit irregular – oscillation is present, a pair of nearly equal eigenvalues stands out of the spectrum and that the associated eigenvectors and PCs are in quadrature. Even for a pure sinusoid, the two associated eigenvalues are not exactly equal (see eqs. (2.7d), (2.7e) of VG), so in practice it can be difficult to tell statistical degeneracy from oscillatory pairing. Ghil and Mo [25] introduced therefore an *ad hoc* criterion for the significance of quadrature between the PCs of a pair, based on their lag correlation. The main difficulty in this approach is the lack of reliable statistical significance estimators of the lag correlation, especially when the processes are nearly periodic, as the PCs are suspected of being.

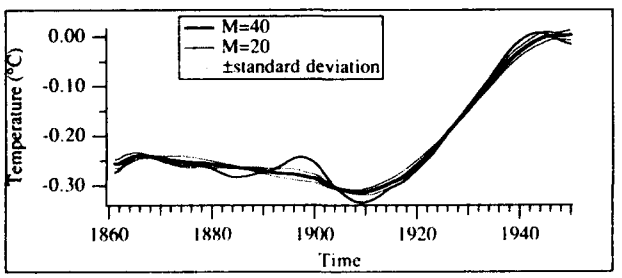

Fig. 8. Same as in the figs. 7a, 7b for the trend components.

We propose here instead two natural criteria based on the spectral properties of the eigenvectors. The first criterion is based on the remark that oscillating pairs of eigenelements $(k, k+1)$ must be spectrally localized around the same frequency. The squares of the reduced Fourier transforms $|\tilde{E}^k(f)|^2$ of EOFs k and $k+1$ are calculated, cf. eq. (2.6), at 500 equally sampled frequencies f between 0 and 0.5 cpu, and the frequency f_k corresponding to the maximum value is estimated. Then, for orders k and $k+1$ to represent an oscillatory pair, the difference $\delta f_k = |f_k - f_{k+1}|$ has to be small. For a pure red-noise process (see VG for the analytical calculation of the EOFs in this case), one has $\delta f_k \approx 1/2M$. Since we want to exclude pairs for this type of process, we impose the criterion $2M\,\delta f_k < 0.75$.

Although necessary, this criterion is not sufficient, since the amplitude of the peaks must also be high. In fact, if the presumed oscillatory pair completely resolves a frequency f^* between f_k and f_{k+1}, the response function $\rho_k(f^*) + \rho_{k+1}(f^*)$ of the reconstruction filter based on components k and $k+1$, given by eq. (2.20), must be close to 1 at this frequency, cf. eq. (2.14). Therefore, the maximum value of $\rho_{\mathcal{A}}(f)$, $\mathcal{A} = \{k, k+1\}$, is calculated and the pair is kept as an oscillatory pair only when this maximum is larger than $\frac{2}{3}$, i.e., only if at least two thirds of the variance of x at the peak frequency f^* is described by the pair in question.

These two criteria are applied to the realizations of the four synthetic processes. Results are summarized in table 2. For $M = 40$, despite the large variance of the noise in P2, the algorithm still finds a pair corresponding to the period 20 for all realizations, whereas the period 7 is identified as a pair in 34 realizations only. For P1 and P3, the algorithm is successful in general, with pair 1–2 corresponding to the period 20 and pair 3–4 to the period 7. Each realization in which the pair 3–4 (and 1–2) is not recovered corre-

Table 2
Oscillatory pairs for the four synthetic processes P1–P4, based on 100 independent realizations, for $M = 20$ and $M = 40$. First row: average number of pairs per realization. Second row: number of realizations showing a pair for the oscillation with period 20. Third row: same as second row for the oscillation with period 7. Last row: average number of spurious pairs.

P1		P2		P3		P4	
$M = 20$	$M = 40$	$M = 20$	$M = 40$	$M = 20$	$M = 40$	$M = 20$	$M = 40$
1.49	1.68	1.14	1.60	2.14	2.46	1.78	5.51
100	100	92	100	100	100	/	/
35	47	18	34	99	100	/	/
0.13	0.20	0.04	0.24	0.16	0.44	1.78	5.51

sponds to values of S smaller than 4 (or 2, respectively). The number of spurious pairs is small for P1, P2 and P3. For $M = 20$, the number of spurious pairs is slightly reduced, as is the number of successful pairs, showing that our criteria are not very sensitive to a change in the window length.

P4 should not be reducible to nearly periodic components, except for the problems arising in the Lorenz system from the presence of embedded (unstable) periodic orbits of arbitrary length, on the one hand, and from finite sample length, on the other. The average number of detected pairs is in fact high, due to these problems. We shall see in section 4.4 that even the most sophisticated spectral methods of classical type find, for these data, a certain number of significant peaks, for the same reasons: they are simply there for any finite segment of a trajectory. Indeed, spells of oscillations occur when the trajectory spirals around the unstable fixed points, for an exponentially distributed length of time, and with varying mean periods. As a consequence, the frequency of the oscillations detected varies with realization, rather than being fixed, as it is for P1, P2 and P3 (see fig. 10 below).

The evolution of the pairing for the IPCC time series was calculated as a function of the ending date (not shown). After the components corresponding to the trend, an average of about three pairs are found (for $M = 40$), associated with rather stable frequencies (see fig. 11 below). For the whole series (ending in 1990), we find five oscillatory pairs with peak periods similar to those found in Ghil and Vautard [23], i.e., 26 years (pair 3–4), 15 years (pair 7–8), 10 years (pair 5–6), 5.2 years (pair 9–10) and 4.6 years (pair 16–17). Fig. 9 shows selected RCs of the IPCC series. The last two pairs just mentioned describe most of the variance with periods of 4–6 years, associated with the low-frequency component of the ENSO phenomenon (see also refs. [7, 22, 26, 53]. While the pairing itself, as a function of ending date, is not very stable for the IPCC data set (cf. also ref. [24]), both the reconstructions (fig. 9) and the dominant periods (fig. 11 below) are quite stable.

4.3. SSA and MEM spectral estimates

Penland et al. [26] advocated the use of SSA for noise reduction before applying the maximum entropy method (MEM) to estimate the power spectrum of a time series. They estimated the power spectra of each of the S significant PCs with MEM, based on the formulation of Burg [32], and truncated eq. (2.15) to these PCs to obtain an approximation of the power spectrum P_x of x. The generally regular behavior of the PCs allowed them to obtain good spectral resolution with low-order AR models. The striking advantage of this SSA prefiltering is to eliminate therewith the spurious peaks inherent to high-order MEM estimates. We refine here this approach by deriving a fully consistent SSA–MEM spectral estimate.

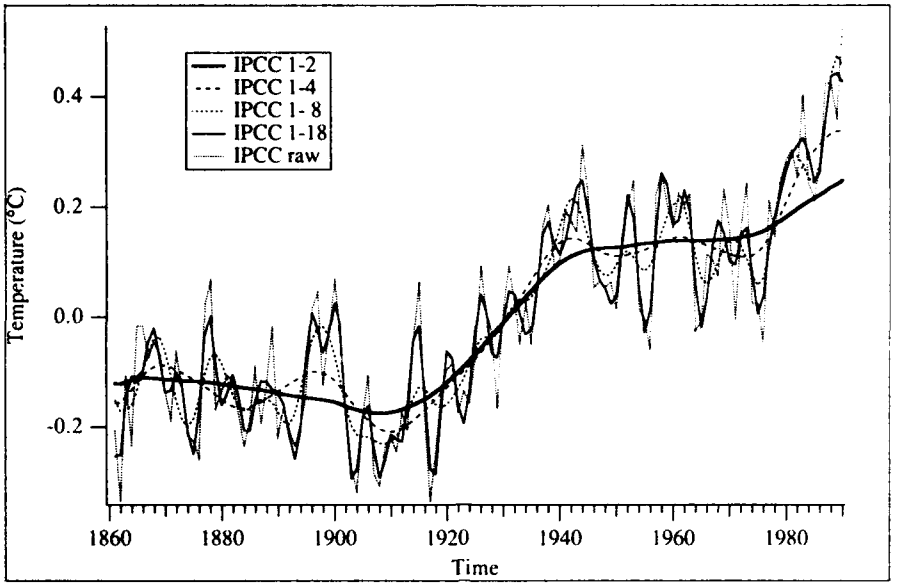

Fig. 9. Reconstructed subsets $R_{\alpha}x$ of the IPCC series with ending date in 1990 only. The global average is removed.

We assume that the autocovariance function $c(j)$ is known up to lag $j = M - 1$. Using the notation of eqs. (2.9), (2.10), an AR process z of order $M - 1$ is fitted to the time series x, using the Yule [33]–Walker [34] method,

$$\Phi(B)\, z_i = v_i\,, \tag{4.3}$$

where v is a white-noise process of variance σ^2 and $\Phi(\zeta)$ a polynomial of degree $M - 1$, with real coefficients, of the complex variable ζ. The PCs b^k of the fitted process satisfy

$$b_i^k = \Psi_k(B)\, \Phi^{-1}(B)\, v_{i+M}\,. \tag{4.4}$$

The power spectrum $P_k(f)$ of a^k may thus be approximated by the spectrum $P_k(f)$ of b^k,

$$P_k(f) = \frac{|\Psi_k(\zeta)|^2}{|\Phi(\zeta)|^2}\,\sigma^2\,, \quad \zeta = \exp(2\pi i f)\,, \tag{4.5}$$

where σ^2 is the variance of the noise process v.

In figs. 10a–10d, the histograms of the peak frequencies of the estimates (4.5) of $P_k(f) + P_{k+1}(f)$ are displayed. Fifty bins between 0 and 0.5 are used for this calculation. For P1, P2 and P3, the spurious peaks are distributed almost uniformly along the frequency axis. The probability of success in the identification of the oscillation with period 20 is close to 1 for all three processes, whereas it varies for the oscillation with period 7, P2 being the worst case and P3 the best, as expected. The spurious peaks, which are described by the oscillatory pairs for P4 (cf. table 2), are concentrated towards the lower frequencies, where the actual power is higher. These remarks hold both for $M = 40$ and $M = 20$, although there is somewhat less success for the latter in identifying the period 7 at high noise levels (figs. 10a, 10b). It follows that, almost independently of (sufficient) window length, SSA separates oscillations from noise even when the noise variance is higher than that of the oscillations.

For the IPCC series, the results are presented in fig. 11, as a function of the ending year. The stablest oscillations are those with periods around 4–5 years, 10 years and 15 years. An interdecadal oscillation with a period of 20–30 years is also in evidence for about half the ending years. Note the similarities with the peaks estimated by Ghil and Vautard [23], using the Jones et al. [37] time series up to 1988 only.

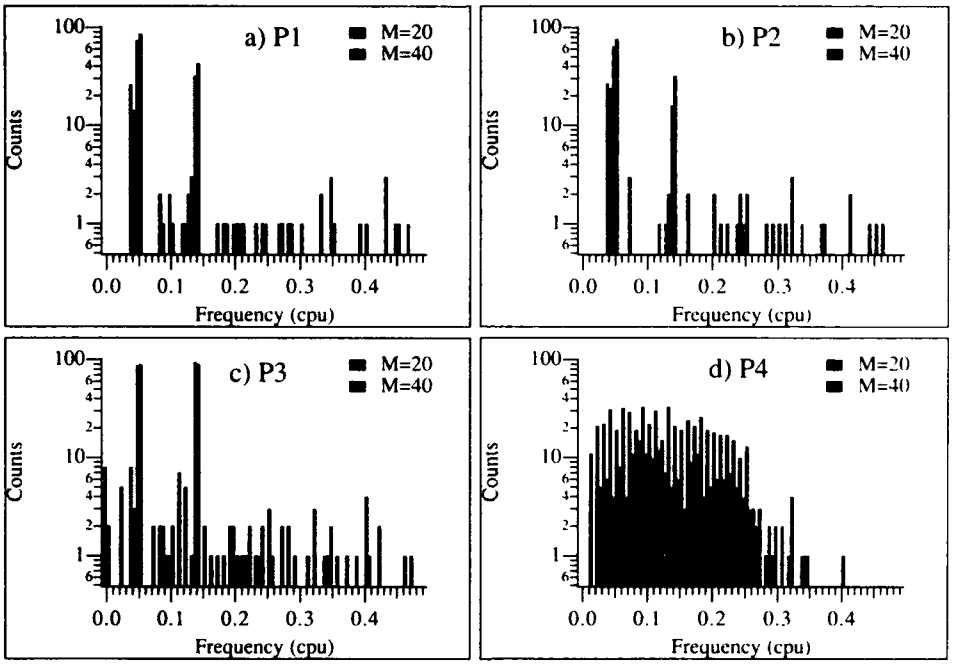

Fig. 10. Histogram of frequencies associated with the oscillatory pairs; frequencies are estimated by the maximum entropy method (MEM). Fifty bins of width 0.01 have been used to count the number of frequencies; the place of the bars for $M = 20$ (shaded) and $M = 40$ (solid) relative to the frequency bins is the same as in fig. 6. (a) P1, (b) P2, (c) P3 and (d) P4.

The theoretical advantage of the formulation (4.5), compared to that of Penland et al. [26], where an AR model is fitted to each individual significant PC, is that the additive property (2.15) of the spectra is conserved exactly. It justifies rigorously the display of *stack spectra* $\mathcal{Q}_p$ of the PCs of the process x: the stack spectrum of order p is the partial sum of (2.15) truncated at order p, i.e.,

$$\mathcal{Q}p(f) = \frac{\sigma^2}{M|\Phi(\zeta)|^2} \sum_{k=1}^{p} |\Psi_k(\zeta)|^2 ,$$
$$\zeta = \exp(2i\pi f) . \qquad (4.6)$$

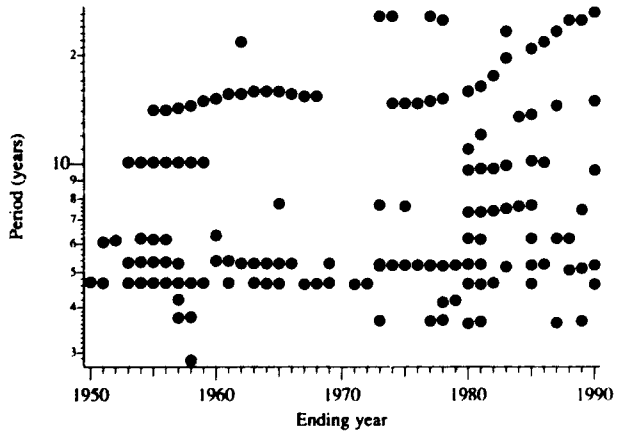

Fig. 11. Periods associated with the quasi-periodic components for the IPCC series, as a function of the moving final year.

Fig. 12 shows the stack spectra for the IPCC series ending in 1990, with $p = 2$, $p = 8$, $p = S = 18$, and $p = M = 40$ (raw MEM). The three low-frequency oscillations described by the pairs (3, 4), (5, 6) and (7, 8) have periods of about 26, 15, and 10 years. Most of the variance associated with PCs 9-to-18 is related to ENSO oscillations, with periods between 4 and 6 years. Note that the peaks found at periods 4.2 and 3.2 years are rejected as noise, as well as most of the variance at periods below 4 years. There is remarkable agreement with the results of Ghil and Vautard [23], using somewhat different raw data [37] and MTM (their fig. 2). Despite the difference between the data sets and the method, we still

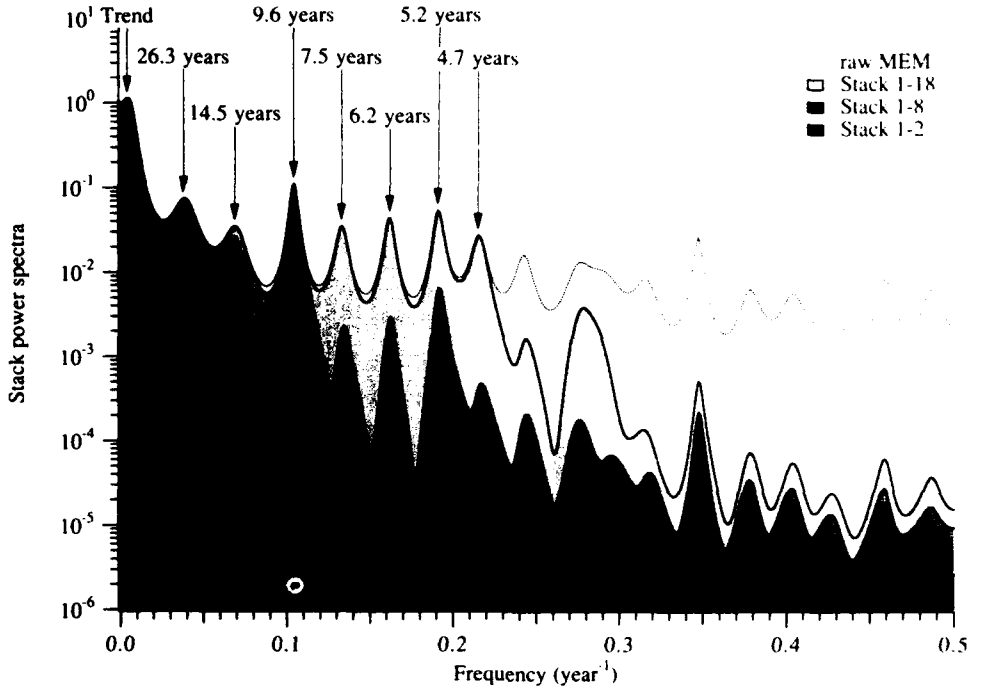

Fig. 12. Stack MEM spectra of the IPCC series (1861–1990), for various subsets of PCs, together with the raw MEM spectrum (i.e., the stack 1–40); $M = 40$.

obtain an interdecadal oscillation, the ENSO 4–6 year activity, and the two other periods (of 10 and 15 years).

4.4. *Multi-taper spectral estimates*

The multi-taper method (MTM) – devised by Thomson [35], based on the work of Slepian [54] – is a nonparametric spectral analysis method, unlike MEM which assumes an AR signal. It provides, moreover, an array of statistical tests for the spectral estimates. MTM was applied to various geophysical time series [55–57] and more recently to several climatic time series, from historic temperature data [23, 50] through tree-ring data [58], to late Pleistocene data [52, 59]. We review briefly the main properties of MTM (see also appendix A of ref. [52] for succint details) and apply it to the previously defined synthetic and IPCC data sets.

MTM aims to eliminate the spectral bias induced by finite sampling. Given a line frequency signal perturbed by white noise, $x_i = \mu \sin(2\pi i f_0) + w_i$, $1 \le i \le N$, and a frequency band $B = (f_0 - W, f_0 + W)$, one wants to minimize the power leakage of f_0 outside B, with a tapered signal $x_i v_i$, $1 \le i \le N$. This goal is achieved with a subset of the $K = [2WN]$ first *Slepian sequences*, otherwise called *discrete prolate spheroidal sequences* (DPSSs). These sequences $(v^{(k)}, 1 \le k \le K)$ are easily computed, given W and N [54, 59].

The tapers are explicitly devised to optimize the estimate of line frequencies f_0 and the corresponding amplitudes μ. An estimate ν of $\mu(f_0)$, for f_0 known, is derived from a least-squares regression with respect to the coefficients of the K tapered signals, yielding

$$\nu(f_0) = \frac{\sum_{k=1}^{K} V_k(0) y_k(f_0)}{\sum_{k=1}^{K} V_k(0)^2} , \tag{4.7}$$

where $y_k(f)$ is the Fourier transform of the kth tapered $xv^{(k)}$ and $V_k(f)$ is the Fourier transform of the kth taper $v^{(k)}$. Notice that the amplitude estimate $\nu(f_0)$ is unbiased when the noise w is

white [56]. In practice, f_0 is not known a priori, and the estimate (4.7) is computed for $\nu(f)$ at different f, to estimate the position f_0^* of the maximum, as well as its value $\nu(f_0^*)$.

One can test the validity of this estimate by calculating the ratio of the explained to the unexplained variance. It turns out that the variable

$$F(f) = \frac{(K-1)|\nu(f)|^2 \Sigma_{k=1}^{K} V_k(0)^2}{\Sigma_{k=1}^{K} |y_k(f) - \nu(f)V_k(0)|^2} \qquad (4.8)$$

follows a Fisher–Snedecor distribution – with 2 and $2K-2$ degrees of freedom for the numerator and the denominator, respectively – when the noise is white [56]. Consequently, one rejects the null hypothesis $\mu = 0$ (i.e., that the series is white) with a probability $1-q$ of being wrong, when the value $F(f)$ exceeds a threshold F_q such that $\mathcal{P}(F < F_q) = q$.

Notice that for a single, finite realization, the maxima of $\nu(f)$ and $F(f)$ will not coincide in position. The position of a maximum in $F(f)$ provides an unbiased – to first order in the detuning $f - f_0$ – estimate of a line component when the noise is white. Hence we use the latter to estimate the position of the peaks. Moreover, the value of F does not depend – to first order – on the magnitude of μ, allowing the detection of small-amplitude oscillations with less ambiguity than traditional spectral analysis methods. This estimate also appears to be robust in practice to the slope of the noise spectrum: the usual white-noise assumption can be replaced by colored noise, yielding a negative rather than zero slope in the frequency domain, like that of most climatic time series [60].

If the process x is composed of several lines, separated by at least $2W$, the procedure still applies in principle, due to the rough independence of the estimates at the different lines. Nonetheless, as we shall see, the test (4.8) detects more sharp lines than actually present in the signal, and the number of spurious peaks appears to be stable in our Monte Carlo experiments, even though the lines themselves occur at random frequencies. For a pure white noise, F-values follow a Fisher distribution. In theory, therefore, if q is the probability of F being less than F_q, the expected number of F-values above F_q is $(1-q)N$. It turns out in our experiments on pure white noise (not shown) that the number of peaks above F_q depends in fact on the bandwidth $2W$ and the number of tapers K; $(1-q)N$ appears therefore to be only a rough upper bound for the number of spurious peaks MTM will exhibit.

We investigate here the effects of SSA noise reduction on MTM. Contrary to MEM, there is no simple algebraic link between MTM and SSA. We have calculated, for the raw series and for the reconstructed noise-reduced series, the MTM spectral estimates, with $WN = 6$ and $K = 8$. The position of the peaks significant at the 95% confidence level is displayed in histogram form in figs. 13a–13d. Only the case of noise reduction with $M = 40$ is discussed, results being similar for $M = 20$.

For P1, the two lines appear for every realization, the period 20 being distributed within two histogram bins and the period 7 within one bin only (fig. 13a). No significant peaks occur in the vicinity of the two lines. The spectral power in a $2W$ band around those frequencies is absorbed by the lines. Indeed – in this case – $W = 0.04$, which corresponds to the gaps on each side of the line peaks. The frequency band beyond 0.2 cpu yields a roughly continuous and flat histogram: all frequencies are spuriously detected in this noise band with equal probability. Hence MTM is an efficient estimator of the real lines in this case, and its spurious frequencies are uniformly distributed. With a 95% statistical confidence level, one expects at most seven peaks in the MTM spectrum of a white-noise process. For P1 (fig. 13a) there are four spurious peaks on average above this threshold, each peak being randomly distributed in the frequency band $(0, 0.5)$ – the two gaps around the line frequencies excepted.

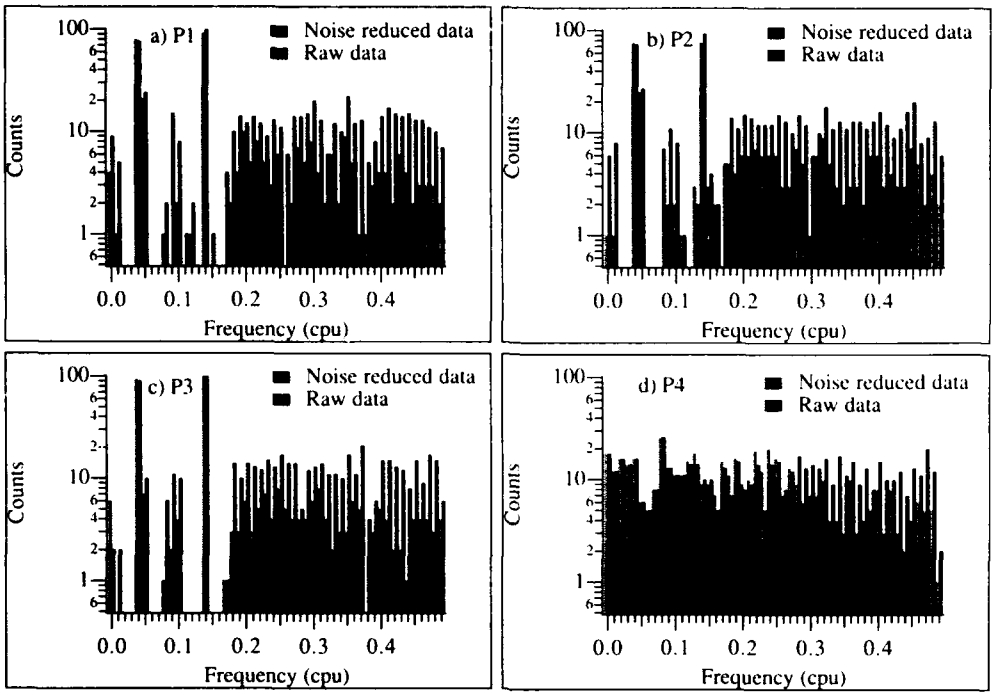

Fig. 13. Histogram of line frequencies identified by the MTM's F-test – at a 95% significance level – before noise reduction (solid bars) and after (shaded bars); $M = 40$. (a) P1, (b) P2, (c) P3 and (d) P4.

The noise reduction algorithm had a drastic effect on the tail of the MEM spectrum, whereas little change is observed for the occurrences of the MTM line peaks. For P1, this procedure reduces the number of spurious peaks exhibited by a factor of 2 – uniformly throughout the noisy part of the spectrum – while the power of the noise is divided by a factor of 10 (not shown). If we increase (P2), or decrease (P3) the white-noise variance, the MTM histograms of peaks are quite similar to those for P1. Therefore, MTM is relatively insensitive to the signal-to-noise ratio, in the case of a quasi-periodic process. Note that the SSA estimates (figs. 10a–10d) count much fewer spurious peaks than MTM. The number of SSA detections of the period 7 is unfortunately also affected by the noise-reduction algorithm, especially for P2 (fig. 10b), which is not the case of MTM estimations. SSA estimates are thus more sensitive to the signal-to-noise ratio, but tend to produce fewer spurious peaks; i.e., SSA is more conservative.

The application of MTM to the process P4 indicates no preferred frequency, proving the robustness of the method. Indeed, MTM considers the Lorenz system as a colored-noise process, with no greater probability of having a line in some band than in another. SSA noise reduction filters out higher frequencies, but the histogram shape for MTM line detections does not change much below 0.3 cpu. SSA estimates, on the other hand, clearly detect peaks with a higher probability at lower frequencies. The difference between the two estimates is clear: SSA does not try to find lines, but rather spectral bands with a high percentage of explained variance.

The detrended IPCC series is again analyzed with a final date moving from 1950 to 1990. In fig. 14, we plot the periods of the peaks significant at the 95% confidence level, in a display format similar to fig. 11. For the detrended, but still noisy data (reconstruction of components from T^* to $M = 40$; open circles in the figure), a sequence of peaks at 15 and 9 years stand out. At lower periods, a number of peaks occur between 2.5 years and 6 years. The SSA noise-

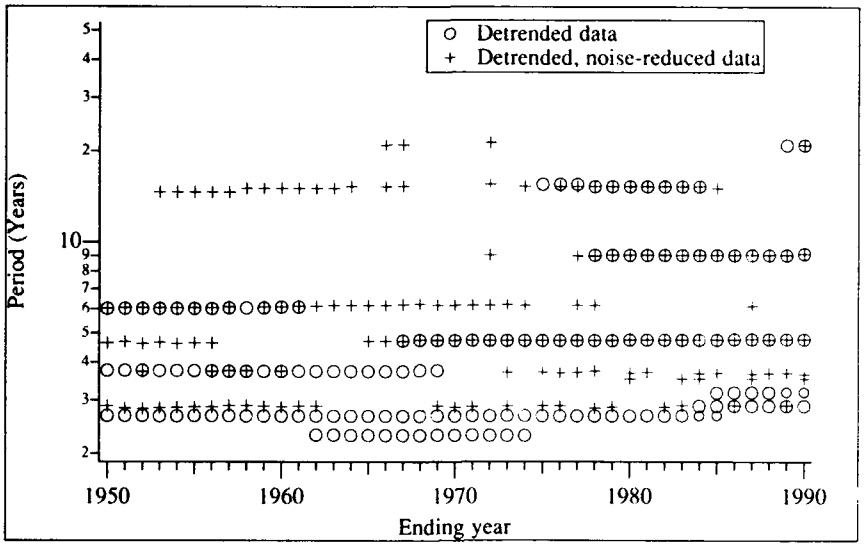

Fig. 14. Evolution of the periods identified by MTM – at the 95% significance level – calculated from the RCs $R_{\mathcal{A}}x$, with $\mathcal{A} = \{T^*, \ldots, 40\}$ (circles), and with $\mathcal{A} = \{T^*, \ldots, S\}$ (plus signs), as a function of the ending year.

reduction filter (RCs T^* to S; pluses in the figure) essentially removes the two highest-frequency peaks. The peaks with periods of 21, 15, 9, 6, 4.6, 3.8, and 2.8 years all appear significant, although the last two have a much lower amplitude. This is in agreement with our MEM results (fig. 12). Note that the interdecadal oscillation with a period of 20–30 years detected by Ghil and Vautard [23] is not very stable at the 95% confidence level. Still, this interdecadal oscillation is significant at the 90% confidence level for every final date (not shown).

5. Application to prediction

Since the PCs are filtered versions of the signal (cf. section 3) and typically band-limited (cf. section 4), their behavior is more regular than that of the raw series, and hence more predictable. This leads to the heuristic idea of forecasting only a subset of PCs, e.g., all the significant ones or the oscillatory pairs exclusively. Thus a – hopefully large – fraction of the variance can be predicted with reasonable skill. The forecast for the entire series is the sum of the expected value of the complementary PCs, i.e., zero, and of the forecast for the selected subset. Keppenne and Ghil [7] showed, by forecasting the Southern Oscillation index (SOI) of ENSO with considerable skill out to two-and-a-half years, that this approach can produce more accurate forecasts on an important and well-studied, but very irregular time series than any other method in current use.

We follow Keppenne and Ghil [7] and fit an AR model to each individual PC using the AR coefficient estimates of Burg [32], with different orders L. The order $L = M - 1$, which seems the most consistent with the SSA analysis (cf. section 4.3) was found to be too large compared with the simple behavior of the PCs: indeed, the variance of the AR coefficient estimates increases with the order [61]. Forecast errors were minimal, for all signals analyzed, when the order was quite low, $L \leq 10$. For small orders, forecast errors are dominated by the lack of resolution; for large orders, by the error made on the coefficients of the model. The results presented here are for $L = \text{const.} = 10$, and remain valid for even smaller orders.

Once forecasts of the individual PCs are produced, the reconstruction algorithm is applied, in order to compare forecasts with real data. Let us

denote by $\mathscr{A}$ the subset of PCs used in the forecast. If the original series is of length N, the forecast for time $N+\tau$ of the sub-signal in question is the reconstruction of the corresponding extrapolated PCs a_i^k, with $1 \le i \le N - M + \tau$. Note that this forecast for time $N+\tau$ differs from the value at time $N+\tau$ produced by a forecast for time $N+\tau'$, with $\tau' > \tau$. Indeed, the forecast for time $N+\tau$ is the end of the reconstructed series, whereas the reconstruction process takes into account PC forecasts out into the future in the latter case. The validation of the forecasts is made by applying the *exact* same procedure to the actual PCs as to the extrapolated PCs.

In fig. 15, we plot – as a function of lead time τ – the average forecast error for different subsets $\mathscr{A}$. The dotted curve represents the average, over the 100 realizations of the four synthetic processes, of the ratio

$$r_1(\tau) = \frac{[F_E(N+\tau) - y(N+\tau)]^2}{u_1}, \qquad (5.1)$$

where $F_E(N+\tau)$ is the MEM forecast at time $N+\tau$, using the raw series x, with $L = 39$; $y(N+\tau)$ is the extrapolated clean signal, calculated from formula (1.5) for P1, P2, and P3, and with the Lorenz equations for P4. In eq. (5.1), u_1 is the measured variance of y. With this normalization, the perfect forecast has an error of 0, and the worst an error of 1, corresponding to the "climatological" forecast, i.e., using the past average as the future forecast. For P1, P2 and P3, these forecast errors are smaller for longer lead times – around $\tau = 40$ – before increasing again. This results from the fact that the spurious oscillations generated by noise have an e-folding time shorter than the significant ones. The forecast is therefore polluted by the effect of noise on the AR coefficient estimates.

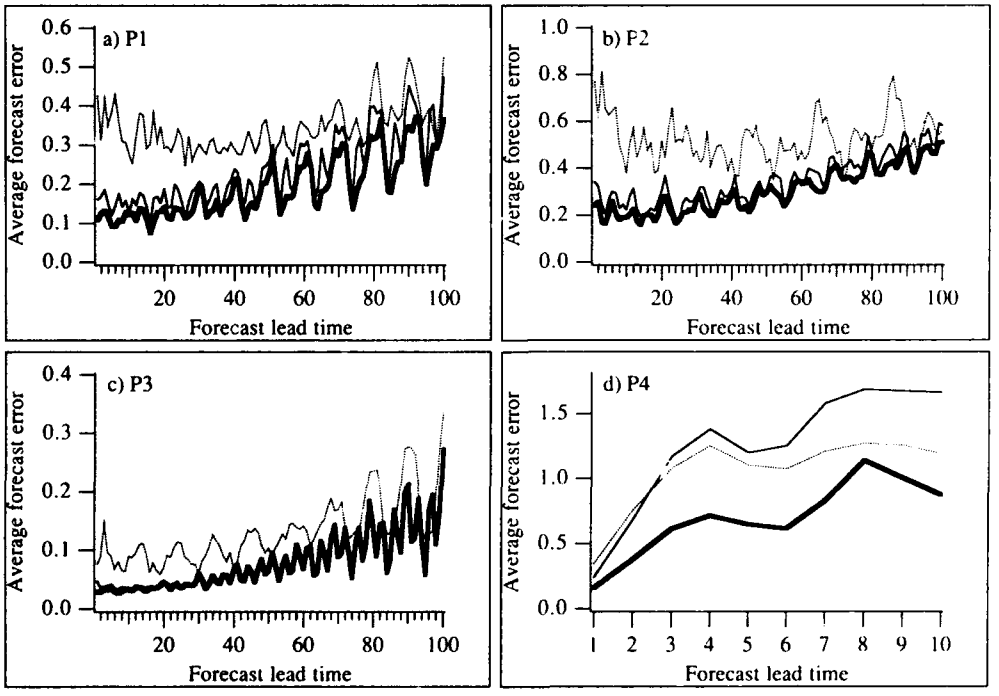

Fig. 15. Average errors of the SSA–MEM forecasts for the RCs $R_{\mathscr{A}}x$, normalized by the variance of the RCs of the clean signal (solid curves). Light lines stand for $\mathscr{A} = \mathscr{S} = \{1, \ldots, S\}$, and heavy lines for $\mathscr{A}$ being the union of the significant oscillating pairs. The dotted line represents the average error of the standard MEM forecast of the raw series, using the AR order $L = 39$. (a) P1, (b) P2, (c) P3 and (d) P4.

The two solid curves show, for two subsets $\mathcal{A}$, the average of the ratio

$$r_2(\mathcal{A}, \tau) = \frac{[F_{\mathcal{A}}(N+\tau) - R_{\mathcal{A}}y(N+\tau)]^2}{u_2} \qquad (5.2)$$

where now u_2 is the measured variance of $R_{\mathcal{A}}y$, while $F_{\mathcal{A}}(N+\tau)$ is the forecast using the above algorithm with $\mathcal{A} = \mathcal{S} = \{1, \ldots, S\}$ (S-forecast: light solid) and $\mathcal{A} = \mathcal{A}_1 \cup \mathcal{A}_2 \cup \cdots \cup \mathcal{A}_Q$, the quasi-periodic pairs $\mathcal{A}_q$ defined in section 4.2 (Q-forecast: heavy solid). Thus, $r_2(\mathcal{A},)$ represents the average forecast error made with respect to the corresponding reconstructed part of the (clean) signal.

Comparison of the solid curves in figs. 15a–15c with the dotted one shows that all forecasts produced by AR extrapolation of the PCs are much better, at all lags, than forecasts performed on the raw signal. For the three processes P1–P3, the error is reduced by a factor of 3 at the beginning and the PC forecasts are good for about 100 time units, i.e., five times the longest deterministic period involved. Raw MEM forecast errors grow more rapidly at longer lags than PC forecasts. Forecasts errors based on the oscillatory pairs only (Q-forecasts) are smaller than forecasts based on all the significant components (S-forecasts).

For the Lorenz equations (fig. 15d), PC-based forecasts are not better than raw MEM forecasts, when compared with the clean signal. After two time units, forecast errors are greater than 1, indicating a total loss of predictive skill. When only oscillatory PCs are considered, a predictability limit of seven time units is found, corresponding to the average period of spiral motion around the unstable fixed points. The (intermittently) oscillatory components describe, in general, more than 50% of the total variance of the finite-length Lorenz signal.

These results leave us with the hope that, for signals with intermittent oscillations, a certain fraction of the variance can be forecast by linear models. When the oscillations are sustained, the predictability limit should be pushed even further, as shown by the results of P1, P2 and P3. The results are fairly stable to a change in window length, since for $M = 20$ (not shown), the behavior of the forecast errors is the same, with somewhat lesser skill.

For the IPCC data, forecast skill is established in a different way. For each year N_y, starting in 1950, the AR coefficients of the PCs are calculated with SSA from the training period (1861, N_y). Then, the AR models for the PCs are used to perform a series of forecasts starting at years N_y, $N_y + 1, \ldots, 1989$. The forecasts are compared to the actual reconstructions, and the error is compared with the error made by the *climatological* forecast (CF hereafter), i.e., the extrapolation of the PCs with the value 0, and by the *persistence* forecast (PF hereafter), i.e., the extrapolation of the PCs with the last known value; CF and PF are standard benchmarks for skill in numerical weather prediction and its extensions.

The average forecast error at lead time τ is given by the average of the quantity

$$e_F(N_y, \mathcal{A}, t, \tau) = [F_{\mathcal{A}}(N_y + t + \tau) - R_{\mathcal{A}}x(N_y + t + \tau)]^2 \qquad (5.3)$$

with respect to the initial years $N_y + t$. The CF error is the average of the quantity

$$e_C(N_y, \mathcal{A}, t, \tau) = [R_{\mathcal{A}}x(N_y + t + \tau)]^2 , \qquad (5.4)$$

and the PF error is the average of

$$e_P(N_y, \mathcal{A}, t, \tau) = [R_{\mathcal{A}}x(N_y + t) - R_{\mathcal{A}}x(N_y + t + \tau)]^2 . \qquad (5.5)$$

Note that for the IPCC time series, we only have at our disposal the raw data to compare with, not the clean signal. This is why, in eqs. (5.3)–(5.5), $R_{\mathcal{A}}x$ stands where $R_{\mathcal{A}}y$ does in eqs. (5.1), (5.2). The forecast errors with respect to the clean signal should obviously be lower.

In table 3 appear the statistics on the ratio of the average forecast error to both the average CF and PF errors, for lead times of $\tau = 1-10$ years, and $M = 40$. Only N_y values ranging from 1950 to 1979 were considered, since after that, average errors are calculated over less than 10 values and loose their statistical significance. If, for year N_y, lead time τ and subset $\mathcal{A}$, the average of the forecast error e_F is lower than the average CF error e_C (or average persistence forecast e_P), the model is successful for those values of the parameters. In table 3, we count the number of successes of the PC-based AR model, as well as the number of failures. Italic characters stand for cases when the number of successes is larger than the number of failures. These numbers are estimated for the subsets $\mathcal{A} = \{T^*, \ldots, S\}$, representing the trendless significant components, as well as for the subset $\mathcal{A}$ including only the quasi-periodic trendless components (S- and Q-forecasts, respectively).

Table 3
The left/right element in each column is the number of initial years N_y, $1950 \le N_y \le 1979$, having an average forecast error lower/higher than the climatological forecast (CLI) or the persistence forecast (PER). The results are calculated with $M = 40$ for the IPCC series. S stands for forecasts of the significant components, i.e., from order T^* to S. Q stands for the quasi-periodic components, i.e., for the union of pairs lying in the interval (T^*, S). The rows indicate the lead time τ, in years. Italic characters indicate that the SSA-MEM forecast is more successful than the comparison forecast. The sum of the elements in each cell is the number of initial years, 30 for the S-forecasts and 29 only for the Q-forecasts – since for year 1970, no oscillatory pair was detected (see also fig. 11).

τ	S/CLI	S/PER	Q/CLI	Q/PER
1	*30/0*	*30/0*	*29/0*	*29/0*
2	*29/1*	*24/6*	*29/0*	*29/0*
3	*23/7*	*19/11*	*29/0*	*28/1*
4	*23/7*	*19/11*	*26/3*	*26/3*
5	*24/6*	14/16	*26/3*	*25/4*
6	*25/5*	7/23	*23/6*	*24/5*
7	*23/7*	8/22	*19/10*	*26/3*
8	*20/10*	8/22	*18/11*	*26/3*
9	*19/11*	7/23	*15/14*	*21/8*
10	*22/8*	9/21	*16/13*	*21/8*

Our S-forecasts are better than CFs at all lead times and better than PFs up to 4 years. Thus PFs are harder to beat than CFs. Careful examination shows that the CFs are, in fact, bad forecasts, because the "detrended" time series has still a small positive trend toward the end. All temperature forecasts produced were slightly below the observed. Climatological forecasts, in particular, lie below the average of the end of the time series. Persistence forecasts are better since the last known value is a better estimate for a series with a (small) trend. Our forecasts decay eventually towards the average (of the past known values), since there is no noise forcing in the AR forecasts. The fact that they remain more successful than CFs indicates, however, that the sign of the anomalies is well forecasted. The phase of the oscillations is correctly estimated, whereas the amplitude is typically underestimated.

The Q-forecasts are better than CFs and PFs for all lead times considered, indicating that pairs do really correspond to linearly predictable phenomena. The price to pay is that Q-forecasts only predict – on average – about 15% of the total variance, 35% of the trendless variance, and 50% of the trendless and noiseless variance. Fig. 16a shows the particularly good forecast initiated from the year $N_y = 1953$, for the significant components 4–14. The forecast matches the series up to 1968, i.e., 15 years ahead, quite well.

Fig. 16b shows the global temperature forecast to the end of the century. Global temperatures should decrease by about 0.2°C up to 1995–1996 before increasing again. For a complete forecast, the trend has to be added back in. If the increase of temperature given by the trend does not change (about 0.08° for the last five years, cf. fig. 9), we should witness a decrease of about 0.12°C for 1995–1996. The global temperature would still be high compared with the beginning of the century, but would be close to the values for the early eighties.

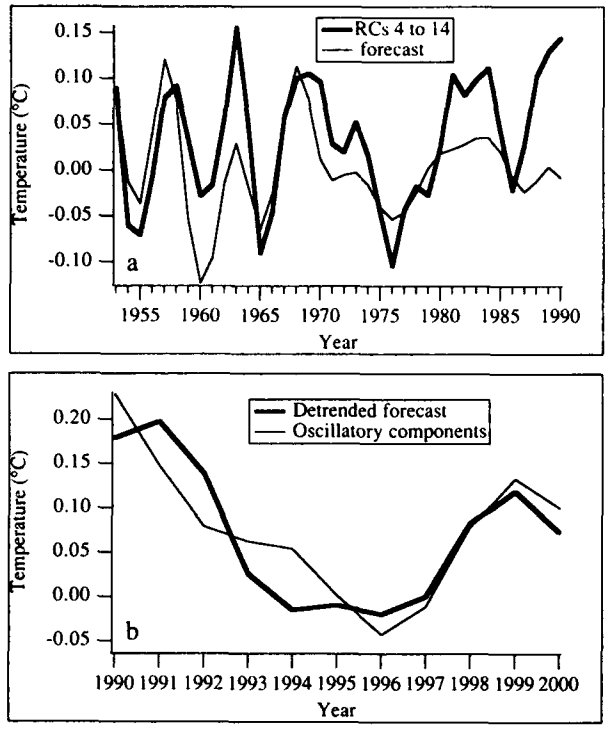

Fig. 16. Global forecasts of detrended temperature, from IPCC data. (a) Based on data prior to 1953 only, of the reconstructed series $R_{\mathscr{A}}x$, with $\mathscr{A} = \{4, \ldots, 14\}$, together with the evolution of the actual quantity forecasted. (b) For the next ten years: heavy curve: $\mathscr{A} = \{3, \ldots, 18\}$; light curve: $\mathscr{A} = \{3, \ldots, 10, 16, 17\}$.

6. Summary and discussion

We have reviewed theoretical and algorithmic properties of singular-spectrum analysis (SSA), from the signal-processing point of view. This method of analysis is particularly useful when little or no knowledge of the underlying dynamical system is available, and the time series at hand are short and noisy. An outline of the main results follows.

(1) Parameter ranges are obtained for applying SSA successfully to the analysis of short signals. A particular method of estimating of the Toeplitz matrix is shown to have little bias compared to other estimates. In order to correctly localize the spells of an oscillation of period T and typical life time T', we suggest to choose the window length M so that $T \leq M \leq T'$.

(2) An algorithm for the reconstruction of isolated components, or groups of components, is presented. It allows one to expand the series x under study into a sum of reconstructed components x^k, corresponding to the kth eigenelement of the Toeplitz matrix, at any given epoch.

(3) We develop a method for the identification of noisy and of significant components. The reconstruction based on the significant components only gives good and statistically stable estimates of the clean signal, whether the noise is white (as in the synthetic examples) or not (as in the IPCC data). This noise-reduction algorithm is shown to be particularly efficient, given short data sets, for processes with a large quasi-periodic component. For purely chaotic processes perturbed by noise, the proposed noise-reduction algorithm involves substantial reduction in the signal as well.

(4) A method is derived to recognize oscillatory pairs of eigenelements. These pairs are shown to correspond to the main periodicities in the data. The periodicities do not necessarily represent sustained harmonic components, but indicate at least intermittent periodic activity in the time series under study. SSA recognizes systematically an oscillation in a short signal (we assumed the knowledge of 150 sample points only) perturbed by white noise with variance as large as twice the variance of the oscillation in question. We also show that SSA can be used for detrending purposes, even for other than linear trends.

(5) Two advanced spectral-analysis methods can be used to good advantage in combination with SSA. First, we derive a fully consistent SSA–maximum-entropy-method (MEM) for power spectrum estimates; this approach respects the additive property of SSA response filters, and allows one to stack spectral estimates of the different components, quantifying therewith the spectral contribution of each eigenelement. Second, when the noise reduction and detrending algorithms are applied prior to multitaper spectral estimation, the number of spurious

spectral peaks is significantly reduced. This eliminates a major drawback of the multi-taper method (MTM), which otherwise provides a significance test for the line components it detects and is robust to noise characteristics.

(6) The regular behavior of the principal components (PCs) makes them easier to forecast than the complete signal. We show that using autoregressive (AR) models for the significant components increases the predictability, especially in the case of quasi-periodic signals embedded in noise. For chaotic dynamical systems with no particular frequency excited, linear models do not perform very well. However, these systems may hide intermittent oscillations. Depending on the variance explained by the latter, at least a fraction of the total variance can be forecasted. For the IPCC temperature data, oscillatory components account for about 50% of the significant variance, after trend removal, and are predictable more than 10 years ahead.

We have focused in this paper on single-channel analysis. The same calculations can be carried out in multi-channel problems. Reconstruction of selected components is done essentially in the same way [19]. The noise-reduction problem can also be approached in a similar manner. The interpretation of the eigenelements is different, since in multi-channel analysis the EOFs are time sequences of "spatial" patterns [18, 62]. Therefore, when a pair of eigenelements emerges, it is usually associated with nearly linear traveling waves, as in the extended EOFs with fixed, small time window already used in meteorology [62, 63].

MEM spectral estimates can be computed using multi-channel AR models [19]. Linear forecasting of the PCs is performed in the same way as in single-channel analysis. An interesting climate modeling application of multi-channel SSA could be to use such simple linear models in order to forecast low-frequency quasi-periodic components, such as the El Niño–Southern Oscillation (ENSO), and use this forecast in combination with a general circulation model, which – in many cases – does not reproduce such oscillations very accurately, but can provide other physical details of interest, related to shorter periodicities [64].

Acknowledgements

It is a pleasure to thank our collaborators in the SSA enterprise: M. Dettinger, C.L. Keppenne, M. Kimoto, K.-C. Mo, M.C. Penland, G. Plaut, Y. Sezginer, and E. Toniolo. G.E. Birchfield, D. Broomhead, L. Smith, P. Switzer, H. Tong and many others asked interesting questions; we hope they will find some of the answers in here. C.K. Folland and D.E. Parker graciously provided the IPCC data set. We also benefited from constructive remarks by P. Manneville, two anonymous reviewers, and the editors of this special issue. The animated atmosphere of the IUTAM/NATO workshop at the University of Warwick was very stimulating. This work was supported at UCLA by NSF grant ATM 90-13217, at LMD by the CNRS, and by a Guggenheim Fellowship to M. Ghil. Computations were done at LMD on SUN Spark workstations.

References

[1] D. Brouwer and M. Clemence, Methods of Celestial Mechanics (Academic Press, New York/London, 1961).
[2] E.N. Lorenz, J. Atmos. Sci. 20 (1963) 130.
[3] E.N. Lorenz, J. Atmos. Sci. 26 (1969) 636.
[4] M. Ghil and S. Childress, Topics in Geophysical Fluid Dynamics: Atmospheric Dynamics, Dynamo Theory and Climate Dynamics (Springer, Berlin, 1987).
[5] S.G.H. Philander, El Niño, La Niña, and the Southern Oscillation (Academic Press, San Diego, 1990).
[6] R.A. Madden and P.R. Julian, J. Atmos. Sci 28 (1971) 702.
[7] C.L. Keppenne and M. Ghil, Adaptive spectral analysis and prediction of the Southern Oscillation Index, in: Proc. 15th Annual climate diagnostics workshop (US Department of Commerce, NOAA/Climate Analysis Center, 1991), 30; see also Adaptive filtering and prediction of the Southern Oscillation Index, J. Geophys. Res., sub judice (1992).
[8] J. Eisenfield and M. Witten, eds., Modeling of Biomedical Systems, Proc. 11th Intern. Assoc. Math. Comput.

Simul. (IMACS) World Congress on Systems, Simulation and Scientific Computing (North-Holland, Amsterdam, 1986).
[9] G. Mayer-Kress, ed., Dimensions and Entropies in Chaotic Systems (Springer, Berlin, 1986); L.A. Smith, Phys. Lett. A 113 (1988) 283; D. Ruelle, Proc. R. Soc. London 427A (1990) 241.
[10] R. Kumaresan and D.W. Tufts, Data-adaptive principal component signal processing, in: IEEE Proc. Conf. on Decision and Control (Albuquerque, 1980) 949.
[11] E.R. Pike, J.G. McWhirter, M. Bertero and C. de Mol, IEEE Proc. 131 (1984) 660.
[12] J.M. Colebrook, Oceanol. Acta 1 (1978) 9.
[13] D.S. Broomhead and G.P. King, Physica D 20 (1986) 217.
[14] K. Fraedrich, J. Atmos. Sci. 43 (1986) 419.
[15] R.W. Preisendorfer, Principal Component Analysis in Meteorology and Oceanography, ed. C.D. Mobley (Elsevier, Amsterdam, 1988).
[16] G.H. Golub and C.F. Van Loan, Matrix Computations (Johns Hopkins Univ. Press, 1983).
[17] D.S. Broomhead and G.P. King, On the qualitative analysis of experimental dynamical systems, in: Nonlinear Phenomena and Chaos, ed. S. Sarkar (Adam Hilger, Bristol, 1986).
[18] M. Kimoto, M. Ghil and K.-C. Mo, Spatial structure of the extratropical 40-day oscillation, in: Proc. 8th Conf. on Atmospheric and Oceanic Waves and Stability (American Meteorological Society, Boston, 1991) 17.
[19] R. Vautard and G. Plaut, Low-frequency oscillations and weather regimes in the Northern Hemisphere, in: Proc. ECMWF Workshop on Predictability (European Centre for Medium Range Weather Forecasts, Reading, 1992) in press.
[20] M. Loève, Probability Theory, 3rd ed. (Van Nostrand, Princeton, 1962).
[21] R. Vautard and M. Ghil, Physica D 35 (1989) 395.
[22] E.M. Rasmusson, X. Wang and C.F. Ropelewski, J. Mar. Syst. 1 (1990) 71.
[23] M. Ghil and R. Vautard, Nature 350 (1991) 324.
[24] M.R. Allen, P.L. Read and L.A. Smith, Bidecadal oscillations and the global temperature record, Nature 355 (1992) 686.
[25] M. Ghil and K.-C. Mo, J. Atmos. Sci. 48 (1991a,b) 752, 780.
[26] C. Penland, M. Ghil and K. Weickmann, J. Geophys. Res. 96 (1991) 22659.
[27] J.D. Horel, J. Clim. Appl. Meteor. 23 (1984) 1660.
[28] K. Hasselmann, J. Geophys. Res. 93 (1988) 11005; C. Penland, Mon. Weather Rev. 117 (1989) 2165.
[29] M.G. Kendall and A. Stuart, The Advanced Theory of Statistics (Griffin, London, 1968).
[30] J.D. Farmer and J.J. Sidorowich, Physica D 47 (1991) 373.
[31] M. Casdagli, Physcia D 35 (1989).
[32] J.P. Burg, Maximum entropy spectral analysis, paper presented at the 37th Annual Meeting of the Soc. Explor. Geophys. (Oklahoma City, OK, 1967); also in Modern Spectrum Analysis, ed. D.G. Childers (IEEE Press, New York, 1978) 34.
[33] G.U. Yule, Phil. Trans. R. Soc. Lond. A 226 (1927) 267.
[34] G. Walker, Proc. R. Soc. Lond. A 131 (1931) 518.
[35] D.J. Thomson, Proc. IEEE 70 (1982) 1055.
[36] J.T. Houghton, G.J. Jenkins and J.T. Ephraums, eds., Climate Change, The IPCC Scientific Assessment (Cambridge Univ. Press, Cambridge, 1990).
[37] P.D. Jones, T.M.L. Wigley and P.B. Wright, Nature 322 (1986) 430.
[38] A. Blanc-Lapierre and B. Picinbono, Fonctions Aléatoires (Masson, Paris, 1981).
[39] G.E.P. Box and G.M. Jenkins, Time Series Analysis, Forecasting and Control (Holden-Day, San Francisco, 1970).
[40] G.M. Jenkins and D.G. Watts, Spectral Analysis and its Applications (Holden-Day, San Francisco, 1968).
[41] T.J. Ulrych and T.N. Bishop, Rev. Geophys. Space Phys. 13 (1975) 183.
[42] J.G. Elsner and A.A. Tsonis, Nature 353 (1991) 551.
[43] J.F. Gibson, M. Casdagli, S.E. Eubank and J.D. Farmer, Principal component analysis and derivatives of time series, Physica D, submitted (1991).
[44] M.I. Fortus, Izv., Atmospheric and Oceanic Physics 9 (1973) 34.
[45] P.A. Devijver and J. Kittler, Pattern Recognition: A Statistical Approach (Prentice-Hall, New York, 1982).
[46] U. Grenander and G. Szegö, Toeplitz Forms and Their Applications (University of California Press, Berkeley, 1958).
[47] W.H. Press, B.P. Flannery, S.A. Teukolsky and W.T. Vetterling, Numerical Recipes, The Art of Scientific Computing (Cambridge Univ. Press, New York, 1989).
[48] S. Ulam, On the Monte Carlo method, in: Proc. 2nd Symp. on Large-Scale Digital Calculating Machinery (1951) 207; R.M. Dole and N.D. Gordon, Mon. Weather Rev. 111 (1983) 1567; R.E. Livezey and W.Y. Chen, Mon. Weather Rev. 111 (1983) 46; R. Vautard, K.-C. Mo and M. Ghil, J. Atmos. Sci. 47 (1990) 1926.
[49] J. Theiler, B. Galdrikian, A. Longtin, S. Eubank and J.D. Farmer, Physica D 58 (1992) 77, these Proceedings.
[50] C. Kuo, C. Lindberg and D.J. Thomson, Nature 343 (1990) 709.
[51] P. Pestiaux, I. van der Mersch, A. Berger and J.C. Duplessy, Climatic Change 12 (1988) 9.
[52] P. Yiou, C. Genthon, M. Ghil, J. Jouzel, H. Le Treut, J.M. Barnola, C. Lorius and Y.N. Korotkevitch, J. Geophys. Res. 96 (1991) 20356.
[53] P.D. Jones, Global temperature variations since 1861, in: Long-Term Variability of Pelagic Fish Populations and their Environment, eds. T. Kawasaki, S. Tanaka, Y. Toba and A. Taniguchi (Pergamon, Oxford, 1989).
[54] D. Slepian, Bell Syst. Tech. J. 57 (1978) 1371.
[55] L.J. Lanzerotti, D.J. Thomson, A. Meloni, L.V. Medford and C.G. Maclennan, J. Geophys. Res. 91 (1986) 7417.

[56] C.R. Lindberg, Multiple Taper Spectral Analysis of Terrestrial Free Oscillations, Ph.D. Thesis (University of California, San Diego, Scripps Institution of Oceanography, 1986).
[57] J. Park, C.R. Lindberg and F.L. Vernon III, J. Geophys. Res. 92 (1987) 14027.
[58] D.J. Thomson, Phil. Trans. R. Soc. Lond. A 330 (1990) 601.
[59] D.J. Thomson, Proc. R. Soc. London A 332 (1990) 539.
[60] H. Le Treut, J. Portes, J. Jouzel and M. Ghil, J. Geophys. Res. 93 (1988) 9365.
[61] H. Akaike, Ann. Inst. Statist. Math. 21 (1969) 243; H. Akaike, IEEE Trans. Autom. Control AC-19 (1974) 716.
[62] K.C. Mo and M. Ghil, Interannual oscillations in the 700 Mb geopotential height field over the Northern Hemisphere, submitted (1992).
[63] B.C. Weare and J.N. Nasstrom, Mon. Wea. Rev. 110 (1982) 481; K.-M. Lau and P.H. Chan, Mon. Weather Rev. 113 (1985) 1889.
[64] J.D. Neelin, M. Latif, M.A.F. Allaart, M.A. Cane, U. Cubasch, W.L. Gates, P.R. Gent, M. Ghil, C. Gordon, N.C. Lau, C.R. Mechoso, G.A. Meehl, J.M. Oberhuber, S.G.H. Philander, P.S. Schopf, K.R. Sperber, A. Sterl, T. Tokioka, J. Tribbia and S.E. Zebiak, Climate Dyn. 7 (1992) 73.

Physica D 58 (1992) 127–137
North-Holland

PHYSICA D

Comparison of algorithms calculating optimal embedding parameters for delay time coordinates

Th. Buzug and G. Pfister
Institut für Angewandte Physik, Universität Kiel, W-2300 Kiel, Germany

Received 30 August 1991
Revised manuscript received 23 January 1992
Accepted 15 February 1992

The success of noise reduction processes and forecasting methods as well as accurate calculations of fractal dimensions and Lyapunov exponents from scalar time series depends strongly on the quality of the reconstructed phase space. We present a comparison of four methods, which simultaneously estimate the two embedding parameters (delay time τ and sufficiently large embedding dimension $\dim_E$) for Takens' delay time coordinates. Recently we introduced a global geometrical measure, the fill-factor, and a local dynamical measure, the averaged integral local deformation. We will discuss these methods briefly and compare them to the topological wavering-product. In addition a simple algorithm is presented, which observes the spreading of trajectories at the transition from $\dim_E$ to $\dim_E + 1$ and gives the opportunity to estimate the correlation entropy K_2.

We applied these algorithms to experimental data series measured from a rotational Taylor–Couette experiment and verified the quality of the obtained embedding parameters by the estimation of correlation dimensions for different reconstructed attractors.

1. Introduction

In many experimental situations the information about the system is contained in a single scalar time series. In the Taylor–Couette experiment e.g. we typically record one observable which is the radial or axial component of the local velocity of the flow. The estimation of the dynamical variables like fractal dimensions and Lyapunov exponents requires a proper reconstruction of an attractor in phase space, in order to extract all relevant components of the dynamics. We will show how an improper choice of the embedding parameters can falsify the results for the dynamical quantities.

N.H. Packard et al. [1] suggested the calculation of successive derivatives of the scalar time series as independent coordinates for a phase space reconstruction. A faster method was published by F. Takens [2] who proposed a reconstruction from delay time coordinates which is commonly used by almost all experimentalists in this field. As a conclusion from his theorem, one can estimate fractal dimensions and Lyapunov exponents of a complex system containing many variables (e.g. the dimension of phase space of Navier–Stokes equations is infinite), when only one is measured.

We briefly describe Takens' method of reconstruction which we use throughout this paper. Let $\xi(t_k)$ the scalar time series, where $k \in K$ and $K := \{k \in N_0;\ k < N_{dat}\}$. N_{dat} is the number of data points, ξ is the observable. State vectors in the reconstructed phase space are given by

$$x(t_s) = \begin{pmatrix} \xi(t_s) \\ \xi(t_s + \tau) \\ \vdots \\ \xi(t_s + \tau(\dim_E - 1)) \end{pmatrix}, \qquad (1)$$

where $s \in S$, $t_s = sT_a$ and $S \in \{\mathbb{N}_0;\ s < N_{dat} -$

0167-2789/92/$05.00 © 1992 – Elsevier Science Publishers B.V. All rights reserved

$\tau/T_a(\dim_E - 1)\}$. $\dim_E$ is the embedding dimension, T_a is the sampling time of the continuous experimental signal and τ is the delay time which is a multiple of T_a. According to Takens' theorem the projection of the orbit of a mapping on an n-dimensional manifold onto a time-delay constructed orbit in $\mathbb{R}^{\dim_E}$ is one to one if $\dim_E \geq 2n + 1$. The delay time τ can be chosen almost arbitrarily. This is correct for time series without noise, with an infinite number of data points and no restriction in resolution; however, none of these conditions holds for experimental data sets. The substantial influence of the delay time on the estimation of dynamical variables from experimental time series is shown in [3–6] and examples will be shown below.

For practical purposes it is important to know the lowest embedding dimension $\dim_E$ which fulfils the condition stated above. This holds especially for algorithms working with matrices where the number of rows and columns depends on $\dim_E$, e.g. calculation of Lyapunov spectra and noise reduction algorithms.

A current method to find the embedding parameters makes use of the redundancy criterion, which measures a more general dependence of coordinates than the autocorrelation function. A. Fraser [7] derived this criterion from mutual information analysis [8]. D.S Broomhead and G.P. King [9] used singular-value-decomposition of the trajectory matrix to obtain the number of nonzero singular values, which yield a sufficiently large embedding dimension. A discussion of these methods can be found in [7].

Below we will only describe algorithms which try to yield an optimal delay time and proper embedding dimension simultaneously and can be implemented even on small computers. We applied the wavering-product algorithm and three methods proposed by us to experimental data series from a rotational Taylor–Couette experiment. The quality of the obtained embedding parameters are verified by the estimation of correlation dimensions for different reconstructed attractors.

2. Algorithms

2.1. Wavering-product

W. Liebert et al. [6] proposed a method which is guided by topological considerations. They focus on neighbourhood relations of points on the attractor: Inner points remain inner points and points within the boundary defining the neighbourhood remain boundary points at the transition from $\dim_E$ to $\dim_E + 1$.

To reveal violation of this property they give two expressions:

$$Q_1(i, k) := \frac{\mathrm{dist}_{\dim_E+1}(i,\ j(k, \dim_E))}{\mathrm{dist}_{\dim_E+1}(i,\ j(k, \dim_E + 1))}\ , \qquad (2)$$

which is the ratio of distances measured in $\mathbb{R}^{\dim_E+1}$ between the reference point $\boldsymbol{x}_i$ and the point $\boldsymbol{x}_{j(k,\dim_E)}$ (the kth neighbour in $\mathbb{R}^{\dim_E}$), and between the reference point and the point $\boldsymbol{x}_{j(k,\dim_E+1)}$ (the kth nearest neighbour in $\mathbb{R}^{\dim_E+1}$), and

$$Q_2(i, k) := \frac{\mathrm{dist}_{\dim_E}(i,\ j(k, \dim_E))}{\mathrm{dist}_{\dim_E}(i,\ j(k, \dim_E + 1))}\ . \qquad (3)$$

Notice that the distances in $Q_2(i, k)$ are calculated in $\mathbb{R}^{\dim_E}$. Fig. 1 shows a situation where a limit cycle is projected from $\mathbb{R}^2$ to $\mathbb{R}^1$.

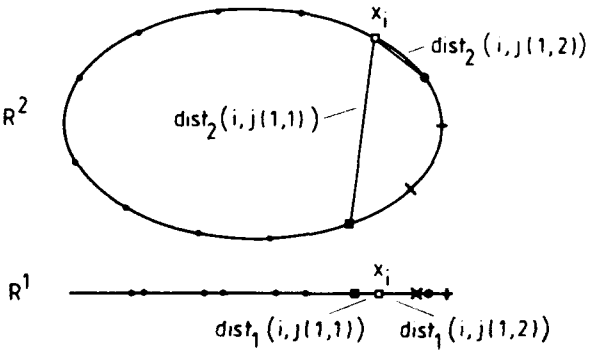

Fig. 1. Schematic representation of the calculation of the wavering-product. It is shown how neighbouring points of the reference point $\boldsymbol{x}_i$ rearrange by the transition from $\mathbb{R}^2$ to $\mathbb{R}^1$. The distances used to measure the degree of violation of the topological properties are marked.

W. Liebert et al. define the averaged wavering-product as

$$\langle W(\dim_E, \tau)\rangle := \log\left(\frac{1}{N_{ref}} \sum_{i=1}^{N_{ref}} \left(\prod_{k=1}^{N_{nb}} Q_1(i,k)\, Q_2(i,k)\right)^{1/2N_{nb}}\right) \tag{4}$$

where N_{nb} is the number of neighbouring points and N_{ref} the number of reference points. For chaotic attractors the explicit τ-dependence can be eliminated by normalizing the wavering-product to $\langle W(\dim_E, \tau)\rangle / \tau$. A minimum of this normalized wavering-product as a function of τ yields the optimum delay time. A sufficiently large embedding dimension is obtained from the convergency of $\langle W(\dim_E, \tau)\rangle / \tau$ to zero. For a detailed discussion of the wavering-product see [6, 10].

2.2. Fill-factor

The fill-factor method which uses purely geometrical considerations guarantees a maximum distance of trajectories. Fig. 2 sketches the basic idea of the fill-factor algorithm using an attractor measured from Taylor–Couette flow. In fig. 2a the trajectories in this two-dimensional reconstruction are maximally separated and the phase space is optimum utilized by data points, while in fig. 2b the attractor tends to collapse. To give a measure of the utilization of a $\dim_E$-dimensional phase space one defines a volume of a parallelepiped spanned by $\dim_E + 1$ points $\boldsymbol{r}_j$ chosen arbitrarily, where $j = 0, \ldots, \dim_E$.

Let $\boldsymbol{r}_0$ a reference point and calculate the displacement vectors $\boldsymbol{d}_p = \boldsymbol{r}_0 - \boldsymbol{r}_p$, where $p = 1, \ldots, \dim_E$. For a proper reconstruction the mean value of $V_{\dim_E, \boldsymbol{r}_0}(\tau) = |\det(\boldsymbol{d}_1, \ldots, \boldsymbol{d}_{\dim_E})|$ is larger than for an insufficient reconstruction if averaged over a number of $(\dim_E + 1)$-tuples $(\boldsymbol{r}_0, \ldots, \boldsymbol{r}_{\dim_E})$. Based on this idea we define as a measure the fill-factor:

$$f_{\dim_E}(\tau) := \log\left(\frac{(1/N_v) \sum_{k=1}^{N_v} V_{\dim_E, \boldsymbol{r}_0(k)}(\tau)}{(\max_{k\in K}\{\xi(t_k)\} - \min_{k\in K}\{\xi(t_k)\})^{\dim_E}}\right). \tag{5}$$

N_v is the number of chosen tuples $(\boldsymbol{r}_0, \ldots, \boldsymbol{r}_{\dim_E})$. The first maxima of $f_{\dim_E}(\tau)$ in

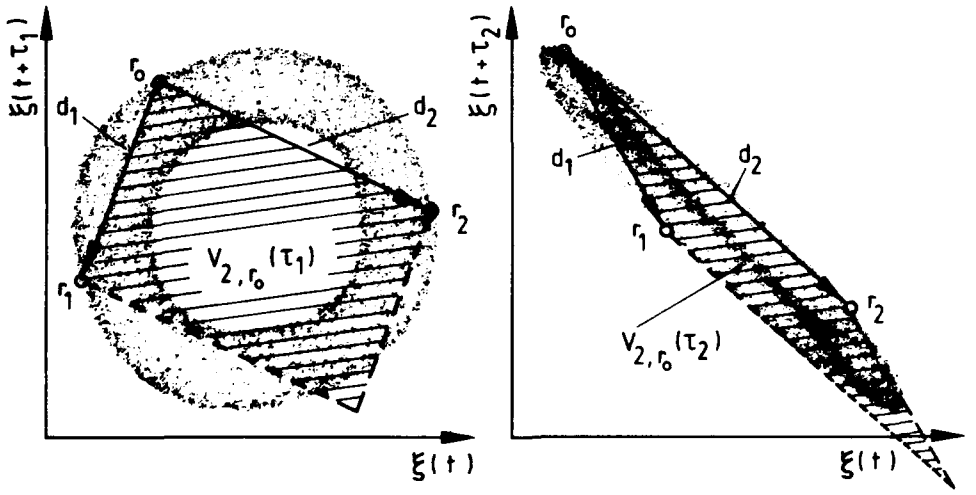

Fig. 2. Two-dimensional schematic representation of the fill-factor algorithm. Left: a proper reconstruction: trajectories are maximum separated. Right: an improper reconstruction: the attractor tends to collapse. r_0, r_1 and r_2 are arbitrarily chosen points on the attractor. For the delay time $\tau = \tau_1$ the mean value of $V_{2,r_0}(\tau) = |\det(\boldsymbol{d}_1, \boldsymbol{d}_2)|$ is larger than for $\tau = \tau_2$ if averaged over a sufficiently large number of triplets (r_0, r_1, r_2).

the interval $0 < \tau < T_c/2$ provide proper choices of the delay time (T_c is the mean recurrence time of the system, i.e. the reciprocal value of the dominant frequency obtained from the power spectrum). For increasing embedding dimensions one recognizes that the qualitative structure of the fill-factor as a function of delay time is preserved and the curves are spaced equidistantly. This behaviour may be used to estimate the sufficiently large embedding dimension. For a detailed description of this algorithm see [5, 11].

2.3. Integral local deformation

The third method considered here describes the local dynamical behaviour of points on the attractor and gives a measure of the homogeneity of the local flow. For real physical systems it is a reasonable assumption that in the original phase space, points on neighbouring trajectories remain neighbouring for small evolution times t_{ev} and are only separated exponentially according to a positive Lyapunov exponent in the chaotic case. We require that this topological behaviour must be preserved in a proper reconstruction. Fig. 3 sketches the idea of this method. It shows an intersection of trajectories in a two-dimensional embedding. At the intersection the flow is ambiguous, in contradiction to the physical understanding. The evolution of the distance $\mathrm{dist}^{t}_{\dim_E,j}(\tau)$ between the reference point $\boldsymbol{x}_j$ and the center of mass of neighbouring points A_j measures the "degree" of noncausal behaviour of the dynamics. For the pictures shown below, we calculate the absolute growth of successive $\mathrm{dist}^{t=q\,t_{ev}}_{\dim_E,j}(\tau)$ with

$$\mathrm{DIST}^{q}_{\dim_E,j}(\tau) := \mathrm{dist}^{t=q\,t_{ev}}_{\dim_E,j}(\tau) - \mathrm{dist}^{t=0}_{\dim_E,j}(\tau) \tag{6}$$

where $q = 1, \ldots, Q$ and $Q = 4$.

To measure the homogeneity of the local flow we define the averaged integral local deformation over N_{ref} reference points

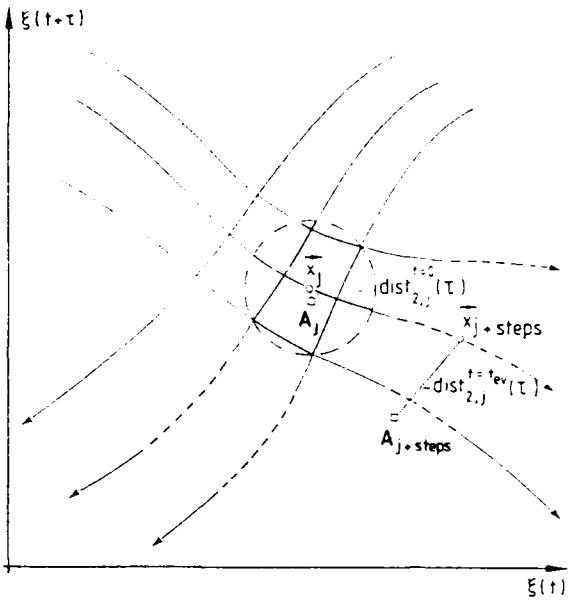

Fig. 3. Two-dimensional schematic representation of measuring homogeneity of the local flow. The measured quantity is the growth rate of the distance from the reference point $\boldsymbol{x}_j$ to the center of mass $\boldsymbol{A}_j$ in time, that is $\|\boldsymbol{x}_{j+\mathrm{steps}} - \boldsymbol{A}_{j+\mathrm{steps}}\| - \|\boldsymbol{x}_j - \boldsymbol{A}_j\|$, where steps $= t_{ev}/T_a$. The dashed segments of the trajectories contain the neighbouring points of $\boldsymbol{x}_j$ at j + steps.

$$\langle \mathrm{ILD}_{\dim_E}(\tau)\rangle := \frac{t_{ev}\sum_{j=1}^{N_{ref}}\left\{\sum_{q=1}^{Q}\left[\mathrm{DIST}^{q-1}_{\dim_E,j}(\tau) + \mathrm{DIST}^{q}_{\dim_E,j}(\tau)\right]\right\}}{2N_{ref}T_a(\max_{k\in K}\{\xi(t_k)\} - \min_{k\in K}\{\xi(t_k)\})} \tag{7}$$

One finds proper delay times at minima of $\langle \mathrm{ILD}_{\dim_E}(\tau)\rangle$, and a sufficiently large embedding dimension is estimated from the convergency at optimal delay times when $\dim_E$ is increased.

For strange attractors the coordinates become more and more uncorrelated as τ is increased so that the local expansion rates of trajectories increase. In first approximation $\langle \mathrm{ILD}_{\dim_E}(\tau)\rangle$ shows a proportionality in τ. So we normalize $\langle \mathrm{ILD}_{\dim_E}(\tau)\rangle$ with τ/T_a. For a comprehensive explanation of this method see [11].

2.4. Simple spreading of trajectories

The last procedure also yields a maximum separation of trajectories. We present a local

measure which additionally provides the correlation entropy K_2. For each pair $(\tau, \dim_E)$ one counts the neighbouring points of a reference point within a given radius R. This is repeated for a sufficiently large number of reference points. With the same set of reference points this procedure is done for $(\tau, \dim_E + 1)$ so we can focus on the ratio $P_{\dim_E}(\tau) := \langle N_{\dim_E+1}(\tau)\rangle / \langle N_{\dim_E}(\tau)\rangle$, where $\langle N_{\dim_E}(\tau)\rangle$ is the averaged number of neighbouring points. At an optimum delay time, i.e. a maximum distance of trajectories, $P_{\dim_E}(\tau)$ will be small, due to the loss of many neighbouring points at the transition from $\dim_E$ to $\dim_E + 1$. For embedding dimensions larger than the first sufficient one, the phase space cannot be blown up in all directions, i.e. no more information can be obtained by adding another coordinate. So the plot of $P_{\dim_E}(\tau)$ as a function of τ will lose significant minima that appear for small embedding dimensions and will converge towards an accumulation line. The relevant information about the delay time is contained in $P_{\dim_E}(\tau)$ when $\dim_E$ is too small and $\dim_E + 1$ sufficiently large. Here the loss of neighbouring points is maximal, due to a maximum separation of trajectories, resulting in minima in $P_{\dim_E}(\tau)$. For an example we show in fig. 4 the calculation of the spreading of trajectories for the Duffing attractor [12] ($\ddot{x} + D\dot{x} + x + x^3 = F \cos \omega t$, where $D = 0.2$, $F = 40$ and $\omega = 1$). The sufficiently large embedding dimension is $\dim_E = 4$ and the relevant minimum is indicated by arrow A ($\tau/T_c \approx 0.07$). If the embedding dimension is too small then a minimum value of $P_{\dim_E}(\tau)$ may give misleading results (arrow B, $\tau/T_c \approx 0.25$).

We may estimate the correlation entropy or order-two Kolmogorov entropy [13] from the logarithm of $P_{\dim_E}(\tau)$ versus delay time. K_2 is defined as

$$K_2 = -\lim_{\dim_E \to \infty} \lim_{\tau \to 0} \frac{1}{\tau} \log \frac{C_2^{\dim_E+1}(\tau)}{C_2^{\dim_E}(\tau)} ; \qquad (8)$$

$C_2^{\dim_E}(\tau)$ is the order-two correlation integral [14].

From the definition of $P_{\dim_E}(\tau)$ we find

$$P_{\dim_E}(\tau) = \frac{\langle N_{\dim_E+1}(\tau)\rangle}{\langle N_{\dim_E}(\tau)\rangle}$$

$$= \frac{1}{N_{dat} N_{ref}} \sum_{i=0}^{N_{dat}-1} \sum_{j=1}^{N_{ref}} \sigma(R - \|x_i - x_j\|_{\dim_E+1})$$

$$\times \left(\frac{1}{N_{dat} N_{ref}} \sum_{i=0}^{N_{dat}-1} \sum_{j=1}^{N_{ref}} \sigma(R - \|x_i - x_j\|_{\dim_E}) \right)^{-1}$$

$$\Rightarrow P_{\dim_E}(\tau) = \frac{C_2^{\dim_E+1}(\tau)}{C_2^{\dim_E}(\tau)} . \qquad (9)$$

$\|\cdot\|_{\dim_E}$ denotes the maximum norm in $\dim_E$-dimensional embedding, σ is the Heaviside function and N_{ref} is the number of arbitrarily chosen reference points. We estimate K_2 from a least squares fit of the slopes of the curves $\log_2(P_{\dim_E}(\tau))$ versus delay time for small τ and higher embedding dimensions.

The estimated entropy is too small, compared to the largest Lyapunov exponent ($\lambda_1 = 1.0$ bits/orbit). This may be caused by a too small number of data points and an improper choice of the radius R ($N_{dat} = 32768$, $R = 3\%$ of the attractor extension). This point needs further investigation.

This method is similar to the one given in [15] where a minimum of the logarithmic correlation integral versus delay time is used for an optimum embedding. With our extension one may identify whether the attractor is a projection from a higher dimension, due to the observation of the transition from $\dim_E$ to $\dim_E + 1$.

We stress the point that for chaotic time series one has to use the smallest delay time where $f_{\dim_E}(\tau)$ ($\langle \mathrm{ILD}_{\dim_E}(\tau)\rangle$, $\langle W(\dim_E, \tau)\rangle$, $\log_2(P_{\dim_E}(\tau))$) has its first maximum (minimum), even when the methods seem to give better values at larger delays. For high embedding dimensions the embedding window $\tau(\dim_E - 1)$ becomes so large that the first and last coordinate may be totally uncorrelated.

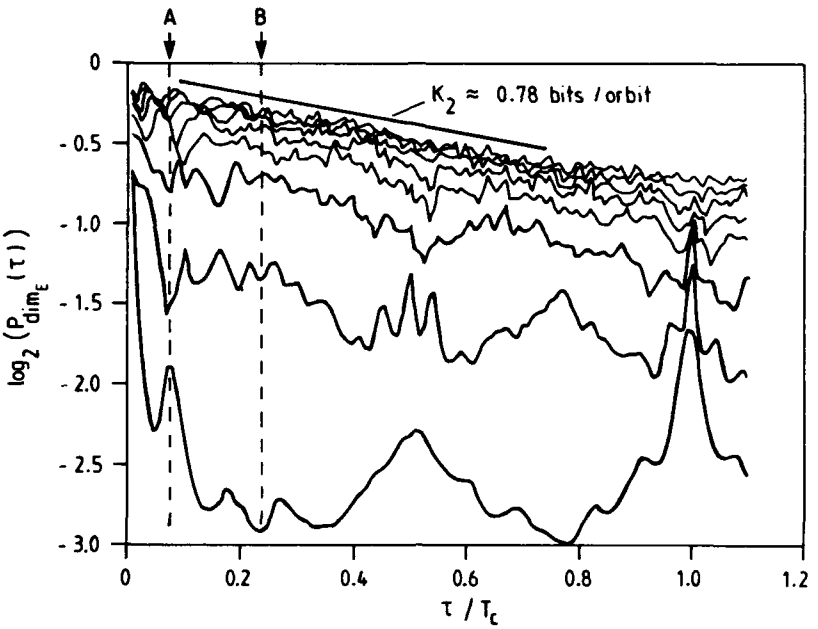

Fig. 4. $\log_2(P_{\dim_E}(\tau))$ for the Duffing attractor. The line indicates $K_2 = 0.78$ bits/orbit. The value for the metric entropy is $h = 1$ bits/orbit. Arrows A and B indicate proper and improper delay times, respectively.

3. Comparison of methods

The goal of our paper is the development of methods applicable to experimental data. Therefore we tested the methods with experimental data measured in rotational Taylor–Couette flow. In order to present two different types of time series we investigated a ten-vortex state showing quasiperiodic dynamics and a two-vortex state showing chaotic behaviour. The physical quantity measured was the axial velocity component obtained with a Laser–Doppler-velocimeter. For signal processing in a digital computer the analogue signal was converted with a resolution of 10 bit. Details of the experiment and the data processing can be found in [16–18].

3.1. *Quasiperiodic attractor*

In order to test the quality of our results we apply all four methods to an attractor with a well known structure, a two-torus. The periods were $T_1 = 1.54$ s and $T_2 = 0.22$ s, respectively with an amplitude ratio of 3.6. We took T_1 as T_c in figs. 5a–5d. The sampling time T_a was 0.02 s in this case. The number of reference points was $N_{ref} = 600$ and the number of data points was $N_{dat} = 32768$.

In fig. 5a–5d the four measures for a proper delay time and embedding dimension are shown as a function of the normalized delay time for various embedding dimensions. To illustrate the significance of the measures we plotted the Poincaré sections of the torus for 9 different delay times in fig. 6. The fill-factor's ($f_{\dim_E}(\tau)$) first two maxima be found at $\tau/T_c \approx 0.05$ and $\tau/T_c \approx 0.09$ in accordance with the first two minima of the integral local deformation ($\langle \mathrm{ILD}_{\dim_E}(\tau) \rangle$), wavering-product ($\langle W(\dim_E, \tau) \rangle$) and spreading ($\log_2(P_{\dim_E}(\tau))$). We show in fig. 6 that one gets a well-spanned torus when using these delays. A comparison between fig. 5 and fig. 6 shows the significance of the relative extrema. We want to stress the point, that proper and improper delay times may be close to each other as can be seen in fig. 6 for $\tau/T_c \approx 0.05$ and $\tau/T_c \approx 0.06$, respectively. For the higher frequency the difference in the delay time of $\tau/T_c = 0.01$ gives already a

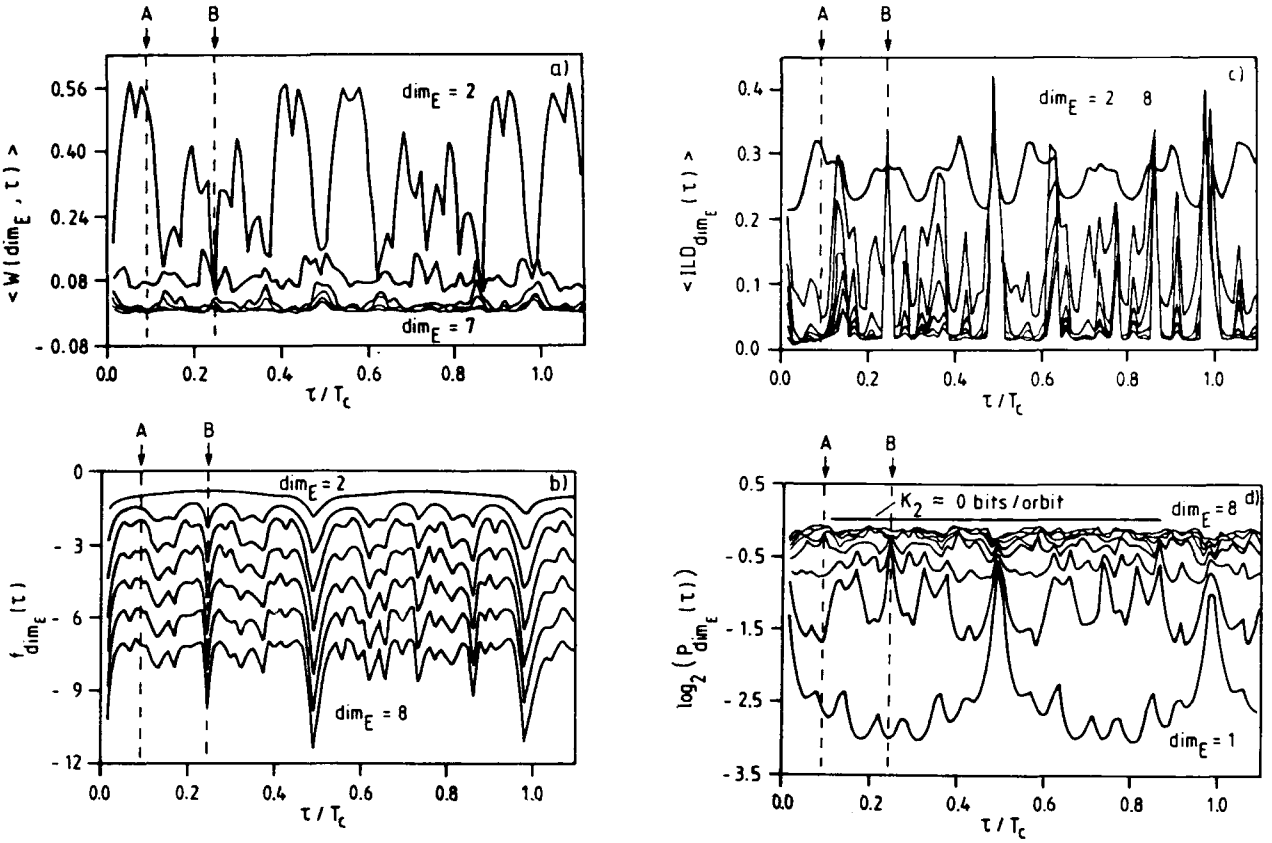

Fig. 5. (a) wavering product $\langle W(\dim_E, \tau)\rangle$, (b) fill-factor $f_{\dim_E}(\tau)$, (c) integral local deformation $\langle \mathrm{ILD}_{\dim_E}(\tau)\rangle$ and (d) spreading $\log_2(P_{\dim_E}(\tau))$ for the reconstructed two-torus from the Taylor–Couette experiment. Arrow (A) indicates a proper, arrow (B) indicates an improper delay time. Sufficient large embedding dimension: $\dim_E = 4$. The entropy $K_2 = 0$ is given by the slope of the line in (d).

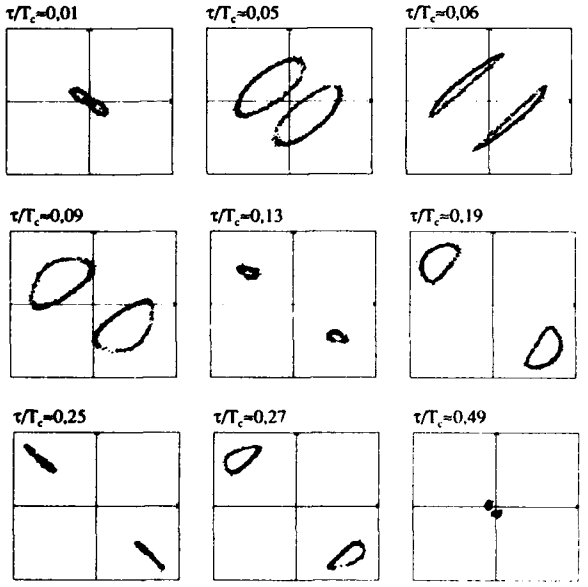

Fig. 6. Poincaré sections for various delay times for the two-torus.

significant phase shift and can cause a collapse of one coordinate.

From the slope of the accumulation line of $\log_2(P_{\dim_E}(\tau))$ versus delay time for higher $\dim_E$ we calculate the correlation entropy $K_2 = 0$ bits/orbit, as expected for a quasiperiodic state.

From the convergency of the four measures as a function of embedding dimension one can estimate $\dim_E = 4$ to be sufficiently large.

For two delay times identified as a proper (arrow A in fig. 5, $\tau/T_c \approx 0.09$) and as an improper delay time (arrow B in fig. 5, $\tau/T_c \approx 0.25$) we calculated the correlation dimension according to Grassberger and Procaccia [14]. The result is given in fig. 7. Fig. 7a shows the local slopes from the double logarithmic plot of the correlation integral versus radius R for the proper delay time. The plot reveals the intrinsic structure of

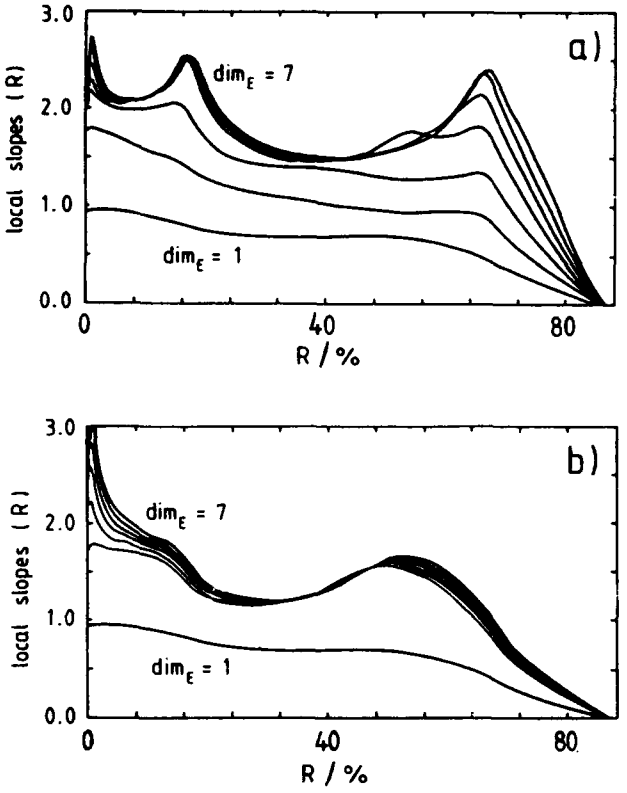

Fig. 7. Local slopes calculated from the double logarithmic correlation integral vs. radius R. The radius is given in percent of the total extention of the attractor. (a) proper reconstruction ($\tau/T_c \approx 0.09$): the local slopes reveal the structure of the torus. (b) improper reconstruction ($\tau/T_c \approx 0.25$): a relevant scaling region for an estimation of the correlation dimension is not found.

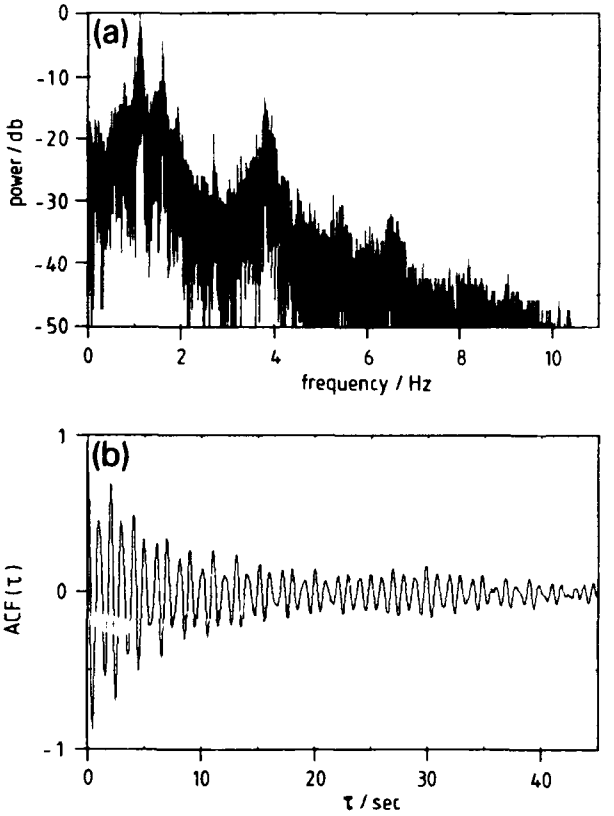

Fig. 8. (a) power spectrum and (b) autocorrelation function for a chaotic time series obtained from the Taylor–Couette experiment.

the torus. D_2 converges for $\dim_E \geq 4$. For the improper delay time no relevant scaling region for the dimension can be found as can be seen in fig. 7b.

3.2. Chaotic attractor

As a second example we examined a two-vortex state showing chaotic dynamics. The number of reference points was $N_{ref} = 600$ and the number of data points was $N_{dat} = 16384$. The sampling time was set to $T_a = 0.03$ s. Fig. 8 shows the velocity power spectrum and the corresponding autocorrelation function. The dominant frequency was 1.11 Hz so we took $T_c = 0.9$ s in this example.

The fill-factor as well as the integral local deformation yield proper delay times at $\tau/T_c \approx 0.17$ (indicated by arrow B) and improper delay times at $\tau/T_c \approx 0.03$ and $\tau/T_c \approx 0.2$ (indicated by arrows A and C). The first minimum of $\langle \mathrm{ILD}_{\dim_E}(\tau) \rangle$ (τ/T_c from 0.1 to 0.17) is wider than the corresponding maximum of the fill-factor. Obviously the local flow of the strange attractor is smooth with maximum utilization in the phase space. The sufficiently large embedding dimension is found to be $\dim_E > 5$. The normalized wavering-product $\langle W(\dim_E, \tau) \rangle / \tau$, shown in fig. 9a, yields only a less significant minimum for $\dim_E = 7$. Fig. 9d shows the spreading of trajectories at the transition from $\dim_E$ to $\dim_E + 1$ for embedding dimensions 1 to 6. Although $\log_2(P_{\dim_E}(\tau))$ versus delay time has significant extrema we must say that this method fails, because one cannot estimate a sufficiently large embedding dimension and the minima of

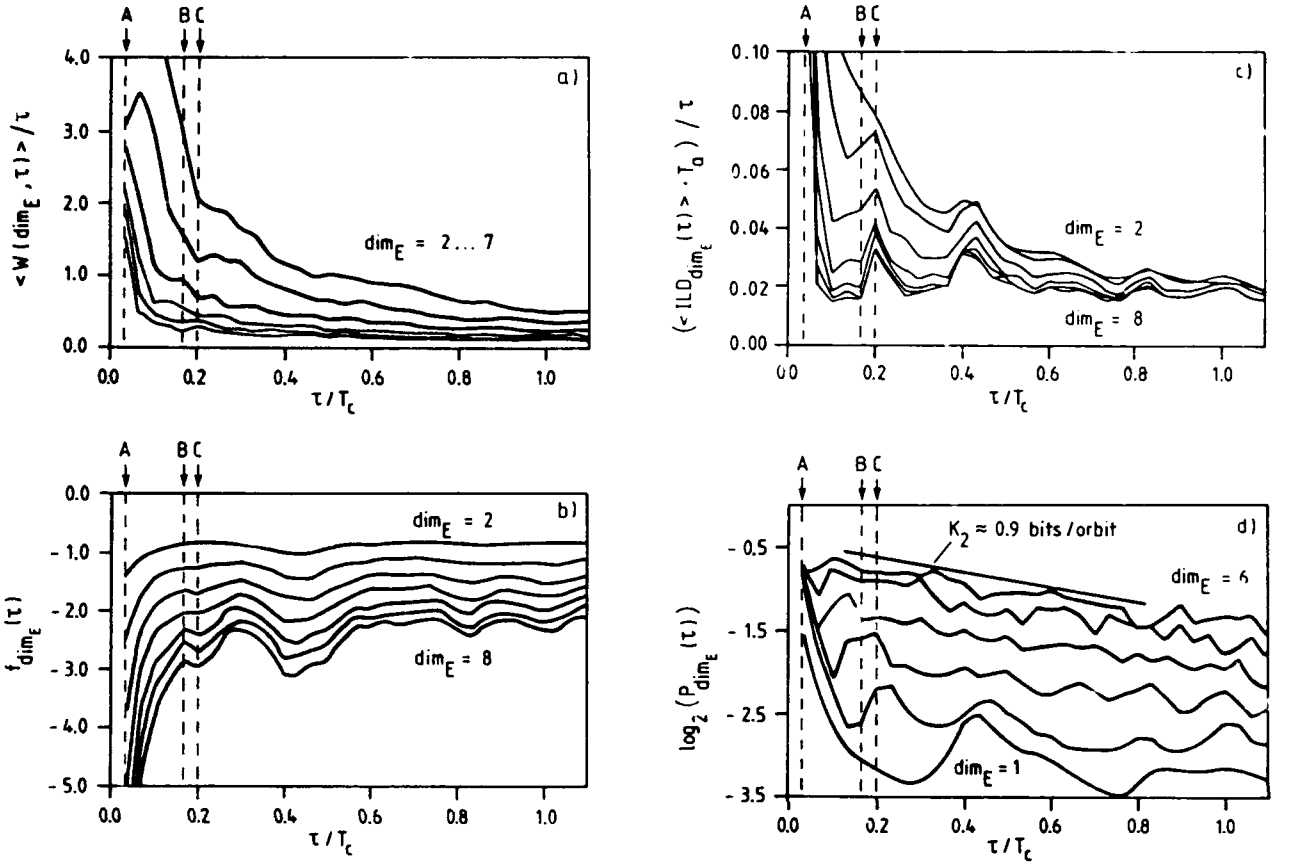

Fig. 9. (a) normalized wavering product, (b) fill-factor, (c) normalized integral local deformation and (d) spreading $\log_2(P_{\dim_E}(\tau))$ for the reconstructed, strange attractor from the Taylor–Couette experiment. Arrow (A) marks a too small delay time ($\tau = T_a$). Arrow (B) marks a proper delay time ($\tau/T_c \approx 0.17$) and arrow (C) an improper delay time ($\tau/T_c \approx 0.2$). The normalized wavering product shows less significant extrema in this region. The slope of $\log_2(P_{\dim_E}(\tau))$ is fitted for embedding dimensions 5 and 6. This rough estimation yields $K_2 \approx 0.9$ bits/orbit.

$\log_2(P_{\dim_E}(\tau))$ vary when $\dim_E$ is increased. This may be caused by a too small number of data points which gives insufficient statistics for higher embedding dimensions. The estimated entropy is $K_2 = 0.9$ bits/orbit.

For the three delay times indicated by A, B and C, respectively, in fig. 9 we calculated the correlation dimension. The results are shown in fig. 10 where the local slopes are plotted as a function of $\log(R)$. As expected from fig. 9 the calculation using $\tau/T_c \approx 0.03$ (arrow A) as delay time does not give any scaling region in the dimension plot fig. 10a. For the proper delay time $\tau/T_c \approx 0.17$ (arrow B) one finds a broad scaling region, yielding a correlation dimension $D_2 \approx 3.1$. The scaling region obtained for the delay time $\tau/T_c \approx 0.2$ (arrow C) becomes smaller but gives approximately the same result for D_2 as before.

3.3. Noise and computer time consumption

Due to its global character the fill-factor is the measure which shows the best robustness against noise. Furthermore, the computer time consumption for this algorithm is low because it does not need any searching and sorting procedures for neighbouring points. For a typical range of delay times and embedding dimensions we estimate the calculation of the fill-factor to be 3 times faster than the simple spreading algorithm, 10 times faster than the averaged inte-

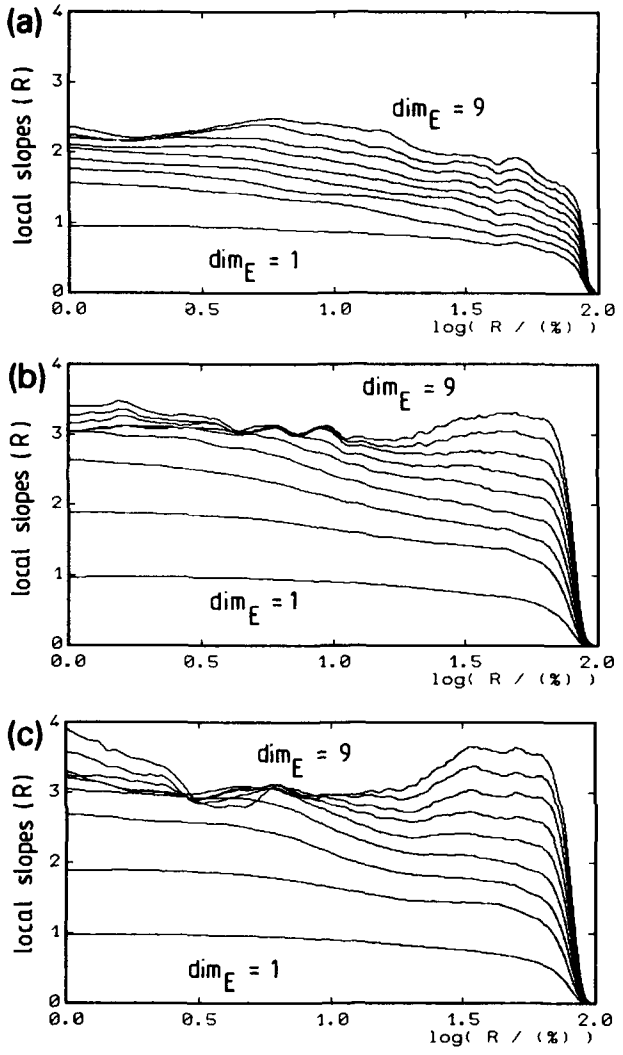

Fig. 10. Local slopes calculated from the double logarithmic correlation integral vs. logarithmic radius R. The radius is given in percent of the total extention of the attractor. (a) improper reconstruction ($\tau/T_c \approx 0.03$): the local slopes do not reveal the structure of the strange attractor. No scaling region is obtained. (b) proper reconstruction ($\tau/T_c \approx 0.17$): one finds a broad scaling interval for an estimation of $D_2 = 3.1$. (c) improper reconstruction ($\tau/T_c \approx 0.2$): the scaling interval becomes smaller.

gral local deformation and about 20 times faster than the averaged wavering-product. One must take this into account when implementing the algorithms on small laboratory computers. We used linearly sorted data set arrays to search for neighbouring points. One may certainly save computation time by using more efficient searching algorithms.

4. Conclusion

The success of the estimation of fractal dimensions depends strongly on the quality of the embedding parameters. We showed that even adjacent delay times yield proper and improper attractor reconstructions.

In this paper we compared four algorithms which provide a proper delay time for the reconstruction of a phase space and give an estimate for a sufficiently large embedding dimension simultaneously. The algorithms were applied to experimental time series and the measures were calculated for several embedding dimensions and a wide range of delay times. By calculating the correlation dimension of two attractors which were reconstructed with proper and improper delay times we could verify a posteriori the common sense criterions used for these algorithms.

References

[1] N.H. Packard, J.P. Crutchfield, J.D. Farmer and R.S. Shaw, Phys. Rev. Lett. 45 (1980) 712.
[2] F. Takens, Lecture Notes in Math. 898 (Springer Verlag, Warwick, 1980) p. 230.
[3] A. Destexte, J.A. Sepulchre and A. Babloyantz, Phys. Lett. A 132 (1988) 101.
[4] H. Haucke, R. Ecke and J. Wheatley, in: Dimensions and Entropies in Chaotic Systems, ed. G. Mayer-Kress (Springer Verlag, Berlin, 1986) p. 198.
[5] Th. Buzug, T. Reimers and G. Pfister, Europhys. Lett. 13 (1990) 605.
[6] W. Liebert, K. Pawelzik and H.G. Schuster, Europhys. Lett. 14 (1991) 521.
[7] A. Fraser, Physica D 34 (1989) 391.
[8] A. Fraser, in: Dimensions and Entropies in Chaotic Systems, ed. G. Mayer-Kress (Springer Verlag, Berlin, 1986) p. 82.
[9] D.S. Broomhead and G.P. King, Physica D 20 (1986) 217.
[10] W. Liebert, Chaos und Herzdynamik, Reihe Physik Bd. 4 (Harri Deutsch, Frankfurt am Main, 1991).
[11] Th. Buzug and G. Pfister, Phys. Rev. A 45 (1992) 7073.
[12] G. Duffing, Erzwungene Schwingungen bei veränderlicher Eigenfrequenz und ihre technische Bedeutung, (Vieweg, Braunschweig, 1918).

[13] J.G. Caputo and P. Atten, Phys. Rev. A 35 (1987) 1311.
[14] P. Grassberger and I. Procaccia, Physica D 9 (1983) 189.
[15] W. Liebert and H.G. Schuster, Phys. Lett. A 142 (1989) 107.
[16] G. Pfister, H. Schmidt, K.A. Cliffe and T. Mullin, J. Fluid Mech. 191 (1988) 1.
[17] Th. Buzug, T. Reimers and G. Pfister, in: Nonlinear Evolution of Spatio-Temporal Structures in Dissipative Continuous Systems, eds. F.H. Busse and L. Kramer (Plenum Press, New York, 1990) p. 7.
[18] G. Pfister, Th. Buzug and N. Enge, (1991), Physica D 58 (1992) 441, these Proceedings.

Physica D 58 (1992) 138–152
North-Holland

PHYSICA D

Problems in estimating dynamics from data

Eric J. Kostelich
Department of Mathematics, Arizona State University, Tempe, AZ 85287, USA

Received 8 October 1991
Revised 25 February 1992
Accepted 2 March 1992

This paper discusses some difficulties in estimating dynamics from time-delay embeddings of experimental data that can be characterized as low-dimensional. A new procedure is described to reduce noise by exploiting the properties of saddle periodic orbits on the reconstructed attractor.

1. Introduction

There are several different approaches to noise reduction in time series data whose underlying dynamics can be described as low dimensional. Kostelich and Yorke [1,2] outlined a procedure that uses an approach originally suggested by Eckmann and Ruelle [3] for computing Lyapunov exponents. Farmer and Sidorowich [4] describe another method for use when the dynamics are known. Schreiber and Grassberger [5] describe a simple time-series based approach. Cawley and Hsu [6] have suggested an approach based on projecting trajectories onto planes that locally approximate the manifold containing the attractor[#1].

Most of these methods involve the estimation of a derivative from the data or in some way require a least squares estimate of the location of some portion of the attractor. This paper describes some of the problems inherent in the estimation of dynamics from data, regardless of the type of model used to approximate the dynamics. These difficulties may arise from the fractal structure of the attractor and errors in all the observations. The problems persist regardless of the amount of available data and affect one's ability to determine an accurate local model of the dynamics, even when an accurate model should be obtainable in principle. These issues are discussed in section 2.

Many of these problems can be circumvented by using as much dynamical information as possible in the formulation of the statistical relationship between the observations. One attempt to do this involves the use of recurrent orbits to derive an accurate linear model of the dynamics in the vicinity of saddle periodic orbits on the attractor. Section 3 describes the method and its application to two experimental data sets previously analyzed in [2].

2. Statistical estimation of dynamical information

A standard procedure in the analysis of chaotic experimental data is to reconstruct the attractor using the method of time delays [8]. Let $\{s_i\}_{i=1}^{N}$ be a time series of N scalar observations, sampled at equal intervals. The reconstructed attrac-

[#1] The reprint collection by Hao [7] contains several articles on the analysis of low dimensional chaotic experimental data.

0167-2789/92/$05.00 © 1992–Elsevier Science Publishers B.V. All rights reserved

tor consists of points of the form

$$\boldsymbol{x}_i = (s_i, s_{i+\tau}, \ldots, s_{i+(m-1)\tau}) \quad (1)$$

where m is the *embedding dimension* m and τ is the *time delay*. (The discrete sampling means that we may still treat the observed dynamics as a map, and $\boldsymbol{x}_i$ refers to the point on the reconstructed attractor whose first coordinate is the ith observation in the time series.) Takens [8] shows that under suitable hypotheses, this reconstruction is equivalent in some sense to the original attractor if m is large enough. (Sauer et al. [9] consider the embedding problem in greater generality. Theiler [10] and Fraser [13] discuss strategies for choosing m and τ.)

The simplest model for estimating the dynamics is a local linear one suggested by Eckmann and Ruelle [3]. Let $\boldsymbol{x}_{\text{ref}}$ be a reference point on the reconstructed attractor, and let $\{\boldsymbol{x}_i\}_{i=1}^n$ be a collection of points in a small neighborhood containing $\boldsymbol{x}_{\text{ref}}$. Let $\{\boldsymbol{y}_i\}$ be the corresponding images; i.e., $\boldsymbol{y}_i$ is the point to which $\boldsymbol{x}_i$ maps at some later time. The "true" dynamics are $\boldsymbol{y}_i = \boldsymbol{f}(\boldsymbol{x}_i)$ for some unknown function $\boldsymbol{f}$. In the Eckmann–Ruelle approach, $\boldsymbol{f}$ is approximated as

$$\boldsymbol{f}(\boldsymbol{x}) \approx A\boldsymbol{x} + \boldsymbol{b}, \quad (2)$$

where A is an $m \times m$ matrix and $\boldsymbol{b}$ is an m-vector. Here A is an estimate of the Jacobian matrix $D\boldsymbol{f}$ evaluated at $\boldsymbol{x}_{\text{ref}}$. This is an accurate model of the dynamics if all the observations and their images are contained in sufficiently small neighborhoods of the reference point and its image.

Estimates of A and $\boldsymbol{b}$ can be found by ordinary linear regression. Although the basic approach is straightforward, there are many factors that affect one's ability to estimate the map A accurately.

Some limiting factors are the result of the dynamics. For instance, the dimension d of the attractor cannot be too large, since the number of data points needed to occupy a ball of a fixed size ϵ around a typical point on the attractor is proportional to $1/\epsilon^d$ [14]. The ball size ϵ cannot be too large, because nonlinearities tend to grow with ϵ, making eq. (2) a less accurate approximation of the dynamics at the point $\boldsymbol{x}$. In most cases, the maximum value of ϵ that yields a good linear approximation depends on the reference point.

These issues are important, but they will not be considered further in this paper. Instead, we are interested in problems that limit one's ability to determine the dynamics from experimental data, even in cases where local linear models like eq. (2) in principle should be good approximations. There are many statistical difficulties arising from the presence of noise and the fractal character of the attractor that deserve more careful attention than they have received in the dynamics literature.

2.1. *Ill conditioned least squares models*

Most low dimensional chaotic attractors have a fractal, striated structure—points tend to form a Cantor set of layers. The layers can be difficult to distinguish because of the limited resolution and size of typical data sets; instead they resemble a curve. Figure 1 shows a portion of the attractor reconstructed from an x-coordinate time series generated by the Hénon map [15]

$$x_{n+1} = 1 - \alpha x_n^2 + y_n,$$
$$y_{n+1} = \beta x_n \quad (3)$$

with the usual parameters $\alpha = 1.4$, $\beta = 0.3$.

If we use eq. (2) to approximate the dynamics in this region of the plane, then we must find the best 2×2 matrix that fits the data. However, all the observations lie nearly along a straight line. In this case, we should change coordinates so that one axis is parallel to the line containing the observations. The map stretches points along this line by an amount that can be determined readily from the images of the observations. The map contracts points in the orthogo-

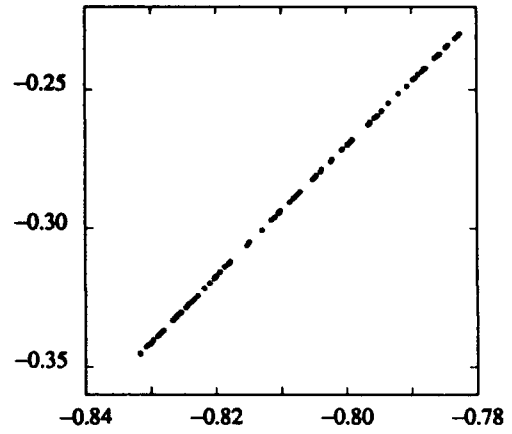

Fig. 1. A typical portion of the Hénon attractor where the points are nearly collinear.

nal direction, but this cannot be quantified readily from these data. It becomes more difficult to estimate the rate of contraction of nearby layers of points as the noise level increases, because noise obscures the structure at small scales. The Lorenz [16] and Rössler [17] attractors are two other familiar examples of attractors where similar problems occur: the points contained in a small box around a typical trajectory tend to be coplanar.

This kind of attractor structure leads to *ill conditioned* least squares problems; i.e., the covariance matrix of the observations is nearly singular. The concept is important because the numerically computed solution of an ill conditioned least squares problem has a large relative error. In this case, ill conditioning means that the Jacobian matrix A in eq. (2) cannot be estimated accurately.

The *singular value decomposition* can be used to detect situations like these. Let $\{x_i\}_{i=1}^n$ be the collection of points plotted in fig. 1, let $\bar{x}$ be their mean, and let X be the $n \times m$ matrix whose ith row is $x_i - \bar{x}$. (We assume $n \geq m$, where $m = 2$ is the embedding dimension for the Hénon data.) Then there exist an $n \times m$ matrix U, an $m \times m$ diagonal matrix Σ, and an $m \times m$ matrix V such that

$$X = U\Sigma V^{\mathrm{T}}. \tag{4}$$

The columns of U and V form an orthonormal basis for the columns and rows of X, respectively [18]. Equation (4) is the *singular value decomposition* of X and can be arranged so that the diagonal elements σ_i of Σ satisfy $\sigma_1 \geq \sigma_2 \geq \cdots \geq \sigma_m \geq 0$. These are the *singular values* of X and correspond to the nonnegative square roots of the eigenvalues of the covariance matrix $X^{\mathrm{T}}X$.

The singular value decomposition allows one to determine whether the least-squares problem in eq. (2) is singular: if the rank of X is r, then only the first r singular values are positive. There is good numerical software for computing the singular value decomposition of a matrix [18]. However, the numerically computed singular values are rarely zero due to roundoff error (even for a singular matrix), but they are small. The *condition number* κ is defined as the ratio σ_1/σ_r. Large values of κ correspond to ill conditioned least-squares problems in that upper bounds for the relative error of the solutions are proportional to κ and sometimes to κ^2. (The relevant theorems are technical and will not be stated here; consult [19] or [18] for more details.)

A difficult question is how to decide whether a problem is ill conditioned when the data in X are known only to a finite accuracy. Some criteria are given in [18] and [19]. Numerical experiments by the author on the Hénon map and laboratory data sets suggest that least squares solutions to eq. (2) are most accurate if the condition number of the problem is of order 10 or less. If the condition number of the original problem with m coordinates (corresponding to the embedding dimension) is larger than 10, then the problem is solved with fewer coordinates. In other words, if $\sigma_1/\sigma_{k+1} > 10$ but $\sigma_1/\sigma_k \leq 10$ then the least-squares problem is solved by first projecting the rows of the observation matrix X onto the subspace spanned by the first k columns of V. In this case, the matrix A computed in eq. (2) has rank k.

The choice of 10 as the upper limit for the condition number is heuristic. A suitable value de-

pends on the noise level and the size of the balls containing the observations for the least squares. If the data are noisy and the fractal character of closely spaced trajectories cannot be distinguished, then 10 probably is a good choice. In this case, the points are smeared along a single thick line, and one cannot estimate the rate at which nearby trajectories are contracted together. A small upper bound like 10 for the condition number usually prevents this.

The points in fig. 1 form an ill conditioned set in that the condition number $\kappa = 348$. The span of the first column of V essentially contains all the observations. So we project them onto the corresponding one dimensional subspace, compute an estimate of the expansion in this direction, and change coordinates back to get the matrix A (whose rank is 1) in eq. (2).

Ill conditioned problems become more common as the embedding dimension increases. For example, the author took a Hénon map time series of 65 536 values to which 0.1% noise had been added and embedded it in 4 dimensions. The resulting least squares problems were ill conditioned (i.e., the condition number of the 4-dimensional least squares problems was larger than 10) about 2/3 of the time.

The dynamics underlying the time series are also important. In some cases, like the Lorenz flow, initial conditions approach the attractor very rapidly, and most of the observations tend to lie along a single sheet. When this happens, it is usually possible to obtain accurate information only about the expansion rates of points on the attractor.

Farmer and Sidorowich [4] have advocated a noise reduction procedure that exploits information about the expanding and contracting directions to locate a new, less noisy trajectory close to the observed one. The idea is to see how a small uncertainty grows in the expanding direction upon forward iteration of the map and how the uncertainty grows in the contracting direction on backward iteration. When the underlying dynamical system is known exactly, their procedure can produce a trajectory of unlimited accuracy. (A similar approach can be used to prove shadowing theorems for numerically generated trajectories of the Hénon map [20]). However, the method requires information about the contracting as well as the expanding directions at each point on the attractor. The above discussion suggests that it may be difficult to adapt their procedure to the case where the dynamics must be estimated from the data, because accurate information about the contracting directions may be unobtainable.

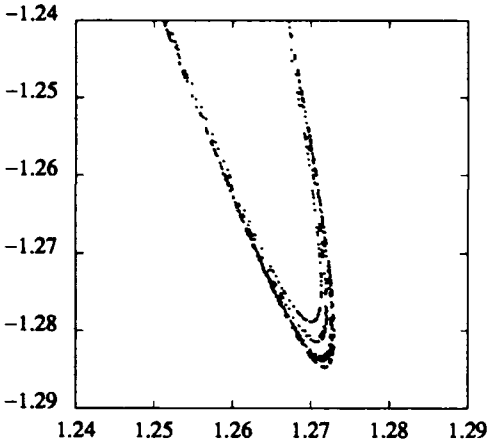

Fig. 2. A portion of the Hénon attractor. Although the points appear to fall along a parabolic curve, the dynamics are well approximated by a linear map.

The singular value decomposition provides a straightforward solution to the problem of ill conditioning, as long as one is interested in a linear model of the dynamics. However, some authors have suggested the use of quadratic and other nonlinear models for local approximations of the dynamics [21,22]. Local nonlinear models complicate the question of the best choice of variables, and the distribution of the observations can be misleading.

Consider the problem of finding the best fit for the collection of points in fig. 2 to their images. Should the linear model of eq. (2) be used with two orthogonal coordinates, or would it be better to use a quadratic model in one variable, i.e., fit the data with a parabola in some suitable coordinates? In fact, these data are generated from

the Hénon map (3), and eq. (2) provides an excellent fit. Despite the appearance of the attractor, the dynamics locally are well described by a linear map.

2.2. Outliers and influential points

Figure 3a shows a set of points selected for a least-squares fit of eq. (2). The data are generated from the Hénon map (3). In this example, the computer is instructed to take the 100 points on the reconstructed attractor closest to the reference point[#2]. Figure 3b shows the same data after 1% uniformly distributed random noise is added. All the observations lie in a box whose sides are less than 2.4% of the attractor extent in length, so eq. (2) provides a good linear approximation of the dynamics. The condition number of the associated least squares problem is about 5, so it is not ill conditioned. Nevertheless, there is a potentially serious problem in estimating the Jacobian matrix.

In this example, the strips of points will be stretched in one direction and pushed together after one iteration of the Hénon map, as illustrated in figs. 3c, d. The problem is that the three rightmost points in figs. 3a, b are relatively far removed from the rest. Here the amount of stretching along the strips is estimated using 100 points, but in the noisy example, the amount of contraction is estimated using only the rightmost 3 points.

These 3 observations are examples of *influential points*. In other words, the determinant of the 2×2 matrix computed from the data is particularly sensitive to small changes in the 3 rightmost points in figs. 3a, b, and its least squares estimate from noisy data is unreliable because the sample is so small.

[#2] The reference point is one of the three points on the right-hand side of the plot in fig. 3a, and distances are measured with the maximum norm. Although the distribution of these points may look peculiar, entirely similar situations are encountered with the use of other norms.

Influential points may be outliers, arising from relatively large "glitches" in the data. More frequently, they result from the fractal structure of the attractor. Figure 4 is a schematic illustration of a common situation. The reference point is located on one of the frequently visited portions of the attractor, represented by the closely spaced curves. (Noise may obscure the attractor structure at the smallest scales, so to the observational accuracy, the closely spaced curves may look like a single thick one.) Regardless of the details of the nearest neighbor lookup strategy, the point selection algorithm often finds a set of points whose distribution is similar to that enclosed in the circle. Suppose the map stretches points along the curves and squeezes the curves together after one iteration. Although there may be a very good linear approximation of the dynamics near the reference point, the rate of contraction is estimated using only a few points chosen from the upper (thin) curve.

The notion of an influential point is a heuristic one, and there is no formal statistical definition. Unlike ill conditioning, influential points do not necessarily affect the accuracy of least squares solutions. For example, the data in figs. 3a, c are known to the numerical precision of the computer. Here the least-squares estimate of the determinant is accurate, even though the three rightmost points are influential. The estimate is less accurate in the noisy case, and the influential points give it a large variance.

For this reason, it is a good idea to check for influential points, particularly when dealing with noisy input data. (See [23] or [24] for extensive discussions of this topic.) Let X be the $n \times m$ matrix of observations as described in section 2.1. The corresponding *prediction matrix* is defined as

$$P = X(X^{\mathrm{T}}X)^{-1}X^{\mathrm{T}}. \tag{5}$$

It can be shown [24,25] that the ith diagonal element p_{ii} of P satisfies $0 \leq p_{ii} \leq 1$ and that $1/p_{ii}$ can be regarded as the number of points in

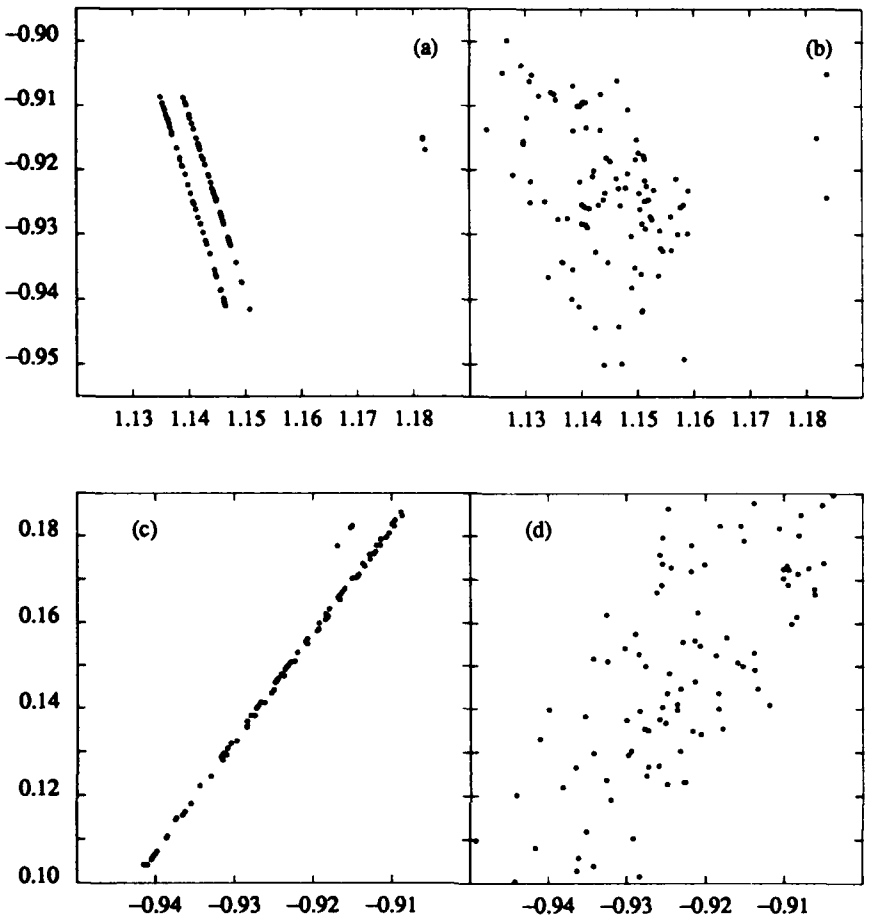

Fig. 3. (a) A collection of 100 points from a numerically generated Hénon attractor. (b) The same points after 1% uniformly distributed random noise has been added. (c), (d) The corresponding images of the points.

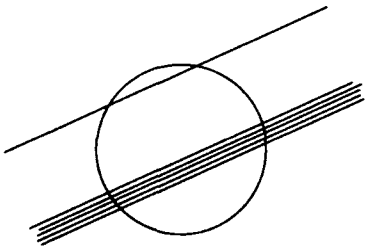

Fig. 4. Schematic illustration of how influential points can arise in least squares problems. The solid curves represent portions of the attractor. The point selection algorithm picks observations from within the circle. The points on the upper curve are influential points.

the fit that determine the corresponding observation y_i. Thus the rows in X for which the corresponding value of p_{ii} exceeds some value, say $p_{ii} > 0.2$, may be influential points [24,26].

However, it is important to note that not all points with a large value of p_{ii} have a disproportionate effect on the least-squares solution, and conversely. There is no single, clear-cut answer to the question of what should be done with influential points in the context of computing local approximations of dynamical systems. In the situation illustrated in figs. 3, the three influential points might be discarded. Although information about the rate of contraction is lost, it may not be readily determinable anyway, particularly from noisy data. (The resulting Jacobian matrix would have rank 1, as described in section 2.1.)

In many statistical applications, it is unwise simply to discard influential points. Graphical analysis of the data and the residuals is generally

recommended. However, this is impractical in applications like Lyapunov exponent estimation and noise reduction in chaotic data, where thousands of multivariate least-squares problems are solved as the attractor is traversed.

In the case of chaotic data, however, one can make reasonable assumptions about the process that generates the observations—points tend to expand in one direction and contract in others. The discarded influential points usually involve only a loss of information about the local contraction rate.

Nevertheless, it is important to assess how much the influential points affect the analysis of a given data set, such as the estimation of the Lyapunov exponents. One procedure is to calculate the Lyapunov exponents first without discarding any influential points. Then the calculation is repeated, perhaps by discarding influential points for which the corresponding value of p_{ii} is particularly large, say $p_{ii} > 0.5$. Next, some smaller values of p_{ii} can be tried (the smaller the value of p_{ii}, the more likely the points are deemed to be influential). The negative Lyapunov exponents are the most likely to be affected by the different rejection criteria. This procedure may yield a useful estimate of the accuracy with which the negative Lyapunov exponents have been calculated.

Influential points are common. For example, in the numerical experiment on the Hénon map described at the end of section 2.1, about 2/3 of the least squares problems had at least one influential point. In this experiment, a point was classified as influential if $p_{ii} > 0.25$.

It should be noted that the prediction matrix P in eq. (5) can be computed inexpensively from the QR decomposition of X. See [18] for details.

The above analysis can be extended to include the image points y_i. Figure 5 is a schematic illustration of the case where a collection of points initially are close together on the attractor but diverge into two or more groups later. This can happen when some trajectories nearly cross each other due to a poor time-delay embedding or due to the complex structure of the attractor. (For example, this situation can arise on the Lorenz attractor where trajectories cross from one lobe to the other.)

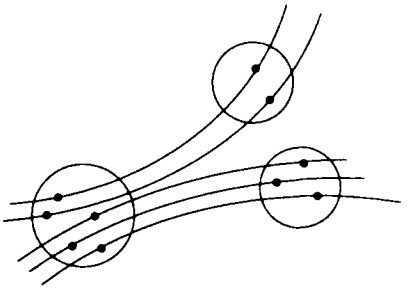

Fig. 5. Schematic diagram of diverging trajectories on an attractor.

One possibility is to form the $n \times 2m$ *augmented* matrix $(X : Y)$ [24]. The ith row of this matrix has as its first m entries the vector $x_i - \bar{x}$ and the vector $y_i - \bar{y}$ as the last m entries. (The bar denotes the mean of the corresponding observations.) The augmented prediction matrix $P_{X,Y}$ is the same as in eq. (5), except that the matrix $(X : Y)$ replaces X. A small value for the ith diagonal entry of $P_{X,Y}$ may indicate that the pair (x_i, y_i) is particularly influential in the fit, perhaps because it is on a diverging trajectory as described above. The use of this procedure may obviate the use of a "global" and a "local" embedding dimension as discussed for instance in [21].

Another alternative is to replace least squares estimation with a different minimizing function, a topic that will not be considered here. The use of so-called "robust statistics" offers many interesting possibilities for the analysis of chaotic experimental data. The monograph by Tong [27] considers the application of robust statistics to certain nonlinear time series models.

2.3. The errors-in-variables problem

Let us consider the problem of fitting a straight line to a collection of data. The classical least-squares problem assumes that

$$y_i = ax_i + b + \epsilon_i, \tag{6}$$

where each observation y_i is a linear function of the independent variable x_i, and the random variables ϵ_i are normally distributed with mean 0 and variance σ^2. In eq. (6), it is assumed that the only error occurs in the measurement of y_i—the values x_i are known exactly.

However, this assumption does not hold when one deals with noisy input data. Instead, all the observations are measured with error. Here the classical least-squares problem is replaced by

$$y_i = a(x_i + \delta_i) + b + \epsilon_i, \tag{7}$$

the so-called *errors in variables* model. Here δ_i and ϵ_i are independent, normally distributed random variables. It can be shown that the classical least-squares estimate of the slope is *biased*; i.e., the slope a is underestimated by an amount that depends on the variance of the δ_i and is independent of the number of observations. Similar results can be obtained in the multivariate case. (The book by Fuller [28] contains a detailed discussion of this problem and an extensive bibliography.)

Each matrix in eq. (2) computed from noisy data is inherently inaccurate as long as ordinary least squares is used to estimate it. This may be important for example in Lyapunov exponent calculations. The standard algorithm [29] for estimating the Lyapunov exponents involves the construction of an orthonormal set of vectors (the Lyapunov basis). At each iteration, the vectors are multiplied by the tangent map (here the matrix A, estimated using a ball of points around the current trajectory point), and the resulting collection of vectors is orthonormalized again. The normalization coefficients are then saved to get an estimate of the Lyapunov exponents. (See [30,31,3] for details.)

This statistical bias may create systematic errors in the estimation of the Lyapunov exponents. In the one dimensional case, for example, the Lyapunov exponent of a chaotic time series probably would be underestimated because the slope of the regression line is biased toward zero. A similar effect may hold in higher dimensions. As a numerical experiment, the author generated a time series of 32 768 x-coordinates from the Hénon map (3) with the usual parameters $\alpha = 1.4$, $\beta = 0.3$. The largest Lyapunov exponent λ_1 obtained from the numerically generated time series, using a procedure similar to that described in [30], is 0.608 bits/iteration. (This is very close to the value $\lambda_1 = 0.607$ bits/iteration obtained by direct iteration of the analytically determined tangent map.) The procedure was repeated after adding 1% uniformly distributed random noise to the original data. The estimated value of λ_1 for the noisy data is 0.562 bits/iteration, an underestimate corresponding to a relative error of 7%.

Noise introduces a tradeoff between a small ball size (needed for an accurate linear approximation of the dynamics) and a large variance in the data relative to the size of the ball. The maximum size of the neighborhood that allows a good local linearization depends on the particular dynamical system, but typically it is not larger than a few percent of the attractor extent. In this case, a noise level of 1% may correspond to a large relative variance, which can obscure the dynamics.

The above numerical experiment to estimate the largest Lyapunov exponent was done with a data set that is easy to analyze: there are 32 000 data points; the attractor is low dimensional (the pointwise dimension [14] of the Hénon attractor is about 1.25); the noise level is relatively small and uniform; and it is possible to obtain a good linearization in a fairly large neighborhood around each point (5% of the attractor extent or so). Nevertheless, noise limits

the accuracy of the Lyapunov exponent calculation. In contrast, laboratory data are more difficult to handle, because they typically generate higher-dimensional attractors, the time series are often relatively short, they may contain occasional large "glitches," and the noise levels may be higher. Even with very large data sets, noise limits one's ability to extract dynamical information like Lyapunov exponents.

3. Noise reduction using periodic orbits

Several procedures for reducing noise have been suggested in cases where the time series is generated by a low dimensional dynamical system [2,4,22,5,6]. All of them share some common features. Typically a *time delay embedding* is used to reconstruct the underlying attractor [8]. A local model of the dynamics, similar to eq. (2), is constructed in each of a set of small neighborhoods covering the attractor[#3]. The observed trajectories in these neighborhoods are then adjusted slightly so that they better satisfy some criterion which depends on the local approximations to the dynamics.

Although these methods can be effective in reducing noise, they have drawbacks. For example, the local approximations to the dynamics usually are determined by fitting the observed points to the model with ordinary least squares. Because all the observations are measured with error, the ordinary least squares solutions for the parameters of the model are biased, as described in section 2.3. Moreover, the adjustment of the trajectories may involve the composition of long sequences of the statistically determined maps, and this may lead to systematic errors.

Recent work has shown that saddle periodic orbits govern the dynamics on typical low-dimensional chaotic attractors [32,33]. In many cases, it is possible to locate saddle orbits on attractors reconstructed from experimental data by finding recurrent trajectories. These can be used to estimate the topological entropy [34] and other invariants associated with the dynamics [35,36].

In this section we describe how saddle periodic orbits can be used to reduce the noise in experimental data. The idea is to linearize around the saddle orbit to find a model that is linear in the parameters like eq. (2). However, the model describes a functional relationship between each recurrent orbit and its successor. That is, the parameters of the map and the adjustments to the observed orbits are determined simultaneously. Only *one* map is calculated for each recurrent orbit. Moreover, the procedure operates directly on sections of the time series without using a time-delay embedding of the attractor. Because only one map is calculated in order to adjust all the points on each of the trajectories near the saddle orbit, the procedure is computationally efficient—over 10 times faster than previous methods.

3.1. Description of the algorithm

The procedure examines the dynamics near saddle periodic orbits. Although saddle orbits are unstable, nearby initial conditions may be pushed away relatively slowly (this is often true of experimental data as discussed below). In such cases, trajectories near the saddle orbit loop around it almost periodically for a time. We say that $\boldsymbol{x}_i$ is an (m,ϵ) *recurrent point* if it returns within ϵ of itself after m iterations of the map, i.e., $\|\boldsymbol{f}^m(\boldsymbol{x}_i) - \boldsymbol{x}_i\| < \epsilon$.

In a time delay embedding, the presence of an (m,ϵ) recurrent point means that there may be consecutive sections of m time series values that are nearly the same. Figure 6 shows a portion of a time series record from an oscillating chemical experiment analyzed in [34]. The reconstructed attractor has many points that recur after $m = 375$ time steps. The marked sections in fig. 6 show some of the respective pieces of the time

[#3] Cawley and Hsu [6] construct a local projection onto the attractor instead of a map.

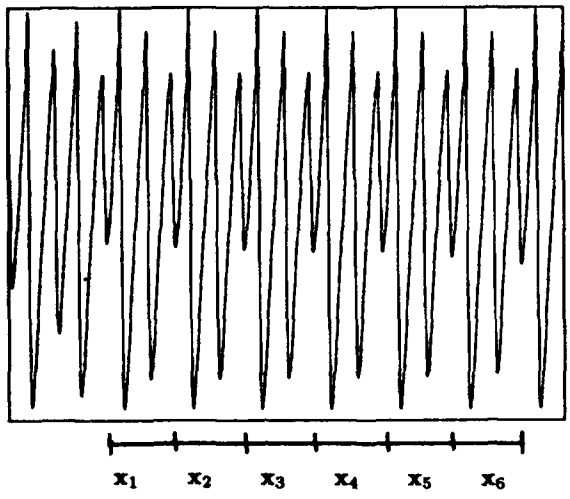

Fig. 6. A portion of a time series from an oscillating chemical experiment. The notation x_i refers to the ith section of the time series which is nearly periodic.

series. These sections appear to correspond to trajectories that loop around a saddle periodic orbit on the attractor. Here x_1 marks the first section near the saddle orbit, and x_2, x_3, etc. refer to successive sections of m values.

We will treat each section as a vector of m components. Each successive section is a function F of the previous one. We write $x_{i+1} = F(x_i)$, where F represents the dynamics near the saddle periodic orbit. This is a natural place to consider the linearized map, as follows.

Let x_f denote the saddle periodic orbit. That is, x_f represents the periodic sequence of m time series values that would be generated if the initial condition were chosen exactly on the saddle periodic orbit and the sampling interval were exactly $1/m$ times the period of the saddle orbit. If x_i and x_{i+1} are sufficiently close to x_f, then

$$x_{i+1} - x_f = F(x_i) - x_f \approx A(x_i - x_f), \qquad (8)$$

where A is the Jacobian matrix of partial derivatives of F evaluated at x_f [37]. Although the map F and its derivatives are unknown, they can be approximated from the data as described in section 2, using a model similar to eq. (2).

In the case of experimental data representing discrete observations from a flow, the recurrence time m can be large. For the data in fig. 6, we have $m = 375$. It is impractical to compute an $m \times m$ approximation of the Jacobian matrix in this example, because it requires an estimate of 140 000 parameters from a small number of recurrent trajectories.

There is considerable redundancy in the observations, however, and the singular value decomposition can be exploited to reduce the problem to the estimation of a $d \times d$ matrix where $d \ll m$ [#4]. Suppose $\{x_i\}_{i=1}^{p}$ is a collection of successive m-recurrent trajectories around some saddle orbit. Let $\bar{x}$ denote the mean of these observations. Let X be the $m \times p$ matrix whose ith column contains $x_i - \bar{x}$, and consider its singular value decomposition given in eq. (4). The columns of U form an orthonormal basis for the columns of X. Moreover, the sum of squares $\sum_{i=1}^{p} \sigma_i^2$ of the singular values equals the total variance σ_{tot}^2 in the observations x_i [19].

We retain only the first d singular vectors (the first d columns of U), where d is the smallest number such that

$$\sum_{i=1}^{d} \sigma_i^2 \geq C\sigma_{\text{tot}}^2 \qquad (9)$$

and project each column of the observation matrix X onto the subspace spanned by them. Here C is a number between 0 and 1, representing some fraction of the total variance. (In general, one can experiment with different values of C to determine the effects of retaining different numbers of singular vectors. In the results described below, we illustrate the analysis with $C = 0.5$ and $C = 0.75$.) In the new coordinates, the m-vector x_i is replaced by a d-vector v_i, whose entries correspond to the components of x_i along each of the d most significant singular vectors. The mean of the original observations is mapped to the origin. The saddle periodic point x_f in the

[#4] Broomhead et al. [12] describe a similar procedure for estimating the local dynamics in large dimensional systems.

original coordinates is now a d-vector v_f in the new coordinates. We let $v_f = 0$ be the initial guess.

The dynamics near the saddle orbit are modeled as in eq. (8), with respect to the basis given by the first d columns of U. The saddle orbit corresponding to the fixed point is near but not exactly at the origin in the new coordinates, and each of the projected observations still contains some error because of the noise. Although the covariance matrix for the remaining errors is not known, we assume it is a multiple of the identity matrix. This is equivalent to the following three assumptions: (1) the errors in the vectors v_i are independent and identically distributed; (2) the variance of the error in each coordinate of each point v_i is the same (this is reasonable since all the observations come from the same time series); (3) any correlation between the errors in different coordinates is negligible.

Following Schwetlick and Tiller [38], we determine values $\hat{A}$ of the Jacobian, $\hat{v}_f$ of the fixed point, and $\hat{v}_i$ of the observations in eq. (8) that minimize

$$S = \sum_i w\|\hat{v}_i - v_i\|^2 + \sum_j \|(\hat{v}_{j+1} - \hat{v}_f) - \hat{A}(\hat{v}_j - \hat{v}_f)\|^2 \qquad (10)$$

It can be shown that these are unbiased estimates under mild additional hypotheses [28]. The first summation in eq. (10) is over all the observations near the fixed point. (Here w is a weighting parameter for the original observations. In the results reported below, we have set $w = 1$.) The second sum is only between those pairs of observations for which one point is the image of the other.

The sum of squares in eq. (10) is similar in spirit to the minimization attempted in an earlier paper by Kostelich and Yorke [2]. The difference here is that the entries of the matrix A are not determined separately from the adjusted observations $\hat{v}_i$. That is, instead of determining A from linear least squares first, then adjusting the observations v_i, we treat both the observations and the entries of A as unknowns in the same nonlinear minimization problem. As mentioned above, we hope to get a better (unbiased) estimate of A, corresponding to the dynamics around the saddle orbit.

Equation (10) involves a relatively small number of successive sections of the original time series. If the procedure is applied to the data in fig. 6, for instance, the first sum in eq. 10 runs from $i = 1$ to 6 and the second sum from $j = 1$ to 5.

Schwetlick and Tiller [38] describe a Gauss–Newton method for minimizing S. It is also possible to proceed more simply and use the Polak–Ribiere conjugate gradient method described in [39]. A suitable initial guess for A usually can be obtained by ordinary least squares, and we set $v_f = 0$ initially. After the points $\hat{v}_i$ are determined, we change coordinates back to obtain the adjusted recurrent orbits.

We conclude this introduction with some remarks about finding recurrent orbits from a given experimental time series. The basic procedure is simple. First reconstruct the attractor using a time delay embedding. For each point on the attractor, find the neighboring points and see whether they return after some multiple of m time steps. (Depending on the sampling time and the underlying dynamics, reasonable values for m might range from 1 to 1000 or more.) One must also verify that successive sections of the corresponding m values in the original time series also remain close.

The size ϵ of the neighborhoods must be not be chosen so large that unrelated trajectories are considered close to the same saddle orbit, and ϵ cannot be so small that recurrent points are missed. (For instance, noise might knock a recurrent point out of a small neighborhood of the saddle orbit.) In the results reported below, different values of ϵ have been used to locate the recurrent orbits, depending on the data set. These values were chosen by trial and error to avoid

the problems just mentioned.

3.2. Results using experimental data

One difficulty that arises in the discussion of various noise reduction schemes is how to quantify the amount of noise removed from a chaotic experimental data set when the "true" dynamics are unknown. The power spectra of chaotic data have a broadband component, and it is difficult to determine how much is attributable to the dynamics and how much comes from the noise.

For the sake of comparison, we consider the two Couette–Taylor data sets previously analyzed in [2]. The first of these is degenerate in some sense because it comes from wavy Taylor vortex flow, whose dynamics are equivalent to a stable limit cycle instead of a saddle orbit. However, in this case power spectra do give a reliable indication of the noise level, since the flow is periodic.

The data set consists of 32 768 time series values that are measurements of one velocity component at equally spaced time intervals in wavy Taylor vortex flow [2]. Nearly all the observations are recurrent with a recurrence time corresponding to 30 time steps. (In general, the recurrence time is not an integer multiple of the sampling time, which always creates some small phase errors. In this data set, the observations can be divided into 5 groups of recurrent orbits—each around the same limit cycle—whose trajectories are nearly in phase.)

For each group of recurrent orbits, the singular value decomposition and the change to singular basis coordinates are done as described in section 3.1. The noise reduction is accomplished by minimizing the sum of squares in eq. (10) in the subspace spanned by first d singular vectors. We illustrate the results obtained when $d = 2$ (accounting for about half the total variance, i.e., $C \approx 0.5$ in eq. (9)) and $d = 5$ (corresponding to $C \approx 0.75$).

Figure 7a shows the power spectrum of the raw data. The power spectrum of the data adjusted with respect to only the first 2 singular basis vectors (fig. 7b) is comparable to that of the data after processing by the Kostelich–Yorke algorithm (see fig. 4 in [2]). A careful examination of the spectra in fig. 7a, b reveals a small peak near 0.3 times the Nyquist frequency in the original data that is missing from the processed data (this also occurs in [2]). However, when the first 5 singular basis vectors are used, the peak remains and the noise floor rises only slightly, as illustrated in fig. 7c. This suggests that the flow may be weakly quasiperiodic. In such cases, the present method may preserve the dynamics more faithfully than the procedure described in [2], provided that d is large enough.

The method is computationally efficient, since only one map needs to be computed for each set of recurrent trajectories. In this example, the minimization of eq. (10) corresponds to the simultaneous adjustment of dozens of trajectories representing hundreds of time series values. On a Silicon Graphics Personal Iris workstation, it takes about 8 seconds to determine all the recurrent orbits in the data set and about 43 seconds to minimize the sum of squares in eq. (10) for each of the 5 groups of recurrent trajectories. All but 1100 of the time series values are adjusted in about 50 seconds of computer time for the case $d = 5$. (In contrast, the noise reduction method described in [2] requires 15 minutes of CPU time.)

We next consider the application of the method to a time series of 32 768 values in a weakly turbulent Couette–Taylor flow [40]. (This is the same data set described in fig. 5 of [2].) A careful examination of the data set suggests that almost 31 000 of the values lie on a single recurrent orbit[#5].

The singular value decomposition and the change of coordinates to the corresponding ba-

[#5] The recurrence time corresponds to approximately 1153 time steps. The search for recurrent orbits was done by embedding the attractor in 6 dimensions and setting ϵ to 8% of the attractor extent.

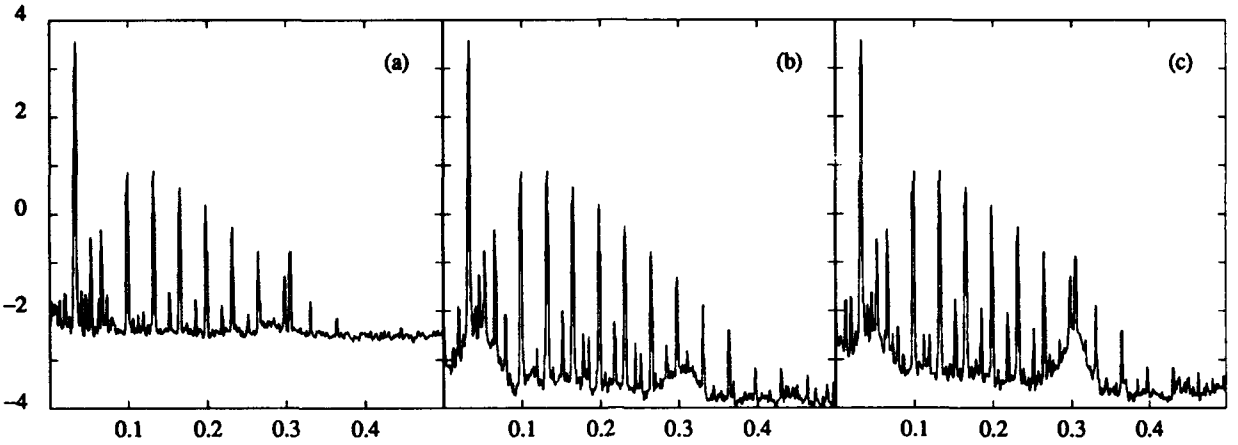

Fig. 7. (a) Power spectrum from wavy Taylor vortex flow. (b), (c) Power spectrum after noise reduction using the first 2 and the first 5 singular basis vectors. The vertical axis is the base-10 logarithm of the power spectral density; the horizontal axis is in multiples of the Nyquist frequency.

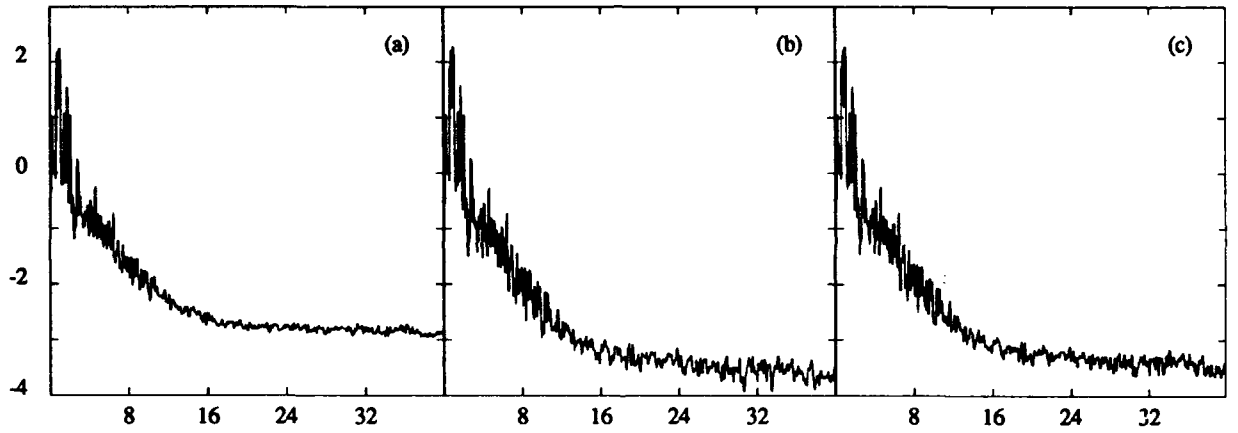

Fig. 8. Power spectra for the weakly chaotic Taylor–Couette data set described in [2]. (a) Power spectrum for the raw data. (b), (c) Power spectra using the noise reduction procedure described in the text with the first 2 and first 5 singular basis vectors, respectively.

sis is computed as described in section 3.1. As above, the noise reduction is done using the first $d = 2$ and $d = 5$ singular vectors (this captures about 50% and 75% of the variance respectively in the recurrent trajectories, like in the periodic case).

Figure 8 shows the resulting power spectra (the units on the plots are the same as those in [40]). The corresponding phase portraits closely resemble those in fig. 5 of [2] and are omitted. The results are comparable to those obtained from the Kostelich–Yorke algorithm [2].

The consistency of the statistical relationship can be checked in a cursory way by plotting the estimated saddle orbit $\hat{v}_f$ in the original time series coordinates. Figure 9 shows the saddle orbit obtained when the sum of squares is minimized using the first 5 singular vectors [#6].

However, in the $d = 5$ case, the power spectral density associated with higher frequencies in the processed data is somewhat larger than that in [2]. Because the data are chaotic, it is difficult to decide whether this higher "noise floor" corresponds to a more faithful preservation of the

[#6] The computer time required is the same as for the periodic data.

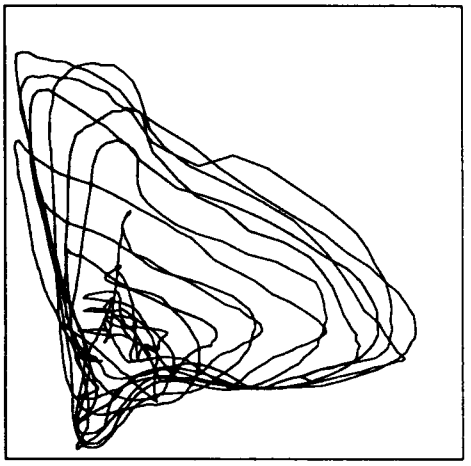

Fig. 9. The saddle orbit estimated from the chaotic Couette–Taylor data.

dynamics, a less effective noise reduction strategy, or some combination of the two.

The calculation of the singular value decomposition is subject to outliers and influential points as described in section 2.2. There are some relatively large "glitches" in these experimental data that could affect the resulting singular vector basis, thus limiting the effectiveness of the noise reduction procedure. The author tried iterating the process (i.e., using the output of one run—where most of the glitches are gone—as the input of the next), but the resulting power spectra are very similar.

Finally, the author checked the effects of different starting values for the matrix A and fixed point v_f in eq. (8). Sometimes the starting guess for A came from ordinary linear regression, and sometimes the initial guess was the identity matrix. Likewise, the fixed point v_f was originally set to zero (corresponding to the mean of the observed trajectories), and sometimes it was chosen slightly away from 0. In all cases, the numerical method converged to the same values of A, v_f, and adjusted observations $\hat{v}_i$.

4. Conclusion and remarks

The noise reduction scheme described here is applicable only to recurrent trajectories near a periodic orbit. Points that are not near a periodic saddle orbit will not be adjusted. A noise reduction method like that in [2] can be used to adjust such non-recurrent points.

In some cases, where the data set is either strongly quasiperiodic or highly chaotic, few points are recurrent, and the method described here is not useful. For example, the distance between two typical nearby points on the Hénon attractor [15] approximately doubles after each iteration of the map. For this reason, few recurrent trajectories can be found in a moderately-sized data set.

However, recurrent trajectories are common in systems that mimic many kinds of experimental data. For instance, the author has found that slightly more than half the points are recurrent in a time series of 65 000 x coordinates obtained by numerical integration of the Lorenz equations [16] with the usual parameters[#7].

The recurrent trajectories near periodic orbits on an attractor are a natural place to find an accurate linear approximation of the dynamics. The time series values comprising the trajectories can be treated as a sequence of long vectors. The singular value decomposition can be exploited to project them onto a low dimensional subspace where a least-squares minimization method can be used to determine an approximate Jacobian matrix and a more self-consistent set of slightly adjusted observations. The adjusted time series is obtained by a simple change of coordinates. In contrast to ordinary least squares, the procedure uses the functional relationship between the recurrent trajectories in the least squares minimization. There is no artificial distinction between dependent and

[#7] The attractor is embedded in 4 dimensions and ϵ is set to 3% of the attractor extent in the search for recurrent points.

independent variables, which may avoid the bias resulting from errors in measurement. The method is computationally efficient, since only one map needs to be determined for each set of recurrent orbits.

Acknowledgements

The author thanks H. Tong and two anonymous referees for helpful comments. This work is supported by the NSF Applied and Computational Mathematics Program under grant No. DMS-9017174.

References

[1] E.J. Kostelich and J.A. Yorke, Phys. Rev. A 38 (1988) 1649.
[2] E.J. Kostelich and J.A. Yorke, Physica D 41 (1990) 183.
[3] J.-P. Eckmann and D. Ruelle, Rev. Mod. Phys. 57 (1985) 617.
[4] J.D. Farmer and J.J. Sidorowich, Physica D 47 (1991) 373.
[5] T. Schreiber and P. Grassberger, A simple noise reduction method for real data, preprint.
[6] R. Cawley and G.-S. Hsu, A local geometric projection method for noise reduction in chaotic maps and flows, preprint.
[7] B.-L. Hao, ed. Chaos II (World Scientific, Singapore, 1990).
[8] F. Takens, in: Dynamical Systems and Turbulence, eds. D.A. Rand and L.-S. Young Lecture Notes in Mathematics, Vol. 898 (Springer, New York, 1981) p. 366.
[9] T. Sauer, J.A. Yorke and M. Casdagli, J. Stat. Phys. (1992), to appear.
[10] J. Theiler, J. Opt. Soc. Am. A 7 (1990) 1055.
[11] D.S. Broomhead and G.P. King, Physica D 20 (1986) 217.
[12] D.S. Broomhead, R. Indik, A.C. Newell and D.A. Rand, Nonlinearity 4 (1991) 159.
[13] A. Fraser and H.L. Swinney, Phys. Rev. A 34 (1986) 1134.
[14] J.D. Farmer, E. Ott and J.A. Yorke, Physica D 7 (1983) 153.
[15] M. Hénon, Commun. Math. Phys. 50 (1976) 69.
[16] E.N. Lorenz, J. Atmos. Sci. 20 (1963) 130.
[17] O.E. Rössler, Phys. Lett. A 57 (1976) 397.
[18] J.J. Dongarra, C.B. Moler, J.R. Bunch and G.W. Stewart, LINPACK User's Guide (Society for Industrial and Applied Mathematics, Philadelphia, 1979).
[19] G.W. Stewart, Introduction to Matrix Computations. (Academic Press, New York, 1973).
[20] S.M. Hammel, J.A. Yorke and C. Grebogi, Bull. Am. Math. Soc. 19 (1988) 465.
[21] R. Brown, P. Bryant and H.D.I. Abarbanel, Phys. Rev. A 43 (1991) 2787.
[22] M. Casdagli, Physica D 35 (1989) 335.
[23] F.R. Hampel, E.M. Ronchetti, P.J. Rousseeuw and W.A. Stahel, Robust Statistics: The Approach Based on Influence Functions. (Wiley, New York, 1986).
[24] S. Chatterjee and A.S. Hadi, Sensitivity Analysis in Linear Regression. (Wiley, New York, 1988).
[25] H. Tong, Non-linear Time Series. (Oxford Univ. Press, Oxford, 1990).
[26] P. Huber, Robust Statistics. (Wiley, New York, 1981).
[27] H. Tong, Threshold models in nonlinear time series analysis, Lecture Notes in Statistics, No. 21 (Springer, Heidelberg, 1983).
[28] W.A. Fuller, Measurement Error Models. (Wiley, New York, 1987).
[29] G. Benettin, L. Galgani, A. Giorgilli and J.M. Strelcyn, Meccanica 15, 9 (1980).
[30] J.-P. Eckmann, S.O. Kamphorst, D. Ruelle and S. Ciliberto, Phys. Rev. A 34 (1986) 4971.
[31] M. Sano and Y. Sawada, Phys. Rev. Lett. 55 (1985) 1082.
[32] D. Auerbach, P. Cvitanović, J.-P. Eckmann, G. Gunaratne and I. Procaccia, Phys. Rev. Lett. 58 (1987) 2387.
[33] C. Grebogi, E. Ott and J.A. Yorke, Phys. Rev. A 37 (1988) 1711.
[34] D.P. Lathrop and E.J. Kostelich, Phys. Rev. A 40 (1989) 431.
[35] N.B. Tufillaro, H.G. Solari and R. Gilmore, Phys. Rev. A 41 (1990) 5717; Phys. Rev. Lett. 64 (1990) 2350.
[36] L. Smith, Quantifying Chaos with Predictive Flows and Maps: Locating Unstable Periodic Orbits. in: Measures of Complexity and Chaos, eds. N.B. Abraham et al. (Plenum, New York, 1989).
[37] See for instance J.M.T. Thompson and H.B. Stewart, Nonlinear Dynamics and Chaos (Wiley, Chicester, 1986) Ch. 8.
[38] H. Schwetlick and V. Tiller, Technometrics 27 (1985) 17.
[39] W.H. Press, B.P. Flannery, S.A. Teukolsky and W.T. Vetterling, Numerical Recipes (Cambridge Univ. Press, Cambridge, 1986).
[40] A. Brandstäter and H.L. Swinney, Phys. Rev. A 35 (1987) 2207.

Physica D 58 (1992) 153–164
North-Holland

PHYSICA D

Controlling chaotic dynamical systems using time delay coordinates

Gregor Nitsche and Ute Dressler
Daimler-Benz Research Institute, Goldsteinstr. 235, 6000 Frankfurt/Main 71, Germany

Received 2 October 1991
Revised manuscript received 17 December 1991
Accepted 17 December 1991

The Ott–Grebogi–Yorke control method is analyzed in the case that the attractor is reconstructed from a time series using time-delay coordinates. It turns out that the control formula of OGY should be modified in order to apply to experimental systems if time-delay coordinates are used. We reveal that the experimental surface of section map does not only depend on the actual parameter but also on the preceding one. In order to meet this dependence two modifications are introduced which lead to a better performance of the control. To compare their control abilities they are applied to simulations of a Duffing oscillator. The issue of measurement noise is considered.

1. Introduction

In 1990, Ott, Grebogi and Yorke (OGY) [1] proposed a new method of controlling a chaotic dynamical system by stabilizing one of the many unstable periodic orbits embedded in a chaotic attractor, using only small time-dependent perturbations in some accessible system parameter.

This method has attracted the attention of many physicists interested in applications of nonlinear dynamics. One reason for this is that OGY stress that all values needed to achieve control can be obtained from an experimental signal starting with the well-known embedding technique [2, 3]. Therefore, the control method can in principle be applied to experimental systems where the dynamical equations are not known. Indeed, Ditto et al. demonstrated recently [4] a first control of a physical system using the method of Ott, Grebogi and Yorke.

With regard to possible applications we investigate the performance of the control method in the case that the chaotic attractor is reconstructed by the embedding technique. This is done by simulating an experimental situation. The damped and driven Duffing oscillator is numerically integrated and the displacements are taken as "experimental" time series $z(t)$. Using delay coordinates, the attractor is reconstructed and the unstable periodic point which one wants to stabilize is determined in an experimental surface of section. It turns out that the control method of OGY should be modified in order to apply to experimental systems if time-delay coordinates are used. The main argument will be that during the control process one switches the control parameter p from p_{i-1} to p_i at times t_i (t_i time of the ith piercing of the surface of section by the trajectory). But, if one uses delay coordinates, the experimental surface of section map $\boldsymbol{P}$ will not only depend on the new actual parameter p_i (as OGY implicitly assume) but also on the preceding one p_{i-1}. Our modifications of the algorithm will consider these dependencies.

The paper is organized as follows. In section 2 we briefly recall the OGY method and introduce

0167-2789/92/$05.00 © 1992 – Elsevier Science Publishers B.V. All rights reserved

our notation. In section 3 the problems arising for the control method using delay coordinates are studied and the modifications mentioned are proposed. In section 4 the performance of the different versions of the method is compared in the case of the Duffing oscillator. With regard to possible applications the robustness of the control method in the presence of measurement noise is briefly considered in section 5.

2. The OGY control method

For simplicity we restrict ourselves to a two-dimensional discrete dynamical system. This restriction is mainly for the ease of presentation. There do also exist extensions of the method to higher dimensional dynamical systems [5, 6]. Let the system depend on some accessible parameter $p \in (p_0 - \delta p_{\max}, p_0 + \delta p_{\max})$ with maximal possible perturbation $\delta p_{\max}$

$$\begin{aligned} &\boldsymbol{\xi}_{i+1} = \boldsymbol{P}(\boldsymbol{\xi}_i, p), \\ &\boldsymbol{\xi}_i \in \mathbb{R}^2, \quad p \in (p_0 - \delta p_{\max}, p_0 + \delta p_{\max}). \end{aligned} \tag{1}$$

We assume that for $p = p_0$ the system is on a chaotic attractor. Let $\boldsymbol{\xi}_F = \boldsymbol{P}(\boldsymbol{\xi}_F, p_0)$ denote the unstable fixed point on the attractor which one wants to stabilize. The control idea is to monitor the system until it comes close to the desired fixed point and then change p by a small amount such that the next state $\boldsymbol{\xi}_{i+1}$ will fall into the stable direction of the fixed point. To do this, one uses the first-order approximation of (1) near $\boldsymbol{\xi}_F$ and p_0,

$$\boldsymbol{\xi}_{i+1} = \boldsymbol{P}(\boldsymbol{\xi}_i, p_i) \cong \boldsymbol{\xi}_F + A(\boldsymbol{\xi}_i - \boldsymbol{\xi}_F) + \boldsymbol{w}(p_i - p_0) \tag{2}$$

or

$$\delta\boldsymbol{\xi}_{i+1} \cong A\,\delta\boldsymbol{\xi}_i + \boldsymbol{w}\,\delta p_i, \tag{3}$$

where $\delta\boldsymbol{\xi}_i = \boldsymbol{\xi}_i - \boldsymbol{\xi}_F$ and $\delta p_i = p_i - p_0$ and $A = D_{\boldsymbol{\xi}}\boldsymbol{P}(\boldsymbol{\xi}_F, p_0)$ is a 2×2 matrix and $\boldsymbol{w} = (\partial \boldsymbol{P}/\partial p)(\boldsymbol{\xi}_F, p_0)$ is a two-dimensional vector.

As the unstable fixed point $\boldsymbol{\xi}_F$ is embedded in a chaotic attractor the linearization of A possesses an eigenvalue λ_s with $|\lambda_s| < 1$ and corresponding eigenvector $\boldsymbol{e}_s$ and an eigenvalue λ_u with $|\lambda_u| > 1$ and eigenvector $\boldsymbol{e}_u$. The eigenvectors $\boldsymbol{e}_s$ and $\boldsymbol{e}_u$ give the directions of the local stable and unstable manifold of the fixed point. Let $\boldsymbol{f}_s$ and $\boldsymbol{f}_u$ be the contravariant basis vectors, i.e. $\boldsymbol{f}_s \cdot \boldsymbol{e}_u = \boldsymbol{f}_u \cdot \boldsymbol{e}_s = 0$ and $\boldsymbol{f}_s \cdot \boldsymbol{e}_s = \boldsymbol{f}_u \cdot \boldsymbol{e}_u = 1$. Then A can be written as $A = \lambda_u \boldsymbol{e}_u \boldsymbol{f}_u + \lambda_s \boldsymbol{e}_s \boldsymbol{f}_s$. The condition that $\boldsymbol{\xi}_{i+1}$ falls on the local stable manifold of the fixed point can now be formulated as

$$\boldsymbol{f}_u \cdot \delta\boldsymbol{\xi}_{i+1} = 0. \tag{4}$$

If $\boldsymbol{\xi}_i$ comes close to $\boldsymbol{\xi}_F$ the linearization (3) holds. The control requirement (4) can then be applied which yields for the new value of the control parameter $p_i = p_0 + \delta p_i$

$$\delta p_i = -\frac{\lambda_u}{\boldsymbol{f}_u \cdot \boldsymbol{w}}\, \boldsymbol{f}_u \cdot \delta\boldsymbol{\xi}_i. \tag{5}$$

The control is only activated if the resulting change in the parameter δp_i is less than the maximal allowed disturbance $\delta p_{\max}$, otherwise δp_i is set to zero. As usual it is assumed that the occurring denominator in (5) does not vanish. After $\boldsymbol{\xi}_{i+1}$ has fallen on the local stable manifold, the parameter perturbation δp_i could be set to zero. But because of errors in the determination of the linearization, measurement errors, or a small amount of noise, the system will in general tend to fall off the stable manifold again. Therefore, the control process (5) has to be activated at every time step i to keep the successive points $\boldsymbol{\xi}_i$ near $\boldsymbol{\xi}_F$.

Finally we note that the control law (5) looks different to the one in ref. [1]. The reason for this is that we use the linearization around $\boldsymbol{\xi}_F$ and p_0 (as is used in ref. [5]) and do not estimate the new position of the fixed point $\boldsymbol{\xi}_F(p)$ as one changes the parameter p.

$$\xi_F(p) = \xi_F(p_0 + \delta p) = \xi_F(p_0) + g\,\delta p\,, \qquad (6)$$

as OGY do. But it is easy to show that these approaches are equivalent and g and w are related through

$$g = (1 - D_\xi P(\xi_F, p_0))^{-1} w\,. \qquad (7)$$

3. OGY control algorithm in the case of delay coordinates

Now we consider the case that the dynamical equations are not known. We assume that the only information about the system is obtained by some measurement process which is mathematically realized by some scalar function Z on the state space M, $Z: M \to \mathbb{R}$. If $Y(t) \in M$ is the state of the system at time t, we obtain the experimental time series $z(t) = Z(Y(t))$. We assume further that the system has settled down on an attractor which lies on some manifold $M_Y \subset M$. Using time delay coordinates with delay τ and embedding dimension d, a d-dimensional delay coordinate vector is formed $X(t) = (z(t), z(t-\tau), \ldots, z(t-(d-1)\tau)) \in \mathbb{R}^d$. For appropriately chosen d and τ [3] there exists a smooth, invertible mapping Φ from M_Y to a submanifold $M_X \subset \mathbb{R}^d$, such that

$$X(t) = \Phi(Y(t))\,, \qquad Y(t) \in M_Y\,, \qquad (8)$$

holds. For a nice visualization see ref. [7]. Let the dynamics in the original phase space be represented by a flow φ such that $Y(t+\tau) = \varphi^\tau(Y(t))$ holds. This continuous dynamical system induces a discrete dynamical system in an appropriately chosen experimental surface of section. It is obtained by the common choice that one component of $X(t)$ equals a constant, e.g. by the condition $(X(t_i))_1 \equiv z(t_i) = c = \text{const}$. This procedure gives the successive points $\xi_i := (z(t_i - \tau), \ldots, z(t_i - (d-1)\tau)) \in \mathbb{R}^{d-1}$ in the surface of section.

In what follows we focus our interest on the so obtained surface of section map $\xi_{i-1} = P(\xi_i)$. For the sake of simplicity let us assume that one wants to stabilize an unstable fixed point ξ_F of P which has been localized by the well-known technique of recurrent points [8–10]. Applying the OGY control algorithm implies that one (instantaneously) changes at the times t_i the parameter p from p_{i-1} to an appropriately chosen parameter p_i using (5). Let us now assume that the time between successive piercings of the surface of section is larger than the lag window, i.e. $t_{i+1} - t_i > (d-1)\tau$.

The reason that one hopes to be able to control the original system $Y(t)$ by observing $X(t)$ is that the introduced embedding Φ gives a bijective relation between the states $X(t)$ and $Y(t)$. The mapping Φ is, however, closely related to the dynamical equations of the system and thus in general dependent on the actual value of the control parameter p_i. We will take this fact into account by writing Φ_{p_i} instead of Φ. Our argumentation is now as follows. The point ξ_i at time t_i in the surface of section is related to the original state by

$$Y(t_i) = \Phi^{-1}_{p_{i-1}}(c, z(t_i - \tau), \ldots, z(t_i - (d-1)\tau))$$
$$= \Phi^{-1}_{p_{i-1}}(X(t_i)). \qquad (9)$$

Here we make use of our assumption that $(d-1)\tau < (t_i - t_{i-1})$, which assures that p_{i-1} is the actual value of p during the whole time interval (t_{i-1}, t_i). The flow in the original state space which describes the development of the system from time t_i to the time t_{i+1} of the $(i+1)$th piercing is in case of activated control given by $\varphi^{t_{i+1}-t_i}_{p_i}$ and thus the state of the system at time t_{i+1} is obtained by

$$Y(t_{i+1}) = \varphi^{t_{i+1}-t_i}_{p_i}(Y(t_i)) \qquad (10)$$

and the corresponding state in the embedding space by

$$X(t_{i+1}) = \Phi_{p_i}(Y(t_{i+1}))\,. \qquad (11)$$

Thus we finally obtain using eqs. (9)–(11)

$$X(t_{i+1}) = (\Phi_{p_i} \circ \varphi_{p_i}^{t_{i+1}-t_i} \circ \Phi_{p_{i-1}}^{-1})(X(t_i)) . \qquad (12)$$

This yields our main conclusion. In the case of activated control (i.e. switching the parameter from p_{i-1} to p_i at time t_i) the experimental surface of section map P does depend not only on the new actual value p_i but also on the preceding value p_{i-1}, i.e.

$$\xi_{i+1} = P(\xi_i, p_{i-1}, p_i) \qquad (13)$$

Note that if the assumption $(t_i - t_{i-1}) > (d-1)\tau$, (for all i), is broken and e.g. only $2(t_i - t_{i-1}) > (d-1)\tau$ holds then the result is straightforwardly generalized to $\xi_{i+1} = P(\xi_i, p_{i-2}, p_{i-1}, p_i)$ i.e. dependencies on further preceding values of p have to be taken into account. For the easiness of notation we restrict ourselves here on the case $(t_i - t_{i-1}) > (d-1)\tau$ for all i.

Taking (13) as starting point the algorithm of OGY is straightforwardly extended. The linearization which one has to consider now is given by

$$\delta\xi_{i+1} \cong A\,\delta\xi_i + v\,\delta p_{i-1} + u\,\delta p_i \qquad (14)$$

with $A = D_{\xi_i} P(\xi_F, p_0, p_0)$, $v = (\partial P/\partial p_{i-1})(\xi_F, p_0, p_0)$, and $u = (\partial P/\partial p_i)(\xi_F, p_0, p_0)$. Demanding $f_u \cdot \delta\xi_{i+1} = 0$ renders the new control formula

$$\delta p_i = -\frac{\lambda_u}{f_u \cdot u} f_u \cdot \delta\xi_i - \frac{f_u \cdot v}{f_u \cdot u}\,\delta p_{i-1} . \qquad (15)$$

When P is not influenced by the preceding parameter perturbation δp_{i-1}, which is equivalent to $v = 0$, the original OGY control formula (5) should be reobtained. To see this we note that the vector w in the control formula (5) is related to u and v by $w = u + v$. This is so because calculating w in practice (see also section 4) means that one changes p_0 to $p_0 + \bar{p}$, $\bar{p}$ small, and observes for a while how the behavior of P changes in the neighborhood of ξ_F, i.e. one looks at $P(\xi_F + \delta\xi, p_0 + \bar{p}, p_0 + \bar{p})$ and therefore one determines $w = u + v$.

The control formula (15) has to be applied in principle all over again even in the absence of measurement errors or noise. In case of activated control, $\delta p_i \neq 0$, the control requirement $f_u \cdot \delta\xi_{i+1} = 0$ does not guarantee that ξ_{i+2} will also fall on the stable manifold. The reason for this is that ξ_F is the fixed point of $P(\cdot, p_0, p_0)$ and not of $P(\cdot, p_0 + \delta p_i, p_{i+1})$, $p_{i+1} = p_0$, which would determine ξ_{i+2} if one does not apply a further perturbation δp_{i+1}. Therefore, ξ_{i+2} will only stay on the local stable manifold of ξ_F (i.e. $f_u \cdot \delta\xi_{i+2} = 0$) if a perturbation δp_{i+1} is chosen according to the control formula (15). This is easily checked using (14).

In section 3 we show examples where the control law (15) is already able to control systems for which the OGY algorithm fails. It is, however, not sufficient for all cases: Consider the case that $|(f_u \cdot v)/(f_u \cdot u)| \geq 1$. Regarding the deviations of $\delta\xi_i$ from zero as stochastic, then, (15) is equivalent to a non-stationary AR (1) (autoregressive of order 1) process (see ref. [11]), i.e. the expectation value of $(\delta p_i)^2$ will diverge for growing i until for some i, δp_i will exceed the maximum allowed value δp_{max}, and the range of control will be left.

To avoid this instability (i.e. the growing of δp_i) we propose an alternative approach. We try to find a control law for δp_i such that δp_{i+1} automatically will become zero. We do this be demanding that the system stabilizes only the next but one step, $i+2$, and that δp_{i+1} equals zero, i.e. by the requirements

$$f_u \cdot \delta\xi_{i+2} = 0 \quad \text{and} \quad \delta p_{i+1} = 0 . \qquad (16)$$

Using the linearization (14) twice, the requirement (16) yields the new control formula

$$\delta p_i = -\frac{\lambda_u^2}{\lambda_u f_u \cdot u + f_u \cdot v} f_u \cdot \delta\xi_i - \frac{\lambda_u f_u \cdot v}{\lambda_u f_u \cdot u + f_u \cdot v}\,\delta p_{i-1} \qquad (17)$$

(where f_u, u, v have again to fulfill the generic condition that the occurring denominators are different from zero).

The new control requirements lead to a self-consistency of the control procedure. Assuming a perfect linearization, absence of noise or measurement errors this time the perturbations could in principle be turned off because the iterate ξ_{i+3} would automatically fall on the stable manifold. In practice, of course, the error in the linearization, which was here even used twice, will always require to activate the control at every time step i.

4. Application of the control algorithms to the Duffing oscillator

The algorithms discussed above have been applied to simulations of a Duffing oscillator [12]. This oscillator is given by

$$\ddot{x} + d\dot{x} + x + x^3 = f\cos\omega t\,, \tag{18}$$

or, equivalently written as

$$\begin{aligned} \dot{x}_1 &= x_2\,, \\ \dot{x}_2 &= -dx_2 - x_1 - x_1^3 + f\cos\omega x_3\,, \\ \dot{x}_3 &= 1\,. \end{aligned} \tag{19}$$

This system has been numerically integrated. As a measurement function the displacement of the oscillator $z(t) \equiv x_1(t)$ is chosen. We use a three-dimensional embedding with delay time $\tau = \frac{1}{4}T$, $T = 2\pi/\omega$ being the period of the driving. The experimental surface of section was obtained by taking $(X(t_i))_1 = z(t_i) = \text{const}$. To insure that the trajectory always pierces the surface of section from one side we added the condition $\dot{z}(t_i) > 0$. In this way a sample of successive points $\xi_i = (z(t_i - \tau),\ z(t_i - 2\tau))$, $i = 1, \ldots, N$ in the two-dimensional surface of section was recorded.

For the localization of fixed points, a method described in refs. [8, 9] was used. From the sample ξ_i, $i = 1, \ldots, N$, the n best recurrent points $\xi_{r_1}, \ldots, \xi_{r_n}$ are determined by

$$\begin{aligned} &\|P(\xi_{r_1}) - \xi_{r_1}\| \leq \cdots \leq \|P(\xi_{r_n}) - \xi_{r_n}\| \\ &\quad \leq \min_{i \neq r_j} \|P(\xi_i) - \xi_i\|\,. \end{aligned} \tag{20}$$

The correct grouping of the recurrent points into classes belonging to the same fixed point can be accomplished by the following procedure: For different values of a "maximum-distance parameter" ϵ, ξ_{r_1} is taken as a master point for the first class. ξ_{r_2} is attached to the same class if $\|\xi_{r_2} - \xi_{r_1}\| < \epsilon$, otherwise it is taken as a master point of a new class, and so on. In general the number of classes obtained by this procedure approaches 1 for large values of ϵ and n for small values; if it, however, remains constant over a broad intermediate range of ϵ values, one can suppose that the correct classification has been found.

Having determined a class of recurrent points, the exact value of the corresponding fixed point ξ_F and the linearization around ξ_F must be found. We do this by fitting an affine mapping

$$P(\xi_{r_i}) \cong A\xi_{r_i} + b\,, \qquad i = 1, \ldots, N_{Cl} \tag{21}$$

to the pairs ξ_{r_i}, $P(\xi_{r_i})$ belonging to the class considered. For this purpose the general least square method described in [13, p. 509 ff., 518 f.] is used. For $k = 1, \ldots, d-1$ it is applied to

$$z_k(i) \cong \sum_{j=1}^{d-1} a_{kj} f_j(i) + b_k g(i)\,, \qquad i = 1, \ldots, N_{Cl} \tag{22}$$

with $z_k(i) = (P(\xi_{r_i}))_k$ and the "nonlinear basis functions" f_j, g given by $f_j(i) = (\xi_{r_i})_j$, and $g(i) \equiv 1$. This fitting method was employed iteratively: As weights for the sample points, we used a function of their distances to the fixed point ξ_F. In the first step, as an initial guess for ξ_F, the master point of the class was taken. Having obtained A and b, a new guess of the fixed point ξ_F was calculated by solving $\xi_F = (1 - A)^{-1} b$. The

iteration was continued until ξ_F and A stayed approximately constant from one step to the other. The eigenvalue λ_u and the corresponding left (contravariant) eigenvector f_u can then be easily found.

What one finally needs to perform control are the vectors u and v. Shifting p to a small constant value $p_0 + \bar{p}$ and observing the behavior of P for a while as it is done in the OGY algorithm only renders the sum $w = u + v$. What one has to do instead is to switch alternatingly on and off the perturbation at every piercing of the surface of section such that $\delta p_i = 0$ for i odd and $\delta p_i = \bar{p}$, for i even, $\bar{p}$ small, respectively. Regarding all pairs (ξ_i, ξ_{i+1}) with even i as one group, and the ones with odd i as another, it is now possible to fit affine mappings in the neighborhood of ξ_F to $P(\cdot, p_0 + \bar{p}, p_0)$ using only pairs (ξ_{r_i}, ξ_{r_i+1}), r_i odd and to $P(\cdot, p_0, p_0 + \bar{p})$ using only pairs (ξ_{r_i}, ξ_{r_i+1}), r_i even, respectively. Using these fits, u and v are then determined by the relations

$$P(\xi_F, p_0 + \bar{p}, p_0) \cong \xi_F + v\bar{p} ,$$
$$P(\xi_F, p_0, p_0 + \bar{p}) \cong \xi_F + u\bar{p} , \qquad (23)$$

one can now try to achieve control.

In fig. 1 a chaotic attractor of the Duffing oscillator (with $d = 0.2$, $f = 36.$, $\omega = 0.661$) in the embedding space is shown. For this attractor the conditions for the surface of section are chosen to be $z(t_i) = 1$, $\dot{z}(t_i) > 0$ and the additional requirement $z(t_i - \tau) < 0$ is used. The surface of section is indicated in fig. 1. In fig. 2 the attractor in the surface of section is shown. Three fixed points (marked as ξ_{F1}, ξ_{F2}, and ξ_{F3}) embedded in the attractor could be determined. The periodic orbits corresponding to these fixed points are presented in fig. 3.

To compare the performances of the three different versions of the control formula we tried to stabilize these three fixed points ξ_{F1}, ξ_{F2}, and ξ_{F3}. As accessible parameter p the amplitude of the driving f, i.e. $p = f$ and $p_0 = f_0 = 36.$ was chosen. The maximal allowed perturbation was

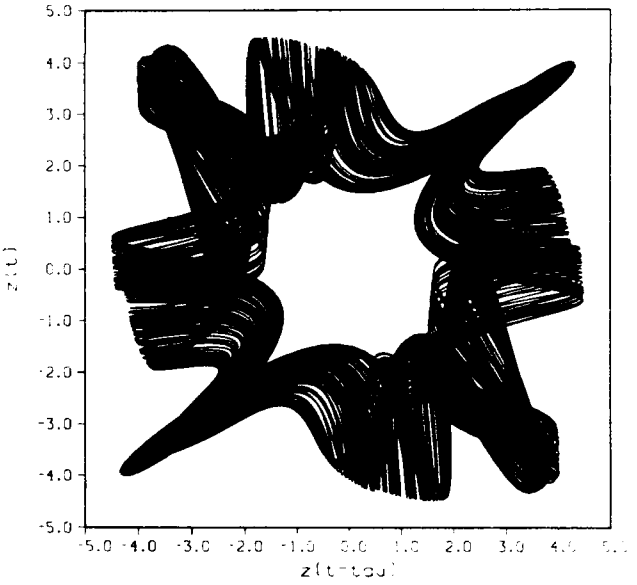

Fig. 1. For the Duffing oscillator ($d = 0.2$, $f = 36.$, $\omega = 0.661$) a two-dimensional projection of the chaotic attractor in the three-dimensional embedding space is shown. As delay time τ we use $\tau = \frac{1}{4}T$ with $T = 2\pi/\omega$. The line marks the half plane which we used as surface of section.

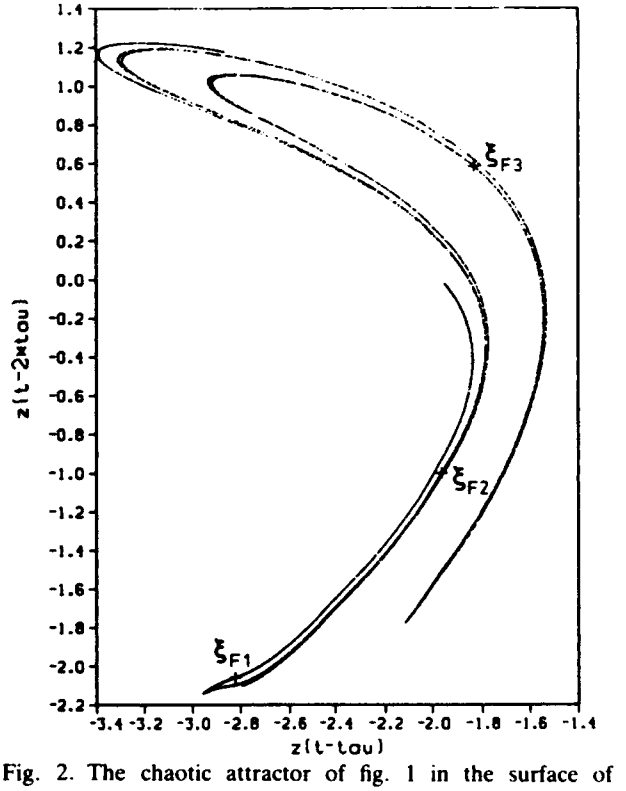

Fig. 2. The chaotic attractor of fig. 1 in the surface of section. The surface of section was obtained by the conditions $z(t_i) = 1.$, $\dot{z}(t_i) > 0$ and $z(t_i - \tau) < 0$. Three unstable fixed points observed are indicated by the crosses. For further reference we call them ξ_{F1}, ξ_{F2} and ξ_{F3}.

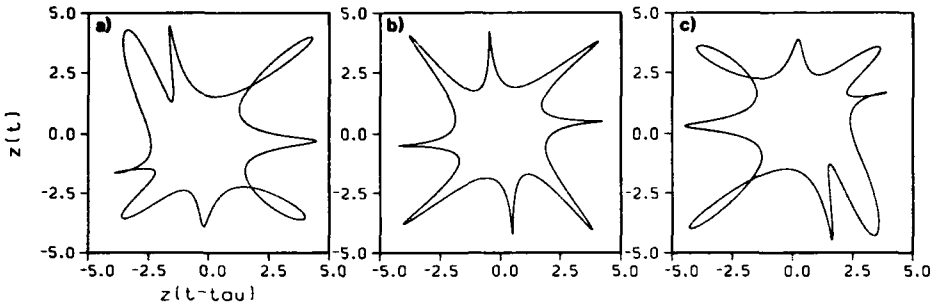

Fig. 3. The periodic orbits corresponding to the fixed points in the surface of section of fig. 2 are plotted in the two-dimensional projection of the embedding space (compare fig. 1) (a) correspond to ξ_{F1}, (b) to ξ_{F2} and (c) to ξ_{F3}.

Table 1
The three control formulas used for control with $u = (\partial P/\partial p_i)\ (\xi_F, p_{i-1}, p_i)$, $v = (\partial P/\partial p_{i-1})\ (\xi_F, p_{i-1}, p_i)$, and $\hat{f}_u = f_u/\|f_u\|$. The constant control coefficients $(a, b_1, \ldots)$ are introduced implicitly.

OGY (5)
$$\delta p_i = -\frac{\lambda_u}{f_u \cdot (u+v)} f_u \cdot \delta\xi_i = a\hat{f}_u \cdot \delta\xi_i$$

MOD1 (15)
$$\delta p_i = -\frac{\lambda_u}{f_u \cdot u} f_u \cdot \delta\xi_i - \frac{f_u \cdot v}{f_u \cdot u}\delta p_{i-1} = b_1 \hat{f}_u \cdot \delta\xi_i + b_2\,\delta p_{i-1}$$

MOD2 (17)
$$\delta p_i = -\frac{\lambda_u}{\lambda_u f_u \cdot u + f_u \cdot v} f_u \cdot \delta\xi_i - \frac{\lambda_u f_u \cdot v}{\lambda_u f_u \cdot u + f_u \cdot v}\delta p_{i-1} = c_1 \hat{f}_u \cdot \delta\xi_i + c_2\,\delta p_{i-1}$$

fixed upon $\delta p_{max} = 0.5$. In table 1 the different control formulas are summarized. The numerically obtained values of the coefficients in the control formulas for the three fixed points are given in table 2. These coefficients are only accurate up to a percentage of about 10. The reason for this is that u and v are usually very small. To determine the coefficients one has to divide by small numbers. Therefore, even slight changes in u and v, which can be caused by changing the number of neighboring points used for the fitting of P, can yield a noticeable change in the coefficients. Fortunately, these variations

Table 2
The numerically obtained values of the coefficients in the control formulas (see table 1) for the three fixed points considered.

	a	b_1	b_2	c_1	c_2	λ_u
ξ_{F1}	−16	−228	−13	39	2.2	−1.87
ξ_{F2}	165	−7	1.04	−9	1.3	4.82
ξ_{F3}	−2.5	−2	0.20	−1.8	0.18	−1.85

in the coefficients did not effect the possibl control ability of the control algorithms.

We start with the stabilization of the fixed point ξ_{F1}. In fig. 4 the three different control formulas are successively applied. As can be

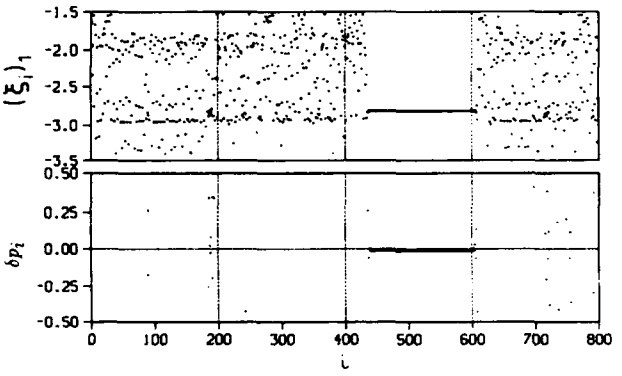

Fig. 4. (a) First component $(\xi_i)_1$ of the points in the surface of section versus i. In order to stabilize the fixed point ξ_{F1} the OGY control law (5) was switched on from $i = 0$–200, the control law (15) from $i = 201$–400, the control law (17) from $i = 401$–600, and again OGY's control law from 601–800. As can be seen only the procedure (17) was able to stabilize ξ_{F1}. (b) The parameter perturbations δp_i versus i used for control are shown. The maximal allowed disturbance was $\delta p_{max} = 0.5$.

seen only the second modification (17) was able to stabilize ξ_{F1}. The coefficients of the control formulas (see table 2) explain why the first modification (15) of the OGY algorithm did not work. The criterium for a stable control algorithm $|b_2| < 1$ was broken. The large absolute value of $b_2 = f_u \cdot v / f_u \cdot u$, here $b_2 = -13.$, indicates further that the influence of the change of the preceding parameter p_{i-1} is relatively larger than that of the actual one p_i. But this is exactly what is neglected if one applies the original approach of OGY without considering the meaning of the time-delay coordinates.

The stabilization of the second fixed point shows different features. Here the generic condition ($f_u \cdot w \neq 0$) of the OGY formula is almost violated. Because of the resulting large value of the coefficient a ($a = 165.$) there were only rare cases where the control requirement $\delta p_i < \delta p_{max}$ was met. But even then the control range was soon left without succeeding in control. In fig. 5 the OGY algorithm is first applied, then the first modification (15) is used to control ξ_{F2}. The coefficient b_2 ($b_2 = 1.04$) just violates the stability criterium. Indeed, the used perturbations δp_i increase at the beginning. But finally, probably due to nonlinear effects, the control procedure stabilizes and the algorithm is capable of achieving control. After 200 iterations at $i = 401$ the second modification (17) is activated. The fixed point ξ_{F2} stays controlled, but the perturbations δp_i needed, drastically decrease. This could be expected thinking of how this control formula (17) was derived using the requirement $\delta p_{i+1} = 0$.

The third fixed point ξ_{F3} could be stabilized by any of the three versions of the control formula. For ξ_{F3} the coefficients of the control formulas are very similar (see table 2). The coefficient b_2 is relatively small ($b_2 = 0.2$) which indicates the small influence of δp_{i-1} compared to δp_i. So one can expect that all the three algorithms will work. In addition, all coefficients are relatively small compared to the ones of ξ_{F1} and ξ_{F2} which also gives a hint that it is not hard to stabilize ξ_{F3}.

In fig. 6 we switched from controlling ξ_{F1} to controlling ξ_{F2} and then ξ_{F3} using the second modification (17) which was able to achieve control for all three fixed points.

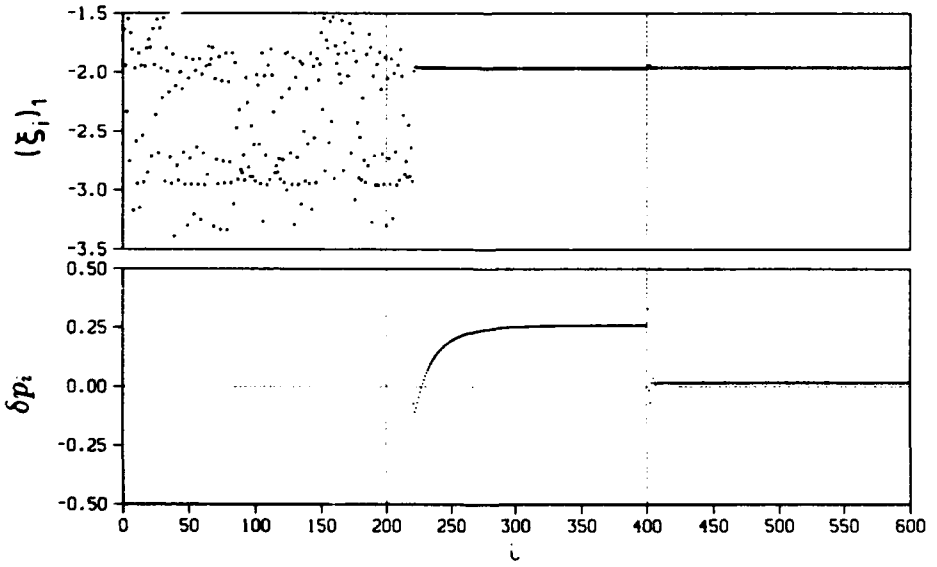

Fig. 5. (a) First component $(\xi_i)_1$ of the points in the surface of section versus i. In order to stabilize ξ_{F2} the control procedures were successively initiated. From 0–200 OGY's law, from 201–400 (15), and from 401–600 (17). (15) and (17) succeeded in stabilizing ξ_{F2}. Because of the large value of the coefficient a ($a = 165.$) in the OGY formula the parameter perturbations δp_i did not happen to fulfill $\delta p_i < \delta p_{max} = 0.5$.

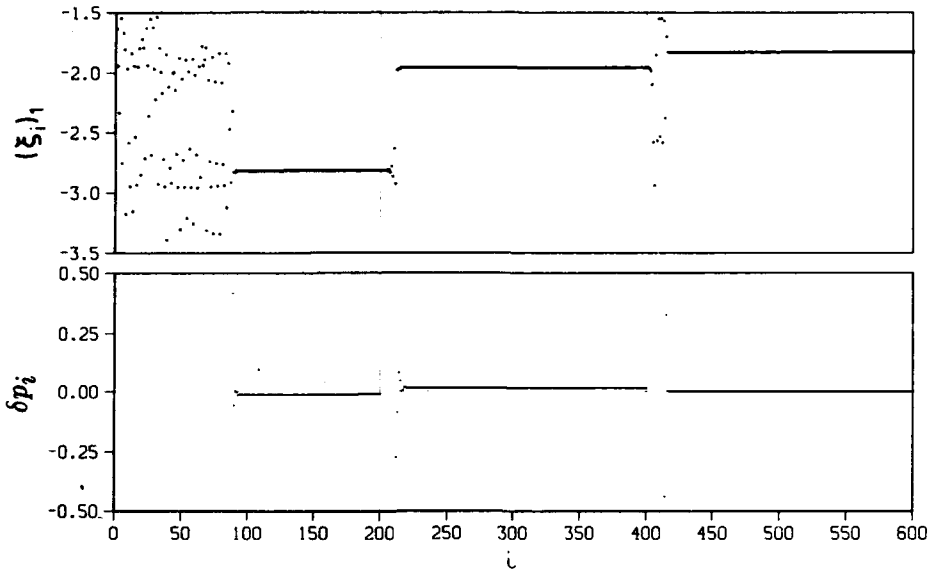

Fig. 6. Using the control law (17) successive control of the fixed points ξ_{F1}, ξ_{F2} and ξ_{F3} could be achieved. From $i = 0$–200 the control formula (17) as applied to stabilize ξ_{F1}, from 201–400 to stabilize ξ_{F2} and from 401–600 to stabilize ξ_{F3}.

Ditto et al. [4] successfully applied the original OGY control formula to a real experiment. Their experimental system was periodically driven with period T. As time series they took a stroboscopic measurement $x(t_i)$, $t_i - t_{i-1} = T$. In this way they obtained a surface of section with points $\xi_i = (x(t_i), x(t_{i-1}))$. We also tested the three versions of the control method using this way of obtaining a surface of section. The periodic motion corresponding to ξ_{F1} could be stabilized by all three algorithms. They were almost equivalent because b_2 and c_2 were nearly zero (of the order of 10^{-4}), so the other coefficients were practically the same ($a \approx b_1 \approx c_1 \approx 2.7$). The periodic motion corresponding to ξ_{F2} could not be stabilized because the embedding in the neighborhood of the fixed point was bad (not injective). The third fixed point finally could only be stabilized using the second modification (17).

Altogether the numerical investigations show that the possibility to stabilize a fixed point is not an intrinsic property of a fixed point, as the eigenvalues λ_u and λ_s are for example. The algorithms were also tested using further surfaces of section. In any case it is confirmed that the quality of the embedding in the neighborhood of the fixed point is of crucial importance for the success of the control procedure. Furthermore, the coefficients of the control formulas differ for different surfaces of section and so do their performances. We always observed that the first modification (15) only worked successfully when the second modification (17) could achieve control, too. The original OGY control formula was able to achieve control only when the two modifications also had success. We never saw that the second modification (17) failed and any of the other methods was successful. But we did observe that the OGY formula failed and the applications of one of the modifications could stabilize the desired fixed points. As a rule this happened when the influence of the preceding parameter was noticeable, which resulted in a non negligible value of $f_u \cdot v$.

5. Measurement noise

With regard to possible applications of the control method to experimental situations the robustness of the method in the presence of

noise is of special interest. Noise can cause several problems. As was already mentioned in ref. [1], noise can kick an orbit out of the control region such that the control requirement $\delta p_i < \delta p_{max}$ gets broken. In case that the attractor has to be reconstructed from a measurement signal further difficulties arise. In what follows we restrict ourselves to the issue of measurement noise.

A major problem already occurs in the preprocessing of the data. The numerically obtained values for the fixed point, its linearization A and the vectors $\boldsymbol{u}$ and $\boldsymbol{v}$ will become more and more imperfect if the noise level increases. This affects directly the resulting control coefficients of the control formulas.

During the control process the exact position of the system in the experimental surface of section is no longer known. Therefore, the control process cannot act exactly in the desired way which limits the control abilities of the control process as well.

To study the effects of measurement noise a noise term $\epsilon\delta$ was added to the measurement function $z(t)$. The random variable δ was chosen to be identically distributed in the interval $[-1, 1]$. The parameter ϵ specifies the intensity of the noise. The surface of section of fig. 1 was used.

For a noise level $\epsilon = 3 \times 10^{-3}$ the second modification was able to stabilize all three fixed points. In fig. 7 the fixed points ξ_{F1}, ξ_{F2}, ξ_{F3} and again ξ_{F1} are successively stabilized. As can be seen the required control signal δp_i is this time much bigger than for the system without noise (see fig. 6). For $\epsilon = 3 \times 10^{-3}$ the second modification gives the only control formula which stabilizes any of the fixed points. While for noiseless data all control formulas could stabilize ξ_{F3} the OGY formula and the first modification lose this ability (see fig. 8). Therefore, the second modification seems to be more robust to measurement noise.

But already the noise level $\epsilon = 5 \times 10^{-3}$ leads to a collapse of the control performance of all

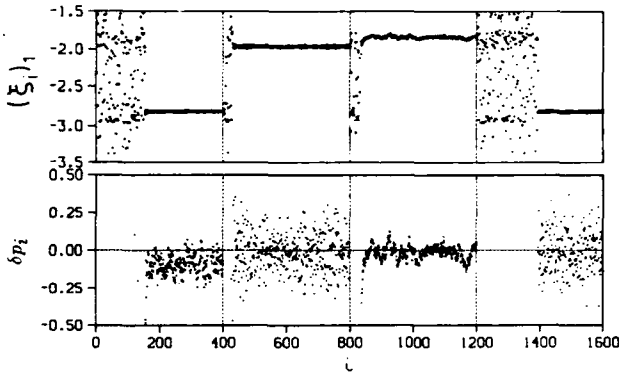

Fig. 7. For a noise level of $\epsilon = 3 \times 10^{-3}$ the fixed points ξ_{F1}, ξ_{F2}, ξ_{F3} and again ξ_{F1} are successively stabilized using the second modification (17). The control parameters were determined from the noisy signal.

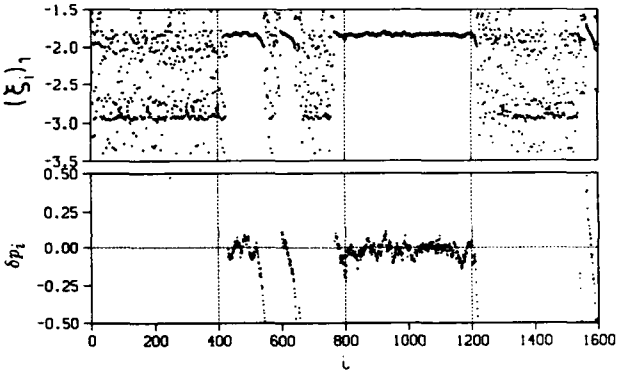

Fig. 8. For a noise level of $\epsilon = 3 \times 10^{-3}$ we tried to stabilize the third fixed point ξ_{F3} using successively the OGY control formula ($i = 1$–400), the first modification ($i = 401$–800), the second modification ($i = 801$–1200), and again the OGY formula ($i = 1201$–1600). Only the second modification was able to stabilize ξ_{F3}.

three versions of the control algorithm. Here the main problem comes from the imperfect numerical determination of the control parameter (control coefficients and position of the fixed points). They were straightforwardly determined without using any noise reduction techniques (e.g. the recently developed techniques [14, 15]). The tolerable noise level can be increased if the control parameters were taken from the noise free data (this is of course not possible in an experimental situation). In fig. 9 the system is spoiled with a noise level $\epsilon = 10^{-2}$. This time the second modification is able to stabilize ξ_{F3} if the noise free

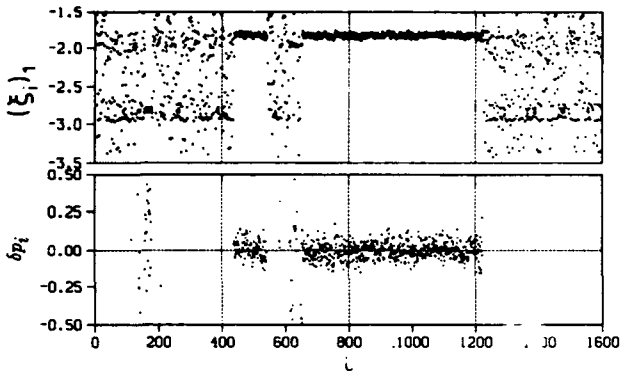

Fig. 9. With the control parameters (Table II) of the noiseless time series the control method was applied to a noisy signal with $\epsilon = 10^{-2}$ to stabilize the third fixed point ξ_{F3}. From $i = 1$–400 OGY's formula was used, from $i = 401$–800 the first modification and from $i = 801$–1200 the second modification and finally from $i = 1201$–1600 again the OGY formula. Only the second modification could stabilize ξ_{F3}.

control parameters are used. The two other versions in contrast fail to control ξ_{F3}. But for the other two fixed points (ξ_{F1}, ξ_{F2}) also the second modification loses its control ability.

So far the numerical simulations show that noise can cause severe problems for the success of the control method. To quantify these problems and to incorporate e.g. noise reduction methods as a remedy a lot of work has to be done in the future.

6. Summary and conclusions

We investigated the control method of Ott, Grebogi and Yorke in the case that one uses time-delay coordinates to reconstruct the attractor from a time series. It turned out that during the control process (switching on and off the parameter perturbations δp_i) the experimental surface of section mapping $\boldsymbol{P}$, whose fixed points one wants to stabilize, does depend not only on the new value p_i at times t_i (t_i time of the ith piercing of the surface of section by the trajectory) but also on the preceding parameter p_{i-1} which was valid in the time interval (t_{i-1}, t_i), i.e. $\boldsymbol{\xi}_{i+1} = \boldsymbol{P}(\boldsymbol{\xi}_i, p_{i-1}, p_i)$ holds. Using this equation as starting point two modifications of the original OGY algorithm were proposed. The first modification (15) is a straightforward extension of the OGY algorithm. It only takes the dependence on p_{i-1} into account which results in the appearance of $\boldsymbol{v} = \partial \boldsymbol{P}/\partial p_{i-1}$ and of δp_{i-1} in the control formula (15).

The second modification (17) was introduced as a remedy for a possible instability (possible increasing of the applied perturbations δp_i) of the first modification. This would occur when the coefficient preceding δp_{i-1} in (15) exceeds 1 which is equivalent to $|\boldsymbol{f}_u \cdot \boldsymbol{v}| > |\boldsymbol{f}_u \cdot \boldsymbol{u}|$. In this case we propose to stabilize $\boldsymbol{\xi}_F$ by requiring that the system stabilizes only the next but one step, i.e. $\boldsymbol{f}_u \cdot \delta \boldsymbol{\xi}_{i+2} = 0$ and that the perturbation needed in the next step δp_{i+1} equals zero. These requirements yield the second modification. In table 1 the original OGY formula and the two modifications are listed.

These three control formulas are applied to simulations of a damped and driven Duffing oscillator. The Duffing oscillator is numerically integrated and its displacements are taken as experimental time series. Using delay coordinates the attractor is reconstructed. The control capabilities of the different control algorithms are demonstrated activating them to stabilize the three fixed points which are determined in the surface of section. We find that the performance of the first modification is superior to the one of the original OGY formula and the second modification outperforms the latter two. However, their performances are similar whenever the influence of the preceding parameter perturbations δp_{i-1} is small which results in a small value of $\boldsymbol{f}_u \cdot \boldsymbol{v}$.

Finally the issue of measurement noise was considered. Only for very small noise levels the second modification preserved its control ability. But already at a noise level of 5×10^{-3} also the second modification failed. At the present stage of the development of the control method the control performance is not satisfactory in the presence of noise. In the immediate future an

improvement might come by applying the recently developed noise reduction methods to get the necessary control parameters more accurate. As in other areas of time series analysis the problem of noise will stay in the center of interest.

In conclusion, we introduced two modifications of the control formula of OGY which can lead to a better performance of the control in the case that the dynamical system is reconstructed using time delay coordinates. Therefore these modifications extend the range of applicability of the OGY control method. With these modifications all remarkable advantages of the OGY control method are preserved, as there are e.g., the dynamics equation are not required, the perturbations of the accessible parameter can be very small, different periodic points can be stabilized in the same parameter range for the same system, and after having determined the control coefficients the computational effort at every iteration is negligible and therefore the possibility of real time applications is given. We expect that the OGY control method will yield important applications in the future also for technical systems.

Acknowledgements

We acknowledge fruitful discussions with C. Mohrdieck and U. Parlitz. One of us (G.N.) was supported by the Studienstiftung des Deutschen Volkes.

References

[1] E. Ott, C. Grebogi and J.A. Yorke, Phys. Rev. Lett. 64 (1990) 1196.
[2] N.H. Packard, J.P. Crutchfield, J.D. Farmer, and R.S. Shaw, Phys. Rev. Lett. 45 (1980) 712.
[3] F. Takens, in: Dynamical Systems and Turbulence eds. D. Rand and L.S. Young (Springer, Berlin, 1981) p. 230.
[4] W.L. Ditto, S.N. Rauseo and M.L. Spano, Phys. Rev. Lett. 65 (1990) 3211.
[5] F.J. Romeiras, E. Ott, C. Grebogi and W.P. Dayawansa, in: American Control Conf. IEEE, 1991.
[6] E. Ott, C. Grebogi and J.A. Yorke, in: Chaos/XAOC Soviet-American Perspectives on Nonlinear Science, ed. D.K. Campbell (American Inst. of Phys., New York 1990) p. 153.
[7] D.S. Broomhead and G.P. King, Physica D 20 (1986) 217.
[8] D.P. Lathrop and E.J. Kostelich, Phys. Rev. A 40 (1989) 4028.
[9] K. Pawelzik and H.G. Schuster, Phys. Rev. A 43 (1991) 1808.
[10] D. Auerbach, P. Cvitanovic, G. Gunaratne J.-P. Eckmann and I. Procaccia, Phys. Rev. Lett. 58 (1987) 2387.
[11] P.J. Brockwell and R.A. Davis, Time series: Theory and Methods (Springer, Berlin, 1987).
[12] U. Parlitz and W. Lauterborn, Phys. Lett. A 107 (1985) 351.
[13] W.H. Press, B.P. Flannery, S.A. Teukolsky and W.T. Vetterling, Numerical Recipes (Cambridge Univ. Press, 1986).
[14] E.J. Kostelich and J.A. Yorke, Physica D 41 (1990) 183.
[15] J.D. Farmer and J.J. Sidorowich, Physica D 47 (1991) 373.

Physica D 58 (1992) 165–192
North-Holland

PHYSICA D

Controlling chaotic dynamical systems

Filipe J. Romeiras[a,b], Celso Grebogi[a,c,d], Edward Ott[a,e,f] and W.P. Dayawansa[f,g]

[a]*Laboratory for Plasma Research, University of Maryland, College Park, MD 20742, USA*
[b]*Centro de Electrodinâmica (INIC) and Departamento de Matemática, Instituto Superior Técnico, 1096 Lisbon Codex, Portugal*
[c]*Department of Mathematics, University of Maryland, College Park, MD 20742, USA*
[d]*Institute for Physical Science and Technology, University of Maryland, College Park, MD 20742, USA*
[e]*Department of Physics, University of Maryland, College Park, MD 20742, USA*
[f]*Department of Electrical Engineering, University of Maryland, College Park, MD 20742, USA*
[g]*Systems Research Center, University of Maryland, College Park, MD 20742, USA*

Received 18 November 1991
Revised manuscript received 16 January 1992
Accepted 16 January 1992

We describe a method that converts the motion on a chaotic attractor to a desired attracting time periodic motion by making only small time dependent perturbations of a control parameter. The time periodic motion results from the stabilization of one of the infinite number of previously unstable periodic orbits embedded in the attractor. The present paper extends that of Ott, Grebogi and Yorke [Phys. Rev. Lett. 64 (1990) 1196], allowing for a more general choice of the feedback matrix and implementation to higher-dimensional systems. The method is illustrated by an application to the control of a periodically impulsively kicked dissipative mechanical system with two degrees of freedom resulting in a four-dimensional map (the "double rotor map"). A key issue addressed is that of the dependence of the average time to achieve control on the size of the perturbations and on the choice of the feedback matrix.

1. Introduction

It is common for systems to evolve with time in a chaotic way. In practice, however, it is often desired that chaos be avoided and/or that the system be optimized with respect to some performance criterion. Given a system which behaves chaotically, one approach might be to make some large (and possibly costly) alteration in the system which completely changes its dynamics in such a way as to achieve the desired objectives. Here we assume that this avenue is not available. Thus we address the following question: Given a chaotic system, how can we obtain improved performance and achieve a desired attracting time-periodic motion by making only *small* controlling temporal perturbations in an accessible system parameter.

The key observation is that a chaotic attractor typically has embedded densely within it an infinite number of unstable periodic orbits [1–5]. In addition, chaotic attractors can also sometimes contain unstable steady states (e.g., the Lorenz attractor has such an embedded steady state). Since we wish to make only small controlling perturbations to the system, we do not envision creating new orbits with very different properties from the already existing orbits. Thus we seek to exploit the already existing unstable periodic orbits and unstable steady states. Our approach is as follows: We first determine some of the unstable low-period periodic orbits and unstable steady states that are embedded in the chaotic attractor. We then examine these orbits and choose one which yields improved system performance. Finally, we apply small controls so as

0167-2789/92/$05.00 © 1992 – Elsevier Science Publishers B.V. All rights reserved

to stabilize this already existing orbit.

Some comments concerning this method are the following:

(1) Before settling into the desired controlled orbit the trajectory experiences a chaotic transient whose expected duration diverges as the maximum allowed size of the control approaches zero.

(2) Small noise can result in occasional bursts in which the orbit wanders far from the controlled orbit.

(3) Controlled chaotic systems offer an advantage in flexibility in that any one of a number of different orbits can be stabilized by the small control, and the choice can be switched from one to another depending on the current desired system performance.

Although we describe the details only in the case of discrete time systems, this method is applicable in the continuous time case as well by considering the discrete time system obtained from the induced dynamics on a Poincaré section.

In order to illustrate the method we apply it to a periodically forced mechanical system (the kicked double rotor), which results in a four-dimensional map. Amongst the examples considered, we study cases where the unstable orbit of the uncontrolled system has two unstable eigenvalues and two stable eigenvalues, and the stabilization is achieved by variation of one control parameter characterizing the strength of the periodic forcing. The present paper generalizes our previous work [6] to the case of higher-dimensional systems [7] and also includes new material illustrating the effect of the choice of stabilization on the length of the chaotic transient experienced by the orbit before control is achieved. Other relevant references on the feedback stabilization of periodic or steady orbits embedded in chaotic attractors are the experiments of Ditto et al. [8], Singer et al. [9], and the paper of Fowler [10]. (Other works in the general field are listed in ref. [11].)

The plan of the paper is as follows. In section 2, we give an implementation of the method, initially developed in ref. [6], by using the "pole placement technique" [7, 12]. In particular, we address the problem of stabilization of periodic orbits with more than one unstable eigenvalue. We also discuss experimental implementation in the absence of an a priori mathematical system model and generalization of the method to deal with cases where delay coordinates embedding is used. In section 3 we present some results for the control of the Hénon map [13], a two-dimensional system that is used as a paradigm in the study of dynamical systems; these results extend those given in ref. [6] in directions relevant to our present study. In section 4 we present results for the control of the double rotor map [14], a four-dimensional system that describes a particular impulsively periodically forced mechanical system. Finally, in section 5 we present the main conclusions of the work.

2. Description of the method

2.1. Formulation

For the sake of simplicity we consider a discrete time dynamical system,

$$\boldsymbol{Z}_{i+1} = \boldsymbol{F}(\boldsymbol{Z}_i, p)\,, \tag{2.1}$$

where $\boldsymbol{Z}_i \in \mathbb{R}^n$, $p \in \mathbb{R}$ and $\boldsymbol{F}$ is sufficiently smooth in both variables. Here, p is considered a real parameter which is available for external adjustment but is restricted to lie in some small interval,

$$|p - \bar{p}| < \delta\,, \tag{2.2}$$

around a nominal value $\bar{p}$. We assume that the nominal system (i.e., for $p = \bar{p}$) contains a chaotic attractor. Our objective is to vary the parameter p with time i in such a way that for almost all initial conditions in the basin of the chaotic attractor, the dynamics of the system

converge onto a desired time periodic orbit contained in the attractor. The control strategy is the following. We will find a stabilizing local feedback control law which is defined on a neighborhood of the desired periodic orbit. This is done by considering the first order approximation of the system at the chosen unstable periodic orbit. Here we assume that this approximation is stabilizable. Since stabilizability is a generic property of linear systems, this assumption is quite reasonable. The ergodic nature of the chaotic dynamics ensures that the state trajectory eventually enters into the neighborhood. Once inside, we apply the stabilizing feedback control law in order to steer the trajectory towards the desired orbit.

For simplicity we shall describe the method as applied to the stabilization of fixed points (i.e., period one orbits) of the map $\boldsymbol{F}$. The consideration of periodic orbits of period larger than one is straightforward and is discussed in section 2.5. Let $\boldsymbol{Z}_*(p)$ denote an unstable fixed point on the attractor. For values of p close to $\bar{p}$ and in the neighborhood of the fixed point $\boldsymbol{Z}_*(\bar{p})$ the map (2.1) can be approximated by the linear map

$$\boldsymbol{Z}_{i+1} - \boldsymbol{Z}_*(\bar{p}) = \mathbf{A}[\boldsymbol{Z}_i - \boldsymbol{Z}_*(\bar{p})] + \boldsymbol{B}(p - \bar{p}), \tag{2.3}$$

where $\mathbf{A}$ is an $n \times n$ Jacobian matrix and $\boldsymbol{B}$ is an n-dimensional column vector,

$$\mathbf{A} = \mathbf{D}_{\boldsymbol{Z}}\boldsymbol{F}(\mathbf{Z}, p), \tag{2.4}$$

$$\boldsymbol{B} = \mathbf{D}_p\boldsymbol{F}(\mathbf{Z}, p), \tag{2.5}$$

and these partial derivatives are evaluated at $\boldsymbol{Z} = \boldsymbol{Z}_*(\bar{p})$ and $p = \bar{p}$. We now introduce the time-dependence of the parameter p by assuming that it is a linear function of the variable $\boldsymbol{Z}_i$ of the form

$$p - \bar{p} = -\boldsymbol{K}^{\mathrm{T}}[\boldsymbol{Z}_i - \boldsymbol{Z}_*(\bar{p})]. \tag{2.6}$$

The $1 \times n$ matrix $\boldsymbol{K}^{\mathrm{T}}$ is to be determined so that the fixed point $\boldsymbol{Z}_*(\bar{p})$ becomes stable. Substituting (2.6) into (2.3) we obtain

$$\boldsymbol{Z}_{i+1} - \boldsymbol{Z}_*(\bar{p}) = (\mathbf{A} - \boldsymbol{B}\boldsymbol{K}^{\mathrm{T}})[\boldsymbol{Z}_i - \boldsymbol{Z}_*(\bar{p})], \tag{2.7}$$

which shows that the fixed point will be stable provided the matrix $\mathbf{A} - \boldsymbol{B}\boldsymbol{K}^{\mathrm{T}}$ is asymptotically stable; that is, all its eigenvalues have modulus smaller than unity.

The solution to the problem of the determination of $\boldsymbol{K}^{\mathrm{T}}$, such that the eigenvalues of the matrix $\mathbf{A} - \boldsymbol{B}\boldsymbol{K}^{\mathrm{T}}$ have specified values, is well known from control systems theory and is called "pole placement technique" (see, for example, Ogata [12]). We summarize the relevant results.

2.2. Review of the pole placement technique

The eigenvalues of the matrix $\mathbf{A} - \boldsymbol{B}\boldsymbol{K}^{\mathrm{T}}$ are called the "regulator poles", and the problem of placing these poles at the desired locations by choosing $\boldsymbol{K}^{\mathrm{T}}$ with $\mathbf{A}$ and $\boldsymbol{B}$ given is the "pole placement problem".

Pole placement problem. Determine the matrix $\boldsymbol{K}^{\mathrm{T}}$ in such a way that the eigenvalues of the matrix $\mathbf{A} - \boldsymbol{B}\boldsymbol{K}^{\mathrm{T}}$ have specified (complex) values $\{\mu_1, \ldots, \mu_n\}$.

The following results [12] give a necessary and sufficient condition for a unique solution of the pole placement problem to exist, and also a method for obtaining it (Ackermann's method).

(1) The pole placement problem has a unique solution if and only if the $n \times n$ matrix

$$\mathbf{C} = (\boldsymbol{B} \vdots \mathbf{A}\boldsymbol{B} \vdots \mathbf{A}^2\boldsymbol{B} \vdots \ldots \vdots \mathbf{A}^{n-1}\boldsymbol{B}),$$

is of rank n. ($\mathbf{C}$ is called the controllability matrix).

(2) The solution of the pole placement problem is given by

$$\boldsymbol{K}^{\mathrm{T}} = (\alpha_n - a_n \ldots \alpha_1 - a_1)\mathbf{T}^{-1},$$

where $\mathbf{T} = \mathbf{C}\mathbf{W}$, and

$$\mathbf{W}=\begin{pmatrix} a_{n-1} & a_{n-2} & \cdots & a_1 & 1 \\ a_{n-2} & a_{n-3} & \cdots & 1 & 0 \\ \vdots & \vdots & & \vdots & \vdots \\ a_1 & 1 & \cdots & 0 & 0 \\ 1 & 0 & \cdots & 0 & 0 \end{pmatrix}.$$

Here $\{a_1, \ldots, a_n\}$ are the coefficients of the characteristic polynomial of $\mathbf{A}$,

$$|s\mathbf{I}-\mathbf{A}| = s^n + a_1 s^{n-1} + \cdots + a_n ,$$

and $\{\alpha_1, \ldots, \alpha_n\}$ are the coefficients of the desired characteristic polynomial of $\mathbf{A} - \boldsymbol{B}\boldsymbol{K}^{\mathrm{T}}$,

$$\Pi_{j=1}^{n}(s-\mu_j) = s^n + \alpha_1 s^{n-1} + \cdots + \alpha_n .$$

2.3. Control parameter

Our considerations so far are based on the linear eq. (2.7) and therefore only apply in the local region near $\boldsymbol{Z}_*(\bar{p})$. On the other hand, the limitation in the size of the parameter perturbations given by (2.2), when combined with (2.6), yields

$$|\boldsymbol{K}^{\mathrm{T}}[\boldsymbol{Z}_i - \boldsymbol{Z}_*(\bar{p})]| < \delta . \tag{2.8}$$

This defines a slab of width $2\delta/|\boldsymbol{K}^{\mathrm{T}}|$. We choose to activate the control according to (2.6) only for values of $\boldsymbol{Z}_i$ inside this slab, and we choose to leave the control parameter at its nominal value (i.e., $p = \bar{p}$) when $\boldsymbol{Z}_i$ is outside this slab. Other choices are possible.

In summary, the control is determined by

$$p - \bar{p} = -\boldsymbol{K}^{\mathrm{T}}[\boldsymbol{Z}_i - \boldsymbol{Z}_*(\bar{p})] \times u(\delta - |\boldsymbol{K}^{\mathrm{T}}[\boldsymbol{Z}_i - \boldsymbol{Z}_*(\bar{p})]|) , \tag{2.9}$$

for arbitrary $\boldsymbol{Z}_i$ [not necessarily close to $\boldsymbol{Z}_*(\bar{p})$], where u is the unit step function defined by

$$u(\alpha) = \begin{cases} 0, & \alpha < 0 , \\ 1, & \alpha > 0 . \end{cases}$$

At this stage it should be pointed out that the matrix $\boldsymbol{K}^{\mathrm{T}}$ can be chosen in many different ways. In principle, any choice of regulator poles inside the unit circle serves our purpose. In ref. [6], the authors made a very special, though quite natural, choice of the gain matrix $\boldsymbol{K}^{\mathrm{T}}$: the resulting value of $p - \bar{p}$ forces the orbit onto the (linear) stable manifold of the fixed point at each iteration. In terms of regulator poles this choice corresponds to setting n_s of these poles equal to the n_s stable eigenvalues of matrix $\mathbf{A}$ and the remaining $n - n_s$ to 0. In terms of the slab (2.8) this choice corresponds not only to orientating it parallel to the stable manifold but also taking an appropriate width.

The choice of the matrix $\boldsymbol{K}^{\mathrm{T}}$ will be discussed at some length in our applications of the method in sections 3 and 4.

2.4. Time to achieve control

The control is activated (i.e., $p \neq \bar{p}$) only if $\boldsymbol{Z}_i$ falls in the narrow slab (2.8). Thus, for small δ, a typical initial condition will execute a chaotic orbit, unchanged from the uncontrolled case, until $\boldsymbol{Z}_i$ falls in this slab. Even then, because of nonlinearity not included in the linearized eq. (2.7), the control may not be able to bring the orbit to the fixed point. In this case the orbit will leave the slab and continue to wander chaotically as if there was no control. Since the orbit on the uncontrolled chaotic attractor is ergodic, at some time it will eventually satisfy (2.8) and also be sufficiently close to the desired fixed point so that control is achieved.

Thus, we create a stable orbit, which, for a typical initial condition, is preceded by a chaotic transient [15–18] in which the orbit is similar to orbits on the uncontrolled chaotic attractor. The length τ of such chaotic transient depends sensitively on the initial condition of the particular orbit. For initial conditions randomly chosen in the basin of attraction the distribution of chaotic transient lengths is exponential [15, 16],

$$\phi(\tau) \simeq \frac{1}{\langle\tau\rangle} \exp\left(-\frac{\tau}{\langle\tau\rangle}\right) , \tag{2.10}$$

for large τ. The quantity $\langle\tau\rangle$ is the characteristic length of the chaotic transient, called in the present case the *average time to achieve control.* Estimates of the scaling of $\langle\tau\rangle$ with δ for small δ are given in Appendix A for the case of two-dimensional maps.

2.5. Control of periodic orbits of period greater than one

The analysis of periodic orbits given in sections 2.1–2.3 can be extended to nontrivial periodic orbits (i.e., orbits with period greater than one). The most direct way is to take the Tth iterate of the map, where T denotes the period of the orbit to be stabilized. For the T times iterated map, any point on the periodic orbit is a fixed point, and we can then apply the discussion sections 2.1–2.3. This method is, however, overly sensitive to noise, especially when long period periodic orbits are involved. Next we outline another method which we believe should, in general, be better. In terms of the treatment of section 2.2, the prescription we give below corresponds to placing the unstable eigenvalues of the uncontrolled problem at zero, while leaving the stable eigenvalues unchanged. (This is only one of many possibilities that could be given.)

We denote the periodic orbit by $\boldsymbol{Z}_{i*}(p)$, where $\boldsymbol{Z}_{(i+T)*}(p) = \boldsymbol{Z}_{i*}(p)$. In addition, we introduce the set of T matrices $\mathbf{A}_i$ which are $n \times n$ and the set of T column vectors $\boldsymbol{B}_i$ which are of dimension n, where

$$\mathbf{A}_i = \mathbf{A}_{i+T} = \mathbf{D}_{\boldsymbol{Z}}\boldsymbol{F}(\boldsymbol{Z}, p)\,,$$

$$\boldsymbol{B}_i = \boldsymbol{B}_{i+T} = \mathbf{D}_p\boldsymbol{F}(\boldsymbol{Z}, p)\,,$$

and the partial derivatives are evaluated at $\boldsymbol{Z} = \boldsymbol{Z}_{i*}(\bar{p})$ and $p = \bar{p}$.

Linearizing as in eq. (2.3), we have

$$\boldsymbol{Z}_{i+1} - \boldsymbol{Z}_{(i+1)*}(\bar{p}) = \mathbf{A}_i[\boldsymbol{Z}_i - \boldsymbol{Z}_{i*}(\bar{p})] + \boldsymbol{B}_i(p_i + \bar{p})\,. \tag{2.11}$$

Say that the periodic orbit has u unstable eigenvalues (i.e., u eigenvalues with magnitude greater than one) and s stable eigenvalues, where $u + s = n$. At each point $\boldsymbol{Z}_{i*}(\bar{p})$ on the $p = \bar{p}$ periodic orbit, determine vectors $\{\boldsymbol{v}_{i,1}, \boldsymbol{v}_{i,2}, \ldots, \boldsymbol{v}_{i,s}\}$ which span the linearized stable subspace. Now let

$$\boldsymbol{\phi}_{i,j} = \mathbf{A}_{i+u-1}\mathbf{A}_{i+u-2}\cdots\mathbf{A}_{i+j+1}\mathbf{A}_{i+j}\,,$$

for $j = 1, 2, \ldots, (u-1)$ and

$$\mathbf{C}_i = (\boldsymbol{\phi}_{i,1}\boldsymbol{B}_i \vdots \boldsymbol{\phi}_{i,2}\boldsymbol{B}_{i+1} \vdots \cdots \vdots \boldsymbol{\phi}_{i,u-1}\boldsymbol{B}_{i+u-2} \vdots \boldsymbol{B}_{i+u-1} \vdots \boldsymbol{v}_{i+u,1} \vdots \boldsymbol{v}_{i+u,2} \vdots \cdots \vdots \boldsymbol{v}_{i+u,s})$$

(One choice of the vectors $\{\boldsymbol{v}_{i,1}, \boldsymbol{v}_{1,2}, \ldots, \boldsymbol{v}_{i,s}\}$ is the stable eigenvectors of $\mathbf{A}_i\mathbf{A}_{i-1}\ldots\mathbf{A}_{i-T+1}$.) The controllability condition (analogous to that in section 2.2) is that $\mathbf{C}_i$ be nonsingular. The desired result for the control is then specified by

$$p_i - \bar{p} = -\boldsymbol{K}_i^{\mathrm{T}}[\boldsymbol{Z}_i - \boldsymbol{Z}_{i*}(\bar{p})]\,, \tag{2.12a}$$

where

$$\boldsymbol{K}_i^{\mathrm{T}} = \boldsymbol{\kappa}\mathbf{C}_i^{-1}\boldsymbol{\phi}_{i,0}\,, \tag{2.12b}$$

and $\boldsymbol{\kappa}$ denotes an n-dimensional row vector whose first entry is one and all of whose remaining entries are zeros.

To derive eqs. (2.12) we iterate (2.11) u times,

$$\boldsymbol{Z}_{i+u} - \boldsymbol{Z}_{(i+u)*}(\bar{p}) = \boldsymbol{\phi}_{i,0}[\boldsymbol{Z}_i - \boldsymbol{Z}_{i*}(\bar{p})] + \boldsymbol{\phi}_{i,1}\boldsymbol{B}_i(p_i - \bar{p}) + \boldsymbol{\phi}_{i,2}\boldsymbol{B}_{i+1}(p_{i+1} - \bar{p}) + \cdots + \boldsymbol{B}_{i+u-1}(p_{i+u-1} - \bar{p})\,. \tag{2.13a}$$

We then demand that $\boldsymbol{Z}_{i+u}$ land on the linearized stable manifold of the periodic orbit through the point $\boldsymbol{Z}_{(i+u)*}(\bar{p})$. That is, we choose the p's such that there exists s coefficients $\alpha_1, \alpha_2, \ldots, \alpha_s$ such that

$$\boldsymbol{Z}_{i+u} - \boldsymbol{Z}_{(i+u)*}(\bar{p}) = \alpha_1\boldsymbol{v}_{i+u,1} + \alpha_2\boldsymbol{v}_{i+u,2} + \cdots + \alpha_s\boldsymbol{v}_{i+u,s}\,. \tag{2.13b}$$

Regarding (2.13a) and (2.13b) as $n = u + s$ equations in the n unknowns, $p_i, p_{i+1}, \ldots, p_{i+u-1}, \alpha_1, \alpha_2, \ldots, \alpha_s$, we then solve for p_i to obtain (2.12).

[Note from the above that at time i we could, once and for all, calculate all the control parameter values to be applied in the next u iterates, $p_i, p_{i+1}, \ldots, p_{i+u-1}$. In the presence of noise, however, this is not a good idea (assuming $u > 1$), since it does not take advantage of the opportunity to correct for the noise on each iterate. Therefore, we believe that, in the presence of noise, it is best to perform the calculation of p_i via eq. (2.12) on each iterate.]

2.6. *Use of delay coordinates*

In experimental studies of chaotic dynamical systems, delay coordinates are often used to represent the system state. This is sometimes useful because it only requires measurement of the time series of a *single* scalar state variable which, we denote $\xi(t)$. A delay coordinate vector can be formed as follows:

$$\mathbf{Z}(t) = (\xi(t), \xi(t - T_D), \xi(t - 2T_D), \ldots, \times \xi(t - MT_D)),$$

where T_D is some conveniently chosen delay time, and the time variable t is assumed continuous. Embedding theorems guarantee that for $M \geq 2n$, where n is the system dimensionality, the vector $\mathbf{Z}$ is generically a global one-to-one representation of the system state. (Actually, for our purposes, we do not require a global embedding; we only require $\mathbf{Z}$ to be one-to-one in the small region near the periodic orbit, and this can typically be achieved with $M = n - 1$.) To obtain a map, one can take a Poincaré surface of section. For the often encountered case of a system which is periodically forced at a period T_F, one can define a "stroboscopic surface of section" by sampling the state at discrete times $t_i = iT_F + t_0$. In this case we have the discrete state variable $\mathbf{Z}_i = \mathbf{Z}(t_i)$.

As pointed out by Dressler and Nitsche [19], in the presence of parameter variation, delay coordinates lead to a map of a different form than

$$\mathbf{Z}_{i+1} = \boldsymbol{F}(\mathbf{Z}_i, p_i),$$

which is the form assumed in sections 2.1–2.5. For example, in the periodically forced case, since the components of $\mathbf{Z}_i$ are $\xi(t_i - mT_D)$ for $m = 0, 1, \ldots, M$, the vector $\mathbf{Z}_{i+1}$ must depend not only on p_i, but also on all previous values of the parameter that were in effect during the time interval $t_i \leq t \leq t_i - MT_D$. In particular, let r be the smallest integer such that $MT_D < rT_F$. Then the relevant map is in general of the form

$$\mathbf{Z}_{i+1} = \boldsymbol{G}(\mathbf{Z}_i, p_i, p_{i-1}, \ldots, p_{i-r}). \tag{2.14a}$$

For $r = 1$ we have

$$\mathbf{Z}_{i+1} = \boldsymbol{G}(\mathbf{Z}_i, p_i, p_{i-1}). \tag{2.14b}$$

We now discuss how the technique of section 2.2 can be applied in the case of delay coordinates, and, for simplicity, we limit the discussion to $r = 1$, eq. (2.14b). Linearizing as in eq. (2.3) and again restricting our attention to the case of a fixed point orbit, we have

$$\mathbf{Z}_{i+1} - \mathbf{Z}_*(\bar{p}) = \mathbf{A}[\mathbf{Z}_i - \mathbf{Z}_*(\bar{p})] + \boldsymbol{B}_a(p_i - \bar{p}) + \boldsymbol{B}_b(p_{i-1} - \bar{p}), \tag{2.15}$$

where $\mathbf{A} = \mathbf{D}_Z \boldsymbol{G}(\mathbf{Z}, p, p')$, $\boldsymbol{B}_a = \mathbf{D}_p \boldsymbol{G}(\mathbf{Z}, p, p')$, and $\boldsymbol{B}_b = \mathbf{D}_{p'} \boldsymbol{G}(\mathbf{Z}, p, p')$, and all partial derivatives are evaluated at $\mathbf{Z} = \mathbf{Z}_*(\bar{p})$ and $p = \bar{p} = p'$.

Now define a new state variable with one extra component by

$$\tilde{\mathbf{Z}}_{i+1} = \begin{pmatrix} \mathbf{Z}_{i+1} \\ p_i \end{pmatrix}. \tag{2.16}$$

and introduce the linear control law,

$$p_i - \bar{p} = -\boldsymbol{K}^{\mathrm{T}}[\boldsymbol{Z}_i - \boldsymbol{Z}_*(\bar{p})] - k(p_{i-1} - \bar{p}) . \tag{2.17}$$

Combining these equations, we obtain

$$\tilde{\boldsymbol{Z}}_{i+1} - \tilde{\boldsymbol{Z}}_*(\bar{p}) = (\tilde{\mathbf{A}} - \tilde{\boldsymbol{B}}\tilde{\boldsymbol{K}}^{\mathrm{T}})[\tilde{\boldsymbol{Z}}_i - \tilde{\boldsymbol{Z}}_*(\bar{p})] , \tag{2.18}$$

where

$$\tilde{\boldsymbol{Z}}_*(\bar{p}) = \begin{pmatrix} \boldsymbol{Z}_*(\bar{p}) \\ \bar{p} \end{pmatrix}, \quad \tilde{\mathbf{A}} = \begin{pmatrix} \mathbf{A} & \boldsymbol{B}_{\mathrm{b}} \\ \mathbf{0} & 0 \end{pmatrix},$$

$$\tilde{\boldsymbol{B}} = \begin{pmatrix} \boldsymbol{B}_{\mathrm{a}} \\ 1 \end{pmatrix}, \quad \tilde{\boldsymbol{K}} = \begin{pmatrix} \boldsymbol{K} \\ k \end{pmatrix}.$$

Since (2.18) is now of the same form as (2.3), the method of section 2.2 can be applied. (A similar result for any $r > 1$ also clearly holds.)

Another method of control for delay coordinates is to reduce (2.14b) directly to the form $\boldsymbol{Z}_{i+1} = \boldsymbol{F}(\boldsymbol{Z}_i, p_i)$ and then proceed as in sections 2.1 and 2.2. This reduction can be done by setting $p_i \equiv \bar{p}$ for every other time step. For example, say $p_i = 0$ for i odd, and $j = \frac{1}{2}i$ for even i. Then making the replacements $\boldsymbol{Z}_i \to \hat{\boldsymbol{Z}}_j$, $p_i \to \hat{p}_j$ for even i, and iterating (2.14b) twice we have

$$\begin{aligned} \hat{\boldsymbol{Z}}_{j+1} &= \boldsymbol{G}[\boldsymbol{G}(\hat{\boldsymbol{Z}}_j, \bar{p}, \hat{p}_j), \hat{p}_j, \bar{p}] \\ &\equiv \hat{\boldsymbol{F}}(\hat{\boldsymbol{Z}}_j, \hat{p}_j) , \end{aligned} \tag{2.19}$$

which is of the required form. We believe, however, that the first method we have given [i.e., that based on eq. (2.18)] should usually be capable of yielding superior results to the method based on (2.19) with respect to noise sensitivity and time to achieve control. This is because our second method does not take advantage of the opportunity to control on each time iterate while our first method does.

3. Controlling the Hénon map

In ref. [6], the authors used the Hénon map to illustrate the control method and, in particular, to test their theoretical predictions concerning the average time to achieve control. As already pointed out, their work is based on a particular choice of the gain matrix $\boldsymbol{K}^{\mathrm{T}}$. In this section we consider how different choices of $\boldsymbol{K}^{\mathrm{T}}$ affect the average time to achieve control for the Hénon map.

The Hénon map [13] is the two-dimensional map

$$\boldsymbol{Z} \mapsto \boldsymbol{Z}' = \boldsymbol{F}(\boldsymbol{Z}) ,$$

defined by

$$\begin{pmatrix} x \\ y \end{pmatrix} \mapsto \begin{pmatrix} x' \\ y' \end{pmatrix} = \begin{pmatrix} a - x^2 + by \\ x \end{pmatrix},$$

where $(x, y) \in \mathbb{R} \times \mathbb{R}$. We keep the parameter b fixed throughout ($b = 0.3$) and allow the control parameter a to vary around a nominal value $\bar{a}$ ($\bar{a} = 1.4$) for which the map has a chaotic attractor.

For $a = \bar{a} = 1.4$ there is an unstable saddle fixed point contained in the chaotic attractor. This fixed point is located at

$$\boldsymbol{Z}_*(a) = x_*(a)\begin{pmatrix} 1 \\ 1 \end{pmatrix},$$

$$x_*(a) = -c + (c^2 + a)^{1/2}, \quad c = \tfrac{1}{2}(1 - b) ,$$

for $a \geq -c^2$. Noting that the Jacobian matrix of partial derivatives of the map is

$$\mathbf{D}_{\boldsymbol{Z}}\boldsymbol{F}(\boldsymbol{Z}) = \begin{pmatrix} -2x & b \\ 1 & 0 \end{pmatrix},$$

and that the stability of the fixed point is determined by the roots of the characteristic equation

$$|\mathbf{D}_{\boldsymbol{Z}}\boldsymbol{F}[\boldsymbol{Z}_*(a)] - s\mathbf{I}| = 0 ,$$

one can easily check that the fixed point is stable for $-c^2 < a < 3c^2$ and unstable for $a > 3c^2$. (Hence the fixed point is unstable for $b = 0.3$, $a = \bar{a} = 1.4$ since $c = 0.35$.)

The quantities that appear in section 2.2 are as follows:

$$\mathbf{A}=\begin{pmatrix}-2\bar{x}_* & b\\ 1 & 0\end{pmatrix},\quad \mathbf{B}=\begin{pmatrix}1\\0\end{pmatrix},$$

$$\mathbf{C}=(\mathbf{B}:\mathbf{AB})=\begin{pmatrix}1 & -2\bar{x}_*\\ 0 & 1\end{pmatrix},$$

$$\mathbf{W}=\begin{pmatrix}2\bar{x}_* & 1\\ 1 & 0\end{pmatrix},\quad \mathbf{T}=\begin{pmatrix}0 & 1\\ 1 & 0\end{pmatrix},$$

$$\boldsymbol{K}^{\mathrm{T}}=(\alpha_1-a_1\quad \alpha_2-a_2),$$

where

$$a_1=2\bar{x}_*=-(\lambda_u+\lambda_s),\quad a_2=-b=\lambda_u\lambda_s,$$

and

$$\alpha_1=-(\mu_1+\mu_2),\quad \alpha_2=\mu_1\mu_2.$$

Here $\bar{x}_*=x_*(\bar{a})$, and λ_u and λ_s are the eigenvalues of matrix **A**,

$$\left.\begin{matrix}\lambda_s\\ \lambda_u\end{matrix}\right\}=-\bar{x}_*\pm(\bar{x}_*^2+b)^{1/2}.$$

The quantities μ_1 and μ_2 are the regulator poles [i.e., the eigenvalues of $(\mathbf{A}-\boldsymbol{B}\boldsymbol{K}^{\mathrm{T}})$].

In order to better illustrate the different choices of regulator poles or, equivalently, of the matrix $\boldsymbol{K}^{\mathrm{T}}$, we have used the plane (α_1, α_2) [cf. fig. 1]. In this plane we have plotted the lines of marginal stability $\mu_1=\pm1$ $(1\pm\alpha_1+\alpha_2=0)$ and $\mu_1\mu_2=1$ $(\alpha_2=1)$; the bounded triangular region delimited by these lines (shown shaded in the figure) is the region where the regulator poles are stable. In addition, we have plotted as dashed lines the axes $(k_1, k_2)=\boldsymbol{K}^{\mathrm{T}}$ which are related to (α_1, α_2) by the translations

$$k_1=\alpha_1-a_1,\quad k_2=\alpha_2-a_2.$$

The straight solid line in the figure going through the origin of the (k_1, k_2) plane has slope $-\lambda_s$ and intersects the line $\alpha_2=0$ at the point Q with coordinates $(\alpha_1, \alpha_2)=(-\lambda_s, 0)$. To this point

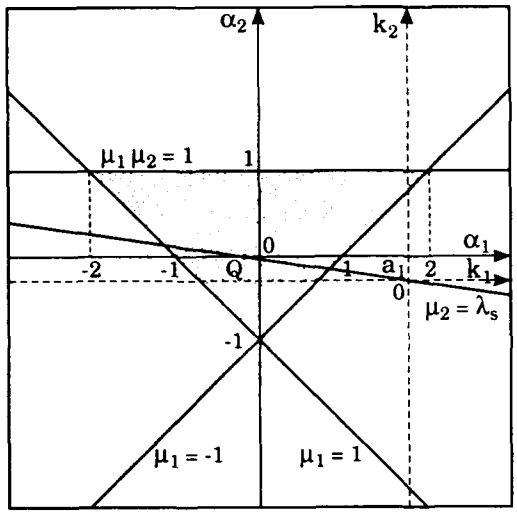

Fig. 1. Hénon map: choice of regulator poles.

corresponds the regulator poles

$$\mu_1=0,\quad \mu_2=\lambda_s,$$

and the matrix

$$\boldsymbol{K}^{\mathrm{T}}=\lambda_u(1\quad -\lambda_s)\equiv\boldsymbol{K}_Q^{\mathrm{T}}.$$

$\boldsymbol{K}_Q^{\mathrm{T}}$ is the special choice of matrix $\boldsymbol{K}^{\mathrm{T}}$ made in ref. [6].

Before proceeding with the discussion, it is convenient to express the vector $\boldsymbol{K}^{\mathrm{T}}$ in polar coordinates

$$\boldsymbol{K}^{\mathrm{T}}=|\boldsymbol{K}^{\mathrm{T}}|(\cos\theta, \sin\theta).$$

We consider the following two ways of varying the vector $\boldsymbol{K}^{\mathrm{T}}$ (inside the triangular region of stability):

(I) θ fixed, $|\boldsymbol{K}^{\mathrm{T}}|$ variable.

(II) $|\boldsymbol{K}^{\mathrm{T}}|$ fixed, θ variable.

In terms of the control slab defined by eq (2.8) we have that in situation (I) the slab is kept orientated in a fixed direction while its width $w=2\delta/|\boldsymbol{K}^{\mathrm{T}}|$ varies, whereas in situation (II) the direction of the slab is rotated while its width is kept fixed at $w=2\delta/|\boldsymbol{K}_Q^{\mathrm{T}}|$. The choice of the $\boldsymbol{K}^{\mathrm{T}}$ in ref. [6] has $\theta=\theta_Q\equiv\tan^{-1}(-\lambda_s)$ and, as we

shall see, this choice is optimal from the point of view of the time to achieve control. (To see that the choice of ref. [6] corresponds to $\theta = \theta_Q$, we note that with this choice one obtains a convergence rate to the periodic orbit of μ_s as in ref. [6].)

In the numerical experiments we calculated the average time to achieve control by the method described in Appendix B. We also allowed for different values of the maximum amplitude of the parameter perturbations, δ.

First we consider the case where θ is fixed (case I) at the value

$$\theta = \theta_Q .$$

This case has a simple interpretation in terms of regulator poles: $\mu_2 = \lambda_s$ is kept fixed while μ_1 is allowed to vary between -1 and $+1$. μ_1 and $|K^T|$ are related by

$$|K^T| = |\mu_1 - \lambda_u|(1 + \lambda_s^2)^{1/2} .$$

Fig. 2 shows results for $\langle \tau \rangle$ for this case. We see that the average time to achieve control increases with μ_1, although only moderately.

Fig. 3 shows results for $\langle \tau \rangle$ versus θ for $|K|^T$ held fixed (case II) at

$$|K^T| = |K_Q^T| = |\lambda_u|(1 + \lambda_s^2)^{1/2} .$$

We see that the average time to achieve control has a strong minimum at $\theta = \theta_Q$.

Fig. 4 shows $\langle \tau \rangle$ versus $|K^T|$ for three values of θ, $\theta = \theta_0$, $\theta = \theta_Q$, and $\theta = \theta_1$, where $\theta_0 < \theta_Q < \theta_1$ and θ_0 and θ_1 are close to θ_Q ($\theta_0 = 170.4°$, $\theta_Q = 171.1°$, $\theta_1 = 172.0°$). We observe that the $\theta = \theta_Q$ result is always below the results for $\theta = \theta_0$ and $\theta = \theta_1$ indicating that the average time

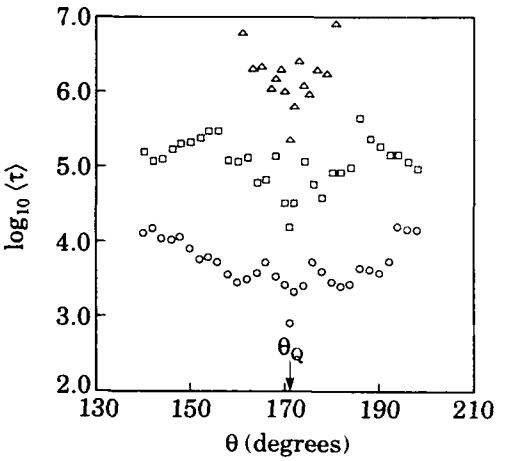

Fig. 3. Hénon map: $\log_{10}\langle \tau \rangle$ versus θ, with $|K^T| = |K_Q^T|$, for (○) $\delta = 10^{-2}$, (□) $\delta = 10^{-3}$, (△) $\delta = 10^{-4}$ ($\bar{a} = 1.4$, $b = 0.3$).

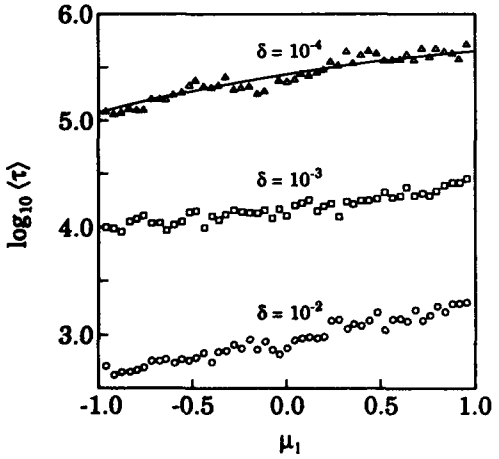

Fig. 2. Hénon map: $\log_{10}\langle \tau \rangle$ versus μ_1, with $\mu_2 = \lambda_s$, for (○) $\delta = 10^{-2}$, (□) $\delta = 10^{-3}$, (△) $\delta = 10^{-4}$. The theoretical curve was calculated using eq. (A.9) of appendix A. ($\bar{a} = 1.4$, $b = 0.3$).

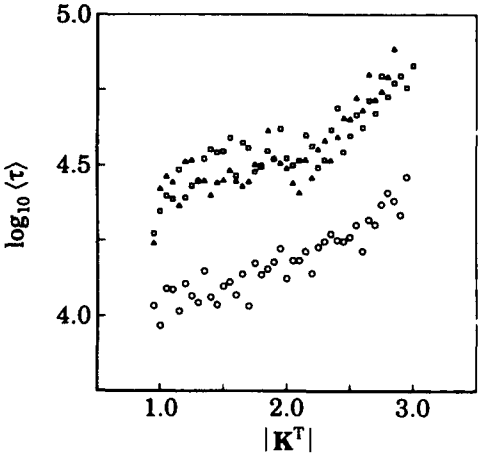

Fig. 4. Hénon map: $\log_{10}\langle \tau \rangle$ versus $|K^T|$ for (○) $\theta = \theta_Q$, (□) $\theta = \theta_0$, (△) $\theta = \theta_1$ ($\theta_0 < \theta_Q < \theta_1$; $\theta_0 = \tan^{-1}[-\lambda_u\lambda_s/(\lambda_u + \lambda_s)] = 170.4°$, $\theta_Q = \tan^{-1}(-\lambda_s) = 171.1°$, $\theta_1 = 172.0°$), and $\delta = 10^{-3}$.

to achieve control has a strong minimum at $\theta = \theta_Q$ not only for $|\boldsymbol{K}^{\mathrm{T}}| = |\boldsymbol{K}_Q^{\mathrm{T}}|$ but for all values of $|\boldsymbol{K}^{\mathrm{T}}|$. Thus the condition $\theta = \theta_Q$ is optimal.

In Appendix A we show how the average time to achieve control can be obtained theoretically in the case of two-dimensional maps and verify that there is excellent agreement between the theoretical and experimental results in the case of the Hénon map.

4. Controlling the double rotor

In this section we apply the control method described in section 2 to a dynamical system known as the double rotor map. We start by deriving the map (section 4.1 and Appendix B), then study its fixed points (section 4.2) and its attractors (section 4.3), including chaotic ones, and finally proceed to control some of the fixed points embedded in one of the chaotic attractors (sections 4.4 and 4.5).

4.1. The double rotor map

The double rotor map is a four-dimensional map which describes the time evolution of a mechanical system known as the kicked double rotor [14]. This system is a four-dimensional extension of the kicked (single) rotor, a two-dimensional system that is described by the well-known dissipative standard map [20].

The double rotor is composed of two thin, massless rods connected as shown in fig. 5. The first rod, of length l_1, pivots about P_1 (which is fixed), and the second rod, of length $2l_2$, pivots about P_2 (which moves). The angles $\theta_1(t)$, $\theta_2(t)$ specify the orientations at time t of the first and second rods, respectively. A mass m_1 is attached at P_2, and masses $\frac{1}{2}m_2$ are attached to each end of the second rod (P_3 and P_4). Friction at P_1 (with coefficient ν_1) slows the first rod at a rate proportional to its angular velocity $\dot{\theta}_1(t) \equiv d\theta_1(t)/dt$; friction at P_2 (with coefficient ν_2) slows the second rod (and simultaneously accelerates the first rod) at a rate proportional to $\dot{\theta}_2(t) - \dot{\theta}_1(t)$. The end of the second rod marked P_3 receives periodic impulse kicks at times $t = T, 2T, \ldots$, always from the same direction and with constant strength f_0. There is no gravity.

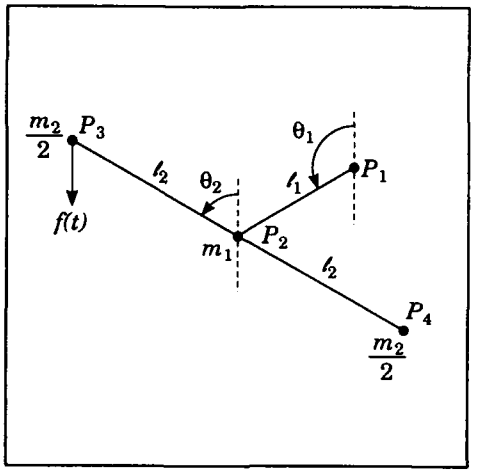

Fig. 5. The double rotor.

In Appendix C we write the differential equations that describe the kicked double rotor and proceed to derive from them the *double rotor map* relating the state of the system just after consecutive kicks. We obtain the four-dimensional map

$$\boldsymbol{Z} \mapsto \boldsymbol{Z}' = \boldsymbol{F}(\boldsymbol{Z}),$$

defined by

$$\begin{pmatrix} \boldsymbol{X} \\ \boldsymbol{Y} \end{pmatrix} \mapsto \begin{pmatrix} \boldsymbol{X}' \\ \boldsymbol{Y}' \end{pmatrix} = \begin{pmatrix} \mathbf{M}\boldsymbol{Y} + \boldsymbol{X} \\ \mathbf{L}\boldsymbol{Y} + \boldsymbol{G}(\boldsymbol{X}') \end{pmatrix}, \tag{4.1}$$

where

$$\boldsymbol{X} = \begin{pmatrix} x_1 \\ x_2 \end{pmatrix} \in \mathrm{S}^1 \times \mathrm{S}^1, \quad \boldsymbol{Y} = \begin{pmatrix} y_1 \\ y_2 \end{pmatrix} \in \mathbb{R} \times \mathbb{R},$$

and

$$\boldsymbol{G}(\boldsymbol{X}') = \begin{pmatrix} c_1 \sin x_1' \\ c_2 \sin x_2' \end{pmatrix}. \tag{4.2}$$

x_1, x_2 are the angular positions of the rods at the instant of the kth kick, $x_j = \theta_j(kT)$, while y_1, y_2

are the angular velocities of the rods immediately after the kth kick, $y_j = \dot{\theta}_j(kT^+)$. S^1 is the circle $\mathbb{R}(\mathrm{mod}\, 2\pi)$. $\mathbf{L}$ and $\mathbf{M}$ are constant 2×2 matrices defined by

$$\mathbf{L} = \sum_{j=1}^{2} \mathbf{W}_j \, e^{\lambda_j T}, \quad \mathbf{M} = \sum_{j=1}^{2} \mathbf{W}_j \, \frac{e^{\lambda_j T} - 1}{\lambda_j},$$

$$\mathbf{W}_1 = \begin{pmatrix} a & b \\ b & d \end{pmatrix}, \quad \mathbf{W}_2 = \begin{pmatrix} d & -b \\ -b & a \end{pmatrix},$$

$$a = \frac{1}{2}\left(1 + \frac{\nu_1}{\Delta}\right), \quad d = \frac{1}{2}\left(1 - \frac{\nu_1}{\Delta}\right), \quad b = -\frac{\nu_2}{\Delta},$$

$$\left.\begin{matrix} \lambda_1 \\ \lambda_2 \end{matrix}\right\} = -\tfrac{1}{2}(\nu_1 + 2\nu_2 \pm \Delta),$$

$$\Delta = (\nu_1^2 + 4\nu_2^2)^{1/2}.$$

Finally, c_1 and c_2 are given by

$$c_j = \frac{f_0}{I} l_j, \quad j = 1, 2,$$

where

$$I = (m_1 + m_2) l_1^2 = m_2 l_2^2.$$

The following relation between matrices $\mathbf{L}$ and $\mathbf{M}$ will be useful below:

$$\mathbf{L} = \mathbf{I} + \mathbf{A}_\nu \mathbf{M}, \tag{4.3}$$

where

$$\mathbf{A}_\nu = \begin{pmatrix} -(\nu_1 + \nu_2) & \nu_2 \\ \nu_2 & -\nu_2 \end{pmatrix}.$$

(λ_1, λ_2 are precisely the eigenvalues of $\mathbf{A}_\nu$.) Note also that

$$|\mathbf{L}| = e^{(\lambda_1 + \lambda_2)T},$$

$$|\mathbf{M}| = \frac{e^{\lambda_1 T} - 1}{\lambda_1} \, \frac{e^{\lambda_2 T} - 1}{\lambda_2},$$

$$|\mathbf{A}_\nu| = \nu_1 \nu_2.$$

From now on we assume that $\nu_1 = \nu_2 \equiv \nu$. This leads to

$$\left.\begin{matrix} \lambda_1 \\ \lambda_2 \end{matrix}\right\} = -\tfrac{1}{2}\nu(3 \pm \sqrt{5}),$$

$$\left.\begin{matrix} a \\ d \end{matrix}\right\} = \tfrac{1}{2}(1 \pm \tfrac{1}{5}\sqrt{5}),$$

$$b = -\tfrac{1}{5}\sqrt{5}.$$

In all the numerical work described in the rest of this section the parameters ν, T, I, m_1, m_2, l_1, and l_2 were kept fixed at the values

$$\nu = T = I = m_1 = m_2 = l_2 = 1,$$
$$l_1 = 1/\sqrt{2}. \tag{4.4}$$

The only parameter which we shall vary is the forcing f_0 used as the control parameter.

4.2. Fixed points of the double rotor map

The fixed points $Z_* = (X_*, Y_*)$ of the map (4.1) are solutions of the system

$$\begin{aligned} X_* &= \mathbf{M} Y_* + X_* - 2\pi N, \\ Y_* &= \mathbf{L} Y_* + G(X_*), \end{aligned} \tag{4.5}$$

where the components of the vector $N = (n_1, n_2)$ are integer and are the rotation numbers in the x_1, x_2 variables. The rotation numbers n_1, n_2 are defined as the multiples of 2π by which x_{1*}, x_{2*} are increased in one iteration of the map before being brought to the interval $[0, 2\pi]$. From eqs. (4.5) we obtain, using (4.3),

$$\begin{aligned} Y_* &= 2\pi \mathbf{M}^{-1} N, \\ G(X_*) &= -2\pi \mathbf{A}_\nu N. \end{aligned} \tag{4.6}$$

Using the definitions of the matrices G and $\mathbf{A}_\nu$ we rewrite the second of the eqs. (4.6) in the form

$$\begin{pmatrix} \sin x_{1*} \\ \sin x_{2*} \end{pmatrix} = -\frac{2\pi\nu I}{f_0} \begin{pmatrix} (1/l_1)(-2n_1 + n_2) \\ (1/l_2)(n_1 - n_2) \end{pmatrix}$$

$$\equiv \frac{1}{f_0} \begin{pmatrix} f_{01} \\ f_{02} \end{pmatrix}. \tag{4.7}$$

where the identity on the right defines the two new quantities f_{01} and f_{02}. These equations show that for each pair of rotation numbers (n_1, n_2) a set of four possible solutions for (x_{1*}, x_{2*}) exists if $|f_0| \geq |f_{0c}|$, where $|f_{0c}| = \max(|f_{01}|, |f_{02}|)$. The four fixed points correspond to the four combinations of values of (x_{1*}, x_{2*}) that have the same pair of values of $(\sin x_{1*}, \sin x_{2*})$. When necessary we will use the notation

$$\boldsymbol{Z}_*^{[N;q]} = (\boldsymbol{X}_*^{[N;q]}, \boldsymbol{Y}_*^{[N]}),$$

or more simply $[N; q]$, to identify the fixed points, where the index q labels the four possible solutions of (4.7) ($q = 1, 2, 3, 4$) and, as shown in fig. 6, corresponds to the ordering

$$x_{1*}^{[N;1]} = x_{1*}^{[N;2]} < x_{1*}^{[N;3]} = x_{1*}^{[N;4]},$$
$$x_{2*}^{[N;1]} = x_{2*}^{[N;3]} < x_{2*}^{[N;2]} = x_{2*}^{[N;4]}$$

Note that $\boldsymbol{Y}_*^{[N]} = (y_{1*}^{[N]}, y_{2*}^{[N]})$ is the same for the four fixed points (i.e., it does not depend on q). Eqs. (4.7) also show that for $|f_0| \geq |f_{0c}|$, $(n_1, n_2) \neq (0, 0)$, another set of four fixed points exists with rotation numbers $(-n_1, -n_2)$. It is easy to see that to each point $(x_{1*}, x_{2*}, y_{1*}, y_{2*})$ of the first set corresponds a point of the second set given by $(2\pi - x_{1*}, 2\pi - x_{2*}, -y_{1*}, -y_{2*})$. This is a reflection of the fact that the double rotor map (4.1) itself is invariant under the change of variables $(x_1, x_2, y_1, y_2) \mapsto (2\pi - x_1, 2\pi - x_2, -y_1, -y_2)$.

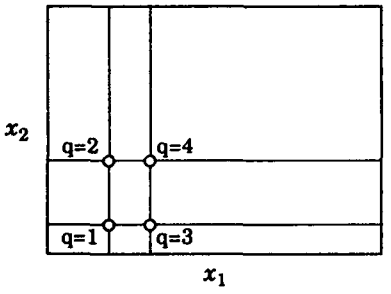

Fig. 6. Double rotor map: labeling of fixed points.

In table 1 we summarize the properties of the five sets of fixed points (36 fixed points) with smaller values of f_{0c} (when the other parameters of the map take the values specified by eqs. (4.4)), with rotation numbers $N = (0, 0)$, $\pm(1, 2)$, $\pm(0, 1)$, $\pm(1, 1)$, $\pm(2, 3)$. Note that the last three sets have the same value of f_{0c}. In fig. 7 we have plotted these fixed points in the plane (x_1, x_2). Their (y_1, y_2) coordinates are given by the first of eqs. (4.6).

Let us now turn our attention to the stability of the fixed points. The basic element of the analysis is the Jacobian (4×4) matrix of partial derivatives of the map (4.1),

$$\mathbf{D}_Z \boldsymbol{F}(\boldsymbol{Z}) = \begin{pmatrix} \mathbf{I}_2 & \mathbf{M} \\ \mathbf{H}(\boldsymbol{X}') & \mathbf{L} + \mathbf{H}(\boldsymbol{X}')\mathbf{M} \end{pmatrix},$$

where

$$\mathbf{H}(\boldsymbol{X}') = \mathbf{D}_x \boldsymbol{G}(\boldsymbol{X}') = \begin{pmatrix} c_1 \cos x_1' & 0 \\ 0 & c_2 \cos x_2' \end{pmatrix},$$

and $\mathbf{I}_n$ denotes the $n \times n$ identity matrix. The characteristic polynomial of $\mathbf{D}_Z \boldsymbol{F}(\boldsymbol{Z}_*)$ is

$$P(s) = |\mathbf{D}_Z \boldsymbol{F}(\boldsymbol{Z}_*) - s\mathbf{I}_4|$$
$$= |s^2 \mathbf{I}_2 - s(\mathbf{I}_2 + \mathbf{L} + \mathbf{HM}) + \mathbf{L}|, \qquad (4.8a)$$

Table 1
Double rotor map: fixed points. The only stable fixed points are: $[(0, 0); 4]$ in the interval $0 < f_0 < 4.27\ldots$; $[(1, 2); 4]$ and $[(-1, -2); 1]$ in the interval $2\pi < f < 7.01\ldots$ [the other parameters are given by eq. (4.4)].

(n_1, n_2)	f_{01}	f_{02}	f_{0c}	h_{11c}	h_{22c}
$(0, 0)$	0	0	0	0	0
$\pm(1, 2)$	0	$2\pi\nu I/I_2$	$2\pi\nu I/I_2$	$\pm 2\pi\nu I_1/I_2$	0
$\pm(0, 1)$	$2\pi\nu I/I_1$	$2\pi\nu I/I_2$	$2\pi\nu I/I_1$	0	$\pm 2\pi\nu(I_2^2/I_1^2 - 1)^{1/2}$
$\pm(1, 1)$	$2\pi\nu I/I_1$	0	$2\pi\nu I/I_1$	0	$\pm 2\pi\nu I_2/I_1$
$\pm(2, 3)$	$2\pi\nu I/I_1$	$2\pi\nu I/I_2$	$2\pi\nu I/I_1$	0	$\pm 2\pi\nu(I_2^2/I_1^2 - 1)^{1/2}$

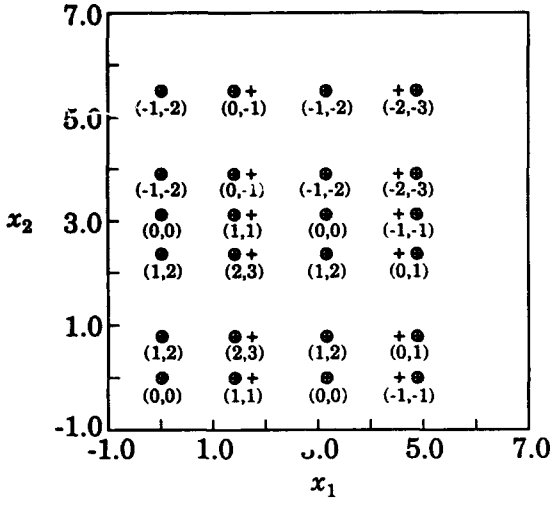

Fig. 7. Double rotor map: fixed points with rotation numbers (n_1, n_2). The symbol (+) denotes fixed points with one unstable eigendirection, while the symbol ⊕ denotes fixed points with two unstable eigendirections. [$f_0 = 9.0$, other parameters given by eq. (4.4)].

where, for simplicity, we have set $\mathbf{H} \equiv \mathbf{H}(X_*)$. The characteristic equation

$$P(s) = 0\,, \tag{4.8b}$$

determines the stability of the fixed points: if all the four roots have modulus smaller than one, the fixed point is stable. The stability of the fixed points as determined from eqs. (4.8) is discussed in appendix D.

For $f_0 = 9.0$, the nominal value in the control experiments of sections 4.4 and 4.5, all the fixed points are unstable. We have indicated in fig. 7 the number of unstable eigendirections at each fixed point.

We observe, from eq. (4.7), that as the forcing f_0 increases, the number of fixed points increases without bound. Not all these fixed points are necessarily embedded in the chaotic attractor, but those that are embedded in it are necessarily unstable. Furthermore, we find that the fixed points are roughly spread throughout the attractor, suggesting that there can be substantial flexibility to select among a variety of asymptotic behaviors by selecting different fixed points for control. (Even more flexibility can be achieved if we also consider periodic orbits of period greater than one.)

4.3. Bifurcation diagram

A bifurcation diagram shows how the attractors of a dynamical system change with a system parameter.

In figs. 8a, 8b we present a bifurcation diagram for the double rotor map, which was obtained in the following way. For each value of the parameter we took a large number of initial

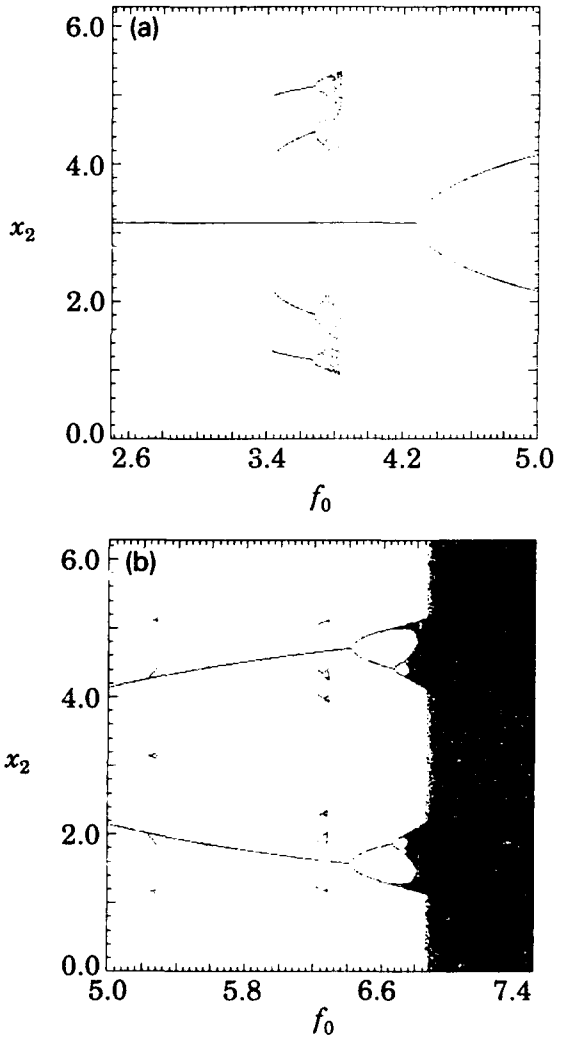

Fig. 8. (a), (b) Double rotor map: bifurcation diagram [parameters given by eq. (4.4); number of values of f_0 in each figure: 251; number of initial conditions for each f_0: 625; snapshot taken after 6000 iterations].

angles (x_1, x_2) with both x_1 and x_2 distributed uniformly in $[0, 2\pi]$ and iterated them starting with zero angular velocity [i.e., $(y_1, y_2) = (0, 0)$]. After iterating a sufficient number of times so that the orbits are essentially on the attractor, we plotted the x_2 component of all the orbits.

The diagram clearly exhibits a main branch that develops continuously for all values of the parameter. This main branch illustrates a period-doubling bifurcation sequence to chaos: a period-1 periodic orbit bifurcates (at $f_0 \simeq 4.27$) to a period-2 periodic orbit which then bifurcates (at $f_0 \simeq 6.42$) to a period-4 periodic orbit which then bifurcates (at $f_0 \simeq 6.67$) to a period-8 periodic orbit, and so on, with an accumulation point of period doublings at $f_0 \simeq 6.75$ beyond which chaos appears. The period-2 periodic orbit in the sequence results from the bifurcation of the stable orbit $\mathbf{Z}_*^{[(0,0);4]} = (\pi, \pi, 0, 0)$ discussed in section 4.2 which exists for $f_0 \geq 0$; at the value $f_{0u}^{[(0,0);4]}$ at which this orbit becomes unstable the stable period-2 periodic orbit is born.

Although it cannot be seen in the diagram, this period doubling sequence is peculiar in the following sense: what appears to be a period-2^m periodic orbit, $m \geq 2$, is in fact 2 period-2^{m-1} periodic orbits. This is a consequence of the symmetry of the double rotor map that forces the period-1 orbit to become unstable (at $f_0 \cong 4.2$) through an eigenvalue 1 instead through -1 as occurs in the normal period doubling bifurcation (an example of which is the bifurcation of the period-1 periodic orbit).

Besides this main branch, there are other period doubling sequences, one of which starts with a period-4 periodic orbit (at $f_0 \simeq 3.42$) and ends with a crisis (at $f_0 \simeq 3.84$). (A *crisis* is the sudden disappearance of a chaotic attractor by collision with an unstable periodic orbit [15, 16].)

It is convenient to have some quantitative characterization of the chaotic attractors revealed by the bifurcation diagram. For this purpose we introduce the spectrum of *Lyapunov exponents*, defined as follows [21, 22].

Consider an n-dimensional map $\mathbf{Z} \mapsto \boldsymbol{F}(\mathbf{Z})$ and its Jacobian matrix of partial derivatives $\mathbf{J}(\mathbf{Z}) = \mathbf{D}_{\mathbf{Z}}\boldsymbol{F}(\mathbf{Z})$. Consider also the sequence $\{\mathbf{Z}_0, \mathbf{Z}_1, \ldots, \mathbf{Z}_{k-1}\}$ generated by successive iteration of the initial condition $\mathbf{Z}_0$. For this sequence introduce the matrix

$$\mathbf{J}_k = \mathbf{J}(\mathbf{Z}_{k-1})\mathbf{J}(\mathbf{Z}_{k-2}) \ldots \mathbf{J}(\mathbf{Z}_1)\mathbf{J}(\mathbf{Z}_0) .$$

Now let

$$\zeta_1(k) \geq \zeta_2(k) \geq \cdots \geq \zeta_n(k) ,$$

denote the n eigenvalues of $(\mathbf{J}_k^T \mathbf{J}_k)^{1/2}$, where $\mathbf{J}_k^T$ is the transpose of $\mathbf{J}_k$. The Lyapunov numbers of the map are then defined by

$$\eta_j = \lim_{k \to \infty} [\zeta_j(k)]^{1/k} , \quad j = 1, \ldots, n ,$$

where the positive real kth root is taken. They satisfy the same ordering as the $\zeta_j(k)$, $j = 1, \ldots, n$. The Lyapunov exponents are the logarithms of the Lyapunov numbers,

$$L_j = \log_e \eta_j , \quad j = 1, \ldots, n ,$$

satisfying the same ordering

$$L_1 \geq L_2 \geq \cdots \geq L_n .$$

Hence, for chaotic attractors of an n-dimensional map there are n Lyapunov exponents, L_j, $j = 1, \ldots, n$. A chaotic attractor is defined to be one which possesses a positive Lyapunov exponent, $L_1 > 0$.

For typical dynamical systems the Lyapunov exponents are the same for almost all initial conditions on the basin of attraction of the attractor. (This is true in particular for the chaotic attractors of the double rotor map for which we calculated Lyapunov exponents; these results are reported below.) Thus the spectrum of Lyapunov exponents may be indeed considered to be a property of the attractor. For maps such that the determinant of the Jacobian matrix is indepen-

dent of the variable Z the Lyapunov exponents satisfy the identity

$$\sum_{j=1}^{n} L_j = \log_e |\mathbf{J}| .$$

This is true in the case of the double rotor map for which we have

$$\sum_{j=1}^{4} L_j = \log_e |\mathbf{L}| = (\lambda_1 + \lambda_2)T = -3\nu ,$$

the last equality applying when $\nu_1 = \nu_2 \equiv \nu$ and $T = 1$.

From the spectrum of Lyapunov exponents define the *Lyapunov dimension*.

$$d_L = k_L + \frac{\sum_{j=1}^{k_L} L_j}{|L_{k_L+1}|} ,$$

where $1 \le k_L \le n-1$ is the largest integer for which $\Sigma_{j=1}^{k_L} L_j \ge 0$. If $L_1 < 0$, we define $d_L = 0$; if $\Sigma_{j=1}^{n} L_j \ge 0$, we define $d_L = n$. (Note that $d_L = n$ is not possible in the case of dissipative systems for which $\log_e |\mathbf{J}| < 0$.) Kaplan and Yorke [23, 24] conjecture that d_L, as given above in terms of the Lyapunov exponents, is typically equal to the fractal dimension of the support of the measure of the attractor (the information dimension).

We have numerically calculated the Lyapunov exponents and the Lyapunov dimension of the chaotic attractor in the main branch of the bifurcation diagram as a function of the forcing f_0. We used the method described in refs. [21, 22] to calculate the exponents of a large number of orbits in the basin of attraction and then took the average of these values. The results of the calculation at evenly spaced values along the f_0 axis are shown in fig. 9. The Lyapunov dimension first becomes positive at the onset of chaos ($f_0 \simeq 6.75$). The attractor dimension goes through the integer values $d_L = 2$ and 3 at $f_0 \simeq 6.88$ and 12.7, respectively.

In the numerical experiments on control that we describe in sections 4.4 and 4.5 we took $\bar{f}_0 = 9.0$ as the nominal value of the control parameter. In Table 2 we list the corresponding values of the four Lyapunov exponents and the Lyapunov dimension. In order to illustrate the point made above regarding the fact that the Lyapunov exponents are the same for almost all initial conditions on the basin of attraction of the

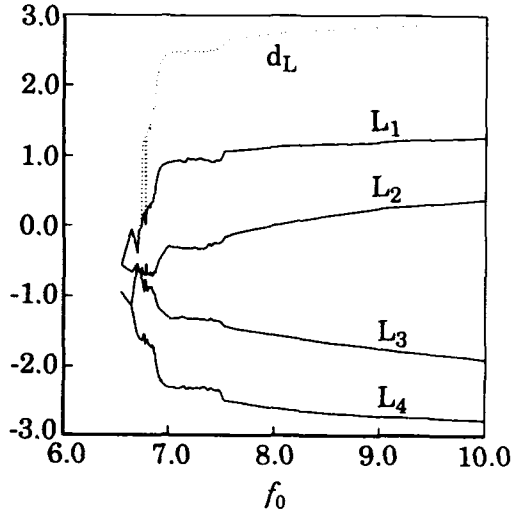

Fig. 9. Double rotor map: spectrum of Lyapunov exponents and Lyapunov dimension of chaotic attractors versus f_0 [eq. (4.4)].

Table 2
Double rotor map: calculation of Lyapunov exponents and Lyapunov dimension of chaotic attractor [$f_0 = 9.0$, other parameters given by eq. (4.4); number of initial conditions = $N_0 = 256$; number of iterations = 10 000]. $d_L = 2 + (L_1 + L_2)/|L_3| = 2.838$.

	j			
	1	2	3	4
$L_j = (1/N_0)\sum_{i=1}^{N_0} L_j^{(i)}$	1.205	0.256	−1.744	−2.717
$\min_{i=1,N_0} L_j^{(i)}$	1.182	0.228	−1.771	−2.734
$\max_{i=1,N_0} L_j^{(i)}$	1.229	0.284	−1.719	−2.693
$[(1/N_0)\sum_{i=1}^{N_0}(L_j^{(i)} - L_j)^2]^{1/2}$	0.00816	0.0102	0.00910	0.00724

attractor, we also give some details on the numerical calculation of these exponents.

We have now described in sufficient detail the two ingredients necessary to the application of the control method to the double rotor map: chaotic attractors and fixed points. It remains to be checked if the fixed points determined in section 4.2 are embedded in the chaotic attractor. By this we mean that any neighborhood of the fixed point contains an infinite number of points of the chaotic attractor. In order to check this, we consider the intersection of the attractor in its four-dimensional phase space with a three-dimensional hyperplane containing the fixed points $\mathbf{Z}_*$ that we wish to check. Numerically we approximate the hyperplane by a very narrow slab through each fixed point of the form

$$|\hat{\boldsymbol{K}}^{\mathrm{T}}(\boldsymbol{Z}-\boldsymbol{Z}_*)|<w\,. \tag{4.9}$$

Actually we took the slabs parallel to the plane (x_1, x_2) which implies that each slab contains the four fixed points with the same rotation number. We then examine a very long orbit and plot only those points satisfying (4.9). The intersection of our 2.8-dimensional attractor with a three dimensional hyperplane is a 1.8-dimensional cross-section. The small scale structure of this 1.8-dimensional intersection is somewhat fuzzed out due to the finite slab thickness. The results, for $f_0 = 9.0$, are given in figs. 10a–10e, which refer to the rotation numbers $N = (0,0)$, $(1,2)$, $(0,1)$, $(1,1)$ and $(2,3)$, respectively. In these figures the relevant fixed points are denoted by a + symbol. The results indicate, with different degrees of certitude, that the first four sets of fixed points are indeed embedded in the attractor while the fifth is not. Note that fig. 10a nicely reveals the symmetry of the map with respect to the point $(\pi, \pi, 0, 0)$. Note also the fractal-like structure in this figure.

We conclude this discussion by mentioning what seems to be an interesting issue: the loss of hyperbolicity due to the existence of fixed points embedded in the attractor that have a number of unstable directions (that is, eigenvalues with magnitude bigger than one) different from the number of unstable directions of the attractor (that is, positive Lyapunov exponents). In fact, from the observation of fig. 7 and table 2, we see that while the chaotic attractor for $f_0 = 9.0$ has two positive Lyapunov exponents some of the unstable fixed points embedded in the attractor have only one unstable eigenvalue.

4.4. Control

We now proceed to apply the method developed in section 2 to control the fixed points of the double rotor map with control parameter f_0. Let us denote by $\bar{\boldsymbol{Z}}_*$ the fixed point to be controlled at the nominal value $\bar{f}_0$ of the parameter. The quantities that were introduced in section 2 now take the following particular form:

$$\mathbf{A} = \begin{pmatrix} \mathbf{I}_2 & \mathbf{M} \\ \mathbf{H}(\bar{\boldsymbol{X}}_*) & \mathbf{L} + \mathbf{H}(\bar{\boldsymbol{X}}_*)\mathbf{M} \end{pmatrix},$$

$$\mathbf{H}(\bar{\boldsymbol{X}}_*) = \frac{\bar{f}_0}{I}\begin{pmatrix} l_1 \cos \bar{x}_{1*} & 0 \\ 0 & l_2 \cos \bar{x}_{2*} \end{pmatrix},$$

$$\boldsymbol{B}^{\mathrm{T}} = \begin{pmatrix} 0 & 0 & \dfrac{l_1}{I}\sin \bar{x}_{1*} & \dfrac{l_2}{I}\sin \bar{x}_{2*} \end{pmatrix},$$

$$\mathbf{C} = (\boldsymbol{B} : \mathbf{A}\boldsymbol{B} : \mathbf{A}^2\boldsymbol{B} : \mathbf{A}^3\boldsymbol{B})\,,$$

$$\mathbf{T} = \mathbf{C}\mathbf{W}\,,$$

$$\mathbf{W} = \begin{pmatrix} a_3 & a_2 & a_1 & 1 \\ a_2 & a_1 & 1 & 0 \\ a_1 & 1 & 0 & 0 \\ 1 & 0 & 0 & 0 \end{pmatrix},$$

$$\boldsymbol{K}^{\mathrm{T}} = (\alpha_4 - a_4 \quad \alpha_3 - a_3 \quad \alpha_2 - a_2 \quad \alpha_1 - a_1)\mathbf{T}^{-1}\,.$$

One immediate conclusion that can be drawn from these results is that the controllability matrix $\mathbf{C}$ is identically zero in the case of the fixed points with rotation numbers $N = (0,0)$ for which $\sin \bar{x}_{1*} = \sin \bar{x}_{2*} = 0$. Hence these points are uncontrollable, at least when the control parameter is f_0. We will show in the next subsection that this set of fixed points can be controlled if we modify the double rotor map to allow for

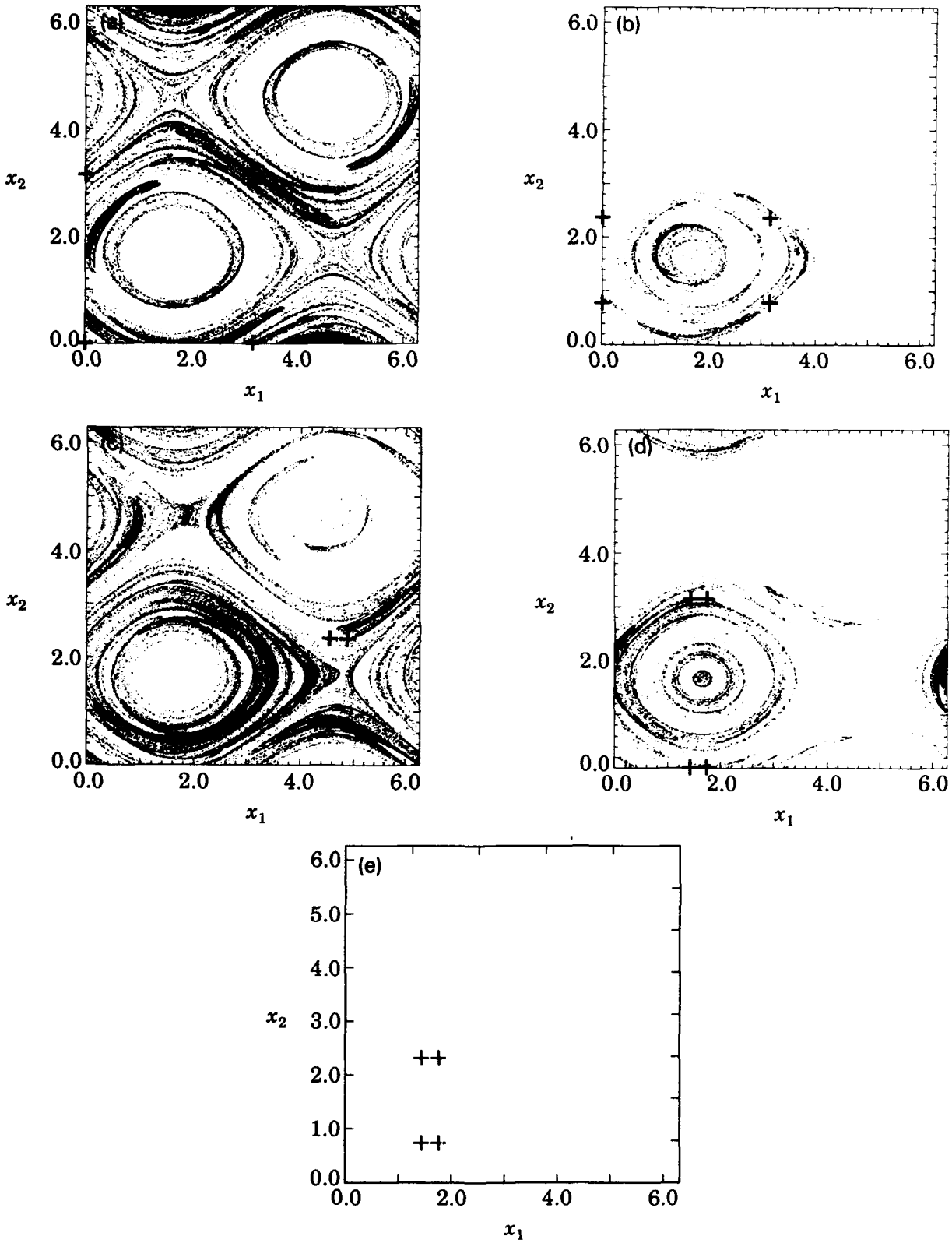

Fig. 10. Double rotor map: sections of chaotic attractor by slab $|\hat{K}^{T}(Z - Z_{*})| < w$, $\hat{K}^{T} = (0, 0, 1, 1)$, $w = 10^{-2}$, through the fixed points (+) with rotation numbers (a) $N = (0, 0)$, (b) $N = (1, 2)$, (c) $N = (0, 1)$, (d) $N = (1, 1)$, (e) $N = (2, 3)$. The map was iterated 10^{8} times [$f_0 = 9.0$, eq. (4.4)].

kicks with variable direction and then take as control parameter the angle the kicks make with the vertical direction in fig. 5.

The method is illustrated in figs. 11a, 11b. The control of the first fixed point was turned on at $i = 0$ with switches to control other fixed points occurring at later times. We plot the x_1 and x_2 coordinates of an orbit as a function of (discrete) time. The parameter perturbations were programmed to control successively four different fixed points of the set with rotation numbers $N = \pm(0, 1)$. The times at which we switched the control from stabilizing one fixed point to stabilizing another are labeled by the arrows in the figure. The figure clearly illustrates the flexibility offered by the method in controlling different periodic motions embedded in the attractor. The figure also shows that the time to achieve control is different from case to case.

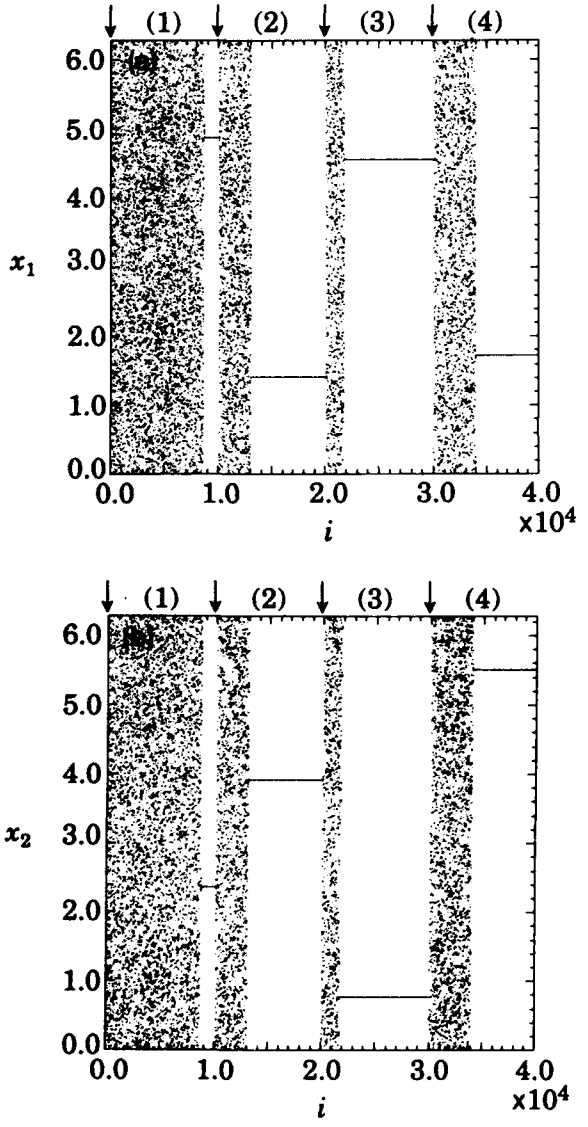

Fig. 11. Double rotor map: successive control of fixed points (1) [(0, 1); 4], (2) [(0, −1); 1], (3) [(0, 1); 1], (4) [(0, −1); 4]. The arrows indicate the times of switching. The regulator poles correspond to projection onto the stable manifold [$\delta = 1.0$, $\bar{f}_0 = 9.0$, eq. (4.4)].

We now report the results of several numerical experiments that were carried out with the purpose of understanding the behavior of the time to achieve control.

The first experiment was intended to confirm that the time to achieve control indeed follows an exponential probability distribution as indicated in section 2.4. We proceeded to control the fixed point [(0, 1); 4] by starting at a large number of different points on the attractor and measuring the time each orbit took to reach the fixed point. We then obtained the distribution function of the time to achieve control $\Phi(\tau)$ by plotting a histogram of τ using bins of constant size. The results are presented as a semilog plot. in fig. 12 and show excellent agreement with the predicted fit to a straight line.

In our next experiment we looked at the dependence of the average time to achieve control on the size of the parameter perturbations, δ. The results are shown in fig. 13, where we have used logarithmic scales in both axes. The two fixed points [(0, 1); 4] and [(0, 1); 1] were controlled. (The first of these points has two unstable eigenvalues while the second has only one unstable eigenvalue.) We see that for the smaller values of δ the results closely follow straight lines indicating a power law dependence,

$$\langle \tau \rangle \sim \delta^{-\gamma},$$

in accord with the theoretical predictions of ref. [6] for two-dimensional maps.

In the experiments described until this point the choice of the regulator poles (eigenvalues of

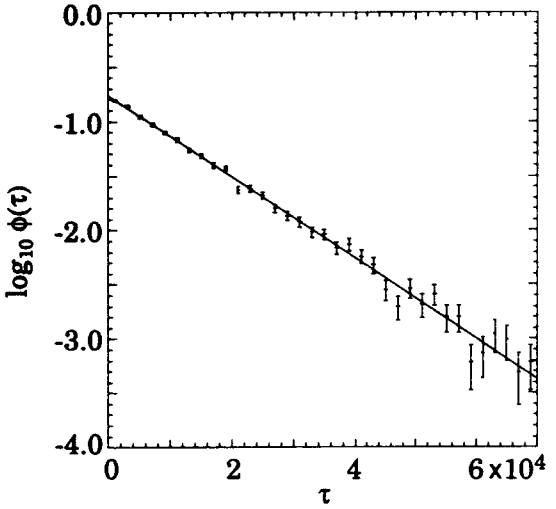

Fig. 12. Double rotor map: histogram of the time to achieve control τ of a sample of 8192 orbits. The fixed point controlled was [(0, 1); 4]. The regulator poles correspond to projection onto the stable manifold. [$\delta = 1.0$, $\bar{f}_0 = 9.0$, eq. (4.4)].

$\mathbf{A} - \boldsymbol{B}\boldsymbol{K}^{\mathrm{T}}$) corresponded to projection onto the stable manifold of the fixed points. That is, the stable eigenvalues of matrix $\mathbf{A}$ were left unchanged, and the unstable eigenvalues were shifted to zero.

In our next set of experiments we looked at how different choices of regulator poles affect the average time to achieve control. We considered the fixed point [(0, 1); 4] with two unstable eigendirections and kept two of the regulator poles equal to the two stable eigenvalues of the fixed point. As regards the other two regulator poles, μ_1 and μ_2, three cases were considered:

(I) $\mu_2 = 0$,
(II) $\mu_2 = \mu_1$,
(III) $\mu_2 = -\mu_1$.

μ_1 was then allowed to vary in the interval $(-1, 1)$. The results of the experiments are shown in fig. 14. In cases (I) and (II) the average time to achieve control essentially increases with μ_1, indicating behavior similar to that found for the Hénon map in fig. 2. In case (III) the average time to achieve control passes through a broad minimum. (Note that the point $\mu_1 = \mu_2 = 0$, which is common to the three cases, corresponds to projection onto the stable manifold.)

4.5. f_0-uncontrollable fixed points

We saw that the set of four fixed points with rotation numbers $N = (0, 0)$ could not be con-

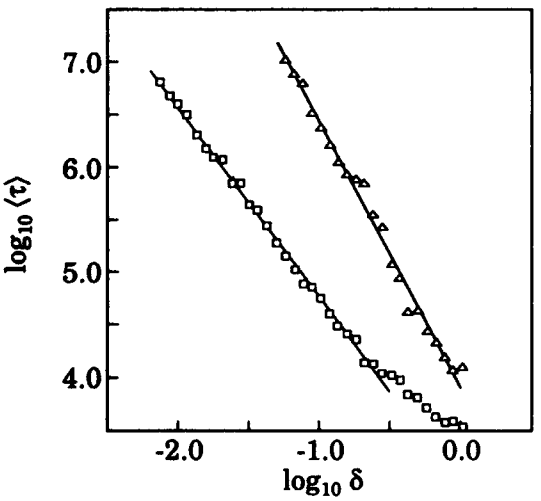

Fig. 13. Double rotor map: $\log_{10}\langle\tau\rangle$ versus $\log_{10}\delta$ for control of the fixed points (□) [(0, 1); 1], (△) [(0, 1); 4]. The regulator poles correspond to projection onto the stable manifold. The straight lines are least square fits to the data [excluding the last nine data points in the case of (□)], [$\bar{f}_0 = 9.0$, eq. (4.4)].

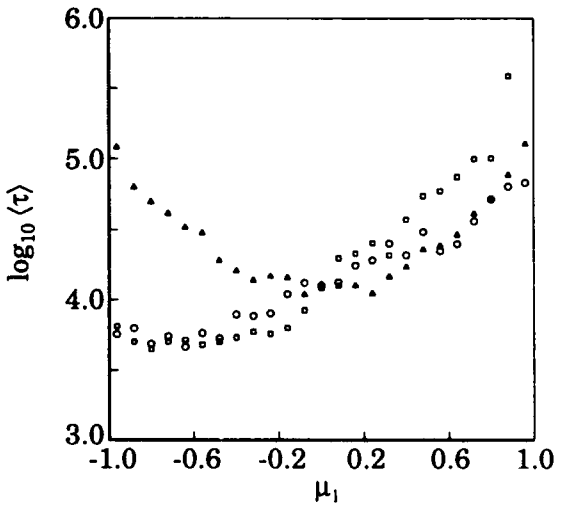

Fig. 14. Double rotor map: $\log_{10}\langle\tau\rangle$ versus μ_1 for (○) $\mu_2 = 0$, (□) $\mu_2 = \mu_1$, (△) $\mu_2 = -\mu_1$. The other two regulator poles were kept equal to the stable eigenvalues of the uncontrolled map. The fixed point controlled was [(0, 1); 4] [$\delta = 1.0$, $\bar{f}_0 = 9.0$, eq. (4.4)].

trolled by changes in the parameter f_0 because the controllability matrix at these points is identically zero.

We show now that these fixed points can be controlled by modifying the double rotor map to allow for kicks with variable direction and then taking the direction of the kicks to be the control parameter, with the nominal value corresponding to the previously fixed direction.

Let us assume that the direction of the kicks makes an angle ψ with the vertical downward direction. Going back to the derivation of the double rotor map in Appendix B, it is easy to verify that the introduction of kicks with variable direction can be taken into account by simply replacing the function G used in the definition of the map and given by eq. (4.2) by the new function

$$\tilde{G}(X) = \begin{pmatrix} c_1 \sin(x_1 - \psi) \\ c_2 \sin(x_2 - \psi) \end{pmatrix}.$$

Taking ψ to be the control parameter with variations around the nominal value $\bar{\psi} = 0$, the application of the method now involves the following quantities:

$$\mathbf{A} = \begin{pmatrix} \mathbf{I}_2 & \mathbf{M} \\ \tilde{\mathbf{H}}(\bar{X}_*) & \mathbf{L} + \tilde{\mathbf{H}}(\bar{X}_*)\mathbf{M} \end{pmatrix},$$

$$\tilde{\mathbf{H}}(\bar{X}_*) = \frac{f_0}{I} \begin{pmatrix} l_1 \cos x_{1*} & 0 \\ 0 & l_2 \cos \bar{x}_{2*} \end{pmatrix},$$

$$\boldsymbol{B}^{\mathrm{T}} = \left(0 \quad 0 \quad -\frac{f_0 l_1}{I} \cos \bar{x}_{1*} \quad -\frac{f_0 l_2}{I} \cos \bar{x}_{2*}\right).$$

The fixed points are now all controllable by small perturbations of the parameter ψ around the nominal value $\bar{\psi} = 0$.

Figs. 15a, 15b illustrate the control of the fixed points $[(0,0);3]$ and $[(0,0);4]$ by kicks of variable direction. The parameter perturbations were programmed to control the first of these points from $i = 0$ to $i = 10^4$ and the second from $i = 10^4$ to $i = 2 \times 10^4$.

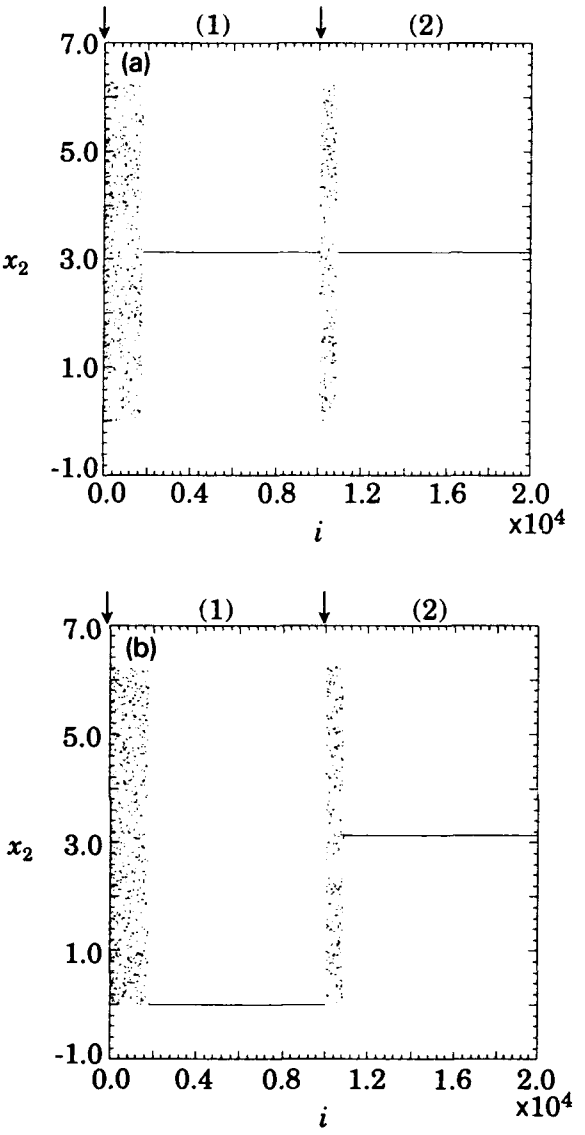

Fig. 15. Modified double rotor map: successive control of fixed points (1) $[(0,0);3]$, (2) $[(0,0);4]$ by kicks of variable direction. The arrows indicate the times of switching. The regulator poles correspond to projection onto the stable manifold [$\delta = 0.05$, $f_0 = 9.0$, eq. (4.4)].

5. Discussion

The transient phase where the orbit wanders chaotically before locking in to a controlled orbit can be greatly shortened by applying the technique discussed by Shinbrot et al. [25]. In the latter paper it was pointed out that orbits can be rapidly brought to a target region on the attrac-

tor (in the present case the neighborhood of the periodic orbit which we wish to stabilize) by using small control perturbations when the orbit is far from the neighborhood of the periodic orbit to be stabilized. The idea was that, since chaotic systems are exponentially sensitive to perturbations, careful choice of even small control perturbations can, after some time, have a large effect on the orbit location and can be used to guide it. Thus the time to achieve control can, in principle, be greatly shortened by properly applying small controls when the orbit is far from the neighborhood of the desired periodic orbit.

One issue which we have not addressed is the effect of noise. If the noise remains small, it may not be sufficient to kick the orbit out of the neighborhood of the chosen periodic orbit where the control is activated. In this case, the orbit remains near the desired periodic orbit indefinitely. However, it may be that the random noise is such that it may occasionally kick the orbit far enough away from the periodic orbit that the orbit falls outside the small controlled phase space region. In this case, after the orbit is kicked out of the controlled phase space region, it wanders chaotically over the attractor until it falls in the controlled region again. Thus there are epochs where the orbit is kept near the desired orbit interspersed with epochs wherein the orbit wanders chaotically far from the desired orbit. If the latter are, on average, relatively much shorter than the former, then one might still regard the control as being effective. See ref. [6] for numerical experiments on this effect using the Hénon map. We also remark that the procedure discussed in the previous paragraph [25] can be used to greatly reduce the duration of the noise induced epochs where the orbit bursts out of the controlled phase space region.

In this paper we have considered the case where there is only a single control parameter available for adjustment. While generically a single parameter is sufficient for stabilization of a desired periodic orbit, there may be some advantage to utilizing several control variables. Therefore, the single control parameter p becomes a vector (e.g., ref. [26] discusses the case where the number of control parameters is equal to the number of unstable eigenvalues). In particular, the added freedom in having several control parameters might allow better means of choosing the control so as to minimize the time to achieve control, as well as the effects of noise.

Finally we wish to point out that full knowledge of the system dynamics is not necessary in order to apply our technique (see also ref. [6]). In particular, we only require the location of the desired periodic orbit, the linearized dynamics about the periodic orbit, and the dependence of the location of the periodic orbit on small variation of the control parameter. Recently, delay coordinate embedding [19, 27] has been utilized in several experimental studies (refs. [8, 28–31]) to extract such information purely from observations of experimental chaotic orbits on the attractor without any a priori knowledge of the system of equations governing the dynamics, and such information has been utilized to control periodic orbits [9]. Hence, application of our method is not limited to cases where a complete knowledge of the system is available.

In conclusion, we have demonstrated that chaotic dynamics can often be converted, by using only a small feedback control, to motion on a desired periodic orbit. Furthermore, by switching the small control, one can switch the time asymptotic behavior from one periodic orbit to another. In some situations, where the flexibility offered by the ability to do such switching is desirable, it may be advantageous to design the system so that it is chaotic. In other situations, where one is presented with a chaotic system, the method may allow one to eliminate the chaos and achieve greatly improved behavior at relatively low cost.

Acknowledgements

This work was supported by the US Department of Energy (Scientific Computing Staff, Of-

fice of Energy Research), the Portuguese Junta Nacional de Investigação Científica e Tecnológica, and the National Science Foundation (Engineering Research Center Program). The computation was done at the National Energy Research Supercomputer Center.

Appendix A. Time to achieve control in the case of two-dimensional maps

We assume that control is achieved if the orbit remains in the slab (2.8) for two consecutive iterations of the map. The two conditions

$$|\boldsymbol{K}^{\mathrm{T}}(\boldsymbol{Z}-\boldsymbol{Z}_{*}(\bar{p}))|<\delta\,,\quad |\boldsymbol{K}^{\mathrm{T}}(\boldsymbol{Z}'-\boldsymbol{Z}_{*}(\bar{p}))|<\delta\,, \tag{A.1}$$

define a control "parallelepiped" P_{c}, where $\boldsymbol{Z}'=\boldsymbol{F}(\boldsymbol{Z},p)$. For small δ, an initial condition will bounce around on the set comprising the uncontrolled chaotic attractor for a long time before it falls in the control parallelepiped P_{c}. At any given iterate the probability of falling in P_{c} is approximately the natural measure (see, for example, [17, 18, 23]) of the uncontrolled chaotic attractor contained in P_{c}. If we follow many orbits this probability $\mu(P_{\mathrm{c}})$ also gives the rate at which these orbits fall into P_{c}. Thus $\mu(P_{\mathrm{c}})$ is the inverse of the average time for a typical orbit to first fall in P_{c},

$$\langle\tau\rangle^{-1}=\mu(P_{\mathrm{c}})\,. \tag{A.2}$$

An estimate for $\mu(P_{\mathrm{c}})$ can be given in the two-dimensional case [23]:

$$\mu(P_{\mathrm{c}})\sim\int_{P_{\mathrm{c}}}\rho|v_{\mathrm{s}}|^{d_{\mathrm{s}}-1}|v_{\mathrm{u}}|^{d_{\mathrm{u}}-1}\,\mathrm{d}v_{\mathrm{s}}\,\mathrm{d}v_{\mathrm{u}}\,, \tag{A.3}$$

where v_{s} and v_{u} denote linear coordinates in the stable and unstable directions. In here d_{u} and d_{s} are the pointwise dimensions [1] for the uncontrolled chaotic attractor at the fixed point in the unstable and the stable directions, respectively; ρ is a normalizing constant. Assuming that the attractor is smooth in the unstable direction we have $d_{\mathrm{u}}=1$, while d_{s} is given in terms of the eigenvalues at the fixed point [1, 17, 18] by

$$d_{\mathrm{s}}=\frac{\log_{\mathrm{e}}|\lambda_{\mathrm{u}}|}{\log_{\mathrm{e}}(1/|\lambda_{\mathrm{s}}|)}\,.$$

In order to determine the control parallelepiped, we need to obtain $\boldsymbol{Z}'$ in the neighborhood of the fixed point $\boldsymbol{Z}_{*}(\bar{p})$ with a better approximation than that provided by the linear map (2.3). We therefore take

$$\boldsymbol{V}'=\mathbf{A}\boldsymbol{V}+\boldsymbol{B}(p-\bar{p})+\tfrac{1}{2}\boldsymbol{Q}(\boldsymbol{V},\boldsymbol{V})+\tfrac{1}{2}\boldsymbol{D}(p-\bar{p})^{2}\,, \tag{A.4}$$

where

$$\boldsymbol{V}=\boldsymbol{Z}-\boldsymbol{Z}_{*}(\bar{p})\,,\quad \boldsymbol{V}'=\boldsymbol{Z}'-\boldsymbol{Z}_{*}(\bar{p})\,,$$

$\mathbf{A}$, $\boldsymbol{B}$ were defined by (2.4), (2.5) and $\boldsymbol{Q}$, $\boldsymbol{D}$ are two vectors with components q_k, d_k $(k=1,2)$ defined by

$$q_k=\sum_{i,j=1}^{2}\left.\frac{\partial^2 f_k}{\partial x_i\,\partial x_j}\right|_{(\boldsymbol{Z}_{*}(\bar{p}),\,\bar{p})}v_i v_j\,,$$

$$d_k=\left.\frac{\partial^2 f_k}{\partial p^2}\right|_{(\boldsymbol{Z}_{*}(\bar{p}),\bar{p})}\,;$$

in here x_k, f_k, and v_k $(k=1,2)$ denote the components of the vectors $\boldsymbol{X}$, $\boldsymbol{F}$ and $\boldsymbol{V}$. Using (2.6) to eliminate $p-\bar{p}$ from eq. (A.4), we obtain

$$\boldsymbol{V}'=\mathbf{A}\boldsymbol{V}+\tfrac{1}{2}\boldsymbol{Q}(\boldsymbol{V},\boldsymbol{V})-\boldsymbol{B}(\boldsymbol{K}^{\mathrm{T}}\boldsymbol{V})+\tfrac{1}{2}\boldsymbol{D}(\boldsymbol{K}^{\mathrm{T}}\boldsymbol{V})^{2}\,. \tag{A.5}$$

The control "parallelogram" P_{c} will therefore be defined by the two equations

$$|\boldsymbol{K}^{\mathrm{T}}\boldsymbol{V}|<\delta\,,\quad |\boldsymbol{K}^{\mathrm{T}}\boldsymbol{V}'|<\delta\,. \tag{A.6}$$

In order to compare with the numerical experimental results described in section 3 we have carried out the calculation of (A.3) in the case of

the Hénon map. Writing this map in the form

$$\begin{pmatrix} x_1 \\ x_2 \end{pmatrix} \mapsto \begin{pmatrix} f_1(x_1, x_2) \\ f_2(x_1, x_2) \end{pmatrix} = \begin{pmatrix} a - x_1^2 + bx_2 \\ x_1 \end{pmatrix},$$

and taking a to be the control parameter while b is kept fixed, we obtain

$$\mathbf{A} = \begin{pmatrix} -2\bar{x}_* & b \\ 1 & 0 \end{pmatrix}, \quad \boldsymbol{B} = \begin{pmatrix} 1 \\ 0 \end{pmatrix},$$

$$\boldsymbol{D} = \begin{pmatrix} 0 \\ 0 \end{pmatrix}, \quad \boldsymbol{Q}(\boldsymbol{V}, \boldsymbol{V}) = \begin{pmatrix} -2v_1^2 \\ 0 \end{pmatrix},$$

$$\boldsymbol{K}^{\mathrm{T}}\boldsymbol{V} = k_1 v_1 + k_2 v_2 ,$$

$$\boldsymbol{K}^{\mathrm{T}}\boldsymbol{V}' = -k_1 v_1^2 + (k_2 - k_1^2 - 2\bar{x}_* k_1) v_1 + k_1 (b - k_2) v_2 .$$

Also we note that for the Hénon map the variables (v_1, v_2) and (v_s, v_u) are related by

$$\begin{pmatrix} v_1 \\ v_2 \end{pmatrix} = \begin{pmatrix} \lambda_s \gamma_s & \lambda_u \gamma_u \\ \gamma_s & \gamma_u \end{pmatrix} \begin{pmatrix} v_s \\ v_u \end{pmatrix}, \tag{A.7}$$

where

$$\gamma_s = (1 + \lambda_s^2)^{-1/2}, \quad \gamma_u = (1 + \lambda_u^2)^{-1/2} .$$

Letting

$$\xi = v_1 , \quad \eta = v_1 + t v_2 , \quad t = k_2 / k_1 ,$$

and using (A.7) to change the variables of integration, eq. (A.3) can be written in the form

$$\mu(P_c) \sim \rho_0 \frac{|r|}{|1 - r|^{d_s}} \int_{P_c} |\xi - r\eta|^{d_s - 1} \, \mathrm{d}\xi \, \mathrm{d}\eta , \tag{A.8}$$

where

$$\frac{1}{r} = 1 + \frac{t}{\lambda_u}$$

and

$$\frac{1}{\rho_0} = \frac{1}{\rho} \gamma_u |\lambda_u| [\gamma_s (\lambda_s - \lambda_u)]^{d_s} .$$

The integration in the variable in the direction of the straight lines $\boldsymbol{K}^{\mathrm{T}}\boldsymbol{V} = \pm\delta$ can be done exactly. On the contrary, except in the case $k_1 = 0$, the integration in the other variable does not seem to be possible in closed form. We have therefore resorted to numerical integration to obtain the results presented in fig. 16 (see below).

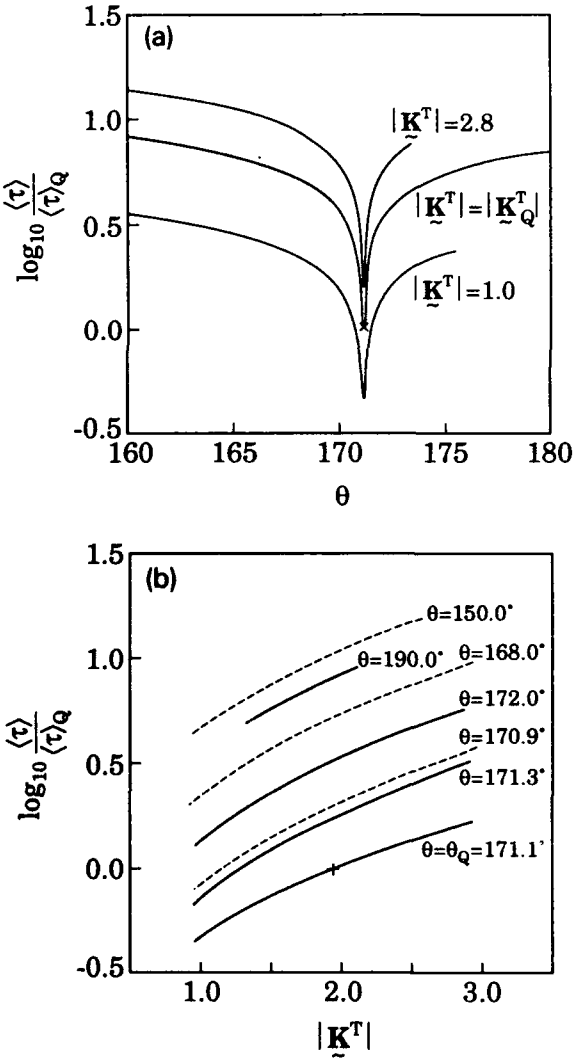

Fig. 16. Hénon map: (theoretical) curves of $\log_{10}(\langle\tau\rangle / \langle\tau\rangle_Q)$ versus $\theta = \arg(\boldsymbol{K}^{\mathrm{T}})$ with $|\boldsymbol{K}^{\mathrm{T}}|$ fixed (a) and of $\log_{10}(\langle\tau\rangle / \langle\tau\rangle_Q)$ versus $|\boldsymbol{K}^{\mathrm{T}}|$ with θ fixed (b). The × (+) denotes the reference value.

An accurate analytical approximation can be obtained in the case $t = -\lambda_s$ (slab parallel to the stable manifold) in the limit $\delta \to 0$:

$$\mu(P_c) \sim \rho_1 g(\mu_1)\, \delta^{\gamma}[1 + 0(\delta)]\,, \tag{A.9}$$

where g is the function defined by

$$g(\mu_1) = \frac{2}{\gamma}\,\frac{(1+\mu_1)^{\gamma} - (1-\mu_1)^{\gamma}}{\mu_1(|\lambda_u| + \mu_1)^{\gamma}}\,,$$

$$\mu_{1m} < \mu_1 < 0 \quad 0 < \mu_1 < \mu_{1M}$$

$$g(0) = 4|\lambda_u|^{-\gamma}\,.$$

and

$$\gamma = \tfrac{1}{2} d_s + 1\,,$$

$$\rho_1 = \frac{\rho_0}{d_s}\,\frac{|r|}{|1-r|^{d_s}}\,, \quad \frac{1}{r} = 1 - \frac{\lambda_s}{\lambda_u}\,,$$

$$\mu_{1m} = -1 + \frac{r^2}{|\lambda_u| - 1}\,\delta + \mathcal{O}(\delta^1)\,,$$

$$\mu_{1M} = 1 - \frac{r^2}{|\lambda_u| + 1}\,\delta + \mathcal{O}(\delta^2)\,.$$

The dependence of $\mu(P_c)$ on δ given by (A.9) is precisely that predicted in ref. [6]. The dependence of $\mu(P_c)$ on μ_1 shows very good agreement with the experimental results – see fig. 2. Note that in plotting the theoretical curve we used as normalizing constant ρ_1 that obtained by least square fitting the theoretical curve to the experimental points.

We have used eq. (A.8) to study the dependence of $\langle \tau \rangle = 1/\mu(P_c)$ on the gain vector $\boldsymbol{K}^T$. In fig. 16a we have plotted curves of $\langle \tau \rangle$ versus $\theta = \arg(\boldsymbol{K}^T)$ with $|\boldsymbol{K}^T|$ kept fixed and in fig. 16b curves of $\langle \tau \rangle$ versus $|\boldsymbol{K}^T|$ with θ kept fixed. $\langle \tau \rangle$ was normalized to its value at the point Q (see section 3 and fig. 1). The results show that $\langle \tau \rangle$ exhibits a strong minimum at $\theta = \theta_Q$ for all values of $|\boldsymbol{K}^T|$ and increases slowly with $|\boldsymbol{K}^T|$ for all values of θ, in agreement with the experimental results of figs. 3 and 4.

Appendix B. Numerical method for calculating $\langle \tau \rangle$

In this appendix we describe the procedure used in sections 3 and 4 to numerically obtain the average time to achieve control, $\langle \tau \rangle$.

From (2.10) we obtain the fraction of chaotic transients with length smaller than some value τ_{max},

$$\rho_{\tau_{max}} = \int_0^{\tau_{max}} \phi(\tau)\, d\tau = 1 - \exp\left(-\frac{\tau_{max}}{\langle \tau \rangle}\right),$$

and the average length of the chaotic transients with length smaller than τ_{max},

$$\langle \tau \rangle_{\tau_{max}} = \int_0^{\tau_{max}} \tau \phi(\tau)\, d\tau$$

$$= \langle \tau \rangle \left[1 - \left(1 + \frac{\tau_{max}}{\langle \tau \rangle}\right) \exp\left(-\frac{\tau_{max}}{\langle \tau \rangle}\right)\right].$$

Combining these two equations we obtain

$$\langle \tau \rangle = \frac{\langle \tau \rangle_{\tau_{max}}}{1 - (1 - \rho_{\tau_{max}})[1 - \log_e(1 - \rho_{\tau_{max}})]}\,, \tag{B.1}$$

which is the required formula. Note that $\rho_\infty = 1$, $\langle \tau \rangle_\infty = \langle \tau \rangle$.

The numerical procedure to calculate the average time to achieve control is as follows. Take a large number N_0 of randomly chosen initial conditions and iterate each of them with the uncontrolled map [i.e., with $\boldsymbol{Z} \mapsto \boldsymbol{F}(\boldsymbol{Z}, \bar{p})$] a sufficient number of times until they are all distributed over the attractor according to its natural measure. Then switch on the control as specified by (2.9) and determine how many further iterates are necessary for $N_f \le N_0$ orbits to fall within a circle of small radius centered at the fixed point. Letting τ_{max} be this number of iterates and $\{\tau_j\}$ with $j = 1, \ldots, N_f$ be the times required for the N_f orbits to fall within the small circle, we have

$$\rho_{\tau_{\max}} = \frac{N_f}{N_0}, \quad \langle \tau \rangle_{\tau_{\max}} = \frac{1}{N_f} \sum_{j=1}^{N_f} \tau_j .$$

Finally we use eq. (P 1) to obtain $\langle \tau \rangle$. In our numerical experiments described in sections 3 and 4, we took $N_0 = 192$, $N_f = 121$, values that led to a good compromise between accuracy and computation time.

Appendix C. Derivation of the double rotor map

The equations of motion of the kicked double rotor are

$$\frac{d}{dt}\left(\frac{\partial L}{\partial \dot{\theta}_j}\right) - \frac{\partial L}{\partial \theta_j} = -\frac{\partial F}{\partial \dot{\theta}_j}, \quad j = 1, 2, \tag{C.1}$$

where the Lagrangian function L is the difference between the kinetic energy,

$$K(\dot{\theta}_1, \dot{\theta}_2) = \tfrac{1}{2} I_1 \dot{\theta}_1^2 + \tfrac{1}{2} I_2 \dot{\theta}_2^2 ,$$

and the potential energy,

$$V(\theta_1, \theta_2, t) = (l_1 \cos\theta_1 + l_2 \cos\theta_2) f(t) ,$$

i.e., $L = T - V$, and Rayleigh's dissipation function F is

$$F(\dot{\theta}_1, \dot{\theta}_2) = \tfrac{1}{2} \nu_1 I_1 \dot{\theta}_1^2 + \tfrac{1}{2} \nu_2 I_2 (\dot{\theta}_2 - \dot{\theta}_1)^2 .$$

The sequence of forcing kicks is given by the semi-infinite comb of delta functions of period T and strength f_0,

$$f(t) = f_0 \sum_{k=1}^{\infty} \delta(t - kT) . \tag{C.2}$$

In here I_1 and I_2 are the moments of inertia,

$$I_1 = (m_1 + m_2) l_1^2 , \quad I_2 = m_2 l_2^2 ,$$

and ν_1, ν_2 are the coefficients of friction.

Elimination of L and F from (C.1) yields

$$\frac{d}{dt}\begin{pmatrix}\dot{\theta}_1 \\ \dot{\theta}_2\end{pmatrix} = \begin{pmatrix} -(\nu_1 + \nu_2 I_2/I_1) & \nu_2 I_2/I_1 \\ \nu_2 & -\nu_2 \end{pmatrix}\begin{pmatrix}\dot{\theta}_1 \\ \dot{\theta}_2\end{pmatrix} + f(t)\begin{pmatrix}(l_1/I_1)\sin\theta_1 \\ (l_2/I_2)\sin\theta_2\end{pmatrix} . \tag{C.3}$$

We now proceed to integrate eq. (C.3). For simplicity we take $I_1 = I_2 \equiv I$.

Since the effect of the kicks is instantaneous (i.e., $f(t) = 0$, for $t \neq kT$, $k = 1, 2, \ldots$) eqs. (C.3) are linear between successive kicks. In particular, for $0 < t < T$, eqs. (C.3) reduce to

$$\frac{d}{dt}\begin{pmatrix}\dot{\theta}_1 \\ \dot{\theta}_2\end{pmatrix} = \mathbf{A}_\nu \begin{pmatrix}\dot{\theta}_1 \\ \dot{\theta}_2\end{pmatrix} ,$$

$$\mathbf{A}_\nu = \begin{pmatrix} -(\nu_1 + \nu_2) & \nu_2 \\ \nu_2 & -\nu_2 \end{pmatrix} . \tag{C.4}$$

This system can be easily solved by the usual methods for linear differential equations with constant coefficients. Denoting by $\dot{\theta}_1(0)$, $\dot{\theta}_2(0)$ the initial angular velocities this solution is

$$\begin{pmatrix}\dot{\theta}_1(t) \\ \dot{\theta}_2(t)\end{pmatrix} = \mathbf{L}(t)\begin{pmatrix}\dot{\theta}_1(0) \\ \dot{\theta}_2(0)\end{pmatrix} , \tag{C.5}$$

where

$$\mathbf{L}(t) = \sum_{j=1}^{2} \mathbf{W}_j e^{\lambda_j t} .$$

λ_1, λ_2 are the eigenvalues of matrix $\mathbf{A}_\nu$.

$$\left.\begin{matrix}\lambda_1 \\ \lambda_2\end{matrix}\right\} = -\tfrac{1}{2}(\nu_1 + 2\nu_2 \pm \Delta) ,$$

$$\Delta = (\nu_1^2 + 4\nu_2^2)^{1/2} ,$$

and $\mathbf{W}_1$, $\mathbf{W}_2$ are the constant matrices

$$\mathbf{W}_1 = \begin{pmatrix} a & b \\ b & d \end{pmatrix}, \quad \mathbf{W}_2 = \begin{pmatrix} d & -b \\ -b & a \end{pmatrix} ,$$

where

$$\left.\begin{matrix}a \\ d\end{matrix}\right\} = \tfrac{1}{2}\left(1 \pm \frac{\nu_1}{\Delta}\right), \quad b = -\frac{\nu_2}{\Delta} .$$

The position of the rods is obtained by integra-

tion of eq. (C.5). Denoting by $\theta_1(0)$, $\theta_2(0)$ the initial positions one obtains

$$\begin{pmatrix}\theta_1(t)\\ \theta_2(t)\end{pmatrix} = \mathbf{M}(t)\begin{pmatrix}\dot\theta_1(0)\\ \dot\theta_2(0)\end{pmatrix} + \begin{pmatrix}\theta_1(0)\\ \theta_2(0)\end{pmatrix}, \qquad \text{(C.6)}$$

where

$$\mathbf{M}(t) = \int_0^t \mathbf{L}(\xi)\,\mathrm{d}\xi = \sum_{j=1}^{2} \mathbf{W}_j \frac{\mathrm{e}^{\lambda_j t} - 1}{\lambda_j}.$$

Eqs. (C.5), (C.6) completely describe the motion of the rotor for $0 < t < T$ (before the first kick).

At $t = T$ the kick instantaneously changes the angular velocity of each rod but not its position; that is, the angular velocity of each rod is discontinuous at $t = T$, while the position is continuous. Denoting by $\theta_j(T^{\pm})$, $\dot\theta_j(T^{\pm})$, $j = 1, 2$ the values of $\theta_j(t)$, $\dot\theta_j(t)$ just before and just after the kick at $t = T$, we therefore have

$$\theta_j(T^-) = \theta_j(T^+) = \theta_j(T), \qquad \text{(C.7)}$$

$$\dot\theta_j(T^+) - \dot\theta_j(T^-) = \frac{f_0}{I} l_j \sin\theta_j(T), \qquad \text{(C.8)}$$

for $j = 1, 2$.

The solution of eqs. (C.3) for $T < t < 2T$ is identical to the solution of the linear system eq. (C.4) for $0 < t < T$ except that the initial conditions $\theta_j(0)$, $\dot\theta_j(0)$, $j = 1, 2$ are replaced by $\theta_j(T)$, $\dot\theta_j(T^+)$, $j = 1, 2$.

The solution of eqs. (C.3) is a composition of the solution of eqs. (C.4) with the effect of the kicks at $t = T, 2T, \ldots$. To study the dynamics of the rotor it is natural to consider only the state of the system immediately after each kick. Thus we obtain from (C.5)–(C.8) the *double rotor map*,

$$\begin{pmatrix}\theta_1^{(k+1)}\\ \theta_2^{(k+1)}\end{pmatrix} = \mathbf{M}(T)\begin{pmatrix}\dot\theta_1^{(k)}\\ \dot\theta_2^{(k)}\end{pmatrix} + \begin{pmatrix}\theta_1^{(k)}\\ \theta_2^{(k)}\end{pmatrix}, \qquad \text{(C.9a)}$$

$$\begin{pmatrix}\dot\theta_1^{(k+1)}\\ \dot\theta_2^{(k+1)}\end{pmatrix} = \mathbf{L}(T)\begin{pmatrix}\dot\theta_1^{(k)}\\ \dot\theta_2^{(k)}\end{pmatrix} + \frac{f_0}{I}\begin{pmatrix}l_1 \sin\theta_1^{(k+1)}\\ l_2 \sin\theta_2^{(k+1)}\end{pmatrix}, \qquad \text{(C.9b)}$$

where

$$\theta_j^{(k)} = \theta_j(kT), \quad j = 1, 2$$

are the positions of the rods at the instant of the kth kick, and

$$\dot\theta_j^{(k)} = \dot\theta_j(kT^+), \quad j = 1, 2$$

are the angular velocities of the rods immediately after the kth kick.

Appendix D. Stability of fixed points for the double rotor map

The coefficients of the characteristic equation (4.8) depend on the fixed point and on the forcing f_0 only through the two non-zero elements of the matrix $\mathbf{H}$, which we are going to denote by h_{11} and h_{22}. The discussion of the stability of the fixed points is conveniently carried out in the plane (h_{11}, h_{22}) by considering the intersections between the lines of marginal stability of the characteristic equation (where one of the roots has modulus unity) and the "orbits" described by the paths followed by the fixed points as the forcing f_0 is varied.

The "orbits" of the fixed points can be obtained by first eliminating x_{j*} $(j = 1, 2)$ between the two equations

$$f_0 \sin x_{j*} = f_{0j}, \quad h_{jj} = \frac{f_0}{I} l_j \cos x_{j*},$$

with the result

$$h_{jj} = \pm \frac{l_j}{I}\,(f_0^2 - f_{0j}^2)^{1/2}, \quad j = 1, 2,$$

and then eliminating f_0 between these two equations, with the result

$$\left(\frac{h_{22}}{l_2}\right)^2 - \left(\frac{h_{11}}{l_1}\right)^2 = \frac{1}{I^2}\,(f_{01}^2 - f_{02}^2),$$

which is the equation of the hyperbola described

by each fixed point in the plane (h_{11}, h_{22}) when f_0 is varied. It should be pointed out that symmetric fixed points with respect to $(x_{1*}, x_{2*}, y_{1*}, y_{2*}) \mapsto (2\pi - x_{1*}, 2\pi - x_{2*}, -y_{1*}, -y_{2*})$ describe the same "orbit." The lines of marginal stability are defined by the equation (see eq. (4.8b))

$$P(e^{i\alpha}) = 0\,, \tag{D.1}$$

where α can take values in the interval $[0, 2\pi)$. When $\alpha = 0$ or $\alpha = \pi$ this equation simplifies considerably. We obtain:

(i) $P(1) = 0 = |\mathbf{HM}| = |\mathbf{H}||\mathbf{M}|$; as $|\mathbf{M}| \neq 0$ this implies

$$h_{11}h_{22} = 0\,.$$

(ii) $P(-1) = 0 = |2(\mathbf{I} + \mathbf{L}) + \mathbf{HM}| = |\mathbf{H} + \mathbf{R}||\mathbf{M}|$, where

$$\mathbf{R} = 2(\mathbf{A}_\nu + 2\mathbf{M}^{-1})\,;$$

writing $\mathbf{R} = \{r_{ij}\}_{i,j=1,2}$ this leads to

$$h_{11}h_{22} + r_{22}h_{11} + r_{11}h_{22} + (r_{11}r_{22} - r_{12}r_{21}) = 0\,.$$

When $\alpha \neq 0, \pi$ it can be shown that the eq. (D.1) has no solutions in the (real) plane (h_{11}, h_{22}); that is, there are no lines of marginal stability with $\alpha \neq 0, \pi$.

In fig. 17 we have plotted in the plane (h_{11}, h_{22}) the lines of marginal stability $P(1) = P(-1) = 0$ (for the parameter values given by eq. (4.4)). The bounded region between these lines, which is the shaded region in the figure, is the only region of the plane where all the roots of the characteristic equation have modulus smaller than unity. We have also plotted the "orbits" of the first five sets of fixed points, the arrows indicating the direction the forcing increases; the critical values of (h_{11}, h_{22}) at $f_0 = f_{0c}$, which occur on the lines $P(1) = 0$, are given in table 1. We see that of all these orbits only two cross the shaded region: one corresponds to the fixed point $[(0, 0); 4]$; the other to the fixed points $[(1, 2); 4]$ and $[(-1, -2); 1]$. These fixed points are therefore stable while their "orbits" remain in the shaded region and become unstable when the "orbits" cross the line $P(-1) = 0$; that is, they are stable in a finite interval of values of f_0, $f_{0c} < f_0 < f_{0u}$. The other fixed points are unstable for all values of f_0. The values of f_{0u} are also given in table 2.

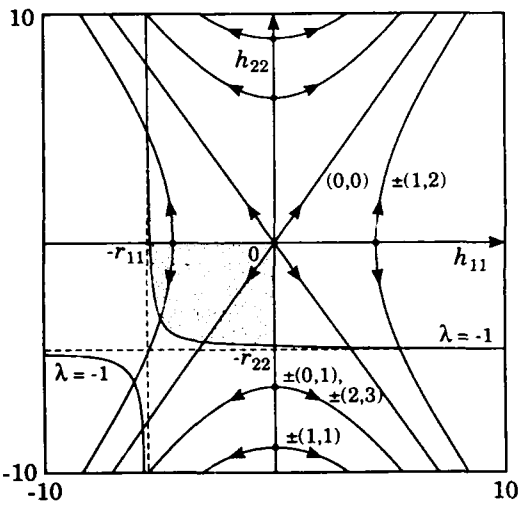

Fig. 17. Double rotor map: stability diagram of the fixed points with rotation numbers (n_1, n_2) $[f_0 = 9.0$, eq. (4.4)].

Fig. 17 only applies for the particular values of the parameters given by eqs. (4.4). For other values the relative positions of the lines of marginal stability and "orbits" of fixed points are different, and fixed points with other rotation numbers may be stable. In general, we can make the following statements regarding the stability of the fixed points: those with rotation numbers $(0, 0)$ are stable over an interval $0 < f_0 < f_{0u}^{(0,0)}$; all the others are either stable over an interval $f_{0c}^{(n_1,n_2)} < f_0 < f_{0u}^{(n_1,n_2)}$ or are always unstable.

References

[1] C. Grebogi, E. Ott and J.A. Yorke, Phys. Rev. A 37 (1988) 1711.

[2] D. Auerbach, P. Cvitanovich, J.P. Eckmann, G. Gunaratne and I. Procaccia, Phys. Rev. Lett. 58 (1987) 2387.

[3] T. Morita, H. Hata, H. Mori, T. Horita and K. Tomita, Prog. Theor. Phys. 78 (1987) 511.
[4] A. Katok, Publ. Math. IHES 51 (1980) 137.
[5] R. Bowen, Trans. Am. Math. Soc. 154 (1971) 377.
[6] E. Ott, C. Grebogi and J.A. Yorke, Phys. Rev. Lett. 64 (1990) 1196.
[7] F.J. Romeiras, E. Ott, C. Grebogi and W.P. Dayawansa, Proc. 1991 Am. Control Conf. (American Automatic Control Council, IEEE Service Center, Piscataway, NJ, 1991), pp. 1112–1119.
[8] J. Singer, Y.-Z. Wang and H.H. Bau, Phys. Rev. Lett. 66 (1991) 1123.
[9] W.L. Ditto, S.N. Rauseo and M.L. Spano, Phys. Rev. Lett. 65 (1990) 3211.
[10] T.B. Fowler, IEEE Trans. on Automatic Control 34 (1989) 201.
[11] A.M. Block and J.E. Marsden, Theor. Comput. Fluid Dyn. 1 (1989) 179;
A. Hübler and E. Lüscher, Naturwissenshaften 76 (1989) 67;
E.A. Jackson, Phys. Lett. A 151 (1990) 478;
B. Huberman and E. Lumer, IEEE Trans. Circuits Syst. 37 (1990) 547;
S. Sinha, R. Ramaswamy and J.S. Rao, Physica D 43 (1990) 118;
B. Peng, V. Petrov and K. Showalter, J. Phys. Chem. 95 (1991) 4957;
T. Tél, Controlling transient chaos, preprint;
A. Azevedo and S.M. Rezende, Phys. Rev. Lett. 66 (1991) 1342;
Y. Braiman and J. Goldhirsch, Phys. Rev. Lett. 66 (1991) 2545.
[12] K. Ogata, Control engineering, Second Ed. (Prentice-Hall, Englewood Cliffs, NJ, 1990), pp. 782–784.
[13] M. Hénon, Commun. Math. Phys. 50 (1976) 69.
[14] C. Grebogi, E. Kostelich, E. Ott and J.A. Yorke, Physica D 25 (1987) 347; Phys. Lett. A 118 (1986) 448; A 120 (1987) 497 (E).
[15] C. Grebogi, E. Ott and J.A. Yorke, Chaotic attractors in crisis, Phys. Rev. Lett. 48 (1982) 1507.
[16] C. Grebogi, E. Ott and J.A. Yorke, Physica D 7 (1983) 181.
[17] C. Grebogi, E. Ott and J.A. Yorke, Phys. Rev. Lett. 57 (1986) 1284.
[18] C. Grebogi, E. Ott, F.J. Romeiras and J.A. Yorke, Phys. Rev. A 36 (1987) 5365.
[19] G. Nitsche and U. Dressler, Controlling chaotic dynamical systems using time delay coordinates, preprint.
[20] G.M. Zaslavsky, Phys. Lett. A 69 (1978) 145.
[21] G. Benettin, L. Galgani, A. Giorgilli and J. Strelcyn, Meccanica 15 (1980) 9.
[22] G. Benettin, L. Galgani, A. Giorgilli and J. Strelcyn, Meccanica 15 (1980) 21.
[23] J.D. Farmer, E. Ott and J.A. Yorke, Physica D 7 (1983) 153.
[24] J. Kaplan and J.A. Yorke, Chaotic behavior of multidimensional difference equations, in: Functional differential equations and the approximation of fixed points, Lecture Notes in Mathematics, eds. H.O. Peitgen and H.O. Walther, Vol. 730 (Springer, Berlin, 1978), p. 228–237.
[25] T. Shinbrot, E. Ott, C. Grebogi and J.A. Yorke, Phys. Rev. Lett. 65 (1990) 3215.
[26] E. Ott, C. Grebogi and J.A. Yorke, Controlling chaotic dynamical systems, in CHAOS/XAOC, Soviet-American perspective on nonlinear science, ed. D. Campbell (American Institute of Physics, New York, 1990), pp. 153–172.
[27] F. Takens, Detecting strange attractors in turbulence, in: Dynamical systems and turbulence, eds. D.A. Rand and L.-S. Young, Lecture Notes in Mathematics, Vol. 898 (Springer, New York, 1980), pp. 366–381.
[28] J.C. Sommerer, W.L. Ditto, C. Grebogi, E. Ott and M. Spano, Phys. Lett. A 153 (1991) 105.
[29] D.P. Lathrop and E.J. Kostelich, Phys. Rev. A 40 (1989) 4028.
[30] G.H. Gunaratne, P.S. Linsay and M.J. Vinson, Phys. Rev. Lett. 63 (1989) 1.
[31] J.C. Sommerer, W.L. Ditto, C. Grebogi, E. Ott and M.L. Spano, Phys. Rev. Lett. 66 (1991) 1947.

Physica D 58 (1992) 193–201
North-Holland

PHYSICA D

A noise reduction method for signals from nonlinear systems

Tim Sauer[1]
Department of Mathematical Sciences, George Mason University, Fairfax, VA 22030, USA

Received 17 September 1991
Accepted 7 January 1992

A numerical algorithm is presented for the purpose of reducing noise from a discretely sampled input signal where the underlying signal of interest has a broadband spectrum. It is designed to be useful even if the clean signal is contaminated with 100% or more noise (signal to noise ratio less than or equal to zero). The method is based on time delay embedding using coordinates generated by local low-pass filtering, which we call a *low-pass embedding*. The singular value decomposition is then used locally in embedding space to distinguish between the dynamics and the noise.

The algorithm is evaluated for chaotic signals generated by the Lorenz and Rössler systems, to which Gaussian white noise has been added.

1. Introduction

For nonlinear systems, the application of traditional linear data filtering techniques is problematic. In the case of data from chaotic systems, for example, the power spectrum of the signal of interest as well as the noise may be broadband. In that case, filters that depend on differentiating signal from noise on frequency considerations are bound to have difficulty in finding the signal.

Embedding methods for the analysis of chaotic experimental data have proved to be quite useful. According to the theory of embedding [1, 2], if the received signal is generated by a sufficiently generic measurement function on the dynamical attractor of the system, then the attractor and its dynamical properties can, in principle, be reconstructed from the signal.

We use the ideas of embedding to design an algorithm that can separate additive noise from a deterministic signal. The algorithm is relatively simple to implement in the sense that the sophisticated ingredients, the Fourier transform and the singular value decomposition, are commonly available numerical algorithms.

Our assumption on the incoming data is that it is the result of a continuous process sampled discretely and evenly in time. We also assume that the noise is additive, and that we have an estimate of the level of the noise. The algorithm is an iterative procedure. On each pass through the data, corrections are added to the data. There are four main steps to the algorithm.

First, the data is embedded using coordinates that are smoothed locally in time using the Fourier transform. One can think of this process as a "low-pass embedding". For a chosen window size of length w, the discrete transform on w points is evaluated. The Fourier components corresponding to the $\frac{1}{2}n$ lowest frequencies are kept for some even integer $n < w$. Since the components are complex numbers, this corresponds to n independent degrees of freedom. The inverse Fourier transform on n points then yields a smoothed version of a windowed section of the signal. The embedding coordinates into $\mathbb{R}^n$ are the n numbers output from the inverse Fourier

[1] Phone: (703) 993-1471; fax: (703) 993-1491; e-mail: TSAUER@GMUVAX.GMU.EDU.

0167-2789/92/$05.00 © 1992 – Elsevier Science Publishers B.V. All rights reserved

transform: in other words, n evenly spaced samples of this smoothed section of length w.

The effect of this step is to smooth the data locally in time so that meaningful neighborhoods can be organized in the second step. Additionally, the low-pass embedding enables us to analyze information which is nominally w-dimensional in n-dimensional space. If n is small compared to w, this can make a significant difference. In the third step, when the corrections to the data are decided, this smoothing will be dropped, and the corrections will be made to the actual unsmoothed data.

The second step is to organize the embedded points in neighborhoods of size r, where r is a rough estimate of the size of the noise. The effect of the first step was to try to insure that all points in a neighborhood of radius r have been perturbed from the same branch of the attractor.

The third step is to project the points in the neighborhood onto the attractor, or at least to push the points in that direction. To do this, we use the singular value decomposition [3] to calculate the principal directions of the set of vectors which connect a fixed base point, say the center of mass of the neighborhood points, to the embedded points. The idea is to correct the raw data by projecting into a few principal directions, as preferred by the locally smoothed data. The use of the SVD to determine the global and/or local principal directions of an embedded attractor was first discussed in refs. [4, 5]. In ref. [6], these ideas were applied to increasing the accuracy of estimates of the correlation dimension of attractors.

Fourth, after the corrections necessary to project the points onto the principal directions are determined, we make use of the fact that the noise is uncorrelated with the signal of interest. (In fact, depending on the application, this may be the definition of noise.) For each embedding coordinate, the random noise in that coordinate has expected value zero. Therefore, to minimize the introduction of new correlations in the noise from our algorithm, we postprocess the corrections to ensure that they add to zero as well. The postprocessing, which we call the "correction decorrelation step", consists of averaging the corrections for the given coordinate across the points in the small neighborhood. Then the average is subtracted from each correction.

Finally, a multiple of the calculated correction is added to the raw data. The multiple is a number between 0 and 1, is small for the first pass through the data set, and is incremented by a fixed value for each additional pass, as the data becomes more consistent with a deterministic process.

To test the effectiveness of the method in reducing noise, we generate clean signals from computer simulations of deterministic systems, add Gaussian white noise of a given level, and then apply the method. The systems used for this study are the Lorenz and Rössler systems. Results are summarized in tables 1 and 2.

Recently, several noise reduction methods for nonlinear signals have been proposed which are in some way based on embedding ideas. Kostelich and Yorke [7, 8] describe a method which uses local linearizations constructed from the raw data to adjust the signal. The purpose is to minimize the self-inconsistency of the signal as much as possible while changing the signal as little as possible. This method has achieved significant noise reduction in cases of low noise. Schreiber and Grassberger [9] have more recently introduced a simpler method which relies on local linearizations which seems to have similar properties.

Hammel [10] and Farmer and Sidorowich [11] have proposed methods which use local linearizations and adjustments along the stable and unstable directions of the dynamical trajectory. This noise reduction idea, referred to as the *refinement step* in refs. [12–14], stemmed from the development of computer-assisted methods for the rigorous verification of existence of shadowing trajectories in computer simulations. This approach can reduce noise several orders of magnitude when the underlying dynamics is

known a priori, but so far has not been demonstrated to work when the dynamics is unknown. For situations where the dynamics is unknown but a true reference orbit is available a priori, Marteau and Abarbanel [15] give a method which can work in the presence of a significant amount of noise.

A method which is closely related to the present work is given by Cawley and Hsu [16]. As in our approach, instead of constructing local linearizations to the dynamics, they try to project noisy data onto the attractor. It may be that the projection approach is less sensitive to errors in the data than constructing local linearizations, and so is more likely to reduce noise in a high-noise context. In the present method, like the methods of refs. [7, 9, 16], no prior knowledge of the underlying attractor, dynamics, stable and unstable directions, or reference orbit is required.

2. Mathematical background

Assume that a system is evolving according to a set of ordinary differential equations, and that the dynamics is confined to a finite-dimensional attractor A in the phase space defined by the equations. By the definition of phase space, the present state of the system is uniquely defined by a point in phase space. The measured signal from the system can be viewed as the evaluation of an observation function h from phase space to the real numbers. If x_i is the point on the attractor that describes the state of the system at time i, then the time series is produced by evaluating the observation function h at the state x_i. The ith point s_i of the time series is $s_i = h(x_i)$.

The embedding method involves using the series of signals $h(x_i)$ to construct a map from the underlying attractor A in phase space to a reconstruction space $\mathbb{R}^n$. Another way to view this map is that n coordinates are being defined that will reconstruct the attractor, if the coordinates are independent and numerous enough. This general approach was advocated in 1980 by Packard et al. [17], in which the authors attribute to Ruelle the idea of using delay coordinates. Roux and Swinney [18] were among the first to analyze laboratory data using delay-coordinate reconstructions.

To be specific, a possible choice for the embedding map $E: A \to \mathbb{R}^n$ is

$$E(x_i) = (h(x_i), h(x_{i+1}), \ldots, h(x_{i+n-1})) = (s_i, s_{i+1}, \ldots, s_{i+n-1}) . \tag{2.1}$$

Takens [1] proved that if A is a smooth manifold of dimension d, if the reconstruction dimension n is at least $2d + 1$, and if the dynamics on A and the observation function h are topologically generic, then the embedding map will be a diffeomorphism. In ref. [2], it is proved that the same conclusion holds if h is generic in a measure-theoretic sense (i.e. probability-one) and furthermore is true in the case that A is perhaps not a smooth manifold, but rather a fractal attractor. In the latter case, the reconstruction dimension n must be strictly greater than twice the box-counting dimension d of the attractor A.

A more general choice than (2.1) is possible. In ref. [2] it is shown that the attractor can as well be reconstructed using

$$F(x_i) = B\begin{pmatrix} h(x_i) \\ \vdots \\ h(x_{i+w-1}) \end{pmatrix} = B\begin{pmatrix} s_i \\ \vdots \\ s_{i+w-1} \end{pmatrix},$$

where $w \geq n$ and B is an $n \times w$ matrix which avoids collapsing periodic points of the underlying dynamical system of integral period less than or equal to w.

3. Low-pass embedding

In the present case, we recommend defining $B = A_3 A_2 A_1$ to be the composition of the following three linear operations:

A_1 = FFT (discrete Fourier transform) of order w;

A_2 = sets to zero all but the lowest $\frac{1}{2}n$ frequency contributions;

A_3 = inverse FFT of order n, using the remaining $\frac{1}{2}n$ frequencies.

The theoretical results we have referred to above state that given a series of data $\{s_i\}$ that is noise-free, the hidden attractor A and the reconstruction $F(A)$ will have identical topological and dynamical properties. That fact motivates using the same approach in practice, where the data is noisy and the length of the series is finite. We embed the signal using F, and then try to correct for noise by locally forcing the data to lie along the principal directions of $F(A)$.

The matrix B has the effect of a low-pass filter, local in time. One starts with a length w section s of the signal, and represents it in the reconstruction by a real vector Bs of length n. If, for example, $w = 64$ and $n = 16$, the information that is contained in s but missing from Bs is essentially the upper three-fourths of the Fourier spectrum (the frequency components above $\frac{1}{4}$ of the Nyquist frequency). If the sampling rate is not too low, it is likely that the lower one-fourth of the spectrum will be sufficient to give a good approximation to the length w section of the clean signal underlying the noise.

To see an example of this, begin with a $w = 64$ point section s of the clean Lorenz signal with sampling period $\Delta t = 0.05$. In fig. 1a, 64 points of the clean signal are plotted as a solid curve, and the 16-vector Bs is plotted as 16 small boxes. The boxes lie very close to the signal, meaning that little information has been lost in going from s to Bs. In fact, the clean signal can be recovered to reasonable accuracy from the boxes by doing a 16 point FFT back to frequency space, filling in the high-frequencies contributions with zeros, and then transforming back with a 64-point FFT. Thus we trade a small amount of information loss for a great deal of advantage in reducing the dimensionality of the embedding.

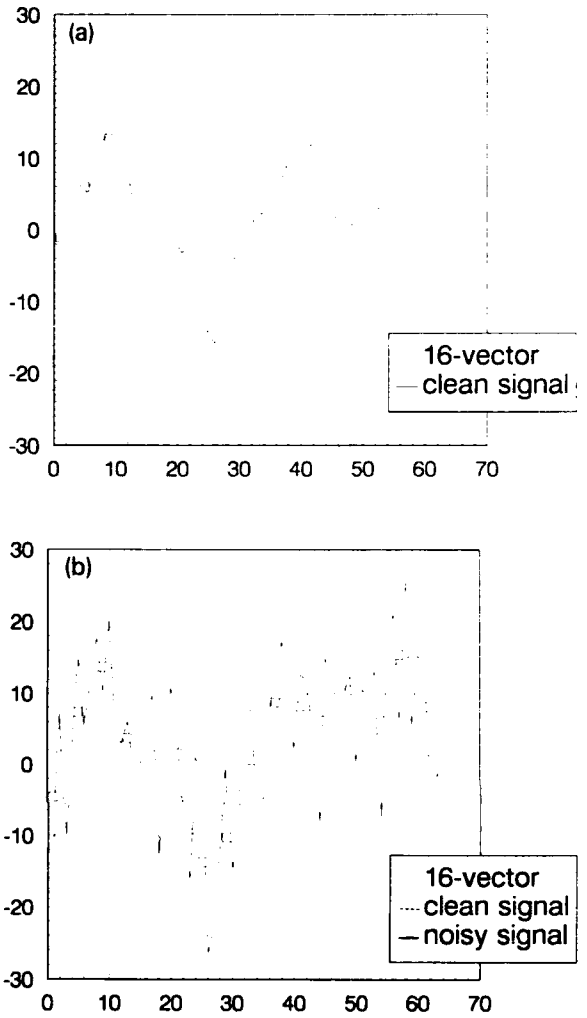

Fig. 1. In both (a) and (b), the sixteen boxes shown are the result of low-pass filtering the 64-point section of the signal shown by the solid curve. The solid curve in (a) consists of 64 contiguous values of the x-coordinates of the Lorenz system sampled at $\Delta t = 0.05$. The solid curve in (b) consists of the same signal with 100% Gaussian white noise added.

Next, begin with a noisy signal s and repeat the exercise. In fig. 1b, the dotted curve is a 64 point clean Lorenz signal, and the solid curve is the clear signal with 100% Gaussian noise added. The small boxes, which represent the 16 points of Bs, track the underlying clean signal to a reasonable degree. For purpose of recovering the clean signal, it can be argued that the 16-dimensional vector Bs has no less information than the 64-dimensional vector s, so that we can safely work in the lower dimension.

4. Algorithm

The derivation of the method makes assumptions on the input data. Specifically, we assume that the signal is the output of a deterministic dynamical system to which white noise has been added. While the degree of success of the method will presumably depend on the extent to which the assumptions hold, it may still be of use where one or more of the assumptions fail.

The method is iterative in nature. Given the original time series $\{s_i: 1 \le i \le L\}$, one pass of the algorithm through the data replaces each s_i by a new value s_i'. The resulting time series should be a less noisy version of the original series. Then the process can be applied to the new series $\{s_i': 1 \le i \le L\}$, and so forth.

The new number s_i' is determined in the following way. Several estimates t_{ij} of the correct value of s_i are generated, and their average $\hat{t}_i$ is computed. Then $s_i' = s_i + m(\hat{t}_i - s_i)$, where $0 \le m \le 1$ is a factor fixed for the entire pass through the data. We typically use $m = 0.1$ for the first pass, and slowly increase m to 0.5 throughout further passes. For example, we used $m = m_p = \max\{0.1 + 0.02(p-1), 0.5\}$ for pass p on the Lorenz attractor runs.

Generating the estimates t_{ij} of the true value of s_i is a four-step process.

1. *Low-pass embedding*

An embedding dimension n and window length w are chosen. There will depend on the nature of the data. For the low-dimensional chaotic attractors we have analyzed so far, we have typically used $n = 16$. The value of w should be larger for finely sampled signals in order to make full use of the data. We suggest that the window contain substantially more than one characteristic period of the signal, if the latter can be determined. In the case of the Lorenz attractor, the oscillations have an average period of roughly 1 time unit. If the sampling rate is $\Delta t = 0.05$, there are around 15–20 data points per oscillation. Therefore we used window lengths of $w =$ 32 and 64, and represented that section of the signal with a vector in $\mathbb{R}^{16}$.

The embedding step is to replace each contiguous section $(s_j, \ldots, s_{j+w-1})$ of the signal, $j = 1, \ldots, L - w + 1$, with the corresponding point x_j in $\mathbb{R}^n$. To accomplish this, apply the FFT of order w to $(s_j, \ldots, s_{j+w-1})$. Then apply the inverse FFT of order n to the $\frac{1}{2}n$ (lowest frequency contributions, including the zero frequency contribution. The result is an n-dimensional real vector x_j which represents the original section of the signal of window length w in the reconstruction.

2. *Neighborhood selection*

Begin by choosing a point x from the embedding into $\mathbb{R}^n$ and a neighborhood radius r. For best results, the distance r should be chosen at around the noise size of the data. Find all points x_j within the neighborhood U centered at x with radius r. Define c to be the center of mass of all points in U, and consider the vectors $v_j = x_j - c$. The vectors v_j connecting the base point c to the other points within distance r will tend to be longer in the direction along the attractor than transverse to the attractor, as long as r is not chosen to be too small.

The number of neighborhoods to construct can be chosen at the user's discretion. In our runs, we did the following. For $w = 32$, we constructed a neighborhood for each reconstructed point x_j that had not yet been contained in a neighborhood. For $w = 64$, we constructed a neighborhood for every second x_j, as long as it had not yet been in a neighborhood, to offset the extra computational time caused by the doubling of the order of the FFT.

3. *Singular value decomposition*

For each neighborhood that contains a sufficient number of points, apply the singular value decomposition to the matrix whose rows are the vectors v_j connecting the vector x_j to the base point c. Define $p(v_j)$ to be the projection of v_j into the linear space spanned by the right singu-

lar vectors corresponding to the M largest singular values, where M is a predetermined number that roughly approximates the local dimension of the attractor. We found that $M = 2$ was most successful for signals from the Lorenz and Rössler systems.

To finish the step, we need to translate $p(v_j) \in \mathbb{R}^n$ back into a corrected value of $(s_j, \ldots, s_{j+w-1})$. This calls for the reverse of the FFT smoothing step above. That is, add the base point c back to $p(v_j)$, apply the order n FFT to $c + p(v_j)$, and use the resulting $\frac{1}{2}n$ complex numbers as the $\frac{1}{2}n$ smallest frequency contributions to an order w FFT, filling in the high-frequency components with zeros. Invert the FFT to get a vector $(u_{jj}, \ldots, u_{j,j+w-1})$, which is a corrected version of $(s_j, \ldots, s_{j+w-1})$.

4. *Correction decorrelation step*

So far $u_{j,j+k}$ is a new estimate for s_{j+k}, for each $x_j \in U$, and for $k = 0, \ldots, w-1$. For each k, replace the estimate $u_{j,j+k}$ by

$$t_{j,j+k} = u_{j,j+k} - \frac{1}{L_U} \sum_{x_j \in U} (u_{j,j+k} - s_{j+k}) , \qquad (4.1)$$

where L_U denotes the number of points in U. After the t_{ji} have been computed for all neighborhoods U, define $\hat{t}_i$ to be the average over j of all contributions t_{ji}, each of which is an approximate to s_i. Finally, $s_i' = s_i + m(\hat{t}_i - s_i)$ is the replacement for s_i in the revised signal.

5. Data

The main goal of this section is to evaluate the effectiveness of the noise reduction method for a range of noise levels and sampling rates. To set up a controlled experiment, artificial data sets with additive Gaussian white noise were generated from the Lorenz and Rössler systems. We used an embedding dimension of $n = 16$ and a window size of $w = 32$ or $w = 64$ for all runs reported.

The Lorenz equations [19] are

$$\begin{aligned} \dot{x} &= \sigma(y - x) , \\ \dot{y} &= \rho x - y - xz , \\ \dot{z} &= -\beta z + xy , \end{aligned} \qquad (5.1)$$

where the parameters are set at the standard values $\sigma = 10$, $\rho = 28$, $\beta = 8/3$. A long trajectory of the Lorenz attractor was generated using the order four Runge–Kutta method with step-size 0.001. To construct a signal with sampling period $\Delta t = 0.05$, the x-coordinate of every 50th point of the trajectory was used for the clean signal. For the signal with sampling period $\Delta t = 0.10$ every 100th point was chosen. To the clean signal was added uncorrelated Gaussian noise whose standard deviation is, respectively, 10%, 100%, and 200% of the RMS Lorenz signal strength. In all cases treated in this section, a time series of 5000 points was used.

The results of the application of the method for various sampling rates and noise levels are given in table 1. The signal-to-noise (SNR) in dB units is defined to be $\mathrm{SNR} = 20 \log_{10}(\bar{c}/\bar{n})$, where $s_i = c_i + n_i$ is the clean signal plus noise, and where $\bar{c} = \langle c_i^2 \rangle^{1/2}$ and $\bar{n} = \langle n_i^2 \rangle^{1/2}$ are the root-mean-square levels of clean signal and noise.

In comparing gains in SNR, it is important to consider the dependence on sampling rate. Increasing the sampling rate and adding uncorrelated noise in the same way would have the effect of moving more of the noise into high frequencies, away from the dominant signal frequencies. For example, in the oversampled case of 100% noisy Lorenz data with $\Delta t = 0.005$, where there are around 200 sample points per oscillation, the method achieves a gain of over 21 dB, much higher than the gains shown in the table, where the sampling rates are lower.

After the maximum gain in SNR has been achieved, one may apply the method with different values of the parameters, e.g. the window length w, to the output signal in hopes of further

Table 1
Results of noise reduction method applied to noisy Lorenz data.

Δt	Avg. pts. per oscill.	Noise level	Window w	Passes	Orig. SNR	Final SNR	Gain (dB)
0.05	20	10%	32	18	20.0	31.7	11.7
0.05	20	100%	32	58	0.0	13.8	13.8
0.05	20	100%	64	15	0.0	14.2	14.2
0.05	20	200%	64	17	−6.0	6.5	12.5
0.10	10	100%	32	19	0.0	11.7	11.7

reduction. In fact, slightly larger gains can be achieved this way, but in order not to complicate our reporting of results for the basic algorithm we do not list them here.

Algorithm performance for the specific case $\Delta t = 0.05$ and 100% noise is illustrated in figs. 2 and 3. In fig. 2 we graph the amount of noise reduction as a function of the number of passes through the data. For this sampling rate and amount of additive noise, the $w = 64$ version of the method reaches a higher level of noise reduction than the $w = 32$ version, and it reaches it with fewer passes. Figure 3 illustrates the total noise reduction achieved on a typical 200-point section of the signal. In fig. 3a, the original noisy

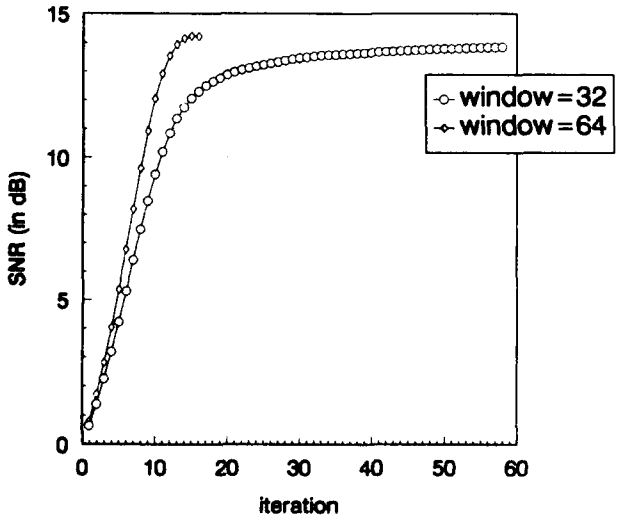

Fig. 2. Noise reduction achieved for the Lorenz data with sampling period $\Delta t = 0.05$ and with 100% noise added is graphed against the number of passes through the data. The circles and diamonds refer to application of the method with window sizes $w = 32$ and $w = 64$, respectively.

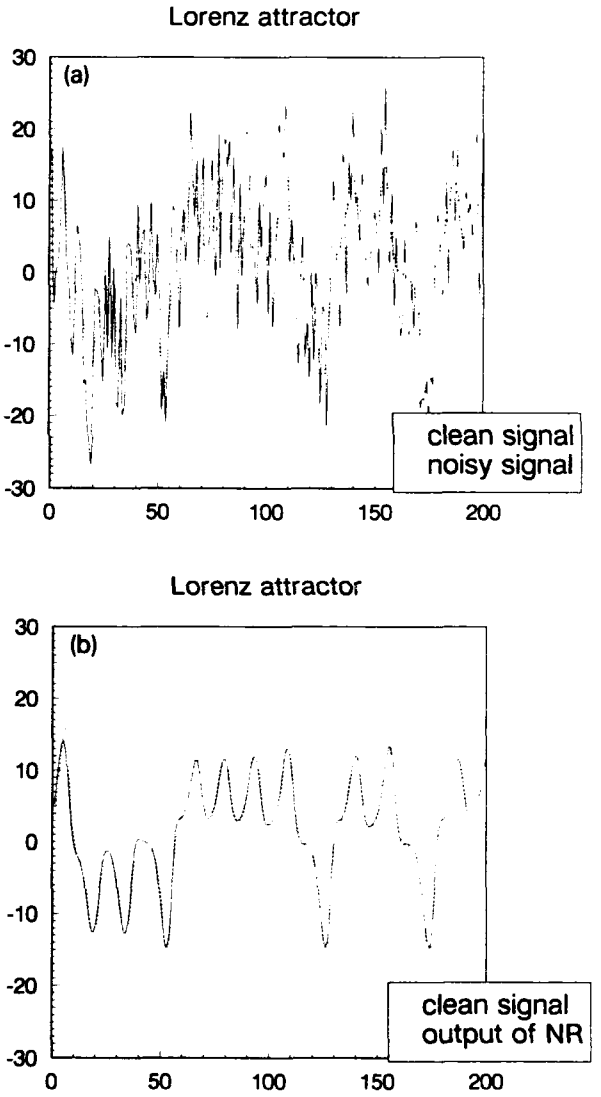

Fig. 3. (a) The solid curve is a 200 point section of the input signal, Lorenz data with sampling period $\Delta t = 0.05$ and 100% additive white noise. The dotted curve is the Lorenz signal before noise was added. (b) The solid curve is the output of the noise reduction method for the same 200 point section as in (a). The dotted curve is the clean signal, as in (a).

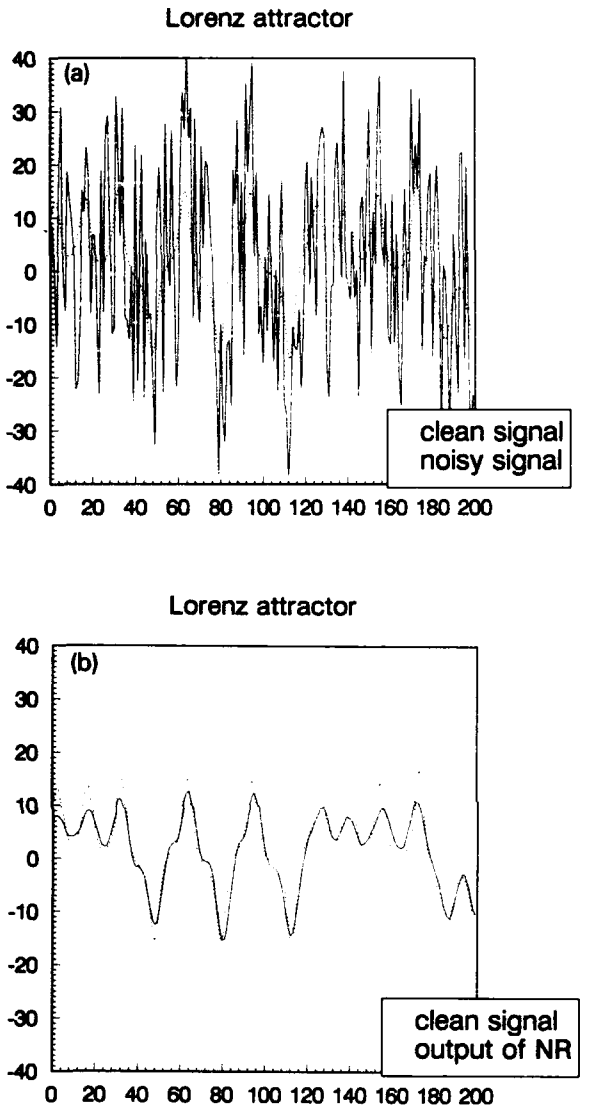

Fig. 4. (a) The solid curve is a 200 point section of the input signal, Lorenz data with sampling period $\Delta t = 0.05$ and 200% additive white noise. The dotted curve is the Lorenz signal before noise was added. (b) The solid curve is the output of the noise reduction method for the same 200 point section as in (a). The dotted curve is the clean signal, as in (a).

signal, Lorenz plus 100% noise, is graphed with a solid curve, and the clean Lorenz signal is the dotted curve. In fig. 3b, the same section of the signal is shown after 15 passes through the data, again plotted against the clean signal. Figure 4 shows similar information as fig. 3b, but for a signal to which 200% Gaussian noise has been added, and for a different section of 200 points.

The Rössler equations [20], motivated by the dynamics of chemical reactions in a stirred tank, are

$$\begin{aligned} \dot{x} &= -(y + z) , \\ \dot{y} &= x + ay , \\ \dot{z} &= bx - cz + xz , \end{aligned} \tag{5.2}$$

where the parameters are set at the standard values $a = 0.36$, $b = 0.4$, $c = 4.5$.

Table 2 summarizes the results of the method applied to data produced by sampling the x-coordinate of the Rössler equations. The sampling period of $\Delta t = 0.4$ is chosen to roughly match the Lorenz data in terms of average points per oscillation. The noise reduction results are in the same general range as those for the Lorenz data.

6. Summary

We have described the use of the delay coordinate embedding method of nonlinear data analysis to separate additive noise from a perturbed signal. The method uses a filtered version of delay coordinate embedding called a low-pass

Table 2
Results of noise reduction method applied to noisy Rössler data.

Δt	Avg. pts. per oscill.	Noise level	Window w	Passes	Orig. SNR	Final SNR	Gain (dB)
0.4	16	10%	32	20	20.0	31.8	11.8
0.4	16	100%	32	45	0.0	13.5	13.5
0.4	16	100%	64	19	0.0	14.3	14.3
0.4	16	200%	64	40	−6.0	7.2	13.2

embedding, and the singular value decomposition to project the input signal along directions belonging to the signal of interest.

The method is tested on artificial data generated by the Lorenz and Rössler systems. Significant noise reduction is measured in terms of signal to noise ratio, as documented in tables 1 and 2. Visually, the output signal appears to recover a good deal of the dynamics of the original signal, as shown in figs. 3 and 4. For example, we recover the characteristic increasing amplitude of the Lorenz oscillations as the trajectory spirals out from the unstable periodic orbit on either side.

The potential utility of this method for the computation of dynamical invariants from noisy data will depend on the success with which the dynamics can be reconstructed. The investigation of this aspect will be the subject of future work.

References

[1] F. Takens, Detecting Strange Attractors in Turbulence, Lecture Notes in Mathematics Vol. 898 (Springer, Berlin, 1981) p. 366.
[2] T. Sauer, J.A. Yorke and M. Casdagli, Embedology, J. Stat. Phys. 65 (1991) 579.
[3] G. Golub and C. Van Loan, Matrix Computations, 2nd ed. (The Johns Hopkins Univ. Press, Baltimore, MD, 1989).
[4] D.S. Broomhead and G.P. King, Physica D 20 (1986) 217.
[5] D.S. Broomhead, R. Jones and G.P. King, J. Phys. A 20 (1987) 563.
[6] A.M. Albano, J. Muench, C. Schwartz, A. Mees and P. Rapp, Phys. Rev. A 38 (1988) 3017.
[7] E. Kostelich and J. Yorke, Physica D 41 (1990) 183.
[8] E. Kostelich and J. Yorke, Phys. Rev. A 38 (1988) 1649.
[9] T. Schreiber and P. Grassberger, A simple noise-reduction method for real data, Phys. Lett. A 160 (1991) 411.
[10] S. Hammel, Phys. Let. A 149 (1990) 421.
[11] J.D. Farmer and J. Sidorowich, Physica D 47 (1991) 373.
[12] C. Grebogi, S. Hammel and J. Yorke, Bull. AMS 19 (1988) 465.
[13] T. Sauer and J. Yorke, Nonlinearity 4 (1991) 961.
[14] C. Grebogi, S. Hammel, J. Yorke and T. Sauer, Shadowing of physical trajectories in chaotic dynamics: containment and refinement, Phys. Rev. Lett. 65 (1990) 1527.
[15] P. Marteau and H. Abarbanel, Noise reduction in chaotic time series using scaled probabalistic methods, preprint.
[16] R. Cawley and G.-H. Hsu, A local geometric projection method for noise reduction in chaotic maps and flows, preprint.
[17] N. Packard, J. Crutchfield, D. Farmer and R. Shaw, Phys. Rev. Lett. 45 (1980) 712.
[18] J.-C. Roux and H. Swinney, in: Nonlinear Phenomena in Chemical Dynamics, eds. C. Vidal and A. Pacault (Springer, Berlin, 1981).
[19] E. Lorenz, J. Atmos. Sci. 20 (1963) 130.
[20] O. Rössler, Z. Naturforsch. 31 (1976) 1168.

Physica D 58 (1992) 202–215
North-Holland

PHYSICA D

Construction of phenomenological models from numerical scalar time series

G. Gouesbet and J. Maquet

Laboratoire d'Energétique des Systèmes et Procédés, INSA de ROUEN, UA CNRS 230, B.P. 08, 76131 Mont-Saint-Aignan Cédex, France

Received 28 August 1991
Revised manuscript received 27 January 1992
Accepted 27 January 1992

The problem of reconstruction of ordinary differential equations from numerical scalar time series is discussed. Techniques are exemplified for Rössler and Lorenz chaotic attractors, with emphasis on improved algorithms with respect to those previously published. The steps which are still required in order to investigate experimental noisy data are discussed.

1. Introduction

Invariants characterizing underlying attractors (generalized dimensions D_q and entropies K_q, associated singularity spectra, Lyapunov exponents) may be evaluated from numerical scalar time series (see 60 pioneering references quoted in ref. [1], and ref. [2] for local evaluations). They depend on control parameters and may be invariant under changes of coordinates (but see ref. [3]). The interest has recently drifted toward the characterization of topological indices, relying on the study of periodic orbits embedded in the attractor, which are independent of changes of coordinate systems but also of changes in the control parameters [4].

We also own algorithms to compute such quantities. For instance, generalized dimensions may be obtained from numerical scalar time series by using fixed-radius or fixed-mass approaches, or from the determination of unstable periodic orbits which are dense in the attractor [5–13]. Many of the evaluations rely on a theorem due to Mañé and Takens [14–16] which is a modified version of a previously stated Whitney theorem.

When the algorithms are successful, valuable information may be obtained. For instance, we may have evaluated the effective number of degrees of freedom required to describe the dynamics, telling us how many ordinary differential equations are needed to construct a phenomenological model of the process. Casdagli however comments that the evaluation of invariants is of little practical interest and that, in particular, no idea is given as how to construct the model itself [17]. He then discusses the inverse problem of map construction, given a sequence of iterates, and addresses the issue of forecasting by using the map as a predictive model.

In this paper, instead of solving the inverse problem to obtain a model as a map, the aim is to reconstruct a vector field. Both problems are closely related: a map may be lifted to a flow and, conversely, a flow integrated with a numerical discrete scheme, is reduced to a map. However, they are also very different in many respects. In particular, there are phenomena oc-

0167-2789/92/$05.00 © 1992 – Elsevier Science Publishers B.V. All rights reserved

curring in maps which are absent from differential systems [18, 19]. We therefore expect that flow models may be safer that map models. Furthermore, in so far as the mathematical language of nature is closer to differential equations than to discrete iterations, flow models might provide us with more accurate insights on the actual physical processes at work.

The problem of vector field reconstruction has been discussed for the Rössler system in refs. [20–21] and for the Lorenz system in refs. [22–23]. This paper again discusses the same systems but by using improved algorithms leading to more accurate evaluations of reconstruction constants, possibly by orders of magnitude. Many complementary comments and discussions given in refs. [20–23] are not repeated here.

The paper is organized as follows. A general mathematical framework, without referring to specific systems, is discussed in section 2. Reconstruction techniques and evaluations of reconstruction constants for the Rössler and Lorenz systems are provided in section 3. Qualitative and quantitatives validations are given in section 4. Conclusions are given in section 5.

2. The general formulation

We consider a dynamical system defined by a set of ordinary differential equations (ODE's):

$$\frac{\mathrm{d}x}{\mathrm{d}t} \equiv \dot{x} = f(x; \mu) , \tag{1}$$

in which $x(t) \in \mathbb{R}^n$ is a vector valued function depending on a parameter t called the time and f, the so-called vector field, is a n-component smooth function generating a flow ϕ_t (see ref. [24]). $\mu \in \mathbb{R}^p$ is the parameter vector with p components, assumed to be constant in this paper.

System (1) is called the original system (OS). The OS may be known, for instance in section 3 where we shall explicitly consider the cases of the Rössler and Lorenz systems. It may also be unknown, for instance when studying experimental systems. In any case, it is assumed that the observer numerically, or experimentally, recorded a scalar time signal. Without any loss of generality, the recorded variable is taken as being $\pi_1 x$, i.e. the projection of x on the first axis of $\mathbb{R}^n$, providing a sampled scalar time series $\{\pi_1 x\}_{i=1}^{N}$.

The aim is thereafter to reconstruct a vector field equivalent (to some sense) to eq. (1) under the form of a standard system (SS) defined by

$$\pi_1 \dot{x} = Y_1 , \tag{2}$$

$$\dot{Y}_1 = Y_2 , \tag{3}$$

$$\ldots$$

$$\dot{Y}_{n-2} = Y_{n-1} , \tag{4}$$

$$\dot{Y}_{n-1} = F(\pi_1 x, Y_1, \ldots, Y_{n-1}) , \tag{5}$$

containing n ODE's, the SS phase space being spanned by n standard coordinates $(\pi_1 x, Y_1, \ldots, Y_{n-1})$. The knowledge of the number of equations to be introduced in the SS must be independently obtained as discussed in refs. [20–23]. These references also heuristically commented on the existence of SS's but a complete study of this problem has been postponed to future work.

Starting from the time series $\{\pi_1 x\}_i$, and using an efficient enough finite-difference scheme, a series of $(n+1)$-uplets $\{\pi_1 x, Y_1, \ldots, Y_{n-1}, \dot{Y}_{n-1}\}_i$ may be obtained. We are then left with a fitting problem to evaluate the standard function F of eq. (5). This problem may be considered as a problem of multivariate modeling of data, to be solved in the framework of the theory of approximations of functions [25–27], leading to $F(\pi_1 x, Y_1, \ldots, Y_{n-1}, \{R_i\})$ in which $\{R_i\}$ is a set of model parameters called the reconstruction constants. The result is a standard recon-

structed syst. . (SRS) which is available even when the OS is unknown.

When the OS is known, the exact standard function F may be known, leading to the standard exact system (SES). In the limit of perfect reconstruction, any SRS must identify with the SES. Also, we may know the direct standard transformation (DST) expressing the standard coordinates $(\pi_1 x, Y_1, \ldots, Y_{n-1})$ versus the original coordinates $\pi_i x$, $i = 1, \ldots, n$ and the inverse standard transformation (IST) expressing the original coordinates versus the standard coordinates. Graphic displays of the SES-trajectories may therefore be obtained by (i) integrating the SES vector field (2)–(5) with F being the exact standard function or (ii) by integrating the OS vector field and applying the DST to the OS trajectory.

Next, we consider inverse standard reconstructed systems (ISRS) which may be studied when the OS is known. They are obtained by starting from SRS's with coordinates $(\pi_1 x, Y_1, \ldots, Y_{n-1})$ and by using the DST to express SRS's in terms of the original coordinates $\pi_i x$. Furthermore, we demand that the components $2, 3, \ldots, n$ of the OS (eq. (1)) be exactly satisfied. Therefore, all numerical errors associated with reconstructions are reported on the first equation for $\pi_1 \dot{x}$. Consequently, ISRS's take the form:

$$\pi_1 \dot{x} = F'(\pi_1 x, \ldots, \pi_n x, \{(R_i)\}) , \tag{6}$$

$$\pi_2 \dot{x} = \pi_2 f(x; \mu) , \tag{7}$$

$$\ldots$$

$$\pi_n \dot{x} = \pi_n f(x; \mu) . \tag{8}$$

When the R_i's are given their exact values, i.e. in the limit of perfect reconstruction, ISRS's become an inverse standard exact system (ISES) which simply identifies with the OS. Other kinds of systems, not discussed in this paper, relevant to the case when the OS is unknown, are discussed in refs. [20–23].

3. The Rössler and the Lorenz systems

Improved algorithms for the determination of the standard function F, leading to gains of accuracy by several orders of magnitude with respect to techniques previously required, are presented in this section. Attention is focussed on OS's and ISRS's. Beside the need to keep this paper under a reasonable length, our choice of focusing the attention here on OS's and ISRS's is essentially due to the fact that these systems provide the most direct and convincing assessments of the quality of reconstructions because, in the limit of perfect reconstructions, ISRS's identify with OS's. For other kinds of systems and validations, see refs. [20–23].

3.1. Mathematical expressions of OS's and ISRS's

The Rössler OS reads

$$\dot{x} = -y - z , \tag{9}$$

$$\dot{y} = x + ay , \tag{10}$$

$$\dot{z} = b + z(x - c) , \tag{11}$$

with the parameter vector $\mu = (a, b, c)$ taken equal to $(0.398, 2, 4)$ for which the asymptotic motion of the system settles down on to a chaotic attractor [18].

The Lorenz OS reads

$$\dot{x} = \sigma(y - x) , \tag{12}$$

$$\dot{y} = Rx - y - xz , \tag{13}$$

$$\dot{z} = -bz + xy , \tag{14}$$

with the parameter vector $\mu = (\sigma, R, b)$ taken equal to $(10, 28, 8/3)$ for which again the asymptotic motion settles down on to a chaotic attractor [18, 28].

Both systems being of order $n = 3$, standard systems read

$$\dot{x} = Y\,, \tag{15}$$

$$\dot{Y} = Z\,, \tag{16}$$

$$\dot{Z} = F(x, Y, Z)\,. \tag{17}$$

For the Rössler system, the exact standard function F may be written as

$$\dot{Z} = ab - cx + x^2 - axY + xZ + (ac - 1)Y + (a - c)Z - \frac{Y}{a + c - x}(x + b - aY + Z)\,. \tag{18}$$

For the Lorenz system, the exact standard function F may be written as

$$\dot{Z} = b\sigma(R - 1)x - b(\sigma + 1)Y - (b + \sigma + 1)Z - x^2Y - x^3\sigma + \frac{Y}{x}[(\sigma + 1)Y + Z]\,. \tag{19}$$

In both cases, we note that these functions exhibit singular coordinate sets of Lebesgue measure 0, $\{x_c = a + c\}$ for the Rössler case and $\{x_c = 0\}$ for the Lorenz case. Discussion of these singularities, their exact nature and numerical consequences, are provided in refs. [20–23].

Both exact standard functions F may be rewritten as a ratio of polynomial expansions, according to

$$Z = \frac{\sum_{j+k+m=0}^{N_0} N_{jkm}x^jY^kZ^m}{\sum_{j+k+m=0}^{N_0} D_{jkm}x^jY^kZ^m}\,. \tag{20}$$

The biggest N_0 generating non-zero contributions is called the degree of the system. Rössler and Lorenz systems are of degree 3 and 4, respectively. Furthermore, in the denominator, one of the D_{jkm}'s must be assigned a constant value (in practice, the simplest one: 1) to remove a degeneracy in the problem. For the Rössler system, we choose $D_{000} = 1$. For the Lorenz system, we have no choice and must set $D_{100} = 1$. The exact values of the constants N_{jkm}, D_{jkm} which are not equal to 0 are given in tables 1 and 2 for the Rössler and Lorenz cases, respectively, except for $D_{000} = 1$ (Rössler) and $D_{100} = 1$ (Lorenz).

With $\dot{Z}$ given by eq. (20), the ISRS of the Rössler system is then found to be

Table 1
Value of constants N_{jkm}, D_{jkm}. Rössler case. $P = -1(a + c)$.

	Exact values	(1)	(2)	(3)
N_{000}	$ab = 0.796$	0.795 996 9	0.796 001 6	0.796 000 008
N_{100}	$abP - c = -4.180\,991\,360$	−4.180 978 7	−4.181 000 0	−4.180 991 338
N_{010}	$ac - 1 + bP = 0.137\,247\,840$	0.137 243 8	0.137 249 3	0.137 247 808
N_{001}	$a - c = -3.602$	−3.601 987 3	−3.602 009 6	−3.601 999 999
N_{200}	$1 - cP = 1.909\,504\,320$	1.909 507 1	1.909 508 4	1.909 504 142
N_{020}	$-aP = 0.090\,495\,680$	0.090 494 8	0.090 497 1	0.090 495 675
N_{110}	$a(Pc - 1) = -0.759\,982\,719$	−0.759 981 0	−0.759 981 5	−0.759 982 548
N_{101}	$1 + P(a - c) = 1.819\,008\,640$	1.819 007 1	1.819 015 0	1.819 008 401
N_{011}	$P = -0.227\,376\,080$	−0.227 374 4	−0.227 373 3	−0.227 375 927
N_{210}	$-aP = 0.090\,495\,680$	0.090 496 3	0.090 494 9	0.090 495 594
N_{201}	$P = -0.227\,376\,080$	−0.227 376 4	−0.227 376 7	−0.227 375 980
N_{300}	$P = -0.227\,376\,080$	−0.227 376 4	−0.227 376 3	−0.227 376 018
D_{100}	$P = -0.227\,376\,080$	−0.227 376 4	−0.227 374 3	−0.227 376 028

Table 2
Values of constants N_{jkm}. Lorenz case.

	Exact values	(1)	(2)	(3)
N_{200}	$b\sigma(R-1)=720$	719.999 131	720.000 215	720.000 097
N_{020}	$\sigma+1=11$	10.999 984	10.999 999 981	11.000 001
N_{110}	$-b(\sigma+1)=-29.(3)$	−29.333 174	−29.333 399	−29.333 350
N_{101}	$-(b+\sigma+1)=-13.(6)$	−13.666 652	−13.666 656	−13.666 667
N_{011}	1	0.999 997	0.999 999 998	1.000 000 161
N_{400}	$-\sigma=-10$	−9.999 985	−10.000 002	−10.000 001
N_{310}	−1	−1.000 002	−0.999 999 050	−0.999 999 980

$$\dot{x}=\frac{-1}{1+z}\Bigg[-bc+x(a+b)+ya^2+zc^2-2xzc+x^2z+\Bigg(\sum_{j+k+m=0}^{3}N_{jkm}x^j(-y-z)^k\times(-b-x-ya+zc-xz)^m\Bigg)\times\Bigg(1+\sum_{j+k+m=1}^{3}D_{jkm}x^j(-y-z)^k\times(-b-x-ya+zc-xz)^m\Bigg)^{-1}\Bigg], \tag{21}$$

$$\dot{y}=x+ay\,, \tag{22}$$

$$\dot{z}=b+z(x-c)\,. \tag{23}$$

For the Lorenz case, the ISRS reads

$$\dot{x}=\frac{1}{R+\sigma-z}\Bigg[(\sigma+1)(Rx-y-xz)+x(xy-bz)+\Bigg(\sum_{j+k+m=0}^{4}N_{jkm}\sigma^{k+m-1}x^j(y-x)^k\times[x(R+\sigma)-y(\sigma+1)-xz]^m\Bigg)\times\Bigg(\sum_{j+k+m=0}^{4}D_{jkm}\sigma^{k+m}x^j(y-x)^k\times[x(R+\sigma)-y(\sigma+1)-xz]^m|D_{100}=1\Bigg)^{-1}\Bigg], \tag{24}$$

$$\dot{y}=Rx-y-xz\,, \tag{25}$$

$$\dot{z}=-bz+xy\,. \tag{26}$$

In both cases, we note again the appearance of singular coordinate sets of Lebesgue measure 0. However, when constants N_{jkm}, D_{jkm} are given their exact values, these ISRS's become OS's owning no singularity. Therefore, for a high-quality reconstruction, the amount of residual parasitic singularities in ISRS's is very small with the result that integrations of the systems do not require any special procedure (see refs. [20–23]).

3.2. *Finite-difference schemes to evaluate derivatives*

In practice, the OS's are integrated with a fourth-order Runge–Kutta technique and a constant time step δt, generating numerical scalar time series $\{x_i\}_{i=1}^{N}$ which are assumed to be all our knowledge concerning the systems. The reconstruction of standard functions F may be achieved from vectorial time series $\{x_i, Y_i, Z_i, \dot{Z}_i\}$, each quadruplet at time step i containing the value x_i of the original variable and three successive derivatives Y_i, Z_i, $\dot{Z}_i$. We therefore need efficient finite-difference schemes to evaluate the derivatives.

All schemes may be deduced from a Taylor expansion of the considered variable (say x) at the considered time t:

$$x(t+\Delta t)=x(t)+\Delta t\,\dot{x}(t)+\tfrac{1}{2}(\Delta t)^2x^{(2)}(t)+\cdots+\frac{1}{n!}(\Delta t)^nx^{(n)}(t)+\mathcal{O}(\Delta t^{n+1})\,. \tag{27}$$

Combining (i) $x(t)$ and $x(t+\Delta t)$ or (ii) $x(t)$ and $x(t-\Delta t)$, we obtain downward and upward (non-centered) first-order schemes reading respectively:

$$\dot{x}(t) = \frac{x(t+\Delta t) - x(t)}{\Delta t} + \mathcal{O}(\Delta t)\,, \tag{28}$$

$$\dot{x}(t) = \frac{x(t) - x(t-\Delta t)}{\Delta t} + \mathcal{O}(\Delta t)\,. \tag{29}$$

In has been systematically observed that non-centered schemes (such as the above first-order ones) led to poorer results than centered schemes, as it could be expected because evaluations of derivatives at time t are actually shifted far away from t, near $(t+\frac{1}{2}\Delta t)$ in (28) and near $(t-\frac{1}{2}\Delta t)$ in (29), the resulting errors being furthermore amplified by the need of successive derivatives. Centered schemes are therefore superior. Writing (27) for $x(t+\Delta t)$ and for $x(t-\Delta t)$, we readily obtain the simplest centered scheme which is of order 2,

$$\dot{x}(t) = \frac{x(t+\Delta t) - x(t-\Delta t)}{2\Delta t} + \mathcal{O}(\Delta t^2)\,, \tag{30}$$

leading to

$$\dot{x}_i = Y_i = (x_{i+1} - x_{i-1})/(2\delta t)\,, \tag{31}$$

$$\dot{Y}_i = Z_i = (x_{i+2} - 2x_i + x_{i-2})/(2\delta t)^2\,, \tag{32}$$

$$\dot{Z}_i = (x_{i+3} - 3x_{i+1} + 3x_{i-1} - x_{i-3})/(2\delta t)^3\,. \tag{33}$$

The fourth-order centered scheme is also discussed. This scheme is obtained from (27) by expressing $[x(t+2\Delta t) - x(t-2\Delta t)]$ and $[x(t+\Delta t) - x(t-\Delta t)]$, leading to

$$\dot{x}_i = \frac{8\Delta_1 - \Delta_2}{12\Delta t} + \mathcal{O}(\delta t^4)\,, \tag{34}$$

in which:

$$\Delta_1 = x_{i+1} - x_{i-1}\,, \tag{35}$$

$$\Delta_2 = x_{i+2} - x_{i-2}\,. \tag{36}$$

To quantify the accuracy of these schemes, we consider N triplets $\{Y_i, Z_i, \dot{Z}_i\} \equiv \{x_i^{(1)}, x_i^{(2)}, x_i^{(3)}\}$ of successive x-derivatives involved in the left-hand sides of standard systems (15)–(17), evaluated using successively the upward first-order scheme (29), the second-order scheme (30) and the fourth-order scheme (34), for the Rössler system, with $\Delta t = \delta t = 10^{-3}$ and $N = 10^4$. These derivatives may also have been evaluated independently directly from the OS and are then noted $\{\tilde{x}_i^{(1)}, \tilde{x}_i^{(2)}, \tilde{x}_i^{(3)}\}$. From (9)–(11), we have

$$\tilde{x}_i^{(1)} = (-y - z)_i\,, \tag{37}$$

$$\tilde{x}_i^{(2)} = (-\dot{y} - \dot{z})_i = -[x + ay + b + z(x-c)]_i\,, \tag{38}$$

and similarly for $\tilde{x}_i^{(3)}$. We may then evaluate scheme errors $\sigma^{(n)}$ in which n designates the order of the derivative according to

$$[\sigma^{(n)}]^2 = \frac{1}{N}\sum_{i=1}^{N} (x_i^{(n)} - \tilde{x}_i^{(n)})^2\,. \tag{39}$$

Results are given in table 3. We observe the deterioration of the scheme errors when the order of the derivative increases and its improvement, by orders of magnitude, when the order of the finite-difference scheme increases. Obviously, still higher-order schemes may be examined.

3.3. *The fitting problem*

When vectorial time series $\{x_i, Y_i, Z_i, \dot{Z}_i\}$ are obtained, we are then left with the problem of determining the standard function F. This is

Table 3
Scheme errors evaluated for several finite-difference schemes. Rössler system.

	Order 1 (non-centered)	Order 2 (centered)	Order 4 (centered)
$\sigma^{(1)}$	1.5×10^{-3}	9×10^{-7}	2.5×10^{-12}
$\sigma^{(2)}$	5.5×10^{-3}	5.5×10^{-6}	9.5×10^{-11}
$\sigma^{(3)}$	2.5×10^{-2}	3.5×10^{-5}	1×10^{-7}

essentially a multivariate interpolation/extrapolation or better approximation problem. See refs. [25–27] for a background, and ref. [17] for a comprehensive review. When global techniques are used, the fitting problem must both define a mathematical structure for F (a model) and then numerically evaluate the values of the reconstruction constants. Generally, F may be expanded on a complete set of basis functions or polynomials, and expansion coefficients (the reconstruction constants) may be evaluated by using a least-square technique. An effective example using Legendre polynomials is provided by Cremers and Hübler [29] for the reconstruction of a limit cycle of a Van der Pol oscillator. Another popular choice in the theory of approximation of functions is the use of rational functions which may be superior to polynomials because they are able to model functions with poles (see ref. [25], ch. 3) which is indeed the case for the exact standard functions of the Rössler and Lorenz systems (section 3.1). Rational functions (20) are therefore used in this paper.

Once the decision of using a global technique with (20) is taken, we must determine the degree N_0 which is in principle unknown. Also, to remove a degeneracy in the problem, one of the denominator constants D_{jkm} must be assigned a constant value that we may choose to be 1. In principle, we also do not know for which constant(s) the assignment of value 1 is possible. Therefore, a general procedure may be to attempt fitting with successive degrees of approximation $N_0 = 1, 2, \ldots$ and simultaneously attempting to set $D_{000} = 1$, then $D_{100} = 1, \ldots$, up we obtain a satisfactory fitting. For the Rössler system, we would determine $N_0 = 3$ and find that we may set $D_{000} = 1$. For the Lorenz system, we would determine $N_0 = 4$ and find that the only possible choice is $D_{100} = 1$. These facts are now considered as being established.

In refs. [20–23], the determination of the reconstruction constants was performed as follows. We first rewrote (20) as a linear equation. For instance, in the Lorenz case, we obtained

$$N_{000} + N_{100}x + \cdots - D_{000}\dot{Z} - D_{010}Y\dot{Z} - \cdots = x\dot{Z}\,, \tag{40}$$

containing 69 constants, constant D_{100} being excluded. When 69 quadruplets $\{x_i, Y_i, Z_i, \dot{Z}_i\}$ are sampled, (40) provides a set of linear equations which may be solved by the Cramer technique to obtain numerical values of reconstruction constants N_{jkm}, D_{jkm}. Actually, for the sake of accuracy, we solve a number of linear sets and carry out averages for each constant. After this step is carried out, we may identify on objective grounds the constants N_{jkm}, D_{jkm} which are theoretically equal to 0, because their values are noise-dominated. Dismissing these constants, (40) simplifies leading us to a similar problem with a smaller number of constants which are again similarly evaluated. It also appears that some sets lead to more accurate results than others, due to outliers. Outliers are eliminated by a discrimination procedure allowing for a refinement of the evaluations. At the outcome of such an algorithm, we obtain the results given in table 1, column (1) for the Rössler system, and in table 2, column (1) for the Lorenz system, with a second-order finite-difference scheme.

The accuracy of the evaluations for constants which are theoretically not equal to 0 may be quantified by using ϵ, the absolute value of the relative difference between the theoretical value of the constant and its reconstructed value. For constants which are theoretically equal to 0, we may use Δ, the absolute difference between the theoretical values and the reconstructed values (not given here), i.e. the modulus of the reconstructed values themselves. For the Rössler and Lorenz systems, the average ϵ per constant in columns (1) are 6×10^{-6} and 2×10^{-6}, respectively.

In this paper, we investigate the use of a least-square method to solve the fitting problem and also the influence of the finite-difference schemes. The example of (40) is considered (Lorenz case). The N_c indeterminates N_{jkm}, D_{jkm}

are arranged in a vector $X_i (i = 1, \ldots, N_c)$ made of N_c lines. When N time steps are recorded, (40) forms a set of linear equations. The coefficients of the left-hand sides are nominals involving variables x, Y, Z, $\dot{Z}$ and form a matrix A_{ij} made of N lines and N_c columns ($i = 1, \ldots, N$; $j = 1, \ldots, N_c$). The right-hand sides form a vector $b_i (i = 1, \ldots, N)$ made of N lines. Knowing A_{ij} and b_i, the problem is to find X_i satisfying the relation (Einstein notation used):

$$A_{ij} X_j = b_i \,. \tag{41}$$

Using $N \gg N_c$, the problem is overdetermined. It may be solved by means of a generalized least-square method (ref. [26], pp. 196, 197), researching the best solution accounting for the overdetermination. We define a residual vector r_i:

$$r_i = b_i - A_{ij} X_j \,. \tag{42}$$

The best solution is the one which minimizes the Euclidean norm of this vector:

$$\| r_i \| = (r_i^2)^{1/2} \,. \tag{43}$$

One them shows that this solution satisfies a normal set of equations [26],

$$B_{ij} A_{jk} X_k = B_{ij} b_j \,, \tag{44}$$

in which $B_{ij} = A_{ji}$ is the transpose of matrix A. Set (44) contains N_c equations ($i = 1, \ldots, N_c$) and N_c unknowns ($k = 1, \ldots, N_c$). Furthermore, for each constant X_i, the quality of the fit is indicated by a standard deviation σ_i which is given by $(C_{i(i)})^{1/2}$, in which $C_{i(i)}$ is the ith diagonal element of the matrix C_{ij} equal to $(B_{ij} A_{jk})^{-1}$. The computer program used to implement this method is Gaussj (see ref. [25]) which relies on a Gauss–Jordan method to solve (44) and invert $(B_{ij} A_{jk})$.

The Rössler and Lorenz systems are integrated with a fourth-order Runge–Kutta algorithm to generate series $\{x_t\}$ with time steps $\delta t = 10^{-3}$ and 10^{-4}, respectively (the pseudo-periods for these systems are 6.22 and 0.73, respectively). Successive derivatives are evaluated by second-order and fourth-order centered schemes. The least-square algorithm is run with $N = 10^5$ time steps, with a sampling time of 10^{-3} in both cases.

Results obtained with second-order finite differences are given in tables 1 and 2, columns (2). The average ϵ's per constant are 6×10^{-6} and 6×10^{-7}, and the average Δ's per constant are 3×10^{-7} and 9×10^{-7}, respectively. The improvement for the ϵ's with respect to columns (1) is not very impressive but it must be remembered that, for these columns, constants theoretically equal to zero were dismissed, while all constants are kept for the least-square method. If we compare the least-square technique (columns (2)) and the Cramer technique with all constants included in the problem (refs. [20–23]), then the gain for ϵ's are by two up to nearly three orders of magnitude, and the gain for Δ's are by nearly one up to two orders of magnitude, for the Lorenz and Rössler systems, respectively. It is of interest to point out that the gain of accuracy is bigger for the Rössler system than for the Lorenz one, in correlation with the fact that we previously found that accurate reconstructions were more difficult for the Rössler case.

Results for fourth-order finite differences are given in tables 1 and 2, columns (3). When compared with the results for second-order finite differences, we find that average ϵ and Δ are more accurate by one order of magnitude for the Rössler system. Conversely, improvements are again, similarly as commented above, less spectacular for the Lorenz system. The gain for average ϵ is only by a factor 3 while we even have a small deterioration of accuracy by a factor 2 for the average Δ. Still, we may conclude that the use of the fourth-order scheme is more efficient than the use of the second order scheme.

Still improved results could be obtained by combining Cramer and least-squares techniques. Noise-dominated constants can effectively be

easily identified by the Cramer technique (refs. [20–23]). Then, dismissing them, we would be left with simpler least-squares problems than the ones we solved, leading expectedly to more accurate results. However, section 4 will show that qualitative and quantitative validations of the quality of our reconstructions are very satisfactory. Therefore, the interest of further improvements is not warranted.

4. Result validations

We start with qualitative validations relying on the visual comparison between attractors produced by the OS's and ISRS's. All displayed trajectories lasted for 100 pseudo-periods. Fig. 1 shows the Rössler OS obtained by integrating the vector field of (9)–(11). Fig. 2 shows the Rössler ISRS obtained by integrating the vector field of (21)–(23). Values of reconstruction constants are taken from table 1, column (3), and the reconstructed values of constants N_{jkm}, D_{jkm} which are theoretically equal to 0 (not given to avoid marginal data proliferation) are also included in the vector field. Both figures compare very favourably. Sensitivity to initial conditions alone is sufficient to prevent figs. 1 and 2 from being identical. For the Lorenz system, we may similarly compare the OS ((12)–(14), fig. 3) and the ISRS ((24)–(26), with N_{jkm} from table 2, column (3), including again the other constants not given, fig. 4). The comparison is exceptionnally good.

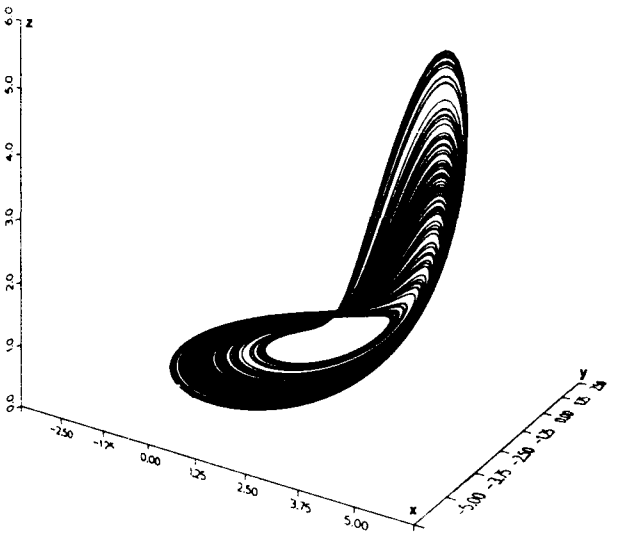

Fig. 2. Rössler case: inverse standard reconstructed system.

For quantitative validations, we shall again compare generalized dimensions evaluated in $\mathbb{R}^3$ with a fixed-radius approach as in refs. [20–23]. Details on algorithms used and notations are in particular available from refs. [1, 20], in which

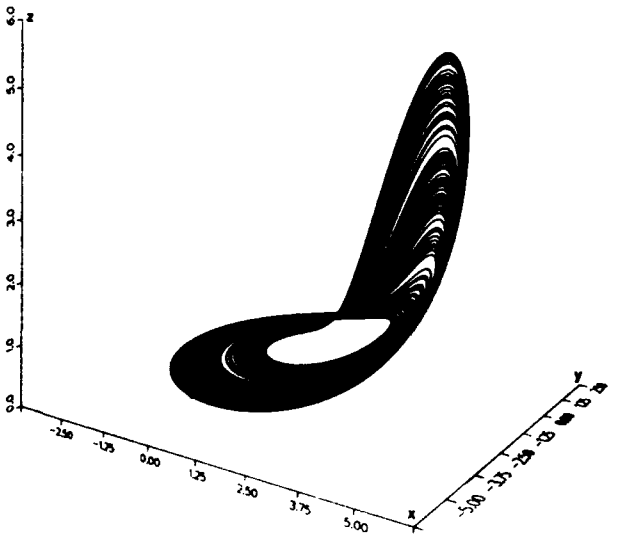

Fig. 1. Rössler case: original system.

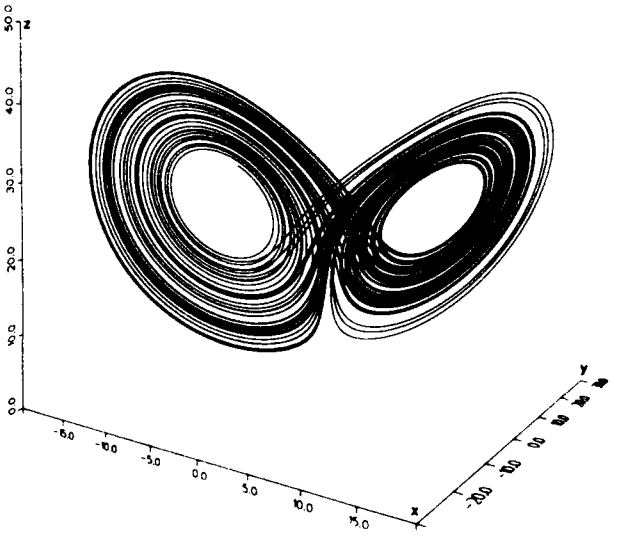

Fig. 3. Lorenz case: original system.

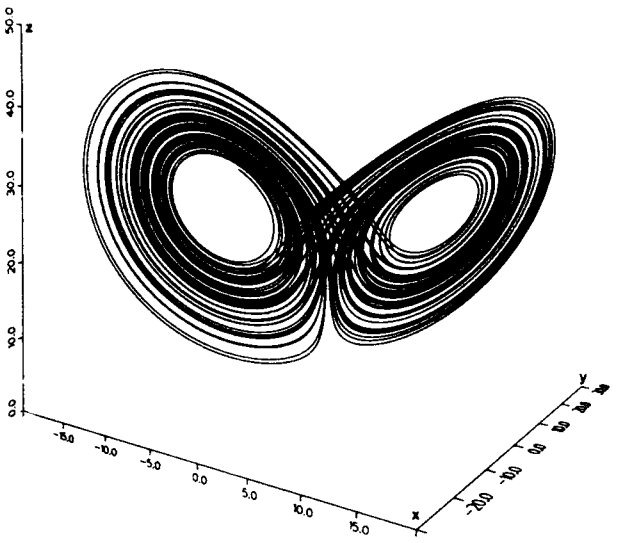

Fig. 4. Lorenz case: inverse standard reconstructed system.

the reader may find extensive quotations concerning the pioneering literature. For both Rössler and Lorenz systems, trajectories are computed with a fourth-order Runge–Kutta algorithm with time step $\delta t = 10^{-3}$. About 62 vectors and 73 vectors were sampled per pseudo-period for the Rössler and the Lorenz systems respectively. The total duration of the trajectories were about 30 000 T_0 in both cases. Local slopes $D_q(r_i)$ are evaluated at 45 r_i-locations separated by equal logarithmic intervals on a range (r_1, r_2). The ranges (r_1, r_2) were $(0.02, 0.8)$ and $(0.2, 4)$ for the Rössler and Lorenz systems respectively. D_q-computations are performed for $q \in [-45, +45]$. D_q-results are obtained by averaging local slopes $D_q(r_i)$ on a range $(r_{\min}, r_{\max})^q$ for which we obtain a plateau of good quality. Ranges $(r_{\min}, r_{\max})$ were $(0.083, 0.345)$ and $(0.368, 1.440)$ for the Rössler and Lorenz systems, respectively. These ranges could have been dramatically increased for some q's (in particular $q = 2$) but, as they have been chosen, they were valid for all q's. This is in contrast for instance with previous computations reported in ref. [20] in which range $(r_{\min}, r_{\max})$ was changed with q. This is in part due to the fact that, by using a more powerful computer, we have been able to afford computations with big resolutions $(N, m) = (2 \times 10^6, 10^4)$ in which N is the size of the temporal sequence, i.e. the number of sampled vectors, and m the number of central vectors used to average local correlation moments. For a given system, the OS and the ISRS are studied under exactly the same specifications. Therefore, comparisons between results make sense even if the D_q-values themselves are biased due to algorithm shortcomings. Finally, we also evaluate $\sigma_D(q)$, the standard mean value over the $D_q(r_i)$'s in the plateau $(r_{\min}, r_{\max})$. These σ_D's therefore provide a quantity evaluating the quality of the plateau. They also provide a clue for the accuracy of the D_q-evaluations, although it is a poor one.

For the Rössler system, some results are provided in table 4 and all resuls are given in figs. 5 and 6. $\epsilon_q\%$ is the relative difference in percent between $D_q(\mathrm{OS})$ and $D_q(\mathrm{ISRS})$ with respect to $D_q(\mathrm{OS})$. $\epsilon_\sigma\%$ is an accuracy indicator equal to 50 $[\sigma_D^q(q, \mathrm{OS})/D_q(\mathrm{OS}) + \sigma_D(q, \mathrm{ISRS})/D_q(\mathrm{ISRS})]$, i.e. to the arithmetic average over OS and ISRS of $\sigma_D(q)/D_q$ in percent. In interpreting these data, we must remember that $q = 1$ is a pivot value. For $q > 1$, D_q's probe parts of the attractor where the measure is most concentrated leading to good statistics and accurate results while, conversely, for $q < 1$, D_q's probe parts of the attractor where the measure is most rarefied leading to poor statistics and inaccurate results. However, even then, fig. 5 expressing D_q's versus q shows a very good agreement between the OS and the ISRS on the whole

Table 4
Some exemplifying results for OS and ISRS generalized dimensions D_q. Rössler system.

q	$D_q \pm \sigma_D$ (OS)	$D_q \pm \sigma_D$ (ISRS)	$\epsilon_q\%$	$\epsilon_\sigma\%$
−30	2.16 ± 0.16	2.14 ± 0.14	1.3	7.0
−10	2.11 ± 0.09	2.09 ± 0.08	0.9	4.0
0	1.9831 ± 0.017	1.9493 ± 0.024	0.6	1.1
1	1.9130 ± 0.009	1.9209 ± 0.017	0.4	0.7
2	1.8939 ± 0.005	1.8982 ± 0.009	0.2	0.4
10	1.8198 ± 0.083	1.8179 ± 0.086	0.1	4.6
30	1.7695 ± 0.173	1.7687 ± 0.179	0.04	9.9

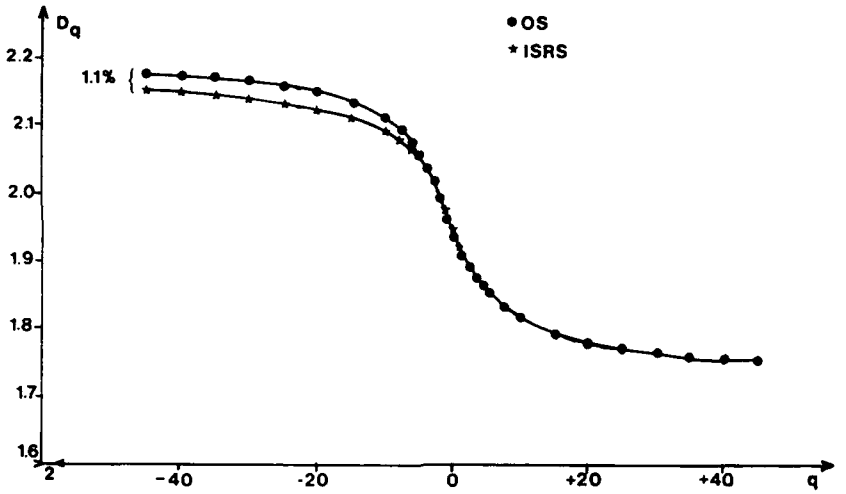

Fig. 5. Rössler case: comparison between generalized dimensions D_q of OS and ISRS.

range of studied q's. In this figure, we first plotted OS results and, afterward, ISRS results, dismissing data when ISRS results are not distinguishable from OS data. For $q > -6$, OS and ISRS results cannot be distinguished in most cases and the agreement is therefore nearly perfect. Even for $q < -6$, the relative differences $\epsilon_q\%$ are very small, being only 1.1% for $q = -45$. This figure should be compared with fig. 5 in ref. [20] showing an impressive improvement. We note that underestimations of D_q's, for $q \geq 0$, in fig. 5, ref. [20], still exist in the present fig. 5 of this paper, but have been significantly reduced. Since this statement holds for both OS and ISRS, we attribute this decrease of underestimations to the increase of the resolution (N, m). Fig. 6 compares $\epsilon_q\%$ and $\epsilon_\sigma\%$. The smallest value of $\epsilon_\sigma\%$ is obtained for $q = 2$ (correlation dimension) which is indeed reputed to be the simplest order to study. ϵ_q is always

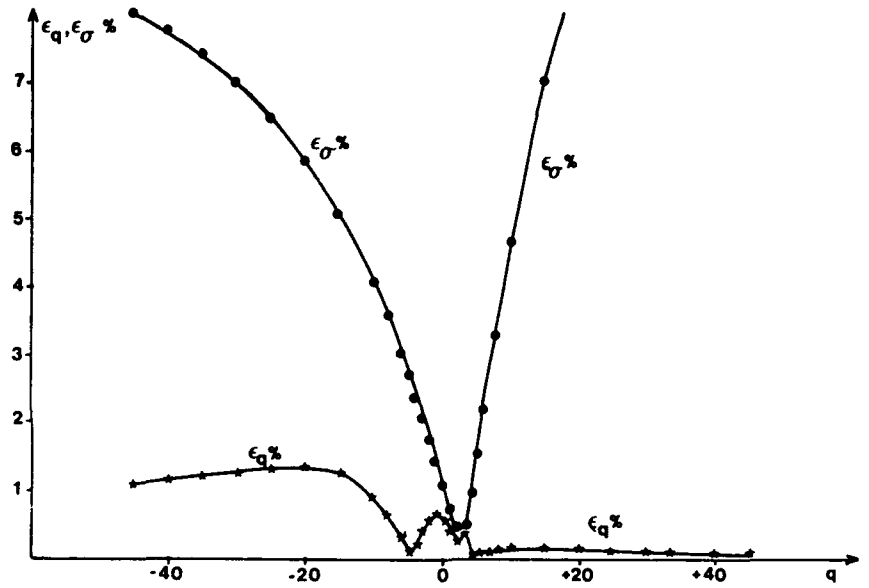

Fig. 6. Rössler case: comparison between ϵ_q, an accuracy criterion for comparison between OS and ISRS, and ϵ_σ a criterion for plateau quality.

smaller than ϵ_σ, and even much smaller, except for a q near the pivot value 1 where the slope dD_q/dq is large. Note also, as expected, that ϵ_q's are much smaller for positive q's than for negative q's. From this discussion, we conclude that the D_q-comparisons between OS and ISRS are very satisfactory. In refs. [21, 22] a more sophisticated approach to discuss the quality of comparisons is provided as a result of the fact that ϵ_σ is indeed a poor statistical criterion of accuracy. This approach relies on making averages on many systems to obtain a more realistic standard deviation σ_D', typically smaller than σ_D, therefore leading to more severe discussions. The qualitative statement that agreements are satisfactory was not modified by this other quantitative approach to evaluate the quality of ϵ_q-values.

For the Lorenz system, results are similarly given in table 5 and figs. 7 and 8. Most comments would be similar and would again lead us to the conclusion that the agreement between OS and ISRS is satisfactory. However, some specific comments are required, linked to the fact that D_q-computations for the Lorenz system are more difficult than for the Rössler case, as

Table 5
Some exemplifying results for OS and ISRS generalized dimensions D_q. Lorenz system.

q	$D_q \pm \sigma_D$ (OS)	$D_q \pm \sigma_D$ (ISRS)	ϵ_q (%)	ϵ_σ (%)
−30	2.9 ± 1.1	2.6 ± 0.9	12	37
−10	2.9 ± 0.9	2.6 ± 0.8	12	31
0	2.0770 ± 0.025	2.0699 ± 0.025	0.3	1.2
1	2.0479 ± 0.002	2.0490 ± 0.001	0.05	0.07
2	2.0690 ± 0.002	2.0697 ± 0.002	0.03	0.1
10	2.1730 ± 0.013	2.1741 ± 0.014	0.05	0.6
30	2.1933 ± 0.020	2.1956 ± 0.019	0.1	0.9

we repeatedly observed in previous works. In fig. 7 agreement seems perfect for $q \geq 0$ but, for $q < 0$, ϵ_q's are much bigger than in the Rössler case. They are however still much smaller than ϵ_σ's (fig. 8) but these ϵ_σ's are also much bigger than for the Rössler system. Actually, all ϵ_q's are smaller or much smaller than ϵ_σ's (fig. 8) but the difference of behaviour between the cases $q > 1$ and $q < 1$ forced us to use two different ordinate scales in fig. 8. Furthermore, computed D_q's increase when q increases for $q \in [1, 25]$. This is an artifact because D_q's must theoretically satisfy the relation $D_q \leq D_p$, $q > p$. Hopefully, computations with still bigger resolutions (N, m) would

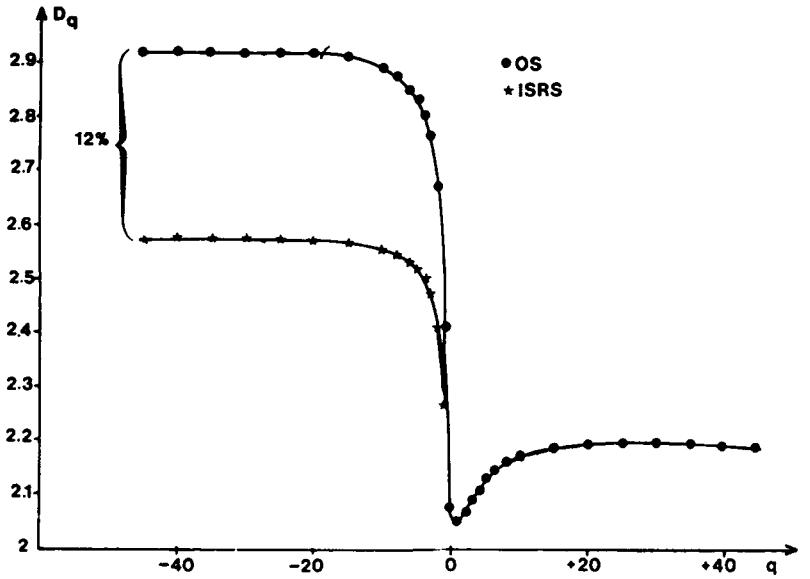

Fig. 7. Lorenz case: comparison between generalized dimensions D_q of OS and ISRS.

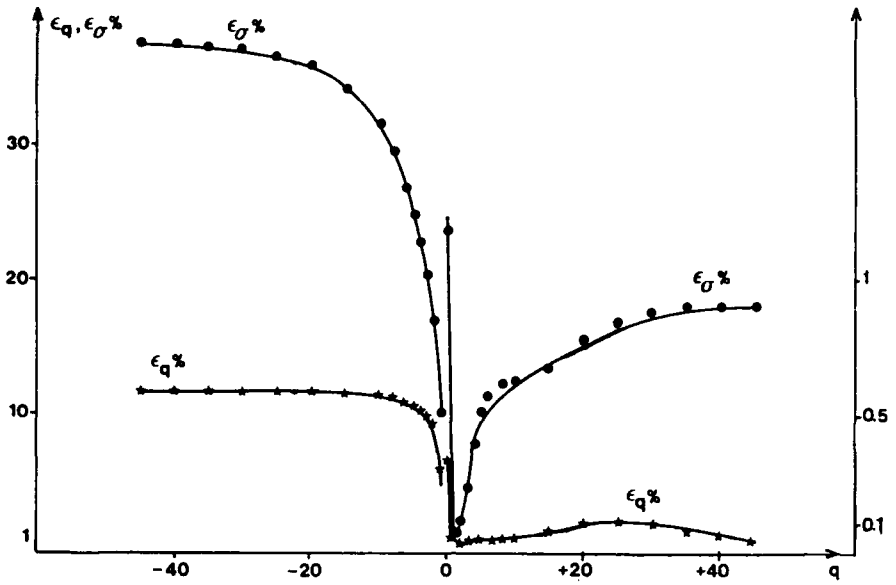

Fig. 8. Lorenz case: comparison between ϵ_q and ϵ_σ.

simultaneously improve the results for small q's and remove the artifact, but such bigger resolutions could be difficult to afford in terms of CPU-requirements. However, we mention that D_q-computations of the OS once performed with $(N, m) = (10^6, 10^5)$ and a time-delay reconstruction technique with variable z did not exhibit the artifact. The reader should refer to ref. [23] for more details on these shortcomings.

5. Conclusions

This paper presented our state of the art in our effort to promote automatic reconstruction of phenomenological models from numerical scalar time series, exemplifying results on two paradigms, namely the Rössler and the Lorenz systems. Beside our main motivation, the discussed techniques open the way to several other lines of research like flow forecasting and others reported in previous references. Our final motivation is, however, to extend and generalize the present work up to the study of experimental noisy systems. One problem is to provide a systematic study of techniques available to model the standard function F. To assess the degree of generality of such techniques, we intend to investigate the example of chaotic attractors produced by a model of thermal lens oscillations [1]. These attractors are generated by a rather exotic vector field which will provide an acid test. The second problem concerns the presence of noise on real data. This addresses the issues of the sensitivity to noise of the techniques we used, and of noise smoothing and removal. We have little doubt that these problems will eventually find adequate solutions, providing the applied scientists with new tools of interest for data and system modelling.

References

[1] G. Gouesbet, Phys. Rev. A 42 (1990) 5928.
[2] J.M. Nese, Physica D 35 (1989) 237.
[3] E. Ott, W.D. Withers and J.A. Yorke, J. Stat. Phys. 36 (1984) 687.
[4] G.B. Mindlin, Xin-Jun Hou., H.G. Solari, R. Gilmore and N.B. Tufillaro, Phys. Rev. Lett. 64 (1990) 2350.
[5] H.G.E. Hentschel and I. Procaccia, Physica D 8 (1983) 435.
[6] P. Grassberger and I. Procaccia, Physica D 13 (1984) 34.
[7] R. Badii and A. Politi, J. Stat. Phys. 40 (1985) 725.
[8] W. Van de Water and P. Schram, Phys. Rev. A 37 (1988) 3118.

[9] J.G. Caputo and P. Atten, Phys. Rev. A 35 (1987) 1311.
[10] C. Grebogi, E. Ott and J.A. Yorke, Phys. Rev. A 37 (1988) 1711.
[11] D. Auerbach, B. O'Shaughnessy and I. Procaccia, Phys. Rev. A 37 (1988) 2234.
[12] G. Broggi, J. Opt. Soc. Am. B 5 (1988) 1020.
[13] M. Ravani, B. Derighetti, G. Broggi and E. Brun, J. Opt. Soc. Am. B 5 (1988) 1029.
[14] R. Mañé, in: Proc. Dynamical Systems and Turbulence, Warwick, 1980, Lecture Notes in Mathematics, Vol. 898 (Springer, Berlin, 1981) p. 230.
[15] F. Takens, in: Dynamical Systems and Turbulence, Warwick, 1980, Lecture Notes in Mathematics, Proc. Vol. 898 (Springer, Berlin, 1981) p. 366.
[16] F. Takens, in: Nonlinear Dynamics and Turbulence, eds. G.I. Barenblatt, G. Iooss and D.D. Joseph (Pitman, London, 1983) p. 314.
[17] M. Casdagli, Physica D 35 (1989) 335.
[18] J.M.T. Thompson and H.B. Stewart, Nonlinear Dynamics and Chaos, (Wiley, New York, 1987).
[19] H.C. Yee, P.K. Sweby and D.F. Griffiths, in: Proc. 12th Int. Conf. Numerical Methods in Fluid Dynamics, Oxford, July 1990, pp. 1–9.
[20] G. Gouesbet, Phys. Rev. A 43 (1991) 5321.
[21] G. Gouesbet, Phys. Rev. A 44 (1991) 6264.
[22] G. Gouesbet, Reconstruction of vector fields. Case of the Lorenz system, Physial Review A, submitted.
[23] G. Gouesbet, in: Proc. 8th Symp. Turbulent Shear Flows, München, 9–11 September 1991.
[24] J. Guckenheimer and P. Holmes, Nonlinear Oscillations, Dynamical Systems, and Bifurcations of Vector Fields, Applied Mathematical Sciences Vol. 42 (Springer, Berlin, 1983).
[25] W.H. Press, B.P. Flannery, S.A. Teukolsky and W.T. Vetterling, Numerical Recipes, the Art of Scientific Computing (Cambridge Univ. Press, Cambridge, 1986).
[26] G. Dahlquist and A. Bjorck, Numerical Methods (Prentice Hall, Englewood Cliffs, NY, 1974).
[27] J.R. Rice, The Approximation of Functions, Vols. 1 and 2 (Addison–Wesley, Reading, MA, 1964 and 1969).
[28] E.N. Lorenz, J. Atmos. Sci. (1963) 130.
[29] J. Cremers and A. Hübler, Z. Naturforsch. A 42 (1987) 797.

Physica D 58 (1992) 216–228
North-Holland

PHYSICA D

Phase space reconstruction for symmetric dynamical systems

G.P. King and Ian Stewart
Nonlinear Systems Laboratory, Mathematics Institute, University of Warwick, Coventry CV4 7AL, UK

Received 21 October 1991
Revised manuscript received 2 March 1992
Accepted 9 March 1992

Since the pioneering work of Packard et al. and Takens it has become customary to reconstruct the topology of attractors in phase space from a time series of one-dimensional experimental observations by using delay coordinates. Many practical refinements of the original methods have been developed.

Many experimental systems possess symmetry, and bifurcations can cause changes in the symmetry of observed states. These changes are quite subtle when the dynamics is chaotic. It is therefore important to reconstruct not just the topology of the attractor, but its symmetry. We indicate how this can be done by extending the Packard–Takens approach to a single *equivariant* observation, taking values not in the real numbers $\mathbb{R}$ but in a linear representation V of the symmetry group G. In effect a single *set* of symmetrically related observations is required. Our central point is that not all plausible choices for such a set can generate embeddings. In order for the method to produce an embedding, it is necessary that V should be "sufficiently complicated". More precisely, the phase space M must be subordinate to V in a sense introduced by Wassermann. This concept is technical, but unavoidable in this context, and it greatly clarifies the issue of embeddability. Using it, we state a symmetric version of the Takens embedding theorem, and sketch the proof. We also discuss the issue of "setwise" versus 'pointwise' symmetry of an attractor, and relate this to the transition from spatial order to spatial disorder in temporally chaotic systems.

1. Introduction

The problem of detecting deterministic chaos in experimental data, and distinguishing it from random noise, has stimulated the development of new methods for analysing time series. The first of these was the *delay coordinate method* of Packard et al. [21] and Takens [29], which permits the topology of phase space, dynamics, and attractors to be reconstructed from a time series of a *single* "generic" observation. This method is justified by the Takens embedding theorem, see ref. [29] theorem 1. It has been refined by Broomhead and King [3, 4] who use principal component analysis to overcome certain practical difficulties in its implementation. Many other variants now exist, not all of which have been given rigorous justification.

Many systems of experimental interest possess symmetry. Fluid flows, combustion, and convection often take place within symmetric containers – cylinders, spheres, rectangular boxes, annuli. Conventional nonlinear dynamics focuses on "generic" behaviour, but symmetry almost by definition is "nongeneric" in the conventional sense. For example, one of the generic hypotheses of the Takens embedding theorem is that the flow should have simple eigenvalues at low-period periodic points. However, in symmetric systems eigenspaces are invariant under the symmetry group, and this can force multiple eigenvalues to occur, because – with very few exceptions – irreducible representations are multidimensional.

It is therefore necessary to modify the theoretical approach, considering systems that are 'generic *subject to possessing the given symmetry*'. Dynamics in the presence of symmetry,

0167-2789/92/$05.00 © 1992 – Elsevier Science Publishers B.V. All rights reserved

or *equivariant dynamics*, has now become a well defined sub-area of dynamical systems theory. For example, Golubitsky et al. [14] have given an extensive treatment of non-chaotic bifurcations. Chaos in symmetric systems has been discussed by many authors including Chossat and Golubitsky [7, 8], Field and Golubitsky [11, 12], and King and Stewart [17]. Several new phenomena occur, notably symmetry-increasing crises ("collisions" of symmetrically related attractors), and intermittency just after such a crisis. The dynamics of crises have been studied by Grebogi et al. [15].

There is evidence that these symmetry-related phenomena occur in experimental systems. Ashwin [1] has detected a symmetry-increasing crisis in a coupled oscillator circuit; and Golubitsky [13] has argued that patterned turbulence in Couette–Taylor flow (such as turbulent Taylor vortices) can usefully be interpreted as symmetric chaos. Further experimental examples are surveyed in King and Stewart [17].

In equivariant dynamics, the emphasis is not just on the topology of attractors, but also on their symmetries. Changes in symmetry are often very robust, and provide excellent opportunities for new experiments on current theories of nonlinear dynamics and chaos. What is lacking are practical techniques for phase space reconstruction that also preserve symmetry, and theoretical foundations for such techniques. In this paper we take a step towards remedying this deficiency by developing an equivariant version of one standard method for reconstructing both the topology and the symmetry of attractors from time series.

The underlying idea is a simple one: to use not just a single numerical measurement, or *observation*, but a multidimensional set of measurements that respects the symmetry – an *equivariant* observation. This is both experimentally and mathematically natural, but by making it explicit we are able to expose, and to some extent deal with, some basic issues that are peculiar to the equivariant case. These involve group-theoretic technicalities: the point we wish to emphasise is that these technicalities *must* be taken into account in order to obtain a general understanding of the nature of the problem.

The fundamental theoretical result that underpins phase space reconstruction methods is the Takens embedding theorem [29]. Correspondingly our central theoretical result is an equivariant version of that theorem (theorem 2 of section 6 below). Its proof involves technical considerations in differential topology, and in this paper we outline only the main points. Again we shall argue that such considerations are not *just* technical: they place restrictions upon the target of a suitable experimental observation, and so have a definite bearing upon the design of experiments to detect symmetric chaos.

2. Experimental motivation

Among the phenomena observed in symmetric systems are "coherent structures": dynamical states that combine local chaos with global pattern. The classic example is the formation of turbulent Taylor vortices in Couette–Taylor flow, see [10].

The most interesting bifurcation for our present purposes is that to turbulent Taylor vortices. The flow is turbulent, with no genuine symmetries; but it possesses the symmetry of Taylor vortices "on the average". That is, ignoring the fine texture of the turbulence, the flow has the same symmetry as Taylor vortices, namely, a reflectional symmetry in the plane of the vortex boundary, together with discrete translational symmetries along the axis (in an infinite cylinder model). Golubitsky [13] traces this *sudden* reappearance of pattern to a symmetry-increasing crisis of conjugate chaotic attractors: see also [17]. The evidence in favour of this explanation is circumstantial but quite strong. Similar ideas apply to some other coherent structures such as spiral turbulence.

Another system rich in symmetry is an elec-

tronic circuit formed from n symmetrically coupled identical oscillators. Ashwin, King, and Swift [2] study systems of this type when the coupling is fully symmetric. The symmetry group is then $\mathbb{S}_n$, the symmetric group of degree n, acting as permutations of the oscillators. The main focus of [2] is non-chaotic dynamics. Ashwin [1] studies chaos in such systems when $n = 3$ or 4. For experiments he uses a system of coupled identical Van der Pol oscillators forced by a sinusoidal signal. The results are visualised by assigning one of n unit vectors, arranged in the plane at angles of $2\pi/n$, to the voltage in each oscillator, and plotting a Poincaré section synchronised with the times at which the forcing signal generator passes through zero from negative to positive. This projection of the voltage data is chosen to preserve symmetry, a theme we take up more generally in section 5 below.

In both of these experimental systems we observe the influence of symmetry of the apparatus upon the dynamics, leading to pattern-formation via symmetry-breaking. Moreover, once the dynamics has become chaotic, we see bifurcations that *increase* the symmetry in some time-averaged sense, leading to certain kinds of coherent structure.

3. Equivariant dynamics

We now describe a theoretical framework in which such effects can be described and analysed. We assume some familiarity with "traditional" dynamical systems theory, see for example [16]. In order to discuss examples from a general viewpoint, we begin by introducing some basic terminology from equivariant dynamics. For simplicity we concentrate on discrete dynamical systems, although similar considerations apply to the continuous case.

A discrete dynamical system is given by an equation of the form

$$x_{t+1} = f(x_t, \lambda)\,. \tag{1}$$

Here $f\colon M \times \mathbb{R}^r \to M$ is a C^∞ mapping (or perhaps C^k for some k) defined on a manifold M, the *phase space*, and $\lambda \in \mathbb{R}^r$ is an r-dimensional *bifurcation parameter*. Usually either $r = 0$ (no bifurcation parameter) or $r = 1$.

Technically, it is normal to assume that f should be a diffeomorphism (invertible smooth map with smooth inverse). This allows the dynamics to be continued for negative time. However, the dynamics of non-invertible maps f can be approximated by projections of those of invertible maps on spaces of double the dimension, as proved in the *shadow lift Lemma* of King and Stewart [17]. We therefore permit non-invertible maps in our examples and numerical experiments.

Similar considerations apply to continuous systems

$$\frac{dx}{dt} = f(x, \lambda)\,, \tag{2}$$

in which case f is a vector field on M.

Some important practical issues in time series analysis are different for continuous systems compared to discrete ones, but both have similar theoretical foundations.

A subset A of M is said to be an *attractor* for (1) if

(a) $f(A) = A$.

(b) A has a dense orbit.

(c) There exists a neighbourhood U of A such that for every $u \in U$ we have $\omega(u) \subset A$, where $\omega(u)$ is the ω-limit set of u.

A similar definition holds for the continuous case.

Suppose that a compact Lie group G acts smoothly on M, so that M becomes a *G-manifold*. Let γm denote the image of $m \in M$ under the action of $\gamma \in G$. We say that f is *G-equivariant* if

$$f(\gamma m) = \gamma f(m)$$

for all $m \in M$, $\gamma \in G$. (For more general maps f between possibly distinct spaces, the actions of G

on source and target may differ.) Make the following definitions:

(a) The *G-orbit* of $m \in M$ is

$$Gm = \{\gamma m | \gamma \in G\} .$$

For equivariant f, if A is an attractor for the dynamics then so is γA for all $\gamma \in G$. We say that γA is *conjugate* to A.

It is important to distinguish the G-orbit of m from its *dynamical orbit*, or *trajectory*. We denote the latter by $O(m)$.

(b) The *isotropy subgroup* of $m \in M$ is

$$\Sigma_m = \{\gamma \in G | \gamma m = m\} .$$

This measures the degree of symmetry of a point m.

(c) We also require a generalisation. If $m \in M$ we define the (*orbital*) *symmetry group* of m to be

$$\Delta_m = \{\gamma \in G | \gamma \overline{O(m)} = \overline{O(m)}\} .$$

Here bars denote topological closure in M.

If A is an attractor having a dense orbit $f^t(m)$, then the *symmetry group* of A, written Δ_A, is defined to equal Δ_m. It is the set of $\gamma \in G$ that leave A *setwise* fixed (but not necessarily pointwise fixed).

(d) If Σ is a subgroup of G (which henceforth we write as $\Sigma \leq G$) then the *fixed-point set* of Σ is

$$\mathrm{Fix}(\Sigma) = \{m \in M | \sigma m = m \quad \text{for all } \sigma \in \Sigma\} .$$

We write this as $\mathrm{Fix}^M(\Sigma)$ when several distinct G-manifolds are under consideration and it is necessary to identify which one is intended.

(e) The *orbit space* M/G is the set of G-orbits of M, with the quotient topology defined by the natural map $M \to M/G$, which sends $x \in M$ to the orbit Gx. In general M/G is not a manifold: it may possess singularities. Intuitively M/G is what remains of M when we identify points that map to each other under the G-action, that is, if we "factor out the symmetry".

4. Symmetry-increasing crises

We briefly describe some examples of crises in symmetric systems. Their occurrence emphasises the need to understand the symmetry of an attractor as well as its topology.

The simplest nontrivial group action is $G = \mathbb{Z}_2$ acting on the line $M = \mathbb{R}$ by $x \mapsto -x$. The *cubic logistic map* $x \mapsto kx(1 - x^2)$ is equivariant for this action. See also [7, 9, 24]. For this map there is an initial bifurcation from a $\mathbb{Z}_2$-symmetric fixed point $x = 0$ to an asymmetric fixed point. This is followed by a period-doubling cascade (of asymmetric points), leading to chaos. There is then a new phenomenon: a sudden "explosion" of the attractor, from an asymmetric interval contained in the positive half-line into a symmetric interval containing both negative and positive values of x. This is an example of the phenomenon that Grebogi et al. [15] call a *crisis*. Two disjoint strange attractors (here related by symmetry) have collided and "fused" into a single attractor. The symmetric attractor that exists after the crisis is not just a union of two separate asymmetric attractors: it is *indecomposable*, that is, it has a dense orbit. The curious feature of such an event is that it *increases* the symmetry of the attractor. In this example, before the crisis there are two distinct attractors A_1, A_2, each with trivial symmetry $\Delta_{A_j} = \mathbf{1}$. After the crisis there is one attractor A with non-trivial symmetry $\Delta_A = \mathbb{Z}_2$. In non-chaotic dynamics, bifurcations tend to *break* symmetry. It is true that reversing the bifurcation parameter trivially turns a symmetry-breaking bifurcation into a symmetry-increasing one, but generally there is a "natural' direction for the bifurcation parameter, in which the degree of nonlinearity increases, often leading from order into chaos; and for non-chaotic states the bifurcations in that direction normally lead to

less and less symmetry. However, when chaotic attractors are present, symmetry-increasing crises are common. They have been reported many times in the literature: see for example [7, 8, 18, 23, 25, 28].

A rich source of numerical examples of symmetry-increasing crises is afforded by mappings of the plane equivariant under the standard action of the dihedral group $\mathbb{D}_n$. Chossat and Golubitsky [8] have studied the family of $\mathbb{D}_n$-equivariant mappings

$$f(z, \lambda) = (\alpha u + \beta v + \lambda)z + \gamma \bar{z}^{n-1} . \qquad (3)$$

Field and Golubitsky [11, 12] have produced high-resolution computer pictures of the attractors of (3) in which pixels are colour-coded according to how many times the point lands on them. This gives a visual representation of the invariant measure on the attractor. Other examples of symmetric crises may be found in Chossat and Golubitsky [8] and King and Stewart [17]. A theoretical explanation of why crises of conjugate attractors in symmetric systems lead to an increase of symmetry has been given by Chossat and Golubitsky [8].

5. Equivariant observations

We now introduce the simple idea that lies behind equivariant phase space reconstruction. First, recall the basis of the Packard–Takens method. Suppose that M is a manifold (phase space) upon which is defined a vector field (continuous dynamic) or diffeomorphism (discrete dynamic) ϕ. Let $h: M \to \mathbb{R}$ be an observation. Then a time series of observations x_j is defined by $x_j = h(\phi^j(x_0))$ for an initial condition x_0. A "window size" N is chosen, and the time series of N-dimensional vectors

$$z_j = (x_j, x_{j+1}, \ldots, x_{j+N-1})$$

is formed. Provided N is large enough ($2n + 1$, where n is the dimension of M, suffices) and h and ϕ satisfy suitable generic hypotheses, the dynamics of z_j in $\mathbb{R}^N$ provide an accurate topological reflection of those of x_0 on M. The most important feature of this method is that a *one-dimensional* observation h is used to deduce topological features of a *multidimensional* dynamic.

The examples and experiments discussed in previous sections motivate a general setting for the analysis of symmetric dynamics, and a symmetric analogue of the Packard–Takens reconstruction method. Suppose that G is a compact Lie group of transformations, acting on the phase space M of the dynamical system. In the discrete case, the dynamics is defined by a diffeomorphism ϕ on M, playing the role of the mapping f in (1). However, ϕ is now G-equivariant. Let $h: M \to V$ be a function, that is, an idealised experimental observation. What kind of structure should the target V of h have?

If we wish to reconstruct the symmetries of attractors of ϕ on M from information lying in V, then V must itself carry symmetry information. That is, V should also be a G-manifold. The simplest and most natural case is when V is a Euclidean G-space, that is, affords a linear representation of G. In this case we can (and henceforth do) assume that G acts orthogonally in some metric: see Golubitsky et al. [14], p. 31.

The natural way to ensure that h conveys information about symmetry is to insist that h should itself be G-equivariant (for the separate actions of G on M and V). That is, that

$$h(\gamma m) = \gamma h(m)$$

for all $m \in M$, $\gamma \in G$. One immediate consequence of equivariance is that V cannot always be assumed one-dimensional as is the case for phase space reconstruction in non-equivariant systems.

In fact, these conditions are natural in experiments aimed at detecting symmetry. For example, in the system studied by Ashwin [1], the

primary measurement made is the triple of voltages (V_1, V_2, V_3) at corresponding points in the three oscillator circuits. Since the symmetry group $\mathbb{S}_n$ acts by permuting the oscillators, the physical interpretation of equivariance is that the measurements should be made in the same way on each oscillator.

If we take an attractor for (3) with full $\mathbb{D}_3$ symmetry and plot its x- and y-coordinates as two separate time series, then the symmetry is by no means apparent. This happens because the x- and y-coordinates are not related in a symmetric fashion; that is, they do not determine an equivariant observation. If instead we plot (fig. 1) time-series for the variables x, $x/2 + \sqrt{3}y/2$, $x/2 - \sqrt{3}y/2$, which are *permuted* by $\mathbb{D}_3$, we observe something rather more interesting.

First, of course, the three time series in fig. 1a, say, are not identical. If they were, it would mean that *every individual* point on the attractor, rather than just the attractor itself, would have $\mathbb{D}_3$ symmetry, so the attractor would be just the origin. However, all three time series do have a remarkably similar appearance. The simplest way to describe this is to say that if we look at randomly selected segments from each, it is very hard to tell which segment is taken from which time series. The same goes for fig. 1b, in which we can even detect, by eye, traces of intermittency caused by the collision of three conjugate $\mathbb{Z}_2$-symmetric attractors. However, in figs. 1c,1d there is a clear distinction: two series look similar but the third is quite different. These correspond to $\mathbb{Z}_2$-symmetric attractors, and the symmetry is clearly "visible" in some statistical sense in the three time series. An explanation of this effect is given in [17] in terms of the concept of *local isomorphism* of time series.

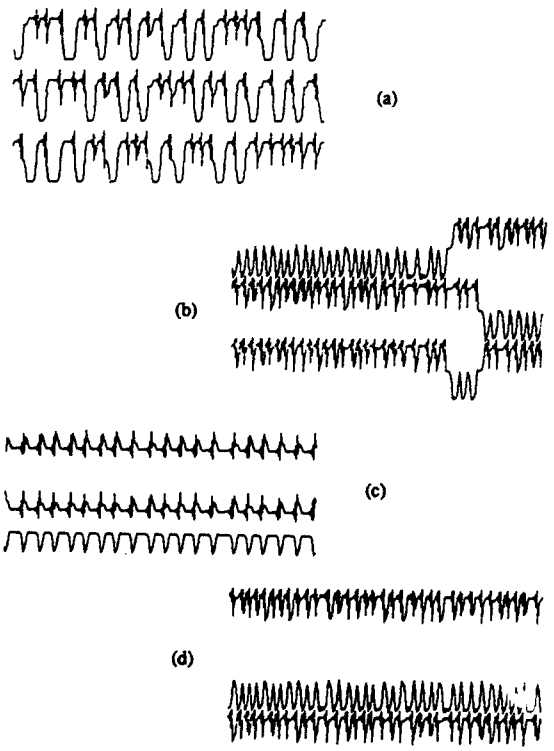

Fig. 1. Four time series for symmetrically placed combinations of the coordinates of a point in an attractor for the $\mathbb{D}_3$-equivariant map (3). (a) $\alpha = -0.9$, $\beta = 0$, $\gamma = -0.8$, $\lambda = 1.3$. (b) $\alpha = -1.1$, $\beta = 0.213$, $\gamma = 0.6$, $\lambda = 1.89$. (c) $\alpha = -0.9$, $\beta = 0$, $\gamma = -0.8$, $\lambda = 1.22$. (d) $\alpha = -1.1$, $\beta = 0.212$, $\gamma = 0.6$, $\lambda = 1.89$.

The choice of equivariant observation is conditioned by the physical interpretation of the symmetry of the system, including questions of what measurements are actually feasible. The *topology* of a dynamical attractor generally lives in some unknown subset of phase space, and hence bears only a loose relation to physically measurable quantities: this is why phase space reconstruction is necessary. The *symmetries* of systems that arise from experiments are normally induced by physical symmetries of the apparatus, and hence have a much more direct interpretation.

One important point must be mentioned here. We will show in section 6 below that the target V of an equivariant observation h must be "sufficiently complicated" in order for reconstruction to have a chance of *embedding* M in a cartesian power of V. For example, suppose we focus upon the conjectured reflectional symmetry-on-average of turbulent Taylor vortices, as described in section 2. The symmetry group is $\mathbb{Z}_2$. Its action on phase space (which here is an infinite-dimensional function space) is by inversion of the axial coordinate, $z \to -z$. Possible equivariant observations include:

(1) The axial component of velocity on the vortex boundary.
(2) The radial component of velocity on the vortex boundary.
(3) A pair of symmetrically related velocity measurements on either side of the vortex boundary.

We show below that neither (1) nor (2) can guarantee an embedding: only (3). (An alternative is to employ (1) and (2) in combination.) We do not consider this restriction to be especially intuitive, but it emerges naturally from the topological/group-theoretic analysis.

An example where an inappropriate choice of equivariant observations leads to difficulties is reported by Lorenz [19]. See ref. [27] for further discussion.

6. An equivariant Takens embedding theorem

We now proceed to our main result: a statement and sketch of the proof of an equivariant Takens embedding theorem. We explain why the truth of such a theorem depends upon the target of the equivariant observation concerned, and describe how Wassermann's concept of phase space being subordinate to a representation of the symmetry group characterises the "good" targets.

The setting for the standard (non-equivariant) theorem is as follows. Work in the category of C^2-smooth manifolds and maps. Let M be an n-dimensional manifold (phase space), and let ϕ be a diffeomorphism on M (discrete dynamical system). Let $h: M \to \mathbb{R}$ be a function (observation). Define the *delay-coordinate map*

$$\Psi_{\phi,h}: M \to \mathbb{R}^{2n+1}$$

by

$$\Psi_{\phi,h}(x) = (h(x), h(\phi(x)), \ldots, h(\phi^{2n}(x))) .$$

Then the Takens embedding theorem (the first and basic version of three similar theorems stated and proved by Takens [29]) is:

Theorem 1. Generically in (ϕ, h), the map $\Psi_{\phi,h}$ is an embedding of M in $\mathbb{R}^{2n+1}$.

The other two embedding theorems in Takens [29] are two versions for continuous dynamics. One is obtained by setting ϕ equal to the time-T forward map for generic T, and the other uses successive derivatives of $h(\phi^t(x))$ at $t = 0$. Sauer et al. [26] improve upon this result by strengthening the genericity assumptions, while making them more explicit.

From our discussion in section 5, we see that the appropriate setting for an equivariant Takens embedding theorem should be as follows. Let G be a compact Lie group. Let M be an n-dimensional G-manifold, and let ϕ be a G-equivariant diffeomorphism on M. Let V be a Euclidean G-space, and let $h: M \to \mathbb{R}$ be a G-equivariant mapping (equivariant observation). Let V^t denote $V \oplus \cdots \oplus V$ with t summands. For given t, define the *delay-coordinate map*

$$\Psi_{\phi,h,t}: M \to V^t$$

by

$$\Psi_{\phi,h,t}(x) = (h(x), h(\phi(x)), \ldots, h(\phi^{t-1}(x))) .$$

We might hope that for sufficiently large t (perhaps $t = 2n + 1$) the map $\Psi_{\phi,h,t}$ is generically a G-equivariant embedding of M in V^t.

However, it is clear in advance that *this may not be the case*, no matter how large t we take

There are "obstacles" to equivariant embedding, which depend upon the structure of V. The following examples capture the nature of the difficulty and motivate the "correct" theorem.

Example 1. Let $M = \mathbb{S}^1$ be the circle, realised as the unit circle

$$\{z | z = e^{i\theta},\ \theta \in \mathbb{R}\}$$

in the complex plane. Let $G = \mathbb{Z}_2$ acting on M by

$z \mapsto \bar{z}$. Let $V = \mathbb{R}$ with the nontrivial representation of G for which $x \mapsto -x$. Let h be any equivariant map from M to V^t for arbitrary t.

By equivariance, h maps $\mathrm{Fix}_M(\mathbb{Z}_2)$ to $\mathrm{Fix}_{\mathbf{R}}(\mathbb{Z}_2)$. The former is $\{0, \pi\}$, the latter $\{0\}$. Therefore $h(0) = h(\pi) = 0$ and h cannot be an *embedding*.

However, h can be an *immersion*. Indeed we can construct such an h using a delay coordinate approach. Define $\phi(z) = z^2$, an equivariant diffeomorphism, and let $k: M \to V$ be given by $k(z) = \mathrm{Im}(z)$. Then k is an equivariant observation. With $t = 2$ we have the delay coordinate map $z \mapsto (\mathrm{Im}(z), \mathrm{Im}(z^2))$. In terms of the coordinate θ this is θ this is $\theta \mapsto (\sin(\theta), \sin(2\theta))$. This is an immersion, and its image, shown in fig. 2, fails to be one-one precisely on $\{0, \pi\}$.

We can modify this map to get an equivariant embedding by introducing an additional coordinate with *trivial* group action, and pulling the crossing apart along that direction. In fact, the system can be equivariantly embedded in $\mathbb{R}^2 = \mathbb{R} \times \mathbb{R}$ with trivial action on the first component and nontrivial action on the second. Indeed, as we have described it, it already *is* embedded in this manner: the first factor is the x-axis in the plane, the second is the y-axis.

An experimental system that realises this phase space and group action is the motion of a bead on a wire loop that is symmetric about the vertical axis, under the influence of gravity and friction. The same group, but not in this precise representation, arises in the Taylor experiment in connection with the reflectional symmetry of turbulent Taylor vortices. The general requirement that both the trivial and the non-trivial representation of $\mathbb{Z}_2$ should occur is the reason why only observation (3) of section 5 guarantees an embedding. Observation (1) involves only the non-trivial representation, and observation (2) only the trivial representation.

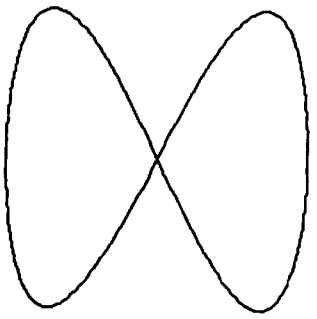

Fig. 2. Equivariant immersion of a circle using delay coordinates.

Example 2. Let $M = \mathbb{T}^2 = \mathbb{S}^1 \times \mathbb{S}^1$ be the two-torus, with angular coordinates (α, β). Let $G = \mathbb{S}^1 = \{\theta\}$ act on M by

$$\theta(\alpha, \beta) = (\alpha + \theta, \beta)$$

so that the action is trivial along the β direction. There are no fixed points.

The natural way to embed a two-torus in Euclidean space is to embed each generating circle $\mathbb{S}^1$ in $\mathbb{R}^2 = \mathbb{C}$ as the unit circle, so that the whole torus embeds in $\mathbb{R}^4 = \mathbb{C}^2$ by $(\alpha, \beta) \mapsto (e^{i\alpha}, e^{i\beta})$. This is equivariant under an action of $\mathbb{S}^1$ that is standard on $\mathbb{C} \times \{0\}$ and trivial on $\{0\} \times \mathbb{C}$. However, the torus can be embedded equivariantly using the *standard* action by rotation on $\mathbb{R}^2$ in *both* factors, even though the action on one generating circle of the phase space M is trivial. To achieve this, map (α, β) to $(e^{i(\alpha+\beta)}, e^{i(\alpha-\beta)})$.

This phase space and group action occurs in the Couette–Taylor experiment if we look at, say, the wavy vortex states in an infinite cylinder model and let G be the group of translations along the axis.

It follows from these examples that if a version of the Takens delay construction is to be used, then the target V of the observation h cannot be *any* Euclidean G-space. It must be "sufficiently complicated". The examples also show that the precise conditions required must be fairly subtle. They may be found in [30], and go back to equivariant embedding theorems of Mostow [20] and Palais [22]. Two alternative approaches are described in [5], but the conditions required on V are not spelt out there. The obstacles to

equivariant embedding are of two kinds: conditions on group orbits, and conditions transverse to group orbits.

First we explain the obstacle transverse to group orbits. Suppose that M is *locally* G-embedded in V' near some point $m \in M$. Let $\Sigma_m \leq G$ be the isotropy subgroup of m. Then the tangent space T_mM is a Euclidean Σ_m-space, and decomposes into irreducibles W_j. Because of the existence of a local G-embedding, each W_j must occur in V' and hence in V. Therefore V must contain at least one copy of every irreducible Σ_m-space that arises locally from the G_m-action on M.

This condition of "local transverse embeddability" can be used to extend embeddings away from G-orbits; but of course those orbits must themselves be embeddable. It is enough to consider just *orbit types*, where two orbits have the same type if their isotropy subgroups are conjugate. The "on orbits" condition is: every orbit (type) of M should embed equivariantly in $V'\backslash\{0\}$ for some t. The origin is deleted to ensure that distinct orbits of the same type can be embedded disjointly. The orbit types are G-diffeomorphic to coset spaces G/Σ as Σ runs through representatives of conjugacy classes of isotropy subgroups of G on M.

More precisely, following Wassermann [30], define M to be *subordinate* to V if for each $m \in M$ there exists a G-invariant neighbourhood U of m that embeds equivariantly into $V'\backslash\{0\}$ for some t. By [22] M is subordinate to V if and only if:

(a) V contains an isomorphic copy of every Σ_m-irreducible occurring in every T_mM;

(b) Every orbit type in M embeds equivariantly into $V'\backslash\{0\}$ for some t.

Let us analyse examples 1 and 2 to check these conditions. For example 1, take V to be $\mathbb{R}$ with nontrivial $\mathbb{Z}_2$-action. Condition (a) is easily checked; but (b) fails since either 0 or π in M must map to 0 under an *equivariant* embedding. In example 2, on the other hand, with $V = \mathbb{R}^2$ and the standard circle action by rotation, (a) is valid since every point has trivial isotropy, and (b) is valid since the only orbit type is a circle with the standard action. Thus Wassermann's conditions explain our previous findings.

The upshot of these considerations is that, if we are to prove an equivariant Takens embedding theorem, then the target V of the equivariant observation h must be subordinate to M. The implications of this condition for experiments are discussed in section 8 below.

In fact this necessary condition is also sufficient. We state the main theorem:

Theorem 2. (*Equivariant Takens embedding theorem*). Let G be a compact Lie group. Let M be an n-dimensional G-manifold, and let ϕ be a G-equivariant diffeomorphism on M. Let V be a Euclidean G-space such that M is subordinate to V, and let $h: M \to \mathbb{R}$ be a G-equivariant mapping. For any t, define

$$\Psi_{\phi,h,t}: M \to V^t$$

by

$$\Psi_{\phi,h,t}(x) = (h(x), h(\phi(x)), \ldots, h(\phi^{t-1}(x))) .$$

Then generically in (ϕ, h), the map $\Psi_{\phi,h,2n+1}$ is an equivariant embedding of M in V^{2n+1}.

Sketch of proof. Argue as in [29], but starting with arbitrary t. Use condition (a) above to ensure that $\Psi_{\phi,h,t}$ is an immersion near fixed points and points of low period; use (b) to choose an appropriate cover of the remainder of M so that the extension argument in [29] can be rendered equivariant. The arguments of Wassermann [30], proposition 1.2, then let us replace t by $2n + 1$.

In practice, since n is generally unknown, the precise bound on t may not be important. However, if estimates of the size of n are available, say by standard dimension-counting arguments or bifurcation analyses, the bound may be useful. As explained in [26] in the non-equivariant

case, it is the box-counting dimension of the attractor under consideration that really controls the size needed for t. This remark presumably extends to the equivariant case.

7. Pointwise and setwise symmetry

If topology is unimportant, there are simpler ways to measure the symmetries of an attractor A in M. One is to use the observation h to define a measure on V and find the symmetries of that measure. Divide V into small boxes, and for each box B in V, count how many times $h(m)$ lies in B. This defines a measure, and under appropriate genericity hypotheses on h and V its (approximate) symmetries will correspond to those of A. This approach is simple, but it has two defects. The first is that it does not also capture the topology of the attractor, so it cannot of itself distinguish chaos from regular dynamics. The other is that it cannot distinguish setwise symmetry of the attractor from pointwise symmetry, which is an important distinction with relevance to experiments. It is implicit in the generalities of section 3, but deserves more detailed explanation, which we now give.

Let us first describe the distinction as it would appear in an experiment. If an attractor has pointwise symmetry, then *at every instant of time* the state of the system has that symmetry. In the case of a chaotic attractor, this would appear as a "spatially ordered, temporally chaotic" state. If the symmetry of the attractor is only setwise, the state at any given instant of time will appear to be asymmetric. The symmetry will be visible only "on the average" as already explained. This would be a "spatially disordered, temporally chaotic" state.

Thus the distinction between pointwise and setwise symmetry is central to the transition from spatially ordered, temporally chaotic states to spatially disordered ones. This is especially true since transitions from pointwise to setwise symmetry are common in symmetric dynamical systems.

We now describe the situation in more abstract terms, to explain why pointwise symmetric attractors can easily arise, and why they can lose stability to setwise symmetric ones. Suppose that A is an attractor in the G-manifold M, having a dense dynamical orbit generated by a point $a \in M$. In section 3 we have distinguished between the symmetry group Δ_A and the isotropy group Σ_a; that is, between the setwise and pointwise symmetries of A.

For example, consider turbulent Taylor vortices, and again restrict attention to $\mathbb{Z}_2$ symmetry. If A is an attractor with $\Delta_A = \mathbb{Z}_2$, then the corresponding flow will have symmetry $\mathbb{Z}_2$ "on average". The radial velocities at symmetrically related points – together forming the equivariant observation – need *not* be the same at each instant. They will be more like fig. 1, with statistically indistinguishable but different time series for the two velocities.

However, if $\Sigma_a = \mathbb{Z}_2$ then by equivariance and continuity every point on A has isotropy subgroup (containing) $\mathbb{Z}_2$ (and for almost all points it is equal to $\mathbb{Z}_2$). The two velocities will be equal at each instant of time, and the two times series will be *identical*.

In both cases, $\Delta_A = \mathbb{Z}_2$. However, in one case there exists a point $a \in A$ for which $\Sigma_a \neq \mathbb{Z}_2$; in the other, $\Sigma_a = \mathbb{Z}_2$ for some (and hence all) $a \in A$. It is important to distinguish these two cases experimentally. This turns out to be quite easy in an equivariant reconstruction. In both, A is fixed *setwise* by $\mathbb{Z}_2$. However, in the first case A is not contained in $\mathrm{Fix}(\mathbb{Z}_2)$, whereas in the second, A *is* contained in $\mathrm{Fix}(\mathbb{Z}_2)$.

Fig. 3 is an example of the first case in the system (3). The setwise symmetry is evident to the eye; but not all points of the attractor lie on the symmetry axis. An example of the second case, also occurring in (3), is shown in fig. 4. Now the entire attractor is concentrated along the symmetry axis.

As noted above, the second type of attractor,

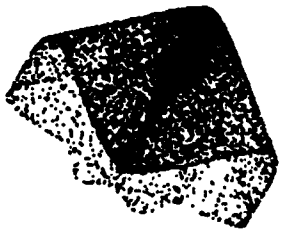

Fig. 3. An attractor A for (3) with $\Delta_A = \mathbb{Z}_2$ but $\Sigma_a = 1$ where the orbit of a is dense in A. Parameter values are $\alpha = -1$, $\beta = 0$, $\gamma = -0.65$, $\lambda = 2$.

with pointwise symmetry, is responsible for "spatially ordered, temporally chaotic" states. For example Caponeri and Ciliberto [6] report convection flows in an annulus that at each instant of time possess spatial dihedral group symmetry $\mathbb{D}_{13}$, but are temporally chaotic.

Spatially ordered, temporally chaotic states may seem puzzling, but they have a very simple explanation in abstract terms. Given a subgroup Σ of G, let $N = \mathrm{Fix}(\Sigma)$, a submanifold of M. By equivariance, it is easy to show that N is invariant under the dynamics ϕ on M. (For example, if z in (3) is real, say $z = x$, then $f(x) = (\alpha x^2 + \beta x^3 + \lambda)x + \gamma x^2$ is also real.) Suppose N is stable to perturbations transverse to N, that is, to symmetry-breaking perturbations. Then the system will naturally assume a state that lies entirely within N, that is, has pointwise symmetry Σ. The dynamics on N can in principle be anything; in particular, it may be chaotic. If so, one observes persistent (stable transverse to N) states with spatial symmetry Σ but temporal chaos. Observe that in this description the symmetry is effectively "factored out", and most phenomena observed will be typical of ordinary dynamics without symmetry – unless they involve singular points of the quotient map $M \to M/G$.

Suppose now a bifurcation occurs that creates an instability transverse to N – a symmetry-breaking instability. An example for (3) is shown in Fig. 5. It is ordinary chaos for the restricted mapping, which in this case is $f(x) = (\alpha x^2 + \lambda)x + \gamma x^2$. Now the dynamics will drift away from N, and the spatial order will break down. There may or may not remain a 'hidden' order "on the average" – it depends on what happens to Δ_A. The symmetry group cannot now be factored out since the dynamics moves away from the fixed-point space N.

Fig. 4. Three attractors A for (3) with $\Delta_A = \mathbb{Z}_2$ and $\Sigma_a = \mathbb{Z}_2$ for all $a \in A$. Parameter values are $\alpha = -1$, $\beta = 0$, $\gamma = -0.6$, and $\lambda = 1.99$, 2.1, 2.18 reading anticlockwise from lower right. Transients are shown to indicate transverse stability.

Fig. 5. Transition to spatial disorder in one of the attractors in fig. 4, caused by instability transverse to the fixed-point space for $\mathbb{Z}_2$. Parameter values are $\alpha = -1$, $\beta = 0$, $\gamma = -0.6$, and $\lambda = 1.99$. Left: unstable invariant set lying in the fixed-point space. Lower right: nearby symmetric attractor (a torus on the verge of breakup) and several superimposed transients to show instability transverse to fixed-point space. Upper right: the resulting symmetric attractor, with transients removed.

8. Implications for experimental design

The practical implication of the equivariant Takens embedding theorem is that for generic equivariant dynamics and generic observations, a delay coordinate approach to equivariant phase space reconstruction can be used, *provided that*:

(a) The "time series" consists of equivariant observations h, which may require several distinct but symmetrically related physical observations.

(b) Phase space, or at least the part of the phase space being reconstructed, is subordinate to the target V of h.

Condition (a) is highly intuitive; (b) is not. *Both* are required.

To perform the reconstruction, take a time series of equivariant observations $\{y_t\} = h(m_t)$, where m_t is the system's state in phase space at time t. Then form a "moving window" of length N, given by vectors $x_i = (y_i, \ldots, y_{i+N-1})$, where the y_i are themselves vectors in V. Then, for large enough N, generically the attractor formed by the x_i in $\mathbb{R}^N$ is topologically equivalent to the original attractor on M, and the dynamics is given by a shift.

It is not always clear how to ensure in advance that conditions (a) or (b) actually hold. (For finite symmetry groups one – rather drastic – answer is to ensure that the target involves *all* irreducible representations.) To verify (b) in particular cases requires some kind of information on the phase space that is being sought, and this is not always available. Analysis of specific models, or theoretical bifurcation scenarios, can sometimes provide such information – for example, they may give clues as to the important "modes" of the system, and the space of modes gives at least local information on the group action on phase space. Another approach would be to factor out the group action and reconstruct M/G using the methods of Sauer et al. [26]. If G is finite, little information about the dynamics will be lost when passing to the orbit space, since orbits are disconnected; but if G has a continuous part, rather a lot of information will be lost.

For practical implementation of such methods, refinements such as those introduced by Broomhead and King [3, 4] must also be developed in the symmetric case. A few remarks along these lines are made in King and Stewart [17]. The topic deserves further study, as do equivariant analogues of alternative reconstruction methods. Clearly many questions remain to be answered in this area: we leave them open for future work.

Acknowledgements

We are grateful to Peter Ashwin, Peter Grassberger, Martin Golubitsky, and James Montaldi for discussions and advice. The first author's research is partially supported by a grant from the Science and Engineering Research Council. Both authors' work is partially supported by a Laboratory Twinning grant from the European Community.

References

[1] P. Ashwin, Nonlinearity 3 (1990) 603.
[2] P. Ashwin, G.P. King and J.W. Swift, Nonlinearity 3 (1990) 585.
[3] D.S. Broomhead and G.P. King, Physica D 20 (1986) 217.
[4] D.S. Broomhead and G.P. King, in: Nonlinear Phenomena and Chaos, ed. S. Sarkar (Adam Hilger, Bristol, 1986) 113.
[5] G.E. Bredon, Introduction to Compact Transformation Groups (Academic Press, New York, 1972).
[6] M. Caponeri and S. Ciliberto, Physica D 127K, these Proceedings.
[7] P. Chossat and M. Golubitsky, SIAM J. Math. Anal 19 (1988) 1259.
[8] P. Chossat and M. Golubitsky, Physica D 32 (1988) 423.
[9] M.Z. Ding and B.L. Hao, Commun. Theor. Phys. (Beijing) 9 (1988) 375; reprinted in Chaos, ed. B.L. Hao (World Scientific, Singapore, 1991) 263.
[10] P.R. Fenstermacher, H.L. Swinney and J.P. Gollub, J. Fluid Mech. 94 (1979) 103.
[11] M.J. Field and M. Golubitsky, Symmetric chaos, Computers in Physics (Sep/Oct 1990) 470.
[12] M.J. Field and M. Golubitsky, Symmetry in Chaos (Oxford Univ. Press, Oxford), to appear.

[13] M. Golubitsky, private communication.
[14] M. Golubitsky, D.G. Schaeffer and I.N. Stewart, Singularities and Groups in Bifurcation Theory Vol. 2 (Springer, New York, 1988).
[15] C. Grebogi, E. Ott, F. Romeiras and J.A. Yorke. Critical exponents for crisis induced intermittency, Phys. Rev. A 36 (1987) 5365.
[16] J. Guckenheimer and P.J. Holmes, Nonlinear Oscillations, Dynamical Systems, and Bifurcation of Vector Fields, Applied Mathematical Sciences 42 (Springer, New York, 1983).
[17] G.P. King and I.N. Stewart, in: Nonlinear Equations in the Applied Sciences, eds. W.F. Ames and C.F. Rogers (Academic Press, New York, 1991) p. 257.
[18] M. Kitano, T. Yabuzaki and T. Ogawa, Phys. Rev. A 29 (1984) 1288.
[19] E.N. Lorenz, Nature 353 (1991) 241.
[20] G.D. Mostow, Ann. Math. 65 (1957) 432.
[21] N.H. Packard, J.P. Crutchfield, J.D. Farmer and R.S. Shaw, Phys. Rev. Lett. 45 (1980) 712.
[22] R.S. Palais, J. Math. Mech. 6 (1957) 673.
[23] J.D. Rodriguez and L. Sirovich, Physica D 43 (1990) 77.
[24] T. Rogers and D.C. Whitley, Math. Modelling 4 (1983) 9.
[25] H. Sakaguchi and K. Tomita, Progr. Theor. Phys. 78 (1987) 305.
[26] T. Sauer, J.A. Yorke, and M. Casdagli, J. Stat. Phys. 65 (1991) 579.
[27] I.N. Stewart, Nature 354 (1991) 113.
[28] K.G. Szabó and T. Tél, J. Stat. Phys. 54 (1989) 925.
[29] F. Takens, in: Dynamical Systems and Turbulence, Warwick 1980, Lecture Notes in Math. 898, eds. D.A. Rand and L.-S. Young (Springer, New York, 1981) 366.
[30] A. Wassermann, Topology 8 (1969) 127.

Physica D 58 (1992) 229–242
North-Holland

PHYSICA D

Topological analysis and synthesis of chaotic time series

Gabriel B. Mindlin and R. Gilmore
Department of Physics and Atmospheric Science, Drexel University, Philadelphia, PA 19104, USA

Received 1 October 1991
Revised manuscript received 30 January 1992
Accepted 7 February 1992

We have developed a topological procedure for analyzing chaotic time series which identifies the stretching and squeezing mechanisms responsible for chaotic behavior in low-dimensional dynamical systems. These mechanisms, quantitatively described by a "template" or "knot-holder", can then be used to model the processes which generate the original chaotic data set.

1. Introduction

A century ago Poincaré observed that the key to a deep understanding of a dynamical system lay in identifying and understanding its unstable periodic orbits [1]. Up to the present time this observation has not been exploited in our attempts to understand the chaotic behavior which is exhibited by low-dimensional dissipative and conservative dynamical systems.

At present, there are two broad approaches to the understanding of chaotic behavior in dynamical systems. These are the metric [2–4] and the topological [5–10] approaches.

The metric approach is based on the study of distances between points in a strange attractor. In this approach it is usual to compute Lyapunov exponents [2], various dimensions [3], scaling functions [4], etc. As a general rule these computations require very large data sets, are computation intensive, and degrade rapidly with noise. The real numbers which are computed lack confidence intervals since there does not yet exist an underlying statistical theory, cannot be independently verified, and do not describe "how to model the dynamics" [8].

The topological approach is newer. It is based on the observation that two mechanisms are responsible for the creation of a strange attractor: stretching and squeezing [9, 10]. The stretching mechanism, which causes nearby points in phase space to diverge from each other, is responsible for "sensitive dependence on initial conditions". The squeezing mechanism, which prevents phase space points from escaping from a compact domain, is responsible for the "recurrence" phenomenon characteristic of chaotic behavior.

These two mechanisms act to organize the strange attractor in phase space in a unique way. In addition, they act to organize the unstable periodic orbits which exist in the neighborhood of the strange attractor (densely for a hyperbolic invariant set [11]) in a unique way. This means that if we can determine how the unstable periodic orbits are organized, we can identify the stretching and squeezing mechanisms which are responsible for the creation of the strange attractor. This identification is topological (homological) and given in terms of a set of integers [9]. The extraction of these integers from time series data is robust against noise and is independently

0167-2789/92/$05.00 © 1992 – Elsevier Science Publishers B.V. All rights reserved

verifiable [10]. Once these mechanisms have been identified, a geometrical model can be constructed which describes how to model the stretching and squeezing mechanisms responsible for generating the original time series. This geometrical model can be used to generate synthetic data sets which have the same topological properties, but not necessarily the same metric properties, as the original data set.

This topological analysis technique which we describe below is applicable to "low"-dimensional dynamical systems. By "low" dimension we mean n-dimensional systems ($n \geq 3$) which possess a chaotic attractor with Hausdorff dimension $d < 3$. This technique has been carried out successfully on experimental data sets from the Belousov–Zhabotinsky reaction (BZ) [10], the laser with saturable absorber (LSA) [12], and the NMR laser [13]. With one exception (explained below in section 5) the steps involved in this topological analysis are illustrated for the BZ data set.

2. Summary of steps

Our topological analysis procedure consists of a number of successive steps. Each is relatively simple. These are summarized in fig. 1 and described briefly below. This description is elaborated upon in the following six sections [10].

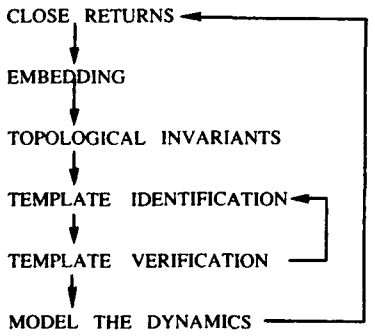

Fig. 1. Six steps in the topological analysis of chaotic time series data. The arrows on the right describe the self consistency checks afforded by this topological procedure for analyzing data.

1. Close returns. This algorithm is used to locate segments in the chaotic time series which can be used as surrogates for the unstable periodic orbits which exist in the neighborhood of the strange attractor.

2. Embedding. An embedding of these orbits into a three-dimensional space is required in order to identify their topological organization. If such an embedding cannot be found, or does not exist (when the Hausdorff dimension $d \geq 3$) the following steps cannot be carried out and the topological analysis cannot be completed.

3. Relative rotation rates and linking numbers. The topological organization of all unstable (surrogate) periodic orbits extracted from the time series is determined by computing the relative rotation rates and linking numbers of all pairs of periodic orbits and the self-relative rotation rates and self-linking number of each individual periodic orbit.

4. Template identification. The template or knot-holder, which supports all unstable periodic orbits in the strange attractor, is identified on the basis of the relative rotation rates or linking numbers of an appropriate subset of orbits.

5. Template verification. Once a template has been tentatively identified, it can be used to predict the (self-) relative rotation rates and (self-) linking numbers for all (orbits) orbit pairs supported by that template. If these predicted (from the template) topological invariants agree with the measured (computed from the surrogate orbits) topological invariants, we have added confidence that the initial template identification was correct. If these invariants do not agree, we can reject the hypothesis that the initial template identification was correct.

6. Model the dynamics. A template serves as a geometrical model for the dynamics (stretching and squeezing mechanisms) which generate the chaotic time series. It is straightforward to build an 'equation free' computer model which drives

a flow through a template. Time series data generated by such an equation free model have topological properties identical to those of the original time series.

The two arrows in fig. 1 indicate "loop closing" procedures. In any analysis it is extremely important to be able to determine, by independent means, if possible, whether the results of the analysis are in fact correct or not. Such "loop closing" procedures are absent from the metric approach to the analysis of chaotic time series, while the topological approach possesses the two indicated.

The template is overdetermined by the topological invariants of periodic orbits extracted from time series data. A subset is used to make the template identification. The compatibility of this identification with the topological properties of the remaining orbits provides an independent test for the validity of this identification.

3. Close returns

The close returns test is predicated on the existence of unstable periodic orbits in the neighborhood of a strange attractor or strange invariant set [6–8, 11, 14]. If a point in the attractor is near an unstable periodic orbit with relatively low period and low Lyapunov exponent, it can evolve in the neighborhood of that orbit long enough to return to an epsilon neighborhood of its starting point. Since chaotic systems are deterministic, this close return provides an initial condition for a segment which evolves in the neighborhood of the segment generated by the initial point.

Such close return segments can be located in the original time series, without embedding, as follows [10]. If $x(i)$ $(i = 1, 2, \ldots, N$, N is the length of the data set) and $x(i + p)$ are coordinates of two points which are neighbors in some appropriate phase space, then $x(i + 1)$ and $x(i + 1 + p)$ will also have approximately equal values, as will $x(i + k)$ and $x(i + k + p)$, for some sequence of values $k = 1, 2, \ldots$, where p is the period of the nearby unstable periodic orbit, measured in units of the sampling time. Such close returns segments can be recognized in the data by making a two-dimensional close returns plot of

$$|x(i) - x(i + p)| \begin{cases} < \varepsilon \rightarrow \text{black}, \\ > \varepsilon \rightarrow \text{white}. \end{cases} \quad (1)$$

Here pixel (i, p) is colored black if the difference $|x(i) - x(i + p)|$ is below some threshold ε, white otherwise. The threshold ε is fixed, typically at a few percent of the diameter of the attractor, $\varepsilon \sim 10^{-2} \times \{\text{Max}[x(i)] - \min[x(i)]\}$. Close returns appear as horizontal line segments whose location in the data set (i_b to i_{f+p}) is clearly indicated. Such segments can usually be used as surrogates for unstable periodic orbits if they satisfy additional weak criteria (e.g., they close up when embedded, cf., section 4). A close returns plot for a portion of the BZ time series [15] is shown in fig. 2. Close returns plots for LSA time series data and NMR laser time series data are similar.

The close returns plot described above is closely related to "recurrence plots" introduced by Eckmann, Kamphorst and Ruelle [16]. Recurrence plots were originally introduced as a tool to determine whether or not a data set was stationary, and have subsequently been used for that purpose [17]. It was also observed that

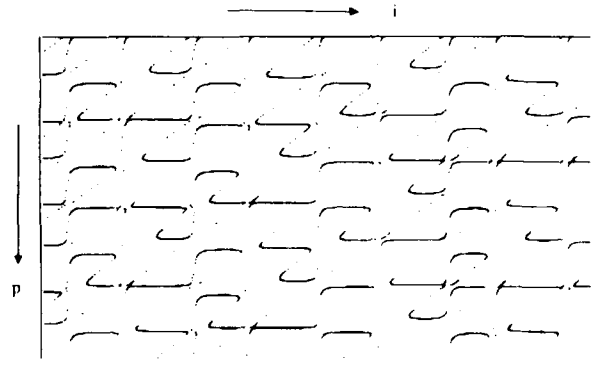

Fig. 2. Close returns plot of the Belousov–Zhabotinsky data. Pixel (i, p) is colored black if $|x(i) - x(i + p)| < \varepsilon$.

recurrence plots provide 'other important and easily interpretable information' [16] but they had not been used to extract periodic orbits from chaotic data. Recurrence plots are generated from embedded data.

The close returns search is robust against additive noise. In fig. 3 we show a sequence of close returns plots on data sets $BZ(i) + f \times GIID(i, \sigma)$ with increasing amounts of noise. Here $BZ(i)$ is an experimental data set from the Belousov–Zhabotinsky reaction [15], GIID is gaussian independent identically distributed with zero mean and standard deviation, σ, equal to that of $BZ(i)$, and f ranges from 0.1 to 2.0. The plot degrades gracefully. Fig. 3f shows how the close returns plot can be recovered from a data set with equal signal to noise ratio ($f = 1.0$ shown in fig. 3d) by using a low pass filter (11 point moving average). Separation of signal from noise is not too difficult when these two components have quite different time scales. In the present case the signal has a time scale of ~130 (samples/cycle) while the noise is independent (time scale of 1).

For large data sets a close returns histogram [14]

$$H(p) = \sum_i \Theta(\varepsilon - |x(i) - x(i+p)|) \qquad (2)$$

can be constructed. Here Θ is the Heaviside theta function. A chaotic data set will exhibit a series of peaks (fig. 4a) while a stochastic data set will generate a uniform distribution (fig. 4b). The peak centered at $p = 0$ in fig. 4a describes dynamic correlations, which must strictly be excluded from Grassberger–Procaccia dimension computations which attempt to characterize geometric correlations (i.e., the peaks centered at $p > 0$). Failure to separate dynamic from geometric correlations has rendered many previous dimension computations "obsolete" [18].

Diagonal segments in close returns plots, and non-zero base lines in close returns histograms, are due to the result that in stationary data sets upward trending segments of data are always followed by downward trending segments (for every "up" there is a "down") which causes accidental close returns. Both the plots and the histograms can be cleaned up by almost any kind of embedding [14].

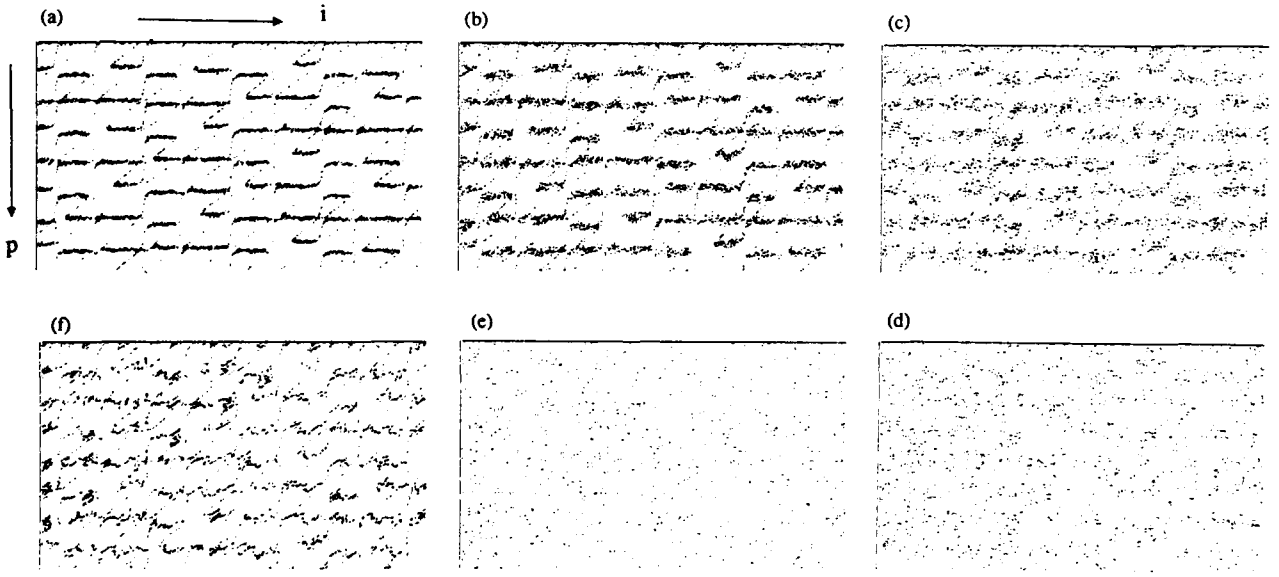

Fig. 3. The close returns plot degrades gracefully with additive noise. Here (see text) (a) $f = 0.10$; (b) $f = 0.25$; (c) $f = 0.50$; (d) $f = 1.0$; (e) $f = 2.0$. (f) The signal can be recovered by a low pass filter, in this case an 11 point moving average on the data set with $f = 1.0$.

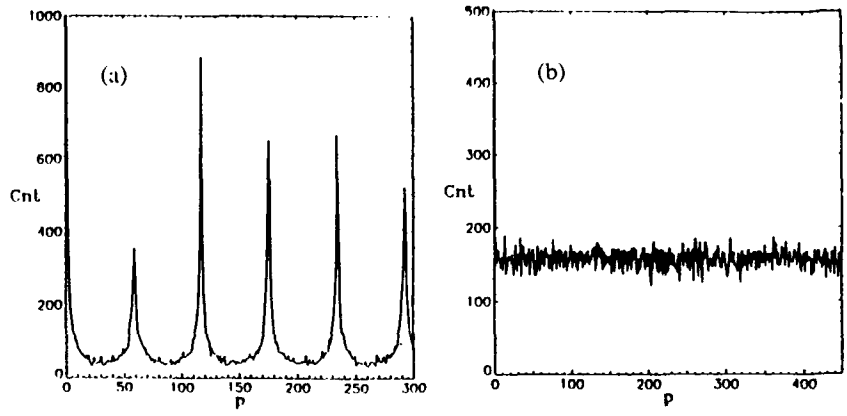

Fig. 4. Close returns histograms. (a) chaotic time series; (b) random series.

4. Embedding

The topological organization of the unstable periodic orbits (and therefore the strange attractor) is determined through their (self-) relative rotation rates [5] and (self-) linking numbers. These can be computed after the orbits have been embedded in $\mathbb{R}^3$ or some other oriented three-manifold. It is therefore necessary to construct a three-dimensional embedding of the strange attractor and the periodic orbits it "contains".

The Takens time delay embedding [19] does not preserve topological (as opposed to metric or geometric) information. We have observed a three-dimensional time delay embedding $x(i) \to y(i) = \{x(i),\ x(i+k),\ x(i+2k)\}$ of Belousov–Zhabotinsky data to undergo self-intersections as the time delay, k, is increased. Such self-intersections show that relative rotation rates and linking numbers are not invariant, but rather depend on the time delay.

We prefer instead an embedding which we call a differential phase space embedding: $x(i) \to y(i) = \{x(i),\ \mathrm{d}x(i)/\mathrm{d}t \sim x(i+1) - x(i-1),\ \mathrm{d}^2x(i)/\mathrm{d}t^2 \sim x(i+1) - 2x(i) + x(i-1)\}$. This particular embedding can be regarded as an affine transformation of a Takens embedding with minimum delay.

We prefer differential phase space embeddings for two reasons. First, the variables x, $\mathrm{d}x/\mathrm{d}t$, $\mathrm{d}^2x/\mathrm{d}t^2$ of this embedding are natural variables to use when attempting to model the dynamics. Second, linking properties of periodic orbits can be determined by inspection at a transverse crossing (if crossings are not transverse, this does not provide an embedding). The tangent at a crossing (fig. 5a) is given by

$$\frac{\mathrm{d}x'}{\mathrm{d}x} = \frac{\mathrm{d}x'/\mathrm{d}t}{\mathrm{d}x/\mathrm{d}t} = \frac{x''}{x'}$$

$$x'' = x' \times \text{slope}\,, \tag{3}$$

Therefore, the acceleration is proportional to the slope at a crossing point. As a result, at crossings with $x' > 0$ the segment with the larger (smaller) slope is over (under) the other, with the reverse situation when $x' < 0$. This means that all linking numbers can be computed by inspection.

A differential phase space embedding of the Belousov–Zhabotinsky data proved inadequate (fig. 6a). All crossings occurred in a single region which could not be resolved despite the fact that the data set is essentially noise free. The dynamic range of the digitized data was 10^4. Taking the first derivative reduced the dynamic range of $\mathrm{d}x/\mathrm{d}t$ to 10^2. A second difference reduced the dynamic range of $\mathrm{d}^2x/\mathrm{d}t^2$ to 10^0, which is the noise level of the digitized data.

As a result we employed an integral–differential filter [10]

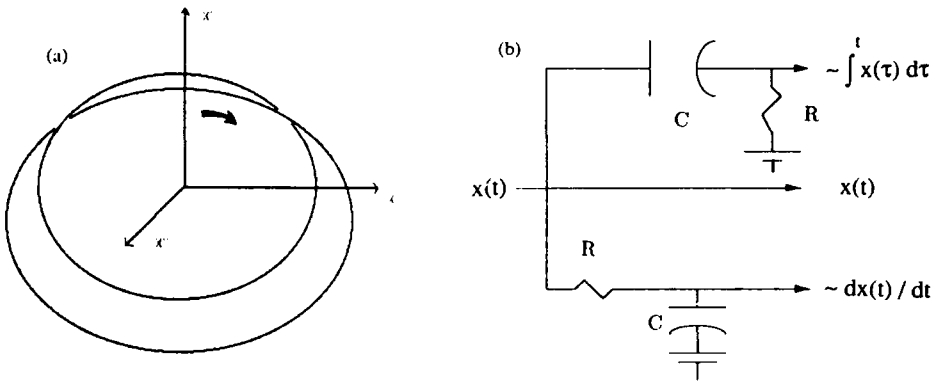

Fig. 5. (a) In a differential phase space embedding the over- and under-crossings at a point of transverse crossing can be determined from the slopes of the segments at the crossings. (b) A simple electronic circuit which generates on line a three dimensional differential-integral phase space embedding.

$$x(i) \rightarrow y(i) = \left\{ y_1(i) = \sum_{j<i} x(j)\, e^{-(i-j)/\tau}, \right.$$

$$\left. y_2(i) = x(i),\ y_3(i) = x(i+1) + x(i-1) \right\}. \qquad (4)$$

This embedding has the same desirable properties as the differential phase space embedding when τ is large (several cycles). The decaying convolution ($e^{-(i-j)/\tau}$) was used instead of a straight integral ($y_1(i) = \Sigma\,[x(j) - x]$) to remove low frequency drift which was present in the data and caused drift in the phase space plot of y_2 against y_1. This embedding is useful for two practical reasons. First it can be implemented on line by a very simple electronic circuit, as shown in fig. 5b. Second, integrating and differentiating both reduce the signal to noise ratio by about an order of magnitude, while differentiating or integrating twice (k times) reduces S/N by about two (k) orders of magnitude. The embedding of the Belousov–Zhabotinsky data with this filter is shown in fig. 6b. Since the strange attractor has a hole in the middle, a (many) Poincaré sections could be defined. The return map on several Poincaré sections was used to construct a consistent symbolic dynamics. The entire data set could be encoded by only two symbols: 0 (orientation preserving) and 1 (orientation reversing). The coding of this data set was independent of Poincaré section used. This embedding was used

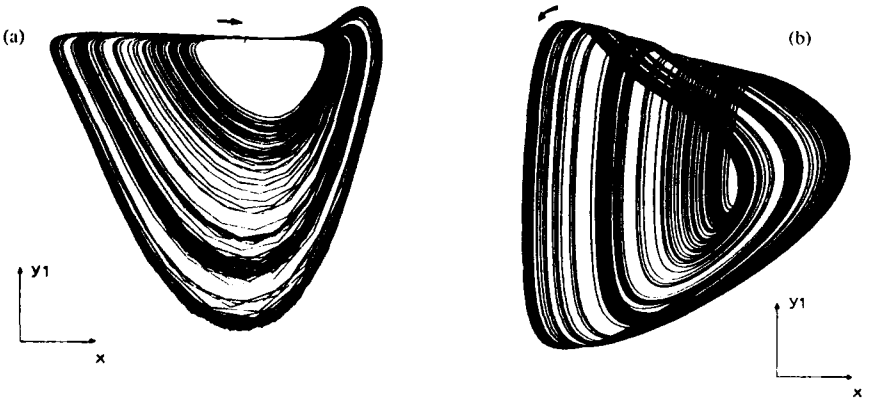

Fig. 6. (a) The degeneracy in the region of crossings cannot be resolved in a differential (x, x', x'') phase space embedding of the Belousov–Zhabotinsky data. (b) A differential–integral phase space embedding (4), performed with the filter shown in fig. 5b, yields a nondegenerate embedding with a hole in the center.

on time series from the LSA and NMR laser, with very similar results.

In general, constructing a consistent symbolic dynamics for time series data is a problem of fundamental importance which is not yet solved. If the system is highly dissipative, as are the BZ and LSA systems, the problem is accessible. Great benefit would result from an algorithmic solution to the problem of assigning a consistent symbolic dynamics to a chaotic time series.

5. Relative rotation rates and linking numbers

Once periodic orbits have been located and a three-dimensional embedding constructed, the topological properties of these orbits can be determined.

We show how to compute linking numbers in fig. 7. Surrogate period two and period three orbits are shown in figs. 7a and 7b. Neither orbit closes, but the period three orbit closes within the pixel resolution of the plot. These orbits are superposed in fig. 7c, which indicates the over and under crossings. The flow direction is shown in fig. 6b. To compute the linking number of these two orbits we construct tangents to the curves at each crossing point. The tangent to the overcross, the tangent to the undercross, and the unit normal to the projection form either a right handed $(+1)$ or left handed (-1) coordinate system. A sign $(+1, -1)$ is assigned to each crossing according to handedness. The linking number of these two orbits is half the sum of signs, summed over all crossings [6, 20]. Linking numbers can also be computed by carrying out a Gaussian integral.

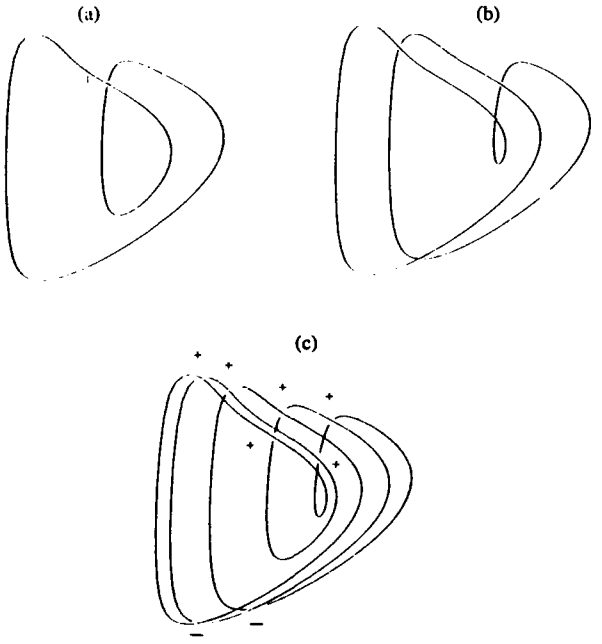

Fig. 7. Embeddings of the period two (a) and period three (b) orbits in the Belousov–Zhabotinsky data. (c) The linking numbers of these two periodic orbits can be determined by counting. The linking number is $[6 \times (+1) + 2 \times (-1)]/2 = 2$.

Relative rotation rates were originally developed to characterize driven dynamical systems [5]. These topological indices (they are sets of fractions) describe roughly how often one orbit rotates around another, on average. More specifically, they are defined as follows. Two orbits A and B, of periods p_A and p_B, intersect a Poincaré section in p_A and p_B points, respectively. A difference vector between one of the intersections of A and one of the intersections of B with the Poincaré section is then propagated forward in time. As it evolves, this difference vector rotates in a plane transverse to the propagation direction. Eventually it will return to its initial position (after $p_A p_B$ periods). This requires an integer rotation through 2π radians. The relative rotation rate, for this pair of initial conditions, is this integer divided by the number of periods, or average rotation per period. A relative rotation rate can be computed for each of the $p_A p_B$ initial conditions. These fractions may not be the same over all initial conditions. The sets of linking numbers and relative rotation rates for periodic orbits provide a unique signature for the underlying template for the strange attractor.

Of the three experimental systems studied, only the NMR laser is periodically driven. The BZ reaction and the LSA are autonomous. Therefore the computations of relative rotation rates, which were developed originally for the analysis of driven dynamical systems [5], pro-

ceeds most easily for the NMR laser. We show in fig. 8 how to carry out the computation of the self-relative rotation rate for a period 4 orbit in data from the NMR laser [13], which is a driven dynamical system. Fig. 8a shows a period 4 orbit, repeated a second time. Each tick represents one driving period. The discontinuity at the repetition of the period 4 orbit is within the pixel resolution of the plot. Figs. 8b, 8c, 8d show superpositions in the x–t plane of the initial orbit with orbits beginning from three other initial conditions in a Poincaré section. The number of crossings is 4, 2, 4 respectively, indicating rotations of the difference vector through $2(2\pi)$, $1(2\pi)$, $2(2\pi)$ radians and relative rotation rates of $\frac{2}{4}$, $\frac{1}{4}$, $\frac{2}{4}$, respectively.

for autonomous dynamical systems (Belousov–Zhabotinsky reaction, LSA). If one can transform an autonomous dynamical system to one which is effectively driven, for example by sweeping a Poincaré section uniformly about an axis through a hole in the attractor, or by carrying out a Hilbert transform, then the computation becomes as simple as that shown above for the NMR laser. Whether or not this is done, the relative rotation rates can be computed by counting crossings. We have developed and implemented an algorithm which does this efficiently [10]. This algorithm was used to determine tables of relative rotation rates for periodic orbits in the BZ data [10] and the LSA data [12].

We show in table 1 the (self-) relative rotation rates for all orbits, up to period 8, extracted from the Belousov–Zhabotinsky data [10]. The linking number of two orbits is the sum of the relative rotation rates over all initial conditions. This is true also of self-linking numbers. Thus, a table of linking numbers can easily be constructed from a table of relative rotation rates. A similar table was constructed for the NMR laser [13]. Experiments were carried out on the LSA under many different operating conditions. Different sets of periodic orbits were found under these different operating condition, and for each set of table of relative rotation rates was constructed [12].

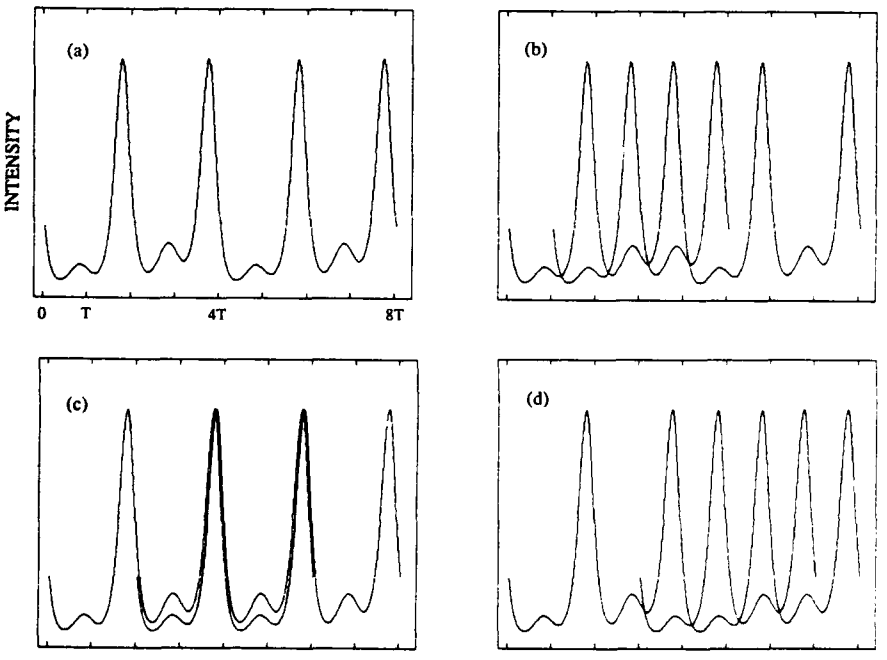

Fig. 8. (a) A period 4 orbit from the NMR laser, repeated a second time (x versus t). Each tick represents a full period. The self relative rotation rates of this orbit can be determined by counting the crossings of this orbit when started from each initial condition in a Poincaré section. These are: (a) 0; (b) 4; (c) 2; (d) 4, for a spectrum: $(\frac{1}{2})^2$, $\frac{1}{4}$, 0 of self-relative rotation rates.

Table 1
Relative rotation rates for periodic orbits extracted from the Belousov–Zhabotinsky data, up to period eight. Each orbit is identified by its symbolic dynamics.

	1 1	2 01	3 011	4 0111	5 01011	6 0110M1	7 0101011	8a 01011011	8b 01010111
1	0								
2	$\frac{1}{2}$	$\frac{1}{2}, 0$							
3	$\frac{1}{3}$	$\frac{1}{3}$	$(\frac{1}{3})^2, 0$						
4	$\frac{1}{2}$	$\frac{1}{2}, \frac{1}{4}$	$\frac{1}{3}$	$(\frac{1}{2})^2, \frac{1}{4}, 0$					
5	$\frac{2}{5}$	$\frac{2}{5}$	$\frac{1}{3}$	$\frac{2}{5}$	$(\frac{2}{5})^4, 0$				
6	$\frac{1}{3}$	$\frac{1}{3}$	$\frac{1}{3}$	$\frac{1}{3}$	$\frac{1}{3}$	$(\frac{1}{3})^4, \frac{1}{6}, 0$			
7	$\frac{3}{7}$	$\frac{5}{14}$	$\frac{1}{3}$	$\frac{11}{28}$	$\frac{13}{35}$	$\frac{1}{3}$	$(\frac{3}{7})^4, (\frac{2}{7})^2, 0$		
8a	$\frac{3}{8}$	$\frac{3}{8}$	$\frac{1}{3}$	$\frac{3}{8}$	$\frac{3}{8}$	$\frac{1}{3}$	$\frac{3}{8}$	$(\frac{3}{8})^7, 0$	
8b	$\frac{1}{2}$	$\frac{1}{2}, \frac{1}{4}$	$\frac{1}{3}$	$(\frac{1}{2})^2, \frac{3}{8}, \frac{1}{4}$	$\frac{2}{5}$	$\frac{1}{3}$	$\frac{3}{8}$	$\frac{3}{8}$	$(\frac{1}{2})^4, \frac{3}{8}, (\frac{1}{4})^2, 0$

6. Template identification

Birman and Williams have proved a remarkable theorem which greatly facilitates the analysis of dynamical systems which exhibit chaos [21–23].

This theorem states that for a dissipative three-dimensional dynamical system which exhibits chaos and has a hyperbolic invariant set, it is possible to project all periodic orbits onto an unstable invariant manifold in the direction of the stable foliation without incurring crossings. This means that the topological organization of the unstable periodic orbits is not changed by the projection. This projection allows us to replace the flaky fractal structure of a strange attractor by a branched two-dimensional manifold. The theorem tells us that the stable direction is not important in understanding the dynamics of the flow. Examples of branched manifolds for four standard flows are shown in fig. 9.

It might appear that the utility of the Birman–Williams theorem, and branched manifolds, to physical systems is restricted. For example, the

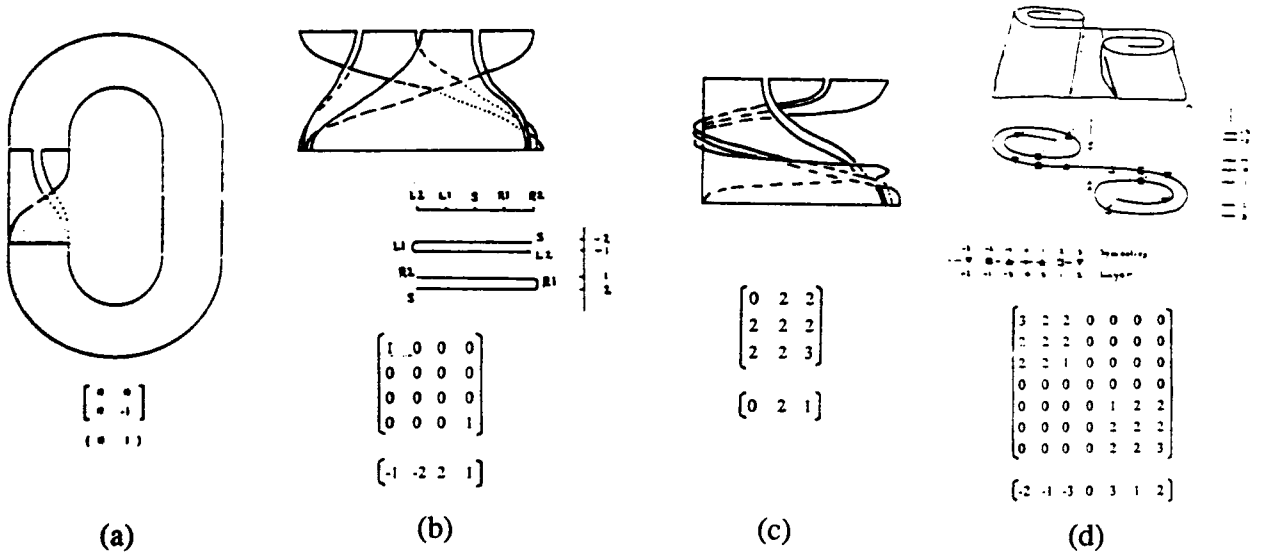

Fig. 9. Templates and their classification by integers for four common nonlinear dynamical systems. (a) Rossler equations; (b) Lorenz equations with large r (>150); (c) van der Pol equations; (d) Duffing equation before homoclinic tangency. The return flow is shown for the Rossler template (a); only the stretching and compressing parts of the remaining templates are shown for the other three flows.

theorem is stated for hyperbolic invariant sets, which are typically not seen in experimental systems. The point is that the linking numbers of orbits which exist in this limit must remain unchanged as long as these orbits exist, when one makes excursions away from the hyperbolic limit and other orbits are "pruned" away [10]. This is the situation we have always encountered in experimental data sets [12, 13].

It also appears that the Birman–Williams theorem is a strictly three-dimensional theorem. However, it remains true for n-dimensional dissipative systems providing these systems have only one unstable direction and are strongly dissipative [24]. In terms of the ordered eigenvalues $\lambda_1 > \lambda_2 > \lambda_3 > \cdots \lambda_n$ this means $\lambda = 0$ (only one unstable direction) and $\lambda_1 < |\lambda_i|$, $i = 3, 4, \ldots$ (strongly dissipative). This means that the Birman–Williams theorem can be applied to systems with a strange attractor whose Hausdorff dimension d is less than 3 (by the Kaplan–Yorke conjecture [25], $d = 2 + \lambda_1/|\lambda_3| < 3$). In essence, the stable directions are not important in determining the dynamics of a strongly contracting flow with one unstable direction.

The projection of a strange attractor to a branched manifold and the identification of periodic orbits in the strange attractor with those in the branched manifold has the following useful result. It is possible to compute the topological organization of the periodic orbits on the template rather easily. Since a transverse section of the template provides a one-dimensional return map, only the kneading theory for one-dimensional return maps is required to locate periodic orbits on the template [26]. The linking properties of these orbits is then determined by the organization of the framed braids in this template [21, 22]. This organization is specified by how the framed braids split apart, wrap around each other, and are joined together.

This organization is completely determined by a set of integers organized into an $n \times n$ symmetric integer valued matrix and a $1 \times n$ integer valued array, where n is the number of branches in the template [9]. The matrix is constructed from period one orbits. Within each branch of the template is exactly one period one orbit. The diagonal matrix element, $T(i, i)$, is the local torsion of the unique period one orbit in the ith branch, measured in units of π. The off diagonal elements, $T(i, j) = T(j, i)$, are twice the linking number of the period one orbits in the ith and jth branches of the template. These integers can also be determined by counting signed crossings: of the ith and jth period one orbits ($T(i, j)$), and of the boundaries of the ith branch ($T(i, i)$). The array information, $A(i)$, indicates the order in which the branches are glued together at the junction. The larger the value of $A(i)$, the nearer to the front is the ith branch.

A simple counting procedure has been encoded to count crossings for any orbits on any template [27]. There are two types of input,

(1) a classification of template, by integers,

(2) a list of orbits, by symbolic dynamics.

The two outputs are

(A) a table of relative rotation rates,

(B) a table of linking numbers.

Thus, given a template, it is possible to compute tables of relative rotation rates and linking numbers for all (or any subset of) periodic orbits supported by that knot-holder. Conversely, given a table of relative rotation rates or linking numbers, it is possible to use the subset of this table restricted to the period one and period two orbits to compute the integers which classify the template: the template matrix and array.

For the Belousov–Zhabotinsky data, dynamics on two symbols suffices. This means that the template has only two branches and can be identified from only three orbits: the two period one orbits 0 and 1, and the period two orbit 01. The period one orbit 0 was not present in the data, so the next lowest period orbit 011 was used to provide the required information. These three orbits uniquely identify the homology of the template. This template, and its topological characterization, is shown in fig. 10 [10]. The flow occurs on a suspension of the Smale horse-

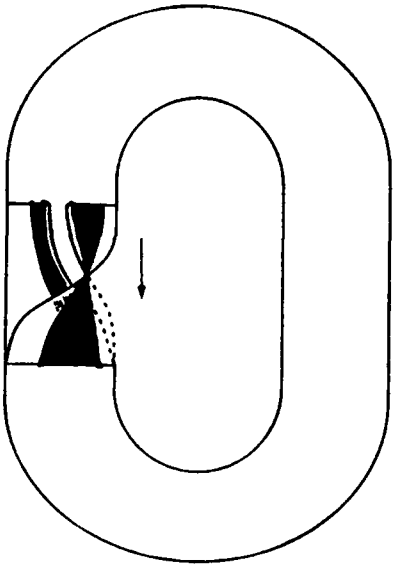

Fig. 10. The template for the Belousov–Zhabotinsky data is a zero torsion lift of a Smale horseshoe. The LSA and NMR laser are described by the same template. The flow is restricted to a subset of the template. The subset has a fractal structure, since it must exclude all pre-images of certain regions.

shoe with zero global torsion. Since not all of the orbits allowed in the hyperbolic limit are seen in the data, the flow is restricted to a subset of this template.

For the LSA data and the NMR laser data two symbols also suffice. In both cases the template was identified as a Smale horseshoe with zero global torsion by using suitable subsets of unstable periodic orbits.

7. Template verification

Once a template has been identified, it can be used to predict the topological invariants, the relative rotation rates and linking numbers, of all periodic orbits which are supported by that knot holder. These invariants are available independently from the periodic orbits extracted from the chaotic time series. Comparison of the predicted (from the template) and measured (from the time series) topological invariants provides an independent check on the validity of the initial template identification. If the predicted and measured matrices of topological invariants are identical, we have added confidence that the initial template identification was correct. If they are not identical, the initial template identification was not correct.

The template underlying the Belousov–Zhabotinskii chaotic data was determined on the basis of the relative rotation rates of the three orbits: 1, 01, 011, shown in table 1. Using this template, the relative rotation rates of the remaining periodic orbits extracted from this data set, up to period eight, were computed. There were no differences between the relative rotation rates computed from the orbits extracted from the data and the corresponding orbits predicted from the template [10]. The templates identified for the LSA and NMR laser were verified in exactly the same way.

Independent checks on the results of an analysis of data are essential in order to provide confidence that the conclusions drawn are correct. The topological method for analyzing time series data provides such independent verification procedures, while the metric approach does not.

8. Model the dynamics

A template provides a qualitative model for the flow which generates chaotic time series.

We have developed a simple computer model for a flow on a horseshoe template. This model generates chaotic time series similar in form to the initial time series. In fact, the two time series have identical topological properties but not necessarily identical metric properties.

The idea behind this modeling effort is illustrated in fig. 11. A three dimensional structure is devised whose horizontal cross section is a "thick spiral". Points in this spiral are measured by their angular displacement from some fixed line and the radial distance in the transverse direction. The coordinates of a point in the spiral in

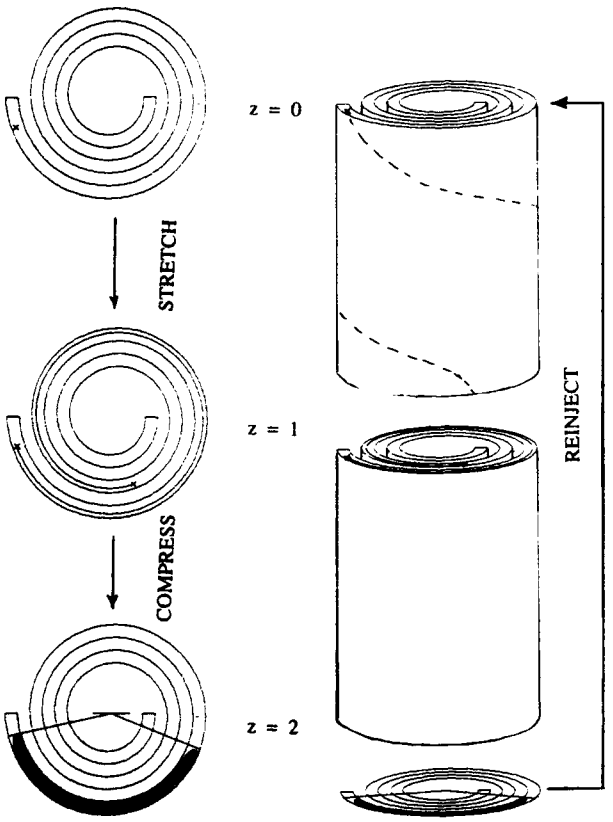

Fig. 11. A template provides a geometric model of the flow. In the spiral template the flow stretches in the angular direction between the planes $z = 0$ and $z = 1$, and is compressed to fit within the part of the spiral between 0 and π between the planes $z = 1$ and $z = 2$. The flow is then reinjected into the $z = 0$ plane from the $z = 2$ plane.

the top ($z = 0$) plane are restricted to be in the 'branch' $0 \leq \theta \leq \pi$. The stretching phase of the evolution occurs in the range $0 < z < 1$. In this phase, the angular value of the phase space point increases uniformly like $\theta(0) \rightarrow \theta(z) = \theta(0) + z(\theta_D + \theta(0)(\lambda - 1))$. The two parameters, θ_D (drift) and λ (Lyapunov exponent) are 'unfolding' parameters for the stretching process. The squeezing phase is carried out between the $z = 1$ and $z = 2$ planes by deforming a circle containing the spiral into a shape which fits into the spiral between the angular variables $0 \leq \theta_0, \theta_\pi \leq \pi$. The angles θ_0, θ_π are "pruning parameters". Reinjection occurs by identifying the $z = 2$ plane with the $z = 0$ plane. As the control (unfolding and pruning) parameters are varied, the flow is restricted to different parts of this structure.

This model seems to describe the properties of many periodically driven nonlinear oscillators at a qualitative level. For example, for fixed Lyapunov exponent λ (roughly comparable to the forcing strength of the driving term), as the drift parameter θ_D (roughly comparable to the period, T, of the driving term) increases, there is a sequence of direct and inverse saddle node bifurcations of period one orbits. Each successive bifurcation creates a saddle and node with global torsion n, the node becomes a flip saddle, initiates a period doubling cascade and chaotic behavior. This behavior then reverses itself (bubble formation), the cascade reverses itself, then the flip saddle becomes a node again, but this time with a global torsion increased by 1 (as the eigenvalue circles the origin in the complex plane). This node then annihilates with the saddle having global torsion $n + 1$ which has meanwhile been created in the succeeding saddle node bifurcation. The spiral template accounts very well for the systematic increase in the global torsion of the period one orbits alternatively created and destroyed in saddle node bifurcations, which has been observed in many driven nonlinear oscillators [28, 29].

9. Model testing

Topological analysis allows the possibility of comparing a model with data it purports to describe, and determining whether the model is not consistent with the data or it is consistent (more correctly, is not inconsistent) with the data.

The procedure is simple. A template is constructed from the experimental data as outlined above. The model is then used to generate a data set for the 'experimentally observed variable'. A template is constructed from this model generated data using exactly the same steps as for the experimental data. If the two templates are dif-

ferent, the model is not consistent with the data. Otherwise, the model is not inconsistent with the data.

We note that templates have handedness. Therefore, if data and model both generate zero global torsion suspensions of the Smale horseshoe, but with opposite handedness, the model can be rejected.

This procedure has been used to compare three-, four-, and five-dimensional models of the LSA with experimental data from the LSA [12]. Each of the models analyzed was compatible with the data.

10. Conclusions

We have developed a topological procedure for analyzing chaotic time series. This procedure has been applied to experimental data sets from the Belousov–Zhabotinsky reaction [10], the laser with saturable absorber [12], and the NMR laser [13].

In this procedure periodic orbits are extracted from the chaotic time series by the method of close returns. They, and the strange attractor, are embedded in a three-dimensional phase space using a differential phase space embedding. The linking numbers and relative rotation rates of these periodic orbits are determined. A subset is used in order to identify the underlying template or knot holder which supports the strange attractor and all the periodic orbits in its neighborhood. This template is then used to compute the topological invariants for all orbits and orbit pairs which exist in the knot holder. A comparison of these topological invariants measured from the data (reconstructed periodic orbits) and those predicted from the template provides added confidence that the initial template identification was correct, or else that it was not correct. The template itself provides a model for the dynamics – the stretching and squeezing mechanisms – responsible for generating the chaotic time series data.

This procedure is useful for data generated by low-dimensional dynamical systems. By "low dimensional" we mean n-dimensional dynamical systems (n arbitrary, $n \geq 3$) which are strongly contracting with only one unstable direction. These have strange attractors with Hausdorff dimension less than three. This is not unreasonable, since the whole procedure depends on constructing a branched two-dimensional manifold in $\mathbb{R}^3$ from a set of topological invariants which can only be defined in $\mathbb{R}^3$. It is remarkable that this procedure is not limited to three-dimensional dynamical systems. For example, the Belousov–Zhabotinsky reaction has been modeled as a dynamical system ranging in dimension from 30 down to five [30]. There are no three-dimensional models for this dynamics. Nevertheless, we have constructed a good three-dimensional embedding, which suggests that this embedding could be used to develop a three-dimensional model of this system. As another example, this analysis has been used to test three-, four-, and five-dimensional models of the LSA against data generated by the LSA [12].

The three experimental systems analyzed so far all lead to the same template, a zero global torsion suspension of the Smale horseshoe. That the horseshoe appears so often in physical systems is not surprising, since it describes the chaotic dynamics generated by a simple homoclinic tangency. For such simple dynamics much information is already conveyed by a return map. So what do we learn from a topological analysis which generates a template that we do not already know from a return map? The topological analysis can distinguish handedness (cf. section 9) as well as global torsion, neither of which can be determined from a return map. Both can be used to compare models with data (section 9). The creation of bifurcation bubbles [28, 29] in driven nonlinear oscillators which is caused by the systematic change in global torsion is evident in a template (cf. section 8), but less so in a return map. More complicated templates, as occur for the van der Pol and the Duffing oscil-

lators, convey much more information than a return map and facilitate analysis of what happens when the symmetry of the Duffing oscillator is broken. Further, a template provides a model for the flow dynamics in a way that a return map cannot.

This topological procedure for analyzing chaotic data can be applied to relatively small data sets, degrades gracefully with noise, is falsifiable, provides a model for the dynamics, and can be used to compare models with experimental data.

References

[1] H. Poincaré, Les Methodes Nouvelle De La Mécanique Céleste (Gauthier-Villars, Paris, 1892).
[2] A. Wolf, J.B. Swift, H.L. Swinney and J.A. Vastano, Physica D 16 (1985) 285.
[3] P. Grassberger and I. Procaccia, Phys. Rev. A 28 (1983) 2591.
[4] T.C. Halsey, M.H. Jensen, L.P. Kadanoff, I. Procaccia and B.I. Shraiman, Phys. Rev. A 33 (1986) 1141.
[5] H.G. Solari and R. Gilmore, Phys. Rev. A 37 (1988) 3096.
[6] N.B. Tufillaro, H.G. Solari and R. Gilmore, Phys. Rev. A 41 (1990) 5717.
[7] P. Cvitanovic, G.H. Gunaratne and I. Procaccia, Phys. Rev. A 38 (1988) 1503.
[8] G.H. Gunaratne, P.S. Linsay and M.J. Vinson, Phys. Rev. Lett. 63 (1989) 1.
[9] G.B. Mindlin, X.-J. Hou, H.G. Solari, R. Gilmore and N.B. Tufillaro, Phys. Rev. Lett. 64 (1990) 2350.
[10] G.B. Mindlin, H.G. Solari, M.A. Natiello, R. Gilmore and X.J. Hou, J. Nonlin. Sci. 1 (1991) 147.
[11] R. Devaney and Z. Nitecki, Commun. Math. Phys. 67 (1979) 137.
[12] F. Papoff, E. Arimondo, F. Fioretto, G.B. Mindlin, H.G. Solari and R. Gilmore, Phys. Rev. Lett. 68 (1992) 1128.
[13] N.B. Tufillaro, R. Holzner, L. Flepp, E. Brun, M. Finardi and R. Badii, Phys. Rev. A 44 (1991) 4786.
[14] D.P. Lathrop and E.J. Kostelich, Phys. Rev. A 40 (1989) 4028.
[15] K. Coffman, W.D. McCormick, Z. Noszticzius, R.H. Simoyi and H.L. Swinney, J. Chem. Phys. 86 (1987) 119.
[16] J.P. Eckmann, S.O. Kamphorst and D. Ruelle, Europhys. Lett. 4 (1987) 973.
[17] A. Babloyantz, in: Measures Of Complexity And Chaos, eds. N.B. Abraham, A.M. Albano, A. Passamante and P.E. Rapp (Plenum, New York, 1989), p. 51.
[18] P. Grassberger, Phys. Lett A 148 (1990) 63.
[19] F. Takens, Lecture Notes in Mathematics 898 (Springer, Berlin, 1981), p. 363.
[20] W.F. Pohl, J. Math. Mech. 17 (1968) 975.
[21] J.S. Birman and R.F. Williams, Topology 22 (1983) 47.
[22] J.S. Birman and R.F. Williams, Cont. Math. 20 (1983) 1.
[23] P. Holmes, in: New Directions In Dynamical Systems, eds. T. Bedford and J. Swift (Cambridge U.P., Cambridge, 1988) p. 150.
[24] R.F. Williams, private communication.
[25] J.L. Kaplan and J.A. Yorke, in: Functional Differential Equations And Approximations Of Fixed Points, eds. H.-O. Peitgen and H.-O. Walther, Lecture Notes in Mathematics Vol. 730 (Springer, Berlin, 1979), p. 204.
[26] J. Milnor and P. Thurston, On Iterated Maps Of The Interval I, II, preprint (Princeton University, 1977).
[27] R. Gilmore, unpublished. Computer code available upon request.
[28] H.G. Solari and R. Gilmore, Phys. Rev. A 38 (1988) 1566.
[29] C. Scheffczyk, U. Parlitz, T. Kurz, W. Knop and W. Lauterborn, Phys. Rev. A 43 (1991) 6495.
[30] L. Gyorgyi, T. Turanyi and R.J. Field, J. Phys. Chem. 94 (1990) 7162.

Physica D 58 (1992) 243–250
North-Holland

PHYSICA D

Dynamical signatures

Lyle Noakes[a] and Alistair Mees[b,1]

[a]*Mathematics Department, The University of Western Australia Nedlands, WA 6009, Australia*
[b]*Santa Fe Institute; Center for Nonlinear Science, Los Alamos National Laboratory, Los Alamos, NM 87545, USA*

Received 4 October 1991
Revised manuscript received 18 December 1991
Accepted 18 December 1991

We describe work in progress on using time series data output from dynamical systems to determine information about phase manifolds. Purely from estimates of the probability density of observations, it turns out to be possible in principle to determine the dimension and genus of the manifold. We also show experimental evidence that our methods may be useful for fractal attractors which have nearly integer dimension and are well-approximated by smooth objects such as smooth manifolds with boundary or branched manifolds. Our methods do not use embedding and do not require knowledge of dimensions or choice of time delays or projections.

1. Introduction

Often, data from a dynamical process is only available as a single scalar measurement even although the phase space of the system is high dimensional and may be non-Euclidean. The standard way to handle this problem is to use the embedding theorem [1–4], and this very powerful result has revolutionised nonlinear data analysis, allowing the calculation of statistics such as fractal dimension [5–7] as well as the building of dynamical models [8–12].

A problem that arises whenever embedding is used is how to construct a good embedding. It would be useful to know in advance the dimension of the phase space[#1] for the dynamics; other information, such as manifold type, would be useful in construction of qualitative (say, geometrical) models of the action of the dynamics which may sometimes be more informative than black-box quantitative models.

In this paper we use an approach which is independent of embedding and does not require choice of embedding dimensions, lags, projections and so on. It gives information about the manifold type if the dimension is known, and in principle can give information about the dimension too. The paper is to an extent a report on work in progress, since the proofs are fairly complex as well as new and it is not yet clear whether one can improve the practical usefulness of the approach; consequently, we concentrate here on noise-free data available in reasonable quantities. We do, however, show some evidence from computer experiments that the method works well in the case for which the theorem was originally designed, namely compact smooth manifolds, and may be extensible to other cases, including certain fractal objects.

The long-term aim is to try to find *dynamical signatures*, which allow a (crude) classification of systems in a simple way. The approach is com-

[1] On leave from The University of Western Australia.
[#1] We use the terms "phase space", "phase manifold", "state space" and "state manifold" interchangeably.

0167-2789/92/$05.00 © 1992 – Elsevier Science Publishers B.V. All rights reserved

plementary to embedding approaches insofar as it provides separate evidence that the phase space has been correctly identified, and in particular it is complementary to other attempts to identify manifolds using embedding plus triangulation [12].

In the rest of the paper we describe the assumptions we make about the dynamical system and the time series of measurements, and state the basic theorem in the case of compact orientable two-manifolds. Then we discuss some of the background and give a brief plausibility argument for the theorem. Following this are some examples of the theorem in use. Finally, we show some experiments on attractors which are approximately manifolds, although with features that go beyond those in the theorem.

2. Manifolds from data

In this section we outline recent work by Noakes [13] which makes it possible in some circumstances to identify manifold type and dimension from data. The approach is to regard a measurement from a dynamical system as a function of the state, and to assume the function is well-behaved. If we have a trajectory, or a set of trajectories, such that the collection of all the states covers the phase manifold uniformly, then, as is known from embedding theory, well-behaved functions of the states preserve certain information. Surprisingly, some of the information – in particular, the manifold type and dimension – survives even drastic surgery such as replacement of the time series by a density estimator.

A *time series* on a smooth manifold M (without boundary) is a sequence $S = \{x_n : n \geq 1, x_n \in M\}$. Let $f: M \to \mathbb{R}$ be a smooth map and write T for the time series $\{y_n \equiv f(x_n) : n \geq 1\}$ on $\mathbb{R}$. Suppose we have a situation where M (and therefore f) and also S is unknown. Can we say anything about the geometry of M by observing T?

Of course, when f is constant we cannot. But most maps are not like that: in fact, an open dense set of smooth maps f is restricted Morse in the sense explained below. For the purpose of this paper we are going to consider only orientable two-manifolds; this makes the explanations easier (we can imagine M as a surface) and, more importantly, ensures that certain features are easy to identify with data sets of reasonable size.

Definitions.

(1) Call $x_i \in M$ *regular* when there is a system (u, v) of local coordinates near x_i in which f takes the form $f(u, v) = u$. When x is not regular call it a *critical point* of f.

(2) Call $x_i \in M$ a *nondegenerate local minimum* when there is a system (u, v) of local coordinates near x_i, in which f takes the form

$$f(u, v) = u^2 + v^2 .$$

Call $x_i \in M$ a *nondegenerate local maximum* when there is a system (u, v) of local coordinates near x_i in which f takes the form

$$f(u, v) = -u^2 - v^2 .$$

(3) Say that x_i is a *nondegenerate saddle* when (u, v) can be chosen so

$$f(u, v) = u^2 - v^2 .$$

We call f *restricted Morse* when it is one-to-one on its set C of critical points, and these critical points are either nondegenerate local maxima or nondegenerate local minima or nondegenerate saddles.

Let f be restricted Morse. Then f has only finitely many critical points, and the integer

$$\chi(M) \equiv \#(\text{local minima}) + \#(\text{local maxima}) - \#(\text{saddles}) , \quad (1)$$

called the Euler characteristic, is independent of f and depends only on the geometry of M. If M is orientable (which we assume), $\chi(M)$ deter-

mines M up to smooth homeomorphisms. For example, in the case of any manifold M diffeomorphic to a sphere it turns out that $\chi(M) = 2$, while for a torus, $\chi(S^1 \times S^1) = 0$. In fact, for a two-manifold, $1 - \frac{1}{2}\chi$ is the number of handles.

If $h: N \to M$ is a smooth homeomorphism, then T might also come from $\tilde{S} \equiv \{\tilde{x}_n = h^{-1}x_n : n \geq 1\}$ by means of the map $\tilde{f} \equiv f \circ h$. So we cannot expect to be able to determine much more about M from the time series than the information given by $\chi(M)$.

This problem, and others, are discussed in ref. [12] in greater detail in the context of manifold triangulation. The present discussion is less ambitious but may be useful in cases where triangulation methods fail for any of a number of reasons; it is also interesting as a method in its own right, since the approach appears to be novel, and may be extensible. One limitation in the present discussion is that S should be more or less uniform with respect to Lebesgue measure; we accept that measures supported by fractal sets are needed in some applications, and we discuss this later. A less essential limitation is that we restrict ourselves here mainly to two dimensional manifolds.

Although the time series T does not give much information about M, we are actually going to throw some away. We forget about the ordering of T, so that it becomes an unordered set of real numbers. On the face of it, there is not a lot we can do now except perhaps construct a histogram or other density estimator for T. For this paper, we are only going to look at histograms and a closely related estimator.

Suppose that the x_n are realisations of a random variable X described by a never-zero smooth density f on M with respect to a never-zero smooth area form μ. Then $y_n = f(x_n)$ is a realization of the random variable $Y \equiv f(X)$. It turns out that Y has a probability density function g, for which we can find an estimate $\hat{g}$ from the data $\{y_n\}$. The following result on the existence of g is nontrivial and is proved in ref. [13] using techniques from differential geometry.

Theorem 1. Let $f: M \to \mathbb{R}$ be restricted Morse. There is a smooth density g for $Y \equiv f(X)$ with the following properties:

(1) g is defined over $f(M) - f(C)$;

(2) if z_0 is the image of a point of local minimum of f then z_0 is a *left cliff* of g, namely

$$\lim_{z \to z_0^+} g(z) > \lim_{z \to z_0} g(z),$$

and if z_0 is the image of a point of local maximum of f then z_0 is a *right cliff* of g, namely

$$\lim_{z \to z_0^-} g(z) < \lim_{z \to z_0} g(z);$$

(3) if z_0 is the image of a saddle of f then z_0 is a *splinter* of g, namely

$$g(z) = -\mathcal{O}(\ln|z - z_0|)$$

for z near z_0.

An idea of why the result holds can be got from thinking about how densities project. Near a point $x_{(0)}$ of local minimum or a restricted Morse function f takes the form $f(u, v) = f(x_{(0)}) + u^2 + v^2$ where u, v are local coordinates in a neighbourhood of $x_{(0)}$. Write $r^2 = u^2 + v^2$. When $Y \geq 0$ the infinitesimal contribution to the probability of $Y \equiv f(X)$ from this neighbourhood is more or less $2\pi r\,\mathrm{d}r = \pi\,\mathrm{d}(r^2) = \pi\,\mathrm{d}Y$ and so the contribution to the density is π. On the other hand, when $Y < 0$ the neighbourhood contributes nothing to the probability of Y. So we have π on the right and 0 on the left, added to which there may be a smooth contribution from regions outside the neighbourhood. The result is a cliff. The argument generalises, of course: for example, a three-manifold gets a contribution of $4\pi r^2\,\mathrm{d}r = 2\pi r\,\mathrm{d}(r^2) = 2\pi Y^{1/2}\,\mathrm{d}Y$, and the cliff is replaced by the positive part of a square root function.

So if we plot $\tilde{g}$, the features characteristic of local maxima and minima and of saddles may

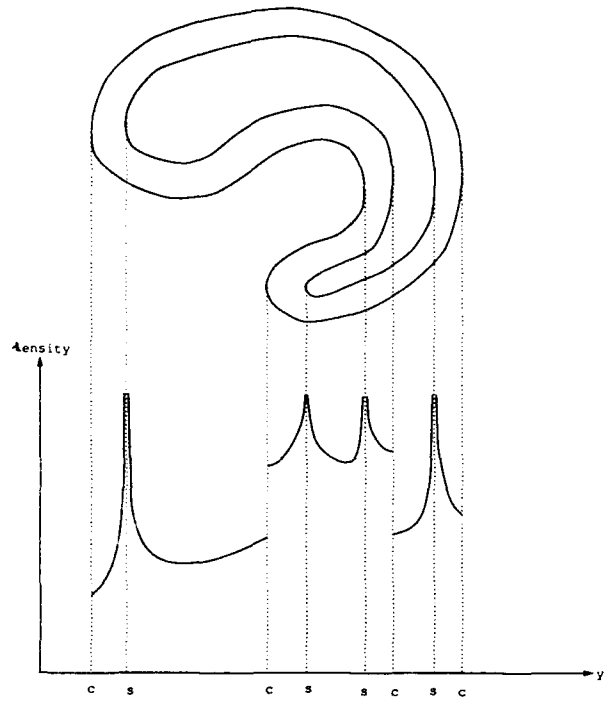

Fig. 1. A possible density for a two-torus embedded in $\mathbb{R}^3$. Cliffs are marked "c" and splinters are marked "s". There are as many cliffs as splinters, implying that $\chi(S^1 \times S^1) = 0$.

stand out. By counting their numbers we should be able to estimate $\chi(M)$. Code for finding a standard equal-width bin histogram is readily available, or is easy to write. The time required for the calculation is, of course, very short. Fig. 1 shows an example for a torus, where the upper part of the picture is a two dimensional projection of a torus embedded in three dimensions and the lower part is the one dimensional projection onto the axis shown. We see cliffs corresponding to "outside curves" from the viewpoint implied by the upper picture, and splinters corresponding to "inside curves". The numbers of cliffs and splinters are the same, so the formula gives $\chi = 0$ as we would expect. Note that one way in which genericity is important is that we do not want a cliff and a splinter (for example) to coincide in the one dimensional projection.

There are analogous, but less informative, procedures for higher dimensional manifolds. The reason they are less informative is that the signatures of extreme points and saddles become less pronounced: for example, we indicated above that for a three-manifold a cliff is replaced by a square root function.

3. Applications

We first describe two examples of direct use of the theorem; for more details and other examples, see ref. [13]. Then we consider how to better estimate the features like cliffs and splinters that we are looking for, and apply a modified estimator to a quasiperiodic signal to reveal the underlying torus.

3.1. Example

We distribute 100 000 points (x_1, x_2, x_3, x_4) uniformly over the torus $S^1 \times S^1$ in $\mathbb{R}^4$, by setting

$$(x_1, x_2, x_3, x_4) = (\cos\theta, \sin\theta, \cos\phi, \sin\phi)$$

for θ and ϕ distributed independently on $(0, 2\pi)$. We define the observation function f by

$$f(x_1, x_2, x_3, x_4) = (x_1 - 1.8)^2 + (x_2 - 3.7)^2 .$$

The critical points of f can be calculated directly and occur at

$(1, 0, 1, 0)$	(minimum)	value 7.93,
$(-1, 0, -1, 0)$	(maximum)	value 29.93,
$(1, 0, -1, 0)$	(saddle)	value 22.73,
$(-1, 0, 1, 0)$	(saddle)	value 15.13.

A histogram of the values of $y = f(x_1, x_2, x_3, x_4)$ is shown in fig. 2. There are two cliffs and two splinters, where the Theorem says they should be. This is also in agreement with eq. (1) since $\chi(S^1 \times S^1) = 0$. The features are clear with a large sample (100 000) and are still visible with a moderate sample (5000).

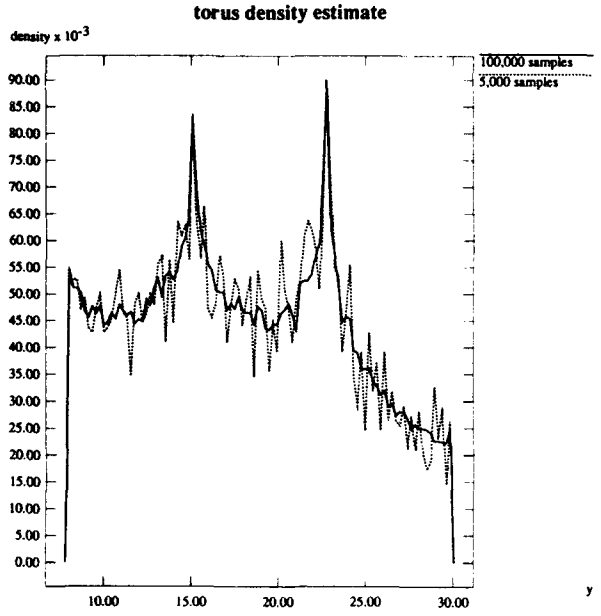

Fig. 2. Density plots (100 bins) for samples from real-valued observations of a uniform distribution on a two-torus embedded in $\mathbb{R}^4$. Solid line: 100 000 samples. Dotted line: 5000 samples. There are two cliffs and two splinters, evident in the 100 000 sample case and visible even in the 5000 sample case.

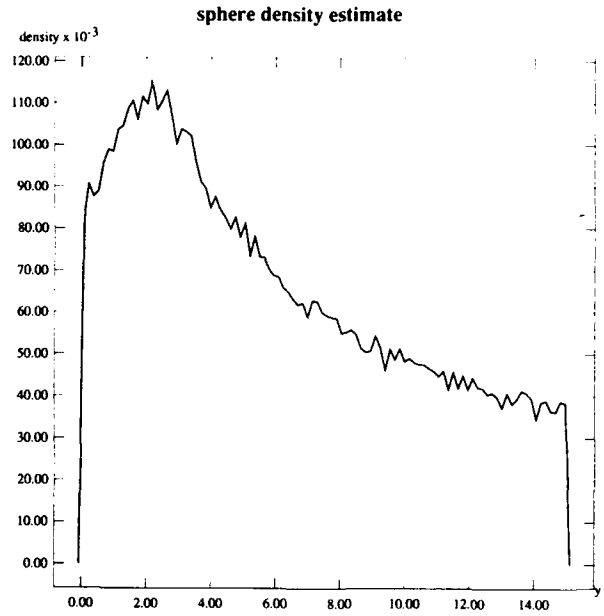

Fig. 3. Density plot (100 bins) for 100 000 samples from a uniform distribution on a two-sphere embedded in $\mathbb{R}^3$. The observation function is $(x+3)(y+1)(z+2)$. There are two cliffs and no splinters.

3.2. *Example*

We take 100 000 points distributed uniformly over S^2 embedded in $\mathbb{R}^3$, with $f(x_1, x_2, x_3) = (x_1+3)(x_2+1)(x_3+2)$. We would have guessed $M \approx S^2$ from formula (1) and the histogram in fig. 3, which has two cliffs and no splinters, implying $\chi(S^2) = 2$.

3.3. *Other methods of density estimation*

A more classically-based approach to estimating the phase manifold M, used in ref. [12], is to use the ordering of T to define an embedding of M in Euclidean space, and then triangulate the resulting cloud of points. This might lead to enhanced estimates, in that smaller samples might be required to estimate $\chi(M)$ accurately, but it may also require a lot of technique to implement successfully, particularly if the data is corrupted by noise or is inaccurate for other reasons. Although we have not discussed the effects of noise on the approach being described here, it is reasonable to expect that small noise on the data should not greatly affect the appearance of the histogram: the main problem will be the blurring of important features, which the risk that, say, a quadratic maximum in the density function becomes indistinguishable from a splinter.

Although we have used large numbers of points in the examples so far, cleverer density estimation techniques could perhaps to used to reduce the size of time series required, at least in the low-noise case. We have not, however, had much success using standard smoothing of histograms; nor would we expect to have much success using smooth kernel approximation, since both of these techniques are intended for estimating smooth densities and obscure precisely the features we wish to find.

A technique which may be better adapted to the present problem is to try to fit the density more carefully in regions where there are many data points. The following simple method first estimates the distribution function (i.e., the inte-

gral $P(y)$ of the density). To do so it sorts the data $\{y_i\}$ into increasing order, giving a series $\{s_i\}$, which gives points $(s_i, i/n)$. A crude piecewise-linear (discontinuous) estimator of P is obtained by fitting straight line segments to subsets of points $(s_i, i/n)$: $i_0 \le i \le i_1$, for various values of i_0 and i_1. The slopes of the lines are then estimates of the density. We have found this useful with subsets ranging in size from 50 to 1000, depending on the number of data points available.

3.4. Example

A sample of 40 000 points (sampled with time interval 0.4) from the function

$$y(t) = \cos t + \sin \omega t \qquad (2)$$

(where $\omega = \exp(1)$) was used as input to this modified density estimator with 100 bins to give the solid line in fig. 4. We do not need such a huge sample, however: the features are still apparent from the dotted line estimate which used only 1000 points and subsets of size 40 (i.e., 25 bins).

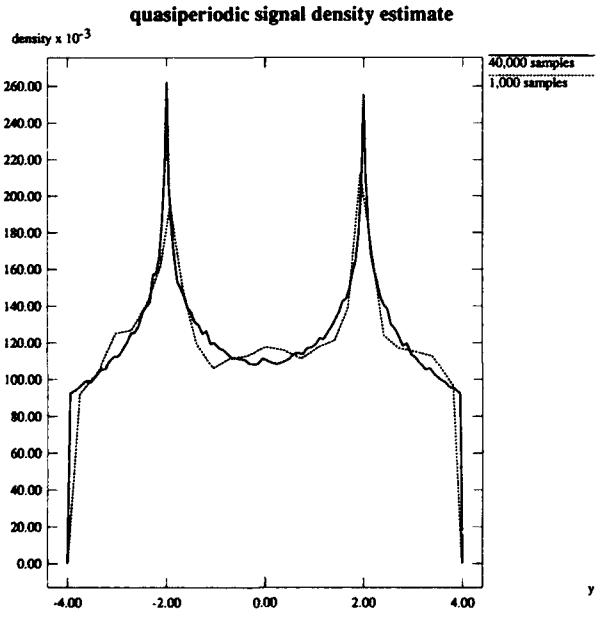

Fig. 4. Modified density estimating algorithm applied to 40 000 data values from the quasiperiodic waveform defined in eq. (2). The phase space is very clearly identified as a torus by the two cliffs and two splinters shown on the solid line (40 000 data values) and the features are also visible with only 1000 data values (dotted line).

The technique we have used here can be regarded as a variable-width binning method, but it is sensitive to noise and, when there is comparatively little data, to subset size; it should probably be used in conjunction with standard histograms. It is certainly worthwhile trying different numbers of bins: for example, with the torus the splinters and cliffs stand out with bins containing very small numbers of points (down to 2 or so) but there are many spurious smaller peaks, while with too many points per bin the splinters are broadened to the extent that they become insignificant.

4. Application to non-manifolds

Encouraged by our success with two-manifolds, we now investigate empirically how much further this kind of analysis can be pushed. Our main interest is in dynamical systems where M is replaced by a fractal set which is "thin" in that its dimension is approximately an integer, and that it is well-approximated by a manifold, possibly with branches or boundaries, and possible non-orientable. (The analysis given earlier can be extended to such more general manifolds, but our interest here is in the fractal objects.)

4.1. Example

We take 9000 points from the Rössler attractor [14] and estimate the density. The resulting graph in fig. 5 has many of the features of the previous examples, especially the cliffs at either end which are characteristic of dimension (approximately) 2. Note also the sharp points which resemble the splinters observed in fig. 1. The approximating surface is made by gluing a Möbius band, which is a non-orientable manifold

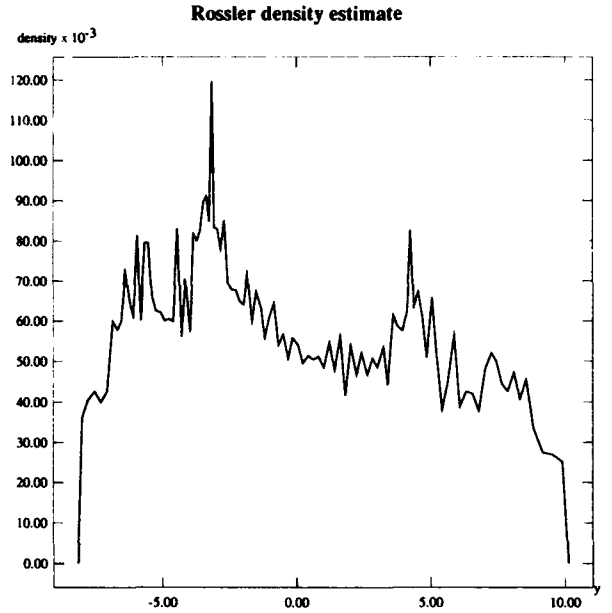

Fig. 5. Modified density estimate (100 bins) for 9000 samples from the Rössler attractor. There appear to be cliffs and perhaps splinters.

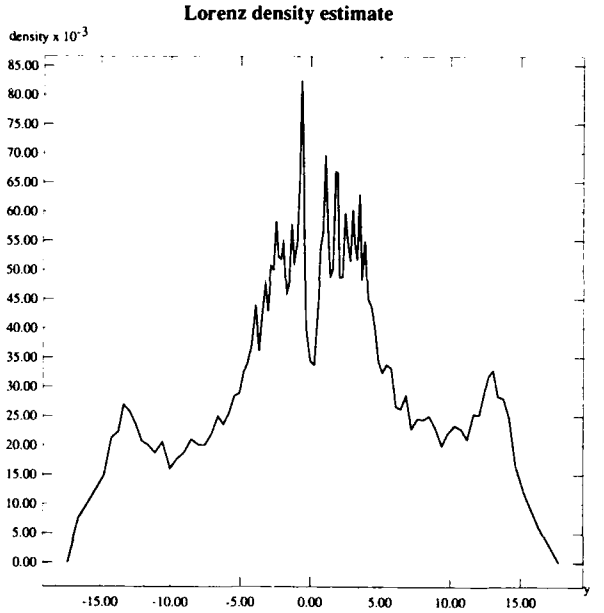

Fig. 6. Modified density estimate (100 bins) for 9000 samples from the Lorenz attractor.

with boundary, to an annulus, which is an orientable manifold with boundary.

4.2. Example

When we do the same thing with 9000 points from the Lorenz attractor [15] we obtain fig. 6. Similar comments apply, except that the cliffs are less pronounced: we need a lot more data to see what is really happening at the edges, and in fact we expect to see fractal structure, rather than actual cliffs. Fractal structure at the edges is one of the features which will show up in a better density estimator: there are already indications in fig. 6, and a better estimator might also show such structure in fig. 5. We are currently in investigating whether we can estimate dimension from such fractal structure.

4.3. Example

To convince ourselves that we are not doing something trivial, we do the same thing with times between geiger counter detections of radioactive emissions from decay of radioactive cobalt. Fig. 7 certainly does not look like a histogram of data collected from a time series whose phase-manifold is two-dimensional, and of

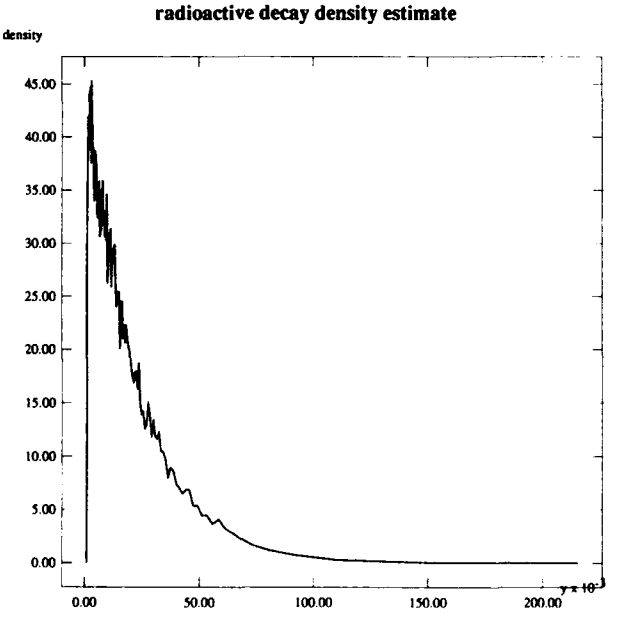

Fig. 7. Modified density estimate (100 bins) for 21 000 intervals between detections of emissions from radioactive cobalt.

course it is not: the data should consist of realisations of independent identically exponentially distributed random variables, which the graph does not contradict.

5. Conclusions

It is a little surprising that information about the nature of the system's state space is available directly from density estimators of a time series or other sample. With the tools we have at present, practical use is limited, and the density approach can best be regarded as complementary to others, but further developments may give rise to a method of increased scope and robustness.

Acknowledgements

A.I.M. thanks the University of Western Australia, the Santa Fe Institute and Los Alamos National Laboratory for support. This research was partially funded by an ARC grant.

References

[1] N.H. Packard, J.P. Crutchfield, J.D. Farmer and R.S. Shaw, Phys. Rev. Lett. 45 (1980) 712.
[2] F. Takens, Detecting strange attractors in turbulence, Lecture notes in Mathematics, Vol. 898 (Springer, New York, 1981).
[3] T. Sauer, J.A. Yorke and M. Casdagli, Commun. Math. Phys. (1991) under consideration.
[4] L. Noakes, The Takens embedding theorem, Intern. J. Bifurc. Chaos 1 (4) (1991) 867.
[5] P. Grassberger and I. Procaccia, Measuring the strangeness of strange attractors, Physica D 9 (1983) 189.
[6] J.D. Farmer, E. Ott and J.A. Yorke, Physica D 7 (1983) 153.
[7] A.M. Albano, A.I. Mees, G.C. deGuzman and P.E. Rapp, in: Chaos in Biological Systems, eds., H. Degn, A.V. Holden and L.F. Olsen (Plenum, New York, 1987), pp. 207–220.
[8] J.-P. Eckmann and D. Ruelle, Rev. Mod. Phys. 57 (1985) 617.
[9] J.D. Farmer and J.J. Sidorowich, Phys. Rev. Lett. 59 (1987) 845.
[10] M. Casdagli, Physica D 35 (1989) 335.
[11] A.I. Mees, Dynamics of Complex Interconnected Biological Systems eds. T. Vincent, A.I. Mees and L.S. Jennings, (Birkhauser, Boston, 1990), p. 104.
[12] A.I. Mees, Dynamical systems and tesselations: detecting determinism in data, Intern. J. Bifurc. Chaos, 1, no. 4 (1991), in press.
[13] L. Noakes, Densities and dynamics, Intern. J. Bifurc. Chaos (1992) in press.
[14] O.E. Rössler, Phys. Lett. (1976) 397.
[15] C.T. Sparrow, The Lorenz equations, Bifurcations, Chaos And Strange Attractors (Springer, New York, 1982).

Physica D 58 (1992) 251–259
North-Holland

PHYSICA D

Extraction of dynamical equations from chaotic data

G. Rowlands[a] and J.C. Sprott[b]

[a]*Department of Physics, University of Warwick, Coventry CV47AL, England*
[b]*Department of Physics, University of Wisconsin, Madison, WI 53706, USA*

Received 26 September 1991
Revised manuscript received 29 January 1992
Accepted 7 February 1992

A method is described for extracting from a chaotic time series a system of equations whose solution reproduces the general features of the original data even when these are contaminated with noise. The equations facilitate calculation of fractal dimension, Lyapunov exponents and short-term predictions. The method is applied to data derived from numerical solutions of the logistic equation, the Hénon equations with added noise, the Lorenz equations and the Rössler equations.

1. Introduction

In many fields of science one measures quantities that fluctuate in time or space with no discernible pattern. Examples include magnetic and electric fields in plasmas, weather and climatological data, variation of biological populations, and stock prices. It has been generally assumed that such situations could be described by a large number of deterministic equations or by stochastic ones. More recently it has been appreciated that ordinary, but nonlinear, differential equations with as few as three degrees of freedom or difference equations with a single degree of freedom can have pseudo-random (chaotic) solutions. This has led to the hope that such simple systems can model the real world.

Ideally, one would like to be able to extract the equations from a fluctuating time series. In the absence of additional information, this goal is unrealistic. The variable observed may not be simply related to the fundamental dynamical variables of the system. The measurement will be contaminated by noise and round-off errors and limited by sample rate and duration. However, it may be possible to find a system of equations which mimic the general features such as the topology in a suitable phase space, and these equations might shed insight into the behavior of the system.

Here we present a method for extracting from a fluctuating time series such a set of equations. These model equations may be used to predict not so much the details of the time evolution, which is limited by sensitivity to initial conditions in chaotic systems, but topological changes such as the change of periodic behavior through a series of period-doubling bifurcations. Furthermore, because the model equations provide in principle an unlimited amount of data, the calculation of fractal dimension [1] and Lyapunov exponents [2] is much simplified, although the relationship between such calculated quantities and the true values remains an intriguing and open question. It is also much simpler to calculate the Lyapunov exponents directly from the equations rather than from the data [3, 4].

Of course there have been previous attempts to extract from a time series a simple set of coupled equations whose solution gives an ap-

0167-2789/92/$05.00 © 1992 – Elsevier Science Publishers B.V. All rights reserved

proximation in some sense to the original data. Difference equations [5–7] corresponding to maps, and differential equations [8–10] corresponding to flows have been deduced. Although the method described here has features common to this earlier work, the novel element is the use of singular value decomposition to choose the appropriate dependent variables that appear in the dynamical equations rather than just using the data and its derivatives. An added advantage of singular value decomposition is that it provides an efficient filter for the noise that is always present in experimental data.

2. Numerical procedure

Until fairly recently the main method of analysis has been to express the time series $T(t)$ in a set of Fourier modes. Then peaks in the associated power spectrum are identified with normal modes of the system. This approach breaks down if there is a large noisy contribution to the measurement or if the underlying system cannot be described in terms of a few modes.

An alternative is to use the method of singular value decomposition [11, 12]. In this method $T(t)$ is expanded in a complete set of modes $\psi_n(t)$, not necessarily Fourier modes, but a set obtained from an analysis of the data rather than imposed from outside. The modes are normalized according to

$$\lambda_m = \frac{1}{N} \sum_{n=1}^{N} |\psi_m|^2 (t = n\tau) , \tag{1}$$

where the original data are assumed given at discrete times $n\tau$ with $1 \le n \le N$. We then approximate $T(t)$ by

$$T(t) = \sum_{m=1}^{d} \psi_m(t) , \tag{2}$$

where the ψ_m's are chosen to correspond to the d largest values of λ_m.

In practice, from the data T_n $(= T(t = n\tau))$ one constructs a set of M-dimensional vectors V_l defined such that $V_l = \{T_l, T_{l+1}, \ldots, T_{M+l-1}\}$ and the auto-correlation function $C(n)$ defined such that

$$C(n) = \sum_{l=1}^{N} T_l T_{l+n} . \tag{3}$$

Using these $C(n)$'s one constructs the symmetric $M \times M$ correlation matrix $\mathbf{M}$ with elements $M_{lp} = C(|l - p|)$. The eigenvalues of this matrix are in fact just the normalization constants introduced in eq. (1), that is λ_m. The corresponding eigenfunctions $(\boldsymbol{\alpha}_m)$ of this matrix give the modes $\psi_m(t)$ according to $\psi_m(t = n\tau) = \boldsymbol{\alpha}_m \cdot \boldsymbol{V}_n$.

Besides giving the best set of orthogonal modes in the sense mentioned above, this method involves some smoothing of the original data. A purely random time series gives $C(n) = C\delta_{n,0}$ so that all the eigenvalues are equal to C.

If when the data are analyzed a few eigenvalues are significantly larger than the rest, then the corresponding eigenfunctions are the ones used in the approximate expansion for $T(t)$ in eq. (2). The neglect of the rest has the effect of removing some of the noise. This whole procedure is analogous to identifying peaks in a Fourier power spectrum. The partial removal of noise by singular value decomposition has been discussed in more detail by Broomhead and King [11]. The choice of which of the eigenvalues are significant is not always obvious, and a subjective judgement has been used here. A more rigorous procedure would follow the treatment of Hediger et al. [13].

From a physical point of view the ψ_m's for $1 \le m \le d$ can be interpreted as coherent structures revealed by the method of singular value decomposition. Modern dynamical systems theory suggests that even small values of d may suffice to encapsulate the essential features of the system. These features are perhaps best appreciated by examining the d-dimensional phase space constructed using the functions ψ_1,

$\psi_2, \ldots, \psi_d$. These topological features are the same as those present using a phase space constructed using the V_n's since the V's are linear combinations of the ψ_m's. Also, features that are masked in the V phase space due to noise may be revealed in the ψ space since some of the noisy component has been removed. The more subtle point of whether a time series of a single variable known just at discrete time intervals can capture the full solution of the underlying problem which exists in continuous time and involves many independent variables has been considered by Takens [14].

Using the d distinct ψ_m's we construct a model equation of the form

$$\psi_m^{n+1} = F_m(\psi_l^n)\,, \tag{4}$$

where $\psi_m^n \equiv \psi_m(t = n\tau)$ and the F_m's are as yet general functions of the ψ's. Guided by the fact that simple forms for the model functions F_m are sufficient to produce chaotic solutions we assume that

$$F_m(\psi_l) = a_{mo} + \sum_{p=1}^{d} a_{mp}\psi_p + \sum_{p,q}^{d} b_{mpq}\psi_p\psi_q + \sum_{p,q,r}^{d} c_{mpqr}\psi_p\psi_q\psi_r\,, \tag{5}$$

where the coefficients a, b, and c are determined by minimizing the variational function

$$J_m = \frac{1}{N}\sum_{n=1}^{N}[\psi_m^{n+1} - F_m(\psi_l^n)]^2 \tag{6}$$

for each value of m. If examination of the phase-space portraits reveals any symmetry then this should be incorporated into the structure of F_m. Of course in some cases a simple polynomial may not be the appropriate form for F_m. For example if the phase-space plots reveal periodic structure then the model functions F_m should be chosen to capture such a structure. A suitable choice of polynomial has been shown [15] to model data arising from the presence of a limit cycle. An F_m expressed as the ratio of two polynomials may have a significantly wider range of application than a simple polynomial since one is then using the power of a Padé approximant [16].

The use of such rational functions has been studied by Casdagli [5] and Gouesbet [10]. However, it is important to note that there is probably no universal panacea, and the form for the model functions F_m should be chosen taking into account all available information about the system. Computer software that carries out the procedure described above as well as many other tests for chaotic time series is available [17].

Singular value decomposition methods or equivalents have been used previously to obtain model equations [18–20], but in those cases the exact equations describing the system are assumed known. The exact equations are then used to generate the model equations. Here we only use the restricted information given by the time series.

Experimental time series $T(t)$ can often be obtained for various values of some control parameter μ. Thus the ψ_m's and F_m's are also functions of μ. Numerical simulations of equations such as those of Lorenz [21] and Rössler [22] and the study of phase transformations using phenomenological models such as the Landau–Ginsburg equation give good reason to believe that the dependence of the coefficients a, b, and c on μ is simple.

3. Numerical examples

To illustrate some of the above techniques we have studied a few selected model situations.

3.1. Logistic equation

First the logistic equation $x_{n+1} = \lambda x_n(1 - x_n)$ has been iterated and x_n identified with T_n. For $\lambda = 4$ the solution is illustrated in fig. 1a. The data have been analyzed using $M = 2$, and the

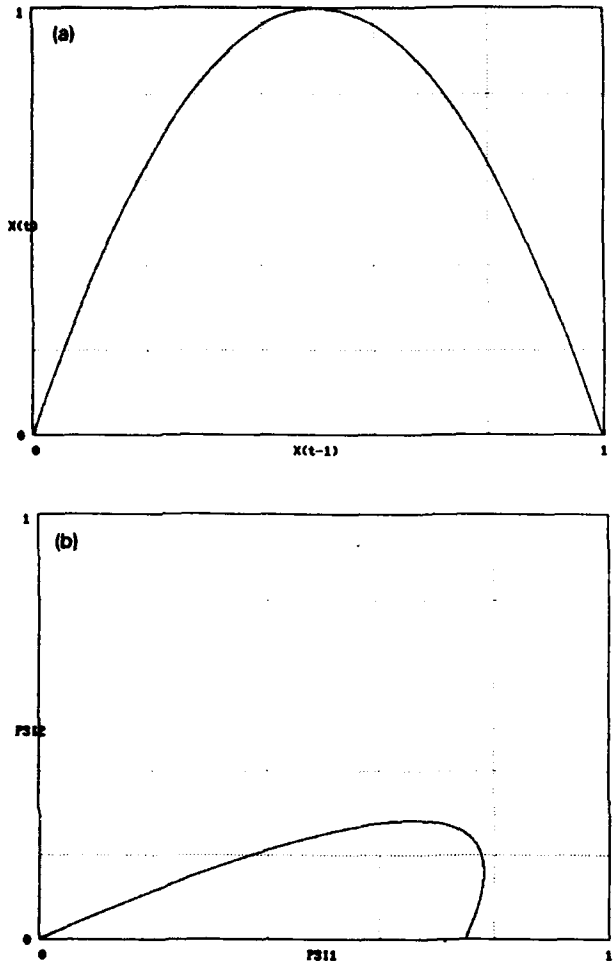

Fig. 1. Phase-space plots of the logistic equation (a) from original data and (b) after singular value decomposition.

phase plane in fig. 1b constructed from the model equations shows a single loop which is a simple distortion of fig. 1a. This simple loop structure still remains if larger values of M are used and the number of model equations is taken equal to M. Even without knowledge of the original equations that generated the data the method shows that a two-dimensional phase plane is sufficient to model the data, and the resulting equations can be linearly combined to recover the logistic equation exactly.

3.2. Hénon equations

The Hénon map, $x_{n+1} = 1 - 1.4x_n^2 + 0.3y_n$, $y_{n+1} = x_n$ has been treated in a similar manner. The results in fig. 2 using $M = 2$ again show that the model equations capture the essential features of the solution, in this case a strange attractor.

A time series of 2300 values was generated by adding normally distributed deviates with zero mean and standard deviation of 0.1. These data for $M = 2$ are shown in fig. 3a. Using these data, two coupled model equations were obtained, solved, and a new time series $X_n = \psi_1^n + \psi_2^n$ generated. This is shown in fig. 3b and is indistinguishable from the Hénon map as given in fig. 2a.

In this case the reduction in noise is solely a

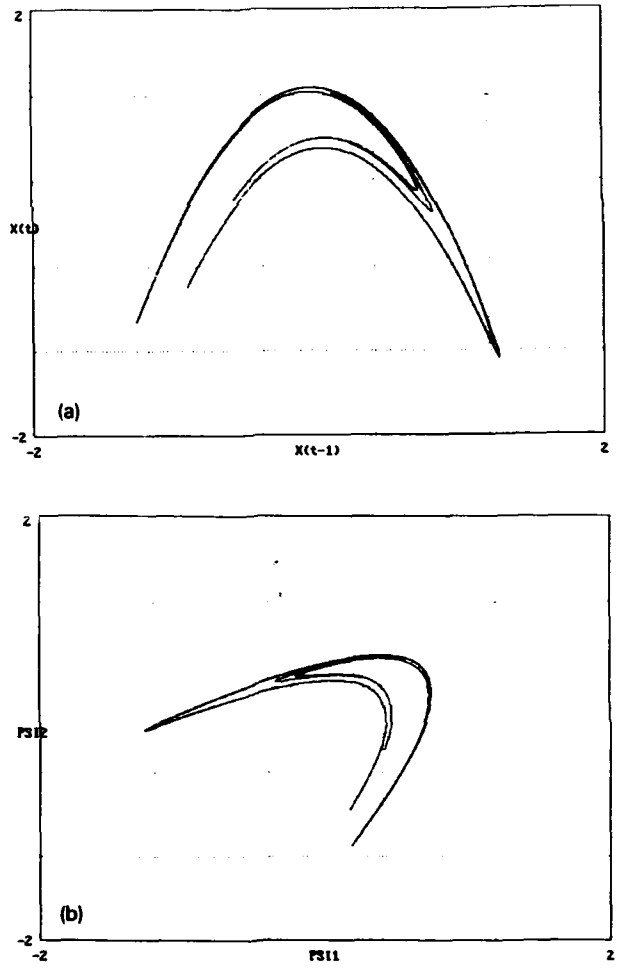

Fig. 2. Phase-space plots of the Hénon map (a) from original data and (b) after singular value decomposition.

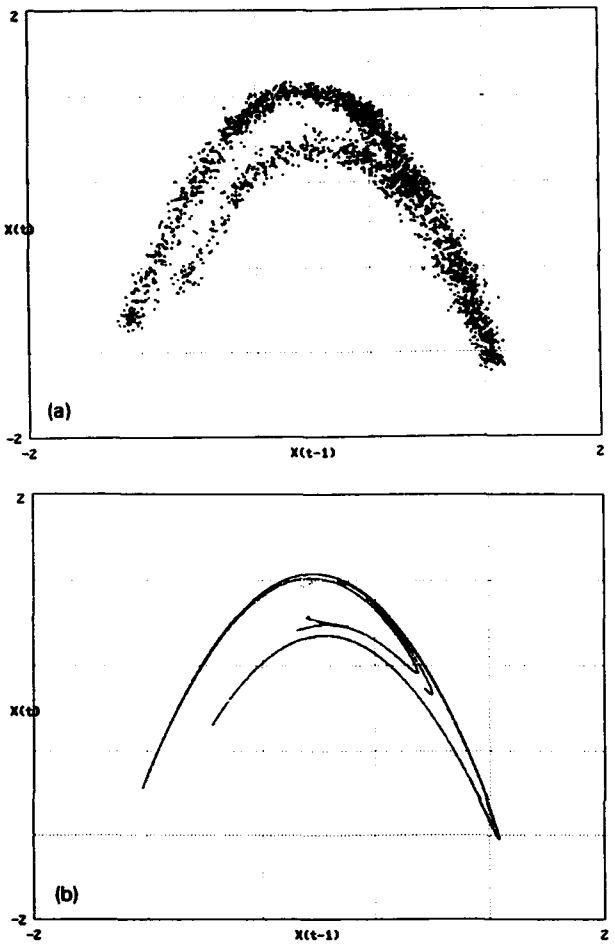

Fig. 3. Phase-space plots of the Hénon map (a) with noise added and (b) from a solution of the model equations fit to the noisy data. A comparison of (b) with fig. 2a shows that the method has completely removed the noise and restored the original data.

result of forcing the data to fit a relatively simple set of equations since only a 2×2 correlation matrix was used and thus all the noise survives the singular value decomposition. Such a method should be used with caution since it tends to simplify the dynamics of the system.

3.3. Lorenz equations

The Lorenz equations

$$\begin{aligned} dx/dt &= \sigma(y - x), \\ dy/dt &= rx - y - xz, \\ dz/dt &= xy - bz, \end{aligned} \tag{7}$$

with $\sigma = 10$, $r = 28$, and $b = 8/3$ were solved numerically and 1000 values of $x(t)$ at $t = 0.05n$ taken as the input time series. These data are shown in fig. 4a. The neglect of the information contained in the variables $y(t)$ and $z(t)$ mirrors the experimental situation where only a limited amount of information is available. The corresponding phase space constructed using three

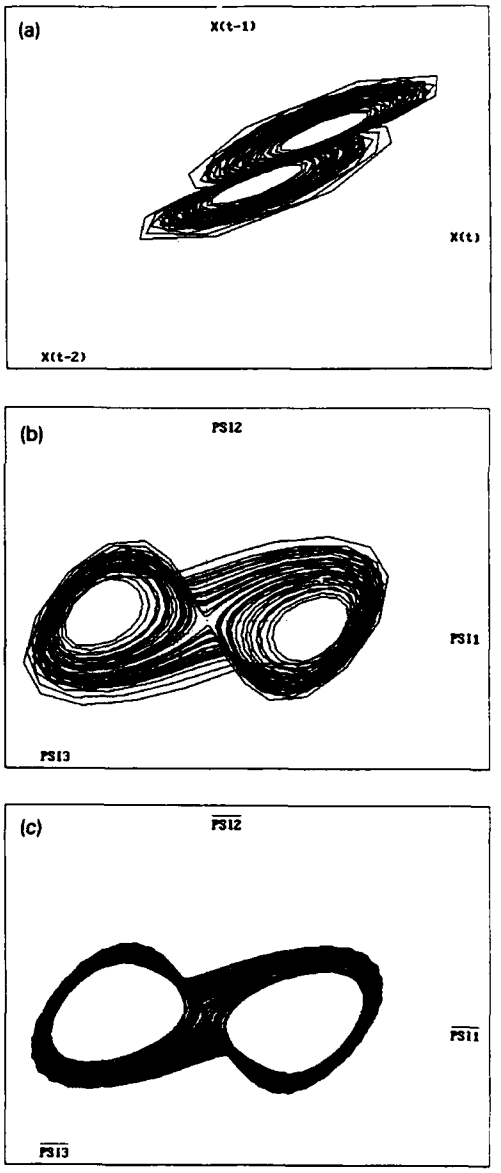

Fig. 4. Three-dimensional phase-space plots of the Lorenz attractor showing that the topology of the attractor is preserved. (a) Original input data, (b) result of singular value decomposition, and (c) solution of the model equations.

eigenfunctions corresponding to the three largest eigenvalues is shown in fig. 4b. This phase-space plot is insensitive to the value of M. A model set of three equations was then constructed using the full cubic form of F given in eq. (5). Their solution is shown in fig. 4c and is seen to capture the essentials of the time behavior. The plots obtained using the model equations are for a much longer time than the original data were given.

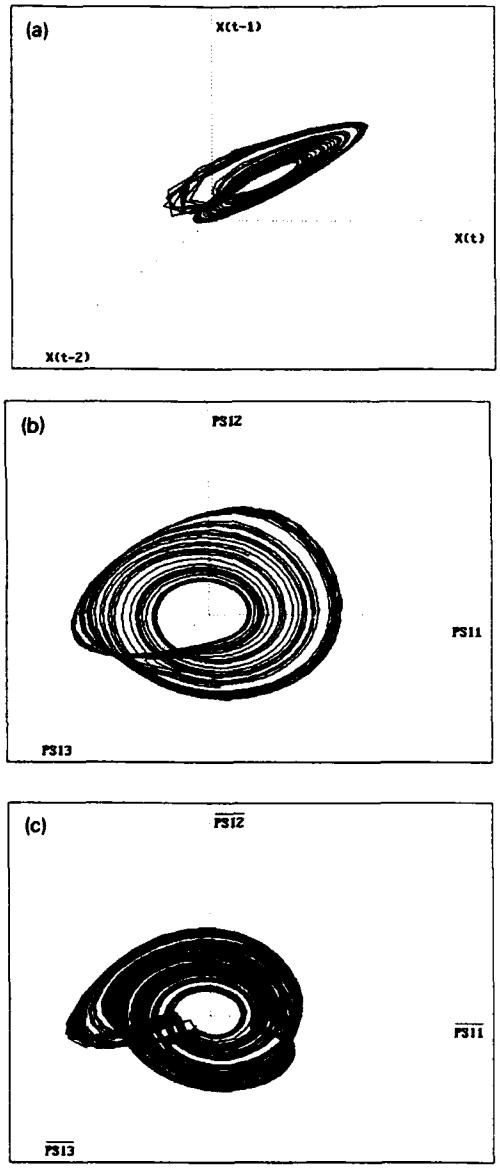

Fig. 5. Three-dimensional phase-space plots of the Rössler attractor showing that the topology of the attractor is preserved. (a) Original input data, (b) result of singular value decomposition, and (c) solution of the model equations.

The correlation dimension calculated using the method of Grassberger and Proccacia [1] with the original data set of 1000 points is 1.97 ± 0.18, and the value calculated from 13 000 values generated by solving the model equations is 2.10 ± 0.10. This is to be compared with the accepted value [1] of 2.05 ± 0.01. It has been pointed out by Ott et al. [23] that correlation dimensions are not necessarily invariant under coordinate changes. However, in the present case, since the ψ_m's are just linear combinations of the $T(n\tau)$'s, the correlation dimension must be invariant.

3.4. *Rössler equations*

A similar treatment has been applied to the Rössler equations

$$\begin{aligned} \mathrm{d}x/\mathrm{d}t &= -(y+z)\,, \\ \mathrm{d}y/\mathrm{d}t &= x + \alpha y\,, \\ \mathrm{d}z/\mathrm{d}t &= \beta + z(x-\gamma)\,, \end{aligned} \tag{8}$$

with $\alpha = \beta = 1/5$, $\gamma = 5.7$, and $t = 0.2n$. The corresponding results are shown in fig. 5. The correlation dimension for this case calculated from the original data set of 1000 points is 1.92 ± 0.08, and the value calculated from 15 000 values generated by solving the model equations is 1.94 ± 0.08. The expected value is slightly greater than 2.0.

4. Sensitivity to parameters

This whole procedure has been carried out for the Lorenz equations for a range of r values between 25 and 90, and in particular the coefficients a, b, and c appearing in eq. (5) were evaluated as a function of r. The variation with r of the coefficients of the largest nine terms is shown in fig. 6a from which it is seen that the variation is reasonably smooth. From the sym-

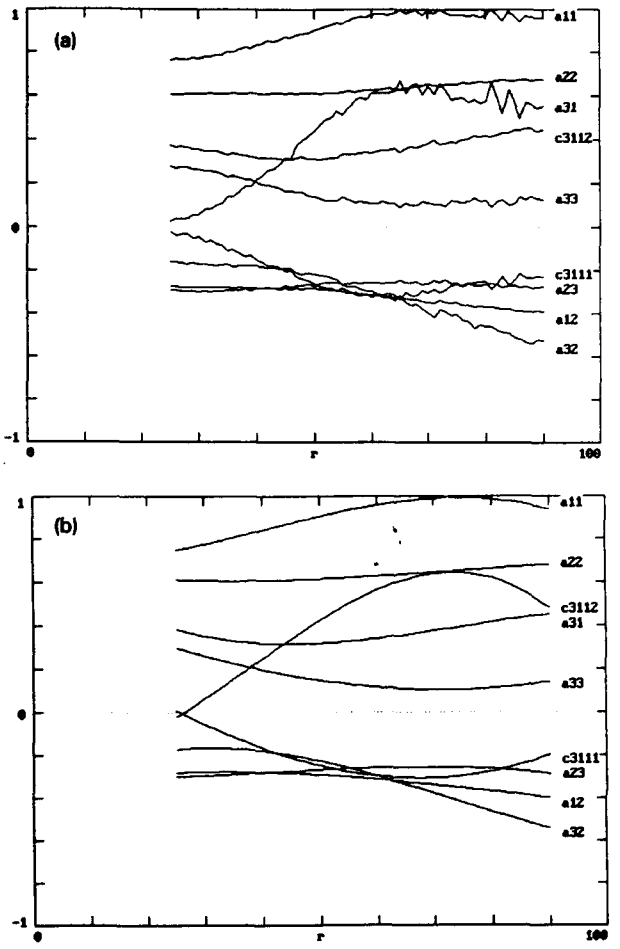

Fig. 6. (a) Variation of the nine largest coefficients of the model equations with the parameter r in the Lorenz equations, (b) along with a least squares fit of each coefficient to a cubic polynomial in r.

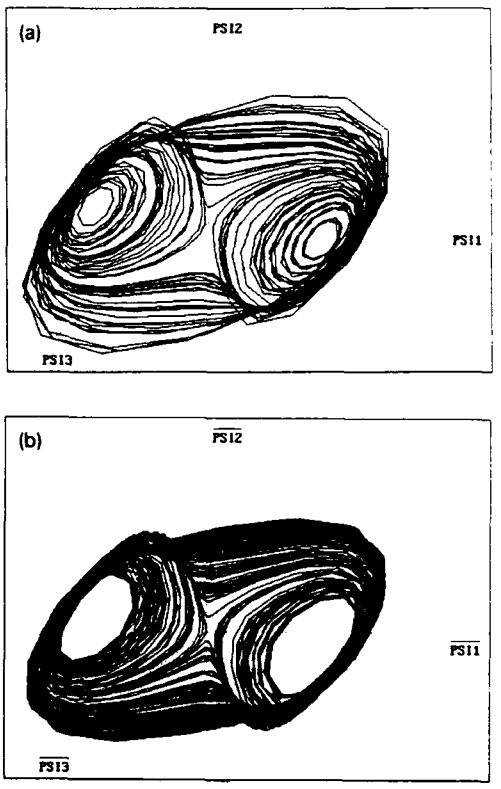

Fig. 7. Phase-space portraits for the Lorenz attractor with $r = 57$ (a) obtained directly from singular value decomposition, and (b) resulting from solution of the model equations with coefficients calculated from least squares fits to cubic polynomials in r.

metry of the Lorenz equations, the terms involving even powers of ψ (a_{mo} and b_{mpq}) are negligibly small. Using the least squares method, the coefficients are readily fitted to simple polynomials in r. A cubic fit as shown in fig. 6b is sufficient.

One now has a set of dynamical equations of the form given by eqs. (4) and (5) where the coefficients a, b, and c are known in the form of simple polynomials in the parameter r. It is on this set of equations that one can base an interpolation or extrapolation procedure. By taking r values other than those measured, and solving the model equations, the behavior of the system can be predicted. This can be in the form of the relevant phase-space plot or by using eq. (2) to form $x(t)$.

The phase-space portrait for $r = 57$ obtained directly from the values of the ψ's is shown in fig. 7a, while the form predicted using the above procedure is shown in fig. 7b. The agreement is good. Extrapolation outside the range of measured values should be applied with caution, however, since the least squares method of fitting curves to polynomials is not ideal.

5. Discussion

In the above method there are two quantities, namely M, the order of the correlation matrix and d, the number of significant eigenfunctions

retained. These are to be considered as parameters of the method which can be adjusted to obtain the best fit between the real system under investigation through the data $T(t)$ and the solution of the model, eq. (4). Since we envisage applying the method to situations where the auto-correlation function shows little structure, we hope the complicated time variation can be attributed to the presence of a strange attractor. Then the parameters M and d are chosen to represent best the topological features of the attractor.

An alternative approach would be to introduce constraints into the quantity that is to be minimized. For example, if it is apparent from the phase-space plots that the phase portrait has certain symmetry properties, then a term

$$\lambda \sum_j \{\psi_m[(s+1)\,\Delta t] - OF_m[\psi_j(s\,\Delta t)]\}^2 \qquad (9)$$

could be added to eq. (6). Here O is the symmetry operator, and λ is a Lagrangian multiplier. Furthermore, one may impose a smoothness condition on the fit by adding a term which minimizes the average second derivative,

$$\sum_j \{F_m[\psi_j(s\,\Delta t)] + F_m\psi_j[(s-2)\,\Delta t] - 2F_m\psi_j[(s-1)\,\Delta t]\}^2 . \qquad (10)$$

The Lagrangian multipliers can then be used to get the best fit to the coefficients a, b, and c. However, the results given here are optimized only by changing M.

The results for the Lorenz and Rössler equations have been obtained using the value of x_n at only 1000 points. The phase-space portraits for the model equations are shown for times longer than a thousand time intervals, illustrating the stability of the equations.

However, the coefficients in the model equations and hence the solution of these equations depend sensitively on the order of the correlation matrix **M**. Though the value of $T(t)$ (that is x) generated using eq. (2) with $d = 3$ is in good agreement (over the time where $x(t)$ is given) with the original data, the associated model equations do not reconstruct the strange attractor. Usually after a short interval of time the solutions tend to become infinite or attract to a fixed point or limit cycle. There is an optimal choice of M for the reconstruction of the attractor. It is reasonable to expect this value to be associated with (a) the maximum difference between λ_3 and the higher eigenvalues and (b) that the elements $C(n)$ used in the correlation matrices span the region where the major variation of C occurs. For the results presented in the case of the Lorenz equation, a value of 9 has been found to be appropriate, while for the Rössler equation, because of the longer correlation time, it was found optimal to make $M = 16$.

The relative difficulty of finding chaotic solutions to the model equations raises the more general question of how common is chaos. A numerical experiment was carried out in which about 10^6 three-dimensional cubic maps of the form given by eqs. (4) and (5) were iterated with the 60 coefficients chosen randomly over a 60-dimensional hypercube with each side extending from -1.2 to 1.2. Initial conditions were chosen near the origin, and the Lyapunov exponent was calculated for each case. About 99% of the solutions were unstable. (This number increases rapidly with the size of the hypercube.) Of the roughly 10 000 stable solutions, which are candidates for modeling bounded physical processes, about two-thirds attract to a fixed point and about one-third are either limit cycles or two-toruses. A small subset of about 4% are strange attractors with positive Lyapunov exponents.

Thus we conclude that for the subset of phenomena that can be represented by three-dimensional cubic maps, nature is chaotic about 4% of the time. There is some evidence to suggest that the regions of parameter space corresponding to chaotic motion are elongated. This means that as long as the parameter change is along the direction of elongation the system has a degree of robustness. The imposition of a symmetry re-

quirement tends to elongate the chaotic region. A by-product of this calculation was the generation of several hundred new examples of strange attractors, no two of which look the same.

6. Conclusion

A method has been described for determining a set of model equations from limited data whose global solutions resemble those of the original data. However, the method is not robust, and the existence of a strange attractor depends sensitively on the value of M. This sensitivity might be reduced by a better choice of the variational function.

Acknowledgements

One of us (G.R.) would like to acknowledge fruitful discussion with J. Alex Thomson at an early stage of this work and the hospitality of the University of Wisconsin – Madison Physics Department. This work was supported in part by the US Department of Energy.

References

[1] P. Grassberger and I. Procaccia, Physica D 9 (1983) 189.
[2] A.M. Lyapunov, Ann. Math. Studies 17 (Princeton Univ. Press, Princeton, NJ, 1949).
[3] G. Benettin, L. Galgani, A. Girogilli and J.-M. Strelcyn, Meccanica 15 (1980) 9.
[4] I. Shimada and T. Nagashima, Prog. Theor. Phys. 61 (1979) 1605.
[5] M. Casdagli, Physica D 35 (1989) 335.
[6] J.D. Farmer and J.J. Sidorowich, Phys. Rev. Lett. 59 (1987) 845.
[7] J.P. Crutchfield and B.S. McNamara, Complex Systems 1 (1987) 417.
[8] N.H. Packard et al., Phys. Rev. Lett. 45 (1980) 712.
[9] J. Cremers and A. Hübler, Z. Naturforsch A 42 (1986) 797.
[10] G. Gouesbet, Phys. Rev. A 43 (1991) 5321.
[11] D.S. Broomhead and G.P. King, Physica D 20 (1986) 217.
[12] R. Vautard and M. Ghil, Physica D 35 (1989) 395.
[13] T. Hediger, A. Passamante and M.E. Farrell, Phys. Rev. A 41 (1990) 5325.
[14] F. Takens, Detecting Strange Attractors in Turbulence, Lecture Notes in Mathematics, D.A. Rand and L.-S. Young, eds. (Springer, Berlin, 1981) p. 366.
[15] J.R. Rice, The Approximation of Functions, Vol. 1 and 2 (Addison-Wesley, Reading, MA, 1969).
[16] P.R. Graves-Morris, Padé Approximants and their Application (Academic, New York, 1973).
[17] J.C. Sprott and G. Rowlands, Chaos Data Analyzer, Physics Academic Software, Box 8202, North Carolina State University, Raleigh, NC 27695.
[18] N. Aubry, P. Holmes, J.L. Lumley and E. Stone, J. Fluid Mech. 192 (1988) 115.
[19] L. Sirovich and J.D. Rodriguez, Phys. Lett. A 120 (1987) 211.
[20] K.S. Ball, L. Sirovich and L.R. Keefe, Int. J. Num Methods Fluids 12 (1991) 585.
[21] E.N. Lorenz, J. Atmos. Sci. 20 (1963) 130.
[22] O.E. Rössler, Phys. Lett. A 57 (1976) 397.
[23] E. Ott, W.D. Withers and J.A. Yorke, J. Stat. Phys. 36 (1984) 687.

Physica D 58 (1992) 260–272
North-Holland

PHYSICA D

Global unpredictability in nonlinear dynamics: capture, dispersal and the indeterminate bifurcations

J.M.T. Thompson

Centre for Nonlinear Dynamics and its Applications, Civil Engineering Building, University College London, Gower Street, London, WC1E 6BT, UK

Received 30 August 1991
Revised manuscript received 6 February 1992
Accepted 6 February 1992

This paper surveys in general terms some of the problems of predictability that arise in regular and chaotic dynamics. These relate to attractors, basins and bifurcations, and a capture-dispersal diagram is introduced to assess relative degrees of global unpredictability. Indeterminate bifurcations emerge as the most severe generators of unpredictability, and some new examples involving both regular and chaotic events are presented as illustrations.

1. Introduction

The unpredictability of a dynamical system can be examined locally, in terms of the uncertainty surrounding the simulation of a required trajectory, or globally in terms of uncertainties of response within families of trajectories. Key qualitative indices for global unpredictability are capture (c) and dispersal (d), a severe phenomenon being one with high c + d that captures a lot of the dynamics and then disperses it widely. Plotted on a capture–dispersal diagram, as in fig. 1, these coordinates give a useful overview of the sources of unpredictability within the attractors, basins and bifurcations of nonlinear dissipative dynamics.

Among the attractors, it is of course steady state chaos that generates the greatest degree of unpredictability. The chaotic attractor captures all trajectories within its basin and disperses them by a spreading, folding and mixing action within a well-defined, albeit fractal, topological structure. Basin boundaries are an obvious mechanism of dispersal within the trajectories of a system. A smooth or fractal boundary can achieve dispersal to an arbitrary number of distinct and remote attractors, the fractal boundary generating additionally the mixing action of chaotic transients associated with chaotic saddle solutions. Basin boundaries thus score well on dispersal, but badly on capture because only trajectories "within" the boundary zone are involved.

The discontinuous-dangerous bifurcations, characterized by the blue-sky disappearance of an attractor, give an inevitable fast dynamic jump to a remote steady state (a point, periodic or chaotic attractor). Most can be indeterminate, in the sense that more than one outcome is possible, the attractor chosen depending sensitively on the precise manner in which the bifurcation is realised. Regular local bifurcations can exhibit this indeterminacy, and an indeterminate tangled saddle–node is a common bifurcational feature in the resonance of softening oscillators [1–3]. These indeterminate bifurcations can be seen as a mechanism for sweeping all trajectories from a basin in phase-control space precisely

0167-2789/92/$05.00 © 1992 – Elsevier Science Publishers B.V. All rights reserved

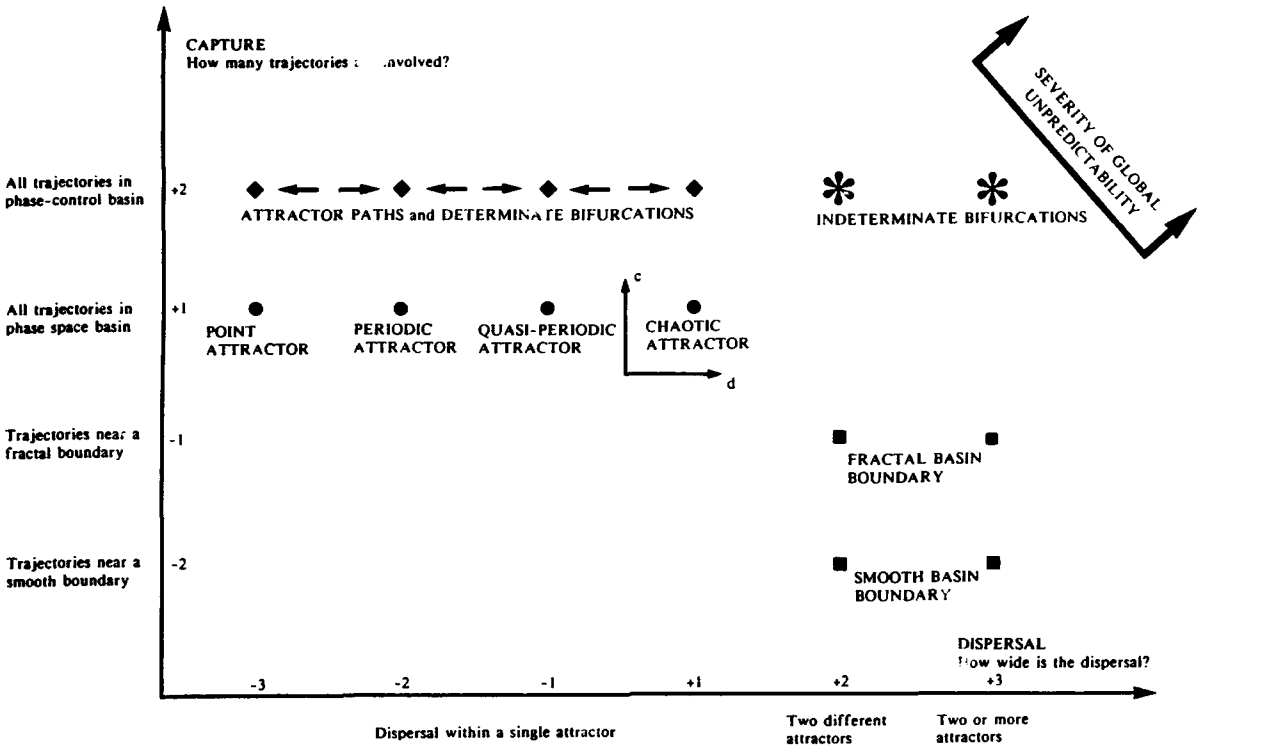

Fig. 1. A notational capture–dispersal diagram, summarizing the degree of global unpredictability generated by different features of the phase-control portrait of a nonlinear dissipative system.

onto a (smooth or fractal) basin boundary, from which they are dispersed to two or more uncorrelated and remote attractors. They achieve the high dispersal of a basin boundary while capturing, during a slow parameter sweep, a full basin of trajectories. The indeterminate bifurcations therefore generate, in a very real sense, the highest degree of global unpredictability in regular and chaotic dynamics.

2. Predictability in simulations

Before addressing the main theme of global uncertainty involving families of trajectories, we review the problem of simulating a single trajectory in the presence of chaotic motions. In nonlinear dynamics, characterized for example by a set of ODEs, there is always a unique trajectory from a given starting condition. So even when the behaviour is in modern parlance *chaotic*, the motion is strictly *deterministic*. However, for even the simplest nonlinear system there is little possibility of a closed-form solution: often there is no analytical solution, as in the presence of chaotic motions. So resort must be made to computers, which brings us to the more pragmatic consideration of *predictability*.

In the real world, be it in an analogue simulation, in a laboratory experiment or in the outside environment, any system is subjected to random external disturbances, described as *noise*: macroscopic mechanical systems also experience internal noise from thermal vibrations of individual molecules. Likewise in digital computations, a required trajectory will be constantly perturbed by numerical noise. This arises firstly from the numerical integration scheme itself, and secondly from round-off errors of the finite precision arithmetic. Referring collectively to analogue, digital and laboratory investigations as *simulations*, what possibility is there of using these to

predict the future in the presence of this all pervasive noise?

To answer this question requires a stochastic analysis. But we gain some insight by considering adjacent motions of the original idealized noise-free dynamical system, S. Noise tends to knock the system from one trajectory to another. So if adjacent trajectories stay close, or better still converge, there is hope that simulations will give a good prediction. Conversely, if adjacent trajectories diverge, we might expect there to be a practical predictability horizon [4] beyond which any simulations will depart significantly from the desired trajectory.

In any large but finite time, T, there is, we recall, a strict continuity of response of system S. If trajectories in phase space from two starting points $x(0)$ and $X(0)$ lead in time T to points $x(T)$ and $X(T)$, then as $x(0)$ approaches arbitrarily close to $X(0)$, so $x(T) \to X(T)$. Similar continuity holds for a small perturbation of S, induced for example by a small change in a control.

Clearly we must consider not just one, but all adjacent trajectories. Now for the autonomous set of first-order differential equations, $\dot{x}_i = F_i(x_j)$, where a dot denotes differentiation with respect to time, t, we have the divergence function

$$\mathrm{div}(x_i) = \partial F_1/\partial x_1 + \partial F_2/\partial x_2 + \partial F_3/\partial x_3 + \cdots .$$

We might suppose that *totally dissipative* systems for which $\mathrm{div}(x_i)$, although not necessarily constant, is everywhere negative, would be the most predictable: and for this reason, we shall focus on them in this section.

With positive definite dissipation, any cloud of starts contracts continuously with its volume tending exponentially to zero as $t \to \infty$. A typical solution will experience a transient converging asymptotically onto a steady state attractor of zero phase volume. These steady states can be point attractors, periodic or quasi-periodic attractors, or chaotic attractors.

It is of course the chaotic attractors that give the greatest predictability problem. In $\mathbb{R}^3$ these have such a rapid contraction onto a sheet that there can be exponential divergence within the sheet, consistent with the overall volume contraction. A repetitive feature of the dynamics, ensures that this sheet is repeatedly folded, as in the making of flaky pastry. The result is an infinitely layered fractal structure in phase space, the chaotic attractor, within which the post-transient motions wander for ever in an essentially random manner. It is the combined effects of *divergence* and *mixing* within a well-defined and localized fractal structure that characterizes a chaotic attractor and poses limits to the detailed predictability of its motions. So even in a totally dissipative system, a trajectory in a chaotic attractor has adjacent diverging trajectories within the sheet. This divergence is exponential, making long term predictions impossible.

Consider, for example, the tracking of a fundamental trajectory of S by an adjacent trajectory of S whose starting coordinates differ by a small perturbation, ϵ. If the error has the form $\epsilon \exp(\lambda t)$ with $\lambda > 0$, this will reach a level of unacceptability, E, at a predictability horizon, H, given by $\lambda H = \ln(E/\epsilon)$. If we repeatedly halve the perturbation to $\epsilon/2$, $\epsilon/4, \ldots$, the new predictability horizon is

$$\lambda H = \ln(E/\epsilon) + \ln(2) + \ln(2) + \cdots .$$

Every time we double the precision of the initial condition, we just succeed in pushing the horizon forward by one step of $\Delta H = (1/\lambda)\ln(2)$. The horizon changes only *linearly* with the number of decimal places used to describe the initial conditions. Moreover the mixing action of a chaotic attractor ensures that beyond the horizon the successively improved simulations do not march towards the required solution in a simple systematic manner.

A similar situation prevails when we try to simulate the response of S, from *a fixed* starting condition using a digital computer. Every time

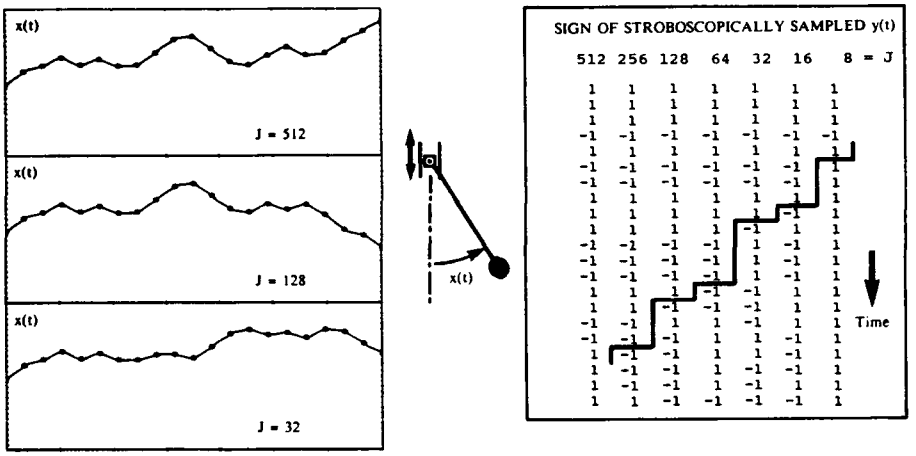

Fig. 2. Chaotic tumbling of a parametrically excited pendulum, showing the variation of the predictability horizon with the size of the Runge–Kutta time step. Parameter values are $\beta = 0.2$, $A = 1.59$, $\omega = 1.79$. All runs start at $x(0) \simeq -1.737$, $y(0) \simeq 2.026$. Window of the time series is $0 < t < 70$, $-14\pi < x < 14\pi$.

we double the precision of the numerical integration we can only expect to increase the predictability horizon by a linear step. This is illustrated in fig. 2 summarizing seven Runge–Kutta simulations of the chaotic tumbling of a parametrically excited pendulum described by

$$\ddot{x} + \beta\dot{x} + [1 + A\cos(\omega t)]\sin(x) = 0\,.$$

The start, roughly on a predetermined chaotic attractor, is held constant throughout. A fourth-order Runge–Kutta algorithm is employed with J steps per forcing cycle, $J = 8, 16, \ldots, 512$. Comparative plots of $x(t)$ are shown in the left-hand graphs. The roughly linear variation of the predictability horizon under halving of J is illustrated in the table which compares the signs of the stroboscopically sampled values of $\dot{x}(t) \equiv y(t)$ at phase $\phi = 0$.

Although detailed correlation is lost at the predictability horizon, the strong phase contraction onto the folding sheet ensures that the more accurate simulations all stay close to a well-defined attracting fractal structure, which is therefore presumed to be that of system S. Fig. 3 shows the similar chaotic attractors obtained at $J = 64$ and 32. Comparable pictures are generated by totally different algorithms, which lends

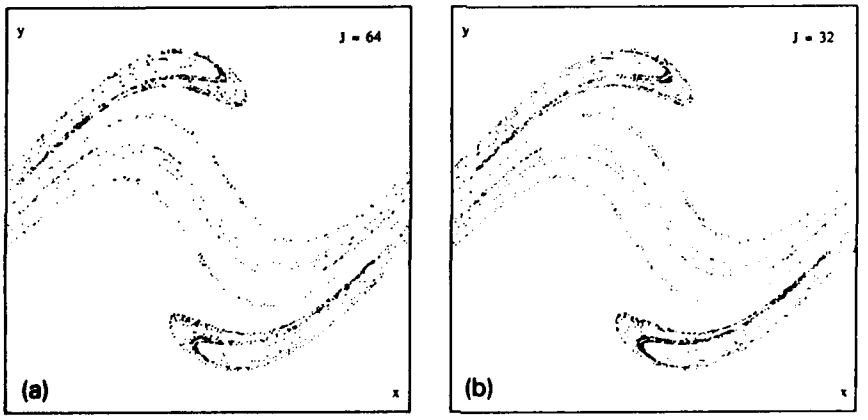

Fig. 3. Stroboscopically sampled chaotic attractor of the tumbling, parametrically excited pendulum. Qualitatively similar attractors obtained at different values of the integration step size. Window is $-\pi < x < \pi$, $-4 < y < 4$. Data as in fig. 2.

support to the view that numerically drawn chaotic attractors are meaningful representations of the underlying dynamics.

In this context we can refer to Grebogi et al. [5] who discuss the relationship between a computer-generated "noisy" trajectory and a true one, with applications to two representative *Hamiltonian* systems. They develop a rigorous procedure to show that some true trajectories remain close to the noisy one for long times. To show that a true trajectory *shadows* the noisy trajectory in this way, they employ a combination of containment, which establishes the existence of an uncountable number of true trajectories close to the noisy one, and refinement, which produces a less noisy trajectory. This is applied successfully to the noisy chaotic trajectories of the standard map and the undamped driven pendulum.

Despite this preservation of the underlying fractal structure, a chaotic attractor will always have a severe predictability horizon for a single trajectory, preventing detailed long term correlations between *any* of the following: (a) the fundamental trajectory of the idealized system; (b) any adjacent trajectory of the idealized system; (c) any trajectory of an idealized perturbed system; (d) any individual trajectory of a laboratory, analogue or digital simulation; (e) any individual trajectory of a real-world prototype system.

3. Capture and dispersal

In a global sense, the degree of unpredictability of a system is clearly related to ideas of capture and dispersal, as we have intimated. So we shall now focus on this aspect, and look in turn at attractors, basins and bifurcations.

3.1. The attractors

An attractor captures all trajectories initialized within its basin and draws them towards a central attracting set. It scores a high capture measure, but has a low (perhaps we should say negative) dispersal. The attractors can therefore be positioned as shown on our schematic capture-dispersal diagram of fig. 1. Here, in recognition of the different compactions achieved, we have assigned increasing dispersal measures as we progress from a point attractor, through periodic and quasi-periodic attractors, to the chaotic attractor.

3.2. The smooth basin boundary

The simplest, and most direct way to obtain a dramatic splitting of two "adjacent" trajectories is to place the two starting points, $x(0)$ and $X(0)$, so that they straddle a point B on a smooth basin boundary. Then, as $t \to \infty$, the two motions will diverge and head towards two totally different and remote attractors. It is important to remember, though, that this behaviour does not violate the continuous dependence on initial conditions in *finite* time, because the essential splitting action will invariably involve slow dynamical motions near an unstable steady state.

Consider first a boundary in a 2D phase space formed by the stable manifold (inset) of a saddle fixed point, D. Trajectories from a line of starts joining $[x(0), X(0)]$ will slow down as they approach D given a line $[x(T), X(T)]$ parallel to the *outset* of D, and approaching it slowly as $T \to \infty$. Increasing T just gives a similar picture, trajectories approaching closer to the outset but still exhibiting the continuous dependency.

Despite this strict mathematical continuity, trajectories from two points straddling the boundary which are located at small but not infinitesimal distances from B, will be perceived to disperse the response to the two remote attractors. In this sense we shall say that a smooth boundary formed by the inset of a saddle in $\mathbb{R}^2$ achieves a dispersal to two different attractors.

An unstable limit cycle is a second example of a basin boundary in a 2D flow. Trajectories initialized just outside the cycle head out to an

exterior attractor while those initialized inside head towards an interior attractor. Once again, the splitting involves infinite time associated with the slow movement away from the cycle.

With such an unstable cycle it is easy to devise a situation in which the interior motions tend, not to a single attractor, but to two or more distinct attractors. This is illustrated in fig. 4a, which has just two interior attracting points, and one exterior attractor, a stable limit cycle. The basins of the two interior attractors wind outwards and spiral onto the unstable limit cycle in what we might call a mosquito-coil structure (not a fractal structure): trajectories initialized just inside the cycle will be attracted to one or other of the fixed points depending sensitively on their starting displacement and phase. So we see that a smooth basin boundary can give dispersal to an

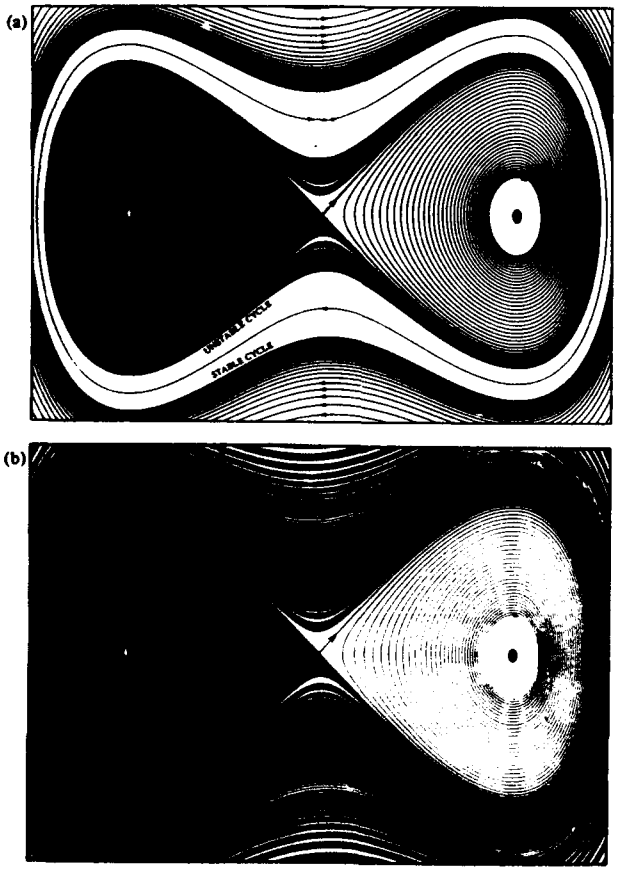

Fig. 4. An indeterminate cyclic fold before (a) and after (b) the coalescence of the two limit cycles. Window is $-0.15 < x < 0.15$, $-0.01 < y < 0.01$.

arbitrary number of alternative attractors (an example involving six exterior point attractors will be seen later in fig. 5).

To generate a significant level of global unpredictibility, we require that a lot of trajectories be involved, and it is here that the smooth boundary does not score highly. To get the dispersal we are obliged to place starts close to the basin boundary: the relevant starts in $\mathbb{R}^2$ must be clustered around a line, rather than filling an area. So not many trajectories are captured by the dispersing action, and we assign the smooth basin boundary the two points shown in the capture-dispersal diagram of fig. 1.

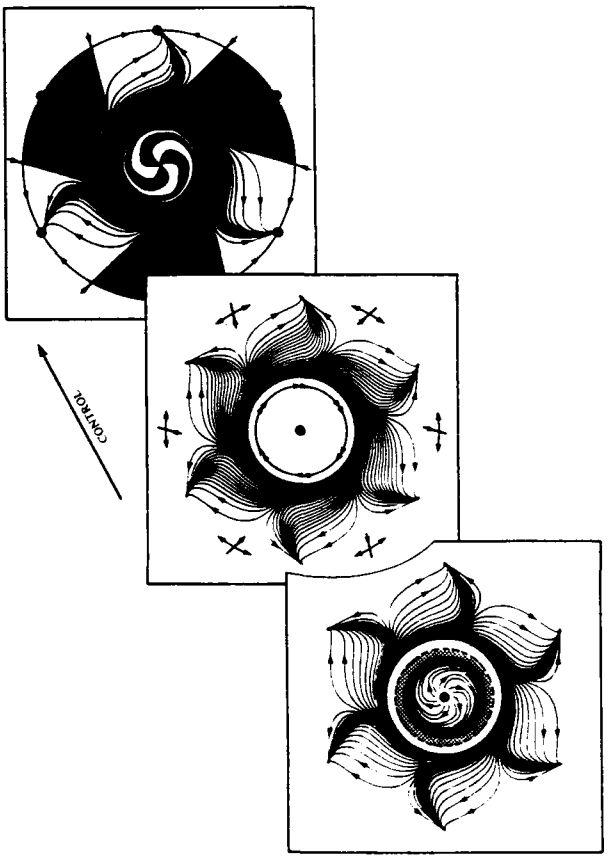

Fig. 5. Multiple dispersal from an indeterminate cyclic fold. Front portrait, $\mu = -0.01$; centre portrait, $\mu = 0$; rear portrait, $\mu = 0.02$. Portrait window, $-3.5 < x, y < 3.5$. In the front portrait the dotted band of width $2(-\mu)^{1/2}$ separates the outer unstable limit cycle (shown as a broken circle) from the inner stable cycle. In the centre portrait, the critical, structurally unstable cycle at $r = 1$ is indicated by double arrows.

3.3. The fractal basin boundary

The mosquito-coiled basins of fig. 4a give a high degree of indeterminacy to trajectories falling inwards off the unstable cycle, because as they approach the cycle the alternating spiral tails of the basins have vanishing thickness.

Fractal basin boundaries [6], generated for example in driven oscillators by homoclinic tangling of the invariant manifolds of a directly unstable saddle cycle [7], achieve such a delicate structure in a more extended region of phase space. It thus seems appropriate to assign to them a greater degree of capture in fig. 1. However, since their fractional dimension is less than that of the phase space, we are still frustrated by the fact that the probability of a start falling precisely on a fractal basin boundary is zero. As with smooth boundaries, fractal boundaries can involve the thin intertwining tails of two or more basins, as recognised by their placing in the figure.

3.4. Attractor paths and determinate bifurcations

We introduce at this stage the concept of an *evolving* system in which a control parameter undergoes a slow sweep. During most of our discussion we can imagine a parameter μ to be either repeated stepped by small increments $\Delta\mu$, or to be a slow function of time. In the latter case, a parametrized flow on $\mathbb{R}^n$, $\dot{x}_i = F_i(x_j, \mu)$, would be replaced by a flow on $\mathbb{R}^{n+1}$, by adding the equation $\dot{\mu} = \epsilon$, and we notice that at any μ the r_i projection of the $\mathbb{R}^{n+1}$ vector field is identical to the $\mathbb{R}^n$ field.

In phase-control space we now have attractor paths with transients settling quickly towards a path. Such a path might be the continuous trace of a point attractor, of a periodic or quasi-periodic attractor, or of a chaotic attractor: and we assign to these the increasing dispersal measures that we used before. Since the capture is now from a basin in phase-control space, we give them all (somewhat arbitrarily) a higher capture measure.

The codimension-one attractor bifurcations that will be typically encountered on such a parameter sweep can be classified as in table 1, following [8–11]. The subtle bifurcations are local events that signal a continuous supercritical growth of a new attractor path. They are safe, in that they do not trigger a fast dynamic jump, or even an instantaneous enlargement of the attracting set. They are, moreover, determinate in outcome, the new path being uniquely defined even in the presence of external noise.

So a subtle bifurcation achieves no dispersal in its own right. It generates, at the most, a determinate change in attractor type, corresponding to a movement between two of the diamond symbols on fig. 1. In terms of dispersal, it is not a significant event on an attractor path. The same conclusion holds for the catastrophic-explosive bifurcations of table 1b. These are global events, characterized by a sudden, instantaneous enlargment of the attracting set, with no jump to a remote disconnected attractor, and no indeterminacy in outcome.

3.5. Indeterminate regular bifurcations

We arrive, finally, at the catastrophic-dangerous bifurcations of table 1c which are characterized by the blue-sky disappearance of an attractor, given an inevitable jump to a remote attractor of any type. These are dangerous in that a system will experience a sudden fast dynamic jump to a distant attractor. With the exception of the saddle–node fold, and the saddle connection, whose 1D outsets (centre-unstable manifolds) ensure, generically, a unique outcome of the dynamic jump, these dangerous bifurcations can all exhibit indeterminate outcomes. Such indeterminacy does not seem to be well documented, and we give first two examples from the regular local bifurcations.

We have seen in fig. 4a how the basins of two (or more) attractors can accumulate onto an

Table 1
Classification of the generic codimension-one attractor bifurcations in dissipative dynamics. In this we speak of a *forward* control sweep as one which generates instability or increased complexity. The | identifies equivalent flow/mapping forms.

(a) Subtle (i.e. continuous) bifurcations
Local bifurcations with the continuous supercritical growth of a new attractor path
Safe with no fast dynamic jump or instantaneous enlargment of the attracting set
Determinate with a single outcome even under small noise excitation
No hysteresis with attractor paths retraced on reversal of control sweep
No basin change, with basin boundary remote from the bifurcating attractors
No intermittency in the steady-state responses of the attractors

| Supercritical Hopf ..... (point to cycle)
Other names: in aeroelasticity, galloping or flutter
Local bifurcation with imaginary conjugate pair of flow eigenvalues λ

| Supercritical Neimark ..... (cycle to torus)
Other names: supercritical secondary Hopf bifurcation
Complex pair of mapping eigenvalues with $|\Lambda| = 1$. Note resonances if Λ^3 or $\Lambda^4 = 1$

Supercritical flip ..... (cycle to cycle)
Other names: supercritical period-doubling bifurcation, subharmonic resonance
Local bifurcation with one mapping eigenvalue, $\Lambda = -1$

(b) Catastrophic (i.e. discontinuous) explosive bifurcations
Global bifurcations with a sudden, instantaneous enlargement of the attracting set
Explosive enlargement, but no jump to remote disconnected attractor
Determinate with a single outcome even under small noise excitation
No hysteresis with attractor paths retraced on reversal of control sweep
No basin change, with basin boundary remote from the bifurcating attractors
Intermittency: supercritical lingering in old domain, flashes through new domain

| Flow explosion ..... (point to cycle)
Other names: omega explosion
Locally a saddle–node whose 1D flow outset forms a closed loop

| Map explosion ..... (cycle to torus)
Other names: mode locking/unlocking
Locally a saddle–node whose 1D mapping outset forms a closed loop or drift ring

Intermittency explosions ..... (cycle to chaos)
Other names: intermittency, interior crisis, interior catastrophe
Locally a fold, subcrit flip or subcrit Neimark; eg. is opening of periodic window

Chaotic explosion ..... (chaos to chaos)
Other names: interior crisis, interior catastrophe
Example is the closing of a periodic window in the logistic map

(c) Catastrophic (i.e. discontinuous) dangerous bifurcations
Blue-sky disappearance of attractor giving jump to a remote attractor of any type
Dangerous with a sudden fast dynamic jump to a distant unrelated attractor,
Determinate or *indeterminate* in outcome, depending on global topology
Hysteresis with original attractor not reinstated on reversal of control sweep
Basin shrinks to zero (c.2) or attractor hits boundary of a residual basin (c.1) & (c.3)
No intermittency (except for a subcritical form in the saddle connection)

(c.1) The local saddle–nodes, with (in)finite residual basins

| Saddle–node fold ..... (from point)
Other names: in elasticity, limit point. Pitchfork (cusp) & transcritical not directly generic
Local saddle–node bifurcation of point attractors with one flow eigenvalue $\lambda = 0$
Indeterminate: can be devised by simultaneous saddle connection, but not generic

| Cyclic fold ..... (from cycle)
Other names: saddle-node, dynamic fold, periodic fold (jump to resonance)
Local saddle-node bifurcation of periodic attractors with one mapping eigenvalue $\Lambda = +1$
Indeterminate: mosquito-coil, this paper, figs. 4–6. Tangled s/n, figs. 9, 10

Table 1 (cont.)

(c.2) The local subcritical bifurcations, with basins shrinking to zero
Subcritical Hopf ..... (from point)
Other names: in aeroelasticity, galloping or flutter
Local bifurcation with an imaginary conjugate pair of flow eigenvalues λ
Indeterminate: aeroelastic galloping in asymmetric well, this paper, figs 7, 8
Subcritical Neimark ..... (from cycle)
Other names: subcritical secondary Hopf bifurcation
Local bifurcation with complex pair of mapping eigenvalues with $\|\Lambda\| = 1$
Indeterminate: no example known to author
Subcritical flip ..... (from cycle)
Other names: subcritical period-doubling bifurcation, subharmonic resonance
Local bifurcation with one mapping eigenvalue, $\Lambda = -1$
Indeterminate: no example known to author
(c.3) Global bifurcations, with (in)finite residual basins
Saddle connection ..... (from cycle)
Other names: homoclinic connection, homoclinic bifurcation
Global homoclinic connection: no mapping form because connection is replaced by tangle
Indeterminate: like the fold, the 1D outflow only allows non-generic indeterminacy
Regular saddle catastrophe ..... (from chaos)
Other names: boundary crisis, chaotic blue sky catastrophe
Chaotic attractor hits saddle on smooth boundary which simultaneously becomes homoclinic
Indeterminate: no example known to author
Chaotic saddle catastrophe ..... (from chaos)
Other names: boundary crisis, blue sky catastrophe
Chaotic attractor hits accessible orbit in a previously tangled basin boundary
Indeterminate: see ref. [1]

unstable limit cycle in a mosquito coil. The unstable cycle can be brought into collision with a surrounding stable cycle, by, for example, sweeping parameter B in the equation

$$\ddot{x} - B\dot{x} + x^2\dot{x} - Ax + x^3 = 0\,,$$

with A constant at 0.01. This is illustrated in fig. 4, the two cycles of fig. 4a at $B = 0.0076$ having disappeared from the portrait of fig. 4b at $B = 0.0075$, due to their mutual annihilation at an intervening cyclic fold. The outcome of this local bifurcation is clearly indeterminate, as described by Abraham [10] and Stewart and Ueda [1] based on sections 1.9 and 7.3 of ref. [12]. The system will settle, after the fold, onto one of the two competing point attractors: the one chosen depending sensitively on the starting conditions at the beginning of the parameter sweep, the rate of the sweep, and any real or numerical noise present in the experiment.

It is easy to devise a cyclic fold that has any desired number of indeterminate outcomes. Consider for example the system described in polar coordinates by

$$\dot{r} = -[(r-1)^2 + \mu](r-3)\,,$$

$$\dot{\theta} = 3 - r + \sin(m\theta)\,.$$

As μ changes from negative to positive, two cycles of radii $1 \pm (-\mu)^{1/2}$ collide at $r = 1$, giving an indeterminate jump from the inner stable cycle to one of the m point attractors that are equally space around the circle $r = 3$. Notice that in devising this scenario we have chosen the form of $\dot{\theta}$ to ensure that $\dot{\theta}$ is always positive if $r < 2$, guaranteeing cycles whenever $\dot{r} = 0$: and to ensure that $\dot{\theta}$ is purely sinusoidal when $\dot{r}$ vanishes at $r = 3$ to give a symmetric pattern of alternating point attractors and saddles.

This scenario is illustrated in fig. 5 for the case

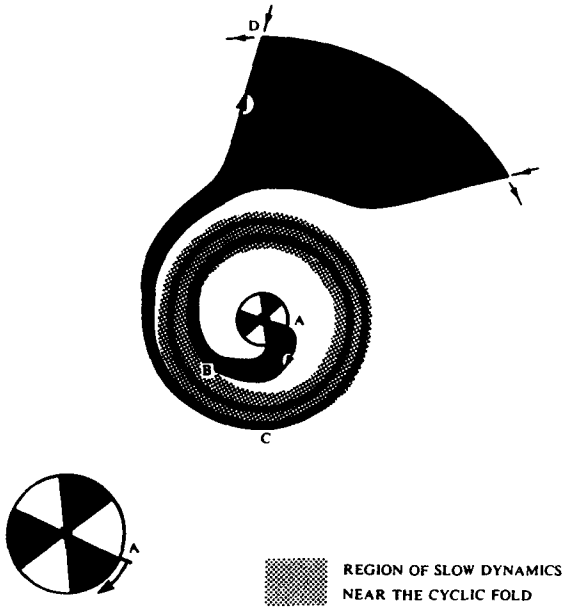

Fig. 6. Multiple dispersal from an indeterminate cyclic fold, showing the behaviour of one of the basins of attraction at $\mu > 0$. The central disc pattern rotates with infinite velocity as $\mu \to 0$.

of $m = 6$. The last portrait, just after the collision of the two cycles, shows how the basins of the six attracting fixed points now pass through the region of slow dynamics at $r \simeq 1$ where $\dot{r}$, although now always positive, is still small.

It is of interest to examine, heuristically, the rate of rotation of the central disc-like basin pattern as $\mu \to 0$. The inset of saddle D in fig. 6 leaves the central disc at A. The initial flow is insensitive to the value of $\mu \simeq 0$, so we can suppose that the inset enters the region of slow dynamics at B with $\theta_B - \theta_A$ equal to a constant C_1. Similarly, between leaving the slow region at C and arriving near D where $\theta = 0$, we can write $\theta_D - \theta_C \simeq C_2$. It is the long time of passage through the slow region around $r = 1$ that depends sensitively on μ. For the canonical fold, $\dot{x} = \mu + x^2$, we can write the solution in terms of $a = \mu^{1/2}$, valid for positive μ, as $x = a \tan(at)$ with $x \to \infty$ at $t_\infty = \pi/2a$. The time of passage from $x = -\infty$ to $x = +\infty$ is therefore π/a, scaling as $\mu^{-1/2}$. So for our cyclic fold we can write $t_C - t_B \propto \mu^{-1/2}$ and assuming that $\dot{\theta}$ is approximately constant in the transit from B to C, $\theta_C - \theta_B \propto \mu^{-1/2}$ and hence $\theta_A = -C_1 - C_2 - C_3\mu^{-1/2}$ giving finally

$$\partial\theta_A/\partial\mu = (\tfrac{1}{2}C_3)\mu^{-3/2}.$$

So the rate of rotation of the central disc scales as $\mu^{-3/2}$. As we approach the cyclic fold from positive μ the disc retains its form but acquires an infinite rate of rotation until it disappears altogether at $\mu = 0$, since the basins do not penetrate to the interior for $\mu < 0$.

At any fixed $\mu > 0$ the central pattern retains its hexagonal symmetry, so there is no great sensitivity to the starting condition $[r(0), \theta(0)]$. For arbitrarily small $\mu > 0$ we can find a finite circle in phase space whose interior points all lie in a prescribed basin. But near the bifurcation the unbounded rate of rotation implies that the point attractor to which a motion flows is infinitely sensitive to the value of μ. As μ decreases towards zero, the radius of the largest sphere in phase-control space whose interior points all lie in one basin will vanish as $\mu^{3/2}$. Notice, however, that this infinite sensitivity to μ is not reflected in the response of the evolving system, $\dot{\mu} = \epsilon$, since the attractor to which a non-evolving trajectory would tend as $t \to \infty$ has no significance under evolving conditions. The characteristics of the local 2D and 3D flows are in fact very simple, and, as we have remarked, they are in no way governed by the invariant manifolds of the distant saddles.

As a second illustration of a regular indeterminate bifurcation, consider the oscillator

$$\ddot{x} + B\dot{x} - C\dot{x}^3 + x + (D-1)x^2 - Dx^3 = 0,$$

which arises in problems of aero-elastic galloping. As the wind-loading parameter B passes from positive to negative the equilibrium at $x = 0$ loses its stability at a sub-critical hopf bifurcation beyond which the divergence is everywhere positive and all trajectories diverge to $x = \pm\infty$. The nonlinear stiffness corresponds to a metastable

well similar to that in fig. 7, parameter D allowing us to vary the relative heights of the two potential barriers. This could correspond to a nominally symmetric structural shell, buckling in the presence of a symmetry-breaking imperfection. Taking the left-hand barrier to be the higher, as drawn, it is clear that if the heights are very different the bifurcation will be determinate, all motions from the bottom of the well tending to $x = +\infty$. Conversely, if the heights are nearly the same, the bifurcation will be indeterminate, with adjacent motions differing perhaps only in their starting phase, heading to either $x = \pm\infty$. The critical condition separating these two types of Hopf bifurcation is represented by the saddle connection illustrated, in which a trajectory climbing out of the well under the positive divergence can just pass from the lower hill-top to the higher hill-top. Phase portraits

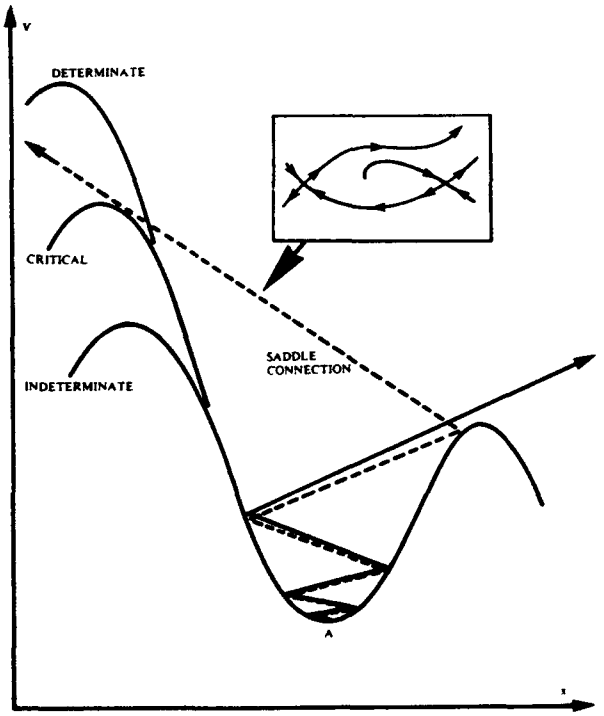

Fig. 7. Sub-critical Hopf bifurcations in an asymmetric potential well. In parameter space the determinate bifurcations, given an inevitable jump to the right, are separated from indeterminate bifurcations, giving jumps to either left or right, by the saddle connection illustrated.

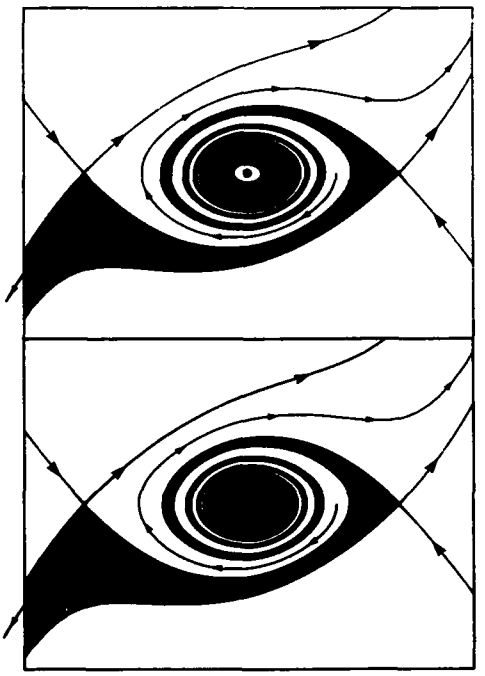

Fig. 8. Indeterminate sub-critical Hopf bifurcation, such as might arise due to aero-elastic galloping in an asymmetric potential well. Phase portraits show the basin structure before (top) and after (bottom) the bifurcation.

corresponding to the indeterminate form of Hopf bifurcation are shown in fig. 8.

3.6. *Indeterminate chaotic bifurcations*

The cyclic fold of fig. 5 is a mechanism for sweeping all trajectories of a phase-control basin precisely onto a smooth basin boundary from which they can be dispersed to a large number of competing attractors. It is an excellent generator of global unpredictability. In a driven system, a cyclic fold can sweep trajectories onto a fractal boundary, scoring equally well on capture–dispersal, and offering additional uncertainties due to the mixing action of the associated chaotic transients.

An example of this has been identified in the resonance of a softening system [2, 3], using the canonical escape equation of our earlier studies [7, 13, 14],

$$\ddot{x} + \beta\dot{x} + x - x^2 = F\sin(\omega t)\,.$$

Typical resonance response diagrams are shown in fig. 9. The top picture shows a safe jump from the saddle–node A which is determinate, the jump to resonance always restabilizing at R. The third picture also shows a determinate jump from A, corresponding now to a direct escape from the cubic well.

Of primary interest is the centre picture, in which saddle–node A is indeterminate, with jumps stabilizing either on the large amplitude harmonic oscillation R; on a coexisting subharmonic, Q, of order $n = 3$; or on the attractor at infinity, P, having escaping out of the well. This indeterminacy arises because at these parameter values we have a *tangled saddle–node* [2, 3], with A located on a fractal basin boundary as illustrated in fig. 10: here the saddle and node are adjacent black-on-white circles near the edge of the grey residual basin. This grey basin will be

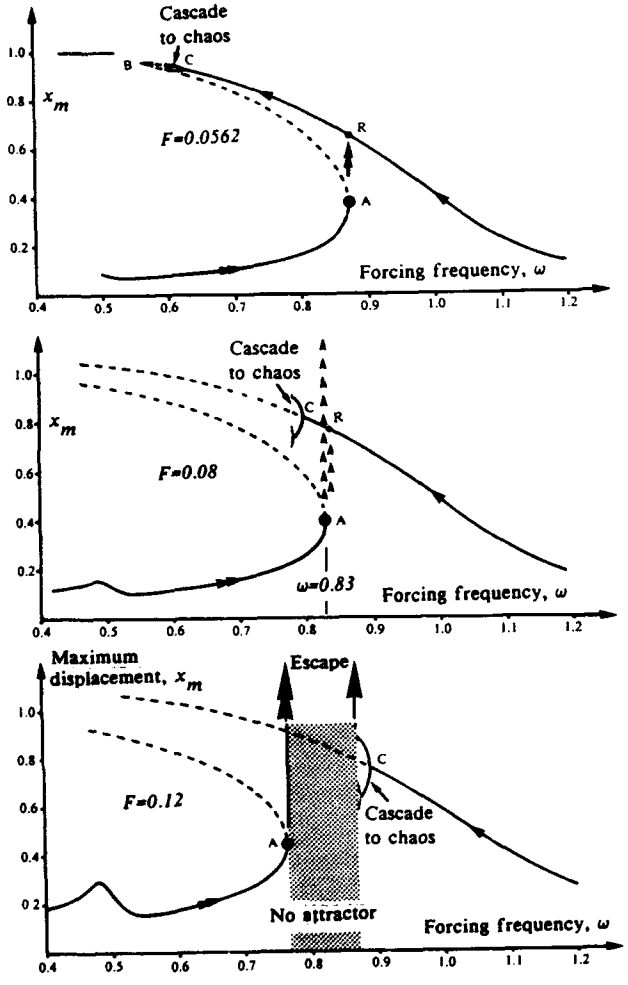

Fig. 9. Three resonance response curves for the canonical escape equation at $\beta = 0.1$, showing the variation of the maximum displacement, x_m, with the forcing frequency, ω. The top picture, at $F = 0.0562$ shows a safe jump to resonance from the saddle-node, A, that always restabilizes on the harmonic attractor, R. The middle picture, at $F = 0.08$, shows an indeterminate jump that may or may not restabilize on R. The bottom picture at $F = 0.12$ shows a determinate jump to infinity, out of the potential well: this occurs once the chaotic bifurcation terminating the cascade from C has passed to the right of A.

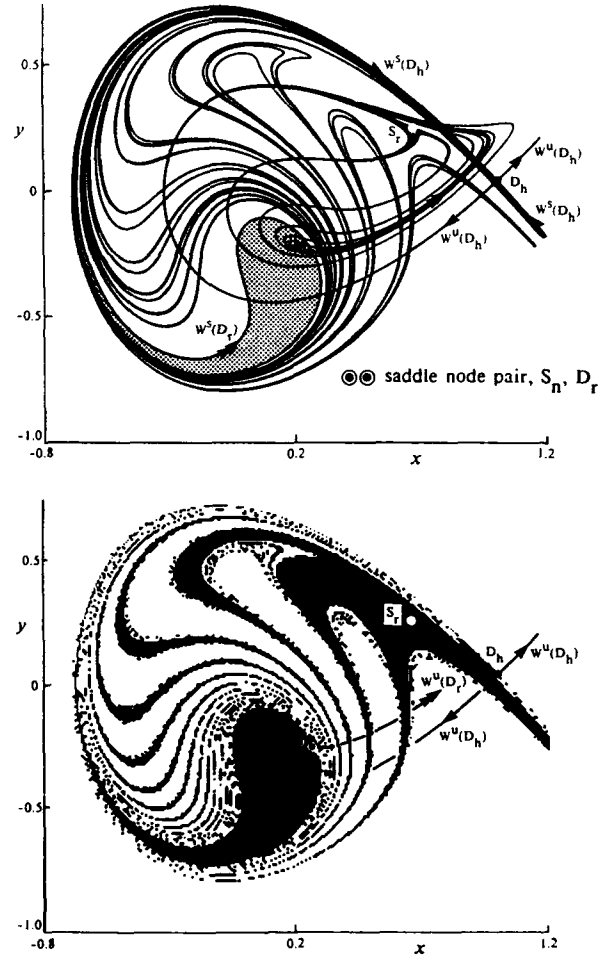

Fig. 10. Invariant manifolds (top) and basins of attraction (bottom) just prior to the tangled saddle-node, A, of the centre picture of fig. 9. Parameter values are $\beta = 0.1$, $\omega = 0.83$, $F = 0.0795$, with the Poincaré section defined at phase $\phi = 180°$. White represents the basin of the attractor at infinity, black the basin of the resonant harmonic oscillation, R, and grey the (residual) basin of the destabilizing node.

instantaneously striated by the basins of P, Q and R, in a manner similar to that of fig. 6, once the saddle and node are annihilated at the imminent cyclic fold [15].

This tangled saddle–node, an indeterminate bifurcation associated with a fractal boundary, gives us perhaps the highest possible degree of global unpredictability, represented by the upper right-hand point of fig. 1. Similar indeterminate bifurcations govern the escape from single-well to cross-well motions in the twin-well Duffing oscillator [1, 16, 17]: and for most softening oscillators there is a boundary crisis [18] near the top of the resonance response diagram which can also be indeterminate [1].

4. Concluding remarks

We have highlighted some of the phenomena that can give high degrees of global unpredictability in nonlinear dissipative dynamics. Indeterminate bifurcations are particularly severe events in terms of our qualitative capture–dispersal criterion. So precursor techniques that spot the imminent approach of a bifurcation in a slowly evolving system will be particularly useful [19]: and chaotic motions are helpful here because their wandering trajectories supply a lot of information about the underlying dynamics [20, 21]. Of course, none of the phenomena violate the continuity of response against starting and control perturbations, outlined in section 2. This is true both for the evolving and the nonevolving systems, but the former can give severe practical unpredictability if they involve a slow passage through an indeterminate bifurcation.

References

[1] H.B. Stewart and Y. Ueda, Proc. R. Soc. London A 432 (1991) 113.
[2] J.M.T. Thompson and M.S. Soliman, Proc. R. Soc. Lond. A 432 (1991) 101.
[3] M.S. Soliman and J.M.T. Thompson, Int. J. Bifurcation Chaos 1 (1991) 107.
[4] M.J. Lighthill, Proc. R. Soc. Lond. A 407 (1986) 35.
[5] C. Grebogi, S.M. Hammel, J.A. Yorke and T. Sauer, Phys. Rev. Lett. 65 (1990) 1527.
[6] S.W. McDonald, C. Grebogi, E. Ott and J.A. Yorke, Physica D 17 (1985) 125.
[7] J.M.T. Thompson, Proc. R. Soc. Lond. A 421 (1989) 195.
[8] J.M.T. Thompson and H.B. Stewart, Nonlinear Dynamics and Chaos (Wiley, New York, 1986).
[9] L.P. Shilnikov, Sov. Phys. Dokl. 20 (1976) 674.
[10] R.H. Abraham, Chaostrophes, intermittency and noise, in: Chaos, Fractals and Dynamics, eds. P. Fischer and W.R. Smith (Dekker, New York, 1985).
[11] E.C. Zeeman, Bifurcation and catastrophe theory, in: Papers in Algebra, Analysis and Statistics, ed. R. Lidl (AMS, Providence, RI, 1982).
[12] J. Guckenheimer and P. Holmes, Nonlinear Oscillations, Dynamical Systems and Bifurcations of Vector Fields (Springer, Berlin, 1983).
[13] J.M.T. Thompson and M.S. Soliman, Proc. R. Soc. Lond. A 428 (1990) 1.
[14] F.A. McRobie, Phil. Trans. R. Soc. London A 338 (1992) 557.
[15] F.A. McRobie and J.M.T. Thompson, Proc. R. Soc. Lond. A 435 (1991) 659.
[16] H.B. Stewart, A chaotic saddle catastrophe in forced oscillators, in: Dynamical Systems Approaches to Nonlinear Problems in Systems and Circuits, eds. F. Salam and M. Levi (SIAM, Philadelphia, 1988) 138.
[17] Y. Ueda, S. Yoshida, H.B. Stewart and J.M.T. Thompson, Phil. Trans. R. Soc. Lond. A 332 (1990) 169.
[18] C. Grebogi, E. Ott and J.A. Yorke, Physica D 7 (1983) 181.
[19] K. Wiesenfeld, J. Stat. Phys. 38 (1985) 1071.
[20] H.B. Stewart and A.N. Lansbury, Forecasting catastrophe by exploiting chaotic dynamics, in: Proc. EPRI Workshop on Applications of Chaos (San Francisco, December 1990) (Wiley, New York), to be published.
[21] J.D. Farmer and J.J. Sidorowich, Exploiting chaos to predict the future and reduce noise, preprint (1988).

Physica D 58 (1992) 273–283
North-Holland

PHYSICA D

Nonlinear analysis of data sampled nonuniformly in time

Joseph L. Breedon and Norman H. Packard

Center for Complex Systems Research – Beckman Institute and the Physics Department, University of Illinois, 405 North Mathews Avenue, Urbana, IL 61801, USA

Received 30 September 1991
Revised manuscript received 3 February 1992
Accepted 7 February 1992

We demonstrate how some of thee common methods in nonlinear data analysis can be modified to account for nonuniform time sampling by using *fuzzy* delay coordinate reconstructions. The effects of measurement noise and time sampling errors are compared. We have also developed a learning algorithm to find optimal fuzzy delay coordinate reconstructions of the data to suit one's goals. This can be employed to find representations optimized for measuring topological invariants, forecasting, control, or other goals.

1. Introduction

The process of observation and analysis is fundamental to science, but has many associated limitations. The most commonly discussed problems are dynamical noise, measurement noise, and small data sets. We will address some of the unique aspects of data sets which have an additional problem: they are not sampled uniformly in time or have an uncertainty in the observation time. In recent years, much work has been done to develop tools for analyzing nonlinear systems, but these techniques have not yet considered nonuniform time sampling. The development of *fuzzy* delay coordinate reconstructions is the primary result of this work. This arises as a natural generalization of delay coordinate state space reconstruction from a time series. We illustrate the implementation of fuzzy delays with mutual information and dimension calculations, and describe an alternate approach to obtaining optimal representations and forecasting which employs a learning algorithm.

[1] E-mail address: [breeden,n]@complex.ccsr.uiuc.edu

The problem of nonuniformly sampled data is often ignored because it is not as prevalent in laboratory experiments as measurement noise. In a controlled environment, slight uncertainties will always exist as to when a measurement was made, but these errors are commonly negligible. Not all scientific endeavors are so fortunate. Astronomers, for instance, must always contend with fluctuating weather conditions and competition for equipment use. Because of this, obtaining long continuous observations of a single object can be extremely difficult. Researchers in many fields are often under constraints which make uniform sampling difficult. We undertake the current investigation to accommodate the analysis of such data.

To develop techniques for nonuniformly sampled data, we must distinguish between discrete time systems (dynamics which could be described by iterative mappings) and continuous time systems (dynamical flows which could be described by differential equations). Data from either type of system might require the techniques to be presented here.

If a discretely timed system is sampled ran-

0167-2789/92/$05.00 © 1992 – Elsevier Science Publishers B.V. All rights reserved

domly, the result is a nonuniformly sampled time series of the kind we are considering. This could arise, for example, in observations of a pulsar under adverse conditions such that not all the emissions could be observed. Because of the potential for chaos in iterative systems, we cannot expect to be able to interpolate between observations. Numerically, we will study this with iterated maps where not every iteration is recorded.

Continuous time systems present a greater range of scenarios. The simplest situation is to have an uncertainty associated with the time of a measurement, $x(t_i \pm \delta t_i)$, similar to measurement noise, $x(t_i) \pm \delta x(t_i)$. We can relate time sampling errors to measurement errors if we assume the dynamics maintain a flow vector field $v(x)$ with probability density $\rho(x)$. By a Taylor series expansion to first order,

$$x_j(t_i \pm \delta t_i) \simeq x_j(t_i) \pm \dot{x}_j\, \delta t_i \equiv x_j(t_i) \pm \delta x_j(t_i)\,, \quad \forall j \in [1, D]\,, \tag{1}$$

where $\delta x_j(t_i) \equiv v_j(x_j(t_i))\, \delta t_i$. Furthermore, if the distribution of time sampling errors is given by $q(\delta t)$ and the system has an ergodic invariant probability distribution over the state space $\rho(x)$, we can relate this to a measurement noise distribution [1] of

$$p(\delta x_j) = \int \frac{\rho(x)\, q(\delta t)}{|(\mathrm{d}v_j/\mathrm{d}t)\, \delta t|} \times \delta(\delta x_j - v_j(x)\, \delta t)\, \mathrm{d}x(\delta t)\,. \tag{2}$$

Of course, this assumes δt is small relative to the typical divergence time of nearby trajectories as given by the Lyapunov exponents [2].

We also consider measurements which are taken nonuniformly in time, $\tau_i \neq i\, \Delta t$, with negligible uncertainty, $\delta t \simeq 0$. This is similar to the problem for discretely timed systems, and is the most interesting application of fuzzy delay coordinates.

In the following sections, we discuss how nonuniformly sampled data and fuzzy reconstructions (section 1) may be implemented in calculations of mutual information for finding good coordinates (section 2), dimension for determining the number of coordinates for a deterministic reconstruction (section 3), optimal representations based upon the experimenter's goals for analysis (section 4), and nonlinear modelling and forecasting (section 5). Finally, we give an example for the analysis of optical emissions of quasar B2 1308 + 326 (section 6).

2. Fuzzy delay coordinates

One of the primary tools in nonlinear analysis is the reconstruction of the state space from a time series. To acquire some basic information about a system's dynamics, one can plot the available time series, $x(t)$ versus derivatives $(\dot{x}(t), \ddot{x}(t), \ldots)$, delay coordinates [3] $(x(t - \tau_1), x(t - \tau_2), \ldots)$, or other reconstructed coordinates [4, 5]. We are using the state space reconstructions to find structure within the time series where none may be apparent, as in chaotic systems.

If the system is well sampled, i.e., the experimenter knows that the state of the system does not change significantly between observations, interpolation can be used to generate a data set which is uniformly spaced in time. However, for sparsely sampled or very noisy systems, interpolation is as likely to degrade as improve the data. In these situations, derivatives and most other reconstructed coordinates also add noise. We introduce *fuzzy* delay coordinate reconstructions, fig. 1, a modification of delay coordinates, so as to use the data unaltered. The state space will be generated using $(x(t), x(t - \tau_1'), x(t - \tau_2'), \ldots)$ where $\tau_i' \in (\tau_i - \delta\tau_i, \tau_i + \delta\tau_i]$. Rather than defining a coordinate by a single delay τ_i, we are allowing for a tolerance window of width $2\,\delta\tau_i$ about τ_i. The point closest to the center of this window will be accepted for the reconstruction. The problem of which coordi-

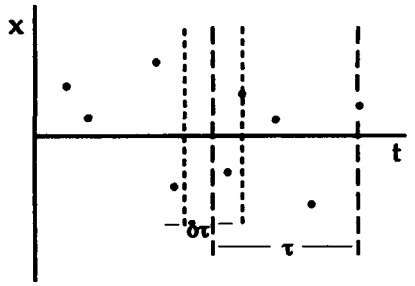

Fig. 1. The generation of fuzzy delay coordinates. τ is the commonly defined delay and $\delta\tau$ is the tolerance window about that delay for accepting sets of points into the state space reconstruction. The point closest to τ within the range $[\tau - \delta\tau, \tau + \delta\tau]$.

nates to use and how many is a major topic of this paper.

It is important to realize that the fuzzy reconstructions we have introduced do not directly smooth the data. The information in the original observation times is still available, and will be exploited in modelling and forecasting, (sections 6 and 7).

Dynamical smoothing of the state space trajectories [6] is sometimes a possibility, but this requires first reconstructing a state space from our nonuniformly sampled data, which brings us back to the need for fuzzy reconstructions. In fact, once the learning algorithm described in section 3 has been applied, we may be able to smooth the original data and interpolate to uniformly spaced measurements.

3. Mutual information

To determine which time delays to use in a state space reconstruction, mutual information [7] is frequently employed. Mutual information is a nonlinear measure of how correlated are two time series, and is calculated from the joint probability distributions as a function of delay, τ, as

$$M(\tau) = \left\langle \log_2\left(\frac{p_{x(t),x(t+\tau)}}{p_{x(t)} p_{x(t+\tau)}} \right) \right\rangle . \tag{3}$$

We are using it to measure the amount of new information introduced by a given choice of delay. The delay corresponding to the first minimum of $M(\tau)$ should give a reconstruction in which the coordinates are maximally independent and avoid the loss of information through chaos that is potentially present in subsequent minima [8]. Topologically, the minima in $M(\tau)$ are those reconstructions for which the dynamics are maximally spread in the state space. This is beneficial to calculating invariants of the dynamics, particularly in the presence of noise.

The calculation of mutual information has always assumed data which was uniformly sampled in time. Since perfectly uniform sampling intervals are almost an experimental impossibility, it is appropriate to ask what tolerance this technique shows to sampling noise. Based upon eq. (2), we have seen that the probability density of time sampling errors, $q(\delta t)$, can be related to an effective probability density of measurement errors, $p(\delta x)$. If the measurements $\{x(t_i)\}$ were made with n-bit resolution, these errors will cause a loss of

$$m = n \, \frac{2\langle \delta x \rangle}{\max(x) - \min(x)} \tag{4}$$

bits leaving $n' = n - m$ bits of information in the observations. Since the maximum of $M(\tau)$ equals the bits of information available, this will cause $M(\tau)$ to decrease with increasing $\langle \delta x' \rangle$. However, this does not suggest any dependence upon τ. Therefore, it is reasonable to expect that while the mutual information will decrease with $\langle \delta x' \rangle$, the location of the minima may be preserved.

We consider the case of a Rössler system [9],

$$\dot{x} = -y - z ,$$

$$\dot{y} = x + 0.343y ,$$

$$\dot{z} = 1.83 + (x - 9.75)z ,$$

sampled nonuniformly producing a finite length data set. By making fuzzy reconstructions, we can choose a width $\delta\tau$ about the delay τ to

maximize the amount of usable data while preserving the location of the minima in $M(\tau)$. If $\delta\tau$ is too small, we are left with so little data that $M(\tau)$ becomes lost in the noise due to finite-size effects. The uncertainty in the mutual information is

$$\delta M \simeq \frac{\beta(\beta-2)}{2N}, \tag{5}$$

where β is the number of bins used in the calculation of the probability distributions and N is the number of data points [10].

The mutual information for a randomly sampled data set from the Rössler system is shown in fig. 2 as a function of τ and $\delta\tau$. Cross-sections of this plot are shown in fig. 3 with the error bars included. From these figures, we find that mutual information is very tolerant to large $\delta\tau$. Although the difference in heights between successive maxima and minima decreases as $\delta\tau$ increases, the locations of those extrema are essentially unchanged. In fact, larger $\delta\tau$ combined with the resulting availability of more data acts to smooth the curve from small $\delta\tau$. This implies that there is

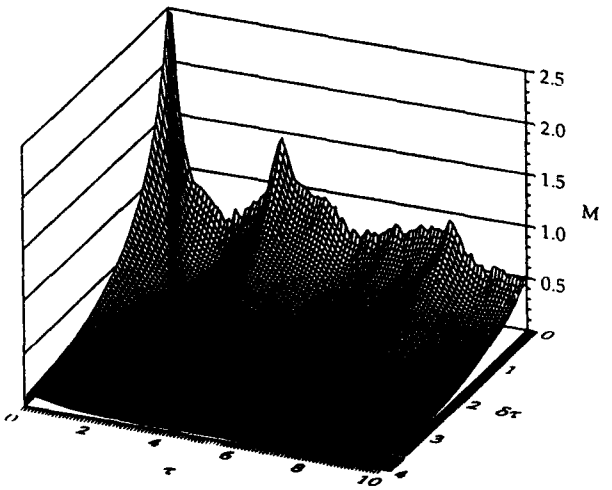

Fig. 2. The mutual information landscape over reconstruction coordinates τ and $\delta\tau$ is shown for the Rössler system. A fixed data set of 25 000 nonuniformly sampled points was used so that as $\delta\tau$ increases, more data becomes available. The ridge corresponding to $\tau = \delta\tau$ occurs because of the asymmetric nature of the windows for $\tau < \delta\tau$. Those values should be ignored.

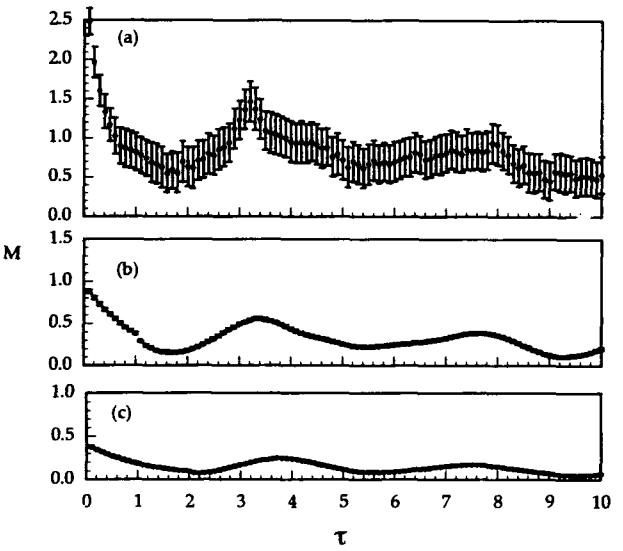

Fig. 3. Slices from fig. 2 are shown with the error bars included: (a) $\delta\tau = 0.05$, (b) $\delta\tau = 1.0$, and (c) $\delta\tau = 2.0$. As $\delta\tau$ increases, the mutual information and the statistical errors therein decrease. Note that even for $\delta\tau = 1.0$, the location of the first minimum is preserved. This is a very large window since the average time to orbit the attractor is ~6.0.

an optimal $\delta\tau > 0$ which gives the best information about the location of the minima. The only time the position of the minima is severely effected is when $\delta\tau > \tau$, which means that τ is actually no longer the most probable delay between points in the reconstruction.

We have conducted the same studies with iterated maps, e.g. Hénon [11] and Ikeda maps, with similar results. The only differences were that $\delta\tau$ increases by integer amounts and minima in M are less informative since the natural delay to use with most maps is $\tau = 1$. The behavior with $\delta\tau$ as documented above remains unchanged.

4. Dimension

Mutual information gives us a criterion with which to choose reconstruction coordinates. By computing the topological dimension of the system, we can estimate how many of these coordinates are required for a deterministic state space representation. It has been shown that if the

fractal dimension of the manifold is m, an embedding of the system can be generated with n coordinates if $n > 2m$ [12].

Many different dimensions can be calculated to characterize a system [13], but we will focus upon the correlation dimension [14] because of its efficiency and broad use. The same generalizations carry over to the other techniques. The limitations of correlation dimension calculations have been examined for measurement noise [15] and sparse data sets [16], but have not yet considered nonuniformly sampled data.

The correlation dimension for a given reconstruction is determined by examining the correlation integral,

$$C(r) = \frac{1}{N^2} \sum_{i \neq j} \Theta(r - |X_i - X_j|) , \qquad (6)$$

where Θ is the Heaviside function and $C(r)$ is the number of pairs of points whose distance is less than r. The vectors X_i are typically constructed from the time series, $x(t)$, with delay coordinates. A high dimensional reconstruction is used to fully unfold the dynamics. If we have a scaling region, $C(r) \propto r^{\nu}$, over a large range of r then ν is taken to be the correlation dimension. Here again we can choose a delay, $\tau' \in [\tau - \delta\tau, \tau + \delta\tau]$, with which to construct a fuzzy state space and perform the calculation. In this case, we can refer back to the mutual information to select the $\delta\tau$ which admits the most data without destroying the state space correlations.

If we consider a nonuniformly sampled continuous system such as our Rössler attractor example, we can show experimentally how the error in the sampling interval $\delta\tau$, is related to measurement noise, fig. 4. We extract the correlation dimension by computing the slope of the scaling region. These plots typically have at least three distinct regions. For very small r, every point appears to be isolated, so the slope is 1. Past a certain large r, the whole attractor is enclosed so $C(r)$ is constant and again the slope is 1. When there is no noise in the system, the

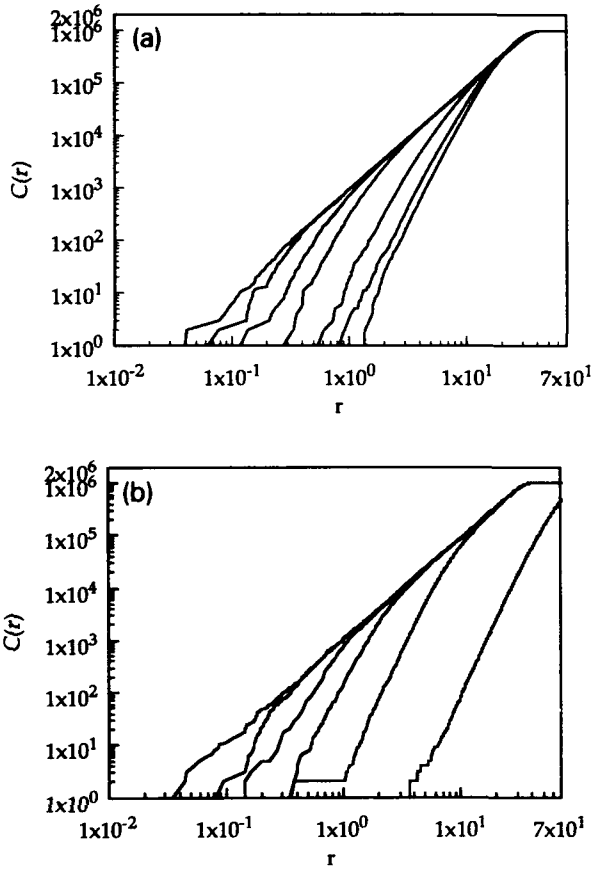

Fig. 4. Correlation dimension calculations are shown for increasing time sampling errors (a), and measurement noise (b). For fig. (a), the curves from left to right correspond to time sampling errors of 0.0, 0.001, 0.01, 0.04, 0.1, 0.4, and 1.0. For fig. (b), noise amplitudes of 0.0, 0.1, 0.4, 1.0, 4.0, and 10.0 are shown. Note that the regions of fractal scaling shrink as the noise amplitudes increase. The calculation was done with a five dimensional embedding space. Below the fractal scaling region, the curves all show a slope consistent with noise in a five dimensional embedding space.

remainder of the curve defines the fractal scaling region and gives $\nu = 1.9$.

When noise of either type is added, the slope does not change; but the scaling region on which it is defined shrinks as the small scale structure of the attractor is destroyed. The slope of the lost region becomes equivalent to the embedding dimension, since the added noise is uniformly space filling. The difference between the two cases is in the rate at which the fractal scaling region disappears. By plotting the size of the scaling region (in $\log(r)$) versus the noise am-

plitude, we obtain a simple relation between time sampling errors and measurement errors, fig. 5.

Although nonuniform time sampling and measurement noise have similar effects upon the calculations, we have more flexibility when dealing with timing errors. Dimension calculations always require large amounts of data, so if we have a very limited data set, we should choose $\delta\tau$ as large as possible. This allows us to obtain a value for ν even though the scaling region is reduced. If, however, we have a large amount of data, we can set $\delta\tau$ very small to increase the scaling region and improve the accuracy of our calculations.

When we consider nonuniformly sampled data from a perfectly timed system, such as an iterated map, we find a very different behavior. Taking randomly sampled data from the Hénon map [11],

$$x_{n+1} = y_n - 1.4x_n^2 + 1 ,$$

$$y_{n+1} = 0.3x_n ,$$

we find that for a given choice of delay coordinate, τ, the long range fractal structure degenerates as $\delta\tau$ is increased, but the small scale structure is intact, fig. 6. This is easily understood if one considers the state space reconstruction resulting from the coordinates $(x_n, x_{n+\tau'})$, $\tau' \in [1, 3]$, i.e., $\tau = 2$ and $\delta\tau = 1$. What we actually have is a superposition of three separate reconstructions, (x_n, x_{n+1}), (x_n, x_{n+2}), and (x_n, x_{n+3}). These three reconstructions have the same topological features, but they cover the state space very differently. This leaves the small scale structure mostly undisturbed, but the longer range fractal scaling breaks down.

These examples for continuous and iterated systems show that fuzzy reconstructions are an effective method for maximizing the use of the available data without disturbing the calculation of the dimension. In combination with mutual information, this provides a possible procedure for obtaining representations of nonuniformly sampled data. For both these statistics, we show that coarse graining the time is similar to measurement noise, which is not surprising. The nontrivial aspect is determining what coarse graining makes best use of the available data.

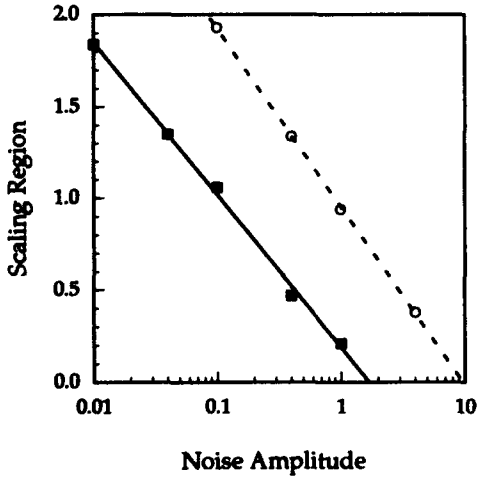

Fig. 5. The size of the fractal scaling regions from fig. 5 are graphed versus the noise amplitude. The filled squares represent time sampling errors and the open circles are measurement noise. A simple fit to the data shows that a sampling error of $\delta\tau$ corresponds to an average measurement noise of $\epsilon 0.5\ (\delta\tau)^{0.9}$. The uncertainty in this exponent is large, and under perfect statistics might be unity.

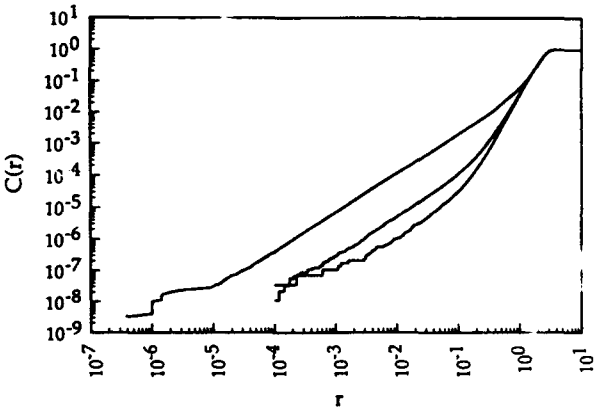

Fig. 6. Correlation dimension calculations for nonuniformly sampled data from the Hénon map. A five dimensional embedding was used with $\tau = 2$. The curves represent $\delta\tau = 0$, 1, and 2 from left to right. Note that the slope of the fractal scaling region is preserved, but the size of this region decreases δt increases. The break down for small distances, r, is due to poor statistics.

5. Optimal representations

The analysis of the two previous sections was an attempt to find a "good" representation of the current state of a dynamical system. This meant finding a representation of the system which was deterministic and well spread in the state space so as to reveal the details of the topology. In this section we examine the concept of an *optimal* representation and discuss modifications to a recently developed learning algorithm [5] to find optimal representations of nonuniformly sampled data.

To determine what is meant by an *optimal representation*, one must consider the ultimate goal of the representation. It is unlikely that any single representation will be optimal for all possible objectives. We have discussed the purpose for using mutual information; however, this representation will not necessarily be optimal for other pursuits, such as forecasting or noise reduction [6], where optimization is done with respect to the future state of the system. If one's goal is forecasting or control [17] of the observed variable only, the quality of a reconstruction of any dimensionality should be based upon the predictability of only the observable, $x(t)$. Many other possibilities can be envisioned. We have proposed a technique for search through the space of possible coordinates to find the representation that best suits the goals of the experimenter. This employs a learning algorithm based upon the genetic algorithm [18] to find optimal representations, because of the potential complexity of the fitness landscape being searched. Since we are searching through dimensions, the dimensionality of the quality landscape is not even known. A search is advantageous, because situations arise in which the best D-dimensional representation is not a subspace of the best $(D+1)$-dimensional representation [19]. In such cases, building a representation by sequentially adding new coordinates would be ineffective. This algorithm is designed to search through the space of possible representations to locate the one best suited to the stated goal. In the present context, we restrict this search to fuzzy delay coordinates.

For the search, each state space reconstruction is encoded in a "genome" where the "genes" describe how each coordinate is generated. For example, genome $(\tau_1, \delta\tau_1; \tau_2, \delta\tau_2)$ specifies a three dimensional representation $(x(t), x(t+\tau_1'), x(t+\tau_2'))$ where $\tau_1' \in [\tau_1 - \delta\tau_1, \tau_1 + \delta\tau_1]$, $\tau_2' \in [\tau_2 - \delta\tau_2, \tau_2 + \delta\tau_2]$. During the search, τ_i, $\delta\tau_i$, and the number of these are all optimized (fig. 7).

As mentioned, many goals and corresponding quality functions are possible. As an example, we will use local linear predictability as our criterion. This is done by modelling a D-dimensional representation locally as

$$\frac{x_i(t_i^1) - x_i(t_i^0)}{t_i^1 - t_i^0} = \boldsymbol{m}_i \cdot \boldsymbol{x} + b_i\,, \quad \forall i \in [1, D]\,, \qquad (7)$$

where $\boldsymbol{m}_i$ and b_i are free coefficients [20], $\boldsymbol{x}$ is the fuzzy delay vector, and $x_i(t_i^0) \rightarrow x_i(t_i^1)$ under the dynamics. To apply this "locally", we partition the state space using a k–D tree data structure [21]. We define the quality of a given reconstruc-

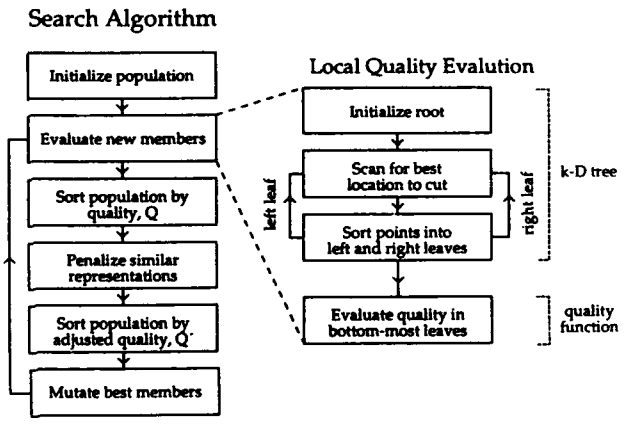

Fig. 7. A schematic of the learning algorithm. The search begins by constructing an initial random population of genes. These representations are evaluated according to the quality function and ranked by the quality, Q. The highest quality members of the population are mutated using the genetic operators. These new members are then evaluated, ranked, and so forth. Eventually the population converges to an optimal representation.

tion as $Q \equiv 1/\eta$ where

$$\eta \equiv \frac{1}{N_\ell} \sum_{k=1}^{N_\ell} \sum_{j=1}^{M_k} \frac{1}{M_k D} \sum_{i=1}^{D} \{x_i^j(t_i^1) - [(\boldsymbol{m}_i \cdot \boldsymbol{x}^j - b_i)(t_i^1 - t_i^0) + x_i^j(t_i^0)]\}^2 , \quad (8)$$

and N_ℓ is the number of leaves and M_k is the number of data points in the kth leaf.

We test this numerically upon the same Rössler system data discussed earlier. In fig. 8, we show the quality is a function of τ and $\delta\tau$. We restricted the analysis to 1,000 data points to illustrate the same interplay between maximizing the data used and minimizing the time sampling errors that was seen for mutual information. Here, we find a preferred reconstruction of $\tau \simeq 0.9$ and $\delta\tau \simeq 0.2$. As before, the values for $\tau < \delta\tau$ are unreliable. Although we show a quality landscape in τ and $\delta\tau$ for two dimensional reconstructions, under normal operation the program would search through this space and in higher dimensions to find the optimal representation.

Note that for this modelling, the observation time is exploited whereas the previous statistics ignored it.

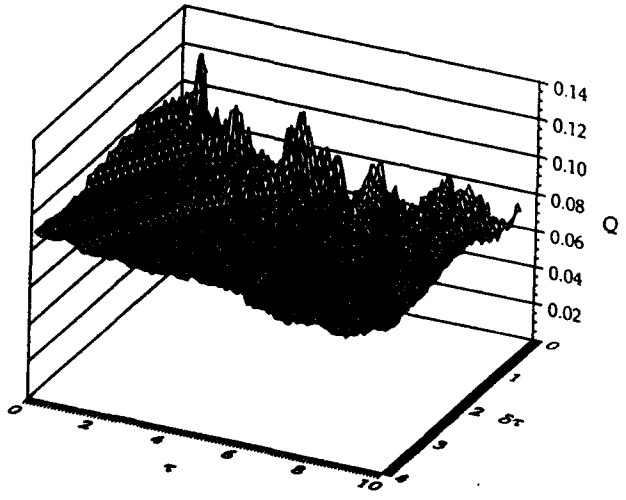

Fig. 8. The quality for prediction using two dimensional reconstructions with delay coordinate τ and width $\delta\tau$ is shown as a function of these variables using 1000 nonuniformly sampled data points from the Rössler system in fig. 2. In order to collect enough data points for the modelling, a value $\delta\tau > 0$ was preferred. The best parameters were $\tau \simeq 0.9$ and $\delta\tau \simeq 0.2$.

6. Modeling and forecasting

To this point, we have focussed our attention upon the fundamental problem of how best to represent nonuniformly sampled time series data. Now, we would like to discuss briefly some of the options available for modelling and forecasting. Even though some methods do both, we distinguish modelling and forecasting, because we can construct models which have explanatory value, or do forecasting without improving our understanding of the system's dynamics.

When we consider nonuniformly sampled data that we may be unable to interpolate, our options are severely limited. If a single, globally defined model of the dynamics is desired, equations of motion in the form of a coupled set of ordinary differential equations (ODEs) may be fit parametrically to the data [22]. In this technique measurements at any time are acceptable since the equations are numerically integrated from t_n to t_{n+1} to compare the predicted and experimental values. This method can be applied when all the variables in the model equations are measured experimentally, or the unobserved variables may be derived from the observed variables via the model [4]. Obviously, this technique works best when one already has a theoretical model for the system with a few free parameters. In fact, this is one of the few modelling procedures in which prior physical knowledge about the system can be easily incorporated directly into the model.

While this method utilizes ODEs to generate a global model, if forecasting is our only objective, it may be more effective to construct several sets of locally defined ODEs. In essence, this is what was done in the Rössler system example of the previous section where local linear difference equations were employed (eq. (7)). Whereas before we were using this to find a state space

representation of the system to provide physical information, we could also use this to predict the future state of the system. In real time applications, this procedure is typically far less computationally intensive than the global modelling procedure.

7. Example: Quasar emissions

To illustrate the application of these concepts, we consider observations of the optical emissions of quasar B2 1308 + 326. The data set consists of 221 nonuniformly sampled measurements of the B magnitude flux (fig. 9). A quick inspection of the data shows that it is unreasonable to consider any interpolation, since we appear to have dynamics on time scales short compared to the observation intervals. This indicates a need for fuzzy delay coordinate analysis.

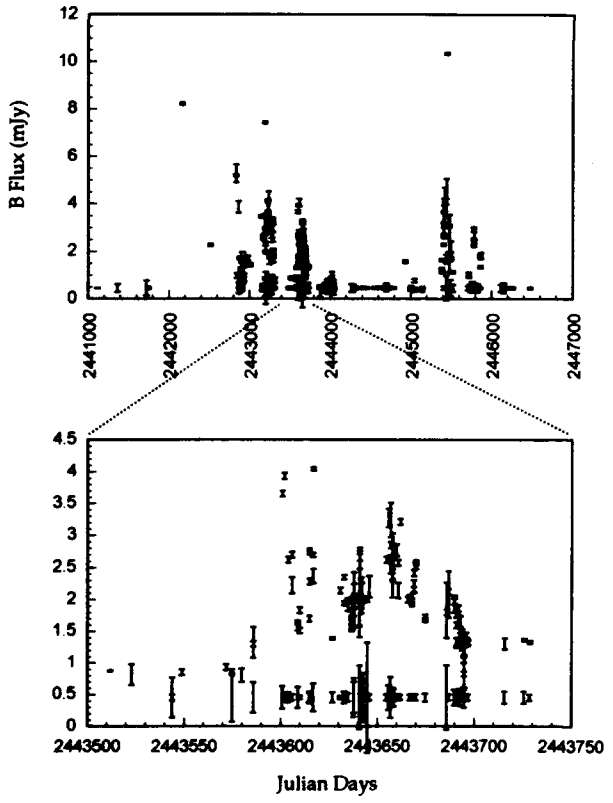

Fig. 9. Measurements of the B flux of quasar B2 1308 + 326 with error bars. The time is given in Julian days and the flux is mJy.

Also, the data is very sparse – so sparse that mutual information or dimension calculations would not be statistically significant. Therefore, we employ the learning algorithm discussed in section 5 to learn a predictive state space reconstruction of the data. Because of the poor quality of the data, we cannot find any of the usual invariants: dimension, Lyapunov exponents, etc. Instead, we just wish to determine if the data comes from a dynamical system rather than a noise process.

To test for dynamics, we first compute the quality of the best learned representation. This was simply $Q = 1/\eta$ where η was the estimation error normalized by the error bars given with the data. To establish a null-hypothesis, we take the original data and shuffle it in time, i.e., we take the original observation times and measurements and randomly pair them to generate a randomized data set. This shuffled data is given to the learning algorithm to maximize the quality. We repeated this process many times and histogrammed the qualities (fig. 10).

We find that the histogram of models for shuffled data has a mean quality of $\mu = 0.011$ and standard deviation of $\sigma = 0.0036$. Since the model of the original data has $Q = 0.26$, it is 69σ away from the null-hypothesis. This means that

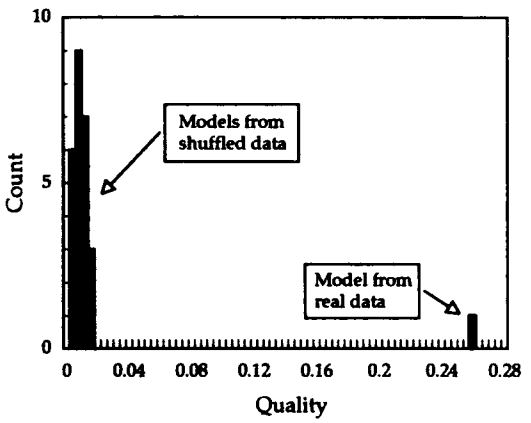

Fig. 10. A histogram of the qualities from the shuffled data tests of the quasar data. The single point at large quality is from the real data. The separation between this point and the shuffled data null-hypothesis indicates a time dependence in the quasar emissions.

with high probability, the time ordering of this data is important for an accurate modelling. This does not exclude a time-correlated noise process, but it is the first evidence that the data is not purely random. The astrophysical implications of the quasar analysis are discussed in greater depth by Breeden, Mufson, and Packard [23].

8. Conclusions

Nonlinear analysis is still in its adolescence. As a logical step in its growth, we felt it necessary to demonstrate that two of the more commonly used tools, mutual information and correlation dimension, are applicable to situations involving nonuniform time sampling. This, in itself, is an important question since almost all data from real experiments exhibit this to some degree. We accomplished this by first generalizing the concept of delay coordinate reconstructions to *fuzzy* reconstructions. These results are not surprising, but we have also found that an intelligent choice of $\delta\tau$ can make much more effective use of the data than some arbitrary binning. Specifically, in sparse data situations, choosing a large window, $\delta\tau$, about the delay coordinate, τ, can improve the accuracy of the calculations by increasing the amount of usable data without destroying the results.

Through analytic calculations and numerical studies of dimension calculations, we have demonstrated the relationship between measurement noise and time sampling errors. By comparing the size of the fractal scaling regions we can quantify the relationship between these effects for a given example.

Fuzzy reconstructions are also a natural extension to the learning algorithm developed to search for optimal representations. In this case, the learning algorithm chooses the best window in delay, $\delta\tau$, as part of the delay coordinates to facilitate the stated goal. This can be a beneficial preprocessor to calculating dynamical invariants (like dimension) to get the fullest use of the data. In a recent application of this technique, optical emissions from a quasar were shown to have some predictability when compared to randomly shuffled versions of the same data [23]. This is despite the fact that the data was nonuniformly sampled, noisy, and sparse – too sparse to apply mutual information or dimension calculations. It is important to notice that while this modelling procedure operated within the fuzzy state space reconstruction, the actual times of the observations were not ignored as in the mutual information and correlation dimension examples. The times are added information which improve the accuracy of the model.

Finally, we commented that nonuniform sampling need not be an impediment to modelling and forecasting. Techniques have been developed for constructing global models (ODEs) which are not at all impaired by this sort of data. Likewise, the learning algorithm coupled with k–D trees and local linear difference equations (or ODEs) is an effective forecasting method which can handle nonuniform sampling well.

Acknowledgements

This work was supported in part by National Science Foundation grant number NSF PHY86-58062 and the research workshop Complexity and Evolution at the Institute for Scientific Interchange, Turin, Italy.

References

[1] A. Papoulis, Probability and Statistics (1989).
[2] A. Wolf, J. Swift, H. Swinney and J. Vastano, Physica D 16 (1985) 285; P. Bryant, R. Brown and H. Abarbanel, Phys. Rev. Lett. 65 (1990) 1523.
[3] N. Packard, J. Crutchfield, J.D. Farmer and R. Shaw, Phys. Rev. Lett. 45 (1980) 712.
[4] J. Breeden and A. Hübler, Phys. Rev. A 42 (1990) 5817.
[5] J. Breeden and N. Packard, Center tor Complex Systems Research, University of Illinois, Technical Report CCSR-91-3 (1991).

[6] E. Kostelich and J. Yorke, Physica D 41 (1990) 183; J.D. Farmer and J.J. Sidorowich, Los Alamos National Laboratory, Technical Report LA-UR-90-653 (1990).
[7] A. Fraser and H. Swinney, Phys. Rev. A 33 (1986) 1134; A. Fraser, IEEE Trans. Information Theory 35 (1989) 245.
[8] R. Shaw, The Dripping Faucet as a Model Chaotic System (Ariel Press, Santa Cruz, CA, 1984).
[9] O. Rössler, Phys. Lett. A 57 (1976) 397.
[10] W. Li, J. Stat. Phys. 60 (1990) 823.
[11] M. Hénon, Commun. Math. Phys. 50 (1976) 69.
[12] T. Sauer, J. Yorke and M. Casdagli, preprint (1991).
[13] J.D. Farmer, E. Ott and J. Yorke, Physica D 7 (1983) 153; H. Hentschel and I. Procaccia, Physica D 8 (1983) 435; Y. Termonia and Z. Alexandrowicz, Phys. Rev. Lett. 51 (1983) 1265; P. Grassberger, Phys. Lett. A 107 (1985) 101.
[14] P. Grassberger and I. Procaccia, Phys. Rev. Lett. 50 (1983) 5; P. Grassberger and I. Procaccia, Physica D 9 (1983) 189.
[15] A. Ben-Mizrachi, I. Procaccia and P. Grassberger, Phys. Rev. A 29, (1984) 975; J. Caputo, B. Malraison and P. Atten, in: G.Mayer-Kress, ed., Dimensions and Entropies in Chaotic Systems, Quantification of Complex Behavior (Springer, Berlin, 1986) p. 180.
[16] N. Abraham, A. Albano, B. Das, G. DeGuzman, S. Yong, R. Gioggia, G. Puccioni and J. Tredicce, Phys. Lett. A 114 (1986) 217; P. Grassberger, Phys. Lett. A 128 (1988) 369; J. Ramsey and H. Yuan, Nonlinearity 3 (1990) 155.
[17] A. Hübler and E. Lüscher, Naturwissenschaften 76 (1989) 67; E.A. Jackson and A. Hübler, Physica D 44 (1990) 407; J. Breeden and N. Packard, Center for Complex Systems Research, University of Illinois, preprint (1992), submitted to 1st IEEE Conf. on Control Applications.
[18] J. Holland, Adaptation in Natural and Artificial Systems (University of Michigan Press, 1975); D. Goldberg, Genetic Althorithms in Search, Optimization, and Machine Learning (Addison-Wesley, 1989); N. Packard, J. Complex Sys. 4 (1990) 543.
[19] F. Richards, T. Meyer and N. Packard, Physica D 45 (1990) 189.
[20] J.-P. Eckmann and D. Ruelle, Rev. Mod. Phys. 57 (1985) 617.
[21] S. Omohundro, J. Complex Syst. 1 (1987) 273.
[22] J. Cremers and A. Hübler, Z. Naturforsch. 42a (1986) 797; J. Crutchfield and B. McNamara, J. Complex Sys. 3 (1987) 417; T. Eisenhammer, A. Hübler, N. Packard and J.S. Kelso, Center for Complex Systems Research Technical Report CCSR-89-7 (1989); J. Breeden, F. Dinkelacker and A. Hübler, Phys. Rev. A 42 (1990) 5827.
[23] J. Breeden, S. Mufson and N. Packard, Center for Complex Systems Research, University of Illinois preprint (1991).

Physica D 58 (1992) 284–287
North-Holland

PHYSICA D

Analysis of noisy signals

A. Rabinovitch[a] and R. Thieberger[a,b]

[a]*Physics Department, Ben Gurion University, Beer Sheva, Israel*
[b]*Department of Physics, N.R.C.N., P.O. Box 9001, Beer Sheva, Israel*

Received 7 October 1991
Revised manuscript received 10 February 1992
Accepted 2 March 1992

A method is developed to obtain all possible pure signals which could have been the origins of a given noisy signal. The method also provides an explicit way to calculate power spectra of these signals.

1. Introduction

Autoregressive moving average (ARMA) models have been extensively used for predicting the time evolution of signals [1]. They constitute both the first approximation to use when the signal is not known to be chaotic, and a general method of obtaining the pattern of the "non deterministic" part of a signal by Wold's decomposition [2]. Recently the ARMA method has been applied, in this sense, to the analysis of chaotic data [3, 4]. Such analysis should however be carried out with care. For chaotic and other essentially non-linear signals the non-deterministic part is only guaranteed to be "uncorrelated", while the ARMA approach implies "independence" [6]. Thus, e.g., an ARMA analysis of the chaotic logistic map $x \to bx(1-x)$ for $b < 4$ yields some "patterned" part [4], while for $b = 4$ a completely "uncorrelated" generator (which can be interpreted as white noise) ensues. A further decomposition of the non-deterministic part can be based on general non-linear methods [5, 7] or on specific more direct methods [8] when chaotic attractors are known or assumed to exist.

When a Box–Jenkins [1] or similar analysis is carried out, a specific ARMA filter is obtained as being responsible for "creating" the signal from a random shock generator. Usually there appears an added white noise as a result of measuring instruments or as an intrinsic property of the process measured itself. The amount of noise included in the signal is generally unknown. This noise brings about alterations in the ARMA parameters obtained [9] and hence also in the predicted time behaviour. Since the exact magnitude of such noise is not usually available, it is evident that a complete unravelling of the "pure" signal from the noisy one is impossible. It would seem however of advantage to have even a partial possibility of "purifying" the signal, such as a knowledge of all possible pure signals which could have played the role of our signal's origin under the addition of different amounts of white noise.

For the ARMA (2, 2) case a complete analysis was carried out previously [10]. By a non-linear transformation the loci of the parameters, for all possible pure signals, were shown to lie on a straight line. The Fourier transform and predicted time evolution could be calculated. Here we will discuss the general ARMA (m, l) case.

0167-2789/92/$05.00 © 1992 – Elsevier Science Publishers B.V. All rights reserved

2. Method

We consider a stationary and invertible signal of an ARMA (m, l) type, $l \le m$, given by

$$\hat{Z}_t = \frac{1 - q_1 B - q_2 B^2 - \cdots - q_l B^l}{1 - p_1 B - p_2 B^2 - \cdots - P_m B^m}\, \hat{\zeta}_t , \qquad (1)$$

where t is the discrete time, $\hat{Z}$ is the "centered" signal (i.e. $\hat{Z}_t = Z_t - \langle Z_t \rangle$), $p_1, \ldots, p_m$, $q_1, \ldots, q_l$ are the AR and MA parameters, respectively, $\hat{\zeta}_t$ is the random shock generator with zero mean and variance σ_ζ^2 and B is the shift operator. We assume that this signal is composed of an original "pure" signal $\hat{X}_t$ with an added white noise $\hat{b}_t$ with variance σ_b^2:

$$\hat{Z}_t = \hat{X}_t + \hat{b}_t . \qquad (2)$$

The pure signal $\hat{X}_t$, has to be of the ARMA (m, m) type [11].

Since the addition of white noise does not change the AR parameters [1] the form of X_t is

$$\hat{X}_t = \frac{1 - q_{1,0} B - q_{2,0} B^2 - \cdots - q_{m,0} B^m}{1 - p_1 B - p_2 B^2 - \cdots - p_m B^m}\, \hat{a}_t . \qquad (3)$$

Here $q_{i,0}$ are the pure signal MA parameters and $\hat{a}_t$ is the generator of the pure signal, having a variance σ_a^2. The values q_i, p_i, σ_ζ^2 are obtained directly from the signal, on using any ARMA program, and we wish to estimate $q_{i,0}$, σ_a and σ_b which are unknown.

Let us denote

$$\hat{Y}_t = (1 - p_1 B - p_2 B^2 - \cdots - p_m B^m)\hat{Z}_t , \qquad (4)$$

then, calculating $E\{Y_t Y_{t+\tau}\}$ and using eqs. (1)–(3) and the white noise character of $\hat{a}_t$, $\hat{b}_t$ and $\hat{\zeta}_t$, we obtain

$$\sigma_a^2 \sum_{i=0}^{m-j} q_{i,0} q_{i+j,0} = \sigma_\zeta^2 \sum_{i=0}^{m-j} q_i q_{i+j} - \sigma_b^2 \sum_{i=0}^{m-j} p_i p_{i+j} , \qquad (5)$$

for $j = 0, 1, \ldots, m$. Here $q_0 \triangleq p_0 \triangleq q_{0,0}$ are defined as -1.

These $m+1$ equations for the $m+2$ unknowns ($q_{i,0}$, $i = 1, 2, \ldots, m$, σ_a^2 and σ_b^2) define the locus of all possible original processes. These equations are non-linear and rather inconvenient to solve directly[*1]. Since they depend upon the autocorrelations they have appeared repeatedly in time series analysis [12]. We present here a transformation which markedly simplifies and facilitates the analysis. Define:

$$u^j = \frac{\sum_{i=0}^{m-j} q_{i,0} q_{i+j,0}}{q_{m,0}} , \quad u_Z^j = \frac{\sum_{i=0}^{m-j} p_i p_{i+j}}{p_m} ,$$

$$u_M^j = \frac{\sum_{i=0}^{m-j} q_i q_{i+j}}{q_m} , \quad j = 0, 1, \ldots, m-1 ,$$

and

$$\delta = \frac{q_m}{p_m}\, \frac{\sigma_\zeta^2}{\sigma_b^2} . \qquad (6)$$

By inserting eq. (6) into eq. (5) one obtains the locus as a straight line in m dimensions:

$$u^j = u_Z^j + b(u_M^j - u_Z^j) , \quad b = \delta/(\delta - 1) \qquad (7)$$

We thus see both the reduction of dimension (m vs. $m+1$ in eq. (5)) and the linear character of the locus in u-space. The marked advantage of the transformation is apparent if the evaluation of the power spectrum[*2] is one's main interest. This point will now be discussed.

[*1] Using MATHEMATICA, we had difficulties in solving the set of equations (5). For example, in the case $m = 4$ discussed in fig. 1, no solution could be obtained on a 386 pc, because of the lack of sufficient memory after running for over 15 minutes.

[*2] Again, since the spectrum is based on the linear analysis, it can be considered as (an important) first approximation to the non-linear approach. In the latter, "polyspectra" are used for handling higher comulants. See e.g. ref. [7].

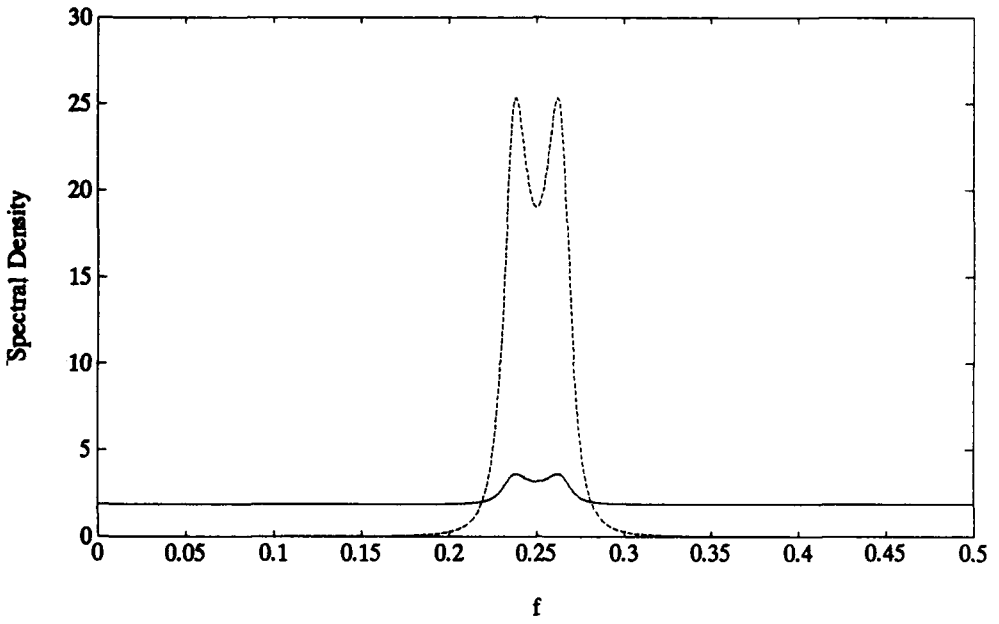

Fig. 1. Comparison of spectral densities, $b = -0.005, -50000$.

3. The power spectrum

No direct subtraction of white noise from the power spectrum is possible. However, the power spectrum of the pure signal can be obtained directly from the points in the u-space. Thus, this power spectrum is given by [1]:

$$g(\omega) = \text{constant} \times \left| \frac{1 - q_{1,0}B - \cdots - q_{m,0}B^m}{1 - p_1 B - \cdots - p_m B^m} \right|^2 ,$$

$$B = \exp(-\mathrm{i}\omega) . \tag{8}$$

Using eq. (6) we can transform eq. (8) to

$$\begin{aligned} g(\omega) = \text{constant} \times & [u^0 + 2u^1 \cos(\omega) + \cdots \\ & + 2u^{m-1} \cos((m-1)\omega) - 2\cos(m\omega)] \\ & \times [u_Z^0 + 2u_Z^1 \cos(\omega) + \cdots \\ & + 2u_Z^{m-1} \cos((m-1)\omega) - 2\cos(m\omega)]^{-1} . \end{aligned} \tag{9}$$

Where the constant is determined by the normalization:

$$\int_0^{0.5} g(f)\,\mathrm{d}f = 1 , \quad f = \omega/2\pi . \tag{10}$$

In fig. 1 we show the results for a demonstration case. We chose ARMA (4, 4) with the following parameters: $q_1 = q_3 = 0$, $q_2 = -1.77$, $q_4 = -0.81$, $p_1 = p_3 = 0$, $p_2 = -1.57$, $p_4 = -0.64$. We choose $b = -0.005$ to represent a noisy signal and $b = -50000$ to represent a fairly cleaned up signal. We see quite clearly the "purifying" effect.

It should be noted that the loss of invertibility or of stationarity can be detected from the power spectrum directly, thus there is no need to transform back to the $q_{i,0}$ for this purpose. This is achieved by detecting a zero (node) at a point in the spectrum which indicates an intersection of the zero of the q_0 polynomial with the unit circle. Similarly, an appearance of negative parts in the "power spectrum" indicates a region of u-space which is not allowed (complex $q_{i,0}$).

References

[1] G.E.P. Box, G.M. Jenkins, Time Series Analysis (Holden-Day, San Francisco, 1976).

[2] H. Wold, A Study in the Analysis of Stationary Time Series, 2nd ed. (Almquist and Wiksell, Stokholm, 1953).

[3] A. Rabinovitch and R. Thieberger, Physica D 28 (1987) 409.
[4] A. Rabinovitch and R. Thieberger, J. Theor. Biol. 131 (1988) 509.
[5] H. Tong, Non-Linear Time Series: a Dynamical System Approach (Clarendon, Oxford, 1990).
[6] M.B. Priestley, Spectral Analysis and Time Series (Academic, New York, 1981).
[7] M.B. Priestley, Non-linear and Non-stationary Time Series Analysis (Academic, New York, 1991).
[8] M. Casdagli, Physica D 35 (1989) 335;
G. Sugihara, B. Grenfell and R.M. May, Phil. Trans. R. Soc. Lond. B 330 (1990) 235;
J.D. Scargle, Astrophys. J. 359 (1990) 469, and references therein.
[9] S.M. Kay, Modern Spectral Estimation (Prentice-Hall, Englewood Cliffs, NY, 1988).
[10] A. Rabinovitch and R. Thieberger, J. Time Series Anal. 13 (1992) 267.
[11] C.W.J. Granger and M.J. Morris, J. R. Stat. Soc. A 139 II (1976) 246.
[12] D.H. Anderson and E.C. Gartland Jr., SIAM J. Sci. Stat. Comput. 6 (1985) 376.

Physica D 58 (1992) 288–298
North-Holland

PHYSICA D

Using cluster analysis to classify time series

C.T. Shaw[a] and G.P. King[b]

[a]*Department of Engineering, University of Warwick, Coventry CV4 7AL, UK*
[b]*Nonlinear Systems Laboratory, Mathematics Institute, University of Warwick, Coventry CV4 7AL, UK*

Received 7 October 1991
Revised manuscript received 3 April 1992
Accepted 3 April 1992

We promote the idea of using the statistical technique of *cluster analysis* in nonlinear data analysis. The technique is illustrated by using it to help identify local oscillators in the wake of the flow past a cylinder.

1. Introduction

Principal component analysis and cluster analysis are two of the most important procedures of multivariate data analysis. Principal component analysis has already been introduced into nonlinear dynamics [1], but to our knowledge cluster analysis has not. *Cluster analysis* is a statistical technique used in many fields to help identify natural groupings in a set of data. The *idea* of cluster analysis is not new in nonlinear dynamics. Indeed, it is central to the algorithms that estimate the spectrum of singularities of the invariant measures of fractal objects and that locate unstable periodic orbits. However, many nonlinear dynamicists are unfamiliar with cluster analysis as a statistical technique. The purpose of this paper is to bring this technique to their attention and illustrate its use by applying it to locate the positions of local oscillators in the flow past a cylinder.

The plan of the paper is as follows. In section 2 we describe the data matrix and the operations of principal component analysis and cluster analysis on this matrix. In section 3 the experimental system is described and our results are given in section 4. In section 5 we discuss our results and our conclusions are given in section 6.

2. Multivariate data analysis

There are a large number of texts that explain in some detail the techniques that can be used to analyse multivariate data. Many such texts are referenced in the comprehensive and practical guide, written primarily for astronomers, by Murtagh and Heck [2].

Central to the procedures employed in multivariate analysis is the specification of a *data matrix*. Principal component analysis and cluster analysis operate on this matrix.

2.1. The data matrix

The data matrix, $\mathbf{X}$, consists of n rows (called the objects) and m columns (called the variables). How one specifies the data matrix is of course problem dependent. For example, in attempts to classify bacterial strains according to the amount of certain fatty acids they contain [3], the objects are the strains and the variables

0167-2789/92/$05.00 © 1992 – Elsevier Science Publishers B.V. All rights reserved

are the different fatty acids. Each strain is then represented as a point in an m-dimensional space, and principle component analysis and/or cluster analysis is used to help discover natural groupings.

The objective of this paper is to suggest that this *taxonomic* approach can be used to help study the structure and dynamics in a spatially extended system. In particular the state of the flow at different locations in the wake of a cylinder are recorded in the form of a time series. Cluster analysis is then employed to identify those parts of the flow that are similar (or dissimilar). For simplicity we use the power spectrum to characterise the state rather than the time series itself. Thus the variables are the frequencies and the objects are the positions at which the measurements are taken. For a particular experiment this procedure may be carried out simply by comparing the different power spectra visually. However, it is easy to see that in a real-world application it is desirable to have a classification procedure executed by computer, since this opens up the possibility of incorporating the procedures and cluster information in an automated control system.

2.2. Principal component analysis (PCA)

In principle component analysis one looks for a few (i.e., less than m) linear combinations of the original variables which account for most of the variance in the data. This is done by first centering the data matrix (i.e., so that each column has zero mean). Then the covariance matrix, $\mathbf{X}^T\mathbf{X}$ (T denotes transpose), is formed and diagonalized to obtain the eigenvectors (principal axes) and eigenvalues (variances). Sometimes it is desirable to scale each variable to have unit standard deviation. If this is done then $\mathbf{X}^T\mathbf{X}$ is the correlation matrix. In our case the scaling is undesirable since it magnifies the noise. Therefore, we use the covariance matrix.

Typically the data matrix is rank deficient. That is, some of the variances are no larger than the variance of the measurement noise. Instead of trying to identify the actual noise level, one sometimes decides to keep only those directions which 'explain' a certain percentage of the variance. Discarding the directions with small variances is what we call PCA *filtered data*. In many problems this type of filtering achieves a large reduction in the dimension of the problem.

2.3. Cluster analysis

In cluster analysis one classifies the objects into natural groupings that contain objects with similar characteristics. There are a variety of clustering techniques, but we will concentrate here on hierarchical techniques [2] which operate on a matrix $\mathbf{D} = (d_{ij})$ of distances between the points $\boldsymbol{x}_1, \ldots, \boldsymbol{x}_n \in \mathrm{R}^m$. Here we use the Euclidean distance

$$d_{ij}^2 = \|\boldsymbol{x}_i - \boldsymbol{x}_j\|^2$$

and refer to $\mathbf{D}$ as the *dissimilarity matrix*.

Once the dissimilarity matrix is calculated, it is scanned and the smallest dissimilarity found (say, d_{ik}). This defines the two closest objects. The two objects are combined (i.e., replaced by a new object, $i \cup k$) and the dissimilarity matrix updated according to an agglomeration algorithm. The whole process is then repeated until only two groups of objects remain. By keeping track of the order in which the objects are agglomerated, the group structure is determined.

Two problems remain. The first concerns the choice of agglomeration algorithm, and the second is deciding how many groups there are in the data.

Agglomerative clustering methods have been motivated by graph theory (linkage-based methods) or by geometry (cluster centre methods) [2]. We shall consider two methods of agglomeration:

(1) *single linkage*, where the dissimilarity matrix is updated by the rule $d_{i\cup k,j} = \min(d_{ij}, d_{kj})$;

(2) *Ward's minimum variance method*, where one seeks to agglomerate two clusters into one such that the variance of the cluster is minimum.

At each stage in the clustering process we know the dissimilarity between two objects. When the output is obtained as a *dendrogram* the links between the objects and the clusters as a function of dissimilarity can be seen. Sudden changes in the value of the dissimilarity suggest the existence of a natural set of clusters. It is important to note that this grouping depends on the clustering technique used, on the dissimilarity measure, and, most importantly, on the investigator!

3. Experimental system

The cluster analysis was carried out on data obtained from measurements of velocity time series in the wake of the flow past a cylinder (for a description of the phenomena, see ref. [4]). Experiments were carried out in a wind tunnel in the regime where vortices are shed periodically. The experimental set up is shown in fig. 1. The cylinder is 1.6 mm in diameter and 76 mm in length. One end of the cylinder was fixed to the wind tunnel floor and the other was free. The free stream velocity was held fixed at 1.2 m/s (Re = 130). The expected shedding frequency for a circular cylinder of this diameter in a uniform stream is 130 Hz [5].

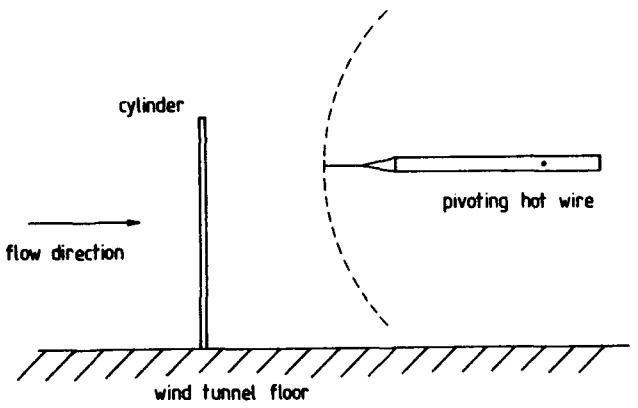

Fig. 1. The experimental arrangement. The cylinder is 1.6 mm in diameter and 76 mm in length. One end of the cylinder was fixed to the wind tunnel floor and the other was free. The free stream velocity was held fixed at 1.2 m/s (Re = 130). The hot-wire probe was mounted to move on an arc in the plane of the cylinder. Thus the grid positions for the measurements were distributed on two parallel arcs. The reference positions of the probe, measured from the axis of the cylinder, were 6.25 and 25 cylinder diameters.

Measurements were made directly behind the cylinder using a single hot-wire probe, a Dantec 55P11, which was controlled by a Dantec 55M-series constant temperature anemometer. The probe was mounted to move on an arc as shown in fig. 1. Thus the grid positions for the measurements were distributed on two parallel arcs in the cylinder wake. The reference positions of the probe for each arc, measured from the axis of the cylinder, were 6.25 and 25 cylinder diameters. The output of the anemometer, which was not linearised, is a measure of the flow velocity at a point. The frequency response of the probe and anemometer is of the order of several kHz, whereas the frequencies we are interested in are those below 250 Hz.

Time series were taken at 21 points spaced uniformly along each arc at intervals of 2° from −25° to 15° (taking a positive angle to be measured away from the tunnel floor and zero to be the horizontal). For each time series the sampling rate was 500 Hz.

4. Results

As mentioned above, we cluster the time series indirectly by applying cluster analysis to the power spectra constructed from them. Thus in our data matrix the objects are the 42 power spectra and the frequencies are the variables. (Before constructing the power spectra, the time series were adjusted to have zero mean.) Time series of various lengths, and hence frequency resolution, (512, 1024 and 2048 points) have been analysed, and the spectra obtained are qualitatively similar. Below we describe our results for 512 point time series (256 frequency

values). Thus our data matrix **X** is 42×256. As we wish to compare the shapes of the spectra, not the amplitudes, each spectrum was normalised by the amplitude of its largest peak (hence after normalisation $\max(x_i) = 1, \forall i$).

4.1. Manual classification

As a first step, a manual classification of the 42 power spectra was performed. An initial look at the spectra showed that the maximum amplitude varied greatly from spectrum to spectrum. The largest peaks did not all occur at the same frequency, but were found to be either 20, 56, 87, 96, 103, 117 or 124 Hz.

When considering the overall shapes of the spectra, several characteristic forms can be seen. The 13 groups suggested by the manual classification are shown in fig. 2. In the figure spatial positions 1–21 correspond to a probe reference position of 6.25 cylinder diameters, and for positions 22–42 a probe reference position of 25 cylinder diameters. The group number for each spatial position is given in the enclosed box and the corresponding spatial positions are given to the left and right of the box. The results of the manual grouping are summarized in table 1, and typical spectra are shown in figs. 3–6.

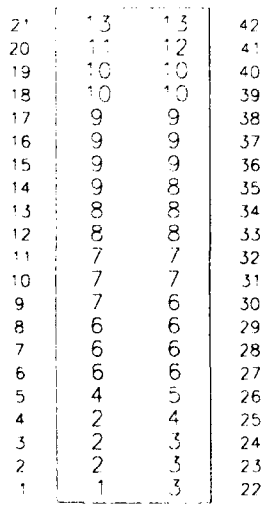

Fig. 2. The groupings derived by visual inspection of the power spectra. The group number for each spatial position is given in the enclosed box; the corresponding spatial positions are given to the left and right of the box. (The figure is sometimes called a dendrogram.)

Having carried out this manual cluster analysis, it is apparent that the classification of the spectra is not a straightforward task as difficult decisions have to be made. For example, the distinction between groups 7 and 8 is not at all clear. Also, if we compare just the main frequencies and not the shape, some of the groups could be combined. However, even though this manual classification process is imperfect, we now have an approximation for the groupings that an automatic classification should produce.

4.2. Cluster analysis of the raw spectra

Ward's minimum variance algorithm and the single linkage algorithm were applied to the normalised spectra. Nine-cluster solutions for each method are shown in fig. 7. Comparing these two figures with each other and with fig. 2, it is clear that Ward's method produces clusters more consistent with the manual classification. The groups in the lower half of the domain being determined quite well, and those in the upper half being formed reasonably, if not quite as expected. There are, however, some errors in

Table 1
Manually classified groups.

Group	Probe position		Main peaks (Hz)	Sample spectrum shown in fig:
	(6.25 dia)	(25 dia)		
1	1		56, 87	3
2	2–4		96	3
3		22–24	87	3
4	5	25	87	3
5		26	117	4
6	6–8	27–30	117	4
7	9–11	31–32	117	4
8	12–13	33–35	100–130	5
9	14–17	36–38	124	5
10	18–19	39–40	20, 124	5
11	20		103	6
12		41	20, 83, 103, 123, 126	6
13	21	42	103	6

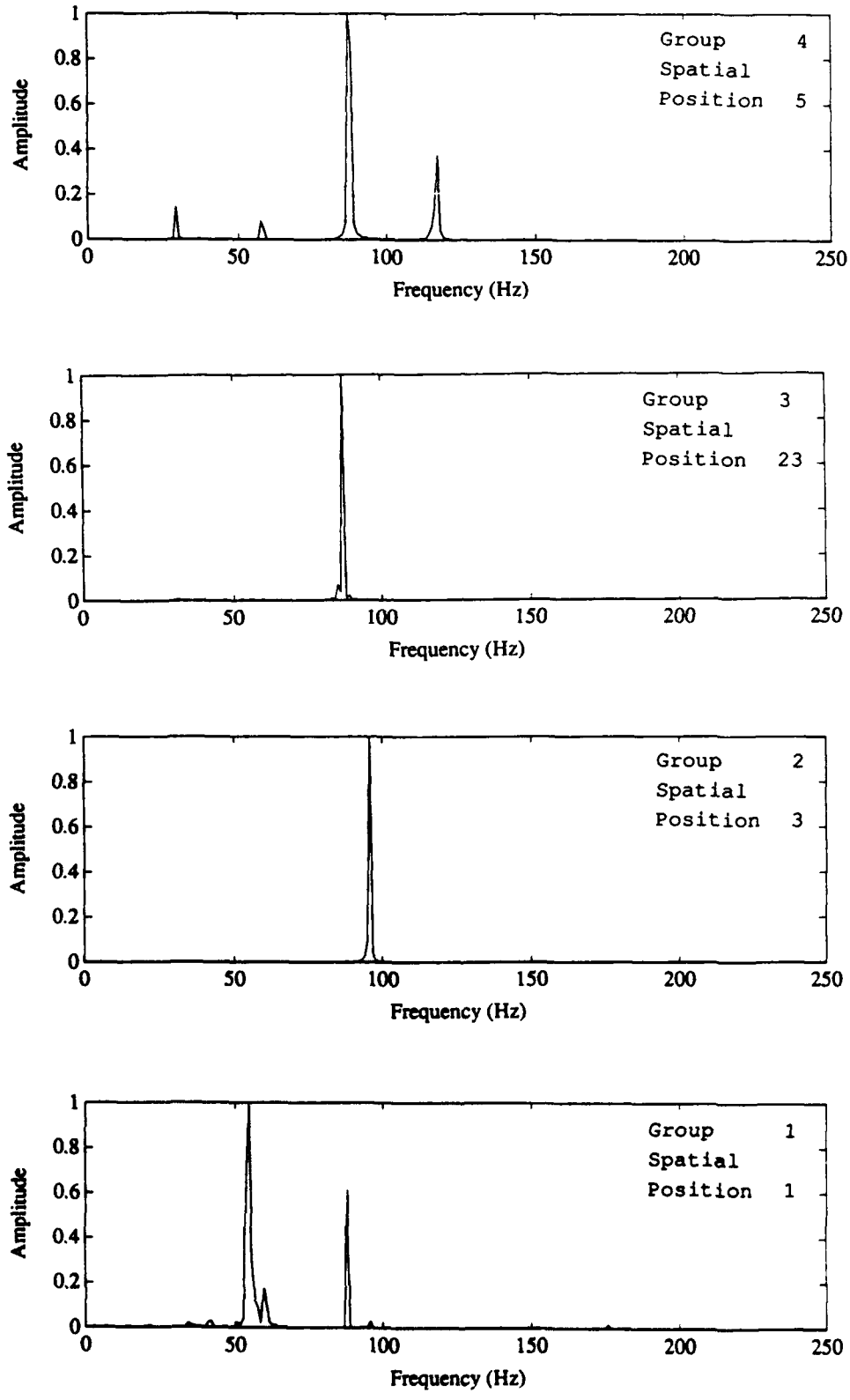

Fig. 3. Representative power spectra from manually identified groups 1–4: grid points 1, 3, 23, 5.

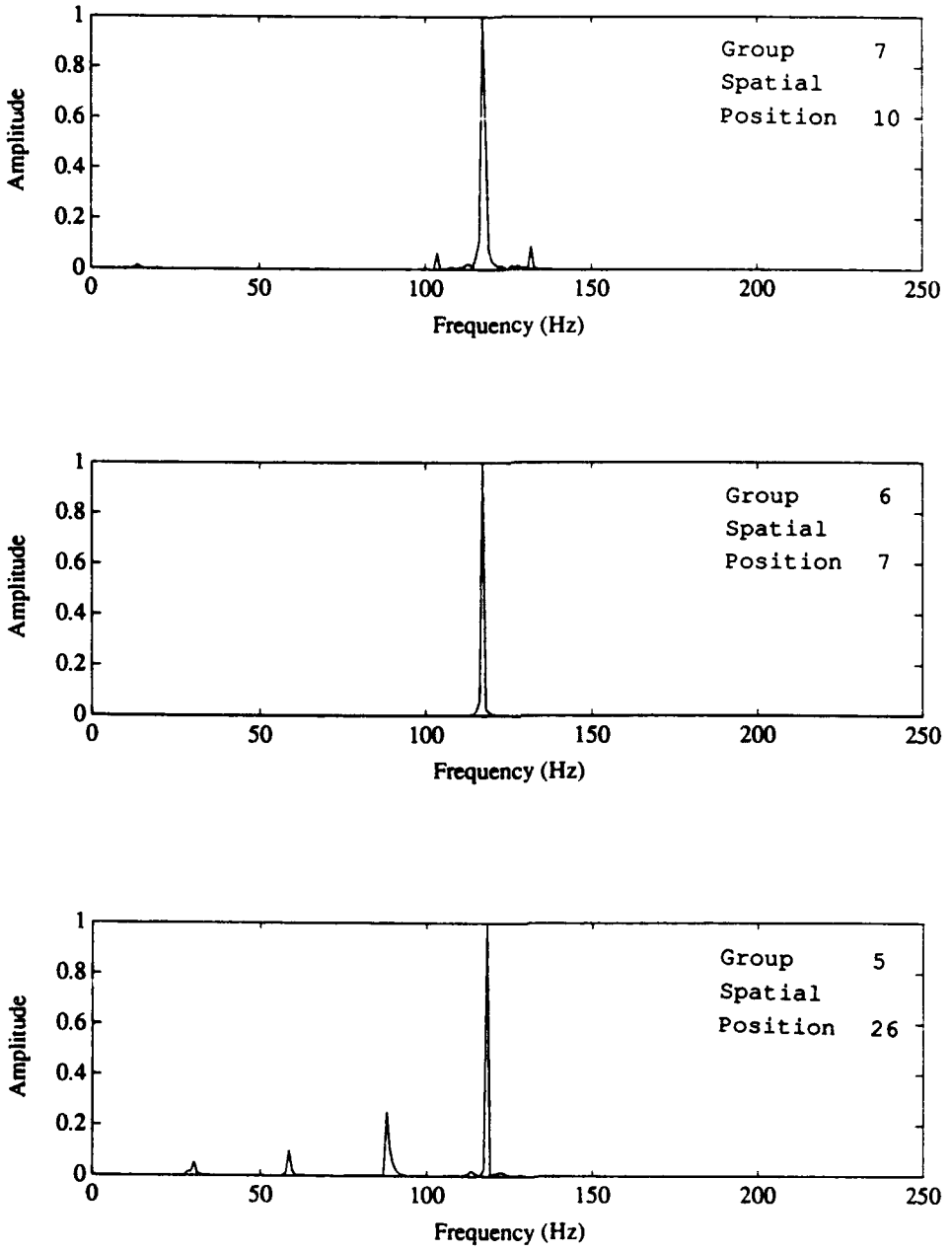

Fig. 4. Representative power spectra from manually identified groups 5–7: grid points 26, 7, 10.

the groupings as some groups contain points in both the upper and lower half of the domain and this is not consistent with the manual groupings. The single link agglomeration seems to have divided the domain into two correctly, but the majority of the groups are not defined correctly. As a result of this, only Ward's method was used in the following.

4.3. Cluster analysis of the PCA filtered spectra

We now give the results of the clustering using the PCA filtered spectra, and examine how sensitive the results are to the number of principal axes retained. Fig. 8a shows the clustering based on using the 4 most significant eigenvectors (54% of the variance), fig. 8b the 7 most significant

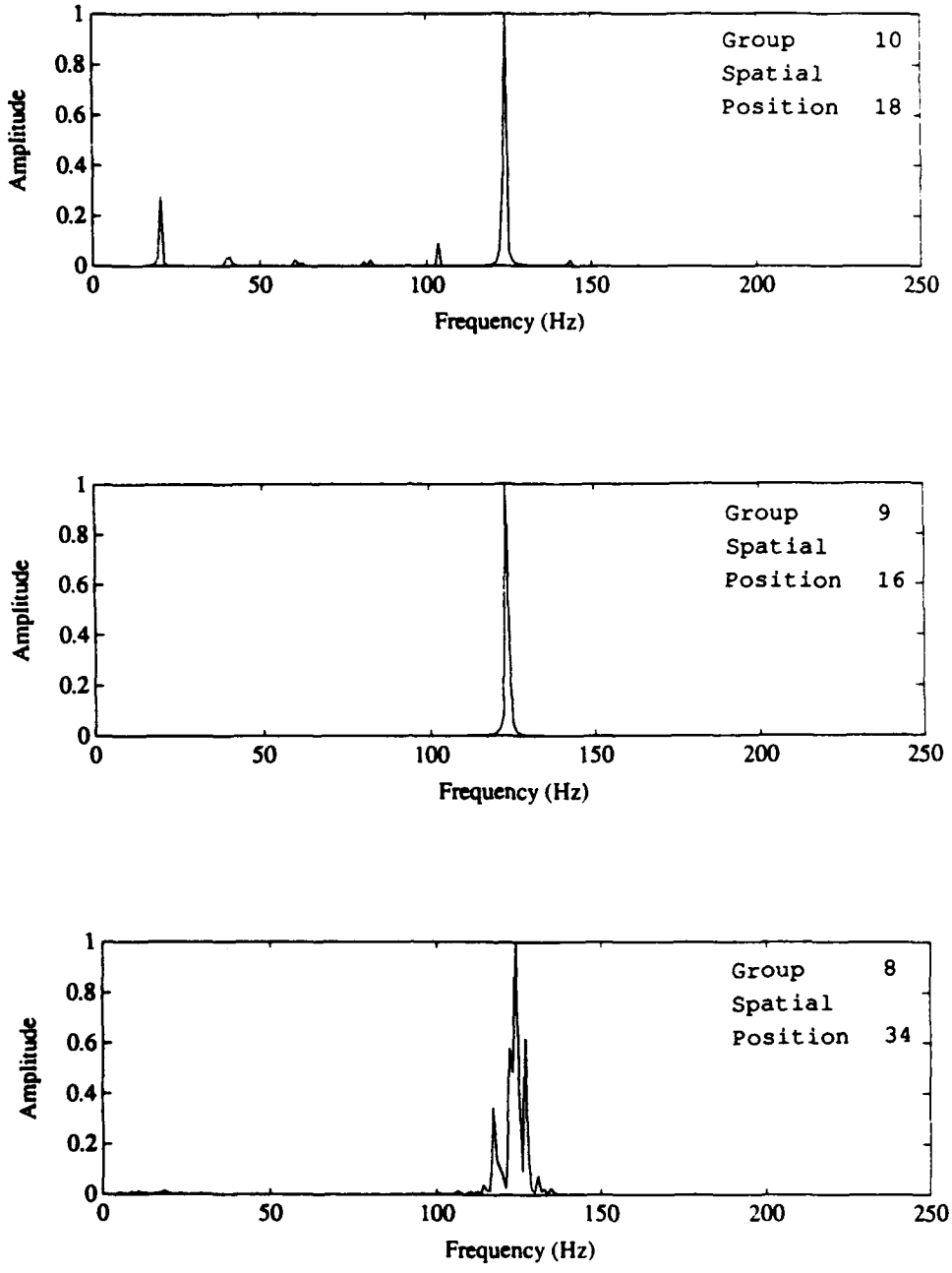

Fig. 5. Representative power spectra from manually identified groups 8–10: grid points 34, 16, 18.

(71% of the variance), and fig. 8c the 14 most significant (93% of the variance).

Comparison of fig. 8c with fig. 7a shows that the groupings produced using 14 axes is very similar to those obtained from clustering the raw spectra. Hence it is clear that the data can be compressed by a factor of 256/14.

Clustering algorithms require large amounts of cpu time. The data compression achieved using PCA significantly reduces the cpu time required to complete the clustering. However, the calculation and diagonalization of the covariance matrix $\mathbf{X}^T\mathbf{X}$, a 256×256 matrix, takes significantly more cpu time than the cluster analysis operating di-

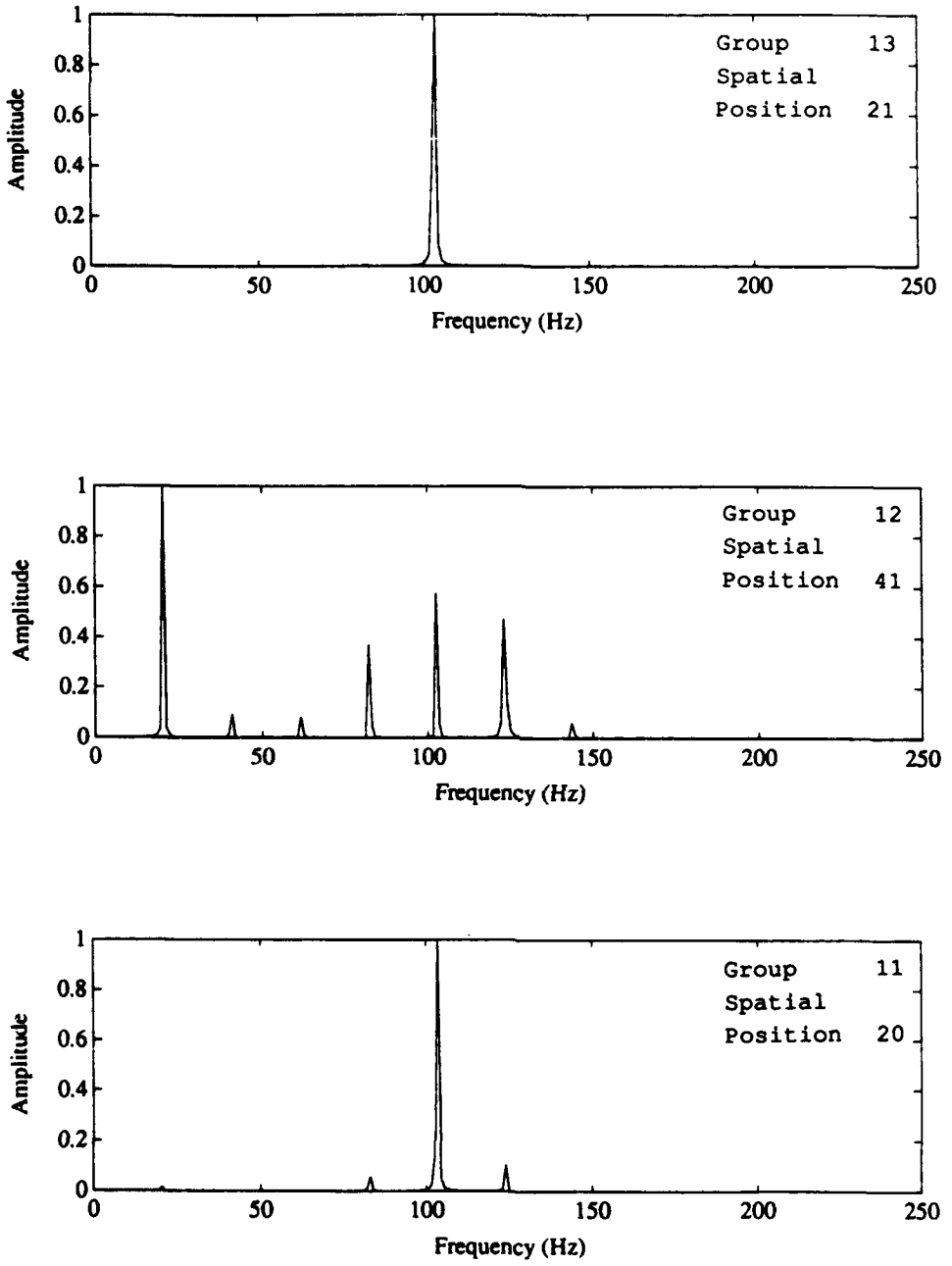

Fig. 6. Representative power spectra from manually identified groups 11–13: grid points 20, 41, 21.

rectly on the 42×256 raw data matrix. Nevertheless in a larger study the number of objects will increase while the number of variables remain constant. Thus at some stage, the cluster analysis of the PCA filtered spectra will be more efficient.

4.4. Cluster analysis of binary coded spectra

As can be seen, the groupings produced by the PCA filtered data was still some way from what was desired. At this point we felt that an improvement might be possible by reducing the

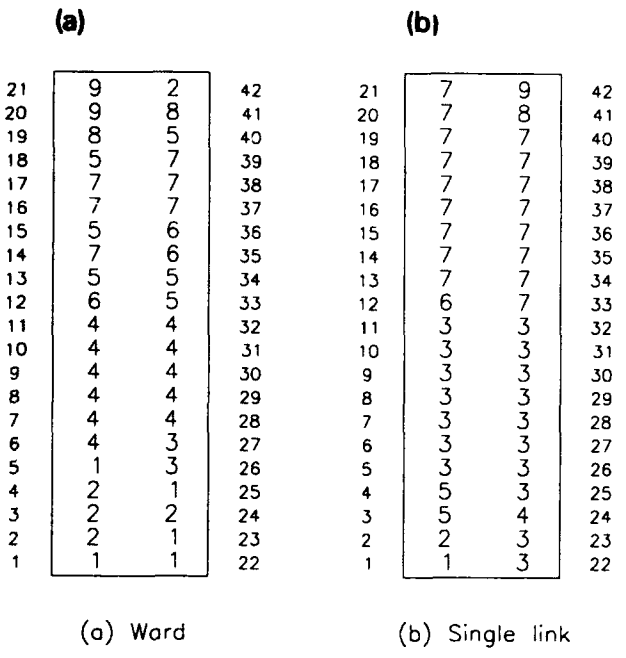

Fig. 7. Clusters obtained from analysis of the normalised spectra using (a) Ward's method and (b) the single linkage method.

information in the spectrum to a binary code. Let x_i denote the power spectrum for grid position i. Then x_{ik} is the power in frequency bin k of spectrum i. We now construct a new data matrix **Y** in the following way. Specify a threshold A_t and then set

$$y_{ik} = \begin{cases} 1 & \text{if } x_{ik} \geq A_t \\ 0 & \text{otherwise} \end{cases}.$$

This effectively produces a spectrum which contains only the dominant frequencies as determined by the value of A_t.

A little thought (or experimentation) reveals a problem. Consider the following set of binary coded spectra:

$$y_1 = (1, 0, 0, \ldots, 0, 0),$$

$$y_2 = (0, 1, 0, \ldots, 0, 0),$$

$$y_3 = (0, 0, 0, \ldots, 0, 1).$$

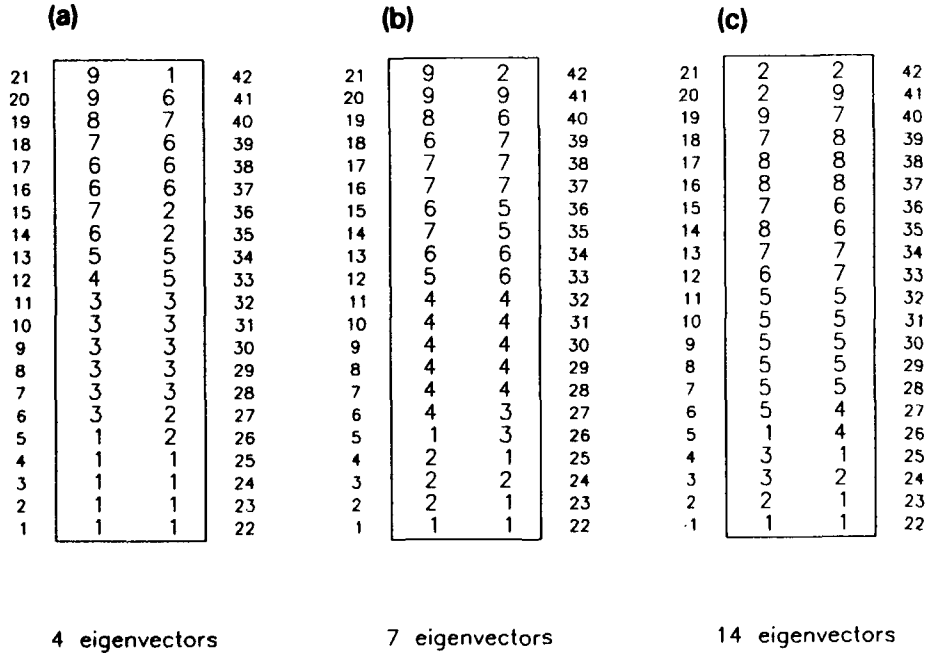

Fig. 8. Clusters obtained using PCA filtered spectra. The spectra were projected onto (a) the 4 most significant directions (54% of the variance), (b) the 7 most significant directions (71% of the variance), and (c) the 14 most significant directions (93% of the variance).

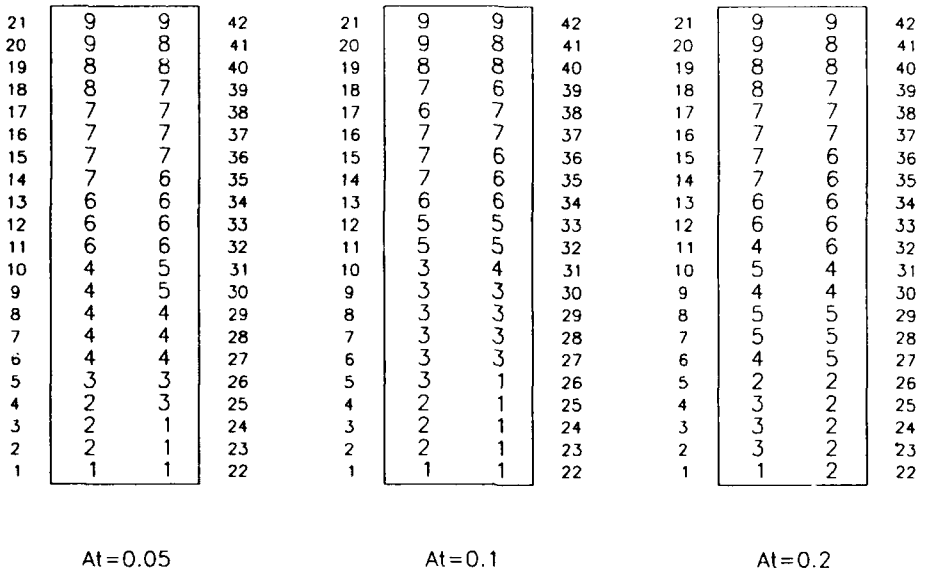

Fig. 9. Clusters obtained from the binary representation of the power spectra (see text). The groupings, from left to right, correspond to thresholds, $A_t = 0.05$, 0.1 and 0.2. As can be seen, the different thresholds all yield slightly different groups, and while none correspond perfectly with the manual groups, they are all closer than the clustering of the PCA filtered spectra.

Since we know that these objects are derived from a power spectrum, it is easy to see that y_1 and y_2 are similar, and that both are much different from y_3. However, when the Euclidean distances between the y_i are calculated, we find $d_{12} = d_{23} = d_{13}$. Clearly something is not quite as it should be, and the obvious conclusion is that we need to measure distances in a way that reflects 'nearness' in frequency. An alternative is to simply recognize that the frequency resolution is too fine. A straightforward remedy is then to decrease the frequency resolution by integrating the power in adjacent frequency bins before reducing to a binary spectrum. This was done using 4 adjacent bins. Thus the spectrum was reduced from 256 to 64 frequencies. The results of the cluster analysis of the binary spectra are shown in fig. 9. The thresholds, $A_t = 0.05$, 0.1 and 0.2, all yield slightly different groups, and while none correspond perfectly with the manual groupings, they are all closer than all other attempts. Thus we may well have reached a limit in the accuracy of the method.

5. Discussion

The choice of agglomeration method crucially affects the groups produced by the clustering. For the data investigated here, Ward's minimum variance method produces a classification much closer to the manual clustering than the single linkage method.

By using PCA, the dimensions of the data can be reduced from 256 to 14. However, there is a penalty to pay for this. The calculation of the covariance matrix and its diagonalization takes considerable cpu time compared to the time taken to cluster even the raw data. Nevertheless, PCA data compression will become more attractive as the sample size increases.

Clear improvements were obtained by representing the spectrum by a binary code and by reducing the frequency resolution. We conclude that these crude qualitative features were close to what the visual system keyed on to achieve the manual grouping. The difficulty in identifying just what set of operations should be carried out

on the data before applying the clustering algorithm illustrates the basic problem faced by designers of machine classifiers.

6. Conclusions

Cluster analysis helps identify objects with similar characteristics. This helps to identify features that need explaining and as a result a deeper understanding of the system will be achieved.

In the present context cluster analysis helped identify regions in space whose dynamics were similar. This reinforces the view that the flow may be thought of as a set of spatially coupled local oscillators. The cluster analysis helps reveal their position and spatial extent and hence suggests where, for example, two probes are best located to study the coupling or interaction of two oscillators in the flow. We hope to carry out such a study in future work.

Another possible use of cluster analysis is in situations where it is possible to employ arrays of sensors distributed over a large spatial extent. It is easy to imagine that in such situations the main difficulty will be the processing of the information from so many probes in a reasonable length of time. Cluster analysis could be used in a preliminary phase of the data acquisition to help determine which probes to "listen to" under different operating conditions.

Acknowledgement

We would like to thank T. Funk for his help on the experiments.

References

[1] D.S. Broomhead and G.P. King, Physica D 20 (1986) 217.
[2] F. Murtagh and A. Heck, Multivariate Data Analysis (Reidel, Amsterdam, 1987).
[3] G.S. Saddler, A.G. O'Donnell, M. Goodfellow and D.E. Minnikin, J. General Microbiol. 133 (1987) 1137.
[4] D.J. Tritton, Physical Fluid Dynamics, Second Edition (Oxford Univ. Press, Oxford, 1989).
[5] C.H.K. Williamson, Phys. Fluids 31 (1988) 2742; J. Fluid Mech. 206 (1989) 579.

Physica D 58 (1992) 299–303
North-Holland

PHYSICA D

Some comments on a bridge between nonlinear dynamicists and statisticians

Howell Tong
University of Kent at Canterbury, Kent, UK

Received 24 September 1991
Revised manuscript received 11 December 1991
Accepted 24 December 1991

We address the question: "Why is a bridge between the two groups desirable?"

1. Introduction

It is a well-known fact that deterministic chaos can generate data which are apparently random and it is equally well known that from time to time statisticians have to resort to simulation to solve analytically intractable problems. One would therefore expect that there should be much common ground between the nonlinear dynamicists and the statisticians. It is interesting to note that it was only relatively recently that the two groups began to interact with each other in a constructive way.

Like other historical developments, there probably does not exist a unique explanation as to why the interaction has been so slow in coming. The basic tenet, written or unwritten, in chaos is that randomness is associated with or even wholly generated by deterministic chaos. On the other hand, statisticians, whether of the frequentist or the Bayesian persuasion, accept randomness as given and try to live with it. This fundamental difference in philosophy may account for much of the differences in methodology of the two groups. Personally, I believe that it is important to probe deeper and analyse the sources of randomness, whilst accepting that there will always remain a *proportion* of the randomness which cannot be adequately explained. In this sense, I believe that a nonlinear dynamicist's approach deals with the deeper layer of randomness.

2. Why is a bridge between the two groups desirable?

I think a bridge is most desirable for both groups for various reasons. First, results in one area might accelerate or clarify development in the other. Second, joint efforts might help solve some hard open problems common to both groups. I shall illustrate these points with some examples, the choice and presentation of which cannot perhaps avoid subjectivity completely.

(i) In chaos one typically (though not invariably nowadays) deals with very large data sets; at the recent Workshop at Warwick University, data sets of the size well beyond 10^6 were frequently mentioned. On the other hand, most statisticians typically deal with a much more

0167-2789/92/$05.00 © 1992 – Elsevier Science Publishers B.V. All rights reserved

modest size, say 10^2. (This difference in emphasis is not so much a question of equipment because with modern computing equipment available to the statisticians, the storage and manipulation of large sample data is not a serious problem.) Therefore, given the different data environment, it is perhaps not surprising that there are different methodological emphases. For example, most statisticians subscribe quite vehemently to the *Principle of Parsimony*: The complexity of the model must be penalised so as to produce *the simplest model that one can get away with. There are, however, sound scientific reasons for always penalising over-fitting, whatever the sample size.* (See, e.g., [15].) As a simple example, let a linear autoregressive (AR) model be fitted to the observations $(X_1, X_2, \ldots, X_N)$, assumed Gaussian and stationary, either by the least squares method or the maximum likelihood method. It is well known that the sum of squares of the residuals (RSS) tends to decrease with increasing 'complexity', in this case the number of past values upon which each current observation is regressed, i.e. the *order* of the linear autoregression. A naive suggestion would then be to fit as high an order as possible. What is the price? The price is that such an over-fitted model has very low predictive power. To quantify this statement, let $E(X_{N+1} - \hat{X}_{N+1})^2$ denote the mean squared error of (one-step-ahead) prediction, where $\hat{X}_{N+1}$ is the prediction obtained from the model fitted to the data $(X_1, \ldots, X_N)$. It turns out that under general conditions for a pth order AR model, AR(p),

$$E(X_{N+1} - \hat{X}_{N+1})^2 = \sigma_p^2\left(1 + \frac{p}{N}\right) + o\left(\frac{1}{N}\right), \qquad (1)$$

where σ_p^2 is the minimum mean squared error of prediction when the model is known. Thus the penalty is measured by the multiplying factor $(1 + p/N)$, which increases with p. In practical terms, (1) suggests that there will come a time when the reduction in RSS (note that RSS/$(N - p)$ is an unbiased estimate of σ_p^2) will not be sufficient to compensate for the increase in the penalty due to overfitting, thus leading to the generally poorer performance in prediction with an over-fitted model. The above discussion is quite heuristic and the interested readers are referred to [15] and the references therein for a more detailed discussion.

It seems to me that the dynamical systems community could benefit greatly from a systematic adoption of the above principle. As an example, recently [3] has considered the estimation of the embedding dimension for a "noisy" dynamical system:

$$X_t = F(X_{t-1}, \ldots, X_{t-d}) + \varepsilon_t, \qquad (2)$$

where F is an *unknown* function and $\{\varepsilon_t\}$ is a sequence of martingale differences with unknown variance σ^2, and d is an unknown positive integer representing the embedding dimension. The objective is to estimate d from the given observations $(X_1, \ldots, X_N)$ of an assumed stationary time series with finite variance and absolutely continuous distribution. As an estimate of $F(z_1, \ldots, z_d)$, we calculate

$$\hat{F}_{N,M}(z_1, z_2, \ldots, z_d) = \frac{\sum_{s \neq t} X_s \prod_{i=1}^{d} k((z_i - X_{s-i})/h_N)}{\sum_{s \neq t} \prod_{i=1}^{d} k((z_i - X_{s-1})/h_N)}, \qquad (3)$$

where, for the present note, k may be taken as any smooth probability density function with finite absolute mean, and h_N is called the *bandwidth*, which controls the amount of smoothing over the neighbourhoods of the z_i's. Note that there is some similarity between (3) and the *localized receptive fields* in neural network. [12]. Let $\hat{F}_N$ denote an analogous estimate but without any deletion. The delete-one procedure is actually a rather subtle way of imposing a penalty on overfitting. Specifically, it may be shown [3] that under quite standard conditions the following scaling law holds:

$$\sum_t \{X_t - \hat{F}_{N,M}(X_{t-1}, \ldots, X_{t-d})\}^2$$
$$= \sum_t \{X_t - \hat{F}_N(X_{t-1}, \ldots, X_{t-d})\}^2$$
$$\times \left[1 + \frac{2\alpha}{h_N^d N} + o_p\left(\frac{1}{h_N^d N}\right)\right], \quad (4)$$

where $\alpha = k(o)$ and o_p denotes the "little O in probability". Note that eq. (4) may be compared with eq. (1). Here the penalty term is principally due to h_N^{-d} (note that $h_d \ll 1$ for sufficiently large N), which increases with d, the embedding dimension.

(ii) An important tool in dynamical systems is the *singular value decomposition* (SVD) introduced to the chaos literature by Broomhead and King [1]. The SVD is founded on the Karhunen–Loéve (KL) expansion. It is perhaps pertinent to repeat briefly the KL expansion here as I believe that further exploitation in the chaos study may still be possible. (For more detail, see e.g. [16].)

Let $\{X(t): \alpha \le t \le \beta\}$, $(\alpha, \beta \in \mathbb{R})$, be a mean-square continuous-time time series and Var $X(t) \le \infty$, all t. Let $\rho(s, t) = \text{corr}(X(s), X(t))$ denote the *autocorrelation function*. Routine consideration of the linear integral equation

$$\int_\alpha^\beta \rho(s, t)\, \psi(s)\, ds = \lambda \psi(t), \quad \alpha \le t \le \beta, \quad (5)$$

where $\rho(s, t)$ acts as the standard Hermitian positive definite kernel, yields upon Mercer's theorem the uniformly convergent series (in both variables)

$$\rho(s, t) = \sum_{j=1}^{\infty} \lambda_j \psi_j(s)\, \overline{\psi_j(t)}, \quad (6)$$

where the λ_j's are called the eigenvalues (>0) and the functions $\psi_j(s)$ are called the eigenfunctions such that

$$\int_\alpha^\beta \psi_j(t)\, \overline{\psi_k(t)}\, dt = \delta_{jk}. \quad (7)$$

A more fundamental result in this approach is that (6) implies and is implied by the following *generalised spectral representation* of the time series:

$$X(t) = \sum_{j=1}^{\infty} \sqrt{\lambda_j}\, \psi_j(t)\, Z_j, \quad (8)$$

where

$$Z_j = \lambda_j^{-1/2} \int_\alpha^\beta X(t)\, \overline{\psi_j(t)}\, dt, \quad (9)$$

so that

$$\text{corr}(Z_j, Z_k) = \delta_{jk}. \quad (10)$$

In statistics (or rather probability), the representation (8) is commonly called the *Karhunen–Loéve (KL) expansion* after K. Karhunen [9] and M. Loéve [10], although the same expansion was introduced independently by many others. (See, e.g., [16]). In particular, when $t \in \{1, 2, \ldots, m\}$, then we have a *finite* collection of random variables $(X(1), \ldots, X(m))$ and the KL expansion reduces to the well-known *principal component analysis* introduced by H. Hotelling in 1933 in his study of educational psychology [8].

It is relevant to point out two facts, which do not seem sufficiently widely appreciated in the chaos literature. First, *stationarity is not necessary* in the above discussion; only finite variance is needed. This is significant because almost all the applications of the KL expansion in the chaos literature are (in my view unnecessarily) restricted to stationary time series. ([6] is a notable exception although the authors still refer to the Toeplitz property of the "covariance" matrix.) Second, although it might be quite reasonable to arrange the sample eigenvalues (obtained from data) in descending order $\hat{\lambda}_1 \ge \hat{\lambda}_2 \ge \ldots$ and use the ratio of the sum of the first few $\hat{\lambda}$'s to the "trace" as a measure of the amount of information explained by the first few principal components, the statistical sampling properties of this ratio statistic is by no means

trivial. See, e.g., [14]. It might also be worthwhile exploring the use of the Principle of Parsimony to the determination of the number of principal components in the context of chaos.

(iii) *Modelling based on local function approximation* is witnessing rapid development in the chaos literature. As recognised by Farmer and Sidorowich [4], Casdagli [2], Grassberger et al. [7] and Sugihara and May [13], the threshold models introduced by me in the late 1970's and early 1980's were a precursor to this development. Of course, much has developed since, as demonstrated in the above references. It is perhaps worth remembering that the basic point of the threshold models may be summarised in the form of the *threshold principle*, which advocates the local approximation over states. I have elaborated this principle elsewhere and most recently in [15]. The fact that only one, two or three thresholds were used in the early development should be seen in perspective because

(a) the choice was made merely for computational convenience (SUN workstations were not available in 1980);

(b) the principle of parismony dictated that the data sets analysed by me and my associates did not warrant too many thresholds.

Of course, once the threshold principle of "divide and rule" is accepted as a useful concept there is then no limit to the computational varieties. Indeed, the statisticians Lewis and Stevens have recently adapted the powerful numerical algorithm of *multivariate adaptive regression splines* (MARS) due to Friedman [5] to provide a versatile and efficient implementation of the threshold principle. [Further details may be found in ref. [11]]. In fact, the area of nonparametric time series modelling provides an excellent common ground for joint exploration.

(iv) To fully comprehend the intimate relationship between order and disorder, low dimensional attractors and high dimensional attractors and so on is a challenge facing both the nonlinear dynamicists and the statisticians. There is much to be gained if there is closer collaboration between the two groups. Quite often knowledge from both areas is essential in order to attack a problem of common concern. For example consider a deterministic model

$$X(t) = F(X(t-1)), \quad t = 1, 2, 3, \ldots, \tag{11}$$

where $X(t) \in \mathbb{R}$. Suppose $X(t)$ is not observable and instead we observe

$$Y(t) = X(t) + e(t), \tag{12}$$

where $e(t)$ is the measurement/observation noise. The above set-up is very common in the chaos literature. Now, from (11) and (12) we may deduce that approximately

$$Y(t) = F(Y(t-1)) + e(t) - F'(y(t-1))\, e(t-1), \tag{13}$$

where F' denotes the derivative. If the Lyapunov exponent of (11) is positive so that the deterministic model is sensitive to initial conditions, then the stochastic model (13) will in general tend not to be *invertible* in the sense that the noise term $e(t)$ will not be measurable with respect to the sigma algebra generated by $Y(t)$, $Y(t-1), \ldots$. Without invertibility, statistical inference/estimation based on maximum likelihood of any parametrised form of F would be extremely difficult. The latter problem is well known in statistical nonlinear time series analysis. (See, e.g., [15], p. 309.)

Another example of particular current concern, some subtleties of which might have been overlooked in the literature, has to do with a model with dynamic (i.e. system) noise:

$$Z_t^{(\varepsilon)} = F^{(\varepsilon)}(Z_{t-1}^{(\varepsilon)}) + e_t^{(\varepsilon)}, \quad t = 1, 2, \ldots, \tag{14}$$

where

$$Z_t^{(0)} = F^{(0)}(Z_{t-1}^{(0)}) \tag{15}$$

corresponds to the underlying deterministic model of interest. For simplicity we assume that both Z and e are real scalars. Let $\lambda^{(0)}$ denote the Lyapunov exponent of the system (15), which is assumed to be ergodic with invariant measure $\mu^{(0)}$ induced by $F^{(0)}$. Similarity, let $\lambda^{(\varepsilon)}$ denote the Lyapunov exponent of the stochastic system (14), again assumed to be ergodic with invariant measure $\mu^{(\varepsilon)}$ induced by $F^{(\varepsilon)}$. Specifically, $\lambda^{(\varepsilon)} = \int \ln |\mathrm{d}F^{(\varepsilon)}(x)/\mathrm{d}x| \mu^{(\varepsilon)}(\mathrm{d}x)$, $\varepsilon \geq 0$. Now, given observations from (14), the obvious sample version $\hat{\lambda}^{(\varepsilon)}$ say of $\lambda^{(\varepsilon)}$ is a natural estimate of $\lambda^{(\varepsilon)}$, *but not* $\lambda^{(0)}$. Therefore, we plainly need to correct $\hat{\lambda}^{(\varepsilon)}$ for bias if it is used to estimate $\lambda^{(0)}$. (A similar remark applies to the Grassberger correlation dimension).

A more fundamental question which does not seem to have been addressed is this: whilst it is well known that $\lambda^{(0)}$ measured the exponential divergence of two initial points in state space upon iteration under $F^{(0)}$, it is not clear to me that $\lambda^{(\varepsilon)}$ measures the "exponential divergence" of two initial distributions, which seems to me the more relevant concept to develop.

Acknowledgments

I would like to thank Sir David Cox and the referee for constructive comments, Professor P.G. Drazin and Dr. G.P. King for inviting me to participate in the IUTAM Symposium and NATO Advanced Research Workshop on Interpretation of Time Series from Nonlinear Mechanical Systems, and the participants for being so tolerant towards the odd statistician in their company. The fundamental difficulties described in section 2 (iv) are the results of on-going joint research with K.S. Chan, and I thank him for his comments. Partial support under the CSS initiative of the SERC is gratefully acknowledged.

References

[1] D.S. Broomhead and G.P. King, Physica D 20 (1986) 217.
[2] M. Casdagli, Physica D 35 (1989) 335.
[3] B. Cheng and H. Tong, J. R. Stat. Soc. (B) 54 No. 2 (1992) 427.
[4] J.D. Farmer and J.J. Sidorowich, in: Evolution, Learning and Cognition, ed. Y.C. Lee (World Scientific, Singapore, 1988).
[5] J.H. Friedman, Ann. Stat. 19 (1991) 1.
[6] M. Ghil and R. Vautarad, Nature 350 (1991) 324.
[7] P. Grassberger, T. Schreiber and C. Schaffrath, Nonlinear time sequence analysis, Tech. Rep., Dept. of Physics, Univ. of Wuppertal, Germany (1991).
[8] H. Hotelling, J. Educ. Psy. 24 (1933) 417; 498.
[9] K. Karhunen, Ann. Acad. Sci. Fennicae, Ser. A., I 34 (1946) 3.
[10] M. Loéve, Rev. Sci. 84 (1945) 297; 84 (1946) 195.
[11] J.G. Stevens, An investigation of multivariate adaptive regression splines for modeling and analysis of univariate and semi-multivariate time series systems, Naval Postgraduate School, Monterey, California, U.S.A., (1991), unpublished.
[12] K. Stokbro, D.K. Umberger and J.A. Hertz, Complex Systems 4 (1990) 603.
[13] G. Sugihara and R.M. May, Nature 344 (1990) 734.
[14] T. Sugiyama and H. Tong, Commun. Statist. - Theor. Meth. A 5(8) (1976) 711.
[15] H. Tong, Nonlinear Time Series: A Dynamical System Approach (Oxford Univ. Press, Oxford, 1990).
[16] A.M. Yaglom, Correlation Theory of Stationary and Related Random Functions I & II (Springer, Heidelberg, 1986).
[17] G.U. Yule, Philos. Trans. R. Soc. A 226 (1927) 267.

Physica D 58 (1992) 304–324
North-Holland

PHYSICA D

Hierarchical resolution of power spectra

R. Badii, M. Finardi,
Paul Scherrer Institut, LUS, 5232 Villigen PSI, Switzerland

G. Broggi
Physik-Institut, Universität Zürich Irchel, 8057 Zurich, Switzerland

M.A. Sepúlveda
Department of Chemistry, University of Washington, 98195 Seattle, USA

Received 16 September 1991
Accepted 20 January 1992

We identify the basic ingredients determining the structure of the power spectra of non-linear dynamical systems in a hierarchical order of importance. The analysis, performed with the help of symbolic methods, shows that dynamical invariants such as topological and metric properties of the symbolic orbits explain the main qualitative features of the spectra, whereas the coordinate-dependent values of the observable itself represent a less relevant contribution. Consideration of simple dynamical models with increasing number of topological transition rules evidences the formation of coherent structures (peaks) and explains their position and size. By constructing the parse tree of the allowed symbolic itineraries, it is possible to estimate conditional probabilities by considering orbits belonging to adjacent tree levels. Accordingly, a Markov transition matrix is obtained for each level l and is used to generate signals with statistical properties which approximate those of the actual one increasingly better for $l \to \infty$. A considerable improvement is achieved by recoding the original signal in terms of variable-length words and by re-applying the above procedure to the transformed signal, which is equivalent to a renormalization operation of the associated dynamical map. The accuracy of the estimates is directly related to the convergence of the scaling function for the conditional probabilities. Analytic results are presented for the simplest five Markov models arising from piecewise-linear, continuous, one-dimensional maps. Numerical studies have been performed for the logistic and Hénon maps and for the Lorenz system.

1. Introduction

Nonlinear dissipative dynamical systems exhibiting chaotic behaviour have been mostly characterized by evaluating dynamical invariants like metric entropies, Lyapunov exponents and fractal dimensions [1, 2] by means of time averages over randomly sampled long trajectories. More traditional statistical indicators, such as power spectra, have been discussed only in connection with phenomena at the border of chaos, because of their non-invariance under smooth coordinate changes. Recent developments in the field, however, suggest reconsidering such an approach within a more general theoretical framework. In fact, it is possible to perform a systematic hierarchical modelling of nonlinear dynamical systems by means of symbolic methods. These allow decomposing the dynamics into sub-processes which can be associated with a tree structure, so that an importance ordering of the relevant features is obtained. As a consequence, the values of the dynamical invariants can be estimated through ensemble ("thermodynamic" [3]) averages which yield higher accuracy than the ordinary time averages, especially when the

0167-2789/92/$05.00 © 1992 – Elsevier Science Publishers B.V. All rights reserved

dynamics folds phase space completely and the topology is simply described by a full (n-ary) tree [4]. In the generic case of partial folding, the symbolic dynamics is represented by incomplete trees. The most efficient description is then obtained by splitting the symbolic signal into variable-length symbolic strings [5] constituting a prefix-free code [6]. This allows one to obtain a renormalized picture of the dynamics by means of a simple recoding process. In the special case of a self-similar signal, such as those produced at the period-doubling accumulation point [7] and at the quasiperiodic transitions to chaos [8], it is possible to achieve an infinite renormalization automatically.

In this work, we apply the procedure introduced in ref. [5] to the resolution of the structure of power spectra, showing that their features are determined, first of all, by the topology of the corresponding trees and, secondly, by the metric properties (probabilities) of the orbits. This first skeleton of the spectra is invariant under smooth coordinate changes. The final contribution is constituted by the values taken by the measured observable along the actual trajectory (not the symbolic one), and is obviously non-invariant. A succession of models is automatically constructed and employed to reproduce signals whose statistical properties approach increasingly better those of the original system. This is obtained by evaluating transition probabilities for blocks of symbols of increasing length. The accuracy achieved by the resulting Markov models is directly connected with the convergence properties of the scaling function [9] for the orbit probabilities. We show that the successive approximations quickly approach a limit curve, for several dynamical systems, if the proper symbolic ordering and the above mentioned coding techniques are used.

This approach allows one to understand the formation of power spectra in generic systems, whereas previous analyses had concerned only simple examples, such as one-dimensional piecewise-linear maps [10, 11] and axiom-A systems [12], or particular phenomena like period-doubling [7], intermittency [13], diffusion [14], and "periodic chaos" [15]; the decay of correlations in area-preserving maps has been investigated in ref. [16]. We illustrate our hierarchical, variable-order, method by presenting numerical studies of the logistic and Hénon maps and of the Lorenz system. Finally, we show how the features of generic spectra (position, width and height of the peaks) can be explained by solving analytically a series of increasingly complicated Markov models describing suitable piecewise-linear, continuous, one-dimensional maps.

2. Shaping of power spectra by incomplete phase-space folding

Dissipative chaotic systems exhibit power spectra characterized by broadened peaks whose position and height are the effect of the complex stretching and folding mechanism acting on phase space. The spectra of conservative dynamical systems present, superimposed on the continuous background, sharp peaks which are usually originated by motion in the vicinity of invariant tori [17]. Although some of these features might be intuitively attributed to the influence of unstable periodic orbits whose neighbourhoods are visited by the trajectory, no causal relation can be identified, in general. Previous investigations, indeed, have been based on quite a wide range of different mathematical approaches and no unique interpretation scheme has emerged. In this section we review some of the major difficulties in a qualitative way, before going to a more systematic treatment of the problem. Consider, for example, the Hénon map [18]

$$(x_{n+1}, y_{n+1}) = (a - x_n^2 + by_n, x_n) \tag{2.1}$$

at standard parameter values ($a = 1.4$, $b = 0.3$). In fig. 1, we show the power spectrum

$$S(f) = \left| \sum_{n=0}^{N-1} x_n \, e^{2\pi i f n} \right|^2 \tag{2.2}$$

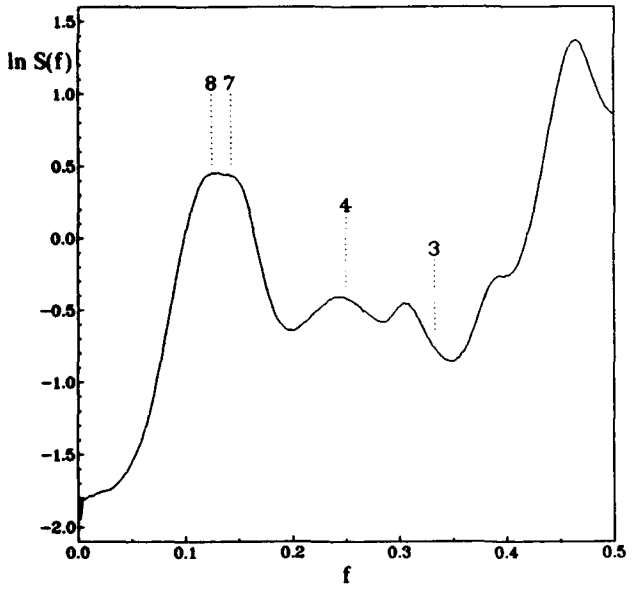

Fig. 1. Natural logarithm of the power spectrum $S(f)$ for the x-coordinate of the Hénon map at ($a = 1.4$, $b = 0.3$), versus the frequency f. The positions corresponding to periodicity 3, 4, 7 and 8 are indicated by dotted lines.

for the x-coordinate, versus the frequency $f = k/N$ ($k = 0, 1, \ldots, N/2$), computed by averaging over 10^4 single spectra obtained by Fourier transforming signals of length $N = 4096$ iterates. The area under the curve has been normalized to 1 and the natural logarithm of $S(f)$ has been taken after subtraction of the zero-frequency component. Although a few peaks seem to be related to integer periods ($f = \frac{1}{4}, \frac{1}{7}, \frac{1}{8}$), others are either displaced from the "expected position" (as the one to the left of $f = \frac{1}{2}$, corresponding to period-two) or close to frequencies corresponding to non-existing periods ($f = \frac{1}{3}$): the lowest-order unstable periodic orbits of the map, in fact, have lengths 1, 2, 4, 6, 7 and 8. Notice that no distinct feature emerges in $S(f)$ which can be trivially associated with a period-six orbit.

Furthermore, the amplitudes of the peaks cannot be explained in terms of the time spent by the chaotic trajectory in the neighborhood of the "corresponding" periodic orbit. Indeed, by using a generating partition [19], one can label phase-space regions with integers and study the occurrence probability of all symbolic sequences produced by the system. This investigation shows that no simple relationship exists between the amplitudes of the peaks and the probability of symbolic sequences of the corresponding length which are periodically extendable [20]. For example, the unstable period-two orbit of the Hénon map can be labelled by the sequence 01, whose probability is roughly twice that of sequence 0111, which labels a period-four orbit: however, the respective peak heights in $S(f)$ differ almost by a factor six.

Finally, the connections between average expansion rates and long-time decay of correlation functions discussed in ref. [10] do not hold exactly in generic systems (for related investigations, see refs. [11, 21]). As a consequence, the widths of the peaks cannot be simply explained in terms of eigenvalues of unstable periodic orbits.

In this work, we show that the structure of the spectra is to be attributed primarily to the incompleteness of the folding mechanism in phase space: this phenomenon is ubiquitous in physical systems without simple symmetries. In fact, maps whose symbolic dynamics can be represented on complete n-ary trees (such as the Bernoulli shift or the tent map and conjugated transformations [22]) have simple spectral features: $S(f)$ is either white or has a broad peak (not necessarily Lorenzian) around $f = 0$. The existence of forbidden orbits (pruned branches on the symbolic tree) is responsible for the appearance of peaks at generic frequencies: no symmetry-induced "cancellations" occur in the Fourier transform of the time-signal. In the Hénon map, e.g., only one period-one orbit (label 1) belongs to the attractor: the motion in its vicinity is not "compensated" in eq. (2.2) by any contribution coming from the neighbourhood of the other fixed point (label 0), which lies at a finite distance from the strange attractor. Finally, another important aspect of the folding process is the amount of rotation of a phase-space element upon the action of the dynamical law: in ref. [10] it was pointed out that the sign

of the local expansion rates (giving rise to either order-preserving or order-reversing transformations, in the one-dimensional case) played a relevant role in the behaviour of the correlation functions. These points will be discussed in detail in the following sections.

3. Hierarchical modelling

Let the state of the system be represented by a point $\boldsymbol{x}$ in a d-dimensional phase space X. If the dynamics is governed by a continuous-time transformation, the procedure to obtain a hierarchical description of it can be started only after having discretized time with the help of a Poincaré section Σ [23] in X. This must be done for both differential flows and experimental (scalar) time series $\{x(\tau), x(2\tau), \ldots\}$ (where the sampling time τ is much smaller than the average recurrence time T on Σ). In the latter case, the trajectories must first be reconstructed in a suitable embedding space [1]. The time evolution on Σ is hence governed by a mapping of the form

$$\boldsymbol{x}_{n+1} = \boldsymbol{f}(\boldsymbol{x}_n), \tag{3.1}$$

where n is an integer and $\boldsymbol{f}$: $\Sigma \to \Sigma$ is a generally unknown nonlinear function. We then introduce a partition $\mathscr{D}$ of Σ consisting of a finite number r of disjoint subsets Δ_i $(i = 0,1, \ldots, r-1)$: i.e., $\Delta_i \cap \Delta_j = \emptyset$, for $i \neq j$, and $\Sigma = \cup_{i=0}^{r-1} \Delta_i$. We further assume that the transformations $\boldsymbol{f}$ admits a natural invariant measure m [1], so that $m[\boldsymbol{f}^{-1}(\Delta_i)] = m(\Delta_i)$, for all $\Delta_i \in \mathscr{D}$, where $\boldsymbol{f}^{-1}$ denotes the inverse of $\boldsymbol{f}$. A generic orbit $w = \{\boldsymbol{x}_0, \boldsymbol{x}_1, \ldots, \boldsymbol{x}_n\}$ visits various elements $\Delta \in \mathscr{D}$. Denoting with the symbol $s_n \in A_0 = \{0, \ldots, r-1\}$ (where A_0 is the alphabet) the index of the domain Δ visited at time n, the trajectory w is mapped to the symbolic sequence $S = s_0 s_1 \ldots s_n$. It is important to notice that sequence S can be produced (in n iterates) only by the points $\boldsymbol{x}_0$ which belong to the intersection $\Delta_S \equiv \Delta_{s_0} \cap \boldsymbol{f}^{-1}(\Delta_{s_1}) \cap \ldots \cap \boldsymbol{f}^{-n}(\Delta_{s_n})$ ($\boldsymbol{f}^n$ being the nth iterate of $\boldsymbol{f}$) [19]. Since the map admits an invariant measure m, the signal $\mathscr{S}_0 = \ldots s_0 s_1 s_2 \ldots$, produced by infinitely iterating $\boldsymbol{f}$, is stationary. The probability $P(S)$ of each finite subsequence S can then be evaluated as the frequency of occurrence of S in $\mathscr{S}_0$. The normalisation is, as usual, $\Sigma_{|S|=n} P(S) = 1$, $\forall n$, where $|S|$ denotes the length (number of symbols) of S. Obviously, $P(S) = m(\Delta_S)$: i.e., the probability of a sequence equals the mass contained in the phase-space region with the same label. Therefore, symbolic strings S with increasing length $|S| = n$ identify smaller and smaller sets in Σ and their probability decreases accordingly. The collection of all admissible two-symbol strings $s_i s_j$ indexes the elements $\Delta_{s_i} \cap \boldsymbol{f}^{-1}(\Delta_{s_j})$ of the first refinement [23] $\mathscr{D}_1$ of the partition $\mathscr{D}$ under $\boldsymbol{f}$; three-symbol strings label the second refinement $\mathscr{D}_2$, and so on. If every infinitely long symbol sequence corresponds to a single point, the partition $\mathscr{D}$ is called generating [23] and the study of the symbolic signal $\mathscr{S}_0$ is "equivalent" to that of the real trajectories of the system.

The phase-space dynamics given by eq. (3.1) is translated, in the space of all bi-infinite sequences over the alphabet A_0, into a dynamical process $\hat{\sigma}$ called shift map, which is defined by $\hat{\sigma}(\ldots s_0 \cdot s_1 s_2 \ldots) = \ldots s_1 \cdot s_2 s_3 \ldots$ (where the extra dot denotes an arbitrary, fixed origin). It is also useful to define the set A_0^* of all finite sequences over A_0 which, for the binary alphabet $\{0, 1\}$, reads $A_0^* = \{0, 1, 00, 01, 10, 11, 000, 001, \ldots\}$. Of course, a generic signal $\mathscr{S}_0$ need not contain, as subsequences, all elements of A_0^*. For example, in most natural languages one never encounters more than three consecutive consonants; the letter "q" is usually followed by the "u"; in a musical score abrupt changes from high to low notes (or vice versa) or among different tonalities are avoided, as well as long repetitions of a single note. The set $\mathscr{L}(\mathscr{S}_0)$ of all admissible subsequences of $\mathscr{S}_0$ is called the language and is usually properly contained in A_0^*. The set $\mathscr{L}$ is invariant under $\hat{\sigma}$: i.e., $\mathscr{L}(\mathscr{S}_0) = \mathscr{L}(\hat{\sigma}(\mathscr{S}_0))$. Each allowed string S corresponds to a succession of $|S|$ enlargements in a non-empty

region of phase space. The pair $(\mathscr{L}, \hat{\sigma})$ constitutes a symbolic dynamical system [23].

According to the previous discussion, we assume that the signal $\mathscr{S}_0$, of length $|\mathscr{S}_0| \gg 1$, is stationary. Hence, we estimate the probability $P(S)$ of each subsequence S, for $|S| = 1,2,\ldots,n_{\max}$: of course, in order to achieve reliable statistics, it is necessary that the number $r^{n_{\max}}$ of a priori possible sequences (with length $n_{\max}$) be much smaller than $|\mathscr{S}_0|$. The aim of the investigation is to furnish a succession of models approximating the unknown dynamics, in such a way that average properties like, e.g., correlation functions are accurately reproduced. These models are first derived for symbolic sequences in A_0^* and then "dressed" with the actual coordinate values x in phase space. Since, in general, the dynamics folds phase space incompletely, not all a priori possible concatentations of the symbols $s_i \in A_0$ are produced (i.e., $\mathscr{L}$ is a subset of A_0^*). Several sequences are forbidden. For example, consider a binary partition ($\Sigma = \Delta_0 \cup \Delta_1$, $\Delta_0 \cap \Delta_1 = \emptyset$) and a system for which no point x belonging to Δ_0 is mapped back to Δ_0 itself in one step (i.e., $f(\Delta_0) \cap \Delta_0 = \emptyset$): the sequence $S = 00$ cannot occur and the only possible continuation after symbol 0 is 1. Therefore, element Δ_0 can be readily renamed as Δ_{01} and the symbolic dynamics yields concatenations of the "words" $w_1 = 1$ and $w_2 = 01$. Such phenomena occur, in nonlinear dynamical systems, at generic parameter values: for example, the symbolic signal produced by the logistic map

$$x_{n+1} = 1 - ax_n^2 \tag{3.2}$$

in a finite region around $a = 1.85$, with $s_n = [1 + \mathrm{sgn}(x_n)]/2$, can be rewritten completely in terms of the three words $w_1 = 1$, $w_2 = 01$ and $w_3 = 001$. Not all combinations of them, however, are allowed: at $a = 1.85$, w_3w_1, $w_3w_2w_3$, $w_3w_2w_2w_1w_3w_2, \ldots$, are not. The list of such irreducible[#1] forbidden words for the Hénon map (2.1) at ($a = 1.4$, $b = 0.3$) begins with 0000, 0010, 0110, 0101000, 0111000, ... etc. [24]. In both these cases it is believed that there is an infinite number of prohibitions. If, instead, the (sub)shift $\hat{\sigma}$ is specified by a finite list of blocks which may not appear in the signal, it is said to be of finite type [23].

Several families of formal languages have been identified so far, the simplest class being represented by the so-called regular languages [25]. They include, in addition to the subshifts of finite type, the sofic systems [26]: the typical example is provided by the logistic map at the period-two band-merging point [22] which yields forbidden words of the form $0(11)^n0$, $\forall n \geq 0$, where w^n indicates the nth consecutive repetition of w. Regular languages can be described by finite automata [25] which produce symbolic strings according to a sequential (usually, stochastic) mechanism. Three examples of these are presented in section 9 (figs. 9a,b,c). Higher-order generation schemes are defined by means of parallel mechanisms, called grammars, which transform symbols in a string S into words chosen from a list $\mathscr{W} = \{w_1, w_2, \ldots\}$. For example, a substitution over the binary alphabet $A_0 = \{a, b\}$ may be specified by a rule of the type ($a \rightarrow \psi(a) = w_1 = ab$; $b \rightarrow \psi(b) = w_2 = bba$): this yields, upon application to the string $S = ab$, $S' = \psi(ab) = abbba$. These "grammatical rules" may depend, in general, on a number of nearest-neighbours of the symbol to be rewritten and be either deterministic or not [25]. Particularly relevant for nonlinear dynamical systems are the two transformations ψ_{PD}: ($0 \rightarrow 01$; $1 \rightarrow 10$) and ψ_{QP}: ($0 \rightarrow 1$; $1 \rightarrow 01$) which model the period-doubling (PD) accumulation point dynamics [7][#2] and the golden-mean quasiperiodic (QP) transition to chaos [8], respectively.

In general, the optimal description of a sub-

[#1] A forbidden word is irreducible if it does not contain another forbidden word.

[#2] The actual symbolic dynamics of the logistic equation at PD is described by a different transformation which is, however, completely equivalent to the more symmetric one considered here (called Morse–Thue substitution and first considered in ref. [27] in connection with PD).

shift dynamics may be given by a mixture of sequential and parallel mechanisms. In our approach, this is searched for having at disposal only the signal $\mathcal{S}_0$, since we do not assume knowledge of the actual dynamical map (3.1) (and of the partition Σ). It is then clear that even just the identification of the basic words (01 and 10 for PD, 1 and 01 for QP) involved in the generation process is a rather difficult problem, which may be even undecidable [25] in some cases: a few results about recognizability of substituted words in grammatical productions *of known origin* can be found in ref. [28]. In general, parallel rewriting rules are expected to generate signals which are most difficult to describe by means of sequential models.

These simple examples suggest that, in order to achieve a condensed representation of $\hat{\sigma}$, it is useful to decompose the signal into a succession of suitable "primitive" words $w_1, w_2, \ldots$, possibly having different lengths, which generate (a superset of) the whole language $\mathcal{L}$ upon concatenations $w_i w_j \ldots$ with one another. They constitute a code [6, 5] and their number may be either finite or not, depending on the nature of $\mathcal{S}_0$ and on the criterion adopted for their definition. They should be chosen in such a way that the most compact description of the dynamics is obtained. For example, if the model to be built must predict all admissible sequences of length $|S| > n_0$ by concatenating primitives, one should minimize the number of forbidden words appearing in this process across the junction between consecutive primitives In fact, if 00 is forbidden and the bare symbols 0 and 1 are chosen as primitives, the tree has a pruned branch at level 2 (obtained when trying to concatenate 0 with 0); if, instead, the primitives are 1 and 01, no topological "defect" occurs (see appendix A for more details).

In the following we suppose that a set of code words has been identified: the technical description of a specific algorithm can be found in appendix A. All admissible sequences are classified hierarchically by constructing a tree (see

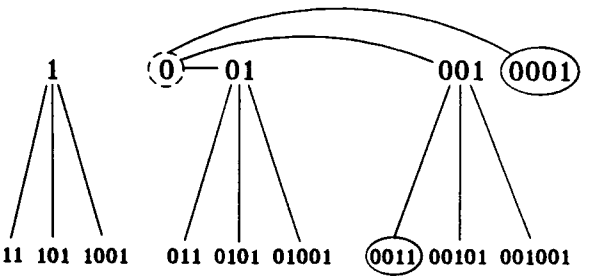

Fig. 2. First two levels of the logic tree for the roof map at $a = (3 - \sqrt{3})/4$ (see appendix A for a description of the construction method).

fig. 2, for an example), the vertices of which are labelled, at the first level, by the primitives themselves. The lth level ($l = 1, \ldots, \infty$) contains concatenations of l such words. All branches leaving a generic vertex S point to the allowed extensions Sw_j, $Sw_k, \ldots$ of sequence S (refinements of subset Δ_S). If the signal is aperiodic, there are branching vertices, corresponding to strings with more than one possible continuation. The method illustrated in appendix A yields a code which satisfies the normalization condition $\Sigma_i P(w_i) = 1$. Furthermore, the probabilities obey the Kolmogorov consistency condition $P(S) = \Sigma_i P(Sw_i)$, so that every complete level of the tree represents a full covering of the phase space (more precisely, of the Poincaré section Σ): in fact, $1 = \Sigma_i P(w_i) = \Sigma_i \Sigma_j P(w_i w_j)$, and so on. Trees constructed in this way are equivalent to "generalized" Markov models, which describe the dynamics as a sequence of events w_i, occurring with measurable transition probabilities, according to unknown rules (determined by the dynamical map f in eq. (3.1)). Since the sequences have variable length at every level, in general, the memory extent depends on the probabilities of the orbits. The order of such models can be estimated by the "average Markov time" per level [5]

$$\bar{\theta} = \lim_{l \to \infty} \frac{1}{l} \sum_{\text{level } l} |S| \, P(S) \tag{3.3}$$

which equals 1 for ordinary trees (also called

block code [6], where the symbols themselves are taken as primitive). A description based on these Markov trees provides a tool for the understanding of the power spectrum $S(f)$ of the signal $\mathcal{S}_0$. In the next sections, the topological and metric (probabilistic) features of the tree will be related to the shape of $S(f)$, by turning the description into an effective model for the generation of signals which are "statistically close" to $\mathcal{S}_0$. Before doing this, we briefly illustrate the criterion for the choice of suitable primitive words.

A particularly relevant role in determining the recurrence (long-term) properties of nonlinear dynamical systems is played by the set Ω of "non-wandering" points [23]: a point x is non-wandering for the map f if, for any neighbourhood U of x, there exists a number $n>0$ such that $f^n(U)\cap U\neq\emptyset$ (an analogous definition can be given for a subshift $\hat{\sigma}$). Correspondingly, a symbolic sequence S which labels a domain Δ_S in Ω will be observed in the signal $\mathcal{S}_0$ with a well-defined frequency of occurrence. The set Ω consists of points with a weak recurrence property: in particular, all periodic points of f belong to Ω [29]. This property suggests a useful criterion to distinguish primitive words from "transient" (i.e., non-recurrent) ones. Following ref. [5], we define a primitive as a string w which can be periodically extended up to the maximum investigated block length n_{max} and which does not contain a prefix with the same property; e.g., 001 is a primitive if 001001... is allowed and 000... is not (see appendix A for details). This is a "strong" condition: namely, one which does not depend on tuning parameters or on statistical weights. Weaker conditions (depending, e.g., on the probabilities $P(S)$) are discussed in ref. [5]. Recall that periodic orbits are dense on the non-wandering sets of hyperbolic (axiom-A) dynamical systems [23].

Our analysis is not restricted to signals produced by nonlinear dynamical systems but can be applied, more generally, to any stationary one-dimensional symbolic pattern, such as a spin configuration generated by a Monte Carlo process or by a cellular automaton [30]. The study of power spectra of parallel-generated sequences has received much attention in the theory of one-dimensional quasi-crystals [31]. All of these systems exhibit a rich structure of subsequences with a recurrent character. If only the data are given and the nature of the physical process is unknown, no theoretical argument can be used to obtain asymptotic estimates (i.e., concerning infinitely long orbits). In such a case, the main limitation of our approach is represented by the size of the available computer memory: with a binary alphabet, one is usually forced to choose $n_{max}\leq 22$.

With generic chaotic signals it is possible to find primitives which are periodically extendable up to n_{max} if the signal is sufficiently long (i.e., if $|\mathcal{S}_0|$ is at least of the order of $10^2 r^{n_{max}}$, where r is the number of symbols in the alphabet A_0). The analysis has been performed for the logistic equation at various parameter values, for several other one- and two-dimensional maps and for some chaotic flows. The first few primitives of the Hénon map at ($a=1.4$, $b=0.3$) are $w_1=1$, $w_2=01$, $w_3=0011101$, $w_4=0011111$, $w_5=00111101$, $w_6=00011101$, $w_7=00011111$, $w_8=000111101$, $w_9=0011110011101$, and so on. The simple examples of period doubling and quasi-periodicity are treated in the appendix. The whole unfolding procedure is applicable independently of the existence of a Markov partition [23] (if one exists, a finite set of primitives is always found: the converse is not true).

4. Iterated coding and renormalization

Before describing the models which can be constructed using the information stored on the tree, we discuss a further very important step in the unfolding scheme. It consists of an iterative procedure which enables us to achieve higher accuracy and to analyze automatically also phe-

nomena at the border of chaos (ergodic, nonmixing). The subdivision of the signal into primitive words constitutes a coarse graining in the time direction, which corresponds to enlargements of some regions of phase space. Because of the arbitrariness of the acceptance condition for the code words (periodic extendability, e.g.) and of the presence of resolution parameters imposed by the finiteness of the amount of data (n_{max}, n_{cut}, see appendix A), this procedure can be viewed as an approximate language-recognition method [32]. The nature of the physical process is, in fact, unknown and the primitives are not expected, in general, to reflect fully asymptotic properties of the system. Also, the resulting hierarchical description may not be the most compact one. This is particularly evident at PD and QP, where the signal, although generated sequentially, can be more efficiently described by means of a parallel algorithm. On the other hand, the dynamics itself may be explicitly of parallel type, as in Monte Carlo updates of spin chains or in cellular automata. The identification of the long-ranged "coherent" structures appearing in such systems is particularly difficult and requires consideration of increasingly long blocks of symbols. The coarse graining of the signal into code words, in such cases, can never be considered as definitive. Therefore, it is necessary to resort to a higher-level modelling procedure, which provides the unfolding method with an explicit parallel mechanism. To this aim, the primitive words w_1, w_2, ... detected in the original signal $\mathcal{S}_0$ are renamed with symbols from a new alphabet $A_1 = \{0, 1, \ldots\}$ and the whole analysis is repeated on the transformed string $\mathcal{S}_1$ thus obtained. The iteration of this procedure yields a progressive coarse graining of the signal (corresponding to an increase of resolution per symbol in phase space). Once the primitives have been recorded in a table, they can be easily recognized while scanning the source signal sequentially, since the method illustrated in the appendix always yields instantaneous (prefix-free [6]) codes. The description of the image signal $\mathcal{S}_k$, obtained after k recoding steps, consists of the derived tree and of the code which keeps track of the previous block-renaming cascade (i.e., of the relations between each symbol in the alphabet A_k and its pre-image string in $\mathcal{S}_0$). The recoding procedure is equivalent to a renormalization-group transformation on the nonlinear map f associated with the subshift [27]: in fact, renaming a sequence S of length n with a single symbol corresponds to considering the nth iterate of f in the phase-space element Δ_S. For perfectly self-similar languages, such as those of PD and QP, the trees obtained at each step are identical: i.e., an exact renormalization is readily achieved [5]. For signals of purely sequential nature, instead, only a few recoding steps are usually possible and useful. However, recoding always yields more asymptotic estimates of the observables associated with the symbolic sequences. For example, after the substitution $(w_1, w_2, w_3) \rightarrow (0, 1, 2)$, in the logistic map at $a = 1.85$, all strings which previously appeared as overlaps between consecutive primitives (like 10, or 100 in $\ldots\ w_2w_2w_1w_2w_3w_2\ldots = \ldots 0\overline{10}110\overline{100}101\ldots \rightarrow \ldots 110121\ldots$, for example) simply disappear. In the new signal, overlap-free probabilities P' are therefore computed and unnecessary sequences are automatically neglected in the tree description. Recalling that in the thermodynamic formalism for nonlinear dynamical systems [3] the role of the Hamiltonian is played by $H(s_1 \ldots s_n) = \ln P(s_1 \ldots s_n)$ [33], it is readily seen that recoding $\mathcal{S}_0 \rightarrow \mathcal{S}_1$ and recomputing the probabilities in $\mathcal{S}_1$ is a completely analogous operation to obtaining a renormalized block Hamiltonian $H' = \ln P'(w_1 \ldots w_m)$ (with $|w_i| \geq 1$, $m \leq n$). In the case of the logistic map at $a = 1.85$, we find $P(1) \approx 0.5896$, $P(01) \approx 0.3236$, $P(001) \approx 0.0868$ in $\mathcal{S}_0$ and $P'(0) \approx 0.451$, $P'(1) \approx 0.401$, $P'(2) \approx 0.148$ in $\mathcal{S}_1$. Another advantage of the renaming process is that the code redundancy may be reduced: in fact the whole signal at PD can be encoded with the first two primitives w_1 and w_2 only, although $P(w_1) + P(w_2) < 1$ in $\mathcal{S}_0$, and all

other code words never occur in the renaming procedure.

5. Reconstruction of power spectra

The trees obtained with the procedure illustrated in the previous section can be used to predict the values of physical observables associated with a level l sequence S, from the knowledge of those corresponding to the orbits allocated at levels 1 to $l-1$. In ref. [5] a notion of complexity was introduced, related to the difficulty of inferring the structure of the system at increasingly finer levels of resolution, by means of estimates based on coarser-scale measurements. In particular, considering the probabilities $P(S)$, it is possible to study sequence-to-sequence transitions and to reconstruct signals with statistical properties which closely approximate those of the actual one. To this aim, the dynamics is modelled by means of a sequence of Markov processes (one for each level l), defined by conditional probabilities, such as $P(S'|S)$, which, in turn, are estimated from the probabilities of lower-level sequences. The accuracy of the model increases with the order l of the level. Although no exact predictions of the actual time dynamics are possible, in general, this method approaches the limit of an "optimal" description in a statistical sense: the reconstructed signals, in fact, exhibit expectation values and transition probabilities which are in close agreement with those of the system under investigation. The dynamics is represented as a succession of deterministic paths (blocks of symbols) which appear at random in time, according to the measured probabilities. The usage of variable-length words furnishes a simple interpretation of the structure of power spectra, in addition to improvements in the convergence of the approximations and in the compactness of the description. In turn, the convergence of the reconstructed power spectra with the order l provides a test for the validity of the model.

The set of all admissible trajectories can be generated with the help of a transition matrix **M** whose elements $M_{ij} = P(S_j|S_i)$ represent the conditional probability of observing sequence S_j, given S_i. They refer to the level l strings (composed of l primitives each) and satisfy the relation $\Sigma_{j=1}^{N(l)} M_{ij} = 1$, where $N(l)$ is the number of orbits at level l. A bi-infinite sequence $\mathcal{S} = \ldots S_{j-1}S_{j_0}S_{j_1}\ldots$ is admissible if $M_{j_n j_{n+1}} > 0$ for all $n \in (\ldots, -1, 0, 1, \ldots)$. The dynamics is then described by a shift map $\hat{\tau}(\mathcal{S}) = \mathcal{S}'$, with $S'_{j_n} = S_{j_{n+1}}$, which advances by l primitives at a time (at variance with $\hat{\sigma}$). When the population $N(l)$ of level l is finite, the set of all admissible sequences $\mathcal{S}$, together with map $\hat{\tau}$, is a generalization of a subshift of finite type [23] with transition matrix **M**. In practice, $N(l)$ is bounded by the number of primitives $N(1, n_{\max})$, found with a finite value of $n_{\max}$, raised to the power l.

Symbolic trajectories $S_1S_2\ldots$ equivalent to the actual signal can be generated with the following simple algorithm. Starting with sequence $S_i (1 \le i \le N(l))$, its successor S_k is determined by choosing a random number u from the uniform distribution over the interval (0, 1) and by comparing it with the values M_{ij}, for all j: the index $1 \le k \le N(l)$ of the successor is the integer which satisfies the relation $\Sigma_{j=1}^{k-1} M_{ij} < u < \Sigma_{j=1}^{k} M_{ij}$. Of course, if some recoding steps had been performed during the unfolding process, each symbol in the current sequence S_k has to be translated back to its pre-image word in the set of primitives found in the analysis of the original signal $\mathcal{S}_0$: in the case of the logistic map at $a = 1.85$, for example, the sequence $w_2w_1w_3 = 102$ is read as $011001 = \psi(102)$, where $\psi(0) = 1$, $\psi(1) = 01$ and $\psi(2) = 001$. The signal is hence generated by the composition of the Markov shift $\hat{\tau}$ with one application of the substitution ψ. For PD and QP, of course, not a single Markov step is needed, since the infinite iteration of the codes ψ_{PD} or ψ_{QP} already produces the exact signal with any input string. In general, the reconstructed signals are given by iteration of a composition of the form $\psi^m\hat{\tau}$, for some ψ (pos-

sibly, the identity), with $m \geq 1$. Some analytical results have been recently obtained for the power spectra of the invariant strings of pure substitutions (including PD and QP) which satisfy certain restrictions [31, 34]. The exactly self-similar structure of such systems allows writing of recursive relations directly for the Fourier amplitudes. In the next section, we present analytical results for a few Markov models describing the simplest examples of incomplete-folding dynamics. So far, an analysis of signals arising from a mixed parallel-sequential dynamics has not been attempted.

The calculation of the matrix elements (conditional probabilities) M_{ij} relative to transitions between level l orbits requires, in principle, taking into account a memory extending over $2l$ primitives. In fact, the probability $P(W|V)$ to observe the sequence $W = w_1 w_2 \ldots w_l$ after $V = v_1 v_2 \ldots v_l$ is defined as the ratio $P(v_1 \ldots v_l w_1 \ldots w_l)/P(v_1 \ldots v_l)$. Since, in general, it is impractical to consider levels l and $2l$, because of the relevant length of the sequences involved, the conditional probabilities can be approximated by comparing two successive levels (i.e., l and $l+1$). The resulting model has then a memory limited to l primitives and reduces to a usual lth order Markov process once the probabilities have been evaluated in the recoded signal. The value of $P(W|V)$ is then estimated as

$$P(w_1 \ldots w_l | v_1 \ldots v_l) \approx P(w_1 | v_1 \ldots v_l) \times P(w_2 | v_2 \ldots v_l w_1) \times \ldots \times P(w_l | v_l w_1 \ldots w_{l-1}), \quad (5.1)$$

where $P(a_{l+1}|a_1 \ldots a_l) = P(a_1 \ldots a_{l+1})/P(a_1 \ldots a_l)$, as usual. All memory effects available up to level l are included, since the dependence on the last l symbols is explicitly taken into account.

6. Model convergence and scaling functions

The validity of the approximation (5.1) and the convergence of the Markov models with the order l can be discussed within the general framework of the thermodynamical formalism for dynamical systems [3] and related to the measure of complexity introduced in ref. [5]. The product on the r.h.s. of eq. (5.1) appears in fact in the coefficients of the lth power of the transfer matrix [3, 5]

$$T_{w_0 w_1' \ldots w_l'; w_1 \ldots w_{l+1}} \equiv \frac{P(w_1 \ldots w_{l+1})}{P(w_1 \ldots w_l)} \delta_{w_1 w_1'} \ldots \delta_{w_l w_l'} \quad (6.1)$$

for a lattice of (variable-size) spin blocks w_i. Matrix **T** describes the conditional probability for the transition between the strings $\ldots w_0 w_1' \ldots w_l' \ldots$ and $\ldots w_1 w_2 \ldots w_{l+1} \ldots$ upon (left) shifting of the signal by one primitive at a time. The two sequences are "connected" only if the last l words of the left one coincide with the first l of the right one (the image), as taken into account by the Kronecker δ's in eq. (6.1). Such a transfer matrix is usually introduced [35, 4, 5] to obtain asymptotic estimates of the generalized metric entropies $K(q)$ [1] from a suitable eigenvalue equation: the function $K(q)$ plays the role of a free energy, while the parameter q is related to the temperature [33]. The convergence properties of the associated thermodynamic sums are therefore the same as those of the Markov models constructed in the previous section, since in both problems the relevant object is the transfer matrix **T**. A detailed description of the asymptotic behaviour of the conditional probabilities can be graphically represented by means of a scaling function $\sigma(t)$ [9] which, for our present purposes, is defined as follows. The level l sequences $S = w_1 w_2 \ldots w_l$ are mapped onto the unit interval by associating a value $t = t(S)$ to each of them. For every $t = t(S)$ the level l approximation $\sigma_l(t)$ of the scaling function $\sigma(t)$ is given by the conditional probability $P(S = w_1 \ldots w_l)/P(w_1 \ldots w_{l-1})$. The definition of the ordering parameter $t = t(S) \in [0, 1]$ can be easily understood by referring to the logic tree of fig. 2. At level $l = 1$, the primitives w_k are con-

sidered in the same order as on the tree (e.g., from left to right) and $t(w_k) = t(w_{k-1}) + P(w_k)$, $k = 1, \ldots, N(1, n_{\max})$ (w_o being the empty string, with $t(w_0) = 0$). Hence, $\sigma_1(t)$ is piecewise constant over $N(1, n_{\max})$ intervals. The generic kth interval is split, at level-two, into subintervals labelled by all sequences $w_j w_k$ ending with w_k and ordered from left to right according to the order of the w_j's on the first level of the tree. In this way, we have $t(w_j w_k) = t(w_{j-1} w_k) + P(w_j w_k)$ and the index k is increased by one after that all j's have been scanned. At level-three, all subintervals of $w_j w_k$ are labelled as $w_i w_j w_k$, with the w_i's ordered as usual, and so on. For example, with a binary tree, the values of t correspond, from left to right, to the sequences 0 and 1 at level one, to 00, 10, 01 and 11, at level two, to 000, 100, 010, 110, 001, 101, 011 and 111, at level three. The widths of the intervals are just the corresponding sequence probabilities, so that forbidden strings do not appear at all [5]. As an illustration, we display in fig. 3 a schematic plot of the first two approximations to $\sigma(t)$ for a tree with the same topology as that of fig. 2. Notice that some intervals are split only into two parts and not three, due to the prohibitions. We have used the short notation P_i for $P(w_i)$, P_{ij} for $P(w_i w_j)$ and, similarly, σ_i for $\sigma(t(w_i))$ and σ_{ij} for $\sigma(t(w_i w_j))$. In fig. 4 we show

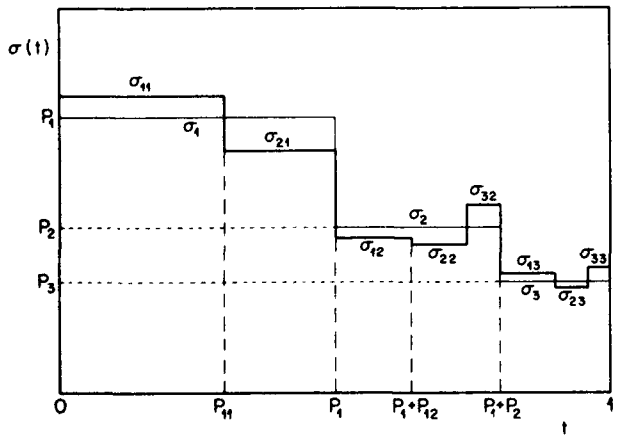

Fig. 3. Schematic plots of the first two levels of approximation to the scaling function $\sigma(t)$ for a tree with the same topology as that displayed in fig. 2.

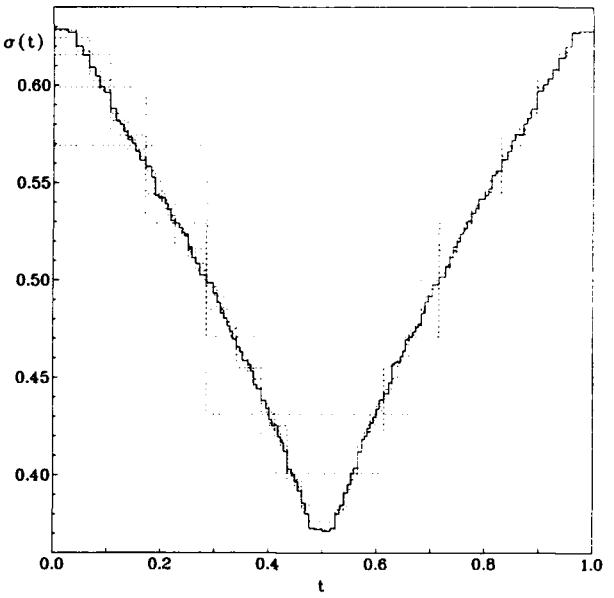

Fig. 4. Approximations to the probability scaling function $\sigma(t)$ of the Lorenz flow at standard parameter values, obtained from the first seven levels of the associated logic tree (dotted lines: $l = 1, \ldots, 6$; solid line: $l = 7$). The ordering parameter t is defined in the text .

the approximations $\sigma_l(t)$ obtained from the first seven levels of the tree for the Lorenz system [36]

$$\dot{x} = 10(y - x)\,,$$

$$\dot{y} = 28x - y - xz\,,$$

$$\dot{z} = -8z/3 + xy\,. \qquad (6.2)$$

The Poincaré section $\Sigma = \{(x, z): \dot{x} = 10(y - x) = 0, \ddot{x}\,\mathrm{sgn}(x) < 0\}$, which is obviously intersected by all trajectories and has the same symmetry as the complete flow, has been divided into two regions by means of the line $x = 0$ (for other choices of the parameters, the generating partition is instead ternary [37]). Notwithstanding the absence of the two period-one cycles, a complete binary-tree description is appropriate, because prohibitions appear only for $|S| > 24 > n_{\max}$ [38]. Within the statistical fluctuations, a fast convergence is observed for increasing l, indicating that Markov models of order as low as

5 or 6 already reproduce the symbolic dynamics with very good accuracy. The memory vanishes exponentially, as it can be seen by inspecting fig. 4, where the distances between consecutive approximations roughly decrease as 2^{-l}. Notice that a perfectly self-similar set is characterized by a piecewise-constant asymptotic scaling function: for system (6.2), instead, the apparent continuity of $\sigma(t)$ indicates the existence of an infinity of scaling rates for the probabilities. The attractor is, in fact, close to an intermittent situation [39]. Convergence of $\sigma_l(t)$ to a function $\sigma(t)$, for $l \to \infty$, indicates that the system is simple, relatively to the chosen unfolding scheme, and that the derived model accurately describes the scaling behaviour of the probabilities.

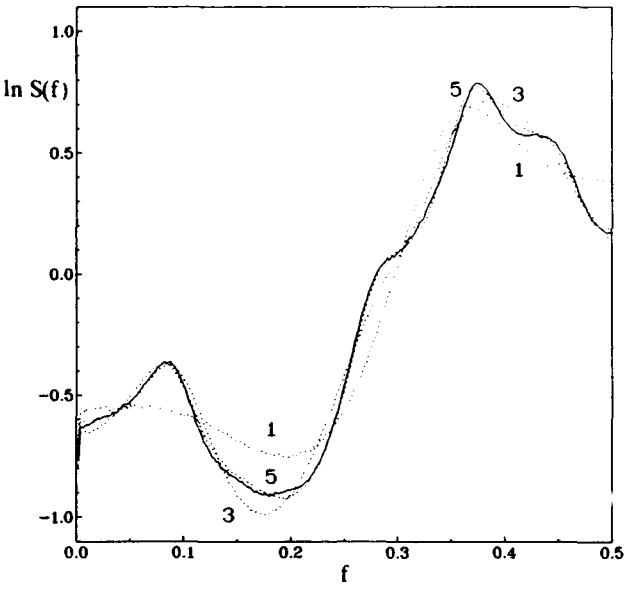

Fig. 5. Comparison between the power spectrum $S(f)$ of the symbolic signal of the logistic map $x' = 1 - 1.85x^2$ (thick line) and those obtained from the level-one, -three and -five reconstructions (dotted lines).

7. Numerical results

The roof map (see the appendix, eq. (A.1)) at $a = (3 - \sqrt{3})/4$ is both topologically and metrically simple [5]: the power spectra of the reconstructed signals are indistinguishable from the true one already at level $l = 2$ (where the longest forbidden sequence $w_3 w_1 = 0011$ is detected). Due to the (piecewise) linearity of this map, the probabilities of compound sequences nearly factorize. In order to show the effect of the nonlinearity, we present, in fig. 5, the power spectrum $S(f)$ of the actual symbolic signal (solid line) of the logistic map at $a = 1.85$, compared with those of the approximations obtained from the level-one, -three and -five Markov models (dotted lines). The area under the curve $S(f)$ versus f (average over 2000 spectra of length 4096) has been normalized to 1, after subtracting the zero-frequency component, and the natural logarithm of $S(f)$ has been plotted. The nonlinearity of this map renders the estimates less accurate, for equal l values, than in the previous case, although the two systems exhibit nearly the same topological tree structure. Since incomplete folding leads to descriptions in terms of variable-length orbits, the position of the peaks in the spectrum finds an easy interpretation. For example, the primitives in both cases have lengths 1, 2 and 3: therefore, a broad peak centred at a frequency between $\frac{1}{3}$ and $\frac{1}{2}$ is expected (recall that $f = \frac{1}{2}$ is the largest measurable frequency in a discrete-time signal). The exact position depends on the probabilities of the corresponding sequences. The quadratic maximum in the logistic equation produces square-root singularities in the invariant measure at the forward images of $x = 0$. In particular, the probability of sequences containing several zeros is higher than in the hyperbolic case. This explains the shape of the main peak in fig. 5, determined by the primitives 01 and 001, which is sharper than the corresponding one of the roof map and is less accurately reproduced for the same l -values. Forbidden sequences at low levels in the tree are responsible for the appearance of secondary peaks, one of which is visible in the figure, around $f = 0.09$. These mechanisms will be discussed in more detail in the next section, where a hierarchy of exactly solvable problems will be introduced. In fig. 6, we show the results ob-

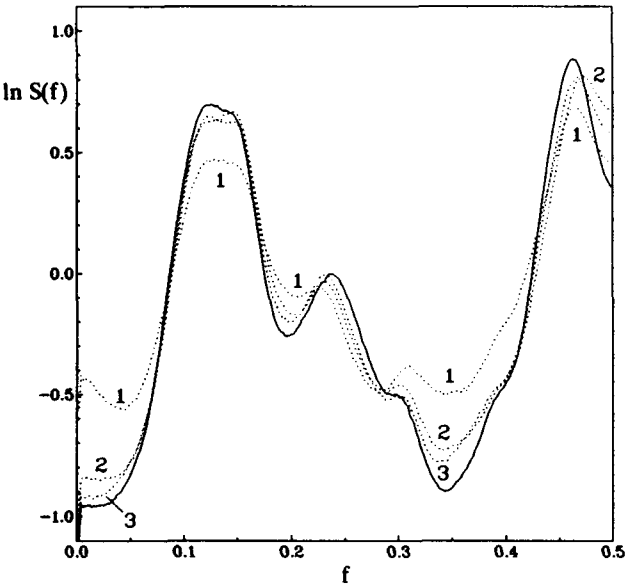

Fig. 6. Same as in fig. 5 for the Hénon map at standard parameter values: the approximations, in this case, have been obtained using level one, two and three.

tained for the Hénon map at ($a = 1.4$, $b = 0.3$), where the population of level one has been truncated after nine primitives (inclusion of more code words did not change the quality of the picture) and reconstructions have been performed with level one, two and three. It is clearly seen that the primitives (of lengths 1, 2, 7, 8, etc.) account for the main peaks at frequencies (close to) $\frac{1}{2}$, $\frac{1}{7}$ and $\frac{1}{8}$. The smaller peak around $f = \frac{1}{4}$ corresponds to the level-three orbit $S = 0111$. In this case, the higher levels contain orbits of length larger than n_{max}. Since their probabilities cannot be estimated directly, approximated values have been calculated using a predictor of the same type as those discussed above.

All spectra displayed in the figures have been obtained by recoding the original signals $\mathcal{S}_0$ into primitives and by computing the probabilities P' in the image signal $\mathcal{S}_1$. The improvement is considerable, especially for the logistic and Hénon maps (spectra reconstructed without recoding are reported in ref. [20]). For PD or QP, iteration of the recoding procedure immediately yields the (unique) exact signal, starting from any seed word, without need of choosing sequences at random with the transition matrix **M**.

The unfolding method requires the detection of variable-length code words whenever they provide the minimal encoding of the source signal. However, it is always possible to construct ordinary (block-code [6]) trees, where equal-length sequences are allocated at each level (i.e., the primitives coincide with the symbols of the alphabet), even in the presence of incomplete-folding dynamics. The whole modelling procedure remains unchanged, except that the description is less compact (as explained before, many unnecessary strings are considered), less asymptotic estimates are obtained (short strings without recurrence properties do not reflect average properties of the system) and, especially, no recoding (renormalization) is possible. The accuracy achievable using block-code trees at some level l of resolution is lower or comparable with that obtained from the variable-length method at a level $l' \approx l/\bar{\theta}$ (where $\bar{\theta}$ is the average Markov time of eq. (3.3)), without recoding: for the logistic map at $a = 1.85$, $\bar{\theta} \approx 1.86$ and the level-three results shown in fig. 5 are quantitatively close to those given by a level-six binary-tree model. If, however, the leftmost peaks in the spectrum correspond to frequencies significantly (i.e., at least twice) smaller than $1/\bar{\theta}$, the convergence of our method is much more rapid: this is the case of the Hénon map, for which the peaks at frequencies $\frac{1}{7}$ and $\frac{1}{8}$ appear already in a level-one reconstruction using only 7 primitives. With a block code, of course, one needs at least 8 levels (i.e., a considerable number of sequences). The parameter $\bar{\theta}$ is a measure of the model's code compression [6] and depends, for a given system, on the criterion used to define the primitives: the value $\bar{\theta} = 1$ indicates no compression (block code).

8. Invariance under smooth coordinate changes

The reconstruction of the symbolic signal $\mathcal{S}_0$ is

based on two ingredients which are invariant under smooth coordinate changes: the topology and the metrics (sequence probabilities) of the logic tree. When dealing with real signals x_n (as, e.g., experimental time series), however, it is necessary to consider the values assumed by the recorded observable x as well. This gives the non-invariant part of the spectrum $S(f)$. Of course, the full signal and the associated symbolic one yield, in general, different power spectra. The topological rules reflect the complicated folding mechanism acting on phase space and represent the most fundamental dynamical properties of the system, while the probabilistic features can affect the shape of the spectra only within the constraints of the topological structure. They are particularly relevant in the non-hyperbolic case, because of the presence of singularities in the invariant measure. Finally, the effect of the actual x-values on $S(f)$ is weaker than or comparable to that of the probabilities. As an example, consider the well-known Bernoulli and tent maps [23] which yield the same symbolic dynamics (a random, δ-correlated, sequence of 0's and 1's) but are, respectively, order preserving and order reversing. In the former case, the spectrum of the signal x_n is Lorenzian (with half-width $\lambda = \ln 2$) whereas, in the second one, it is white (as that of the symbolic signal). As a further illustration of these differences, we show, in fig. 7, the spectrum of the symbolic signal of the Lorenz system and, in fig. 8, the corresponding one for the x-variable on the Poincaré section: an average over 2000 trajectories of length $N = 4096$ has been taken. In this case, the two spectra have nearly the same shape, apart from a rescaling of the vertical axis: the symbolic dynamics can be approximated by a nonlinear version of the Bernoulli shift which does not reach completely the two fixed points at $x = 0$ and $x = 1$, where the motion is close to intermittency [39]. Therefore, the peak visible in the figures around frequency zero is mainly determined by the distribution of the times spent by the system in the intermittent regions, rather

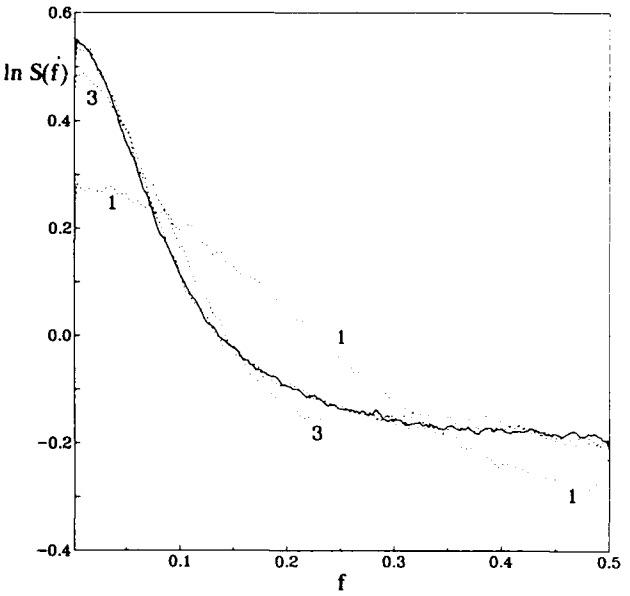

Fig. 7. Same as in fig. 5, for the Lorenz system at standard parameter values, using level one, two and three, (the latter reconstruction being nearly coincident with the true spectrum).

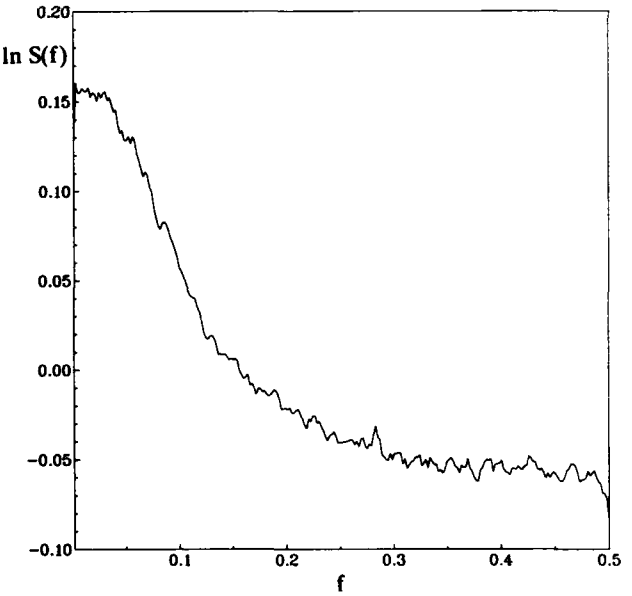

Fig. 8. Power spectrum of the x-coordinate in the Poincaré section $\Sigma = \{(x, z)\colon \dot{x} = 10(y - x) = 0,\ \ddot{x}\,\mathrm{sgn}(x) < 0\}$ of the Lorenz system at standard parameter values.

than by the x-values (as it was instead for the Bernoulli map), and it is not Lorenzian. Indeed, also in the much more complicated case of the

Hénon map only minor modifications of the overall shape are imputable to the coordinate values. These can be included in the reconstructed signals by associating to each sequence S a number $n = |S|$ of x-values given by $\bar{x}_0 = \langle x \rangle_{\Delta_S}$ (the center of mass of phase-space element Δ_S), $\bar{x}_1 = \langle x \rangle_{f(\Delta_S)}, \ldots, \bar{x}_{n-1} = \langle x \rangle_{f^{n-1}(\Delta_S)}$, where $f^k(\Delta)$ denotes the kth image of set Δ under the action of map f. When the symbolic string S is chosen, the real sequence $\{\bar{x}_0, \ldots, \bar{x}_{n-1}\}$ is attached to the reconstructed signal to be Fourier transformed. A further improvement is obtained by adding to each center of mass $\bar{x}_k$ a (Gaussian-distributed) random number with variance $\sigma_k = [\langle x^2 \rangle_{f^k(\Delta_S)} - \bar{x}_k^2]^{1/2}$, which is also evaluated from the coordinates of the phase-space points falling in element $f^k(\Delta_S)$ [20]. In this way, the dynamics is split into a macroscopic part, given by the (finite-time) jumps between elements in phase space, and a microscopic random contribution which represents the unresolved motion within each element of the covering.

Finally, notice that the power spectrum of a continuous-time system may differ substantially from that computed on the Poincaré section Σ, when the return times of the trajectory on Σ have a broad distribution (cf., for example, figs. 7 and 8 with the spectrum of the full signal generated by the Lorenz system (6.2), reported in ref. [40]). The hierarchical modelling proposed in ref. [5] and illustrated above can be complemented with local maps which approximate the real trajectories from a phase-space element on the Poincaré section Σ to its image on Σ itself. These transformations are determined by fitting the orbits with suitable polynomials [37].

9. A hierarchy of Markov models

The intuitive interpretation of the shape of power spectra given in the previous section can be rendered more rigorous by studying a few analytically solvable examples. We consider Markov models corresponding to the simplest five subshifts of finite type, in a hierarchy characterized by an increasing number (or length) of forbidden words. The resulting topology of the tree will determine the main features in the spectrum, whereas variation of the transition probabilities will cause smooth modifications, within the limits imposed by the topology.

The finite automaton which describes a given regular language can be represented by a directed graph $D = (V, A)$, where $V = \{v_1, \ldots, v_m\}$ is a set of vertices and $A = \{\ldots v_k v_l, \ldots\}$ is a set of ordered pairs of vertices, called arcs [25] (arc $v_k v_l$ obviously leading from v_k to v_l). The arcs are labelled with symbols s_i from the alphabet $A_0 = \{0, \ldots, r-1\}$ (which we take as binary, for simplicity), where i ranges from 1 to the number of arcs in the graph. At most $r = 2$ arcs can leave a vertex: the language is the set of the symbolic words generated by following any allowed path on the graph. Furthermore, each arc $v_k v_l$ is charactered by a transition probability p_{kl} which satisfies the relation $\Sigma_l p_{kl} = 1$, $\forall k$ (i.e., there is a unit probability to leave any vertex v_k). When the automaton is used to generate a signal, a random choice is made at each bifurcating vertex, according to the attached probabilities (see fig. 9). Therefore, the process can be described by a Markov transition matrix $\mathbf{R}$, analogous to those considered in section 5. Notice that no memory is taken into account in these simple models: a given arc is followed with a given probability, independently of the past, at variance with what happens when using trees, where all allowed paths are explicitly considered, together with the respective weights. The autocorrelation function $C(\tau)$ can be computed analytically from the knowledge of the graph by following a straightforward procedure [41]. The necessary information is stored in the matrix $\mathbf{R}$, whose generic element R_{ij} represents the probability of the arc-to-arc transition $s_i \rightarrow s_j$: this quantity can be easily computed from the arc (vertex-to-vertex transition) probabilities p_{kl} defined above. Representing the binary symbols

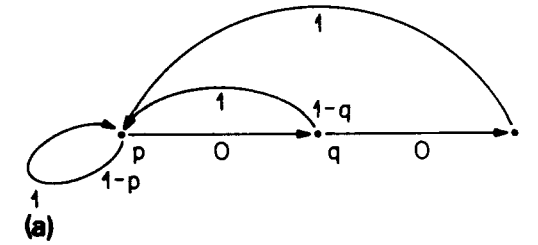

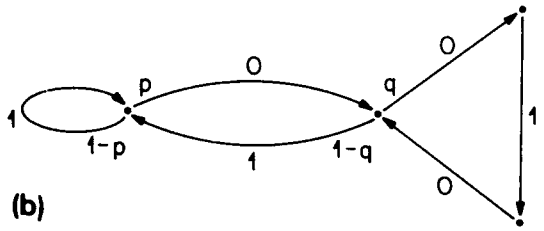

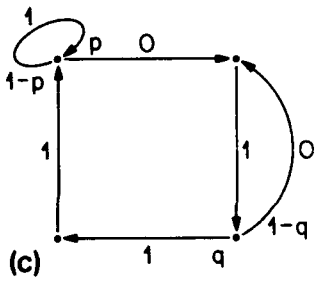

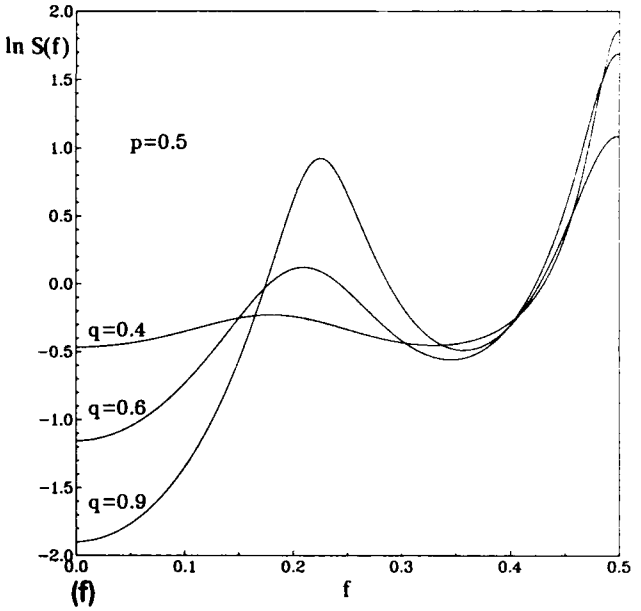

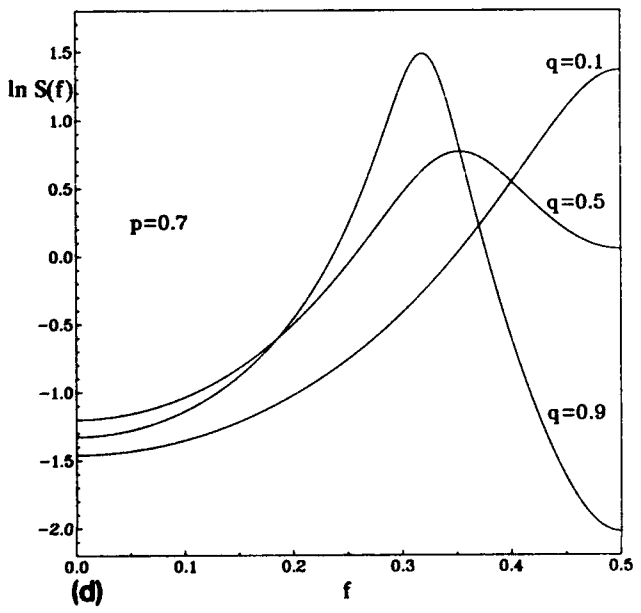

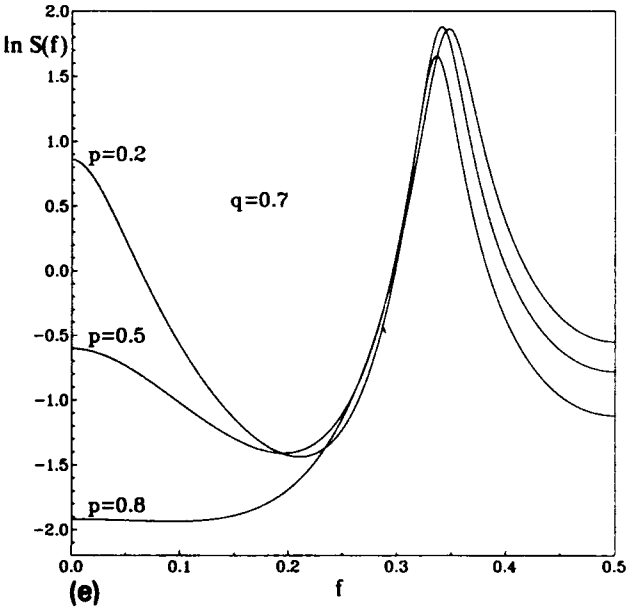

Fig. 9. Directed graphs (a, b and c) representing the allowed transitions in models 3, 4 and 5 of section 9 and corresponding power spectra (d, e and f), for various choices of the parameters.

$\{s_1, s_2, \dots\}$ attached to the arcs (taken in any order) and their corresponding steady-state probabilities $\{\pi_1, \pi_2, \dots\}$ as vectors $\vec{s}$ and $\vec{\pi}$, the autocorrelation function $C(\tau) = \langle s_{i_0} s_{i_\tau} \rangle - \langle s \rangle^2$, $\tau = 0, 1, \dots$, is given by the expression [41]

$$C(\tau) = \overrightarrow{\pi s} \cdot \mathbf{R}^\tau \cdot \vec{s} - (\vec{\pi} \cdot \vec{s})^2 , \tag{9.1}$$

where $\mathbf{R}^\tau$ is the τth power of $\mathbf{R}$ and $\overrightarrow{\pi s} = \{\pi_1 s_1, \pi_2 s_2, \dots\}$.

We discuss, with the help of this procedure, five Markov models related to continuous piecewise-linear maps, showing that the presence of forbidden sequences causes the emergence of "coherent" structures, starting from a flat spectrum.

As already mentioned, the symbolic dynamics of the tent map (eq. (A.1) with $a = 0$) is a random process with

$$C(\tau) = \begin{cases} p(1-p), & \text{if } \tau = 0, \\ 0, & \text{otherwise}, \end{cases} \tag{9.2}$$

where $p = P(0)$, so that $S(f) = 1$, $\forall f$. A well-known metric modification of such a complete-topology system is provided by the telegraphic signal [42], whose spectrum is a Lorenzian centered at the origin. The simplest topological alteration of the full binary tree is obtained by forbidding the sequence 00: this case corresponds to the roof map at $a = \frac{1}{2}$. The resulting primitives are then 1 and 01, so that a complete binary tree is recovered. The transition matrix $\mathbf{R}$ has the three real eigenvalues $\lambda_1 = 0$, $\lambda_2 = 1$ and $\lambda_3 = -p$, where $p = P(01) = 1 - P(1)$. Using eq. (9.1), one finds [41]

$$C(\tau) = \frac{p}{(p+1)^2} (-p)^\tau . \tag{9.3}$$

Hence, the power spectrum is a Lorenzian centered at $f = \frac{1}{2}$.

Our third model shows how a peak at a generic frequency $0 < f < \frac{1}{2}$ is produced. We consider the roof map at $a = (3 - \sqrt{5})/4$, where the dynamics yields all combinations of the three primitives 1, 01 and 001, being 000 the only forbidden word. The critical point belongs to a period-four orbit with kneading sequence [22] $C100$. The corresponding Markov graph is displayed in fig. 9a. The 5×5 matrix $\mathbf{R}$ can be reduced to a 3×3 matrix with two non-trivial eigenvalues (the other one being equal to 1), which are the roots $z = z_1$ and $z = z_2$ of the equation $z^2 + pz + pq = 0$. The meaning of the parameters $0 < p < 1$ and $0 < q < 1$ is clear from the figure. Accordingly, one obtains

$$C(\tau) = \frac{p}{1 + p + pq} (k_1 z_1^{\tau+1} + k_2 z_2^{\tau+1}) , \tag{9.4}$$

where $k_j = (z_j + q)(1 - z_j)^{-1}(z_j^2 - pq)^{-1}$. When the z_j's become complex, the power spectrum (see fig. 9d) presents a peak at a frequency between $\frac{1}{3}$ and $\frac{1}{2}$, depending on the values of p and q. This can be easily verified by writing the roots in the exponential form $z_j = \rho_j \exp(i\omega_j)$ and computing the angular part for the limit values 0 or 1 which p and q can assume. In fact the changes in the probabilities modify the shape of the spectrum only within the bounds imposed by the topology: the lengths of the primitives (1, 2 and 3) clearly indicate the region in which a peak is expected.

The last two examples concern the appearance of a second peak, related to the presence of a further prohibition in the language. In particular, we consider two equivalent cases by taking either three primitives with a level-two forbidden concatenation or two primitives with a level-three prohibition. The first model has the same topology as the roof map at $a = (3 - \sqrt{})/4$, where the forbidden sequences are 000 (determining the primitives 1, 01 and 001) and $0011 = w_3 w_1$. The corresponding graph is displayed in fig. 9b. The 6×6 matrix $\mathbf{R}$ has three non-trivial eigenvalues z_j, given by the roots of the equation $z^3 + pz^2 + pqz + (pq - q) = 0$ and the correlation function reads

$$C(\tau) = \frac{1 - q}{1 - q + p + 2pq} \sum_{j=1}^{3} k_j z_j^\tau , \tag{9.5}$$

where

$$k_j = \frac{(z_j^3 + pq - q)(z_j^3 + z_j pq - q)}{z_j p(1-q)(z_j^3 + 2q) + (z_j^3 - q)^2} .$$

Three power spectra are shown in fig. 9e, for $q = 0.7$ and various choices of p. A second peak around frequency zero develops when p decreases from 1. The final example has the same tree topology as the roof map at $a = \frac{5}{8}$, where the dynamics yields all concatenations of the two primitives 1 and 01, except for $01101 = w_2 w_1 w_2$ (see fig. 9c). The critical point belongs to a period-five orbit with kneading-sequence $C1011$. Also in this case the transition matrix has size 6 and three non-trivial eigenvalues, roots of the equation $z^3 + pz^2 + (p + q - 1)z + pq = 0$. The correlation function has the same form as in the previous case:

$$C(\tau) = \frac{1}{q + 2p + pq} \sum_{j=1}^{3} k_j z_j^{\tau} , \qquad (9.6)$$

where

$$k_j =$$

$$[(1-p)z_j^3 + pz_j^2 + (p + q - 1)z_j + pq] \times [qz_j^3 + pqz_j^2 + q(p + q - 1)z_j + pq(q + 1)] \times [(1-p)z_j^2(z_j^2 + q - 1)^2 + 2pqz_j(2z_j^2 + q - 1)]^{-1} .$$

The power spectrum, shown in fig. 9f, exhibits a second peak to the left of frequency $f_0 \leq \frac{1}{4}$ (corresponding to the orbit 0111, which is the only allowed extension of 011), in addition to the first one, centered around $f = \frac{1}{2}$ and determined by the primitives (of lengths 1 and 2). In fact, every prohibition corresponds to a vertex with a single outgoing arrow (for a binary alphabet) in the transition graph D, so that relatively short cycles can appear in D with a small number of exit branches (and an associated small escape probability). Finally, notice that position, height and width of the peaks depend on the eigenvalues of the transition matrix $\mathbf{R}$, which cannot be simply related to properties (lengths, Lyapunov exponents) of the unstable periodic orbits in the dynamical map f.

10. Conclusions

We have shown that power spectra of nonlinear dynamical systems are determined by the topological and metric properties of the symbolic dynamics, representable on a logic tree, and by the actual numerical values of the recorded observable x. The former two ingredients are dynamical invariants and affect the shape of the spectra more deeply than the latter one, which is obviously non-invariant. Therefore, the evaluation of power spectra (which is often the simplest operation to perform on experimental data) assumes a new importance: in fact, the presence of broad peaks can be immediately related to the topology of the logic tree (primitives and first few levels). This information constitutes a guidance in the construction of simple Markov models and in the search of the relevant unstable periodic orbits of the system. Moreover, the spectra contain information about the metric features of the dynamics and possibly depend on the coordinate values x. Finally, we have evaluated numerically the probability scaling function for all examples presented, displaying, in particular, the results obtained for the Lorenz system. The relation between the convergence of the Markov models and the scaling function has been discussed in terms of a suitable complexity measure.

Acknowledgements

We are grateful to P. Talkner and R. Weber for several exchanges of ideas and for a careful reading of the manuscript. One of us (R.B.) thanks E. Pollak for useful discussions. This work has been partly supported by the Swiss National Foundation.

Appendix A

In this appendix we illustrate an algorithm for the identification of periodically extendable primitives. This is a generalization of the method proposed in ref. [5]. The purpose is to select those strings which exhibit some distinguished recurrence properties, as explained in section 3. All substrings S of the signal $\mathcal{S}_0$ are tested in order of increasing length n, starting from the single symbols ($n = 1$) themselves. We want to individuate either periodic sequences (i.e., cyclically repeating up to the largest available string-length n_{max}) or, if none are found, orbits which can be extended periodically up to a limited total length (number of symbols) $n_{min} \leq n_{max}$.

Single symbols s_i are considered first: those which are found to be n_{min}-extendable (i.e., such that $s^{n_{min}}$ is observed at least once in $\mathcal{S}_0$) are accepted as primitives, while all others are classified as "transient". Choosing $n_{min} = n_{max}$ (as we usually do) is equivalent to requiring full periodicity. If, however, no unstable fixed point lies infinitesimally close to the attractor, this condition may not be fulfilled for large n_{min} (if no symbol repeats enough many times consecutively in $\mathcal{S}_0$). When this happens, all blocks of length 2 must be examined. The n_{min}-extendable ones are then taken as primitives. All others which have positive probability are transient orbits (notice that some blocks of length 2 might be forbidden altogether). If, in turn, no primitive block of length 2 has been found, those of length 3 are analyzed, and so on up to a cutoff length $n_{cut} \leq n_{min}$. If still no primitive has been identified, the acceptance condition is weakened to an extendability length $n'_{min} = n_{min} - 1$ and the whole process is restarted from the beginning ($n = 1$). In this way, primitives of some length $n \leq n_{cut}$ are necessarily found (all other allowed strings with the same length n being transient orbits) since, in the worst case, n'_{min} can decrease down to n_{cut} itself. The parameter n_{cut} is introduced only because of computer memory limitations, as well as n_{max}, and represents the longest range in which we try to detect differences in the recurrence behaviour of the various orbits. If the procedure is unsuccessful (i.e., if n'_{min} reaches the value n_{cut} and all orbits with that length exist), an ordinary block-code tree is constructed. Usually, $n_{cut} \leq n_{min}/2$ (to identify possible blocks of length n_{cut} having at least one full cyclic extension).

In general, the set of primitives found with the above procedure is still incomplete: all longer ones are missing, unless a block code has been chosen.

Example 1. Consider the piecewise-linear roof map defined by

$$x_{n+1} = \begin{cases} a + 2(1-a)x_n\,, & \text{if } x_n \in [0, \tfrac{1}{2})\ (s_n = 0)\,, \\ 2(1-x_n)\,, & \text{if } x_n \in [\tfrac{1}{2}, 1]\ (s_n = 1)\,. \end{cases} \tag{A.1}$$

For $a = (3 - \sqrt{3})/4$ [5], a Markov partition exists: in fact, the critical point $x = \frac{1}{2}$ belongs to an unstable period-five orbit with symbolic label (kneading sequence [22]) $C1001$, where the letter C denotes $x = \frac{1}{2}$ itself. The unit interval can be divided into three subsets, labelled by the sequences $w_1 = 1$ (interval $[\frac{1}{2}, 1]$), $w_2 = 01$ (left pre-image of element 1) and $w_3 = 001$ (left pre-image of 01). The symbolic dynamics yields all possible random combinations of these three primitive strings, except for the forbidden orbit $w_3 w_1 = 0011$: this is the minimal description, which we want to discover from the analysis of the signal $\mathcal{S}_0$. Clearly, only symbol 1 is periodically extendable: symbol 0 occurs at most twice consecutively in the signal and is, therefore, transient. In fig. 2, we display the corresponding logic tree: symbol 1 is allocated at level one, whereas symbol 0 is reported only for convenience of illustration, encircled with a dashed line.

The construction of the tree then proceeds by forming new sequences $S' = Sw$ as concatenations of any admissible string S (including transient orbits) with a primitive w. If sequence S' in turn exists (i.e., if $P(S') > 0$), it is allocated on the tree, at the position determined by its paren-

tal relations. The possible combinations of length two are 01 (transient–primitive) and 11 (primitive–primitive), both admissible. Sequence 11 is the descendent of 1 and, therefore, appears at level 2. Sequence 01 is the second primitive: in fact, transient strings are attributed a virtual level 0 and all primitives formed by concatenations have a transient prefix. Eventually, level 1 will contain all primitives. Transient orbits play a role only in the search of the code words: they are totally neglected once the latter ones have been all found (or when all sequences up to $|S| = n_{max}$ have been considered). The possible combinations of length 3 are then 001, 011, 101 and 111: 001 is the third primitive, 011 and 101 are allocated at level two and 111 at level three. Notice that sequences such as 10, 010 or 100 are not even generated with this procedure: they are irrelevant for a left-to-right sequential reconstruction of the signal. When forming the sequences of length 4, we discover that 0001 and 0011 do not exist: they are topological prediction errors and appear encircled with a solid line in fig. 2. When a new combination is formed, if it happens to contain one of these forbidden orbits (as, for example, $10011 = w_1 w_3 w_1$), it is obviously rejected a priori. Notice that a more redundant model for the symbolic dynamics would be obtained using the four-element Markov partition, with the associated nine prohibitions. The same tree is obtained for the logistic map (3.2), at $a = 1.85$, up to the second level (differences appearing from level three).

For a generic language, it may happen that, at the end of the process, some tree level is not complete because it should contain sequences longer than n_{max}, the probability of which cannot be measured. This is the case of the Hénon map at standard parameter values. Then, a normalization to one of the total probability of level one is carried out (if the code is not complete, otherwise this is automatically obtained) and the rest of the tree is completed by using suitable predictors (see the next section) for the probabilities $P(S)$ of the missing sequences S. The errors introduced by this procedure are negligible if n_{max} is sufficiently large. Finally, notice that primitive sequences have little in common with "prime" sequences (strings which cannot be decomposed into a number $k > 1$ of repetitions of a single subword [4]).

Example 2. Periodic chaos is also automatically handled: if the attractor consists of p chaotic regions, which alternate periodically, the lengths of the primitives are all multiples of p. No block shorter than p, in fact, can be extended periodically to arbitrary length: for the detection of the "right" code words it is sufficient to choose $n_{cut} \geq p$. This is equivalent to studying the pth iterate of the map, which admits a generating partition composed of r^p elements (the pth refinement of the original one).

Examples 3 and 4. In the signals generated at PD and QP (see section 3), instead, no substring repeats consecutively more than twice. In fact, one has: $\mathcal{S}_0 = 01101001\ldots$ at PD and $\mathcal{S}_0 = 10101101\ldots$ at QP. The appropriate coarse-graining of the signal is hence automatically obtained when n'_{min} has decreased to 4 or 2, respectively, yielding the code words $w_1 = 01$, $w_2 = 10$, $w_3 = 0010$, $w_4 = 1101, \ldots$ (for PD, with $n_{cut} = 2$) and $w_1 = 1$, $w_2 = 01$ (for QP, with $n_{cut} = 1$). In the former case, although the whole signal can be encoded with the two words 01 and 10 only, an infinity of primitives is found, since the relation $\Sigma_i P(w_i) = 1$ holds by construction. Usage of a larger n_{cut} yields directly a higher-order coarse graining, in which the primitives w' are the images under ψ_{PD} of those given above: for $n_{cut} = 4$, one finds the second-generation encoding $w'_1 = 0110 = \psi_{PD}(w_1)$, $w'_2 = 1001 = \psi_{PD}(w_2)$, and so on.

Our procedure yields a so-called prefix-free code: i.e., no code word is the prefix of another one. Hence, if one is given the set of primitives, it is possible to recognize them immediately in the signal, as soon as they are received by the source [6]. In this way, recoding of the primitives into new symbols $(w_1, w_2, \ldots) \rightarrow (0, 1, \ldots)$ is a straightforward task.

References

[1] J.P. Eckmann and D. Ruelle, Rev. Mod. Phys. 57 (1985) 617.

[2] Hao Bai-Lin, Chaos (World Scientific, Singapore, 1984); P. Cvitanović, Universality in Chaos, (Hilger, Bristol, 1984).

[3] D. Ruelle, Encyclopedia of Mathematics and its Applications, Vol. 5. Thermodynamic Formalism (Addison-Wesley, Reading, MA, 1978).

[4] R. Artuso, E. Aurell and P. Cvitanović, Nonlinearity 3 (1990) 325, 361.

[5] R. Badii, Europhys. Lett. 13 (1990) 599; R. Badii, Quantitative Characterization of Complexity and Predictability, Weizmann preprint, Rehovot, Israel (1988); R. Badii in: Measures of Complexity and Chaos, eds. N.B. Abraham, A. Albano, T. Passamante and P. Rapp (Plenum, New York, 1990); R. Badii, M. Finardi and G. Broggi, in: Information Dynamics ed. H. Atmanspacher et al. (Plenum, New York, 1991); R. Badii, M. Finardi and G. Broggi, in: Chaos, Order and Patterns, eds. R. Artuso, G. Casati and P. Cvitanović (Plenum, New York, 1991).

[6] R. Hamming, Coding and Information Theory (Prentice-Hall, Englewood Cliffs, NJ, 1986).

[7] M.J. Feigenbaum, J. Stat. Phys 19 (1978) 25; Phys. Lett. A 74 (1979) 375; Commun. Math. Phys. 77 (1980) 65; M. Nauenberg and J. Rudnick, Phys. Rev. B 24 (1981) 493.

[8] M.J. Feigenbaum, L.P. Kadanoff and S.J. Shenker, Physica D 5 (1982) 370; D. Rand, S. Ostlund, J. Sethna and E.D. Siggia, Phys. Rev. Lett. 49 (1982) 132; Physica D 8, (1983) 303.

[9] M.J. Feigenbaum, J. Stat. Phys. 52 (1988) 527.

[10] R. Badii, K. Heinzelmann, P.F. Meier and A. Politi, Phys. Rev. A 37 (1988) 1323.

[11] H. Mori, B.C. So and T. Ose, Prog. Theor. Phys. 66 (1981) 1266; H. Fujisaka and T. Yamada, Z. Naturforsch. 33a (1978) 1455.

[12] D. Ruelle, Phys. Rev. Lett. 56 (1986) 405; J. Stat. Phys. 44 (1986) 281.

[13] J.A. Hirsch, B.A. Huberman and D.J. Scalapino, Phys. Rev. A 25 (1982) 519; I. Procaccia and H. Schuster, Phys. Rev. A 28 (1983) 1210; P. Manneville, J. Phys. (Paris) 41 (1980) 1235; T. Geisel and S. Thomae, Phys. Rev. Lett. 52 (1984) 1936; H. Mori, H. Okamoto, B.C. So and S. Kuroki, Prog. Theor. Phys. 76 (1986) 784; V. Baladi, J.-P. Eckmann and D. Ruelle, Nonlinearity 2 (1989) 119.

[14] T. Geisel and W. Nierwetberg, Phys. Rev. Lett. 48 (1982) 7; S. Großmann and H. Fujisaka, Phys. Rev. A 26 (1982) 1779.

[15] S. Großmann and S. Thomae, Z. Naturforsch. 32a (1977) 1353; J. Stat. Phys. 26 (1981) 485; T. Yoshida and K. Tomita, Prog. Theor. Phys. 76 (1986) 752.

[16] J.D. Crawford and J.R. Cary, Physica D 6 (1983) 223; J.D. Meiss, J.R. Cary, C. Grebogi, J.D. Crawford, A.N. Kaufman and H.D.I. Abarbanel, Physica D 6 (1983) 375.

[17] M.A. Sepúlveda, R. Badii and E. Pollak, Phys. Rev. Lett. 63 (1989) 1226; B. Eckhardt, J.M. Gomez-Llorente and E. Pollak, Chem. Phys. Lett. 174 (1990) 325.

[18] M. Hénon, Comm. Math. Phys. 50 (1976) 69.

[19] V.M. Alekseev and M.V. Yakobson, Phys. Rep. 75 (1981) 287.

[20] M.A. Sepúlveda and R. Badii, Symbolic Dynamical Resolution of Power Spectra, in: Measures of Complexity and Chaos, eds. N.B. Abraham, A. Albano, T. Passamante and P. Rapp (Plenum, New York, 1990).

[21] F. Christiansen, G. Paladin and H.H. Rugh, Phys. Rev. Lett. 65 (1990) 2087.

[22] P. Collet and J.P. Eckmann, Iterated Maps on the Interval as Dynamical Systems (Birkhäuser, Basel, 1980).

[23] J. Guckenheimer and P. Homes, Nonlinear Oscillations, Dynamical Systems and Bifurcations of Vector Fields (Springer, Berlin, 1986).

[24] P. Grassberger, H. Kantz and U. Moenig, J. Phys. A 22 (1990) 5217.

[25] J.E. Hopcroft and J. D. Ullman, Introduction to Automata Theory, Languages and Computation (Addison-Wesley, Reading, Ma, 1979); G. Rozenberg and A. Salomaa, The Mathematical Theory of L Systems (Academic Press, New York, 1980).

[26] B. Weiss, Monatsh. Math. 77 (1973) 462.

[27] I. Procaccia, S. Thomae and C. Tresser, Phys. Rev. A 35 (1987) 1884.

[28] M. Queffelec, Lecture Notes in Mathematics, Vol. 1294 Substitution Dynamical Systems: Spectral Analysis (Springer, Berlin, 1987).

[29] P. Walters, An Introduction to Ergodic Theory (Springer, Berlin, 1982).

[30] S. Wolfram, Rev. Mod. Phys. 55 (1983) 601.

[31] C. Godrèche and J.M. Luck, J. Phys. A 23 (1990) 3769.

[32] R.M. Wharton, Inform. Contr. 26 (1974) 236.

[33] R. Badii, Riv. Nuovo Cimento 12, (1989) 1.

[34] E. Bombieri and J.E. Taylor, J. Phys. (Paris) 47, Coll. C3 (1986) 19.

[35] M.J. Feigenbaum, M.H. Jensen and I. Procaccia, Phys. Rev. Lett. 57 (1986) 1503.

[36] E.N. Lorenz, J. Atmos. Sci. 20 (1963) 130.

[37] M. Finardi, R. Badii and G. Broggi, unpublished.

[38] C. Sparrow, The Lorenz Equations: Bifurcations, Chaos and Strange Attractors (Springer, New York, 1982).

[39] Z. Kaufmann, P. Szépfalusy and T. Tél, Acta Phys. Hung. 62 (1987) 321; Z. Kaufmann and P. Szépfalusy, Phys. Rev. A 40 (1989) 2615.

[40] Y. Aizawa, Prog. Theor. Phys. 68, (1982) 64.

[41] W. Li, Complex Systems 1 (1987) 107.

[42] A. Papoulis, Probability, Random Variables and Stochastic Processes (McGraw-Hill, New York, 1984).

Physica D 58 (1992) 325–330
North-Holland

PHYSICA D

Evaluation of probabilistic and dynamical invariants from finite symbolic substrings – comparison between two approaches

R. Stoop
Institute of Mathematics, Swiss Federal Institute of Technology (ETH) of Zurich, CH-8092 Zurich, Switzerland

and

J. Parisi[1]
Physics Institute, University of Zurich, CH-8001 Zurich, Switzerland

Received 7 October 1991
Revised manuscript received 24 December 1991
Accepted 20 January 1992

While evaluating scaling functions of fractal dimensions and Lyapunov exponents from time series in the traditional way, assumptions are made concerning the grammar of the underlying dynamical system: it is implicitly assumed that the length of the substrings considered is *sufficient* to capture the grammatical properties of the system. In this contribution, we show where this assumption becomes relevant. We give an example of a simple grammatical rule which leads to badly behaving convergence properties of the associated scaling functions. As another consequence of our investigations, we conclude that, whenever a finite grammar is encountered, the cycle expansion approach of Cvitanović using periodic orbits should preferably be used.

1. Introduction

As it is common use to define a chaotic attractor as the closure of its nonforbidden periodic orbits [1], it should not be too surprising that the grammatical rules, which allow only part of the periodic orbits to exist, exert a nonnegligible influence on the associated scaling functions (not of the Feigenbaum type). Whereas the appearance of nonhyperbolic contributions can be traced in the scaling functions derived from time series without knowledge of the underlying grammar, the effect of changing grammatical rules is far less easy to investigate. However, in the present contribution, we intend to make clear that such an influence can, nonetheless, not be neglected: it will be shown to have a large impact on the form of the associated scaling functions. Although in the generic case of experimental time series a large number of nonhyperbolic points is to be expected [2], we restrict ourselves to a hyperbolic model, in order to be able to work out this influence against dominating nonhyperbolic effects. In the evaluation of experimentally obtained time series, two different directions are commonly followed. In one approach (subsequently called the "probabilistic" approach), the generalized Renyi dimensions are calculated, from which the well-known entropy-like scaling function $f(\alpha)$ can be derived. The other approach deals with the logarithmic stretching rates describing the stability

[1]Correspondence to: Priv.-Doz. Dr. Jürgen Parisi, Physics Institute, University of Zurich, Schönberggasse 9, CH-8001 Zurich, Switzerland, Phone +41-1-2572911, Fax +41-1-2616323.

0167-2789/92/$05.00 © 1992 – Elsevier Science Publishers B.V. All rights reserved

of the system, called Lyapunov exponents, for which an entropy-like scaling function can be derived much in the same way. It is this scaling function that we consider, in order to demonstrate the properties mentioned above. Traditionally, the so-called thermodynamic averages [3, 4] are calculated from the "canonical" partition function [5], and only partial use is made of periodic orbits. However, a more recent work by Cvitanović and collaborators suggests that the use of a "grandcanonical-like" partition, which takes explicitly account of the unstable periodic orbits of the system, should numerically be more suited for these purposes [6].

In our contribution, we consider different restrictions imposed on a three-scale Cantor set by simple but nontrivial grammars. We investigate the effects they exert upon the scaling behavior and discuss the relationship with experimentally obtained time series. We show that the traditional approach, although not entirely worthless, leads to severe numerical problems of various nature so that it is difficult to extrapolate the asymptotic behavior from finite symbolic substrings of the length accessible to the computer. And, finally, we point out that the discovery of hidden grammatical rules can lead to a rather drastic change of the scaling functions. To demonstrate this exemplarily, we consider a three-scale Cantor set. For the relevance of such a model, see e.g. ref. [7]. The generalized entropy function [8, 9] which contains all the relevant information on the scaling behavior of the system is then calculated, (a) from the partition function upon increasing the length of the substrings considered, (b) from the zeta-function approach of Cvitanović [6] and Ruelle [3]. From the generalized entropy function, the thermodynamic averages can easily be derived.

2. Thermodynamic formalism

The thermodynamic formalism starts with a partition of the phase space which is compatible with the iteration of the dynamical map. Using a partition consisting of M symbols, in analogy to statistical mechanics, the partition function [5]

$$Z_G(q, \beta, n) = \sum_{j \in (1, \ldots, M)^n} l_j^{\beta} p_j^q \tag{1}$$

is defined. Here the size of the jth region R_j of the partition is denoted by l_j, whereas the probability of falling into this region is denoted by p_j ($p_j = \int_{R_j} \rho(x)\, dx$, where $\rho(x)$ means the natural measure). β and q are sometimes called "filtering exponents"; n denotes the "level" of the partition. Local scaling of l and p in n is expected. In this way, the length scale l and the probability p give rise to scaling exponents ε and α through

$$l_j = e^{-n\varepsilon_j}, \tag{2}$$

$$p_j = l_j^{\alpha_j}, \tag{3}$$

respectively. Using the above expression, from the partition function the generalized free energy F_G can be derived [4, 8, 9]:

$$F_G(q, \beta) = \lim_{n \to \infty} \frac{1}{n} \log \sum_{j \in (1, \ldots, M)^n} e^{-n\varepsilon_j(\alpha_j q + \beta)}, \tag{4}$$

where log denotes the natural logarithm. A generalized entropy function $S_G(\alpha, \varepsilon)$ is then introduced through the "global" scaling assumption that the number of regions N which have scaling exponents between (α, ε) and $(\alpha + d\alpha, \varepsilon + d\varepsilon)$ scales as

$$N(\alpha, \varepsilon)\, d\alpha\, d\varepsilon \sim e^{S_G(\alpha, \varepsilon)}\, d\alpha\, d\varepsilon. \tag{5}$$

From the generalized free energy F_G, in a standard way the relationship with the generalized entropy S_G is found [5–9],

$$S_G(\alpha, \varepsilon) = F_G(q, \beta) + (\alpha q + \beta)\varepsilon, \tag{6}$$

where those values of α and ε leading to the maximum of Z_G (as a function of given q and β)

have been chosen [9]. The free energy F_G or the generalized entropy S_G describe in this way the scaling behavior of the dynamical system equivalently. For $\beta = 0$, the information-theoretical Renyi entropies evolve from (4).

From the generalized free energy, two more specific free energies and entropies can be derived by restriction: For $q = 1$, we obtain the generalized Lyapunov exponents [10], whereas for $q = 0$ the free energy is gained which leads to the maximum value of $S_G(\alpha, \varepsilon)$ with respect to variation of α alone for given ε [11]. The latter free energy and the associated entropy are denoted by $F_G(\beta)$ and $S_G(\varepsilon)$, respectively. For the discussion of a dynamical system, the scaling function $S_G(\varepsilon)$ is, in some respect, better suited than the scaling functions of the generalized Lyapunov exponents. The fractal dimensions (see refs. [5, 12, 13]) are obtained as the zeros $\beta_0(q)$ of $F_G(q, \beta)$ for given q. Therefore, via (1) and the generalized entropy function, the characteristic thermodynamic functions can, in principle, be calculated from an approximation of the system by strings of a finite length n, for experimental settings as well as for model systems [9].

3. Model systems

In order to demonstrate the rather generic convergence properties, we consider the following situation: Assume that in the sequence space the system can be coded with the help of three symbols. Therefore, as an appropriate model for a dissipative dynamical system, we consider a three-scale Cantor set and use for the symbolic description the symbols A, B, and C. We, furthermore, impose a grammar by the requirement that a three-fold repetition of one symbol, C, cannot occur. For the symbols A, B, and C, the length scales and the associated probabilities are specified. At level $n = 1$, the following length scales and probabilities are observed: $l_A = 0.1$, $l_B = 0.2$, $l_C = 0.3$; $p_A = 0.2$, $p_B = 0.3$, $p_C = 0.5$. We then presume that a hierarchical discovery is being made in the following sense: While at level 2 the branching probabilities remain, at level 3 the particularity of the sequence CCC, which is not allowed, is detected. For simplicity, we assume that, as the effect of this discovery, the forbidden substring is proportionally distributed to the neighboring branches CCA and CCB [14, 15].

In this way, a nontrivial grammar is imposed on the fractal. In contrast to what could be expected, it is not possible to exclude at a given level n, once and for all, the generation of the forbidden substring: The generation of the fractal is "not closed" with respect to the iteration number n. The hope is then that an increase of the length n could remedy the situation. Taking into account the structure of the grammar, it is easily seen that this expectation can only partially be justified. In order to investigate the convergence of the approach, we now start from the ensemble of all possible substrings of length n and calculate the generalized entropy function $S_G(\alpha, \varepsilon)_n$. Then, we derive the entropy-like functions $f(\alpha)_n$ and $S_G(\varepsilon)_n$, for different lengths n [16].

4. Results

In ref. [9], the form of the generalized entropy function of the unrestricted Cantor set has already been discussed. While the restriction is imposed, upon increasing the length of the substrings considered, the support of the entropy function converges towards the modified, asymptotic form (fig. 1). As a function of n, we obtain a rather oscillatory convergence (fig. 2) which is due to the fact that different symbolic substrings could not yet be excluded at the given level n. However, this convergence is affected in part by the numerical inaccuracy of the computational tools. For example, the numerical accuracy is limited by the computation time used for the summation of the partition function up to length

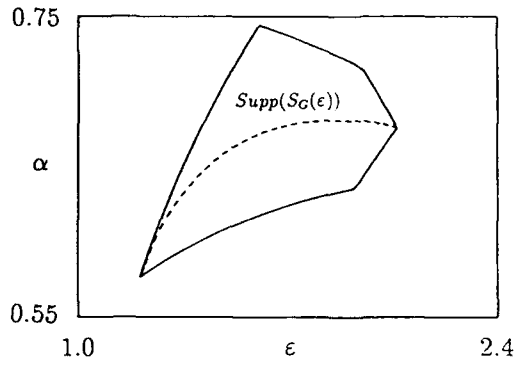

Fig. 1. Asymptotic form of the generalized entropy function, calculated from the zeta-function approach. Shown is the support of $S_G(\alpha, \varepsilon)$, i.e., the region in the (α, ε)-plane for which $S_G(\alpha, \varepsilon)$ is a nonzero, convex function. The dashed line indicates the support of $S_G(\varepsilon) = S_G(\alpha, \varepsilon)|_{q=0}$.

of 12. Furthermore, the use of high values of the weighting exponents q and β poses severe numerical problems (in our computations, we use a range from -30 to 30 for both parameters). Nevertheless, it can be seen that it is possible to unveil some remaining, important invariant properties of the system. For instance, the maximum of $S_G(\varepsilon)$ is rather well-approximated by $S_G(\varepsilon)_n$ (see fig. 3). The fact that these entropy functions do not come down to zero could be taken as an indication of a phase-transition-like effect [9, 17]. However, the second approach shows that this is not the case. (The problem of

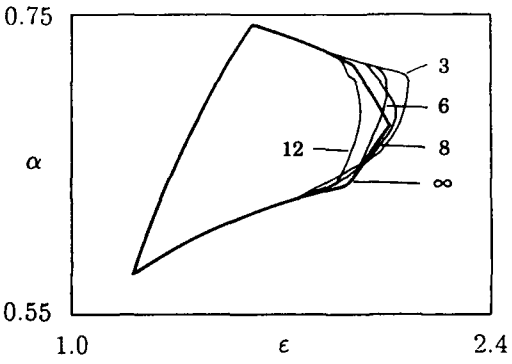

Fig. 2. Oscillatory convergence towards the asymptotic generalized entropy function which is due to the fact that at a given level of n not all sequences which would be forbidden for larger n can be excluded without suppressing other, allowed, sequences. Shown is again the support of the entropy function.

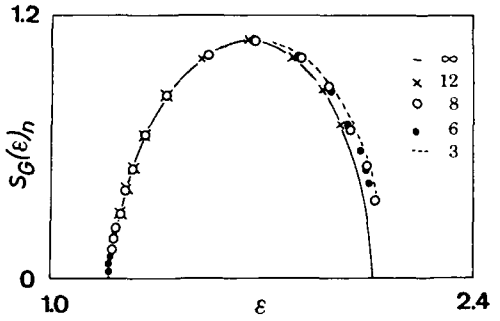

Fig. 3. Convergence of the entropy functions $S_G(\varepsilon)_n$ towards the asymptotic entropy function $S_G(\varepsilon)_{n=\infty}$. The convergence is limited by poor resolution for large n (see text).

phase transitions will be discussed extensively in a forthcoming publication.) Note that the asymptotic entropy function was calculated by making use of the zeta-function approach [6].

Having pointed out the intrinsic superiority of the "grandcanonical-like" approach for our problem, we proceed by investigating the effect upon the associated, more specific scaling functions $f(\alpha)$, $\phi(\lambda)$, and $S_G(\varepsilon)$, if the same rules are applied alternatively to the symbol strings AAA, BBB, respectively. In this case, the effects on the scaling functions are seen to be of a rather different nature: We obtain asymptotically the supports of the generalized entropy functions, as shown in figs. 4 and 5. From these figures, the effects of the restrictions exerted upon the specific scaling functions can already be esti-

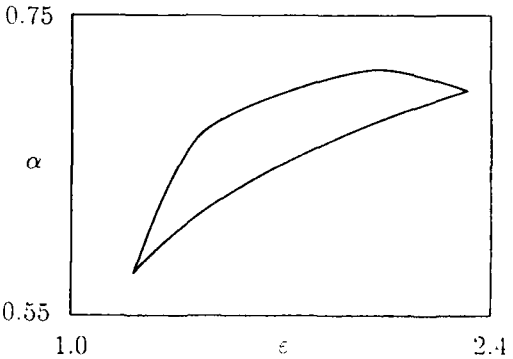

Fig. 4. Support of the generalized entropy function for the case of forbidden substring AAA.

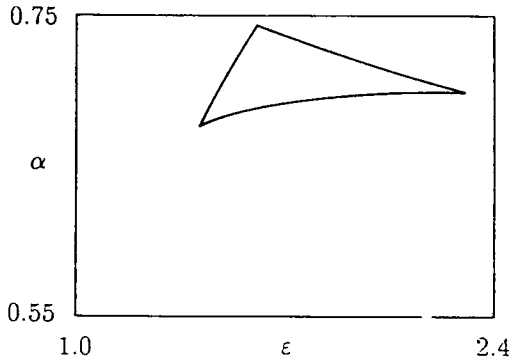

Fig. 5. Support of the generalized entropy function for the case of forbidden substring *BBB*.

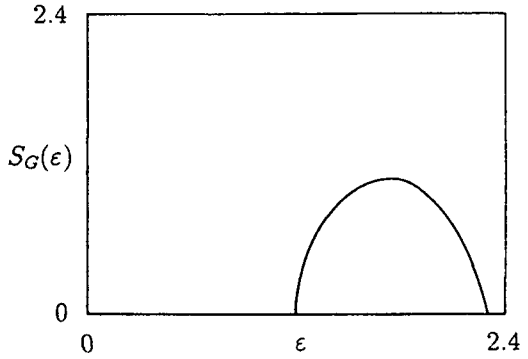

Fig. 6. $S_G(\varepsilon)$ obtained for the model with forbidden substring *AAA*.

mated. In the figs. 6 and 7, we display the associated scaling functions $S_G(\varepsilon)$. Note, however, no phase-transition-like behavior is obtained in this way.

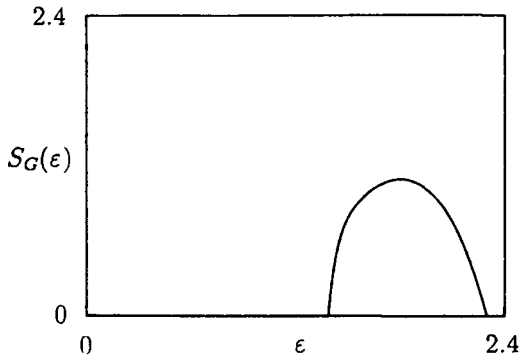

Fig. 7. $S_G(\varepsilon)$ obtained for the model with forbidden substring *BBB*.

5. Conclusions

Let us emphasize that the effects described are very similar to those observed during the evaluation of, e.g., the "dynamical" or "geometrical" scaling functions $\phi(\lambda)$ from experimental time series. Upon increasing the length of the substrings considered, different shapes of the associated scaling function $\phi(\lambda)$ are obtained, seemingly contradicting the law of independent averages, due to the nontrivial role of the grammar of the system. At least for experimental systems with a finite grammar, the approach via zeta functions has been shown to lead to an accuracy of the scaling function not known to be attained by the traditional approach. For infinite grammars, however, the situation is far less favorable; the cycle expansions typically converge but poorly.

Our results indicate that the use of the zeta-function approach for the evaluation of the thermodynamic averages can be superior to that of the more traditional ones. Much of the success of this approach, however, depends on the fact that the alphabet associated with our model can be reformulated to constitute a complete one. As a consequence, for an experimental setting or a model with a complex grammar, the application of this powerful tool may not be straightforward. Therefore, the evaluation via the more traditional approach, with all its disadvantages, will often be a reasonable alternative, if complete as possible information about the scaling behavior of a system is to be extracted. Investigations of nonhyperbolic systems are discussed elsewhere in detail [18].

References

[1] J.P. Eckmann and D. Ruelle, Rev. Mod. Phys. 57 (1985) 617;
R.L. Devaney, An Introduction to Chaotic Dynamical Systems (Benjamin Tumminyi, Menlo Park, CA, 1986).
[2] D. Ruelle, Elements of Differentiable Manifolds and Bifurcation Theory (Academic, San Diego, 1989).

[3] D. Ruelle, Thermodynamic Formalism (Addison-Wesley, Reading, MA, 1978).
[4] T. Tél, Z. Naturforsch. 43a (1988) 1154.
[5] T.C. Halsey, M.H. Jensen, L.P. Kadanoff, I. Procaccia and B. Shraiman, Phys. Rev. A 33 (1986) 1141.
[6] P. Cvitanović, in: Nonlinear Physical Phenomena, Brasilia 1989 Winter School, A. Ferraz, F. Oliveira and R. Osorio, eds. (World Scientific, Singapore, 1990);
R. Artuso, E. Aurell and P. Cvitanović, Nonlinearity 3 (1990) 325;
R. Artuso, E. Aurell and P. Cvitanović, Nonlinearity 3 (1990) 361.
[7] G. Gunaratne, M.H. Jensen and I. Procaccia, Nonlinearity 1 (1988) 157.
[8] M. Kohmoto, Phys. Rev. A 37 (1988) 1345.
[9] R. Stoop and J. Parisi, Phys. Rev. A 43 (1991) 1802.
[10] H. Fujisaka, Prog. Theor. Phys. 70 (1983) 1264.
[11] Y. Oono and Y. Takahashi, Prog. Theor. Phys. 63 (1980) 1804.
[12] A. Renyi, Probability Theory (North-Holland, Amsterdam, 1970).
[13] P. Grassberger and I. Procaccia, Physica D 13 (1984) 34.
[14] R. Stoop, J. Parisi and H. Brauchli, Helv. Phys. Acta 64 (1991) 950.
[15] R. Stoop, J. Parisi and H. Brauchli, Z. Naturforsch 46a (1991) 642.
[16] R. Stoop and J. Parisi, Phys. Lett. A 161 (1991) 67.
[17] R. Stoop, J. Peinke, and J. Parisi, Physica D 50 (1991) 405.
[18] R. Stoop, Z. Naturforsch. 46a (1991) 1117.

Physica D 58 (1992) 331–338
North-Holland

PHYSICA D

Dynamical description of spatial disorder

V.S. Afraimovich, A.B. Ezersky, M.I. Rabinovich, M.A. Shereshevsky[1] and A.L. Zheleznyak

Institute of Applied Physics, Russian Academy of Sciences, 46 Uljanov Street, 603600 Nizhny Novgorod, Russia

Received 7 October 1991
Revised manuscript received 31 January 1992
Accepted 15 February 1992

We propose a new approach to the analysis of chaotic spatial field distributions (including the snapshots of the fields evolving with time), taking as a basis a translational dynamical system with d times. A space series is used to determine quantitative characteristics of disorder such as spatial correlation and pointwise dimensions.

1. Introduction

The disordered spatial field distribution (density, temperature, velocity, etc.) or simply *disorder* is usually analysed in terms of its simplest statistical characteristics such as spatial spectrum, correlation scale, and the like [1]. Knowledge of these standard characteristics is extremely important for the analysis of chaotic structures. They enable us, in particular, to distinguish short-range and long-range order, to determine the size of domains, to describe statistical properties of a random field picture, and so on. However, traditional approaches to the analysis of spatial disorder give no information about its deterministic origin. In particular, they do not show that a finite dimensional dynamical system may generate disorder.

A "dynamical" approach to spatial disorder appears to be extremely interesting. Actually, even the fact that disorder may be described by a low-dimensional dynamical system gives additional information about its origin. Time variation of the properties of a "spatial" dynamical system that generates a snapshot answers the question about evolutionary peculiarities of disorder. Finally, "dynamical" disorder may be separated from spatial (speckle) noise.

Our paper is concerned with the description of spatial disorder in terms of nonlinear dynamics. To this end we introduce the concept of a "translational dynamical system". Its meaning is readily understood by use of an example of a one-dimensional space series, i.e. an instantaneous field distribution with one spatial coordinate. In this case, the spatial coordinate, say x, can be treated as time and the space series, $u(x)$, will be an observable, i.e. a function of the point on a trajectory of the dynamical system which will be referred to as a translational dynamical system. Employing the approach proposed by Packard and Takens [2, 3], we can reconstruct the invariant set that contains this trajectory and calculate, for instance, its fractal dimension. This procedure is very much like the processing of time series, but in our case we know in advance that the translational dynamical system describing the space series $u(x)$ is "reversible", because such a system for isotropic unbounded media (it is only these media that we consider here) must

[1] Current address: Mathematics Institute, University of Warwick, Coventry CV4 7AL, UK.

0167-2789/92/$05.00 © 1992 – Elsevier Science Publishers B.V. All rights reserved

be invariant on substituting $-x$ for x. Therefore, the translational dynamical system of interest must possess the properties similar to those of a Hamiltonian system.

Thus we can use a direct spatio-temporal analogy for a one-dimensional space series. For d spatial coordinates this analogy can be used in a wider sense; then instead of a traditional dynamical system we propose to employ a dynamical system with d times (the so-called action of $\mathbb{Z}^d$ or $\mathbb{R}^d$ groups). These dynamical systems were considered, for example, in ref. [4].

The motion along the trajectory of such a dynamical system in the direction of any "time" x_k is equivalent to the shift of the spatial picture along the kth spatial coordinate.

The concept of the trajectory of an invariant set of a translational dynamical system with "d times" is essential for the generalization of the Packard–Takens approach that will be proposed here. Besides, we will generalize Grassberger–Procaccia's algorithm [5] for the calculation of the correlation dimension of space series with d spatial coordinates.

The merits of this approach are illustrated by an example of chaotic capillary ripples observed on the surface of a horizontal layer of fluid excited parametrically [6]. It was revealed, in particular, that the spatial dimension of the snapshot of ripples increases with supercriticality.

2. Translational dynamical system

When formalizing the characteristics of spatial distribution snapshots we will need notions such as *phase space*, *translational dynamical system*, *dimension*.

Consider a set of continuous (vector-) functions $u(x)$, $x \in \mathbb{R}^d$ ($u \in \mathbb{R}^p$) employing conventional procedures of summation and scaling. Introducing into this set a distance we obtain a metric space B that will be referred to as the phase space of the system. Let each d-dimensional vector $\alpha = (\alpha_1, \ldots, \alpha_d) \in \mathbb{R}^d$ correspond to the translation map $T^\alpha: B \to B$ that is determined from the expression $T^\alpha u(x) = u(x + \alpha)$. Thus we determine the action of the group $\mathbb{R}^d$ on B or, in other words, we are concerned with a dynamical system with d times that will be referred to as a translational dynamical system.

If the process under study is such that knowing the initial state (initial field distribution) one can unambiguously determine the subsequent states at any moment of time, then a semigroup of evolution operators $\{S^t\}_{t \geq 0}$ also acts on B, i.e. an evolution dynamical system is determined as well. The behaviour of the trajectories of translational and evolutional dynamical systems in the common phase space B gives a full mathematical description of the spatio-temporal properties of the nonequilibrium medium of interest.

3. The characteristics of snapshots

The characteristics of the snapshot $u(x)$ do not, evidently, depend on the reference system in $\mathbb{R}^d$. In other words, these characteristics must describe an invariant set of points along the trajectory of a translational dynamical system: $\{T^\alpha u(x)\}_{\alpha \in \mathbb{R}^d} \equiv A_{u(x)}$. Accordingly, the value $C(A_{u(x)})$ ($C(M)$ is the limit capacity of the set M) will be referred to as the limit capacity, or the fractal dimension, of the snapshot $u(x)$. The Hausdorff dimension of the snapshot and other measure-independent characteristics are determined in a similar fashion. If a measure μ that is invariant relative to T^α is determined on $A_{u(x)}$, then the μ-dependent characteristics (e.g., pointwise or correlation dimensions) will also be referred to as the characteristics of the snapshot (see appendix).

Note that if, for example, a two-dimensional snapshot is periodic with respect to x_1 and x_2, then the set $A_{u(x)}$ is merely a two-dimensional torus; if the snapshot has a quasi-periodically repeating structure, then $A_{u(x)}$ is also a torus but now of a higher dimension; while for the pat-

terns chaotically distributed over the plane, $A_{u(x)}$ will be a fractal set. The time evolution of the snapshots (space series) corresponds to the motion of the set A_u in the space B: $A_{u(x)} \xrightarrow{s^t} A_{s^t u(x)}$.

Bearing in mind the analogy with ordinary dynamical systems and for the sake of simplicity, below we will consider the space and time to be discrete, i.e. instead of $\mathbb{R}^d$ we will use $\mathbb{Z}^d$ and instead of $\mathbb{R}_+$ we will take $\mathbb{Z}_+$.

Generalizing the Takens approach [3] to systems with d-dimensional time, we can consider the snapshots to be generated by a finite-dimensional dynamical system, provided that its fractal dimension is finite. The snapshot $u(j)$, $j = (j_1, \ldots, j_d) \in \mathbb{Z}^d$ will be called a finite-dimensional one if: (1) there exists a dynamical system with d-dimensional time and a finite phase space M; (2) there exists a Lipschitz-continuous one-to-one map $h: A_u \to M$ such that the inverse map h^{-1} is also Lipschitz-continuous. Here $\bar{A}_u$ = closure $\{T^\alpha u\}$, $\alpha \in \mathbb{Z}^d$.

We will provide the space of the sequences $B = \{u(j), j \in \mathbb{Z}^d\}$ with the norm $\|\underline{u}\| = \Sigma_j |u_j| / 2^{|j|}$, where $|j| = |j_1| + \cdots + |j_n|$ and $|u_j|$ is the usual norm in $\mathbb{R}^p$. We can readily verify that B is a Banach space. Let for a fixed snapshot $u(j)$ the fractal dimension of the set $\bar{A}_{u(j)}$ be finite: $C(\bar{A}_{u(j)}) < \infty$ and the set be compact. Let $m > 0$ be an integer such that $m^d \geq 2C(\bar{A}_{u(j)}) + 1$. Through C_m^d we will denote an integral d-dimensional cube with the side m, i.e. $C_m^d = \{j^0 = (j_1, \ldots, j_d) \in \mathbb{Z}^d,\ 0 \leq j_i \leq m\}$. Let also $M_m = \{v(j), j \in C_m^d,\ v(j) \in \mathbb{R}^p\}$. Apparently, M_m is the m^d-dimensional subspace of the space B. Let $\Pi_m: B \to M_m$ be a natural projection, i.e. the map which establishes the correspondence of the snapshot $u(j)$ to the element $v(j) \in M_m$ such that $u(j) = v(j)$ for any $j \in C_m^d$. According to the Mañe theorem [7], one-to-one (and bicontinuous) projections are typical among $B \to M_m$ on the set $A_{u(j)}$. Assume that Π_m is a typical natural projection. Then a dynamical system generated by the map $\tilde{T}^\alpha = \Pi_m \circ T^\alpha \circ \Pi_m^{-1}$, $\alpha \in \mathbb{Z}^d$ and having d-dimensional time is determined on the image $E = \Pi_m(A_{u(j)})$ and the snapshot $u(j)$ will be finitely generated, provided that $\Pi_m(\bar{A}_{u(j)})$ is a Lipschitz-continuous map.

4. Numerical algorithms

The lemmas proved in the appendix allow us to propose the algorithms for the calculation of the correlation and pointwise dimensions generalizing the algorithms from refs. [5, 8]. Let us take a two-dimensional snapshot ($d = 2$) in the form of a two-dimensional array $\{u_{i,j}, i, j \in \mathbb{Z}_+\}$. In reality the array, naturally, has a limited size: $i \leq N_1$, $j \leq N_2$. For each integer $m \geq 1$ we will construct $m \times m$ matrices:

$$A_{K,L}^{(m)} = \{(u_{k,l}), k = K_1, \ldots, K + m - 1,\ l = L, \ldots, L + m - 1\}.$$

Let us define the correlation integral in the form

$$C^{(m)}(\varepsilon) = \frac{R^{(m)}(\varepsilon)}{[(N_1 - m)(N_2 - m)]^2},$$

$$R^{(m)}(\varepsilon) = \#\{((K, L,), (K', L')): \operatorname{dist}(A_{K,L}^{(m)}, A_{K',L'}^{(m)}) \leq \varepsilon\};$$

where $\#(E)$ is the number of elements in the set E.

Then the ratio $\log C^{(m)}(\varepsilon)/\log \varepsilon$ for sufficiently small ε can be approximately equal to the correlation dimension D_c of the two-dimensional snapshot in the m-dimensional embedding space.

Following ref. [9] we will estimate the minimal size of the array $(U_{i,j})_{N_1 \times N_2}$ that is needed for correct evaluation of the dimension within the range $[\varepsilon', \varepsilon'']$ of values of ε. Since

$$D_c \cong \frac{\log_2 C^{(m)}(\varepsilon'') - \log_2 C^{(m)}(\varepsilon')}{\log_2 \varepsilon'' - \log_2 \varepsilon'},$$

$$C^{(m)}(\varepsilon') \geq \frac{1}{N_1^2 \cdot N_2^2}, \quad C^{(m)}(\varepsilon'') \leq 1,$$

then, assuming $\varepsilon'' = 2^K \varepsilon'$, we have the estimate

$$D_c \leq \frac{2}{K} \log_2(N_1 \cdot N_2) . \quad (1)$$

Note that for a d-dimensional snapshot such an estimate has the form

$$D_c \leq \frac{2}{K} \sum_{l=1}^{d} \log_2 N_1 .$$

Thus, when determining the correlation dimension of a multidimensional snapshot one must bear in mind that the number of discretization points along each time coordinate may be much smaller than in the case of a one-dimensional time.

Since the construction of the correlation integral needs a great number of calculations of the distances between the matrices, we preferred to compute the distance in the form:

$$\operatorname{dist}(A^{(m)}_{K,L}, A^{(m)}_{K',L'}) = \max_{\substack{k=K,\ldots,K+m-1 \\ k'=K',\ldots,K'+m-1 \\ l=L,\ldots,L+m-1 \\ l'=L',\ldots,L'+m-1}} (|u_{k,l} - u_{k',l'}|). \quad (2)$$

The number of calculations may be reduced significantly by comparing the matrices $A^{(m)}_{K,L}$ to the array of reference matrices

$$\{A_{K_i,L_j}, i \leq i_{\mathrm{ref}}, j \leq j_{\mathrm{ref}}\} .$$

In this case the correctness of the calculation of the correlation dimension of a two-dimensional snapshot is determined by an estimate similar to (1):

$$D_c \leq \frac{1}{K} \log_2(N_1 \cdot N_2 \cdot i_{\mathrm{ref}} \cdot j_{\mathrm{ref}}) . \quad (3)$$

The testing showed that the behaviour of the correlation integrals does not, in fact, depend on the turn of the snapshot by an arbitrary angle, which indicates that the algorithm is robust. Fig. 1 shows the plots of $\log_2 R^{(m)}(r)$ versus $\log_2 r$ ($r = 2^{10}(\varepsilon/\varepsilon_{\max})$) for a two-dimensional snapshot $U(x, y) = \sin x \sin \sqrt{\frac{3}{2}}\, y$ which is a two-dimensional torus in the corresponding phase space. The correlation dimension was calculated to be $D_c \in [1.96; 2.03]$, when $N_1, N_2 = 256$, j_{ref}, $j_{\mathrm{ref}} = 4$.

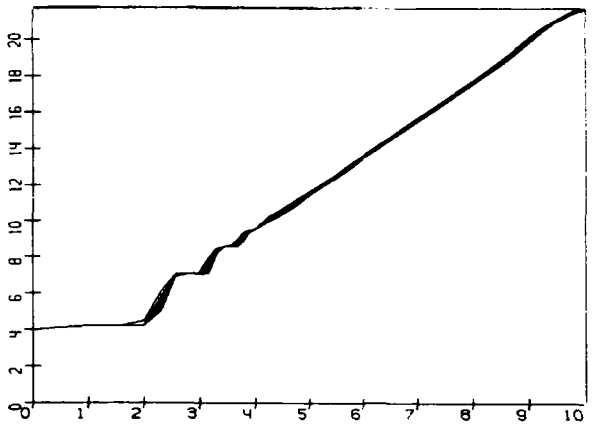

Fig. 1. The plot $\log_2 R^{(m)}(r)$ versus $\log_2 r$ for the two-dimensional field $U(x, y) = \sin x \sin\sqrt{3/2}y$ for different values m of the dimension of the embedding space.

5. The dimension of spatial disorder for capillary ripples

The procedure for the calculation of the correlation dimension presented above was employed for the description of the spatio-temporal chaos of parametrically excited capillary ripples.

Experiments on the dynamics of capillary waves were performed on a fluid placed in a flat couvette vibrating in the vertical direction. It is known [10] that, if the amplitude A of vibration is higher than the critical value A_c, a system of capillary waves is generated on the surface of the fluid. If the size of the couvette is much larger than the wavelength of capillary ripples, then the parametrically excited ripples are a superposition of two mutually perpendicular pairs of counter-propagating waves, independent of the shape of the couvette, which may be round or square. As

the supercriticality $s = A/A_c - 1$ increases, there appear envelope waves propagating perpendicular to the originally excited pairs. When the amplitude of vibrations is sufficiently high, the system of envelope waves becomes chaotic – turbulence is formed. This is a quite general scenario of the transition to wave turbulence although its details may differ in fluids of different viscosities (see ref. [6]).

It would appear natural that the correlation dimension calculated by the snapshots of capillary ripples would increase with the growth of the supercriticality. To prove these intuitive ideas we have made quantitative measurements and processed them, employing the correlation dimension of snapshots. The correlation dimension D_c has been calculated for patterns of capillary ripples for the supercriticalities $s \in [0.15, 1.85]$ (see fig. 2).

The correlation integrals corresponding to the snapshots are presented in fig. 3. Our facilities (we perform calculations on an EC-1037 which is comparable with an IBM 4341) allow for the processing of 512×512 matrices that are constructed by the images of capillary ripples, with the number of reference points being N_l, $N_l = 8$.

Results of calculations show that, as the supercriticality s increases from 0.15 to 1.85, the correlation dimension of the snapshots increases. For equal supercriticalities the correlation dimensions are found to be approximately equal (see fig. 4).

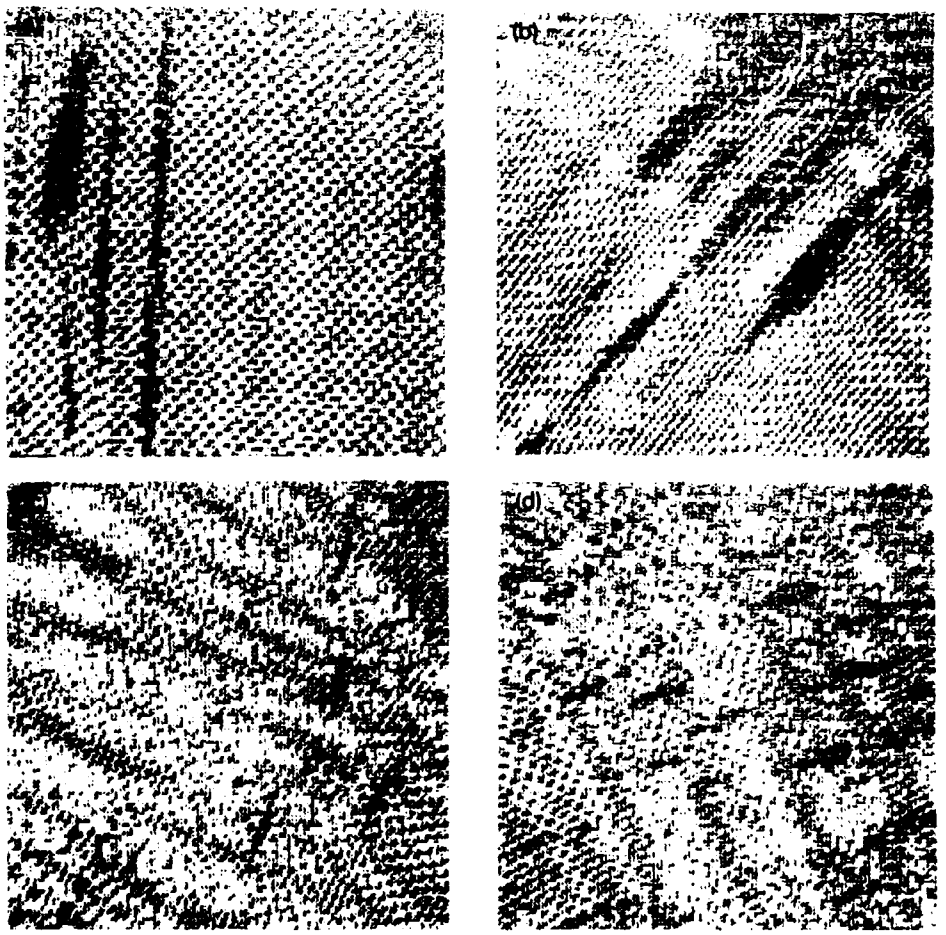

Fig. 2. Snapshots of capillary ripples for supercriticalities: (a) $s = 0.15$, (b) 0.81, (c) 1.1, (d) 1.85.

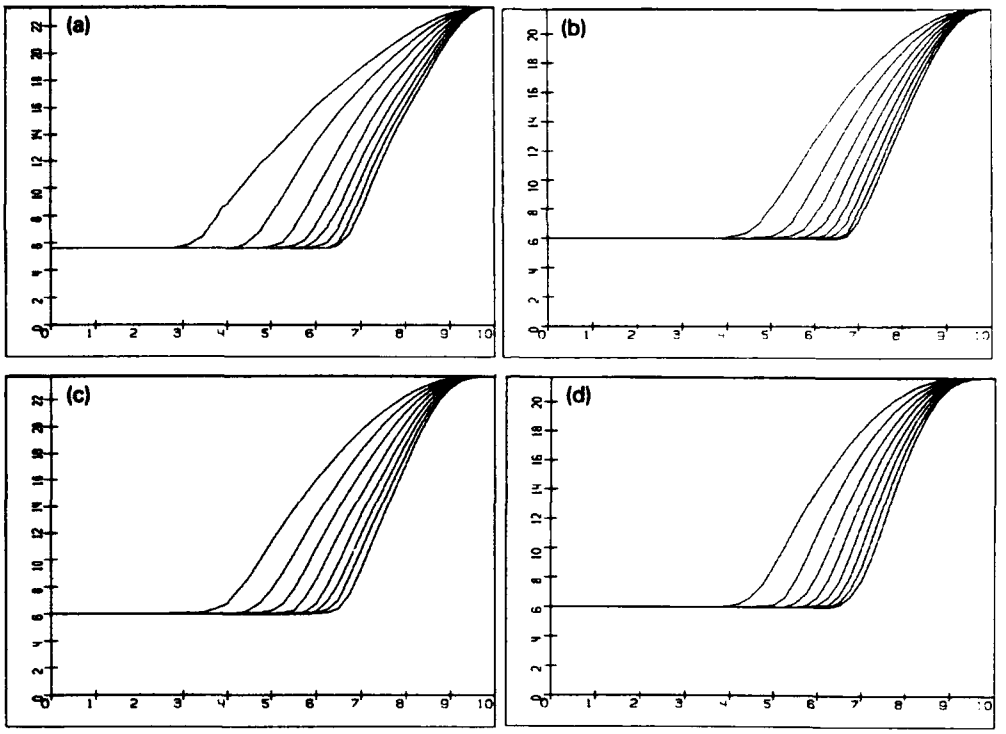

Fig. 3. Correlation integrals corresponding to fig. 2: (a) $D_c = 6.3$, (b) 7.0, (c) 7.4, (d) 8.0.

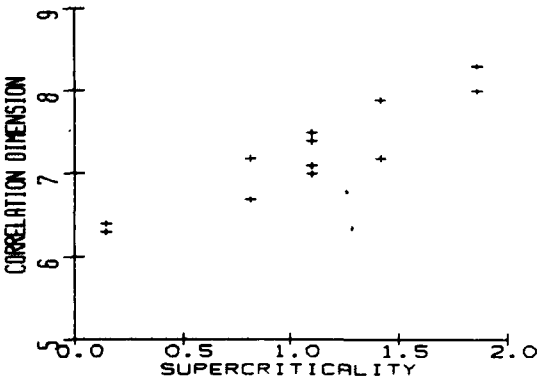

Fig. 4. Correlation dimension of snapshots of capillary ripples as a function of the supercriticality.

6. Discussion

The analysis of the dimension of space series, or snapshots of a medium (field) presented in this paper may be interesting from different viewpoints.

(1) The investigation of the temporal behaviour of the dimension of spatial patterns allows for the new understanding of the evolution of turbulence (from an initial state) and of the reverse problem – the establishment of organized structures from spatial disorder. In particular, the dimension, D_c, of the snapshot is a very handy tool for the investigation of critical phenomena in nonequilibrium media. For example, it was revealed in ref. [11] that within a complex Ginzburg–Landau equation D_c changes abruptly in the transition from the regime of phase turbulence to amplitude turbulence.

(2) As in the case of dynamical systems described by ordinary differential equations [12], one can distinguish in the snapshots a deterministically generated component against the background of spatial noise.

(3) Analysis of snapshots may employ, besides the dimension, other characteristics of deterministic chaos, for instance, topological and met-

rical entropies (see ref. [13]) and, perhaps, Lyapunov exponents. Investigation of the time evolution of these characteristics seems to be promising for the prediction of the temporal behaviour of snapshots.

Appendix. Pointwise and correlation dimensions of snapshots

Assume that $A_{u(x)} \equiv X$ is a compact set and there exists a probability measure μ that is invariant relative to the translational dynamical system $T^{\alpha}: X \to X$, $\alpha = (\alpha_1, \ldots, \alpha_d) \in \mathbb{Z}^d$. Assume also that the measure μ is ergodic with respect to this dynamical system (i.e. any set $D \subset X$ such that $T^{\alpha} D = D$, $\alpha \in \mathbb{Z}^d$ has a measure $\mu(D) = 0$ or $\mu(D) = 1$). Let us designate through C_N^d an integral d-dimensional cube with the side N, i.e.

$$C_N^D = \{\alpha = (\alpha_1, \ldots, \alpha_d) \in \mathbb{Z}^d,\ 0 < \alpha_1 \le N\} .$$

By virtue of the generalized ergodic Birkhoff theorem for a dynamical system with d-dimensional time [4] the relation

$$\lim_{a \to \infty} \frac{1}{\#(C_N^d)} \sum_{\alpha \in C_N^d} \varphi(T^{\alpha} u) = \int \varphi \, d\mu \qquad \text{(A1)}$$

is valid for any function $\varphi \in L^1(X, \mu)$ and for μ of almost any $u \in X$, where $\#(E)$ is the number of elements in the set E. Apparently, $\#(C_N^d) = N^d$.

Let us describe the generalizations of the algorithms for the calculation of the dimension of an ergodic invariant set [5, 8] to the case of d-dimensional time.

For arbitrary $x \in X$, $N > 0$ and $\varepsilon > 0$ we take

$$L_N(u, \varepsilon) = \#\{\alpha \in C_N^d: \operatorname{dist}(T^{\alpha} u, u) \le \varepsilon\} .$$

Taking in (A1) $\varphi(y) = \chi_{D(u,\varepsilon)}$, where $D(u, \varepsilon) = \{y \in X, \operatorname{dist}(u, y) \le \varepsilon\}$ is a sphere of radius ε with the centre at the point u and χ is a characteristic function:

$$\chi_D(y) = \begin{cases} 1, & y \in D \\ 0, & y \notin D \end{cases},$$

and considering the point u to be typical with respect to the measure μ, we obtain

$$\lim_{N \to \infty} \frac{1}{N^d} L_N(u, \varepsilon) = \mu(D(u, \varepsilon)) . \qquad \text{(A2)}$$

Designating through G_{μ} a set of points typical relative to μ (by the ergodic theorem, $\mu(G_{\mu}) = 1$) we obtain from (A2) the following lemma.

Lemma 1. For any $x \in G_{\mu}$,

$$\lim_{\varepsilon \to 0} \lim_{N \to \infty} \frac{1}{\log \varepsilon} \log\left(\frac{1}{N^d} L_N(u, \varepsilon)\right) = d_{\mu}(u) ,$$

if there exists

$$d_{\mu}(u) = \lim_{\varepsilon \to 0} \frac{\log D(u, \varepsilon)}{\log \varepsilon} .$$

It should be borne in mind that the quantity $d_{\mu}(u)$ is a pointwise dimension of the measure μ at the point u.

We now assume that

$$R_N(u, \varepsilon) = \#\{(\alpha, \beta) \in C_N^d \times C_N^d: \operatorname{dist}(T^{\alpha} u, T^{\beta} u) \le \varepsilon\} ,$$

and there exists a limit

$$D_u(\mu) \stackrel{\text{def}}{=} \lim_{\varepsilon \to 0} \lim_{N \to \infty} \frac{1}{\log \varepsilon} \log\left(\frac{1}{N^{2d}} R_N(u, \varepsilon)\right) . \qquad \text{(A3)}$$

We will show that for typical points u, $D_u(\mu)$ is a correlation dimension under some additional assumptions. Let us represent $R_N(u, \varepsilon)$ in the form

$$R_N(u, \varepsilon) = \sum_{\alpha \in C_N^d} L_N(u, T^{\alpha} u, \varepsilon) , \qquad \text{(A4)}$$

where $L_N(u, v, \varepsilon) \stackrel{\text{def}}{=} \#\{\alpha \in C_N^d: \operatorname{dist}(T^{\alpha} u, v) \le$

$\varepsilon\}$. Apparently, $L_N(u, u, \varepsilon) = L_N(u, \varepsilon)$. The property of ergodicity yields (cf. (A2))

$$\lim_{N\to\infty} \frac{1}{N^d} L_N(u, v, \varepsilon) = \mu(D(v, \varepsilon)),$$

in particular,

$$\lim_{N\to\infty} \frac{1}{N^d} L_N((u, T^\alpha u, \varepsilon) = \mu(D(T^\alpha u, \varepsilon)),$$
$$\alpha \in \mathbb{Z}^d. \qquad \text{(A5)}$$

Lemma 2. If $u \in G_\mu$, the convergence in (A5) is uniform with respect to $\alpha \in \mathbb{Z}^d$ and there exists a limit

$$\Delta(\mu) = \lim_{\varepsilon\to 0} \frac{\log \int \mu(D(v, \varepsilon))\, d\mu(v)}{\log \varepsilon},$$

then $D(\mu) = \Delta(\mu)$.

Proof. By virtue of (A5) we have

$$D_u(\mu) = \lim_{\varepsilon\to 0} \frac{1}{\log \varepsilon} \left(\lim_{N\to\infty} \frac{1}{N^d} \times \sum_{\alpha\in c_N^d} \frac{1}{N^d} L_N(u, T^\alpha u, \varepsilon) \right)$$
$$= \lim_{\varepsilon\to 0} \frac{1}{\log \varepsilon} \left(\lim_{N\to\infty} \frac{1}{N^d} \times \sum_{\alpha\in c_N^d} \mu(D(T^\alpha u, \varepsilon)) \right).$$

In the latter equality we assume that the convergence of $L_N(u, T^\alpha u, \varepsilon)/N^d$ to $\mu(D(T^\alpha u, \varepsilon))$ is uniform with respect to α. Further, because $u \in G_\mu$, by virtue of the ergodicity theorem we obtain

$$D_u(\mu) = \lim_{\varepsilon\to 0} \log \int \mu(D(y, \varepsilon))\, d\mu(y) = \Delta(\mu).$$

References

[1] J.M. Ziman, Models of Disorder (Cambridge Univ. Press, Cambridge, 1979).
[2] N.H. Packard, J.P. Crutchfeld, J.D. Farmer and R.S. Shaw, Phys. Rev. Lett. 45 (1980) 712.
[3] F. Takens, in: Dynamical Systems and Turbulence, Warwick, 1980. Lecture Notes in Mathematics Vol. 898 (Springer, Berlin, 1981) p. 230.
[4] A.B. Katok, Ya.G. Sinai and A.M. Stepin, in: Modern Problems of Mathematics. Fundamental Research, Vol. 2 (VINITI, Moscow, 1985) p. 5.
[5] I. Procaccia, P. Grassberger and H.G.E. Hehtschel, in: Lecture Notes in Physics, Vol. 179 (Springer, Berlin, 1983) p. 212.
[6] A.B. Ezersky and M.I. Rabinovich, Europhys. Lett. 13 (1990) 243.
[7] R. Mañe, in: Dynamical Systems and Turbulence, Warwick, 1980. Lecture Notes in Mathematics, Vol. 898 (Springer, Berlin, 1981) p. 366.
[8] Y. Termonia and Z. Alexandrowicz, Phys. Rev. Lett. 51 (1983) 1265.
[9] D. Ruelle, Proc. R. Soc. A 427 (1990) 1873, 241.
[10] M. Faraday, Trans. R. Soc. London 121 (1831) 299.
[11] M.V. Bazhenov, M.I. Rabinovich and A.L. Fabrikant, Phys. Lett. A 163 (1992) 87.
[12] A. Ben-Mizrachi, I. Procaccia and P. Grassberger, Phys. Rev. A 29 (1984) 2, 975.
[13] K. Smith, Algebraic Ideas in Ergodic Theory. Conf. Board Math. Sci. Regional Conf. Ser. in Math., AMS, Providence, RI, V. 76 (1990).

Physica D 58 (1992) 339–364
North-Holland

PHYSICA D

Spatiotemporal pattern formation and chaos in passive optical systems

M. Brambilla[1], G. Broggi and F. Prati[1]
Physik-Institut der Universität Zürich, Winterthurerstrasse 190, 8057 Zürich, Switzerland

Received 8 October 1991
Revised manuscript received 15 January 1992
Accepted 7 February 1992

The interaction and competition of transverse cavity modes in passive optical systems can lead to the formation of spatial field structures whose symmetry differs from that of the empty cavity, while the time behaviour can become irregular. After having introduced dynamical equations in which the spatial dependence of the electric field is described by frequency-degenerate Gauss–Laguerre (GL) modes, the stationary solutions corresponding to a single or many modes are calculated and their stability is discussed. A scan of the parameter space allows for the identification of several interesting dynamical regimes. An extensive study of the chaotic states is performed in order to understand the relation between GL mode excitation and the relevant active degrees of freedom. Based on this analysis, the conditions for the onset of spatiotemporal chaos, for its characterisation and experimental observation are finally discussed.

1. Introduction

Within the framework of the theoretical and experimental investigation of dissipative dynamical systems, much effort has been devoted to the study of nonlinear optical systems, which display a rich variety of periodic, quasiperiodic and chaotic behaviour [1]. In the modeling of optical systems, in order to simplify the mathematical description, large use has been made of the plane-wave approximation, which assumes the uniformity of the electric field in the planes orthogonal to the direction of propagation of the radiation beam. Obviously, this approximation ignores completely any effects that may arise in the transverse directions and lead to the formation of spatial patterns. The theoretical modeling and systematic investigation of these transverse effects have recently received increasing interest, for both passive and laser systems [2].

In optical systems, the onset of spatial and spatiotemporal phenomena can be profitably described in terms of interaction and competition among the modes of the empty cavity. Relevant for the evolution are the mode frequency and the spatial configuration of each mode with respect to that of the available gain and of the loss profile [3, 4]. This mode interaction can lead to the formation of spatial patterns having symmetry properties different from those of the empty cavity and cause the onset of irregular spatiotemporal regimes [5]. In such situations, diffraction assumes a role equivalent to that played by diffusion in the spatiotemporal chaotic evolutions observed in hydrodynamical [6] and open chemical systems [7, 8]. The theoretical understanding of these phenomena, still very rudimentary, is being pursued following approaches typical to low-dimensional chaos- and turbulence theory [9–11].

[1] Also Dipartimento di Fisica dell'Università, Milan, Italy.

0167-2789/92/$05.00 © 1992 – Elsevier Science Publishers B.V. All rights reserved

In section 2 we introduce the model equations describing the evolution of the slowly varying envelopes F and P of the electric field and of the polarisation for a two-level absorbing medium in a ring cavity. Using the empty-cavity modes to describe the transverse structure of the field in the filled cavity, and provided that the absorbing region is much smaller than the Rayleigh length z_0, one can describe the space dependence of tne electric field in terms of frequency-degenerate Gauss–Laguerre (GL) modes $A_{pl}(\rho, \varphi)$, while the system's evolution is determined by the time behaviour of the GL modal amplitudes $f_{pl}(t)$. In suitable conditions, the dynamical equations admit stationary solutions, whose configuration may correspond to a single or to many GL modes. In both situations we identify some prototypical conditions in which the steady state solution can be obtained analytically and derive its expression. The section is completed by a linear stability analysis showing how the onset of the modes of a higher-order family ($q = 1$) destabilises the singlemode TEM_{00} stationary solution, giving rise to more complex spatiotemporal structures.

In section 3 we study the dynamical regimes that are observed scanning the parameter space. We prove the existence of points in the transverse plane where the electric field intensity vanishes; such points are singularities for the electric field phase and, therefore, can be regarded as optical vortices [3]. We present some of the many different dynamical patterns that the system displays and identify experimentally-accessible parameter regions where the time behaviour becomes irregular.

Section 4 is devoted to the detailed study of the irregular time regions. We test the chaoticity of the evolution and the dimensionality of the attractor by measuring Kolmogorov metric entropy $K(1)$ and information dimension $D(1)$, while the relation between GL mode excitation and degrees of freedom effectively determining the dynamics is investigated by studying systematically the time correlations among GL modal amplitudes $f_{pl}(t)$ and the degree of spatial coherence of the field intensity.

Finally, in section 5, we discuss possible future observation of spatiotemporal chaos in passive optical systems in both numerical and real experiments.

2. Description of the model

2.1. Deduction of the dynamical equations

We consider a ring cavity with two spherical mirrors 1 and 2 having radius of curvature R_0 and transmissivity T and two perfectly reflecting plane mirrors 3 and 4 (fig. 1). The total length of the cavity is $\mathscr{L}$, while L is the distance between the two spherical mirrors and L_A is the length of the absorbing medium, which is assumed to be a homogeneously broadened collection of two-level atoms with transition frequency ω_a and linewidth $\gamma_\perp$; α is the absorption rate per unit length experienced by the

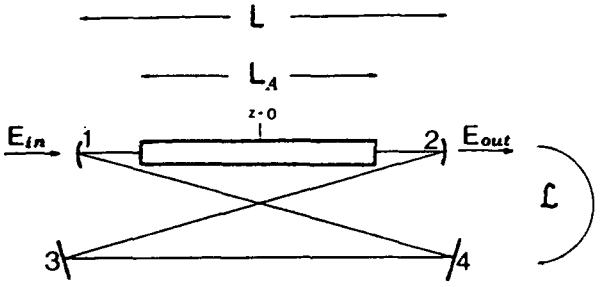

Fig. 1. Ring cavity with two partially reflecting spherical mirrors (1 and 2) and two perfectly plane mirrors (3 and 4). L_A is the length of the active medium. L is the distance between the two spherical mirrors and $\mathscr{L}$ is the total length of the cavity.

light passing through the medium. An external coherent field E_{in} is injected into the resonator through mirror 1 and we assume that it is matched with the fundamental Gaussian mode of the cavity.

In the paraxial and slowly varying envelope approximations, and choosing, in accordance with the system's symmetry, cylindrical coordinates, the Maxwell equation for the slowly varying envelopes F and P of the electric field and of the atomic polarisation is

$$\frac{1}{2ik_{in}} \nabla_{\perp}^2 F(r, \varphi, z, t) + \frac{\partial}{\partial z} F(r, \varphi, z, t) + \frac{1}{c} \frac{\partial}{\partial t} F(r, \varphi, z, t) = \alpha P(r, \varphi, z, t) \,. \tag{1}$$

where $k_{in} = \omega_{in}/c$ is the wave vector associated to the frequency of the input field ω_{in} and

$$\nabla_{\perp}^2 \equiv \frac{\partial^2}{\partial r^2} + \frac{1}{r} \frac{\partial}{\partial r} + \frac{1}{r^2} \frac{\partial^2}{\partial \varphi^2} \,. \tag{2}$$

Our study is based on the assumption that the empty cavity modes are suitable also to describe the transverse structure of the field in the filled cavity [12]. These modes are in general complicated functions of the spatial coordinates. We shall consider the limit

$$z_0 = \tfrac{1}{2} k_{in} w_0^2 \gg L_A \,, \tag{3}$$

where z_0 is the Rayleigh length and w_0 is the minimum waist of the beam. In this limit the modal functions assume the simple form of the Gauss–Laguerre functions

$$A_{pl}(\rho, \varphi) = \sqrt{\frac{2}{\pi}} (2\rho^2)^{|l|/2} \left[\frac{p!}{(p + |l|)!} \right]^{1/2} L_p^{|l|}(2\rho^2) \, e^{-\rho^2} e^{il\varphi} \,, \tag{4}$$

where $\rho = r/w_0$ is the normalised radial coordinate, $p = 0, 1, \ldots$ is the radial index, $l = 0, \pm 1, \ldots$ is the angular index and $L_p^{|l|}$ are the Laguerre polynomials of the indicated argument. The functions A_{pl} obey the orthonormality relation

$$\int_0^{2\pi} d\varphi \int_0^{\infty} d\rho \, \rho A_{pl}^*(\rho, \varphi) \, A_{p'l'}(\rho, \varphi) = \delta_{pp'} \delta_{ll'} \tag{5}$$

and form an orthonormal set in the transverse plane. The geometrical parameters of the cavity $\mathscr{L}$, L and R_0 determine the eigenfrequencies of the resonator according to the formula [12]

$$\omega_{npl} = \frac{c}{\mathscr{L}} \left[2\pi n + 2(2p + |l| + 1) \cos^{-1} \sqrt{\left(1 - \frac{L}{R_0}\right)\left(1 - \frac{\mathscr{L} - L}{R_0}\right)} \right], \tag{6}$$

where $n = 0, 1, 2, \ldots$ is the longitudinal index. An important consequence of eq. (6) is that the frequency of the GL modes depends on the transverse indices p and l only via the combination $2p + |l|$, thus introducing degeneracy. The modes gather in degenerate families, labelled by the index $q = 2p + |l|$ as shown in fig. 2. In the following we shall denote the transverse modes of the cavity by the couple of indices (p, l). The degenerate family of order q consists of $q + 1$ modes. In the literature mode $(0, 0)$ is usually designated as TEM_{00} and modes $(0, \pm l)$ are called TEM_{0l}^* hybrid modes or also doughnut modes because of their annular intensity profile.

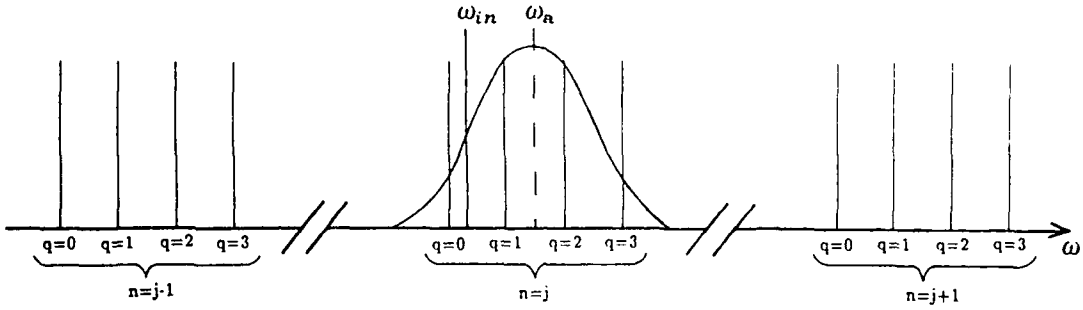

Fig. 2. Scheme of the frequencies of the eigenmodes of the empty cavity. In our model we assume that the separation between longitudinal modes is much larger than the separation between transverse modes with the same longitudinal index. In addition, only few transverse modes lie under the atomic line.

At this point we consider some limiting assumptions that allow for a considerable simplification of the analytical description:

$$\gamma_\perp \ll c/\mathscr{L}\,, \tag{7}$$

$$\omega_{n01} - \omega_{n00} \ll c/\mathscr{L}\,, \tag{8}$$

$$\alpha L_A \ll 1\,, \tag{9}$$

$$T \ll 1\,, \tag{10}$$

$$2C = \alpha L_A/T \quad \text{finite}\,, \tag{11}$$

$$\theta = \frac{\omega_{n00} - \omega_{in}}{cT/\mathscr{L}} \quad \text{finite}\,. \tag{12}$$

The physical meaning of eqs. (7) and (8) is that only the modes belonging to the longitudinal family nearest to the input field can be excited, whereas all the other longitudinal modes do not play any role in the dynamics (see fig. 2). Eq. (9) means that the interaction between electric field and atoms is arbitrarily small and gives foundation to our initial assumption that the source term in the Maxwell equation can be treated perturbatively. Eq. (10) describes an almost perfect reflection from the spherical mirrors so that the field remains confined in the cavity long enough to experience significant nonlinearities (the cooperative parameter $2C$ does not vanish). Conditions (7)–(12) correspond to a generalisation of the well-known mean-field limit [13] and allow to neglect the dependence of the electric field in the atomic sample on the longitudinal coordinate z.

Taking into account the orthonormality property (5), it is possible to expand the slowly varying envelope of the electric field $F(\rho, \varphi, t)$ in terms of the GL functions (4), obtaining:

$$F(\rho, \varphi, t) = \sum_{pl} f_{pl}(t)\, A_{pl}(\rho, \varphi)\,, \tag{13}$$

where the modal amplitudes f_{pl} are in general complex functions. We assume that the input field is matched with the TEM_{00} mode of the cavity so that its slowly varying envelope can be written as

$$F_{in}(\rho, \varphi) = Y A_{00}(\rho, \varphi)\,, \tag{14}$$

where Y is the normalised amplitude, which is taken real with an appropriate choice of the reference frequency. Including these expressions in the Maxwell equation for the electric field interacting with the atomic medium, making use of the approximations we have introduced and projecting onto the modal eigenfunctions, we obtain a set of integro-differential equations which describe the temporal evolution of the modal amplitudes [14]:

$$\frac{\mathrm{d}f_{pl}}{\mathrm{d}t} = -k\left[(1 + \mathrm{i}\theta + \mathrm{i}a_{pl})f_{pl} - Y\delta_{p,0}\delta_{l,0} + 2C\int_0^{2\pi}\mathrm{d}\varphi\int_0^{\infty}\mathrm{d}\rho\,\rho A^*_{pl}(\rho,\varphi)\,P(\rho,\varphi,t)\right], \tag{15}$$

where $k = cT/\mathscr{L}$ is the cavity linewidth and a_{pl} denotes the difference between the frequency of the mode of indices p, l and that of the fundamental TEM_{00} mode, normalised to k: $a_{pl} = (\omega_{npl} - \omega_{n00})/k$. P is the normalised slowly varying envelope of the atomic polarisation. Eq. (15) must be coupled with the atomic Bloch equations, which read

$$\frac{\partial P}{\partial t} = \gamma_\perp[F(\rho,\varphi,t)\,D(\rho,\varphi,t) - (1 + \mathrm{i}\Delta)P(\rho,\varphi,t)], \tag{16}$$

$$\frac{\partial D}{\partial t} = -\gamma_\parallel[\mathrm{Re}(F^*(\rho,\varphi,t)\,P(\rho,\varphi,t)) + D(\rho,\varphi,t) - 1], \tag{17}$$

where D is the normalised population inversion, $\gamma_\parallel$ is its relaxation rate and Δ is the detuning of the atomic transition from the frequency of the input field, normalised to $\gamma_\perp$: $\Delta = (\omega_a - \omega_{n00})/\gamma_\perp$.

In expansion (13) one should consider a priori all the modal amplitudes f_{pl} with $p = 0, 1, \ldots$ and $l = 0, \pm1, \ldots$. However, in real devices, transverse modes of high order (large values of q) usually suffer from high diffraction losses due to the finite size of the mirrors, the limited diameter of the active medium and the presence of intracavity elements such as pinholes, modulators, etc. Our model can describe the mode selection operated by such devices simply by limiting the expansion (13) to those values of p and l which do not exceed an upper limiting value of the family index q. This is a particular feature of optical systems that allows one to easily control the number of modes in play, both in the experimental devices and in the dynamical equations. The advantage with respect to other physical systems such as fluids, where the number of modes is always extremely large, is evident.

2.2. *Numerical integration of the dynamical equations*

Before proceeding to the study of the stationary solutions of the dynamical equations (15)–(17), we describe briefly how we perform their numerical integration. We first of all discretise the spatial dependence of P and D by introducing a grid of points (ρ_m, φ_n) $[m = 1 \ldots M;\ n = 1 \ldots N]$ in the transverse plane. Points φ_n are equally spaced in the interval $[0, 2\pi]$, while points ρ_m are chosen in such a way that $2\rho_m^2$, $[m = 1 \ldots M]$ are the zeroes of the Laguerre polynomial of order M. In this way the double integral of eq. (15) can be approximated by a double-weighted sum over the indices l and m (Gaussian quadratures), while eqs. (16) and (17) transform into a set of $2M \cdot N$ ordinary differential equations for $P_{mn}(t) = P(\rho_m, \varphi_n, t)$ and $D_{mn}(t) = D(\rho_m, \varphi_n, t)$:

$$\frac{\mathrm{d}f_{pli}}{\mathrm{d}t} = -k\left[(1 + \mathrm{i}\theta + \mathrm{i}a_{pl})f_{pli} - Y\delta_{p,0}\delta_{l,0} + 2C\sum_{m=1}^{M}\sum_{n=1}^{N} w_{mn}\bar{A}_{pli}(\rho_m,\varphi_n)\,P_{mn}\right], \tag{18}$$

$$\frac{dP_{mn}}{dt} = \gamma_\perp [F_{mn} D_{mn} - (1 + i\Delta) P_{mn}] , \tag{19}$$

$$\frac{dD_{mn}}{dt} = -\gamma_\parallel [\mathrm{Re}(F^*_{mn} P_{mn}) + D_{mn} - 1] , \tag{20}$$

where

$$F_{mn}(t) = \sum_{pl} \bar{A}_{pli}(\rho_m, \varphi_n)\, f_{pli}(t) \tag{21}$$

and w_{mn} is a set of weights for Gaussian quadratures.

In eqs. (18)–(21) the doughnut Gauss–Laguerre functions $A_{pl}(\rho, \varphi)$, which depend on the angular variable φ via the exponential factor $e^{il\varphi}$ (see eq. (4)), have been replaced by their linear combination $\bar{A}_{pli}(\rho, \varphi)$, defined in the following way

$$\bar{A}_{p0}(\rho, \varphi) = A_{p0}(\rho, \varphi) , \tag{22}$$

$$\begin{aligned} \bar{A}_{pl1}(\rho, \varphi) &= \frac{1}{\sqrt{2}} [A_{pl}(\rho, \varphi) + A_{p-l}(\rho, \varphi)] \\ &= \frac{2}{\sqrt{\pi}} (2\rho^2)^{l/2} \left[\frac{p!}{(p+l)!} \right]^{1/2} L_p^l(2\rho^2)\, e^{-\rho^2} \cos(l\varphi) , \end{aligned} \tag{23}$$

$$\begin{aligned} \bar{A}_{pl2}(\rho, \varphi) &= \frac{1}{\sqrt{2}i} [A_{pl}(\rho, \varphi) - A_{p-l}(\rho, \varphi)] \\ &= \frac{2}{\sqrt{\pi}} (2\rho^2)^{l/2} \left[\frac{p!}{(p+l)!} \right]^{1/2} L_p^l(2\rho^2)\, e^{-\rho^2} \sin(l\varphi) . \end{aligned} \tag{24}$$

Accordingly, the angular index l takes only non-negative values $l = 0, 1, 2 \ldots$. Since the $\bar{A}_{pli}(\rho, \varphi)$ are real functions, this substitution allows for a straightforward separation of the real and imaginary parts in eq. (18), thus reducing the CPU time required by the adaptive Runge–Kutta integration method. In sections 4 and 5 we shall refer to this latter modal decomposition.

2.3. *Stationary solutions*

The stationary equations are obtained by setting the time derivatives in eqs. (15)–(17) equal to zero. The atomic variables' stationary states are given by

$$P^{(st)}(\rho, \varphi) = \frac{(1 - i\Delta) F^{(st)}}{1 + \Delta^2 + |F^{(st)}|^2} , \qquad D^{(st)}(\rho, \varphi) = \frac{1 + \Delta^2}{1 + \Delta^2 + |F^{(st)}|^2} , \tag{25}$$

where

$$F^{(st)}(\rho, \varphi) = \sum_{p,l} A_{pl}(\rho, \varphi)\, f_{pl}^{(st)} . \tag{26}$$

By substituting the expression for $P^{(st)}$ in the stationary equations for the modal amplitudes of the field, one obtains

$$Y = f_{00}^{(st)}(1 + i\theta) + 2C(1 - i\Delta) \sum_{p',l'} \int_0^{2\pi} d\varphi \int_0^{\infty} d\rho\, \rho \frac{A_{00}^* A_{p'l'}}{1 + \Delta^2 + |\Sigma_{r,m} A_{rm} f_{rm}^{(st)}|^2} f_{p'l'}^{(st)}, \tag{27}$$

$$0 = f_{pl}^{(st)}(1 + ia_{pl} + i\theta) + 2C(1 - i\Delta) \sum_{p',l'} \int_0^{2\pi} d\varphi \int_0^{\infty} d\rho\, \rho \frac{A_{pl}^* A_{p'l'}}{1 + \Delta^2 + |\Sigma_{r,m} A_{rm} f_{rm}^{(st)}|^2} f_{p'l'}^{(st)}, \tag{28}$$

where we have isolated the equation for the TEM_{00} mode (the only one that experiences the driving field Y).

2.3.1. *Singlemode TEM_{00} solution*

The singlemode solution is such that in eq. (26) only the amplitude f_{00} of the TEM_{00} mode is different from zero, and is an exact solution of eqs. (27) and (28) only in the limit in which it is possible to neglect all the modes belonging to families with $q \geq 2$.

In this limit the dynamic behaviour of the system is governed by the three modes (0, 0) and (0, ±1) of the families $q = 0$ and $q = 1$, that are described by the modal functions

$$A_1(\rho) \equiv A_{00}(\rho) = \sqrt{\frac{2}{\pi}}\, e^{-\rho^2}, \tag{29}$$

$$A_2(\rho, \varphi) \equiv A_{01}(\rho, \varphi) = \frac{2}{\sqrt{\pi}}\, \rho\, e^{-\rho^2} e^{i\varphi}, \tag{30}$$

$$A_3(\rho, \varphi) \equiv A_{0-1}(\rho, \varphi) = \frac{2}{\sqrt{\pi}}\, \rho\, e^{-\rho^2} e^{-i\varphi}, \tag{31}$$

and the electric field can be written as

$$F(\rho, \varphi, t) = \sum_{i=1}^{3} f_i(t) A_i(\rho, \varphi). \tag{32}$$

It is easy to show that the choice

$$f_1^{(st)} \equiv f_{00}^{(st)} \neq 0, \qquad f_2^{(st)} \equiv f_{01}^{(st)} = 0, \qquad f_3^{(st)} \equiv f_{0-1}^{(st)} = 0,$$

satisfies eqs. (27) and (28). In particular, eq. (27) becomes

$$Y = f_1^{(st)}(1 + i\theta) + 2C(1 - i\Delta) 2\pi \int_0^{\infty} d\rho\, \rho \frac{|A_1(\rho)|^2}{1 + \Delta^2 + |A_1(\rho)\, f_1^{(st)}|^2} f_1^{(st)}. \tag{33}$$

By multiplying each side of eq. (33) by its complex conjugate one obtains an expression that links the modulus of the output field $x_1 = \sqrt{2/\pi}\, |f_1^{(st)}|$ to that of the input field $y_1 = \sqrt{2/\pi}\, Y$ [15]:

$$y_1 = x_1 \left[\left(1 + \frac{2C}{x_1^2} \ln \frac{1 + \Delta^2 + x_1^2}{1 + \Delta^2} \right)^2 + \left(\theta - \frac{2C\Delta}{x_1^2} \ln \frac{1 + \Delta^2 + x_1^2}{1 + \Delta^2} \right)^2 \right]^{1/2}. \tag{34}$$

The corresponding steady state curve, for suitable sets of parameters, displays the typical S-shape of optical bistable systems.

2.3.2. Multimode $l = 0$ solutions

When the modes belonging to families with $q \geq 2$ are included in the model the singlemode stationary solution described in the previous section does not exist any longer, for the integrals that appear in eqs. (27) and (28) couple mode (0, 0) with all the modes $(p, l = 0)$.

Let us consider for example what happens if we include in the model the modes of the family $q = 2$. They are described by the modal functions

$$A_4(\rho) \equiv A_{10}(\rho) = \sqrt{\frac{2}{\pi}}\,(1 - 2\rho^2)\,\mathrm{e}^{-\rho^2}\,, \tag{35}$$

$$A_5(\rho, \varphi) \equiv A_{02}(\rho, \varphi) = \frac{2}{\sqrt{\pi}}\,\rho^2\,\mathrm{e}^{-\rho^2}\,\mathrm{e}^{2\mathrm{i}\varphi}\,, \tag{36}$$

$$A_6(\rho, \varphi) \equiv A_{0-2}(\rho, \varphi) = \frac{2}{\sqrt{\pi}}\,\rho^2\,\mathrm{e}^{-\rho^2}\,\mathrm{e}^{-2\mathrm{i}\varphi}\,, \tag{37}$$

that must be added to those of eqs. (29)–(31), so that the total electric field is

$$F(\rho, \varphi, t) = \sum_{i=1}^{6} f_i(t) A_i(\rho, \varphi)\,. \tag{38}$$

The multimode $l = 0$ solution is in this case the solution such that only the modal amplitudes $f_1^{(\mathrm{st})} \equiv f_{00}^{(\mathrm{st})}$ and $f_4^{(\mathrm{st})} \equiv f_{10}^{(\mathrm{st})}$ do not vanish and their values are given by the following equations:

$$Y = f_1^{(\mathrm{st})}(1 + \mathrm{i}\theta) + 2C(1 - \mathrm{i}\Delta)2\pi \int_0^\infty \mathrm{d}\rho\,\rho\,\frac{|A_1(\rho)|^2 f_1^{(\mathrm{st})} + A_1(\rho)^* A_4(\rho) f_4^{(\mathrm{st})}}{1 + \Delta^2 + |A_1(\rho) f_1^{(\mathrm{st})} + A_4(\rho) f_4^{(\mathrm{st})}|^2}\,, \tag{39}$$

$$0 = f_4^{(\mathrm{st})}(1 + \mathrm{i}a_{10} + \mathrm{i}\theta) + 2C(1 - \mathrm{i}\Delta)2\pi \int_0^\infty \mathrm{d}\rho\,\rho\,\frac{A_4(\rho)^* A_1(\rho) f_1^{(\mathrm{st})} + |A_4(\rho)|^2 f_4^{(\mathrm{st})}}{1 + \Delta^2 + |A_1(\rho) f_1^{(\mathrm{st})} + A_4(\rho) f_4^{(\mathrm{st})}|^2}\,. \tag{40}$$

Since all the modes with $l = 0$ are independent of the angular coordinate φ, the intensity profiles of these kind of solutions possess cylindrical symmetry and they are not, in general, very different from that of the TEM_{00} solution, for the contributes of the modes with $p \geq 1$ are usually small.

2.3.3. Generic multimode solutions

Other multimode solutions exist in which modes with $l \neq 0$ are present. For these solutions the r.h.s. of eqs. (27) and (28) are very complicated implicit functions of the $f_{pl}^{(\mathrm{st})}$ and, in general, also their numerical solution is very difficult, so that it is easier to integrate numerically eqs. (15)–(17) and analyse the steady state they reach at regime.

The intensity profile of one of these solutions is shown in fig. 3. In this case the parameters are $C = 100$, $\Delta = 10$, $\theta = -2$, $a_{01} = 4$, $k/\gamma_\perp = 1$, $\gamma_\parallel/\gamma_\perp = 1$ and the modes belonging to families $q = 0, 1, 2, 3, 4$ are active. As one can see, the presence of modes with angular index l difference from zero causes a breaking of the cylindrical symmetry in the intensity profile.

Even though the stationary configurations we have described so far can be represented by linear combinations of the empty cavity eigenmodes, it must be noted that, in general, it is not true that *any* linear combination of such modes is a stable solution of the dynamical equations. Because of the nonlinear interaction among the atoms and the electric field, which is manifest in eqs. (27) and (28), the

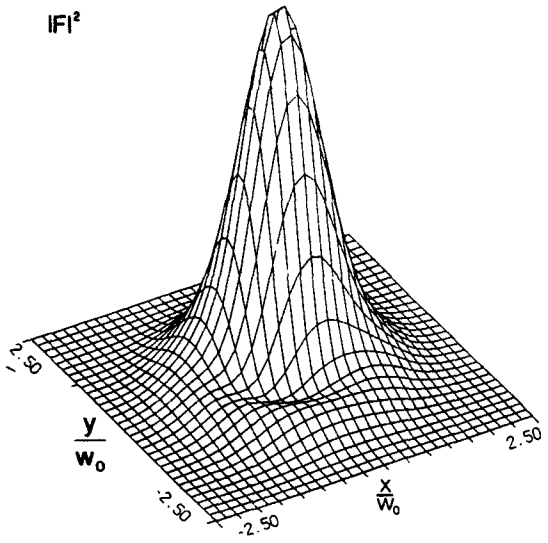

Fig. 3. Intensity profile of a multimode stationary solution in the transverse plane.

system selects only *particular* linear combinations of the modes, that represent fixed points in the phase space whose coordinates are the real and the imaginary parts of the model amplitudes f_{pl}. The same picture in terms of attractors holds for the dynamical regimes that we describe in the following section, where the modal amplitudes are functions of time.

2.4. *Destabilisation of the TEM_{00} single mode steady state*

In this section we restrict our analysis again to the three modes model and describe how the onset of the modes of family $q = 1$ can destabilise the singlemode TEM_{00} stationary solution (34), giving rise to more complex spatiotemporal structures.

In order to check the stability of the singlemode stationary solution we consider a small perturbation

$$\delta F(\rho, \varphi, t) = \sum_{i=1}^{3} A_i(\rho, \varphi)\delta f_i(t) = F(\rho, \varphi, t) - F^{(st)}(\rho, \varphi)$$
$$= F(\rho, \varphi, t) - A_1(\rho) f_1^{(st)}, \tag{41}$$

$$\delta P(\rho, \varphi, t) = P(\rho, \varphi, t) - P^{(st)}(\rho, \varphi), \tag{42}$$

$$\delta D(\rho, \varphi, t) = D(\rho, \varphi, t) - D^{(st)}(\rho, \varphi) \tag{43}$$

and linearise the dynamical eqs. (15)–(17) around the steady state. Then we introduce the usual exponential Ansatz

$$\begin{pmatrix} \delta f_i(t) \\ \delta f_i^*(t) \\ \delta P(\rho, \varphi, t) \\ \delta P^*(\rho, \varphi, t) \\ \delta D(\rho, \varphi, t) \end{pmatrix} = e^{\tilde{\lambda}\gamma_\perp t} \begin{pmatrix} \delta f_i^0 \\ \delta f_i^{0*} \\ \delta P^0(\rho, \varphi) \\ \delta P^{0*}(\rho, \varphi) \\ \delta D^0(\rho, \varphi) \end{pmatrix}, \tag{44}$$

obtaining a closed set of linear equations for the variables δf_2^0, δf_2^{0*}, δf_3^0, δf_3^{0*}.

The condition for the existence of a non-vanishing solution of these equations leads to a transcendental secular equation in $\tilde{\lambda}$:

$$\begin{aligned}\tilde{\lambda}/\tilde{k} = &-1 - C(\Phi(x_1, \tilde{\gamma}, \tilde{\lambda}, \Delta) + \Phi(x_1, \tilde{\gamma}, \tilde{\lambda}, -\Delta)) \\ &\pm \{4C^2\Psi(x_1, \tilde{\gamma}, \tilde{\lambda}, \Delta)\Psi(x_1, \tilde{\gamma}, \tilde{\lambda}, -\Delta)x_1^4 \\ &- [\theta + a_{01} + C(\Phi(x_1, \tilde{\gamma}, \tilde{\lambda}, \Delta) - \Phi(x_1, \tilde{\gamma}, \tilde{\lambda}, -\Delta))]^2\}^{1/2}, \end{aligned} \tag{45}$$

where

$$\tilde{k} = k/\gamma_\perp, \qquad \tilde{\gamma} = \gamma_\parallel/\gamma_\perp, \tag{46}$$

$$\Phi(x_1, \tilde{\gamma}, \tilde{\lambda}, \Delta) = \int_0^\infty d\rho \, \frac{4\rho^3 e^{-2\rho^2}[2(1+\Delta^2)(\tilde{\gamma}+\tilde{\lambda})(1+\tilde{\lambda}-i\Delta) - \tilde{\gamma}\tilde{\lambda}(1+i\Delta)x_1^2 e^{-2\rho^2}]}{(1+\Delta^2+x_1^2 e^{-2\rho^2})\{(\tilde{\gamma}+\tilde{\lambda})[(1+\tilde{\lambda})^2+\Delta^2] + \tilde{\gamma}(1+\tilde{\lambda})x_1^2 e^{-2\rho^2}\}}, \tag{47}$$

$$\Psi(x_1, \tilde{\gamma}, \tilde{\lambda}, \Delta) = \int_0^\infty d\rho \, \frac{4\rho^3 e^{-2\rho^2}[\tilde{\gamma}(\tilde{\lambda}+2)(1-i\Delta)]}{(1+\Delta^2+x_1^2 e^{-2\rho^2})\{(\tilde{\gamma}+\tilde{\lambda})[(1+\tilde{\lambda})^2+\Delta^2] + \tilde{\gamma}(1+\tilde{\lambda})x_1^2 e^{-2\rho^2}\}}. \tag{48}$$

The existence of a root of eq. (45) with $\mathrm{Re}\,\tilde{\lambda} > 0$ indicates the instability of the (0, 0) solution. Eq. (45) can be solved, in general, only numerically. Here we consider two particular cases in which the treatment can be considerably simplified and the instability boundaries in the parameter space can be easily calculated.

A first simplified approach to the stability analysis consists in observing that, as eq. (45) clearly shows, the eigenvalue $\tilde{\lambda}$ is proportional to $\tilde{k}$. Hence, if $\tilde{k}$ is small, one can solve perturbatively the eigenvalue problem by assuming that

$$\tilde{\lambda} = \tilde{\lambda}_0 + \tilde{k}\tilde{\lambda}_1 + \mathcal{O}(\tilde{k}^2). \tag{49}$$

We note that the self-consistency of this method requires that the frequency spacing between mode (0, 0) and the input field is of the order of k, while the frequency spacing between all other modes and the input field is of the order of $\gamma_\perp$ [12]. In other terms, we require that

$$\theta = \frac{\omega_{n00} - \omega_{in}}{k} = \mathcal{O}(1), \qquad \eta = \tilde{k}a_{01} = \frac{\omega_{n01} - \omega_{n00}}{\gamma_\perp} = \mathcal{O}(1). \tag{50}$$

The calculation of the first two terms of the expansion (49) yields

$$\tilde{\lambda}_0 = \mp i\eta, \tag{51}$$

$$\tilde{\lambda}_1 = -2C\Phi(x_1, \tilde{\gamma}, \tilde{\lambda} = \tilde{\lambda}_0, \Delta) - 1 \pm i\Delta. \tag{52}$$

As $\tilde{\lambda}_0$ is purely imaginary, the instability condition amounts to

$$\mathrm{Re}\,\tilde{\lambda}_1 > 0. \tag{53}$$

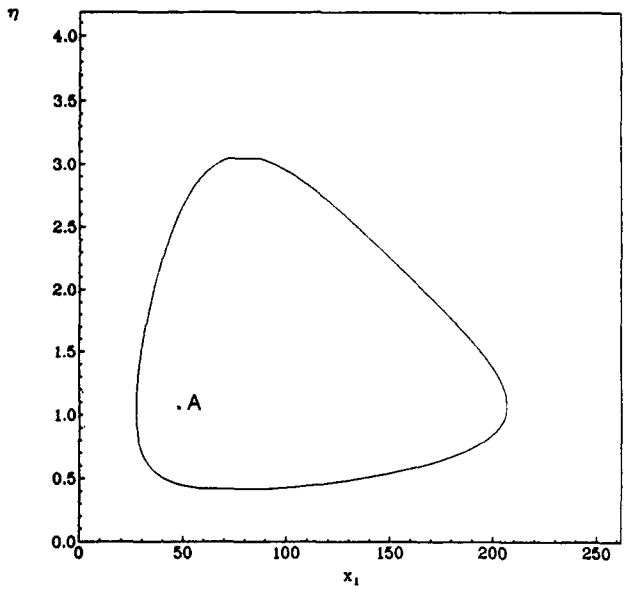

Fig. 4. Instability domain of the singlemode $TEM_{(0)}$ solution in the (x_1, η) plane in the case $\tilde{k} \ll 1$, for $C = 600$, $\Delta = 20$, $\tilde{\gamma} = 1$. In correspondence to the solid line the real part of the eigenvalue vanishes. Point A indicates the values of x_1 and η that have been used in fig. 6.

Fig. 4 shows, in the parameter subspace (x_1, η), the instability boundary Re $\tilde{\lambda}_1 = 0$, surrounding the unstable region. The onset of this instability is marked by the change of sign in the real part of a complex eigenvalue (Hopf instability).

Another kind of instability occurs when both Re $\tilde{\lambda}$ and Im $\tilde{\lambda}$ vanish simultaneously. The boundary of the instability domain are found by setting $\tilde{\lambda} = 0$ in eq. (45) and no assumption is made on the value of $\tilde{k}$. It is worth noting that this procedure amounts to revealing the existence of Turing instabilities [16]. In fig. 5 the solid line encloses the instability domain in the parameter space (x_1, a_{01}); all other parameters have been fixed at the values specified in the captions.

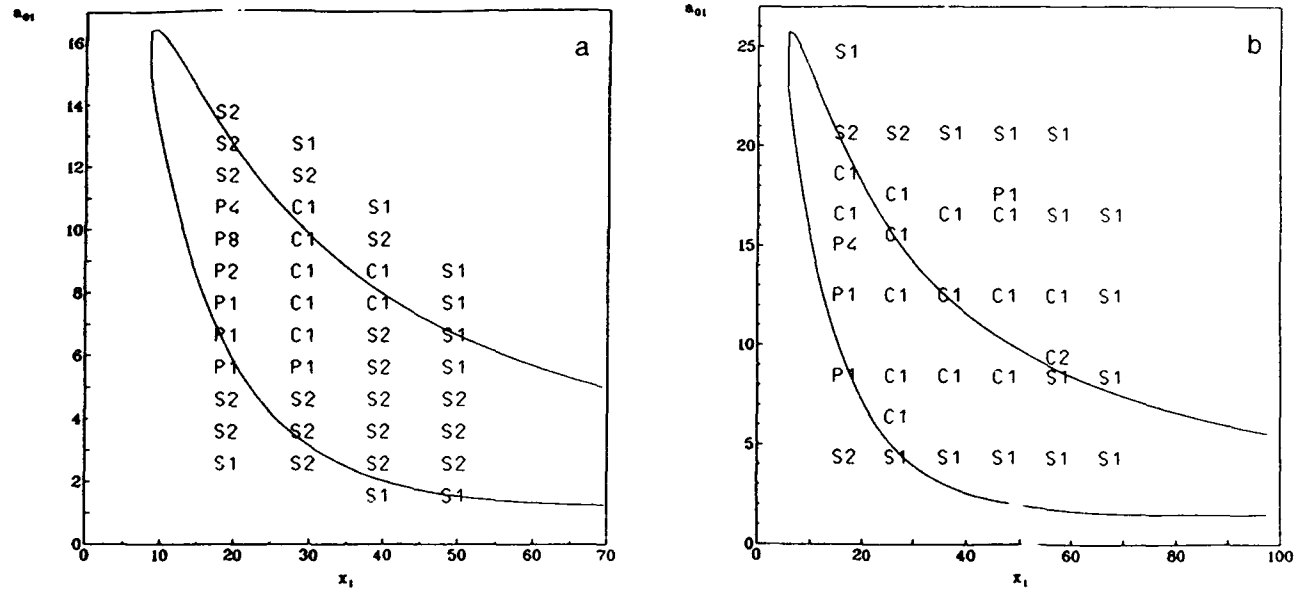

Fig. 5. Instability domains of the singlemode TEM_{00} solution in the (x_1, a_{01}) plane. In correspondence to the solid line both the real and the imaginary part of the eigenvalue vanish. The values of the other parameters are $\Delta = 10$, $\theta = -2$, $\tilde{\gamma} = 1$ and (a) $C = 100$, (b) $C = 150$. The meaning of the lettering is explained in the text.

3. Dynamical regimes

In this section we describe the various regimes that have been observed in the analysis of the dynamical behaviour of our system. These regimes are rather different in the case $k \ll \gamma_\perp, \gamma_\parallel$ (good cavity limit) and in the case $k \sim \gamma_\perp \sim \gamma_\parallel$, therefore we treat the two cases separately.

3.1. Good cavity limit

This limit is defined by the condition $\tilde{k} \ll 1$. In this situation the instability condition for the singlemode TEM_{00} solution is given by eq. (53). We have observed that the patterns that arise from this instability are always characterised by the fact that only the (0, 0) mode and one of the (0, ±1) doughnut modes contribute to the electric field. Their intensities are constant, but each of them oscillates with its own frequency. If we assume for definiteness that the doughnut mode with positive helicity is active, the electric field has the form

$$F(\rho, \varphi, t) = \sqrt{\frac{2}{\pi}} [f_1 + \rho\sqrt{2} f_2 \, e^{i(\varphi - \eta\tau)}] \, e^{-\rho^2} , \tag{54}$$

where $\tau = \gamma_\perp t$ and η is the difference between the frequencies of the two families, normalised to $\gamma_\perp$. Eq. (54) yields the following expression for the field intensity:

$$|F(\rho, \varphi, t)|^2 = \frac{2}{\pi} [|f_1|^2 + 2\rho^2 |f^2|^2 + 2\sqrt{2}\rho |f_1| \, |f_2| \cos(\varphi - \eta\tau - \varphi_0)] \, e^{-2\rho^2} , \tag{55}$$

where φ_0 is the phase lag between f_1 and f_2 at time $t = 0$. Eq. (55) clearly describes a counterclockwise rotating pattern; the rotation is clockwise if the doughnut with negative helicity is active. The dynamics of the modulus of the field is depicted in the sequence of fig. 6, obtained with the following set of parameters: $C = 600$, $\Delta = 20$, $\tilde{\gamma} = 1$, $\eta = 1$, $x_1 = 50$, (corresponding to point A in fig. 4) $\theta = 30$ and $\tilde{k} = 0.01$.

As one expects from the inspection of fig. 6, there exists a point in the transverse plane where the electric field intensity vanishes. Such a point is a singularity for the electric field phase and, therefore, it can be regarded as an optical vortex, in the sense of ref. [3]. This point is easily identified in eq. (55) as the one having polar coordinates

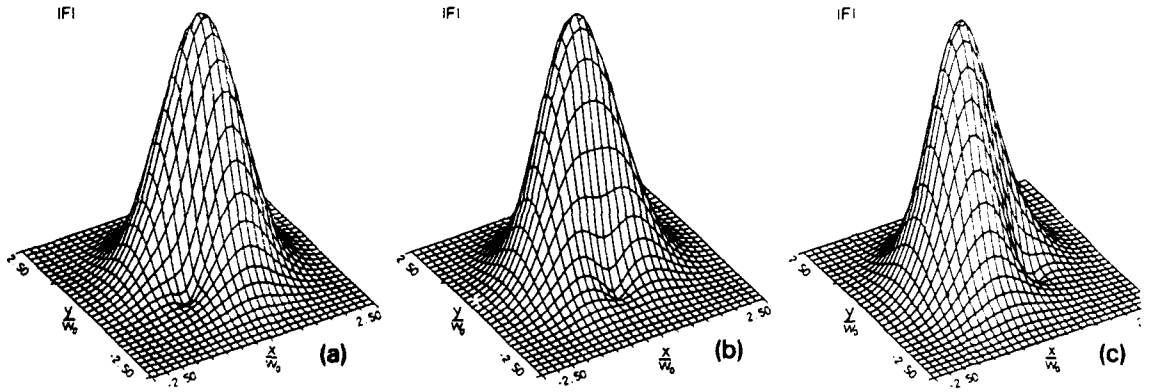

Fig. 6. Evolution of the modulus of the field for a choice of the parameters corresponding to point A in fig. 4. The rotation of the whole structure and the presence of a vortex are clearly visible.

$$\rho_v = \frac{|f_1|}{\sqrt{2}|f_2|}, \qquad \varphi_v = \eta\tau + \varphi_0 + \pi . \tag{56}$$

Obviously, the vortex moves on a circular orbit around the optical axis with angular frequency η. The existence of the same dynamical pattern has been theoretically predicted in active systems [17] and is presently being experimentally investigated by the group of Weiss and collaborators.

3.2. The case $k \sim \gamma_\perp \sim \gamma_\parallel$

A rich variety of dynamical patterns has been found in this case. In fig. 5 the solid lines show the domains of instability predicted by the analysis of the three-modes model. We have used these results as a starting point for our study based on the integration of eqs. (15)–(17) up to family $q = 2$ (i.e. we considered the six–modes model). Our results are illustrated schematically in the same figure, where we indicate the multimode $l = 0$ stationary solutions with S_1 and the generic multimode stationary solutions with S2. The symbol Pn, with $n = 1, 2, 4, 8$, refers to regimes where the total intensity is periodic with period n, whereas C1 and C2 denote two different chaotic regimes. As one can see there exist extended areas of chaotic behavior. Period doubling routes have been identified for both regimes C1 and C2. Conversely, when the mode separation is increased the systems tends to reach the S1 configuration, because all other higher order families are disfavoured. The presence of unstable behaviour outside the instability domain and, vice versa, of stable regimes inside it is not surprising, for we are comparing the numerical results relative to the six–mode model with the theoretical predictions of the three–mode model, which is the only one to be analytically treatable.

Fig. 7 illustrates a period-4 behaviour which is observed for the parameters values of fig. 5b, with $a_{01} = 13.5$ and $x_1 = 20$. Figs. 7a and 7b show the projections of the trajectory onto the planes Re f_{00}–Im f_{00} and Re f_{01}–Im f_{01}, respectively.

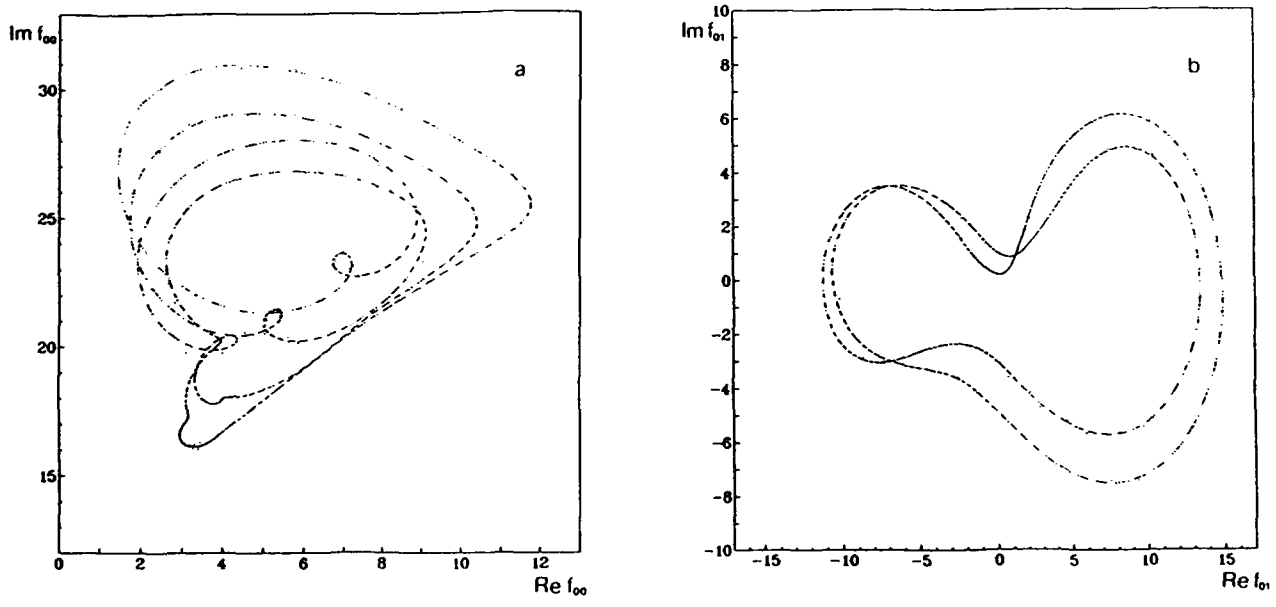

Fig. 7. Example of periodic behaviour: (a) projection of the trajectory on the (Re f_{00}, Im f_{00}) plane; (b) projection of the trajectory on the (Re f_{01}, Im f_{01}) plane.

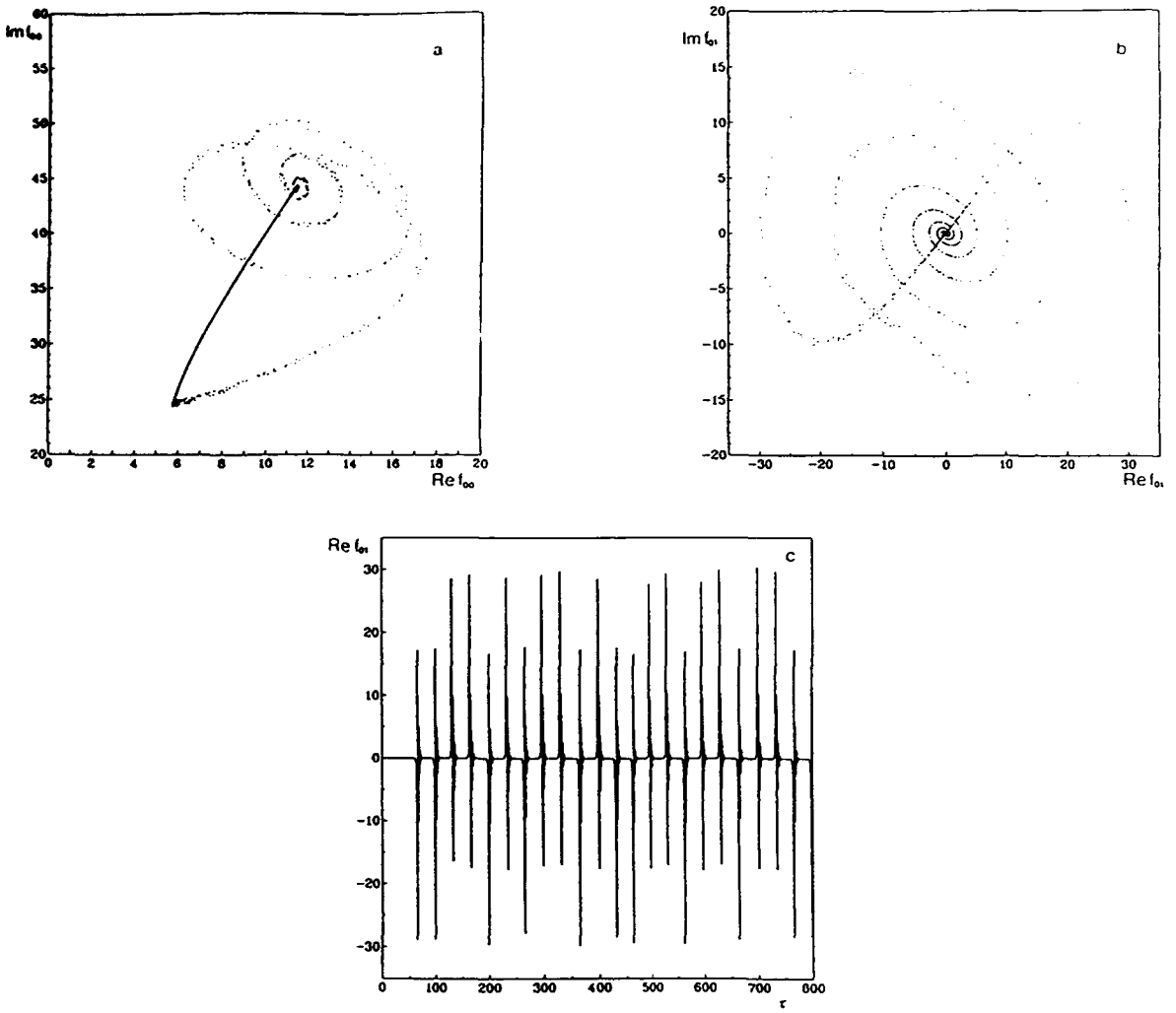

Fig. 8. Example of Šilnikov-like chaotic behaviour: (a) projection of the trajectory on the (Re f_{00}, Im f_{00}) plane; (b) projection of the trajectory on the (Re f_{01}, Im f_{01}) plane. (c) temporal evolution of Re f_{01}.

A second type of chaotic behaviour has been observed for the parameters of fig. 5b (with $x_1 = 60$) and for several values of a_{01} in the range $8.5 < a_{01} < 14$. In this case, the trajectory remains for a long time interval (extending for approximately 50 τ-units) on a regular path. Correspondingly, f_{00} drifts along the solid line of fig. 8a, while f_{01} remains equal to zero, as shown in figs. 8b, 8c. Then, suddenly, the system experiences an abrupt push, subsequently to spiral back to the regular orbit, a behaviour reminiscent of Šilnikov chaos [18].

The chaotic behaviour indicated in fig. 5b with C1 is observed also for parameter values within the experimental reach. An extensive analysis of this regime is presented in the following section.

4. Study of the chaotic states

In this section we study extensively the behaviour of the system in the chaotic regime, having as a goal the understanding of the relation between spatial pattern formation and temporal irregular

dynamics. To this end we concentrate on the case $\tilde{k} = 1$, $\tilde{\gamma} = 1$, $C = 100$, $\Delta = 10$, $\theta = -2$, $a_{01} = 9$, $x_1 = 30$ (cf. fig. 5a), which we study for increasing number of active GL modes. Namely, we consider in the expansion (13) the families $q \leqslant 2$, $q \leqslant 3$ and $q \leqslant 4$, respectively. In all three cases we peformed the numerical integration of eqs. (18)–(20) and collected the time series of the expansion coefficients $f_{pl}(t)$ of eq. (21). In the analysis of extended systems, a complete characterisation of the dynamics may require the recording of huge amounts of data, an obstruction that, in many instances, can preclude the quantitative understanding of the system's behaviour. In our case the mode expansion offers the advantage of synthesising the space information, thus avoiding all problems related with the choice of a proper spatial sampling. Nevertheless, in order to perform analyses which have become standard in the theory of low-dimensional chaos, one has to record several hundred thousand data points per expansion coefficient, which brings very soon, for increasing q, to the limit capacity of currently available mass-storage devices. The analyses discussed in the following are based on three data sets: for $q \leqslant 2$ we recorded, for each of the 6 complex expansion coefficients, $n = 1\,138\,000$ points, at a rate of one point each $\Delta t = 0.15$; for $q \leqslant 3$, for each of the 10 complex coefficients, $n = 300\,000$ points with $\Delta t = 0.3$; for $q \leqslant 4$, for each of the 15 complex coefficients, $n = 300\,000$ points with $\Delta t = 0.3$. The integration of the dynamical equations, carried out on an Alliant FX8 vector-parallel minicomputer, required several days of CPU time.

4.1. *Characterisation of the chaotic time behaviour*

In this section we present the results of the analysis of the time series $f_{pl}(t)$, whose first step is the determination of the low-dimensional nature of the dynamics.

A first insight into the system's behaviour can be obtained by inspecting the projections obtained by plotting the nth attractor point versus the $(n+1)$st, for each of the time series. The existence of a relation between the shape of the attractor and the spatial configuration of the electric field is apparent. Independently of how many modes are active, the attractor's shape is mainly determined by the parity and magnitude of the angular index l, whereas the radial coefficient p and the phase coefficient i have little influence. Typical attractor shapes are seen in fig. 9, for $q \leqslant 4$ and time interval between subsequent points $\Delta t = 0.6$. Real and imaginary parts are plotted separately. We notice that the attractors related to modes with odd l's have the shape of symmetric (with respect to both diagonals) loops. An increase in $|l|$ is accompanied by a higher density and a more complicated folding in the areas adjacent to the origin. If l is even the attractors have no evident symmetry properties and become very irregularly dense for increasing $|l|$.

The relation spatial modal indices – time behaviour of the amplitudes becomes even more evident studying the probability distributions of the values $f_{pl}(t)$ illustrated in fig. 10. The shape of the histograms is again rather independent of q, p and i, whereas it depends strongly on the parity and the modulus of l. While the considerations we have made with reference to the symmetry properties of the attractors extend quite obviously to the probability distributions, it is here remarkably clearer how an increase in $|l|$ causes the histograms to be sharply peaked around the origin. Thus, modes with high angular coefficients are governed, for the given parameter values, by an intermittent dynamics. Further comments about the time fluctuations of modal amplitudes will be made in section 4.2.

As mentioned in section 2.2, time series $f_{pl}(t)$ are actually the result of the numerical integration of a set of very many coupled nonlinear ordinary differential equations (in our case 972, 980 and 990 equations for $q \leqslant 2$, $q \leqslant 3$ and $q \leqslant 4$, respectively). In order to investigate the low-dimensional nature of

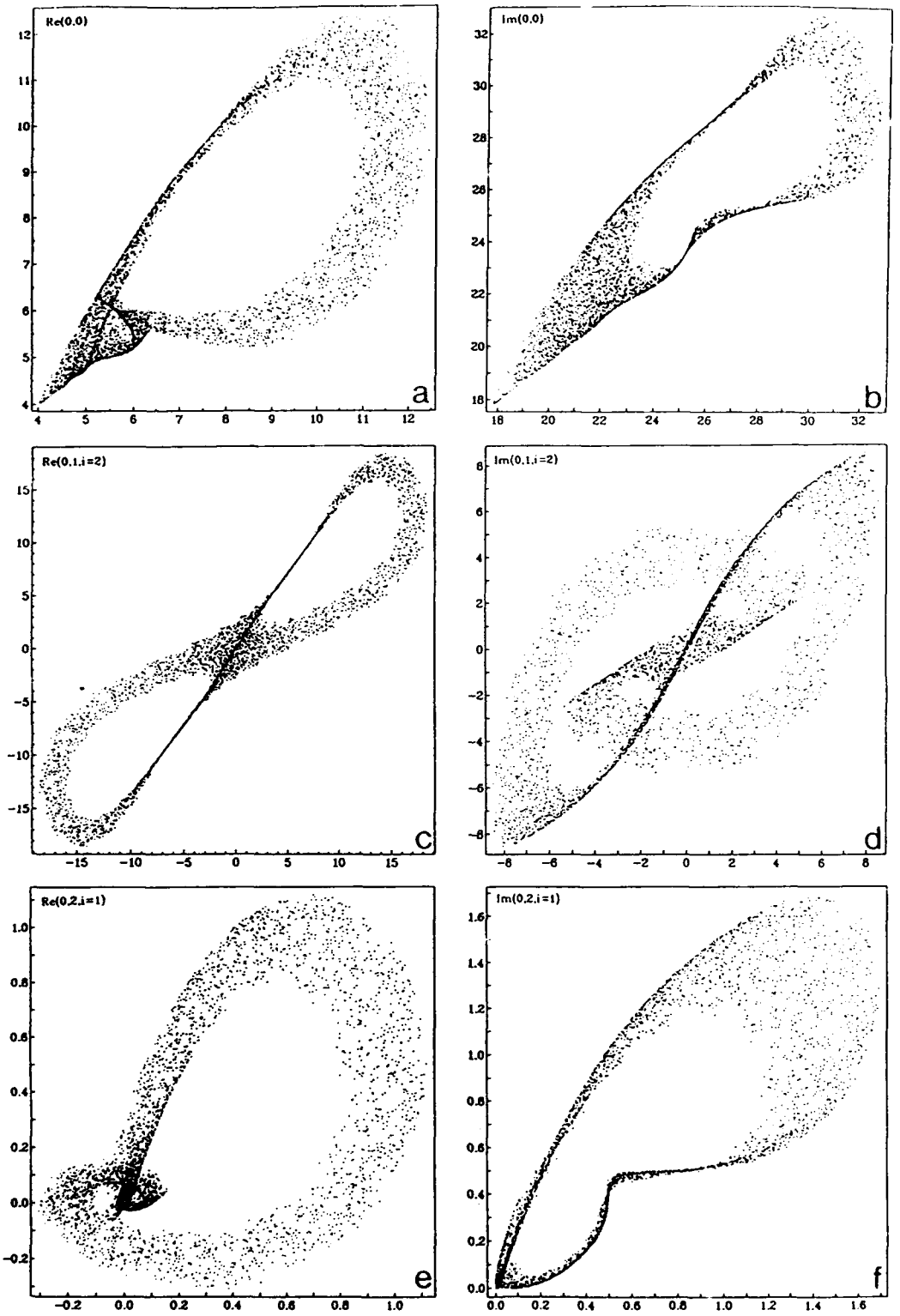

Fig. 9. Two-dimensional projections of the Gauss–Laguerre coefficients $f_{pl}(t)$, for $q \leq 4$, $\tilde{k} = 1$, $\tilde{\gamma} = 1$, $C = 100$, $\Delta = 10$, $\theta = -2$, $a_{01} = 9$, $x_1 = 30$. Each attractor point is projected against the preceding one. The coefficients are identified by the indices p, l and, if $l \neq 0$, i; real and imaginary parts are plotted separately. Each figure contains 5000 points sampled at a rate of one point each $\Delta t = 0.6$.

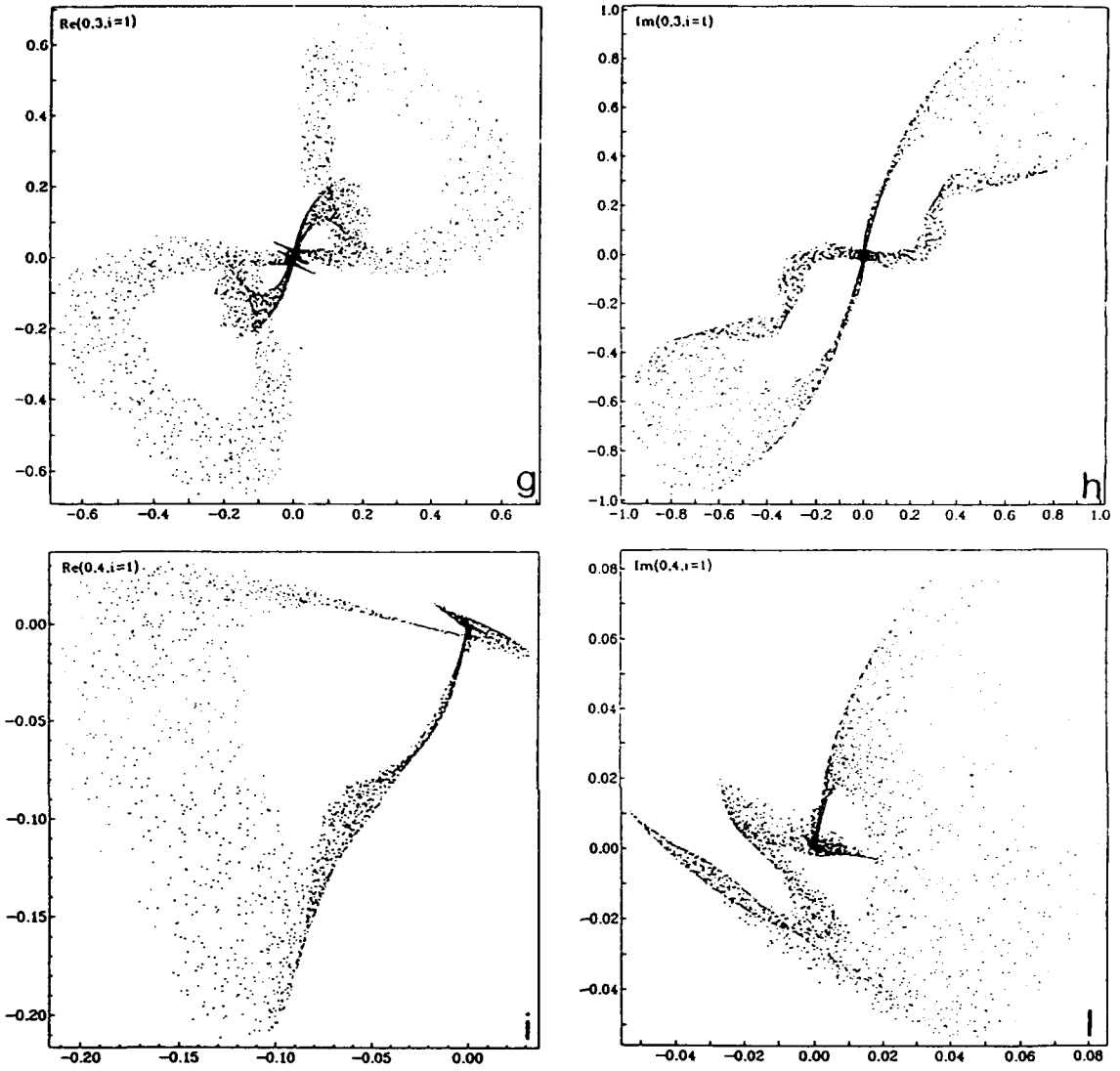

Fig. 9 (cont.).

the irregular time dynamics we have proceeded to the measurement of fractal dimensions and entropies [20, 19], adopting the constant-mass method [21, 22].

The first set of results, illustrated in fig. 11, was obtained by considering the $f_{pl}(t)$ as coordinates in a phase-space whose dimension is the number of the active GL modes (actually, twice this number, since real and imaginary parts are considered separately). The information dimension $D(1)$ [19] is plotted in fig. 11a for $q \leqslant 2$, in fig. 11b for $q \leqslant 3$ and in fig. 11c for $q \leqslant 4$ versus the number of considered attractor points n (given in powers of $b = 1.18$) for several orders of nearest-neighbours (n − n) k. Fig. 11 should be understood in the following way. In each of the three cases, $m = 8192$ points were chosen on the attractor, at random with respect to the natural measure, as reference points. $D(1)$ is determined by measuring the exponential scaling of the average distance of the kth n − n with n, by means of a regression procedure carried out in an n-range of 12 powers of b [22]. These plots allow one to study at the same time the convergence with both n and k: in the cases (a) and (b) all n-n distances have reached

their asymptotic scaling for the available n-values [in (a) the typical fluctuations due to lacunarity have already set in], whereas in (c) only the lowest-order n-n distances have converged (as one expects because of the increased phase-space dimension). In all cases the convergence is satisfactory: giving a higher weight to lower-order n-n's one measures: (a) $D(1) = 2.6$, (b) $D(1) = 2.3$, and (c) $D(1) = 2.5$, the errors being smaller than 0.2 in all three cases. The phenomenon is therefore unequivocably low-dimensional and $2 < D(1) < 3$. Relevant to us is the absence of any systematic increase in the

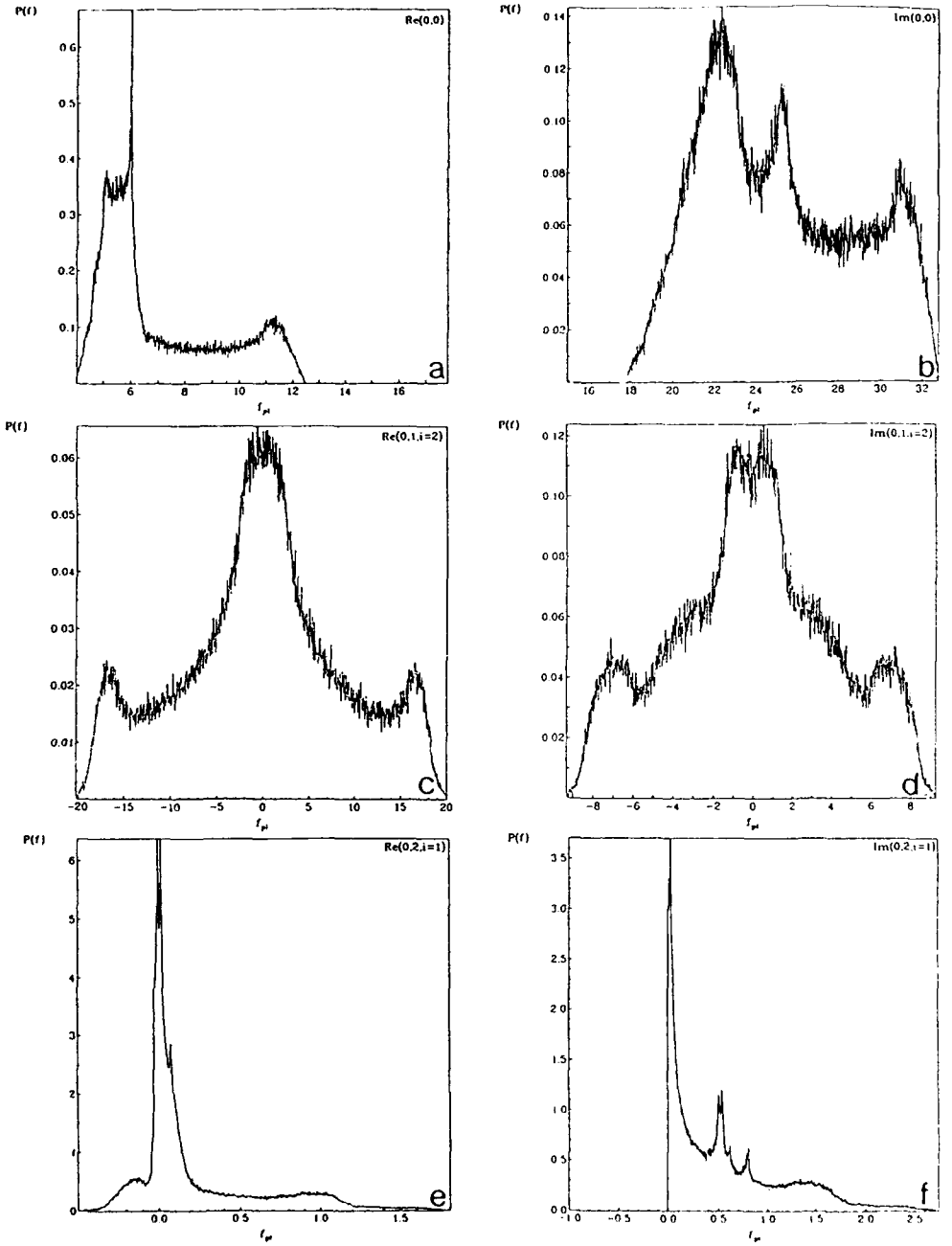

Fig. 10. Probability distributions of the Gauss–Laguerre mode amplitudes $f_{pl}(t)$, for the cases of fig. 9. The histograms have been constructed by distributing 250 000 values over 512 bins.

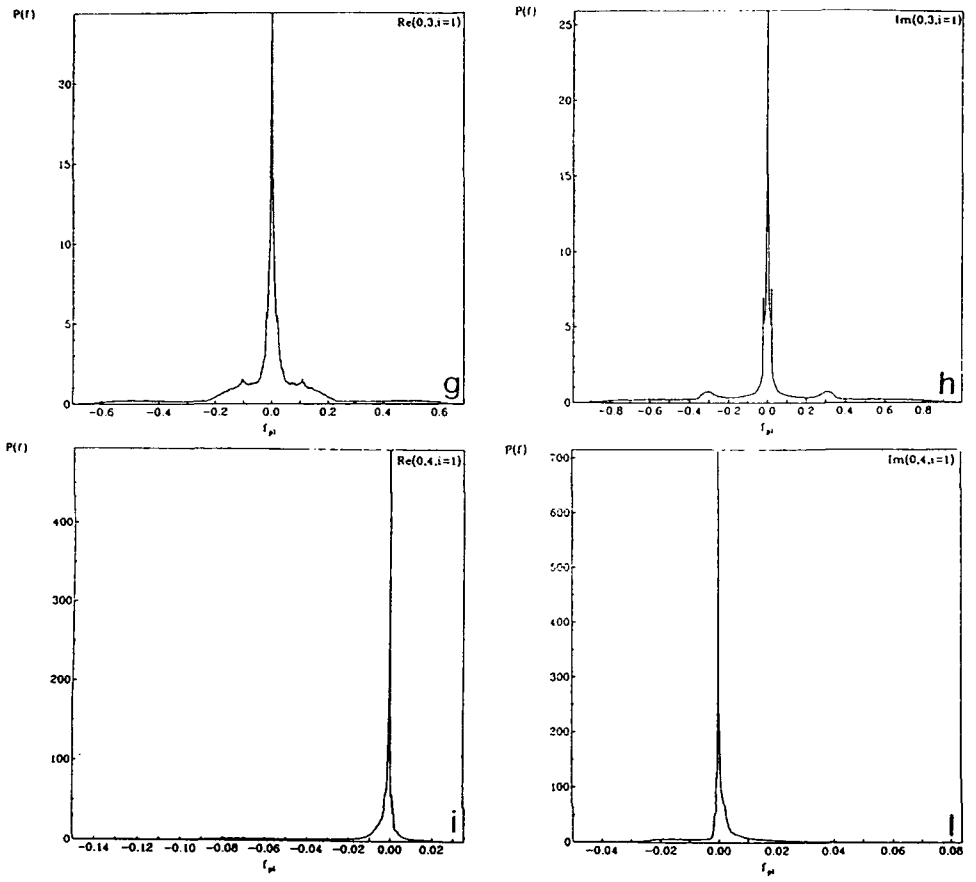

Fig. 10 (cont.).

information dimension with the number of active GL modes, that, therefore, cannot be easily related with the degrees of freedom governing the system's time dynamics.

The second set of results concerns measurements of the information dimension $D(1)$ and of the Kolmogorov metric entropy $K(1)$ [23] of the single time series $f_{pl}(t)$ and of the total electric field intensity $|F(t)|^2 = \Sigma_{pl} f_{pl}(t) f^*_{pl}(t)$, after time-delay reconstruction in a suitable E-dimensional embedding space. Our scope was twofold. On the one side, we wanted to check that our numerical procedure for the integration of the dynamical equations preserved the correct coupling of all variables: this has been clearly proved, for all signals $f_{pl}(t)$ have shown to have the same dimension and entropy. On the other side, we were interested in testing the suitability of the total intensity $|F(t)|^2$ as scalar observable for the investigation of the time dynamics, since this is by far the easiest quantity to measure in an experiment. Moreover, if in future numerical integrations many more modes will be considered, it will be impossible, because of storage space, to record long sequences of all the $f_{pl}(t)$'s for the measurements of the scaling properties of the time attractors. Therefore, we are interested in showing that these latter measurements can be performed on $|F(t)|^2$. The comparison between the values of figs. 11 and 12a provides evidence that this is indeed possible.

A very satisfactory convergence to a finite value is shown also by the measured metric entropy $K(1)$ (fig. 12b). Our result, namely $K(1) = 0.18 \pm 0.$., should be compared with that for the Lorenz model, $K(1) = 1.1$, which indicates that a slower average exponential separation occur in our case than on the Lorenz attractor.

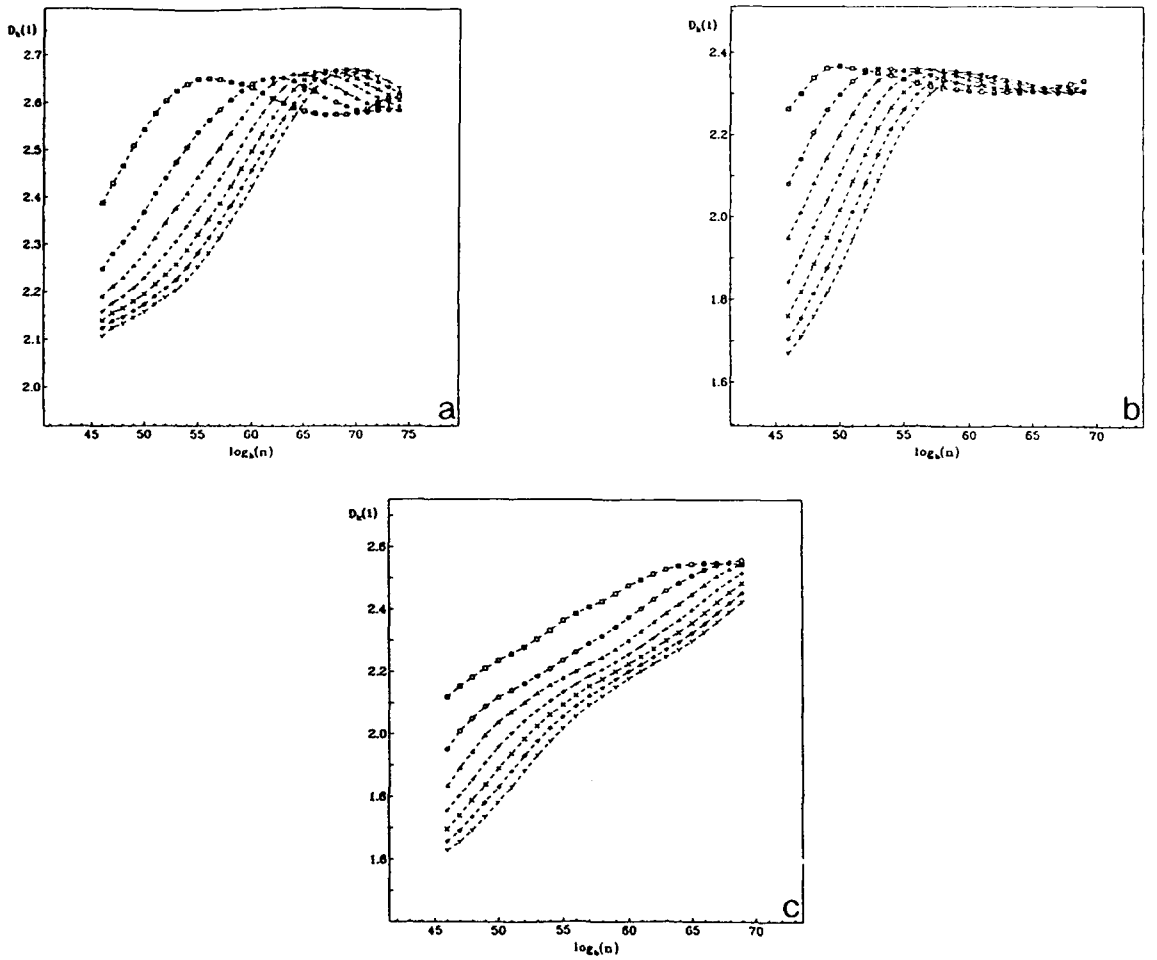

Fig. 11. Information dimension $D(1)$ for (a) $q \leq 2$, (b) $q \leq 3$, (c) $q \leq 4$ (other parameter values as in fig. 9) versus the number of considered attractor points n [in (a) $n \leq 284\,672$, in (b) and (c) $n \leq 126\,947$]. The x-axis scale is given in powers of $b = 1.18$. Each curve represents the behaviour of different-order nearest-neighbour distances k, namely $k = 5$ (squares), $k = 10$ (circles), $k = 15$ (triangles), $k = 20$ (crosses), $k = 25$ (St. Andrew's crosses), $k = 30$ (diamonds), $k = 35$ (Y's).

Since the system's asymptotic motion takes place on an attractor of dimension $D(1) < 3$, if follows that some of the GL coefficients $f_{pl}(t)$ must necessarily show non-decaying time correlations. In the following we discuss the results of a systematic investigation of the linear correlation functions

$$C_{pl,p'l'}(\tau) \equiv \lim_{T \to +\infty} \frac{1}{2T} \int_{-T}^{T} \mathrm{d}t \, f_{pl}(t+\tau) \, f^{*}_{p'l'}(t) \tag{57}$$

for sets of modal indices coinciding (autocorrelation) or distinct (cross-correlation).

Let us consider first the autocorrelations: we have observed two typical time-decay modes, the first of which (fig. 13a) is displayed, independently of the values of the other indices, by the coefficients of GL modes having odd l, and the second (figs. 14a and 14b) by those having even l. The former is characterised by a very fast decay, followed by oscilations of very small amplitude and periods distributed around the average period of the GL mode $\Delta\tau \approx 5$ (fig. 13a, cf. also the behaviour of the autocorrelations of the x and y variables of the Lorenz model). These oscillations generate the peaks in

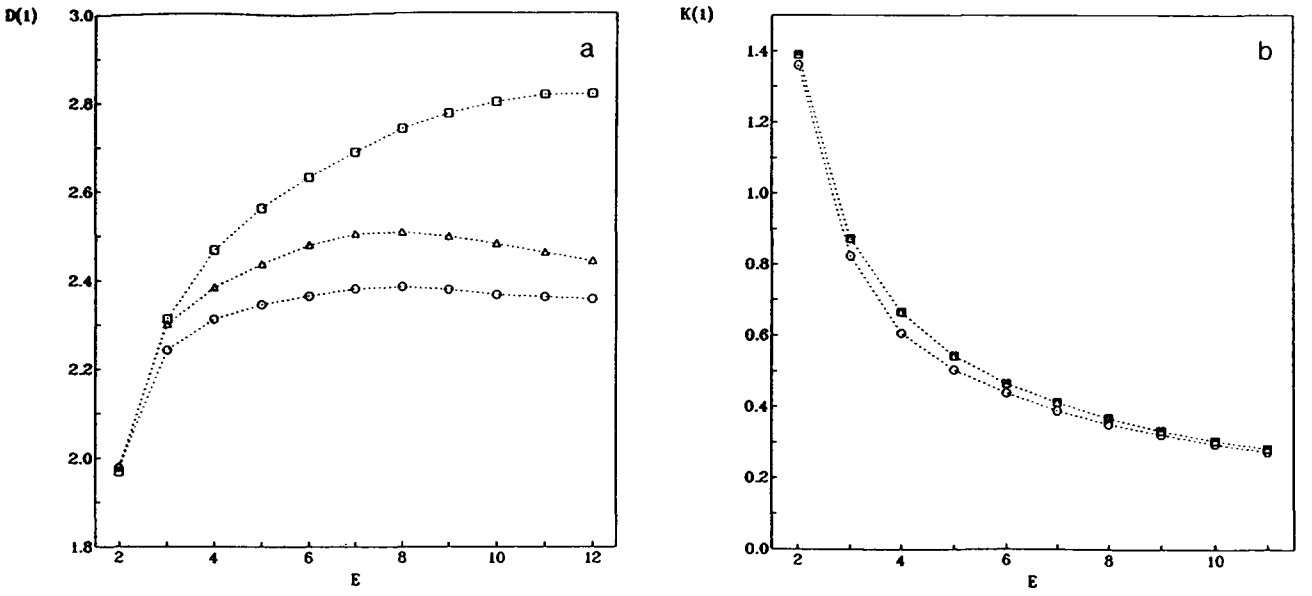

Fig. 12. Information dimension $D(1)$ (a) and Kolmogorov metric entropy $K(1)$ (b) of the total electric field intensity $|F(t)|^2$ versus embedding dimension E, for $q \leq 2$ (squares), $q \leq 3$ (circles), $q \leq 4$ (triangles) (other parameter values as in fig. 9). The measurements have been performed using $m = 8192$ reference points, $n = 284\,672$ data points and considering the scaling of the 5th n-n distances. $k(1)$ is in units of $\Delta t = 0.6$.

the power spectrum around $f = 0.03$ (fig. 13b). The latter decay mode is characterised by large oscillations, again having period $\Delta\tau \sim 5$ (fig. 14a, cf. also the behaviour of the autocorrelation of the z-variable of the Lorenz model). Their envelope presents first an exponential decay, with rate $\vartheta_e \approx 250$, followed by persisting oscillations of amplitude ≈ 0.1 and period $\Delta\tau_e \approx 500$ (fig. 14b). Correspondingly, many low-frequency peaks are visible in the power spectrum (fig. 14c).

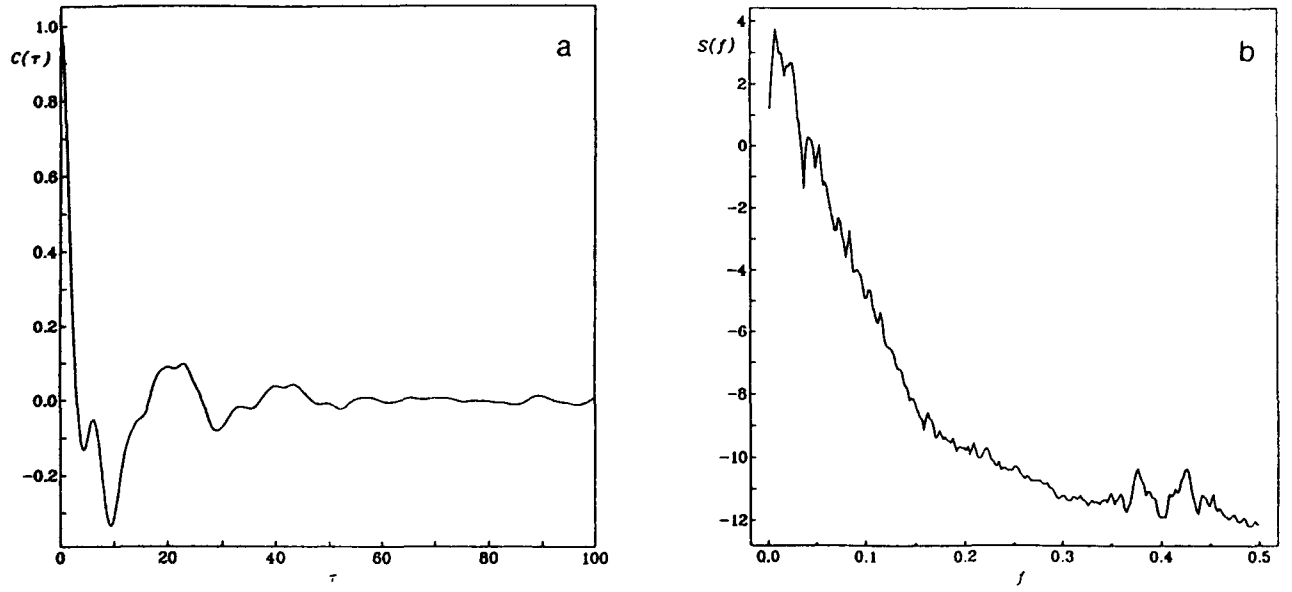

Fig. 13. (a) Autocorrelation function of the real part of Gauss–Laguerre coefficient $f_{01}(t)$, for $i = 1$, $q \leq 2$, computed over 131 072 data points. (b) Power spectrum of the same variable, computed over 1 048 072 data points. The x-axis scale is determined by the sampling time $\Delta t = 0.15$ (i.e. $f = 0.5$ corresponds to an oscillation of period $\Delta t = 0.3$).

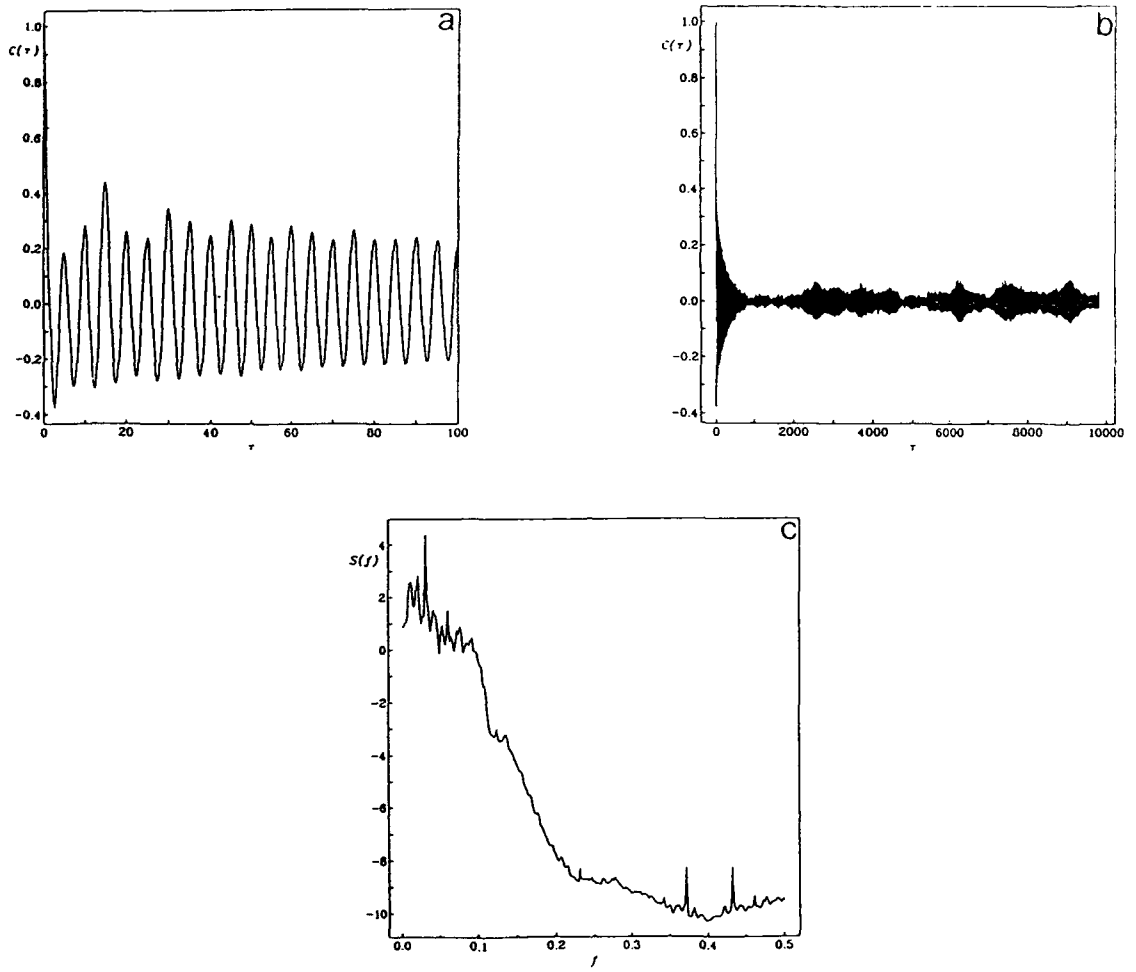

Fig. 14. (a), (b): Autocorrelation function of the real part of Gauss–Laguerre coefficient $f_{10}(t)$, for $i = 1$, $q \leq 2$, computed over 131 072 data points. (c): Power spectrum of the same variable, scales as in fig. 13.

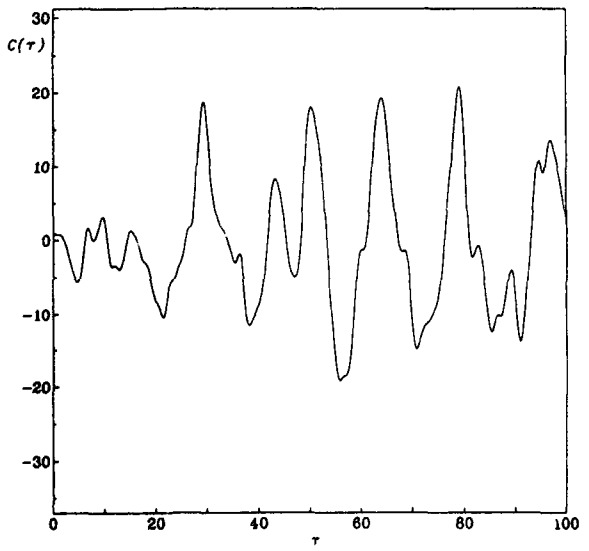

Fig. 15. Cross-correlation function of the real parts of Gauss–Laguerre coefficients $f_{01}(t)$ and $f_{10}(t)$, for $i = 1$, $q \leq 2$, computed over 131 072 data points.

Whereas the cross-correlations of the couples Re (f_{pl})-Im (f_{pl}) decay, according to the value of l, in the same way we have described with reference to the autocorrelations, we observe that in general cross-correlations of generic coefficients present irregular oscillations (distributed around $\Delta\tau \approx 5$) that do not decay in amplitude (fig. 15), with the exception of the case in which both modes have angular coefficients l of the same parity. In this latter case they decay as in figs. 13a and 14a, 14b, for l odd or even, respectively. The analysis of the linear correlation functions has confirmed, therefore, that systematic correlations among the $f_{pl}(t)$'s are present also in the case of chaotic time evolution and that the nature of these correlations depends on the symmetry of the spatial patterns arisen from the symmetry-breaking instabilities. In the following we proceed to the investigation of these relations by evaluating the degree of spatial coherence of the system.

4.2. Spatiotemporal effects

The relations between space patterns and time behaviour evidenced in the preceding section suggest to study indicators depending on both the dynamical regime and the transverse field configuration of the system. We introduce therefore the degree of spatial coherence of the (complex) variable $V(\boldsymbol{r}, t)$:

$$\Gamma_{r_0}(\boldsymbol{r}) \equiv \frac{\lim_{T\to+\infty}(1/2T)\int_{-T}^{+T} \mathrm{d}t\, V(\boldsymbol{r}_0, t)\, V^*(\boldsymbol{r}, t)}{\lim_{T\to+\infty}(1/2T)\int_{-T}^{+T} \mathrm{d}t\, |V(\boldsymbol{r}_0, t)|^2}\,, \tag{58}$$

where $\boldsymbol{r}_0$ is the position of a reference point (the origin, in our case) and $\boldsymbol{r}$ is the position vector in the transverse plane. Notice that a laser oscillating in a single transverse mode has perfect spatial coherence (i.e., $\Gamma \equiv 1$). As variable V we have chosen $F(\rho, \phi, t) - \langle F(\rho, \phi, t)\rangle$ ($\langle\cdot\rangle$ indicates time averaging) and $|F(\rho, \phi, t)|^2 - \langle |F(\rho, \phi, t)|^2\rangle$; the latter quantity turned out to be the most convenient, also in view of the feasibility of a direct measurement of Γ in a future experiment (e.g. averaging over photographic frames taken at different times). In fig. 16 $\Gamma(x, y)$ is displayed for (a) $q \leqslant 2$ and (b) $q \leqslant 4$. In order to allow for an easier comparison, the x and y coordinates have been normalised to the mode maximum spatial extent L, defined, with some arbitrariness, as the value of the radial coordinate beyond which the modulus of any A_{pl} does not exceed 10^{-10} ($L \cong 5.17$ for $q \leqslant 2$ and $L \cong 5.52$ for $q \leqslant 4$). In both cases Γ has a very regular bell-shape, not very different from the one obtained for periodic motion in time.

As it is seen from fig. 16, the reduction in extent of the correlation region is of few percent upon doubling of $q_{\max}$. This is a further indication that the predominance of low-order modes and the presence of relevant correlations among mode coefficients prevents the system from losing spatial coherence even when many modes become active and the time dynamics chaotic. If $\Gamma(x, y)$ is compared, using the same parameter values, for a simulated evolution in which the $f_{pl}(t)$'s are substituted by Gaussian random numbers, its behaviour loses smoothness and the size of the central peak is reduced by a factor 2. In a similar simulation with $q \leqslant 16$ the shape of $\Gamma(x, y)$ is already very irregular, and the (vaguely-defined) correlation length $\xi(\phi)$ satisfies $\xi(\phi) < \frac{1}{12} L$, $\forall\phi$. Because of the presence of the time correlations in the $f_{pl}(t)$'s discussed in the preceding section, the value of $q_{\max}$ for which we expect the system to show a similar behaviour is much higher. Moreover, one should not forget that, hitherto, we have discussed just linear correlations, whereas higher-order effects can be relevant and further limit the ability of the system to lose spatial coherence. We plan to extend our analysis of mode amplitude correlation to full nonlinearity by considering the mutual information of the relevant variables. If we consider the condition $\xi \ll L$ as necessary for the onset of spatiotemporal chaos

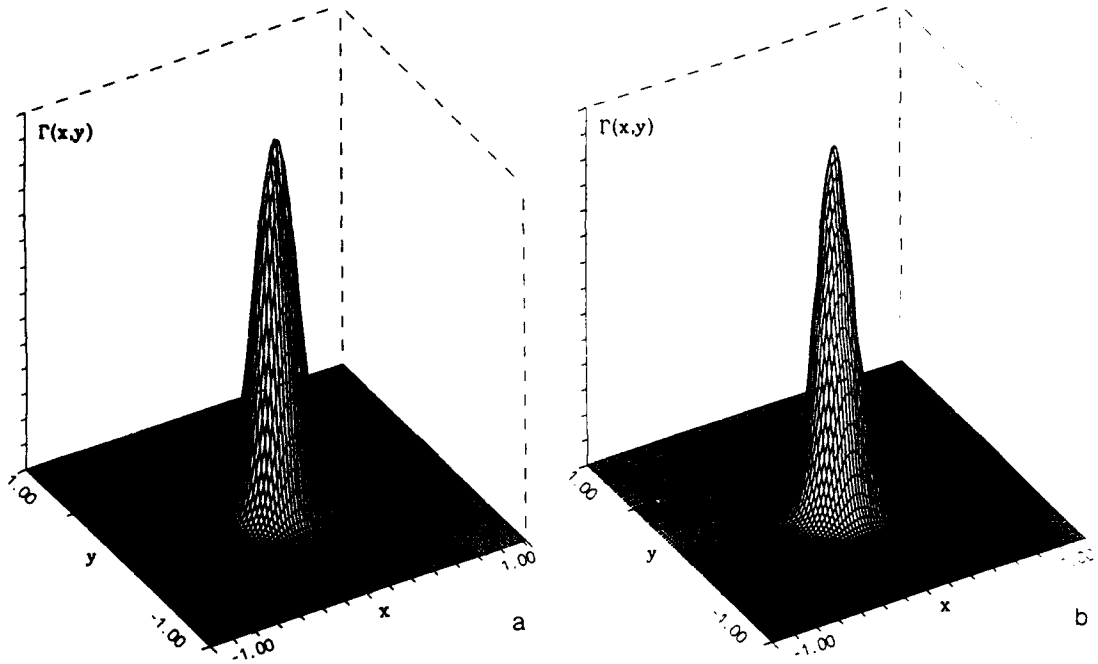

Fig. 16. Degree of spatial coherence $\Gamma(x, y)$ of the electric field intensity $|F(x, y, t)|^2 - \langle |F(x, y, t)|^2 \rangle$ for (a) $q \leq 2$ and (b) $q \leq 4$. The x and y coordinates are normalised to the mode maximum spatial extent L. Γ has been evaluated on a square space grid of 100×100 points by averaging over 4096 time configurations, sampled at intervals $\Delta t = 0.6$.

[9], we do not expect, therefore, optical systems of our type to display this kind of behaviour until (i) very many GL modes are active (ii) out of these, sufficiently many uncorrelated modes contribute to the dynamics with comparable amplitudes (i.e., spatiotemporal chaos could emerge only for selected parameter values among those yielding irregular time dynamics). We point out again that linear uncorrelation may not be sufficient for the fulfillment of condition (ii). A very efficient way of testing condition (ii) is the study of the time fluctuations of modal amplitudes $P(f_{pl})$ introduced in section 4.1, from which one can rapidly evaluate the contribution to the dynamics of relevant high-order modes. Moreover, if, instead of GL modes, one considers spatial Fourier modes (for instance by Fourier-transforming along the radial direction for a chosen phase), one expects the time amplitudes of the terms having wavelength much larger than the correlation length ξ to be Gaussian-distributed [9]. Obviously, the distributions of the time fluctuations of the Fourier coefficients can be straightforwardly calculated from the knowledge of the $f_{pl}(t)$.

5. Concluding remarks

The integration of the dynamical equations with a number of modes sufficiently great for irregular spatial structures to arise cannot be performed, unfortunately, by using the method illustrated in section 2.2, because of the exceedingly large CPU-time that would be required. The theoretical study of the system's behaviour in this limit must therefore be pursued with the help of new, more sophisticated numerical techniques.

Conversely, the experimental observation of the onset of spatiotemporal chaos in passive optical systems (if it occurs at all) seems to be, at least in principle, achievable, since a cavity (whose size is usually of the order of 1 cm) can support very many modes, and their number can be controlled by adjusting the intracavity aperture. Special consideration deserve the already mentioned difficulties arising from the huge amount of data that should be recorded in order to characterise an extended system. An acquisition apparatus based on a space grid of photosensitive devices, for instance, would be extremely expensive, and would also have such a high information output that the data channels and the storage system would be very soon saturated. In our case, at least for a first set of experiments, one can focus on more global quantities. As discussed in section 4.1, dimensions and entropies can be suitably determined from the total output intensity, while the degree of spatial coherence Γ can be measured by using series of photographic snapshots. In order to test the onset of spatiotemporal chaos, one can study the distributions of the long-wavelength Fourier mode coefficients calculated e.g. fast-Fourier transforming (in space) the intensity data sampled along the radial direction by a small number of photosensitive devices. Histograms of the fluctuations of the model amplitudes can be obtained already after suitably short observations. The experimenter could vary the system parameters until these distributions approach a Gaussian.

In section 2 we have modeled the dynamical behaviour of an absorbing nonlinear optical medium in a ring cavity by means of a set of equations in which the slowly varying envelope of the electric field is described by frequency-degenerate Gauss–Laguerre modes. A procedure for their numerical integration has also been illustrated. In suitable conditions, these equations admit stationary solutions. We have shown that the steady-state configuration may correspond to a single or to many GL modes. In the former situation we have derived the analytic expression of the solution for some simple cases and performed a linear stability analysis. Varying the control parameters the system experiences different dynamical regimes, some of which have been illustrated in section 3. In general, the symmetry properties of the solutions differ from those of the empty cavity, and the time behaviour may become irregular. An extensive study of such a situation has been presented in section 4. By measuring dimension and entropy, we have proved that the asymptotic motion of the system takes place on a low-dimensional strange attractor. Evidence for the existence of systematic non-decaying linear time correlations among GL modal amplitudes $f_{pl}(t)$ has been provided, thus clarifying the relation between mode excitation and relevant active degrees of freedom. The measurement of the degree of spatial coherence Γ, presented in section 4.2, has further circumstantiated the role of this relation. Finally, we have discussed the conditions for the onset of spatiotemporal chaos, coming to the conclusion that this kind of behaviour cannot be displayed by the optical systems we have modeled until very many (i.e., hundreds of) GL modes are active. Moreover, sufficiently many of these modes must display decaying correlations and contribute to the dynamics with comparable amplitudes. The influence of higher order correlations remains unexplored and may constitute a further obstruction to the onset of spatiotemporal chaos.

Acknowledgements

We are indebted to L.A. Lugiato and R. Badii for useful discussions and to the Swiss National Science Foundation for financial support. M.B. and F.P. acknowledge support from the EEC Esprit Basic Research Action, project T.O.P.P.

References

[1] See the feature issues on Instabilities in Active Optical Media, N.B. Abraham, L.A. Lugiato and L.M. Narducci, eds., J. Opt. Soc. Am. B 2 (1985) and on Nonlinear Dynamics of Lasers, D.K. Bandy, A.N. Oraevsky and J.K. Tredicce, eds., J. Opt. Soc. Am. B 5 (1988); Instabilities and Chaos in Quantum Optics, F.T. Arecchi and R. Harrison, eds. (Berlin, 1987); Instabilities and Chaos in Quantum Optics II N.B. Abraham, F.T. Arecchi and L.A. Lugiato, eds. (New York, 1988), and references therein.

[2] G. Giusfredi, J.F. Valley, R. Pon, G. Khitrova and H.M. Gibbs, J. Opt. Soc. A. B 5, 1181 (1988); W.J. Firth and C. Paré, Opt. Lett. 13 (1988) 1096; R. Chang, G.P. D'Alessandro, W.J. Firth, A. Geddes, R. Indik, J.V. Moloney, E.M. Wright and G.S. McDonald, to be published; G. Grynberg, Opt. Comm. 66 (1988) 321; G. Grynberg, E. Le Bihan, P. Verker, P. Simoneau, J.R.R. Leite, D. Bloch, S. Le Boiteux and M. Duclay, Opt. Comm. 67 (1988) 363; J.H. Moloney, in Chaos, Noise and Fractals, R. Pike and L. Lugiato, eds. (Hileger, Bristol 1988); see also the feature issues on Transverse Effects in Nonlinear Optical Systems, N.B. Abraham and W.J. Firth, eds., J. Opt. Soc. Am. B (June and July 1990) and references therein.

[3] M. Brambilla, F. Battipede, L.A. Lugiato, V. Penna, F. Prati, C. Tamm and C.O. Wiess, Phys. Rev. A 43 (1991) 5090.

[4] W. Klische, C.O. Weiss, B. Wellegehausen, Phys. Rev. A 39 (1989) 919; C. Green, G.B. Mindlin, E.J. D'Angelo, H.G. Solari and J.R. Tredicce, Phys. Rev. Lett. 65 (1990) 3124.

[5] F.T. Arecchi, G. Giacomelli, P.L. Ramazza and S. Residori, Phys. Rev. Lett. 65 (1990) 2531.

[6] S. Ciliberto and P. Bigazzi, Phys. Rev. Lett. 60 (1988) 286; S. Ciliberto and M. Caponeri, Phys. Rev. Lett. 64 (1990) 2775; preprint (1991); S. Ciliberto, S. Douady and S. Fauve, Europhys. Lett. 15 (1991) 23; S. Ciliberto and B. Nicolaenko, Europhys. Lett. 14 (1991) 303.

[7] J.A. Vastano and H.L. Swinney, Phys. Rev. Lett. 60 (1988) 1773; W.Y. Tam, J.A. Vastano, H.L. Swinney and W. Horsthemke, Phys. Rev. Lett. 61 (1988) 2163; W.Y. Tam and H.L. Swinney, Physica D 46 (1990) 10; J.A. Vastano, T. Russo and H.L. Swinney, Physica D 46 (1990) 23.

[8] A. Arneodo and J. Elezgaray, Phys. Lett. A 143 (1990) 25; A. Arneodo, J. Elezgaray, J. Pearson and T. Russo, Physica D 49 (1991) 141.

[9] P.C. Hohenberg and B.I. Shraiman, Physica D 37 (1989) 109.

[10] G. Giacomelli and A. Politi, Europhys. Lett. 15 (1991) 387.

[11] K. Kaneko, Physica D 37 (1989) 60; G. Mayer-Kress and K. Kaneko, J. Stat. Phys. 54 (1989) 1489; K. Kaneko, Physica D 34 (1989) 1; J.P. Crutchfield and K. Kaneko, in Directions in Chaos, Hao Bai-Lin ed., Vol. 1 (Singapore, 1987) 272.

[12] L.A. Lugiato, F. Prati, L.M. Narducci, P Ru, J.R. Tredicce and D.K. Bandy, Phys. Rev. A 37 (1988) 3847.

[13] L.A. Lugiato, in Progress in Optics, E. Wolf ed., XXI, 71 (Amsterdam, 1984).

[14] L.A. Lugiato, G.L. Oppo, J.R. Tredicce, L.M. Narducci and M.A. Pernigo, J. Opt. Soc. Am. B 7 (1990) 1019.

[15] L.A. Lugiato and M. Milani, Z. Phys. B 50 (1983) 171.

[16] A.M. Turing, Philos. Trans. R. Soc. London Ser. B 237 (1952) 37.

[17] M. Brambilla, M. Cattaneo, L.A. Lugiato and F. Prati, in Proceedings of the ECOOSA Conference, Int. Phys. Conf. Ser. No. 115, sec. 3 (IOP Publ., 1991).

[18] L.P. Šilnikov, Sov. Math. Dokl. 6 (1965) 163.

[19] A. Renyi, Probability Theory (Amsterdam, 1970).

[20] Grassberger and I. Procaccia, Phys. Rev. Lett. 50 (1983) 346.

[21] R. Badii and A. Politi, J. Stat. Phys. 40 (1985) 725.

[22] G. Broggi, J. Opt. Soc. Am. B 5 (1988) 1020; Numerical Characterisation of Chaotic Experimental Signals, Ph.D. Thesis, University of Zurich (1988).

[23] V.M. Alekseev and M.V. Yakobson, Phys. Rep. 75 (1981) 290 and references therein.

Physica D 58 (1992) 365–383
North-Holland

PHYSICA D

Thermodynamic aspects of the transition to spatiotemporal chaos

M. Caponeri[a] and S. Ciliberto[b,1]

[a]*Istituto Nazionale di Ottica, Largo E. Fermi 6, 50125 Firenze, Italy*
[b]*Ecole Normale Supérieure de Lyon, 46 Allée d'Italie, 69364 Lyon, France*

Received 29 August 1991
Revised manuscript received 24 February 1992
Accepted 2 March 1992

The general features of the onset of spatiotemporal chaos observed in several physical systems are reviewed with special emphasis on the statistical properties. The possibility of constructing a thermodynamics of spatiotemporal chaos is discussed by considering an experiment on thermal convection. It is shown that, by analogy with a system near thermal equilibrium, it is possible to define two quantities, which behave like an energy and an entropy and are related by standard thermodynamic relationships. The fluctuation-dissipation is also verified.

1. Introduction

The transition to chaos in spatially extended systems is now widely investigated in many natural phenomena such as hydrodynamic [1–6] and optical instabilities [7, 8], flames [9], chemical reactions [10], pattern formation in biology [11] and information storage in the brain [11]. There are also technical applications in which the analysis of the transition to spatiotemporal chaos is important in order to understand the stability of devices, for example, Josephson junction and laser diode arrays [12]. Theoretically, the general properties of this transition are studied in simple mathematical models such as coupled maps [13–15][*1], partial differential equations [14, 16–18] and cellular automata [19–21]. The reason for this interest is to attempt to understand the complex space-time evolution of the above-mentioned systems, using concepts of either statistical mechanics or low-dimensional dynamical systems, which have been extensively studied in the last decade [22].

It is important to point out immediately the differences between low dimensional chaos, spatiotemporal chaos and fully developed turbulence. In order to make such a distinction we follow Hohenberg and Shraiman [23], who made this point very clear by defining three characteristic length scales: the dissipation length l_D, the excitation length l_E and the correlation length ξ. The ratios of these lengths with respect to each other and to the characteristic system size L determine the state of the system. The dissipation length is the minimum length below which all the modes are damped. The excitation length l_E is the characteristic length in which energy is injected into the system. For small systems $L \simeq l_E$ and, for moderate values of the control parameter, $l_E \simeq l_D$. Then only a few modes are excited and the dynamics can be explained by the interaction of a small number of modes. In contrast, for a large system, that is, when $l_E \ll L$, one needs to introduce the correla-

[*1] See also the references in [18b].
[1] To whom all correspondence should be addressed.

0167-2789/92/$05.00 © 1992 – Elsevier Science Publishers B.V. All rights reserved

tion length ξ which can be defined in terms of the correlation function $C(r, t)$. In many cases this function decays exponentially like $\exp(-r/\xi)$ thus defining ξ in a natural way. When $\xi \simeq L$ the system is coherent in space but may evolve chaotically or regularly, that is, it behaves like a small dynamical system. In these regimes dynamical systems may present interesting spatial features such as mode competition, travelling waves and localized oscillations, that do not destroy the spatial order. When the correlation length $\xi \ll L$ the dynamical behavior is incoherent in space and the system may be chaotic in both space and time. This regime, which occurs for $L \gg l_E \simeq l_D$, is the regime of spatiotemporal chaos or weak turbulence and usually corresponds to the evolution of coherent structures of the size of the correlation length. This regime has to be distinguished from fully developed turbulence which implies an energy cascade, that is, Fourier spectra with power law decay [24, 25], which does not necessarily appear in spatiotemporal chaos.

One of the main goals in the research of spatiotemporal chaos is to understand properties that do not depend on the particular system considered. For example, several experimental [1, 3, 4] and numerical works (13a, 14] have shown that the transition to spatiotemporal chaos has several properties of a second order phase transition, although the details of the transition may depend on the specific system. For example, in surface waves [1] (two spatial dimensions plus time) it is reminiscent of transition in the orientational order. When the system can be considered almost one dimensional, the transition is dominated by spatiotemporal intermittency [2, 3, 4, 13a, 14, 17], whose dynamics presents a mixture of ordered and disordered regions that are competing, as described in sections 2 and 3. The space-time evolution in the above mentioned works was always characterised in terms of local variables whose dynamics can be rather complex. However, it is also important to see if global variables of the system can be useful in describing spatiotemporal chaos, or, in other words, if one could expect to find simpler statistical properties in those variables than in the local ones and eventually to construct a statistical mechanics of spatiotemporal chaos [13b, 23, 26]. Furthermore, the dynamics of global variables may be related to some local dynamics as was observed in a recent experiment [5] on the Faraday instability (surface waves induced excited parametrically). Specifically it has been shown that the fluctuations of the driving acceleration, which is a global parameter, are strongly correlated with the dynamics of defects of the surface wave pattern.

The first step toward the construction of a statistical mechanics of spatiotemporal chaos is the determination of the distributions of the local fluctuations and those of the Fourier mode amplitudes. This has been applied to the solutions of the Kuramoto-Sivashinsky (KS) equation [27–29]. Specifically Pumir [27] has studied the fluctuations in real and Fourier space for the solutions of KS. Yakhot [28] and Zalesky [29] tried to explain the dynamics of long wavelength Fourier modes as driven by a stochastic noise produced by the short wavelength Fourier modes.

In addition, Kaneko [13b] has extensively investigated the thermodynamic properties of spatiotemporal chaos of coupled maps. He mainly studied the scaling of the Lyapunov dimension and Kolmogorov–Sinai entropy as functions of the size of the subspace used to measure. He found that these two quantities scale linearly with size, thus indicating that they can be considered extensive thermodynamic variables. He also suggested the use of these two quantities to characterize space-time chaos in experimental systems, but the well known difficulty of measuring Lyapunov exponents in systems that have dimension greater than 5 makes this test almost impossible [30].

The statistical properties of space-time chaos have been also measured in several experiments on surface waves [1a], Rayleigh–Bénard convec-

tion [26] and in an optical device [7]. In all of these experiments it has been observed that the amplitude of the long wavelength Fourier modes has Gaussian statistics although the local dynamics may have strong deviations from a Gaussian. This rather strange result, that we will discuss in section 4, is due to the fact that long wavelength Fourier modes are coarse grained variables of the system. Therefore, they imply an average over many correlation lengths, and thus the central limit theorem ensures that the amplitude of long wavelength Fourier modes have a Gaussian distribution even though the local dynamics does not [23,]. In the above-mentioned experiments [26] on Rayleigh–Bénard convection an attempt has also been made to construct a thermodynamics by introducing some global quantities, related by simple thermodynamic relationships, that are able to characterize space-time chaos and are easily measurable in experiments.

Another important problem that has to be solved in the research of spatiotemporal chaos is the measure of at least the order of magnitude of the number of degrees of freedom involved in the dynamics. Clearly the number of positive Lyapunov exponents will be useful. However, as we mentioned before, in experiments the calculation of these exponents is impossible once the number of positive ones is greater than 4. Thus other methods have been tested. A very promising one is is the Karhunen–Loève decomposition that has been applied to experimental [32, 33] and numerical data sets [32, 34, 35]; it can be very useful not only in estimating the number of the main degrees of freedom involved in the dynamics [32], but also in constructing models of the system under study [33].

In this review, in order to describe in more detail all of the above-mentioned aspects of the research on space-time chaos, we consider a specific experiment [3, 26, 32] in which many of those aspects have been analysed. We will also try to compare the results of this experiment with those of other experiments and of numerical simulations. The experiment considered here is on thermal convection in a horizontal fluid layer heated from below, that is Rayleigh–Bénard convection. This fluid instability can be viewed as a general example because as a function of the control parameter and of boundary conditions, it presents a periodic stationary pattern, low dimensional chaos, spatiotemporal chaos and turbulence.

The paper is organized as follows; in section 2 we recall the main features of Rayleigh–Bénard convection and those of our experiment. We also describe the different states observed as a function of the control parameter. In section 3 we analyse the transition to spatiotemporal chaos in terms of local variables, showing that this transition presents features of a second order phase transition. In section 4 the possibilities of constructing a thermodynamics in the spatiotemporally chaotic regimes is discussed, starting with the definition of a temperature of the system. We also show that if a thermodynamic formalism is applied the transition to space–time chaos still presents features of a second order phase transition in the global variables. In section 5 the application of the Karhunen–Loève decomposition in estimating the number of degrees of freedom on experimental and numerical data sets is described. It is shown that this method seems to give a number close to the number of positive Lyapunov exponents. Finally, in section 6 a general discussion and conclusions are presented.

2. A specific system

2.1. Rayleigh–Bénard convection in annular geometry

The features of Rayleigh–Bénard convection may be found in standard texts and review papers [36], thus we recall here only the main ones. Let us consider a fluid layer confined between two horizontal solid plates and heated from

below. The most relevant parameter of this instability is the Rayleigh number $R = \beta g \Delta T d^3/\nu\chi$, where β is the volumetric expansion coefficient, g the acceleration of gravity, ν the kinematic viscosity, χ the thermal diffusion coefficient, d the depth of the layer and ΔT the difference of temperature between the two horizontal plates. When Ra exceeds the threshold value Rc steady convection arises, producing a pattern of parallel rolls with a well defined wavenumber k. The rolls are parallel to the shortest side of the cell containing the fluid. The values of Rc and k depend on the size of the cell and on the boundary conditions. For example, in the case of an infinite layer and perfect conducting plates $\mathrm{Rc} = 1708$ and $k_c = 3.11/d$. Thus, from an experimental point of view, it is very important to define two other parameters, namely the aspect ratios $\Gamma_x = L_x/d$ and $\Gamma_y = L_y/d$, where L_x and L_y are the two horizontal lengths of the cell. The time dependent regimes of Rayleigh–Bénard convection observed at $\mathrm{Ra} \gg \mathrm{Rc}$ are strongly influenced by the aspect ratios and also by the Prandtl number $\mathrm{Pr} = \nu/\chi$. Indeed, in the experiments in which the transition to low dimensional chaos has been studied [37], Γ was of the order of $2\pi/k$. As we mentioned in section 1, this corresponds to the correlation length of the system being of the order of the system size, i.e. $\xi \simeq L$.

In the experiment that we describe in this paper the cell containing the working fluid is annular. Indeed, with this configuration and a suitable choice of the radial aspect ratio, it is possible to construct a pattern that is almost a one dimensional chain of radial rolls (roll axis along radial directions, see also fig. 1 with periodic boundary conditions. These features of the spatial pattern are very useful in order to compare the results of our experiment with those obtained by the mathematical models mentioned in section 1. The inner and outer diameters of the cell are 6 and 8 cm respectively, whereas the depth d of the layer is 1 cm. Thus the azimuthal aspect ratio, measured on the circle of radius of mean diameter, is 22, and the radial one is 1. The fluid is silicone oil with a Prandtl number of 30 and the critical temperature difference, computed for an infinite layer, is $\Delta T_c = 0.06°\mathrm{C}$. The different states of the system will be labeled with $\eta = \Delta T/\Delta T_c$. The experimental details have been described elsewhere [38]. The set up provides

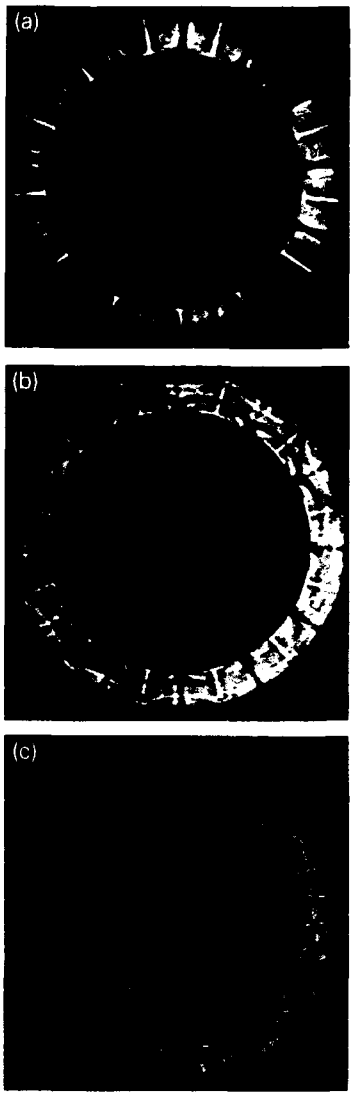

Fig. 1. Shadowgraphs of typical spatial patterns. White and dark regions correspond to cold and hot currents respectively. (a) Stationary spatial pattern at $\eta = 100$; (b) Snapshot of the spatial pattern at $\eta = 190$ in a time dependent biperiodic regime; (c) Snapshot of the spatial patterns at $\eta = 230$ in a spatiotemporal intermittent regime. Notice the simultaneous presence of ordered and disordered regions in different parts of the annulus.

the possibility of measuring on the circle of mean diameter the two components of the thermal gradient averaged in the vertical direction, in the polar coordinate reference frame r, θ. Below we describe the properties of only the component of the gradient perpendicular to the roll axis, because those of the other component (the radial one) are the same. The azimuthal component (made dimensionless by dividing it by $\Delta T_c/d$) is called $u(x, t)$, where $x = \theta/2\pi$ indicates the position on the circumference of mean diameter, thus $0 < x < 1$. The function $u(x, t)$ is sampled at N points in space. In time dependent regimes $u(x, t)$ is recorded for at least 5000 times, in order to have sufficient statistical accuracy. The time series length was about 500 times the mean period of oscillation of the system. N was equal to 128 in several runs and 256 in others. However, no sensitive dependence of the results on N has been noticed.

2.2. Spatial patterns

Analysing the fluid behavior as a function of $\eta = \Delta T/\Delta T_c$, we observe that for η around 1 there are about 22 rolls. This number increases with η and reaches 38 at η around 200. A detailed analysis of the wavenumber selection process has been reported elsewhere [38]. In fig. 1a we show the shadowgraph of the spatial pattern at $\eta = 100$. Dark regions correspond to the hot currents rising up and white regions to the cold ones, going down. We note that the configuration constrains the spatial structure to an almost one dimensional chain of rolls.,

The spatial structure remains stationary for $\eta < 164$ where a subcritical bifurcation to the time dependent regime takes place. For $\eta > 164$ the time evolution is chaotic but, reducing η, the system presents either periodic or quasiperiodic oscillations, and at $\eta = 149$ it is again stationary. In the range $149 < \eta < 200$ the time dependence consists of rather localized fluctuations that slightly modulate the convective structure, which maintains its periodicity. This is clearly seen in fig. 1b where a snapshot of the spatial structure at $\eta = 190$ is shown. The presence of hot and cold currents transverse to the main set of rolls merits a special comment. Such a two dimensional effect certainly influences the dynamics. However, considering that the ratio between the length and the width of the annulus is roughly 22, we expect that the system can be considered almost one dimensional for what concerns the propagation time of thermal fluctuations along the circle. because the two time scales are very well separated. Besides, we also observe that the time dependent fluid motion is still well correlated along the radius.

The space–time evolution of $u(x, t)$ and the corresponding time evolution of the point $x = 0$ at $\eta = 164$ are shown in fig. 2a and fig. 2b. In fig. 2b we clearly see that the time evolution is

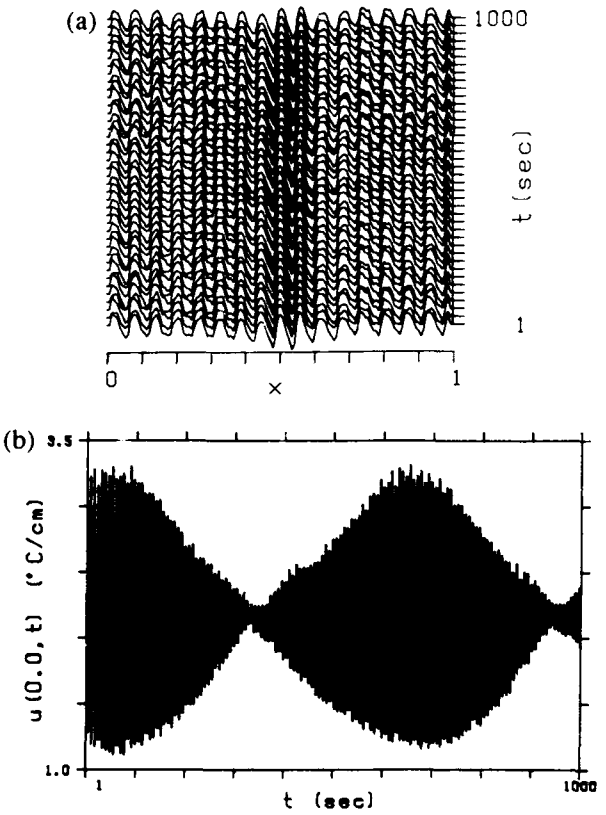

Fig. 2. (a) Space–time evolution of $u(x, t)$ at $\eta = 164$; (b) Corresponding time evolution of the point $x = 0$. The vertical scale has been amplified in (b) because the time dependent modulation slightly perturbs the spatial pattern shown in (a), where the maximum amplitude is roughly 4°C/cm.

quasiperiodic. However, this time dependent modulation is hardly seen in fig. 2a, because it slightly perturbs the spatial pattern that maintains its original periodic structure. Increasing η (<200) the time evolution becomes chaotic but there is still spatial order. The fractal dimension and the orthogonal decomposition (see section 5) indicate that the number of degrees of freedom of the dynamics is around 3.

At higher η the spatial order begins to be destroyed because of the appearance of bursts, detaching from the boundary layer. This spatiotemporally intermittency appears at $\eta > 200$. The snapshot of a typical spatial pattern at $\eta = 230$ is shown in fig. 1c. It presents several domains where the spatial periodicity is lost (we will refer to them as turbulent) and other regions (that we call laminar) where the spatial coherence is still maintained. The alternation between ordered and disordered regions is clearly observed in the space–time evolution of $u(x, t)$ at $\eta = 216$, shown in figs. 3a, 3b) at two different times. We notice that for $1000 < t < 1040$ there are strong oscillations that locally destroy the spatial order, whereas for $1500 < t < 1540$ the pattern is again very regular. In the following sections we will describe in detail the statistical properties of this spatiotemporal intermittency, but we want to discuss first the spatial Fourier spectra in the different regimes described in this section.

The time averaged spatial Fourier spectra at $\eta = 164$, $\eta = 216$, $\eta = 347$ are shown in figs. 4a, 4b, and 4c respectively.

The spatial spectrum of fig. 4a, corresponding to a biperiodic time dependent regime, presents well defined peaks, because the spatial structure, although modulated in time, is still very ordered. In contrast fig. 4b, corresponding to a value of η that is very close to the threshold for spatiotemporal intermittency, presents a broadened third harmonic. This indicates that the most important length scales for this transition are the shortest ones. Finally, in fig. 4c the spectrum, corresponding to a value of η far above the transition point, is totally broadened because the spatial

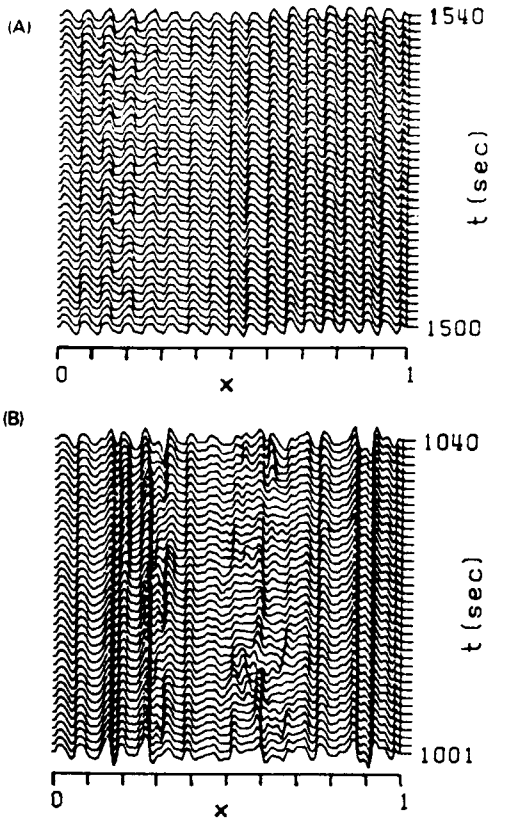

Fig. 3. Space–time evolutions of $u(x, t)$ at $\eta = 216$ at two different time intervals of 40 s each.

order has been destroyed. Notice the exponential decay at high k and the flat region for the small ones. These features are rather similar to those observed in the turbulent regimes of the Kuramoto–Sivashinsky equation [39]. The evolution of the spatial Fourier spectra as a function of η clearly shows the increasing disorder of spatial patterns and confirms the description made in the introduction. Furthermore, the cor-

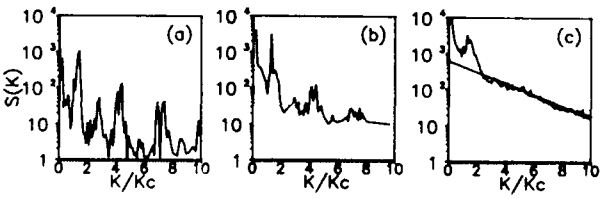

Fig. 4. Spatial power spectra at different values of η: (a) $\eta = 164$; (b) $\eta = 216$; (c) $\eta = 348$. k_c is the critical wavenumber which is about 3.11 cm $^{-1}$.

relation length for $\eta = \eta_c \simeq 200$, where the system presents either a stationary or a chaotic time evolution, is very close to 1.

3. The weak turbulence

3.1. Reduction to a binary code

As we discussed in the previous section, for $\eta > 200$ the space–time evolution of $u(x,t)$ shows that in the turbulent domains the time evolution is characterised by the appearance of large oscillatory bursts that locally destroy the spatial order. By contrast, in laminar regions the oscillations remain very weak. Thus the two regions can be identified by measuring the local peak to peak amplitude u_{pp}, for a time interval δt comparable with the mean period of the oscillation, that is,

$$u_{pp}(x, t) = \max[u(x, \tau)] - \min[u(x, \tau)] \qquad (1)$$

with $t < \tau < (t + \delta t)$. Choosing a cutoff α, setting to 1 all the points in which $u_{pp} > \alpha$ and to 0 all the other points, the space-time dynamics is reduced to a binary code in which 1 stands for "turbulent" and 0 for "laminar". As an example of such a code we show the space–time evolution of $u(x, t)$ at $\eta = 216$, in fig. 5a), and $\eta = 248$ in fig. 5b), the black and white regions corresponding to turbulent and laminar domains respectively. We remark that the qualitative features of these pictures are rather independent of the precise value of the cutoff. We can easily verify that the code catches the main properties of the dynamics by comparing fig. 5a with figs. 3a and 3b. Indeed, we clearly see that the most oscillating and disordered regions of fig. 3 correspond to black points in fig. 5a, whereas ordered and not oscillating regions are represented by white points.

At $\eta = 216$ (fig. 5a) a wide laminar region surrounds completely the turbulent patches that remain localized in space, after their appearance.

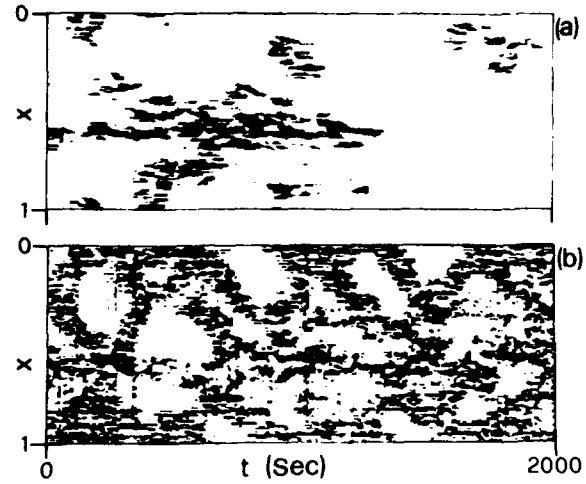

Fig. 5. Binary representation, at $\alpha = 1.5$°C/cm, of the space-time evolution of $u(x, t)$ at (a) $\eta = 216$ and (b) $\eta = 248$. The dark and white areas correspond to turbulent and laminar domains respectively.

Furthermore, the nucleation of a turbulent domain has no relationship with the relaxation of another one. In contrast, at $\eta = 248$ (fig. 5b), the turbulent regions migrate and slowly invade the laminar ones. This last regime that sets for $\eta > 245$ is very similar to those obtained in theoretical models [13–14]. The change from the regime of fig. 5a to that of fig. 5b is reminiscent of a percolation [40]. Indeed, percolation has been proposed as one of the possible mechanisms for the transition to spatiotemporal intermittency.

3.2. Statistical distribution of ordered regions

Following a method also used in numerical models [13, 14], we quantitatively characterize such a behaviour by computing, over a time interval of 10^4 s (this time corresponds to roughly 10^3 characteristic times of the system), the distribution $P(x)$ of the laminar domains of length x. For $\eta < 248$ $P(x)$ decays with a power law. The exponent does not depend within our accuracy, either on α or on η. Its average value is $\mu = 1.9 \pm 0.1$. On the other hand, for $\eta > 248$, the decay of $P(x)$ for $x > 0.1$ is exponential with a characteristic length $1/m$. The existence of two different regimes is clearly seen in fig. 6a, 6b

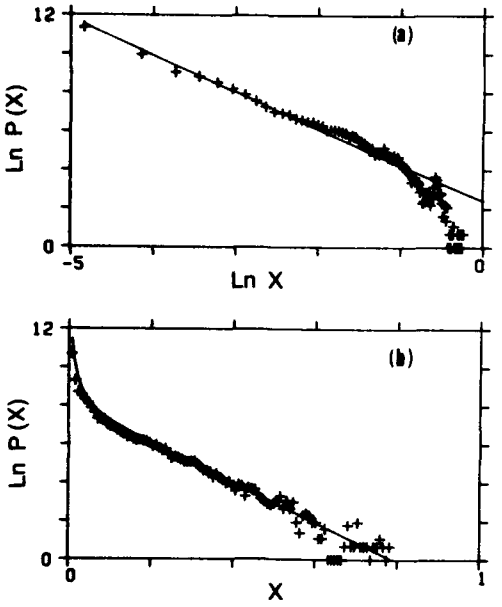

Fig. 6. Distribution $P(x)$ of the laminar regions of length x: (a) $\eta = 241$, algebraic decay with exponent 1.9; (b) $\eta = 310$ and $\alpha = 1.6$°C/cm, exponential decay with a characteristic length $1/m = 0.10$. The solid lines are obtained from eq. (4).

which display $P(x)$ versus x at $\eta = 241$ and $\eta = 310$. Looking at fig. 6a we clearly see that the decay of $P(x)$ begins for a length scale that is smaller than the roll size. This rather strange result has an explanation, because, as we remarked in section 2b, the main energy contribution to the time dependent regimes comes from the high spatial frequencies.

We find that the dependence of m on η is the following:

$$m(\alpha, \eta) = m_0(\eta) \exp(-\alpha/\alpha_0) \qquad (2)$$

with $\alpha_0 = (0.87 \pm 0.06)$°C/cm independent of η. The dependence of m_0 versus η is reported in fig. 7). The linear best fit for $\eta > 246$ of the points of fig. 7 gives the following result:

$$m_0(\eta) = m_1\left(\frac{\eta}{\eta_s} - 1\right)^{1/2} \qquad (3)$$

with $\eta_s = 247 \pm 1$ and $m_1 = 117 \pm 2$. This equation shows the existence of a well defined

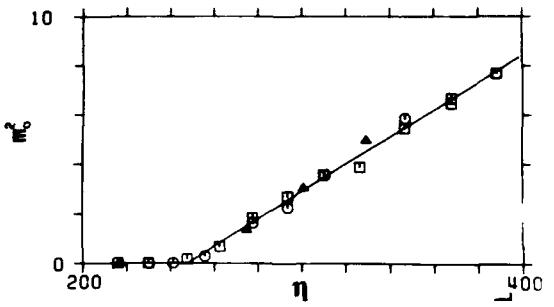

Fig. 7. Dependence of m_0^2 on η. The different symbols pertain to different sets of measurements done either increasing or decreasing η. The solid line is obtained from eq. (3).

threshold η_s for the appearance of an exponential decay in $P(x)$. We also see that the characteristic length $1/m_0$ diverges at $\eta = \eta_s$. In the range $200 < \eta < 400$, $P(x)$ is very well approximated by the following equation:

$$P(x) = (Ax^{-\mu} + B) \exp[-m(\alpha, \eta)x] , \qquad (4)$$

where $m(\alpha, \eta)$ is given by (2), μ has the previously determined values and A, B are free parameters that can be easily determined. A fit to our experimental $P(x)$, in the range 0.4°C/cm $< \alpha <$ 3°C/cm, yields $A = 10$, $B \simeq 4 \times 10^3$ for $\eta > \eta_s$ and $B = 0$ for $\eta < \eta_s$.

The features of $P(x)$ displayed by eqs. (3), (4) are typical of phase transitions. Since the transitions point η_s is very close to the point where the behaviour like that of fig. 5b sets in, we conclude that the transition to this behaviour may be a phase transition. The main features of $P(x)$ and m for $\eta > \eta_s$ qualitatively agree with those obtained in coupled maps [13–15], partial differential equations [14, 17], and in a phenomenological cellular automata model [19] of spatiotemporally intermittent regimes.

The presence of a power law decay of $P(x)$ for $\eta_c < \eta < \eta_s$ may be due to finite size effects. Indeed, a cellular automaton model of this transition [19] presents the same features when the number of cells is reduced.

Recently, another method has been suggested to identify the characteristic length involved in

the dynamics [41]. It is based on the comparison of the root mean square value of the field with that of its derivatives. Therefore, there is no need to define a threshold as we have done. However, we have not checked this method on our data and we are not aware of other papers on the subject.

4. Thermodynamics of space–time chaos

In the previous sections we have analysed the transition to spatiotemporal chaos in terms of local variables. We now want to discuss the behaviour of global variables of the system.

4.1. Statistical properties of fluctuations

We are interested in knowing the statistical properties of the fluctuations $W(x, t) = u(x, t) - \langle u(x, t)\rangle$ ($\langle\ \rangle$ means time average), of their spatial Fourier transform $\tilde{W}(k, t)$, of the energy $E(t)$ and of a suitably defined entropy $S(t)$. The energy is defined in the following way:

$$E(t, N_v) = \sum_{i=0}^{N_v} u^2(x_i, t)\,, \tag{5}$$

with $2 < N_v < N$ where N is the total number of spatial points. The total energy is $E(t) = E(t, N)$. The dependence of the energy on N_v shows how the root mean square (r.m.s.) value, $\Delta E(N_v)$, of the energy fluctuations scales as a function of the volume of integration N_v.

The spectral entropy [42] is defined in the following way:

$$\sigma(t) = \frac{S(t)}{S_0} = \frac{-1}{S_0} \sum_{k=1}^{N/2} \Phi_k(t) \log(\Phi_k(t)) \tag{6}$$

where $\Phi_k(t) = |\tilde{u}(k, t)|^2/E(t)$, $S_0 = \log(N/2)$ is the equipartition value of $S(t)$ and $N/2$ the total number of Fourier modes. The parameter σ is 1 at the equipartition and 0 when only one mode is excited. It is important to stress that $E(t)$ and $\sigma(t)$ are not exactly an energy and an entropy but they behave like these two thermodynamic quantities. We want also to stress that the properties that we will show are almost independent of the specific way in which the entropy is defined. An example of this can be found in ref. [49], where an entropy, which is well defined from a statistical point of view, has been used to analyse our data, showing a good agreement with the results reported here. Our entropy is defined in Fourier space because, as we will see, the Fourier modes present more interesting statistical properties. There is no distinction in defining the energy either in real or in Fourier space.

We now analyse the statistical properties near the transition point for spatiotemporal chaos η_s. In fig. 8 we show, for two values of η, the

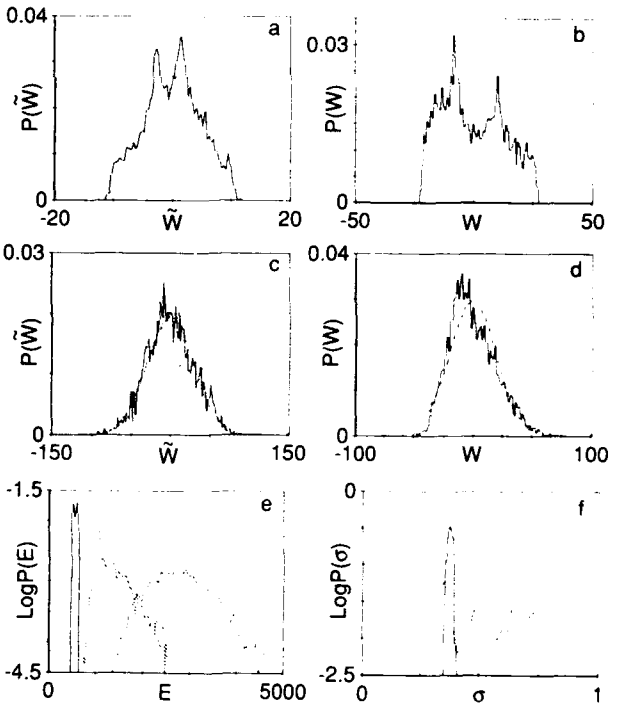

Fig. 8. Distributions of the fluctuations of the spatial Fourier mode amplitude $\tilde{W}_r(k, t)$ (a), (c) and the fluctuations in real space $W(x, t)$ (b), (d) at $x = 0.5$ and $k/k_c = 2$ for different values of η: (a), (b) $\eta = 164$; (c), (d) $\eta = 300$. Dashed lines correspond to Gaussian fits. Distributions of E (e), and of σ (f), at $\eta = 164$ solid lines; $\eta = 219$ dotted lines; $\eta = 248$ dashed lines.

distributions $P_k(\tilde{W}_r)$, of the real part $\tilde{W}_r$ of $\tilde{W}(k, t)$ at $k/k_c = 2$ (k_c is the critical wavenumber of the instability), and $P_x(W)$, of $W(x, t)$, at $x = 0.5$. We clearly see that at $\eta = 164$ (when the time evolution is biperiodic) $\tilde{W}_r(k, t)$ and $W(x, t)$ have a two-peaked distribution. For $\eta > \eta_s$ (fig. 8c), $P(\tilde{W}_r)$ tends to a Gaussian distribution; in contrast $P(W)$ (fig. 8d) is a Gaussian. The fact that the Fourier mode amplitudes have Gaussian distributions, whereas the local dynamics does not, has also been reported in ref. 1b and widely discussed in refs. [23, 31]. The reason for this effect is that the small k Fourier modes are coarse grained variables of the system because they imply on average over many correlation lengths [23, 31]. In figs. 8e, 8f we show, for different values of η, the distributions $P(E)$ and $P(\sigma)$ of $E(t)$ and $\sigma(t)$ respectively. We observe that above the transition point η_s the entropy fluctuations are clearly enhanced and that the average value of σ grows as a function of η.

Although the distributions for $\eta > \eta_s$ assume a characteristic bell shape, they are not Gaussians, because a significant asymmetry is observed. The existence of this asymmetry is quite reasonable because the distribution of a nonlinear function of Gaussian distributed variables (the $\tilde{W}$ in our case) is not, in general, Gaussian [43].

The deviation of a generic distribution $P(v)$ from a Gaussian may be studied in a better way by computing

$$M_i(v) = \Psi_i(v - v_a)/\Psi_2^{i/2}(v - v_a) \qquad (7)$$

where $\Psi_i(v - v_a)$ is the moment of order i of the variable $v - v_a$ and v_a is the mean value of v. For a Gaussian, M_3 (the skewness) and M_4 (the flatness) are equal to 0 and 3 respectively. These two quantities have been computed for $P(W)$, $P(\tilde{W}_r)$, $P(E)$ and $P(\sigma)$ at different values of η. The results for $P(\tilde{W}_r)$ are shown in figs. 8a, 8b as a function of η for several values of k (the imaginary part $\tilde{W}_j$ behaves in the same way). The statistical accuracy in the calculation is of the order of ± 0.3, and it has been computed using

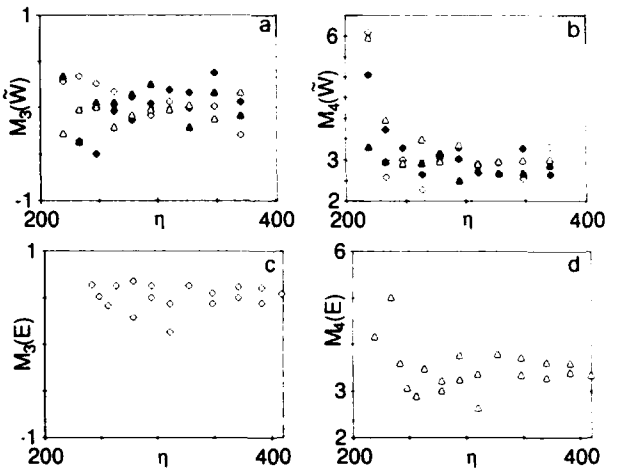

Fig. 9. (a) The skewness $M_3(\tilde{W}_r)$ and (b) the flatness $M_4(\tilde{W}_r)$, of the distribution of $\tilde{W}_r$, versus η for different values of k: ◇, $k/k_c = 1$; ◆, $k/k_c = 1.5$; △, $k/k_c = 2$; ▲, $k/k_c = 3$. (c) $M_3(E)$ and (d) $M_4(E)$ versus η.

standard methods. The skewness (fig. 9a) is always close to zero because the distributions of our data are always rather symmetric with respect to the mean. In contrast, the flatness, which accounts for the tails of the distributions, changes considerably as a function of η; see fig. 9b. $M_4(\tilde{W}_r)$ tends to 3 for almost all the modes for $\eta > \eta_s$ confirming the transition to a Gaussian distribution. We point out that the same transition does not occur in $M_4(W)$ for all the spatial points, indicating that the local dynamics does not, in general, have a Gaussian distribution.

In fig. 9c and 9d we show, as a function of η, $M_3(E)$ and $M_4(E)$ respectively. We observe that in this case M_4 does not reach 3 for $\eta > \eta_s$, and M_3 is different from zero, confirming the existence of the strong asymmetry seen in fig. 8e). Furthermore, the fact that the $M_3(E)$ and $M_4(E)$ are constant for $\eta > \eta_s$ indicates that the shape of distribution does not change as a function of η.

We now analyse the behaviour, as a function of N_v, of the r.m.s. energy fluctuations, $\Delta E(N_v)$. For $\eta < \eta_c = 200$ the relative fluctuations $\delta E = \Delta E(N_v)/E(N_v)$ do not follow a well defined law as a function of N_v. In contrast, for $\eta > \eta_c$, we find that δE decreases as a function of N_v as a power law N_v^{μ}, in the range $2 < N_v < N$ (fig.

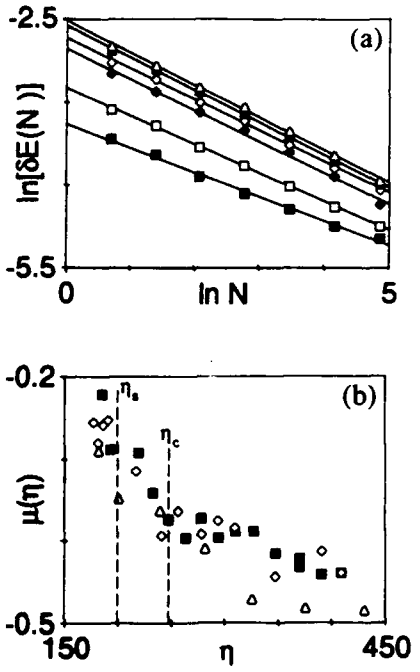

Fig. 10. (a) Dependence on N_v of the relative energy fluctuations δE for different values of η: □, $\eta = 219$; ■, $\eta = 233$; ◇, $\eta = 247.5$; ◆, $\eta = 278$; △, $\eta = 310$; ▲, $\eta = 327$. (b) Dependence on η of the exponent μ, the different symbols pertain to different runs.

10a). The exponent $\mu(\eta)$ tends asymptotically to $-1/2$ (fig. 10b). The value of μ indicates that above η_s, $E(t, N_v)$ behaves, as a function of the number of points, as an additive thermodynamic quantity.

4.2. *Fluctuation-dissipation theorem*

Summarizing the results up to this point we observe that the distributions of the Fourier mode amplitudes tend to a Gaussian distribution for $\eta > \eta_s$. Furthermore, δE decreases as function of the integration volume. These findings support a thermodynamical description of the transition to spatiotemporal chaos, in which the Fourier modes may be considered as an ensemble of non-interacting degrees of freedom. An important question is how a "generalized temperature" of the system may be defined [23]. The main difficulty arises from the fact that $\Psi_2(\tilde{W})$ is not constant as a function of k but presents a high-frequency cutoff as in all hydrodynamic systems [31].

This problem has been bypassed by Hohenberg and Shraiman [23], who suggested using the fluctuation-dissipation theorem (FDT) [43] to define the temperature of the system. An extension of this theorem has recently been proposed by Falcioni et al. [44], who have demonstrated that it can also be successfully used in dynamical systems presenting a chaotic time evolution.

The application of the fluctuation dissipation theorem implies the knowledge of the linear response, $\delta(x, t)$, of the system, which can be measured by perturbing it with a very small signal. From a practical point of view this is a very difficult task even in numerical systems [44], because a very small signal (the response to the perturbation) has to be extracted from the natural fluctuations of $u(x, t)$, that are much bigger than $\delta(x, t)$. Therefore, the error in the calculation of the response may be very large.

In order to verify the approach proposed by Hohenberg and Shraiman, we perturbed our system locally with a heat source constructed with a small resistor having a negligible thermal response time and a size smaller than one half the depth of the layer. The resistor was heated periodically by electric current pulses, whose frequency, amplitude and duty cycle were changed in order to measure $\delta(x, t)$ at many different frequencies and amplitudes. At a fixed η we sent a series of about ten pulses while we were measuring the space-time evolution of the system $u_p(x, t) = u(x, t) + \delta(x, t)$, that is, the natural fluctuation plus the response to the perturbation. The time 0 of these series coincides with the first pulse. We repeated this operation at least 100 times, and by synchronously averaging the different time series we obtained the space–time evolution $\delta(x, t)$. This happens because the mean of $u(x, t)$ is zero as a consequence of its chaotic time evolution. As an example we show in fig. 11a the time evolution of $\delta(x, t)$ produced by pulses of 0.1 s with a duty

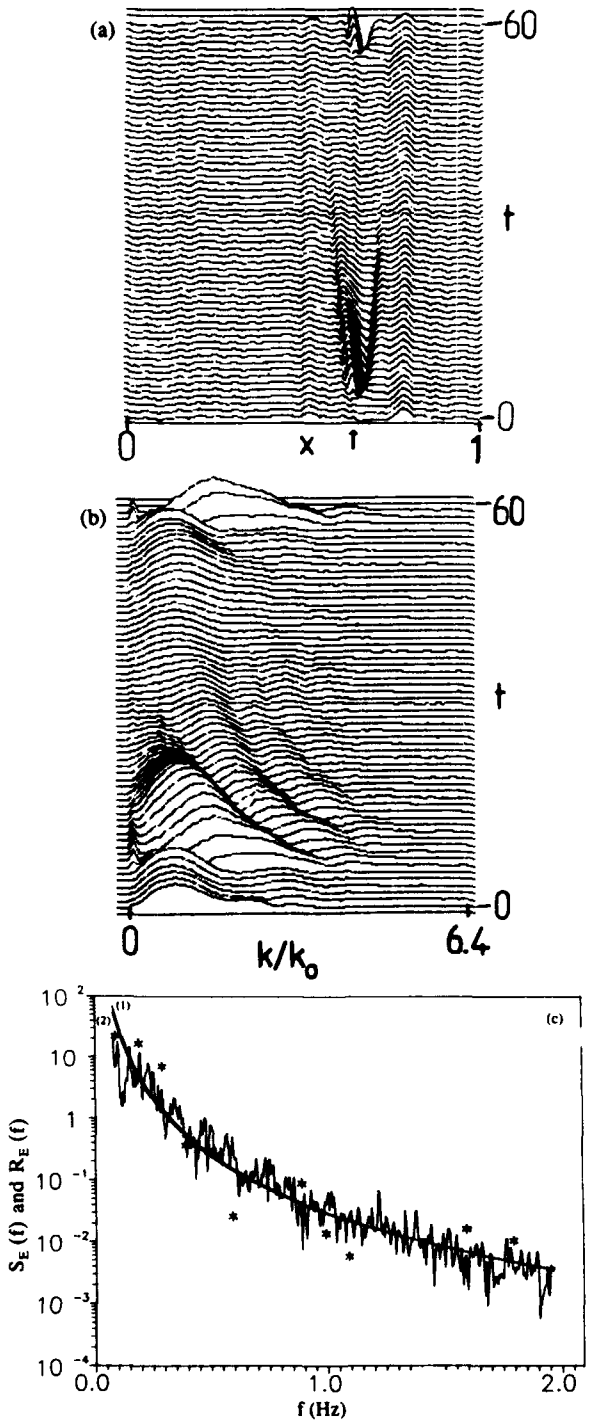

Fig. 11. (a) Space–time evolution of the perturbation produced by the heater at $\eta = 230$; the arrow indicates the position of the heater producing the perturbation; (b) Time evolution of the spatial Fourier spectrum of the perturbation at $\eta = 230$; (c) Spectrum $S_E(f)$ of the energy at $\eta = 300$. Stars correspond to $R_E(f) = I(f)/f$ measured at different frequencies. The two continuous lines are the best fit of $S_E(f)$ (1) and of $R_E(f)$ (2).

cycle of 50 s at $\eta = 230$. We observe the existence of a propagation, starting from the point where the perturbation is produced (arrow in the figure). The propagation is damped before it can invade all the structure. In fig. 11b we show the time evolution of the spatial Fourier spectrum of the perturbation of fig. 11a. Here we clearly see an inverse cascade of energy going towards small k and starting from wavevectors corresponding to the characteristic size of the perturbation (length of the heating resistor). It is interesting to notice that the maximum of the Fourier spectrum never goes below the length scale of k_c.

The FDT has been verified by comparing the spectrum $S_E(f)$ of $E(t)$, directly measured, with that computed from the response function. Specifically, once $\delta(x, t)$ is obtained, we compute the corresponding energy

$$E_\delta(t) = \sum_{i=0}^{N} \delta^2(x_i, t) \tag{8}$$

and its Fourier transform is divided by the excitation spectrum in order to have a normalized response. The imaginary part of this normalized Fourier transform is $I(f)$. The FDT implies that:

$$S_E(f) = AI(f)/f, \tag{9}$$

where A is a constant (proportional to the temperature). In fig. 11c we show the spectrum $S_E(f)$ obtained at $\eta = 300$. The stars in this figure represent $R_E(f) = I(f)/f$, which has been translated by log A in order to superimpose it on S_E. The two continuous lines (almost indistinguishable) correspond to best fits of $S_E(f)$ and $R_E(f)$. The good agreement between the computed spectrum and the measured one shows that the FDT is satisfied within experimental errors, and thus a temperature of the system can be defined, at least using a spatially averaged variable such as the energy. It would certainly be more interesting if we could show that FDT holds also for long wavelength Fourier modes. We also tried this measurement, but the results

were dependent on the model that we used to schematize the spatial distribution of the perturbation. Thus we do not have a clear check of FDT for all k. Furthermore the above-mentioned difficulties of measuring the response function do not allow us to use FDT to follow how the temperature, defined by eq. (9), changes as a function of the control parameter. Indeed, the spectrum shown in fig. 11c took almost two days of averaging to be obtained. So we propose here an approach that is rather similar to that of [23], but it uses the natural fluctuations of the system.

4.3. *Definition of a temperature*

We know that [43], for a thermodynamic system at constant pressure and volume, the r.m.s. fluctuations of energy and entropy are proportional to $K_B^{1/2}C_v^{1/2}T$ and $K_B^{1/2}C_p^{1/2}$ respectively, where C_v and C_p are the specific heats at constant volume and constant pressure, T is the temperature of the system and K_B is the Boltzmann constant.

To check these points we show in fig. 12 the mean values of E, σ and the r.m.s. values ΔE, $\Delta\sigma$ of their fluctuations, as functions of η. We see that $\langle E\rangle$ (fig. 12a) and $\langle\sigma\rangle$ (fig. 12b) are monotonically increasing as a function of η. The behaviour of σ above $\eta_c = 200$ indicates that the power spectrum shape does not change as a function of η. From fig. 12d we immediately realise that $\Delta\sigma$ increases by a considerable amount near η_c, as indeed we have already observed in the distributions of fig. 8e. In fig. 12d, we also notice that $\Delta\sigma$ is almost constant above η_s. As a consequence, we can make the hypothesis that C_p of our "thermodynamic system" is constant above η_s. Since we cannot distinguish in our system between a constant volume and a constant pressure process, we assume $C = C_p \simeq C_v$. Such a hypothesis has to be verified a posteriori.

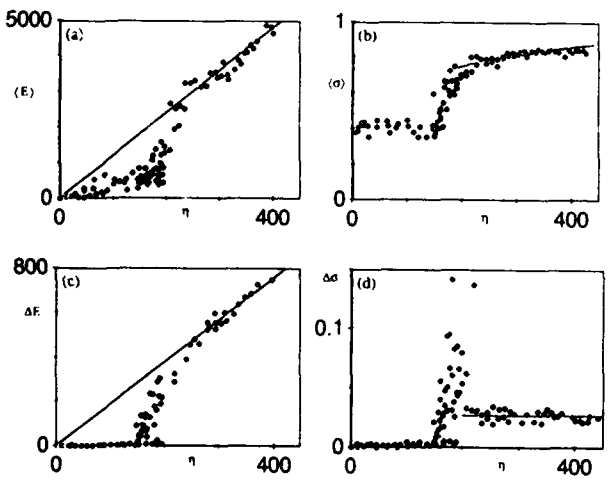

Fig. 12. Dependence on η of the mean values of the energy E (a), the entropy σ (b), and of the r.m.s. values of their fluctuations ΔE (c), $\Delta\sigma$ (d).

Fig. 12c shows that for $\eta > \eta_s$, ΔE grows linearly as a function of η (solid line in fig. 12c). As a consequence, the ratio $(\Delta E/\Delta\sigma)$ may be considered proportional to the "generalized temperature" $(\tilde{T} = r\eta)$ of the system for $\eta > \eta_s$ where the Fourier mode amplitudes have a Gaussian distribution. From the data we obtain $r = 73 \pm 1$.

In order to demonstrate that our definitions are self-consistent, we construct for $\eta > \eta_s = 248$ a free energy F:

$$F = -Cr\eta \ln(r\eta) + (\sigma_0 + C)r\eta\,, \qquad (10)$$

where $\sigma_0 = 0.817 \pm 0.005$, $C = 0.165 \pm 0.005$. From this free energy we may compute $\langle E\rangle$, $\langle\sigma\rangle$ and C as a function of η, via appropriate thermodynamic relationships [43]. The solid lines, shown in Fig. 12a and 12b, are the result of the calculations, and are in agreement with the experimental points. This verifies all the hypotheses made to define the "generalized temperature" of the system.

In fig. 13a we show the behaviour of the free energy F versus η. We see that F is a decreasing and rather smooth function of η. In order to see if this function behaves like a free energy, we have measured the time evolution of F when the control parameter η is suddenly changed. The result of one measurement is shown in fig. 13b

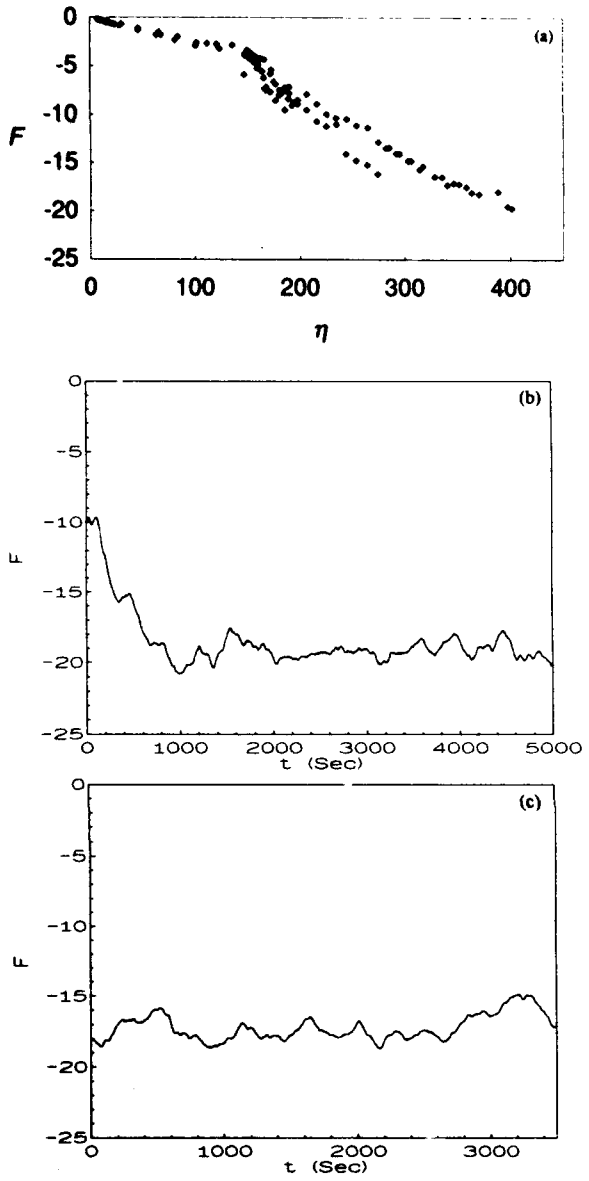

Fig. 13. (a) Dependence of the free energy F as a function of η; (b) Transient behaviour of F when η is suddenly changed from 330 to 452; (c) Time evolution of F in the steady state at $\eta = 415$.

where F is shown as a function of time when η is changed from 330 to 452 at time 0. The mean entropy and the mean energy were computed on an interval of time of about 100 sec. We see that F relaxes to the new value without strong oscillations, whose amplitude is similar to the free energy fluctuations in the steady state shown in fig. 13c. This kind of dynamical behaviour shows that the function F that we defined behaves like a free energy also from a dynamical point of view.

4.4. *Extension of the results to small* η

We want now to compare these results, based on the analysis of global variables of the system, with those obtained in section 3 using a local analysis. In the previous section we have seen that using the characteristic length of turbulent regions as an order parameter, we were able to identify a well defined transition point η_s for the appearance of space–time intermittency. In this section we have seen that above η_s the system displays thermodynamic properties and that a temperature can be defined. Now there is the important question of understanding the transition between a state below η_s that does not display thermodynamic properties to a state about η_s that does display these properties. To the best of our knowledge there is not a clear answer to this problem. Since we do not have our own, we call attention to some other relevant experimental facts which should provide useful information for a more complete understanding of the phenomenon. We consider the fluctuations of the entropy $\Delta\sigma$. In looking at fig. 12 we see that, close to the transition point for $\eta \simeq 200$, $\Delta\sigma$ is much higher than for any other value of η. If we force our thermodynamic analogy, the divergence of $\Delta\sigma$ corresponds to a divergence of the specific heat C near the transition point, which is a typical feature of second order phase transition. To see if our thermodynamic analogy could be extended to a thermodynamic formalism that could relate the different quantities via standard thermodynamic relationships, even below η_s we adopted the following procedure. We made a best fit of $\langle\sigma\rangle$ versus η in the full measurement range. The fit is shown as a continuum line in fig. 14a. By using the standard thermodynamic relationship $C = (\partial\sigma/\partial\eta)\eta$ one can compute C versus η from the best fit of $\langle\sigma\rangle$. Taking into account the value of K_B previously

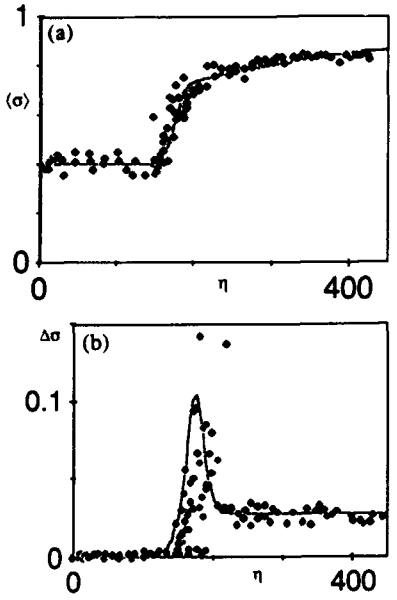

Fig. 14. (a) Spectral entropy σ versus η, the continuous line is a best fit of the data; (b) Entropy fluctuations versus η, the continuous line is obtained from the fit of σ via standard thermodynamic relationships.

computed, one obtains the fluctuations of $\Delta\sigma$ as function of η. The result of these calculations is the continuous line in fig. 14b that fits rather well the divergence of entropy fluctuations. This result indicates that an extension of our thermodynamic formalism is reasonable, although there are no theoretical justifications to do that. If one believes this thermodynamic analogy, one concludes that some macroscopic variables present features of a second order phase transition (divergence of the specific heat) as presented by the statistics of the local variables used in section 3.

5. Estimating the number of "degrees of freedom"

In this section we want to analyse the number of "degrees of freedom" that may produce the behaviour described in previous sections. By "degrees of freedom" we mean a number which is close to the Lyapunov and fractal dimensions [22].

However, as we have already mentioned in the introduction, the direct calculation of these two quantities on experimental signals is almost impossible when the dimension of phase space is greater than 5 [30, 45]. To overcome this problem we have applied the Karhunen–Loève (K.L.) decomposition, which has recently been applied to spatiotemporal dynamics [33–35] and to low-dimensional chaos [50].

Here we report only a summary of the results because the details can be found in ref. [32]. Let us recall very briefly what K.L. decomposition is. If we have a field $W(x, t)$ this method allows us to find a basis of orthonormal functions $\Psi_n(x)$ by solving an integral equation whose kernel is the two-point correlation function $K(x, x') = \langle w(x, t)\, w(x', t)\rangle$ ($\langle\ \rangle$ means time average). The functions $\Psi_n(x)$ are the eigenfunctions of the integral equation

$$\int_0^L K(x, x')\, \Psi_n(x')\, \mathrm{d}'x = \lambda_n\, \Psi_n(x)\,, \tag{11}$$

whose eigenvalues are λ_n. Then we can write

$$W(x, t) = \sum_{n=1}^{\infty} A_n(t)\, \Psi_n(x) \tag{12}$$

with $A_n(t)$ and $\Psi_n(x)$ that satisfy the following conditions:

$$\frac{1}{L}\int_0^L \Psi_n(x)\, \Psi_m(x)\, \mathrm{d}x = \delta_{n,m}\,, \tag{13}$$

$$\lambda_n \delta_{n,m} = \langle A_n(t)\, A_m(t)\rangle\,. \tag{14}$$

Here L is the size of the system, $\delta_{n,m}$ is the Kronecker symbol, λ_n is the energy of the mode n and

$$E = \sum_{n=1}^{\infty} \lambda_n \tag{15}$$

is the total energy of the system. To apply the method we first compute the two-point correlation function $K(x, x')$ and then eq. (11) is solved. Finally, once the $\Psi_n(x)$ are known the

$A_n(t)$ can be obtained by projecting the space–time evolution onto this basis, using eq. (12) and eq. (13). Here the field $W(x, t)$ to be decomposed using the K.L. method represents the fluctuations of $u(x, t)$ with respect to the time averaged spatial pattern $\langle u(x, t)\rangle$. We have studied how the energy of $W(x, t)$ is distributed among the $\Psi_n(x)$ as a function of the control parameter η. To do this we define the quantity

$$R(m) = \sum_{n=1}^{m} \frac{\lambda_n}{E}, \tag{16}$$

which is the percentage of energy contained in the first m modes. The quantity $R(m)$ versus m is shown in fig. 15a for five different values of η. We clearly see that the initial slope of $R(m)$ at $m = 1$ decreases as a function of η. This means that the number of modes that contain a certain percentage of the total energy increases as a function of η. In figs. 14b we show this number, that is, the minimum value M of m for which $R(m) > 0.93$, as a function of η. The value of 93% has been chosen because in the case of periodic oscillation this is the amount of the total energy contained in the first 2 modes. If a different threshold is used, M can change by 1 or 2 but the shape of the curve remains the same. In looking at fig. 15a we see that M is less than 10 for $148 < \eta < 175$ where the system presents periodic, biperiodic and weakly chaotic oscillations, while retaining spatial coherence (see section 2. Then it has a big jump at $\eta = 190$ where the system presents a bursting regime that leads to spatiotemporal intermittency (see section 2). Above $\eta = 240$ we note a saturation that in part is due to the limited number of data points in space, but we notice that the behaviour of M as a function of η is rather similar to that of the spectral entropy computed in section 4 (see fig. 12).

We computed the maximum number M that can be accurately estimated with a given number of samples in space. This check has been done by reducing the number of samples in our data. We find that M remains reliable up to roughly 1/2 of the maximum number of data points that are sampled in space. We also checked the results by increasing the number of spatial samples from 128 to 256 and we found that, for $\eta > 240$, the value of significant eigenfunctions is about 75, thus the correction is not very large.

The K.L. method converges very rapidly towards the final result even on data sets for which calculations of the fractal dimension (f.d.) or the Lyapunov exponents give a wrong result because of an insufficient number of points. In the insert of fig. 15b we show an expanded view of the region in fig. 15b with $140 < \eta < 165$, where the system presents a low dimensional chaotic regime. The stars represent the number M, whereas the crosses are the values of the f.d. for the same values of η. The fractal dimension has been computed using the method of Grassberger and

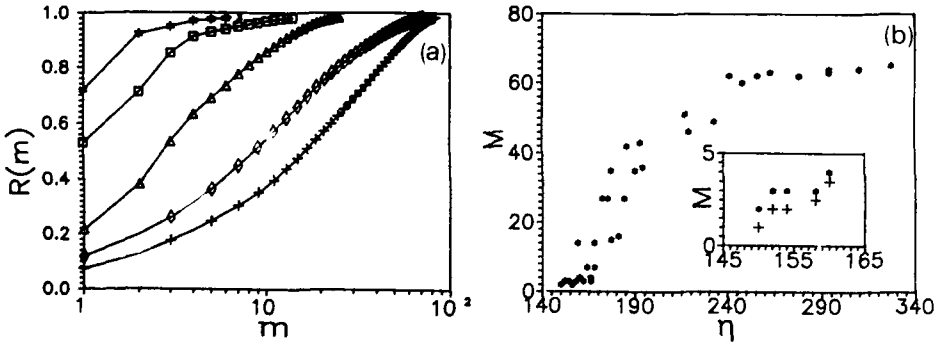

Fig. 15. (a) Dependence of $R(m)$ versus m for five different η: ★, $\eta = 150$; □, $\eta = 160$; △, $\eta = 168$; ◇, $\eta = 219$; +, $\eta = 310$. (b) Dependence of M on η. The insert is an expanded view of the interval $145 < \eta < 165$ (not all the experimental points are shown). Dots correspond to M whereas crosses represent the values of the fractal dimension.

Procaccia [46]. The phase space has been constructed using 64 time series simultaneously recorded at uniformly spaced spatial points. This method is clearly better than using delayed coordinates because it eliminates the ambiguity of the choice of the delay time [47][#2]. When looking at the insert of fig. 3b, we see that there is a remarkable agreement between M and f.d. if the latter is less than 5. Specifically M is equal to the next integer larger than f.d. This point has been clearly discussed also in ref. [50)]. To see if the first M eigenfunctions form a sufficient basis to describe the space–time dynamics of the system we computed f.d. using $A_n(t)$ with $1 < n < M$ to reconstruct the phase space. The results are in perfect agreement with those computed using 64 time series.

In contrast, when M is larger than 10, although we observed an increase of f.d., we were not able to estimate the fractal dimension reliably. This quantity was greater than 6 for $\eta >$ 170 but the error was more than 50% even when using 16 000 data points for each of the 64 time series. The reason for the large error is the appearance of the intermittent behaviour, which does not allow enough resolution (data points) during the intermittent bursts. So we can only say that the f.d. is probably greater than 6 but, in this case, we cannot make a comparison with M. This comparison can be made only on numerically generated dynamics whose number of degrees of freedom are exactly known. This has been done in the Kolmogorov–Spiegel–Sivashinsky equation [16] for which the Lyapunov dimension is known to scale with the system size [48]. Using the same criterion as that used on experimental data, we find that M, computed with K.L., is very close to the Lyapunov dimension, which was about 30 for the specific case. More details about this numerical test can be found in ref. [32].

[#2] There is no ambiguity in the choice of spatial points because the different points, either in real or Fourier space, can be considered as independent variables of the system and this is not in general true for delayed coordinates.

The numerical results [32, 34, 35, 45b] in spatiotemporal system (namely partial differential equations and coupled maps) indicate that there is a correlation between the value of M and the number of main degrees of freedom (in the sense of Lyapunov dimension) involved in the dynamics. There is not a clear explanation of the correlation [35, 45b] because the value obtained by K.L. is a linear estimate. However, from numerical tests one could conclude that the system spends a large amount of time in a linear subspace and only occasionally does it visit the other part of the phase space. This can be another way of describing the strong intermittency observed in spatiotemporal chaos. Because of the relationship between M and the Lyapunov dimension observed in numerical experiments, we assume that the value of M can be considered as a rough estimate of the number of the main degrees of freedom involved in the dynamics.

If this estimation is true, we can claim that probably the number of main modes involved in the spatiotemporal chaotic regimes of our systems is about 80. This result is rather interesting because it shows that important statistical features, like those shown in section 4, may be found even with a rather small number of modes involved in the dynamics.

6. Conclusions

Using the results of an experiment on Rayleigh–Bénard convection in an annular geometry, we have reviewed several methods that can be used in order to analyse the transition to spatiotemporal chaos. The example that we have chosen is very useful to investigate the transition from low dimensional chaos to weak turbulence because its behaviour is rather similar to the one observed in many other one dimensional systems.

In summary, the onset of spatiotemporal inter-

mittency in our cell displays features of a phase transition that is reminiscent of a percolation. This result has been obtained by reducing the space–time dynamics to a binary code, which captures the relevant features of the phenomenon. The universality class to which this phenomenon belongs is not detectable in a laboratory experiment because of the strong finite size effects. However, accurate numerical simulations on cellular automata show that it could be a percolation [19, 15b].

Above the transition point to space–time chaos the system displays thermodynamic properties: the Fourier mode amplitudes have Gaussian distributions, the energy of the system scales as an additive thermodynamic quantity and the fluctuation-dissipation theorem is satisfied for the energy. Furthermore, a thermodynamic temperature, which is proportional to the control parameter, can be defined using the natural fluctuations of the system. The most relevant fact is that a phase transition-like behaviour is recovered in the global variables of the system, just as in the local ones.

Finally, a rough estimate of the number of degrees of freedom (in the sense of Lyapunov dimension) involved in the dynamics shows that such a statistical behaviour is produced by the interaction of about 80 modes. This estimate has been given using the Karhunen-Loève decomposition that allows us to give also some information on the most important spatial structures of the dynamics [32].

The limited number of modes involved and the thermodynamic properties of this system clearly show the importance of non-standard statistics [49] in describing such phenomena.

This review on thermodynamic properties of space-time chaos is far from complete because at least two other important aspects have been left out. One concerns two dimensional systems, the other defect-induced turbulence. Information about these features can be found in other papers [1, 5, 18].

Acknowledgements

We thank F.T. Arecchi, F. Bagnoli, H. Brandt, S. Fauve, P. Hohenberg, R. Livi and S. Ruffo for useful discussions and suggestions. We also thank L. Albavetti for very useful technical support.

This work has been partially supported by G.N.F.M. and by CEE contract number sci-0035-c(cd).

References

[1] (a) N.B. Tufillaro, R. Ramshankar and J.P. Gollub, Phys. Rev. Lett. 62 (1989) 422; (b) J.P. Gollub and R. Ramshankar, in: New Perspective in Turbulence, S. Orzag, L. Sirovich eds. (Springer, Berlin, 1990).

[2] M. Rabaud, S. Michalland and Y. Couder, Phys. Rev. Lett. 64 (1990) 184.

[3] S. Ciliberto and P. Bigazzi, Phys. Rev. Lett. 60 (1988) 286.

[4] S. Daviaud, M. Dubois and P. Bergé, Europhys. Lett. 9 (1989) 441; F. Daviaud, M. Bonetti and M. Dubois, Phys. Rev. A 42 (1990) 3388.

[5] S. Cilberto, S. Douady and S. Fauve, Europhys. Lett. 23 (1991) 15.

[6] P. Kolodner, J.A. Glazier and H. Williams, Phys. Rev. Lett. 65 (1990) 1579; J.A. Glazier and P. Kolodner, Phys. Rev. A 43 (1991) 4269.

[7] F.T. Arecchi, G. Giacomelli, P.L. Ramazza and S. Risidori, Phys. Rev. Lett. 65 (1990) 2531.

[8] J.V. Moloney and A. Newell, Physica D 44 (1990) 1.

[9] P. Clavin, in: Physico Chemical Hydrodynamics (interfacial phenomena), ed. M. Velarde (Plenum, New York, 1988).

[10] V. Castets, E. Dulos and J. Boissonade, Phys. Rev. Lett. 64 (1990) 2953; H. Mike, S. Muller, B. Hess, Phys. Lett. 25 (1989) 141; K. Coffman, W.D. McCormick, Z. Noszticzius, R.H. Simoyi, H.L. Swinney, J. Chem. Phys. 86 (1987) 119.

[11] Proc. Les Houches Conf. Complexity and Evolution (Nova Commack, New York, 1991).

[12] K.Y. Tsang and K. Weisenfeld, Appl. Phys. Lett. 56 (1990) 5;
J. Berkemeier, T. Dirksmeyer, G. Klempt and H.G. Purwins, Z. Phys. B 65 (1986) 255.

[13] (a) K. Kaneko, Prog. Theor. Phys. 74 (1985) 1033; (b) K. Kaneko, Prog. Theor. Phys. Suppl. No. 99 (1989) 263.

[14] H. Chaté and P. Manneville, Phys. Rev. Lett. 54 (1987) 112; Europhys. Lett. 6 (1988) 591; Physica D 32 (1988) 409.

[15] J. Crutchfield and K. Kaneko in: Direction in Chaos, ed. B.L. Hao (World Scientific, Singapore, 1987); L. Bunimovich, A. Lambert and R. Lima, J. Stat. Phys. 61 (1990); (b) P. Grassberger and T. Schreiber, Physica D 50 (1991) 177.
[16] B. Nicolaenko, in: CHAOS 87, ed. M. Duong-Van (North Holland, Amsterdam, 1988).
[17] H. Chaté and B. Nicolaenko, in: Proc. Conf. New trends in nonlinear dynamics and pattern forming phenomena (Plenum, New York, 1991).
[18] (a) P. Coullet, L. Gil and J. Lega, Physica D 37 (1989) 91; (b) J. Lega, Thesis University of Nice (1989).
[19] F. Bagnoli, S. Ciliberto, A. Francescato, R. Livi and S. Ruffo, in: Chaos and complexity, M. Buiatti, S. Ciliberto, R. Livi and S. Ruffo eds. (World Scientific Singapore 1988); F. Bagnoli, S. Ciliberto, A. Francescato, R. Livi and S. Ruffo, in: Proc. School on Cellular Automata, Les Houches (1989).
[22] J.P. Eckmann and D. Ruelle, Rev. Mod. Phys. (1987); P. Bergé, Y. Pomeau and C. Vidal, L'Ordre dans le Chaos (Hermann, Paris, 1984).
[23] P.C. Hohenberg and B.I. Shraiman, Physica D 37 (1989) 109.
[24] L.D. Landau and E.M. Lifshitz, Fluid Mechanics (Pergamon, Oxford, 1980).
[25] D.J. Tritton, Physical Fluid Dynamics (Van Nostrand, Princeton, 1977); A.S. Monin and A.M. Yaglom, Statistical Fluid Mechanics (MIT Press, Cambridge, 1975).
[26] S. Ciliberto and M. Caponeri, Phys. Rev. Lett. 64 (1990) 2775.
[27] A. Pumir, J. Phys. (Paris) 46 (1985) 511.
[28] V. Yakhot, Phys. Rev. A 24 (1981) 642.
[29] S. Zalesky, Physica D 34 (1989) 427.
[30] J.P. Eckmann, S. Oliffson-Kamphorst, D. Ruelle and S. Ciliberto, Phys. Rev. A 34 (1986) 4971.
[31] R.H. Kraichnan and S. Chen, Physica D 37 (1989) 160.
[32] S. Ciliberto and B. Nicolaenko, Europhysics Letters 303 (1991) 14.
[33] N. Aubry, P. Holmes, J.L. Lumley, E. Stone, J. Fluid Mech., 192 (1988) 115; Physica D 37 (1989) 1.
[34] L. Sirovich, in: Contemporary Machematics, A.M.S., Vol. 99, B. Nicolaenko ed. (1988); Physica D 37 (1989) 126; Phys. Rev. Lett. 65 (1990) 1356.
[35] R. Guyonnet and R. Lima, preprint CPT Luminy; N. Aubry, M.P. Chauve and R. Guyonnet, preprint CPT-90/PE.2434.
[36] S. Chandrasekar, Hydrodynamic and Hydromagnetic Stability (Clarendon Press, Oxford, 1961); F.H. Busse, Rep. Prog. Phys. 41 (1978) 1929; Ch. Normand, Y. Pomeau and M. Velarde, Rev. Mod. Phys. 49 (1977) 581.
[37] A. Libchaber, C. Laroche and S. Fauve, J. Phys. (Paris) Lett. 43 (1982) 221; M. Giglio, S. Musazzi and U. Perini, Phys. Rev. Lett. 53 (1984) 2402; M. Dubois, M. Rubio and P. Bergé, Phys. Rev. Lett. 51 (1983) 1446.
[38] S. Ciliberto, M. Caponeri and F. Bagnoli, Nuovo Cimento D 12 (1990) 6.
[39] Y. Pomeau, A. Pumir and P. Pelcé, J. Stat. Phys. 37 (1984) 39.
[40] Y. Pomeau, Physica D 23 (1986) 3.
[41] D.S. Stassinopoulos, G. Huber and P. Alstrom, Phys. Rev. Lett. 64 (1990) 3007.
[42] R. Livi, M. Pettini, S. Ruffo, M. Sparpaglione and A. Vulpiani, Phys. Rev. A 31 (1985) 1039.
[43] L.D. Landau and E.M. Lifshitz, Statistical Physics (Pergamon, Oxford, 1980).
[44] M. Falcioni, S. Isola and A. Vulpiani, Phys. Lett. A 144 (1990) 341; G.F. Carnevale, M. Falcioni, S. Isola, R. Parini and A. Vulpiani, Phys. Fluids A3 (1991) 2247.
[45] (a) A. Politi in, Characterizing space–time chaos, ed. N. Abraham (Plenum, New York, 1989); (b) A. Torcini, A. Politi, G.P. Puccioni and G. D'Allessandro, Physica D 53 (1991) 85.
[46] P. Grassberger and I. Procaccia, Phys. Rev. Lett. 50 (1983) 346.
[47] A.M. Fraser, H.L. Swinney, Phys. Rev. A 33 (1986) 1134.
[48] P. Manneville, in: Macroscopic Modelling of Turbulent Flows and Fluid Mixtures, ed. O. Pirennau, Lecture Notes in Physics (Springer, Berlin, 1985).
[49] S. Isola, S. Ruffo, J. Phys. (Paris) II 1 (1991) 1349.
[50] D.S. Broomhead and G.P. King, Physica D 20 (1986) 217;
D.S. Broomhead, R. Jones and G.P. King, J. Phys. A (1987) L563.

Physica D 58 (1992) 384–391
North-Holland

PHYSICA D

Invariant measure in coupled maps

A. Politi[1] and G.P. Puccioni
Istituto Nazionale di Ottica, 50125 Firenze, Italy

Received 3 October 1991
Revised manuscript received 25 February 1992
Accepted 2 March 1992

The invariant measure associated with a chain of coupled maps is investigated by performing a local orthogonal decomposition. The same approach is also applied to the tangent space.

1. Introduction

The investigation of spatio-temporal chaos has recently attracted much interest. There is indeed hope that its understanding will shed new light on the evolution of systems with many degrees of freedom. In particular, a very general question arises as to whether a truly random signal can be distinguished from an infinite-dimensional chaotic one.

Statistical mechanics has provided the most powerful tool to describe low-dimensional strange attractors [1]. Likewise, we expect it to play an essential role also in the characterization of spatio-temporal chaos. However, we are still far from a satisfactory development of this line of thought. Rigorous results have been established only in the limited case of a chain of everywhere expanding maps, when the invariant measure covers the whole phase space [2]. In more realistic dissipative systems, difficulties arise which prevent a straightforward application of statistical-mechanics concepts. For instance, the exponential contraction of volumes enforces the overall attractor to fill a lower-dimensional manifold. Hence, unlike in Hamiltonian systems, here, many degrees of freedom remain inactive in the asymptotic evolution, yielding no contribution to the stationary properties.

More specifically, let us refer to a chain of coupled one-dimensional maps. The state of the system is represented by the time-dependent scalar field x_{t+1}^i obeying the equation [3]

$$x_{t+1}^i = f(\tfrac{1}{2}\sigma x_t^{i-1} + (1-\sigma)x_t^i + \tfrac{1}{2}\sigma x_t^{i+1}) , \qquad (1.1)$$

where i and t are discrete space and time variables, respectively; $f(\,)$ is a map of the interval into itself, and σ is a parameter controlling the strength of the diffusive coupling.

Previous simulations in spatially extended systems have shown that the fraction $\nu(\lambda)$ of the number of Lyapunov exponents larger than λ tend to be independent of the chain length L for $L \to \infty$ (thermodynamic limit) [4]. In other words, the spectrum of Lyapunov exponents is a well-defined entity. The existence of a limit spectrum straightforwardly implies that the dimension D of the attractor (as determined from the Kaplan–Yorke formula) is an extensive quantity, linearly dependent on the length L

$$D = \rho L , \qquad (1.2)$$

[1] INFN Sezione di Firenze; e-mail address: politi@fi.infn.it.

0167-2789/92/$05.00 © 1992 – Elsevier Science Publishers B.V. All rights reserved

where ρ is the so-called density of dimensions. In the case of non-invertible dynamics, the sum of all Lyapunov exponents can remain strictly positive, so that Kaplan–Yorke formula cannot apply [this is for instance the case of eq. (1.1) for a sufficiently small coupling strength σ]. In order to avoid such problems, we have always chosen parameter values such that a meaningful Lyapunov dimension can be determined (e.g. $\sigma = \frac{2}{3}$ and $f(x) = 2 - x^2$, yielding a dimension density $\rho \simeq 0.6$).

The state of affairs is much less clear when we pass from closed chains (as above) to sub-chains of an – in principle – infinite lattice [5]. This second approach somehow corresponds to the canonical-ensemble picture of statistical mechanics: the system of interest (sub-chain of length E) is coupled with a thermal bath given by the rest of the chain. From the previous considerations, the attractor corresponding to an isolated system would fill, for E sufficiently large, a ρE-dimensional manifold (let us forget about multifractal corrections, whose presence does not affect the validity of the following argument). The main effect of the coupling with the heat bath is to add a sort of "external noise" dressing the manifold along all directions, and thus making the resulting invariant measure to become E-dimensional. However, this seemingly trivial result does not provide a complete information about the scaling behaviour of the probability density. In fact, in the case of spatially extended systems, two independent scaling parameters are to be taken into account: the size ε of the boxes used to cover the phase space, and the length E of the chain. The coarse-grained dimension $D(\varepsilon, E)$ is a function of both parameters. The previous argument, together with careful numerical simulations [6], strongly support the hypothesis that, taking first the limit $\varepsilon \to 0$ (as required by the definition of dimension), $D(\varepsilon, E)$ converges to E itself. Instead, it is not clear what is to be expected if we first take the limit $E \to \infty$ (i.e. we observe the chain at fixed, finite, resolution). Numerical simulations presented below in this paper empower the conjecture that

$$D(\varepsilon, E) \simeq \rho_e(\varepsilon) E \,, \tag{1.3}$$

where ρ_e is close to the dimension density ρ defined in eq. (1.2). A rough theoretical argument is presented to justify this conclusion. Although all the numerical results presented in this paper have been obtained from simulations with logistic maps for the same parameter values, test runs made for different parameters and different maps indicate that they are more general.

The plan of the paper is as follows. First we introduce local orthogonal decomposition (OD), then we apply it to a chain of maps to extract information about the nonuniformity of probability distribution and to better comprehend the reason of the slow convergence exhibited by $D(\varepsilon, E)$. In section 3 we put forward the first elements of a possible application of OD to tangent space, as well. The hope is to be finally able to obtain a more detailed local description of the invariant measure, and perhaps construct more rigorous theoretical arguments about the structure of the invariant measure.

2. Local orthogonal decomposition

The idea of analysing the possible states of a sub-chain of length E requires to construct the vectors

$$\mathbf{v}_i \equiv (x_t^i, x_t^{i+1}, \ldots, x_t^{i+E-1}) \,, \tag{2.1}$$

and then to investigate their probability distribution in the corresponding E-dimensional space. This sort of spatial-embedding procedure is equivalent to projecting the invariant measure of the – in principle – infinite chain down onto an E-dimensional space. Previous numerical simulations revealed an increasingly slow convergence of $D(\varepsilon, E)$ to its limit value for increasing E [6]. These results have been interpreted as the indi-

cation that the invariant measure covers an increasingly thin subset along suitable directions in the embedding space. Here, we further investigate this point by performing a local orthogonal decomposition. Let us first recall the standard global implementation of OD [7]. Being $\mathbf{v}_t$ a vector lying in a given embedding space, we start computing the correlation operator

$$K_{i,j} \equiv \langle v_t^i v_t^j \rangle - \langle v_t^i \rangle \langle v_t^j \rangle \,, \quad \forall i, j \,, \tag{2.2}$$

where $\langle\ \rangle$ indicates the average with respect to the actual measure. The eigenvalues λ_n of the matrix $K_{i,j}$ can be interpreted as the average square sizes of the distribution along the principal axes, i.e. along the corresponding eigenvectors ψ_n. In the case of a probability distribution uniformly filling a thin parallelepiped, the relevant information about the thickness of the support is revealed by OD in terms of the existence of a small eigenvalue. After deforming the parallelepiped to a still thin, but curved manifold, such an information is immediately lost, the true local thickness being masked by the nonlinear character of the support. In such a case, we can separately apply OD to different smaller subsets so as to decrease nonlinear effects.

More precisely, we restrict the averages in eq. (2.2) to the points falling inside the same box $B(r, \varepsilon)$, with r representing its (randomly chosen) center, and ε its size. In order to construct global indicators, the box-dependent eigenvalues are then averaged over different reference points. Feasibility of the simulations impeded us to handle more than 200 such points.

It is not difficult to show that in case of a uniform distribution in a box of size ε, all the eigenvalues are equal

$$\lambda_n = \tfrac{1}{3}\varepsilon^2 \,. \tag{2.3}$$

Therefore, it is convenient to introduce the rescaled variables

$$w_n \equiv \frac{3\langle \lambda_n \rangle_r}{\varepsilon^2} \,. \tag{2.4}$$

which immediately provide information about the deviation from a uniform distribution. Actually, the dependence of λ_n on n, more than estimating the nonuniformity, characterizes local anisotropy. However, the average over different reference points present in eq. (2.4) allows one to obtain true information about the nonuniformity. Think for instance of a radial-dependent spherical-symmetric distribution. OD applied to a box set around the center of the sphere does not detect any nonuniformity, but any other choice of the reference point reveals nonuniformity as a local anisotropy.

For any smooth probability distribution appears more and more uniform when the resolution is increased, all w_n's are expected to converge to 1 for $\varepsilon \to 0$. This cannot be the case of the logistic map ($f(x) = a - x^2$), as a uniform density around $x = 0$ is transformed into an inverse-square root singularity around the maximum. In a chain of logistic maps, the same phenomenon leads to the Cartesian product of many such singularities. In order to get rid of this problem (which is not the main cause of the slow convergence of coarse-grained dimensions [6]), we have numerically performed a change of coordinate from x to y, transforming the single-site probability density $P(x)\,dx$ into a constant distribution.

As already mentioned in the introduction, we have performed the numerical simulations for $a = 2$ and $\sigma = \frac{2}{3}$ when fully developed spatio-temporal chaos is present with an exponential decay of spatial correlations. This is a case which exhibits an increasingly slow convergence of the coarse-grained fractal dimension [6]. It is worth mentioning that such phenomenon does not appear to be pathological of these parameter values, as the same behaviour has been also observed in simulations performed with different maps (e.g. tent map) [8].

In fig. 1 we have reported the dependence of

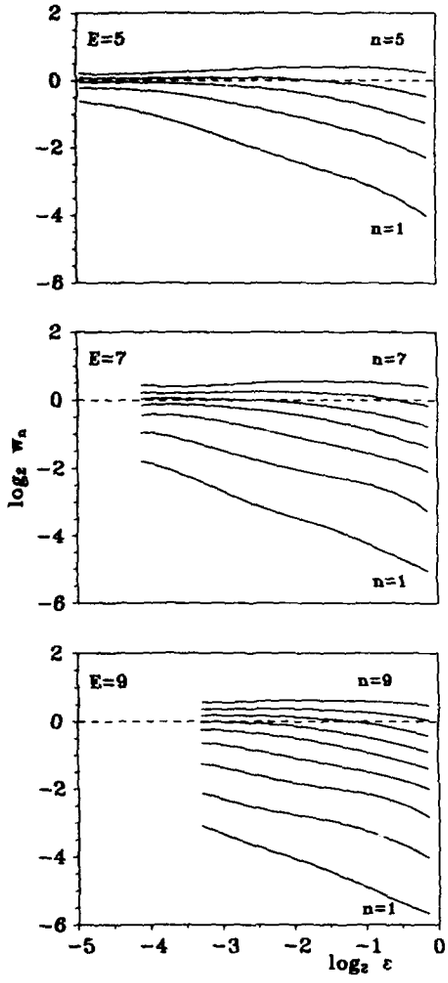

Fig. 1. Dependence of the nonuniformity coefficients w_n arising from the application of orthogonal decomposition to the probability densities in boxes of different sizes ε. The simulations have been performed for a chain of logistic maps, ($f(x) = 2 - x^2$, with a coupling strength $\sigma = \frac{1}{3}$). The dashed horizontal curve denotes the asymptotic value corresponding to a uniform distribution.

w_n on ε for $E = 5$, 7 and 9. The results have been obtained by iterating a chain of length $L = 1000$ and processing 2×10^9 data points. Some curves show a clear-cut convergence towards the expected asymptotic value $w_n = 1$. In the other cases the "large scale" convergence is followed by a "small scale" pseudo-divergence. The latter phenomenon turns out to be the consequence of a systematic error originated from the low statistics in the smaller boxes. In fact, simulations performed with fewer data showed the same phenomenon already for bigger boxes.

Moreover, notice that the smallest "thickness" w_1 decreases for increasing embedding dimension. To better elucidate the dependence of w_n on E, let us introduce the notion of nonuniformity spectrum

$$W(\nu \equiv n/E) = w_n \,. \tag{2.5}$$

Analogously to the spectrum of Lyapunov exponents, we expect that, in the thermodynamic limit, all spectra should tend to superimpose when plotted according to eq. (2.5). From fig. 2, where we have reported the results obtained for different chain lengths with global OD, we observe indeed a convergence towards a limit shape. Notice that the spectrum plotted in fig. 2 is [apart from the normalization of eq. (2.4), which simply leads to a vertical shift in a logarithmic scale, and from a possible reordering of the eigenvalues] the spatial Fourier spectrum. In fact, whenever translational invariance holds, the principal eigenvectors coincide with Fourier modes. However, this is no longer true when we consider smaller boxes.

When the embedding dimension is increased, it soon becomes unfeasable to generate enough points to fill a small box in a realistic amount of CPU time. Therefore, it is crucial to take into

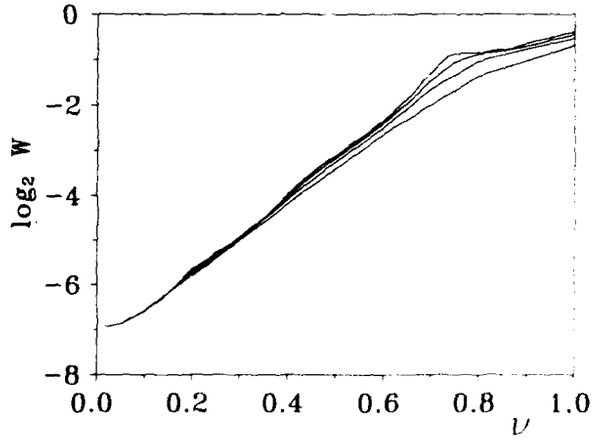

Fig. 2. Nonuniformity spectra, as arising from global OD, for increasing chain lengths.

account finite-size effects to better extrapolate the asymptotic results already from short-length simulations. It is reasonable to assume that finite-size effects can be accounted for by a power-series expansion in the smallness parameter $1/E$. Retaining only the first order [9], we have

$$\nu \equiv \frac{n}{E} + \frac{\alpha}{E} . \tag{2.6}$$

where the coefficient α is determined so as to yield the best superposition of the spectra in the small-ν region (since we are interested to extrapolate the minimum value $W(0)$). The results, plotted in fig. 3 for two different resolutions, clearly reveal a tendency to converge to a limit shape.

Let us now try to interpret these result in the spirit of the conjecture raised in ref. [6]. First of all, $W(0)$, for any finite choice of the box-size ε, is presumably limited from below by nonlinearities (unless nonlinear corrections tend to vanish for $E \to \infty$). Therefore, if the width of the distribution locally decreases for $E \to \infty$, $W(0)$ should decrease for $\varepsilon \to 0$, staying however finite as long as $\varepsilon > 0$. If instead, the distribution were uniformly filling an ellipsoid, then $W(0)$ would increase as ε^2, when the resolution is initially increased (see definition (2.3)).

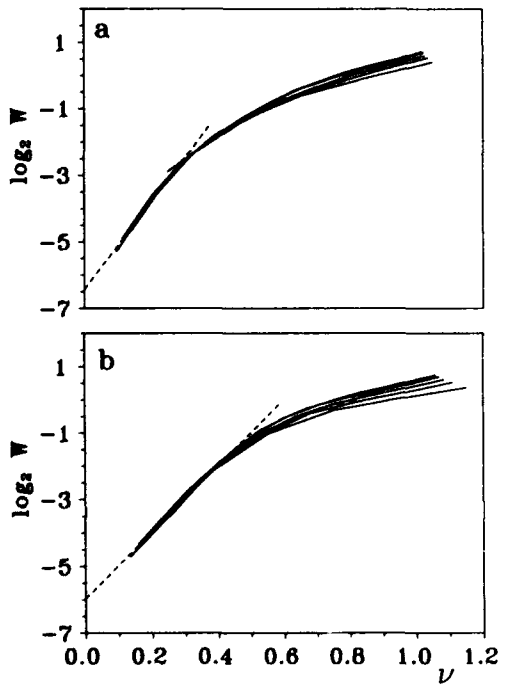

Fig. 3. Nonuniformity spectra for two different resolutions: $\varepsilon = 0.42$ (a), 0.18 (b) (ε is scaled in such a way that $\varepsilon = 1$ corresponds to the actual size of the set). The dashed lines extrapolate the curves towards $W(0)$.

From the results of figs. 2 and 3, we see that $W(0)$ neither decreases nor increases as fast as ε^2. This means that nonlinear effects are very important in lowering the convergence of fractal dimension estimates, but they do not seem to be so strong as to justify the existence of an increasingly thin manifold.

However, there is a simple argument in favour of the latter conjecture. As already mentioned in the Introduction, the evolution of a sub-chain of length E can be seen as a deterministic evolution inside an E-dimensional phase space, plus a sort of random noise, due to the coupling with the rest of the chain. As this coupling acts only at the boundaries, its overall size is independent of the chain-length. In order to clarify the role played by such a "noise", it is useful to project it along the position-dependent stable and unstable directions. If the invariant manifolds were likely to assume all possible directions, then the amplitude of the "noise" along each direction should, on the average, be of the order of $1/\sqrt{E}$. On the one hand, a small noise along an unstable direction is amplified but, as the attractor is already continuous along such a direction, its effect on the invariant measure is not qualitatively relevant. On the other hand, a noise acting along a stable direction is damped, but it is sufficient to provide a finite width to the probability density. However, as the "noise" amplitude goes to 0 for $E \to \infty$, the thickness does the same. Actually, it is not true that the manifold points equally likely along all directions, as the Lyapunov vectors are more or less localized [9], but this cannot affect the previous argument. In fact, since the overall intensity of the coupling is of order $\mathcal{O}(1)$, there can be at most a finite number of stable directions charac-

terized by a noise amplitude independent of E. Now, a finite number of directions escaping our previous arguments does not make a relevant difference in the thermodynamic limit. On the contrary, it is in principle possible to imagine invariant manifolds pointing along quasi-forbidden directions and characterized by a noise amplitude decreasing faster than $1/\sqrt{E}$.

Our numerical simulations having shown a slowly increasing $W(0)$, are not in agreement with the previous analysis. However, we must recall that the above arguments are entirely based onto a linear analysis, while it is not obvious whether nonlinear terms are negligible at the relatively short embedding dimensions used in the simulations. In fact, we have been able to reach at most $E = 13$, which means an average noise amplitude about $2\sqrt{\frac{1}{13}} = 0.554$ (there are two forcing terms acting at the extrema of each sub-chain).

Before passing to a direct investigation of the invariant manifold, let us comment about the convergence of the fractal-dimension estimates. From the knowledge of the density of points in the various boxes, it is obviously possible to measure coarse-grained dimensions. The average value is plotted in fig. 4 versus E, for two different resolutions. In both cases we observe

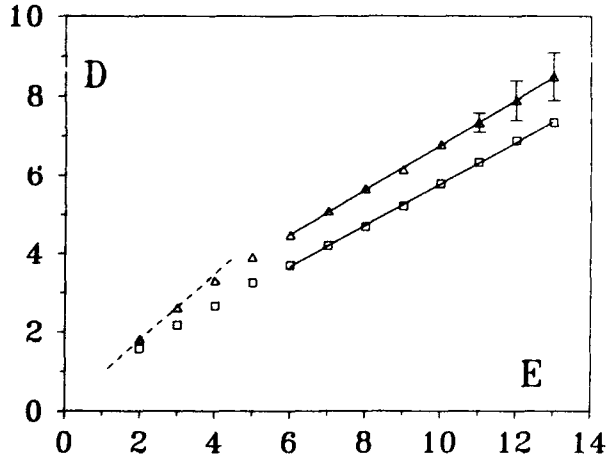

Fig. 4. Coarse grained dimension D versus the embedding dimension E for two different resolutions: $\varepsilon = 0.42$ (squares), 0.18 (triangles). The error bars are drawn only when the uncertainty is larger than the size of the symbols.

an almost linear increase with a slope about 0.53 and 0.56, respectively. Both slopes are definitely smaller than 1, the value that we would have obtained by first taking the limit $\varepsilon \to 0$. Furthermore, the slope is close to the density of dimensions ($\simeq 0.6$), i.e. the value that we would have expected for an isolated chain. A possible explanation of this fact goes as follows. We have seen that the effect of external noise is confined to small length scales, the smallness depending on the length E of the chain. Therefore, it is not possible to distinguish the probability density observed for E sufficiently large, from that one of an isolated chain. Accordingly, $D(\varepsilon, E) \simeq \rho E$, i.e. eq. (1.3) holds, together with the equality $\rho_e = \rho$. As a consequence, for ε sufficiently small, one should be able to detect two distinct regimes in the behaviour of $D(\varepsilon, E)$: (i) a small-E region, where the resolution is sufficient to reveal the presence of the coupling, characterized by the scaling behaviour $D(\varepsilon, E) \simeq E$; (ii) a large-$E$ region, where the asymptotic law is found. Some evidence of this behaviour is shown in fig. 4, where the curve obtained for $\varepsilon = 0.18$ (triangles) exhibits a somehow larger slope at small E-values (see dashed curve). A more clear evidence of a cross-over between two different regimes could be reached for smaller boxes. Unfortunately, this is practically unfeasible, because of the enormous number of data points required to fill such boxes.

Let us conclude this section, by noting that eq. (1.3) provides, in principle, a tool to distinguish an infinite-dimensional chaotic signal (C) from a random one (R). In fact, by interpreting the spatial variable i as a time variable, the embedding procedure sketched in eq. (2.1) becomes the typical temporal-embedding technique used to reconstruct strange attractors, and our signal $x_t^i, x_t^{i+1}, \ldots$ can be interpreted as an infinite-dimensional chaotic signal. In both C- and R-cases, the fractal dimension $D(0, E)$ coincides with the embedding dimension itself. However, for a random signal, we expect that, instead of eq. (1.3), the equality $D(\varepsilon, E) = E$ again holds

at sufficiently high resolutions. This answers the question formulated in ref. [10] and recalled at the beginning of this paper.

3. Orthogonal decomposition in tangent space

In the previous section we have applied local OD to the invariant measure in the phase space. We have seen that, on the one hand, this approach is able to confirm the slow convergence of fractal dimension estimates but, on the other hand, it does not lead to reliable conclusions about the local structure of the probability distribution for increasing embedding dimensions.

From the analysis of low-dimensional chaos, it is well known that Lyapunov exponents contain enough information so as to provide a complete characterization of the chaotic properties (e.g. fractal dimension and metric entropy). In the following we shall combine such a philosophy with the ideas expounded in section 2, to describe spatially extended systems.

Let us consider a chain of length L with a Lyapunov dimension ρL. The implementation of Kaplan–Yorke formula implicitly associates a partial dimension to each invariant (either stable, or unstable) direction. More precisely, the directions corresponding to the first $l = [\rho L]$ (i.e. the integer part of ρL) Lyapunov vectors are characterized by partial dimensions equal to 1 (such directions include the whole unstable manifold plus some of the less contracting directions). The $(l+1)$st direction is characterized by a fractal structure, and the remaining stable directions are to be associated with a zero partial dimension.

Here, we make the stronger assumption that the invariant measure covers smoothly a regular ρL-dimensional manifold. In other words, we neglect the single direction characterized by a non-integer dimension: this approximation does not appear to be so severe in the thermodynamic limit. Moreover, we neglect multifractal corrections. They are not small in principle, since the fluctuations of pointwise dimension are proportional to the chain length [11]. However, the volume of the regions characterized by a dimension value other than the average one is asymptotically 0. Finally, if a stable direction is characterized by a zero partial dimension, it is not necessarily true that the attractor has a point-like structure along such a direction. We do not know if such anomaly is going to occur generically in high dimensional systems. In the lack of rigorous statements we use the Occam's razor, making the simplest assumption.

We now go back to the problem of projecting locally the invariant measure, to exploit the assumption about the smoothness of the probability density. More precisely, we assume that the distribution around a generic point $X \equiv (x_1, \ldots, x_L)$ covers uniformly a ρL-dimensional subspace identified by the corresponding Lyapunov vectors u_i. The projection P is simply performed by retaining E spatially consecutive coordinates of the point X and of the Lyapunov vectors. As a result, we determine the directions spanned by the probability distributions in the embedding space. Obviously, since $\rho L > E$, the resulting vectors overspan the E-dimensional space. However, nothing is known a priori about the directions exhibited by the projected vectors Pu_i. To investigate this point, we have interpreted such vectors as points in an E-dimensional space and applied OD to them. The results (averaged over different reference points) are shown in fig. 5, where the smallest coefficient w_1 is plotted versus E for two different chain lengths. The clean straight-line behaviour indicates an exponential decrease of w_1. This means that the projection of a ρL-dimensional hypercube onto an E- dimensional space, is mostly concentrated along suitable directions, while being very thin along some other ones. However, this result proves only a necessary, but far from sufficient, condition to explain the existence of directions characterized by a small thickness. In fact, in the above analysis, we have implicitly assumed that the probability density around a generic point S_E in the embedding

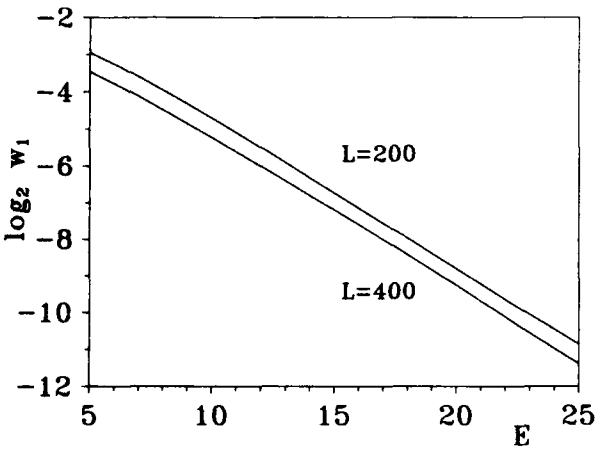

Fig. 5. Smallest eigenvalue w_1 (from the projection of Lyapunov vectors) versus the dimension E of the projection space for different chain length L.

space derives from the projection of the invariant measure around just one point S_L in the L-dimensional space ($S_E = PS_L$). This is not true, for there are infinitely many different S_L points in the global phase space, whose projection yields the same point S_E in the embedding space. Therefore, one should superimpose all such distributions before applying OD to the Lyapunov vectors. The computation of the resulting nonuniformity spectra is a much more cumbersome task, which we plan to undertake in the near future.

References

[1] J.-P. Eckmann and D. Ruelle, Rev. Mod. Phys. 57 (1985) 617.
[2] L.A. Bunimovich and Ya. G. Sinai, Nonlinearity 1 (1989) 491.
[3] K. Kaneko, Prog. Theor. Phys. 72 (1984) 480.
[4] Y. Pomeau, A. Pumir and O. Pelce, J. Stat. Phys. 37 (1984) 39.
[5] P. Grassberger, Physica Scripta 40 (1989) 346.
[6] A. Torcini, A. Politi, G.P. Puccioni and G. D'Alesandro, Physica D 53 (1991) 85.
[7] D.S. Broomhead and G.P. King, Physica D 20 (1986) 217; N. Aubry, P. Holmes, J.L. Lumley and E. Stone, J. Fluid. Mech. 192 (1988) 115.
[8] A. Politi and G.P. Puccioni, unpublished.
[9] G. Giacomelli and A. Politi, Europhys. Lett. 15 (1991) 387.
[10] G. Mayer-Kress and K. Kaneko, J. Stat. Phys. 54 (1989) 1489.
[11] A. Politi and A. Torcini, to be published.

Physica D 58 (1992) 392–401
North-Holland

PHYSICA D

Phase-space analysis of bursting behavior in Kolmogorov flow

Dieter Armbruster, Randy Heiland, Eric J. Kostelich and Basil Nicolaenko
Dept. of Mathematics, Arizona State University, Tempe, AZ 85287-1804, USA

Received 7 October 1991
Revised manuscript received 16 December 1991
Accepted 16 December 1991

PDE simulations for the Kolmogorov flow are analyzed in terms of phase-space concepts. The tool used is the proper orthogonal decomposition method which extracts coherent structures and prominent features of a random or turbulent dataset. We analyze a quasiperiodic regime and an intermittent regime. We derive two eigenfunctions that determine the dynamics and structure of the quasiperiodic case and find a third one associated with the unstable manifold of the bursts of the intermittent regime. Calculations are performed for streamfunction data and vorticity data which show substantial differences. It is argued that the streamfunction data demonstrate the low dimensional phase-space dynamics of the large scales whereas the vorticity data show an enstrophy cascade.

1. Introduction

Recent large scale simulations of periodically forced 2D Navier–Stokes equations (Kolmogorov flow) have revealed a quasiturbulent regime characterized by a periodically modulated drifting laminar flow interspersed by unpredictable, sometimes violent eruptions of turbulence [1]. In the spirit of recent approaches to connect spatially and temporally complex behaviour to finite dimensional attractors, one hopes to explain those simulations through structurally stable features of dynamical systems. An important ingredient for such an idea is the symmetry structure of these simulations. The latter are performed with periodic boundary conditions which, together with the periodic forcing (wavelength $2\pi/k$), introduce a $D_k \times O(2)$ symmetry under which the governing equations are equivariant. Because of these symmetry constraints, our working hypothesis for the turbulent bursts is that they are governed by structurally stable homoclinic connections between the quasiperiodic laminar solutions, and phase-shifted laminar solutions which are related to each other via group operations [2]. Unfortunately, while similar behavior appears in the Kuramoto–Sivashinsky equation, where such a regime occurs essentially as a secondary bifurcation which can be explained by a two-mode analysis [3], our intermittently turbulent regime occurs after many previous bifurcations have happened and therefore the basic flow is unstable to many modes. Hence a group theoretic analysis would involve the interaction of many different representations of the symmetry group making a full analysis unfeasible.

A suitable tool to extract phase-space information out of large scale PDE simulations seems to be the proper orthogonal decomposition (POD) also known as Karhunen–Loève decomposition [4, 5]. This was recently demonstrated for the Kuramoto–Sivashinsky equation in refs. [6, 7]. Simulations for Kolmogorov flow in refs. [1, 8, 9] clearly give the impression of a finite, in fact very low dimensional dynamics for this regime. Con-

0167-2789/92/$05.00 © 1992 – Elsevier Science Publishers B.V. All rights reserved

sequently our long term goal is to come up with a reasonably low dimensional dynamical system derived via a proper orthogonal decomposition and amenable to traditional phase-space analysis. While we have not yet *synthesized* such a system we have *analyzed* the simulations. We think our preliminary results give very interesting partial answers and raise some new and crucial questions about the nature of turbulence.

Using POD we extract the dominant features of the data as spatial eigenfunctions of the covariance matrix and project the data onto the first few eigenfunctions. Doing this for a time sequence we can reconstruct the time evolution of the flow using a suitable number of these eigenmodes. Specifically we are reconstructing two regions of the simulations: The region believed to be predominantly laminar and the region containing a burst, respectively. While the PDE numerical code integrates a streamfunction, turbulence theory prefers to deal with vorticity. Performing a POD on both we get the surprising result that the dimensions derived from an energy criterion on the POD and visual comparison of reconstructed and original data, as well as those derived from an embedding algorithm [10], do not coincide for stream-function and vorticity data. We offer interpretations and speculations on the reasons for that discrepancy in our conclusion.

Another interesting result concerns the implication of the streamfunction analysis for Kolmogorov flow: We confirm that the laminar flow can be described as a modulated travelling wave. Its basic POD eigenfunctions are calculated and their Fourier components are known. We can also quantify the dimension of the burst regime. In particular we can identify modes that are associated with the unstable manifold of the modulated travelling wave.

The remainder of the paper is organized as follows: In section 2 we describe the relevant features of the bursting regime in Kolmogorov flow. Section 3 reviews the proper orthogonal decomposition insofar as it applies to phase-space analysis of partial differential equations. Section 4 reports on our results for streamfunction data and section 5 deals with vorticity data. The conclusion discusses these results in terms of low dimensional phase-space dynamics versus enstrophy cascade.

2. The Kolmogorov flow: Bursting regimes

The two dimensional Kolmogorov flow is the solution of the 2D Navier–Stokes equation with a uni-directional force $f = (\nu k_f^3 \cos k_f y, 0)$. It was introduced by Kolmogorov in the late 1950's as an example on which to study transition to turbulence. For large enough viscosity ν, the only stable flow is the plane parallel periodic shear flow $u_0 = (k_f \cos k_f y, 0)$, usually called the "basic Kolmogorov flow". The macroscopic Reynolds number of the basic flow is easily found to be $1/\nu$; this will be used later as a free parameter to define the bifurcation sequence. It was shown by Meshalkin and Sinai [11] that large-scale instabilities are present for Reynolds numbers exceeding a critical value, $\sqrt{2}$. This large-scale instability has been shown by Nepomnyachtchyi [12] and Sivashinky [13] to be of negative-viscosity type, in the sense that the basic anisotropic flow generates a negative viscosity for large scale perturbations. In a 2π-periodic square box the equations are

$$\frac{\partial u}{\partial t} + u \cdot \nabla u + \nabla p = \nu \nabla^2 u + f \,, \tag{1}$$

$$\nabla \cdot u = 0 \,, \tag{2}$$

$$f = (\nu k_f^3 \cos k_f y, 0) \,, \quad 0 \leq x, y \leq 2\pi \,. \tag{3}$$

Sequences of bifurcations have been investigated in refs. [8, 14] (see also ref. [15]. Recently interesting transitions that occur at higher Reynolds number have been studied in refs. [1, 16, 9]. They lead to sparsely distributed bursts in time for a fairly large range of Reynolds number from a threshold of about $\mathrm{Re} \approx 20.5$ for $k = 8$ to about

$\mathrm{Re} \approx 120$. The most striking feature of this transition is that the bursts generate substantial spatial disorder and drive developed turbulence. Typically, near threshold the dynamics follows a long laminar regime, then undergoes a strong chaotic burst, then seems to settle down to a laminar regime at the same level as before; then another explosion follows. Intervals between bursts are not constant and fluctuate randomly. A study of the Fourier modes [1, 16, 9] suggests that

- the laminar regime can be described by a traveling modulated system of eddies with well defined symmetries (symmetry of a square lattice rotated by 45°);
- successive laminar intervals do not correspond to identical dynamical states but rather to a sequence of states mapped onto each other under some group action. These group actions in particular act on the phases of the complex Fourier coefficients as demonstrated in refs. [1, 16, 9];
- spatial order is destroyed during the bursts, with spatial dynamics on a much smaller space-scale.

In refs. [1, 16] this kind of behavior is discussed in terms of heteroclinic and homoclinic loops in phase space involving an analysis of the symmetry groups of the system. These symmetries enable the heteroclinic loops to become structurally stable which is in accord with the observation that the bursting persists up to and beyond $\mathrm{Re} = 120$ (for $k_f = 8$). As the Reynolds number increases, the time between bursts becomes shorter, so that the coherent vortices ultimately appear only during brief intermittencies and the bursts dominate nearly all of the dynamics. It should be pointed out that the Reynolds number $\mathrm{Re} = 1/\nu$ is only a macroscopic number. Effective (local) Reynolds numbers vary from 500 ($\nu = \frac{1}{25}$) to 1500 ($\nu = \frac{1}{120}$).

In this work we focus on a regime just beyond, yet very close to the bifurcation from the modulated travelling wave; specifically $\mathrm{Re} = 20.545$, $k_f = 8$ (the laminar states are still stable at $\mathrm{Re} = 20.540$). One of our goals is to obtain more information on the unstable manifold of the hyperbolic tori in a situation where the dynamics is still weakly chaotic and remain for a very long time in a neighborhood of the tori. Fig. 1 shows a typical plot of the vorticity: There is a large-scale structure underlying two prominent localized eddies in the upper left and the lower right corner and a diagonal wavestructure. Plots of the maximal vorticity against time in typical time series at $\mathrm{Re} = 20.545$ reveal long laminar sequences with "microbursts" spaced far apart. There is no phase shift before and after such microbursts and the dynamics does not (yet) track a full heteroclinic connection. Hence by doing a POD analysis on these microbursts we hope to be able to reveal the trigger mechanism for the chaotic bursting.

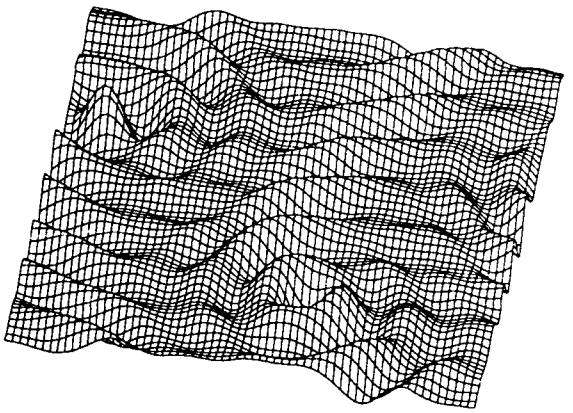

Fig. 1. Typical data vector (snapshot) showing the vorticity (z-direction) above an (x, y) grid. Note the two circular eddies in the upper left and the lower right corner and the remnants of the period 8 basic Kolmogorov flow.

3. The Proper Orthogonal Decomposition

This procedure has been proposed by Lumley [4] and subsequently used by many groups to extract coherent structures from turbulent data.

We briefly summarize the method and refer the reader to ref. [5] for details. Basically one looks for eigenfunctions that optimally capture the dynamics of a certain flow. The eigenfunctions have the interpretation of maximizing an averaged quadratic functional which, for data representing a velocity, corresponds to the kinetic energy. Therefore we generally refer to the 'energy' of the data. Mathematically equivalent, the eigenfunctions maximize the correlation of the flow fields in each coordinate direction. Specifically, if $u(x, t)$ represents the spatio-temporal evolution of the PDE in question, then we choose ψ_1 such that

$$\lambda_1 = \lim_{T\to\infty} \frac{1}{T} \int_0^T (\psi_1, u)^2 \, dt \tag{4}$$

is a maximum with the side constraint that $(\psi_1, \psi_1) = 1$. Proceeding inductively, the resulting variational problem leads to a Fredholm type integral equation

$$\int K(x, y)\, \psi(y) = \lambda \psi(x) , \tag{5}$$

where the kernel $K(x, y) = \langle u(x, t)\, u(y, t) \rangle$ and the brackets denote time average. Consider a truncated expansion of the flow in terms of the $\{\psi_n\}$, namely

$$u(x, t) \approx \sum_{n=1}^{N} a_n(t)\, \psi_n(x) . \tag{6}$$

Then we observe that the modes are uncorrelated in time as $\langle a_j(t)\, a_k(t) \rangle = \lambda_j \delta_{jk}$ and furthermore, the eigenvalue λ_j corresponds to the statistical variance in the jth coordinate direction, and is maximal.

We face two problems with that type of data analysis: As is obvious from eq. (4) one usually performs time averages over very long samples. However, this tends to obscure short lived events like the intermittent bursts, and it smooths out all temporal details of the flow. Therefore we carefully select the data for our two analyses (Fig. 2): We cut the data containing a microburst into two pieces. The first one is laminar (by visual inspection); the second one contains a large part of laminar flow but also includes a burst. Keeping a laminar part in our burst timeframe ensures that we are processing those data, that come from small exponential growth along the unstable manifold of the torus.

The second problem concerns the traveling of our data field. Theoretical analysis shows [5] that the POD eigenfunctions for a travelling wave become sinusoids. We are, however, not interested in the Fourier decomposition of the traveling wave but want to treat it as one coherent

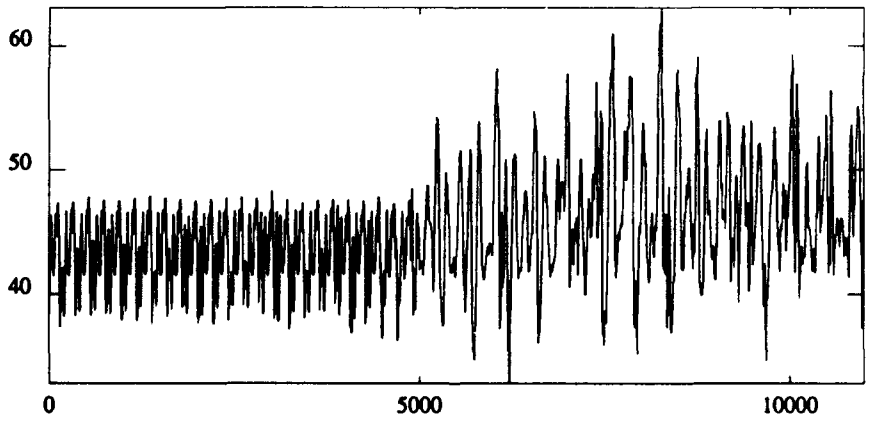

Fig. 2. Time series of the maximal vorticity over the sample. Our laminar phase comprise data in the first 30% of the sample, our burst phase is centered around $t = 5000$.

structure. Hence we process our data first, calculate the wave speed and go into a co-moving coordinate frame. The mean of the so-called "untraveled" data then corresponds to the traveling structure. We subtract the mean and perform our POD on the remaining data, both for the laminar and the bursting regime.

The technical details are the following: Our simulation data come from a 64×64 pseudo spectral algorithm for the streamfunction. Unless otherwise noted we use a shell of Fourier modes incorporating all modes of the form (m, n) with $-10 \leq m \leq 10$, $-10 \leq n \leq 10$ (shell 10). The POD is performed as a snapshot method [5] with 200 time frames on either the physical data (a 64×64 vector calculated by inverse FFT from the shell 10 Fourier modes) or on the Fourier coefficients directly one snapshot vector now corresponding to the approximately 200 Fourier amplitudes in our shell 10.

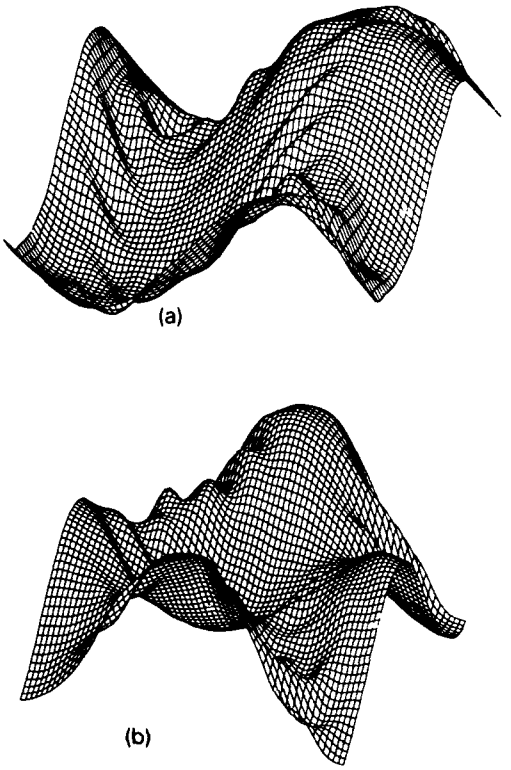

Fig. 3. First two eigenfunctions for the POD of the streamfunction data in the laminar phase. (a) with 89.9% of the energy, (b) with 9.4% of the energy.

4. Analyzing the streamfunction data

We perform the described POD analysis on the laminar regime using the data in the streamfunction formulation. Ordering the eigenfunctions according to the magnitude of the eigenvalue ("energy") we have 98.7% of the energy in the first two modes which are displayed in Fig. 3. A reconstruction of the data using just those two modes together with the mean flow gives an almost perfect agreement between data and reconstruction. Using the POD on the Fourier amplitudes we capture almost the same amount of energy in the first few eigenfunctions. We confirmed that the linear operations of Fourier transformation and POD commute, i.e., the Fourier transformation of the first two eigenfunctions in physical space gives us the first two eigenfunctions of the proper orthogonal decomposition, performed directly on the Fourier amplitudes. Fig. 4 shows the two eigenfunctions in Fourier space. One sees that although the modes $(0, 1)$ and $(1, 0)$ are very dominant, there are higher modes (smaller scales) that also play a role. Hence a simple description of this limit cycle in terms of Fourier modes does not seem to be feasible.

Analyzing the burst for the streamfunction data shows some surprising results. We can now capture 98.0% of the energy in three modes (fig. 5).

The first mode in the laminar regime is roughly the same as the first mode in the bursting regime, whereas modes two and three in the bursting regime both seem to be related to mode two in the laminar regime. It appears that they are real and imaginary parts of the same complex eigenfunction. This suggests that if the limit cycle lies in a real subspace, then its unstable manifold is in the imaginary subspace. This is corroborated by the observation that the POD eigenfunctions two and three in the Fourier repre-

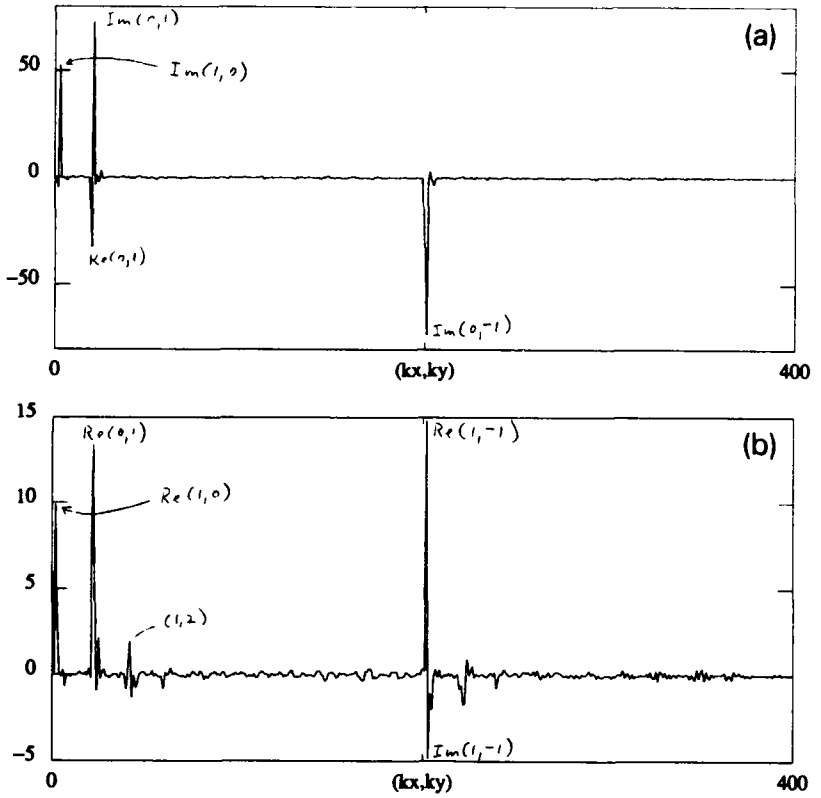

Fig. 4. Two POD eigenfunctions in Fourier space that span the limit cycle of the laminar flow in streamfunction formulation. The labelling on the x-axis is done as follows: $(k_x = 0...9,\ k_y = 0)$, $(k_x = 0...9,\ k_y = 1)$ and so on to $k_y = 9$ and then repeat for $k_y = -1...-9$. A few labels (k_x, k_y) for the real and imaginary parts of the Fourier modes are indicated.

sentation (fig. 6) contain basically the same modes and hence span a complex Fourier mode. If these subspaces can be shown to be invariant under some subgroup of the full symmetry

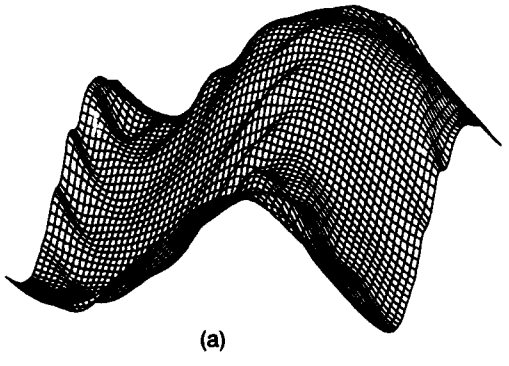

Fig. 5. (a)–(c) First three eigenfunctions for the POD of the streamfunction in the burst phase. Compare to the principal eigenfunctions of fig. 3. Energies are 80.9%, 12.1% and 5.5%.

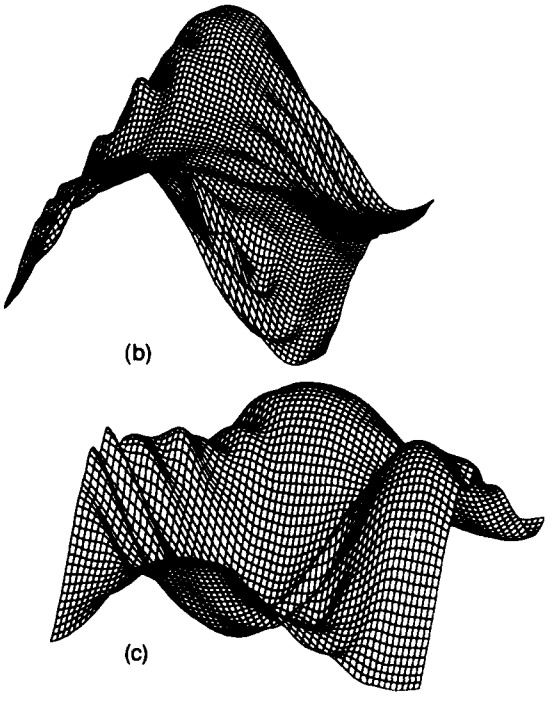

Fig. 5 (cont.).

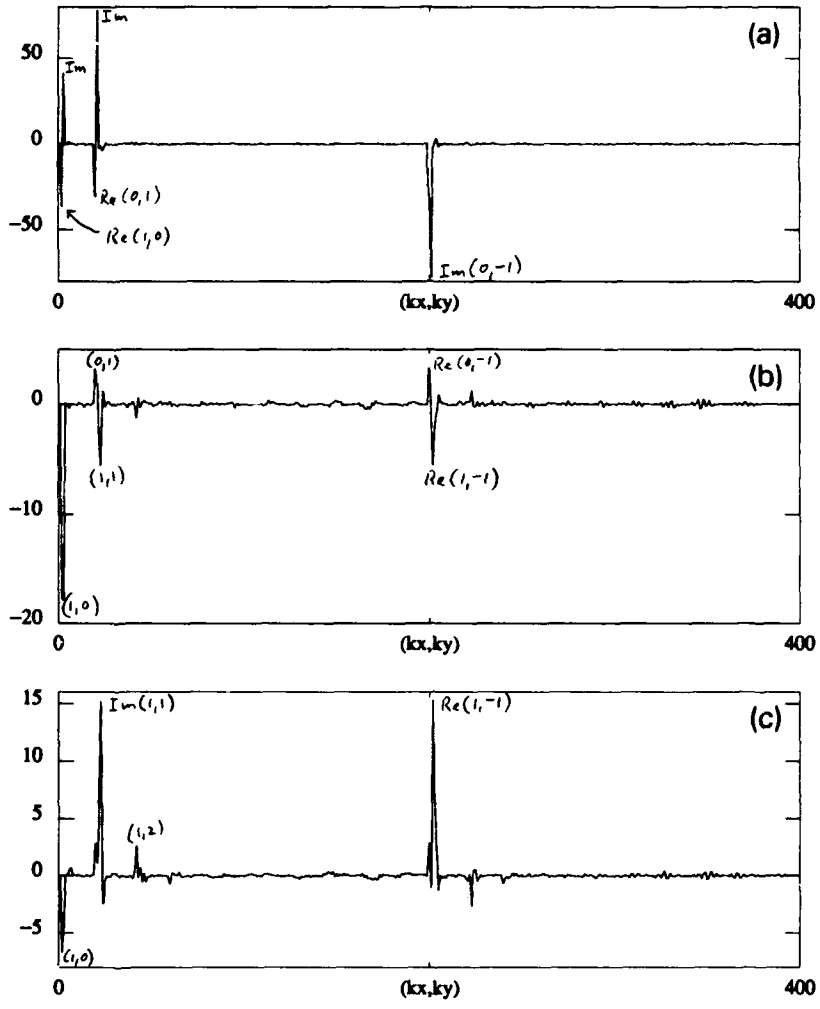

Fig. 6. The first three POD eigenfunctions for the burst phase of the streamfunction data in Fourier space. Compare to fig. 5. Note also that eigenfunction two and three seem to span a complex eigenfunction.

group, then this observation might give us a clue to fully analyze the symmetry operations that are involved with the heteroclinic orbits. However, we have trouble reconstructing the data. Comparing reconstruction and data we see that the large scale flow is resolved well but the characteristic burst dynamics in the center of the two eddies is not captured by the three mode reconstruction. It turns out that a number of modes (e.g. 7, 8, and 11 (see fig. 7) with energies around 0.1%) are very localized on these eddies. Including them in a reconstruction substantially improves it.

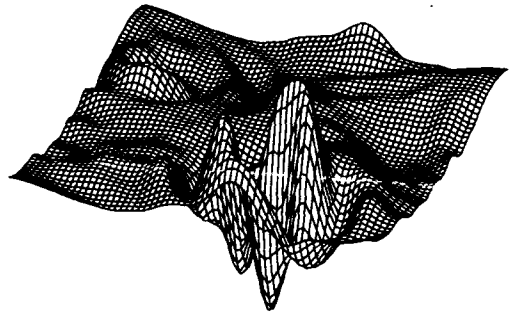

Fig. 7. Eigenfunction eight for the streamfunction data in the burst phase. Energy is only ≈0.1%. Note the highly localized structure in the lower right eddy.

5. Analyzing the vorticity data

Let us consider the flow simulations in a vorticity representation $w = -\nabla^2\psi$ where $\psi(x, y)$ is the streamfunction. Visual inspection of the data in this representation indicates sharper gradients in space and time (i.e., changes in the picture happen more abruptly and with larger amplitude) but a very similar overall dynamics. We note that the POD eigenvalues now physically represent enstrophy, i.e., $\int |w|^2 \, dx \, dy$. It turns out that, although the visual impression of the dynamics is not very different from the dynamics of the streamfunction data, we now need five (eight) POD eigenfunctions to capture 96% (99%) of the energy of the laminar flow. Worse yet, we need 20 POD eigenfunctions for the burst to capture 95% of the energy. Also, typically these eigenfunctions have a very complicated Fourier spectrum, showing substantial contributions from the smaller scales (fig. 9).

It seems, however, that these Fourier spectra lead to constructive interference such that the corresponding transformed functions in physical space lead to relatively smooth structures (fig. 8). Inspecting the POD eigenfunctions in the laminar and bursting regime we find that the first two eigenfunctions are roughly the same whereas the third eigenfunction (figs. 8, 9) for the burst is a new one which cannot be found among the first

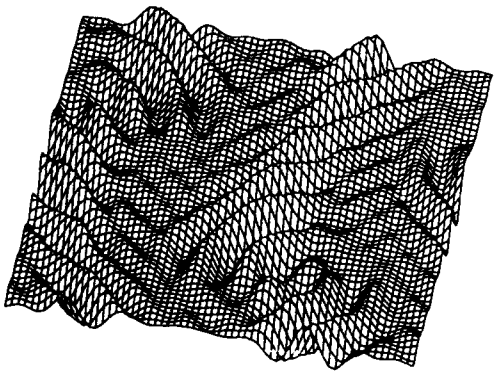

Fig. 8. Third POD eigenfunction of the vorticity data in the burst phase. This eigenfunction captures an energy of about 8.7% and seems to play no role in the dynamics of the laminar phase.

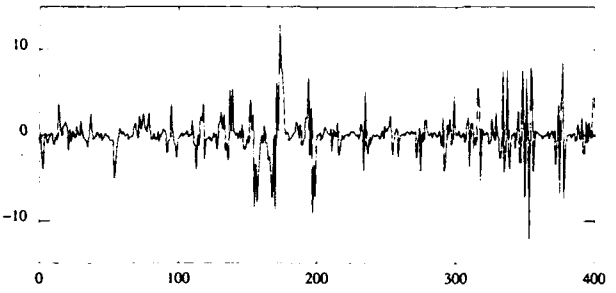

Fig. 9. Third POD eigenfunction of the vorticity data in the burst phase in Fourier space. See fig. 8.

five of the laminar regime. This indicates, as with the streamfunction data, that this mode could be responsible for the bursting dynamics. Reconstruction and visual comparison shows that about eight eigenfunctions in the laminar case and 15 in the bursting capture the small scale dynamics in the eyes of the eddies reasonably well whereas a smaller number of modes (around five and ten) seem to capture the large scale dynamics. Due to the more pronounced nature of the small scale activity in the vorticity data it is more difficult to separate small and large scales visually.

6. Conclusion

Due to the ongoing nature of this research only few definite conclusions can be drawn but several interesting comments and speculations are in order.

– Clearly the laminar phase is a modulated traveling wave. Its wavespeed can be calculated by observing the change in phase of a Fourier mode. In a coordinate frame moving with the traveling part, the oscillation is described by a limit cycle which is spanned by the first two eigenfunctions of the POD decomposition for the streamfunction data. We independently confirmed this by extracting a scalar "averaged" quantity from the field (summing up a norm over a 16×16 grid in physical space). On the time series for that scalar quantity we performed a time-delay embedding and calculated the fractal

dimension d_F [10]. For both streamfunction and vorticity data we found $d_F = 1.0$.

– There exists a low dimensional large scale dynamics that drives the burst. The unstable manifold of the laminar phase apart from containing the T^2-torus is very flat, concentrating the burst mainly along one dimension. This is again supported by plots of a time-delay embedding. Fig. 10 shows such a two-dimensional time-delay plot. One sees the remnants of the basic limit cycle with faster oscillations superimposed. Computations of fractal dimensions suffer from too small a data set and are not very accurate. Initial calculations give $d_F = 1.24$ and $d_F = 1.65$ for streamfunction and vorticity data, respectively. Both numbers are consistent with a POD embedding dimension between three and five.

– The biggest mystery of this analysis is the large discrepancy between the number of relevant eigenfunctions for streamfunction and vorticity data. From a dynamical systems point of view, if this system has a finite dimensional attractor then there exists only *one* dimension and all numbers for vorticity and streamfunction should agree with each other. However, the Laplacian obviously acts as a nonlinear weight function giving largest weight to the smallest scales of the PDE simulation. Therefore the general noise level of the vorticity data is increased up to a margin of about 5% of the POD energy. In order to check the dependence of the POD results on the resolution of the PDE simulation we enlarged our data set and used *all* Fourier modes available from the 64×64 pseudo-spectral grid. The result is that we needed even more POD eigenfunctions (25 versus 20) to capture 95% of the energy in the vorticity burst data. At the same time visual inspection of the reconstruction was satisfactory with fewer POD modes (10 modes versus 16). These results suggest that there are two types of dynamics going on during the burst phase: A large scale, low dimensional one which can be described by a structurally stable homoclinic orbit and which has very definite symmetry properties. This dynamics is best captured by looking at the behavior of the streamfunction. Riding on top of that dynamics is a small-scale dynamics characterized by an enstrophy cascade: Enstrophy is accumulating in the modes which are barely resolved and have the smallest scales. Better spatial resolution leads to an accumulation of enstrophy in the new, yet smaller scales. Such an enstrophy cascade during a burst was already pinpointed in ref. [1]. While some of these scales which do not belong to the large-scale dynamics have some distinct visual impact on the flow – they drive the burst in the eyes of the eddies – we believe the modes in the enstrophy cascade to be basically driven by the large-scale dynamics and noise. In particular, they possibly play a role in triggering the burst event and hence in the randomness of the time between bursts, but they do not contribute to the overall shape of the attractor. This view is consistent with recent two fluids turbulence theories and with a similar study of intermittent behavior in boundary layers triggered by midstream pressure fluctuations [17].

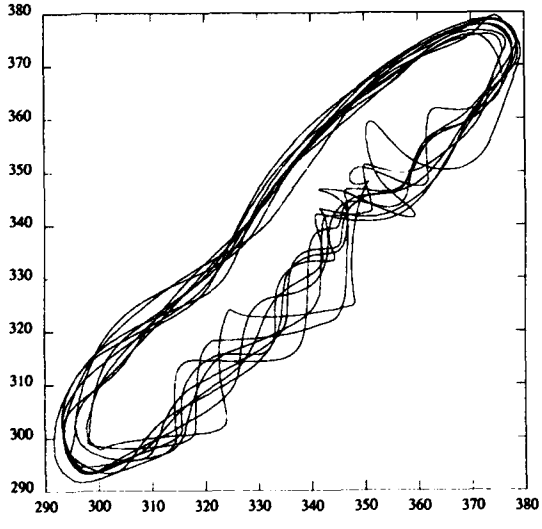

Fig. 10. Two-dimensional time-delay plot for an averaged scalar function of the vorticity field. One can distinguish a laminar dynamics following closely the original limit cycle and a faster, oscillatory phase with motion transverse to the limit cycle.

Acknowledgement

We thank Z.S. She for the use of his Kolmogorov flow simulation code and for fruitful discussions. This research was supported by the Air Force Office for Scientific Research through its URI grant to the Mathematics Department at ASU and through NSF grant DMS-9017174.

References

[1] B. Nicolaenko and Z.S. She, Symmetry-breaking homoclinic chaos in the Kolmogorov flows, in: Nonlinear World, Intern. Workshop on Nonlinear and Turbulent Processes in Physics (Kiev, 1989), eds. V.G. Baryakhtar et al. (1990) p. 602.

[2] J. Guckenheimer and P.J. Holmes, Math. Proc. Camb. Phil. Soc. 103 (1988) 189.

[3] D. Armbruster, J. Guckenheimer and P.J. Holmes, SIAM J. Appl. Math. 49 (1989) 676.

[4] J.L. Lumley, in: Atmospheric Turbulence and Radio Wave Propagation, eds. A.M. Yaglom and V.I. Tatarski (Nauka, Moscow), (1967) 166.

[5] L. Sirovich, Quart. Appl. Math. Vol XLV (3) (1987) 561.

[6] N. Aubry, R. Guyonnet and R. Lima, Spatio-temporal symmetries and bifurcations via the bi-orthogonal decomposition, preprint (1991); N. Aubry, W.-Y. Lian and E. Titi, Preserving symmetries in the proper orthogonal decomposition, preprint (1991).

[7] M. Kirkby and D. Armbruster, Reconstructing phase space for PDE simulations, to appear in ZAMP (1992).

[8] Z.S. She, Proc. on Current Trends in Turbulence Research, AIAA (1988) p. 374.

[9] Z.S. She and B. Nicolaenko, in: Topological Fluid Mechanics, eds. H.K. Moffatt, (Cambridge Univ. Press, Cambridge, 1990) p. 256.

[10] E.J. Kostelich and H.L. Swinney, Phys. Scr. 40 (1989) 436.

[11] L.D. Meshalkin and Ya. G. Sinai, J. Appl. Math 25 (1961) 1700.

[12] A.A. Nepomnyachtchyi, Prikl. Math. Makh. 40 (1976) 886.

[13] G.I. Sivashinsky, Physica D17 (1985) 243.

[14] Z.S. She, Phys. Lett. A 124 (1987) 161.

[15] N. Platt, L. Sirovich and N. Fitzmaurice, Phys. Fluids A 3 (1991) 681.

[16] B. Nicolaenko and Z.S. She, Eur. J. Mech. B/Fluids 10 (1991) 67.

[17] N. Aubry, P. Holmes, J.L. Lumley and E. Stone, J. Fluid Mech. 192 (1988) 115.

Physica D 58 (1992) 402–406
North-Holland

PHYSICA D

Low dimensional models of the wall region in a turbulent boundary layer: New results*

Gal Berkooz[a], Philip Holmes[b] and John L. Lumley[c]

[a]*Center for Applied Mathematics, Cornell University, Ithaca, NY 14853, USA*
[b]*Theoretical and Applied Mechanics, Center for Applied Mathematics, Cornell University, Ithaca, NY 14853, USA*
[c]*Sibley School of Mechanical and Aerospace Engineering, Cornell University, Ithaca, NY 14853, USA*

Received 13 September 1991
Revised manuscript received 10 February 1992
Accepted 15 February 1992

Using an optimally convergent representation, a low dimensional model is constructed, which embodies in a streamwise-invariant form the effects of streamwise structure. Results of Stone show that the model is capable of mimicking the stability change due to favorable and unfavorable pressure gradients. Results of Aubry et al. suggest that polymer drag reduction is associated with stabilization of the secondary instabilities, as has been speculated. Results of Bloch and Marsden indicate that drag can be reduced by feedback, and that this is mathematically equivalent to polymer drag reduction. The authors showed that dynamical systems based on the Proper Orthogonal Decomposition have, on the average, the best short term tracking time (the time that a model tracks the true system accurately; essential for control) for a given number of modes. In recent work, the authors have shown that several assumptions made on an intuitive basis in the work of Aubry et al. may be justified formally. Berkooz has made rigorous estimates using the proper orthogonal decomposition showing that a structured turbulent flow, such as the wall layer, has a phase space representation that remains within a thin slab centered on the most energetic modes for most of the time. Campbell and Holmes have shown several results in connection with symmetry breaking in systems with structurally stable heteroclinic cycles. This work is relevant to our models of interacting coherent structures in boundary layers with discrete spanwise symmetry, such as that caused by riblets, which are known to produce drag reduction.

1. Background

Objective analysis of experimental measurements indicates that there are recurrent streamwise rolls present in the wall region, at least in the quadratic mean sense [16, 23]. Representation theorems [24] permit optimal expansion of the instantaneous velocity field in the wall region in terms of these streamwise rolls [25]. Without involving ourselves in the question of the source of these rolls, we ask how they will behave dynamically. Severely truncating our system, and using Galerkin projection, we obtain a closed set of non-linear ordinary differential equations with ten degrees of freedom. The methods of dynamical systems theory are applied to these equations. Loss to unresolved modes is represented by a Heisenberg parameter [6].

We find that for large values of the Heisenberg parameter (large loss), we obtain stable streamwise rolls having the experimentally observed spacing. For smaller values of the parameter, we have traveling waves (corresponding to cross-stream drift of the rolls); we also find a hetero-

* Supported in part by Contract No. AFOSR 89-0226, jointly funded by the US Airforce Office of Scientific Research (Control and Aerospace Programs) and the US Office of Naval Research, in part by the US National Aeronautics and Space Administration, Langley Research Center, under Contract No. NAG-1-954, and in part by the US National Science Foundation under Grants Nos. DMS-88-14553 and MSM 86-11164.

0167-2789/92/$05.00 © 1992 – Elsevier Science Publishers B.V. All rights reserved

clinic attracting orbit giving rise to intermittency; and finally a chaotic state showing ghosts of all of the above.

The intermittent jump from one equilibrium point to the other in the heteroclinic case resembles in many respects the burst observed in experiments. Specifically, the time between jumps, and the duration of the jumps, is approximately that observed in a burst; the jump begins with the formation of a narrowed and intensified updraft, like the ejection phase of a burst, and is followed by a gentle, diffuse downdraft, like the sweep phase of a burst. During the jump a spike of Reynolds stress is produced, as is observed in a burst, although the magnitude is limited in our model by the truncation of the high wavenumber components.

The behavior is quite robust, much of it being due to the symmetries present (Aubry's group has examined dimensions up to 64 real and demonstrated persistence of the global behavior [4]). We have examined eigenvalues and coefficients obtained from experiment [18], and from exact simulation [29], which differ in magnitude. Similar behavior is obtained in both cases; in the latter case, the heteroclinic orbits connect limit cycles instead of fixed points, corresponding to cross-stream waving of the streamwise rolls. The bifurcation diagram remains structurally similar, but is somewhat distorted.

The role of the pressure term derived from the permeable boundary between the wall region and the outer layer is made clear – it triggers the intermittent jumps, which otherwise would occur at longer and longer intervals, as the system trajectory is attracted closer and closer to the heteroclinic cycle. The pressure term results in the jumps occurring at essentially random times, and the magnitude of the signal determines the average timing. This clarifies the question of whether bursting scales with wall variables or with outer variables – evidently the structure of a burst scales with wall variables, while the time between bursts should scale in a complex way with both inner and outer variables [30, 31].

Change of the third order coefficients, corresponding to acceleration or deceleration of the mean flow, changes the heteroclinic cycles from attracting to repelling, increase or decreasing the stability, in agreement with observations [30].

The existence of fixed point is an artifact introduced by the projection; however, a decoupled model still displays the rich dynamics [8, 12, 20].

2. Recent work

In recent work, Berkooz [7, 8], in collaboration with Holmes and Lumley, has shown that several assumptions made on an intuitive basis in the work of Aubry et al. may be justified formally, namely: that the Heisenberg model used gives the correct dissipation within a constant of order unity, as assumed; that the Leonard stresses (stresses coming from resolved modes–unresolved modes interaction) may be neglected in the case of modeling with no streamwise variation, as assumed; that the previous result holds for an arbitrary number of eigenfunctions when no streamwise variation is present; that models with no streamwise variation in effect average the streamwise dynamics, as conjectured by Holmes.

In connection with our attempts to control the wall region, Berkooz [8] introduced the notion of short term tracking T_s. Consider the wall layer starting from an initial condition. The model starts from an initial condition which is the projection of the initial condition for the full system. If one fixes a distance in phase space, ε, one expects that the dynamics of the model and those of the projection of the full system will diverge. The time it takes this divergence to get to size ε (on the average) is T_s and measured in wall units. This is a measure of the time over which a dynamical systems model tracks the true dynamics accurately. T_s is of fundamental importance in the control application, and it must be of the order of the wall-region time scales to make control possible. Berkooz [8] then showed

that dynamical systems based on the proper orthogonal decomposition have, on the average, the best T_s for a given number of modes.

Berkooz [7] has made rigorous estimates using the proper orthogonal decomposition showing that a structured turbulent flow, such as the wall layer, has a phase space representation that remains within a thin slab centered on the most energetic modes for most of the time. This result appears in a seminal form in Foias et al. [17] and was shown independently by Aubry et al. [5]. However, exits from this region, which is all that our low-dimensional models include, should not be ignored, since they typically correspond to violent events, such as the bursting phenomenon. Berkooz and Holmes are trying to develop a theory in which deterministic, low-dimensional dynamics governing the low modes apply most of the time, passages from and returns to this being modeled probabilistically. This might be viewed as a dynamical closure. They plan to test their theory on problems including the 32 and 54 dimensional projections of Aubry and Sanghi.

Campbell and Holmes [15] are continuing their studies of breaking translation/reflection symmetry into discrete translation and reflection, specifically dihedral, $(O(2) \to D_4)$ in systems with structurally stable heteroclinic cycles. They have proved that no analytic (second) integral of motion exists in a certain limiting case and that only two pairs of the continuum of O(2) symmetric heteroclinic cycles persist in general. They are studying the bifurcations from these survivors. This work is relevant to our models of interacting coherent structures in boundary layers with discrete spanwise symmetry, such as that caused by riblets. This is to our knowledge the first analytical contribution to our understanding of the drag reduction caused by riblets.

3. Control

Polymer drag reduction is known to increase the time between bursts, and to increase the scale of the wall region, leaving it geometrically the same [27]. In our model, stretching of the wall region to increase its scale reduces the drag, and requires stabilization of the bursts, to increase the time between bursts [5]. It is thus completely consistent with the observations. Our sort of relatively simple model could be used as a "black box" in active feed-back systems to control the boundary layer. Bloch and Marsden [14] showed that feeding back eigenfunctions with the proper phase (in the presence of noise) can delay the bursting, (the heteroclinic jump to the other fixed point), thereby decreasing the average drag. It is also possible to speed up the bursting, thus increasing mixing, to control separation Bloch and Marsden [5] also showed that polymer drag reduction is formally equivalent to delaying the bursts by active feedback (increasing the mean time between bursts. Hence, we may expect an actively controlled layer to resemble a passively polymer-drag-reduced layer.

The simplest system that contains the essential features of our low-dimensional model is the O(2)-symmetric 1:2 wavenumber interaction studied by Armbruster et al. [1]. This is the simplest system that shares the essential properties of the models developed by Aubry et al. [6]. This can be written in complex modal coordinates (spanwise Fourier amplitudes) a_j as

$$\begin{aligned} \partial_t a_1 &= a_1^* a_2 + a_1(\mu_1 + e_{11}|a_1|^2 + e_{12}|a_2|^2) \\ &\quad + \varepsilon \xi_1(t)\,, \\ \partial_t a_2 &= -a_1^2 + a_2(\mu_1 + e_{21}|a_1|^2 + e_{22}|a_2|^2) \\ &\quad + \varepsilon \xi_2(t)\,, \end{aligned} \tag{1}$$

where the $\xi_j(t)$ are complex valued IID Wiener processes representing the pressure perturbation from the outer part of the boundary layer. With suitable choices of the real parameters μ_j, e_{ij}, for $\varepsilon = 0$, this system has attracting heteroclinic cycles which for $\varepsilon > 0$ lead to bursts at irregular intervals with a skewed distribution of interevent times having an exponential tail remark-

ably similar to those seen experimentally [22, 30].

It was felt that the energy expenditure required for conventional stabilization of the saddle points in heteroclinic cycles (and hence complete suppression of bursting) might be excessive and that a more modest strategy of *delaying* bursting should be developed. Consequently, in their preliminary study of control strategies for ODEs such as (1) [14] explored this possibility primarily by shifting the saddle eigenvalues toward the left-hand half of the complex plane. This was done in the context of linear control by adding a term $\mathrm{Ba} = -\beta\,\mathrm{diag}\{\mu_1^2 a_1, \mu_2^2 a_2\}$ to (1), which shifts the unstable eigenvalue λ_u leftward by $O(\beta)$. In physically relevant parameter regimes the system (1) has only one unstable eigenvalue. Since the mean interburst time is $\langle T\rangle = \lambda_u^{-1}\ln(1/\varepsilon)$ and the distribution tail goes as $\exp(-\lambda_u T)$ [31, 32], any such reduction in λ_u delays bursting on average.

The substantial problem of designing and implementing a feedback law to effect this has not yet been addressed. The general idea is to construct a "smart" wall, with sensors and actuators (piezoelectric or magnetoelastic) to effect local geometry changes at the wall in response to sensed velocity fields, hence modifying the coherent structures. This, in turn, changes the coefficients of the model. We do not yet know specific details (direct numerical simulations are being undertaken to investigate them), but it is clear that, in general, *all* the coefficients e_{ij} and μ_j, nonlinear as well as linear, will be affected, and therefore we are really in the realm of nonlinear control rather than the linear controller assumed by Bloch and Marsden [14].

A second complication of the simple strategy proposed by Bloch and Marsden [14] is that models such as that above, and the multi-mode elaborations of Aubry et al. [6], are local, since they are produced by projection of the governing equations on a small domain. The modeling strategy relies on the fact that this domain is large enough to contain a range of structures, yet small enough that bursts do not occur in it at all times, and hence one does not average away the dynamics [8, 20]. In common with the strategy of numerical simulations, one assumes that a two-dimensional array of such periodic domains covering a large surface will adequately reproduce the statistics of an extended turbulent layer. In reality, exactly periodic arrays of structures all bursting in step are not seen and phase relationships between distant spacial points may not be simple. Thus, to adequately model a spacially extended boundary layer, one should probably take an array of systems such as the above, weakly coupled and excited by weakly correlated "pressures" $\xi_j(t)$. As far as we know, the problem of controlling such a distributed nonlinear system, with stochastic excitation but strong underlying symmetry and phase space structure of this individual units, has not yet been addressed.

We are currently studying the construction and properties of extended models using projection onto spacially localized wavelet bases [9]. The Kuramoto–Sivashinsky equation, more tractable than the full boundary layer problem but sharing features such as symmetries and heteroclinic cycles [2], is being used in this work. Once these systems are better understood, it will be possible to pose the control problem more clearly.

References

[1] D. Armbruster, J Guckenheimer and P. Holmes, Physica D 29 (1988) 257.

[2] D. Armbruster, J. Guckenheimer and P. Holmes, SIAM J. Appl. Math. 49 (1989) 676.

[3] N. Aubry, R. Guyonnet and R. Lima, J. Stat. Phys. 64 (314) (1991) 683.

[4] N. Aubry and S. Sanghi, Proc. July meeting of ASME, New York, ed. Ghia.

[5] N. Aubry, P. Holmes and J.L. Lumley, Theor. Comput. Fluid Dynam., 1 (1990) 229.

[6] N. Aubry, P. Holmes, J.L. Lumley and E. Stone, J. Fluid Mech. 192 (1988) 115.

[7] G. Berkooz, in: The Lumley Symposium: Recent Developments in Turbulence, eds. T. Gatski and C. Speziale (Springer, Berlin), to appear.

[8] G. Berkooz, Ph.D. Thesis (Cornell, Ithaca, 1991).

[9] G. Berkooz, J. Elezgaray and P. Holmes, Proc. DARPA/ONERA Conf. on Wavelets and Applications, (Princeton, June 1991).
[10] G. Berkooz, J. Guckenheimer, P. Holmes, J.L. Lumley, J. Marsden, N. Aubry and E. Stone, AIAA Paper No. 90–1639 (1990).
[11] G. Berkooz, P. Holmes and J.L. Lumley, in: The Global Geometry of Turbulence ed. Javier Jiménez (Springer, Berlin, 1990), in press.
[12] G. Berkooz, P. Holmes and J.L. Lumley, J. Fluid Mech. 230 (1991) 75.
[13] G. Berkooz, P. Holmes and J.L. Lumley, Decaying turbulence and heteroclinic cycles in the wall layer. in preparation.
[14] A.M. Bloch and J.E. Marsden, Theoretical and Comput. Fluid Dynamics. 1 (3) (1989) 179.
[15] S. Campbell and P. Holmes, Bifurcation from O(2)-symmetric heteroclinic cycles with three interacting modes, Nonlinearity, in press.
[16] E.R. Corino and R.S. Brodkey, J. Fluid Mech. 37 (1) (1969) 1.
[17] C. Foias, O. Manley and L. Sirovich, Phys. Fluids A, 2 (1990) 464.
[18] S. Herzog, The large scale structure in the near-wall region of turbulent pipe flow, Ph.D. thesis, Cornell University (1986)
[19] P.J. Holmes, in: Whither Turbulence? Turbulence at the crossroads, Lecture Notes in Physics Vol. 357, ed. J.L. Lumley (Springer, Berlin, 1990) 195.
[20] P.J. Holmes, Appl. Mech. Rev. 43 (5,2) (1990) S23.
[21] P.J. Holmes, in: Whither Turbulence? Turbulence at the crossroads. Lecture Notes in Physics Vol. 357, ed. J.L. Lumley (Springer, Berlin, 1990) p. 306.
[22] P. Holmes and E. Stone, in: The Lumley Symposium: Recent Developments in Turbulence, eds. T. Gatski and C. Speziale, (Springer, Berlin), to appear.
[23] S.J. Kline, W.C. Reynolds, F.A. Schraub and P.W. Rundstadler, J. Fluid Mech. 30(4) (1967) 741.
[24] M. Loève, Probability Theory (Van Nostrand, New York, 1955).
[25] J.L. Lumley, in: Atmospheric Turbulence and Radio Wave Propagation, eds. A.M. Yaglom and V.I. Tatarski (Nauka, Moscow, 1967). p. 166–178.
[26] J.L. Lumley, in: Transition and Turbulence, ed. R.E. Meyer (Academic Press, New York, 1981) p. 215.
[27] J.L. Lumley and I. Kubo, in: The Influence of Polymer Additives on Velocity and Temperature Fields, ed. B. Gampert (Springer, Berlin, 1985) p. 3.
[28] H.K. Moffat, Fixed points of turbulent dynamical systems and suppression of non-linearity, in: Whither Turbulence? Turbulence at the crossroads. Lecture Notes in Physics Vol. 357, ed. J.L. Lumley (Springer, Berlin, 1989) p. 250.
[29] P. Moin, in: Proc. AIAA 22nd Aerospace Sciences Meeting (1984).
[30] E. Stone and P. Holmes, Physica D 37 (1989) 20.
[31] E. Stone and P. Holmes, SIAM J. Appl. Math. 50 (1990) 726.
[32] E. Stone and P. Holmes, Phys. Lett. A 155 (1991) 29.
[33] E. Stone, A Study of Low Dimensional Models for the Wall Region of a Turbulent Boundary Layer. Ph.D. Thesis (Cornell University, Ithaca, NY, 1989).

Physica D 58 (1992) 407–413
North-Holland

PHYSICA D

Complex bi-orthogonal decomposition of a chain of coupled wakes

M.P. Chauve and P. Le Gal

UM0033, Université d'Aix-Marseille II, C.N.R.S., Institut de Mécanique Statistique de la Turbulence, 12, Avenue du Général Leclerc, 13003 Marseille, France

Received 9 October 1991
Revised manuscript received 3 February 1992
Accepted 7 February 1992

This work is devoted to the experimental analysis of the flow created by a row of cylinders. As each cylinder wake appears by the Hopf bifurcation of a global oscillating mode, this experiment is similar to a chain of coupled non-linear oscillators and this dynamic system can be modelled using a Ginzburg–Landau type equation. A video analysis technique is performed on visualization pictures in order to obtain the spatio-temporal evolution of the wakes. This diagram is then analysed using the bi-orthogonal decomposition extended to its complex form. It is shown that only a few eigenmodes are excited, giving a low-dimensional dynamic system that enables the different parameters of the model to be estimated.

1. Introduction

The goal of our experimental analysis is the study of the flow consisting of a row of coupled wakes [1]. The so-called Bénard–Von Karman street appearing in the wake of a cylinder by the Hopf bifurcation of a global mode [2], constitutes one of the most simple non-linear oscillators of fluid mechanics. If we consider a row of N parallel cylinders placed in a plane perpendicular to a flow, the row of wakes is similar to a chain of non-linear coupled oscillators, and can be modelled using the system of N equations [3]:

$$\frac{\mathrm{d}A_i(t)}{\mathrm{d}t} = (j\omega + \varepsilon(1 + \mathrm{j}c_0))A_i(t) - (1 + \mathrm{j}c_2)|A_i(t)|^2 A_i(t) + \nu(1 + \mathrm{j}c_1) \times (A_{i+1}(t) + A_{i-1}(t) - 2A_i(t)),$$

where A_i represents the complex order parameter associated with the spanwise motions in the wake of the ith cylinder, ε the control parameter of the flow (i.e the reduced Reynolds number), $\omega + \varepsilon c_0$ the natural frequency at the corresponding Reynolds number, and c_2 is a parameter representing the variations of this frequency with non-linearity. The coefficient $\nu(1 + \mathrm{j}c_1)$ gives the complex intensity of the coupling, where an interaction to first neighbours only has been considered. This equation can be seen as a discrete form of the generalized Ginzburg–Landau equation (GGL equation), which represents the spatio-temporal evolution of a system of waves propagating in unstable flows [4]. Recently, some erratic spatio-temporal behaviour has been observed in numerical simulation of the GGL equation [5] and also in some experiments [3, 6]. We can, therefore, assume that the spatial aspect of turbulence, absent in the temporal theories of transition towards deterministic chaos, might be recovered in the notion of spatio-temporal chaos [7]. But the different aspects of the solutions of the GGL equation (laminar or turbulent) depend on the values of its coefficients. For instance, if $1 + c_1c_2 < 0$, the system is unstable and

0167-2789/92/$05.00 © 1992 – Elsevier Science Publishers B.V. All rights reserved

phase turbulence appears [7]. The challenge of our experimental analysis is, therefore, to answer the following questions: Is the GGL equation a good model for our experiment of coupled wakes? If so, are we able to calculate its coefficients?

In order to study the spatio-temporal evolution of these coupled wakes, we apply the bi-orthogonal decomposition [8] to experimental signals resulting from a video image analysis. As the GGL model is written in the complex plane, we first build an analytical signal using the Hilbert transform [9], and secondly apply the bi-orthogonal decomposition in its complex form to determine the eigenmodes of our system. The projection of the GGL equation onto these modes leads to a tensorial equation which generalizes the notion of dispersion relation. The parameters of this relation can be calculated by resolving a system of algebraic equations. Thus we obtain the values of the coefficients of the GGL equation corresponding to our experimental system. A numerical simulation of the model is then realised in order to compare the original flow with the numerical solution.

2. Experimental results

A row of 16 cylinders is placed in the 200 mm × 200 mm working section of a hydrodynamic water tunnel. Each cylinder is 2 mm in diameter and its length is equal to the side of the cross section of the channel. The distance between each cylinder axis is set to a value of 8 mm for which some strong coupling between the vortex streets exist [10]. Through a small aperture (diameter 0.5 mm) in the middle of each cylinder, we inject some dye (an emulsion of silicon oil) in order to visualize the flow. The flow velocity is very low (around 0.04 m/s) and this technique is suitable for visualizing the waves that occur on the streak lines behind each cylinder. Fig. 1 presents a snap-shot of such a visualization for a Reynolds number (based on the cylinder diameter) of 80. This low value has been chosen in order to avoid three-dimensional effects that could take place along the cylinder axes [11]. A successful verification of the bi-dimensionality of the flow allows us to consider the spatio-temporal deformations of the dye filaments as the order parameters describing each wake. We observe in fig. 1 that wakes 4 and 11 have stopped oscillating. These events appear in a completely erratic manner and can affect any wake. We believe that these amplitude holes are similar to some defects discovered recently in a theoretical analysis [12] or in numerical simulations [5] of the GGL equation. As we have no three-dimensional effects, these holes are different from some amplitude modulations that may appear in the wake of one cylinder [11]. The chaotic appearance of these holes seems to be the basic ingredient of the spatio-temporal chaos observed in these different situations and might be a universal process of turbulence genesis.

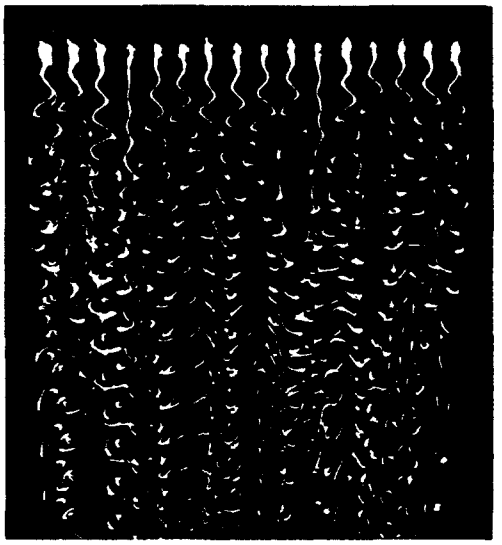

Fig. 1. Snapshot of the flow around the 16 cylinders for a Reynolds number of 80.

To achieve a better understanding of our dynamic system, we build spatio-temporal diagrams using the video movie of our visualization. We realise real-time acquisitions of one video line placed at a distance of 12 mm behind the

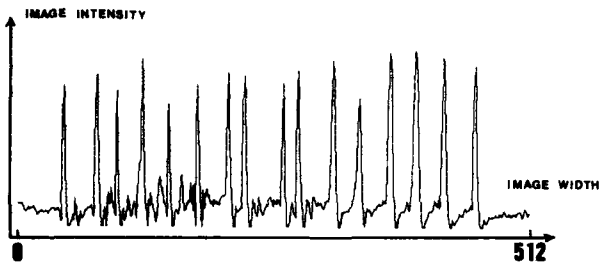

Fig. 2. A video line showing the 16 peaks corresponding to the 16 wakes merging from the noisy background.

row of cylinders. Fig. 2 shows such a line at a given time. It has been digitized on 512 pixels and consists essentially of a row of peaks merging from a constant level. This low level is simply the dark background of the picture and each of the 16 peaks is the intersection of the video line with the white dye streak. The position of the maximum value of each peak is easily obtained and constitutes parameter A_i associated with the ith cylinder. Fig. 3 shows a spatio-temporal diagram composed of 256 lines which have been stored every 40 ms. Several holes are clearly visible and illustrate the complexity of the flow. We observe in this diagram that a difference of about 15% can exist between the frequencies of the coupled oscillators, thus the gradients of phase seem to be at the origin of the formation of the wake oscillation intermittent deaths [5, 1].

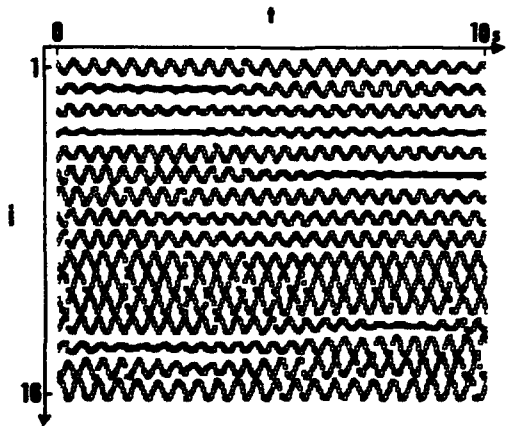

Fig. 3. Spatio-temporal diagram. Some amplitude holes are clearly visible.

To study this diagram in a quantitative manner, we chose to apply the complex bi-orthogonal decomposition to this field. It should be noted that a great advantage of this technique is to catch and synthesize the essential spatio-temporal features of our flow in a set of a few eigenmodes.

3. Bi-orthogonal decomposition

3.1. Analysis tools

Bi-orthogonal decomposition is an extension in space and time of the proper orthogonal decomposition (or the Kahrunen–Loève decomposition) proposed by Lumley [13] for the identification of coherent structures in turbulence. Bi-orthogonal decomposition has only recently been introduced [8] and consists of a decomposition into spatial orthogonal modes, called topos, and temporal orthogonal modes called chronos. It has been shown [8] that a canonical decomposition exists for any complex space-time signals (providing they are finite energy functions of x and t) which can be written as:

$$U(x, t) = \sum_k \alpha_k \bar{\psi}_k(t)\, \varphi_k(x)\,,$$

where the overbar denotes the complex conjugate, α_k are the square roots of the eigenvalues of a spatial (or temporal) two-point correlation function and $\varphi_k(x)$ (or $\psi_k(t)$) are the corresponding spatial (or temporal) eigenfunctions. These two sets of functions are, in fact, composed of orthonormal functions. It follows that an analysis similar to that given by the proper orthogonal decomposition can be performed. It is, however, interesting to mention here that the notion of coherent structures is extended to the time direction: each space structure is associated with a temporal structure: a coherent structure is then defined by a couple of chrono and topo. The energy of a structure is simply given by its eigen-

value and the global energy of the signal is equal to the sum of the eigenvalues:

$$E(u) = \sum_k \alpha_k^2 .$$

The effective number of degrees of freedom of the signal or its dimension is given by the number of non-zero eigenvalues.

Up to now, this decomposition has only been used in its restrictive real form. As the GGL model uses a complex order parameter $A_i(t)$, it is necessary to extend our measurements to the complex plane. This means that each real signal is analytically extended by the calculation of an imaginary part by the use of the Hilbert transform [9]. This transformation is just an amplifier which has a gain of 1 and that shifts the phase of 90°. By this means the bi-orthogonal decomposition can be used in its complex form and takes into account the phase dynamics of the signals (exactly like the sine and cosine functions, both are necessary to represent phase dynamics in the Fourier space).

3.2. *Experimental application*

The spatio-temporal diagram of fig. 3 is supposed to be the real part of a complex field. By using the Hilbert transform we obtain the corresponding imaginary part. This complex field is represented by a matrix of 16 spatial points by 256 temporal ones. As this matrix is not a square matrix, we chose to calculate a spatial correlation matrix which is a tractable 16×16 Hermitian matrix. In order to compute the eigenvalues of this matrix, we first convert it into a 32×32 real symmetric one. Then a Householder reduction to a tridiagonal form followed by a QL iteration [14] is used to obtain the double real eigenvalues α_k^2, and the corresponding complex spatial eigenfunctions $\varphi_k(x)$. The chronos are obtained by a scalar product of the original signals by the topos.

Fig. 4a shows the decrease of $p_k = \alpha_k^2/E$ versus k, which are the normalized energies of each mode k: it will be shown that the energy is concentrated in the first modes. The accumulated energy is presented in fig. 4b where we observe that 90% of the global signal energy is caught only in the first three modes, proving that the dynamics of our system are contained in a low-dimension space.

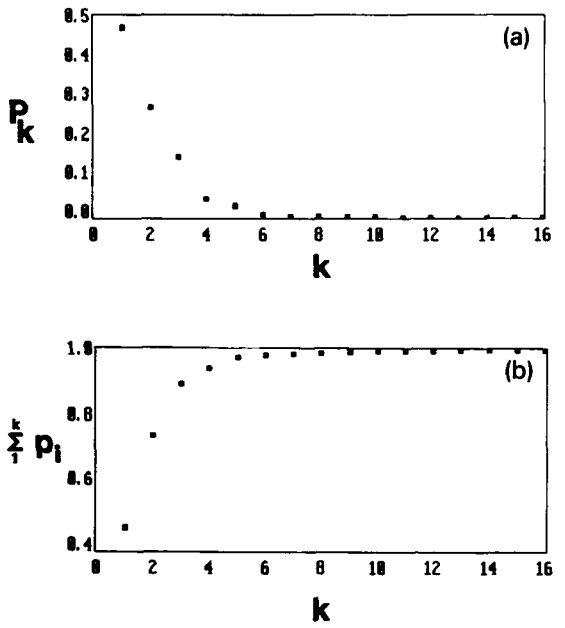

Fig. 4. (a) Evolution of the normalized energy p_k versus the number k of the mode. (b) Cumulated energy showing that only three modes contain 90% of the total energy.

Fig. 5 gives the evolution of the six first complex chronos (fig. 5a: real part, fig. 5b: imaginary part). It can be seen that the first chronos consist of a nearly homogeneous rapid oscillation which characterizes the basic Von Kármán wake. The number of periods present in these functions allows an estimation of the basic frequency of the wakes. The value obtained is 30% lower than the classical value of the Von Karman street [11]. It has been verified that the wakes are bi-dimensional [1] and this implies that this difference cannot be a consequence of an oblique shedding effect [11] and is probably due to the wake coupling. However, this rapid oscillation is modulated in amplitude with a very long period. For

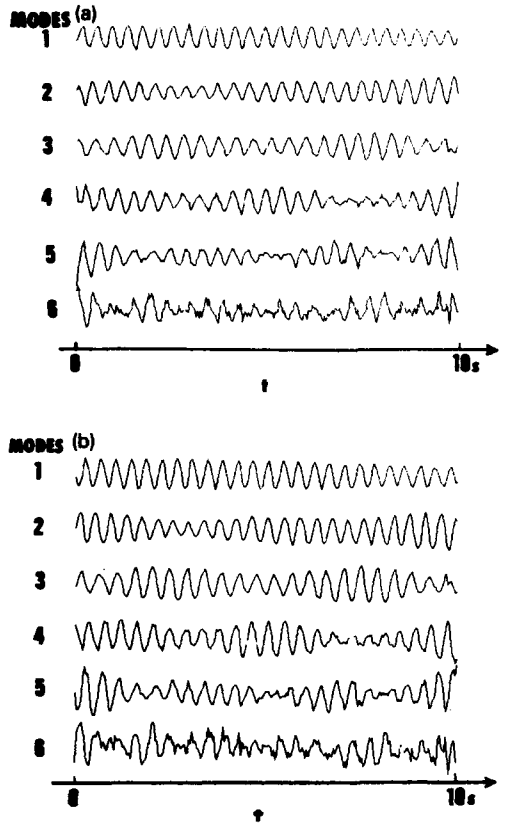

Fig. 5. The real (a) and imaginary (b) parts of the 6 first chronos.

the two first chronos, this period covers the entire temporal window. We would point out that there is a shift of π between the modulations of chronos 1 and 2. Chronos 3 and 4 present the same features, but now the modulations appear twice in the window and there is still a phase of π between both modulations. The fifth chrono is also constituted by the rapid mode which is modulated in amplitude with the third harmonic. Therefore, an entire hierarchy of modulations is captured by this set of chronos. We think that the dynamics of the wake deaths are included in these phase variations of the modulations. In the range 6–16, the chronos carry a small amount of energy and are only linked to the noise.

Fig. 6 is a reconstruction of the real part of the signal on only the first three modes:

$$A_j(t) = \sum_k \alpha_k \bar{\psi}_k(t)\, \varphi_k(i)\,, \quad k = 1, 3\,.$$

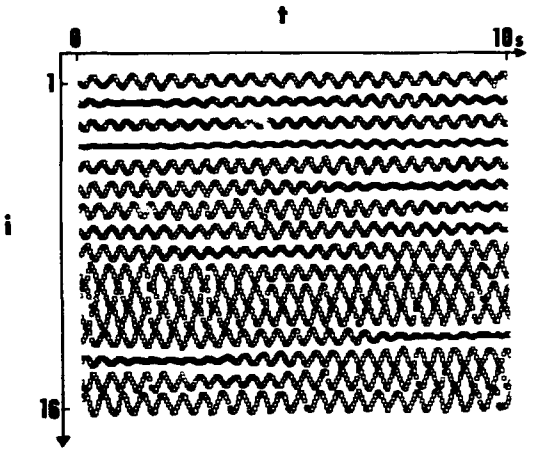

Fig. 6. Real part of the calculated signal on the three first modes.

We can verify that this spatio-temporal diagram agrees very well with the original measured one in fig. 3. Up to now, we have not been able to see any remarkable features on the topos.

4. Comparison with the GGL model

Having calculated the decomposition of the complex field $A_i(t)$ on the two sets of orthonormal functions:

$$A_i(t) = \sum_k \alpha_k \bar{\psi}_k(t)\, \varphi_k(i)\,,$$

we project the function $|A_i(t)|^2 A_i(t)$, which appears in the GGL equation onto the same set of chronos and topos:

$$|A_i(t)|^2 A_i(t) = \sum_{jk} \beta_{jk} \bar{\psi}_j(t)\, \varphi_k(i)\,.$$

By replacing these two functions with their expressions in the GGL equation, we obtain:

$$\sum_k \alpha_k \frac{\mathrm{d}\bar{\psi}_k(t)}{\mathrm{d}t}\, \varphi_k(i) = [\mathrm{j}\omega + \varepsilon(1 + \mathrm{j}c_0)] \sum_k \alpha_k \bar{\psi}_k(t) \times \varphi_k(i) - (1 + \mathrm{j}c_2) \sum_{jk} \beta_{jk} \bar{\psi}_j(t)\, \varphi_k(i) + \nu(1 + \mathrm{j}c_1) \sum_k \alpha_k \bar{\psi}_k(t)[\varphi_k(i+1) + \varphi_k(i-1) - 2\varphi_k(i)]\,.$$

Using the properties of orthonormality of the topos and chronos, we project this equation first onto $\bar{\varphi}_l$:

$$\alpha_l \, \mathrm{d}\bar{\psi}_l(t)/\mathrm{d}t = [\mathrm{j}\omega + \varepsilon(1 + \mathrm{j}c_0)]\alpha_l\bar{\psi}_l(t) - (1 + \mathrm{j}c_2)\sum_j \beta_{jl}\bar{\psi}_j(t) + \nu(1 + \mathrm{j}c_1)\sum_k \alpha_k\bar{\psi}_k(t)\langle\bar{\varphi}_l(i)/(\varphi_k(i+1) + \varphi_k(i-1) - 2\varphi_k(i))\rangle_i ,$$

where $\langle / \rangle_i$ represents the scalar product of topos. Then, in the same manner, we project again this last equation onto ψ_s:

$$\alpha_l\langle(\mathrm{d}\bar{\psi}_l(t)/\mathrm{d}t)/\psi_s\rangle_t = (\mathrm{j}\omega + \varepsilon(1 + \mathrm{j}c_0))\alpha_l\delta_{sl} - (1 + \mathrm{j}c_2)\beta_{sl} + \nu(1 + \mathrm{j}c_1)\alpha_s\langle\bar{\varphi}_l(i)/(\varphi_s(i+1) + \varphi_s(i-1) - 2\varphi_s(i))\rangle_i ,$$

where $\langle / \rangle_t$ is now the scalar product between two chronos, and δ_{sl} the Kronecker symbol. We note Ω_{sl} the term $\langle(\mathrm{d}\bar{\psi}_l(t)/\mathrm{d}t)/\psi_s\rangle_t$ and K_{sl} the term $\langle\bar{\varphi}_l(i)/(\varphi_s(i+1) + \varphi_s(i-1) - 2\varphi_s(i))\rangle_i$ in order to write the GGL equation in the following condensed form:

$$\alpha_l\Omega_{sl} = (\mathrm{j}\omega + \varepsilon(1 + \mathrm{j}c_0))\alpha_l\delta_{sl} - (1 + \mathrm{j}c_2)\beta_{sl} + \nu(1 + \mathrm{j}c_1)\alpha_s K_{sl} .$$

The quantities Ω_{sl}, β_{sl} and K_{sl} can be calculated from the eigenfunctions obtained previously. If we call C_0 the quantity $(j\omega + \varepsilon(1 + jc_0))$, C_1 the quantity $\nu(1 + \mathrm{j}c_1)$, C_2 the quantity $(1 + \mathrm{j}c_2)$ and γ_{sl} the ratio β_{sl}/α_l, the last equation can be written in the following way:

$$\Omega_{sl} = C_0\delta_{sl} - C_2\gamma_{sl} + C_1(\alpha_s/\alpha_l)K_{sl}$$

This relation is an extension of the dispersion relation of the Fourier space. The anti-hermitian tensor Ω_{sl} is a generalization of the notion of frequency and the Hermitian tensor K_{sl} a generalization of the notion of wavenumber.

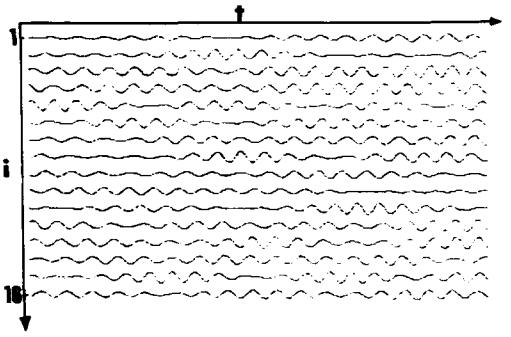

Fig. 7. Real part of a simulated field using the calculated coefficients from the experimental analysis (arbitrary units).

Therefore, the problem we are dealing with is obtaining the equation of the plane representing this dispersion relation in the space (γ, Ω, K). From the previously performed analysis, three different triplets $(\gamma_{II}, \Omega_{II}, K_{II})$ can be calculated from the first three most energetic modes. The resolution of three linear equations leads to the three parameters C_0, C_1 and C_2 and finally to an estimation of the three numerical coefficients of the GGL equation. With these coefficients, it is possible to come back to the model and perform a numerical simulation. An example of such a result is presented in fig. 7 where some holes of amplitude can be observed as in the original signal (see fig. 3).

5. Conclusion

As in numerical simulations of the generalized Ginzburg–Landau equation, spatio-temporal chaos has been observed in an experiment of coupled wakes. This chaos is apparent in the erratic formation of amplitude extinctions of the Bénard–Von Kármán streets. This dynamic system has been analysed by the use of a video imaging system and analytically extended to the complex plane using the Hilbert transform. In order to extract the most energetic space-time structures and use them as a basic set of functions to project the GGL model, a complex bi-orthogonal decomposition has been per-

formed. It has been shown that the dynamics of the system studied is included in a three-dimensional proper space. The concerned eigenmodes present long wave modulations which contain the dynamics of amplitude holes. The projection of the GGL equation onto the first three eigenmodes leads to a generalized dispersion relation whose solution produces an estimation of the GGL coefficients. A numerical simulation with these last coefficients shows behaviour similar to the experimental system. Thus we confirm that the GGL equation is a good model for our experimental coupled wakes. In particular, the chaotic appearance of these holes (experimental or numerical) seems to be a universal process of turbulence genesis requiring further investigation.

References

[1] P. Le Gal, Compt. Rend. Acad. Sci. Paris, 313 (1991) 1499.

[2] M. Provansal, C. Mathis and L. Boyer, J. Fluid Mech. 182 (1987) 1; J.M. Chomaz, P. Huerre and G. Redekopp, Phys. Rev. Lett. 60 (1988) 25; K.R. Sreenivasan, P.J. Strykowsky and D.J. Olinger, in: Proc. Forum Unsteady Flow Sep., Ed. K.N. Ghia 52 (ASME, New York, 1990) p. 1.

[3] O. Cardoso, H. Willaime and P. Tabeling, Phys. Rev. Lett. 65 (1990) 1869.

[4] Y. Kuramoto, Springer series in synergetics, Vol. 19 (Springer, Berlin, 1984); K. Stewartson and J.T. Stuart, J. Fluid Mech. 48 (1971) 529.

[5] L. Gil, preprint (Nice, 1991).

[6] M. Rabaud, S. Michalland and Y. Couderc, Phys. Rev. Lett. 64 (1990) 184.

[7] P. Coullet, L. Gil and J. Lega, Phys. Rev. Lett. 62 (1989) 1619.

[8] N. Aubry, R. Guyonnet and R. Lima, J. Stat. Phys. 64 (1991) 683; N. Aubry, M.P. Chauve, R. Guyonnet, preprint (Marseille, 1990).

[9] J. Max, Méthodes et Techniques de Traitement du Signal et Applications aux Mesures Physiques, tome 1 (Masson, Paris, 1989).

[10] H.J. Kim and P.A. Durbin, J. Fluid Mech. 196 (1988) 431; P. Le Gal, M.P. Chauve, R. Lima and J. Rezende, Phys. Rev. A 41 (1990) 4566.

[11] C.H.K. Williamson, J. Fluid Mech. 206 (1989) 579.

[12] N. Bekki and K. Nozaki, Phys. Lett. A 110 (1985) 133.

[13] J. Lumley, Stochastic Tools in Turbulence (Academic Press, New York, 1970).

[14] W.H. Press, B.P. Flannery, A.A. Teukolsky and W.T. Vetterling, Numerical Recipes (Cambridge Univ. Press, 1986).

Physica D 58 (1992) 414–422
North-Holland

PHYSICA D

Turbulent convection in helium gas

Emily S.C. Ching[1], Leo P. Kadanoff, Albert Libchaber[2] and Xiao-Zhong Wu[3]
The James Franck Institute and the Department of Physics, The University of Chicago, Chicago, IL 60637, USA

Received 27 August 1991
Revised manuscript received 15 October 1991
Accepted 9 December 1991

Various changes in measured signals were observed in thermal convective experiments of low-temperature helium gas, indicating that there are more than one turbulent states in the system. The more recently observed transition occurs at a Rayleigh number of about 10^{11}, within the hard turbulence regime. It was first observed [Wu et al., Phys. Rev. Lett. 64 (1990) 2140] in the analyses of the frequency power spectra, measured at the center of the experimental cell. In this paper, it is shown that the power spectra can be equally well fitted by three different fitting functions, each having a different physical interpretation. Thus, the transition is not well characterized by the power spectra. On the other hand, the study of root-mean-squared temperature derivatives clearly indicates and quantifies this transition.

1. Introduction

Recently, there has been a lot of interest in studying the Rayleigh–Bénard convection of low-temperature helium gas [1–6]. The advantage of using low-temperature helium gas is that a wide range of Rayleigh numbers can be covered by changing the gas density [7, 8]. Thus, the system can be used to study the development of different flow states. Specifically, it is ideal for studying turbulence which remains as an essentially unsolved problem in fluid mechanics.

The experimental system consists [1–3] of a cylindrical cell, of diameter 20 cm and height (L) 40 cm, which is filled with helium gas at about 5 degrees Kelvin. The cell is heated from below and the temperature difference between the top and the bottom plates, Δ, is of the order of 100 mK. Temperature as a function of time, $T(t)$, at various points inside the cell is measured by arsenic-doped silicon bolometers. These bolometers are small in size, about 0.2 mm, with a high sensitivity of 2 mK/Ω, and short response time of the order of 1 millisecond.

The system is described by the Boussinesq equations [9] of an incompressible fluid:

$$\frac{\partial \boldsymbol{u}}{\partial t} - \nu\nabla^2\boldsymbol{u} + \boldsymbol{u}\cdot\nabla\boldsymbol{u} + \nabla p = g\alpha T\boldsymbol{e}_3\,, \tag{1a}$$

$$\frac{\partial T}{\partial t} - \kappa\nabla^2 T + \boldsymbol{u}\cdot\nabla T = 0\,, \tag{1b}$$

$$\nabla\cdot\boldsymbol{u} = 0\,, \tag{1c}$$

where $\boldsymbol{u}$ is the velocity field, p the pressure divided by density and T the temperature field, while $\boldsymbol{e}_3$ is the unit vector in the vertical direction. Further, α is the volume thermal expansion coefficient, g is the acceleration due to gravity, and κ and ν are the thermal diffusivity and kinematic viscosity of the gas, respectively. Eq.

[1]Address after August 1992: Institute for Theoretical Physics, University of California, Santa Barbara, CA 93106, USA.

[2]Present address: Department of Physics, Princeton University, Princeton, NJ 08544, USA, and NEC Research Institute, Princeton, NJ 08540, USA.

[3]Present address: Exxon Research and Engineering Company, Annandale, NJ 08801, USA.

0167-2789/92/$05.00 © 1992 – Elsevier Science Publishers B.V. All rights reserved

(1) defines two dimensionless parameters: the Rayleigh number (Ra) which is given by

$$\mathrm{Ra} = \frac{\alpha g \Delta L^3}{\kappa \nu} \tag{2}$$

and the Prandtl number which is the ratio ν/κ. In this helium experiment, the Prandtl number is of order unity and is almost constant, thus a flow state is characterized by the Rayleigh number.

As the Rayleigh number is increased, the fluid progresses from a laminar state to a turbulent state which exhibits both temporal and spatial disorder. Two different turbulent states have been observed which are designated as the soft and hard turbulence [1–3]. The soft-to-hard transition occurs at Ra about 10^8. The main difference between the soft and the hard turbulent states is that hard turbulence is a self-similar state in which all measured quantities exhibit scaling behavior. These measured quantities include the Nusselt number, Nu, which is the ratio of the actual heat flux to that would occur were there only heat conduction, namely:

$$\mathrm{Nu} = \frac{H}{k\Delta/L}\,, \tag{3}$$

where H is the actual heat flux and k is the thermal conductivity of the gas. Above the soft-hard transition, Nu scales with Ra:

$$\mathrm{Nu} \sim \mathrm{Ra}^{0.290 \pm 0.005}\,. \tag{4}$$

The scaling exponent 0.290 ± 0.005 agrees with the theoretical result [3] of 2/7 which is also confirmed in a two-dimensional numerical simulation [10]. The other quantities are the root-mean-squared fluctuations, Δ_c, and the large scale flow velocity, U, which scale with Ra as follows:

$$\frac{\Delta_c}{\Delta} \sim \mathrm{Ra}^{-0.146 \pm 0.007}\,, \quad \frac{UL}{\kappa} \sim \mathrm{Ra}^{0.49 \pm 0.02}\,. \tag{5}$$

Moreover, the soft-to-hard transition is also characterized by other changes. First, the probability distribution of temperature fluctuations, recorded at the center of the cell, changes from Gaussian-like to exponential-like [1–3]. Second, there is a change in the shape of the frequency power spectrum [4].

More recently, Wu et al. [4] observed a change in the high-frequency parts of the power spectra at Ra about 10^{11}. For $\mathrm{Ra} \leq 7.3 \times 10^{10}$, when the frequency and power are properly rescaled, the whole power spectra (except for the initial flat region with frequencies smaller than that corresponding to the large scale flow) can be described by a universal function. However, this does not work for the high-frequency parts for data of higher Rayleigh numbers. Instead, the data for $\mathrm{Ra} \geq 7.3 \times 10^{10}$ can be made to "collapse" into one single curve only by a more complicated multifractal-like transformation. Frisch and Vergassola [11] showed that just this kind of scaling arises in the Parisi–Frisch multifractal model of turbulence [12].

This second transition at Ra about 10^{11} is only a change in the high-frequency parts of the power spectra. The other measured characteristics of hard turbulence remain unchanged. The scaling behavior of the various quantities mentioned above continues to hold for values of Ra well beyond 10^{11}. This paper gives a detailed analysis of the power spectra, particularly at the higher frequencies. In section 2, we describe these analyses and the results obtained. We discuss the results in section 3 and show that the data can be equally weli fitted by three different fitting functions each having a physical interpretation. Thus, the transition is not well characterized by the power spectra. We then include the results of another analysis which clearly indicates and quantifies this transition. Conclusions are given in section 4.

2. Analyses of frequency power spectra

The frequency power spectra, $P(\omega)$ are ob-

tained by Fourier transforming $T(t)$ and taking the absolute square,

$$P(\omega) = \frac{\left| \sum_{j=0}^{N-1} T(t_0 + j\tau_0)\, e^{2\pi i j \tau \omega} \right|^2}{N/\tau}, \qquad (6)$$

with ω being an integer times $1/(\tau N)$ where τ is the experimental sampling period. In the actual calculation, $T(t_0 + j\tau)$ is multiplied by a Hanning window (see e.g. ref. [13]). We fit $P(\omega)$ of sixteen Rayleigh numbers, ranging from 1.1×10^8 to 4.3×10^{14}, by three different functional forms, each with three fitting parameters. In the following, we shall first describe these different fitting forms and then the results obtained.

According to ref. [4], the highest frequency part of the spectra can be described by $\exp[-(\omega/\omega_h)^\beta]$ with $\beta = 0.55 \pm 0.05$ and ω_h is some frequency depending on Ra. Therefore, we first fit the data by the following form,

$$F_1(\omega) = A_1 \omega^{-x_1} \exp[(-\omega/\omega_1)^{1/2}], \qquad (7)$$

where A_1, x_1 and ω_1 are parameters fitted for each Ra. We shall call this fit the exponential one-half fit. The second functional form we use is similar to the first one but with an exponential cutoff.

$$F_2(\omega) = A_2 \omega^{-x_2} \exp(-\omega/\omega_2), \qquad (8)$$

with A_2, x_2 and ω_2 being the fitting parameters. Therefore, we call it the exponential fit. This form conforms to standard ideas about power spectra in turbulence [14, 15] and was used by Procaccia et al. [6]. It can be shown (see appendix and ref. [16]) that a multifractal-like fit [4] with a structure like that of eq. (8) can be given in the form

$$F(\omega) = P_0 \left(\frac{\mathrm{Ra}}{R_0}\right)^{c_1} \left(\frac{\omega}{\omega_0}\right)^{-x_2} \exp[-c_2(\omega/\omega_0)^{S_0/S}],$$
$$\text{with} \quad S = \ln(\mathrm{Ra}/R_0), \qquad (9)$$

where P_0, R_0 ω_0, S_0, c_1, c_2 and x_2 are constants. Thus, we choose the last fitting form to be a power-law decay of exponent -1.3 with a stretched-exponential cutoff,

$$F_3(\omega) = A_3 \omega^{-1.3} \exp[-(\omega/\omega_3)^\beta], \qquad (10)$$

with A_3, ω_3 and β the fitting parameters and call it the stretched-exponential fit.

We perform a nonlinear least-square fit to obtain the parameters, As a preliminary check, we plot the result of the fit together with the data in the same graph. We find that the three fits work almost equally well. In order to see better the quality of these different fits, we plot the ratio of the data to the result of fit, r, for each Ra. Typical plots of r for the three fits are shown for four Ra in fig. 1. We do not expect the fits to work either for the initial flat region where frequencies are smaller than that corresponding to the large scale flow, or near the highest frequency end where thermal noise levels off the data. This is reflected in fig. 1 in which r is much smaller than 1 for the initial flat region and much larger than 1 for the highest frequencies. We observe that there is an intermediate region in which r is around 1, showing that the different forms fit the data approximately.

The exponential one-half fit works better for the first few lowest Ra studied but does not work as well for the intermediate range of Ra. For the highest Ra studied ($\sim 10^{13}$–10^{14}), it fits the data better again and is close to the stretched-exponential fit which is similar to the exponential fit for lower Ra. This can be seen from the value of the parameters β which is approximately 1 for low Ra and close to $\frac{1}{2}$ for higher Ra (see below). The intermediate range of Ra ($10^9 \lesssim \mathrm{Ra} \lesssim 10^{12}$) is best fitted by the exponential fitting form. As mentioned above, the power spectra "collapsed" into one universal curve for $\mathrm{Ra} \lesssim 7.3 \times 10^{10}$ [4]. Thus, we expect that the data of lower Ra should also be better fitted by the exponential fit. The result that the exponential one-half fit actually works better for the data of the first few lowest Ra is understood as follows. For the data of the

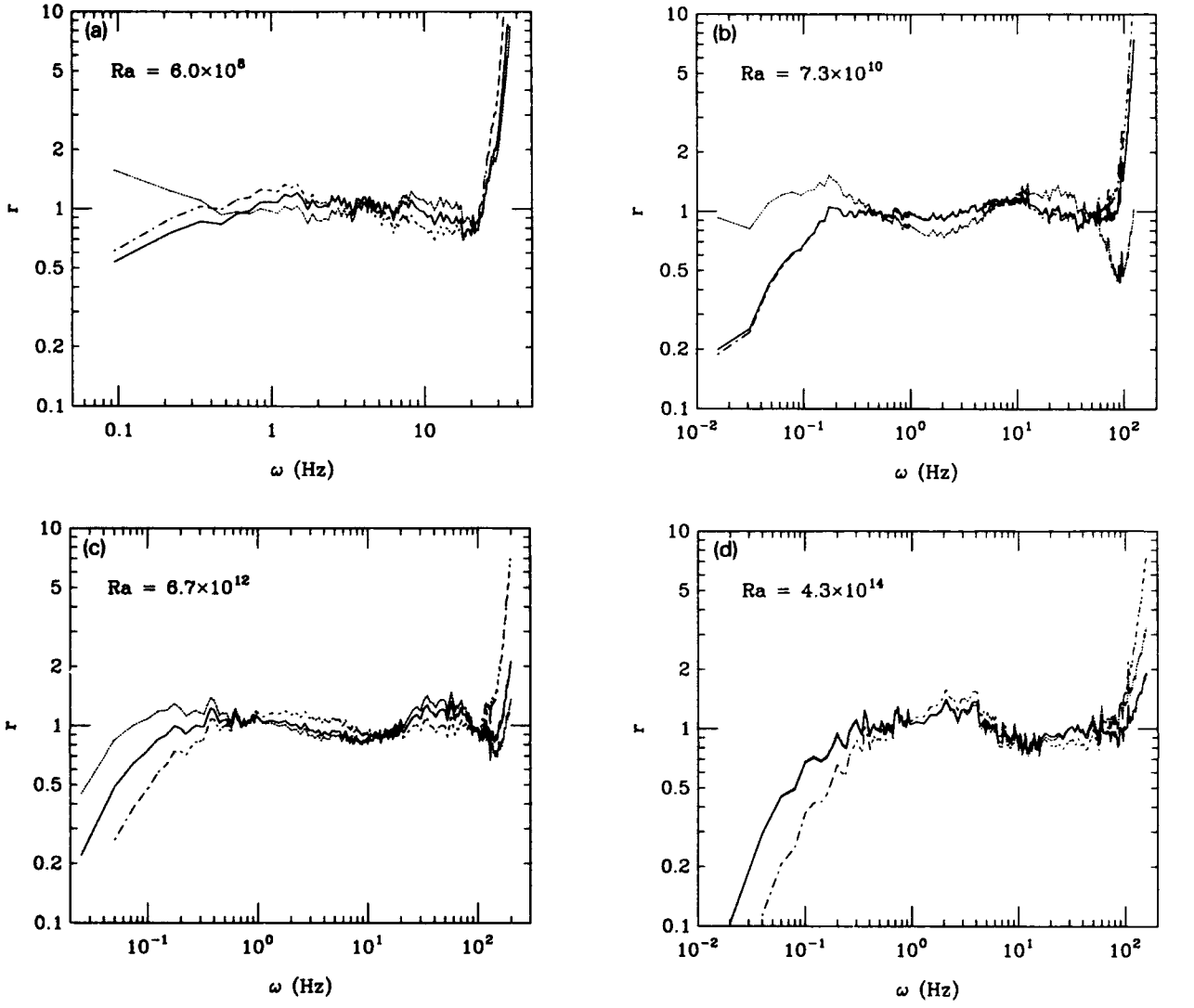

Fig. 1. Quality-checking of the three different fitting forms, the exponential one-half, the exponential and the stretched-exponential fits (see eqs. (7), (8) and (10), respectively), for four different Rayleigh numbers. (a) $Ra = 6.0 \times 10^8$, (b) $Ra = 7.3 \times 10^{10}$, (c) $Ra = 6.7 \times 10^{12}$, and (d) $Ra = 4.3 \times 10^{14}$. We plot the ratio of the data of the power spectrum to the result of fit, r, versus the frequency, ω. The dotted line is for the exponential one-half fit, the dot-dashed line is for the exponential fit and the solid line is for the stretched-exponential fit. It can be seen that none of the three fitting forms works too well for the highest Ra.

first few lowest Ra studied here, the range of the power law is very short so it is very difficult to fit the data with a power-law decay and then an exponential cutoff. Rather, the whole region is better approximated by just an exponential one-half decay (the value of x_1 is about 0 for the lowest Ra, see below). None of the three fitting forms fits the data of $Ra = 4.3 \times 10^{14}$ (the highest Ra studied) well.

The exponential fit is good for data of intermediate values of Ra but not as well for higher Ra. This point has already been noted in ref. [6]. In particular, if one plots

$$G(\omega) \equiv P(\omega) \exp\left(\frac{\omega}{\omega_2}\right) \tag{11}$$

versus ω in a log–log plot, one does not get a reasonably good straight line. Instead, the curve

appeared [6] to develop into two straight lines, suggesting $G(\omega)$ might be a combination of two power-law decays, or at least a more complicated form than a single power-law decay.

After checking the quality of the various fits, we then investigate how the fitting parameters vary with Ra. The dependence of the three parameters, x_1, x_2 and β, on Ra is shown in figs. 2, 3 and 4, respectively. We see that both x_2 and β display a change in behavior at Ra about 10^{11}: x_2 scatters around 1.3 and then increases to 1.8, while β scatters around 0.9 and then decreases to about 0.4. Instead, x_1 behaves quite differently: except for some slight scattering, it increases monotonically from about 0 to 1.4. Comparing eq. (10) with eq. (9), one sees that if the multifractal-like fit is good, then β corresponds to S_0/S above the transition. Thus, the reciprocal of β should increase linearly with ln Ra. In fig. 4, we plot $1/\beta$ versus ln Ra and find that this indeed is true except for the highest Ra. This fact, together with the above observation that the stretched-exponential form does not fit too well the highest Ra data, indicates that the multifractal-like transformation may work only for an intermediate range of Ra as was noted already in ref. [4]. The slope obtained is 0.15 ± 0.01 which

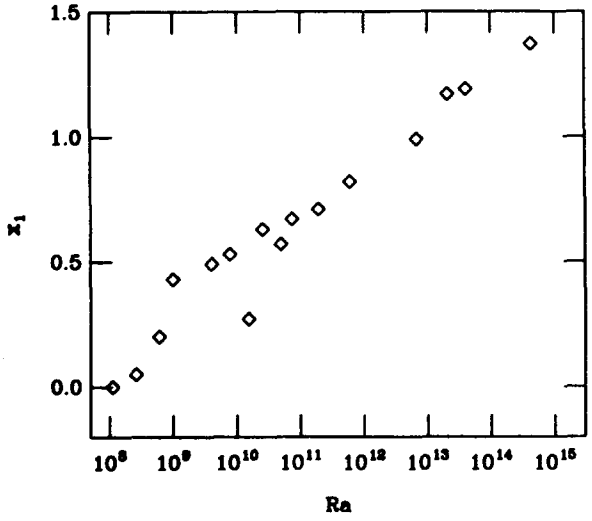

Fig. 2. The behavior of the fitted parameter x_1 (see eq. (7)) as a function of Ra.

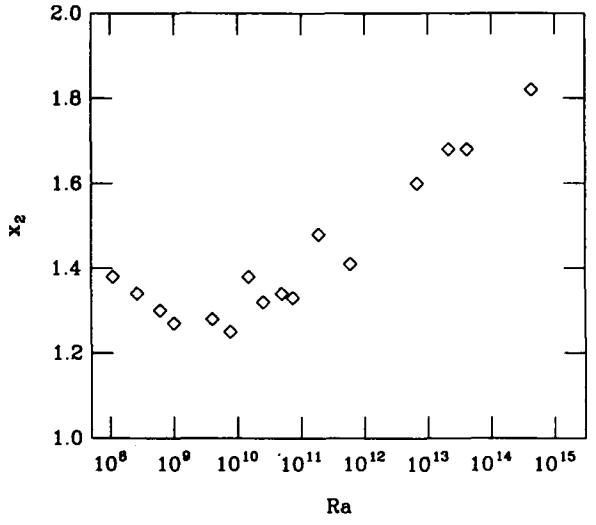

Fig. 3. The behavior of the fitted parameter x_2 (see eq. (8)) as a function of Ra. It can be seen that there is a change in behavior at Ra about 10^{11}.

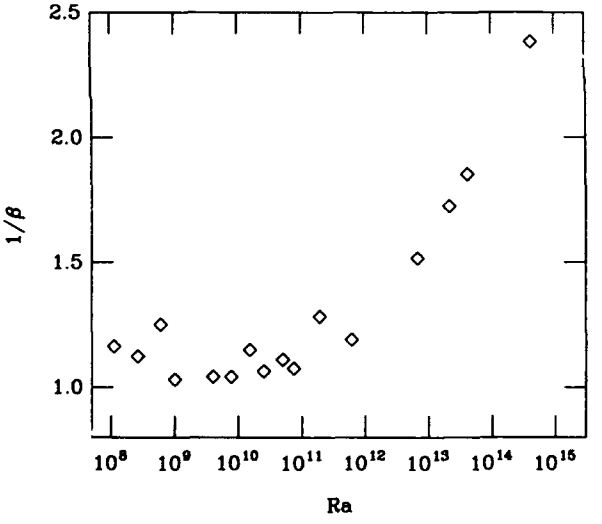

Fig. 4. The dependence of the fitted parameter β (see eq. (10)) on Ra. A change in behavior is seen at Ra about 10^{11}.

agrees with $1/S_0 = 0.152$ (see appendix for the value of S_0).

Next, we compare the three frequencies ω_1, ω_2 and ω_3 which are the typical scales describing dissipation. In fig. 5 we present a log–log plot of these frequencies versus Ra. Below the transition, ω_2 and ω_3 are indistinguishable within measurement errors. This fact, together with the fact

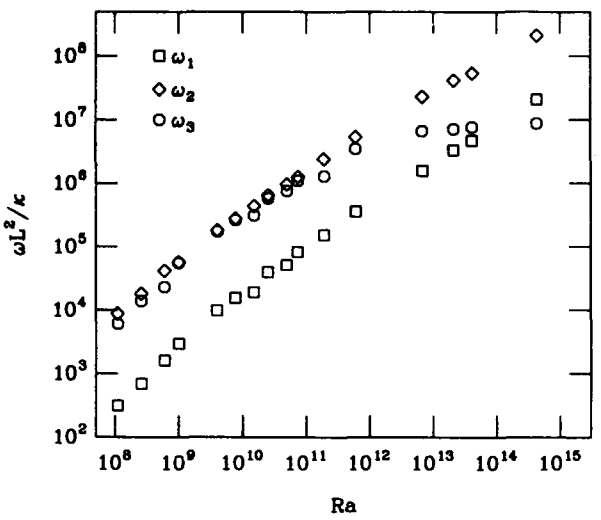

Fig. 5. The dependence of the three characteristic frequencies, ω_1, ω_2 and ω_3 (se eqs. (7), (8) and (10)) on Ra.

that β is close to one in this region of Ra, just echo the result [6] that eq. (8) with $x_2 = -1.3 \pm 0.1$ is a good description of the power spectra for lower values of Ra. However, for higher values of Ra, the two frequencies deviate from each other significantly and behave differently as a function of Ra. The frequency ω_1 is smaller than ω_2 by more than an order of magnitude but it seems to be proportional to ω_2. In fact, the three frequencies all scale as a power of Ra:

$$\frac{\omega_1 L^2}{\kappa} \sim \begin{cases} \mathrm{Ra}^{0.77\pm0.09} & \text{for Ra} \lesssim 10^{11}, \\ \mathrm{Ra}^{0.62\pm0.05} & \text{for Ra} \gtrsim 10^{11}, \end{cases} \tag{12}$$

$$\frac{\omega_2 L^2}{\kappa} \sim \begin{cases} \mathrm{Ra}^{0.79\pm0.06} & \text{for Ra} \lesssim 10^{11}, \\ \mathrm{Ra}^{0.57\pm0.08} & \text{for Ra} \gtrsim 10^{11}, \end{cases} \tag{13}$$

and

$$\frac{\omega_3 L^2}{\kappa} \sim \begin{cases} \mathrm{Ra}^{0.8\pm0.1} & \text{for Ra} \lesssim 10^{11}, \\ \mathrm{Ra}^{0.07\pm0.06} & \text{for Ra} \gtrsim 10^{11}. \end{cases} \tag{14}$$

Thus, all the three frequencies have essentially the same scaling behavior for $\mathrm{Ra} \lesssim 10^{11}$. This implies that, below the transition, a well-defined characteristic frequency scale describing dissipation exists, which is independent of whatever functional form assumed for dissipation. Above the transition, this is no longer true as the behavior of the frequency obtained depends crucially on the functional form assumed which is a priori unknown. This point will be elaborated in the following section.

3. Discussion

We see that the data of the power spectra do not distinguish sharply between the different fitting functions. In the following, we shall argue that this ambiguity allows for different interpretations of the transition.

Using standard ideas in power spectra, we associate the power-law decay with cascade of quantities, like kinetic energy flux [14] or T^2 flux [15, 17], from larger scales down to smaller scales and the exponential or stretched-exponential cutoff with the dissipation of these quantities when viscosity or thermal diffusivity becomes important. The stretched-exponential fitting form then implies that, above the transition, the cascade remains unchanged but the form of dissipation changes. With β decreasing as Ra increases, it suggests that the dissipation decreases as compared to that extrapolated from below the transition. On the other hand, the exponential fit with the picture that $G(\omega)$ (eq. (11)) changing form implies that above the transition, the cascade changes, possibly from cascade of one quantity to another giving rise to a second power-law, while the form of dissipation remains unchanged.

This possibility of more than one interpretation is related to another interesting question: what is the functional form describing dissipation? It is known [18] that the wavenumber power spectra (spatial Fourier transform) must decay at least as fast as an exponential, or else the temperature field becomes unbounded contrary to experimental evidence. However, not very much can be said about the relationship between the wavenumber and the frequency except for the usually assumed frozen-flow hypoth-

esis [19]. The results of the above analysis show that the present data do not distinguish sharply between the three different functional forms of dissipation.

Hence, from analyzing the power spectra, we can conclude that a transition occurs at Ra about 10^{11} but it is difficult to characterize it. It is then natural to search for another, better characterization. The study [6] of the root-mean-squared temperature derivative via the dimensionless quantity Q,

$$Q^2 \equiv \frac{\overline{(\partial T/\partial t)^2}}{\Delta_c^2 \kappa^2 / L^4}\,, \tag{15}$$

with the overbar denoting a time average and Δ_c the root-mean-squared temperature fluctuation,

$$\Delta_c^2 = \overline{(T-\bar{T})^2}\,, \tag{16}$$

shows that Q has a sharp change of behavior at Ra about 10^{11}:

$$Q \sim \begin{cases} \mathrm{Ra}^{0.67\pm0.04} & \text{for } \mathrm{Ra} \lesssim 10^{11}\,, \\ \mathrm{Ra}^{0.48\pm0.06} & \text{for } \mathrm{Ra} \gtrsim 10^{11}\,. \end{cases} \tag{17}$$

This change in the scaling exponent clearly quantifies the transition.

The study of Q provides other clues to the nature of the transition. Q is essentially the rate of temperature fluctuations, in units of $\Delta_c \kappa / L^2$. Since Δ_c is the measured root-mean-squared temperature fluctuation, Q just defines a frequency scale, in units of κ/L^2, over which fluctations occur. We expect Q to be dominated by fast fluctations, thus this frequency scale is the inverse of the shortest timescale appeared in the problem. The shortest timescale, τ_1, previously identified in the problem, was found [20] to scale as a power of Ra:

$$\frac{\tau_1}{L^2/\kappa} \sim \begin{cases} \mathrm{Ra}^{-(0.73\pm0.06)} & \text{for } \mathrm{Ra} \lesssim 10^{11}\,, \\ \mathrm{Ra}^{-(0.4\pm0.1)} & \text{for } \mathrm{Ra} \gtrsim 10^{11}\,. \end{cases} \tag{18}$$

We compare $1/Q$ and τ_1 in fig. 6 and see that they indeed have the same scaling behavior. The increase of the scaling exponent in eq. (18) implies that above the transition, the typical timescale, over which fluctuations occur, increases as compared to that extrapolated from below the transition. Using the frozen-flow type argument [19], a longer timescale means a longer lengthscale. As we expect most of the temperature changes occur across the cap of thermal plumes (which are one of the coherent structures observed [21] in the problem), a longer lengthscale then suggests that the surface of the plumes is more convoluted. This may thus be related to the suggestion that this transition arises from the roughening of thermal plumes [6]. However, we have to admit that all these arguments are highly speculative.

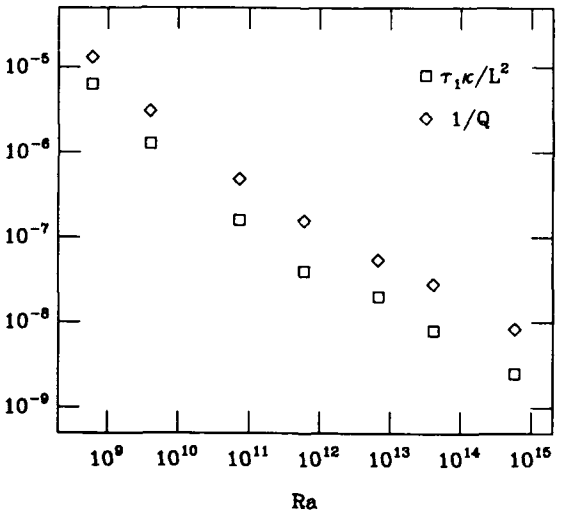

Fig. 6. Comparison of $1/Q$ (see eq. (15) for definition of Q) with $\tau_1\kappa/L^2$ where τ_1 is the shortest timescale identified in the problem. It can be clearly seen that the two quantities behave similarly.

4. Conclusion

We perform a detailed analysis on the frequency power spectra of temperature fluctuations and show that data are equally well fitted by three different fitting forms. Consequently, different physical interpretations of the nature of the transition are allowed. Therefore, it is difficult to characterize the transition using power spectra. On the other hand, the dimensionless root-mean-squared temperature derivative, Q,

scales as a power of Ra, with the exponent decreasing from 0.67 ± 0.04 to 0.48 ± 0.06 at Ra about 10^{11}. This decrease in dissipation clearly quantifies the transition.

Acknowledgement

This work was supported in part by the University of Chicago Materials Research Laboratory.

Appendix. Derivation of eq. (9)

It was shown in ref. [4] that all the power spectra, for $\mathrm{Ra} \geq 7.3 \times 10^{11}$, collapse into one single curve, $f(\alpha)$, under the following multifractal-like transformation,

$$f = \frac{\ln[P(\omega)/P_0]}{\ln(\mathrm{Ra}/R_0)}, \qquad \alpha = \frac{\ln(\omega/\omega_0)}{\ln(\mathrm{Ra}/R_0)}, \tag{19}$$

where P_0, ω_0 and R_0 are some constants. This implies that for $\mathrm{Ra} \geq 7.3 \times 10^{11}$, $P(\omega)$ is described by

$$F(\omega) = P_0 \exp[Sf(\alpha)] \quad \text{with } S = \ln\left(\frac{\mathrm{Ra}}{R_0}\right). \tag{20}$$

The functional form of $f(\alpha)$ can be obtained by assuming that the multifractal-like fit has a structure of eq. (8). This is justified by the observation that the data of $\mathrm{Ra} = 7.3 \times 10^{11}$ is also well appproximated by eq. (8) (see fig. 1c). Rewriting eq. (8) in terms of α, we have

$$F_1(\omega) = P_0 \exp[S(c_1 - x_2\alpha - c_2 e^{S_0\alpha})],$$

where

$$c_1 = -\frac{\ln P_0}{S_0} - \frac{x_2}{S_0}\ln\left(\frac{\omega_0}{\tilde{\omega}}\right),$$

$$c_2 = \frac{\omega_0}{\omega_2 S_0}, \quad S_0 \equiv S|_{\mathrm{Ra}=7.3\times10^{10}}, \tag{21}$$

with $\tilde{\omega}^{x_2} = A_2$. Comparing eq. (20) with eq. (21), we find

$$f(\alpha) = c_1 - x_2\alpha - c_2 e^{S_0\alpha} \tag{22}$$

agreeing with the form given by Castaing [16]. Using $P_0 = (5.8 \pm 0.7) \times 10^{-7}$, $\omega_0 L^2/\kappa = (1.1 \pm 0.2) \times 10^5$ and $R_0 = 1 \times 10^8$ from ref. [4], and $x_2 = 1.33$, $\tilde{\omega} L^2/\kappa = 1.35 \times 10^3$ and $\omega_2 L^2/\kappa = 1.26 \times 10^6$ from the fit of eq. (8) for $\mathrm{Ra} = 7.3 \times 10^{10}$; we have

$$S_0 = 6.59, \quad c_1 = 1.29, \quad c_2 = 0.013. \tag{23}$$

Except for c_1, these values agree with Castaing's results [16]. Finally, using eqs. (20) and (22), we see that the multifractal-like fit with a structure of eq. (8) can be given in the following form:

$$F(\omega) = P_0\left(\frac{\mathrm{Ra}}{R_0}\right)^{c_1}\left(\frac{\omega}{\omega_0}\right)^{-x_2} \times \exp[-c_2(\omega/\omega_0)^{S_0/S}]. \tag{24}$$

This is just eq. (9).

References

[1] F. Heslot, B. Castaing and A. Libchaber, Phys. Rev. A 36 (1987) 5870.
[2] M. Sano, X-Z. Wu and A. Libchaber, Phys. Rev. A 40 (1989) 6421.
[3] B. Castaing, G. Gunaratne, F. Heslot, L.P. Kadanoff, A. Libchaber, S. Thomae, X.-Z. Wu, S. Zaleski and C. Zanetti, J. Fluid Mech. 204 (1989) 1.
[4] X.-Z. Wu, L.P. Kadanoff, A. Libchaber and M. Sano, Phys. Rev. Lett. 64 (1990) 2140.
[5] X.-Z. Wu and A. Libchaber, Phys. Rev. A 43 (1991) 2833.
[6] I. Procaccia, E.S.C. Ching, P. Constantin, L.P. Kadanoff, A. Libchaber and X.-Z. Wu, Phys. Rev. A 44 (1991) 8091.
[7] D.C. Threlfall, Ph.D. Thesis, University of Cambridge (1976); J. Fluid Mech. 67 (1975) 17.
[8] X.-Z. Wu, Ph.D. Thesis, University of Chicago (1991).
[9] S. Chandrasekhar, Hydrodynamic and Hydromagnetic Stability (Dover, New York, 1981).
[10] J. Werner, E.E. DeLuca, R. Rosner and F. Cattaneo, Phys. Rev. Lett. 67 (1991) 3519.

[11] U. Frisch and M. Vergassola, Europhys. Lett. 14 (1991) 439.
[12] G. Parisi and U. Frisch, in: Proc. Turbulence and Predictability in Geophysical Fluid Dynamics, Varenna, 1983, eds. M. Ghil, R. Benzi and G. Parisi, p. 84.
[13] W.H. Press et al., Numerical Recipes: The Art of Scientific Computing, (Cambridge University Press 1986).
See also the Hewlett Packard 3562A Dynamic Signal Analyzer Operating Manual.
[14] A.N. Kolmogorov, J. Fluid Mech. 13 (1962) 82.
[15] R. Bolgiano Jr., J. Geophys. Res. 64 (1959) 2226;
A.M. Obukhov, Dokl. Akad. Nauk. SSSR 125 (1959) 1246.
[16] B. Castaing, Phys. Rev. Lett. 65 (1990) 3209.
[17] I. Procaccia and R. Zeitak, Phys. Rev. Lett. 62 (1989) 2128;
V.S. L'vov and G.E. Fal'kovich, Conservation laws and two-flux spectra of hydrodynamic convective turbulence, preprint (1991).
[18] C. Foias and R. Temann, J. Funct. Anal. 87 (1989) 359;
C. Foias, O. Manley and L. Sirovich, Phys. Fluids A 2 (1990) 464.
[19] G.I. Taylor, Proc. R. Soc. London A 164 (1938) 476.
[20] E.S.C. Ching, Phys. Rev. A 44 (1991) 3622.
[21] G. Zocchi, E. Moses and A. Libchaber, Physica A 166 (1990) 387.

Physica D 58 (1992) 423–440
North-Holland

PHYSICA D

Combined approaches and characterizations of experimental chaotic attractors in thermal lensing

S. Meunier-Guttin-Cluzel, B. Maheu and G. Gouesbet
LESP, URA CNRS CORIA, INSA de Rouen, B.P. 8, F-76131 Mont Saint Aignan cedex, France

Received 7 October 1991
Revised manuscript received 6 February 1992
Accepted 15 February 1992

Local heating of a liquid just below its surface may generate surface waves and hydrodynamical oscillations. The resulting system exhibits a great wealth of behaviour when a laser beam is used for heating, leading to the creation of an unsteady thermal lens. Chaotic time signals have been recorded and analyzed using combined approaches: power spectra, 3D projections, Poincaré sections, periodic orbits, generalized Renyi dimensions. These approaches are applied to the characterization of one typical experimental chaotic attractor. The usefulness of each technique is outlined and, finally, a likely value for the information dimension of the attractor is found to be close to 4.

1. Introduction

In the rapidly growing field of nonlinear dynamics, there still exists a need for typical, well controlled and cheap experiments. To our knowledge, the most celebrated and most studied experiments seem to be Rayleigh–Bénard instability [1–4], Belousov–Zhabotinsky reaction [5, 6], nonlinear electrical circuits [7, 8], lasers [9] or Couette–Taylor systems [10].

The above list is by no means a complete review of the existing experiments but it only recalls well-known examples of experimental nonlinear dynamical systems.

The oscillatory thermal lens is another good candidate for being a generic experimental nonlinear dynamical system.

To our knowledge, this phenomenon was first mentioned in 1973 in a very brief report [11]. It was independently discovered by our group in 1981 [12] and since that time we have been continuously studying it. Progressively our work has set the oscillations of the thermal lens in the very middle of nonlinear dynamics with connections to bifurcation and instability theory, Feigenbaum cascade, quasiperiodicity and chaos. When the oscillations are due to the thermal lens produced by absorption of the laser beam, a beautiful ring pattern is the consequence of interferences inside the beam passing through the thermal lens. Oscillations of the thermal lens are easily detected by oscillations of the ring pattern. They look like heartbeats at frequencies close to 1 Hz and, accordingly, the phenomenon has been named optical heartbeat (HB).

Recently, Bazhenov et al. [13], Viznyuk and Sukhodol'skii [14] published papers on experimental study of the oscillations of a heated surface and their work witnesses an increasing interest about these free surface instabilities.

The present paper is focused on description and analysis of experimental results and data. More precisely we will concentrate on new results about chaotic experimental signals and outline the usefulness of multiple approaches for analyzing experimental time series. Only short outlines will be devoted to experimental results for non chaotic regimes and we will skip discus-

0167-2789/92/$05.00 © 1992 – Elsevier Science Publishers B.V. All rights reserved

sion of theoretical models. Details about non chaotic regimes of the HB-system can be found in refs. [15–20] and about the theoretical models in refs. [21–23].

2. Experiments

2.1. Experimental set-up and data acquisition (*HB1 system*)

Quantitative and detailed information about experiments has been reported elsewhere [12, 15–20,24–31]. Let us only recall that all experiments basically rely on a continuous heating of a liquid close to the free surface. Many geometries, configurations and liquids have been tested. In the present experiment called heartbeat 1 (HB1-experiment), a horizontal laser beam is focused below the free surface of an absorbing liquid (fig. 1). Hence, the focus point is heated and becomes surrounded by a refractive index gradient acting as a diverging lens. After crossing the thermal lens, the laser beam diverges and a high contrast ring pattern is produced by what may be understood as thermal lens aberrations. This pattern can be projected onto a screen and, as the pattern is large (0.1 m up to 1 m), it is the best way for showing and analyzing the very small thermal lens ($\simeq 10^{-4}$ m). Thermal lensing is a well-known phenomenon which was reported in the sixties, for instance, by Gordon et al. [32]. Conversely, oscillations of a thermal lens have been studied more recently, in the eighties [12]. This phenomenon occurs when the distance between the heated point and the surface is small enough for feed back from surface waves to the heated zone. When the thermal lens departs from steadiness, the ring pattern evolves to HB's. To take a picture, the ring patterns behave like quiet heartbeats when the hydrodynamical system oscillates periodically and they can be compared to a heart attack when chaos is reached (this comparison holds between the aspects of the optical pattern and of the human heart. Conversely, the underlying electrical activity of the human heart may follow chaotic dynamics when healthy and may depart from chaos in case of a heart attack [33].)

Fig. 2 is a schematic of the experimental set-up: the source is an Argon ion laser (item 1). Laser power P is adjusted by rotation of the plane of polarization relative to a polarizer (Glan prism and polarizer, item 3). Then, the laser light comes through a window inside a thermoregulated box (item 11) which contains all other

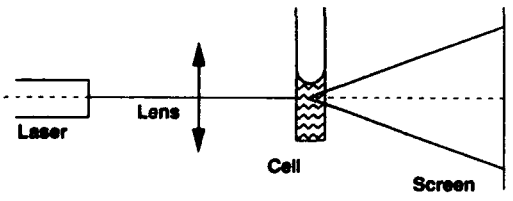

Fig. 1. Heartbeat 1 experiments (principle).

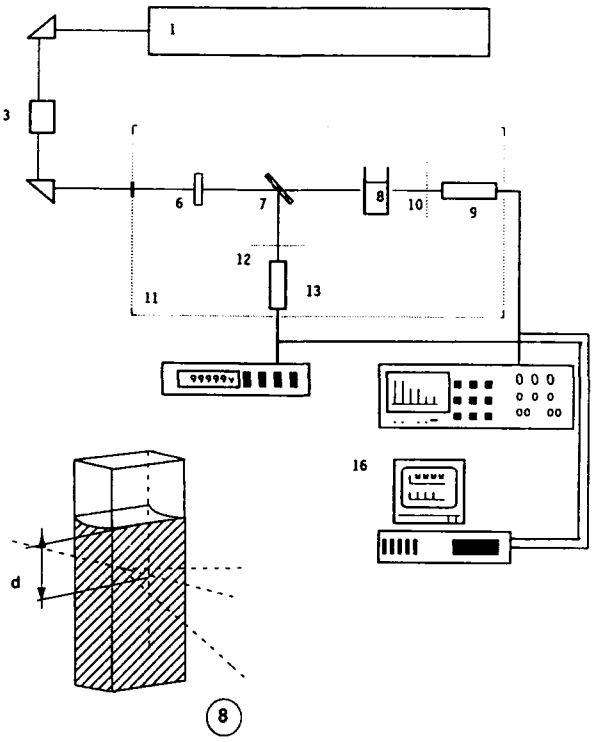

Fig. 2. Experimental set-up for HB1: (1) Ar^+ laser; (3) power adjustment; (6) focusing lens; (7) pellicle beam splitter; (8) sealed cell containing liquid and colorant; (9) photodiode; (10) translucent screen; (11) thermoregulated room; (12) neutral attenuator; (13) photodiode; (16) data acquisition and storage.

pieces of the set-up except data storage and processing.

Inside the thermoregulated box we find a pellicle beam splitter (item 7) allowing permanent control and measurement of the incident laser power (photodiode + attenuator, items 12–13). Item 6 is the lens focusing the beam on the sealed cell containing a solution of toluene with 50 mg/ℓ Red Organol BX 1750 dye (item 8). A micropositioner allows variation of the distance d between laser beam and surface. Finally the HB's fringes are smoothed by a translucent screen (item 10) and measured by a photodiode (item 9). The experimental signals from both photodiodes are fed to an acquisition interface and, after processing, they are stored in a PC (item 16).

A real time acquisition and sampling of experimental data is performed by the PC interface. The signal from photodiode 9 is sampled at a chosen fixed frequency, then it is possibly amplified and extracted from continuous background. Finally it is stored as a two-byte integer.

Sampling frequency, amplification ratio and offset can be adjusted in the range 0 Hz–1000 Hz, 1–128 and 0 V–10 V, respectively. The bandpass cut-off of the time signal is about 100 Hz.

2.2. Physical understanding of experiments

HB experiments essentially rely on *buoyancy*, *thermal diffusion* and *Marangoni effect*.

Buoyancy and *thermal diffusion* are the agents which transfer heat from the heated region up to the free surface. d being the distance between surface and heated zone, buoyancy is likely to be predominant for high d values and thermal diffusion for small d values.

The *Marangoni effect*, due to a negative temperature derivative of surface tension ejects hot liquid away when it reaches the surface.

When the parameters are correctly adjusted, oscillations can grow inside the liquid together with surface waves.

Various stationary behaviours can be obtained by varying the thermophysical properties of the liquid (nature of the liquid, boundary temperature), the distance d from the surface and the rate of heating. However, the pertinent thermophysical parameters have not yet been identified and, up to now, we cannot a priori predict which gas-liquid interfaces will exhibit unsteady behaviours.

Typical physical quantities are the frequency of the phenomenon ($\simeq$1–10 Hz) and the maximal distance, between the free surface and the heated zone ($\simeq 5 \times 10^{-3}$ m). Inside the fluid the typical scales are very small (down to 5×10^{-5} m), accordingly the temperature field remains unknown.

In all experiments performed by our group, the variable parameters are distance d and rate of heating, while the nature of the liquid and the boundary temperature are kept fixed.

2.3. Field of dynamical state

Fig. 3 shows a HB1 state diagram in parameter plane (P, d), P being the laser power and d the distance between focus point and free surface. The external (boundary) temperature is monitored and held fixed at a constant value (25 ± 0.05°C). The liquid is toluene colored by Red Organol BX1750 (0.05 kg/m^3). Dynamical states and bifurcations have been identified by the power spectra of the experimental time signals, and checked by other approaches (see section 4). Curve CT1 is the frontier between steadiness (below, labelled S) and periodicity (above, labelled P). The transition on CT1 is a supercritical Hopf bifurcation.

In the experiment, the operator scans over d at fixed power P. Scanning for both increasing and decreasing d values shows no evidence for hysteresis within experimental accuracy.

Although each power value was scanned very precisely (d-steps up to 20 μm), at high d's, the location of curve CT1 suffers high uncertainties (see error bars on fig. 3) because of the very low

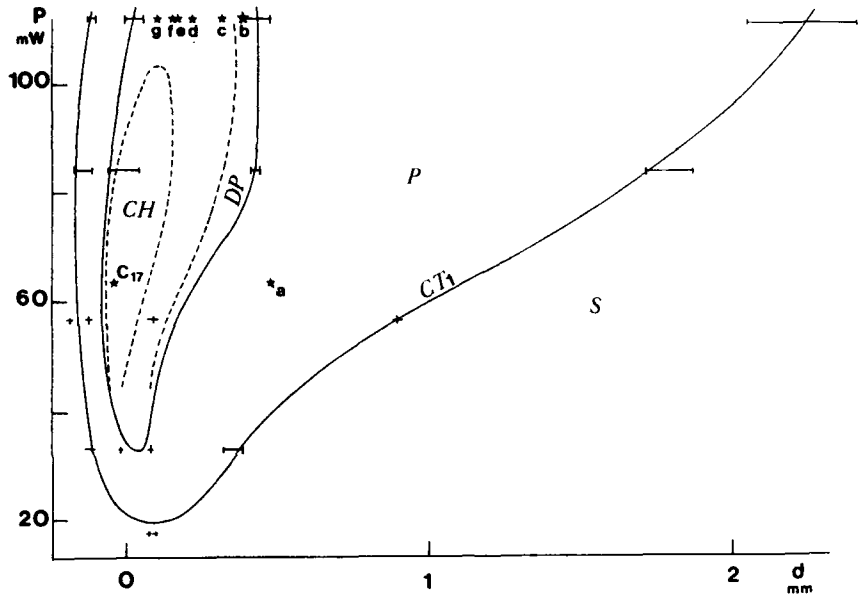

Fig. 3. Power-distance state plane of HB1 system (toluene with 0.05 kg/m^3 Red Organol BX1750; fixed boundary temperature: 25 ± 0.05°C). Continuous and dashed lines are the frontiers between steadiness (S), periodicity (P), period doubling (DP) and chaos (CH). Points with labels refer to experimental results reported in the paper.

amplitude of the oscillations and because of their intermittency.

Only the firmly established periodic (label P), doubly periodic (label DP) and chaotic (label CH) zones of diagram (P, d) have been shown on fig. 3. Smaller windows have been observed (chaos, periodicity, quasi-periodicity, chaos with periodic component) but their size is too small to ensure reproductibility and precise location on diagram (P, d).

With silicon oils whose thermophysical properties are better adapted to the hydrodynamical experiment, the state diagram can be drawn with a higher precision and the following behaviours have been observed [18, 19, 25]:

Periodic with one fundamental frequency, *periodic with subharmonics* corresponding to a Feigenbaum cascade, and *quasiperiodic* with two fundamental frequencies. *Frequency lockings* have also been observed when the two fundamental frequencies of the quasiperiodic signals become commensurable, leading to the experimental observation of *devil staircases*. *Hysteresis* also has been detected.

However, temporal chaos has not been observed with silicon oils though it has been observed with toluene. Hence, section 4 which is devoted to chaotic HB1 behaviour relies on experiments with toluene.

3. Combined approaches and characterization of chaotic regimes

Chaotic regimes can be detected by their high level continuous background in power spectra. However, such a continuous background is not a unique signature of chaos and a precise characterization requires going beyond power spectra toward quantitative characteristics of chaos.

The present section briefly recalls the main features of the (classical) approaches that we used for the characterization of chaotic time series, namely, qualitative 2D projections of 3D embeddings, Poincaré sections, detection of recurrent points and unstable orbits and quantitative characterization by Renyi dimensions.

Applications of the above approaches for

analyzing experimental time series will be reported in section 4.

3.1. Qualitative approaches of the chaotic regimes

3.1.1. n-dimensional reconstruction and 2D projection of 3D embeddings

The analysis of the chaotic experimental signal begins by the reconstruction of a trajectory in an n-dimensional phase space. By using the time delay method first proposed by Packard [34] and established by Takens [35, 36], we reconstruct a projection of the (assumed) underlying attractor embedded in $\mathbb{R}^n$. For sake of brevity, this geometric structure will be called "attractor" throughout the rest of the paper. Roughly speaking, the time delay method operates as follows: the physical signal $x(t)$ is sampled into time series of N experimental points $x(t_0 + i\,\Delta t)$ $(1 \leq i \leq N$; Δt sampling time; t_0 beginning of measurements). N-point trajectories (more exactly $\mathrm{INT}([N-(n-1)p]/m)$ can be reconstructed in $\mathbb{R}^n$, vector X_j having coordinates $X_{jk} = x(t_0 + jm\,\Delta t + kp\,\Delta t)$ $(0 \leq j \leq \mathrm{INT}([N-(n-1)p]/m)$; $0 \leq k \leq n-1$; m and p "well chosen" strictly positive integers). $p\,\Delta t$ is the time delay. A result of the time delay method is that the X_j's are randomly distributed with respect to the natural measure over the reconstructed attractor.

Firm foundations of $\mathbb{R}^n$ reconstructions are provided by the Mañé theorem [37] (although contested by Sauer et al. [38]) about parametrization of compact sets by real coordinates and by its extension to Takens' theorem [35] proving that, for $n \geq 2D_H + 1$, topology preserving reconstructions are dense among reconstructions.

$\mathbb{R}^3$ reconstructions can easily be 2D-projected on computer screens and are a big help in characterizing the attractor. Obviously, we know that $\mathbb{R}^3$ is not a good choice for reconstructing and embedding the experimental attractor since it does not comply with Takens' criterion. Furthermore, dimension computations exhibit a dimension close to 4 for the experimental attractor (see section 4). 3D embedding will then reduce the attractor. Nevertheless, 2D projections of 3D embeddings can be used as an interactive tool showing real time evolution of the dynamical states and simplifying the analysis of power spectra which can be associated with the aspect of the 3D embedding (e.g. fig. 4).

3.1.2. Poincaré sections, recurrent points and periodic orbits

Poincaré sections containing the crossing points between the reconstructed phase space trajectory and a given surface [39] are useful to evidence periodic and quasi-periodic oscillations. Well defined clusters of points on the Poincaré section are the signature of periodicity or quasi-periodicity. Conversely, cloudy sections do not allow sharp-cut conclusions because these sections may result either from high dimension quasi-periodicity or from chaos.

Another approach that we followed only in a qualitative way is the extraction of recurrent points and periodic orbits from the attractor. ϵ-recurrent points of order m are defined by the fact that the phase trajectory comes into a neighbourhood ϵ of these points after lag time $m\,\Delta t$ [40, 41]. The peaks, in the histograms of these ϵ-recurrent points as a function of order m, reveal possible periodic orbits in the attractor. Theory of dynamical systems establishes that many chaotic strange attractors have a skeleton of unstable periodic orbits which are dense on the attractor [42, 43]. The real phase trajectory will be captured by unstable orbits along the stable manifold and sooner or later will leave the orbits because of the divergence along the unstable manifold. Thus, the detection of portions of periodic orbits reveals the underlying skeleton of the attractor and may help in understanding its organization as well as its evolution under change of parameters.

3.2. Quantitative characterization of the attractor

A given attractor can be quantitatively charac-

terized by numbers like Renyi dimensions, generalized metric entropies and Lyapunov exponents. We mainly computed dimensions because they are a first clue for the estimation of the real phase space dimension.

Renyi dimensions D_q (q real) are global characterizations of the distribution of a given quantity (mass, charge, density, probability of presence, ...) over a support set defined by its geometric measure μ [44–46]. For dynamical systems and attractors, the involved quantity is the distribution of trajectory points in phase space and the geometric object is the set of representative phase space points for time tending to infinity. The D_q dimension is the (space) scaling exponent of the μ-weighted $(q-1)$th moment of the probability $p(i, r)$ that a point of the attractor lie inside ball i with radius r.

Furthermore, the measure μ itself is the probability of presence which is the "natural measure" over the attractor. Thus, given a partition B of the attractor by boxes of equal size r, the following scaling law holds in the limit $r \to 0$ and defines the set of Renyi dimensions:

$$\lim_{r\to 0} \sum_{B} \{p(i,r)[p(i,r)]^{q-1}\} \simeq r^{D_q(q-1)}, \quad q \neq 1. \tag{1}$$

The natural probability measure being ergodic, the partition B can be replaced by averaging over m boxes randomly distributed with respect to the measure and the scaling law can then be written either with respect to the radius (fixed radius) or with respect to the probability (fixed mass) [47].

The relevant formulae are

$$\lim_{r\to 0} \frac{1}{m} \sum_{i=1}^{m} [p(i,r)]^{q-1} \simeq r^{D_q(q-1)}, \quad q \neq 1 \tag{2}$$

for the fixed radius approach, and

$$\lim_{p\to 0} \frac{1}{m} \sum_{j=1}^{m} [\delta(j,p)]^{\gamma} \simeq p^{\gamma/D(\gamma)}, \quad \gamma \neq 0 \tag{3}$$

for the fixed mass approach, $\delta(j, p)$ being the size of box j containing probability p and $D(\gamma)$ being connected to Renyi dimensions by

$$D_q = D(\gamma = (1-q)D_q). \tag{4}$$

In the limit $q \to 1$ ($\gamma \to 0$) eqs. (2), (3) reduce to the definition of the information dimension D_1:

$$\lim_{r\to 0} \sum_{i=1}^{m} \frac{1}{m} \log p(i,r) \simeq D_1 \log r, \tag{5}$$

$$\lim_{p\to 0} \frac{1}{m} \sum_{j=1}^{m} \log[\delta(j,p)] = \log p^{1/D(0)}. \tag{6}$$

In practical computations, probability $p(i, r)$ is equal to the ratio N_i/N, the number of points lying inside box i over the total number of points on the attractor. Similarly, in the fixed mass approach, $\delta(j, p)$ is the distance of the kth nearest neighbour if p is taken equal to k/N. However, for experimental time series, the resolution of the data is finite and N also remains finite. Accordingly, the limits $r \to 0$ and $p \to 0$ cannot be reached and the actual scaling properties which can be computed do not necessarily identify with the true ones: (i) in the fixed radius method, the scaling law will hold only over finite, and sometimes unidentifiable r-intervals, specially for the case $q \leq 0$ when the poorly filled boxes significantly contribute to the r.h.s. of eqs. (2) and (5), (ii) in the fixed mass approach, the asymptotic behaviour for $N \to \infty$ sometimes will not be reached and the resulting overestimation of δ may significantly bias $D(\gamma)$ for $\gamma \geq 0$ (eqs. (3) and (6)).

Such limitations and biases which are due mainly to finite sets of points, lacunarity, drift and noise [48–51], may also arise from the finite precision of data (below 12-bit resolution [52]) or from a badly chosen sampling frequency [53]. In the present work, we handle sets of more than 10^5 data points with 15 bit precision. The sampling frequency has been chosen small enough to avoid underestimation of dimensions ($p\,\Delta t \simeq$

one eighth of pseudo-period) and the embedding dimension and time step have been empirically adjusted by trial and error until the largest scaling intervals were obtained (see section 4.2).

Systematic optimization of these empirical procedures is desirable [54, 55] but likely would only bring minor improvements of our results.

A last remark about Renyi dimensions is that the set of Renyi dimensions D_q complies with the inequality [45]

$$q \geq p \rightarrow D_q \leq D_p \,. \tag{7}$$

The higher q, the more significant will be the relative contribution of dense regions of the attractor to summation in eq. (2). Conversely, sparsely occupied regions will significantly influence the value of D_q for strongly negative q. Hence scanning on q from $-\infty$ to $+\infty$ is equivalent to scanning on probability density from less densely filled regions to most densely filled ones. However, each D_q value is an average of the scaling exponent over the attractor and it does not give any insight on the location of local scaling exponents on the attractor (local dimensions) [56]. Badii and Broggi [51] have pointed out that the fixed radius method is better suited for high q-values whereas the fixed mass approach operates better for small q's.

4. Experimental chaotic attractors

As stated in the introduction of the present paper, chaotic attractors have been detected in the experimental time series of the HB1 experiment. The present section is devoted to these experimental results. We shall show how the HB1 system evolves when varying the parameters and then characterize one of the experimental attractors.

4.1. Evolution of the system under changes of parameters

Figs. 4a–4g gather a sequence of 7 different

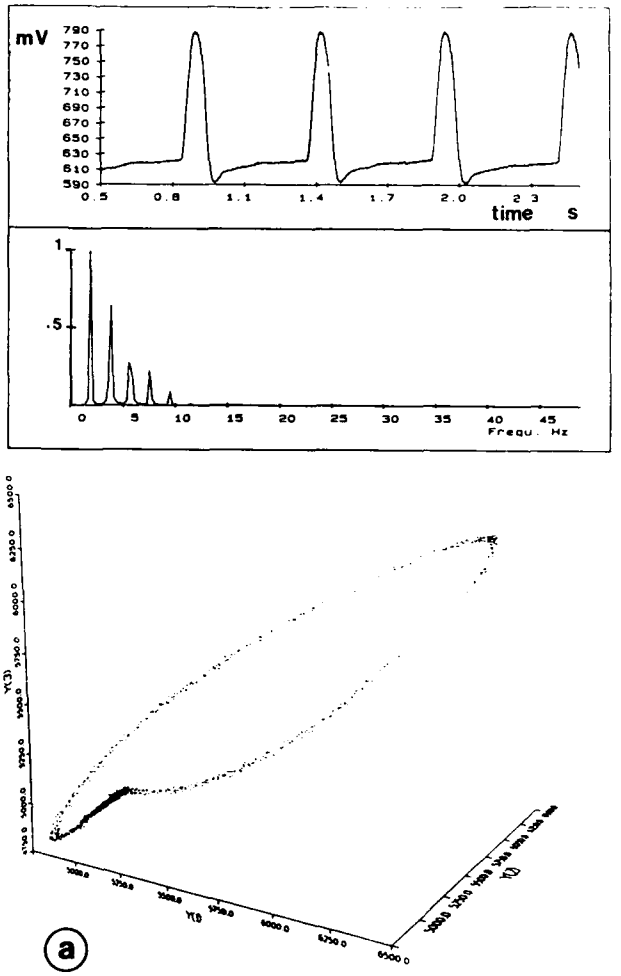

Fig. 4. Time signal, power spectrum (ordinate is the square root of the amplitude with arbitrary units) and 3D-projection of a sequence of dynamical states for decreasing focus–surface distance (labels a–g in fig. 3). (a) periodic state (laser power: 66 mW; distance from bottom of meniscus: 0.49 mm). (b)–(g) period doubling, interwoven orbits, periodic orbit, and random jumps between periodic orbits (laser power: 121 mW; distance from bottom of meniscus in mm: 0.39; 0.32; 0.22; 0.18; 0.16; 0.11.

dynamical states of the thermal lens. All states, but the first one, have been recorded with the same laser power $P = 121$ mW and they are ordered from high to low focus-surface distances (except the first one, experiments are located on the same horizontal line at the top of fig. 3. They are ordered from right to left.)

For each state of the system, we give a part of the time signal, the associated power spectrum

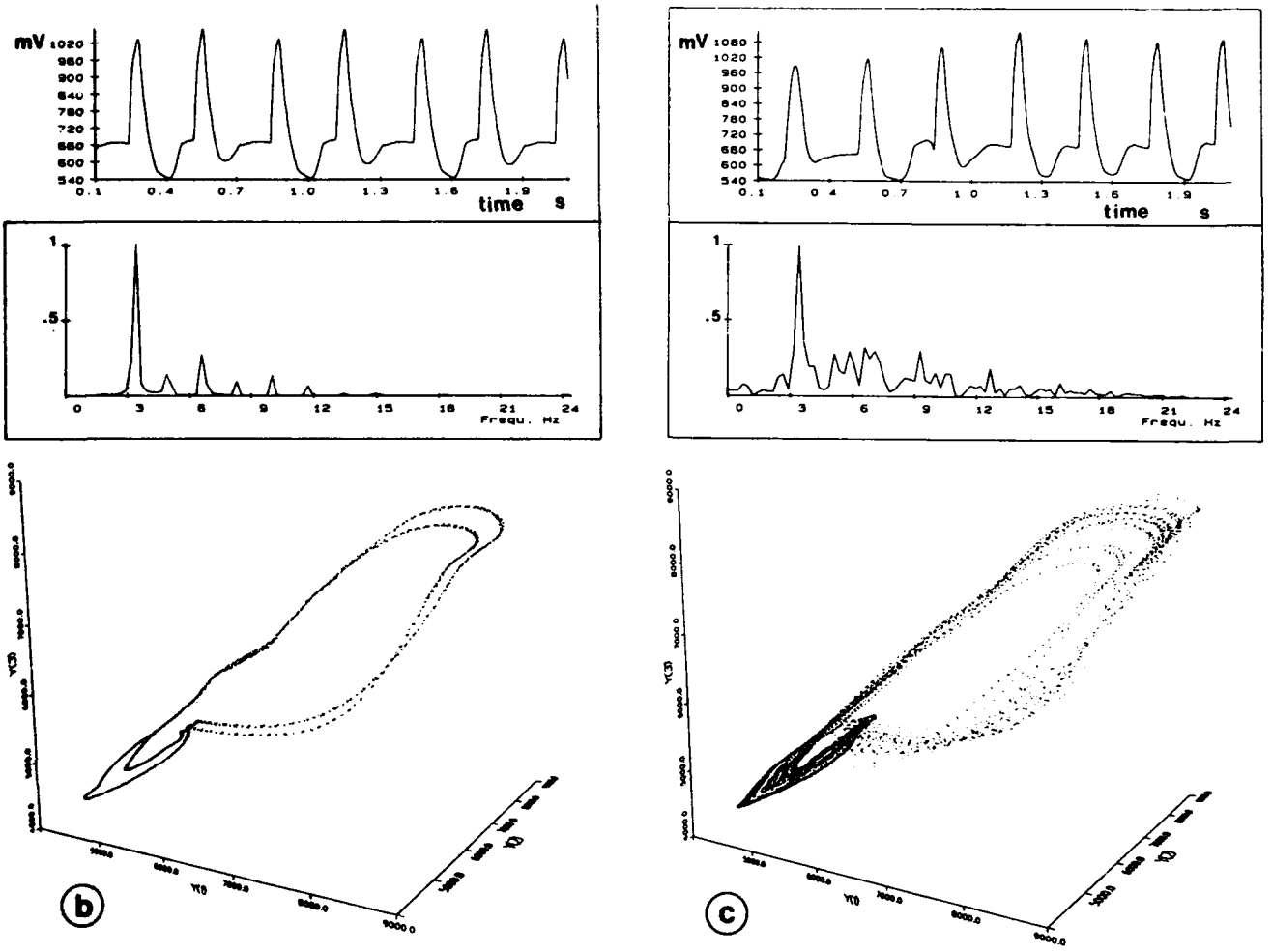

Fig. 4. Continued.

and a 3D projection. We choose high sampling frequencies (1000 or 2000 Hz) which give high resolution on 3D embeddings. For dimension computations, the sampling frequency must be lower.

The 2D projections of 3D embeddings bring much more information than the time signals and power spectra alone. For high distances d, we observe a periodic state with fundamental frequency at about 2 Hz and several harmonics. The 2D projection shows a cycle with two different regions: a concentrated zone and a large sparsely populated orbit. The corresponding phenomena in the time signal are a slow variation of light intensity followed by a sharp peak (fig. 4a). When we decrease the distance d, period doubling is observed and the 2D projection precisely shows that the system alternatively follows each part of the twin orbit (fig. 4b) [57]. Decreasing d values further, we find the power spectrum evolves to a well defined periodic peak surrounded by a continuous background and the 2D projection reveals that the system randomly chooses between interwoven periodic orbits (fig. 4c). The other states of the sequence successively show a well defined periodic orbit (fig. 4d), and a new growth of the orbit thickness (2D projection) and of the noisy background (power spectrum) suggesting the existence of a chaotic attractor (figs. 4e and 4f). When the focus point is

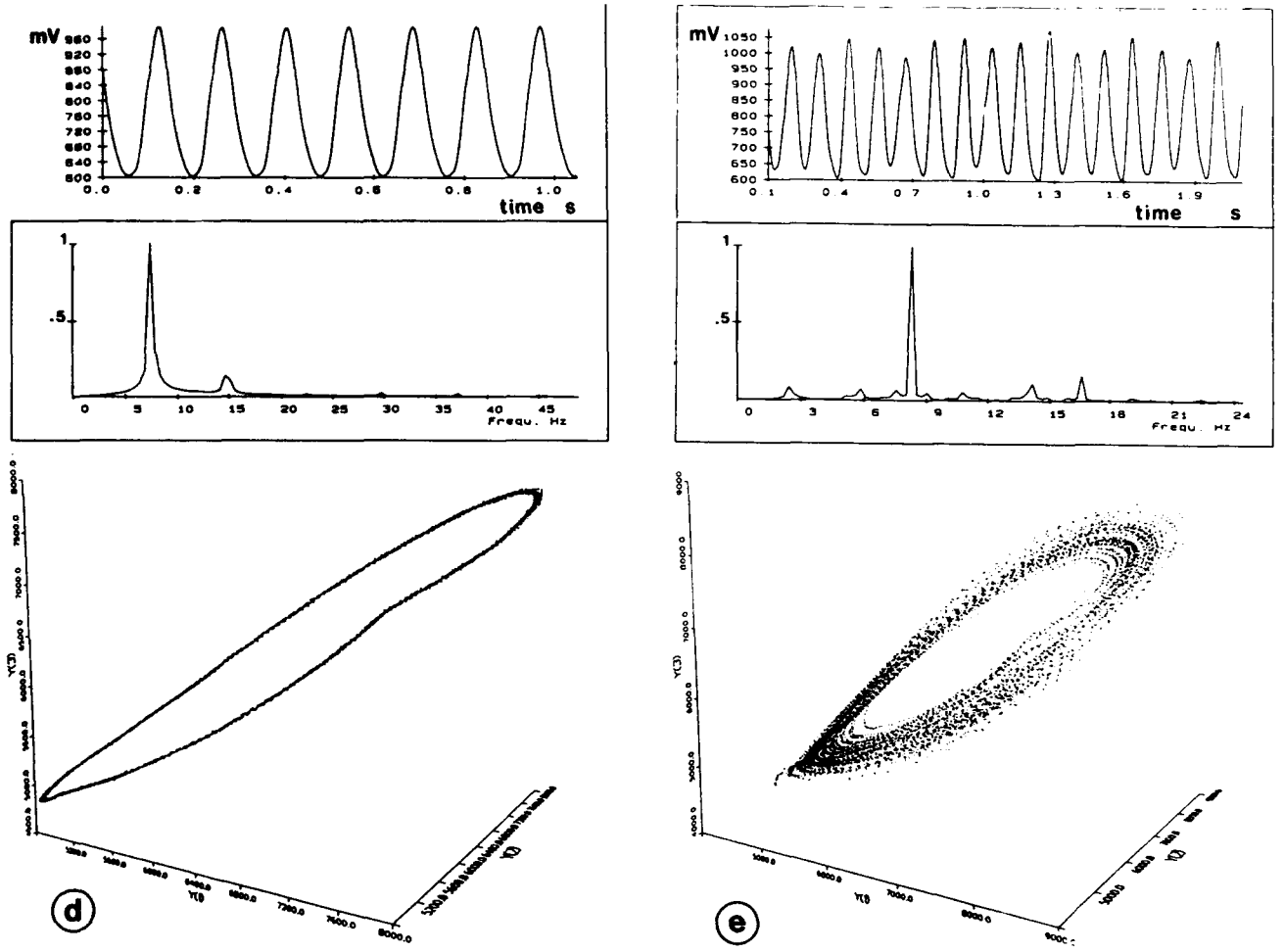

Fig. 4. Continued.

close to the surface, a periodic state is reached again but with a small and noisy signal which gives a thick periodic orbit in the 2D projection (fig. 4g).

4.2. *Characterizations of a chaotic attractor*

Several chaotic states of the HB1 experiment have been recorded and analyzed. From these, we have chosen one example to report some results of the approaches described in section 3. This example is a dynamical state labelled C17 in fig. 3. The incident laser power is 66 mW, the focus is 0.08 mm above the bottom level of the meniscus and the sampling frequency is 200 Hz. 163 840 data points have been stored.

The 2D projection of the 3D embedding of the attractor and a Poincaré section are given by figs. 5a, 5b, respectively. Fig. 5a shows a cloud of points without evident structure apart from a short thick curve in the left lower part and a very dense area in the middle. The curve is the track of a well defined motif in the time evolution of the thermal lens and the dense area witnesses that the oscillations almost stop and the data accordingly cluster around the same value before dispersing again. The Poincaré section of fig. 5b is the intersection of the 3D projection with the plane $Y(3) = 4500$ for trajectories going downward. Again, no clear structure can be detected in the Poincaré section which shows two diffuse clouds. Other sections in different regions of the

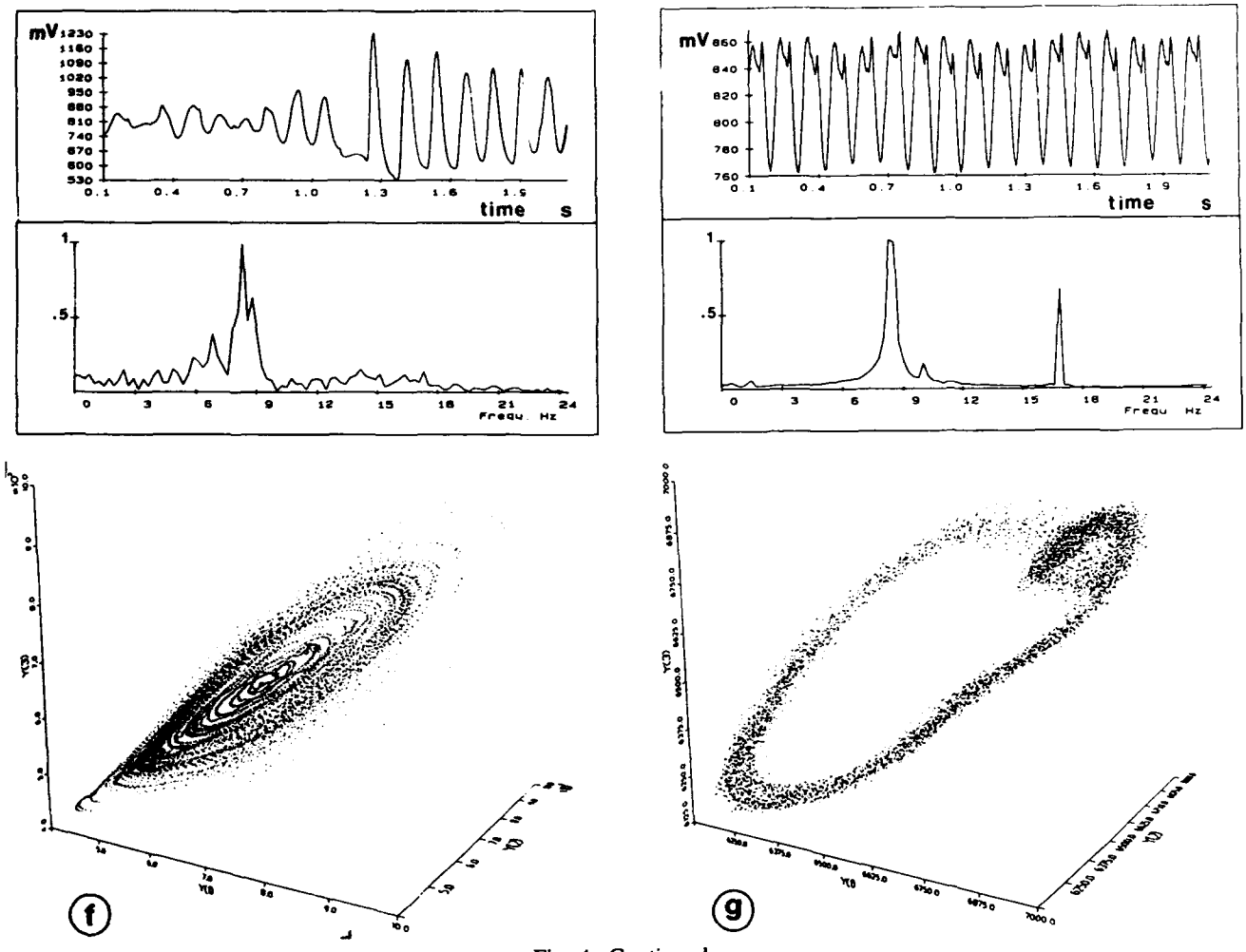

Fig. 4. Continued.

attractor have confirmed that it is sensible to discard the possibility that this is either a periodic or quasiperiodic dynamical state. With experimental data like ours, Poincaré sections cannot be used much beyond the detection of periodicity and quasiperiodicity because of the small number of points inside a given section. Hence the analysis of Poincaré sections often must be restricted to qualitative observations and remarks.

Between qualitative and quantitative analysis, lies the identification of recurrent points. Fig. 6a is the histogram giving the number of ϵ-recurrent points as a function of the order m of the recurrence. Peaks indicate possible periodicities. On the histogram, recurrence orders (e.g. $m = 11, 21, 22, 69, 93, 163, 326, 491 \ldots$) can be identified for $\epsilon = 20$ (that is about 0.01 diameter of the attractor). Peaks 163, 326 and 491 are the typical signature of a strongly recurrent behaviour, the phase space trajectory following the same way at equally repeated time intervals. Once the orders of recurrence have been identified, it is then possible to draw the corresponding portions of the phase space trajectory and to detect how recurrences are due to the sticking of the trajectory in the neighbourhood of a periodic orbit (e.g. figs. 6c–e). Hence, it appears that recurrence peaks 21–22 cover two different orbits, the first one exhibiting a single medium size

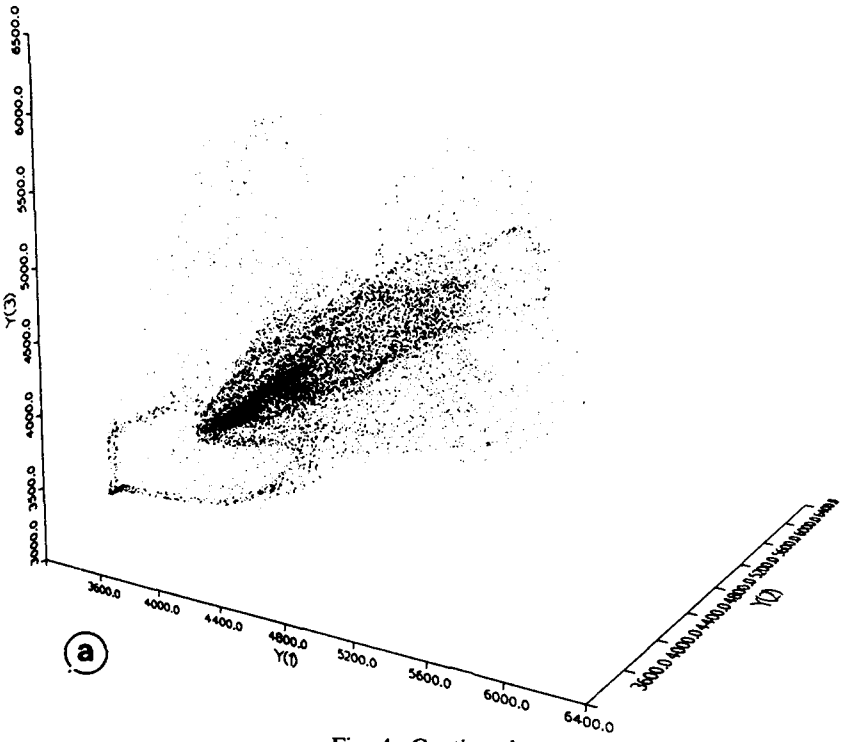

Fig. 4. Continued.

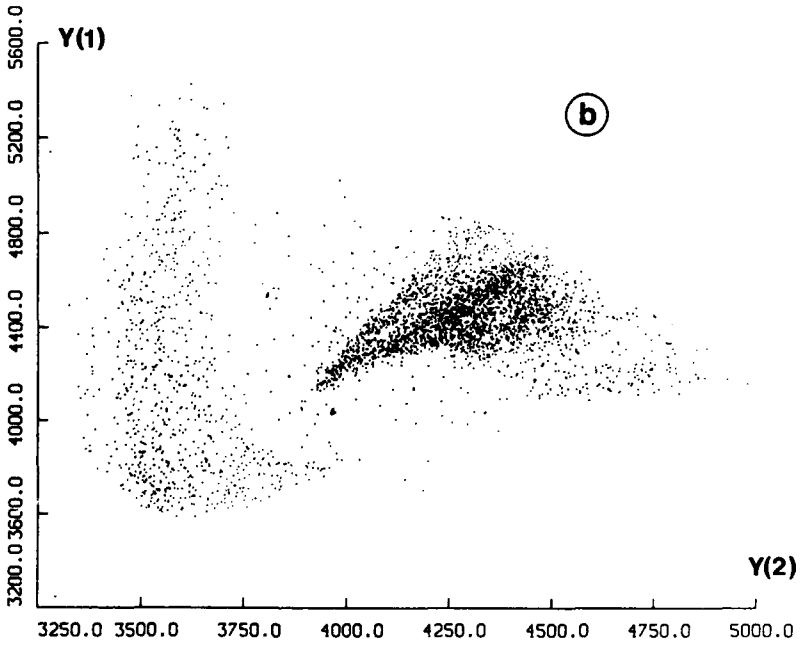

Fig. 5. A typical experimental chaotic time series (dynamical state labelled C17 in fig. 3). (a) 3D display; (b) Poincaré section ($Y(3) = 4500$, trajectory going downward).

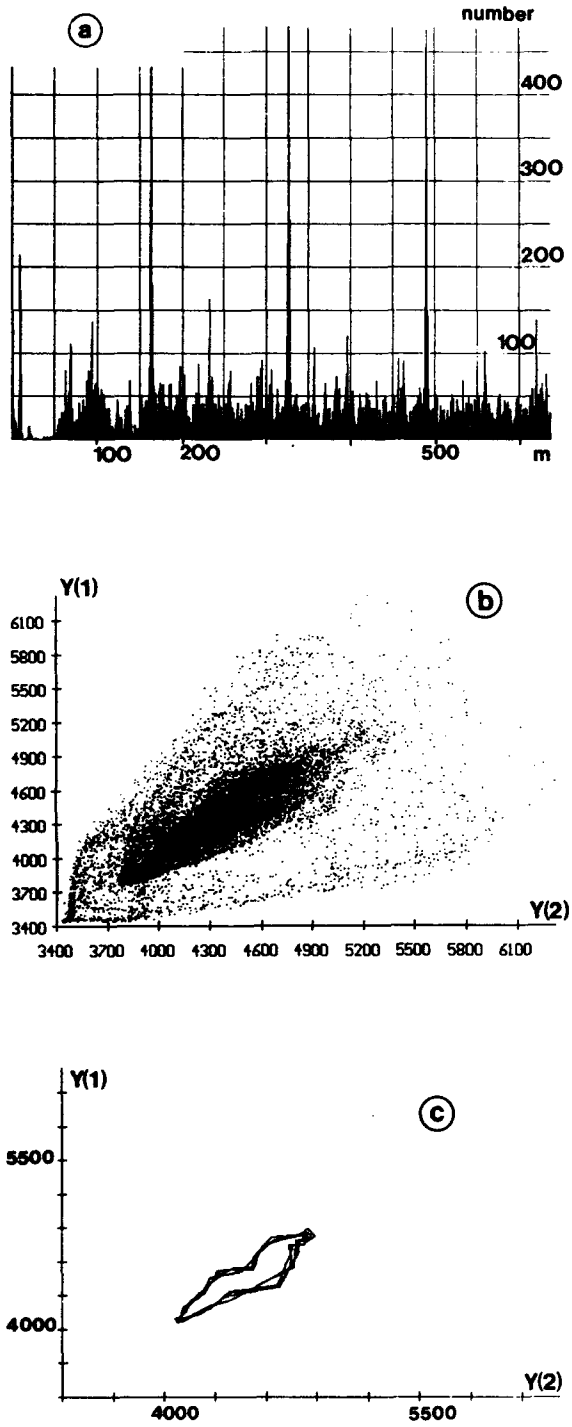

Fig. 6. Detection of ϵ-recurrent points and periodic orbits ($\epsilon = 20$; sampling frequency 200 Hz). (a) number of ϵ-recurrent points vs recurrence order m ($\mathbf{R}^3$ embedding. $\mathbf{R}^{10}$ exhibits the same features but with a more noisy histogram). (b)–(e) 2D-projections of the attractor (b) and of orbits corresponding to recurrence orders 21 (c), 22 (d), (69) (e) (same axes and scales).

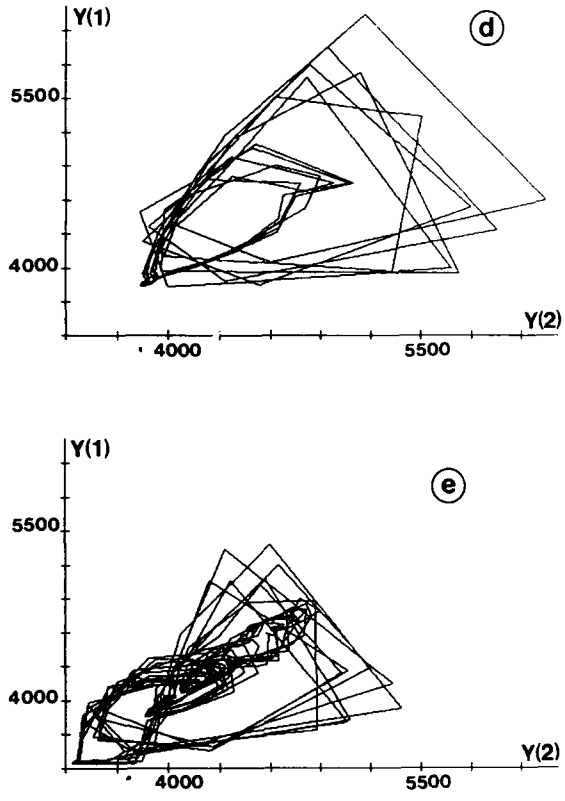

Fig. 6. Continued.

loop on 2D projection (fig. 6c) and the second one being a large two-loop orbit (fig. 6d). For a higher recurrence order like 69 (fig. 6e), the 2D projection of the orbit is more complex showing at least four loops. In fig. 6, each presumably unstable orbit is shadowed by several portions of trajectory close to each other that have been evidenced by colors which, unfortunately, cannot be reproduced in this paper. The portions of trajectory look like broken lines because the sampling time ($5\ 10^{-3}$ s) is only 40 times smaller than the pseudoperiod of the signal. Lack of time explains why it has only been possible to draw fig. 6 as a 2D projection without 3D embedding. For the same reason and also owing to the small amount of experimental data, we have not yet been able to extract from periodic orbits further information like winding numbers or symbolic dynamics. In principle this would be feasible [58, 59] but it still requires a lot of work.

Quantitative characterization of the attractor

have been carried out by dimension computations (see section 3.2). The time series contains $N = 163\,840$ data points. Averages involved by eqs. (2)–(6) have been carried over $m = 10\,000$ points randomly distributed with respect to the probability measure. The sampling frequency is 200 Hz and the pseudo frequency of the time signal (highest peak in power spectrum) is 5 Hz. Hence, the time series contains about 40 points per pseudo period. The time delay has been adjusted to obtain the best stability of the information dimension D_1 in the fixed radius approach: in $\mathbb{R}^{10}$, a time delay of 25×10^{-3} s (that is choosing one data point each five) gives the largest and most stable plateau for the estimation of D_1. This value has been retained for all other computations.

Figs. 7–10 summarize the results of the fixed radius approach. Fig. 7 shows eq. (5) for different dimensions of the embedding phase space. The ordinate in fig. 7 is the l.h.s of eq. (5), i.e. the average logarithm of the probability, and the

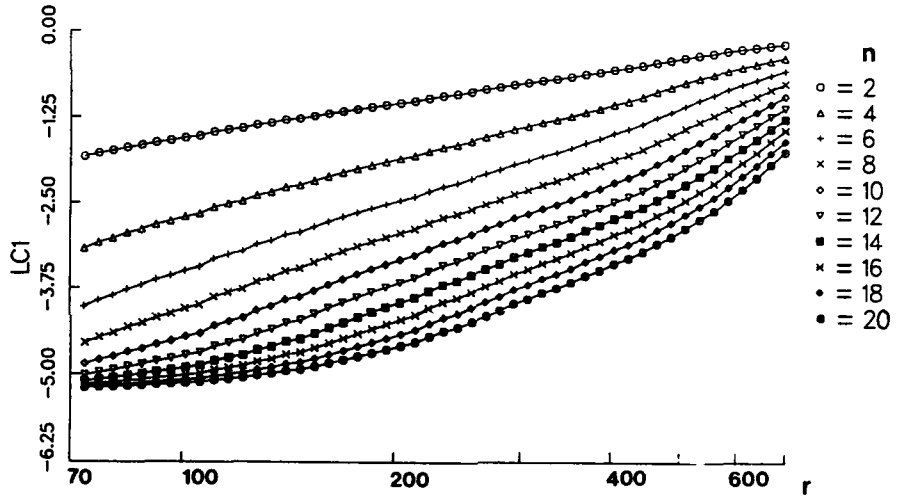

Fig. 7. Eq. (5): Average logarithm of the probability of a box as a function of box size r (log scale). Different curves correspond to different dimensions n of the embedding phase space.

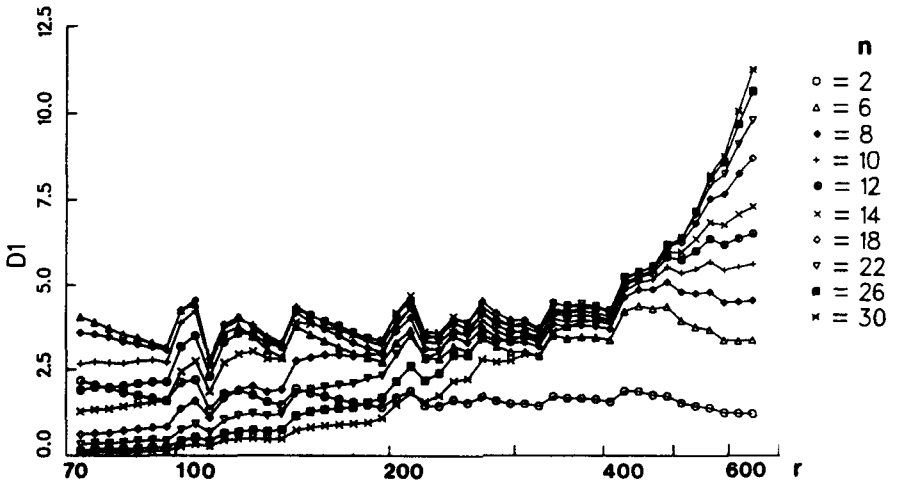

Fig. 8. Local slope of curves of fig. 7.

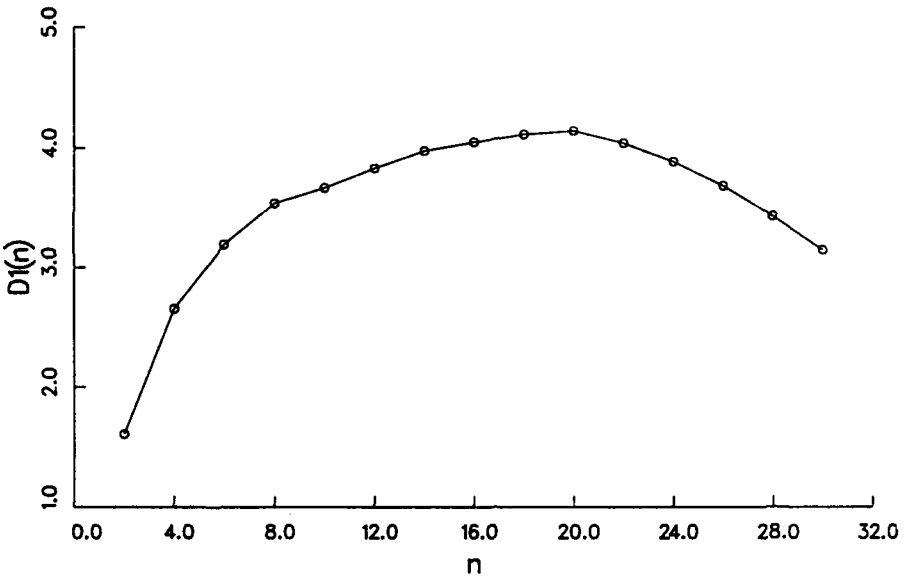

Fig. 9. Information dimension D_1 vs. dimension of the embedding phase space.

abscissa is the logarithm of the box size r. If the scaling law (5) holds, the slope is the information dimension D_1. The embedding phase space dimensions range over [2, 20] and r over [70, 700]. A scaling zone where the different curves are parallel straight lines can be located for $230 < r < 420$ (that is about $0.06 \ll 0.12$ in units of the attractor diameter). The local slopes of the curves of fig. 7 are shown by fig. 8 where the scaling zones more or less look like plateaus.

For increasing embedding phase space dimensions, noise progressively invades and submerges small r-values due to decreasing statistics which smoothes small scale structures of the attractor

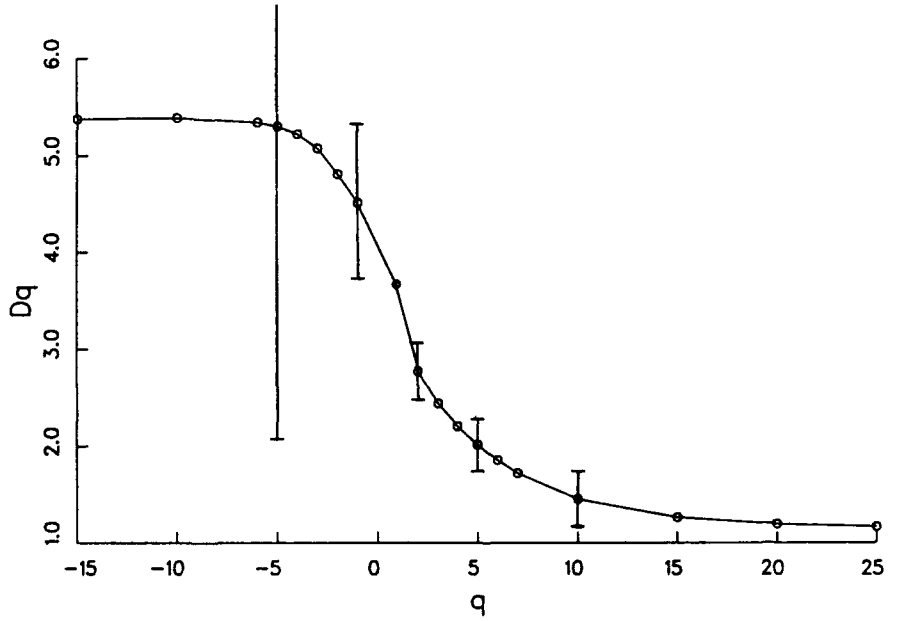

Fig. 10. Spectrum of Renyi dimensions D_q. (Some standard deviations are given, they increase for decreasing q.)

(slope decreasing to zero). Simultaneously the curves are shifted upward to an asymptotic level. On the right, the curves steepen because a high embedding dimension stretches the attractor, setting many points at large distances that are of the order of the size of the attractor.

The information dimension D_1 has been computed as an average of the local slopes over the scaling zone, the scaling zone itself being determined by an automatic procedure which avoids subjective or ad hoc choices. It would require too much space to detail here the procedure. Basically, the procedure does not involve human interpretation except the choice of the value of the error bar for the ordinate of the plateau (see ref. [60]).

The results of the average is displayed by fig. 9 as a function of the embedding phase space dimension n. D_1 decreases for low dimensions and for high dimensions. For high dimensions, the decrease is due to noise and for low dimensions it automatically results from the fact that D_1 cannot be higher than n for nD-embeddings. For intermediate dimensions an asymptotic value around 4 is obtained: For instance $D_1 = 4.0$ in $\mathbb{R}^{16}$ (std dev. 0.3) and $D_1 = 4.1$ in $\mathbb{R}^{18}$ (std dev. 0.3).

Finally, fig. 10 shows the spectrum of Renyi dimensions D_q computed with the fixed radius method in $\mathbb{R}^{10}$ (although $\mathbb{R}^{16}$ is better suited for the computation of D_1, $\mathbb{R}^{10}$ is the best compromise when computing D_q's for various q-values). q ranges from -15 to 25 but, for negative values, the results are only rough estimates with high standard deviation. As a matter of fact, due to empty boxes, the local slopes are strongly underestimated when the radii of the boxes are small. Thus we have been obliged to abandon the automatic procedure of averaging the local slopes and to come back to approximate and subjective manual procedures with subsequent adjustments to fit both procedures on the same figure. However, fig. 10 displays a typical profile of a D_q spectrum complying with inequality (7) and, without giving too much significance to the numerical values of the dimensions, there is no doubt that they range over a pretty broad range (roughly between 1 and 5). Accordingly, we can conclude that the attractor is likely to be strongly inhomogeneous because the dimensions of sparsely filled regions are clearly different from those of densely filled regions (see comment on eq (7)). Local dimensions have been computed with the purpose of assessing the inhomogeneity of the attractor but the set of experimental data is too small to obtain any sensible values and distribution of local dimensions over the attractor.

A specific remark is necessary about $D_q < 2$: in principle, chaos requires $D_q \geq 2$. Results lower than 2 likely are due to finite resolution of data. At smaller scales (experimentally unattainable), the points should be distributed over the attractor in such a manner that $D_q \geq 2$.

The fixed mass approach (see section 3.2) confirms the results of the fixed radius one. Fig. 11 shows the results of the fixed-mass approach on the same time series and with the same parameters ($m = 10\,000$, time delay 25×10^{-3} s and a space dimension of 10). The $D(0)$ dimension is plotted as a function of the number N of points, for different values of the number of neighbours.

The first point to emphasize is the good asymptotic behaviour of the curves. Hence, we are not obliged to take an average value on a quite subjective number of points, and the result is more stable than with the fixed radius method.

The second point is that the value of $D(0)$ compares well with D_1 computed previously: $D(0) = 3.8 \pm 0.1$. Both methods thus agree about a dimension of the attractor close to 4. Such a pretty high dimension a priori may be suspected because the computations are sensitive to various biases. However, the quality of our data and the coherence of our results strongly witness for an actual dimension about 4 (see following section).

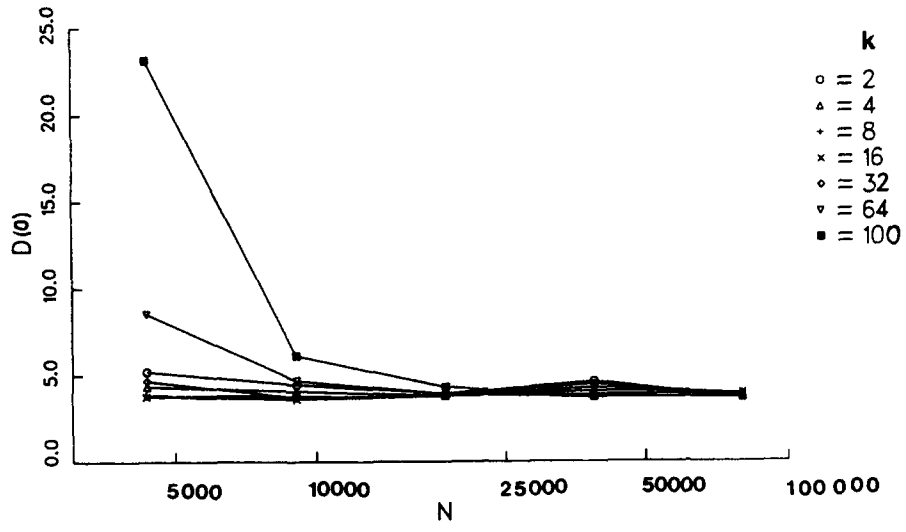

Fig. 11. Asymptotic behaviour of $D(0)$ dimension function vs. number of data points N. (Fixed mass method.) Each curve is for a given number of nearest neighbours k.

4.3. *A plea for the use of combined approaches*

The physicist dealing with experimental chaotic systems as we do here should be convinced that combined approaches of the experimental attractor are not only useful but almost necessary. In thermal lensing, owing to the complexity of the involved hydrodynamical properties, we ignore much more than we know about the physics of the experiment. Thus, any single result remains questionable and combined approaches are the unique means for assessing firm results. For instance, an attractor dimension about 4 a priori seems too high to establish low dimensional chaos and this result may raise the scepticism of the reader. And so did we look at our first dimension computations. But, combining further several approaches, we note that the fixed mass dimension confirms the fixed radius one, that the power spectra and the 3D embeddings assess the quality of the signal with low noise level and that the Poincaré sections and periodic orbits show the possibility of qualitative insight into the structure of the attractor. Isolated, one of these observations remains weak but their convergence sets our conclusions to a reasonable confidence level.

Combined approaches do not only assess the final results that are published in scientific papers, they also enrich the researcher's feeling and analysis of the dynamical systems. Let us emphasize three features that we have experimented to be significant but that are only poorly reflected in the static, frozen, scientific papers: (i) graphical displays give access to a powerful *global perception* of the results because our vision system is well suited for catching and analysing a large amount of data (ii) real-time observation of displays reveals the *chronology* of the phenomenon as the points lighten successively on the screen (iii) on-line implementation of graphical tools helps the researcher in choosing and monitoring the *parameters* of the experiment because it immediately shows the evolution of the graphical display when parameters are changed.

5. Conclusion

Heating just below the free surface of a liquid can induce oscillations and various kinds of dynamical states. The heartbeat experiments use heating by a focused laser beam which simulta-

neously gives an enlarged picture of the dynamical system due to thermal lensing. Thus the experiment owns the advantages of visual evidence and of optical based diagnostics and measures. We have recorded many time series from the HB1 experiment, some of them being chaotic. For the analysis of the experimental time series and for the understanding of the dynamical system, the use of multiple and complementary approaches is not only desirable but almost necessary. Particularly powerful are 2D and 3D displays which introduce to a global visual perception of the behaviour of the system and of its evolution when the parameters are changed. These graphical tools give their best when they allow permanent feedback by implementation in real time processing of experimental data. Several chaotic attractors have been detected by analysis of HB1 time series and one example has been reported in the present paper. 3D reconstructions, power spectra, Poincaré sections have assessed the presence of temporal chaos. The analysis of recurrent points has revealed some of the underlying presumably unstable periodic orbits. The computations of Renyi dimensions with Grassberger–Procaccia algorithm have been done and published both with the fixed radius approach and with the fixed mass one. They give an information dimensions of the attractor about 4. This value suggests that theoretical models of HB experiments should involve at least four or five ordinary differential equations. Other papers report some significant work which has been done to design such theoretical models of the HB system, reducing the actual system to a dynamical system with few degrees of freedom [21–23]. For instance, two (well-designed) coupled ODE's suffice to approach the understanding of the first Hopf bifurcation and with three coupled ODE's, secondary instabilities can be modelled.

Forthcoming work will aim at completing the analysis of chaotic time series (entropies, Lyapunov exponents) and at obtaining similar behaviours with a hot wire experiment. Then, probably the way will be open to produce and analyze spatial-temporal chaos in heated surface instabilities.

Acknowledgements

We acknowledge Alain Souillard for improving the English of the paper and Jean-Guy Caputo for helpful and motivating discussions.

References

[1] P. Bergé, Lecture notes in Physics 104 (Springer, Berlin, 1979) p. 189.
[2] P. Bergé, M. Dubois, in: Scattering Techniques Applied to Supramolecular and Nonequilibrium Systems", eds. S.H. Chen, B. Chu and R. Nossal (Plenum, New York, 1981) p. 493.
[3] A. Libchaber and J. Maurer, in: Nonlinear Phenomena at Phase Transitions and Instabilities, ed. T. Riste (Plenum, New York, 1982) p. 259.
[4] A. Libchaber, C. Laroche and S. Fauve, J. Phys. (Paris) Lett. 43 (1982) L211.
[5] C. Vidal, S. Bachelart and A. Rossi, J. Phys. (Paris) 43 (1982) 7.
[6] R.H. Simoyi, A. Wolf and H.L. Swinney, Phys. Rev. Lett. 49 (1982) 245.
[7] P. Linsay, Phys. Rev. Lett. 47 (1981) 1349.
[8] J. Testa, J. Perez and C. Jeffries, Phys. Rev. Lett. 48 (1982) 714.
[9] F.T. Arecchi, R. Meucci, G. Puccioni and J. Tredicce, Phys. Rev. Lett. 49 (1982) 1217.
[10] C.D. Andereck, R. Dickman and H.L. Swinney, Phys. Fluids 26 (1983) 1395.
[11] E. Jakeman, E.R. Pike and J.M. Vaughan, RRE Newsletter and Research Review, No. 12 (1973).
[12] R. Anthore, P. Flament, G. Gouesbet, M. Rhazi and M.E. Weill, Appl. Opt. 21 (1982) 2.
[13] V.Yu Bazhenov, M.V. Vasnetsov, M.S. Soskin and V.B. Taranenko, JEPT Lett. 49 (1989) 376.
[14] S.A. Viznyuk and A.T. Sukhodol'skii, Sov. Phys. Tech. Phys. 33 (1988) 609.
[15] G. Gouesbet, M. Rhazi and M.E. Weill, Appl. Opt. 22 (1983) 304.
[16] G. Gouesbet and E. Lefort, Appl. Opt. 26 (1987) 2940.
[17] G. Gouesbet, M.E. Weill and E. Lefort, AIAA J. 24, (1986) 1324.
[18] G. Gouesbet and E. Lefort, Phys. Rev. A 37 (1988) 4903.
[19] G. Gouesbet and E. Lefort, in: Proc. Nat. Fluid Dyn. Cong. (Cincinnati, OH, July 1988) Paper 88-3814.

[20] G. Gouesbet, Int. J. JSME, Ser. II 32 (1989) 301.
[21] G. Gouesbet, J. Maquet, Comm. Heat Mass Trans. 16 (1989) 133.
[22] G. Gouesbet, Dynamical states and bifurcations in a new thermodynamical nonlinear system: optical heartbeats and associated phenomena, Entropie (France) 153/154 (1990) 47.
[23] G. Gouesbet, Phys. Rev. A 42 (1990) 5928.
[24] M. Rhazi, Etude des oscillations créées par une source de chaleur placée à proximité d'une surface libre. Thèse de 3ème cycle, Rouen (France) 18 Avril (1984).
[25] E. Lefort, Caractérisation des bifurcations et de la dynamique d'une lentille thermique par analyse spectrale. Thèse de 3ème cycle, Rouen (France) 6 Mai (1987).
[26] C. Rozé, Etude des oscillations créées par un fil chaud placé juste au-dessous de la surface libre d'un liquide. Thèse de l'Université de Rouen (France) 14 Décembre (1989).
[27] M.E. Weill, M. Rhazi and G. Gouesbet, Compt. Rend. Acad. Sci. Paris 294 Ser. II (1982) 567.
[28] M.E. Weill, M. Rhazi and G. Gouesbet, J. Phys. (Paris) 46 (1985) 1501.
[29] G. Gouesbet, Phys. Chem. Hydrodyn. 8 (1987) 349.
[30] G. Gouesbet, J. Maquet, C. Rozé and R. Darrigo, Phys. Fluids A 2 (1990) 903.
[31] C. Rozé, G. Gouesbet and R. Darrigo, New investigation of oscillatory instabilities produced by temperature-controlled hot-wire heating below an interface, in preparation.
[32] J.P. Gordon, R.C.C. Leite, R.S. Moore, S.P. Porto and J.R. Whinnery, J. Appl. Phys. 36 (1965) 3.
[33] A. Destexhe, G. Nicolis and C. Nicolis, in: Measures of complexity and chaos, eds. N.B. Abraham, A.M. Albano, A. Passamante and P.E. Rapp (Plenum, New York, 1989) p. 339.
[34] N.H. Packard, J.P. Crutchfield, J.D. Farmer and R.S. Shaw, Phys. Rev. Lett. 45 (1980) 712.
[35] F. Takens, in: Dynamical systems and turbulence (Warwick, 1980), Lecture notes in Mathematics 898 (Springer, Berlin, 1981) 366.
[36] F. Takens, in: Nonlinear dynamics and turbulence, eds. G.I. Barenblatt, G. Iooss and D.D. Joseph (Pitman, London, 1983) p. 314.
[37] R. Mañé, in: Dynamical systems and turbulence (Warwick, 1980), Lecture notes in Mathematics 898 (Springer, Berlin, 1981) p. 230.
[38] T. Sauer, J.A. Yorke and M. Casdagli, Embedology, Phys. D 58 (1992) 193, these Proceedings.
[39] P. Bergé, Y. Pomeau and C. Vidal, L'ordre dans le chaos (Hermann, Paris, 1984).
[40] J.P. Eckmann, S.O. Kamphorst and D. Ruelle, Europhys. Lett. 4 (1987) 973.
[41] A. Babloyantz, in: Measures of complexity and chaos, eds. N.B. Abraham et al. (Plenum Press, New York, 1989) p. 51.
[42] D.P. Lathrop and E.J. Kostelich, in: Measures of complexity and chaos, eds. N.B. Abraham et al. (Plenum, New York, 1989) p. 147.
[43] D.P. Lathrop and E.J. Kostelich, Phys. Rev. A 40 (1989) 4028.
[44] A. Renyi, Probability theory (North-Holland, Amsterdam, 1970).
[45] H.G.E. Hentschel and I. Procaccia, Physica D 8 (1983) 435.
[46] P. Grassberger and I. Procaccia, Phys. Rev. Lett. D 5 (1983) 346.
[47] P. Grassberger, R. Badii and A. Politi, J. Stat. Phys. 51 (1988) 135.
[48] P. Grassberger, Phys. Lett. A 128 (1988) 369.
[49] C.L. Sayers, in: OSA Proc. on Nonlinear Dynamics in Optical Systems, eds. N.B. Abraham, E. Garmire and P. Mandel, Vol. 7 (Optical Society of America, Washington DC, 1991) p. 5.
[50] N.B. Abraham, A.M. Albano, B. Das, G. de Guzman, S. Yong, R.S. Gioggia, G.P. Puccioni and J.R. Tredicce, Phys. Lett. A 114 (1986) 217.
[51] R. Badii and G. Broggi, Phys. Lett. A 131 (1988) 339.
[52] Möller and Mitschke, Phys. Lett. A 138 (1989) 176.
[53] J.G. Caputo, Dimension et entropie des attracteurs associés à des écoulements réels: estimation et analyse de la méthode. Thèse de l'Université de Grenoble (France, 1986).
[54] T. Buzug and G. Pfister, Physica D 58 (1992) 127, these Proceedings.
[55] T. Buzug and G. Pfister, Europhys. Lett. 13 (1990) 605.
[56] T.C. Halsey, M.H. Jensen, L.P. Kadanoff, I. Procaccia and B.I. Shraiman, Phys. Rev. A 33 (1986) 1141.
[57] Actually the first peak in power spectrum is too small to be visible because the system is very close to period doubling bifurcation.
[58] G.B. Mindlin, X. Hou, H.G. Solari, R. Gilmore and N.B. Tufillaro, Phys. Rev. Lett. 64 (1990) 2350.
[59] R. Badii, in: Measures of complexity and chaos, eds. N.B. Abraham et al. (Plenum, New York, 1989) p. 147.
[60] S. Meunier-Guttin-Cluzel, Caractérisations et modélisations des régimes chaotiques de la lentille thermique. Thèse de l'Université de Rouen (France, 1990).

Physica D 58 (1992) 441–454
North-Holland

PHYSICA D

Characterization of experimental time series from Taylor–Couette flow

G. Pfister, Th. Buzug and N. Enge
Institut für Angewandte Physik, Universität Kiel, W-2300 Kiel, Germany

Received 30 October 1991
Revised manuscript received 10 February 1992
Accepted 15 February 1992

Rotational Taylor–Couette flow shows a rich variety of well-defined and controllable scenarios. Even for short cylinders, where the number of possible flow states is found to be very small, period doubling cascades, intermittencies, homoclinic orbits and n-tori can be found depending on boundary conditions. We characterize these flow states by fractal dimensions, Lyapunov spectra and entropies. In the experiments the axial velocity component was measured using laser–Doppler anemometry and the phase space was reconstructed by using delay time coordinates. A simple noise reduction algorithm was applied to the noisy data set to improve the accuracy of the estimation of the dynamical variables.

1. Introduction

The flow of a viscous fluid between two rotating coaxial cylinders has long been one of the most prominent examples in the study of hydrodynamic instabilities [1]. Though the experiment is comparatively easy to perform and the external parameters can be satisfactorily controlled, the theoretical calculations lead to exact solutions of the Navier–Stokes equation for small Reynolds numbers only and if the cylinders are considered to be infinitely long. Nevertheless many ideas concerning hydrodynamic instabilities and the route to chaos could be examined experimentally and verified numerically [2–12]. For a better understanding of the Taylor–Couette flow one has to know all solutions as a function of their location in the control parameter space. This requires the analysis of many points in the parameter space. For the estimation of dynamic variables like fractal dimensions and Lyapunov spectra, which can handle noisy data sets restricted in resolution and number, one needs efficient algorithms.

To limit the number of solutions we focus on Taylor–Couette flow with short cylinders where this number of solutions is assumed to be moderately small ([9] and papers cited therein). Even with this restricted configuration, we can show that there is no universal route to chaos for Taylor–Couette flow. Instead there exists a rich variety of scenarios. In this paper we present experimental results of three of them: period doubling, n-torus and intermittency. The interpretation of the results shows the necessity of noise reduction methods and we present a simple algorithm implemented by us.

2. Flow apparatus and measuring techniques

The inner cylinder of the Taylor–Couette apparatus used in the experiments was machined from stainless steel having a radius of $r_1 = 12.5$ mm, while the outer cylinder was made from optical polished glass with a radius of $r_2 = 25$ mm. The accuracy of the radii is better than 0.01 mm over the entire length of 640 mm. The

0167-2789/92/$05.00 © 1992 – Elsevier Science Publishers B.V. All rights reserved

flow was confined between a rotating inner cylinder and a stationary outer cylinder and stationary bottom and top plates. The length of the gap could be varied continuously by moving the metal collar which provides the top surface of the flow domain. The aspect ratio Γ used as a geometrical control parameter is defined as the ratio of gap height to gap width. We used silicon oil as the working fluid with different viscosities depending on the flow situation. Working at very low gap height to width ratios, it turned out that even small dirt particles (<1 mm) in the fluid can perturb the flow in some cases. So the fluid was cleaned with a filter having a mesh size of 5 μm.

The external control parameter is the Reynolds number defined as $\mathrm{Re} = (\Omega\ d\ r_1)/\nu$, where Ω is the angular frequency of rotation of the inner cylinder, $d = r_2 - r_1$ the gap width and ν the kinematic viscosity. The temperature of the fluid was kept constant to within 0.01 K by circulating thermostatically controlled silicon oil through a surrounding square box. A phase-locked loop circuit controlled the speed of the inner cylinder to better than one part in 10^{-4} in the short term and better than one part in 10^{-7} in the long term average. Thus the accuracy of the absolute value of the Reynolds number was about 1% and for relative changes better than 10^{-5}. The local velocity was measured by a real fringe laser–Doppler-anemometer and recorded by a phase-locked-loop analogue tracker. According to the statistics of scattering particles the signal shows Doppler-phase noise. The analogue output voltage of the tracker, which is proportional to the local velocity component, was filtered by an analogue Bessel filter of fourth order with a cutoff frequency depending on the flow situation and the highest significant frequency of the system. The velocity signal was fed into an AD-converter with 10 or 12 bit resolution and then into a computer where the data processing was performed. For more details of the experimental setup see [9–11].

The first step in analyzing the time series obtained is the reconstruction of the attractor by delay time coordinates. New methods enable us to choose a proper delay time and a sufficiently large embedding dimension. Data sets with a high noise level are treated by a noise reduction method described below. The received data sets and those with a low initial noise level can now be characterized by classical analysis (power spectra and autocorrelation function) and modern techniques yielding fractal dimensions, Lyapunov spectra and entropies.

2.1. *Bifurcations of Taylor–Couette flow*

The basic flows considered in this paper are illustrated in the upper part of fig. 1 where the flow pattern in a radial plane of the two flow types existing for aspect ratios $\Gamma \leq 1.2$ are shown. i and o indicate inner and outer cylinder, respectively. The two cell flow (s for symmetric) is mirror symmetric relative to the midplane with a maximum outward flow velocity in this plane and a slower reflux at top and bottom plate. For this flow mode the axial velocity component v_z in the midplane is zero for all Reynolds numbers. The single-cell flow (a for asymmetric) appears in two equivalent modes with one big vortex and a small weak one near the bottom or top plate.

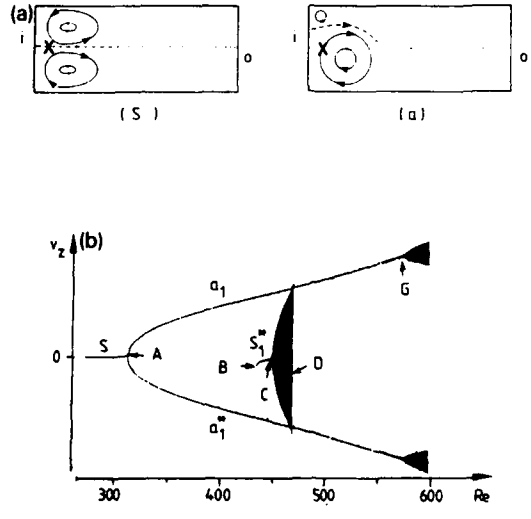

Fig. 1. (a) Flow patterns for the symmetric two-vortex state (s) and the single vortex state (a_1) drawn after a visualization experiment. (b) corresponding bifurcation diagram.

respectively. The vortices have contrary directions of rotation. In contrast to the symmetric mode, the axial velocity component of the single vortex mode is non-zero in most locations in the midplane. With a proper position of the measurement volume it is possible to characterize the actual flow mode by measurement of a single velocity component. The approximate location of the measurement volume is indicated by X in the schematic representation of the flow pattern.

The lower part of fig. 1 shows a bifurcation diagram of these two flow modes at an aspect ratio of $\Gamma = 0.47$. For this measurement the Reynolds number was increased at a quasistatic rate from $\mathrm{Re} = 200$ to $\mathrm{Re} = 600$ and v_z was recorded. This procedure was repeated for all branches.

For Reynolds numbers smaller than 320 the axial velocity component is zero, indicating the symmetric two vortex state. The branch of this flow mode is marked with S. At point A a supercritical bifurcation appears: the symmetric solution loses stability and the two asymmetric modes, marked with a_1 in the diagram, appears. At this point A a critical slowing down takes place, i.e. the time constant diverges, so special care has to be take while passing the point. This bifurcation is disconnected due to very small imperfections in the apparatus and thus there is a smooth development of one of the single-cell flows. The other branch can be reached by sudden starts or finite perturbations of the flow. Those branches are marked with an asterisk. Following the branches of the two single-cell modes to higher Reynolds numbers a Hopf bifurcation occurs (marked with G).

The time dependent flow modes can either be an $m = 2$ mode (m being the azimuthal wave number) or an $m = 3$ mode, depending on the aspect ratio Γ.

The symmetric solution which loses stability at point A restabilizes at point B, starting a secondary symmetric branch S_1^*. This branch can be obtained experimentally only by a sudden jump from the stable symmetric solution (S) to Reynolds numbers Re above the critical value B. For higher Reynolds numbers this branch shows a Hopf bifurcation at point C.

Depending on slight changes of flow geometry and aspect ratio the time periodic flow starting at B can show quite different scenarios on the route to chaos. (As an example a period doubling cascade will be shown below.)

The basis of a full understanding of this flow is the knowledge of all critical points. In fig. 2 we plot all known critical points as a function of the control parameters, the Reynolds number and the aspect ratio Γ, taken from measurements and numerical calculations [9].

For this Γ–Re plot hundreds of bifurcation diagrams like the one shown in fig. 1 had to be recorded, most of them by ramping the Reynolds number in both directions to detect hysteresis effects.

The solid lines marked with G indicate the loci of Hopf bifurcations, evolving from the station-

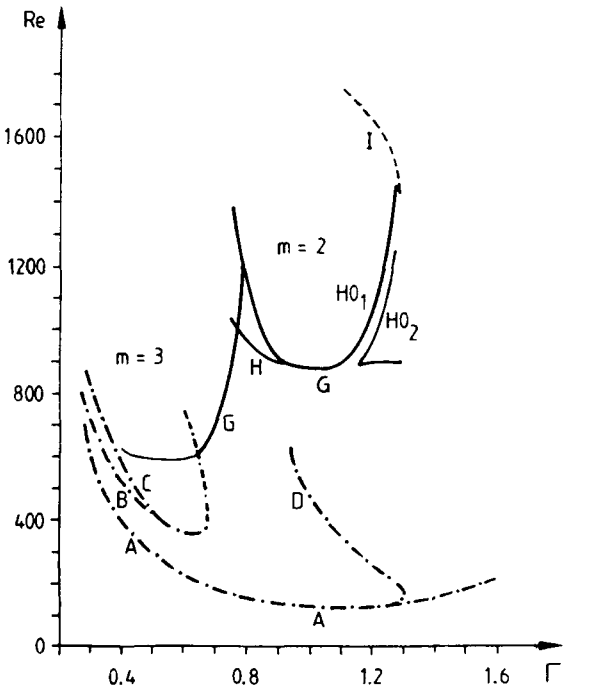

Fig. 2. Stability diagram in Re–Γ plane. Dashed-dotted lines: region of steady solutions, solid lines: regime of time dependent asymmetric solutions and dashed line: regime of intermittent solutions.

ary single cell mode. For aspect ratios $\Gamma < 0.8$ an oscillatory state with an azimuthal wave number $m = 3$ occurs, for $\Gamma \geq 0.8$ an $m = 2$ mode. This $m = 2$ mode is of particular interest, because it shows a hysteresis region marked by H and two lines of homoclinity, marked with HO_1 and HO_2, respectively. This gives a band of stationary flow which extends up to Reynolds number $Re = 1400$. Approaching this band from both sides in the Γ–Re plane, the frequency of the $m = 2$ mode goes to zero while a constant amplitude is preserved (details can be found in [13]). The development of these time periodic states towards higher Reynolds numbers depends strongly on the flow mode. Even for the same basic flow we find quite a lot of scenarios depending on the aspect ratio Γ. The work on this topic has been started recently, so we present here exemplarily three scenarios: quasiperiodicity, period doubling and intermittency.

3. Reconstruction of phase space from scalar time series

The analysis of chaotic time series requires a careful application of methods which yield fractal dimensions, Lyapunov exponents and entropy of attractors in phase space. In many experimental situations only a few of the system's observables can be obtained.

We reconstruct the phase space from states of the Taylor–Couette experiment where only one component of the local velocity is measured by the use of Takens' delay time coordinates [14]. $\{v_z(t_k)\}$ with $k = 0, \ldots, N_{dat} - 1$ is the scalar time series, N_{dat} is the number of sampled data points. Vectors in the embedding space are given by

$$\boldsymbol{x}(t_s) = \begin{pmatrix} v_z(t_s) \\ v_z(t_s + \tau) \\ \cdot \\ \cdot \\ \cdot \\ v_z(t_s + \tau(\dim_E - 1)) \end{pmatrix}, \tag{1}$$

where $s \in S$ and $S := \{\mathbb{N}_0;\ s < N_{dat} - (\tau/T_a)(\dim_E - 1)\}$, $\dim_E$ is the embedding dimension, τ is the delay time and T_a the sampling time. For convenience we write x_s instead of $x(t_s)$. The choice of a proper delay time and a sufficiently large embedding dimension, which is not known a priori, is not trivial for time series restricted in resolution and number of data points. Recently we developed two methods to calculate optimal embedding parameters. The first algorithm yields a global statical measure, called fill factor, which gives an estimate of the phase space utilization for (quasi-)periodic and strange attractors and leads to a maximum distance of trajectories [15]. The second algorithm, the integral local deformation, describes the local dynamical behaviour of points on the attractor and gives a measure of the homogeneity of the local flow [16]. A comparison of different algorithms is presented in [17].

4. Characterization of time series

To characterize chaotic time series it is often insufficient to calculate power spectra or autocorrelation functions, only. Recently more powerful tools have been developed. With the results of these algorithms one can distinguish between different chaotic states of a nonlinear system.

4.1. The fractal dimension

A useful parameter characterizing the geometry of strange attractors is the fractal dimension. For the results presented here we calculated the correlation dimension [18]

$$D_2 = \lim_{R \to 0} \frac{\log(C(R))}{\log(R)}, \tag{2}$$

where $C(R)$ is the correlation integral

$$C(R) \approx \frac{1}{N_{ref}} \sum_{j=0}^{N_{ref}-1} \frac{1}{N_{dat}} \sum_{i=0}^{N_{dat}-1} \sigma(R - \|x_i - x_j\|), \tag{3}$$

where R: scaling radius, N_{ref}: number of reference points and σ: Heaviside function.

For inhomogeneous attractors it is often useful to calculate the distribution of local or pointwise dimensions

$$D_{pw} = \lim_{R\to 0} \frac{\log(C^j(R))}{\log(R)} , \tag{4}$$

where $C^j(R)$ is the local correlation integral

$$C^j(R) := \frac{1}{N_{dat}} \sum_{i=0}^{N_{dat}-1} \sigma(R - \|x_i - x_j\|) . \tag{5}$$

4.2. The Lyapunov exponents

The most significant parameter to detect and distinguish between chaotic dynamics is the spectrum of Lyapunov exponents (LE)

$$\lambda_k = \lim_{t_{ev}\to\infty} \frac{1}{t_{ev}} \log\left(\frac{p_k(t_{ev})}{p_k(0)}\right) , \tag{6}$$

where $p_k(0)$ is the radius of the $\dim_E$-sphere at the starting point and $p_k(t_{ev})$ are the principal axes of the $\dim_E$-ellipsoid at some evolution time t_{ev}. The LE describe the sensitivity of a system to small variations of initial conditions. So LE give an estimate of the "strength of chaoticity". A review of the algorithm we used is given in [19].

In an experiment a $\dim_E$-dimensional linearized flow map has to be approximated. Strong efforts are made to identify true and spurious LE when the embedding dimension is larger than the number of relevant degrees of freedom. Some algorithms are based on the observation that the true LE change their signs upon time reversal whereas the spurious exponents do not [20]. Other algorithms use singular value decomposition techniques to restrict the linearized flow map to the relevant subspace [21].

4.3. The entropy

The entropy of a system's state is the essential measure of chaoticity, the average loss of information. Closely related to the LE, the metric entropy for homogeneous attractors [22] is given by

$$h = \sum_k \lambda_k^+ , \tag{7}$$

where λ_k^+ denote the positive exponents. The order-two Kolmogorov entropy or correlation entropy [22] is given by

$$K_2 = -\lim_{\dim_E\to\infty} \lim_{\tau\to 0} \frac{1}{\tau} \log \frac{C_{\dim_E+1}}{C_{\dim_E}} \tag{8}$$

where $C_{\dim_E}$ denotes the correlation integral in $\dim_E$-dimensional embedding space. K_2 can be estimated from the slope of the logarithm of the ratio of successive correlation integrals versus delay time at the accumulation line for higher $\dim_E$ and small τ [17]. For further practical estimates of K_2 see [23].

5. Noise reduction

Experimental attractors from the Taylor–Couette experiment are always noisy, due to the Doppler-phase noise on the LDV signal. This effect is caused by the arrival statistics of the light scattering particles.

Recently many efforts have been made to find the underlying noiseless attractor [24–27] to ensure accurate calculations of fractal dimensions and Lyapunov spectra. It is well known that using filters in the time domain can affect the values of the dynamical variables [28, 29].

The new noise reduction method presented here eliminates high frequency noise while preserving the original dynamics. The noise reduced attractor enables us to estimate the dynamical variables more precisely. We tested our new approach on experimental (Taylor–Couette) as well as on numerical (Duffing oscillator) time series.

5.1. The noise reduction method

The method presented here uses the average flow vector instead of an approximation of the linearized flow map. We define a local average displacement vector $f(x_i)$ as the difference between the center of mass of a cloud of neighbouring points at the reference point x_i and the center of mass of the same ensemble one time step later. Considering a window of p points x_{i+k}, $0 \le k \le p-1$, one obtains new points $\hat{x}_{i+k}$, by minimizing the sum

$$\sum_{k=0}^{p-1} \|\hat{x}_{i+k} - f(\hat{x}_{i+k-1})\|^2 + \|\hat{x}_{i+k} - x_{i+k}\|^2 . \qquad (9)$$

The minimization satisfies the following two conditions:

– The new points must be reconstructable from a time series.

– Only those coordinates are varied, which are independent from the points outside the window.

The first term of expression (9) describes the deviation from the averaged direction, the second term describes the distance from the old data points. The attractor will be noise reduced successively for all data points. The whole procedure is repeated until the noise level is reduced below a given threshold. This procedure works only if the number of data points per mean period of the attractor is sufficiently high. The algorithm is comparatively easy to implement even on small computers. The work on this noise reduction algorithm and a comparison with other methods is still in progress.

5.2. Test of the noise reduction method

Below we present the results of our method for a quasiperiodic time series from Taylor–Couette flow and for a numerical, chaotic time series (Duffing oscillator: $\ddot{x} + D\dot{x} + x + x^3 = F\cos\omega t$, where $D = 0.2$, $F = 40$ and $\omega = 1$). The number of points per mean cycle is 78 for the experimental time series and 126 for the numerical data.

To demonstrate the noise reduction scheme we applied this algorithm to the quasiperiodic attractor. Fig. 3a shows the phase space reconstruction, Poincaré section and circle map of a torus that was low pass filtered with a cut off frequency of $f_{lp} = 500$ Hz, which is above 100 times higher than the fundamental frequency in the system. Fig. 3b shows the same state after the noise reduction procedure.

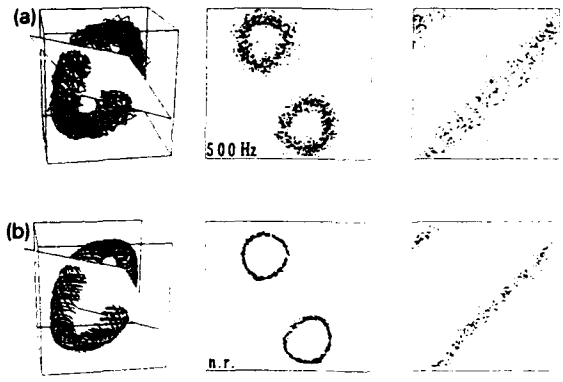

Fig. 3. Reconstructed attractors, Poincare sections and circle maps of the experimental quasiperiodic time series (a) 500 Hz low pass filtered, (b) noise reduced.

The power spectra for these two cases shown in fig. 4 demonstrate, that the noise between the two frequencies is reduced while the intensity ratio is left unchanged. In fig. 5 the slope of the double logarithmic plot of the correlation integral versus scaling radius is shown for both cases. The noise reduction scheme yields a proper estimate of the correlation dimensions. The expected value of D_2 for the torus is indicated by dotted lines. The noise reduction scheme was applied directly to the data set shown in fig. 3a, whereas the best procedure is to start with a proper setting of the analogue filter.

In order to show that the method works with chaotic attractors as well, we added about 4% white noise to the numerical time series from the Duffing system. The number of data points is $N_{dat} = 32\,768$ at a resolution of 10 bit. To compare the quality of the noise free, noise covered and noise reduced time series we estimated the first two LE for embedding dimensions up to $\dim_E = 12$. The LE were estimated by calculating the linearized flow map. Fig. 6 illustrates that the

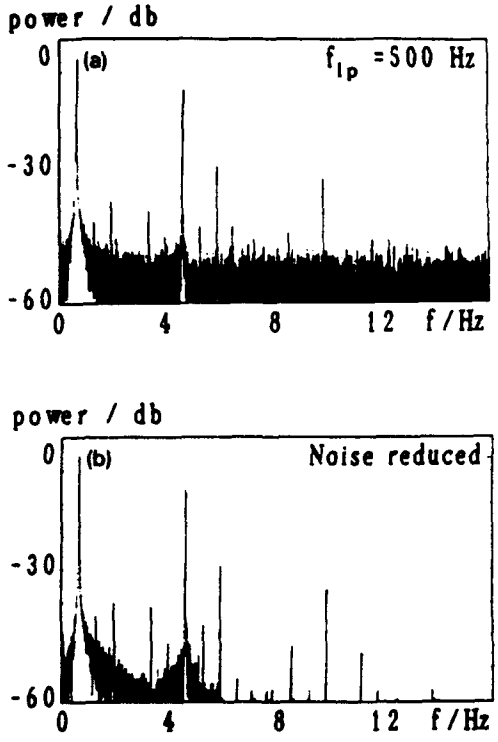

Fig. 4. Power spectra of the time series shown in fig. 3.

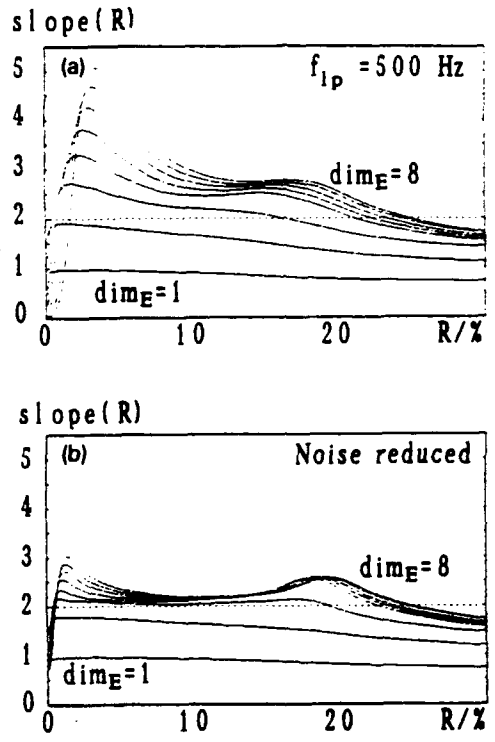

Fig. 5. Slope of the double logarithmic plotted correlation integral of the time series shown in fig. 3.

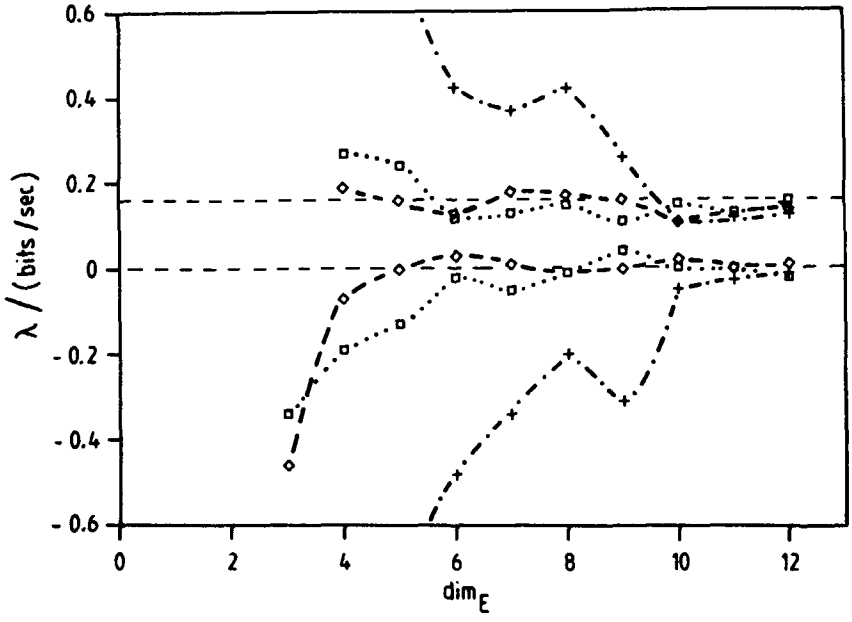

Fig. 6. The non-negative Lyapunov exponents versus embedding dimension for the noise free (dashed lines), noise covered (dashed dotted lines) and noise reduced Duffing-attractor (dotted lines). The horizontal dashed lines indicate the correct values for the first two Lyapunov exponents.

Table 1
Lyapunov spectra for the noise free, noise covered and noise reduced Duffing attractor in comparison with the theoretical values.

	Noise free time series	Noise covered time series	Noise reduced time series	Theor.
λ_1	0.15 ± 0.01	0.40 ± 0.11	0.16 ± 0.02	0.16
λ_2	0.00 ± 0.01	-0.65 ± 0.34	-0.04 ± 0.02	0.00
λ_3	-0.51 ± 0.05	-5.70 ± 1.40	-0.57 ± 0.10	-0.45

results obtained from the noise reduced time series agree with the noise free data. The dotted lines indicated the first two exponents calculated directly from the known linearized flow map. The exponents are hardly to be estimated from the noise covered time series. In table 1 the first three LE are shown for the different time series. We averaged the relevant exponents for $\dim_E = 4$ to $\dim_E = 12$. The given errors are the statistical inaccuracy of the means.

6. Scenarios

In this section we exemplarily present experimental results from the Taylor–Couette flow. The goal is to show the variety of scenarios and how the algorithms work when applied to the given experiment.

6.1. Period doubling

The Hopf bifurcation evolving from the restabilized symmetric two cell state, indicated with line C in fig. 2, can show quite different scenarios on the route to chaos depending on slight variations of the aspect ratio. The most remarkable scenario is a period doubling cascade.

Figs. 7a to 7d shows the fundamental limit cycle and three period doubling bifurcations leading to 8 times the fundamental period. For Reynolds numbers larger than the accumulation point the flow becomes chaotic (7e), then shows restabilization (7f) for higher Reynolds numbers. For this scenario we calculated the correlation dimension (circles), the mean pointwise dimension (diamonds) and the Kaplan–Yorke dimension (squares) shown in fig. 8a. As expected, the dimensions increase rapidly to values larger than 2, above the critical Reynolds number 568 we found experimentally the period-3 window, which agrees with the simple logistic model. The dimensions are found to be 1.4 instead of 1, which we think is caused by noise and in addition to having not met the correct Reynolds number for the periodic window.

Fig. 8b shows the Lyapunov spectra in the same range of the Reynolds number (circles, squares and diamonds are the first three expo-

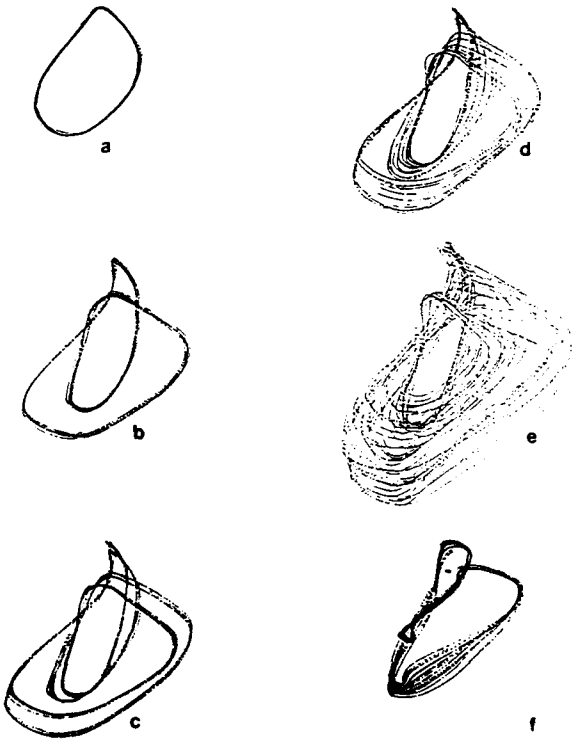

Fig. 7. Phase space reconstruction of a period doubling cascade.

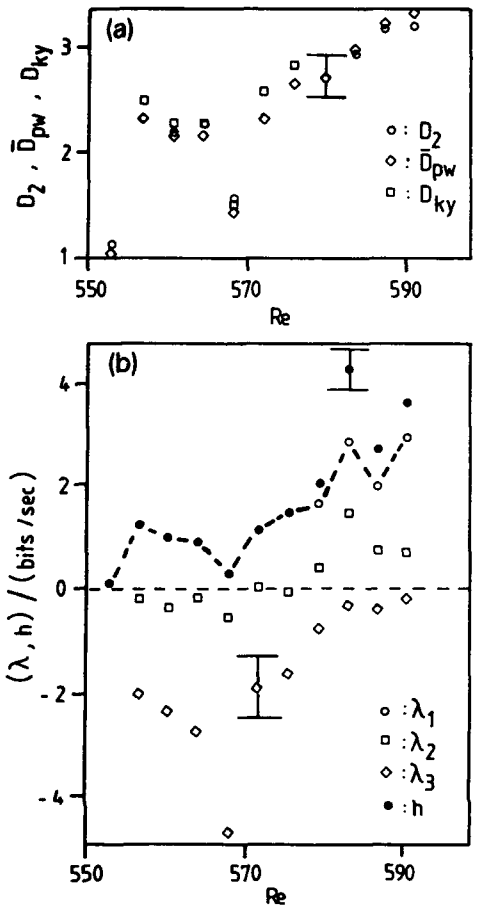

Fig. 8. (a) Different dimensionalities for a period doubling cascade versus Reynolds number, (b) Lyapunov spectra and metric entropy versus Reynolds number. The dotted line shows the first Lyapunov exponent, the given uncertainties are the standard deviations of the averaging process.

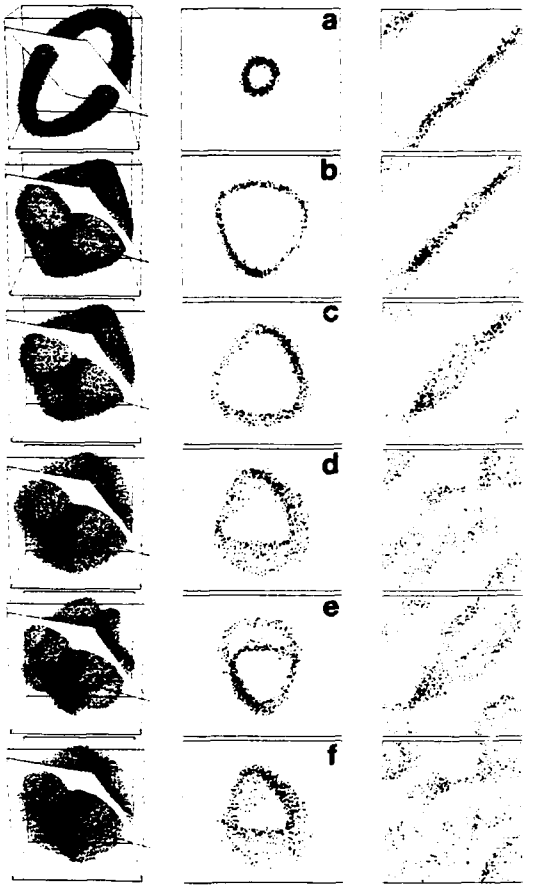

Fig. 9. Reconstructed attractors, Poincaré sections and circle map for a quasiperiodic sequence.

nents, respectively, the full circles are the values of the metric entropy). This result is in good agreement with the plot above. The error bars are estimated from the standard deviation of the averaging process over several embedding dimensions. This analysis shows that the finite resolution of these measurements allows only the detection of the largest periodic window in this scenario.

6.2. *Quasiperiodic sequence*

The Hopf bifurcation occurring at the restabilized two vortex flow can show quasiperiodic behaviour for different values of aspect ratio Γ. We find this scenario also in the evolution of $m = 2$ and $m = 3$ modes and often in scenarios at larger aspect ratios with many vortices. The break-up of a two-torus in Taylor–Couette flow was the first scenario which was analyzed by A. Brandstätter and H. Swinney [6] using modern nonlinear techniques.

Fig. 9 shows the evolution of a quasiperiodic state towards higher Reynolds numbers. The three columns show the reconstructed phase space with the orientation of the Poincaré plane, the Poincaré section and the corresponding circle map, respectively. In contrast to the Ruelle–Takens–Newhouse scenario which was analyzed in [6] we found a stable three-mode state. From the Poincaré sections and circle maps shown in fig. 9d and 9f we cannot decide whether this state

is chaotic or not. Therefore we estimate the dimension and entropy of the state shown in fig. 9d. In fig. 10 the evaluation of the dimension is shown. Fig. 10a gives the local slopes of the double logarithmic plot of the correlation integral versus $\log(R)$. We find a plateau at about $R = 4\%$ and estimated the correlation dimension to be $D_2 \approx 3.2$. In fig. 10b the distributions of pointwise dimensions are shown; then indicate a homogeneous attractor. The mean pointwise dimension D_{pw} agrees with the correlation dimension.

We want to point out that, although the circle

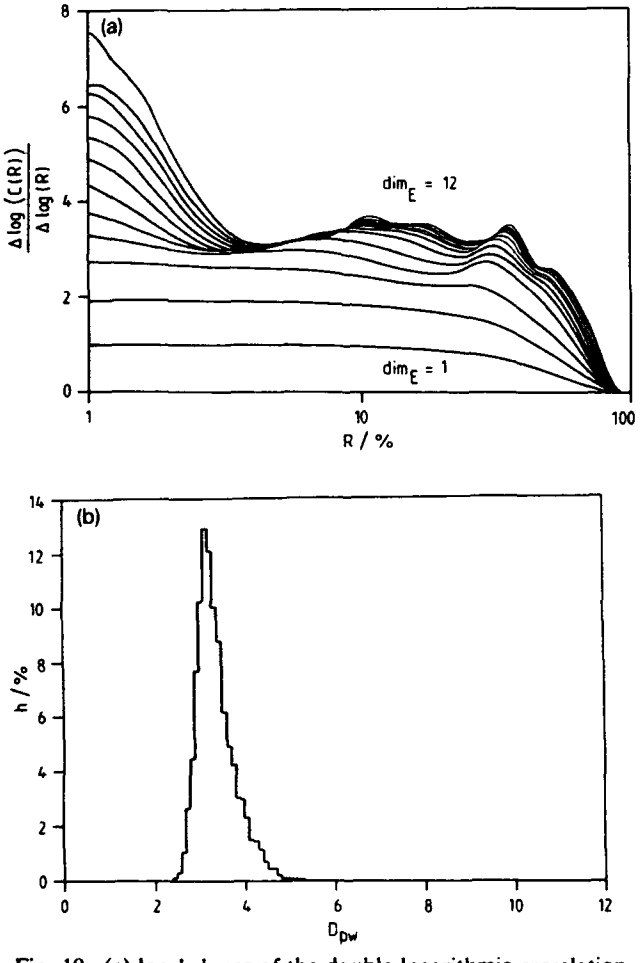

Fig. 10. (a) local slopes of the double logarithmic correlation integral versus logarithmic radius (given in percent of the total extension of the attractor). (c) Distribution of pointwise dimension for $\dim_E = 12$ showing a homogeneous attractor yielding $D_{pw} \approx 3.2$.

map for case (9d) suggests non-invertibility and $D_2 = 3.2$, we found that this state is a three-torus. In fig. 11a the logarithm of the ratio of successive correlation integrals is plotted versus normalized delay time as suggested by eq. (8). From a fit of the accumulation line one estimates $K_2 = 0$ bits/orbit. In fig. 11b the calculation of the correlation entropy is plotted versus embedding dimension.

Fig. 12 gives the estimated dimensions for the whole quasiperiodic scenario. The arrows marked with a,b,d and e correspond to the states shown in fig. 9. At a Reynolds number Re = 550, marked with a, the flow shows a second Hopf bifurcation and the limit cycle with a dimension of about 1 (experimentally) changes to a two-torus with a dimension of about 2. At Reynolds numbers about 580, marked with b in fig. 12, another Hopf bifurcation occurs, giving a three-torus. The flow modes, showing three fundamental frequencies, are physically quite different and we did not find any phase locking. (Recently we found phase locking of similar flow modes in a twelve-vortex state. results will be published elsewhere.) The frequencies of the three modes are functions of the Reynolds number. So the modes are not incommensurate for all Reynolds numbers. We caught only the ratio $f_3/f_1 = \frac{1}{2}$, where the dimension is decreased by one.

The estimated dimensions are systematically too high, which we think is due to the noise level of the experiment. This effect shows the need for efficient noise reduction algorithms. Noise reduction has not yet been applied to the data for the considered range in fig. 12.

6.3. *Intermittency near a homoclinic orbit*

As shown in fig. 2, Taylor–Couette flows for aspect ratios $1.05 < \Gamma < 1.35$ show a Hopf bifurcation, which evolves from the single cell state at Reynolds numbers $\mathrm{Re} > 900$. The flow mode with an azimuthal wave number $m = 2$ is intersected in the Re–Γ-plane by two lines of homoclinity. This effect will be described elsewhere.

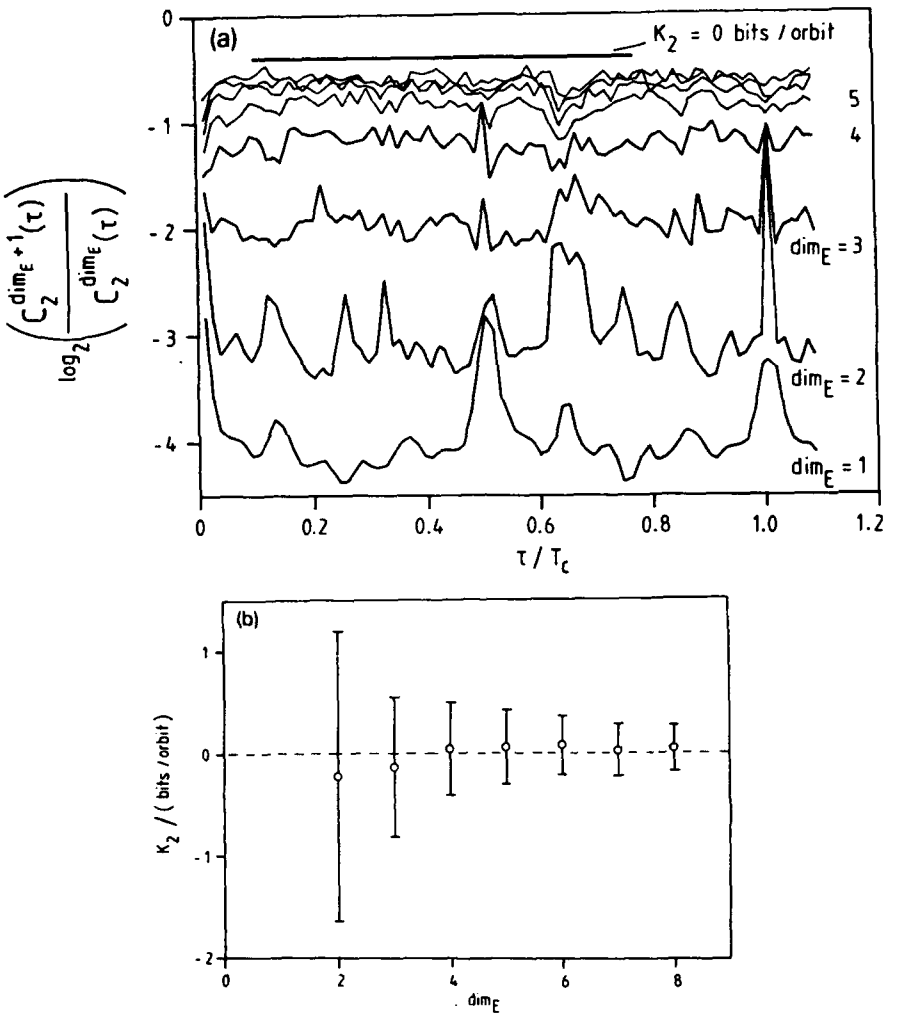

Fig. 11. (a) logarithmic ratio of successive correlation integrals versus normalized delay time (T_c is mean recurrence time). The correlation entropy K_2 is estimated to be 0 bits/orbit. (b) Correlation entropy versus embedding dimension estimated from fig. 10a for embedding dimensions 2 to 8 in the delay interval $\tau/T_c = 0.1$–0.4. The errors are the standard deviations.

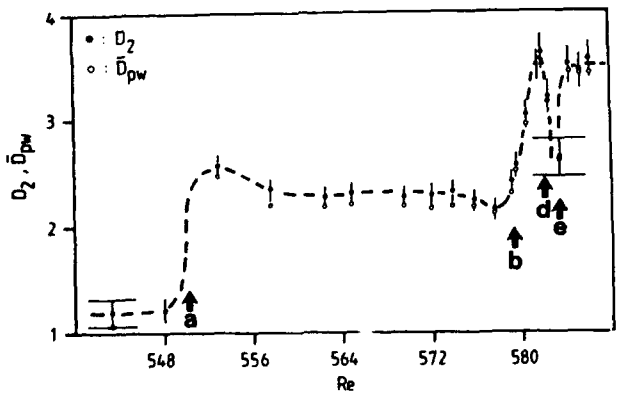

Fig. 12. Correlation dimension and averaged pointwise dimension for the quasiperiodic sequence. At the arrows a and b new incommensurate modes appear, at arrow e two modes become commensurate (ratio of 1:2).

We focus on a scenario occurring for values of Γ larger than 1.1 and Re $\approx$ 1500. Figs. 13a–13c show the time series, reconstructed attractors and the distribution of pointwise dimensions for $\Gamma = 1.2$ and three Reynolds numbers. The embedding dimension is $dim_E = 12$ in all cases. Fig. 13a shows a noisy limit cycle at Re = 1400, in fig. 13b intermittent behaviour is shown. As can be seen from the reconstructed phase space, the kind of the limit cycle does not change. Also a high dimensional region with an approximate fractal dimension of 6 occurs. For Reynolds numbers Re = 1800 the laminar phase disappears

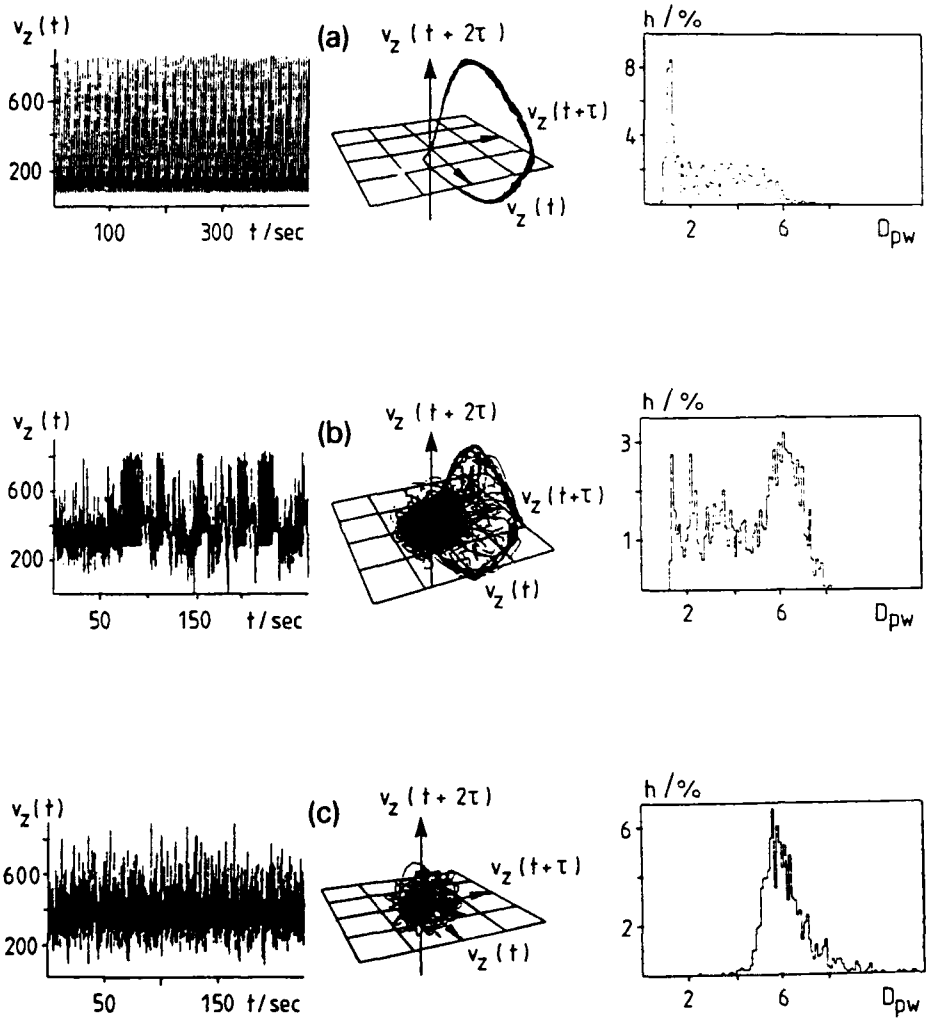

Fig. 13. Time series, reconstructed attractor and distribution of pointwise dimension for (a) Re = 1400, noisy limit circle, (b) Re = 1658, intermittency and (c) Re = 1800, chaotic state.

and only the high dimensional part of the attractor remains, showing the same fractal dimension as before.

For a better understanding of this intermittency we recorded the distribution of the length of laminar phases, seen in fig. 14a. For this plot the length of 500 laminar phases were recorded with a resolution of 1 second. (The period of the limit cycle was in the order of 1 second, which limits the accuracy of the time estimate.) The statistics are not sufficient to estimate an exact value for the exponent of the expected distribution $P(T) \propto T^{-\alpha}$. A rough estimate gives a value on the order of $\alpha \approx 1$ [30].

The mean length $\langle T \rangle$ of the laminar phases as a function of Reynolds numbers is shown figure 14b. The solid line is a fit of the measurement points to the function $\langle T \rangle = a(\varepsilon)^{-1}$, where $a = 7.236$. This is the expected scaling law with $\varepsilon = \mathrm{Re} - \mathrm{Re}_c$ and $\mathrm{Re}_c = 1652$. From the experimental data we can only exclude type I and type III intermittency. Further investigations will be done to decide whether the intermittency is of type II or a new kind.

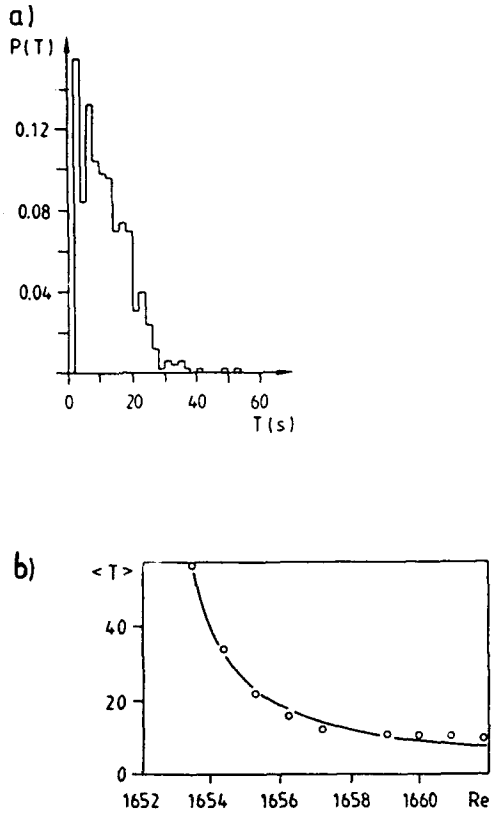

Fig. 14. Distribution of laminar flow $P(T)$ versus duration T for Re = 1658. (a) resolution of 1 s, (b) mean duration of the laminar flow versus Reynolds number.

7. Conclusion

One motivation to find efficient algorithms for the analysis of chaotic time series is to characterize all states of a nonlinear system in a given control parameter space. In this paper we showed that in Taylor–Couette flow a rich variety of scenarios exists even for a very limited geometry. Starting from various stationary and periodic states we investigated a period doubling cascade, a 3-torus and an intermittent scenario. The experimental results show that noise reduction is necessary to obtain the required accuracy in the estimation of dynamical variables.

Acknowledgements

We thank J. Müller from the Institut für Angewandte Physik der Universität Kiel for reading the manuscript and for useful comments.

References

[1] R.C. Di Prima and H.L. Swinney, in: Hydrodynamic instabilities and transition to turbulence, eds. H.L. Swinney and J.P. Gollub (Springer, Berlin, 1980) p. 128.
[2] T.B. Benajamin and T. Mullin, J. Fluid Mech. 121 (1982) 219.
[3] A. Brandstäter, J. Swift, H.L. Swinney, A. Wolf, J.D. Farmer, E. Jen and J.P. Crutchfield, Phys. Rev. Lett 51 (1983) 1442.
[4] G. Pfister, Lecture Notes in Physics 235 (Springer, Berlin, 1985) 199.
[5] T. Mullin and K.A. Cliffe, in: Nonlinear Phenomena and Chaos, ed. S. Sarkar (Adam Hilger, Bristol) p. 96.
[6] A. Brandstäter and H.L. Swinney, Phys. Rev. A 35 (1987) 2207.
[7] T. Mullin, K.A. Cliffe and G. Pfister, Phys. Rev. Lett. 58 (1987) 2212.
[8] T. Mullin, IMA Appl. Math. 46 (1991) 109.
[9] G. Pfister, H. Schmidt, K.A. Cliffe and T. Mullin, J. Fluid. Mech. 191 (1988) 1.
[10] A. Schulz, Diplomarbeit, Universität Kiel (1988); G. Pfister and A. Schulz, in preparation.
[11] G. Pfister, U. Gerdts, A. Lorenzen and K. Schätzel, in: Photon Correlating Techniques in Fluid Mechanics (Springer, Berlin, 1983) p. 256.
[12] G. Pfister, K. Schätzel and U. Gerdts, in: Laser Anemometry in Fluid Mechanics (Lisbon, 1984) p. 37.
[13] G. Pfister, A. Schulz and B. Lensch, Eur. J. Mech., B/Fluids 10 (1991) 247.
[14] F. Takens, Lecture Notes in Math. 898 (Springer, Warwick, 1980) p. 230.
[15] Th. Buzug, T. Reimers and G. Pfister, Europhys. Lett. 13 (1990) 605.
[16] Th. Buzug and G. Pfister, Phys. Rev. A 45 (1992) 7073.
[17] Th. Buzug and G. Pfister, Comparison of Algorithms calculating Optimal Embedding Parameters for Delay Time Coordinates, to appear in Physica D 58 (1992) 127, these Proceedings.
[18] P. Grassberger and I. Procaccia, Physica D 9 (1983) 189.
[19] Th. Buzug, T. Reimers and G. Pfister, in: Nonlinear Evolution of Spatio-Temporal Structrues in Dissipative Continuous Systems, eds. F.H. Busse and L. Kramer (Plenum, New York, 1990) p. 7.
[20] U. Parlitz, Identification of true and spurious lyapunov exponents from time series, preprint (1991).

[21] R. Stoop and J. Parisi, Physica D 50 (1991) 89.
[22] H.G. Schuster, Deterministic Chaos (VCH-Verlag, Weinheim, 1988).
[23] J.G. Caputo and P. Atten, Phys. Rev. A 35 (1987) 1311.
[24] E.J. Kostelich and J.A. Yorke, Physica D 41 (1990) 183.
[25] T. Schreiber and P. Grassberger, A simple noise-reduction method for real data, preprint (1991).
[26] J.D. Farmer and J.J. Sidorowich, Physica D 47 (1991) 373.
[27] J.I. Salisbury, Noise reduction using chaotic theory, preprint (1991).
[28] R. Badii and A. Politi, in Dimensions and Entropies in chaotic Systems, ed. G. Mayer-Kress (Springer, Berlin, 1989) p. 67.
[29] A. Chennaoui, K. Pawelzik, W. Liebert, H.G. Schuster and G. Pfister, Phys. Rev. A 41 (1990) 4151.
[30] B. Lensch, Diplomarbeit, Universität Kiel (1988).

Physica D 58 (1992) 455–468
North-Holland

PHYSICA D

Applications of singular systems analysis to 'Baroclinic chaos'

P.L. Read[1]
Robert Hooke Institute, Clarendon Laboratory, Parks Road, Oxford, OX1 3PU, UK

Received 7 October
Revised manuscript received 2 March 1992
Accepted 2 March 1992

The method of singular systems analysis (SSA) is applied to the phase portrait analysis of high precision time series of measurements of temperature and total heat transport obtained in a high Prandtl number (Pr = 26) fluid contained in a rotating, cylindrical annulus subject to a horizontal temperature gradient. Global SSA is found to be a highly effective means of separating weak high frequency oscillatory components from a signal dominated by strong oscillations at low frequency, revealing the possible presence of weak inertia–gravity oscillations within a large-scale baroclinic wave flow. SSA embeddings may fail in practice, however, for signals modulated in amplitude where the carrier and modulation frequencies differ widely, unless a sufficiently long window is used. A modification of global SSA with short windows, consistent with Takens' 'Method of Delays', is proposed and verified using data from a chaotic regime of the rotating annulus, which may improve SSA embeddings for such cases. Local SSA is applied to the estimation of topological dimension in quasi-periodic and chaotic flows, and produces results consistent with more conventional dimension measures.

1. Introduction

In characterising complex behaviour in the context of low dimensional chaos, the theory of dynamical systems has emphasised the geometric and topological properties of a system's behaviour as viewed in its phase-space. This approach was given further impetus with the proposal [1] that essential aspects of the time behaviour of a dynamical system could actually be reconstructed from a suitable set of measurements in a K-dimensional state space (K integer) constructed using time delays (hereafter the 'method of delays' or MOD). This approach was originally proposed as a generic analysis tool applicable to virtually any dataset. In practice, however, results obtained are found to be sensitive to factors such as the delay timescale τ and assumed embedding dimension K, and to measurement noise. Consideration of these factors led Broomhead and King ([2], hereafter BK) and Fraedrich [3] to propose the application of singular system analysis (SSA), a technique developed from the information theory of Pike et al. [4] and related to the Karhunen–Loève transformations used in statistics, to the problems of dynamical systems analysis. BK showed how the "deterministic" components of a time series could be separated from the noisy or 'stochastic' components, and reconstructed in a statistically optimal way using a subset of the most significant singular vectors. In subsequent papers, Broomhead et al. [5, 6] further extended SSA to analyse the *local* geometric properties of a reconstructed attractor. Such methods were promoted as offering significant advantages in dealing with real (i.e. noise-contaminated) data over earlier phase-portrait techniques based on MOD.

In the present paper, we apply both global and

[1]Present address: Atmospheric, Oceanic and Planetary Physics, Department of Physics, University of Oxford, UK.

0167-2789/92/$05.00 © 1992 – Elsevier Science Publishers B.V. All rights reserved

local SSA methods to the analysis of high precision measured time series of temperature and total heat transport in a rotating annulus. Thermal convection in a rotating, cylindrical fluid annulus, differentially heated in the *horizontal*, has been studied for many years [7] as a laboratory analogue of the large scale circulation of a planetary atmosphere. Such a system may serve both as a valuable source of physical insight, as well as providing a useful 'test bed' for the development of analysis techniques which might eventually be applied to meteorological data and models. The annulus is its typical form possesses circular azimuthal symmetry about the rotation axis in its boundary conditions, and exhibits a rich variety of flow regimes depending upon the external conditions (principally temperature contrast ΔT and rotation rate Ω). These regimes range from steady, laminar axisymmetric convection (analogous to tropical Hadley flow, at low Ω), through regular steady or periodic *baroclinic waves* (at moderate Ω) to highly irregular aperiodic 'geostrophic turbulence' (at high Ω). As in the mid-latitude atmosphere of the Earth, waves develop as a result of a potential energy-releasing (*baroclinic* [7]) instability of the azimuthally-symmetric component of the flow associated with buoyancy contrasts driven by differential solar heating between equator and poles. In studying how regular flow regimes in the rotating annulus break down into more complex and disordered flows, therefore, insight may be gained into a range of nonlinear dynamical processes which promote varying degrees of disorder, and which may also contribute actively towards limiting the finite predictibility of atmospheres [8] and oceans (if not necessarily those of the Earth).

In the present work, particular emphasis is placed on regions of parameter space close to observed transitions to 'baroclinic chaos' ([9], hereafter RBJS). Section 2 briefly describes the experimental system and analysis methods, and section 3 presents some results from the application of global SSA to the data. Some of the advantages of SSA in facilitating the extraction of small amplitude components of the signal are demonstrated, though a practical limitation of SSA in the presence of a noisy time series with widely separated timescales is also discussed. An extension to the conventional SSA is proposed which may overcome some of these limitations. Section 4 presents some results of the application of local SSA to quasi-periodic in and chaotic flows, and some concluding remarks are offered in section 5.

2. Apparatus and phase portrait reconstruction

The working fluid was contained in a cylindrical annulus between two coaxial thermally-conducting cylinders at radii $r = 2.0$ cm and $r = 8.5$ cm, and between rigid insulating boundaries in contact with the fluid at $z = 0$ and $z = 14.0$ cm respectively. The apparatus was rotated about its vertical axis of symmetry at angular velocity Ω and differentially heated in the *horizontal* at the sidewalls (the outer typically being the warmer). The annulus was designed for the precision measurement of fluid and boundary temperatures and of total heat transport, and was essentially the same as described by Hignett et al. [10] and RBJS. The working fluid consisted of a 25% solution by volume of glycerol in water, with a Prandtl number of 26.4. Temperatures at the boundaries and in the fluid were measured using copper–constantan thermocouples (sensitivity $\sim 40\,\mu$V per K). In the fluid, 32 thermocouples were equally-spaced in azimuth at mid-height and mid-radius, enabling the azimuthal wavenumber spectrum to be obtained readily by fast Fourier Transf ın techniques [10]. The total heat transport through the inner side boundary was measured using the method described by Hignett [10] from the coolant (water) flow rate and the difference in temperature between the inlet and outlet. Total heat transport on timescales as small as 10 s could be measured to an absolute precision of $\sim \pm 2\%$, though much

smaller relative changes (~parts in 10^3) could be detected.

A variety of different procedures were used to take in and analyse the data. Short time series of measurements at all thermocouples in the fluid and boundaries, and of the total heat transport, were recorded and used to identify the dominant flow type and to measure wave drift rates and (where appropriate) frequencies of time variations in amplitude or structure. In the work presented here, at selected points in parameter space much longer time series (a) of temperature at one of the ring thermocouples in the fluid, and (b) the total heat transport, averaged over 1–2 s, were recorded simultaneously for up to 250 drift periods of the dominant wavenumber (requiring up to 20 h of measurements). This procedure was adopted as a compromise between the more desirable course of recording simultaneous measurements at many different locations in the flow and the practical limitations of the data acquisition system (mainly on sampling rate and storage capacity) available at the time the experiments were carried out.

Phase portraits were constructed by the usual method of time-delay embedding or 'method of delays' (MOD) – [1, 11]), in which scalar series e.g. of temperature $T(t)$ are represented as a trajectory in a K-dimensional embedding space by denoting the state of the flow at time t by the vector $[T(t), T(t+\tau), T(t+2\tau), \ldots, T(t+(K-1)\tau)]$. This global embedding was further refined by the use of SSA (see BK) to reproject the trajectory onto a statistically optimum orthogonal basis. The latter comprises the eigenvectors of the $n \times n$ covariance matrix computed using a sliding 'window' of n points (where $n \gg$ maximum required embedding dimension), which is stepped along the time series. As discussed in BK, this method avoids some of the arbitrary choices necessary in the simple 'method of delays' (especially of the delay time τ). For the present work, time series were typically sampled at 1–2 s intervals, placing 200 or more samples per wave drift period (though rather fewer per typical period of amplitude or structural modulation, which ranged from 50–300 s). A window length τ_w of between 75 s and 100 s proved suitable in most cases, given the relatively long wave drift periods. This value of τ_w is somewhat longer than would be suggested from BK (their eq. (3.20)), though is still somewhat less than most typical timescales observed in the flow (see RBJS). For some cases to be discussed below, however, even this length of window proved to be too short to resolve significant structure in the reconstructed attractor.

3. Global analyses

In addition to the improved objectivity in constructing embeddings using MOD, a number of other advantages for 'phase portrait' reconstruction were claimed by the original promoters of SSA (e.g. see BK). In particular, it was noted that use of a truncated set of the derived eigenvectors effectively introduces a filter into the analysis, eliminating many of the unwanted non-deterministic components of the signal. In the present work, a 50-point window ($K = 50$, see above) was used except where stated, and analyses performed upon reconstructions involving only the first few (≤ 6) eigenvectors. In the following, we describe two examples of the use of SSA in the analysis of periodic and chaotic time series obtained in the apparatus outlined above, which illustrate (a) some of the advantages of SSA in extracting small signal components in a remarkably efficient way, but also (b) a limitation of the simplest form of SSA in constructing embeddings for flows containing components modulated in amplitude with widely differing timescales in the presence of noise.

In the following sub-sections we illustrate aspects of the use of SSA in the analysis of time series with reference to a number of data series obtained at various parameter settings in the above mentioned apparatus. The cases discussed include a sub-set of those presented by RBJS,

and comprise four separate experiments carried out at fixed temperature contrast $\Delta T \simeq 10$ K and variable rotation rate Ω. The salient details of each run are summarised in table 1, including the values of the relevant non-dimensional control parameters (e.g. see [7]), viz. the stability parameter or 'thermal Rossby number':

$$\Theta = \frac{g\alpha\,\Delta T\,D}{[\Omega(b-a)]^2} \tag{3.1a}$$

and Taylor number, Ta, taken to be

$$\mathrm{Ta} = \frac{4\Omega^2[b-a]^5}{\nu^2 D}\,, \tag{3.1b}$$

where g is the acceleration due to gravity, α the volumetric expansion coefficient, ΔT the imposed thermal contrast, Ω the system rotation rate, D, a and b the annulus depth, inner and outer radius respectively, and ν is the kinematic viscosity.

3.1. *Separating 'fast' waves from 'slow'*

One of the most remarkable flow regimes of the rotating thermal annulus is the so-called 'steady wave' regime, typically found over a range of parameters intermediate between the steady axisymmetric state (at low Ω) and fully developed 'geostrophic turbulence' (obtained at high Ω [7]). In this regime, the flow pattern comprises a single dominant azimuthal wavenumber component and its harmonics, which drifts steadily at constant amplitude around the apparatus at a rate determined by the flow structure and apparatus geometry [7, 10].

Table 1
Experimental parameters.

Case	Flow Type	ΔT (K)	Ω (rad s^{-1})	Θ	Ta ($\times 10^6$)
A	$m=3$	9.98	2.030	0.422	5.86
B	$m=3$AV	10.06	1.873	0.500	4.99
C	$m=3$MAV	10.01	1.716	0.593	4.19
D	$m=3$SV	9.95	3.420	0.148	16.6

The existence of such a pure steady wave state has been disputed by Pfeffer et al. [12, 13], who report a direct transition between states with the same azimuthal wavenumber but which are either modulated periodically in amplitude or structure (known respectively as 'amplitude vacillation' AV and 'structural vacillation' SV; see [7, 12]). The source of this controversy may be due in part to a matter of definition (Hignett [14], for example, defines a flow as AV only if amplitude fluctuations exceed 5% of the mean amplitude). RBJS found that the modulation index η of AV, defined as

$$\eta = \frac{A_{\max} - A_{\min}}{A_{\max} + A_{\min}} \tag{3.2}$$

(where $A_{\max}$ and $A_{\min}$ are respectively the maximum and minimum wave amplitudes) decreased uniformly towards zero with increasing Ω, with no clearly-defined transition point. Even so, flows were found over a range of parameters in which amplitude fluctuations were very small (η typically $<10^{-2}$).

Time series from a steady wave flow would be expected to take a very simple from, in which local temperatures oscillate periodically at the drift frequency of the dominant azimuthal wavenumber and the total heat transport through each sidewall is constant. Fig. 1 shows the singular spectrum obtained for the temperature measured at a fixed location in the flow from such a steady wave state in the present apparatus (case A; see table 1), in which each singular value σ_n is normalised to indicate the proportion of the variance accounted for by each eigenvector (a typical phase portrait constructed from the first 2–3 eigenvectors for this flow, taking the form of a limit cycle, is illustrated in fig. 9a and RBJS). Thus, some 99.9% of the variance is contained in the first three eigenvectors, though some 16 components appear to lie above a well-defined 'noise floor' around $\sigma_n^2 = 10^{-4}\%$.

The apparent pairing of eigenvalues 4 and 5

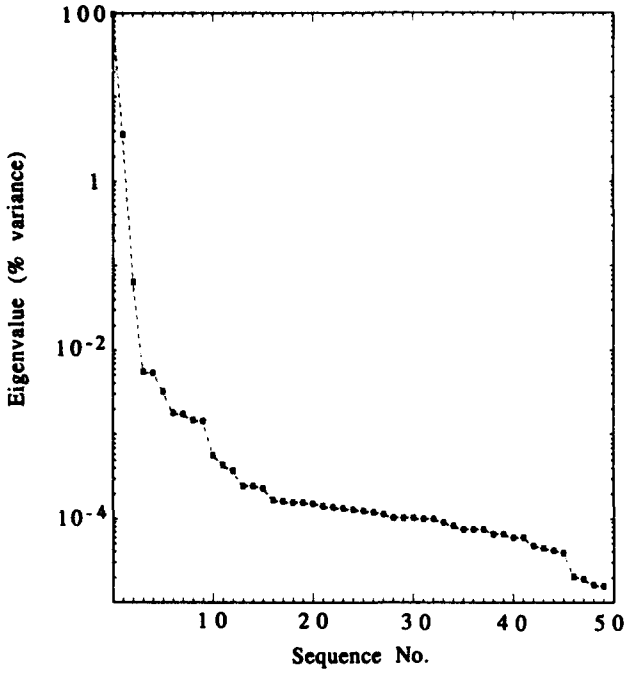

Fig. 1. Singular spectrum obtained from a time series of 4×10^4 temperature measurements in a steady wave flow in the rotating annulus experiments of [9]. Analysis employed a window of 50 points sampled every 2 s ($\tau_\omega = 100$ s), and eigenvalues have been normalised to show the proportion of the total variance represented. The 95% confidence interval for each each eigenvalue [3, 15] corresponds to $\Delta\sigma/\sigma \sim 0.6\%$.

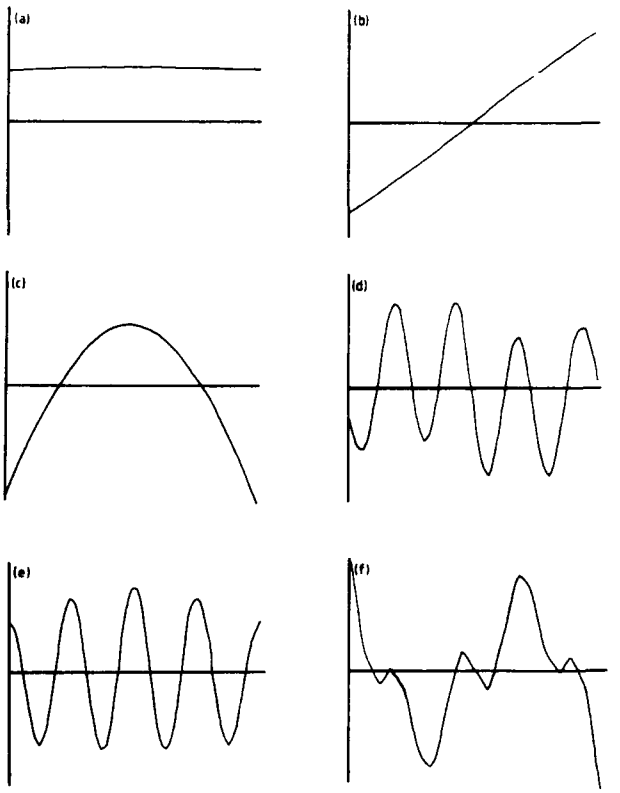

Fig. 2. (a)–(f) Profiles of the first six singular vectors corresponding to the singular spectrum shown in fig. 1.

(and others) indicates the possibility of additional oscillatory components independent of the dominant mode (cf. [15]). This is further confirmed in the sequence of eigenvectors c_n for $n = 1$–5 (see fig. 2), in which the nodal complexity of each eigenvector increases by one from $n = 1$–3 but jumps sharply for $n = 4$ and 5 (figs. 2d and 2e). Eigenvectors c_4 and c_5 both contain a smoothly oscillating, nearly-sinusoidal component at high frequency (period ~ 20 s) and form a complex pair in relative phase quadrature.

On projection of the original signal onto c_1, a smoothed version of the original time series is recovered (cf. figs. 3a and 3b). Projection of the time series onto c_4 or c_5 (fig. 3c), however, reveals a sequence of short bursts of oscillation of very small amplitude (peak amplitude ~ 0.1) at a frequency $\omega \sim 0.3$ rad s^{-1}, each lasting around 200 s and repeated at the same point within every drift period of the dominant wave ($\tau_d \sim 900$ s). The rapid oscillation is evidently strongest just after the passage of the temperature minimum in the main drifting wave. Such weak oscillations around the temperature minimum are just visible in the raw data itself (see fig. 3a). We may construct a Poincaré section around the local minimum in the signal projected onto c_1 (by taking the plane $c_2 = 0$), and plot intersections in the sub-plane (c_4, c_5) to obtain fig. 4. This clearly shows an open toroidal structure, indicating that the flow is actually quasi-periodic on a torus of very narrow cross-section. It should be noted that such a clear signature of quasi-periodic behaviour could not readily be obtained without the use of SSA (e.g. using simple MOD).

These bursting oscillations are quite weak in amplitude, and are undetectable in the full 32-

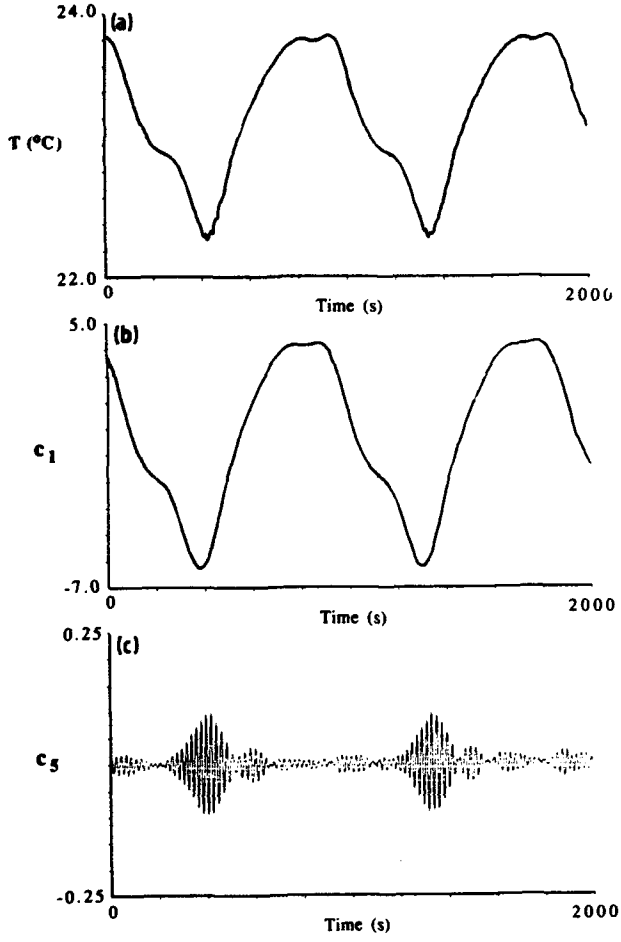

Fig. 3. (a) Extract from the temperature time series obtained at mid-depth and mid-radius in the steady wave flow regime of the rotating annulus (see figs. 1 and 2); (b) projection of the time series onto the first singular vector of fig. 2(a); (c) projection onto the 5th singular vector (fig. 2e).

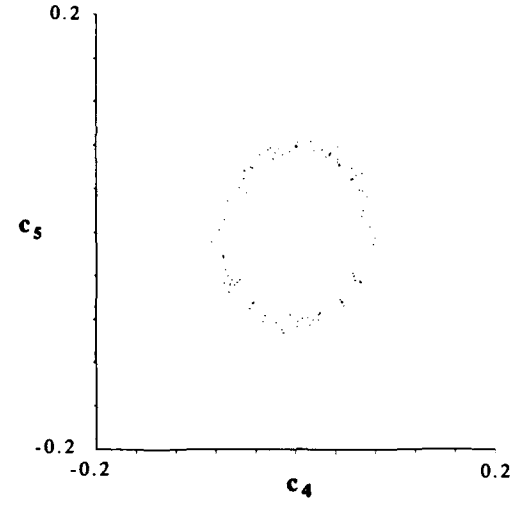

Fig. 4. Poincaré section obtained from the temperature time series shown in fig. 3a projected onto the singular vectors of fig. 2. Section shows the intersections of the reconstructed trajectory with the plane $c_1 = 0$, plotted onto the sub-plane (c_4, c_5).

point thermocouple data (owing to a reduced signal-to-noise ratio). We therefore have very little information with which to determine the nature of this phenomenon. However, the clear synchronization of the bursts with the wave drift would suggest that the oscillation arises from an interaction with the apparatus itself, perhaps even with the thermocouple probe itself. Furthermore, the observed carrier frequency of the bursts is quite close to that of the mean buoyancy frequency N, defined as

$$N^2 = -g\alpha \frac{\partial T}{\partial z}, \tag{3.3}$$

estimated to be ~ 0.4 rad s^{-1} from the fluid properties and experimental parameters. It is conjectured, therefore, that these weak oscillations represent a form of inertia–gravity wave associated with the passage of a certain portion of the main wave past a stationary topographic obstacle, such as the thermocouple ring, though more detailed and sensitive spatially-resolved measurements and/or a numerical simulation would be needed to confirm this interpretation.

3.2. *Embedding flows with slow modulations*

In the previous section, a clear example was presented of a situation in which global SSA greatly facilitated the extraction of a weak high frequency periodic signal component from a much stronger oscillation at a significantly lower frequency. With the benefit of hindsight, it must be acknowledge that more conventional band-pass filters would probably be equally effective in enabling the extract of the high frequency inertia-gravity wave signal in this case. It is unlikely, however, that such methods would have given such immediate prominence as SSA

to this component of the time series, which in this case prompted further investigation of a previously unrecognized dynamical phenomenon.

In the following, in contrast to the above, we discuss a case in which SSA was unable to produce a satisfactory embedding, and present an extension which enables the construction of an improved embedding for signals comprising a fast oscillation which is slowly modulated in amplitude. As an example of this type of signal, RBJS discussed a baroclinic flow regime in which two or more incommensurate azimuthal wavenumber components were each modulated in amplitude at two distinct and widely separated timescales. This regime was identified as chaotic (see RBJS), and arose via a transition from a simpler quasi-periodic flow in which a *single* azimuthal wavenumber was periodically modulated in amplitude (i.e. 'amplitude vacillation' or AV; see [7, 12] and case B of table 1). A typical time series is presented in fig. 5, which shows the variation with time of the total heat transport $H(t)$. The heat transport signal is modulated about its mean value $H \simeq 45$ W due to the fast modulation of the amplitude of the dominant wave (largely responsible for radial heat transfer) at the 'vacillation frequency' ω_v (corresponding to a period around 150 s). The modulation index η of the 'vacillation' is itself modulated at an even lower frequency $\sim\omega_m$ (hence this regime is referred to as a 'modulated amplitude vacillation' or MAV; see RBJS and case

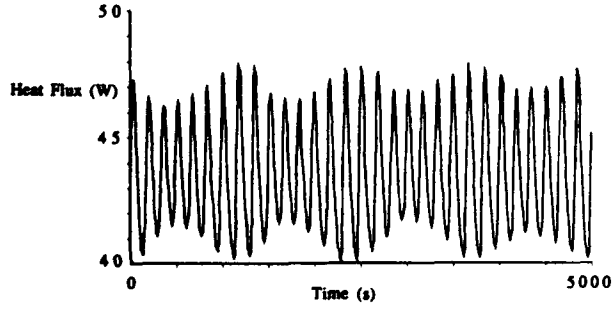

Fig. 5. Extract from time series of total heat flow, obtained from a chaotically-modulated baroclinic wave flow (MAV – Case C; see table 1 and RBJS) in a rotating annulus.

C of table 1), though the long-period secondary modulation is apparently aperiodic in form with a period ~1500 s.

Phase portraits derived from $H(t)$ for this case are organised about a limit cycle at ω_v but are spread by the slow modulation into a disk-like structure of finite radial extent (see RBJS). A typical Poincaré section from such a phase portrait using a moderate length window ($\tau_w = 100$ s) is illustrated in fig. 6a, showing the points clustered along a linear structure with a thickness comparable to the scatter attributable to experimental noise and drifts. However, indications that this disk-like appearance was masking the true dynamics were provided by return maps of the projection of the Poincaré section onto the c_2 axis (see RBJS). These maps showed a closed elliptical form which suggested that the $H(t)$ flow was really organised about a torus, but that the modulation was too slow to change its phase significantly within either one period of the main oscillation at ω_v or an interval of τ_w. Attempts were made to vary the window length (up to $\tau_w = 1000$ s, obtained by resampling the time series more sparsely at 10 s intervals), but all failed to resolve the toroidal nature of the phase portrait in any projection except when $\tau_w \sim$ 1000 s (see fig. 6c), suggesting a fundamental inability of this form of SSA to embed modulated signals with widely separated carrier and modulation frequencies ($\omega_v/\omega_m \geq 10$) unless $\tau_w \sim \tau_m$ ($=2\pi/\omega_m$). When $\tau_w \sim \tau_m$, fig. 6c clearly reveals the underlying toroidal structure with an intriguingly clumped distribution of points around the torus 'walls' with some indication of finger-like extensions suggestive of a 'wrinkling' of the toroidal surface.

RBJS were able to produce an improved embedding of this flow using *short* windows by constructing a modified state space which employed two timescales. The coefficients $c_1(t)$, $c_2(t)$, $c_3(t)\ldots$, constructed using a window length of only $\tau_w = 100$ s, were regarded as an alternative set of 'observables' in the sense of Takens [1], and a new delay embedding (termed

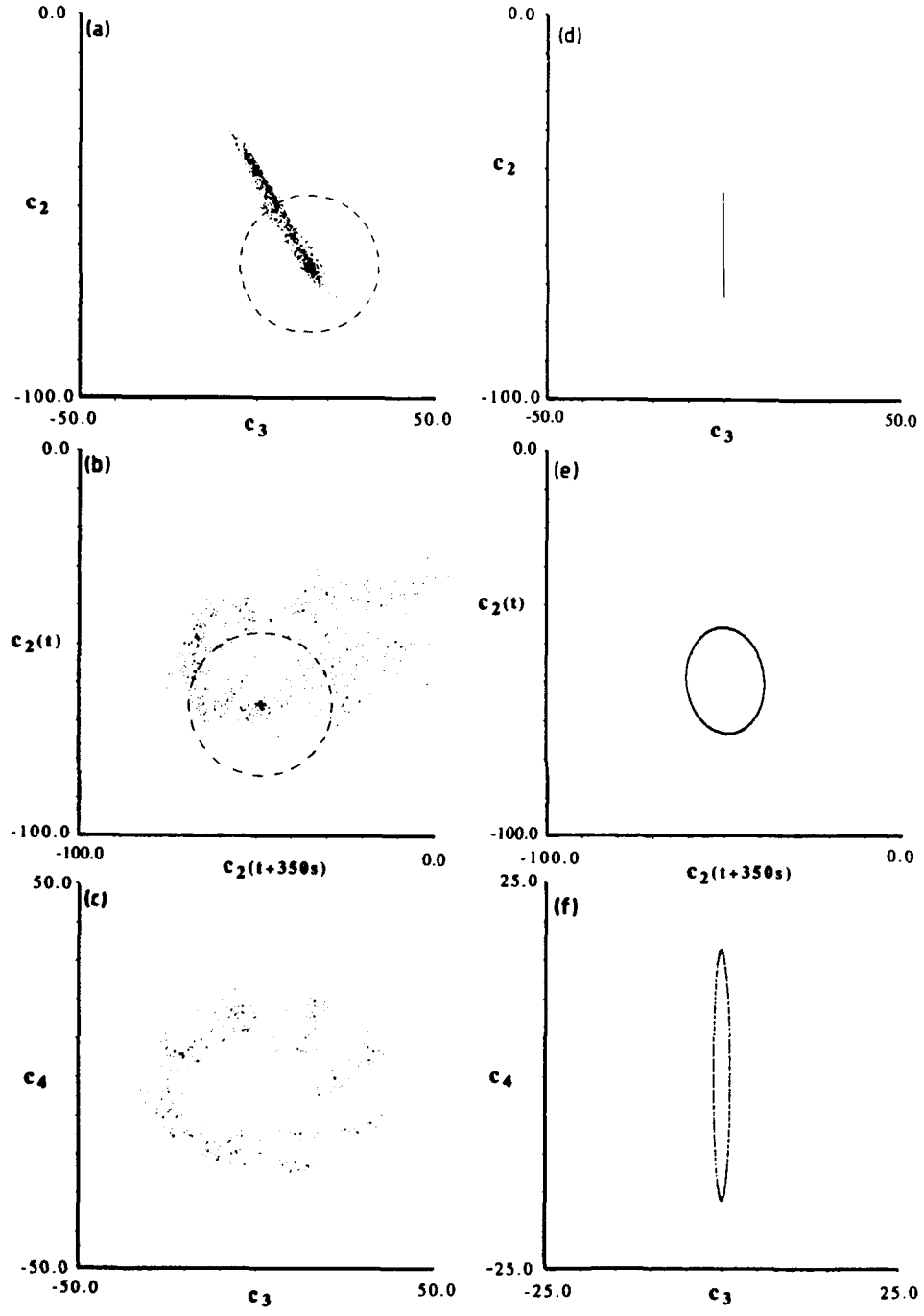

Fig. 6. Poincaré sections obtained in SSA coordinates ((a)–(c)) from the heat transport time series shown in fig. 5, and ((d)–(f)) from the artificial time series given by eq. (3.2): (a) and (d) are sections in normal SSA coordinates with $\tau_\omega = 100$ s, showing the intersections of the trajectory with the plane $c_1 = 0$ plotted onto the sub-plane $(c_2(t), c_3(t))$; (b) and (e) are sections in hybrid delay SSA coordinates showing intersections with the same plane as in (a) and (d) but plotted onto the sub-plane $(c_2(t), c_2(t + \tau_D))$, where $\tau_D = 350$ s; (c) and (f) are sections in normal SSA coordinates with $\tau_\omega = 1000$ s, showing intersections with the plane $c_1 = 0$ on the sub-plane $(c_3(t), c_4(t))$.

hereafter 'hybrid delay SSA' or HDSSA) was then constructed by taking the first three coordinates at time t to be $(c_1(t), c_2(t), c_2(t+\tau_D)\ldots)$, where τ_D was chosen to take account of the slow modulation with a period τ_m. Further coordinates could comprise projections onto higher eigenvectors, with or without additional time delays. In the present example, $\tau_D \sim \tau_m/4$, where $\tau_m \simeq 1500$ s. Fig. 6b shows the same Poincaré section as in fig. 6a but projection onto the new basis, and now clearly shows a toroidal structure (cf. the Poincaré section with $\tau_w = 1000$ s in fig. 6c). The thickness of the torus 'walls' is somewhat greater than the experimental noise and drift, with some suggestion of undulations in the exterior surface as noted above for fig. 6c. The robustness of such structures would tend to favour the interpretation of the irregular nature of the long-period modulation as low-dimensional chaotic behaviour, as inferred by RBJS.

The effectiveness of this construction in resolving the toroidal structure of slowly-modulated quasi-periodic signals is further illustrated in figs. 6d and 6e, which show the same analysis applied to a surrogate artificial time series $A(t)$ generated from the function

$$A(t) = A_0 + (A_1 + A_2 \sin \omega_1 t) \sin \omega_2 t\,, \qquad (3.4)$$

with $\omega_2 = \omega_v$ and $\omega_1 \sim \omega_m$ (cf. RBJS). The basic form of SSA using a window of $\tau_\omega \sim 100$ s produces extremely elongated Poincaré sections in which all points collapse onto a near-vertical line at $c_3 = 0$. In extreme cases, points collapse completely onto a line, forming a section which is completely degenerate (see fig. 6d). With larger windows, Poincaré sections projected onto higher order eigenvectors were able to reveal the toroidal character of the signal reasonably clearly, though still exhibited a tendency towards strongly elongated patterns which would still be difficult to distinguish in the presence of noise (cf. fig. 6f). With the HDSSA embedding, however, the Poincaré section (fig. 6e) opens out to reveal the toroidal structure quite clearly. In all the above discussion, it is important to emphasise that the toroidal nature of $H(t)$ could not readily be established using the simple form of MOD with any reasonable value of τ, despite extensive attempts to investigate a wide range of projections, because of the high degree of dynamical 'noise' and long correlation timescales of the slow modulation in the signal which typically obscures the underlying structure.

4. Local analyses

4.1. Local dimension

Having achieved a satisfactory embedding of a trajectory from a time series, it is then commonly required to estimate the values of invariants characterising the reconstructed attractor. These may include various measures of attractor dimension, metric entropy and the spectrum of Lyapunov exponents [11]. For the flows discussed above, RBJS reported estimates of the pointwise dimension D_p [16] and largest non-negative Lyapunov exponent λ_1 (derived using a form of the algorithm due to Wolf et al. [17]), and Smith [18] has presented evidence for low-dimension behaviour in several cases from the same data using an extension of the Grassberger–Procaccia correlation dimension estimator. A significant difficulty with this approach to dimension estimation, found in the analysis of the flows considered here, however, is that the local curvature of the reconstructed attractor varies strongly with location on the attractor. This leads to difficulties in identifying a range of length scales over which integrals exhibit identifiable scaling behaviour; a difficulty which can be partially overcome by the use of pointwise dimension and other *local* estimators.

4.2. Local SSA and topological dimension

Although it may be argued [3] that the singular spectrum from global SSA provides an esti-

mate of the dimension of an attractor from the number of significant eigenvalues, this estimate is not robust since, in general, it depends upon the window length (BK [5, 15]). Broomhead, Jones and King [5] proposed an alternative method employing SSA to examine the geometry of localised regions of an attractor where the manifold is *locally linear*, and thereby to obtain an estimate of the *topological* dimension k. Their procedure may be summarised as follows.

A reference point is selected on the reconstructed attractor with position vector $\boldsymbol{x}$ in the space spanned by the first d eigenvectors in a global SSA. Nearby points within a ball of radius ε are identified and the ε-neighbourhood matrix $\mathbf{B}_\varepsilon(\boldsymbol{x})$ constructed with rows comprising the vectors $\{(\boldsymbol{x}_j - \boldsymbol{x})^{\mathrm{T}} : |\boldsymbol{x}_j - \boldsymbol{x}| < \varepsilon\}$. The singular vectors of $\mathbf{B}_\varepsilon$ are obtained and correspond to an optimal orthogonal coordinate system centered on $\boldsymbol{x}$. As discussed by [5], the geometry of the manifold is characterised from a consideration of the variation of the magnitudes of the singular values σ_i (equal to the square root of the eigenvalues) of $\mathbf{B}_\varepsilon$ as the ball radius ε is varied. For small enough ε, a neighbourhood of an m-manifold in $\mathbb{R}^d$ will have k approximately equal singular values above a 'noise floor', and these will grow linearly with ε until saturation or the effects of curvature in the manifold become apparent. The remaining $\{\sigma_i : i > k\}$ should remain approximately constant until values of ε where they are significantly affected by curvature. Singular values affected by curvature then vary approximately as ε^2 or faster until they also saturate.

This behaviour is clearly seen in an example from the rotating annulus taken from RBJS, for which the flow comprises a quasi-periodic 'amplitude vacillation' (case B of table 1). The resulting temperature series $T(t)$ at a fixed location in the flow contains two dominant frequencies ω_d and ω_v respectively (where ω_d is the drift frequency of the dominant azimuthal wavenumber), and phase portraits clearly show the trajectory to lie on a well-defined two-torus. A typical Poincaré section from such a flow is shown in fig. 7a. Fig. 7b shows the result of a local SSA analysis, centered on the point indicated by the cross in

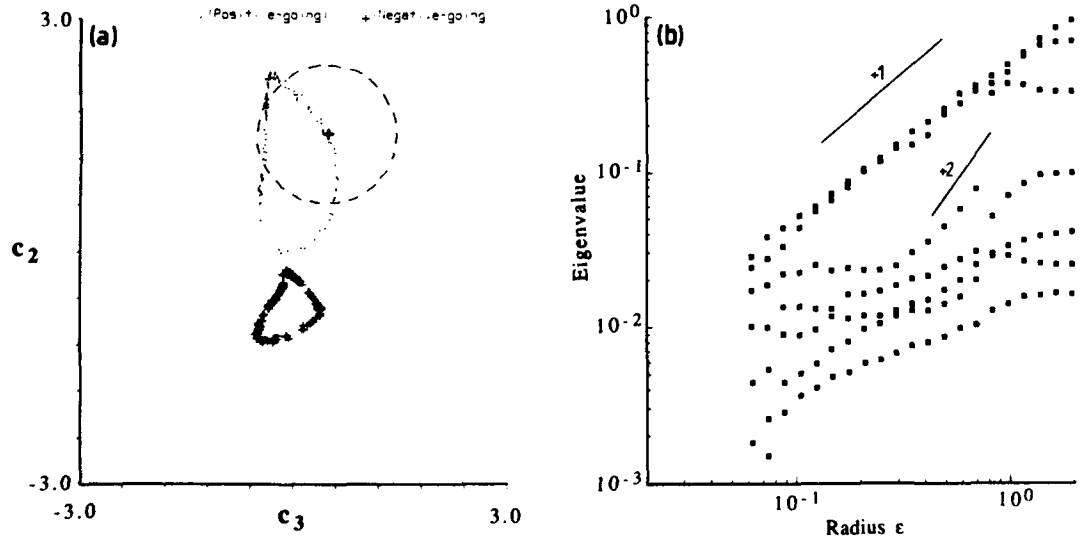

Fig. 7. Poincaré section (a) and local SSA analysis (b) from a temperature time series obtained in a periodically-modulated regular baroclinic wave flow (AV – Case B; see table 1 and RBJS): (a) section in SSA coordinates showing intersections with $c_1 = 0$ plotted onto the plane (c_2, c_3); (b) local analysis centred on the point indicated by the cross in (a) over the neighbourhood enclosed within the dashed circle. Note that the 95% confidence interval on the relative magnitude of eigenvalues [3, 15] varies with ε from ±3% at the largest values of ε to ±50% at small ε.

fig. 7a and carried out for $d = 7$ over a neighbour extending out to the radius indicated by the dashed circle. For $\varepsilon \leq 0.6$, a pair of singular values dominate and both clearly scale as ε over almost the entire range considered. The remaining σ_i are approximately constant for $\varepsilon \leq 0.3$, after which σ_3 grows rapidly, reaching an amplitude comparable to σ_1 and σ_2 around $\varepsilon = 1$. Saturation effects are apparent in $\sigma_1 - \sigma_4$ beyond $\varepsilon = 1$, around which the ball size becomes comparable with the walls of the torus (cf. fig. 7b).

4.3. Local analysis and HDSSA

For the MAV flow discussed above in section 3.2 (case C of table 1), it was noted that global SSA can fail to produce a satisfactory embedding for amplitude-modulated flows with widely differing carrier and modulation timescales unless $\tau_\omega \sim \tau_m$. It might be expected that this could influence adversely the estimation of invariants from the reconstructed attractor. As discussed by RBJS, pointwise dimension estimates for $H(t)$ from the flow discussed in 3.2 indicated a value for D_p around 2 for the scales resolvable, while Lyapunov exponent estimates suggested a significantly positive value for λ_1 indicative of low-dimensional chaos. The results of section 3.2 above, however, suggest that much of the two-dimensional character of the $H(t)$ attractor may be due to the failure of the embedding, which causes the (basically toroidal) attractor to collapse onto a sheet-like structure.

This apparent two-dimensional character of the attractor reconstructed using simple SSA with short windows is also reflected under local SSA analysis, except at small ε. Fig. 8a shows a typical local SSA analysis for $d = 7$, centered at the point indicated by the cross in fig. 6b and surrounded by the dashed circle at $\varepsilon = 20$. Two singular values scaling as ε clearly emerge for virtually all values of ε. σ_3 and σ_4 appear to scale as though affected by local curvature around $\varepsilon \sim 2$–3 until they saturated for $\varepsilon > 5$. When the HDSSA method is used to construct the embedding, however, evidence for some higher dimensional activity is revealed. Fig. 8b shows the local SSA analysis comparable to that of fig. 8a for the same region of the attractor, embedded using $d = 7$ for global coordinates given by

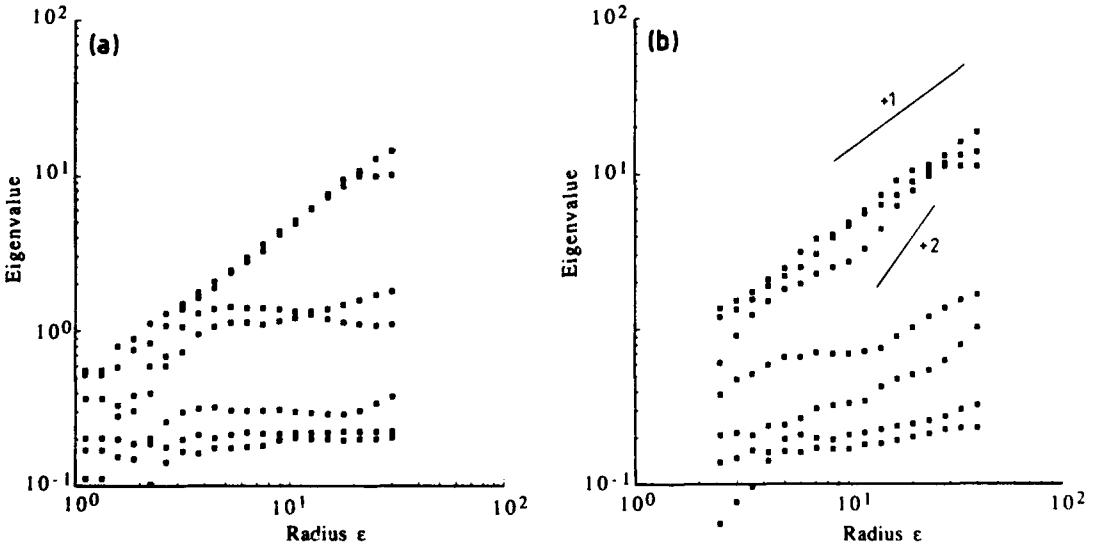

Fig. 8. Local SSA analyses from the heat transport time series shown in figs. 5 and 6 (a and b) in normal global SSA coordinates (a) and HDSSA coordinates (b). Analyses are centred on the points indicated by crosses over the neighbourhoods enclosed within the dashed circles in figs. 6a and 6b respectively. Confidence intervals on eigenvalues vary over the same range as in fig. 7.

$$\boldsymbol{x}(t) = (c_1(t), c_2(t), c_2(t+\tau_D), c_3(t) \ldots c_6(t)) . \quad (4.1)$$

In this case, the analysis shows three dominant singular values which scale as ε, the others remaining roughly constant except for $\varepsilon > 15$ where curvature effects start to become significant. σ_3 appears to scale as ε^2 around $\varepsilon \sim 3$, though the statistical error on these points is relatively large owing to the relatively few points remaining inside the ball. This would indicate that the topological dimension $k = 3$ for this flow, which is more likely to be consistent with the low-dimensional chaotic behaviour inferred from λ_1 and the evidence for simple spatial structure etc. (see RBJS). Curiously, the estimate for λ_1 was scarcely affected by changing to the embedding defined by (4.1) in estimates derived using the Wolf et al. [17] algorithm. Values were found typically to reduce by only ~10% from those obtained using the simple global SSA embedding with $\tau_\omega \sim 100$ s.

4.4. *A transition to chaos in four dimensions?*

The other principal type of transition to disordered flow observed in the thermal annulus entails, as an intermediate stage, bifurcations from the steady wave state (cf. section 3.1) to one in which rapid fluctuations take place primarily in the *structure* of the dominant wave (so-called 'structural vacillation' or SV [7]; see case D of table 1). This SV state is now widely recognized as the first stage towards the emergence of fully-developed 'geostrophic turbulence', in which the flow structure, dominant wavenumber and amplitude is constantly changing in a disordered and aperiodic manner (e.g. see RBJS [13]). Such a complex flow is likely at least to represent chaotic flow on an attractor of relatively high dimension (assuming it is chaotic in a formal sense at all – e.g. see RBJS). Guckenheimer and Buzyna [19] presented evidence from rotating annulus experiments which indicated an increase in attractor dimension up to $D_p \simeq 7$ as the SV regime approached 'geostrophic turbulence'.

In the present work, RBJS presented estimates of D_p spanning the SV regime which suggested an increasing attractor dimension, though none of the estimates exceeded $D_p = 4$. There were, however, some inconsistencies between dimension estimates obtained from simultaneous $T(t)$ and $H(t)$ time series, and evidence for satisfactory scaling regions was often marginal, suggesting that the estimates of D_p in this regime were poorly defined. Fig. 9 shows two examples of phase portraits obtained from $T(t)$ spanning the transition from steady wave flow to SV. Fig 9a and 9c show the phase portraits (a) from a steady wave flow (case A; see table 1), and (b) from a well developed SV (case D; see table 1). As remarked by RBJS, the onset of SV appears to result in a uniform thickening of the steady wave limit cycle via irregular bursts of high frequency oscillations, but with little evidence of any systematic structure; the SV flow appears to be immediately chaotic (via a narrow band of temporal intermittency in parameter space) with no intermediate quasi-periodic state (see RBJS).

Figs. 9b and 9d show typical local SSA analyses for these reconstructed attractors, centered upon the points in figs. 9a and (c) surrounded by the dashed circles, again for $d = 7$. Fig. 9b shows only one singular value rising above the noise level (around $\sigma_i = 10^{-2}$) and scaling as ε. To within the limitations of experimental noise and drifts, therefore, $k = 1$ for this flow, confirming it as a simple steady wave. In fig. 9d, however, there is clearly more structure in evidence. The limit cycle about which the flow is organised, representing quasi-steady wave drift, dominates the singular spectrum for $\varepsilon > 0.5$. In the range $0.2 \leq \varepsilon \leq 0.5$, however, four singular values are found to be of comparable magnitude and scale roughly as ε, indicating a dimension $k = 4$ within the resolution of the data. For $\varepsilon \leq 0.2$, all singular values are comparable with the noise and ill-defined because of poor statistics. This would

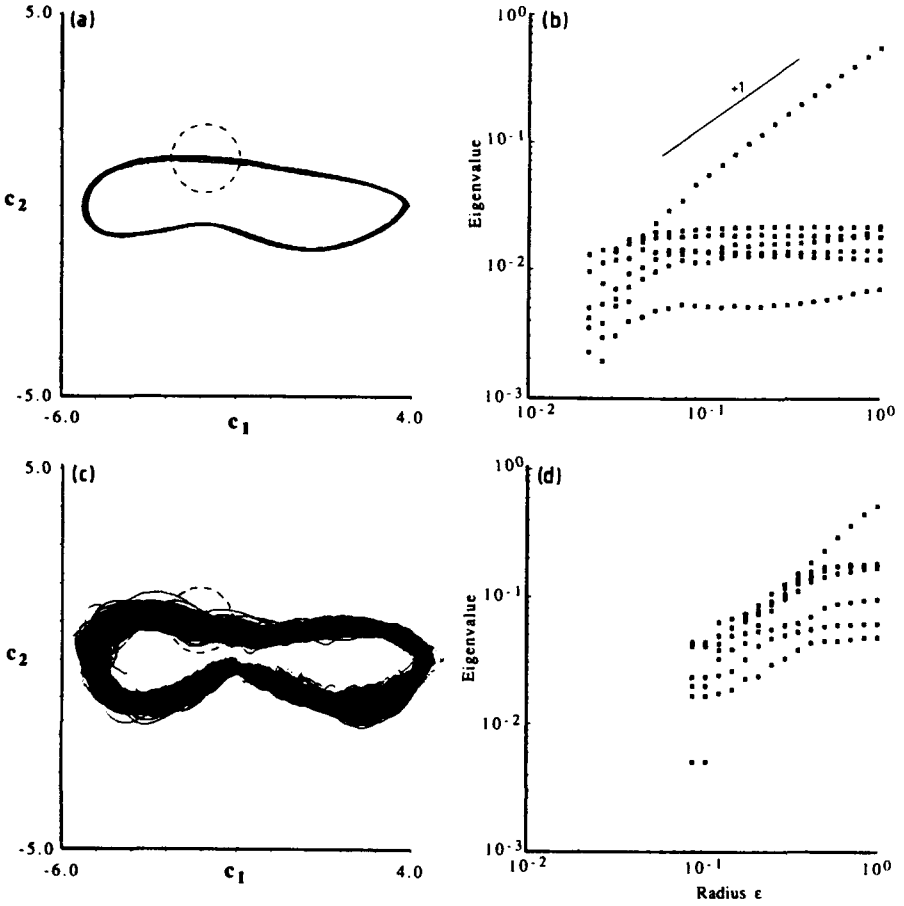

Fig. 9. SSA phase portraits ((a) and (c)) and local SSA analyses ((b) and (d)) from temperature time series obtained from a steady baroclinic wave flow (Case A; see table 1) (a), (b) and a chaotic structurally-modulated baroclinic wave (SV – Case D; see table 1 and RBJS) ((c), (d)). Local analyses are centred upon the points enclosed within the dashed circles shown in (a) and (c) respectively. Confidence intervals on eigenvalues vary over the same range as in fig. 7.

seem to support the conclusion (see RBJS) that SV may be consistent with low-dimensional chaos, with an attractor dimension in $T(t)$ of $3 < D_p < 4$.

5. Discussion

Results presented above have clearly demonstrated the effectiveness of global SSA in extracting very weak bursts of high frequency oscillations from a signal dominated by a much stronger component ($\sim 10^2$ larger in amplitude) of complex structure at a much lower frequency. It is noteworthy that, in contrast to more conventional filtering methods, no tuning of the technique was necessary in order to achieve a very clear separation of the two signal components. The present work has also shown, however, that embeddings obtained using SSA can apparently fail when the signal comprises a very slow periodic or irregular modulation of a high frequency carrier unless relatively large windows (based on the *slow* timescale in the signal) are employed (note that this also applies to the case discussed in section 3.1), which may lead to excessive computational expense in some cases. Although alternative methods are available from engineering practice to treat the demodulation of amplitude-modulated carrier signals (e.g. [20]),

the HDSSA approach proposed herein would seem to offer a simple extension to the more conventional MOD which can readily enable such signals to be embedded successfully for phase-plane analysis in cases where it may be impractical to use very long windows.

Local SSA is shown to provide a viable alternative means of analysing the local structure of a reconstructed attractor, if used with care and providing the underlying global embedding is well-posed. In the present work, we have obtained estimates of topological dimension which are consistent with alternative, more conventional, dimension estimates, and provide supporting evidence for two distinct types of chaotic behaviour of low dimension in a rotating, thermally stratified fluid (so-called 'baroclinic chaos'). It is important to remark, however, that, like the more conventional box-counting or correlation dimension estimators, local SSA does rely on being able to identify scaling behaviour over a reasonable range in radius of the chosen neighbourhood; a property which experience suggests may not always be straightforward to find, and which places considerable demands on data quality and quantity for attractor dimensions significantly greater than around 3. The apparent success of local SSA in the present context, however, does provide some encouragement to apply the approach to the evaluation of more complex quantities such as the estimation of the spectrum of Lyapunov exponents [6].

Acknowledgements

It is a pleasure to thank Prof. R. Hide for his support and encouragement during this work and for many lively discussions. I am also grateful to Dr. P. Hignett and W.D.N. Jackson for their contribution to the development of the apparatus, and to D.W. Johnson and R.M. Small for their assistance in running the experiments. Thanks are especially due to Dr. M.J. Bell for his contributions to the data analysis and interpretation, and for his original suggestion which led to the development of the HDSSA proposed herein. I am also grateful to Dr. D. Broomhead, Dr. L.A. Smith and Dr. R.L. Smith for helpful discussions concerning the analysis of the data, and to anonymous referees whose suggestions led to improvements in the presentation. This work was carried out under project RE20Z of the Meteorological Office research programme.

References

[1] F. Takens in: Dynamical Systems and Turbulence, eds D. Rand and L.S. Young, Lecture Notes in Mathematics (Springer, Berlin, 1981) 366.
[2] D.S. Broomhead and G.P. King, Physica D 20 (1986) 217 referred to as BK.
[3] K. Fraedrich, J. Atmos. Sci. 43 (1986) 331.
[4] E.R. Pike, J.G. McWhirter, M. Bertero, and C. De Mol, Proc. IEEE 131 (1984) 660.
[5] D.S. Broomhead, R. Jones and G.P. King, J. Phys. A 20 (1987) L563.
[6] D.S. Broomhead and G.P. King, in: Nonlinear Phenomena and Chaos, ed. S. Sarkar (Adam Hilger, Bristol, 1986) p. 113.
[7] R. Hide, and P.J. Mason, Adv. Phys. 24 (1975) 47.
[8] J. Shukla, Adv. Geophys. 28B (1985) 87.
[9] P.L. Read, M.J. Bell, D.W. Johnson and R.M. Small, J. Fluid Mech. 238 (1992) 599, referred to as RBJS.
[10] P. Hignett, A.A. White, R.D. Carter, W.D.N. Jackson and R.M. Small, Quart. J. R. Met. Soc. 111 (1985) 131; P. Hignett, Geophys. Astrophys. Fluid Dyn. 19 (1982) 293.
[11] J.-P. Eckmann, and D. Ruelle, Rev. Mod. Phys. 57 (1985) 617.
[12] R.L. Pfeffer, G. Buzyna, and R. Kung, J. Atmos. Sci. 37 (1980) 2129.
[13] G. Buzyna, R.L. Pfeffer, and R. Kung, J. Fluid Mech. 145 (1984) 377.
[14] P. Hignett, Geophys. Astrophys Fluid Dyn. 31 (1985) 247.
[15] R. Vautard, and M. Ghil, Physica D 35 (1989) 395.
[16] J.D. Farmer, E. Ott, and J. Yorke, Physica D 7 (1983) 153.
[17] A. Wolf, J.B. Swift, H.L. Swinney, and J.A. Vastano, Physica D 16 (1985) 285.
[18] R.L. Smith, J. R. Stat. Soc. (1991), submitted.
[19] J. Guckenheimer, and G. Buzyna, Phys. Rev. Lett. 51 (1983) 1438.
[20] R.N. Bracewell, The Fourier Transform and its Applications, 2nd Ed. (McGraw Hill, New York, 1978); L.R. Rabiner and B. Gold, Theory and Applications of Digital Signal Processing (Prentice Hall, New Jersey, 1975).

PHYSICA D

Physica D 58 (1992) 469–481
North-Holland

Correlation of local stretchings as a way of characterising chaotic dynamics amid noise

C.D. Bertram[1] and X. Tian

Centre for Biomedical Engineering, University of New South Wales, Kensington, Sydney, Australia 2033

Received 3 October 1991
Revised manuscript received 29 January 1992
Accepted 7 February 1992

A positive Lyapunov exponent can result from either chaotic dynamics or noise. As a possible means of assessing the degree to which the exponent is noise-affected, and as a possible index in its own right, the localised divergence of two neighbouring trajectories from a fiducial trajectory is compared, in the expectation of finding strong correlation when the source of stretching is deterministic chaos, and little or no correlation when the source is coloured or uncoloured noise. The method is applied to various equation systems and to a periodic time series from the self-excited oscillation of flexible tube collapsed by external pressure and conveying a flow.

1. Introduction

This work arose out of investigations of the intriguing properties of a collapsed tube conveying a flow. In concept, this is a model of many of the conduits in the human body. The essentials are that the tube walls are flexible, and that pressure outside exceeds that inside. This situation occurs in the circulation in the larger veins, and also in the pulmonary airways, in the urethra and in the larynx. When a cuff is applied to the arm for the measurement of blood pressure, these conditions occur in the brachial artery. A comprehensive list of the physiological occurrences is given by Shapiro [1].

The self-excited oscillations that such a system will undergo are of particular interest. These oscillations are the basis of lung wheezing, of the action of the vocal cords, and of the vibration of a trumpet-player's lips, and are related to events underlying the Korotkov sounds heard by stethoscope or microphone downstream of the arm cuff. We seek to understand the mechanism of the oscillations through analysis of experimentally observable behaviour, since this system, although apparently simple, has proved resistant to quantitatively accurate theoretical prediction [2].

In the course of analysis of the aperiodic oscillations, we find that the dynamics appear to include an inherent noise component considerably in excess of that due to measurement. This, the experimental viewpoint, is better expressed analytically by saying that the dynamics appear very complicated or high-dimensional. We are thus led to consider ways to quantify an aperiodic system that will differentiate between deterministic and noise sources of orbital divergence.

2. The experiment

The system under consideration is shown in fig. 1. It consists of a fairly short uniform segment of silicone rubber tube, mounted between

[1] E mail address: chrisb@mr_plod.cbme.unsw.edu.au.

0167-2789/92/$05.00 © 1992 – Elsevier Science Publishers B.V. All rights reserved

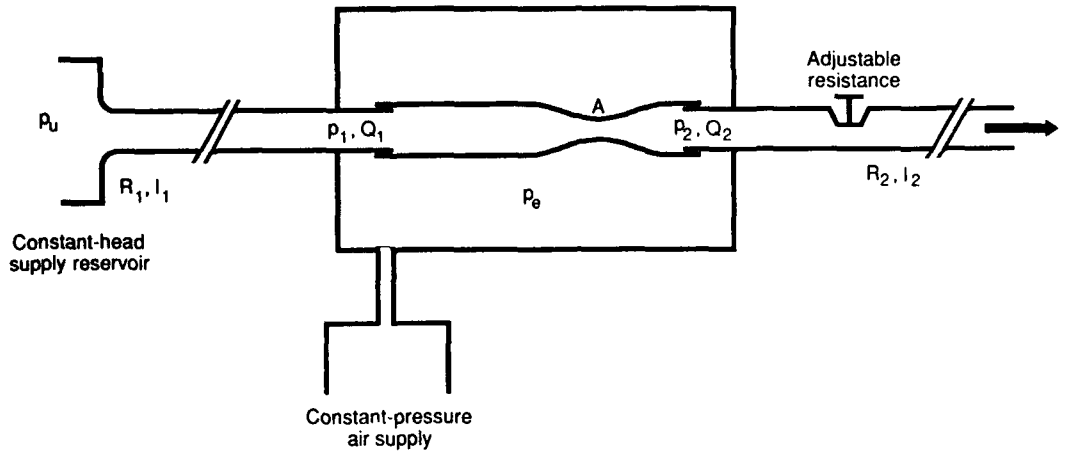

Fig. 1. Schematic of the system investigated experimentally, showing the flexible tube mounted in the pressure chamber and perfused from a constant-head reservoir. The fluid inertia and resistance to flow both upstream and downstream of the flexible tube are calibrated parameters. The control variables are the pressures in the reservoir (p_u) and the chamber (p_e). The time signals recorded are the pressures (p_1, p_2) and volume flow-rates into and out of the tube, and the cross-sectional area at the site of maximal oscillation, near the downstream end.

rigid pipes which form the opposite ends of a pressure chamber. Compressed air in the chamber causes the tube to collapse, or flatten out. In cross-section the tube is then dumbbell-shaped, with opposite-wall contact in the middle. Water is propelled through the tube from a constant-head reservoir.

Behaviour depends on at least ten dimensionless parameters [3]. There are the tube parameters of length and wall stiffness, plus wall mass and longitudinal tension. The fluid density and viscosity set the Reynolds number. In addition the rest of the apparatus contributes fluid inertia and resistance to flow, both upstream and downstream of the collapsible tube.

A two-dimensional slice of that parameter space has been characterised, by varying the tube length and the flow resistance downstream. For each of twelve locations on that slice, a control-space diagram in two further dimensions has been drawn up [4]. The axes of this are the control pressures setting the flow-rate and the degree of collapse. Each diagram includes various zones of different behaviour. These behaviours include steady flow, both when the tube is open and when it is collapsed, various different types of oscillation, defined by frequency range or waveform shape, and exponential instability or divergence.

A rich variety of qualitatively distinct modes of oscillation has been recorded. For those oscillations which are markedly aperiodic, we seek to demonstrate underlying order. This is equivalent to asking whether we have low-dimensional chaos, since high-dimensional deterministic chaos and non-deterministic variation are equally intractable as far as today's analysis tools are concerned. Assuming provisionally the presence of low-dimensional chaos, we seek to characterise the degree of chaos, despite having access only to experimental data with an inevitably limited signal-to-noise ratio. Most investigations overcome this difficulty by substituting a low-dimensional simplified model of the experiment. Such models exist for this system (e.g. ref. [3]) but have been shown to represent the experimental system inadequately. Even the most recent theoretical models (e.g. ref. [5]) fail in their quantitative predictions. A further complication of this system is that even if there is a chaotic attractor, it is not necessarily intrinsic to the self-excited oscillator. It might be that at

some operating points the oscillator simply becomes sensitively dependent on the time-varying details of the arriving turbulent flow.

3. Methods of characterisation

One well-known way to reduce the complexity of a system is to apply the techniques of singular value decomposition (SVD) as developed for this purpose by Broomhead and King [6]. This method gives information including the maximum sensible embedding dimension and an estimate of attractor dimension at localised points [7], but can be regarded for these purposes as simply a particularly adept way of low-pass filtering.

A computationally efficient way then to characterise the degree of chaos is the positive Lyapunov exponent, which by quantifying how fast neighbouring points get separated indicates how rapidly the ability to predict future position is lost. Wolf et al. [8] have promoted this index and provided algorithms for use with experimental data.

The problem with λ_1, the global Lyapunov exponent, is that its value depends on the noise level; see fig. 2, where the log of the λ_1-value is plotted against the log of the *inverse* of the signal-to-noise ratio. We find this noise-to-signal approach logical, in that we add noise to the data as a way of investigating its effects. The signal-to-noise ratio is estimated either from phase portraits or from the amplitude spectrum.

Our phase-portrait method is explained with reference to fig. 3, a phase-portrait-style plot of one state variable against another. This example is close to periodic, although there is a secondary oscillation during one phase of the cycle which produces a two-torus. A measure of the experimental signal-to-noise ratio, i.e., that which characterises the transducers and data acquisition, is provided by comparing the strip width where all trajectories converge maximally with the overall size of the limit cycle. The procedure assumes that there is a part of the cycle when the dynamical system follows consistently the same trajectory. To the extent that this assumption is false, the estimate of signal-to-noise will be conservative.

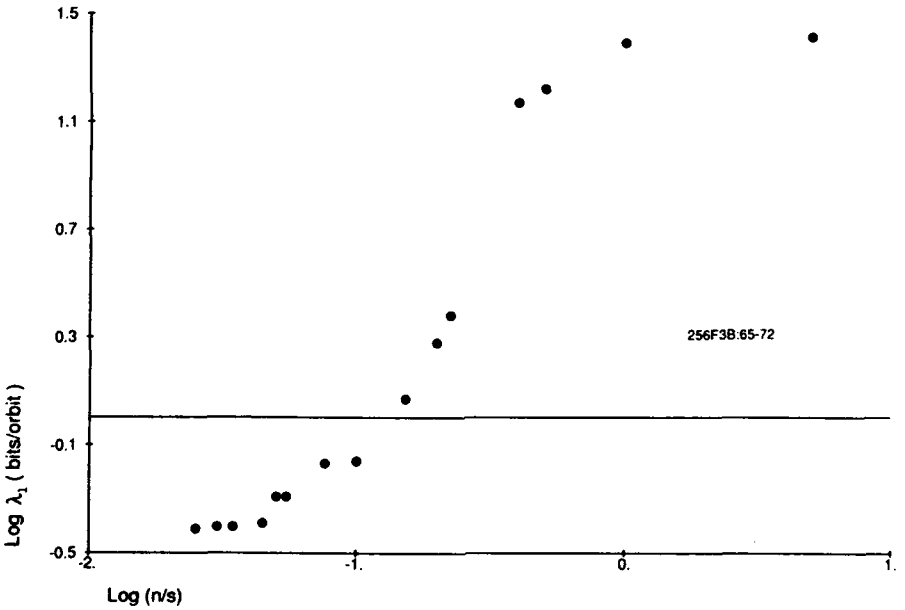

Fig. 2. The logarithm (base 10) of the noise-to-signal amplitude ratio versus the logarithm of the largest Lyapunov exponent (λ_1), for aperiodic experimental data with added pseudo-random noise of varying amplitude.

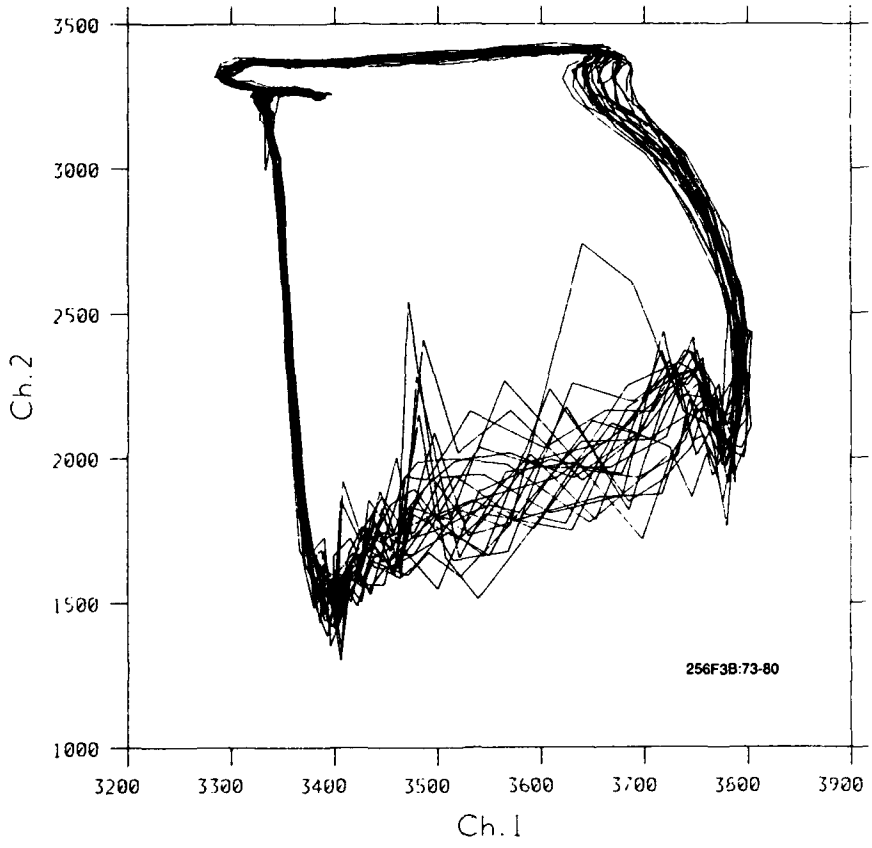

Fig. 3. Typical phase-plane portrait of p_1 versus p_2 during low-frequency oscillation. The topology is basically that of a limit cycle, which by virtue of a secondary oscillation of randomised phase around part of the cycle becomes a two-torus.

Alternatively, when there is marked trajectory variation at all phases of the cycle, the noise level can be estimated from the Fourier spectrum. The peak-to-peak amplitude of pseudo-random white noise giving the same level of noise floor to the spectrum as that present at the high-frequency end of the experimental spectrum is found and compared with the peak-to-peak signal amplitude. Since the spectral noise floor for the signal is not completely flat and devoid of signal power, this method too gives a conservative estimate of the signal-to-noise ratio.

Having estimated the signal-to-noise ratio of the original data, we plot this λ_1 at the left-hand side in fig. 2. Then pseudo-random noise of varying amplitude is added to the data and λ_1 is re-calculated each time. The value is seen to increase along with the noise level. There is a suggestion of a leveling-out to a constant value on the left, and indeed for attractors based on equations, for which a low noise-to-signal ratio can be obtained, a constant value is reached, as shown in fig. 4. Here an example of a periodic system (a noisy sine wave) is compared with the Lorenz attractor. The Lorenz returns a significantly positive λ_1, the sine wave an insignificantly positive one. (Significance is defined by computing the cumulative mean of the localised stretch and its standard error once the cumulative average has ceased to converge.)

Now λ_1 is the cumulative average of all the local stretching estimates, each such estimate being computed as

$$S(t) = \frac{1}{N\,\delta t} \log \frac{L(t)}{L(t - N\,\delta t)} ,$$

where L is the distance between the fiducial orbit

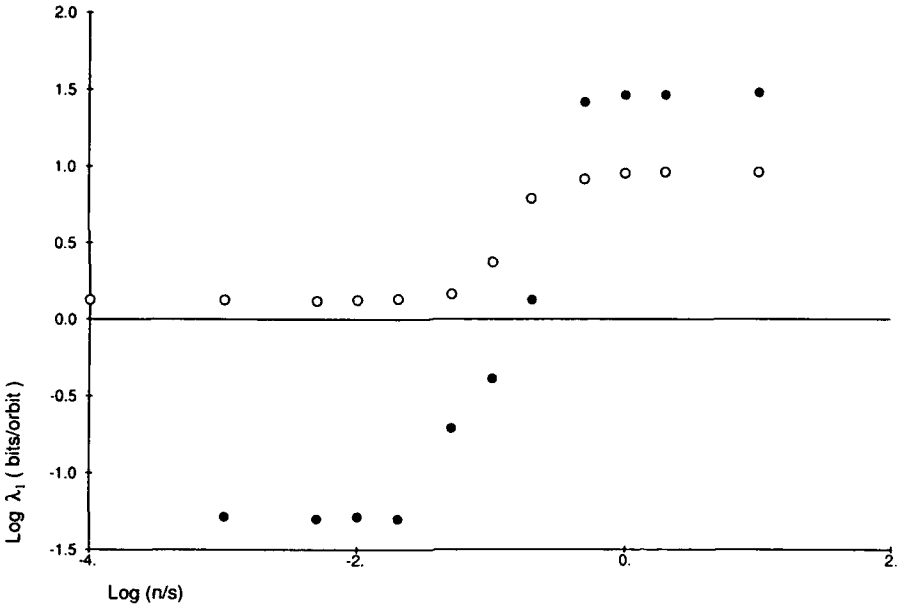

Fig. 4. As fig. 2, but for (●) a sine wave and for (○) the Lorenz attractor ($\sigma = 10$, $b = \frac{8}{3}$, $R = 28$).

point and the neighbour-orbit point, δt is the data sampling interval and N is an integer. What extra information is available from looking in detail at the individual stretch estimates? On a noise-free attractor, regions of stretching and folding should give rise to somewhat similar behaviour on many different orbits. The main idea explored in this paper is to compute not one but two local stretchings (S_1 and S_2), by tracking the divergence of two neighbouring trajectories from a fiducial trajectory. (The procedure has similarities with the use of three trajectories to compute $\lambda + \lambda_2$. But in this case we are concerned with linear distance of each neighbour from the fiducial orbit instead of the area of the triangle formed by the current point on each of the three orbits.) We hypothesised that the behaviour of two such stretchings should be highly correlated when the stretching is the result of deterministic processes, and uncorrelated when the computed divergence is the result of noise. We postulated that such a comparison of S_1 and S_2 might usefully distinguish between chaos and noise where λ_1 does not, and in particular might help to quantify chaos in the presence of noise.

4. Implementation

Except where embedding dimension is specifically varied, or where the equation system is four-dimensional, all calculations have been done in a three-dimensional embedding space, using two equal delays to generate coordinates from a one-dimensional array of x-values from the numerical integration of the equations. We concentrate on single-centre attractors (e.g. the Rössler, Shaw's velocity-forced Van der Pol system), as opposed to two-centre systems (Lorenz, double potential well), since the experimental data fall in this category. For these systems we can define an arbitrary centre around which orbits rotate as seen in two-dimensional projection. Many orbits can then be compared in terms of an angle ϕ which defines the region of phase space. The local stretchings are then distributed for the Rössler attractor as shown in fig. 5. Classically, Lyapunov exponents are expressed as bits/second of lost information, but conversion to bits/orbit allows comparison of different attractors. Points above zero represent divergence of neighbouring trajectories, and those below, con-

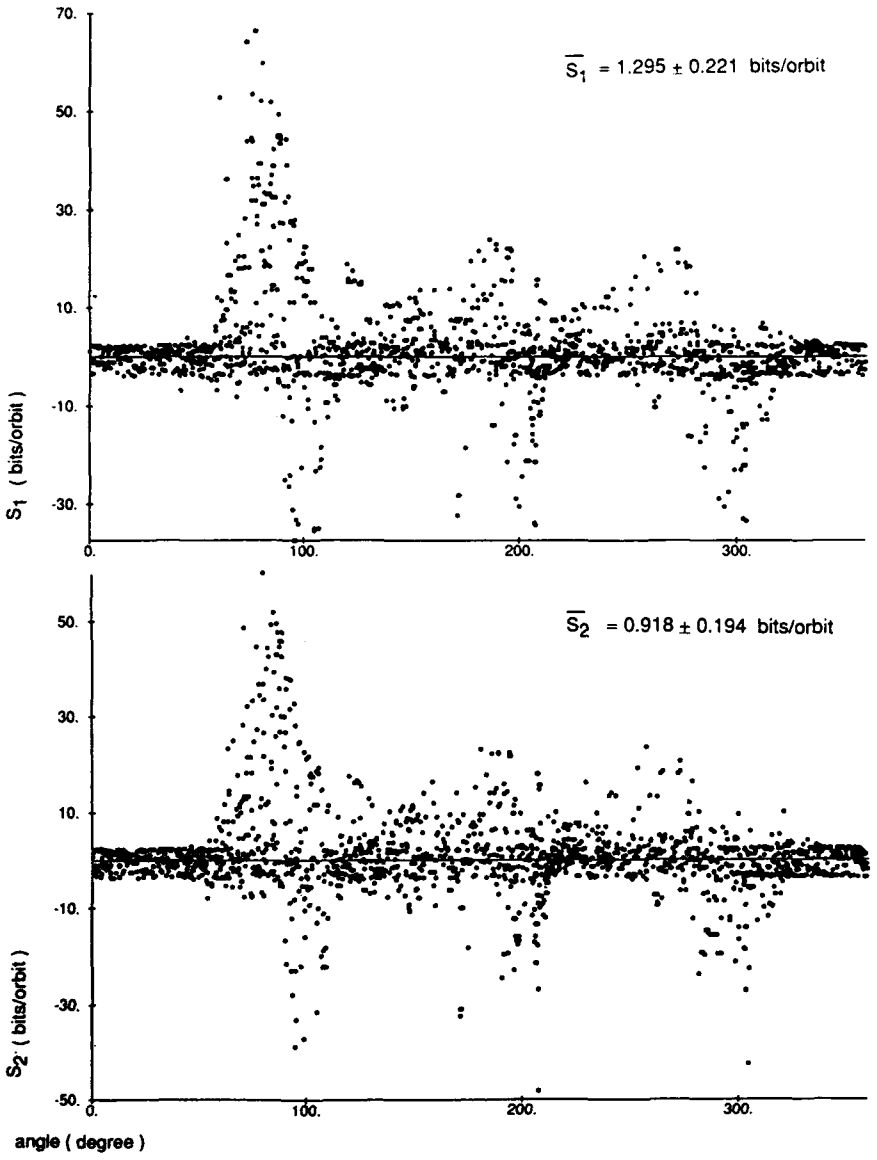

Fig. 5. Position in terms of angular location (ϕ) on the reversed-time Rössler attractor ($a = 0.15$, $b = 0.2$, $c = 10$) versus the two local stretchings S_1 and S_2 (see text). The computation used 2048 data points calculated at $\delta t = 0.3$ s, with stretch calculated over each five δt.

vergence. In keeping track of the two neighbouring orbits, if the current distance to one (former) neighbour exceeds the maximum allowed, both neighbours are replaced simultaneously. As a result there are more replacements overall and the global mean of each of the two stretchings is slightly altered; $\overline{S_1}$ is higher than λ_1 as computed using only one neighbour orbit, and $\overline{S_2}$, which is computed using always the second choice of nearby orbit, is lower. But clearly both see the same features in the attractor, whether they be divergence, convergence or cross-over, which is a combination of the two.

The criteria to be satisfied by a replacement mean that the chosen orbit is not always the closest. The search for an S_1 replacement is conducted on the principle that the nearest neighbour is selected, subject to the constraint

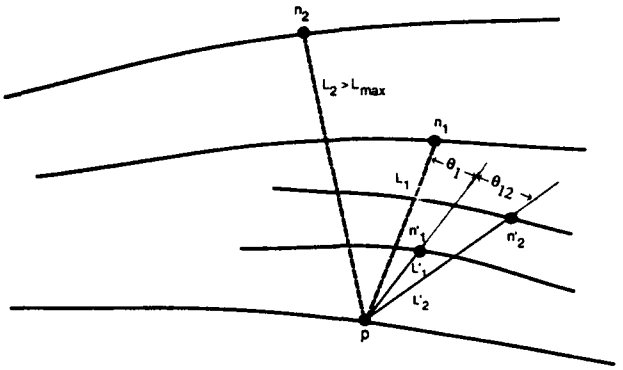

Fig. 6. Diagram illustrating the angular constraints that control the process of selecting replacement neighbour orbits when the maximum separation L_{max} is exceeded. Notation: p: current fiducial orbit point; n_1, n_2: current points on the first and second nearby orbits at the time when replacement is required; n'_1, n'_2: points found on two candidate replacements orbits by successive application of a box-search algorithm.

that the angle θ_1 (see fig. 6) between the vector to the last point used on the old orbit and the first used on the new orbit not exceed a preset maximum. This ensures that the computation always tracks a measure of the same Lyapunov exponent through the dataset. On occasion the local sparseness is such that no replacement satisfying this angular criterion can be found within the maximum allowed distance for a neighbour, and in this case the angular criterion is relaxed. These search principles are as established by Wolf et al. [8]. The S_2 replacement is then found on similar principles, minimising the distance to the new neighbour while controlling the angle θ_{12} between the vectors from the current point on the fiducial orbit to the current point on each of the replacement orbits. Normally θ_1 and θ_{12} are limited to 30° or less, but the three limit parameters are chosen so as to ensure that the percentage of instances when the angular criteria have to be relaxed is kept small.

S_1 and S_2 can also be treated as two linear data arrays and cr s-correlated. The zero-delay cross-correlation has the form

$$\mathrm{cc}_{12} = \frac{E[(S_1 - \overline{S_1})(S_2 - \overline{S_2})]}{\sigma_1 \sigma_2},$$

where the numerator is the covariance of S_1 and S_2, and σ_1 and σ_2 are the standard deviations of S_1 and S_2 respectively. The single number thus obtained characterises the extent to which the data are noise-affected. This can be demonstrated as in fig. 7 by observing how the normalised cross-correlation between the two local stretching trains varies when noise is added. At low noise levels, cc_{12} is like λ_1 a characteristic measure of the attractor. For the Rössler attractor the asymptotic level of cross-correlation is 0.64, whereas for the Lorenz it is 0.69, and for a continuously differentiable periodic signal it is unity.

That this measure of the behaviour of the attractor contains different information from λ_1 can be seen by comparing the ordering of the same three attractors by λ_1. Whereas the cross-correlation established the Lorenz as situated "between" the Rössler and the sine-wave, λ_1 has the Rössler in the middle of the three.

In the noise-afflicted region, the various attractors examined all suffer reducing cross-correlation, along what looks to be a common or universal path. The aperiodic collapsible-tube data subscribe to this path, as shown in fig. 8, indicating that pre-processing by some means such as singular system analysis is required before the attractor can be characterised further.

To test whether an asymptotic cc_{12}-value could be derived from noisy data using SVD, we added that amplitude of noise to the Rössler attractor which gave approximately the noise-to-signal ratio characteristic of the experiments, i.e. $\log_{10}(n/s)$ slightly greater than -2. Then we applied singular value decomposition to the resulting x-variable time series and reconstructed the attractor in three dimensions using the first three singular vectors. Proceeding as described above, we computed the zero-lag cross-correlation of the S_1 and S_2 time series and compared it with the value found for the noise-free Rössler system (see the left-hand side of fig. 9a). The estimate found after using SVD to remove noise is close to that computed for the original noise-

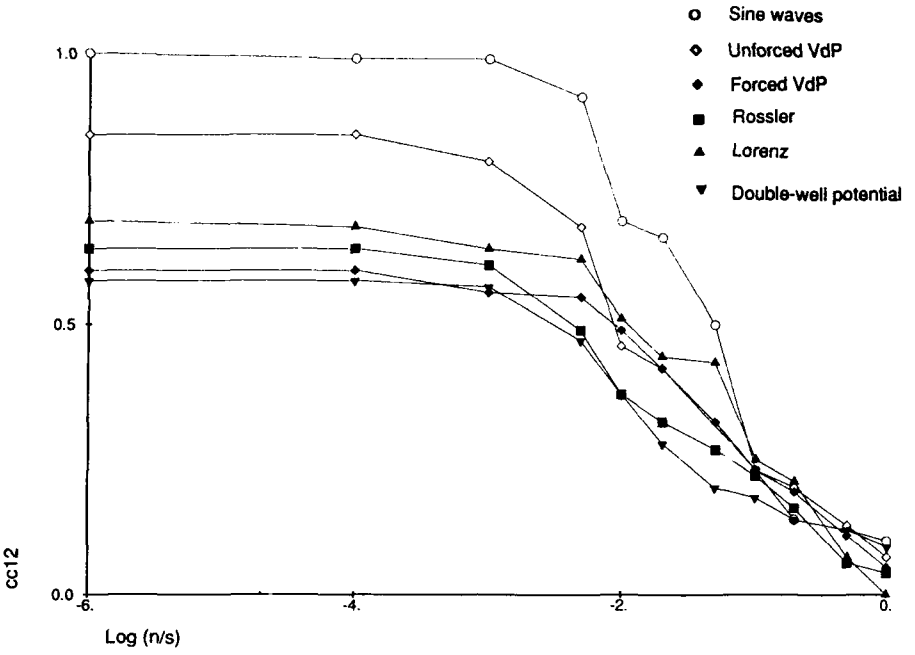

Fig. 7. The log(noise-to-signal ratio) versus the zero-lag normalised cross-correlation cc_{12} of the S_1 and S_2 time series for (○) a sine wave, (◇) the unforced van der Pol attractor ($\omega = 1$, $\alpha = 10$), (◆) Shaw's forced Van der Pol system ($\omega_0 = 1.57$, $A = 0.25$), (■) the Rössler attractor as in fig. 5, (▲) the Lorenz attractor as in fig. 4, and (▼) the double potential well system ($\omega = 0.83$, $f = 0.16$, $\delta = 0.1$), all with noise added as in fig. 2. Note that the two periodic systems yield markedly higher cross-correlation than the chaotic systems.

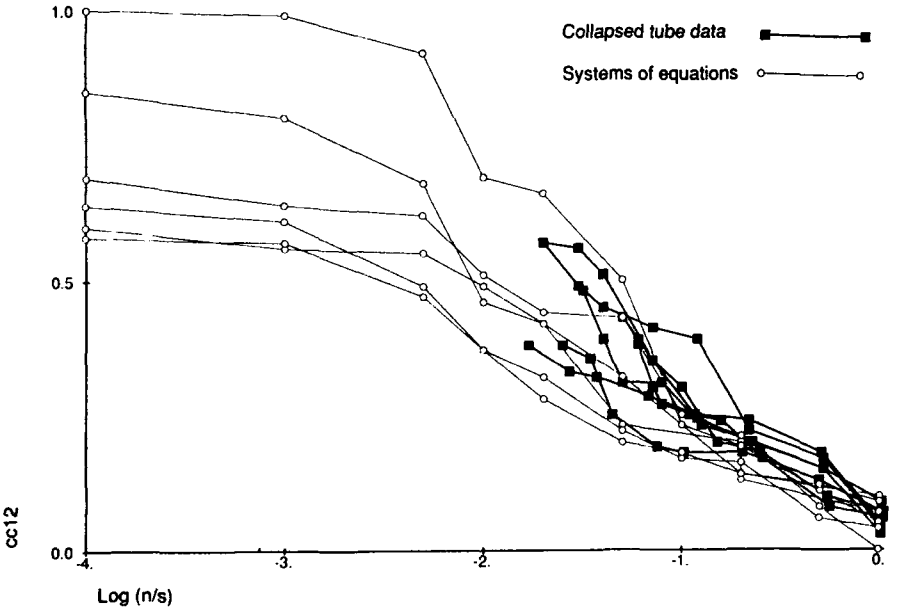

Fig. 8. As fig. 7, but with the addition of cc_{12} calculations for several different experimental time series from the collapsible-tube system.

free system. Increasing amounts of noise were then added once more to the SVD reconstruction, and new cc_{12}-values were computed, giving the curve delineated by open symbols. This curve was found to follow closely the cc_{12}-values given by the original attractor with added noise (filled symbols).

Figs. 9b–9d show the results of applying this procedure to three other equation systems. Similar behaviour is apparent, encouraging us to believe that the procedure is viable for use on experimental data where no noise-free value is available. The outcome of treating examples of the experimental data similarly is shown in figs. 9e–9f. The value of cross-correlation found with the aid of SVD at low noise-to-signal ratio can be regarded as an estimate of the asymptotic value to which the system would tend in the absence of instrumental noise and high-dimensional dynamical influences.

It may reasonably be asked how sensitive the value of cc_{12} is to variations in the parameters which are specified to the computation of λ_1 by the method of Wolf et al. [8] and which are also used in the derivation of cc_{12}. These include the embedding dimension, the delay used to produce the phase portraits, and internal parameters specifying limits on the size of $L(t)$, the distance between the fiducial and neighbour orbits, and the angular deviation allowed at the time of replacement. In addition the cc_{12}-calculation introduces further parameters such as θ_{12}. Fig. 10 shows for the Rössler attractor how cc_{12} varies with some of the parameters. Whereas we find that the behaviour of λ_1 as a function of each parameter is somewhat unpredictable, and not always apparently systematic, cc_{12} consistently reaches a maximum in the region which by other criteria represents a physically or numerically reasonable choice for that parameter. Calculations on other equation systems and on collapsible tube data show similar behaviour. This suggests that cc_{12} may have a further use, as a way of determining the optimal or most appropriate choice of the computational parameters involved in the calculation both of cc_{12} itself and of λ_1. Further work is under way to determine how reliable this idea is.

5. Discussion

The notion of examining the localised rate of trajectory divergence for an attractor in phase space is of course not new; Nese [10] reviews the several ways in which this idea has been quantified, and adds his own analyses of the local predictability of the Lorenz attractor. The idea is sufficiently appealing that it appears frequently, for recent instance in the work of Caputo et al. [11]. In general the fact that the divergence rate varies systematically around an attractor is well established. However, we are not aware of previous work in which the extent of the *coordination* of the localised divergence has been examined as a tool to distinguish via its local dynamics the behaviour of a chaotic attractor from stochastic additive noise or extrinsic high-dimensional forcing.

As originally envisaged, the notion of comparing the localised stretch around the attractor was to have involved the use of a cloud of nearby points rather than simply two. This was abandoned for pragmatic reasons. Whether for reasons of data storage or of stationarity in the experimental conditions, the recorded time series cannot be extended arbitrarily. Consequently there is a finite limit on the density of sampling of the phase space. Use of more than the minimum number of neighbouring orbits then necessitates extending the distance that defines "neighbouring"; this should always be minimised. Secondly, the computation is most economic when only two neighbours are tracked.

Even when it is accepted that two neighbours will be used, there remains the question of how exactly to compare the localised stretching calcu-

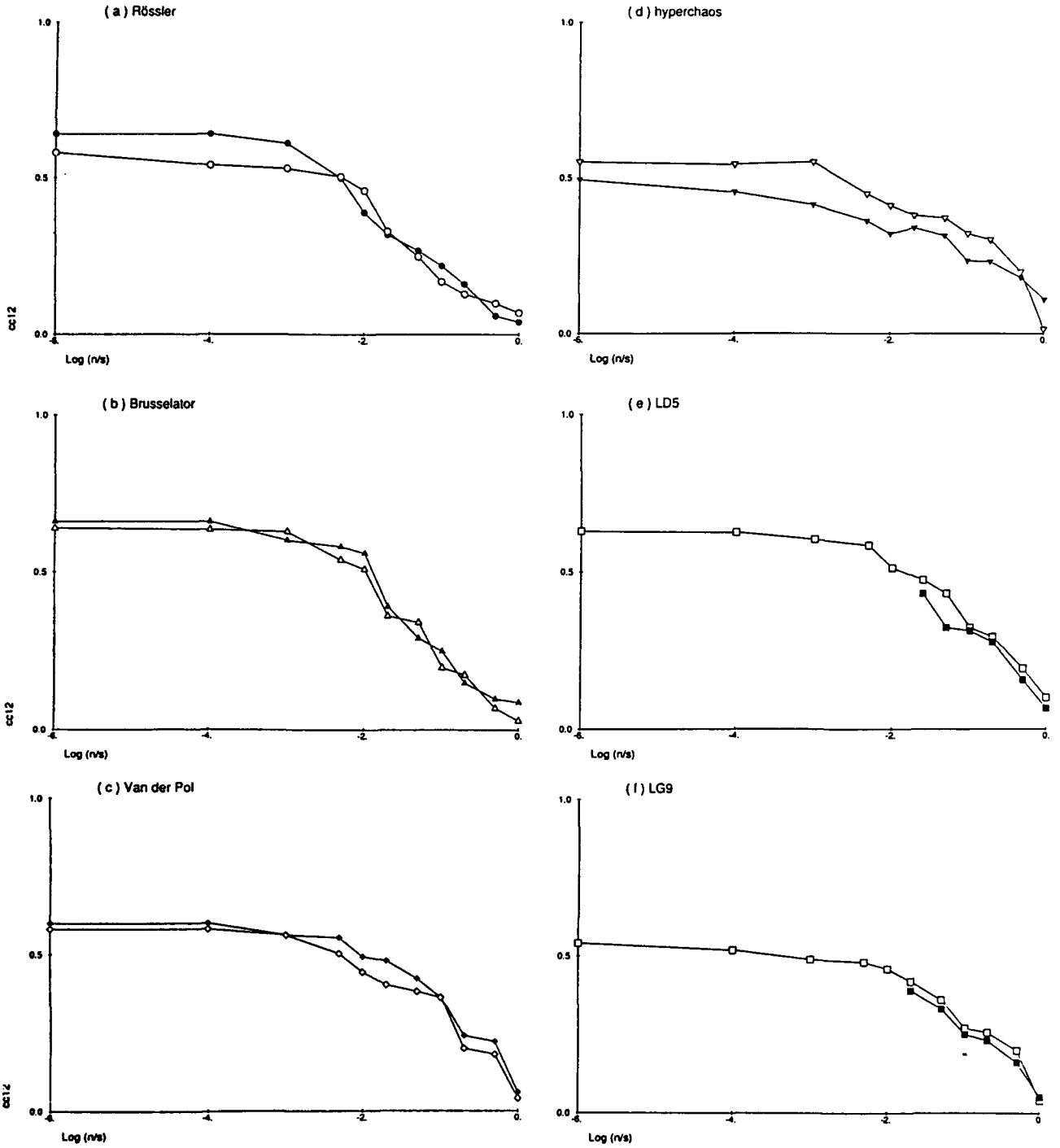

Fig. 9. (a) $\log(n/s)$ versus cc_{12} for (●) the Rössler system, time-delay reconstructed in R^3 with $\delta t = 0.7$ s. At $n/s = 0.02$, corresponding to n/s for the experimental data without additional noise (see fig. 8), singular value decomposition (window length $\tau_w = 0.49$ s) is used to effect a noise-free R^3 reconstruction, which is then the basis of further noise addition and cc_{12} calculations (○). (b) As fig. 9a, but for (▲, △) the forced Brusselator equations ($A = 0.4$, $B = 1.2$, $\alpha = 0.08$, $\omega = 0.91$) with $\delta t = 0.1$ s and $\tau_w = 0.7$ s. (c) As fig. 9a, but for (◆, ◇) Shaw's van der Pol system as in fig. 7 ($\delta t = 0.1$ s, $\tau_w = 0.7$ s). (d) As fig. 9a, but for (▼, ▽) Rössler's four-variable hyperchaotic system [9] and therefore reconstructed in R^4. $\delta t = 0.1$ s and $\tau_w = 2.5$ s. (e), (f) As figs. 9a–9c, but for (■, □) aperiodic collapsible-tube time series, and therefore lacking results for low n/s without SVD. For LD5, $\delta t = 0.0005$ s and $\tau_w = 0.0065$ s. For LG9, $\delta t = 0.002$ s and $\tau_w = 0.05$ s.

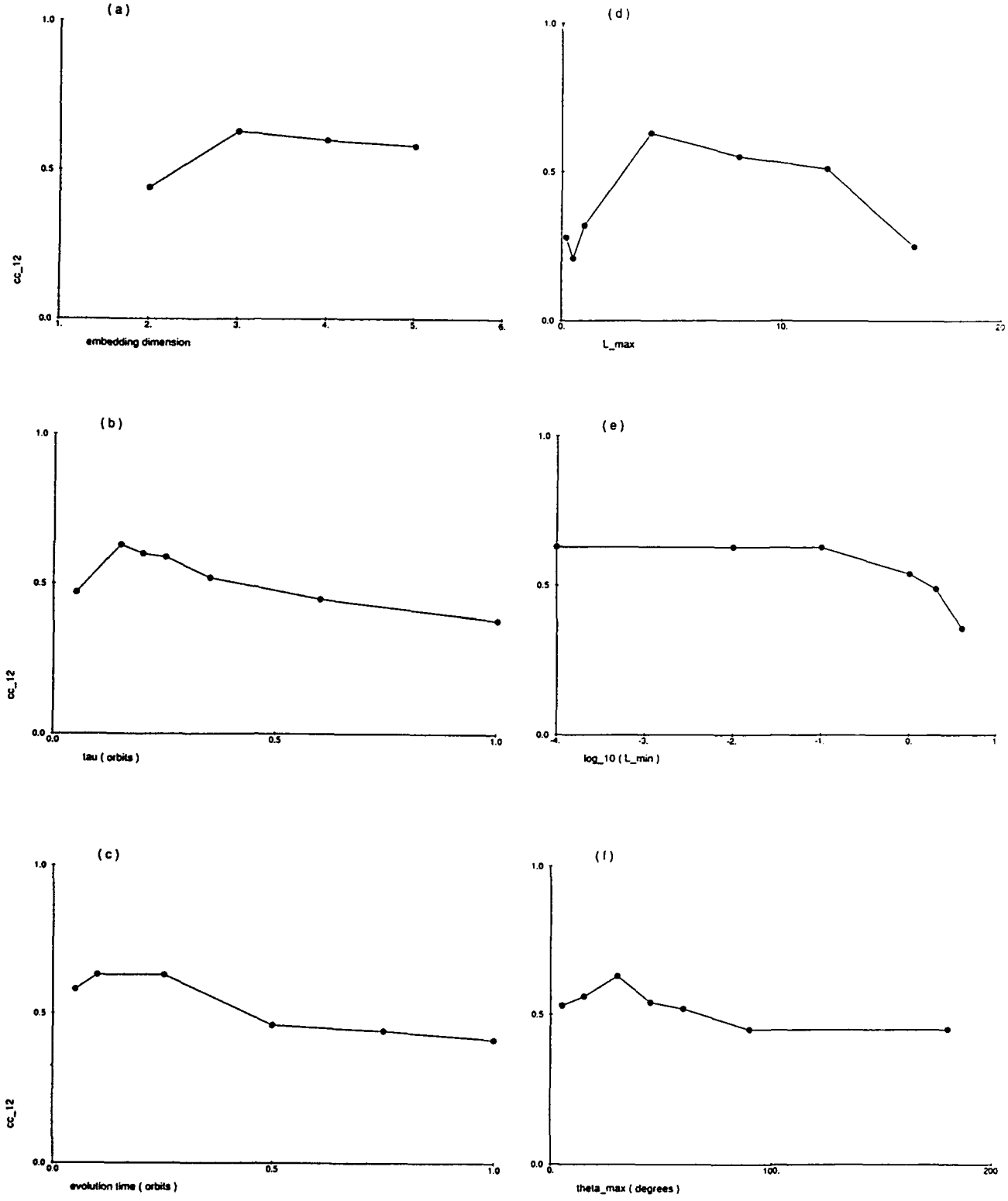

Fig. 10. The variation of cc_{12} for the Rössler attractor with (a) embedding dimension, (b) embedding delay time, (c) evolution time (N in the definition of $S(t)$), (d) maximum distance $L(t)$ before replacement, (e) minimum distance $L(t)$ after replacement, and (f) maximum angular deviation allowed at replacement for both θ_1 and θ_{12}.

lated between the fiducial orbit and each neighbour. The raw data are the stretch time series; we have opted to compare them by cross-correlation, using the correlation at zero lag as an index of the dynamical system. (In all cases we have investigated, the cross-correlation falls off rapidly at non-zero lag.) Alternatives include the cross-power spectrum, which would present information equivalent to the cross-correlation at all lags in terms of frequency. We have tried other possibilities. The normalised cross-corelation compares only the shape and phase of two waveforms; it does not reflect differences in amplitude. WIthout normalisation, the index becomes sensitive to the absolute rates of divergence that characterise the attractor; this property is already expressed in the Lyapunov exponent. We have also computed a modified function that retains the normalisation, yet decreases as the amplitude difference between the two input series increases. However, the results are not markedly affected by this modification.

The maximum value of the index cc_{12}, at low noise-to-signal ratio and with the computation parameters optimised as in fig. 10, appears on the basis of the testing so far to be a robust characteristic of a given attractor. However, given that this result is supported by studies of only a limited number of numerical systems, apart from the experimental data from the collapsible tube, it should be regarded as provisional pending further work.

Since the collapsible-tube data were shown to inhabit the region of the diagram of noise ratio vs. stretching cross-correlation where the cross-correlation value depends on the noise level, a procedure based on the use of singular value decomposition was devised whereby an estimated noise-free value could be estimated. This value was supported, first by the correspondence between the decline of the SVD-processed cross-correlation with added noise and that of the raw data, and secondly by the similarity between the correlation-decline curves of SVD-processed and raw data for other single-centre attractors. Nevertheless the putative noise-free value of cross-correlation found for the collapsible-tube data through the use of SVD must be treated with caution. Essentially the procedure devised is an extrapolation. The source of complicated behaviour in the collapsible-tube data is thought to be largely the high-dimensional dynamics, mimicking noise of unknown colouration which arises in conjunction with the signal itself, whereas the noise in the equation systems is additive and white. Furthermore, the equation systems are all very low-dimensional. These differences mean that it cannot be inferred with complete certainty that the behaviour of the cross-correlation of the SVD-processed collapsible-tube data with added noise is indicative of how a putative noise-less collapsible-tube recording would behave. Indeed the very concept of a noise-free collapsible-tube experiment is ill-defined if the source of noise-like variation is the high-dimensional dynamics, i.e., is inherent to the physical process whereby the aperiodic time series are generated. Nevertheless, to the extent that these uncertanties permit, the procedure devised yields a potential useful characterisation of the system.

In summary, an index has been devised which measures the extent to which the local divergence or stretch is organised on a phase-space regional basis. It can be used in at least two ways. One is as a measure of the extent to which the data are noise-corrupted, bearing in mind that for the aperiodic collapsible-tube data the greater part of the "noise" is seen as a reflection of high-dimensional attractor dynamics. In this role, the cross-correlation is used to factor interpretation of other measures such as λ_1. The second use is as an independent criterion of the attractor organisation, giving information beyond that contained in the global Lyapunov exponent and in previously devised measures of local stretch. A possible third role is as an objective quantitative criterion for the optimal choice of computational parameters involved in the calculation of the largest Lyapunov exponent.

Acknowledgements

C.D.B. gratefully acknowledges invaluable discussions with Professor Alan Wolf, Cooper Union School of Engineering, New York, NY.

References

[1] A.H. Shapiro, in: Proc. 6th Canadian Congress of Applied Mechanics (Vancouver, 1977) p. 883.
[2] R.D. Kamm and T.J. Pedley, ASME J. Biomech. Eng. 111 (1989) 177.
[3] C.D. Bertram and T.J. Pedley, J. Biomech. 15 (1982) 39.
[4] C.D. Bertram, C.J. Raymond and T.J. Pedley, J. Fluids Struct. 5 (1991) 391.
[5] O.E. Jensen, J. Fluid Mech. 220 (1990) 623.
[6] D.S. Broomhead and G.P. King, Physica D 20 (1986) 217.
[7] D.S. Broomhead, R. Jones and G.P. King, J. Phys. A 20 (1987) L563.
[8] A. Wolf, J.B. Swift, H.L. Swinney and J.A. Vastano, Physica D 16 (1985) 285.
[9] O.E. Rössler, Phys. Lett. A 71 (1979) 155.
[10] J.M. Nese, Physica D 35 (1989) 237.
[11] J.G. Caputo, G. Gouesbet, B. Maheu and S. Meunier-Guttin-Cluzel, IUTAM Symp. and NATO Advanced Research Workshop (University of Warwick, Coventry, UK, August 1991).

Physica D 58 (1992) 482–488
North-Holland

PHYSICA D

A technique for measuring fractal dimensions from time series on a real-time scale

A. Namajūnas and A. Tamaševičius
Semiconductor Physics Institute, Goštauto 11, Vilnius 2600, Lithuania

Received 7 October 1991
Revised manuscript received 31 January 1992
Accepted 31 January 1992

A dedicated electronic instrument for measuring fractal dimension of chaotic systems called "dimensiometer" is described. The pointwise correlation dimension can be obtained from experimental time series on a real-time scale. This technique employs a discrete sequence of the time intervals between the successive intersections of a single variable $x(t)$ and an arbitrary level c. The "dimensiometer" is tested by means of a simple electronic chaos oscillator. The experimental results are compared with the numerical calculations carried out for the corresponding dynamical model.

1. Introduction

Many nonlinear physical systems exhibit chaotic temporal behaviour. In recent years the qualitative description of this phenomenon based on the visual inspection of the bifurcation diagrams, Poincaré sections, power spectra, etc., has evolved to the quantitative characterization employing dimensions, entropies and Lyapunov exponents [1]. In particular dimensions can be used to distinguish between random noise and deterministic temporal chaos. In addition, this quantitative measure makes it possible to follow the evolution of a system from one chaotic state to another.

Various digital methods have been proposed for determining fractal [2] and integer [3] dimensions of chaotic systems from time series data sets.

Several attempts have been made to develop analog techniques for determining dimensions without the need of digital computing equipment. An optical technique for measuring fractal dimensions of planar Poincaré maps has been described [4]. Also an electronic technique for measuring the phase space dimension from chaotic time series has been suggested [5].

The instrument described in our previous paper [5] is restricted to the minimum phase space dimension or the number of degrees of freedom, which is an integer. Here we report on a modified electronic tool ("dimensiometer") for estimating the fractal pointwise correlation dimension.

2. Procedure

Usually the method of delays [6, 7] is used to reconstruct the attractor in n-dimensional phase space from a single observable $x(t)$:

$$\boldsymbol{X}^n(t) = \{x(t), x(t+T), \ldots, x(t+(n-1)T)\}\,. \tag{2.1}$$

This continuous flow is digitized in discrete time steps $\mathrm{d}t$ (as a rule $\mathrm{d}t = T$). So one obtains a set

0167-2789/92/$05.00 © 1992 – Elsevier Science Publishers B.V. All rights reserved

of n-dimensional vectors $\{X_i^n\}$, $i = 1, 2, \ldots, N$, where

$$X_i^n = \{x(iT), x((i+1)T), \ldots, x((i+n-1)T)\}, \quad (2.2)$$

convenient for digital processing.

When designing the analog electronic instrument we have modified the procedure in the following way. Let us set the condition

$$x(t) = c, \quad (2.3)$$

where c is an arbitrary chosen fixed level, e.g. the mean $\langle x \rangle$ is a suitable value for c. The given condition can be fulfilled at certain time moments, say $t_1, t_2, \ldots, t_i, \ldots$. Denoting the differences $t_{i+1} - t_i$ as T_i we obtain a sequence of the time intervals between the successive intersections of the variable $x(t)$ and the constant level c, i.e. the "return" times

$$\{T_1, T_2, \ldots, T_i, \ldots\}. \quad (2.4)$$

From this sequence we construct m-dimensional vectors $\{T_i^m\}$, $i = 1, 2, \ldots$, where

$$T_i^m = \{T_i, T_{i+1}, \ldots, T_{i+m-1}\}. \quad (2.5)$$

Apparently, the dimension of an attractor obtained from $\{T_i^m\}$ (the "T" approach) is one less than the dimension obtained from the actual set $\{X_i^n\}$ (the "X" approach):

$$d_T = d_X - 1. \quad (2.6)$$

This is due to the employed condition (2.3), similarly to the case of the Poincaré sections (see also the appendix).

3. The instrument

A sketch of the "dimensiometer" is shown in fig. 1. The comparator (see also fig. 2) produces

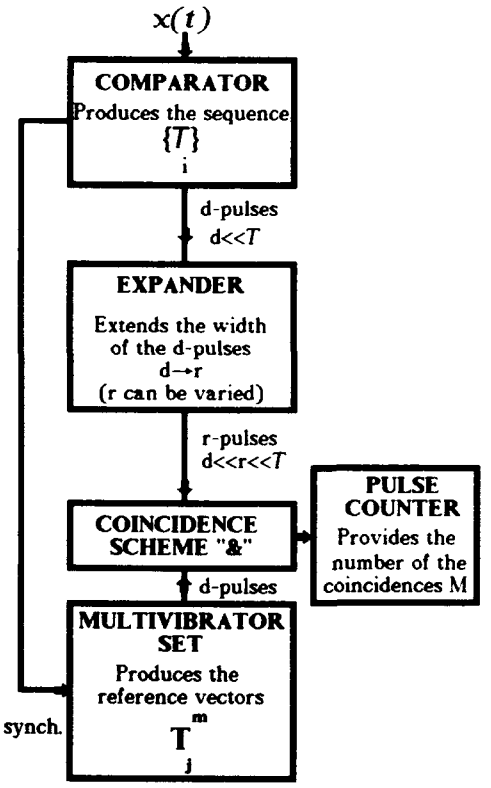

Fig. 1. Block diagram of the instrument for the correlation dimension measurements.

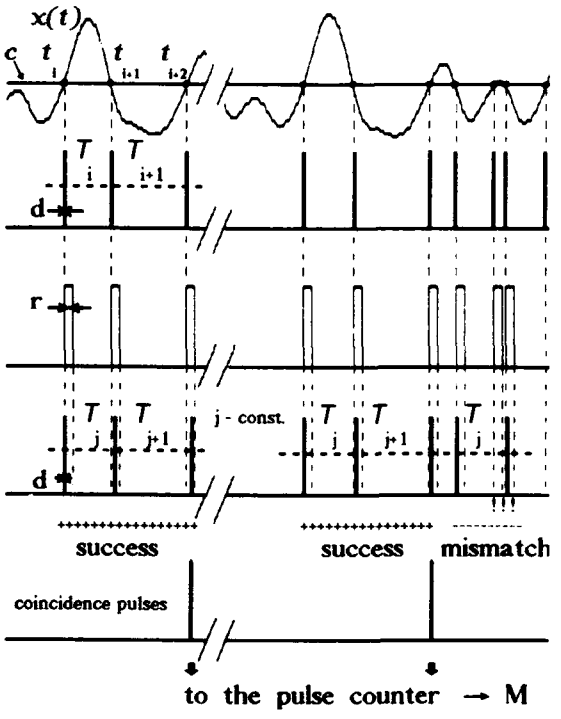

Fig. 2. Time diagram of the signals in the "dimensiometer".

a train of short d-pulses corresponding to the time instants when the variable $x(t)$ "crosses" the given level c. Thus the continuous chaotic signal $x(t)$ is converted in to a discrete sequence of pulses separated from each other by chaotically varying intervals $\ldots, T_i, T_{i+1}, \ldots$ according to (2.4). These short d-pulses are extended in the expander. The width of the extended pulses (r-pulses) can be regulated electronically in the instrument. The width r plays the role of the size of the hyperspheres similar to the scaling parameter in the digital algorithm [2].

The multivibrator set also produces a sequence of d-pulses but with externally adjusted time intervals $T_j, T_{j+1}, \ldots, T_{j+m-1}$ (it must be noted, that only the "first" d-pulse in the multivibrator set is synchronized with the one in the comparator). These two sets of pulses, namely the r-pulses and the d-pulses (produced in the multivibrator set) are compared with each other in the coincidence scheme "&". So, if the respective sets of the intervals $\{\boldsymbol{T}_i^m\}$ and $\{\boldsymbol{T}_j^m\}$ (fig. 2 illustrates the case of $m = 2$) coincide in time within an accuracy r the scheme "&" generates a single coincidence pulse (the bottom trace in fig. 2). The latter pulses are counted in a pulse counter or a frequency meter.

The "dimensiometer" constructs m-dimensional vectors $\boldsymbol{T}_i^m$ (2.5) along with m-dimensional vectors $(\boldsymbol{T}_i^m + \boldsymbol{R}^m)$, where

$$\boldsymbol{R}^m = \{r_1, r_2, \ldots, r_m\}\,, \tag{3.1}$$

(for simplicity $r_1 = \cdots = r_m = r$). In addition it produces an artificial reference vector

$$\boldsymbol{T}_j^m = \{T_j, T_{j+1}, \ldots, T_{j+m-1}\}\,, \quad j = \text{const.} \tag{3.2}$$

The coincidence pulses do appear if

$$T_{i+k-1} < T_{j+k-1} < (T_{i+k-1} + r)\,, \quad k = 1, 2, \ldots, m\,, \tag{3.3a}$$

or

$$(T_{j+k-1} - r) < T_{i+k-1} < T_{j+k-1}\,. \tag{3.3b}$$

The total number of the points given by (2.5) appearing in the neighbourhood of the reference point (3.2) can be written as

$$M_j^m(r) = \sum_i \prod_k^m \{H(r - (T_{j+k-1} - T_{i+k-1})) \times H(T_{j+k-1} - T_{i+k-1})\}\,, \tag{3.4}$$

where $H(x)$ is the Heaviside function. This number behaves roughly as a power law

$$M_j^m(r) \sim r^{d^*(m)}\,, \tag{3.5}$$

where $d^*(m)$ saturates at large embedding dimensions m to a certain value d^* called the pointwise correlation dimension (the sum in (3.4) is taken over i, but not j).

The above procedure implies a local analysis of an attractor ($j = \text{const}$, $r \ll T$). Obviously, other parts of the attractor, if necessary, can be explored in the same way setting appropriate reference vectors $\boldsymbol{T}_i^m$. Moreover, in contrast to digital methods employing time series data sets the "dimensiometer" can easily choose the vectors $\boldsymbol{T}_j^m$ in the neighbourhood of the most often visited parts of the attractor. This is achieved by adjusting $\boldsymbol{T}_j^m$ in order to select the maximum of M per time unit (such points have the maximum statistical weight in the averaging procedure).

4. Chaotic oscillator

The "dimensiometer" was tested by means of the electronic chaos oscillator [8] employed in an earlier work [5]. This nonlinear oscillator (fig. 3) is similar to the Van der Pol oscillator but with an additional nonlinear chain consisting of the inductor L_1 and the semiconductor diode D. Fig.

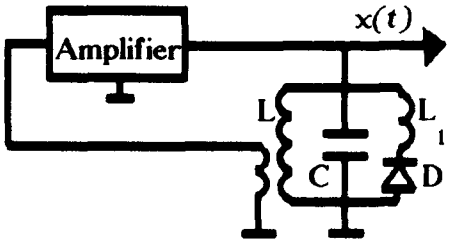

Fig. 3. Circuit diagram of the chaos oscillator used to test the "dimensiometer".

4 illustrates the chaotic behaviour of the oscillator. The frequency range, in general, depends on the values of L, C and L_1 (in our experiments the central frequency of the broadband continuous spectrum was near 10 kHz).

A previous analysis [5] indicated this oscillator to have *three* degrees of freedom, i.e. the minimum phase space dimension $k_{\min} = 3$, sufficient to specify the chaotic state. So the dynamics of this chaos oscillator can be described by the set of *three* ordinary differential equations

$$\mathrm{d}x/\mathrm{d}\theta = ax + y - z\,, \quad \mathrm{d}y/\mathrm{d}\theta = -x\,,$$
$$\mathrm{d}z/\mathrm{d}\theta = bx - bF(z)\,, \tag{4.1}$$

where $F(z) = \ln(kz + 1)$ if $z \geq 0$ and $F(z) = kz$ if $z < 0$ is a function representing the nonlinear current voltage characteristic of the semiconductor diode. The dimensionless variables and parameters in (4.1) are given by

$$x = U_C/U_0\,, \quad y = \rho I/U_0\,, \quad z = \rho I_1/U_0\,,$$
$$\theta = t/\sqrt{LC}\,, \tag{4.2}$$

where U_C is the voltage across the capacitor C (the output signal), I and I_1 the current through the inductor L and L_1 respectively,

$$a = \rho/R\,, \quad b = L/L_1\,, \quad k = R_\mathrm{d}/\rho\,,$$
$$U_0 = k_\mathrm{B}T/e\,, \quad \rho = \sqrt{L/C}\,, \quad R_\mathrm{d} = U_0/I_\mathrm{s}\,, \tag{4.3}$$

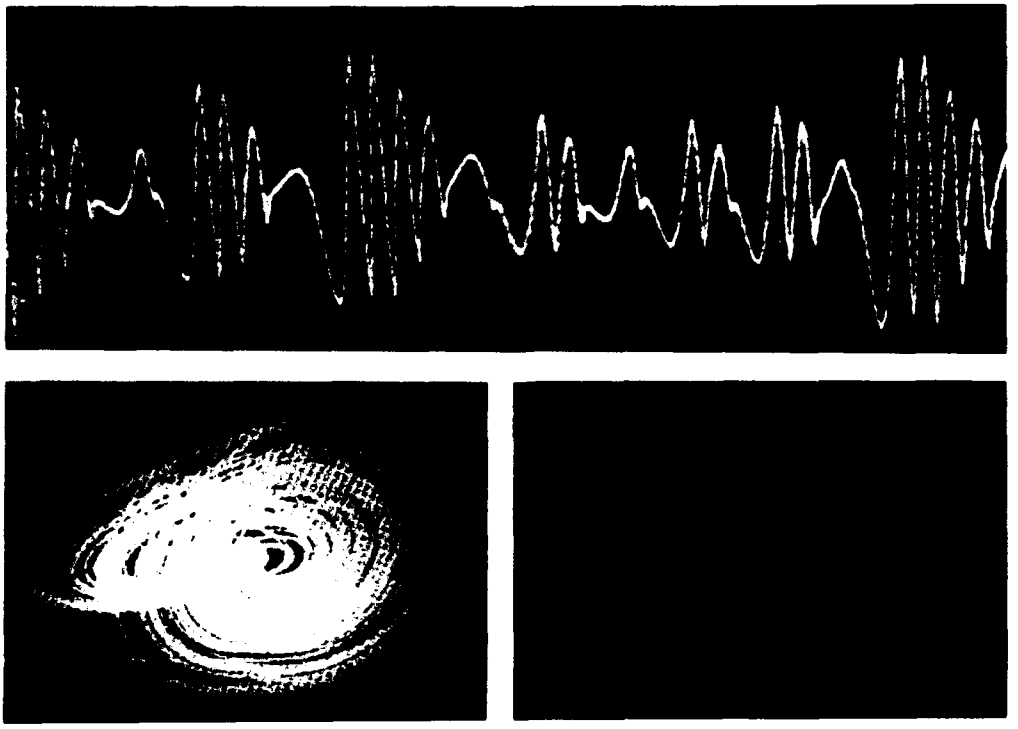

Fig. 4. Illustration of the output signal produced by the chaos oscillator; (top) snapshot of time series, (bottom left) phase portrait $\mathrm{d}x/\mathrm{d}t$ versus x (bottom right) Poincaré section $\mathrm{d}x/\mathrm{d}t$ versus $\int x\,\mathrm{d}t$ at $x = 0$.

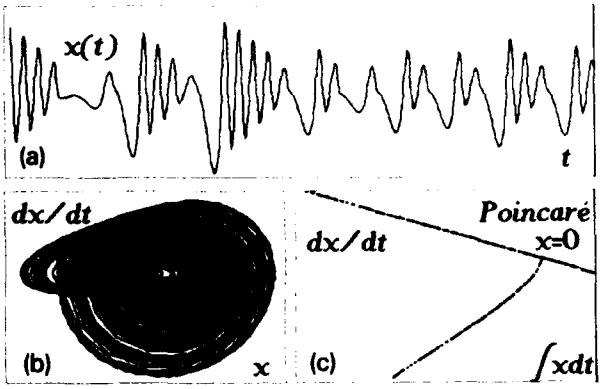

Fig. 5. Numerical results for model (4.1) with $a = 0.91$, $b = 10$, $k = 500$; (top) snapshot of time series, (bottom left) phase portrait, (bottom right) Poincaré section.

where R is the modulus of the negative resistance contributed to the LC-contour by the amplifier and the positive feedback, k_B, T and e denote the Boltzmann constant, the temperature and the electron charge, I_s is the saturation current of the diode.

The results of the numerical integration (fig. 5) exhibit a good agreement of the model (4.1) with the experimental results (fig. 4).

5. Correlation dimension

5.1. Experimental results

The results obtained by means of the "dimensiometer" are presented in fig. 6. The coincidence rate was high enough, e.g. ~3 kHz for $m = 2$, $r = r_0$, so the pulse counter operated in the frequency meter mode. Thus the values of M in fig. 6a were taken per 1 s. The scaling law of $M(r)$ seems to be in satisfactory agreement with (3.5). In fig. 6b along with the main result (2) some other measurements, namely random noise analysis (1) and periodic oscillations treatment (3), are presented for comparison. The low value of the correlation dimension ($d^* = 0.82$, i.e. $d^* < 1$) obtained in the experiment conform with the quasi-linear structure of the Poincaré section

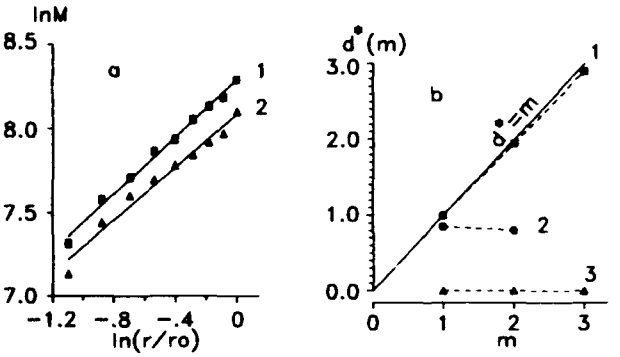

Fig. 6. (a) Log–log plot of the pointwise correlation integral M versus r as measured from chaotic oscillations for different embedding dimensions (1) $m = 1$, (2) $m = 2$. (b) Correlation exponent $d^*(m)$ as a function of m for different types of signals (1) random noise (no saturation), (2) deterministic chaos (the saturated value $d^* = 0.82$), (3) periodic oscillations (the saturated value $d^* = 0$). $c = 0$.

(fig. 4). This is the case of the so-called "small" strange attractor.

5.2. Numerical results

The pointwise correlation dimension for model (4.1) was calculated from the variable $x(t)$ employing the T approach as in the case of the "dimensiometer". An algorithm similar to (3.4) was used:

$$M_j^m(r) = \sum_i^N \prod_k^m H(r - |T_{j+k-1} - T_{i+k-1}|) \qquad (5.1)$$

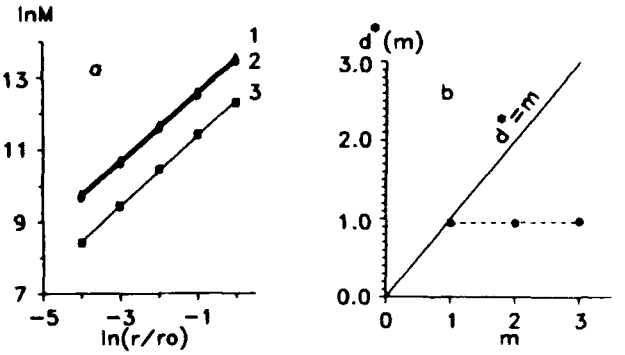

Fig. 7. (a) Log–log plot of the pointwise correlation integral M versus r obtained from the single observable x for model (4.1) with different embedding dimensions (1) $m = 1$, (2) 2, (3) 3. (b) Corelation exponent $d^*(m)$ as a function of m (the saturated value $d^* = 0.95$). $c = 0$.

($N = 14000$). The coordinates of the three-dimensional reference vector T_j^3 were the following, $T_j = 1.53$, $T_{j+i} = 0.94$, $T_{j+2} = 2.70$.

The results are presented in figs. 7a, 7b.

6. Conclusion

An analog technique has been achieved for the quantitative analysis of chaotic time series from nonlinear systems. This electronic instrument ("dimensiometer") enables us to estimate the pointwise correlation dimension from a single observable. The real time operating mode is a valuable feature of its performance.

Appendix

The purpose of this appendix is to illustrate relation (2.6), i.e. to compare the T and the X approaches. Numerical calculations have been performed for model (4.1) with the control parameters given in fig. 5. The global correlation dimensions have been computed according to ref. [2],

$$C^n(r) = \sum_{j\neq i}^{N}\sum^{N} \prod_{k}^{n} H(r - |T_{j+k-1} - T_{i+k-1}|) \sim r^{d(n)}, \tag{A1}$$

$$C^n(r) = \sum_{j\neq i}^{N}\sum^{N} \prod_{k}^{n} H(r - |X_{j+k-1} - X_{i+k-1}|) \sim r^{d(n)}. \tag{A2}$$

The results are shown in figs. 8a, 8b and figs. 9a, 9b, respectively. This is an evidence for $d_T = d_X - 1$.

The small value of the dimension $d = 1.92$, i.e. $1 < d < 2$, may seem to be puzzling in the case of the three-dimensional chaotic flow. However, it must be emphasized that the value of the dimension is obtained as a result of the averaging procedure all over the attractor (double sum in (A1) and (A2)). If an attractor is of sufficiently simple topology, such as the Rossler attractor, it is quite acceptable that there is a great number of points j where the local values $d^* < 2$, except for a small fraction of points j in the sites of the intersection between the flat sheets where the local values $2 < d^* < 3$. Consequently, it may appear that the average value $1 < d < 2$, e.g. $d = 1.548$, for the Rossler attractor [9].

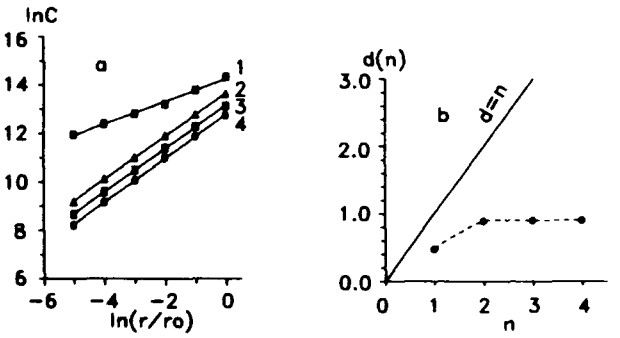

Fig. 8. (a) Log–log plot of the correlation integral C (global) versus r for model (4.1) obtained in the T approach with different embedding dimensions (1) $n = 1$, (2) 2, (3) 3, (4) 4. (b) Corelation exponent $d(n)$ as a function of n (the saturated value $d_T = 0.92$). $c = 0$.

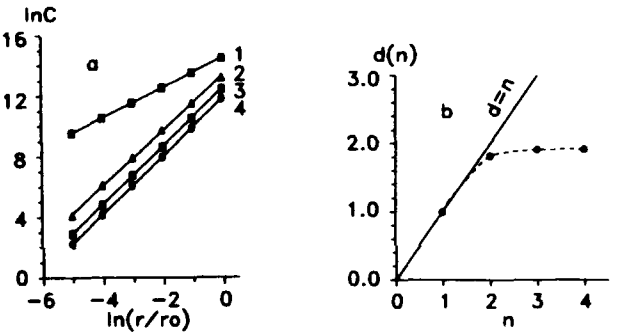

Fig. 9. The same as in fig. 8 but calculated in the usual X approach (the saturated value of the correlation exponent in (b) $d_X = 1.92$).

References

[1] G. Mayer-Kress, ed., Dimensions and Entropies in Chaotic Systems (Springer, Berlin, 1986).

[2] P. Grassberger and I. Procaccia, Phys. Rev. Lett. 50 (1983) 346.

[3] D.S. Broomhead, R. Jones and G.P. King, J. Phys. A 20 (1987) L563.
[4] C.-K. Lee and F.C. Moon, Phys. Lett. A 114 (1986) 222.
[5] A. Namajūnas, J. Požela and A. Tamaševičius, Phys. Lett. A 131 (1988) 85.
[6] N.H. Packard, J.P. Crutchfield, J.D. Farmer and R.S. Shaw, Phys. Rev. Lett. 45 (1980) 712.
[7] F. Takens, in: Lecture Notes in Mathematics, Vol. 989, eds. D.A. Rand and L.-S. Young (Springer, Berlin, 1981) p. 366.
[8] R.A. Pikšrys, K.A. Pyragas and A. Tamaševičius, Radiotekhnika 9 (1986) 43 [English translation in Telecommun. Radio Eng.].
[9] A.K. Agarwal, K. Banerjee and J.K. Bhattacharjee, Phys. Lett. A 119 (1986) 280.

Physica D 58 (1992) 489–496
North-Holland

PHYSICA D

Estimation of the persistence of strain from experimental recordings from cardiac tissue

H. Zhang, A.V. Holden
Department of Physiology and Centre for Nonlinear Studies, The University, Leeds LS2 9JT, UK

M. Lab and M. Moutoussis
Department of Physiology, Charing Cross and Westminster Medical School, London W6 8RF, UK

Received 16 September 1991
Revised version received 17 February 1992
Accepted 24 February 1992

The "persistence of strain" σ^2 has been ported from fluid mechanics into nonlinear dynamics, as a measure of the geometry of attracting sets that reflects both stretching (sensitivity to initial conditions) and folding. We outline a method for estimating σ^2 from experimental time series and apply it to electrical and mechanical signals recorded from the surface of the heart during experimentally induced ventricular fibrillation.

1. Introduction

Chaotic dynamics is characterised by a sensitivity to initial conditions, whereby trajectories starting at neighbouring points in phase space diverge exponentially fast. This divergence may be quantified by the Lyapunov exponent spectrum of the dynamical system, where for an n-dimensional phase space an infinitesimal n-sphere of initial conditions, with the centre of the n-sphere on the attractor, will evolve into an n-ellipsoid. The average growth rate of the norm of the ith principal axis $\boldsymbol{a}_i(t)$ of this n-ellipsoid gives the ith Lyapunov exponent

$$\lambda_i = \lim_{t\to\infty} \frac{1}{t} \log_2\left(\frac{|\boldsymbol{a}_i(t)|}{|\boldsymbol{a}_i(0)|}\right) \text{ bits/s},$$

and the maximal Lyapunov exponent and the entire spectrum of Lyapunov exponents, may be estimated from an experimental time series [1–3].

If one visualises phase space as a physical space, and trajectories as flows, then the Lyapunov exponents give a measure of how volume in phase space expands or contracts during the flow: a positive Lyapunov exponent is a measure of how the dynamics stretches state space in the direction of the eigenvector associated with the Lyapunov exponent. For a trajectory to be confined to a compact attractor this stretching in a given direction must be counteracted by a folding back; chaotic motion is characterised by stretching and folding. The "persistence of strain", originally a measure of the balance between shear dominated and vorticity dominated flow in a fluid mechanical system, was introduced into nonlinear dynamics by Dresselhaus and Tabor [4] as a measure of both stretching and folding.

The reconstruction of an attractor from experimental time series provides a means of visualising the geometry underlying the behaviour, and this geometry may be quantified by mea-

0167-2789/92/$05.00 © 1992 – Elsevier Science Publishers B.V. All rights reserved

sures such as the fractal dimensions, Lyapunov exponents and entropies. The persistence of strain is a measure that can be defined for a system of nonlinear ODEs, and that provides a means for characterising the attractor.

An autonomous n-dimensional system of nonlinear ODEs

$$\mathrm{d}x/\mathrm{d}t = F(x, t), \quad x(0) = x_0, \tag{1}$$

can be linearized near a given point $x(0)$, $x = x(0) + \delta x(0)$, to yield a linear, but nonautonomous (depending on $x(0)$) system of equation

$$\mathrm{d}\delta x(t)/\mathrm{d}t = \mathbf{A}(x(0))\,\delta x(0), \tag{2}$$

where $\mathbf{A}(x(0))$ is the Jacobian matrix

$$A_{i,j}(x(0)) = \partial_j F_i|_{x(0)} \quad \text{for } i, j = 1, 2, 3, \ldots, n. \tag{3}$$

The solution of (2) is

$$\delta x(t) = \int \mathbf{A}(x(0))\,\delta x(0)\,\mathrm{d}t. \tag{4}$$

In the tangent space, we can think that $\delta x(t)$ is the map of $\delta x(0)$ by the tangent map matrix $\mathbf{T}^t(x(0))$. That is

$$\delta x(t) = \mathbf{T}^t(x(0))\,\delta x(0). \tag{5}$$

If we divide the time t into K subintervals of Δt, according to the chain rule [5, 6]

$$\mathbf{T}^t(x(0)) = \mathbf{T}^{K\,\Delta t}(x(0) = \mathbf{T}^{\Delta t}(x(k-1)) \cdots \mathbf{T}^{\Delta t}(x(1)) \cdot \mathbf{T}^{\Delta t}(x(0)). \tag{6}$$

When $\Delta t \to 0$, $\mathbf{T}^{\Delta t}(x(i)) = \mathbf{A}(x(i))\,\Delta t$. If the eigenvalues of the matrix $\mathbf{A}$ are complex conjugate pairs $(\alpha_i + i\beta_i)$ the persistence of strain σ^2 is defined as the second trace of $\mathbf{A}$ [4]:

$$\sigma^2 = \tfrac{1}{2}\,\mathrm{Tr}\,\mathbf{A}^2 = \tfrac{1}{2}\sum_i^n (\alpha_i^2 - \beta_i^2). \tag{7}$$

$\sigma^2 > 0$ implies stretching, and $\sigma^2 < 0$ implies folding. Since these processes occur at different parts of the attractor, averaging σ^2 over the whole trajectory will allow the two processes to cancel each other. Stretching and folding can be separated by

$$\bar{\sigma}(I) = \frac{1}{\mathrm{vol}(I)} \int \mathrm{d}x\,[\sigma^2(x, t)]^{1/2} = \bar{\sigma}_{\mathrm{Re}}(I) + \mathrm{i}\bar{\sigma}_{\mathrm{Im}}(\mathrm{I}), \tag{8}$$

where I is an invariant set such as an attractor. The ratio between stretching and folding can be used as a characteristic to quantify a strange attractor [6, 7].

$$\gamma = \bar{\sigma}_{\mathrm{Rm}}/\bar{\sigma}_{\mathrm{Im}}. \tag{9}$$

2. Algorithm

We bear in mind that the persistence of strain σ^2 is calculated from the eigenvalues of the Jacobian matrix $\mathbf{A}$. For a physical system, if its dynamical equations are known, it is quite easy to calculate the persistence of strain from its dynamical equations. However, in practice we are often confronted with some physical systems whose dynamical equations are unclear. What we can get from such physical systems is only a sample of an experimental time series of a single-state variable obtained at regular and discrete time intervals.

We start with a time series, $x(t_0)$, $x(t_1), \ldots, x(t_n)$, with $x(t_i) \in \mathbb{R}$, and $t_1 = t_0 + i\tau$, $i = 0, 1, 2, \ldots, n$, where τ is the time interval. We assume the time series is stationary and is produced by a nonlinear dynamical system with a low-dimensional attractor. A time series is manifestly one-dimensional and presents a projection π: $\mathbb{R}^M \to \mathbb{R}$ from the full state vector $x(t) \in \mathbb{R}^M$.

The time delay method provides us with a procedure [8] to reconstruct the state space by embedding the time series into a higher-dimensional space. A vector, $x(t) \in \mathbb{R}^m$, is created

$$x(t) = (x(t), x(t-\tau), \ldots, x(t-(m-1)\tau)\,. \quad (10)$$

Here $x(t)$ can be thought as the mapping π: $\mathbb{R}^M \to \mathbb{R}^m$ from the full state space $x(t) \in \mathbb{R}^M$ to the reconstructed state space $x(t) \in \mathbb{R}^m$. Takens [9] and Mañé [10] have proved that when $m \geq 2D+1$, where D is the Hausdorff dimension of the attractor, the embedding procedure provides a topologically equivalent reconstruction of the attractor from an 1-D time series.

Now let us examine the evolution of the vectors on the reconstructed attractor. Mathematically we can think that the evolution of the vector on the attractor is a flow produced by the tangent map $\mathbf{T}^{\Delta t}(x_i)$ mapping the state x_i to x_{i+1}. The matrix of the linearised flow $\mathbf{T}^{\Delta t}(x_i)$ can be approximated from a single trajectory by using the structure of the reconstructed attractor. This is done by tracing the time evolution of the difference vectors between x_i and an other point x_j of the same trajectory on the attractor, which are the ε-distance neighbours of x_i. Centred at point x_i, N ε-distance neighbours consist of a set of difference vectors $x_i - x_j$, where $j = 1, 2, \ldots, N$. With the evolution time Δt, x_i maps into x_i', while x_j maps into x_j', where $j = 1, 2, \ldots, N$, and the initial N difference vectors in the ball $B(\varepsilon)$,

$$B(\varepsilon) = \{x_i - x_j \,|\, \|x_i - x_j\| \leq \varepsilon\}\,, \quad (11)$$

evolve into N difference vectors in the ellipsoid ball $B(\varepsilon')$,

$$B(\varepsilon') = \{\mathbf{T}^{\Delta t}(x_i) - \mathbf{T}^{\Delta t}(x_j)\}\,. \quad (12)$$

If we denote the N difference vectors in the ball $B(\varepsilon)$ and $B(\varepsilon')$ by $\{y^i \,|\, i = 1, 2, \ldots, N\}$, and $\{z^i \,|\, i = 1, 2, \ldots, N\}$ individually, an $N \times N$ map matrix $\mathbf{T}_j$ is determined, such that the average of the squared error norm of all the maps $\{y^i \to z^i\}$ takes a minimum

$$\min_{\mathbf{T}_j} S = \min \frac{1}{N} \sum_{i=1}^{N} \|z^i - y^i\|^2\,. \quad (13)$$

This equation can be solved for the matrix $\mathbf{T}_j$

$$\mathbf{T}_j = \boldsymbol{C}\boldsymbol{V}^{-1} \quad \text{with} \quad ((\mathbf{V}))_{kl} = \frac{1}{N} \sum_{i=1}^{N} y_k^i y_l^i\,,$$

$$((\mathbf{C}))_{kl} = \frac{1}{N} \sum_{i=1}^{N} z_k^i y_l^i\,. \quad (14)$$

If the distance ε and the time interval are small enough, the matrix $\mathbf{T}_j$ can be used as a good approximation of the tangent map $\mathbf{T}^{\Delta t}(x_i)$.

We calculate the persistence of strain by the following procedures:

(i) Reconstruct the dynamical attractor from experimental time series in the phase space by the time delay method.

(ii) Divide the evolution of the trajectory into a series of small time intervals, and obtain the tangent map in this time interval by a least-squares fit.

(iii) Calculate the persistence of the strain from the tangent map.

(iv) Compute the average of σ^2 obtained from each time interval, and then calculate $\bar{\sigma}_{\mathrm{Re}}$ and $\bar{\sigma}_{\mathrm{Im}}$.

2.1. Calibration

The persistence of the strain, σ^2, estimated from an experimental time series contains some information about the system. For a chaotic motion, σ^2 oscillates between a positive and negative magnitude. However, $\bar{\sigma}^2$ provides more valuable information than σ^2. The σ^2 series estimated from a pseudo time series obtained by numerical solution of a system's equations differs from what we calculate from system's equations directly. Figure 1 shows the σ^2 series for the Lorenz equations with parameters $R = 45.92$, $\sigma = 16$, $b = 4$ calculated from equations and from a pseudo time series. The difference between them are drastic.

The reason that the σ^2 series calculated from a pseudo time series differs from calculated results

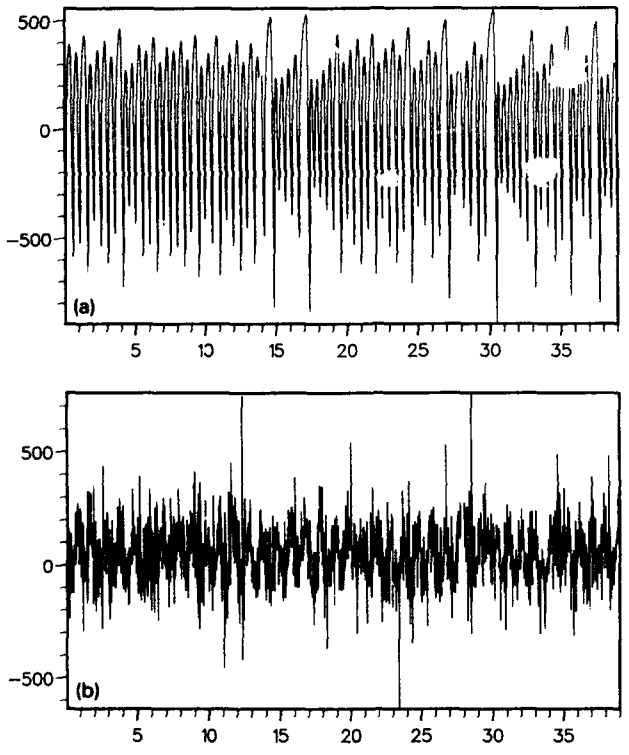

Fig. 1. The series of persistence of strain for Lorenz equations with parameters $R = 45.92$, $\sigma = 4$, $b = 10$. (a) The series of persistence of strain calculated from equation. (b) The series of persistence of strain calculated from a pseudo time series.

is that in the computation process we choose the N ε-distance neighbours with a randomly chosen probability. The error is produced from the N neighbours being nonuniformly chosen in N different directions. If we take the advantage of the SVD [11] method to extract an orthogonal basis at the reference point of the trajectory, and then project the ball composed of by the N difference vectors to the basis, by tracing the evolution of the projected ball, the procedure would be improved. Meanwhile, the parameters such as embedding dimension and sampling time interval also influence the estimated result.

However, after averaging over the whole trajectory (50 000 points), from a pseudo time series, we get $\gamma = 1.75$, $\bar{\sigma}_{\mathrm{Re}} = 10.35$, $\bar{\sigma}_{\mathrm{Im}} = 5.91$, all of which are quite similar to the calculated results from equations, of which $\gamma = 1.68$, $\bar{\sigma}_{\mathrm{Re}} = 10.20$, $\bar{\sigma}_{Im} = 6.05$.

3. Case study: ventricular fibrillation

In ventricular fibrillation the ventricles no longer contract synchronously, but different parts of the ventricular muscle contract at different times, which redistributes blood within the ventricular chamber. The effect of ventricular fibrillation is that the pump function of the heart fails and systemic blood flow, including that through the coronary arteries of the heart itself, stops. Consequently the metabolic status of the ventricles deteriorates progressively and so do the electromechanical signals. A continuous sample of signals which are stable for the duration required for our analysis is not possible. One way of overcoming this difficulty is to induce fibrillation while coronary artery flow is maintained. Retrograde perfusion of the coronary arteries in an isolated heart was chosen for maintaining a stable biological microenvironment while collecting data during ventricular fibrillation.

New Zealand White rabbits, weighing about 2.5 kg were injected with a mixture of pentobarbitone sodium (200 mg/ml Expiral) heparin (Monoparin 1000 units/ml) into a marginal ear vein until no corneal reflex remained. The heart was exposed, removed, and immediately plunged into a mixture of ice-cold Krebs solution containing heparin and massaged to remove any excess blood from the coronary circulation, thereby reducing clot formation. The heart was then attached to the Langendorff apparatus via the aorta for retrograde perfusion of the coronary arteries. The Krebs solution was first passed through a filter to remove invisible particulate matter and heated by a water jacket to 37°C.

The Krebs solution was bubbled with 95% O_2/5% CO_2 mixture. The heart was paced, via electrodes on the atrium or ventricle, faster than intrinsic rate by stimulating pulses which were about 1.5–2 times threshold.

Monophasic action potentials (MAPs) were recorded using two suction electrodes [12] placed on the ventricular epicardium, with care being

taken not to place them over major blood vessels. A tripodal device operated by vacuum and with strain gauges attached was sucked on to the epicardium. This provided an analogue signal of epicardial segment motion that provides an index of length changes in the cardiac muscle fibers [12].

The heart was paced progressively faster until it could no longer adequately follow the stimuli, and then slowed back until it could. This rate, about 150 ms between beats, was maintained. After a period ranging between 2–5 min electromechanical signals went through episodes of regular alternans (alternate large and small signals), tachycardia (heart rate spontaneously very fast but regular), and disorganised rhythm. This ended in a period of maintained ventricular fibrillation, where the ventricular muscle showed writhing movements, with irregular electrical and mechanical activity at any point on the surface of the heart, and no synchronisation of activity between distant points. During the latter part of the protocol the pH of the coronary effluent dropped from around 7.3 to 6.8.

We have used the method described in section 2 to analyze electrical and mechanical recordings from the ventricular epicardial surface during this period of maintained ventricular fibrillation. The result of analysing the electrical signals are presented in fig. 2.

Figure 2a shows 0.4 seconds of the electrical activity: irregularity is apparent both in the size of the spike-like components of the signals (which correspond to ventricular action poten-

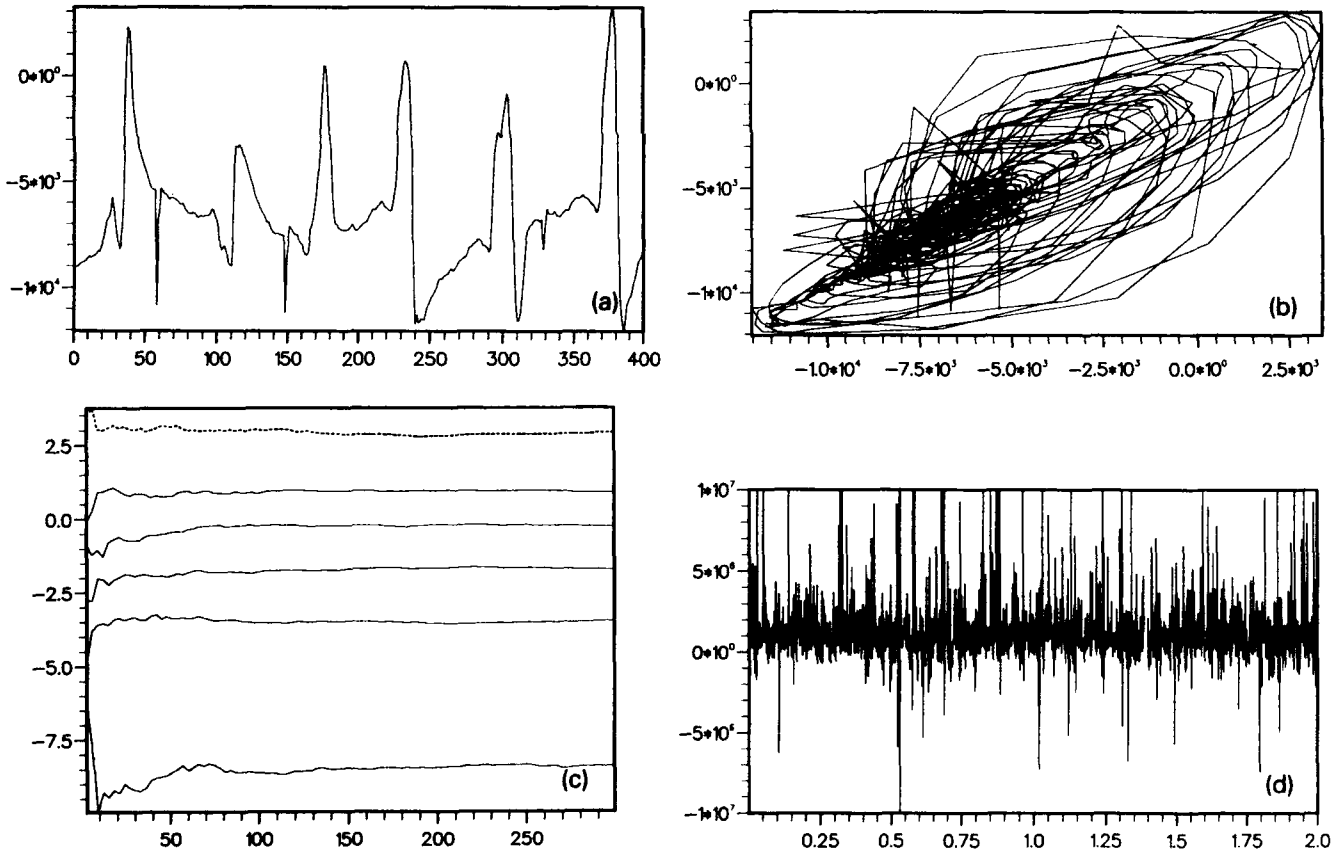

Fig. 2. The characteristics for electrical ECG data recorded from a rabbit heart during ventricular fibrillation with sampling frequency 1000 Hz. (a) The irregular time series for 2 seconds time. (b) The attractor portrait projected to the plane associated with the first two principle eigenvectors after SVD. (c) The Lyapunov exponents spectrum, assumed embedding dimension 6 (d) The series of persistence of strain, assumed embedding dimension 6.

tials) and their timing. The projection of the reconstructed attractor into the plane formed by the first two principal eigenvectors, obtained by singular value decomposition, suggests chaotic behaviour. The correlation dimension saturates at 3.8 at an embedding dimension of 6. Estimation of the six Lyapunov exponents converge to their limits value after the first second of the data: the two largest are clearly positive. Thus on the criteria of a low, noninteger attractor dimension and positive Lyapunov exponent the signal is chaotic, and represents a sample of motion on a strange attractor generated by stretching and folding. The stretching and folding of the trajectory on the attractor is illustrated by the plot of $\sigma^2(t)$ in fig. 2d, where if $\sigma^2 > 0$, stretching of the trajectory in state space predominates over folding, and if $\sigma^2 < 0$, folding predominates over stretching.

The same analysis has been applied to the mechanical signals recorded simultaneously during ventricular fibrillation in fig. 3. Once again, on the criteria of a noninteger attractor dimension ($D_2 = 3.5$) and positive Lyapunov exponent the signal is clearly chaotic. The Lyapunov exponents are given in table 1.

Although there are quantitative differences (due to the different bandwidth and signal to noise ratio of the two signals) the qualitative features are similar: their results can be used to identify (and quantify) chaos in these two functionally related signals, but not to distinguish

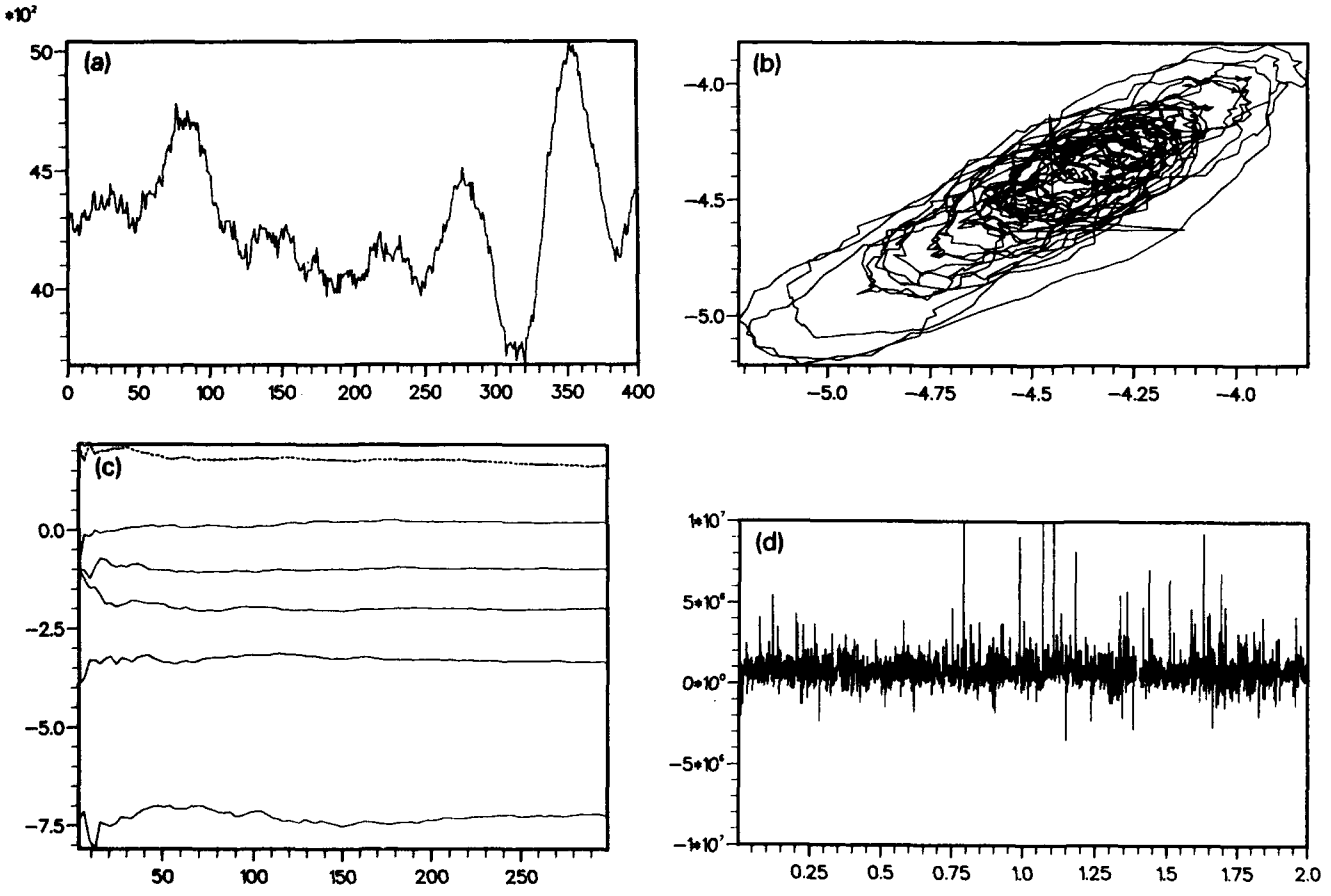

Fig. 3. The characteristics for mechanical ECG data recorded simultaneously from a rabbit heart during ventricular fibrillation with sampling frequency 1000 Hz. (a) The irregular time series for 2 seconds (b) The attractor portrait projected to the plane associated with the first two principle eigenvectors after SVD. (c) The Lyapunov exponents spectrum, assumed embedding dimension 6. (d) The series of persistence of strain, assumed embedding dimension 6.

Table 1
The Lyapunov exponents spectrum for electrical and mechanical signals recorded from a rabbit heart during ventricular fibrillation. The assumed embedding dimension is 6. The sampling frequency is 1000 Hz.

	λ_1	λ_2	λ_3	λ_4	λ_5	λ_6
electrical	3.1	1.0	−0.29	−1.7	−3.5	−8.3
mechanical	1.7	0.46	−0.92	−2.0	−3.2	−6.9

Table 2
The persistence of strain for electrical and mechanical signals recorded from a rabbit heart during ventricular fibrillation. The assumed embedding dimension is 6. The sampling frequency is 1000 Hz.

	$\bar{\sigma}_{Re}$	$\bar{\sigma}_{Im}$	$\bar{\sigma}_{Rm}/\bar{\sigma}_{Im}$
electrical	9.8	1.4	6.5
mechanical	7.9	0.7	10.1

between them or different models for their functional interaction. The plot of $\sigma^2(t)$ for the mechanical signal in fig. 3d is different from that of the electrical signal: $\sigma^2(t) > 0$ for most of the time series. Stretching of the trajectory in state space predominates over folding.

These different roles of stretching and folding of the trajectory in state space can be quantified by the estimation of $\bar{\sigma}_{Re}$ and $\bar{\sigma}_{Im}$ provided in table 2.

The ratio of the stretching to folding is clearly much greater for the mechanical signal.

4. Conclusions

This is an on-going discussion as to whether ventricular fibrillation (in clinical practice, or induced in animal, or isolated heart, experiments) is an example of chaotic or spatio–temporal chaotic behaviour, or is irregular behaviour generated by a complicated, highly structured system; see papers in refs. [13–16].

A positive maximum estimated Lyapunov exponent is a characteristic of a chaotic process, and is found both for time series generated by a dynamical system (modeled by ODEs or a map) and for activity at a point during spatio–temporal chaos.

Both the electrical and mechanical signals may be identified as chaotic, on the basis of their positive maximal estimated Lyapunov exponents. This identification of chaos in both the electrical and mechanical activity is consistent with the view that electrical activity triggers the mechanical activity, and so if the first is chaotic, then so is the second. The normalised ratio γ distinguishes between the two chaotic signals. The different behaviours of γ distinguishes the two signals, and so provides a measure of distinguishing between models of mechanical–electric interaction in cardiac tissue. The types of physiological model for the mechanisms underlying ventricular fibrillation are (a) local chaotic dynamics *or* the result of propagating, re-entrant waves (an example of spatio–temporal chaos) [17] and (b) electrical activity triggers mechanical activity, *or* electrical activity triggers mechanical activity, which in turn alters electrical activity [18].

All combination of these two types of model can generate irregular fluctuations in mechanical and electrical activity; the persistence of strain measure provides additional constraints on the behaviours of the models and so may be of value in distinguishing between the different classes of model.

Acknowledgements

This work was supported by grants from the MRC (SPG 9017859 to AVH) and the British Heart Foundation and Wellcome Trust (to ML).

References

[1] A. Wolf, J.B. Swift, H.L. Swinney and J.A. Vastano, Physica D 16 (1985) 285.
[2] G. Bennetin, L. Galgani, A. Giorgilli and J.-M. Strelcyn, Meccanica 15 (March 1980) 9.
[3] Meyer-Kress, ed., Dimensions and Entropies in Chaotic Systems, (Springer, Berlin, 1986).
[4] E. Dresselhaus and M. Tabor, J. Phys. A 22 (1989) 971.

[5] I. Shimada and T. Nagashima, Prog. Theor. Phys. 61 (1979) 6.
[6] J.-P. Eckmann, S.O. Kamphorst, D. Ruelle and S. Ciliberto, Phys. Rev. A 34 (1986) 4971.
[7] H. Zhang and A.V. Holden, The application of the persistence of strain to quantify the geometrical change of an attractor, Chaos, solitons and fractals, submitted.
[8] N.H. Packard, J.P. Crutchfield, J.D. Farmer and R.S. Shaw. Phys. Rev. Lett. 45 (1980) 712.
[9] F. Takens, in: Proc. Dynamical Systems and Turbulence, Warwick, 1980, Lecture Notes in Mathematics 898 (Springer, Berlin, 1981).
[10] R. Mañé, in: Proc. Dynamical Systems and Turbulence, Warwick, 1980, Lecture Notes in Mathematics 898 (Springer, Berlin, 1981).
[11] D.S. Broomhead and G.P. King, Physica D 20 (1986) 217.
[12] M.J. Lab and K.V. Woollard, Cardiovasc. Res. 12 (1978) 555.
[13] A.V. Holden, M. Markus and H.G. Othmer, eds., Nonlinear Waves in Excitable Media, NATO ASI series (Plenum, New York, 1991).
[14] J. Jalife, ed., Mathematical Approaches to Cardiac Arrhythmias, Ann. N.Y Acad. Sciences Vol. 591 (NY Acad. Sciences, New York, 1990).
[15] H. Degn, A.V. Holden and L.F. Olsen, eds., Chaos in Biological Systems. NATO ASI series (Plenum, New York, 1987).
[16] D.T. Kaplan and R.J. Cohen, Circ. Res. 67 (1990) 886.
[17] A. Panfilov and A.V. Holden, Int. J. Bifurc. Chaos 1 (1991) 219.
[18] M.J. Lab and A.V. Holden, in: Theory of Heart, L. Glass, ed. (Springer, Berlin, 1991).

List of participants

A.M. Albano
Bryn Mawr College

A. Arnéodo
C.N.R.S., Pessac

A. Babloyantz
Free University of Brussels

R. Badii
Paul-Scherrer Institute, Villigen

C.D. Bertram
University of New South Wales

M.A. Boudourides
University of Thrace

D.S. Broomhead
R.S.R.E., Malvern

W. Brüstle
University of Stuttgart

C. Budd
University of Bristol

J.-G. Cuputo
C.N.R.S., Rouen

M.-P. Chauve
I.M.S.T., Marseille

S. Ciliberto
Ecole Normale Supérieure, Lyon

P.G. Drazin
University of Bristol

U. Dressler
Daimler-Benz AG, Frankfurt

I. Dvořák
Psychiatric Research Institute, Prague

M. Dykman
Daly City, California

G. Eilenberger
K.F.A., Jülich

A. Fowler
University of Oxford

M. Ghil
University of California, Los Angeles

R. Gilmore
Drexel University

M. Gorman
University of Houston

S. Goshen
N.R.C.N., Beer-sheva

P. Grassberger
University of Wuppertal

C. Grebogi
University of Maryland

A. Grossmann
Centre de Physique Théorique, Marseille

A. Holden
University of Leeds

A. Hübler
University of Illinois

J. Huke
R.S.R.E., Malvern

T. Kapitaniak
Technical University of Lodz

M. Kimoto
Japan Meteorology Agency

G.P. King
University of Warwick

E. Kostelich
Arizona State University

E. Kreuzer
Technical University of Hamburg–Harburg

P.S. Landa
Moscow State University

V.Ya. Levchenko
U.S.S.R. Academy of Sciences, Novosibirsk

D. Lowe
R.S.R.E., Malvern

J.L. Lumley
Cornell University

B. Maheu
I.N.S.A., Rouen

P. McClintock
University of Lancaster

A. Mees
University of Western Australia

C. Myers
Lockheed Sanders Inc., U.S.A.

R. Narasimha
National Aeroautical Laboratory, India

B. Nicolaenko
Los Alamos National Laboratory

A.R. Osborne
C.N.R., Torino

G. Pfister
University of Kiel

E.R. Pike
King's College, London

A. Politi
Istituto Nazionale di Ottica, Italy

A. Provenzale
C.N.R., Torino

A. Rabinovitch
Ben Gurion University of the Negev

P.L. Read
University of Oxford

G. Rowlands
University of Warwick

V.A. Sabelnikov
Central Aero-hydrodynamic Institute, Zhukovsky

H. Sato
Institute of Flow Research, Tokyo

T. Sauer
George Mason University

C.T. Shaw
University of Warwick

L. Smith
University of Warwick

C. Sparrow
University of Cambridge

C. Sprott
University of Wisconsin

I.N. Stewart
University of Warwick

R. Stoop
University of Zürich

A. Tamaševičius
Academy of Sciences of Lithuania

W.W. Taylor
RTA Corporation, U.S.A.

J. Theiler
Los Alamos National Laboratory

R. Thieberger
Ben Gurion University of the Negev

J.M.T. Thompson
University College, London

H. Tong
University of Kent

W. van de Water
Eindhoven Institute of Technology

List of observers

K. Aihara
Tokyo Denki University

O. Coté
U.S. Air Force, London

F.E. Culick
California Institute of Technology

R.D. Ryan
O.N.R., London

C. Tebaldi
University of Bologna

List of young scientists

O.A. Akala
Imperial College, London

S.T. Bauer
University of Miami

J.L. Breeden
University of Illinois

G. Broggi
University of Zürich

T. Buzug
University of Kiel

E. Ching
University of Chicago

A.G. Darbyshire
University of Oxford

M. Davies
University College, London

C. de Groot
Interdisciplinary Center for Supercomputing, Zürich

E. Del Rio
Complutense University of Madrid

F. Dux
University of Bristol

W.-G. Fruh
University of Oxford

P. Ghilardi
University of Pavia

G. Giacomelli
Istituto Nazionale di Ottica, Italy

J. Glover
University of Cambridge

J. Healey
University of Cambridge

A.J. Homburg
University of Groningen

S. Hotson
University of Warwick

J. Hyde
University of Leeds

K. Judd
Tokyo Denki University

G. Kember
University of Oxford

A. Kosinov
U.S.S.R. Academy of Sciences, Novosibirsk

H. Lamba
University of Bristol

J. Maquet
I.N.S.A., Rouen

S. Meunier-Guttin-Cluzel
I.N.S.A., Rouen

M.R. Muldoon
University of Warwick

T. Otaguro
Institute of Computational Fluid Dynamics, Tokyo

G. Papaïoannou
University of Patras

U. Parlitz
University of Darmstadt

P. Pokorny
Free University of Brussels

M. Potts
R.S.R.E., Malvern

P.L. Ramazza
Istituto Nazionale di Ottica, Italy

T. Reimers
University of Kiel

S. Residori
Istituto Nazionale di Ottica, Italy

T. Schreiber
University of Copenhagen

F.N. Shaikh
University of Cambridge

D.K. Siegwart
University of Oxford

N.D. Stein
University of Lancaster

N.G. Stocks
University of Lancaster

U. Smart
Queen's University, Belfast

J.C. Vassilicos
University of Cambridge

R. Wang
Free University of Berlin

H. Wilson
K.F.A., Jülich

H. Zhang
University of Leeds

A.L. Zheleznyak
U.S.S.R. Academy of Sciences, Nizhny Novgorod

List of lectures

The name of each speaker is in italics, below the title of his or her lecture.

Wavelets and fractals in physics
A. Arnéodo

Complexity and hierarchical modelling of chaotic signals
R. Badii and M. Finardi

Control of the wall region of a turbulent boundary layer: new results
G. Berkooz, P. Holmes and *J.L. Lumley*

The collapsible-tube oscillator as a test-bed for empirical dynamical system analyses
C.D. Bertram

A learning algorithm for optimal representations of experimental data
J.L. Breeden and N.H. Packard

Topology from a time series
D.S. Broomhead, J.P. Huke, R.S. MacKay and *M.R. Muldoon*

Linear filters and nonlinear systems
D.S. Broomhead, J.P. Huke and M.R. Muldoon

Applications of the bi-orthogonal decomposition in fluid mechanical experiments
M.P. Chauve and P. Le Gal

On non-parametric order determination and chaos
B. Cheng and *H. Tong*

Characterizing space-time chaos
S. Ciliberto and B. Nicolaenko

Phase space reconstruction in physical experiments
A.G. Darbyshire and T. Mullin

Modelling and forecasting of univariate time series by parsimonious feedforward connectionist nets
C. de Groot and D. Wuertz

Power spectra of underdamped noise-driven nonlinear systems and stochastic resonance
M.I. Dykman and P.V.E. McClintock

Testing for nonlinearity in time series: the method of surrogate data
S. Eubank, J.D. Farmer, B. Galdrikian, A. Longtin and *J. Theiler*

Climatic trends and variability: diagnosis and prediction
M. Ghil

Topological analysis and synthesis of chaotic time series
R. Gilmore

Using power spectra to identify chaos in flames
M. Gorman and M. el-Hamdi

Construction of phenomenological models for numerical scalar time series
G. Gouesbet and *J. Maquet*

Control of chaos
C. Grebogi

Compound wavelets
A. Grossmann

Optimal modelling for a control of high dimensional evolving systems
A. Hübler

Flow randomization in boundary-layer transition
Y.S. Kachanov and *V.Y. Levchenko*

The 40-day oscillation in the extratropical atmosphere as identified by multi-channel singular spectrum analysis
M. Kimoto, M. Ghil and K.-C. Mo

Periodic saddle orbits, noise reduction, and nonlinear prediction
E. Kostelich

Combined approaches of a chaotic attractor in dynamics of a laser heated interface
S. Meunier-Guttin-Cluzel, *B. Maheu* and G. Gouesbet

A simple dynamical system that mimics open-flow turbulence
R. Narasimha

Detecting symmetry breaking intermittent chaos in turbulence
B. Nicolaenko, E. Kostelich and Z.-S. She

Characterization of experimental time series from Taylor–Couette flow
G. Pfister, Th. Buzug and N. Enge

Singular systems theory
E.R. Pike

Transitions in convective turbulence: the role of thermal plumes
I. Procaccia, *E.S.C. Ching*, P. Constantin, L.P. Kadanoff, A. Libchaber and X.-Z. Wu

Deterministic chaos versus random noise from the analysis of measured data
A. Provenzale and A.R. Osborne

Analysis of noisy signals
A. Rabinovitch and R. Thieberger

Chaotic regimes in rotating, stably-stratified flow
P.L. Read

Extraction of dynamical equations from chaotic data
G. Rowlands and J.C. Sprott

Objective search of patterns in turbulence signals
H. Sato and T. Otaguro

Embedology
T. Sauer, J.A. Yorke and M. Casdagli

A simple noise-reduction scheme and some results on shadowing
T. Schreiber and *P. Grassberger*

Identification and prediction of deterministic dynamical systems
L.A. Smith

Symmetric attractors and chaotic time series
I. Stewart

Scaling functions of Lyapunov exponents from time series – a new interpretation
R. Stoop and J. Parisi

Issues pertaining to applying nonlinear prediction to a signal separation problem
W.W. Taylor

Capture, dispersal and unpredictability in chaotic dynamics
J.M.T. Thompson

A dedicated computer for measuring fractal dimension
W. van de Water

Are turbulent interfaces fractal or spiral?
J.C. Vassilicos and J.C.R. Hunt

List of posters

The names of the authors follow the title of their poster.

Dimension of spatial field distributions of nonequilibrium media
V.S. Afraimovich, A.B. Ezersky, M.I. Rabinovich, M.A. Shereshevsky and A.L. Zheleznyak

Using neural nets to look for chaos
A.M. Albano, A. Passamante, T. Hediger and M.E. Farrell

Indicators on space complexity in extended chaotic systems
F.T. Arecchi, G. Giacomelli, P.L. Ramazza and S. Residori

Evidence for slow brain waves: a dynamical approach
A. Babloyantz

Empirical low-order El Niño dynamics
S.T. Bauer and M.G. Brown

Interpretation of aperiodic time series: distinction between strange chaotic and strange nonchaotic attractors
J. Brindley, T. Kapitaniak and J. Wojewoda

Characterisation of spatiotemporal chaos in lasers
G. Broggi

Deterministic properties and fractal dimension of the volcano source system from volcanic tremor records
W. Brüstle and R. Schick

Time series analysis of a discontinuous dynamical system
C. Budd and H. Lamba

Optimal embedding parameters by the analysis of the global statistical and local dynamical behaviour of strange attractors
Th. Buzug and G. Pfister

Local dimensions and divergence rates for dynamical systems
J.-G. Caputo, B. Maheu and S. Meunier-Guttin-Cluzel

Probability density functions of temperature differences in Rayleigh–Bénard convection
E.S.C. Ching

Oscillations and onset of chaos and related bifurcation results for a nonlinear oscillator with possible escape to infinity
E. Del Rio, A. Rodriguez-Lozano and M.G. Velarde

COREX: user friendly program for estimating correlation exponent of EEG
I. Dvořák, J. Wackermann and M. Paluš

Observations of stochastic resonance in a bistable system with periodically modulated noise intensity
M.I. Dykman, D.G. Luchinsky, P.V.E. McClintock, N.D. Stein and N.G. Stocks

Bifurcation diagrams of Duffing-type oscillators derive from circle maps
G. Eilenberger and K. Schmidt

Global and local analysis of brain attractors
D. Gallez and A. Babloyantz

Deterministic chaos versus random noise in rainfall time series
P. Ghilardi

Determining fixed points from data.
J. Glover

Calculating fractal dimensions
S. Goshen and R. Thieberger

Reconstruction and quantification of attractors from single and multi-channel neural signals
A.V. Holden, H. Zhang, H. Pockberger, I. Dvořák, M. Paluš, J. Wackermann and F.L. Li

An improved estimator of dimension
K. Judd

Random sampling and the Grassberger–Procaccia algorithm
G. Kember and A.C. Fowler

Using multivariate data analysis to compare time series
G.P. King and C.T. Shaw

On the determination of dimension from sampled data
E. Kreuzer

Quantitative characteristics of chaotic motion and problems of diagnostics and identification
P.S. Landa and M.G. Rosenblum

Nonlinear time series forecasting, adaptive networks and numerical optimisation strategies
D. Lowe and A. Webb

Modeling chaotic systems with hidden Markov models
C. Myers, B. Shin and A. Singer

A technique for measuring fractal dimensions from time series in a real time scale
A. Namajūnas and A. Tamaševičius

Controlling chaos using time delay components
G. Nitsche and U. Dressler

Dynamical signatures
L. Noakes and A. Mees

Fractality and chaotic dynamics in turbulent flows
A.R. Osborne

Cognition of patterns in a fully developed turbulence
T. Otaguro, H. Sato and S. Takagi

Evidence of low dimensional chaotic attractor in weather temperature time-series data in Greece
G. Papaioannou, T. Bountis and L. Karakatsanis

Estimation of Lyapunov exponents from chaotic time series based on approximations of the flow map by radial basis functions
U. Parlitz

Evaluation of time series from forced excitable systems
P. Pokorny and M. Marek

Fractal-dimension analysis of coupled maps
A. Politi and G.P. Puccioni

Experimental studies of time series obtained from transition to turbulence in pipe flow
T. Reimers and V. Wilkening

Wavelet analysis of fully developed turbulence data at high Reynolds number
V.A. Sabelnikov, A.A. Praskovsky and D.A. Usikov

Computer package for chaotic time series analysis
J.C. Sprott

Effect of quasi-monochromatic noise on nonlinear systems
N.D. Stein, M.I. Dykman, P.V.E. McClintock and N.G. Stocks

Noise induced escape across fractal basin bondaries
N.G. Stocks, P.V.E. McClintock, N.D. Stein and R. Mannella

Convergence of thermodynamic averages
R. Stoop and J. Parisi

The shape of turbulent friction
W. van de Water and E. van de Wetering

Estimation of the persistence of strain from experimental recordings from cardiac tissue
H. Zhang, A.V. Holden, M. Lab and M. Moutoussis

List of contributors

Afraimovich, V.S. 331
Albano, A.M. 1
Armbruster, D. 392

Badii, R. 304
Berkooz, G. 402
Bertram, C.D. 469
Brambilla, M. 339
Breedon, J.L. 273
Broggi, G. 304, 339
Buzug, Th. 127, 441

Caponeri, M. 365
Chauve, M.P. 407
Ching, E.S.C. 414
Ciliberto, S. 365

Dayawansa, W.P. 165
Doyne Farmer, J. 77
Dressler, U. 153
Dykman, M.I. 10

Enge, N. 441
Eubank, S. 77
Ezersky, A.B. 331

Farrell, M.E. 1
Finardi, M. 304

Galdrikian, B. 77
Ghil, M. 95
Gilmore, R. 229
Gouesbet, G. 202, 423
Grebogi, C. 165

Hediger, T. 1
Heiland, R. 392
Holden, A.V. 489
Holmes, P. 402

Kadanoff, L.P. 414
King, G.P. 216, 288
Kostelich, E.J. 138, 392

Lab, M. 489
Le Gal, P. 407
Libchaber, A. 414
Longtin, A. 77
Lumley, J.L. 402

Maheu, B. 423
Maquet, J. 202
McClintock, P.V.E. 10
Mees, A. 243
Meunier-Guttin-Cluzel, S. 423
Mindlin, G.B. 229
Moutoussis, M. 489
Murante, G. 31

Namajūnas, A. 482
Nicolaenko, B. 392
Nitsche, G. 153
Noakes, L. 243

Ott, E. 165

Packard, N.H. 273
Parisi, J. 325
Passamante, A. 1
Pfister, G. 127, 441
Politi, A. 384
Prati, F. 339
Provenzale, A. 31
Puccioni, G.P. 384

Rabinovich, M.I. 331
Rabinovitch, A. 284
Read, P.L. 455
Romeiras, F.J. 165
Rowlands, G. 251

Sauer, T. 193
Sepúlveda, M.A. 304
Shaw, C.T. 288
Shereshevsky, M.A. 331
Smith, L.A. 31, 50
Sprott, J.C. 251
Stewart, I. 216
Stoop, R. 325

Tamaševičius, A. 482
Theiler, J. 77
Thieberger, R. 284
Thompson, J.M.T. 260
Tian, X. 469
Tong, H. 299

Vautard, R. 95
Vio, R. 31

Wu, X.-Z. 414

Yiou, P. 95

Zhang, H. 489
Zheleznyak, A.L. 331

PHYSICS LETTERS A

Nonlinear Science

CONTENTS

Volume 167, number 1 6 July 1992

Quantum corrections to semi-classical laser theory
A.A. Bakasov and G. Denardo 37
Dynamical properties of DNA promoters
M. Salerno 49
Soliton experiments in a damped ac-driven nonlinear electrical transmission line
T. Kuusela 54
On the nature of nonchaotic turbulence
S.V. Ershov and A.B. Potapov 60
Friction coefficient of a Brownian particle: dependence on size and mass
L.F. Rull, J.J. Morales and M.J. Nuevo 65

Volume 167, number 2 13 July 1992

Hamiltonian dynamics of orbits homoclinic to a resonance band
G. Kovačič 137
Dissipative dynamics of orbits homoclinic to a resonance band
G. Kovačič 143
On the information entropy of squeezed states and the entropic uncertainty relation
C.H. Keitel and K. Wódkiewicz 151
A new kind of *R*-matrix associated with the Hopf algebra $U_q(A_2(\mu))$
M.-L. Ge and X.-F. Liu 161
A discrete Neumann system
O. Ragnisco 165
On the analytical description of multisolitons within the KP1 equation
V.M. Galkin and Yu.A. Stepanyants 172
Coherence of Josephson soliton oscillators in the millimeter-wave range
M. Cirillo, I. Modena, F. Santucci, P. Carelli and R. Leoni 175
Chaos and noisy periodicity in forced ocean–atmosphere models
J. Brindley, T. Kapitaniak and A. Barcilon 179
Regular and chaotic behavior in the new Lorenz system
C. Masoller, A.C. Sicardi Schifino and L. Romanelli 185

Volume 167, number 3 20 July 1992

Allowed transformations and symmetry classes of variable coefficient Korteweg–de Vries equations
P. Winternitz and J.P. Gazeau 246
On the explicit symmetry breaking in the Taylor–Couette problem
D. Armbruster and A. Mahalov 251
Any nonlinear gate, with linear gates, suffices for computation
S. Lloyd 255
Non-linear excitations on a disordered spin chain
C.E. Cordeiro 261
Conformal dynamics for vortex motions
B. Legras and V. Zeitlin 265

Volume 167, number 4 27 July 1992

Quantum Volterra model
A.Yu. Volkov 345
Global asymptotics of the second Painlevé transcedent
A. Kapaev 356
Many-body Green functions of q-deformed oscillators
J.L. Birman 363
Solitonic defects in hydrogen-bonded systems at finite acidity
L.N. Christophorov and Yu.B. Gaididei 367
Soliton interaction with change of form in the classical Boussinesq system
L. Martínez Alonso and E. Medina Reus 370

Volume 167, number 5,6 3 August 1992

Unitary polynomials in normal matrix models and wave functions for the fractional quantum Hall effects
L.-L. Chau and Y. Yu 452
***R*-matrices for the semicyclic representations of $U_q\widehat{sl}(2)$**
I.T. Ivanov and D.B. Uglov 459
On the instability of three-dimensional flows of an ideal incompressible fluid
A. Lifschitz 465
Randomly interrupted diffusion
J. Łuczka, M. Niemiec and E. Piotrowski 475
Semiline solution of a nonlinear diffusion–convection equation
S. de Lillo 479

Volume 168, number 1 10 August 1992

Diffusion in uniformly hyperbolic one-dimensional maps and Appell polynomials
P. Gaspard 13
Transport as a dynamical property of a simple map
H.H. Hasegawa and D.J. Driebe 18
Solvable quantum many-body problems in two dimensions
M.-L. Yan and B.-H. Zhao 25
Wavelet electrodynamics
G. Kaiser 28
A nonequilibrium phase transition with colored noise
J. García-Ojalvo, J.M. Sancho and L. Ramírez-Piscina 35
Robust new routes to chaos in differential equations
P. Glendinning 40
Multi-fractal aspects of the intermittency corrections to the spectrum of temperature fluctuations in isotropic turbulence
B.K. Shivamoggi 47
Irreversible phase transitions in the dimer–monomer surface reaction process on fractal media
E.V. Albano 55

Volume 168, number 2 17 August 1992

A dynamical system model for interference effects and the two-slit experiment of quantum physics
A. Boyarsky and P. Góra 103
A class of solutions of the Konopelchenko–Rogers equations
J.J.C. Nimmo 113
Asymptotic permanent profile of the ion acoustic wave driven by the Langmuir wave
D.J. Kaup, A. Latifi and J. Leon 120
Nonlocal angular instability of a Kolmogorov-like wave turbulence spectrum
G.E. Falkovich and M.D. Spector 127
Collapse of wave fronts in reaction–diffusion systems
V. Pérez-Muñuzuri, M. Gómez-Gesteira, V. Pérez-Villar and P. Hanusse 133

Volume 168, number 3 24 August 1992

Reentrant hexagonal Turing structures
J. Verdasca, A. de Wit, G. Dewel and P. Borckmans 194

Volume 168, number 4 31 August 1992

Stationary dissipation due to quantum chaos: simulated light absorption with quantum maps
K. Ikeda 248
Correlation functions of the *XXZ* model for $\Delta < -1$
M. Jimbo, K. Miki, T. Miwa and A. Nakayashiki 256
Completely integrable model of interacting *q*-bosons
N.M. Bogoliubov and R.K. Bullough 264
A coupled Lorenz-cell model of Rayleigh–Bénard turbulence
E.A. Jackson and A. Kodogeorgiou 270
Discrete model of spatially mixing system
A.S. Pikovsky 276

PHYSICS LETTERS A

FORTHCOMING PAPERS IN Nonlinear Science:

J. Avan, w_∞-currents in three-dimensional Toda theory

E.A. Bartnik, K.J. Blinowska and J.A. Tuszyński, Stability of quantum capture in Langmuir–Blodgett monolayers against positional disorder

M.S. Benilov, Appearance of structures with slow variations in large-size reaction–diffusion and current systems

A. Brizard, Hermitian structure for linearized ideal MHD equations with equilibrium flows

M. Bruschi, P.M. Santini and O. Ragnisco, Integrable cellular automata

Y. Chen, Exact solutions of grey solitons in uniform self-defocussing media

A.A. Chernikov and G. Schmidt, Chaotic streamlines in convective cells

O.A. Chubykalo, V.V. Konotop, L. Vázquez and V.E. Vekslerchik, Some features of the repulsive discrete nonlinear Schrödinger equation

F. Colomo, A.G. Izergin, V.E. Korepin and V. Tognetti, Correlators in the Heisenberg $XX0$ chain as Fredholm determinants

X. Dai, P.H. Hor, L. Gao and C.W. Chu, Inversion solution of equation of motion and the flux relaxation law in high T_c superconductor YBCO

M.E. Davies, An iterated function approximation in shadowing time series

W. Deng and Y. Liu, Generalized Möbius inverse formulas

P.J. Forrester, Some statistical properties of the eigenvalues of complex random matrices

G. Gaeta, Solitons in planar and helicoidal Yakushevich model of DNA dynamics

J. González and D. Jou, Extended thermodynamics and the nonequilibrium Einstein relation

N. Grønbech-Jensen, Phase-locking of soliton motion in uniformly driven sine-Gordon systems

K. He and G. Hu, Reversal of phase velocity of negative-energy mode and bistability in driven–damped drift wave system

S. Homma and S. Takeno, Soliton scattering by an impurity on a nonlinear lattice

H. Isliker, A scaling test for correlation dimensions

J. Jiménez, J. Moreno, G.J. Ruggeri and A. Marcano, Detecting chaos with local associative memories

J.A.S. Kelso, S.L. Bressler, S. Buchanan, G.C. DeGuzman, M. Ding, A. Fuchs and T. Holroyd, A phase transition in human brain and behavior

Yu.S. Kivshar, O.H. Olsen and M.R. Samuelsen, Hysteresis loop induced by rf radiation in Josephson junctions: an analytical approach

E.R. Korutcheva, Domains of attraction in neural network models with correlated patterns

R.A. Kosiński, Spatio-temporal diagrams for domain wall dynamics

R.A. Kraenkel, S.M. Kurcbart, J.G. Pereira and M.A. Manna, Effects of a temperature dependent viscosity in surface nonlinear waves propagating in a shallow fluid heated from below

N.A. Kudryashov, Partial differential equations with solutions having movable first-order singularities

continued on next page

Editors:

V.M. Agranovich
*A.R. Bishop**
J.I. Budnick
J. Flouquet
*A.P. Fordy**
B. Fricke
*D.D. Holm**
A. Lagendijk
A.A. Maradudin
M. Portolab
J.P. Vigier

* Nonlinear Science

PHYSICS LETTERS A

FORTHCOMING PAPERS IN Nonlinear Science:

Y.-T. Lau, Large-period turbulent solutions of the Kuramoto–Sivashinsky equation

P.G.L. Leach, Comment on an aspect of a Letter of Shivamoggi and Muilenburg

M. Li, S.J. Liu, N.X. Chen, Y.G. Teng, W.X. Zhang and S.Z. Zhang, Modified Möbius inversion transform and interatomic pair potentials in bcc-metal Mo and Cr

F. Leyvraz and T.H. Seligman, Structural invariance and the statistics of quasi-energies

A. Mees, K. Aihara, M. Adachi, K. Judd, T. Ikeguchi and G. Matsumoto, Deterministic prediction and chaos in squid axon response

K. Okamoto and K. Nomura, Fluid-dimer critical point in $S=\frac{1}{2}$ antiferromagnetic Heisenberg chain with next nearest neighbor interactions

A. Ramani, B. Grammaticos and J. Satsuma, Integrability of multidimensional discrete systems

T. Shinbrot, C. Grebogi, E. Ott and J.A. Yorke, Using chaos to target stationary states of flows

P.B. Slater, Maximum-entropy estimation of a two-particle density matrix from a mixture of a particle into two nonorthogonal states

R. Van de Weygaert, B.J.T. Jones and V.J. Martínez, The minimal spanning tree as an estimator for generalized dimensions

K. Wada and T. Uchida, On the anti-causal path probability method by Kikuchi

R.-H. Zhou and P.-L. Cao, Molecular cluster analysis of O_2 adsorption and dissociation on Pt(111)

Z. Zhou, Explicit solutions of N-wave equation in $1+2$ dimensions

For more information and/or a free inspection copy please contact the publisher.

Editors:

V.M. Agranovich
*A.R. Bishop**
J.I. Budnick
J. Flouquet
*A.P. Fordy**
B. Fricke
*D.D. Holm**
A. Lagendijk
A.A. Maradudin
M. Porkolab
J.P. Vigier

* Nonlinear Science

NORTH-HOLLAND
P.O. BOX 103, 1000 AC, AMSTERDAM, THE NETHERLANDS
In the U.S.A. and Canada: Elsevier Science Publishing Co. Inc. 655 Ave. of the Americas, New York, NY 110

Note to authors

Physica is published in four sections:

Physica A (*Statistical and theoretical physics*) contains papers in all fields of statistical physics as well as on general theoretical physics subjects. The emphasis of the journal is on fostering the interaction between experimental, theoretical and computational research in statistical physics. The field of statistical physics is meant to comprise any phenomena where the relationship between microscopic properties and macroscopic behaviour plays a role.

Physica B (*Condensed matter*) contains papers and review articles in the realm of physics of condensed matter. Both experimental and theoretical contributions are invited, although theoretical papers should preferably be related to experimental results.

Physica C (*Superconductivity*) serves as a rapid channel for publications on superconductivity and related subjects. This includes theoretical papers on the fundamental issues raised by high-T_c superconductivity, reports on measurements of a wide variety of physical properties of high-T_c superconductors, on new materials and new preparation techniques, on thin-film and device-oriented work and on theoretical results pertinent to such experiments. New results in the traditional areas of superconductivity as well as on novel phenomena (e.g., heavy-fermion superconductivity) will also be included.

Physica D (*Nonlinear phenomena*) contains papers and review articles reporting experiments, techniques and ideas which, although they may be derived and explained in the context of a particular field, advance the understanding of nonlinear phenomena in general. Contributions of this type in the recent literature have dealt with: wave motion in physical, chemical and biological systems; chaotic motion in models relevant to turbulence; quantum and statistical mechanics governed by nonlinear field equations; instability, bifurcation, pattern formation and cooperative phenomena.

Instructions to authors for Physica D

Submission. Manuscripts should be sent in *triplicate* to one of the editors (addresses given on the inside front cover page).

Submission of a paper will be taken to imply that it represents original work not previously published, that it is not being considered elsewhere for publication, and that if accepted for publication it will not be published elsewhere in the same form, in any language without the consent of the publisher.

The master copy and original drawings will be returned to the authors in case their paper is not accepted for publication.

Proposals for review articles (approximately 500–1000 words) should be sent to any one of the editors. The editors will evaluate each proposal on the basis of 1) subject matter and 2) presentation and readability.

Manuscripts should be written in English and typed with double spacing, wide margins and on one side of the page only.

The *title* should be concise and specific. When the length of the title exceeds 45 letters, a *running* title should be indicated. The name of the institute where the research was carried out should be stated with each author's name.

An *abstract* of not more than 150 words should be provided in English, summarizing the new information and the author's conclusions.

Keywords (five or less) should be provided for the subject index, and, if possible, the appropriate PACS classification codes.

References in the text should be numbered (e.g., "Jones and Smith [1] have reported that . . .") in ascending order, and listed on a separate sheet stating the author, journal, volume and the year of publication (in brackets) and the number of the first page. Example: [1] S. Jones and P. Smith, Phys. Rev. 190 (1964) 2016.

Formulae should be clearly written. Vectors will be printed in bold-face italics (heavy, slanting type), and should be indicated by a wavy underlining in the type-script.

Special attention should be paid to characters that can be easily misread, such as i (lower case), I (cap.), l (el), 1 (one), ′ (prime); o (lower case), O (cap.), 0 (zero), ° (degree); u, v (vee), ν (Greek nu), V (cap.); ×, x, X; z, Z; p, P, ρ (Greek rho); etc.

Drawings and any *lettering* should be done in India ink, or by means of a high-quality printing device. Lines should be bold, the frame lines of graphs slightly finer than those of the plotted curves. The figures should be numbered and the captions listed on a separate sheet.

For *colour illustrations*, see Physica D, Volume 53, No. 1 (1991) p. v, or contact the editors.

Alterations in the text cannot be permitted once the paper has been typeset. Authors may be charged for extra corrections resulting from their inattention.

Refereeing. All papers are subjected to refereeing, and in case a paper cannot be accepted in the form it was submitted, the submitting author will be informed about the referee's comments.

Acceptance. Acceptance forms will be sent by the editor. There is *no* page charge. Upon acceptance of an article by the journal, the author(s) will be asked to transfer copyright of the article to the publisher. This transfer will ensure the widest possible dissemination of information.

Reprints. 50 reprints of each article will be supplied to the first author free of charge (in case of an article with colour illustrations this amounts to 200 reprints free of charge). An order form for reprints will be provided with the author's proof. It should be returned to the publishers together with the corrected author's proof.

North-Holland Delta Series

The Delta Series includes a selection of carefully edited volumes providing timely reviews and state-of-the-art reports in all fields of physics. Both established and emerging fields are covered, thus presenting a broad range of topics at the forefront of today's physics.

Geometrical and Algebraic Aspects of Nonlinear Field Theory

S. De Filippo, M. Marinaro, G.Marmo and G. Vilasi *(editors)*
1989 x + 248 pages
US $81.00/Dfl.158.00
ISBN 0-444-87359-7

High Gain, High Power Free Electron Laser: Physics and Application to TeV Particle Acceleration

R. Bonifacio, L. De Salvo Souza and C. Pellegrini *(editors)*
1989 xvi + 310 pages
US $99.50/Dfl.194.00
ISBN 0-444-87395-3

Turbulence and Nonlinear Dynamics in MHD Flows

M. Meneguzzi, A. Pouquet and P.L. Sulem *(editors)*
1989 x + 280 pages
US $99.50/Dfl.194.00
ISBN 0-444-87396-1

Nonlinear Phenomena in Complex Systems

A.N. Proto *(editor)*
1989 viii + 256 pages
US $110.50/Dfl.215.00
ISBN 0-444-88035-6

Scattering in Volumes and Surfaces

M. Nieto-Vesperinas and J. Dainty *(editors)*
1990 viii + 324 pages
US $94.50/Dfl.184.00
ISBN 0-444-88529-3

Between Science and Technology

A. Sarlemijn and P.A. Kroes *(editors)*
1990 viii + 214 pages
US $48.50/Dfl.95.00
ISBN 0-444-88659-1

Strongly Coupled Plasma Physics

S. Ichimaru *(editor)*
1990 xxiv + 708 pages
US $128.00/Dfl.250.00
ISBN 0-444-88363-0

Mechanics, Analysis and Geometry: 200 Years after Lagrange

M. Francaviglia *(editor)*
1991 xii + 560 pages
US $123.00/Dfl.240.00
ISBN 0-444-88958-2

Thermal Field Theories

H. Ezawa, T. Arimitsu and Y. Hasimoto *(editors)*
1991 xvi + 606 pages
US $115.50/Dfl.225.00
ISBN 0-444-88903-5

Nonlinear Phenomena in Fluids, Solids and Other Complex Systems

P. Cordero and B. Nachtergaele *(editors)*
1991 xii + 482 pages
US $115.50/Dfl.225.00
ISBN 0-444-88791-1

Neutron, X-Ray and Light Scattering

P. Lindner and T. Zemb *(editors)*
1991 x + 376 pages
US $89.50/Dfl.175.00
ISBN 0-444-88946-9

Photochemical Processes in Organized Molecular Systems

K. Honda *(editor)*
1991 xiv + 538 pages
US $102.50/Dfl.200.00
ISBN 0-444-88878-0

Dynamics and Mechanisms of Photoinduced Electron Transfer and Related Phenomena

N. Mataga, T. Okada and H. Masuhara *(editors)*

1992 xviii + 566 pages
US $148.50/Dfl.260.00
ISBN 0-444-89191-9

TO ORDER

Contact your regular supplier or:

ELSEVIER SCIENCE PUBLISHERS

P.O. Box 211
1000 AE Amsterdam
The Netherlands

Customers in the USA and Canada:

ELSEVIER SCIENCE PUBLISHING CO. INC.

P.O. Box 882
Madison Square Station
New York, NY 10159, USA

No postage will be added to prepaid book orders. US $ book prices are valid only in the USA and Canada. In all other countries the Dutch guilder (Dfl.) price is definitive. Customers in The Netherlands please add 6% BTW. In New York State please add applicable sales tax. All prices are subject to change without prior notice.

NORTH-HOLLAND

(AN IMPRINT OF ELSEVIER SCIENCE PUBLISHERS)